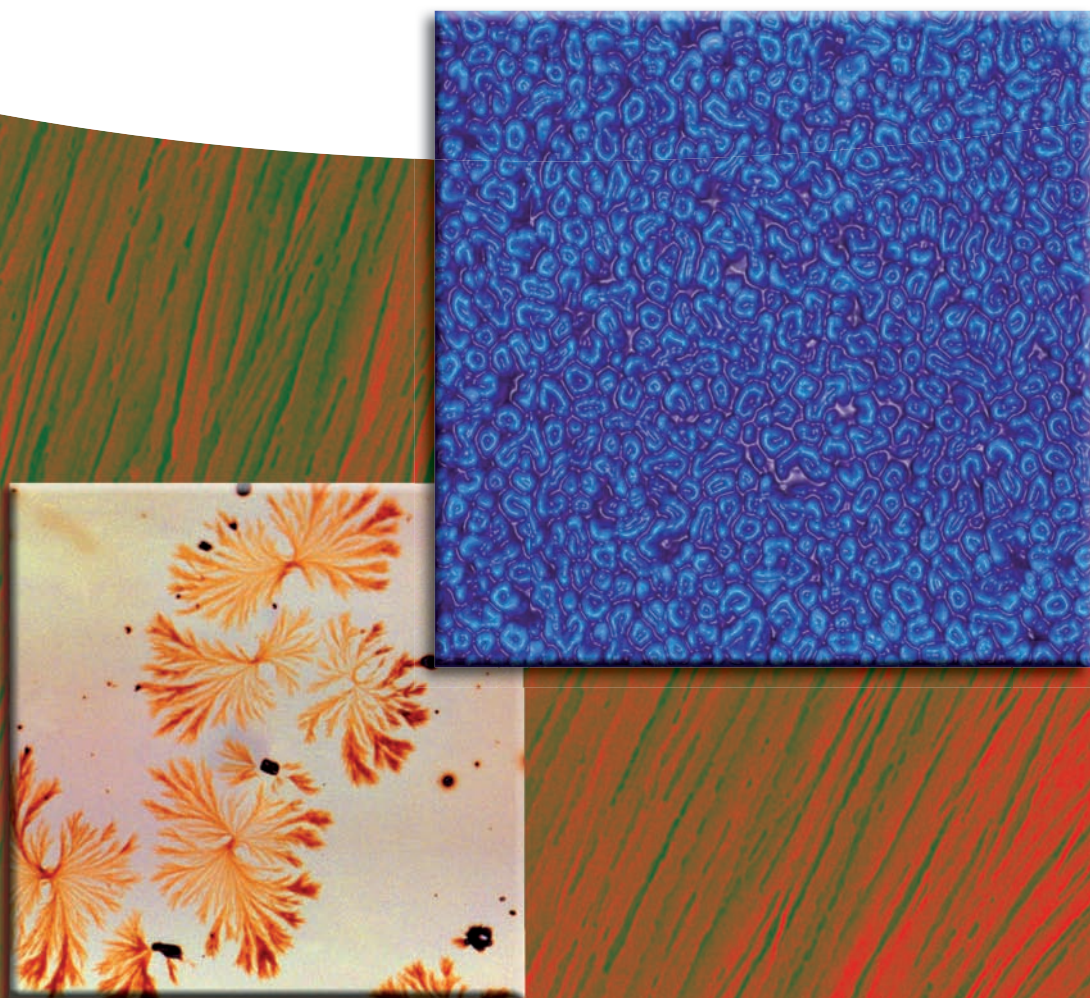


Edited by S. Thomas, Y. Grohens,  
and P. Jyotishkumar

# Characterization of Polymer Blends

Miscibility, Morphology and Interfaces







*Edited by*  
*S. Thomas,*  
*Y. Grohens, and*  
*P. Jyotishkumar*

**Characterization of  
Polymer Blends**

## ***Related Titles***

Thomas, S., Durand, D., Chassenieux, C., Jyotishkumar, P. (eds.)

### **Handbook of Biopolymer-Based Materials From Blends and Composites to Gels and Complex Networks**

2013

ISBN: 978-3-527-32884-0 (Also available in electronic formats)

Isayev, A. I. (ed.)

### **Encyclopedia of Polymer Blends**

Volume 1: Fundamentals

2010

ISBN: 978-3-527-31929-9

Isayev, A. I. (ed.)

### **Encyclopedia of Polymer Blends**

Volume 2: Processing

2011

ISBN: 978-3-527-31930-5

*Edited by S. Thomas, Y. Grohens, and P. Jyotishkumar*

## **Characterization of Polymer Blends**

Miscibility, Morphology and Interfaces

**WILEY-VCH**  
Verlag GmbH & Co. KGaA

## The Editors

### **Prof. Dr. Sabu Thomas**

Mahatma Gandhi University  
School of Chemical Sciences  
Priyadarshini Hills P.O.  
686-560 Kottayam, Kerala  
India

### **Prof. Dr. Yves Grohens**

Université de Bretagne Sud  
Laboratoire LIMATB  
Rue St Maudé  
56100 Lorient  
France

### **Prof. Dr. P. Jyotishkumar**

Mahatma Gandhi University  
School of Chemical Sciences  
Priyadarshini Hills P.O.  
686-560 Kottayam, Kerala  
India

## Cover

*The transmission electron micrograph in the background, optical micrograph on the left, and atomic force micrograph on the right side of the cover were created by Dr. Muruganathan Ramanathan and Dr. Seth B. Darling, [Ramanathan, M. and Darling, S.B., Soft Matter, 2009, 5, 4665-4671] and are reproduced with kind permission from the authors.*

All books published by **Wiley-VCH** are carefully produced. Nevertheless, authors, editors, and publisher do not warrant the information contained in these books, including this book, to be free of errors. Readers are advised to keep in mind that statements, data, illustrations, procedural details or other items may inadvertently be inaccurate.

### **Library of Congress Card No.:** applied for **British Library Cataloguing-in-Publication Data**

A catalogue record for this book is available from the British Library.

### **Bibliographic information published by the Deutsche Nationalbibliothek**

The Deutsche Nationalbibliothek lists this publication in the Deutsche Nationalbibliografie; detailed bibliographic data are available on the Internet at <http://dnb.d-nb.de>.

© 2015 Wiley-VCH Verlag GmbH & Co. KGaA,  
Boschstr. 12, 69469 Weinheim, Germany

All rights reserved (including those of translation into other languages). No part of this book may be reproduced in any form – by photoprinting, microfilm, or any other means – nor transmitted or translated into a machine language without written permission from the publishers. Registered names, trademarks, etc. used in this book, even when not specifically marked as such, are not to be considered unprotected by law.

**Print ISBN:** 978-3-527-33153-6

**ePDF ISBN:** 978-3-527-64562-6

**ePub ISBN:** 978-3-527-64561-9

**Mobi ISBN:** 978-3-527-64563-3

**oBook ISBN:** 978-3-527-64560-2

**Cover Design** Grafik-Design Schulz, Fußgönheim,  
Germany

**Typesetting** Thomson Digital, Noida, India

**Printing and Binding** Markono Print Media Pte Ltd,  
Singapore

Printed on acid-free paper



## Contents

### List of Contributors   XXI

### Volume 1

- 1     Polymer Blends: State of the Art, New Challenges, and Opportunities   1**  
*Jyotishkumar Parameswaranpillai, Sabu Thomas, and Yves Grohens*
  - 1.1   Introduction   1
  - 1.2   Miscible and Immiscible Polymer Blends   2
  - 1.3   Compatibility in Polymer Blends   3
  - 1.4   Topics Covered in this Book   3
  - References   5
  
- 2     Miscible Blends Based on Biodegradable Polymers   7**  
*Emilio Meaurio, Natalia Hernandez-Montero, Ester Zuza, and Jose-Ramon Sarasua*
  - 2.1   Introduction   7
  - 2.2   Thermodynamic Approach to the Miscibility of Polymer Blends   8
    - 2.2.1   Introduction   8
    - 2.2.2   Molecular Size and Entropy   8
    - 2.2.3   The Regular Solution   10
    - 2.2.4   The Flory–Huggins Model   13
    - 2.2.5   The Hildebrand Approach   17
    - 2.2.6   Extension of the Flory–Huggins Model to Systems with Specific Interactions   19
    - 2.2.7   The Dependence of Miscibility on Blend Composition and Temperature   24
    - 2.2.8   The Painter–Coleman Association Model (PCAM)   25
    - 2.2.9   Analysis of the Miscibility Using Molecular Modeling Calculations   26
      - 2.2.10   Classification of Miscible Systems   27
        - 2.2.10.1   Entropically Driven Miscible Systems   27
        - 2.2.10.2   Enthalpically Driven Miscible Systems   28

2.3	Revision of Polymer Blends Based on Biodegradable Polyesters	29
2.3.1	Blends Containing Poly(lactic acid) or Poly(lactide) (PLA)	29
2.3.1.1	PLA/PLA Blends	30
2.3.1.2	PLA Blended with Poly(ethylene glycol) (PEG) and Poly(ethylene oxide) (PEO)	34
2.3.1.3	PLA Blended with Poly(vinyl alcohol) (PVA) and Poly(vinyl acetate)	36
2.3.1.4	PLA/Poly( $\epsilon$ -caprolactone) (PCL) Blends	37
2.3.1.5	PLA/Poly((R)-3-Hydroxybutyric acid) (PHB) Blends	40
2.3.1.6	PLA Blended with Poly(methyl methacrylate) (PMMA) and Poly(methyl acrylate) (PMA)	41
2.3.1.7	PLA/Poly(4-vinylphenol) (PVPh) Blends	43
2.3.1.8	PLA Blended with Poly(butylene succinate) (PBS) and Poly(ethylene succinate) (PESu)	45
2.3.1.9	PLA Blended with Poly(propylene carbonate) (PPC) and Poly(trimethylene carbonate) (PTMC)	47
2.3.1.10	PLA/Poly(styrene) (PS) Blends	48
2.3.1.11	PLA Blended with Other Polymers	48
2.3.1.12	PLA Blended with Other Copolymers	50
2.3.2	Blends Containing Poly( $\epsilon$ -caprolactone) (PCL)	50
2.3.3	Blends Containing Poly(hydroxy butyrate) (PHB)	50
2.3.4	Blends Containing Poly(p-dioxanone) (PPDO)	51
2.3.5	Blends Containing Poly(glycolic acid) (PGA) or Polyglycolide	52
2.4	Revision of Blends Based on Natural Polymers	52
2.4.1	Blends Containing Starch	52
2.4.2	Blends Containing Cellulose	54
2.4.3	Blends Containing Chitosan	55
2.4.4	Blends Containing Collagen	56
	Appendix 2.A Relevant Research Papers	57
	Appendix 2.B List of Abbreviations and Nomenclature	83
	2.B.1 Chemical Terms	83
	2.B.2 Polymers and Copolymers	83
	2.B.3 Notations	84
	2.B.4 Symbols	85
	2.B.5 Greek Letters	86
	Acknowledgments	86
	References	86
<b>3</b>	<b>Thermodynamics and Morphology and Compatibilization of Polymer Blends</b>	<b>93</b>
	<i>Zdeněk Starý</i>	
3.1	Introduction	93
3.2	Thermodynamics of Polymer Blends	95
3.2.1	Enthalpy of Mixing	95
3.2.2	Entropy of Mixing	96

3.2.3	Flory–Huggins Theory	98
3.3	Phase Behavior of Polymer Blends	100
3.3.1	Phase Diagrams	101
3.3.2	Phase Separation	104
3.3.3	Interfaces in Polymer Blends	107
3.4	Morphology of Polymer Blends	111
3.4.1	Morphology Development During Melt Processing	114
3.4.2	Stability of Blend Morphology	119
3.5	Compatibilization of Polymer Blends	120
3.5.1	Morphology Development in Compatibilized Blends	121
3.5.2	Compatibilization Techniques	123
3.5.2.1	Addition of Preprepared Copolymer	124
3.5.2.2	Addition of Reactive Polymer	125
3.5.2.3	Addition of Reactive Low-Molecular-Weight Compounds	125
3.5.2.4	Other Compatibilization Techniques	126
	References	126
<b>4</b>	<b>Characterization of Polymer Blends: Rheological Studies</b>	<b>133</b>
	<i>Yingfeng Yu</i>	
4.1	Introduction	133
4.1.1	General Description of Thermoset Rheological Behaviors	133
4.1.2	Thermosetting Resins: Gelation, Vitrification, and Viscoelasticity	134
4.1.3	Methods of Rheological Measurement	137
4.2	Thermosetting Blend Systems with Rubbers and Thermoplastics	138
4.2.1	Phase Separation and Rheological Behavior of Rubber-Modified Systems	138
4.2.2	Phase Separation and Rheological Behavior of Thermoplastic-Modified Systems	140
4.2.3	Viscoelastic Properties of the Blends	143
4.2.4	Gelation Behaviors of the Blends	148
4.3	Thermosetting Systems with Nanostructures	150
4.4	Conclusions	153
	References	153
<b>5</b>	<b>Characterization of Phase Behavior in Polymer Blends by Light Scattering</b>	<b>159</b>
	<i>Petr Svoboda</i>	
5.1	Introduction	159
5.2	Amorphous/Crystalline Polymer Blends	160
5.3	Light Scattering	161
5.4	Cloud-Point Determination	162
5.5	Time-Resolved Light Scattering	165
5.5.1	Immiscible Blends	165
5.5.2	Spinodal Decomposition	166
5.5.3	Crystallization by $H_v$ Light Scattering	169

5.5.4	Model Blend of Poly( $\epsilon$ -Caprolactone) (PCL) and Poly(Styrene-co-Acrylonitrile) (SAN)	170
5.5.5	Samples Preparation	171
5.5.6	Phase Separation and Phase Dissolution in Poly( $\epsilon$ -Caprolactone)/Poly(Styrene-co-Acrylonitrile) Blend	172
5.5.7	Crystallization Kinetics by Optical Microscopy and by $H_v$ Light Scattering	181
5.5.8	Competition of Phase Dissolution and Crystallization	190
5.6	Determination of Virtual UCST Behavior	197
5.6.1	Evaluation of Particle Size in Immiscible Blends	204
	Acknowledgments	205
	References	205
<b>6</b>	<b>Characterization of Polymer Blends by X-Ray Scattering: SAXS and WAXS</b>	<b>209</b>
	<i>Jitendra Sharma</i>	
6.1	Introduction	209
6.1.1	Development of SAXS Techniques for Polymers	212
6.1.2	Instrumentation and the Synchrotron Advantage	212
6.2	Basics of X-Ray Scattering	213
6.2.1	Elastic Scattering of Electromagnetic Radiation by Single Electron	213
6.2.2	Scattering by Assembly of Electrons: Scattering Geometry and Interference	215
6.2.3	Scattered Intensity	216
6.3	Small- and Wide-Angle X-Ray Scattering (SAXS and WAXS)	218
6.4	Polymer Blend Morphology	219
6.4.1	Blends of Homopolymers	219
6.4.1.1	Structural Characterization: SAXS Data	220
6.4.1.2	Crystallinity: WAXS Data	224
6.4.2	Blends of Block Copolymers	224
6.4.3	Time-Resolved Studies: Kinetics of Crystallization and Melting	228
6.5	Conclusions	231
	References	232
<b>7</b>	<b>Characterization of Polymer Blends and Block Copolymers by Neutron Scattering: Miscibility and Nanoscale Morphology</b>	<b>237</b>
	<i>Kell Mortensen</i>	
7.1	Introduction	237
7.2	Small-Angle Scattering	237
7.2.1	Contrast	239
7.2.2	Scattering Function	242
7.2.3	Gaussian Chain	244



7.3	Thermodynamics of Polymer Blends and Solutions. Flory–Huggins Theory	246
7.4	The Scattering Function and Thermodynamics	249
7.4.1	The Forward Scattering	250
7.4.2	Random Phase Approximation (RPA)	254
7.4.3	Beyond Mean Field	258
7.5	Block Copolymers	260
7.5.1	Ordered Phases	264
	References	268

## **8      Ultrasound in Polymer Blends** 269

*Sangmook Lee and Jae Wook Lee*

8.1	Introduction	269
8.2	High-Frequency Ultrasound	270
8.2.1	Static Characterization	270
8.2.1.1	Miscibility of Solution Blends	270
8.2.1.2	Compatibility	273
8.2.1.3	Density	274
8.2.1.4	Phase Inversion	275
8.2.1.5	Molecular Orientation	276
8.2.2	In-Line Monitoring	278
8.2.2.1	Morphology	278
8.3	Power Ultrasound	280
8.3.1	Injection Molding	280
8.3.1.1	Weld Line Strength Improvement	280
8.3.2	Batch Melt Mixing	281
8.3.2.1	Compatibilization	282
8.3.3	Extrusion	283
8.3.3.1	Molecular Weight Control	284
8.3.3.2	Tensile Properties Enhancement	284
8.3.3.3	Compatibilization	286
8.3.3.4	Rheological Modification	287
8.3.3.5	Morphology Control	289
8.3.3.6	Die Swell Reduction	290
8.4	Summary	292
	References	293

## **9      Characterization of Polymer Blends: Ellipsometry** 299

*Éva Kiss*

9.1	Ellipsometry	299
9.1.1	Principles of Ellipsometry	299
9.1.2	Thickness and Optical Properties of Layers on Solid Supports	300
9.1.2.1	Linear EMA	301
9.1.2.2	Maxwell–Garnett EMA	301
9.1.2.3	Bruggeman EMA	302

9.1.3	Depth Profiling	303
9.1.4	Sample Preparation	303
9.1.5	Types of Instrument and Measurements	303
9.1.5.1	Spectroscopic Ellipsometry, Real-Time Measurement	304
9.2	Applications in the Characterization of Polymer Blend Films	304
9.2.1	Phase Separation in Thin Polymer Blend Films	304
9.2.2	Analysis of Interfacial Thickness and Interfacial Reaction	305
9.2.2.1	Miscibility	305
9.2.2.2	Reactive Compatibilization	308
9.2.3	Morphology, Roughness, and Pattern Formation in Nanolayers	309
9.2.4	Biomaterial Surfaces	312
9.2.5	Surface Modification, Adsorption from Solution	312
9.2.5.1	Biomaterial Blends	313
9.2.5.2	Distribution and Release of Drugs	315
9.2.6	Composite Layers for Organic Solar Cells	317
9.3	Concluding Remarks	322
	Acknowledgments	322
	References	323
<b>10</b>	<b>Inverse Gas Chromatography</b>	<b>327</b>
	<i>Kasylda Milczewska and Adam Voelkel</i>	
10.1	Concept and History of Inverse Gas Chromatography (IGC)	327
10.2	Theoretical Background	328
10.3	Thermodynamic Aspects: Parameters Used for Polymer Blend Characterization	330
10.3.1	Flory–Huggins Interaction Parameter for Polymer–Test Solute Systems	331
10.3.2	Flory–Huggins Interaction Parameter for “Multiple” Systems	333
10.4	Procedures Used in IGC Experiments Leading to the Determination of Polymer Blend Characteristics	334
10.5	Application of Chemometric Methods	336
10.6	Transport Properties of Polymeric Mixtures	337
10.7	Usefulness of IGC: Applications of IGC-Derived Parameters in the Characterization of Various Systems	340
10.8	Advantages and Drawbacks of IGC	341
	References	342
<b>11</b>	<b>Thermal Analysis in Polymer Blends</b>	<b>347</b>
	<i>Ramesh T. Subramaniam and R. Shanti Rajantharan</i>	
11.1	Introduction to Polymer Blends	347
11.1.1	The Principle of Polymer Blending	348
11.2	Experimental	349
11.2.1	System 1: PVC/PEO Blends	349
11.2.2	System 2: PVC/PEO:LiCF <sub>3</sub> SO <sub>3</sub> Blends	350
11.2.3	System 3: PVC/PEO-LiCF <sub>3</sub> SO <sub>3</sub> -DBP:EC Blends	351

11.2.4	System 4: PVC/PEO-LiCF <sub>3</sub> SO <sub>3</sub> -DBP-EC:SiO <sub>2</sub> Blends	351
11.3	Instrumentation	351
11.3.1	Sample Weight	352
11.3.2	Testing Temperature Range	352
11.3.3	Gas Environment	352
11.3.4	Heating Rate	353
11.4	Thermal Analysis	353
11.4.1	Information Obtained from TGA	353
11.4.2	Thermal Process	353
11.4.3	The Value of the TGA Information	354
11.5	Results and Discussion: Thermal Analysis	355
11.5.1	Pure PVC	355
11.5.2	Pure PEO	359
11.5.3	System 1: PVC/PEO Blends	359
11.5.4	System 2: PVC/PEO:LiCF <sub>3</sub> SO <sub>3</sub> Blends	360
11.5.5	System 3: PVC/PEO-LiCF <sub>3</sub> SO <sub>3</sub> -DBP-EC Blends	361
11.5.6	System 4: PVC-PEO-LiCF <sub>3</sub> SO <sub>3</sub> -DBP-EC:SiO <sub>2</sub> Blends	362
11.6	Conclusion	362
	References	363
<b>12</b>	<b>Dynamic Mechanical Thermal Analysis of Polymer Blends</b>	<b>365</b>
	<i>José-David Badia, Laura Santonja-Blasco, Alfonso Martínez-Felipe, and Amparo Ribes-Greus</i>	
12.1	Dynamic Mechanical Thermal Analysis (DMTA)	365
12.1.1	The DMTA Analyzers	366
12.1.2	Using DMTA to Analyze the Viscoelastic Behavior of Polymers	368
12.1.3	Description of DMTA Results: The Viscoelastic Spectra	369
12.1.3.1	The Glassy State	369
12.1.3.2	The Glass–Rubber Relaxation	371
12.1.3.3	Rubbery Plateau	372
12.1.3.4	Recrystallization or Curing	372
12.1.3.5	Flowing	373
12.1.4	Modeling the Viscoelastic Behavior	373
12.2	Miscibility Studies	373
12.2.1	Binary Systems	374
12.2.2	Ternary Systems	376
12.2.3	Influence of Type of Processing	376
12.2.4	Recovering Plastic Waste by Polymer Blending	377
12.2.5	Influence of Nanoparticles	377
12.2.6	The Study of the Rubbery Plateau as an Indicator of Miscibility	378
12.2.7	Theoretical Approaches to Calculating the Glass–Rubber Relaxation Temperature	379
12.3	Segmental Dynamics, Fragility Index, and Free-Volume	379
12.4	Effects of Plasticizers and Chemical and Physical Crosslinks	381

12.4.1	Influence of Plasticizers on Viscoelastic Performance of Polymer Blends	382
12.4.2	Influence of Chemical and Physical Crosslinkers on the Viscoelastic Performance of Polymer Blends	383
12.4.3	Strategies to Tune the Heat Distortion Temperature by Polymer Blending	384
12.5	Summary	386
	References	387
<b>13</b>	<b>Thermomechanical Analysis and Processing of Polymer Blends</b>	<b>393</b>
	<i>Suchart Siengchin</i>	
13.1	Introduction	393
13.2	Polymer Toughness	394
13.3	Thermomechanical Analysis and Manufacture of Polymer Blends	395
13.3.1	Theoretical Background	396
13.3.1.1	Dynamic Mechanical Thermal Analysis (DMTA)	396
13.3.1.2	Creep Response	397
13.3.1.3	Thermogravimetric Analysis	399
13.3.2	Latex and Online-Manufacturing Concept of Polymer Blends	399
13.3.3	Materials Systems Studied	402
13.4	Results and Discussion	403
13.4.1	POM/PU Blend	403
13.4.2	PA-6/HNBR Blend	408
13.5	Summary	412
13.5.1	Greek Symbols	413
	Acknowledgment	413
	References	413
<b>14</b>	<b>Water Sorption and Solvent Sorption Behavior</b>	<b>417</b>
	<i>Fatemeh Sabzi</i>	
14.1	Introduction	417
14.2	Water Sorption	418
14.2.1	Chitosan Blends	418
14.2.2	PVP/Polysulfone Blend	420
14.2.3	PEOX Blends	422
14.2.4	PES/PEO Blend	422
14.2.5	Phenoxy Blends	423
14.2.6	Poly(ethylene terephthalate) (PET) Nanocomposites	423
14.2.7	PMMA/HHIS and PMMA/HS	424
14.2.8	PVC/EVAc	425
14.2.9	PBI/PI	428
14.2.10	PP/EVA	428
14.2.11	PVA/P(AA-AMPS)	430
14.2.12	PVP/PEG	431
14.2.13	iPHB/aPHB and iPHB/PECH	431



14.2.14	Epoxy Resin/PEI	432
14.2.15	PMMA/PEO	433
14.3	Pervaporation	434
14.3.1	THF/Water Mixtures	434
14.3.2	Acetic Acid/Water Mixture	435
14.3.3	Ethanol/Water Mixture	435
14.3.4	DMF/Water Mixtures	436
14.3.5	1,4-Dioxane/Water	436
14.4	Vapor Permeation	437
14.4.1	Chitosan/CPA	437
14.4.2	Natural Rubber Blends	437
14.4.3	NBR Blends	440
14.4.4	LCP Blends	441
14.4.5	PU/PDMS	442
14.4.6	EEA-CB	442
14.4.7	PVC/EVAc	443
14.4.8	PHB/PEO and PHB/PMMA	443
14.4.9	PVA/PAA	443
14.5	Gas Permeation	444
14.5.1	PVA/PEI/PEG	444
14.5.2	PS/PC	444
14.5.3	PS/PPO	445
14.5.4	PS/PTMPS	445
14.5.5	Matrimid/PSF	446
14.5.6	Matrimid/P84	446
14.5.7	Matrimid/PBI	447
14.5.8	CA/PMMA	447
14.5.9	PU/PMMA	448
14.5.10	EVA-45/H-48	448
14.5.11	PS/PVME	448
14.5.12	TLCP/PET	449
14.5.13	CELL/PVA	449
14.5.14	Trogamid Blends	449
14.5.15	TPX/Siloxane	450
14.5.16	PTMSMMA/3-Methylsulfolane	450
14.5.17	BCPC/PMMA	450
14.6	Conclusions	451
	References	451
<b>15</b>	<b>Modeling and Simulation</b>	<b>457</b>
	<i>Yingrui Shang and David Kazmer</i>	
15.1	Introduction	457
15.1.1	Numerical Models for Polymer Blends	457
15.1.2	Spinodal Decomposition	461
15.1.3	Cahn–Hilliard Equation	464

15.1.4	Numerical Method	465
15.2	Numerical Simulation of Phase Separation of Immiscible Polymer Blends on a Heterogeneously Functionalized Substrate	466
15.2.1	Fundamentals	467
15.2.2	Numerical Method	468
15.2.3	Implementation	470
15.2.4	Results and Discussion	471
15.2.5	Summary	479
15.3	Numerical Simulation of the Self-Assembly of a Polymer–Polymer–Solvent Ternary System on a Heterogeneously Functionalized Substrate	481
15.3.1	Introduction	481
15.3.2	Thermodynamics	481
15.3.3	Numerical Method	484
15.3.4	Implementation	485
15.3.5	Results and Discussion	486
15.3.6	Summary	496
15.4	Verification of Numerical Simulation of the Self-Assembly of a Polymer–Polymer–Solvent Ternary System on a Heterogeneously Functionalized Substrate	497
15.4.1	Experiment	498
15.4.2	Implementation	499
15.4.3	Results and Discussion	501
15.4.4	Summary	511
15.5	Effects of Pattern Shapes and Block Copolymer	513
15.6	Conclusions	515
	Acknowledgments	517
	References	517

## Volume 2

<b>16</b>	<b>Optical Microscopy (Polarized, Interference, and Phase-Contrast Microscopy) and Confocal Microscopy</b>	<b>523</b>
	<i>Muruganathan Ramanathan and Seth B. Darling</i>	
16.1	Introduction	523
16.2	Optical and Confocal Microscopy: A Brief Overview	524
16.3	Mesoscale Morphologies in Polymer Blends: Spherulites and Microcrystallites	526
16.4	Optical Characterization of Mesoscale Morphologies in Polymer Blends	528
16.4.1	Crystalline–Crystalline Blend	528
16.4.2	Crystalline–Amorphous Blend	531
16.4.3	Role of Polymer Tacticity on Polymer Blend Morphologies	535

16.4.4	Crystallization Morphologies in Stereocomplexationable Chiral Blends	537
16.4.5	Mesoscale Morphologies in Conducting Polymer Blends	540
16.5	Confocal Microscopy Characterization of Polymer Blends	543
16.6	Summary	547
	Acknowledgments	547
	References	548
<b>17</b>	<b>Electron Microscopic Analysis of Multicomponent Polymers and Blends</b>	<b>551</b>
	<i>Rameshwar Adhikari</i>	
17.1	Introduction and Overview	551
17.2	Sample Preparation Techniques	552
17.2.1	Thin-Film Preparation	552
17.2.2	Staining of Thin Sections	553
17.2.3	Etching of the Surface	554
17.2.4	Specimens for Fracture Behavior Analysis	554
17.3	Morphological Characterization	555
17.3.1	Blends of Semicrystalline Polymers	555
17.3.2	Blends of Amorphous Polymers	561
17.3.3	Nanostructured Copolymers and Blends	563
17.4	Special Techniques and Applications	567
17.5	Deformation Studies on Polymer Blends	571
17.6	Concluding Notes	574
	Acknowledgments	575
	References	575
<b>18</b>	<b>Characterization of Polymer Blends Using SIMS and NanoSIMS</b>	<b>579</b>
	<i>Vanna Torrisi</i>	
18.1	Introduction	579
18.2	Thin Films and Ultrathin Films of Polymer Blends	580
18.2.1	Phase-Separation Phenomena	583
18.2.2	Technological Applications of Thin and Ultrathin Films of Polymer Blends	586
18.2.3	The Necessity of Compositional Information	588
18.3	SIMS: The Techniques and Outputs	589
18.3.1	ToF-SIMS: The Technique	592
18.3.1.1	Spectra, Profiling, and Imaging Mode	592
18.3.1.2	ToF-SIMS: Spatially Resolved Molecular Information	593
18.3.1.3	Multivariate Analysis of ToF-SIMS Images	595
18.3.2	NanoSIMS: The Technique	597
18.3.2.1	NanoSIMS: Ion Optical Set-Up	597
18.3.2.2	NanoSIMS: The Mass Spectrometer	597

18.3.2.3	NanoSIMS: Highly Spatially Resolved Elemental Information	598
18.4	3D Imaging of Polymer Blends	599
18.5	Conclusions and Perspectives	602
	References	603
<b>19</b>	<b>Fluorescence Microscopy Techniques for the Structural Analysis of Polymer Materials</b>	<b>609</b>
	<i>Hiroyuki Aoki</i>	
19.1	Introduction	609
19.2	Fundamentals of Fluorescence Microscopy	609
19.3	Fluorescence Imaging of Polymer Blend Systems	612
19.3.1	Real-Space Measurement of 3D Structure	612
19.3.2	Spectroscopic Information	614
19.4	Fluorescence Microscopy Beyond the Diffraction Barrier	615
19.4.1	Near-Field Optical Microscopy	615
19.4.2	Super-Resolution Optical Microscopy	617
19.4.3	Conformational Analysis of Single Polymer Chain	620
19.5	Summary	621
	References	622
<b>20</b>	<b>Characterization of Polymer Blends with FTIR Spectroscopy</b>	<b>625</b>
	<i>Ufana Riaz and Syed Marghoob Ashraf</i>	
20.1	Introduction	625
20.2	Methods of Investigating Miscibility	626
20.2.1	FTIR as a Spectroscopic Tool for the Characterization of Polymer Blends	626
20.2.2	Determination of Miscibility Through Hydrogen Bonding	628
20.3	Characterization of Vinyl Polymer Blends using FTIR Spectroscopy	628
20.3.1	Poly(vinylphenol) (PVPh) Blends	628
20.3.2	Poly(vinylpyrrolidone) (PVP) Blends	632
20.3.3	Poly(vinyl alcohol) (PVA) Blends	637
20.4	Characterization of Blends of Polyethers (PE) using FTIR Spectroscopy	643
20.4.1	Polyethylene Oxide (PEO) Blends	643
20.4.2	Poly (vinyl methyl ether) (PVME) Blends	650
20.5	Characterization of Acrylate Blends with FTIR Spectroscopy	655
20.5.1	Poly(methylmethacrylate) (PMMA) Blends	655
20.5.2	Poly-(3-hydroxybutyrate-co-3-hydroxyvalerate) (PHBV) Blends	657
20.6	Characterization of Synthetic Rubber using FTIR Spectroscopy	661



20.7	Characterization of Natural Polymer Blends Using FTIR Spectroscopy	663
20.7.1	Collagen Blends	663
20.7.2	Chitosan Blends	664
20.8	Study of Blends by Polarization Modulation and 2D-FTIR Spectroscopy	665
20.9	Analysis of Polymer Blends Using FTIR Microspectroscopy	668
20.10	Conclusions	669
	Acknowledgments	670
	Abbreviations	670
	References	671
<b>21</b>	<b>Characterization of Polymer Blends with Solid-State NMR Spectroscopy</b>	<b>679</b>
	<i>Mohammad Mahdi Abolhasani and Vahid Karimkhani</i>	
21.1	Introduction	679
21.2	Miscibility	680
21.3	Proton Spin-Lattice Relaxation Experiments	680
21.4	Experiments for the Direct Observation of Proton Spin-Diffusion	688
21.5	Molecular Dynamics	692
21.5.1	$^2\text{H}$ NMR Line Shape Analysis	692
21.5.2	Polarization Inversion Spin Exchange at the Magic Angle (PISEMA) Experiment	694
21.5.3	Two-Dimensional Widelane Separation (WISE) NMR	695
21.6	Organic Solar Cells	696
21.7	Conclusions	700
	References	702
<b>22</b>	<b>Characterization of Polymer Blends by Infrared, Near-Infrared, and Raman Imaging</b>	<b>705</b>
	<i>Harumi Sato, Miriam Unger, Dieter Fischer, Yukihiro Ozaki, and Heinz W. Siesler</i>	
22.1	Instrumentation for Mid-Infrared and Near-Infrared Imaging	705
22.2	Raman Microspectroscopy	709
22.3	Characterization of Polymer Blends by FT-IR Imaging	711
22.3.1	Investigation of Phase Separation in Biopolymer Blends	711
22.3.1.1	Poly((3-Hydroxybutyrate)(PHB)/Poly(L-Lactic Acid)(PLA) Blends	711
22.3.1.2	FT-IR Imaging of Anisotropic PHB/PLA Blend Films	714
22.3.1.3	Variable-Temperature FT-IR and Raman Imaging Spectroscopy of a Phase-Separated PHB/PLA 50/50 wt% Blend Film	717
22.3.1.4	FT-IR Imaging of the State of Order of PHB/PCL Blend Films	720
22.3.1.5	FT-IR and FT-NIR Imaging of the Spherulitic Structure of Poly(3-Hydroxy-Butyrate) and Cellulose Acetate Butyrate Blends	724

22.3.1.6	Raman Mapping Measurements of the Influence of a Compatibilizer on Phase Separation of the Polymer Blend Polypropylene/Polyamide 6	728
	References	730
<b>23</b>	<b>Electron Paramagnetic Resonance Spectroscopy and Forward Recoil Spectrometry</b>	<b>731</b>
	<i>Krzysztof Kruczała and Ewa Szajdzińska-Piętek</i>	
23.1	Introduction	731
23.2	Electron Paramagnetic Spectroscopy	732
23.2.1	EPR Background	732
23.2.1.1	Multifrequency EPR	736
23.2.1.2	Pulsed EPR	737
23.2.1.3	EPR Imaging	738
23.2.1.4	Simulation of EPR Spectra	741
23.2.1.5	Spin Probes and Spin Labels	744
23.2.2	EPR Applications in Studies of Polymer Blends	747
23.2.2.1	Spin Probing of the Structure and Dynamics	747
23.2.2.2	Radical Processes Induced by Ionizing Radiation	755
23.2.2.3	Conductive Materials	761
23.3	Forward Recoil Spectrometry	766
23.3.1	FRES Fundamentals	767
23.3.2	Technique Developments	769
23.3.2.1	Time-of-Flight FRES	770
23.3.2.2	Low-Energy FRES	771
23.3.2.3	Heavy Ion FRES	772
23.3.3	Applications to Polymer Blend Studies	773
23.3.3.1	Tracer Diffusion	773
23.3.3.2	Reaction Kinetics	775
23.3.3.3	Surface and Interfaces	776
23.3.3.4	Phase Separation	778
	Acknowledgments	782
	References	783
<b>24</b>	<b>Characterization of Polymer Blends Using UV-Visible Spectroscopy</b>	<b>789</b>
	<i>Mamdouh H. Abou-Taleb</i>	
24.1	Introduction	789
24.2	Electromagnetic Radiation	791
24.3	Interaction of Radiation (UV/VIS) with Matter	792
24.4	The Nature of Electronic Excitations in Matter (Polymer Blends)	793
24.5	Relationship of Structure of Matter to the Electronic Absorption Spectrum	796
24.6	The Correspondence of Color and Transparent Spectrum	796

24.7	Relationship of Polymer Blends to Material Characterization	798
24.8	Optical Properties of Semiconductors (Polymers and Polymer Blends)	801
24.9	Optical Absorption Spectra of Materials	802
24.9.1	Extended-to-Extended State Transitions	803
24.9.2	Extended-to-Localized and Localized-to-Extended State Transitions	803
24.9.3	Localized-to-Localized State Transitions	804
24.9.4	Exciton Absorption	807
24.9.5	Free Carrier Absorption	807
24.10	Instrumentation	809
24.10.1	Single-Beam Spectrophotometry	809
24.10.2	Double-Beam Spectrophotometry	810
24.11	Radiation Sources	811
24.11.1	Xenon Lamp (Xenon Arc Lamp)	811
24.11.2	Deuterium Lamp	811
24.12	Monochromator	811
24.12.1	Wavelength Selection	812
24.13	Detection Area and Detectors	812
24.13.1	Photomultiplier	812
24.13.2	Silicon Photodiode	813
24.13.3	Photodiode Array	813
24.14	Data Acquisition	814
24.15	Classification of Errors in Spectrophotometry	814
24.15.1	Spectral Band Width and Slit Width	815
24.15.2	Slit Height	816
24.15.3	Stray Light	816
24.15.4	Solvents	817
	References	817
<b>25</b>	<b>Fluorescence Spectroscopy</b>	<b>821</b>
	<i>Gabriel Bernardo and Jorge Morgado</i>	
25.1	Introduction	821
25.2	Fundamentals of Fluorescence Spectroscopy	822
25.2.1	Theory	822
25.2.2	Steady-State Fluorescence	823
25.2.3	Time-Resolved Fluorescence	823
25.2.4	Fluorescence Quenching	827
25.2.5	Fluorescence Microscopy	830
25.3	Intrinsically Fluorescent Polymer Blends	830
25.4	Systems Requiring Extrinsic Fluorescent Labels	840
25.5	Conclusions	844
	Nomenclature	844
	Acknowledgments	845
	References	846

<b>26</b>	<b>Characterization of Polymer Blends by Dielectric Spectroscopy and Thermally Simulated Depolarization Current</b>	<b>849</b>
	<i>Samy A. Madbouly and Michael R. Kessler</i>	
26.1	Introduction	849
26.1.1	Dielectric Relaxation Spectroscopy and Thermally Stimulated Depolarization Current	849
26.1.2	Analysis of Relaxation Spectrum	850
26.1.3	Effect of Temperature on Relaxation Spectrum	852
26.2	Dielectric Relaxation Spectroscopy of Amorphous Polymer Blends	853
26.3	Dielectric Relaxation Spectroscopy of Semicrystalline Polymer Blends	862
26.4	Dielectric Relaxation Spectroscopy of Chemically Reactive Polymer Blends	868
26.5	Conclusions	872
	References	873
<b>27</b>	<b>Positron Annihilation Spectroscopy: Polymer Blends and Miscibility</b>	<b>877</b>
	<i>Chikkakuntappa Ranganathaiah</i>	
27.1	Introduction	877
27.2	Positron Annihilation Spectroscopy	878
27.2.1	The Positron Annihilation Process	878
27.2.2	Positronium	880
27.2.2.1	Positron and Positronium Sensitivity to Defects and Free Volume	882
27.2.2.2	Models Predicting Positronium Formation	883
27.3	Free Volume Theory	884
27.3.1	Free Volume Model and Positronium Lifetime Connection	885
27.4	Characterization of Polymer Blends by PAS	887
27.5	Experimental Methods of PAS	888
27.5.1	Positron Annihilation Lifetime Spectroscopy (PALS)	888
27.5.1.1	Free Volume Distribution-Lifetime Analysis by Laplace Transform Method	891
27.5.1.2	Free-Volume Distributions in Polymer Blends	892
27.5.1.3	Angular Correlation of Annihilation Radiation (ACAR) Method	893
27.5.1.4	Doppler Broadening of the Annihilation Radiation (DBAR) Method	894
27.6	Miscibility in Polymer Blends and Free Volume	896
27.6.1	Free Volume and Miscibility Studies in Blends	901
27.7	Future Outlook	916
	Acknowledgments	916
	References	916
	<b>Index</b>	<b>921</b>

## List of Contributors

### ***Mohammad Mahdi Abolhasani***

University of Kashan  
Chemical Engineering Department  
Kashan  
Iran

### ***Mamdouh H. Abou-Taleb***

Cairo University  
Faculty of Science  
Physics Department  
Giza  
Egypt

and

Taif University  
Faculty of Science  
Physics Department  
21974 Taif  
Saudi Arabia

### ***Rameshwar Adhikari***

Tribhuvan University  
Central Department of Chemistry  
Kirtipur  
Kathmandu  
Nepal

and

Nepal Polymer Institute (NPI)  
Kathmandu  
Nepal

### ***Hiroyuki Aoki***

Kyoto University  
Advanced Biomedical Engineering  
Research Unit  
Kyoto-Daigaku-Katsura  
Nishikyo  
Kyoto 615-8510  
Japan

### ***Syed Marghoob Ashraf***

Jamia Millia Islamia (A Central  
University)  
Department of Chemistry  
Materials Research Laboratory  
Maulana Mohammad Ali Jauhar  
Marg  
New Delhi 110025  
India

### ***José-David Badia***

Universitat Politècnica de València  
Instituto de Tecnología de Materiales  
Camino de Vera, s/n  
46022 València  
Spain

**Gabriel Bernardo**

University of Minho  
Institute for Polymers and  
Composites/I3N  
Campus de Azurém  
4800-058 Guimarães  
Portugal

**Seth B. Darling**

Argonne National Laboratory  
Center for Nanoscale Materials  
9700 South Cass Avenue  
Argonne, IL60439  
USA

and

University of Chicago  
Institute for Molecular Engineering  
5801 South Ellis Avenue  
Chicago, IL 60637  
USA

**Dieter Fischer**

Leibniz-Institute for  
Polymer Research  
Hohe Str. 6  
01069 Dresden  
Germany

**Yves Grohens**

Université de Bretagne Sud  
Laboratoire Ingénierie des Matériaux  
de Bretagne  
Rue St Maudé  
56100 Lorient  
France

**Natalia Hernandez-Montero**

University of the Basque Country  
(UPV/EHU)  
School of Engineering  
Department of Mining-Metallurgy  
Engineering & Materials Science  
POLYMAT – Basque Center for  
Macromolecular Design and  
Engineering  
Alameda de Urquijo s/n.  
48013 Bilbao  
Spain

**Vahid Karimkhani**

Amirkabir University of Technology  
Department of Polymer Engineering  
and Color Technology  
Tehran  
Iran

and

Case Western Reserve University  
Department of Macromolecular  
Science and Engineering  
2100 Adelbert Road  
Cleveland, OH 44106  
USA

**David Kazmer**

University of Massachusetts at Lowell  
Department of Plastics Engineering  
1 University Avenue  
Lowell, MA 01854  
USA

**Michael R. Kessler**

Washington State University  
School of Mechanical and Materials  
Engineering  
Pullman, WA 99164  
USA

**Éva Kiss**

Eötvös Loránd University  
Institute of Chemistry  
Laboratory of Interfaces and  
Nanostructures  
Pázmány P. s. 1/a  
1117 Budapest  
Hungary

**Krzysztof Kruczała**

Jagiellonian University  
Faculty of Chemistry  
Ul. Ingardenia 3/139  
30-060 Krakow  
Poland

**Jae Wook Lee**

Sogang University  
Department of Chemical and  
Biomolecular Engineering  
Applied Rheology Center  
Seoul 121-742  
Korea

**Sangmook Lee**

Dankook University  
Division of Chemical Engineering  
126, Jukjeon-dong, Suji-gu  
Gyeonggi-do 448-701  
Korea

**Samy A. Madbouly**

Iowa State University  
Department of Materials Science and  
Engineering  
Ames, IA 50011  
USA

and

Cairo University  
Faculty of Science  
Department of Chemistry  
Orman-Giza 12613  
Egypt

**Alfonso Martínez-Felipe**

Universitat Politècnica de València  
Instituto de Tecnología de Materiales  
Camino de Vera, s/n  
46022 València  
Spain

**Emilio Meaurio**

University of the Basque Country  
(UPV/EHU)  
School of Engineering  
Department of Mining-Metallurgy  
Engineering & Materials Science  
POLYMAT – Basque Center for  
Macromolecular Design and  
Engineering  
Alameda de Urquijo s/n.  
48013 Bilbao  
Spain

**Kasylda Milczewska**

Poznan University of Technology  
Institute of Chemical Technology and  
Engineering  
pl. M. Skłodowskiej-Curie 2  
60-965 Poznan  
Poland

**Jorge Morgado**

Instituto de Telecomunicações  
Av. Rovisco Pais  
1049-001 Lisbon  
Portugal

and

Instituto Superior Técnico  
Department of Bioengineering  
UL, Av. Rovisco Pais  
1049-001 Lisbon  
Portugal

**Kell Mortensen**

University of Copenhagen  
Niels Bohr Institute  
Universitetsparken 5, D306  
2100 Copenhagen  
Denmark

**Yukihiro Ozaki**

Kwansei Gakuin University  
School of Science and Technology  
Sanda  
Hyogo 669-1337  
Japan

**Jyotishkumar Parameswaranpillai**

Cochin University of Science and  
Technology  
Department of Polymer Science and  
Rubber Technology  
Cochin  
Kerala 682022  
India

**R. Shanti Rajantharan**

University of Malaya  
Faculty of Science  
Department of Physics  
Centre for Ionics University of  
Malaya  
Jalan Lembah Pantai  
50603 Kuala Lumpur  
Malaysia

**Muruganathan Ramanathan**

Oak Ridge National Laboratory  
Center for Nanophase Materials  
Sciences  
One Bethel Valley Rd  
Oak Ridge, TN 37831  
USA

**Chikkakuntappa Ranganathaiah**

University of Mysore  
Department of Studies in Physics  
Manasagangotri  
Mysore 570006  
India

and

University of Western Australia  
School of Physics  
ARC Center of Excellence – Center  
for Antimatter-Matter Studies  
35 Stirling Highway Crawley  
Perth WA 6009  
Australia

**Ufana Riaz**

Jamia Millia Islamia (A Central  
University)  
Department of Chemistry  
Materials Research Laboratory  
Maulana Mohammad Ali Jauhar  
Marg  
New Delhi 110025  
India

**Amparo Ribes-Greus**

Universitat Politècnica de València  
Instituto de Tecnología de Materiales  
Camino de Vera, s/n  
46022 València  
Spain

**Fatemeh Sabzi**

Shiraz University of Technology  
Department of Chemical  
Engineering  
Modarres Blv.  
Shiraz 71555-313  
Iran



**Laura Santonja-Blasco**

Universitat Politècnica de València  
 Instituto de Tecnología de Materiales  
 Camino de Vera, s/n  
 46022 València  
 Spain

**Jose-Ramon Sarasua**

University of the Basque Country  
 (UPV/EHU)  
 School of Engineering  
 Department of Mining-Metallurgy  
 Engineering & Materials Science  
 POLYMAT – Basque Center for  
 Macromolecular Design and  
 Engineering  
 Alameda de Urquijo s/n.  
 48013 Bilbao  
 Spain

**Harumi Sato**

Kobe University  
 Graduate School of Human  
 Development and Environment  
 Nada-ku  
 Kobe  
 Hyogo 657–8501  
 Japan

**Yingrui Shang**

Tianjin University  
 College of Material Science and  
 Engineering  
 Department of Polymer Science and  
 Engineering  
 Tianjin  
 China

**Jitendra Sharma**

Shri Mata Vaishno Devi University  
 School of Physics  
 Kakriyal Katra  
 Reasi  
 Jammu & Kashmir 182320  
 India

**Suchart Siengchin**

King Mongkut's University of  
 Technology North Bangkok  
 The Sirindhorn International  
 Thai-German Graduate School of  
 Engineering (TGGS)  
 Department of Mechanical and  
 Process Engineering  
 1518 Wongsawang Road  
 Bangsue  
 Bangkok 10800  
 Thailand

**Heinz W. Siesler**

University of Duisburg-Essen  
 Department of Physical Chemistry  
 Schuetzenbahn 70  
 45117 Essen  
 Germany

**Zdeněk Starý**

Friedrich-Alexander-University  
 Erlangen-Nuremberg  
 Institute of Polymer Materials  
 Martensstrasse 7  
 91058 Erlangen  
 Germany

**Ramesh T. Subramaniam**

University of Malaya  
 Faculty of Science  
 Department of Physics  
 Centre for Ionics University of  
 Malaya  
 Jalan Lembah Pantai  
 50603 Kuala Lumpur  
 Malaysia

**Petr Svoboda**

Tomas Bata University in Zlin  
Faculty of Technology  
Department of Polymer Engineering  
Nam. T. G. Masaryka 275  
762 72 Zlin  
Czech Republic

and

Tomas Bata University in Zlin  
University Institute  
Centre of Polymer Systems  
Nad Ovcirnou 3685  
760 01 Zlin  
Czech Republic

**Ewa Szajdzińska-Piętek**

Jagiellonian University  
Faculty of Chemistry  
Ul. Ingardenia 3/139  
30-060 Krakow  
Poland

**Sabu Thomas**

Mahatma Gandhi University  
International and Interuniversity  
Centre for Nanoscience &  
Nanotechnology  
Priyadarshini Hills  
Kottayam  
Kerala 686560  
India

**Vanna Torrisi**

University of Catania and CSGI  
Department of Chemical Sciences  
Laboratory for Molecular Surfaces  
and Nanotechnology (LAMSUN)  
Viale A. Doria 6  
95125 Catania  
Italy

**Miriam Unger**

CETICS Healthcare Technologies  
GmbH  
Schelztorstraße 54–56  
Esslingen am Neckar  
Germany

**Adam Voelkel**

Poznan University of Technology  
Institute of Chemical Technology and  
Engineering  
pl. M. Skłodowskiej-Curie 2  
60-965 Poznan  
Poland

**Yingfeng Yu**

Fudan University  
Department of Macromolecular  
Science  
State Key Laboratory of Molecular  
Engineering of Polymers  
Shanghai 200433  
China

**Ester Zuza**

University of the Basque Country  
(UPV/EHU)  
School of Engineering  
Department of Mining-Metallurgy  
Engineering & Materials Science  
POLYMAT – Basque Center for  
Macromolecular Design and  
Engineering  
Alameda de Urquijo s/n.  
48013 Bilbao  
Spain

## 1

**Polymer Blends: State of the Art, New Challenges, and Opportunities**

*Jyotishkumar Parameswaranpillai, Sabu Thomas, and Yves Grohens*

## 1.1

**Introduction**

A polymer blend is a mixture of two or more polymers that have been blended together to create a new material with different physical properties. Generally, there are five main types of polymer blend: thermoplastic–thermoplastic blends; thermoplastic–rubber blends; thermoplastic–thermosetting blends; rubber–thermosetting blends; and polymer–filler blends, all of which have been extensively studied. Polymer blending has attracted much attention as an easy and cost-effective method of developing polymeric materials that have versatility for commercial applications. In other words, the properties of the blends can be manipulated according to their end use by correct selection of the component polymers [1]. Today, the market pressure is so high that producers of plastics need to provide better and more economic materials with superior combinations of properties as a replacement for the traditional metals and polymers. Although, plastic raw materials are more costly than metals in terms of weight, they are more economical in terms of the product cost. Moreover, polymers are corrosion-resistant, possess a light weight with good toughness (which is important for good fuel economy in automobiles and aerospace applications), and are used for creating a wide range of goods that include household plastic products, automotive interior and exterior components, biomedical devices, and aerospace applications [2].

The development and commercialization of new polymer usually requires many years and is also extremely costly. However, by employing a polymer blending process – which is also very cheap to operate – it is often possible to reduce the time to commercialization to perhaps two to three years [2]. As part of the replacement of traditional polymers, the production of polymer blends represents half of all plastics produced in 2010. Today, the polymer industry is becoming increasingly sophisticated, with ultra-high-performance injection molding machines and extruders available that allow phase-separations and viscosity changes to be effectively detected or manipulated during the processing stages [3]. Whilst this modern blending technology can also greatly extend the performance capabilities of

polymer blends, increasing market pressure now determines that, for specific applications, polymer blends must perform under some specific conditions (e.g., mechanical, chemical, thermal, electrical). This presents a major challenge as the materials must often function at the limit of the properties that can be achieved; consequently, in-depth studies of the properties and performance of polymer blends are essential.

## 1.2

### Miscible and Immiscible Polymer Blends

Generally, polymer blends are classified into either homogeneous (miscible on a molecular level) or heterogeneous (immiscible) blends. For example, poly(styrene) (PS)–poly(phenylene oxide) (PPO) and poly(styrene-acrylonitrile) (SAN)–poly(methyl methacrylate) (PMMA) are miscible blends, while poly(propylene) (PP)–PS and poly(propylene)–poly(ethylene) (PE) are immiscible blends. Miscible (single-phase) blends are usually optically transparent and are homogeneous to the polymer segmental level. Single-phase blends also undergo phase separation that is usually brought about by variations in temperature, pressure, or in the composition of the mixture.

Since, ultimately, the properties of a polymer blend will depend on the final morphology, various research groups have recently undertaken extensive studies of the miscibility and phase behavior of polymer blends. In practice, the physical properties of interest are found either by miscible pairs or by a heterogeneous system, depending on the type of application. Generally, polymer blends can be completely miscible, partially miscible or immiscible, depending on the value of  $\Delta G_m$  [4].

The free energy of mixing is given by

$$\Delta G_m = \Delta H_m - T\Delta S_m \quad (1.1)$$

For miscibility (binary blend), the following two conditions must be satisfied: the first condition  $\Delta G_m < 0$ ; and the second condition

$$\left( \frac{\partial^2(\Delta G_m)}{\partial \phi_i^2} \right)_{T,p} > 0 \quad (1.2)$$

where  $\Delta G_m$  is the Gibbs energy of mixing,  $\phi$  is the composition, where  $\phi$  is usually taken as the volume fraction of one of the components.

$\Delta S_m$  is the entropy factor and is a measure of disorder or randomness, is always positive and, therefore, is favorable for mixing or miscibility especially for low-molecular-weight solutions. In contrast, polymer solutions have monomers with a high molecular weight and hence the enthalpy of mixing ( $\Delta H_m$ ) is also a deciding factor for miscibility.  $\Delta H_m$  is the heat that is either consumed (endothermic) or generated (exothermic) during mixing. If the mixing is exothermic then the system is driven towards miscibility. The mixing is exothermic only when strong specific interactions occur between the blend components. The most common specific interactions found in polymer blends are hydrogen bonding,

dipole–dipole, and ionic interactions. Several techniques that can be used to understand the specific interaction in polymers, such as Fourier transform infrared (FTIR) spectroscopy, small-angle neutron scattering, ellipsometry, neutron reflectivity, and nuclear magnetic resonance (NMR) spectroscopy.

Experimentally observed phase diagrams in polymer blend systems may be lower critical solution temperature (LCST), upper critical solution temperature (UCST), combined UCST and LCST, hourglass-, and/or closed-loop-shaped. The most commonly observed phase diagrams are LCST (phase separation of a miscible blend during heating) and UCST (phase separation of a miscible blend during cooling). Phase separation in polymer solutions may proceed either by nucleation and growth (NG) or by spinodal decomposition (SD), or by the combination of both [5]. Experimentally, phase separation can be followed by a number of experimental techniques that include light scattering, neutron scattering, ellipsometry, and rheology. The generated morphology can be characterized using scanning electron microscopy (SEM), atomic force microscopy (AFM), transmission electron microscopy (TEM) fluorescence microscopy, infrared, near-infrared and Raman imaging, and confocal microscopy.

### 1.3

#### Compatibility in Polymer Blends

In general, the compatibility between the polymer phases decides the properties of a heterogeneous polymer blend [6,7]. The interface between the polymer phases in a polymer system is characterized by the interfacial tension which, when approaching zero, causes the blend to become miscible. In other words, if there are strong interactions between the phases then the polymer blend will be miscible in nature. Large interfacial tensions lead to phase separation, with the phase-separated particles perhaps undergoing coalescence; this will result in an increased particle size and, in turn, decreased mechanical properties. The interfacial tension can be reduced by the addition of interfacial agents known as compatibilizers [8]; these are generally molecules with hydrophobic and hydrophilic regions that can be aligned along the interfaces between the two polymer phases, causing the interfacial tension to be reduced and the compatibility of the polymer blends to be increased. Compatibility results in a reduction of the dispersed particle size, an enhanced phase stability, and increased mechanical properties [8]. The physical properties of miscible, compatibilized and uncompatibilized blends can be characterized using techniques such as thermogravimetric analysis, dynamic mechanical thermal analysis, and universal testing machines.

### 1.4

#### Topics Covered in this Book

The following chapters in this book provide a comprehensive overview on the miscibility, phase separation, morphology and other fundamental properties of

polymer blends, using a wide range of state-of-the-art techniques. For example, Chapter 2 relates to the miscibility of polymer blends, and provides an overview of the theory behind the phase separation of polymer blends, with specific examples. Chapter 3 describes the compatibility of polymer blends and discusses the influence of compatibilizers on phase morphology and structural properties. Chapter 4 provides a comprehensive review of the rheological properties of thermosetting blends and composites, while Chapter 5 provides details of the light scattering of polymer blends and outlines the theory and applications of light-scattering techniques for studying the phase behavior of polymer blends. In Chapter 6, a survey is provided of the characterization of polymer blends, using X-ray scattering techniques, while Chapter 7 details the basis for using neutron scattering when studying the phase behavior of polymer blends and block copolymer systems. In Chapter 8, the applications of ultrasound on polymer blends are reviewed; these include the characterization of polymer blends, polymer modification, property enhancement and the monitoring of polymer processing. The theories and applications of ellipsometry on polymer blends are discussed in Chapter 9, applications include phase separation, morphology, nanoporosity, adhesive and adsorption properties. Chapter 10 discusses the theories and applications of inverse gas chromatography on polymer blend systems; the advantages and drawbacks of inverse gas chromatography are also discussed in detail. In Chapter 11, the thermal stability of polymer blends is discussed, outlining the changes in thermal stability by blending, together with some specific examples. The application of dynamic mechanical thermal analysis (DMTA) for the study of polymer blends is described in Chapter 12, together with details of the theoretical bases underlying viscoelastic theory, the study of segmental dynamics, free volume and dynamic fragility, and the study of miscibility or the effect of adding plasticizers and chemical or physical crosslinkers. An overview of the thermomechanical properties of polymer blends is provided in Chapter 13, where the importance of particle size on polymer toughening is stressed. Chapter 14 provides a comprehensive review on water sorption and solvent sorption behavior that can be expected from miscible or immiscible but compatible polymer blends. The authors of this chapter concluded that miscibility depends on the molecular structures of the both polymers, morphologies and blend composition, as well as the processes of the blends. Numerical simulation models and methods for polymer blends are covered in Chapter 15, while Chapter 16 deals with the latest microscopic techniques that have the capability to observe the three-dimensional structural details in polymer blend films. In Chapter 17, the morphologies of different types of polymer blends investigated by various microscopic techniques are discussed, with special reference to sample preparation and comparison among SEM, TEM and AFM. In Chapter 18, the most sensitive surface technique, namely secondary ion mass spectrometry (SIMS), is described, which allows molecular and highly spatially resolved lateral information to be obtained. In Chapter 19, the authors discuss the morphology of different types of polymer blends, using fluorescence microscopy to determine the quantitative spatial distribution and molecular information of the polymer components. In Chapter 20, the potential of FTIR techniques for

determining the properties of polymers blends both quantitatively and qualitatively is highlighted, while in Chapter 21 hydrogen-bonding interactions between the polymer components, determined using NMR spectroscopy, are discussed. Chapter 22 provides details of the phase morphology of polymer blends using infrared, near-infrared and Raman imaging, while in Chapter 23 the application of, and recent advances in, the characterization of polymer blends using electron spin resonance (ESR) spectroscopy and forward recoil spectroscopy, are discussed. In Chapter 24, attention is focused on the optical properties of polymer blends, in both ultraviolet and visible ranges of light, to investigate the miscibility of polymer blends, while Chapter 25 focuses on the driving forces that produce miscibility in polymer blends, using fluorescence spectroscopy. Chapter 26 provides a comprehensive overview of recent developments and progress in the molecular dynamics, miscibility, nature of interaction, crystallization behavior, and curing kinetics of representative examples of polymer blends using dielectric relaxation spectroscopy (DRS) and thermally stimulated depolarization current (TSDC) techniques. Finally, in Chapter 27 attention is focused on the miscibility of polymer blends, using positron annihilation spectroscopy.

## References

- 1 Paul, D.R. (1989) Control of phase structure in polymer blends, in *Functional Polymers* (eds D.E. Bergbreiter and C.R. Martin), Plenum Press, New York, p. 1–18.
- 2 Scobbo, J.J., Jr and Goettler, L.A. (2003) Applications of polymer alloys and blends, in *Polymer Blends Handbook* (ed. L.A. Utracki), Kluwer Academic Publishers, pp. 951–976.
- 3 White, J.L. and Bumm, S.H. (2011) Polymer blend compounding and processing, in *Encyclopedia of Polymer Blends* (eds A.I. Isayev and S. Palsule), Wiley-VCH, Weinheim, pp. 1–26.
- 4 Flory, P.J. (1953) *Principles of Polymer Chemistry*, Cornell University Press, New York.
- 5 Jyotishkumar, P., Ozdilek, C., Moldenaers, P., Sinturel, C., Janke, A., Pionteck, P., and Thomas, S. (2010) Dynamics of phase separation in poly(acrylonitrile-butadiene-styrene)-modified epoxy/DDS system: kinetics and viscoelastic effects. *J. Phys. Chem. B*, **114**, 13271–13281.
- 6 Jiang, R., Quirk, R.P., White, J.L., and Min, K. (1991) Polycarbonate-polystyrene block copolymers and their application as compatibilizing agents in polymer blends. *Polym. Eng. Sci.*, **31**, 1545.
- 7 George, S.M., Puglia, D., Kenny, J.M., Causin, V., Parameswaranpillai, J., and Thomas, S. (2013) Morphological and mechanical characterization of nanostructured thermosets from epoxy and styrene-block-butadiene-block-styrene triblock copolymer. *Ind. Eng. Chem. Res.*, **52** (26), 9121–9129.
- 8 Chen, C.C. and White, J.L. (1993) Compatibilizing agents in polymer blends: Interfacial tension, phase morphology, and mechanical properties. *Polym. Eng. Sci.*, **33**, 923–930.





## 2

### Miscible Blends Based on Biodegradable Polymers

*Emilio Meaurio, Natalia Hernandez-Montero, Ester Zuza, and Jose-Ramon Sarasua*

#### 2.1

##### Introduction

This review reports the advances in the field of biodegradable polymer blends with both natural and synthetic polymers. These materials have attracted industrial and academic attention because they can be tailored to improve certain properties, such as biocompatibility and biodegradability, to the specific requirements of the different applications in the biomedical, pharmaceutical and packaging fields. In addition, they can be produced using simple techniques. The present chapter is divided in two main sections following this brief introduction. The first section provides the necessary theoretical knowledge to understand the overall miscibility behaviors observed in real polymer blends. The thermodynamic theory presented here is based on the simple but highly flexible Flory–Huggins theory, incorporating the regular solution theory to account for the enthalpic contribution. This simple theoretical model is extended here with the appropriate approaches to systems presenting specific interactions, providing an overall general picture of the miscibility behavior of polymer blends. The second section reviews the structure, preparation, miscibility and properties of different biodegradable polymer blends investigated up to now. Particularly, the biodegradable blends based on polylactides have been thoroughly revisited and discussed in great detail. In addition, the miscibility behavior of other commercially available biopolymers of great interest such as poly( $\epsilon$ -caprolactone) (PCL), poly(3-hydroxybutyrate) (PHB), poly(*p*-dioxanone) (PPDO) and polyglycolide (PGA) is also briefly reviewed. Finally, Appendix 2.A shows a short outline of the research works used to develop the miscibility study presented here, recapping the chemical structures of the polymers, their solubility parameters and brief comments summarizing the research works.

## 2.2

### Thermodynamic Approach to the Miscibility of Polymer Blends

#### 2.2.1

##### Introduction

Both in case of low-molecular-weight mixtures or polymer blends, the equilibrium phase behavior is determined by the free energy of mixing of the system,  $\Delta G_m$ :

$$\Delta G_m = \Delta H_m - T\Delta S_m \quad (2.1)$$

where  $\Delta H_m$  is the enthalpy of mixing,  $\Delta S_m$  is the entropy of mixing and  $T$  is the temperature [1–3]. To observe a single-phase system, the following two conditions must be fulfilled: first  $\Delta G_m < 0$  and second:

$$\left( \frac{\partial^2(\Delta G_m)}{\partial \phi_i^2} \right)_{T,p} > 0 \quad (2.2)$$

where  $\phi_i$  represents the volume fraction of component  $i$ . The last condition assures a concave upward  $\Delta G_m$  versus  $\phi_i$  curve at any composition, assuring the stability of the system and preventing phase separation [1–3].

#### 2.2.2

##### Molecular Size and Entropy

Historically, the simplest miscible system has been the mixture of *ideal gases*, consisting on noninteracting point particles. This system can be analyzed using simple arguments based on classical thermodynamics [1]. The enthalpy of mixing is zero ( $\Delta H_m = 0$ ) and the entropy of mixing ( $\Delta S_m$ ) is given by:

$$\Delta S_m = -R(n_1 \ln x_1 + n_2 \ln x_2) \quad (2.3)$$

where  $n_i$  is the number of moles of the  $i$ -th component,  $x_i$  is the molar fraction, and  $R$  is the ideal gas constant [1].

Equation (2.3) also works properly for mixtures of nonpolar solvents of similar molecular volume, and is considered the classical expression for the entropy of mixing of *ideal* solutions [1]. These solutions present random molecular mixing, and Eq. (2.3) can actually be derived from the statistical thermodynamic analysis of a lattice model randomly filled with spheres of identical size [4,5]. In addition, in an *ideal* solution the average strength of the intermolecular interactions between the components of the mixture is identical to the average strength of the interactions occurring between the pure components [1]. Therefore, the enthalpy of mixing in these systems is zero ( $\Delta H_m = 0$ ) and miscibility arises from the entropic contribution to the free energy of mixing ( $\Delta G_m = -T\Delta S_m$ ).

Investigations dealing with the thermodynamic properties of polymer solutions revealed that Eq. (2.3) underestimates  $\Delta S_m$  in these systems, and is not valid for mixtures of compounds with grossly different molar volumes [6]. The statistical

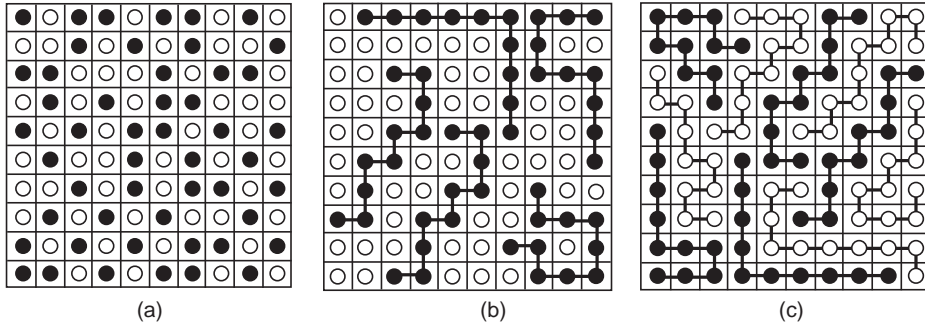


**Figure 2.1** (a) Lattice with random mixing of two types of sphere ( $10^{30}$  possible combinations); (b) Lattice with random mixing of polymer and solvent ( $10^{16}$  combinations); (c) Lattice with random mixing of two types of polymer chain ( $10^3$  combinations).

thermodynamic analysis of such solutions was carried out by Flory–Huggins, using a simple lattice representation for the polymer solution and calculating the total number of ways the lattice can be occupied by small molecules and by connected polymer segments,  $\Omega$  (see Figure 2.1b) [2,6,7]. In this model, each lattice site accounts for a solvent molecule or a polymer segment with the same volume as the solvent molecule (not necessarily the repeat unit of the polymer). The entropy of mixing and the total number of arrangements  $\Omega$  are related according to Boltzmann's law:

$$\Delta S_m = k \ln \Omega \quad (2.4)$$

where  $k$  is the Boltzmann constant. The Flory–Huggins analysis assumes a random arrangement for the chain segments (equal probabilities for all the configurations). The final expression for the entropy of mixing is [2,6]:

$$\Delta S_m = -R(n_1 \ln \phi_1 + n_2 \ln \phi_2) \quad (2.5)$$

Equation (2.5) is apparently very similar to the classical *ideal* Eq. (2.3). The only difference is that volume fractions,  $\phi_i$ , replace mole fractions,  $x_i$ . This apparently subtle change is actually crucial to account for the effect on the entropy of mixing associated to the large difference of molecular size between the molecules of the solvent and the polymer. This effect is best understood with the aid of examples based on the lattice models in Figure 2.1. Figure 2.1a–c represent a mixture of solvent molecules, a polymer solution, and a polymer blend respectively, in all cases being  $\phi_1 = \phi_2 = 0.5$ . According to Eqs (2.4) and (2.5), in the Flory–Huggins treatment the number of microstates for the lattice models in Figure 2.1 can be obtained from  $\ln \Omega = -(N_1 \ln \phi_1 + N_2 \ln \phi_2)$ , where  $N_i$  is the number of molecules. In case of the lattice representing the solvent mixture (Figure 2.1a),  $N_1 = N_2 = 50$ , and  $\Omega \approx 10^{30}$ . In case of the lattice representing the polymer solution (Figure 2.1b),  $N_1 = 50$ ,  $N_2 = 5$ ; therefore,  $\Omega \approx 10^{16}$ . The reduction in the number of microstates is a consequence of reducing the total amount of molecules in the system ( $\Delta S_m \propto N_i$ ) as a consequence of introducing larger molecules. Note that if

molar fractions (present in the “classical” Eq. (2.3)) were used instead of volume fractions, the number of microstates calculated would be noticeably reduced ( $x_1 = 50/55$ ,  $x_2 = 5/55$ ,  $\Omega \approx 10^7$ ). The main reason for this discrepancy is that in the lattice models of the Flory–Huggins theory, solvent molecules can be allocated in a total of 100 lattice sites (even though only 50 sites are occupied at the same time); the large number of cells available being due to the large size of the polymer molecules. In this respect, the “classical” calculation actually assumes that the solvent molecules can only be distributed among a total of 55 sites. These simple calculations indicate, in agreement with experimental measurements, that adding solvent molecules to big molecules adds more entropy to the system than that predicted by the “classical” model [6]. Finally, Figure 2.1c represents a polymer blend with  $N_1 = N_2 = 5$ , therefore  $\Omega \approx 10^3$ . For this last system the number of microstates is further reduced, and because the blend contains molecules of identical size, volume fractions and molar fractions are equivalent and the “classical” and the Flory–Huggins models predict the same number of microstates. Hence, the Flory–Huggins model predicts the same  $\Omega$  for the system in Figure 2.1c as the one predicted by the “classical” equation for one blend containing spherical molecules of the same size as the polymer molecules. This implies that the Flory–Huggins model does not account for any conformational contribution to the entropy (arising from the different conformations accessible to the flexible polymer chains in Figure 2.1c); it only accounts for the so-called combinatorial entropy (also referred to as “translational entropy”), that is, the entropy resulting from all the possible combinations for the centers of masses of the molecules.

### 2.2.3

#### The Regular Solution

In real solutions, the thermodynamic magnitudes  $\Delta G_m$ ,  $\Delta H_m$  and  $\Delta S_m$ , deviate from the *ideal* values, and the excess functions can be defined as the difference between the real values and the ideal values. For example, the excess enthalpy is [1]:

$$H^E = \Delta H_{m,real} - \Delta H_{m,ideal} \quad (2.6)$$

A case of particular interest is the so-called *regular solution*, a mixture in which the excess entropy and the excess volume are zero, but the average interactions in the blend are different from those in the pure components. Since  $S^E = 0$ , the *regular solution* maintains the random molecular order of the ideal solution. In addition,  $V^E = 0$  implies that the volume of mixing is also zero ( $\Delta V_m = 0$ ) and for a mixing process at constant pressure enthalpies can be equated to internal energies; hence, the enthalpy of mixing,  $\Delta H_m$ , can be calculated according to:

$$\Delta H_m = \Delta E_m = E_f - E_o = E_m - E_1 - E_2 \quad (2.7)$$

where  $\Delta E_m$  is the internal energy of mixing,  $E_m$  is the internal energy of the mixture, and  $E_i$  are the internal energies of the pure components. Considering an

isothermal process, the internal energy contributions associated to internal motions (such as vibrational or rotational motions) can be excluded from the calculation as they should be unaffected by the mixing process [1]. The only relevant contributions are therefore those associated to the intermolecular interactions. For simplicity, consider the lattice in Figure 2.1a representing a mixture of low-molecular-weight compounds [2–5]. In this lattice model, each solute segment is surrounded on average by  $\phi_1 z$  neighbors of solvent molecules (where  $z$  is the coordination number of the lattice and solvent is component-1), and by  $\phi_2 z$  neighbors of solute molecules (solute is component-2). Since the total number of sites in the lattice is  $n_0$ , the lattice contains  $n_0 \phi_2$  solute segments each interacting in this manner, hence, the total number of 1–2 contacts is  $n_0 \phi_2 \phi_1 z$  and the total number of 2–2 contacts is  $\frac{1}{2} n_0 \phi_2 \phi_2 z$  (the factor  $\frac{1}{2}$  enters here to avoid counting each contact twice; one time per molecule participating in the 2–2 contact). Similarly, the total number of 1–1 contacts is  $\frac{1}{2} n_0 \phi_1 \phi_1 z$ . Regarding the initial pure solutions, the lattice representing the pure solvent contains  $n_0 \phi_1$  molecules and  $\frac{1}{2} n_0 \phi_1 z$  1–1 contacts (the factor  $\frac{1}{2}$  avoids again counting each contact twice), while the lattice representing the pure solute contains similarly  $\frac{1}{2} n_0 \phi_2 z$  2–2 contacts. Defining  $w$  as the attractive energy corresponding to each contact,  $\Delta H_m$  is therefore:

$$\Delta H_m = n_0 \phi_1 \phi_2 z w_{12} + \frac{1}{2} n_0 \phi_1^2 z w_{11} + \frac{1}{2} n_0 \phi_2^2 z w_{22} - \frac{1}{2} n_0 \phi_1 z w_{11} - \frac{1}{2} n_0 \phi_2 z w_{22} \quad (2.8)$$

and recalling that  $\phi_1 + \phi_2 = 1$ , Eq. (2.8) can be simplified to:

$$\Delta H_m = n_0 \phi_1 \phi_2 z w_{12} - \frac{1}{2} n_0 \phi_1 \phi_2 z w_{11} - \frac{1}{2} n_0 \phi_1 \phi_2 z w_{22} \quad (2.9)$$

The simplification step from Eq. (2.8) to Eq. 2.9 eliminates the contributions due to the autoassociation contacts occurring in the mixture (second and third terms in the right-hand side of Eq. (2.8)) with identical terms arising from the pure components. Therefore, only the contacts that are actually modified (broken or formed) contribute to  $\Delta H_m$  in Eq. (2.9); and the enthalpy of mixing is the energetic balance corresponding to the process of breaking identical amounts of 1–1 and 2–2 contacts and replacing them by 1–2 contacts [2–5].

According to Eq. (2.9), the formation of each 1–2 contact involves breaking half 1–1 and half 2–2 contacts on average. The *interaction energy* corresponding to the formation of each 1–2 contact,  $\Delta w_{12}$ , is defined according to [2–5]:

$$\Delta w_{12} = w_{12} - \frac{1}{2} w_{11} - \frac{1}{2} w_{22} \quad (2.10)$$

and the enthalpy of mixing corresponding to the regular solution is therefore:

$$\Delta H_m = n_0 z \phi_1 \phi_2 \Delta w_{12} = \frac{V}{V_r} z \phi_1 \phi_2 \Delta w_{12} \quad (2.11)$$

where  $n_0 = V/V_r$  ( $V$  is the total volume of the lattice and  $V_r$  is the molar volume of the lattice sites) has been considered. All the constant terms in Eq. (2.11) can be included in a new constant term,  $B$ :

$$B = \frac{z\Delta w_{12}}{V_r} \quad (2.12)$$

$B$  is the product of the interaction energy corresponding to each 1–2 contact ( $\Delta w_{12}$ ) by the density of contacts (the quotient  $z/V_r$ ), and is termed the *interaction energy density*.  $B$  represents the interaction energy density achieved by the solute lattice sites at infinite dilution (when they are exclusively surrounded by solvent molecules and can establish  $z$  1–2 contact). It is therefore a property of the system independent of the lattice parameters. This can be rationalized considering for example the case of  $n$ -alkanes in solution: choosing two methylene units ( $-\text{CH}_2-\text{CH}_2-$ ) as reference instead of one ( $-\text{CH}_2-$ ) reduces the density of lateral contacts by half, but the interaction energy of each contact is doubled, and therefore  $B$  remains constant. In systems with dispersive interactions exclusively, and if the surface-to-volume ratios of the mixed molecules are similar (as they usually are in many organic systems),  $B$  is nearly constant with composition [8]. Finally, note that the product  $BV_r$  represents the *interaction energy per lattice site*, and can be used to compare the strength of the dispersive interactions between different systems, as long as the same (arbitrarily chosen)  $V_r$  value is used in all cases. The enthalpy of mixing,  $\Delta H_m$ , written in terms of  $B$  is:

$$\Delta H_m = BV\phi_1\phi_2 \quad (2.13)$$

This form of equation for the enthalpy of mixing is known as van Laar-type equation. In spite of being derived for a lattice filled with molecules of equal size, Eq. (2.13) also works correctly for mixtures of molecules of different size. For example, the enthalpy of mixing at infinite dilution calculated per mole of solute is  $\Delta H_\infty = BV_{02}$  (since  $B\phi_1 \approx B$  and  $V\phi_2 = V_2$  in Eq. (2.13); in addition  $V_2 = V_{02}$  considering one mole of solute), indicating that  $\Delta H_\infty$  scales linearly with the molar volume of the solute,  $V_{02}$ . Following with the  $n$ -alkanes as an example, doubling the length of the solute doubles  $\Delta H_\infty$ , as expected.

Many nonelectrolyte solutions of small molecules obey approximately Eq. (2.13) [8]. Experimental studies have shown that the *regular* solution model is appropriate for binary mixtures *without specific interactions*, including systems containing polymer chains [8]. In general, specific interactions (hydrogen bond, charge transfer, etc.) modify molecular order and the free volume of the blend, affecting the dependence of the excess enthalpy with composition ((randomness was assumed in Eq. (2.13)), and modifying the excess entropy (no longer zero). Temperature dependences are also modified, as they become governed by the evolution of the interactions with temperature [8,9].

## 2.2.4

**The Flory–Huggins Model**

This theoretical model adopts the Flory–Huggins treatment for the entropy of mixing, Eq. (2.5), and the *regular* solution treatment for the enthalpy of mixing, Eq. (2.13), leading to the following expression for the Gibbs free energy of mixing [2]:

$$\Delta G_m = RT(n_1 \ln \phi_1 + n_2 \ln \phi_2) + BV\phi_1\phi_2 \quad (2.14)$$

Equation (2.14) can be considered a general expression valid for *regular* solutions, regardless of the size of the components (solvents or polymers). Note that the entropic term scales with the number of molecules, and the enthalpic term with the volume of the system; hence, both terms scale differently with the size of the system, and implicitly with the size of the molecules comprising the system. To explore the effect of these size-related aspects on  $\Delta G_m$ , Eq. (2.14) is rewritten as an intensive property, usually referenced to the volume corresponding to one mole of lattice sites,  $V_r$ . The number of lattice sites occupied by component  $i$  is given by its molar volume ratio,  $r_i$ , defined as:

$$r_i = \frac{V_i}{V_r} = \frac{M_i}{\rho_i V_r} = \frac{m_i M_{0i}}{\rho_i V_r} = \frac{m_i V_{0i}}{V_r} = m_i r_{0i} \quad (2.15)$$

where  $V_i$  is the molar volume of component  $i$ ,  $m_i$  is the polymerization degree ( $m_i = 1$  in the case of a solvent),  $V_{0i}$  is the molar volume of the repeat unit,  $M_{0i}$  is the molar mass of the repeat unit, and  $\rho_i$  is the density in the amorphous state. The total number of lattice cells occupied by the  $n_i$  moles of component  $i$  is  $r_i n_i$ , and its volume fraction is therefore:

$$\phi_i = \frac{r_i n_i}{n_0} \quad (2.16)$$

where  $n_0$  stands for the total number of lattice sites ( $n_0 = \sum r_i n_i$ ). Using Eqs (2.15) and (2.16), and recalling that  $n_0 = V/V_r$ , Eq. (2.14) can be rewritten as:

$$\frac{\Delta G_m}{n_0} = RT \left( \frac{\phi_1}{r_1} \ln \phi_1 + \frac{\phi_2}{r_2} \ln \phi_2 \right) + BV_r \phi_1 \phi_2 \quad (2.17)$$

Equation (2.17) provides  $\Delta G_m$  per mole of lattice sites, or *per  $V_r$  volume units of mixture*. It is valid for any type of *regular* solution, regardless of the difference in size between the components of the mixture. In Eq. (2.17), the entropic term is always negative ( $\ln \phi_i < 0$ , since  $\phi_i < 1$ ) and therefore favorable to the miscibility. The plot of this term versus composition is concave upwards for any system at any temperature. Miscibility depends therefore on the sign and magnitude of the enthalpic term. If  $B < 0$ , the enthalpic term is also concave upwards and the plot

of  $\Delta G_m$  versus composition maintains the same curvature, indicating complete miscibility (one single phase at any composition). However, in systems with  $B > 0$ , the enthalpic contribution is always positive and adopts a concave downwards curvature. As long as  $B$  is small enough, the curvature corresponding to the entropic term still dominates and the plot of  $\Delta G_m$  versus  $\phi$  still indicates complete miscibility. However, when  $B$  exceeds a certain critical value, the plot of  $\Delta G_m$  versus composition shows two minima, with one concave downwards central region, where phase separation occurs.

Phase separation begins at the critical conditions, when the two minima of the  $\Delta G_m$  versus  $\phi$  plot meet at the same point, and also meet the two inflection points limiting the concavity regions. Therefore, the following conditions apply [1–5]:

$$\frac{\partial^2(\Delta G_m)}{\partial \phi_A^2} = \frac{\partial^3(\Delta G_m)}{\partial \phi_A^3} = 0 \quad (2.18)$$

Applying Eqs (2.18) to (2.17), the following relationship is obtained for the critical conditions [2–5]:

$$BV_r = \frac{RT}{2} \left( \frac{1}{r_1^{1/2}} + \frac{1}{r_2^{1/2}} \right)^2 \quad (2.19)$$

Equation (2.19) relates the critical interaction energy  $(BV_r)_c$ , the critical temperature,  $T_c$ , and the critical molecular sizes,  $r_{ic}$  ((related to the critical polymerization degrees according to Eq. (2.15)). As can be seen, the critical interaction energy decreases with increasing molecular size, and Eq. (2.19) can be used to compare the ability of solvent solutions and polymer blends to form miscible systems. Assuming, for simplicity, that  $V_r = V_{01} = V_{02}$ , in case of a mixture of solvents at room temperature  $r_1 = r_2 = 1$  (since  $m_1 = m_2 = 1$  in the case of solvents), and  $(BV_r)_c = 2RT \approx 5 \text{ kJ mol}^{-1}$  according to Eq. (2.19). In the case of a solution of a high-molecular-weight polymer,  $m_1 = 1$  and  $1/(m_2)^{1/2} \approx 0$ , hence  $(BV_r)_c \approx (RT)/2 \approx 1.2 \text{ kJ mol}^{-1}$ . In this case, the unfavorable enthalpic contribution necessary to begin the phase separation is smaller, which explains why the amount of solvents available for high-molecular-weight polymers is reduced compared to low-molecular-weight substances. Finally, for a blend of high-molecular-weight polymers of identical degrees of polymerization ( $m_1 = m_2 = m$ ), Eq. (2.16) simplifies to  $(BV_r)_c = (2RT)/m$ . Assuming a typical degree of polymerization of about  $10^3$ , then  $(BV_r)_c = 0.005 \text{ kJ mol}^{-1}$ , and hence phase separation at room temperature already starts at extremely small repulsive interactions. Note that  $(BV_r)_c$  is reduced four times on passing from a solvent mixture to a polymer solution, but on passing to a polymer blend the critical interaction energy is reduced  $r$  times ( $10^3$  in this example). Hence, the occurrence of attractive specific interactions is usually considered a requirement to observe miscibility in polymer blends [8].

There is, however, another important difference between the low- and high-molecular-weight mixtures seldom discussed in the literature: according to the



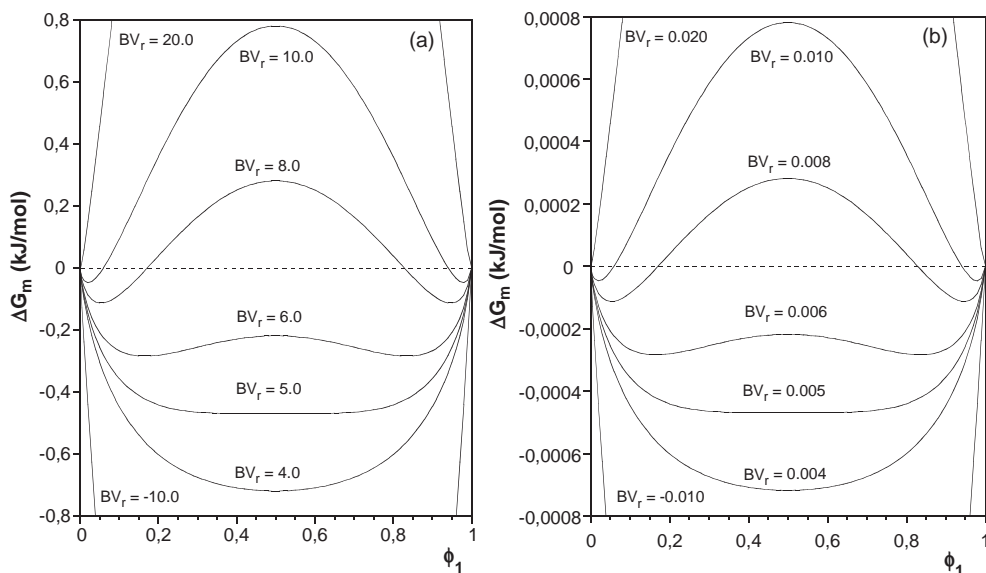


**Figure 2.2** Gibbs free energies of mixing versus composition for systems of different interaction energies ( $BV_r$ , kJ mol<sup>-1</sup>) calculated using the Flory–Huggins model (Eq. (2.17)).

(a) Mixtures of low-molecular-weight solvents of identical molar volume; (b) Blends of polymers of degree of polymerization  $m = 10^3$  and identical repeat unit molar volume.

Flory–Huggins theory, partial miscibility is also very improbable in polymer blends compared to low-molecular-weight mixtures. Figure 2.2 shows the Gibbs free energy of mixing versus composition for mixtures of two solvents, A and B; and for polymer blends with different interaction energies. As before, the systems are assumed to consist of components of equal  $V_0$  values. As can be seen in Figure 2.2a, solvent mixtures with  $BV_r = 6$  kJ mol<sup>-1</sup> and solvent feed compositions in the range 16–84 vol.% will phase separate in one A-rich phase containing about 84 vol.% A and in one B-rich phase containing about 16 vol.% A. However, if the interaction energy increases to  $BV_r = 10$  kJ mol<sup>-1</sup>, then the amount of the minority component in the two phases reduces to about 2 vol.%. There is a relatively wide range of molar interaction energies (from 5 kJ mol<sup>-1</sup> to ca. 10 kJ mol<sup>-1</sup>) for which partial miscibility can be claimed, and a number of systems can be found with  $BV_r$  values within this range; hence, partial miscibility is a rather frequent behavior. However, in the case of polymer blends, and assuming again  $m_1 = m_2 = 10^3$ , partial miscibility with phases containing the minority component in significant amounts can be observed only within a very narrow  $BV_r$  range (see Figure 2.2b), from  $BV_r = 0.005$  kJ mol<sup>-1</sup> to about 0.010 kJ mol<sup>-1</sup>. Increasing  $BV_r$  from 0.010 kJ mol<sup>-1</sup> to 0.020 kJ mol<sup>-1</sup> reduces the volume fraction of the minority component in the separated phases from two-hundredths to below one-thousandth, where immiscibility should be claimed. Therefore, according to the Flory–Huggins model, partial miscibility in polymer blends only occurs within an extremely narrow range of interaction

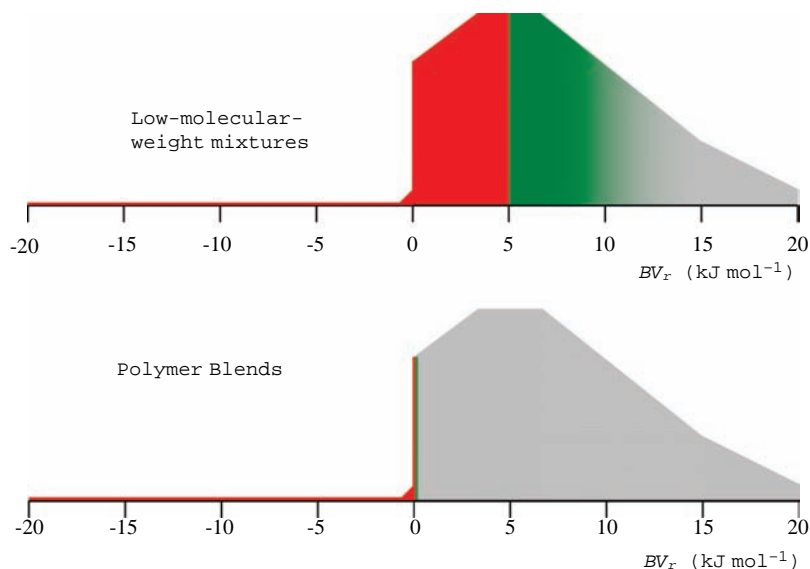


**Figure 2.3** Classification of the miscibility regions according to the interaction energy ( $BV_r$ ) intervals: miscible (red), partially miscible (green) and immiscible (gray) systems. The upper graph shows low-molecular-weight mixtures; the lower graph shows polymer blends (see text for details).

energies located next to the critical value (for the particular example considered here,  $BV_r$  ranges from 0.005 to about  $0.010 \text{ kJ mol}^{-1}$ ). Partial miscibility is therefore also a very rare phenomenon in polymer blends compared to low-molecular-weight compounds [10].

These ideas can be clarified by using the simple graphs in Figure 2.3, that classify the miscibility behavior of both low-molecular-weight mixtures and polymer blends according to their molar interaction energies ( $BV_r$ ). The red-colored regions indicate miscible systems, green-colored regions indicate partial miscibility, while gray regions indicate phase-separated systems. The graph heights have only qualitative validity, and are related to the probability of finding systems with the  $BV_r$  values in the abscissa (or to the number of systems actually possible). As can be seen, similar distributions of  $BV_r$  values have been assumed in both cases, since both polymers and their low-molecular-weight analogs exhibit intermolecular interactions of similar strength. Negative  $BV_r$  values can only be observed when the systems contain specific chemical groups capable of establishing attractive interactions that overcome the ubiquitous dispersive interactions (of repulsive nature) [8]. This is the principle of the so-called “complementary dissimilarity” [8], a fairly uncommon feature, and therefore the heights are small when  $BV_r < 0$ . Positive interaction energies will be observed in most cases. The areas of the red and green regions are related (qualitatively) to the probability of finding completely miscible and partially miscible systems, respectively. As can be

seen, both regions are strongly reduced in case of blends of homopolymers of high molecular weight (in this numeric example, to about one-thousandth). Therefore, not only miscibility but also partial miscibility can be considered the exception rather than the rule in the case of polymer blends [8,10].

Finally, in the Flory–Huggins treatment the strength of the interactions is frequently expressed in terms of the interaction parameter,  $\chi$ , defined by Flory as the ratio between the interaction energy and the thermal energy:

$$\chi = \frac{BV_r}{RT} \quad (2.20)$$

The Flory–Huggins equation is therefore:

$$\frac{\Delta G_m}{n_0} = RT \left( \frac{\phi_1}{r_1} \ln \phi_1 + \frac{\phi_2}{r_2} \ln \phi_2 + \chi \phi_1 \phi_2 \right) \quad (2.21)$$

Note that both the interaction energy,  $BV_r$ , and the interaction parameter,  $\chi$ , are proportional to the size of the system, or  $V_r$ . For example, for blends with polyethylene,  $V_r$  can be adopted as the molar volume of one methylene unit or as the molar volume of one dimethylene unit. Doubling  $V_r$  implies doubling  $BV_r$  and  $\chi$ . To allow comparisons in the strength of the interactions between different systems, some authors prefer to work with an arbitrarily chosen constant value for  $V_r$  instead of changing its value from one system to another [11].

### 2.2.5

#### The Hildebrand Approach

This approach estimates the strength of the dispersive interactions in mixtures of solvents, and is straightforwardly extended to mixtures involving polymers [8,9]. The *cohesive energy*,  $E_{coh}$ , is defined as the internal energy of vaporization ( $\Delta E_v$ ) from the liquid state to the ideal gas state (where intermolecular forces are suppressed). The energy necessary for this transformation is mainly spent pulling the molecules apart, since other molecular contributions to the total internal energy (such as vibrational energies, etc.) should remain unaffected because of the isothermal nature of the process. Therefore,  $E_{coh}$  is a measure of the intermolecular attractive energy, and for low-molecular-weight compounds it can be obtained from the enthalpy of vaporization ( $\Delta H_v$ ) according to:

$$E_{coh} = \Delta E_v = \Delta H_v - p\Delta V \approx \Delta H_v - RT \quad (2.22)$$

Cohesive energies are therefore positive since  $\Delta E_v > 0$ . The cohesive energy density (CED; Eq. (2.23)) is defined as the cohesive energy per unit volume, and measures the intermolecular attraction energy per unit volume in pure substances. In addition, the solubility parameter,  $\delta$ , is defined as the square-root of the cohesive energy density, ( $\delta = (\text{CED})^{1/2}$ ):

$$\delta^2 = \text{CED} = \frac{E_{coh}}{V} \quad (2.23)$$

Cohesive energy densities can be used to estimate the value of the interaction energy density,  $B$ , using the Hildebrand approach [9]. The total number of contacts in a lattice containing  $n_0$  lattice sites is  $\frac{1}{2}n_0z$  (the factor  $\frac{1}{2}$  avoids counting each contact twice), and the total attractive energy in the case of identical contacts is  $\frac{1}{2}n_0zw$ . Therefore, the CED of a pure substance  $i$  is related to the lattice parameters as follows:

$$\text{CED}_i = \frac{E_{coh}}{V} = -\frac{\frac{1}{2}n_0zw_{ii}}{n_0V_r} = -\frac{\frac{1}{2}zw_{ii}}{V_r} \quad (2.24)$$

The negative sign is introduced because the interaction energies are negative but the CEDs are positive (see Eq. (2.23)). As can be seen, the CED of a pure component provides the energy density of the autoassociation contacts, terms that already appeared when calculating the interaction energy density,  $B$  (see Eq. (2.12)). Unfortunately, the energy density for the interassociation contacts cannot be measured since, in addition to the 1–2 contacts, real mixtures always contain 1–1 and 2–2 contacts. This issue is overcome using the Hildebrand approach, assuming that the 1–2 attractive energy can be estimated as the geometric mean of the attractive energies of the pure components ( $w_{12} = (w_{11}w_{22})^{\frac{1}{2}}$ ) [9]. Therefore, the CED that would be obtained from a hypothetical mixture containing exclusively 1–2 contacts (denoted as  $\text{CED}_{12}$ ) can be estimated according to:

$$\text{CED}_{12} = -\frac{\frac{1}{2}zw_{12}}{V_r} \approx -\frac{\frac{1}{2}z(w_{11}w_{22})^{\frac{1}{2}}}{V_r} = (\text{CED}_1)^{\frac{1}{2}}(\text{CED}_2)^{\frac{1}{2}} \quad (2.25)$$

Substituting the values of the attractive energy densities in terms of the CEDs of the pure components in the definition of  $B$  (Eq. (2.12)), and recalling that  $\delta^2 = \text{CED}$ :

$$B = \text{CED}_1 + \text{CED}_2 - 2(\text{CED}_1)^{\frac{1}{2}}(\text{CED}_2)^{\frac{1}{2}} = (\delta_1 - \delta_2)^2 \quad (2.26)$$

Substituting in Eq. (2.13), the enthalpy of mixing can be estimated according to:

$$\frac{\Delta H_m}{V} = \phi_1\phi_2(\delta_1 - \delta_2)^2 \quad (2.27)$$

This equation indicates that the contribution of the dispersive interactions to the enthalpy of mixing is always positive, and therefore unfavorable to miscibility [8,9].

Unfortunately, polymers are nonvolatile compounds, and solubility parameters cannot be obtained directly from the enthalpies of vaporization. Several indirect methods, such as swelling measurements, inverse gas chromatography and solubility testing, can be used to measure the  $\delta$  values [12]. In addition, different group contribution methods have been developed to estimate their solubility parameters [13]. Due to the wide range of methods available, and to the errors associated with each method, values found in the literature usually extend over a rather wide range [12]. Among the different experimental methods available to obtain  $\delta$  values, solubility testing is usually considered the most reliable [14].

## 2.2.6

**Extension of the Flory–Huggins Model to Systems with Specific Interactions**

In the Flory–Huggins model, randomness is assumed in the derivations of both the entropic term and the Van Laar-type enthalpic term. However, in systems containing specific interactions (such as hydrogen bonding, dipole–dipole, charge transfer, etc.) the number of specific contacts usually exceeds the value expected when considering random mixing [8]. These systems are said to maximize the number of specific interactions, and randomness is therefore lost. In addition, the energetic contribution associated with the establishment of the specific contacts is usually much larger than the energetic contribution associated with the establishment of the dispersive contacts, which means that even slight deviations from randomness can be accompanied by dramatic changes in the dependence of  $\Delta G_m$  with composition. Equation (2.17) is therefore no longer appropriate for these systems.

The simplest approaches to extend the Flory–Huggins model to systems with specific interactions seek the introduction of corrections to Eq. (2.17) that account for the particularities of these systems [8]. Assuming a quasi-random mixture and neglecting free-volume effects, the entropic term can be maintained and the product of volume fractions in the enthalpic term can be retained as a reasonable approach to count the number of interassociating contacts. However, the *interaction energy density*,  $B$ , is no longer independent of the composition in systems with specific interactions. This can be rationalized by considering a mixture of low-molecular-weight compounds of identical molar volume in which the two components of the blend contain respectively one and two interacting groups. When the compound at infinite dilution is the one establishing double interactions, the lattice cells containing the dilute compound will interact with about double strength than in the opposite case (when the compound at infinite dilution is the one that is only able to establish single contacts).

To account for the composition dependence,  $B$  can be modified by adding correction terms defined in a parallel manner to the original dispersive term. At infinite dilution of component-2 (when  $\phi_1 \rightarrow 1$ ), the correction term should be the product of the density of specific contacts achieved by the dilute component,  $z_{02}/V_{02}$ , (where  $z_{02}$  is the number of specific contacts per molecule, or per repeat-unit-2 in the case of a polymer, and  $V_{02}$  is the molar volume of component-2, or of the repeat-unit-2) by the interaction energy of the specific contacts,  $\Delta w_{si}$ . A similar correction term can be proposed when  $\phi_2 \rightarrow 1$ . At intermediate concentrations, the rule of mixtures can be assumed. Hence,  $B$  can be redefined according to:

$$B = \frac{z\Delta w_{12}}{V_r} + \left( \phi_1 \frac{z_{02}}{V_{02}} + \phi_2 \frac{z_{01}}{V_{01}} \right) \Delta w_{si} \quad (2.28)$$

Equation (2.28) has been written assuming the occurrence of only one type of specific interaction in the system (characterized by  $\Delta w_{si}$ ), but in the case of the coexistence of different types of specific interaction it can be easily extended. In addition, the dispersive part in Equation (2.28) (the first term on the right-hand

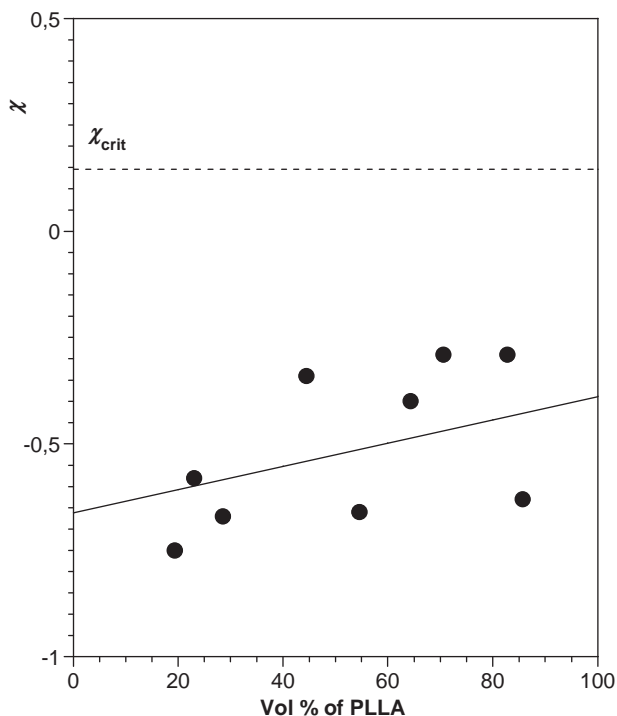


**Figure 2.4** Values of the interaction parameter,  $\chi$ , obtained from MD simulations for PLLA/PVPh blends of different composition. The continuous line is the fit of the calculated data to Eq. (2.29), using the constants in Table 2.1 and  $\Delta u_{si} = -1.7 \text{ kJ mol}^{-1}$ .

side) can be estimated from  $(\delta_{d1} - \delta_{d2})^2$ , where  $\delta_{di}$  are the dispersive solubility parameters, calculated using specially developed group contribution methods that account only for the dispersive part of the interactions [8,15].

Testing Eq. (2.28) against real polymer blends is not a trivial task, however, because there is no simple experimental procedure to measure  $B$  (or  $\chi$ ) at different compositions in these systems. Molecular modeling techniques represent an alternative approach to investigate the miscibility of polymer blends and to calculate the values of  $B$  or  $\chi$  as a function of composition (the fundamentals of this procedure are briefly discussed in Section 2.1.9 of this chapter) [16,17]. Molecular Dynamics (MD) simulations of blends of poly(L-lactide) (PLLA) with poly(vinyl phenol) (PVPh) were performed using the Materials Studio (v. 4.0) software package from Accelrys [17]. This software suite includes the COMPASS (Condensed-phase Optimized Molecular Potentials for Atomistic Simulation Studies) force-field, specially optimized to provide an accurate condensed-phase equation of state and cohesive properties for molecules containing a wide range of functional groups. Figure 2.4 presents the values calculated for  $\chi$  using MD simulations [17]. For PLLA-rich systems, the calculated data are also in good agreement with the value obtained from melting point depression measurements,  $\chi = -0.4$  (note,

**Table 2.1** Constant parameters used in Figure 2.4 to fit the values of  $\chi$  obtained from MD simulations for the PLLA/PVPh system to Eq. (2.29).

Parameter	PLLA	PVPh	Comments
$M_0$ (g mol <sup>-1</sup> )	72	120	Molar mass of the repeat unit
$\rho$ (g cm <sup>-3</sup> )	1.247	1.25	Exp. density of amorphous polymer [17]
$V_0$ (cm <sup>3</sup> mol <sup>-1</sup> )	57.7	96.0	Molar volume, calculated as $V_0 = M_0/\rho$
$\delta_d$ (cal cm <sup>-3</sup> ) <sup>1/2</sup>	10.1	10.6	Dispersive interaction parameters [8,15,18]
$z_0$	1.0	1.0	Number of specific contacts per repeat unit

however, that the experimental value is actually valid at the melting temperature of PLLA, about 190 °C, but MD calculations were performed at 25 °C [18]. The calculated data have been fitted to Eq. (2.29), obtained from Eqs (2.28) and (2.20), letting  $\Delta w_{si}$  as the only fitting parameter. The remaining constant parameters present in Eq. (2.29) are listed in Table 2.1 [17]. As can be seen in Figure 2.4, Eq. (2.29) fits properly the calculated data using  $\Delta w_{si} = -1.7$  kJ mol<sup>-1</sup>. The interaction parameter is larger when PLLA is the dilute component because the interaction energy density is larger because of the smaller molar volume of PLLA:

$$\chi = \frac{V_r}{RT} \left[ (\delta_{d1} - \delta_{d2})^2 + \left( \phi_1 \frac{z_{02}}{V_{02}} + \phi_2 \frac{z_{01}}{V_{01}} \right) \Delta w_{si} \right] \quad (2.29)$$

A brief analysis of the  $\Delta w_{si}$  parameter can provide additional insight into the nature of the specific interactions in the PLLA/PVPh system. The main specific interactions present in this system and the corresponding hydrogen-bonding enthalpies are hydroxyl–carbonyl interassociation ( $h_A = -3.8$  kcal mol<sup>-1</sup>) and hydroxyl–hydroxyl autoassociation through dimer formation ( $h_2 = -5.6$  kcal mol<sup>-1</sup>) and through multimer formation ( $h_B = -5.2$  kcal mol<sup>-1</sup>) [8]. Recalling that interaction energies were defined as the energy corresponding to the formation of one interassociation bond at the expense of breaking half of the autoassociation bond of each component, in a hypothetical scenario where pure PVPh was assumed to be exclusively autoassociated through dimer formation, the interaction energy would be  $\Delta w_{si} = -3.8 - \frac{1}{2} \times (-5.6) = -1.0$  kcal mol<sup>-1</sup> ( $= -4.0$  kJ mol<sup>-1</sup>). This (actually unrealistic) scenario predicts a favorable contribution to miscibility arising from specific interactions, even though the stronger O—H···O—H interactions are replaced by the weaker O—H···O=C interactions. The actual reason is that, in this hypothetical situation, the number of formed bonds doubles the number of broken bonds. Nevertheless, this simple calculation explains that weaker interactions can replace stronger interactions if the total number of specific contacts increases. In the infrared (IR) spectrum, this change should be observed as a blue shift of the OH-stretching band [8]. A more realistic estimation should consider that in actual polymer blends, interassociation peaks at about 80% of the hydrogen-bonded C=O groups [8,19], and that in pure PVPh the percentage of autoassociated OH groups is about 60%, mainly in the form of multimers [8,20,21], in which internal OH groups establish two hydrogen bonds (the

coordination number is therefore 2 for the nonterminal hydroxyls, but should be in the range of 1.5–2.0 on average [22]). With these assumptions,  $\Delta w_{si} = 0.8 \times (-3.8) - \frac{1}{2} \times 1.75 \times (-5.2) = -0.31 \text{ kcal mol}^{-1}$  ( $= -1.3 \text{ kJ mol}^{-1}$ ) is obtained. This more realistic calculation makes evident the complexity of the balance of interactions. Since increasing the hydroxyl density favors the formation of multimers (and the autoassociation in general), a reduced miscibility can be anticipated for polymers such as poly(vinyl alcohol) (PVA) compared to PVPh.

Finally, it is interesting to analyze how the introduction of specific interactions modifies the miscibility behavior in polymer blends. According to the simple treatment presented here, when the density of specific contacts of the two polymers is identical ( $(z_{01}/V_{01} = z_{02}/V_{02})$ ; see Eq. (2.28)),  $B$  is independent of composition and the  $\Delta G_m$  versus composition diagrams show improved symmetry, resembling those shown in Figure 2.2. However, when the specific contact densities of the components of the blend are different,  $B$  depends on composition, and the free energy curves show significant changes. Figure 2.5 shows  $BV_r$  and  $\Delta G_m$  versus composition plots for blends between two polymers of different specific contact density, calculated assuming varying relative strengths of the specific to dispersive interactions. The parameters used in Eq. (2.28) for polymer-1 were  $z_{01} = 1$ ,  $V_{01} = 50 \text{ cm}^3$ , and  $m_1 = 10^3$ ; and for polymer-2  $z_{02} = 1$ ,  $V_{02} = 100 \text{ cm}^3$ , and  $m_2 = 500$ . Hence, both polymeric chains present the same molecular size, but the former doubles the specific contact density of the latter. The same interaction energy as in the PLLA/PVPh system has been assumed,  $\Delta w_{si} = -1.7 \text{ kJ mol}^{-1}$ , and the strength of the dispersive interactions has been varied by acting on the difference of the dispersive solubility parameters,  $\Delta\delta_d$ , in Eq. (2.28).

As can be seen, the overall shape of the curves changes dramatically; in particular they become extremely asymmetric. Complete miscibility requires  $\Delta G_m < 0$  and  $\partial^2(\Delta G_m)/\partial\phi_1^2 > 0$  (the curve is concave upwards). Calculating the second derivative of Eq. (2.28) and equating to zero reveals that the critical dispersive interaction is  $\Delta\delta_d = 0.74 (\text{cal cm}^{-3})^{1/2}$ , the critical composition being  $\phi_1 = 0.98$ . All of the  $\Delta G_m$  curves with  $\Delta\delta_d$  above the critical value show a concave-downwards region between two concave-upwards regions. When  $\Delta\delta_d$  is in the range 0.74 to 2.9, the concave-upwards region located to the left is actually due to  $B < 0$  (specific interactions prevail over dispersive interactions), while the concave-upwards region to the right (observable only at high magnification) is due to the prevalence of the entropic term over the enthalpic term, occurring always at high dilution levels. Strictly speaking, partial miscibility should be claimed when  $0.74 < \Delta\delta_d < 2.9$ , but from the experimental point of view partial miscibility should not be easily observed in the range  $0.74 < \Delta\delta_d < 2.0$ , because negative second derivatives occur within relatively short composition ranges (when  $\Delta\delta_d = 1.5$ , negative  $\partial^2(\Delta G_m)/\partial\phi_1^2$  values occur in the range  $0.82 < \phi_1 < 0.997$ , and when  $\Delta\delta_d = 2.0$  the range is  $0.68 < \phi_1 < 0.998$ ).

Figure 2.5 predicts some interesting trends. First, partial miscibility – which was considered a very unusual result in systems with dispersive interactions – now becomes a real possibility. Second, the systems in Figure 2.5 showing partial miscibility separate in a partially miscible phase and a nearly pure polymer; hence,



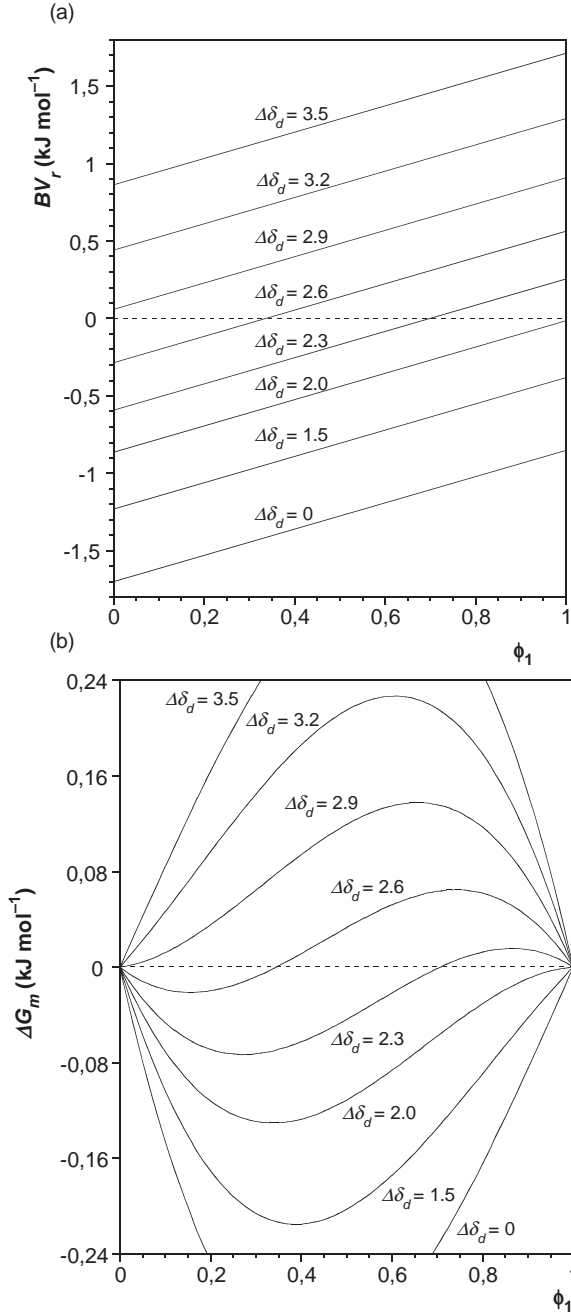


**Figure 2.5** Interaction energy (a) and Gibbs free energy (b) of mixing versus composition for systems with specific interactions of fixed strength,  $\Delta w_{si} = -1.7 \text{ kJ mol}^{-1}$ , and varying dispersive interactions according to the  $\Delta\delta_d$  values.

one of the polymers can be partially miscible in the second polymer, but not vice versa. Third, the polymer with a higher density of specific contacts (usually the one with the smaller repeat unit) is the one with enhanced miscibility. For example, blends of polylactides (PLAs) with poly(methyl methacrylate) (PMMA) show single glass transition temperatures, of enlarged width for the PMMA-rich blends (see also Section 2.2.1.6) [23]. This behavior is compatible with the curves in Figure 2.5 with  $\Delta\delta_d$  in the range of 1.5–2.0. In addition, poly(ethylene oxide) (PEO) is partially miscible with PLLA up to about 20–50 wt% PEO (the amount is controversial), the second phase being nearly pure PLA (see also Section 2.2.1.2) [24]. This behavior is consistent with the curve with  $\Delta\delta_d = 2.6$  in Figure 2.5. In addition, both the PLA/PMMA and the PLA/PEO systems show, as expected, a constrained miscibility for the component of higher molar volume. In contrast, for blends of PLA with PVPh, a partial miscibility was reported by Zhang *et al.*, who observed phase separation in a nearly pure PVPh phase and a PLA-rich phase containing up to about 15–20 wt% PVPh [25,26]. These results are at odds with the theoretical model discussed here since, according to Zhang *et al.*, the polymer with the repeat unit of higher molar volume, PVPh, is the one that is partially miscible in the second polymer. The miscibility of the PLA/PVPh system was reexamined a few years later by the present authors' research group, and complete miscibility was actually found to occur in that system [18,27,28]. The results reported by Zhang *et al.* were attributed to the occurrence of phase separation during the casting step due to the  $\Delta\chi$  effect [18,27]. In summary, even though some systems containing specific interactions may not conform to the trends predicted in this section due to the simplistic nature of the theoretical model, in the authors' opinion it provides in most cases valuable intuitive guidelines.

### 2.2.7

#### The Dependence of Miscibility on Blend Composition and Temperature

In the original Flory–Huggins model, the interaction parameter  $\chi$  (or  $B$ ) reflected exclusively enthalpic contributions to the free energy of mixing [2]. However, this description was soon extended when assuming that  $\chi$  includes contributions of both enthalpic and entropic nature to  $\Delta G_m$  [2–5]. As discussed in the preceding sections, specific interactions introduce nonrandomness and other effects that need to be considered for a correct description of the actual behavior of polymer blends. Both, theoretical and empirical corrections to  $\chi$  (or  $B$ ) have been proposed [8]. Regarding the dependence on composition, the simplest empirical approach assumes a linear dependence of  $B$  with composition ( $B = a + b\phi_1$ ). This type of approach has actually been used in Eq. (2.28) and applied to the PLLA/PVPh system in Section 2.1.6 in this chapter.

Regarding the temperature dependence of the interaction parameter  $\chi$  (or  $B$ ), in the original Flory–Huggins model the unfavorable enthalpic term is constant with temperature, but the favorable entropic term increases with temperature (see Eq. (2.14) or (2.17)). The model predicts phase diagrams with an Upper Critical Solution Temperature (UCST), or miscibilization upon heating. However, systems

with specific interactions usually present Lower Critical Solution Temperature (LCST) phase diagrams. In these systems, thermal agitation decreases the number specific interassociating contacts, and the system shows phase separation upon heating. In general, the temperature dependence of the  $\chi$  parameter has usually been described (empirically) by [3]:

$$\chi = a + \frac{b}{T} \quad (2.30)$$

where the constant  $a$  represents an entropic contribution to  $\chi$ , and  $b$  represents the enthalpic contribution. For most systems, both  $a$  and  $b$  will depend on the blend composition. A positive value for the constant  $b$  is associated with the mixture exhibiting an UCST, while a negative  $b$  corresponds to LCST behavior. Although Eq. (2.30) has proven useful, more complex relationships may also occur. For example,  $\chi$  may show a parabolic dependence on  $T$ , reflecting the simultaneous existence of both an UCST and a LCST [29].

According to Eqs (2.20) and (2.30), the following dependence on temperature can be deduced for the interaction energy density:  $B = a + bT$ . In addition,  $B$  depends on composition (recall the simple dependence discussed here,  $B = a + b\phi_1$ ). A general expression can be proposed for  $B$  combining both dependences:  $B = A_1 + A_2T + A_3\phi_1 + A_4\phi_1T$ , where the  $A_i$  coefficients are now constant coefficients that depend only on the nature of the system. Several expressions of different complexity can be found in the literature [30,31].

### 2.2.8

#### The Painter–Coleman Association Model (PCAM)

Coleman and Painter combined an association model with the Flory–Huggins theory to develop a theory that would describe the miscibility behavior of polymer blends with hydrogen bonding [8,32,33]. The theory is based on the assumption that the enthalpic contribution to the Gibbs free energy of mixing  $\Delta G_m$  consists of “weak” or “physical” or “dispersive” interactions, and “strong” or “chemical” or “specific” interactions. The free energy of mixing per mole of lattice sites is given by:

$$\frac{\Delta G_m}{RT} = \left( \frac{\phi_A}{m_A} \ln \phi_A + \frac{\phi_B}{m_B} \ln \phi_B \right) + \chi \phi_A \phi_B + \frac{\Delta G_H}{RT} \quad (2.31)$$

The first two terms represent the combinational entropy of mixing. Since these entropy terms are usually small in polymer blends,  $\Delta G_m$  is dominated by the balance between the third and fourth terms. The third term represents physical forces that can be estimated using Hildebrand’s approach from solubility parameters calculated using group contribution methods for a set of carefully chosen groups which are free from association (see also Section 2.1.6) [8,15]. The fourth term represents the favorable hydrogen-bonding contribution to  $\Delta G_m$ . Its

magnitude depends on two major factors. One factor is the relative strength of self-association to interassociation; if the strength of interassociation between two dissimilar polymers is greater than that of the self-association of either of them, then miscibility is favored. The second factor is the density of specific interacting sites in the blend; increasing this density can be expected to render the otherwise immiscible blends miscible.

Coleman *et al.* uses Fourier transform infrared (FTIR) spectroscopy to obtain the association constants,  $K_i$ , for all of the hydrogen-bonding equilibria occurring in the pure polymers, and in the blends. Using a van't Hoff-type plot, the enthalpies of hydrogen bonding can be calculated.

$$\ln K = \frac{-\Delta G}{RT} = \frac{-\Delta H}{RT} + \frac{\Delta S}{R} \quad (2.32)$$

With these data and the equations developed in their association model, the  $\Delta G_m$  curves can be calculated at any temperature. The phase behavior of the system can be thus quantitatively described (binodal and spinodal calculations, heats of mixing, etc.) [8,32]. However, the original model included an erroneous excess entropy term within the  $(\Delta G_H/RT)$  term of Eq. (2.32) [34]; this erroneous term was based on an incorrect reference state and allowed a nice agreement between theory and experiment. However, when the association constants obtained from FTIR experiments in polymer blends were used in the correct theory, the agreement was poor [34]. Coleman *et al.* realized that the poor agreement was a consequence of unaccounted effects in the initial theoretical model. Accordingly, in addition to correcting the reference state, the theoretical model was also modified to take into account intramolecular screening and “spacing” effects [35]. One unanticipated advantage of these investigations was that standard self-association and interassociation equilibrium constants, which are more easily obtained from appropriate model low-molar-mass compounds, can now be used to calculate the hydrogen-bonding contribution to the free energy of mixing in polymer blends. Although phase diagrams have been successfully calculated with the new model, all in all the corrections introduced have increased its complexity so that currently it has been only been tested in a few systems [35].

### 2.2.9

#### Analysis of the Miscibility Using Molecular Modeling Calculations

The MD approach is based on Eq. (2.7): recalling that changes of internal energy associated with the mixing process can be estimated as changes in the cohesive energy (with opposite sign, since  $E < 0$  but  $E_{coh} > 0$ ), dividing both sides by the total volume of the mixture,  $V$ , and considering also that  $V\phi_2 = V_2$  and  $V\phi_1 = V_1$ , it can be readily shown that [36]:

$$\frac{\Delta E_m}{V} = \phi_1 \left( \frac{E_{coh}}{V} \right)_1 + \phi_2 \left( \frac{E_{coh}}{V} \right)_2 - \left( \frac{E_{coh}}{V} \right)_{mix} \quad (2.33)$$

Hence, by building modeling cells for the pure polymers and for the mixture, and by calculating the CEDs for each of those cells, the internal energy of mixing per unit volume of mixture,  $\Delta E_m/V$ , can be obtained. Using also Eqs (2.20) and (2.13) and recalling that  $\Delta H_m \approx \Delta E_m$ , the interaction parameter can be obtained from:

$$\chi = \left( \frac{\Delta E_m}{V} \right) \frac{V_r}{RT\phi_1\phi_2} \quad (2.34)$$

In principle, MD simulations carried out using accurate force fields and careful procedures should lead to accurate determinations of the interaction parameter, which is the dominant contribution to  $\Delta G_m$ . The entropic contribution is not determined using Eq. (2.33), but this seems a minor drawback [36]. However, MD simulations seem to show a limited accuracy in some calculations. For example, several groups have reported that calculated solubility parameters are usually below the experimental values [16,37,38], with Gestoso *et al.* obtaining  $\delta = 8.7 \pm 1.2 \text{ (cal cm}^{-3})^{1/2}$  for PVPh [38], significantly less than the experimental value obtained from solubility testing,  $\delta = 12.0 \text{ (cal cm}^{-3})^{1/2}$  [39]. As solubility parameters are obtained from CEDs, MD simulations seem to underestimate the strength of the intermolecular interactions. However, when the CEDs are calculated to obtain  $\Delta H_m$  according to Eq. (2.33), an important error cancellation can be anticipated as the errors associated with the blend and with the pure polymer cells are subtracted. Recently, several polymeric mixtures have been investigated using the MD approach [16,17,21,37], and a very good agreement has been found in all cases with the experimental results with regards to the miscibility behavior. Hence, MD calculations are currently considered very reliable tools in the investigation of the miscibility of polymer blends.

## 2.2.10

### Classification of Miscible Systems

As discussed, miscibility is a rare phenomenon in polymers. However, miscibility conditions can be satisfied in the following cases.

#### 2.2.10.1 Entropically Driven Miscible Systems

This section encompasses the systems with very similar chemical structures, for which  $\Delta H_m$  is positive but very small (smaller than the favorable entropic term). This situation is very rare but can occur in the cases listed below:

- i) In nonpolar mixtures of homopolymers with very similar chemical structures. Traditionally, the 1,2-polybutadiene/*cis*-1,4-polyisoprene system [39], has been considered to fall within this category, since only van der Waals dispersion forces are expected between the blend components. However, a negative Flory's interaction parameter  $\chi_{12}$  has been recently estimated using excess volume measurements, and a stereostructural effect for mixing has been suggested [39]. Nevertheless, this mechanism is theoretically possible, and is therefore cited in this review.

- ii) In mixtures of copolymers with the same comonomers and similar chemical compositions.
- iii) Including also blends of oligomers, the number of miscible systems can be significantly increased, since the favorable  $\Delta S_m$  term is larger than in the case of high-molecular-weight polymers.

All of these systems are adequately described by the Flory–Huggins model.

### 2.2.10.2 Enthalpically Driven Miscible Systems

This section covers the polymeric systems that, in spite of the dissimilar chemical structures of the blend partners, show miscibility. This is because  $\Delta H_m$  takes in these cases values generally negative, ensuring the miscibility of the system. This situation is made possible via two mechanisms: (i) specific interactions; and (ii) if at least one component of the blend is a copolymer, the so-called “intramolecular repulsion effect” or “copolymer repulsion effect.”

The first mechanism usually controls miscibility in the case of mixtures of homopolymers. It occurs in systems with “complementary dissimilarity” – that is, when the polymeric chains are very different but contain chemical groups that establish specific interactions, leading to a negative enthalpy of mixing [8]. The most common specific interactions are hydrogen bonds, but other possible interactions to consider are dipole–dipole, ionic, acid–base, cation– $\pi$  (cations interacting with aromatic rings) and charge transfer complexes. In this case, it is interesting to note that an effective way to obtain a homogeneous mixture of two polymers which, a priori, were immiscible, is the chemical modification of one or both of them with varying amounts of groups capable of establishing specific interactions. Sometimes, the simple introduction of a small number of “active” groups makes it possible to preserve the bulk properties of the starting homopolymers, but with a marked improvement in their ability to form miscible blends. For example, introducing just 1 mol.% of vinyl phenol groups into polystyrene makes possible to achieve miscibility with PMMA [8].

Experimentally, there are many miscible polymer pairs in which at least one of the components is a random copolymer but specific interactions are not present [40]. This phenomenon is attributed to the so-called “intramolecular repulsion effect.” Within the familiar Flory–Huggins description, and in the case of a random copolymer  $A_xB_{1-x}$  blended with a homopolymer C, three interaction parameters,  $\chi_{AB}$ ,  $\chi_{AC}$  and  $\chi_{BC}$  are required to describe the enthalpy of mixing. Using a mean field theory, the mixture can be described in terms of one parameter  $\chi_{eff}$  given by:

$$\chi_{eff} = x\chi_{AC} + (1-x)\chi_{BC} - x(1-x)\chi_{AB} \quad (2.35)$$

Assuming high-molecular-weight polymers, miscibility requires this parameter to be either zero or negative. As the equation shows, this can be accomplished even if all parameters are positive (i.e., systems without specific interactions), provided that  $\chi_{AB}$  is sufficiently large; hence, the phrase “intramolecular repulsion”

[40]. In other words, copolymer–homopolymer and copolymer–copolymer blends may be miscible in a certain range of compositions and temperatures, even though the respective constituent homopolymers are pairwise immiscible due to the so-called “copolymer repulsion effect.” In these systems the repulsion between segments of the copolymer is greater than the average repulsion of each of these segments with the homopolymer; hence, the net energy of interaction between the homopolymer and the copolymer is negative within a certain range of compositions of the copolymer, and miscibility is observed within the so-called “miscibility window” [40].

## 2.3

### Revision of Polymer Blends Based on Biodegradable Polyesters

In this section, the structure, preparation, miscibility and properties of different polymer blends based on biodegradable polyesters are reviewed. Polylactide-based blends are first revisited and discussed, and the miscibility behaviors of other commercially available biopolymers of great interest such as poly( $\epsilon$ -caprolactone) (PCL), poly(3-hydroxybutyrate) (PHB), poly(*p*-dioxanone) (PPDO) and polyglycolide (PGA) are briefly reviewed. Finally, Appendix 2.A provides a brief outline of the investigations used to develop the miscibility study presented here. In this recap, it is possible to find the chemical structures of the polymers and their solubility parameters, and also some brief comments summarizing the research studies.

#### 2.3.1

##### Blends Containing Poly(lactic acid) or Poly(lactide) (PLA)

Poly(lactic acid) or poly(lactide) (PLA) belongs to the family of aliphatic polyesters derived from  $\alpha$ -hydroxy acids. Lactic acid (2-hydroxypropionic acid) and lactic acid (LA) are chiral molecules which exist in two optically active forms; D-(–)-(R) or L-(+)-(S). Depending on the proportions of the enantiomers, PLAs with different properties can be derived, allowing the production of a wide spectrum of PLA polymers to match specific performance requirements [41,42]. The synthesis of PLA starts with the production of LA via the bacterial fermentation of corn starch or cane sugar. The production of an optically pure isomer requires using bacterial strains that produce exclusively the desired form of LA, namely L-lactic acid (L-LA) or D-lactic acid (D-LA), from which the optically pure polymers (L-PLA and D-PLA) can be synthesized. The polycondensation reaction of the lactic acids usually leads, however, to low-molecular-weight PLA. In order to obtain high-molecular-weight PLA, two molecules of LA are dehydrated to lactide (a cyclic lactone) and subsequently subjected to ring-opening polymerization (ROP). PLA has reasonably good optical, physical, mechanical, thermal and barrier properties compared to existing petroleum-based polymers. Furthermore, PLA is a biodegradable and biocompatible polymer that has been approved by the Food and Drug

Administration (FDA) and is therefore widely used in fields of biomedicine and packaging [42].

The commercial forms of PLA are the homopolymer poly(L-Lactide) (L-PLA or PLLA) and the copolymer poly(D,L-Lactide) (D,L-PLA or PDLLA), which are produced from L-lactide and D,L-lactide, respectively. The L-isomer constitutes the main fraction of PLA derived from renewable sources, since the majority of lactic acid from biological sources exists in this form [43]. Polylactides (PLAs) exhibit different properties depending on the D/L unit ratio and sequence distribution. Generally, the crystallinity of PLLA and PDLA decreases with increasing racemic content. PLA polymers with an L-content >90% tend to be semicrystalline, while those with a lower optical purity are generally amorphous [43–45].

### 2.3.1.1 PLA/PLA Blends

The optically pure polylactides L-PLA (or PLLA) and D-PLA (or PDLA) are semicrystalline polymers with glass transition and melting temperatures of about 60 °C and 180 °C, respectively. In contrast, DL-PLA (or PDLLA) is an amorphous polymer that consists of racemic lactate units and is crystalline only when the D and L unit sequence is completely alternating; such a polymer is termed poly (*meso*-lactide) [44]. The blending of PLAs can result in new materials that present with unexpected synergisms, such as those observed in the equimolar blends between the optically pure polylactides, PLLA and PDLA.

Numerous studies have been performed to understand the behavior of miscible PLLA/PDLA blends [45–49]. Ikada *et al.* [49] first reported that the 1/1 blend of PLLA with PDLA produces a stereocomplex with melting temperature ( $T_m$ ) around 230 °C, which is 50 °C higher than the melting point of the optically pure polymers. PLLA/PDLA blends were also investigated by Sarasua *et al.* [47], who reported the occurrence of heterogeneous crystallization after solidification from the melt, with a population of  $\alpha$  homocrystals melting at about 180 °C and a population of  $\eta$  stereocomplex crystals melting at about 230 °C. The crystallization of pure PLLA and of the PLLA/PDLA 50/50 complex were investigated using FTIR spectroscopy to gain insight into the interactions driving the stereocomplexation. In particular, the C—H and C=O stretching regions of the stereocomplex were found to evolve differently during the crystallization process compared to the pure polymers.

Figure 2.6 shows the spectra obtained for the isothermal crystallization of the stoichiometric blend PLLA/PDLA 50/50 at 190 °C, after melting for 2 min at 240 °C. At room temperature, the C=O stretching band of amorphous PLLA is located at about 1759 cm<sup>-1</sup>, but at 190 °C the maximum occurs at 1755 cm<sup>-1</sup>, as can be seen in Figure 2.6. The C=O stretching band of amorphous PLAs is known to be sensitive to chain conformation; at room temperature the C—O(ester), O—Ca, and Ca—C bonds in the main chain of PLAs adopt predominantly the *trans*, *gauche* and *trans* conformations, respectively, but at higher temperatures conformers of higher energy gain importance, explaining the aforementioned shift in the location of the C=O stretching band. During crystallization at 190 °C, where only stereocomplex crystallization can occur, the crystalline band is located at about



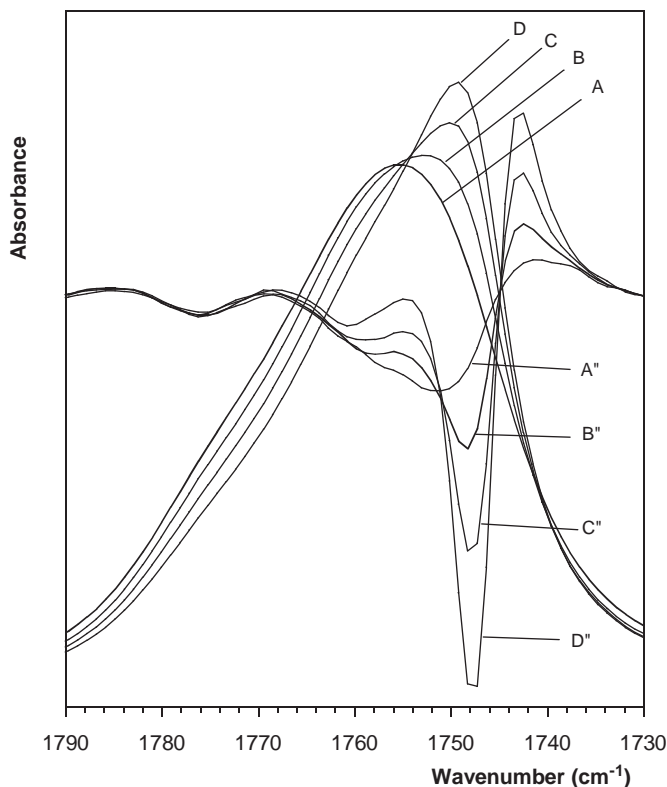


**Figure 2.6** Carbonyl stretching region of PLLA/PDLA 50/50 blend (A, B, C, and D) and second derivatives (A'', B'', C'' and D'') recorded during isothermal crystallization at 190 °C. A = 0 min (amorphous blend); B = 4 min; C = 30 min; D = 8 h.

1748  $\text{cm}^{-1}$  (Figure 2.6). Since the crystalline band in pure PLLA is located at about 1759  $\text{cm}^{-1}$  (*trans-gauche-trans* conformation), the C=O stretching band of the stereocomplex suggests the occurrence of specific interactions that shift the location of the C=O stretching band by about 11  $\text{cm}^{-1}$ .

The C—H stretching region of the PLA stereocomplexes was also investigated. Polylactides show three peaks in this region located at about 2995, 2944, and 2880  $\text{cm}^{-1}$ . The absorption at higher wavenumbers (2995  $\text{cm}^{-1}$ ) is actually a composite band consisting of two  $\text{CH}_3$  asymmetric stretching modes, while the band at about 2944  $\text{cm}^{-1}$  is assigned to the  $\text{CH}_3$  symmetric stretching mode; finally, the lower wavenumber band located at about 2880  $\text{cm}^{-1}$  is due to the  $\text{C}_\alpha\text{H}$  stretching mode. During the crystallization of pure PLAs, the crystalline components emerge at about the same locations; therefore band narrowing is the overall change occurring in the crystallization process. Figure 2.7a and b display respectively the  $\text{CH}_3$  asymmetric stretching region and the  $\text{C}_\alpha\text{H}$  stretching region for a PLLA/PDLA 50/50 blend during crystallization at 190 °C. As can be seen, crystallization is

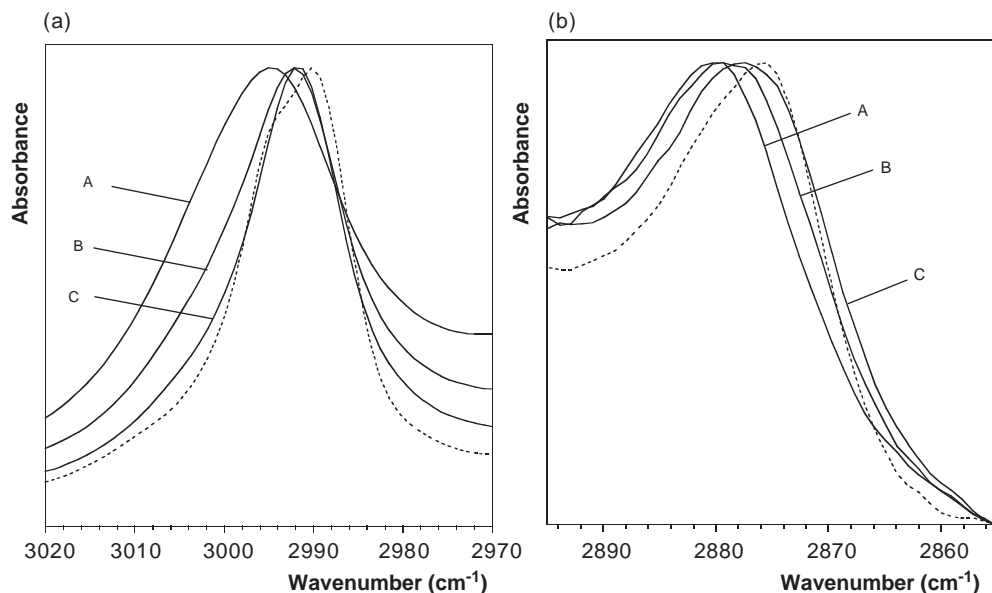


**Figure 2.7** (a) Autoscaled CH<sub>3</sub> asymmetric stretching region and (b) C<sub>α</sub>H stretching region for the PLLA/PDLA 50/50 blend recorded during isothermal crystallization at 190 °C. A = 0 min (amorphous blend); B = 30 min; C = 480 min.

accompanied by a noticeable red shift in both the CH<sub>3</sub> and the C<sub>α</sub>H stretching regions. In this spectral region, red shifts are sensitive to temperature, but the room temperature shift recorded for the stereocomplex bands compared to pure PLAs was about 4 cm<sup>-1</sup> in both the CH<sub>3</sub> and the C<sub>α</sub>H stretching regions. Hence, FTIR analysis suggested the occurrence of CH<sub>3</sub>···O=C and C<sub>α</sub>H···O=C hydrogen-bonding interactions between both stereoisomers of polylactide [47].

Although the occurrence of double hydrogen bonds (one C=O acceptor group hydrogen-bonded with two donor groups) had already been reported for other low-molecular-weight systems, it was still unreported in the case of polymer blends. Those interactions are, nevertheless, more restrictive than the establishment of single hydrogen bonds, since a very good stereocomplementarity is required to establish double hydrogen bonds with all the C=O groups within the crystalline lamellae (recall that “free” crystalline bands were not observed). Therefore, molecular models of the stereocomplex chains were built to confirm the feasibility of the interactions suggested by FTIR. Figure 2.8a shows one PLLA and one PDLA chain in parallel orientation, at the same relative distance as in the unit cell reported by Brizzolara. As can be seen, the model shows the possibility of simultaneous C<sub>α</sub>H···O=C and CH<sub>3</sub>···O=C hydrogen bonds with similar hydrogen-bonding distances of about 2.9 Å, and hydrogen bonding angles of about 120° and 150°, respectively. Considering that the cut-off distance and the angle for the C—H···O hydrogen bonds are respectively 3.0 Å and 110°,

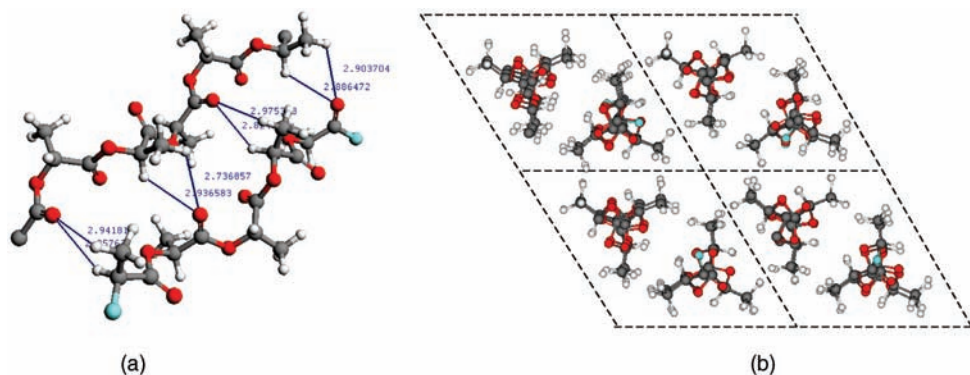


**Figure 2.8** (a) PDLA (top) and PLLA (bottom) chains in parallel orientation, as located in the stereocomplex crystal. The model has been built by bringing the chains until they fit in the experimental dimensions of the unit cell. Hydrogen-bonding angles for the interactions

suggested by FTIR are  $120^\circ$  and  $150^\circ$  for  $C=O \cdots H$  and  $CH_3 \cdots O$  bonds, respectively, and the hydrogen bond distance is about  $2.9 \text{ \AA}$ ; (b) Stereocomplex crystal lattice built from chains in the arrangement proposed.

the molecular models support the feasibility of the interactions suggested by FTIR analysis. Finally, the strength of the hydrogen-bonding interactions estimated from the observed spectral shifts using known  $\Delta H - \Delta \nu$  relationships is  $\Delta H \approx 1.3 \text{ kcal mol}^{-1}$ .

Finally, Tsuji and coworkers performed extensive studies of the stereocomplexation of PLLA/PDLLA blends [50] with different molecular weights. Increasing molecular weights were found to reduce the growth rate (G), regularity and crystallinity, presumably due to an increase of the number of entanglements between the PLLA and PDLLA chains [50]. Thus, increasing the molecular weight was found to hinder the stereocomplexation of PLAs.

Other PLA-based blends have also been investigated with different purposes. For example, Cha and Pitt [51] investigated blends of PLLA with poly(glycolic acid-co-L-lactic acid) (PGLA) containing 83 mol.% of lactide. Blending was performed to modify the rates of hydrolytic degradation of the material and, consequently, the rates of biodegradation-controlled delivery of drugs. It was shown that, despite the incompatibility of the blends, the rate of hydrolytic chain scission of each component could be significantly modified by the presence of the second polymer. Poly(aspartic acid-co-L-lactide) (PAL) copolymers are actually PLA-based polymers modified with minor amounts of aspartic acid (2–20 mol.%) to accelerate the hydrolysis of PLLA. Both, Oyama *et al.* [52] and Shinoda *et al.* [53] proposed the blending of PLLA with PAL copolymers in order to study effects of the PAL composition on the blend structure and the kinetics of hydrolysis. In general, phase separation was observed for the PLLA/PAL blends, but when PLLA was blended with the PAL copolymers with lower aspartic acid contents the dispersed phase observed using transmission electron microscopy was finer, indicating an

improved compatibility. These authors observed that the addition of PAL did not accelerate the hydrolysis of the PLLA in air, but that degradation was significantly accelerated in water. Hence, nontoxic biomaterials could be successfully generated that would barely degrade during handling or storage in air, but would easily disintegrate in water to form harmless decomposition products.

### 2.3.1.2 PLA Blended with Poly(ethylene glycol) (PEG) and Poly(ethylene oxide) (PEO)

Poly(ethylene glycol) (PEG) belongs to the family of polyethers due to the presence of ether groups in the chain backbone. PEG is a thermoplastic crystalline homopolymer of low molecular weight that is obtained from either ethylene glycol or ethylene oxide [54,55]. PEGs contain terminal hydroxyl groups, are available in molecular weights ranging from 400 to 40 000 g mol<sup>-1</sup>, and are water-soluble within this range. PEG is also soluble in some organic solvents such as acetone, alcohol and chloroform, but not in hydrocarbons. The molecular weight of PEGs is a significant variable that influences many features. For example, the end groups are known to be hydroxyl only in the case of lower-molecular-weight species, whereas the glass transition temperature ( $T_g$ ) can vary from -40 °C to -70 °C [55,56]. One other outstanding characteristic is that PEG is biocompatible and lacks antigenicity and immunogenicity [54].

Blends of PLAs with PEG have been briefly studied during the past four decades. Due to the high hydrophilic character of PEG, the PLA/PEG blends are used to enhance both the hydrophilicity and the degradation rate of PLAs [57]. The solubility parameters of PLLA and PEO are 10.1 and 9.9 (cal cm<sup>-3</sup>)<sup>1/2</sup>, respectively (calculated according to the group contribution method of Coleman *et al.* that accounts only for the dispersive part of the cohesive energy). The closeness of these values suggests that the miscibility of PLLA with PEO is thermodynamically possible. However, Younes *et al.* [58] reported PLLA/PEG blends that comprised two crystalline phases, with both components being able to crystallize. Finally, it was concluded that the system was partially miscible, due to a depression of the melting point and the existence of some chain interpenetration. The results of another study, performed on solvent cast blends with up to 30 wt% of PEG, reported the miscibility in the melt for the PLLA/PEG blends to be within the investigated compositions range. Blends presented a unique  $T_g$ , and the Fox relation was applied to fit the empirical  $T_g$  behaviors [59]. Additional studies presented similar conclusions with regards to microphase separation and partial miscibility for this system [60–62]. When Lai *et al.* [63] used PEG samples of very low molecular weight (2000 g mol<sup>-1</sup>), their differential scanning calorimetry (DSC) analyses of the blends showed that PEG and PLLA were miscible in the melt up to 70 wt% of PEG. Moreover, the effect of the end groups of PEG on the miscibility and crystallization behavior of PEG/PLA blends was also investigated, with miscibility being shown to decrease in the following order: PEG(2CH<sub>3</sub>)/PLLA, PEG(1OH-1CH<sub>3</sub>)/PLLA and PEG(2OH)/PLLA.

Moreover, the melt blending of up to 30 wt% PEG to PLLA decreased the  $T_g$  of PLLA by about 20 °C [55]. Hu *et al.* [61,64] also found a single  $T_g$  up to 30 wt% PEG, but compositions exceeding 20 wt% PEG were not stable at ambient

temperature. In addition, blends with PEG contents high enough to decrease the  $T_g$  below ambient temperature exhibited aging under ambient conditions, but the amorphous phase was found to remain miscible after the aging process. Pillin *et al.* [65] studied PEGs with molecular weights in the range 200 to 1000 g mol<sup>-1</sup> as plasticizers for polylactides, and compared them with other plasticizers. Their results confirmed that PEGs were highly efficient for  $T_g$  reduction, exhibited small interaction parameters with PLAs, and showed excellent fits to the Fox relation. At about 20 wt% PEG the  $T_g$  was observed to reach a plateau, and crystallization of PLLA was found to be enhanced by the mobility increase due to the plasticizing effect of PEG. Similar results were found by Baiardo *et al.* [66].

According to Ran *et al.* [67], the copolymer poly(ethylene glycol-co-propylene glycol) (PEPG) is also a good macromolecular plasticizer for PLA, due to their good compatibility. Furthermore, the authors observed good compatibility with samples of PLA of different optical purities, and also noted that the crystallization behavior of the blends was, as expected, noticeably influenced by the optical purity of the polylactide.

Poly(ethylene oxide) (PEO) has the same chemical structure as PEG, and can be considered a high-molecular-weight PEG [54]. According to several groups, PLA/PEO blends form a heterogeneous system whether prepared from their solutions or from the melt [68–72]. One study of PLA/PEO blends, applying melt blending as the preparation method, was presented by Ghosh *et al.* [70]. In this case, it was shown that in a 50/50 wt% PLLA/PEO blend, the PLLA and PEO system was biphasic, containing a homogeneous PLLA/PEO phase and a PEO-rich phase. Subsequently, this feature was used to fabricate scaffolds with a macroporous lamellar architecture and microporous walls. Another study was conducted with the aim of producing porous PLLA films by water extraction of PEO [71]; subsequent DSC analyses revealed that the PLLA and PEO were phase-separated at least after solvent evaporation. A comparison of blend films before and after extraction suggested that a small amount of PEO had become trapped in the amorphous region between the PLLA crystallites, even after water extraction. Similarly, Honarbaksh *et al.* [69] prepared electrospun blends of PLA/PEO in order to produce a highly porous fibrous structure as a drug-delivery matrix with enhanced hydrophilicity. The incorporation of PEO into the matrix introduces preferable sites to which aqueous compounds can be attached, while retaining the overall structural integrity and porous morphology.

Nijenhuis *et al.* [24] prepared PEO/PLLA blends by solution precipitation, and also found that PEO is partially miscible with PLLA. These authors observed that the melting endotherm corresponding to the PEO fraction was not detected in blends containing less than 20 wt% PEO, indicating completely amorphous blends. They also observed evidences pointing to the possibility of a completely miscible system, such as a slight shift to lower temperatures in the melting point of PLLA with the addition of PEO. However, as recognized by these authors, this phenomenon alone is not absolute proof of miscibility. The PLLA/PEO blends demonstrated complex DSC thermograms due to the overlapping of different phenomena (such as crystallization and melting processes), which made the

determination of possible intermediate  $T_g$ s difficult. In addition, the high crystallinity of PEO limits the accuracy when determining its  $T_g$  [58]. Because of these limitations, the authors could not ascertain the occurrence of single intermediate  $T_g$ s in the whole range of compositions for the PLLA/PEO blends, and therefore miscibility could not be conclusively proved.

### 2.3.1.3 PLA Blended with Poly(vinyl alcohol) (PVA) and Poly(vinyl acetate)

Poly(vinyl acetate) (PVAc) is an inexpensive, high-tonnage bulk commodity polymer which, unlike most vinyl polymers, is moderately biodegradable [73]. It is an amorphous material with a  $T_g$  of about 30 °C. In contrast, poly(vinyl alcohol) (PVA) is a synthetic, hydrophilic, biodegradable, biocompatible and highly flexible polymer, in spite of its highly crystalline structure. The  $T_g$  and  $T_m$  of PVA are about 80 °C and 230 °C, respectively. PVA is obtained by the hydrolysis of PVAc, and usually contains a small amount of residual vinyl acetate groups. Partial hydrolysis of PVAc is a simple route to obtain poly(vinyl acetate-co-vinyl alcohol) [P(VAc-co-VA)] copolymers.

The hydroxyl groups in PVA can establish hydrogen bonds with the ester groups of polyesters. By taking advantage of the possibility of such specific interactions in the blends, miscibility or partial miscibility might be achieved between PLA and PVA [74]. Although the large difference in experimental solubility parameters ( $\Delta\delta$ ) between PLLA and PVA points to phase-separated systems, the difference of dispersive terms (calculated using the group contribution method proposed by Coleman *et al.*) is small, which suggests that in the case of achieving sufficiently high interassociation densities, miscibility is still possible. However, most studies have reported immiscibility or partially miscibility for the PLLA/PVA system. Blend films of this mixture were obtained by Shuai *et al.* [74], who showed (using DSC) that the amorphous regions of the PLA/PVA blends were phase-separated. Nonetheless, an interassociation through the formation of hydrogen bonds in the PLLA/PVA blends was demonstrated using FTIR analysis and  $^{13}\text{C}$ -pulse saturation transfer/magic angle spinning nuclear magnetic resonance (PST MAS NMR) measurements. For this reason, the authors concluded that the PLLA/PVA system is partially miscible. Tsuji *et al.* [75] also found phase separation in PLLA/PVA blends, and the PLLA-rich and PVA-rich phases both formed a continuous domain in the blend film with PLLA weight fraction  $X_{\text{PLLA}} = 0.5$  [ $X_{\text{PLLA}}(\text{w/w}) = \text{PLLA}/(\text{PVA} + \text{PLLA})$ ].

Molecular modeling calculations using atomistic molecular dynamics and mesoscopic dynamics of polymer melts, along with thermodynamic approaches, were applied to predict the miscibility behavior of the PLLA/PVA blends. For the PLLA/PVA 1:9 (mol: mol) composition, the calculated interaction parameter  $\chi_{23}$  was smaller than the critical interaction parameter, and miscibility was therefore predicted for this composition (note also that molecular modeling calculations were carried out with chains of very low molecular weight). Increasing the PLLA content resulted in higher  $\chi_{23}$  than  $\chi_{23,\text{critical}}$ ; therefore these polymer blends were predicted to be immiscible. From the peak of the computing radial distribution function (RDF) it was proposed that hydrogen-bonding interactions with the C=O

group were responsible for the small miscibility window observed at low PLLA contents.

The miscibility behavior of PLA/PVAc blends was reported by Gajria *et al.* [76], who investigated their physical properties, degradation and surface tension. A single-phase behavior was observed, and the mechanical properties exhibited synergism in the range of 5 to 30 wt% PVAc. The miscibility of this system was also confirmed by Park *et al.* [77] according to the single  $T_g$  criterion. The  $T_g$ -composition dependence was found to follow the Fox–Flory equation, and the Flory–Huggins interaction parameter was negative. Moreover, the presence of PVAc in the interlamellar region of PLLA suggests a good interaction between both components. Similar results were also observed for this system when prepared by solvent-casting [78]. Some research groups have proposed that the likely interactions between the carbonyl groups of PLA (proton acceptors) and the  $\alpha$ -hydrogens of PVAc (proton donors) could serve as the driving force for the miscibility of these polymer blends [76,78]. Finally, the study was extended to blends of PLLA with P(VAc-*co*-VA) copolymers with different degrees of hydrolysis. The insertion of a small amount of vinyl alcohol units in the PVAc chains was found to preclude the miscibility with PLLA, and the PLLA/P(VAc-*co*-VA) blends were found to be immiscible according to the observation of two glass transitions and phase-separated morphologies.

PLLA has also been blended with poly(ethylene-*co*-vinyl acetate) (EVAc) copolymers [79]. EVAc# copolymers (where # denotes the wt% of VAc in the copolymer) are synthetic random copolymers of an amorphous nature with  $T_g$ s below room temperature and a low viscosity compared to PLA [80]. Miscibility was found for the PLLA/EVAc85 system according to the single  $T_g$  criterion, and to the slightly negative Flory–Huggins interaction parameter. On the other hand, immiscibility was observed for the PLLA/EVAc70 system. Thus, the introduction of 30 wt% ethylene into the vinyl acetate chains is able to hinder the miscibility with PLLA.

#### 2.3.1.4 PLA/Poly( $\epsilon$ -caprolactone) (PCL) Blends

PCL is an aliphatic semicrystalline polyester obtained by the ROP of a relatively economical monomeric unit,  $\epsilon$ -caprolactone; thus, it is composed of hexanoate repeat units. PCL is known to be a highly processable polymer of low  $T_g$  value ( $\sim -60^\circ\text{C}$ ) and low melting point ( $\sim 60^\circ\text{C}$ ), and is soluble in a wide range of organic solvents. One outstanding mechanical property of this polymer is its extremely high elongation at rupture [41]. PCL has been used as adhesive and packaging material, though owing to its biocompatible and biodegradable nature it has also been employed in the biomedical field as scaffold in tissue engineering applications and implantable biomaterials in long-term drug-delivery systems [54,81]. Furthermore, PCL can form miscible blends with different polymer such as poly(vinyl chloride) (PVC) [82], poly(carbonate) (PC) [83], poly(vinyl phenol) (PVPh) [84], poly(vinyl methyl ether) (PVME) [85], and poly(styrene-*co*-acrylonitrile) (SAN) [86]. PCL is also mechanically compatible with polyethylene, polypropylene, natural rubber and PVA [81]. The carbonyl group present in the repeat unit of PCL

can potentially establish intermolecular interactions with different polymers, in particular with hydrogen-bond donors [87–90].

Blends of PLA with PCL have been investigated in order to toughen the PLA matrix and broaden the application possibilities of both polymers. In spite of the proximity between the solubility parameters of PLA and PCL (10.1 and  $9.2 \text{ cal}^{0.5} \text{ cm}^{-1.5}$ , respectively), the bibliographic revision shows that PLA/PCL blends are immiscible [59,91–98]. This fact suggests a lack of favorable specific interactions between these two components [15,91]. Even though the blends of these two polymers did not show the desired properties as a consequence of their immiscible nature, there are some interesting and noteworthy results.

By means of DSC, polarized optical microscopy (POM) and dynamic mechanical thermal analysis (DMTA), Tsuji *et al.* [99] found phase separation in solvent cast mixtures of PDLA with PCL, but they could not conclude immiscibility for the PDLA/PCL system because of the probability that the cosolvent molecules might have induced the phase separation during solvent evaporation. Furthermore, Lopez-Rodriguez *et al.* [100] observed phase separation for both melt-blended and solvent-cast PLA/PCL blends over the whole range of compositions. The shift in the mechanical loss ( $\tan \delta$ ) peak observed by means of DMTA suggested that PCL could be partially soluble in the PLA-rich phase. The morphology of the tensile-fractured surfaces of PLLA, PCL, and their blends was investigated using scanning electron microscopy (SEM) (see Figure 2.9). The images of PCL revealed ductile fractures with an irregular morphology, while those of PLLA (Figure 2.9a) revealed brittle fractures. All PLLA/PCL blends were clearly phase-separated. The border compositions, PLLA/PCL 80/20 (Figure 2.9b) and PLLA/PCL 20/80 (Figure 2.9d), showed spheres of dispersed phase into a continuous matrix. However, the fracture surface of PLLA/PCL 80/20 was smooth, consistent with the brittle behavior shown by the PLLA-rich blend in tensile tests, while the characteristics of the SEM micrograph of its PCL-rich counterpart (PLLA/PCL 20/80) revealed a ductile fracture mode. The intermediate equimolar blend, PLLA/PCL 60/40, showed an interconnected morphology and a ductile fracture mode (Figure 2.9c). Sharp interphase boundaries could be observed in all cases, with no signs of any good adhesion between PLLA and PCL.

Yang *et al.* [59] used DSC and optical microscopy to investigate the PLLA/PCL system and reported phase separation in the melt, but also found that the crystallization rate of PLLA was enhanced by blending with PCL. Moreover, the partial miscibility between these two polymers was suggested to increase the crystallization rate of PLLA. In addition, the existence of LCST phase behavior was probed by Meredith *et al.* [101] for the PCL/PDLA blends. The critical temperature exhibited by the PCL/PDLA blends was  $86^\circ\text{C}$  and the critical composition was 0.36 (PCL mass fraction). The thermally induced phase separation at the critical and off-critical compositions proceeded via spinodal decomposition, resulting in a cocontinuous structure. This was in contrast to the dispersed particle-matrix structure that resulted from the nucleation and growth mechanisms. In addition to these reports, other investigations regarding the crystallization, morphological



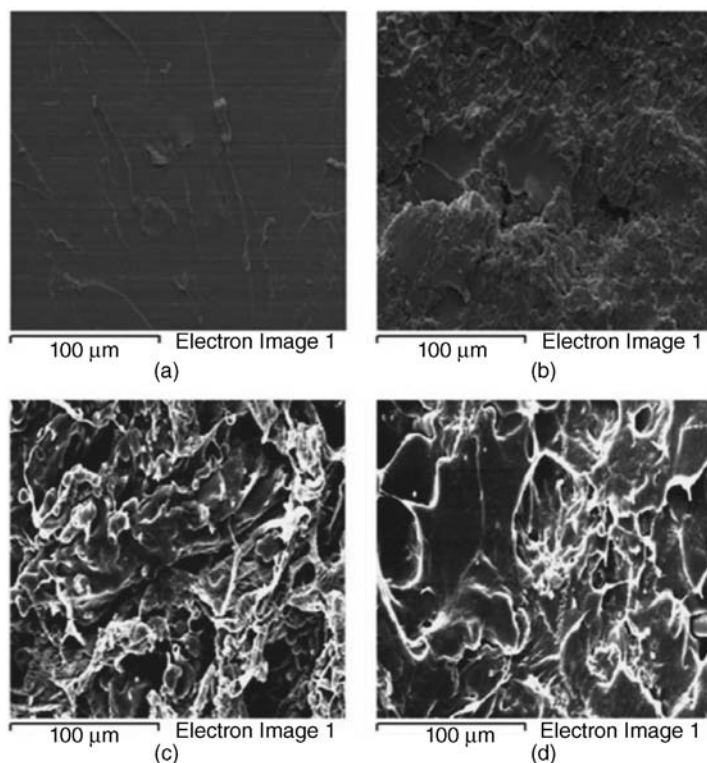


**Figure 2.9** Scanning electron microscopy images of fracture surfaces of (a) PLLA, (b) PLLA/PCL 80/20, (c) PLLA/PCL 60/20, and (d) PLLA/PCL 20/80.

and mechanical behavior of PLA/PCL blends have also been undertaken [102–104].

Alternatively, other studies have focused on improving the miscibility of this system by using copolymers of a similar chemical nature to the main components. For example, Dell’Erba *et al.* [93] used a high-efficiency melt mixing to obtain a fine dispersion of PCL domains in immiscible PLLA/PCL blends. Moreover, by adding small amounts of PLLA-PCL-PLLA triblock copolymer it was possible to achieve a more homogeneous distribution of particle size and to lower the fraction of large domains; hence the copolymer acts as an interfacial agent in the phase boundary. In another study, Na *et al.* [105] examined the behavior of blends of PLA with block copolymers of PCL and PEG (PCL-*b*-PEG), and observed isolated PCL domains free from PLA chains in the blends when the PEG chains of the copolymer were mixed into the amorphous region of PLA. This indicated a compatibilizing effect of the PCL-*b*-PEG copolymers, and this was confirmed by means of mechanical properties and morphological analyses. The authors concluded that the PEG copolymer blocks were miscible with PLA while the PCL

phase was still immiscible with the PLA matrix. Moreover, a similar study of PLLA/PCL blends in the presence of PLLA-PEO and PLLA-PCL-PLLA block copolymers showed the PEO block of the former copolymer to be a better emulsifier than the central PCL block of the latter triblock copolymer [92]. Whilst the thermal properties of the prepared blends were virtually unaffected by the presence of the copolymers, but the interface-related properties – such as morphology or mechanical properties – were noticeably influenced.

### 2.3.1.5 PLA/Poly((R)-3-Hydroxybutyric acid)) (PHB) Blends

Poly(3-hydroxybutyrate) (PHB) was first discovered in *Bacillus megaterium* during the 1920s by Maurice Lemoigne, a French microbiologist. It is thought that bacteria store PHB as an energy source, and during recent years several chemical synthetic routes have been developed for its synthesis. PHB is a semicrystalline isotactic biodegradable polymer that presents  $T_g$  and  $T_m$  values in the ranges of  $-5$  to  $20^\circ\text{C}$  and  $160$  to  $180^\circ\text{C}$ , respectively. It is soluble in a wide range of solvents, and can be processed into different shapes and structures, such as films, sheets, spheres, and fibers [41]. The semicrystalline copolymers of PHB and 3-hydroxyvalerate (PHB-PHV), show similar properties to PHB, but with lower melting temperatures depending on the HV content. Since the homopolymer PHB is a tough, brittle polymer, the less brittle and tougher copolymer has greater potential as a biomaterial. Another unique property of PHB-PHV is its piezoelectricity, which makes it a potential candidate for orthopedic applications as electrical stimulation is known to promote bone healing.

The polymer partner that has been examined most intensively for obtaining blends with PHB is PLA, and several studies have focused on understanding the interactions in PLA/PHB blends. The miscibility, crystallization and melting behavior of PLA/PHB blends were investigated by Blumm and Owen [106], who studied the spherulitic structure and melting behavior of the blends and found the miscibility of the blends to be heavily dependent on the molecular weight of PLLA. When the molecular weight of PLLA was low ( $M_n = 1759$ ), the blends were miscible with PHB ( $M_n = 222\,000$ ) in the melt over the whole composition range, but when the molecular weight of PLLA was higher ( $M_n = 159\,400$ ) the blends showed phase separation. The dependence of the molecular weight of PLLA on the miscibility of the PLLA/PHB blends (PHB  $M_n = 300\,000$ ) was examined in detail by Koyama *et al.* [107], who used PLLA with molecular weights ranging from  $9900$  to  $530\,000$  Da. The reported critical molecular weight of PLLA to obtain miscible blends with PHB was about  $18\,000$ – $20\,000$  Da, from which a difference in solubility parameter of about  $0.34 (\text{J cm}^{-3})^{1/2}$  could be estimated using the Flory–Huggins equation. According to Yoon *et al.* [108], miscibility was observed only when the molecular weight of PLLA was  $11\,700$ , or less. Although the PEG-*b*-PLA copolymer can compatibilize the blends because of the miscibility of PEG with PHB, when the molecular weight of PLLA was high (i.e.,  $56\,000$ ), the block copolymer did not function effectively as a compatibilizer for the PHB/PLA blends. Along the

same lines, when Ohkoshi *et al.* [109] investigated the miscibility of PLA/PHB blends with different molecular weights, miscibility was demonstrated for low-molecular-weight PHB, while for PHB with  $M_w = 9400$  a single  $T_g$  was observed up to 50 wt% PHB in the blend. However, for high-molecular-weight PLA/PHB blends ( $M_w$  (PHB) = 140 000), two  $T_g$ -values at 59 °C and 0 °C were observed, corresponding to the neat components. Moreover, Zhang *et al.* [110] reported improved miscibilities in the blends obtained by melt blending compared to those obtained by solvent casting. Whilst the latter blends were completely immiscible, the melt-blended samples showed some evidence of partial miscibility, such as a depression of  $T_m$  and a decrease in the crystallinity of PHB in the blends.

Other research groups have also investigated the behavior of this system by using different molecular weights, and have reported similar results to those discussed above [111,112]. Malinová *et al.* [112] examined the miscibility of a commercial sample of PHB ( $M_v = 285\,500$ ) with low- ( $M_v = 9200$ ) and high- ( $M_v = 153\,000$ ) molecular weight PLLAs, and found PHB to be miscible with the former in the whole compositions range but immiscible with the latter. Wasantha *et al.* [113] reported a partial miscibility for high-molecular-weight blends, while Focarete *et al.* [114] observed miscibility for blends of high-molecular-weight PLA with low-molecular-weight PHB.

Other reports have also been made with regards to the miscibility of PHB with lactide-based copolymers. Focarete *et al.* [114] reported a partial miscibility for blends comprising low-molecular-weight PHB and poly(L-lactide-co-glycolide) (PLGA) copolymers. Koyama and coworkers [115] synthesized random copolymers of  $\epsilon$ -caprolactone (CL) and (D,L)-lactide (LA), P(CL-co-LA), with a wide range of compositions (0–100 mol.% LA) and molecular weights ( $M_n = 1500$ –40 000), and then blended the P(CL-co-LA) copolymers with high-molecular-weight PHB. The blends of PHB with P(CL-co-LA) containing ~40 mol.% LA were miscible, independent of the molecular weight of the P(CL-co-41 mol.% LA) component ranging in  $M_n$  values from 1500 to 33 000. Miscibility or partial miscibility was claimed for blends of PHB with the remaining P(CL-co-LA) copolymers, depending on the molecular weight of the copolymer. Moreover, the miscibility analysis of PHB with a poly(D,L-lactide)-co-poly(ethylene glycol) (PELA) copolymer containing 8 wt% ethylene glycol revealed phase separation [116]. When Furukawa *et al.* [117,118] compared the miscibility of PLA with both PHB and the poly(3-hydroxybutyrate-co-3-hydroxyhexanoate) copolymer (P(HB-co-HHx)), immiscibility was noted for both the PLA/PHB and the PLA/(P(HB-co-HHx)) systems. Nevertheless, PLLA showed a better compatibility with P(HB-co-HHx) than with PHB.

#### 2.3.1.6 PLA Blended with Poly(methyl methacrylate) (PMMA) and Poly(methyl acrylate) (PMA)

PMMA is a linear, amorphous, synthetic, nonbiodegradable polymer with a high transparency and good mechanical properties. It is classified as a hard and rigid –

but brittle – material, but its tensile, compressive and flexural strengths are satisfactory for most applications. The two main advantages of PMMA are its easy availability and preparation. Although some of these properties are common to several other polymers, few of these are produced from liquid, nonvolatile and low-cost monomers [119]. The miscibility of PLA with PMMA and PMA has been investigated in several studies. Eguiburu *et al.* [23] prepared blends by solution/precipitation and reported the miscibility of PMA with both amorphous and crystalline PLAs (PLLA and PDLLA were actually used). The PLA/PMMA systems showed single but enlarged  $T_g$  widths for the PMMA-rich blends, indicating that the system might be close to the miscibility limits. Nevertheless, additional experimental data obtained by means of DMTA and enthalpy relaxation supported the miscibility of the PLA/PMMA system. Recent reports have also confirmed the miscibility of the PLA/PMMA blends [120,121]. When applying the Gordon–Taylor equation to both systems, the  $k$ -value for the PLA/PMA system was higher than that for the PLA/PMMA system, which suggests that PMA has a greater ability to form miscible blends with PLA than does PMMA. When Zhang *et al.* [120] prepared PDLLA/PMMA blends by both solvent casting and solution/precipitation, they observed two  $T_g$ -values for the former, which suggested the presence of two segregated phases in the solvent cast blends. In contrast, a single  $T_g$  was found for the solution/precipitation blends, indicating their miscibility. Phase separation in miscible systems prepared by solvent casting is usually attributed to the  $\Delta\chi$  effect. The crystallization of PLLA was found to be greatly restricted by amorphous PMMA showing the typical behavior of miscible blends with amorphous polymers with a higher  $T_g$ -value than that of the semicrystalline component. Finally, similar tendencies were observed in the amorphous state for both PDLLA and PLLA to form miscible blends with PMMA [120].

Li and coworkers provided an alternative explanation for the miscibility behavior of the PLA/PMMA system [122,123]. The same group also reported two  $T_g$ -values in the first DSC scans for solvent-cast PLLA/PMMA blends, although after heating at high temperatures ( $\sim 250^\circ\text{C}$ ), phase homogenization of the two polymers led to miscibility on the basis of a single  $T_g$  observed in a subsequent DSC scan. According to these authors, these results can be attributed to UCST phase behavior (the system is miscible at high temperature but becomes phase-separated on cooling). The possibility of transesterification reactions at temperatures around the UCST was excluded in the blends by means of NMR analysis. However, the authors did not include any blends obtained by solution/precipitation, and consequently their results may appear inconclusive, in the sense that the initial phase separation might actually have been due to the  $\Delta\chi$  rather than to the UCST behavior. It should be noted that although the authors were able to observe a miscibilization of the system at high temperatures upon heating, they did not report any phase separation in the melt (above the crystallization temperature of PLLA) upon cooling. They also investigated the effect of the tacticity of PMMA on its miscibility with PLA, and observed similar phase behaviors for both the atactic PMMA (aPMMA) and the syndiotactic PMMA (sPMMA). The isotactic PMMA

(iPMMA) was, however, immiscible at any temperature up to the degradation temperature.

### 2.3.1.7 PLA/Poly(4-vinylphenol) (PVPh) Blends

PVPh is a synthetic amorphous polymer that contains a hydroxyl group attached to a pendant phenyl ring, and is a strong proton donor. Interactions of the hydroxyl group of PVPh with proton-accepting functional groups (such as ester, carbonyl, ether, and pyridine groups) originates intermolecular hydrogen bonding [124–127]. Furthermore, in the case of the blends of PVPh with PLA, the small difference in the solubility parameter of PVPh ( $10.6 \text{ cal}^{0.5} \text{ cm}^{-1.5}$ ) and PLLA ( $10.1 \text{ cal}^{0.5} \text{ cm}^{-1.5}$ ), indicates that this polymer pair can be miscible.

The miscibility of high-molecular-weight PLAs with PVPh was first investigated by Zhang *et al.* [25,26], who reported a partial miscibility for this system. According to their results, the  $T_g$  of the PVPh-rich phase remains almost invariant, while the  $T_g$  of the PLA-rich phase increases steadily with the content of PVPh in the blend. Thus, the authors concluded that the system was actually phase-separated, with one phase containing almost pure PVPh and the PLA-rich phase containing up to 17 wt% PVPh. Blends of PLA with a low-molecular-weight PVPh samples ( $M_w = 13\,000$ ) were later investigated by Chen *et al.* [128], who observed complete miscibility over the whole range of compositions. Subsequently, Chen *et al.* argued that the conflict between their results and those of Zhang *et al.* was due either to the different molecular weights of PVPh (Zhang *et al.* used PVPh samples of higher  $M_w$ , from 22 000 to 30 000), or to the different solvents (dimethylformamide versus tetrahydrofuran and, consequently, the different casting temperatures) used in the blend preparation. The miscibility of the system was finally revisited by Meaurio *et al.* [17,18,27,28], who blended high-molecular-weight samples of PLA and PVPh ( $M_v = 30\,000 \text{ g mol}^{-1}$ ) and observed a similar phase behavior to that reported by Zhang *et al.* when the blends were prepared by solvent casting. However, complete miscibility was shown in the second DSC scans when the blends had been prepared by the solution/precipitation method. Phase separation for the solvent-cast blends was attributed to the  $\Delta\chi$  effect, which takes into account that the phase behavior of a solvent(1)–polymer(2)–polymer(3) ternary system depends not only on the polymer–polymer interaction parameter  $\chi_{23}$  but also on the difference in strengths of the polymer–solvent interaction parameters,  $\Delta\chi = |\chi_{12} - \chi_{13}|$ . Provided that  $\Delta\chi$  is sufficiently large compared to  $\chi_{23}$ , theoretical models of ternary systems can predict phase separation even if the polymers are compatible ( $\chi_{23} < 0$ ) because these systems can show closed immiscibility regions in the ternary phase diagram, leading to phase-separated systems during the solvent casting step [129].

The interassociation interactions in the PLA/PVPh blends were analyzed using FTIR analysis [18]. Figure 2.10 shows the hydroxyl stretching region for pure PVPh and PLLA/PVPh blends of different composition. The spectrum of pure PVPh shows a broad, complex band due to the addition of contributions arising from a wide number of different species. The shoulder observed at about  $3535 \text{ cm}^{-1}$  has been attributed in the traditional literature to free OH groups,

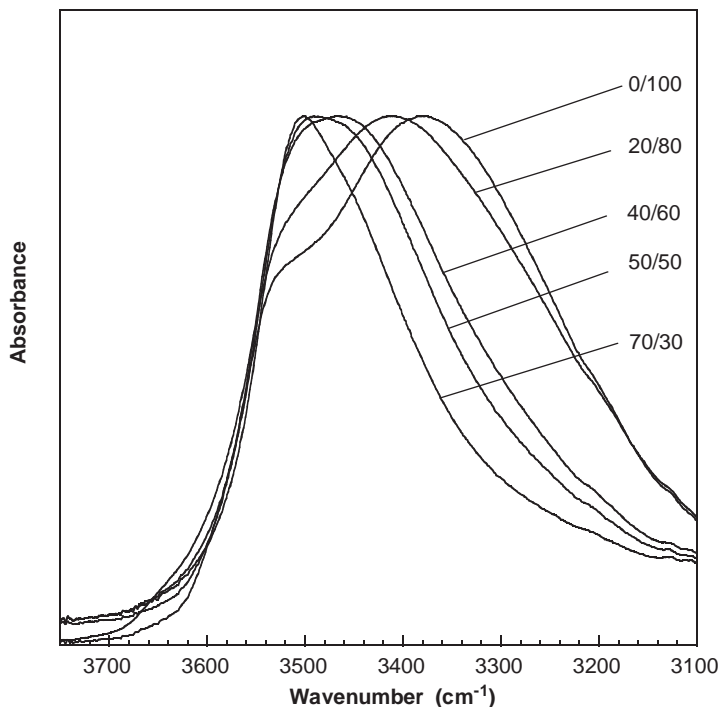


**Figure 2.10** Hydroxyl stretching region for PLLA/PVPh blends of different composition at room temperature.

though recent investigations have indicated that it should be assigned to hydroxyl groups interacting with aromatic rings ( $\text{OH} \cdots \pi$  interactions) [130]. The free OH stretching band has been claimed to occur at about  $3600 \text{ cm}^{-1}$ , but is undetectable in the spectrum of pure PVPh [131]. Hydroxyl–hydroxyl autoassociation occurs in a wide range of different species including dimers and trimers, and results in a very broad band centered at about  $3360 \text{ cm}^{-1}$  [18,132–134]. Upon mixing with PLLA, the maximum of the OH stretching band shifts to higher frequencies. The location of the hydrogen-bonded hydroxyl stretching band is related to the strength of the hydrogen bond interactions, and fact Coleman *et al.* [135] have used the frequency difference ( $\Delta\nu$ ) between the hydrogen-bonded hydroxyl absorption and the free hydroxyl absorption to measure the average strength of the intermolecular interaction. The observed blue shift indicates that the  $\text{OH} \cdots \text{O}=\text{C}$  interassociation interactions formed upon the addition of PLLA to PVPh are weaker than the initially existing  $\text{OH} \cdots \text{OH}$  autoassociating interactions. This behavior is consistent with the negative deviation relative to the Fox equation observed for the dependence of  $T_g$  on composition in this system. In addition, in the PLLA-rich compositions, most of the OH groups of PVPh should be interassociated, and the location observed for the PLLA/PVPh 80/20 composition

( $3500\text{ cm}^{-1}$ ) can be actually assigned to the  $\text{OH}\cdots\text{O}=\text{C}$  interactions. This value is larger than the typical value observed for other polyester/PVPh systems ( $3440\text{ cm}^{-1}$ ). Interestingly, the analysis of the OH stretching region reveals that the  $\text{OH}\cdots\text{O}=\text{C}$  hydrogen bonds in the PLA/PVPh system are weaker than in similar polyester/PVPH systems.

The polymer–polymer interaction parameter for the PLA/PVPh system, obtained from melting point depression measurements,  $\chi_{23} = -0.4$ , was also smaller than the typical values reported for other polyester/PVPh systems ( $\chi_{23}$  values in the range of  $-1.0$  to  $-1.4$ ), in agreement with the analyses performed using FTIR. The weaker nature of the interassociating  $\text{OH}\cdots\text{O}=\text{C}$  interactions in the PLA/PVPh systems was explained in terms of functional group accessibility issues, which when considered as a whole include several steric effects such as intramolecular screening, steric hindrances, steric shielding effects, group spacing, and chain stiffness [27]. Among these effects, steric shielding (where a portion of the molecule shields the functional group) was considered the most relevant factor for explaining the weaker nature of the interactions in the PLA/PVPh blends [27].

In addition to the experimental analyses, MD simulations using the COMPASS force-field were performed to gain insight into the miscibility behavior of the PLLA/PVPh and PDLA/PS blends [17]. Figure 2.11 shows the snapshots of amorphous unit cells of PLLA/PVPh blends of different compositions. In agreement with the experimental results, molecular modeling calculations predicted miscibility for the PLLA/PVPh system. The calculated Flory–Huggins interaction parameter ( $\chi$ ) was also in reasonable agreement with the experimental results, and also with estimations based on existing miscibility models. Finally, although the dependence of the interaction parameter with composition and the prediction of miscibility were correct, the molecular modeling analyses were found to underestimate the strengths of the interactions.

### 2.3.1.8 PLA Blended with Poly(butylene succinate) (PBS) and Poly(ethylene succinate) (PESu)

Poly(butylene succinate) (PBS) is a highly crystalline biodegradable polyester with  $T_g$  and  $T_m$  values of about  $-30^\circ\text{C}$  and  $115^\circ\text{C}$ , respectively. PBS is produced via a polycondensation reaction of 1,4-butanediol and succinic acid, both of which monomers can be obtained from renewable sources. The tensile yield strength of unoriented specimens may reach 30–35 MPa, and is comparable to that of polypropylene. PBS is a flexible material with a Young's modulus in the range 300–500 MPa, depending on the degree of crystallinity [136]. Therefore, the blending of PBS with PLA should increase the toughness and the rate of crystallization of the PLA, without compromising the biodegradability of the final material [137,138].

The miscibility of PLA/PBS has been investigated by several groups, and immiscibility has been reported in all cases [137–142]. For example, Park and Im [138] observed a jump in specific heat at temperatures close to the  $T_g$  of PLLA for the whole range of blend compositions, indicating the existence of a PLLA-rich

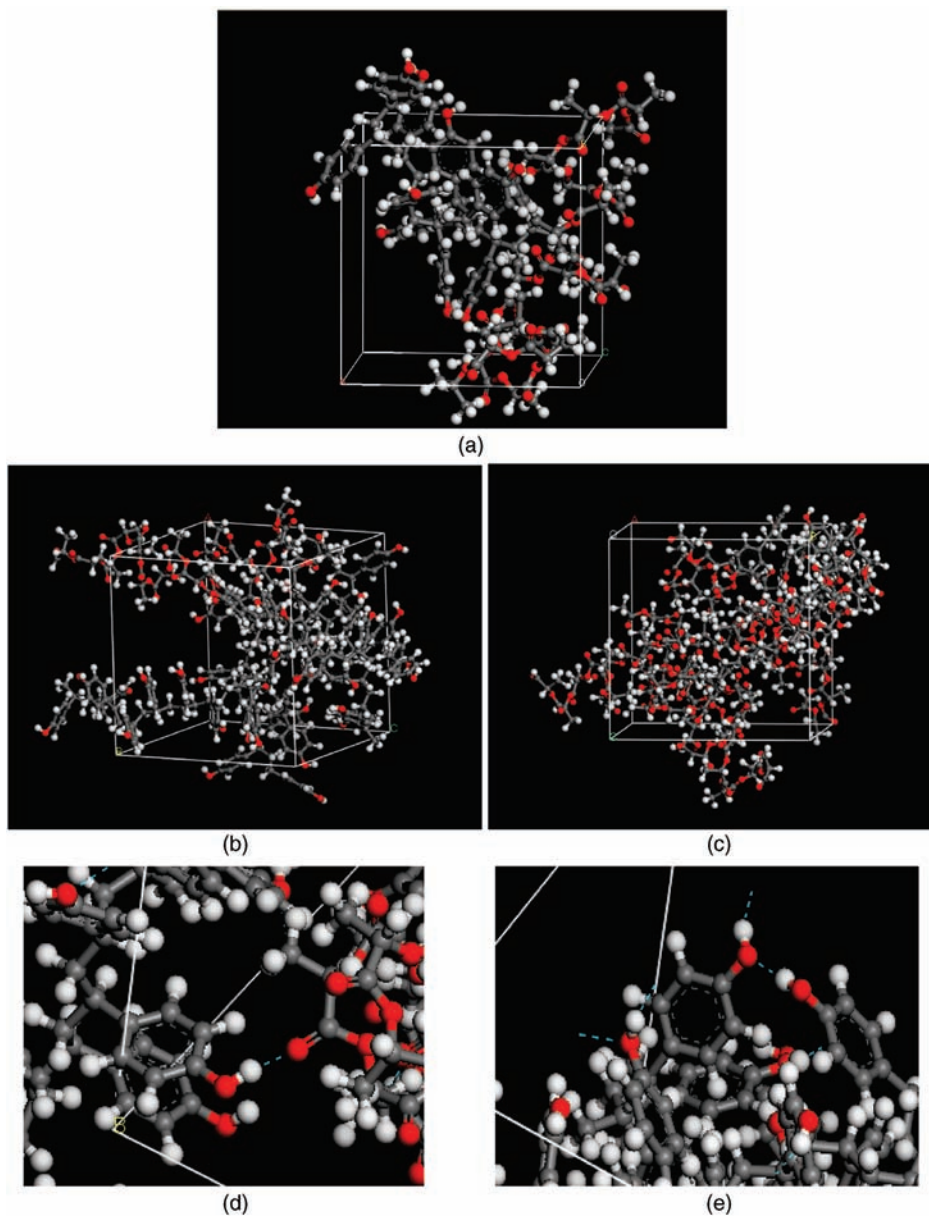


**Figure 2.11** Snapshots of the amorphous unit cells of PLLA/PVPh blends of different composition, containing (a) 1-1, (b) 1-4 and (c) 4-1 chains of PLLA-PVPh. Snapshots (d) and (e) display respectively  $\text{O}-\text{H} \cdots \text{O}=\text{C}$  and  $\text{O}-\text{H} \cdots \text{O}-\text{H}$  hydrogen bonds.



phase. Both, Bhatia *et al.* [139] and Shibata *et al.* [143] also investigated this system and found that the blends showed some compatibility when the composition of PBS was below 20 wt%. In contrast, immiscibility in the molten state was reported by Yokohara *et al.* for high-molecular-weight PLA/PBS blends ( $M_{w\text{PLA}} = 3.5 \times 10^5$  and  $M_{w\text{PBS}} = 1.5 \times 10^5$ ) [137]. The blends exhibited a phase-separated structure, while a system comprised of 5–20 wt% PBS exhibited a PBS dispersed phase in the PLA matrix. The interfacial tension of PBS and PLA, as estimated from a rheological emulsion model, was  $3.5 \text{ mN m}^{-1}$ . This result was also indicative of the immiscibility of this polymer pair.

Poly(butylene succinate-co-butylene carbonate) (PEC) is a random copolymer which has been recently developed by Mitsubishi Gas Chemical Company as a new biodegradable thermoplastic. PEC contains a small amount of butylene carbonate units ( $\sim 10 \text{ mol.}\%$ ) that reduce the crystallization degree of the butylene succinate repeat units without significantly affecting the transition temperatures ( $T_g = -26^\circ\text{C}$  and  $T_m = 106^\circ\text{C}$  in the case of PEC), that remain close to the values of PBS [144]. When Hirano *et al.* [145] investigated the miscibility of PEC ( $M_w = 10^5$ ) with low-molecular-weight PLA ( $M_w = 2000 \text{ g mol}^{-1}$ ), miscibility was observed for the polymer/oligomer system, and the dependence of  $T_g$  on composition was found to follow the Fox equation.

Poly(ethylene succinate) (PESu) is also a crystalline biodegradable polyester with  $T_g$  and  $T_m$  values of  $-10^\circ\text{C}$  and  $105^\circ\text{C}$ , respectively. Lu *et al.* [146] studied the miscibility of blends of PESu with PLA, and reported an immiscibility of the system. Woo and coworkers [147] recently conducted another study which confirmed UCST behavior for the PLA/PESu blends. The cast blends were found to be immiscible at room temperature, but were transformed into homogeneous mixtures on heating to high temperatures. The PLA/PESu blends could also be locked into a quasi-miscible state by quenching from above the UCST. These quasi-miscible blends were analyzed to assess the strength of the interactions by using a melting-point-depression method; this led to an interaction parameter  $\chi = -0.73$ , and suggested moderate to strong interactions, as might be expected for carbonyl-containing polymers. Furthermore, characterization of the spherulite growth rates of PESu in the UCST-quenched PLA/PESu blends of different composition revealed that the amorphous component of higher  $T_g$  (PDLLA) significantly depressed the growth rates of the blends, supporting the quasi-miscible state of the UCST-quenched PLA/PESu blends. Finally, the L/D configuration in PLAs did not influence the phase behavior of this system; rather, the UCST was elevated with increasing  $M_w$  of PLAs in the blends.

### 2.3.1.9 PLA Blended with Poly(propylene carbonate) (PPC) and Poly(trimethylene carbonate) (PTMC)

Poly(propylene carbonate) (PPC) is a biodegradable aliphatic polycarbonate that is synthesized from carbon dioxide and propylene epoxide. It is an amorphous polymer with  $T_g$  at about  $20^\circ\text{C}$  that can be used as a toughening agent [148–150]. Both, PLA and PPC were reported to be compatible materials; adding PLA to PPC

enhanced the  $T_g$  and the thermal stability (measured by thermogravimetric analysis) of PPC in blends. Several possible interactions between the chains of PLA and PPC were suggested according to the FTIR analysis [150].

Poly(trimethylene carbonate) (PTMC) is an amorphous elastomeric biomaterial with a  $T_g$  of about  $-15^\circ\text{C}$ . PTMC exhibits good mechanical properties, including high toughness and tensile strength. Blends of PTMC and PLA were reported by Moon *et al.* [151]. The miscibility of PTMC and PLLA at the air/water interface was found to depend on the pH of the subphase. The PTMC/PLLA blends were miscible at neutral conditions (pH 7.4), whereas phase separation was observed in basic conditions (pH 10.7). The phase-separation behavior at pH 10.7 was related to the interruption of the attractive interaction between PTMC and PLLA, induced by extra sodium and hydroxide ions existing at the air/water interface. On the basis of these results, a mechanism for the hydrolytic degradation of PTMC and PLLA was proposed.

#### 2.3.1.10 PLA/Poly(styrene) (PS) Blends

Poly(styrene) (PS) is a synthetic nonbiodegradable polymer. The interfacial tension between PLA and PS, measured using a modified deformed drop retraction (DDR) method, was  $6.1\text{ mN m}^{-1}$  at  $200^\circ\text{C}$ , indicating immiscibility for the PLA/PS system [152,153]. Mohamed *et al.* [154] studied the PLA/PS system by means of Fourier transform infrared-photoacoustic spectroscopy (FTIR-PAS), with the aim of probing the level of intermolecular interactions between the components of the blend. This analysis suggested the existence of  $n-\pi$  interactions between PLA and PS, indicating some extent of molecular impingement. However, immiscibility was concluded according to DSC results. Miscibility can be enhanced through the incorporation of  $-\text{OH}$  side groups into PS, as proposed by Zuza *et al.* [155], who synthesized poly(styrene-co-hydroxystyrene) (PSHS) copolymers (also termed poly(styrene-co-vinylphenol) (PSVPh) copolymers) with different hydroxystyrene (HS) contents which were subsequently blended with PDLLA. A molar content of about 16 mol.% HS (PSHS16) was found necessary to promote complete miscibility of the PDLLA/PSHS system. The SEM micrographs in Figure 2.12 show clear phase-separated morphologies for the PDLLA/PS system, while homogeneous single-phase morphologies were found for the PDLLA/PSHS16 system. Different properties of the immiscible PLA/PS systems have also been investigated by others [156–158].

#### 2.3.1.11 PLA Blended with Other Polymers

In addition to the systems discussed above, other studies documenting the miscibility of PLA with several blend partners have been conducted. Nonetheless, the literature dealing with each of these systems is scarce, and it was preferred that these were included in a different section. Blends of polyamide (PA) with PLA were recently reported by Feng *et al.* [159]. When these authors studied the structure and properties of blends by means of FTIR, DMTA, DSC and SEM analysis, the DSC scans showed two  $T_g$ -values located at about the glass transition temperatures of PLA and PA, and slightly shifted towards each other. This behavior

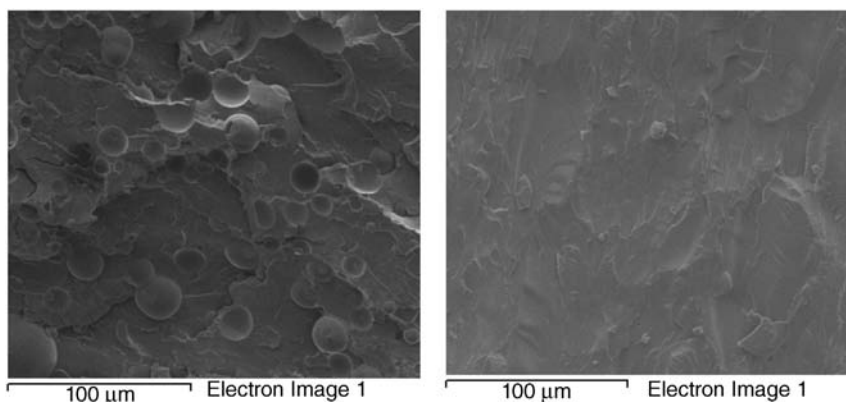


**Figure 2.12** Scanning electron microscopy images of fractured surfaces. (a) PDLLA/PS 75/25; (b) PDLLA/PSHS16 50/50.

suggested a partially miscible system, probably due to hydrogen bonding between the molecules of PA and PLA. In addition, a strong interfacial adhesion was claimed to explain the improved tensile properties of this system. The same research group also investigated blends of PLA with a thermoplastic polyurethane (TPU) [160], the chemical structure of which was similar to that of the PA, but the TPU contained an ether group in its repeat unit. The PLA/TPU blends showed improved toughness, and the  $T_g$ -values of PLA and TPU in the blends were also shifted towards each other; this suggested a partially miscible system, presumably because of hydrogen-bonding interactions between the molecules of TPU and PLA. The morphological analysis showed well-dispersed spherical particles of TPU in the PLA matrix.

Poly(ethylene terephthalate) (PET) is a commercially important engineering thermoplastic with good thermal and mechanical properties, low permeability, and chemical resistance. It is widely used for producing bottle containers and food packaging, and is therefore an interesting blend partner for PLAs. Its  $T_g$  is in the region of 70 °C (quenched, amorphous PET) to 80 °C (crystalline PET), and its  $T_m$  is about 250 °C. When binary blends of PET and PLA were studied by Chen *et al.* [161], using DSC and X-ray scattering, the mixture was found to be miscible in the melt over the entire composition range, according to the single  $T_g$  criterion. Moreover, PET was found to have a higher ability than PLA to form the rigid amorphous fraction (RAF), leading to a large solid fraction once the PET had crystallized.

Lin *et al.* [162] modified PLA with a biodegradable hyperbranched poly(ester amide) (HBP) and reported that mixtures presented lower  $T_g$ -values than the neat polymers, indicating a partial miscibility of the blends that was attributable to hydrogen-bonding interactions between the carbonyl group of PLA and the hydroxyl and/or amine groups of HBP. This component was found to act primarily as a plasticizer that improves the mechanical properties of PLA. When Zhang

*et al.* [163] studied melt-blended PLA/HBP systems containing up to 20 wt% HBP, the miscibility of HBP in PLA was found to decrease with an increase in HBP concentration, indicating a partial miscibility for this system. Subsequent FTIR analysis demonstrated intermolecular hydrogen bonding between PLA and HBP, thus restricting the mobility of PLA. DSC thermograms revealed two  $T_g$ -values for compositions exceeding 10 wt% HBP, and miscible blends were only found for compositions below 10 wt% HBP. Other new high-molecular-weight plasticizers for PLA were proposed by Okamoto *et al.* [164]. These new plasticizers were polyester-diols (PED), and the blends of these components with PLA resulted in homogeneous or phase-separated blends, depending on the composition. Miscible blends were formed with 20 wt% of polyethylene adipate (PEA) or polydiethylene adipate (PDEA), while phase-separated blends were obtained with 20 wt% of polybutylene adipate (PBA) or polyhexamethylene adipate (PHA). The PEDs miscible with PLA were those with solubility parameters,  $\delta$ , closest to that of PLA.

### 2.3.1.12 PLA Blended with Other Copolymers

This section describes the blends of PLA with copolymers that are not discussed in the preceding paragraphs. Thermoplastic Konjac glucomannan (TKGM) is a graft copolymer synthesized from konjac glucomannan (a high-molecular-weight polysaccharide) grafted with vinyl acetate and methyl acrylate. Hence, TKGM contains polyether and mannose as soft and hard polymer segments, respectively. Melt blends of TKGM and PLA were thermodynamically miscible, as evidenced by a single composition-dependent  $T_g$ , single-phase morphologies, and the establishment of interactions between TKGM and PLA in the blends [165].

## 2.3.2

### Blends Containing Poly( $\epsilon$ -caprolactone) (PCL)

PCL is a biodegradable, biocompatible, and semicrystalline aliphatic polyester with  $T_g$  and  $T_m$  at about  $-60^\circ\text{C}$  and  $60^\circ\text{C}$ , respectively [166]. Blends with PCL are probably among the most widely investigated series of blends involving one or more crystallizable components and, in this context, provide information that enhances the general understanding of polymer blends. PCL forms miscible blends with PVPh [84], poly(vinyl chloride) (PVC) [82], poly(carbonate) (PC) [83], poly(*p*-chlorostyrene) (PpClS) [167], polyphenols [168], phenolics [169], poly(phenyl methacrylate) (PPhMA) [170], poly(benzyl methacrylate) (PBzMA) [171], poly(styrene-*co*-acrylonitrile) (SAN) [86], poly(4-hydroxystyrene-*co*-methoxystyrene) (HSMS) [89] and poly(vinyl methyl ether) (PVME) [85]. In contrast, immiscibility was reported on blends of PCL with PGA, PLA [91], PHB, PHBV [172], CAB [173] and PS [174].

## 2.3.3

### Blends Containing Poly(hydroxy butyrate) (PHB)

In addition to PLAs and PCL, PHB is among the most widely studied of the biopolymers. PHB is a thermoplastic aliphatic polyester that is produced by bacterial

fermentation and belongs to the group of poly(hydroxyalkanoate)s (PHAs). Miscible blends were prepared by mixing PHB with PVAc [175], PVC [176], PEO [177], cellulose acetate butyrate (CAB) [178], cellulose acetate propionate (CAP) [179], PVPh [180], poly(epichlorohydrin) (PEC) [181], poly(ethylene succinate) (PES) [182], poly(vinylidene chloride-co-acrylonitrile) (P(VDC-AN)) [180,183], and poly(vinyl acetate-co-vinyl alcohol) (P(VAc-co-VA)) [184]. In addition, microbial isotactic PHB is miscible with synthetic atactic PHB, the atactic PHB being located in the amorphous region between the crystalline lamellae of microbial PHB [185]. On the other hand, immiscibility or partial miscibility has been determined between PHB and certain blend partners such as PMMA [186], PVA [187] and PCL [188].

#### 2.3.4

##### **Blends Containing Poly(*p*-dioxanone) (PPDO)**

PPDO is a colorless, semicrystalline polymer prepared by the ROP of *p*-dioxanone. The polymer exhibits a very low  $T_g$  in the range of  $-10^\circ\text{C}$  to  $0^\circ\text{C}$ , and melts at about  $110^\circ\text{C}$ . PPDO undergoes degradation by the nonspecific scission of the ester moieties located in the chain backbone. However, due to the high crystallinity and hydrophobicity of the polymer, it can be considered a slow to moderately degrading polymer [41]. PPDO is actually an aliphatic polyether-ester with particular characteristics that are owed to the coexistence of ether and ester groups that endow PPDO with special characteristics, such as excellent biodegradability and flexibility [189]. In spite of the outstanding properties of PPDO compared to other commercially available absorbable polymers (e.g., polylactide or polyglycolide), investigations focused on PPDO are few in number. Most studies with this polymer have been directed towards its structural characterization or biodegradation behavior. In fact, only a few studies have been conducted to date examining the miscibility of PPDO, and the only miscible counterpart reported until now is poly(ethylene succinate) (PES) [190]. The chemical structures of both PPDO and PES are very similar, and in fact the  $T_g$  difference between PPDO and PES is less than  $5^\circ\text{C}$ ; the  $T_m$  difference is also less than  $5^\circ\text{C}$ , and therefore PES seems not to be an interesting mate to modify the mechanical properties of PPDO. On the other hand, immiscible blends of PPDO have been reported with PHB [191], PLLA [192], PDLLA [193], and PVA [194]. In a recently study, PPDO and PVPh were found to be completely miscible over the whole range of compositions, according to the single  $T_g$  criterion [195]. The dependence of  $T_g$  on composition showed a negative deviation relative to the Fox law. The splitting observed in the  $\text{C}=\text{O}$  stretching band of amorphous PPDO was explained in terms of the intramolecular ether-ester interactions that occur in the oxyethanoate structures ( $-\text{O}-\text{CH}_2-\text{CO}-\text{O}-$ ) present in the repeat unit of PPDO. Based on this preliminary analysis, the FTIR spectra of the blends were analyzed and it was established that interassociation contacts occur almost exclusively with the  $\text{C}=\text{O}$  groups of PPDO, while the number of contacts with the ether groups of PPDO is not significant. The red shift observed in the  $\text{C}=\text{O}$  stretching band relative to the

“free” C=O groups was about  $23\text{ cm}^{-1}$ , in good agreement with the values observed in other polyester/PVPh systems.

### 2.3.5

#### Blends Containing Poly(glycolic acid) (PGA) or Polyglycolide

Polyglycolide can be considered one of the first biodegradable synthetic polymers investigated for biomedical applications. PGA is a highly crystalline polymer (45–55% crystallinity) that exhibits a high tensile modulus with very low solubility in organic solvents. The  $T_g$  of the polymer ranges from 35 to 40 °C, and the melting point exceeds 200 °C. In spite of its low solubility, PGA has been fabricated into a variety of forms and structures, with extrusion, injection and compression molding, as well as particulate leaching and solvent casting, being some of the techniques used to develop PGA-based structures for biomedical applications [41]. Blends of PGA were reviewed by Rocha *et al.* [196], who investigated blends of PGA with PCL, poly(D,L-lactide), and poly(3-hydroxybutyrate-co-3-hydroxyvalerate) (PHBV). The specific heat jumps that corresponded to the glass transitions of the pure polymers were found not to be shifted upon blending, indicating a lack of miscibility, as expected according to thermodynamic estimations [197]. In another study, Ellis *et al.* [198] found that blends of PGA with polycarbonate showed the presence of two  $T_g$ -values that were unchanged relative to those of the pure components, and concluded the immiscibility of the blend.

## 2.4

### Revision of Blends Based on Natural Polymers

Natural materials are often complex composites with outstanding mechanical properties. Such complex structures, which have evolved over hundreds of millions of years of evolution, are currently inspiring materials scientists to design novel materials. *Blending* represents one of the simplest methods for designing new materials, and natural polymers have attracted a great deal of attention during the past few decades when new materials have been sought for potential biomedical applications, whether mixed with themselves or combined with synthetic polymers. This final section of the chapter provides a brief revision of the most widely studied and applied natural polymers such as starch, cellulose and chitosan (which are polysaccharides), and collagen (which is a protein).

### 2.4.1

#### Blends Containing Starch

Starch, a biodegradable carbohydrate obtained from natural resources, is composed of D-glucose units polymerized enzymatically by plants. During starch synthesis, two different types of polysaccharide are generated: 10–20% amylose (D-glucose monomers linked through  $\alpha(1 \rightarrow 4)$  glycosidic bonds forming linear

chains) and 80–90% amylopectin (amylose chains branched through  $\alpha(1 \rightarrow 6)$  glycosidic linkages at about every 30 glucose units). Native starch adopts the form of small granules of very characteristic sizes, depending on its origin. The structure of the starch granules is governed by the structure of the dominant polysaccharide, amylopectin; the radially aligned chains are hydrogen-bonded, and the number of branches increases with radius in the amounts required to fill up the space [199–202]. Starch has been used as a filler for plastics for the past two decades. It has the advantages of being renewable, biodegradable, abundantly available, and cheap. However, the major drawback of using starch in polymers is its high moisture sensitivity, which limits its application and increases its susceptibility to thermomechanical degradation during processing [200,203].

Many reports have been made concerning the use of starch with other polymers, and some of these have focused on the miscibility and mechanical properties of the blends. The combination of starch with water-soluble polymers such as PVA and/or polyalkylene glycols has been widely considered since 1970 [201,202]. Blends of starch with PVA have been shown to be compatible; compared to with pure starch, blends present an improved tensile strength, elongation and processability [202,204]. Blends of starch with poly(ethylene-co-vinyl alcohol) (EVA) have been shown to form an “interpenetrated” structure that results in the total insolubility of starch [201,202,205,206]. Other systems that have been investigated are based on incompatible synthetic polymers such as cellulose, cellulose derivatives, or aliphatic polyesters [203,207]. With regards to aliphatic polyesters, blends with PLA showed two distinct  $T_g$ -values, although the  $T_g$ -value corresponding to the PLA-rich phase shifted towards the  $T_g$  of starch with changing blend compositions, indicating some degree of interaction [208]. Observations made using microscopy revealed nonuniformly dispersed PLA inclusions in the starch matrix, and confirmed that phase separation had occurred [209]. The tensile strength and elongation was decreased almost linearly as the starch content was increased. As a consequence of its heterogeneous structure and incompatibility, starch has mainly been studied with other nonbiodegradable polymers such as HDPE and LDPE, in order to obtain plastics with improved biodegradability [210].

Other aliphatic polyesters blended with starch include PCL, polybutylene succinate adipate (PBSA) and PHAs [202,203,207]. Starch/PCL blends observed using SEM showed a dispersion of the starch-rich phase within the continuous PCL matrix; however, these blends showed poor tensile properties [207]. With regards to PHAs, poly(3-hydroxybutyrate) (PHB) has been blended with both starch and thermoplastic starch (TS; this is starch plasticized with glycerol). In the case of PHB/starch blends, the  $T_g$  of PHB was shifted slightly to higher temperatures with the addition of starch, and the addition of up to 30 wt% starch only slightly improved the mechanical properties of PHB, indicating a certain degree of compatibility. Interestingly, blending PHB with TS caused a notable rise in both the  $T_g$  and the mechanical properties of the polyhydroxyalkanoate. Detailed analyses of miscibility behaviors in this PHB/TS system are complex, due to the chemical complexity of this ternary system [211]. Studies of different types of starch blended with PHBV have shown that all the blends presented a general worsening

of the mechanical properties [212,213]. As a consequence, compatibilizers were introduced into the systems to improve the compatibility between aliphatic polyesters such as PCL, PBS and PHBV and starch. In most cases, the compatibilizer would contain an anhydride functional group and was incorporated to the polyester backbone. The results of these studies showed that tensile strengths close to that of the synthetic polyester could be obtained with only small amounts of compatibilizer [214].

#### 2.4.2

##### **Blends Containing Cellulose**

Cellulose is the most abundant natural polymer, and is the structural component of the primary cell wall of green plants. It is a linear polysaccharide consisting of 10 000 to 15 000 D-glucose units linked together by  $\beta$ -(1  $\rightarrow$  4) glycosidic bonds. The main difference between cellulose and other D-glucose-based polysaccharides is that the glucose residue in cellulose is in the  $\beta$  configuration while that in amylose, amylopectin and glycogen is in the  $\alpha$  configuration. This difference provides cellulose with unique physical and chemical properties [215]. In particular, the natural cellulose molecule adopts an extended and rather stiff rod-like conformation, aided by the equatorial conformation of the glucose residues. The multiple hydroxyl groups on the glucose from one chain form hydrogen bonds with oxygen atoms on the same or on a neighbor chain, so that the chains are held firmly together side-by-side and form microfibrils with high tensile strength. This structure is important in conferring rigidity to plant cells, but makes cellulose a very difficult-to-dissolve linear polymer. In fact, only a few specialized solvents, such as *N*-methylmorpholine-*N*-oxide (NMMO) and ionic liquids will dissolve cellulose without chemical modification, and are in fact used to produce regenerated celluloses (e.g., viscose and cellophane) from dissolved pulps. Notably, the constrained solubility of cellulose has hindered investigations of its miscibility, for which many studies have utilized cellulose either in the form of fibers or as cellulose derivatives which have much broader solubilities.

Cellulose has been reported as being miscible with strong hydrogen-bond acceptors such as poly(4-vinylpyridine) [216] and poly(vinylpyrrolidone) [217]. In addition, miscibility has been reported in blends of cellulose with PVA, a system presenting a complex interassociation pattern, since the hydroxyl groups present in both polymers can act as both hydrogen bond donors and acceptors [216,218]. In contrast, phase separation has been observed in blends with PCL, nylon 6 and poly(acrylonitrile) (PAN) [216,219]. The compatibility of the chitin/cellulose system was studied using the D<sub>2</sub>O sorption method in films of varying composition, and by small-angle neutron scattering. The structure of the films was shown to change from homogeneous to microheterogeneous with an increasing content of the second component, while good compatibility was observed only for those blends containing very small amounts (up to 2.5 wt%) of the second component [220,221].

Blends based on cellulose derivatives have been widely investigated, and their review is beyond the scope of this chapter. For example, when cellulose acetate



butyrate was blended with PHBV, using melt compounding, the structure and mechanical properties were shown to depend on the PHBV content. Notably, when the PHBV content was below 50 wt% the blends were amorphous, but they became semicrystalline at higher polyhydroxyalkanoate contents. Partial miscibility was observed with high PHBV contents [202,207,222].

#### 2.4.3

#### Blends Containing Chitosan

Chitin and chitosan are natural, biodegradable polymers that occur abundantly in the natural world, forming the main components of the cell walls of fungi and the exoskeletons of arthropods such as crustaceans and insects. Chitin is a linear homopolymer composed of units of *N*-acetylglucosamine (a derivative of  $\beta$ -glucose). Chitosan is obtained by the deacetylation of chitin (enzymatically driven in Nature, or via strong bases in the laboratory), a reaction that converts a fraction of the *N*-acetylglucosamine units into *N*-glucosamine units. Similar to cellulose, chitin is very difficult to dissolve. When chitin is deacetylated to at least 50 wt%, it becomes soluble in diluted acids and is then referred to as chitosan. The latter material has great potential in pharmaceutical and cosmetic applications due to its biocompatibility, high charge density, nontoxicity and mucoadhesion. Recently, chitosan has attracted attention because the range of its applications has been extended to medical, wastewater treatment, biomembranes and hydrogel development [223–227]. It can also be used in many formulations employed for drug delivery.

Many research groups have attempted to modify the properties of chitosan, and to develop new methods for preparing polymer blends of chitosan and chitin with natural and synthetic polymers. The applications of these materials have been reviewed by Rogovina *et al.* [228]. Chitosan has been shown miscible with PVP, and possible applications have been discussed for this material [229]. Miscibility has also been reported for blends with other tertiary polyamides, namely poly(*N*-methyl-*N*-vinyl acetamide), poly(*N,N*-dimethyl acrylamide), poly(2-methyl-2-oxazoline), and poly(2-ethyl-2-oxazoline). Both, PEO and PVA are synthetic polymers currently used in biomedical applications on the basis of their biocompatibility, and hence they are interesting candidates to be blended with chitosan. Although miscibility has been reported for the chitosan/PEO system, immiscibility has been demonstrated for the chitosan/PVA system, most likely due to the strong autoassociation of PVA [230]. Miscibility has also been reported in blends of chitosan with collagen. Other interesting synthetic biocompatible polymers are PLA and nylon 6, although their blends with chitosan show phase separation [231–233]. PCL has been used together with chitosan in the preparation of several materials for medical applications; in particular, blends of chitosan with PCL have been studied both as a membrane and also as particles [234]. Chitosan has also been blended with several other polysaccharides derived from plants, such as cellulose [235,236], alginates [237], and dextran [238].

## 2.4.4

**Blends Containing Collagen**

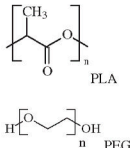
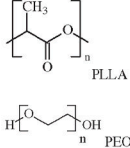
Collagen is the most abundant protein in animals, where it provides the principal structural and mechanical support. It is a major structural protein, forming molecular strands that strengthen the tendons as well as vast resilient sheets that support the skin and internal organs. Collagen is a rather stiff and hard protein that has been compared to steel in structures – not because of its strength but rather because it is a basic structural component of the body [166,215].

The solubility of collagen depends heavily on the age of the tissue from which it is derived [239]. For soluble collagen, it is possible to obtain a blend with the synthetic polymer using a common solvent. Collagen-based materials are widely used in reconstructive medicine, pharmacy and cosmetics. Several reports have been made concerning blends of collagen, some of which have focused on the miscibility of the systems [166]. By using viscometric analysis, miscibility has been demonstrated for binary blends containing collagen and PVP [240]; the collagen/PVA system also showed miscibility at the molecular level. The specific interactions responsible for miscibility in the aforementioned systems have been analyzed in thin films, using FTIR spectroscopy. The amide carbonyl group of PVP in the collagen/PVP system was observed to shift to lower wavenumbers, suggesting hydrogen-bonding interactions between collagen and PVP. In another study, viscometric data obtained for binary blends containing collagen/PEO and collagen/PEG showed that collagen and these polymers were immiscible, although the FTIR spectra revealed some minor interactions between collagen and PEO and/or PEG in the solid state [241]. When the collagen/PLA system was investigated by means of DSC, SEM, tensile tests and biodegradation studies, it was concluded that PLA/collagen forms an immiscible system where collagen separates into a coarse phase. In this case, the mechanical properties were drastically reduced compared to pure PLA, and only the rate of biodegradability was improved by the addition of collagen [242].

Many studies have been conducted with blends based on collagen and chitosan [116,243,244]. The ultimate properties and applications of these blends depend mainly on the concentrations of the individual components. Sionkowska *et al.* [243] investigated the molecular interactions between collagen and chitosan by using viscometry, wide-angle X-ray scattering and FTIR analysis, and showed that the collagen/chitosan blends were miscible at the molecular level. These authors also observed that the interassociation interactions altered the initial helical conformation of collagen and, in turn, its overall physical properties. More recently, tertiary blends have attracted much attention, and such blends composed of PCL, elastin and collagen have been prepared to mimic the structure of native arteries. Subsequently, the electrospinning of these blends led to the production of nanofibrous to microfibrous three-layered, small-diameter vascular grafts in which each layer demonstrated distinct material properties [245].

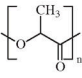
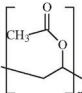
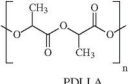
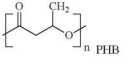
Appendix 2.A Relevant Research Papers

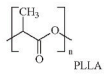
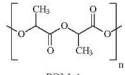
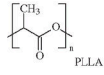
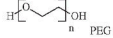
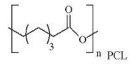
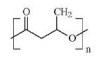
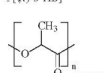
Summary of current research papers on miscibility studies of polymer blends based on poly(lactide) (PLA).

Materials/Blend	Chemical structure	Colleman-Painter $\delta$ (cal cm <sup>-3</sup> ) <sup>1/2</sup>	Points/Conclusion	Year/ Ref
Poly(lactic acid) (PLA) $M_n = 28\,000$ g mol <sup>-1</sup> Poly(ethylene glycol) $M_w = 15\,000$ g mol <sup>-1</sup> $M_w = 3400$ g mol <sup>-1</sup> $M_w = 6000$ g mol <sup>-1</sup> $M_w = 35\,000$ g mol <sup>-1</sup>	 PLA PEG	$\delta_{PLA} = 10.1$ $\delta_{PEG} = 9.4$	1. Blends were obtained by casting using CHCl <sub>3</sub> . 2. PLA/PEG blends comprised two crystalline phases, with both components able to crystallize. 3. Some phase blending occurs, as revealed by the depression of the melting point. 4. IR spectroscopy data indicated the absence of intercomponent hydrogen bonding. 5. In this system, it is believed that the conformation and spatial arrangement of the chains play a fundamental role much more than solubility parameters.	1988 [58]
Poly(L-lactide) (PLLA) $M_n = 800\,000$ g mol <sup>-1</sup> Poly(ethylene oxide) (PEO) $M_w = 4\,000\,000$ g mol <sup>-1</sup>	 PLLA PEO	$\delta_{PLA} = 10.1$ $\delta_{PEO} = 9.4$ $\delta_{PEG} = 9.4$	1. Blends were obtained by solution-precipitation method, using CH <sub>2</sub> Cl <sub>2</sub> as solvent and diethyl ether as precipitant. 2. High-molecular-weight PEO and PLLA are miscible in the amorphous state. A single $T_g$ intermediate was observed between the $T_g$ of the pure components. 3. The equilibrium melting point of PLLA also decreases with increasing PEO concentration in the blend.	1996 [24]

(continued)

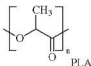
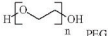
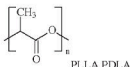
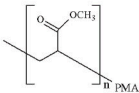
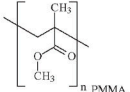
Appendix 2.A (Continued)

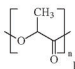
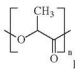
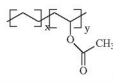
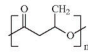
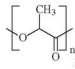
Materials/Blend	Chemical structure	Colleman-Painter $\delta$ (cal cm <sup>-3</sup> ) <sup>1/2</sup>	Points/Conclusion	Year/ Ref
Poly(lactic acid) (PLA) $M_w = 137\,000\text{ g mol}^{-1}$ Poly(vinyl acetate) (PVAc) $M_w = 187\,000\text{ g mol}^{-1}$	<div></div> <div>PLA</div> <div></div> <div>PVAc</div>	$\delta_{\text{PLA}} = 10.1$ $\delta_{\text{PVAc}} = 9.6$	<ol style="list-style-type: none"><li>1. The mixtures were prepared by melt blending in a single-screw extruder.</li><li>2. DSC results showed a single <math>T_g</math> for all PLA/PVAc blend compositions, indicating that PLA and PVAc form miscible blends.</li><li>3. This was also shown in an enzymatic degradation study.</li></ol>	1996 [76]
Poly(DL-lactide) (PDLLA) $M_w = 43\,000\text{ g mol}^{-1}$ Poly( $\beta$ -hydroxybutyrate) (PHB) $M_w = 30\,000\text{ g mol}^{-1}$	<div></div> <div>PDLLA</div> <div></div> <div>PHB</div>	$\delta_{\text{PLA}} = 10.1$ $\delta_{\text{PHB}} = 11.1$	<ol style="list-style-type: none"><li>1. Blends were obtained by casting using CHCl<sub>3</sub>.</li><li>2. Even though it was found in the second heating scan of DSC analysis some changes in the blends such a slight <math>T_m</math> depression, it was concluded that this system is immiscible in the amorphous state because the blend exhibited two <math>T_g</math>s corresponding to the <math>T_g</math>s of plain PHB and PLA.</li><li>3. It was suggested that the changes on the blends occurred where a heat treatment was applied, because of transesterification between the PHB and PLA chains.</li></ol>	1996 [246]

Poly(L-lactide) (PLLA) $M_n = 1\,300\,000\text{ g mol}^{-1}$ Poly(DL-lactide) (PDLLA) PDLLA300, $M_w = 400\,000\text{ g mol}^{-1}$ PDLLA40, $M_w = 59\,000\text{ g mol}^{-1}$ PDLLA6.5, $M_w = 14\,000\text{ g mol}^{-1}$	 PLLA  PDLLA	$\delta_{\text{PLA}} = 10.1$ $\delta_{\text{PDLLA}} = 10.1$	1. Blends were prepared by casting using methylene chloride, dichloromethane. 2. PDLLA is miscible with PLLA, irrespective of the molecular weight of PDLLA, and increases entanglement between PLLA and PDLLA with increasing molecular weight to reduce the growth rate and regularity of PLLA spherulites and PLLA crystallinity.	1996 [50]
Poly(L-lactide) (PLLA) $M_n = 85\,000\text{ g mol}^{-1}$ Poly(ethylene glycol) (PEG) $M_w = 10\,000\text{ g mol}^{-1}$ Poly( $\epsilon$ -caprolactone) (PCL) $M_w = 15\,000\text{ g mol}^{-1}$	 PLLA  PEG  PCL	$\delta_{\text{PLA}} = 10.1$ $\delta_{\text{PEG}} = 9.4$ $\delta_{\text{PCL}} = 9.4$	1. Blends were obtained by casting using $\text{CHCl}_3$ and temperature. 2. PLLA/PEG blends were miscible in the melt over the composition range investigated. The miscibility promoted the spherulite growth rate but depressed the nucleation density of PLLA. The crystallizability of PEG was decreased by blending with PLLA, while that of PLLA was not affected noticeably upon blending with PEG. 4. Phase-separated morphology was identified for PLLA/PCL blends. The crystallization rate of PLLA could be improved by blending with PCL.	1997 [59]
Poly[(R)-3-hydroxybutyric acid, P [(R)-3-HB] $M_n = 300\,000\text{ g mol}^{-1}$ $M_w = 650\,000\text{ g mol}^{-1}$ Poly[(S)-lactic acid], P[(S)-LA] $M_n = 300\,000\text{ g mol}^{-1}$ $M_w = 530\,000\text{ g mol}^{-1}$	 P[(R)-3-HB]  P[(S)-LA]	$\delta_{\text{P}[(\text{R})\text{-3HB}]} = 11.1$ $\delta_{\text{P}[(\text{S})\text{-LA}]} = 10.1$	1. Blends were obtained by casting using $\text{CHCl}_3$ . 2. Blends with high-molecular-weight values showed two phases in the melt, while blends with low-molecular-weight were miscible. 3. On the basis of the relationship between the miscibility of blend and the molecular weight of P[(S)-LA] component, the difference in $\delta_1$ and $\delta_2$ of the blends components in the Flory-Huggins equation was estimated to be $(0.34\text{ J cm}^{-3})^{1/2}$ .	1997 [107]

(continued)

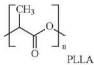
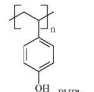
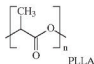
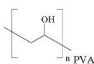
## Appendix 2.A (Continued)

Materials/Blend	Chemical structure	Colleman-Painter $\delta$ (cal cm <sup>-3</sup> ) <sup>1/2</sup>	Points/Conclusion	Year/ Ref
Poly(lactic acid) (PLA) with 96% L and $M_w = 140\,000$ g mol <sup>-1</sup> (approx.) Poly(ethylene glycol) (PEG) $M_w = 20\,000$ g mol <sup>-1</sup>	 	$\delta_{PLA} = 10.1$ $\delta_{PEG} = 9.4$	<ol style="list-style-type: none"> <li>1. PLLA and PEG were melt-blended, using a counter-rotating twin-screw extruder.</li> <li>2. Based on thermal analysis, it was found that PLA and PEG form miscible blends in compositions less than 50/50.</li> <li>3. Both components were able to crystallize, and PEG enhances the crystallization of PLA, however the crystallinity of PEG was suppressed. DMTA results indicated that blends showed some level of plasticization.</li> </ol>	1997 [55]
Poly(L-lactide) PLLA $M_w = 100\,000$ g mol <sup>-1</sup> Poly(D-lactide) PDLA $M_w = 110\,000$ g mol <sup>-1</sup> Poly(methyl acrylate) (PMA) $M_w = 38\,000$ g mol <sup>-1</sup> Poly(methyl methacrylate) (PMMA) $M_p = 480\,000$ g mol <sup>-1</sup>	  	$\delta_{PLLA} = 10.1$ $\delta_{PDLA} = 10.1$ $\delta_{PMA} = 9.6$ $\delta_{PMMA} = 10.2$	<ol style="list-style-type: none"> <li>1. Blends were prepared either by casting from dioxane solution or by the solution/precipitation method (dioxane/hexane).</li> <li>2. PMA and PDLA form miscible blends, it was observed a single <math>T_g</math> composition-dependent.</li> <li>3. PDLA/PMMA blends also are considered as a miscible blend even though the enlargement of the <math>T_g</math> width, observed a high PMMA content, suggesting that the system is in the miscibility limits.</li> <li>3. Both blends, PLLA/PMA and PLLA/PMMA, presented some degree of miscibility in the melt; but after cooling if an adequate thermal treatment is applied, the crystallization tendency of PLLA acted as the driving force for phase separation and the formation of segregated crystalline micro-domains.</li> </ol>	1998 [23]

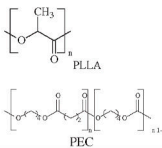
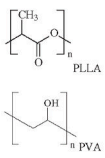
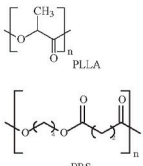
<p>Poly(L-lactic acid) (PLLA)</p> <p>Was study a <math>M_w</math> range, <math>1.0 \times 10^4</math>–<math>9.8 \times 10^5 \text{ g mol}^{-1}</math></p> <p>Poly(D-lactide) (PDLA)</p> <p>Was study a <math>M_w</math> range, <math>2.2 \times 10^4</math>–<math>1.0 \times 10^6 \text{ g mol}^{-1}</math></p>	 <p>PLLA, PDLA</p>	<p><math>\delta_{\text{PLLA}} = 10.1</math></p> <p><math>\delta_{\text{PDLA}} = 10.1</math></p>	<ol style="list-style-type: none"> <li>1. Blends were obtained by casting using <math>\text{CH}_2\text{Cl}_2</math>.</li> <li>2. The enthalpy of melting for stereo complex crystallites in 1:1 blend films was higher than that of homocrystallites when the molecular weight of polymers was below <math>2 \times 10^5</math>, while this relationship was reversed when <math>M_w</math> increased to <math>1 \times 10^6</math>.</li> <li>3. Spherulites formation was suppressed in 1:1 blend, whereas large-sized spherulites were formed for nonblended PLLA and PDLA films, irrespective of the molecular weight.</li> </ol>	<p>1999</p> <p>[45]</p>
<p>Poly(L-lactic acid) (PLLA) star-shaped</p> <p>Poly(ethylene-co-vinyl acetate) (EVA)</p> <p>EVA70 = 70 wt% vinyl acetate</p> <p>EVA85 = 85 wt% vinyl acetate</p>	 <p>PLA</p>  <p>EVA</p>	<p><math>\delta_{\text{PLLA}} = 10.1</math></p> <p><math>\delta_{\text{EVA70}} = 9.9</math></p> <p><math>\delta_{\text{EVA85}} = 10.4</math></p>	<ol style="list-style-type: none"> <li>1. Blends were obtained by casting using <math>\text{CHCl}_3</math> as a solvent.</li> <li>2. Blends of PLLA/EVA70 were immiscible in the whole composition range: <math>T_g</math> and <math>G</math> were nearly constant.</li> <li>3. PLLA/EVA 85 blends were miscible, determined by <math>T_g</math> equilibrium <math>T_m</math> and <math>G</math>. The Flory–Huggins interaction parameter was negative.</li> </ol>	<p>1999</p> <p>[79]</p>
<p>Poly[(R,S)-3-hydroxybutyric acid], P[(R,S)-3-HB] or ataPHB</p> <p><math>M_w = 9400 \text{ g mol}^{-1}</math></p> <p><math>M_w = 21\,000 \text{ g mol}^{-1}</math></p> <p><math>M_w = 140\,000 \text{ g mol}^{-1}</math></p> <p>Poly[(S)-lactic acid], PLA</p> <p><math>M_w = 778\,000 \text{ g mol}^{-1}</math></p>	 <p>P[(R,S)-3-HB]</p>  <p>PLA</p>	<p><math>\delta_{\text{P}[(\text{R,S})\text{-3HB}]} = 11.1</math></p> <p><math>\delta_{\text{P}[(\text{S})\text{-LA}]} = 10.1</math></p>	<ol style="list-style-type: none"> <li>1. Blends were obtained by casting using <math>\text{CHCl}_3</math> as a solvent.</li> <li>2. PLA and low-molecular-weight ataPHB are miscible in the melt within the ataPHB content up to 50 wt%. This blend showed a single <math>T_g</math>. In contrast, the binary blends with high-molecular-weight of ataPHB showed two <math>T_g</math>s.</li> <li>3. Small amounts of ataPHB facilitated the crystallization of PLA.</li> </ol>	<p>2000</p> <p>[109]</p>

(continued)

Appendix 2.A (Continued)

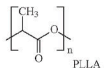
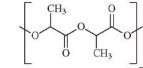
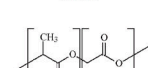
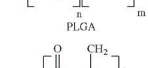
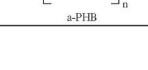

Materials/Blend	Chemical structure	Collerman-Painter $\delta$ (cal cm <sup>-1</sup> ) <sup>1/2</sup>	Points/Conclusion	Year/ Ref
			4. Lamellar thickness of PLA crystals decreased slightly with an increased in ataPHB. 5. Relaxation phenomena were detected at two different temperatures, indicating phase separation.	
Poly(L-lactide) (PLLA) $M_n = 82\,000$ g mol <sup>-1</sup> $M_w = 153\,000$ g mol <sup>-1</sup> Poly(4-vinylphenol) $M_n = 13\,000$ g mol <sup>-1</sup> $M_w = 25\,000$ g mol <sup>-1</sup>	  PLLA PVPh	$\delta_{\text{PLLA}} = 10.1$ $\delta_{\text{PVPh}} = 10.6$	1. Blends were obtained by casting using DMF. 2. Small-angle scattering (SAXS) with the measurement of absolute intensity probed the semi-crystalline morphology of melt-miscible PLLA/PVPh blends. 3. The presence of PVPh in the interlamellar regions enhanced the electron density contrast ( $\Delta n$ ) between the crystalline and amorphous layers.	2000 [128]
Poly(L-lactide) (PLLA) $M_n = 133\,000$ g mol <sup>-1</sup> Poly(vinyl alcohol) atactic (aPVA) and sidiotactic (sPVA) 99% of saponification	  PLLA PVA	$\delta_{\text{PLLA}} = 10.1$ $\delta_{\text{PVA}} = 9.8$	1. Blends were obtained by casting using HFIP. 2. Formation of interpolymer hydrogen bonding in PLLA/PVA with low PLLA contents was demonstrated by FTIR and <sup>13</sup> C-PST MAS NMR measurements. However, two $T_g$ s were detected. 3. WAXD measurements demonstrated that PLLA and PVA crystallize separately.	2000 [74]

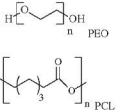
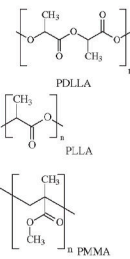


Poly(l-lactic acid) (PLLA) $M_w = 2000 \text{ g mol}^{-1}$ Poly(ester carbonate) = Poly (butylene succinate-co-butylene carbonate) (PEC) $M_w \approx 100\,000 \text{ g mol}^{-1}$		$\delta_{\text{PLLA}} = 10.1$ $\delta_{\text{PEC}} = 10.8$	<ol style="list-style-type: none"> <li>1. Blends were obtained by casting using <math>\text{CHCl}_3</math>.</li> <li>2. Miscibility was found according with the blends "single <math>T_g</math> and Fox equation was used to fit the <math>T_{g,s}</math>."</li> <li>3. The change in birefringence of PLLA spherulites indicated the penetration of PEC lamellae into PLLA spherulites.</li> </ol>	2001 [145]
Poly(l-lactide) (PLLA) $M_w = 330\,000 \text{ g mol}^{-1}$ Poly(vinyl alcohol) (PVA) atactic DP = 2000, 99.5% hydrolyzed		$\delta_{\text{PLLA}} = 10.1$ $\delta_{\text{PVA}} = 9.8$	<ol style="list-style-type: none"> <li>1. Blends were obtained by casting using HFIP and then melt quenched.</li> <li>2. PLLA and PVA molecules were phase-separated in their blends films and PLLA-rich and PVA-rich phases formed a continuous domain in the blends film with a <math>X_{\text{PLLA}}</math> of 0.5, these results were observed by DSC, POM, SEM and X-ray diffractometry.</li> <li>3. It was also discussed a water absorption, a dynamic contact angle and a mechanical study.</li> </ol>	2001 [45,247]
Poly(l-lactic acid) (PLLA) $M_w = 367\,000 \text{ g mol}^{-1}$ Poly(butylene succinate) (PBS) $M_w = 120\,000 \text{ g mol}^{-1}$		$\delta_{\text{PLLA}} = 10.1$ $\delta_{\text{PBS}} = 10.8$	<ol style="list-style-type: none"> <li>1. Blend were prepared by melt-mixing using a twin-screw.</li> <li>2. Blend system exhibited a single <math>T_g</math>.</li> <li>3. A depression of the equilibrium melting point of the PLLA component was observed. The interaction parameter between PLLA and PBS showed a negative value of <math>-0.15</math>.</li> <li>4. Small-angle X-ray scattering revealed that PBS component was expelled out of the interlamellar regions of PLA.</li> </ol>	2002 [138]

(continued)

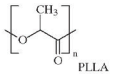
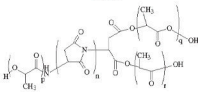
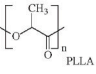
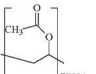
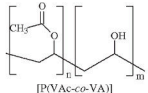
Appendix 2.A (Continued)

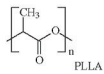
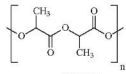
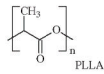
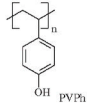
Materials/Blend	Chemical structure	Colleman-Painter $\delta$ (cal cm <sup>-3</sup> ) <sup>1/2</sup>	Points/Conclusion	Year/ Ref
Poly(L-lactide) (PLLA) $M_w = 40\,000$ g mol <sup>-1</sup>		$\delta_{\text{PLLA}} = 10.1$	1. Blends were obtained by casting using CHCl <sub>3</sub> . 2. The a-PHB/PD11A blends are miscible over the whole composition range, all blends show a single $T_g$ . On the other hand, blends of a-PHB with PL5GA and PL16GA show partial miscibility. 3. The solubility limit of a-PHB in PLGA is around 20 wt% in both cases.	2002 [114]
Poly(DL-lactide) (PDLLA) (D/L = 50/50) $M_w = 44\,000$ g mol <sup>-1</sup>		$\delta_{\text{PDLLA}} = 10.1$		
Poly(L-lactide-co-glycolide) (PLGA) PL5GA = 5%mol of glycolide, $M_w = 64\,000$ g mol <sup>-1</sup>		$\delta_{\text{PL5GA}} = 10.2$		
PL16GA, $M_w = 53\,000$ g mol <sup>-1</sup>		$\delta_{\text{PL16GA}} = 10.3$		
PL52GA, $M_w =$ not determined owing to sample insolubility		$\delta_{\text{PL52GA}} = 10.9$		
Poly[(R,S)-3-hydroxybutyrate] (a-PHB) $M_w = 1300$ g mol <sup>-1</sup>		$\delta_{\text{a-PHB}} = 11.1$		

<p>Poly(ethylene oxide) (PEO)  <math>M_w = 100\,000\text{ g mol}^{-1}</math>  Poly(<math>\epsilon</math>-caprolactone) (PCL)  <math>M_w = 14\,300\text{ g mol}^{-1}</math></p>		<p><math>\delta_{\text{PEO}} = 9.4</math>  <math>\delta_{\text{PCL}} = 9.4</math></p>	<ol style="list-style-type: none"> <li>1. Blends were obtained by solution with <math>\text{CHCl}_3</math> and temperature.</li> <li>2. From phase-contrast microscopy it was proven that PEO/PCL blends were immiscible.</li> <li>3. The crystallization rate of PEO decreases with the increases of PCL content in the blends, while the crystallization mechanism did not change.</li> </ol>	<p>2003  [248]</p>
<p>Poly(DL-lactide) (PDLLA)  <math>M_w = 150\,000\text{ g mol}^{-1}</math>  Poly(L-lactide) (PLLA)  <math>M_w = 55\,000\text{ g mol}^{-1}</math>  Poly(methyl methacrylate) (PMMA)  <math>M_w = 1\,000\,000\text{ g mol}^{-1}</math></p>		<p><math>\delta_{\text{PDLLA}} = 10.1</math>  <math>\delta_{\text{PLLA}} = 10.1</math>  <math>\delta_{\text{PMMA}} = 10.2</math></p>	<ol style="list-style-type: none"> <li>1. Blends were obtained by solution-precipitation method, using dioxane as solvent and petroleum ether as precipitant.</li> <li>2. On the basis of DSC results, in solution/precipitation blends, PDLLA is miscible with PMMA because a single <math>T_g</math> suited between the <math>T_g</math>s of the two pure components.</li> <li>3. In the PLLA/PMMA blend, the crystallization of PLLA was restricted by PMMA. Once the thermal history of the blends was destroyed, PLLA and PMMA were miscible.</li> <li>4. The <math>T_g</math> composition relationship for both PDLLA/PMMA and PLLA/PMMA miscible systems obeyed the Gordon-Taylor equation.</li> <li>5. Experimental results that there is no more favorable tendency of PDLLA to form miscible blends with PMMA than PLLA does when PLLA is in the amorphous state.</li> </ol>	<p>2003  [120]</p>

(continued)

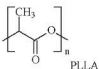
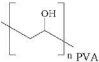
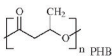
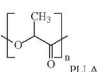
Appendix 2.A (Continued)

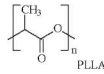
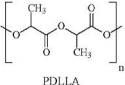
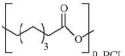
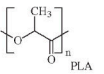
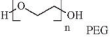
Materials/Blend	Chemical structure	Colleman-Painter $\delta$ (cal cm <sup>-2</sup> ) <sup>1/2</sup>	Points/Conclusion	Year/ Ref
Poly(L-lactic acid) (PLA) $M_w = 139\,000\text{ g mol}^{-1}$ $M_w = 283\,000\text{ g mol}^{-1}$ Poly(aspartic acid-co-lactide) (PAL) $M_w = 14\,700\text{ g mol}^{-1}$	 PLLA  PAL	$\delta_{\text{PLLA}} = 10.1$ $\delta_{\text{PAL}} =$	1. Blends were obtained by casting using a mixture of CHCl <sub>3</sub> and methanol. 2. PAL was miscible with PLA and produced homogeneous transparent blend films without impairing the inherent mechanical properties of PLA. 3. A small amount of added PAL enhanced the degradation rate of PLA effectively in water, soil and compost.	2003 [53]
Poly(L-lactic acid) (PLLA) $M_w = 139\,000\text{ g mol}^{-1}$ Poly(vinyl acetate) (PVAc) $M_w = 167\,000\text{ g mol}^{-1}$ Poly(vinyl acetate-co-vinyl alcohol) [P(VAc-co-VA)] [P(VAc-co-VA)]10 = 10% of degree of hydrolysis [P(VAc-co-VA)]20 [P(VAc-co-VA)]30	 PLLA  $\eta\text{PVAc}$  [P(VAc-co-VA)]	$\delta_{\text{PLLA}} = 10.1$ $\delta_{\text{PVAc}} = 9.6$ $\delta_{[\text{P(VAc-co-VA)]10}} = 9.6$ $\delta_{[\text{P(VAc-co-VA)]20}} = 9.6$ $\delta_{[\text{P(VAc-co-VA)]30}} = 9.7$	1. Blends were obtained by casting using CHCl <sub>3</sub> . 2. PLA/PVAc blends exhibited a single $T_g$ over the entire composition range, indicating that blends were miscible. In contrast, for the blends with even 10% hydrolyzed PVAc copolymer, phase separation was observed. 3. The interaction parameter indicated negative values for up to 10% hydrolyzed samples, but positive values at more than 20% hydrolyzed samples. 4. SAXS analysis revealed that the PVAc component was located in the interlamellar region. 5. POM analysis showed that the [P(VAc-co-VA)] component seemed to be expelled from the interfibrillar regions. 6. SEM analysis showed a significant phase separation with an increasing degree of hydrolysis.	2003 [77]

Poly(L-lactide) (PLLA) $M_n = 323\,800\text{ g mol}^{-1}$ Poly(DL-lactide) (PDLLA) $M_n = 319\,400\text{ g mol}^{-1}$	 <p>PLLA</p>  <p>PDLLA</p>	$\delta_{\text{PLLA}} = 10.1$ $\delta_{\text{PDLLA}} = 10.1$	1. Blends were obtained by melt blending. 2. PLLA/PDLLA blends after solidification were found heterogeneous with $\alpha$ type and $\eta$ type crystals melting.	2005 [46]
Poly(L-lactide) (PLLA) $M_n = 320\,000\text{ g mol}^{-1}$ Poly(4-vinylphenol) $M_n = 20\,300\text{ g mol}^{-1}$	 <p>PLLA</p>  <p>PVPh</p>	$\delta_{\text{PLLA}} = 10.1$ $\delta_{\text{PVPh}} = 10.6$	1. Blends were obtained by casting with dioxane and by solution-precipitation method, using dioxane as solvent and <i>n</i> -hexane as precipitant. 2. Miscibility was found in the PLLA/PVPh system in all the compositions range for blends obtained by solution/precipitation in the dioxane/hexane pair. However, phase separation was observed for PVPh-rich blends obtained by casting from dioxane solutions. 3. By FTIR analysis, hydrogen bonding between both components was established. 4. Equilibrium melting point depression method was applied and a negative interaction parameter and energy density were found. The negative value of the interaction parameter confirms a thermodynamically miscible blend.	2005 [18]

(continued)

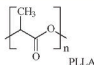
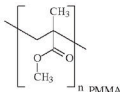
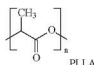
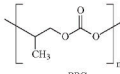
Appendix 2.A (Continued)

Materials/Blend	Chemical structure	Colleman-Painter $\delta$ (cal cm <sup>-3</sup> ) <sup>1/2</sup>	Points/Conclusion	Year/ Ref
Poly(L-lactide) (PLLA) $M_w = 100\,000$ g mol <sup>-1</sup> Molecular weight calculated: Repeat units = 10, $M_w = 900$ g mol <sup>-1</sup> Poly(vinyl alcohol) (PVA) (syndiotactic) Molecular weight calculated: Repeat units = 21, $M_w = 924$ g mol <sup>-1</sup>	 	$\delta_{\text{PLLA}}$ (COMPASS) = 8.65 $\delta_{\text{PLLA}}$ (GCM) = 8.10 $\delta_{\text{PLLA(esp)}}$ = 5.43 $\delta_{\text{PLLA}}$ (Colleman) = 10.1 $\delta_{\text{PVA}}$ (COMPASS) = 11.02 $\delta_{\text{PVA}}$ (GCM) = 10.03 $\delta_{\text{PVA(esp)}}$ = 12.60 $\delta_{\text{PVA}}$ (Colleman) = 9.8	<ol style="list-style-type: none"> <li>1. The reported data on blend miscibility studies of PLLA and PVA polymers were validated using the COMPASS force field and MD simulations protocols.</li> <li>2. It was confirmed that a 1:9 PLLA/PVA blend is miscible because <math>\chi</math> is smaller than <math>\chi_{\text{critical}}</math>, whereas at other compositions these blends are immiscible.</li> <li>3. From the peak obtained by RDF it was found that the C=O group is responsible for the minimal miscibility occurring at low PLLA content of the blend.</li> </ol>	2006 [16]
Poly (3-hydroxybutyrate) (PHB) $M_w = 600\,000$ g mol <sup>-1</sup> Poly(L-lactic acid) (PLA) $M_w = 150\,000$ g mol <sup>-1</sup> $M_w = 4300$ g mol <sup>-1</sup>	 	$\delta_{\text{PHB}} = 11.1$ $\delta_{\text{PLLA}} = 10.1$ $\delta_{\text{PLLA}} = 10.1$	<ol style="list-style-type: none"> <li>1. Blends were obtained by casting using CHCl<sub>3</sub> and temperature.</li> <li>2. The crystallization behavior of immiscible and miscible PHB/PLLA blends was discussed..</li> <li>3. The crystallization dynamics of PLLA and PHB were greatly affected by their miscibility in the blends.</li> <li>4. In the immiscible PHB/PLLA blend, the presence of the PHB component did not affect the crystallization mechanism, but the crystallization rate was substantially depressed.</li> <li>5. In contrast, to the stepwise crystallization of PHB and PLLA in the immiscible blends, an almost simultaneous crystallization of PHB/PLLA miscible blend was observed.</li> </ol>	2006 [111]

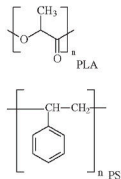
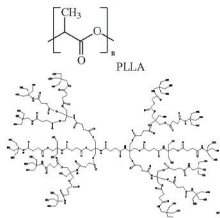
Poly(L-lactide) (PLLA) $M_v = 2250 \text{ g mol}^{-1}$ Poly(DL-lactide) (PDLLA) $M_v = 2320 \text{ g mol}^{-1}$ Poly( $\epsilon$ -caprolactone) (PCL) $M_v = 1280 \text{ g mol}^{-1}$	 <p>PLLA</p>  <p>PDLLA</p>  <p>PCL</p>	$\delta_{\text{PLLA}} = 10.1$ $\delta_{\text{PDLLA}} = 10.1$ $\delta_{\text{PCL}} = 9.4$	<ol style="list-style-type: none"> <li>1. PLLA was melt-blended with PCL and PDLLA was cast-blended in <math>\text{CHCl}_3</math>.</li> <li>2. Phase separation with sharp phase boundaries was revealed in all blends, by direct observation of their morphologies using SEM.</li> <li>3. Consistent with the nonvariation of the melting point with blend composition, the POM revealed a separated crystallization of both components in the blend.</li> </ol>	2006 [249]
Poly(lactic acid) (PLA) $M_w = 74\,000 \text{ g mol}^{-1}$ Poly(ethylene glycol) (PEG) $M_w = 200 \text{ g mol}^{-1}$ $M_w = 400 \text{ g mol}^{-1}$ $M_w = 1000 \text{ g mol}^{-1}$	 <p>PLA</p>  <p>PEG</p>	$\delta_{\text{PLA}} = 10.1$ $\delta_{\text{PEG}} = 9.4$	<ol style="list-style-type: none"> <li>1. PEG was employed as a plasticizer and was blended with PLA by melt-blending.</li> <li>2. PEG was efficient for the <math>T_g</math> reduction; it clearly appears that for compositions higher than 20% of plasticizer, all blends present a limit of miscibility and the <math>T_g</math> reaches a plateau value.</li> <li>3. PEGs exhibit lower interaction parameters with PLA than other plasticizers and yield a better fit with the Fox relation.</li> <li>4. PEGs induce a decrease in the cohesion of these materials, shown by a very low stress at breaking.</li> </ol>	2006 [65]

(continued)

Appendix 2.A (Continued)

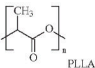
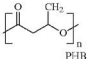
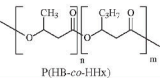
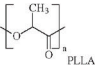
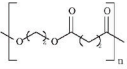
Materials/Blend	Chemical structure	Colleran-Painter $\delta$ (cal cm <sup>-2</sup> ) <sup>1/2</sup>	Points/Conclusion	Year/ Ref
Poly(L-lactide) (PLLA) $M_w = 320\,000$ g mol <sup>-1</sup> Poly(methyl methacrylate) (PMMA) $M_w = 100\,000$ g mol <sup>-1</sup>	 	$\delta_{\text{PLLA}} = 10.1$ $\delta_{\text{PMMA}} = 10.2$	<ol style="list-style-type: none"> <li>1. Blends were obtained by melt blending.</li> <li>2. In a previous study, it was established that PLLA/PMMA blends, which are mixed with a solution/precipitation method, are miscible [120]. In the present study it was confirmed that PLLA/PMMA blends, which are mixed with a two-roll mill, are also miscible.</li> <li>3. The <math>T_g</math> behavior indicated the miscibility of PLLA and PMMA blends.</li> <li>4. The hydrolytic degradation rate of PLLA/PMMA blend can be widely controlled by PMMA content.</li> </ol>	2006 [121]
Poly(L-lactic acid) (PLLA) $M_w = 160\,000$ g mol <sup>-1</sup> $M_w = 220\,000$ g mol <sup>-1</sup> Poly(propylene carbonate) (PPC) $M_w = 70\,000$ g mol <sup>-1</sup> $M_w = 110\,000$ g mol <sup>-1</sup>	 	$\delta_{\text{PLA}} = 10.1$ $\delta_{\text{PPC}} = 10.2$	<ol style="list-style-type: none"> <li>1. Blends were obtained by melt-blending in a screw extruder.</li> <li>2. PLLA/PPC are partially miscible but compatible to some extent because of the similar chemical natures of the blend components.</li> <li>3. The compatibility of PLA and PPC enhances <math>T_g</math> and <math>T_{max}</math> of PPC in blends.</li> <li>4. There are several specific interactions between the chains of PLA and PPC: C—H and =O—C and C=O...O=C and C=O...O—C dipole-dipole interactions.</li> </ol>	2006 [150]

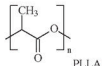
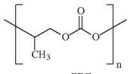
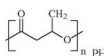
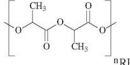
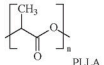
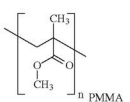


Poly(lactic acid) (PLA) Poly(styrene) (PS)	 <div>PLA</div> <div>PS</div>	$\delta_{\text{PLA}} = 10.1$ $\delta_{\text{PS}} = 9.5$	<ol style="list-style-type: none"><li>1. Compounding of blends was accomplished by melt extrusion into a twin-screw extruder.</li><li>2. PLA/PS blends showed two composition-dependent <math>T_g</math>s; however, FTIR-PAS investigation suggested the existence of <math>\pi</math>-<math>\pi</math> interactions between both polymers.</li><li>3. The blends also displayed <math>T_m</math> and <math>T_c</math> values which varied with composition.</li></ol>	2007 [154]
Poly(lactide) (PLA) $M_n = 80$ kDa Hyperbranched poly(ester amide) (HBP) $M_n = 4.2$ kDa	 <div>PLLA</div> <div>HBP</div>	$\delta_{\text{PLA}} = 10.1$ $\delta_{\text{HBP}} = \text{NA}$	<ol style="list-style-type: none"><li>1. Blends were prepared by melt-mixing up to 20% (w/w) of HBP.</li><li>2. A slight depression of <math>T_g</math> was observed with the increase of HBP component, indicating partial miscibility of the blend system, which resulted from H-bonding between carbonyl of PLA with hydroxyl and amine of HBP.</li><li>3. The HBP component acted as a heterogeneous nucleating agent and improved the crystallization capability of PLA.</li><li>4. HBP as a modifier improved the processability and thermal and mechanical properties of PLA.</li></ol>	2007 [162]

(continued)

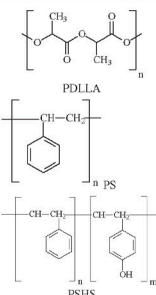
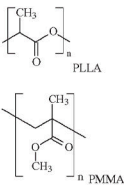
Appendix 2.A (Continued)

Materials/Blend	Chemical structure	Colleman-Painter $\delta$ (cal cm <sup>-3</sup> ) <sup>1/2</sup>	Points/Conclusion	Year/ Ref
Poly(l-lactic acid) (PLLA) $M_w = 150\,000$ g mol <sup>-1</sup>		$\delta_{\text{PLLA}} = 10.1$	1. Blends were obtained by casting using CHCl <sub>3</sub> and temperature. 2. The combination of DSC, WAXD, and IR microspectroscopy revealed that both PHB/PLA and P(HB-co-HHx)/PLLA blends are immiscible, but the P(HB-co-HHx)/PLLA blends are somewhat more compatible.	2007 [118]
Poly[(R)-3-hydroxybutyric acid (PHB) $M_w = 600\,000$ g mol <sup>-1</sup>		$\delta_{\text{PHB}} = 11.1$		
Poly[(R)-3-hydroxybutyrate-co-(R)-3-hydroxyhexanoate) (P(HB-co-HHx)) $M_w = 638\,000$ g mol <sup>-1</sup>		$\delta_{\text{P(HB-co-HHx)}} = 10.9$		
Poly(lactic acid) (PLA) $M_w = 300\,000$ g mol <sup>-1</sup>		$\delta_{\text{PLA}} = 10.1$	1. Blends were obtained by melt blending. 2. It was found that PLA and PBS are immiscible in the molten state and the blends exhibit a phase-separated structure. 3. The interfacial tension between PLA and PBS was found to be 3.5 mN m <sup>-1</sup> . 4. Blending PBS accelerates the crystallization of PLA.	2008 [137]
Poly(butylene succinate) (PBS) $M_w = 150\,000$ g mol <sup>-1</sup>		$\delta_{\text{PBS}} = 10.8$		

Poly(L-lactic acid) (PLLA) $M_w = 160\,000\text{ g mol}^{-1}$ $M_w = 220\,000\text{ g mol}^{-1}$ Poly(propylene carbonate) (PPC) $M_w = 70\,000\text{ g mol}^{-1}$ $M_w = 110\,000\text{ g mol}^{-1}$ Carbon black(CB) as a filler	 <p>PLLA</p>  <p>PPC</p>	$\delta_{PLA} = 10.1$ $\delta_{PPC} = 10.2$	1. Blends were obtained by melt-blending and then pressed. 2. An interaction existed between the matrix and CB particles, revealed by FTIR. 3. PLLA/PPC are partially miscible because their similar chemical natures as it was introduced before.	2008 [149]
Poly(3-hydroxybutyrate) (PHB) $M_w = 230\,000\text{ g mol}^{-1}$ Poly(D,L-lactic acid) (RPLA)	 <p>PHB</p>  <p><sup>n</sup>RPLA</p>	$\delta_{RPLA} = 10.1$ $\delta_{PHB} = 11.1$	1. Blends were obtained by solution-precipitation method, using $\text{CHCl}_3$ and temperature as solvent and hexane as precipitant. 2. Decreases of a single $T_g$ from both mt-DSC and mFTM experiments, with increase RPLA content in blends. Verified miscibility of PHB-RPLA for above 50% RPLA content.	2008 [113]
Poly(L-lactide) (PLLA) $M_w = 152\,000\text{ g mol}^{-1}$ Poly(methyl methacrylate) (PMMA) $M_w = 53\,500\text{ g mol}^{-1}$ $M_w = 100\,000\text{ g mol}^{-1}$ $M_w = 350\,000\text{ g mol}^{-1}$	 <p>PLLA</p>  <p>PMMA</p>	$\delta_{PLLA} = 10.1$ $\delta_{PMMA} = 10.2$	1. Blends of PLLA and PMMA were prepared by casting using $\text{CHCl}_3$ . 2. UCST behavior in PMMA/PLLA blends was demonstrated, where the UCST phase reversibility is possible via solvent re-dissolution. 3. The phase diagrams with respect to temperature for the PMMA/PLA blend system are highly dependent on the molar mass, which contributes to entropic terms. 4. Possibilities of chemical reactions and transreactions at temperatures around the UCST are excluded in the blends from NMR analysis of heat-homogenized blend samples.	2008 [122]

(continued)

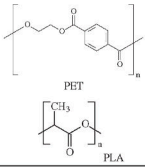
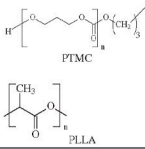
## Appendix 2.A (Continued)

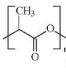
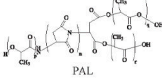
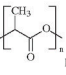
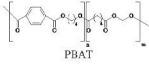
Materials/Blend	Chemical structure	Colleman-Painter $\delta$ (cal cm <sup>-3</sup> ) <sup>1/2</sup>	Points/Conclusion	Year/ Ref
Poly(DL-lactide) (PDLLA) $M_n = 290\,000$ g mol <sup>-1</sup> Poly(styrene) (PS) $M_n = 110\,000$ g mol <sup>-1</sup> Poly(styrene-co-hydroxystyrene (PSHS) PSHS8 PSHS12 PSHS16, $M_n = 10\,000$ g mol <sup>-1</sup>	 <p>PDLLA</p> <p>PS</p> <p>PSHS</p>	$\delta_{PDLLA} = 10.1$ $\delta_{PS} = 9.5$ $\delta_{PSHS8} = 9.6$ $\delta_{PSHS12} = 9.6$ $\delta_{PSHS16} = 9.7$	<ol style="list-style-type: none"> <li>PSHS copolymers containing different HS content were synthesized and blended with PDLLA. Blends were prepared both by the solution-precipitation method (THF/hexane) and by melt mixing.</li> <li>Incorporation of -OH groups into PS by copolymerization with hydroxystyrene caused specific OH...O=C interactions with carbonyl groups of PDLLA.</li> <li>It was found that a mole content of about 16% of HS (PSHS16) was necessary in copolymer chains to establish enough hydrogen bonds to assure the complete miscibility of the system.</li> <li>By heating above the <math>T_g</math> of the polymers promoted miscibility.</li> <li>Blends showed a single <math>T_g</math>.</li> </ol>	2008 [155]
Poly(L-lactic acid) (PLLA) $M_w = 152\,000$ g mol <sup>-1</sup> Poly(methyl methacrylate) (PMMA) iPMMA, $M_w = 300\,000$ g mol <sup>-1</sup> sPMMA, $M_w = 50\,000$ g mol <sup>-1</sup> aPMMA, $M_w = 53\,500$ g mol <sup>-1</sup> $M_w = 100\,000$ g mol <sup>-1</sup> $M_w = 350\,000$ g mol <sup>-1</sup>	 <p>PLLA</p> <p>PMMA</p>	$\delta_{PLLA} = 10.1$ $\delta_{PMMA} = 10.2$	<ol style="list-style-type: none"> <li>Blends of PLLA and PMMA were prepared by casting using CHCl<sub>3</sub>.</li> <li>In continuing the previous studies proving existence in <math>M_w</math>-dependence UCST behavior in blends of atactic PMMA with PLLA, this study investigated the relationship between the chain configuration in PMMA and blends miscibility or UCST behavior.</li> <li>The conclusion was that tactic configuration in PMMA does influence the phase behavior in the blends.</li> <li>iPMMA/PLLA blend, unlike either sPMMA/PLLA or aPMMA/PLLA, immiscible from ambient to high temperature of thermal degradation, showing no signs of UCST.</li> <li>The solubility parameter for PLLA is closer to that for aPMMA and sPMMA, respectively, but apparently differs more significantly from that for iPMMA.</li> </ol>	2008 [123]

(continued)

(continued)

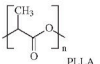
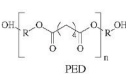
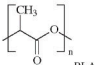
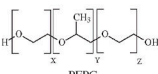
Appendix 2.A (Continued)

Materials/Blend	Chemical structure	Coleman-Painter $\delta$ (cal cm <sup>-3</sup> ) <sup>1/2</sup>	Points/Conclusion	Year/ Ref
Poly(ethylene terephthalate) (PET) $M_n = 25\,000\text{ g mol}^{-1}$ Poly(lactic acid) (PLA)	 <p>PET</p> <p>PLA</p>	$\delta_{\text{PET}} = 12.4$ $\delta_{\text{PLA}} = 10.1$	<ol style="list-style-type: none"> <li>1. Blends were prepared by casting with HFIP.</li> <li>2. PET/PLA blends were found to be miscible in the melt over the entire composition range. Both quenched amorphous and semicrystalline blends exhibit a single, composition-dependent <math>T_g</math>.</li> <li>3. PET can crystallize in all blends. In contrast, PLA crystallization is strongly affected by the mobility of the PET fraction.</li> </ol>	2009 [161]
Poly(trimethylene carbonate) (PTMC) $M_n = 27\text{ kDa}$ Poly(L-lactide) (PLLA) $M_n = 53\text{ kDa}$	 <p>PTMC</p> <p>PLLA</p>	$\delta_{\text{PTMC}} = 9.9$ $\delta_{\text{PLA}} = 10.1$	<ol style="list-style-type: none"> <li>1. Blends were prepared by casting with CHCl<sub>3</sub>.</li> <li>2. PTMC/PLLA blends were miscible at neutral condition (pH 7.4), whereas they have the phase separation on basic condition (pH 10.7). This phase separation behavior at pH 10.7 was related to the interruption of the attractive interaction between PTMC and PLLA, brought about by sodium and hydroxide ions.</li> </ol>	2009 [151]

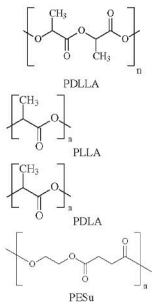
<div><div>Poly(L-lactic acid) (PLLA)</div><div>Poly(aspartic acid-co-lactide) (PALs)</div><div><math>M_n = 1000 \text{ g mol}^{-1}</math></div><div><math>M_n = 4300 \text{ g mol}^{-1}</math></div></div>	<div><div></div><div></div></div>	<div><math>\delta_{\text{PLLA}} = 10.1</math></div> <div><math>\delta_{\text{PAL}} = \text{NA}</math></div>	<div><div>1. PLLA and PAL were melt-mixed.</div><div>2. The addition of PAL did not accelerate the hydrolysis of the PLLA in air.</div><div>3. The degradation of PLLA was significantly accelerated by the addition of PAL in water, with the degradation rate constant increasing linearly with increase in the PAL concentration, when the same PAL was used for the blend preparation.</div><div>4. The distribution of PALs with higher [LA]/[As] occurs at a smaller scale in blends, and implies that a higher miscibility of the PAL with PLLA results in a larger contact area between the components, thereby accelerating the degradation efficiently.</div></div>	<div>2009</div> <div>[52]</div>
<div><div>Poly(lactic acid) (PLA)</div><div><math>M_w = 200 \text{ kDa}</math></div><div>Poly(butylene adipate-co-terephthalate) (PBAT)</div><div><math>M_w = 145 \text{ kDa}</math></div></div>	<div><div></div><div></div></div>	<div><math>\delta_{\text{PLA}} = 10.1</math></div> <div><math>\delta_{\text{PBAT}} = 11.5</math></div>	<div><div>1. PLA and PBAT blend were prepared by melt-blending in an internal mixer.</div><div>2. The degree of crystallinity of PLA in various blends all markedly was increased, and the crystallization mechanism was almost unchanged.</div><div>3. The equilibrium melting point of PLA initially decreased with the increase of PBAT content, and then increased when the PBAT content in the blends was 60 wt% compared no neat PLA.</div><div>4. The spherulitic morphology of PLA was influenced apparently by crystallization temperature and blending with PBAT. The crystal structure of PLA was not modified by the blending, and the crystal structure almost remained unchangeable, based on WAXD measurements.</div></div>	<div>2009</div> <div>[251]</div>

(continued)

## Appendix 2.A (Continued)

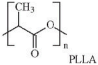
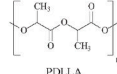
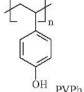
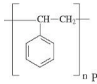
Materials/Blend	Chemical structure	Colleman-Painter $\delta$ (cal cm <sup>-3</sup> ) <sup>1/2</sup>	Points/Conclusion	Year/ Ref
Poly(lactic acid) (PLA) $M_w = 170 \text{ kg mol}^{-1}$ Polyester-diols (PED) $M_w = 2000 \text{ g mol}^{-1}$ Polyethylene adipate (PEA): $R = (\text{CH}_2)_2$ Poly(butylene adipate) (PBA): $R = (\text{CH}_2)_4$ Poly(hexamethylene adipate) (PHA): $R = (\text{CH}_2)_6$ Poly(diethylene adipate) (PDEA): $R = (\text{CH}_2)_2\text{-O-}(\text{CH}_2)_2$	  PLLA PED	$\delta_{\text{PLA}} = 10.1$ $\delta_{\text{PEA}} = 10.0$ $\delta_{\text{PBA}} = 9.6$ $\delta_{\text{PHA}} = 9.4$ $\delta_{\text{PDEA}} = 9.9$	1. PLA/PEG blends were prepared by melt-blending. 2. The PLA/PEA 80/20 blend and the PLA/PDEA 80/20 blend are miscible with PLA, while the PLA/PBA 80/20 blend and the PLA/PHA 80/20 blend are partially miscible with PLA. 3. The miscibility of PEA, PBA, PHA is roughly explained by solubility parameter calculated by the method of Small. The $T_g$ of the PLA-rich phases decreases with decreasing differences in solubility parameter values between PLA and PED. 4. The good miscibility of PDEA with PLA would be due to large configurational entropy caused by chain flexibility of PDEA with the ether bond. 5. Thermal analysis by DSC shows an enhanced crystallization of the PLA/PEA and the PLA/PDEA miscible blends.	2009 [164]
Polylactide (PLA) PLA1 = L-lactide content of 98%. $M_w = 207 \text{ kDa}$ PLA2 = L-lactide content of 88%. $M_w = 320 \text{ kDa}$ Poly(ethylene glycol-co-propylene glycol) (PEPG) $M_n = 12 \text{ kDa}$	  PLA PEPG	$\delta_{\text{PLA}} = 10.1$ $\delta_{\text{PEPG}} = 9.1$	1. PLA/PEG blends were prepared by melt mixing using a twin-screw. 2. PEPG was miscible with the two types of PLA in the blend composition range of 5–20 wt%, and can effectively decrease the $T_g$ of PLA. 3. Neat PLA2 lost the ability to crystallize in the DSC and DMTA measurements; however, it could crystallize more easily due to the improved crystallizability with the addition of PEPG.	2010 [67]

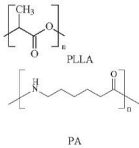
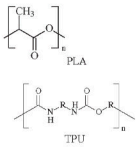


<p>Poly(D,L-lactic acid) (PDLLA)  <math>M_w = 157\,000\text{ g mol}^{-1}</math>  Poly(L-lactic acid) (PLLA)  <math>M_w = 152\,000\text{ g mol}^{-1}</math>  Poly(D-lactic acid) (PDLA)  <math>M_w = 124\,000\text{ g mol}^{-1}</math>  Poly(ethylene succinate) (PESu)  <math>M_w = 10\,000\text{ g mol}^{-1}</math></p>	 <p>PDLLA  PLLA  PDLA  PESu</p>	<p><math>\delta_{PDLLA} = 10.1</math>  <math>\delta_{PLLA} = 10.1</math>  <math>\delta_{PDLA} = 10.1</math>  <math>\delta_{PESu} = 11.7</math></p>	<ol style="list-style-type: none"> <li>1. PLA/PESu were prepared by casting using <math>\text{CHCl}_3</math> as a solvent.</li> <li>2. PLA/PESu blends are of UCST systems. Namely, this blends turn from two-phase mixtures at ambient temperature into homogeneous miscible mixtures at high temperatures; the phase boundary between the two-phase to one-phase mixtures is UCST.</li> <li>3. Cast-blends of PLA/PESu reveals two <math>T_g</math>s. However, when quenched from UCST, the blends of PESu with PLA all exhibit a single, composition-dependent <math>T_g</math>, suggesting miscibility in blends.</li> <li>4. The PLA/PESu blends can be locked into a quasi-miscible state by quenching rapidly from above UCST.</li> <li>5. The interaction strength parameter suggests that there is interaction, albeit not strong.</li> <li>6. PDLLA significantly depresses the blend's growth rates, supporting the quasi-miscible state of UCST-quenched PLA/PESu blends.</li> <li>7. The L/D configuration in PLAs does not influence the phase behavior of PLA/PESu blends; however, the molecular weights are apparently correlated with the temperature of UCST phase diagrams. Generally, UCST is elevated with increase of <math>M_w</math> of PLAs in the blends.</li> </ol>	<p>2010  [147]</p>
--	--	--	---	------------------------

(continued)

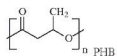
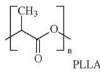
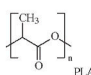
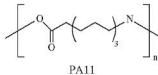
Appendix 2.A (Continued)

Materials/Blend	Chemical structure	Colleman-Painter $\delta$ (cal cm <sup>-3</sup> ) <sup>1/2</sup>	Points/Conclusion	Year/ Ref
Poly(L-lactide) (PLLA) Molecular weight calculated: Repeat units = 20, $M_w = 1440$ g mol <sup>-1</sup>		$\delta_{PLLA(MD)} = 8.5$ $\delta_{PLLA(exp)} = 10.6$ $\delta_{PLLA}$ (Colleman) = 10.1 $\delta_{PDLLA(MD)} = 8.6$ $\delta_{PDLLA(exp)} = 10.6$	1. Miscibility state of PLLA with PVPh was investigated using MD simulations. Molecular modeling based on COMPASS force-field predicted selected critical properties for the miscibility behavior of polymer systems. 2. The solubility parameters and molecular weight of each polymer studied by employed this simulations were calculated. The miscibility state of PLA blends with PS and PVPh was subsequently investigated. 3. The interaction parameters estimated using known miscibility models with some simple assumptions provided a closer approach to the experimental results. 4. The fact that the COMPASS force-field is parameterized using low-molecular-weight compounds may explain some of the observed deviations, since polymer-specific features such as cooperativity effects are not expected to occur in those compounds.	2010 [17]
Poly(D,L-lactide) (PDLLA) Molecular weight calculated: Repeat units = 20, $M_w = 1440$ g mol <sup>-1</sup>		$\delta_{PDLLA}$ (Colleman) = 10.1 $\delta_{PVPh(MD)} = 10.4$ $\delta_{PVPh(exp)} = 12.0$ $\delta_{PVPh}$		
Poly(vinylphenol) (PVPh) Molecular weight calculated: Repeat units = 10, $M_w = 1200$ g mol <sup>-1</sup>		$\delta_{PVPh}$ (Colleman) = 10.6 $\delta_{PS(MD)} = 8.4$ $\delta_{PS(exp)} = 9.4$ $\delta_{PS(Colleman)} = 9.5$		
Poly(styrene) (PS) Molecular weight calculated: Repeat units = 10, $M_w = 1040$ g mol <sup>-1</sup>				

<p>Poly(l-lactic acid) (PLLA)  <math>M_n = 100\,000\text{ g mol}^{-1}</math>  Polyamide (PA)  Terpolymer:PA6/PA66/PA610,  with a monomer ratio 38/35/27,  was used to reduce melting point  of PA</p>	 <p>PLLA</p> <p>PA</p>	<p><math>\delta_{\text{PLLA}} = 10.1</math>  <math>\delta_{\text{PA}} = 10.5</math></p>	<ol style="list-style-type: none"> <li>1. PLA/PA blends were prepared by melt-blending.</li> <li>2. Two <math>T_g</math>s of PLA and PA in blends were found, and these shifted to the inside of their respective original <math>T_g</math> suggestive of a partially miscible system due to hydrogen bonding between PLA and PA.</li> <li>3. The addition of PA reduces the spherulite size of the blends.</li> <li>4. PLA/PA blends showed an almost constant melting temperature, and the crystallinity of PA phase increased with increasing PA content but decreased for the PLA phase.</li> <li>5. Spherical particles of PA were found dispersed homogeneously in the PLA matrix.</li> <li>6. The strong interfacial adhesion of the two phases was beneficial for the improvement of the tensile properties of the blends.</li> </ol>	<p>2010  [159]</p>
<p>Poly(lactide) (PLA)  <math>M_w = 100\,000\text{ g mol}^{-1}</math>  Thermoplastic polyurethane  (TPU)  <math>M_w = 47\,000\text{ g mol}^{-1}</math></p>	 <p>PLA</p> <p>TPU</p>	<p><math>\delta_{\text{PLA}} = 10.1</math>  <math>\delta_{\text{TPU}} = 13.8</math>  <math>R = \text{CH}_2 = 13.8</math></p>	<ol style="list-style-type: none"> <li>1. Blends of PLA/TPU were melt-blending.</li> <li>2. The two <math>T_g</math>s of PLA and TPU in the blends shifted to the inside of their respective original <math>T_g</math>s; this was suggestive of a partially miscible system because of hydrogen bonding between the molecules of TPU and PLA.</li> <li>3. Spherical particles of TPU dispersed homogeneously in the PLA matrix.</li> <li>4. The use of TPU greatly improved the fracture toughness of PLA.</li> </ol>	<p>2011  [160]</p>

(continued)

Appendix 2.A (Continued)

Materials/Blend	Chemical structure	Coleman-Painter $\delta$ (cal cm <sup>-3</sup> ) <sup>1/2</sup>	Points/Conclusion	Year/ Ref
Poly (3-hydroxybutyrate) (PHB) $M_e = 285\,000\text{ g mol}^{-1}$ Poly(L-lactic acid) (PLLA) $M_e = 9200\text{ g mol}^{-1}$ $M_v = 153\,100\text{ g mol}^{-1}$	 	$\delta_{\text{PLA}} = 10.1$ $\delta_{\text{PHB}} = 11.1$	1. PHB/PLLA blends were prepared by casting using $\text{CHCl}_3$ . 2. Miscibility of a commercial sample of PHB with a low and high molar mass PLLA was studied. 3. PHB and low molar mass PLLA are miscible within the whole concentration range; a single $T_g$ was observed. 4. In the case of PHB/high molar mass PLLA mixtures, the presence of separated peaks of cold crystallization on the DSC trace disallowed $T_g$ to be read. Hence, $T_g$ blends was studied by temperature modulated DSC (TMDSC). 5. PHB and high molar mass PLLA presented immiscibility of the mixtures.	2011 [112]
Polylactide (PLA) $M_w = 188\,000\text{ g mol}^{-1}$ Polyamide11 (PA11) $M_w = 25\,000\text{ g mol}^{-1}$	 	$\delta_{\text{PLA}} = 10.1$ $\delta_{\text{PA11}} = 9.4$	1. Blends of PLA/PA11 were melt-blending with a twin-screw. 2. The study revealed good self-compatibility of PLA/PA11 immiscible binary blends without using a compatibilizing agent. This compatibility was suggested by the micronic to submicronic dispersion of the minor component in the matrix of the mayor component. 3. The experimental findings for this blend vouch in favor of neutral interactions between the unlike chains. 4. PA11 did not operate with a nucleating effect on PLA, both upon cooling and heating. This was evidence of no capability of PLA for epitaxial crystallization onto the PA11 crystal surface.	2011 [252]

NA, data not available.

## Appendix 2.B List of Abbreviations and Nomenclature

The abbreviations of individual monomers, polymers and copolymers are based on those used by the original authors and are identified within the text. However, some more generally used abbreviations are as follows.

### 2.B.1

#### Chemical Terms

Prefixes: R-, alkyl-, Me-, methyl-, Et-, ethyl-, Bu-, butyl-, Pr-, propyl-, Ac-, acetyl-

---

ethylene acrylic acid	EAA
glycolic acid	GA
L(+) or S(+) lactic acid	LLA
D(−) or R(+) lactic acid	DLA
3(or $\beta$ )-butyrolactone	3(or $\beta$ )BL
3(or $\beta$ )-hydroxybutyric acid	3-HBA
propylene glycol	PG
R-3-hydroxybutyric acid	R3HBA
triethyl citrate	TEC
4(or $\gamma$ )-hydroxybutyric acid	4-HBA
3-hydroxyvaleric acid	3-HVA
methyl methacrylate	MMA

---

### 2.B.2

#### Polymers and Copolymers

---

poly( $\alpha$ - or 2-hydroxy acid)	P $\alpha$ HA
poly(glycolic acid)	PGA
poly(lactic acid)	PLA
poly(L-lactic acid)	PLLA
poly(D-lactic acid)	PDLA
poly(D,L- or R,S-lactic acid)	P(D,L or R,S)LA
polylactide	PLA
poly( $\epsilon$ -caprolactone)	PCL
poly(valerolactone)	PVL
poly( $\beta$ -D,L-butyrolactone)	P( $\beta$ (D,L)BL)
poly(hydroxyalkanoate)	PHA
poly(3- or $\beta$ -hydroxyalkanoate)	P(3 or $\beta$ )HA
poly(3-hydroxybutyrate)	P3HB
atactic poly(3-hydroxybutyrate)	a-PHB
poly(R-3-hydroxybutyrate)	PR3HB
poly(RS)-hydroxybutyrate	P(RS)HB
poly(3-hydroxyvalerate)	P3HV

poly(4-hydroxybutyrate)	P4HB
poly(6-hydroxyhexanoate)	PHH
polyethylene	PE
polystyrene	PS
poly(vinyl alcohol)	PVA
poly(ethylene oxide)	PEO
poly(vinyl acetate)	PVAc
polypropylene	PP
poly(ethylene terephthalate)	PET
poly(vinyl chloride)	PVC
poly(methyl methacrylate)	PMMA
poly(ethylene glycol)	PEG
poly(sebacic anhydride)	PSA
poly( <i>p</i> -dioxanone)	PPDO
poly(vinyl acetate- <i>co</i> -vinyl alcohol)	[P(VAc- <i>co</i> -VA)]
poly(carboxyphenoxyhexane)	PCPH
poly(1,4-ethylene adipate)	PEA
poly(cyclohexyl methacrylate)	PCHMA
poly(epichlorohydrin)	PEC
poly(carboxyphenoxyvaleric acid)	PCPV
poly(glycolic acid- <i>co</i> -lactic acid)	PGLA
poly(lactic acid- <i>co</i> -glycolic acid)	PLGA
poly(D,L-lactic acid- <i>co</i> -glycolic acid)	P(D,L)LGA
hyperbranched poly(ester amide)	HBP
polyester diols	PED
polyethylene adipate	PEA
polydiethylene adipate	PDEA
polybutylene adipate	PBA
polyhexamethylene adipate	PHA
poly(trimethylene carbonate)	PTMC
thermoplastic Konjac glucomannan	TKGM
poly(ethylene- <i>co</i> -vinyl acetate)	EVA
poly(butylene succinate- <i>co</i> -butylene carbonate)	PEC
poly(aspartic acid- <i>co</i> -lactide)	PAL
poly(ethylene glycol- <i>co</i> -propylene glycol)	PEPG
Poly(vinyl chloride)	PVC

---

### 2.B.3

#### Notations

COMPASS = Condensed-phase optimized molecular potentials for atomistic simulation studies

DSC = Differential scanning calorimetry

DMTA	= Dynamic mechanical thermal analysis
FDA	= Food and Drug Administration
FTIR-PAS	= Infrared photoacoustic spectroscopy
FTIR	= Fourier transform infrared spectroscopy
HM	= High molecular weight
$^1\text{H}$ NMR	= Proton nuclear magnetic resonance
MW	= molecular weight
LW	= Lower-molecular-weight
LCST	= Lower Critical Solution Temperature
O. M.	= Optical microscopy (also OM)
[(polymer)]	= amount/concentration of the cited polymer
POM	= Polarized optical microscopy
SALS	= Small-angle light scattering (also SALLS)
SAXS	= Small-angle X-ray scattering
SEM	= Scanning electron microscopy
RDF	= Computing radial distribution function
RAF	= Rigid amorphous fraction
ROP	= Ring-opening polymerization
TMDSC	= Modulated DSC
UCST	= Upper Critical Solution Temperature
WAXS	= Wide-angle X-ray scattering

#### 2.B.4

##### Symbols

$C_p$	= heat capacity under constant pressure
$b$	= thickness of a monomolecular crystal layer
$B_{12}$	= interaction density
$D$	= coefficient of diffusion
$G$	= isothermal spherulite growth rate
$k$	= Avrami constant for primary crystallization processes
$k'$	= Avrami constant for secondary crystallization processes
$n$	= Avrami exponent for primary crystallization processes
$R$	= spherulite radius
$R$	= universal gas constant
$T_c$	= bulk crystallization temperature
$T_{c,cold}$	= cold crystallization temperature
$T_g$	= glass transition temperature
$T_m$	= measured melting temperature of the crystalline phase
$T_m^o$	= theoretical melting temperature for crystalline lamellae of infinite thickness
wt%	= weight percentage
$X_c$	= total degree of crystallinity

2.B.5

**Greek Letters** $\chi_{12}$  = polymer–polymer interaction parameter $\delta$  = solubility parameter**Acknowledgments**

The authors are thankful for funds from Basque Government, Department of Education, Universities and Research (GIC10/152-IT-334-10) and Department of Industry & Innovation (Ref. Etortek IE10-276), and from the Spanish Government, Ministry of Science and Innovation, MICINN (BIO2010-21542-C02-01). A predoctoral grant for N. H. M. from the University of the Basque Country (UPV/EHU) is also acknowledged.

**References**

- Atkins, P.W. (1998) *Physical Chemistry*, 6th edn, Oxford University Press, Oxford, UK.
- Flory, P.J. (1953) *Principles of Polymer Chemistry*, Cornell University Press, New York.
- Rubinstein, M. and Colby, R.H. (2003) *Polymer Physics*, Cornell University Press, New York.
- Boyd, R.H. and Phillips, P.J. (1993) *The Science of Polymer Molecules*, Cambridge University Press, Cambridge.
- Robeson, L.M. (2007) *Polymer Blends: A Comprehensive Review*, Hanser, Munich, pp. 254–331.
- Flory, P.J. and Krigbaum, W.R. (1951) *Annu. Rev. Phys. Chem.*, **2**, 383–402.
- Flory, P.J. (1989) *Statistical Mechanics of Chain Molecules*, Hanser, Munich, Germany.
- Coleman, M.M., Graf, J.F., and Painter, P.C. (1991) *Specific Interactions and the Miscibility of Polymer Blends*, Technomic Publishing Inc., Lancaster, PA.
- Hildebrand, J.H. (1964) *The Solubility of Nonelectrolytes*, Dover Publications, New York.
- Tufano, C., Peters, G.W.M., Anderson, P.D., and Meijer, H.E.H. (2008) *J. Colloid Interface Sci.*, **325**, 130–140.
- Lefebvre, A.A., Balsara, N.P., Lee, J.H., and Vaidyanathan, C. (2002) *Macromolecules*, **35**, 7758–7764.
- Gulke, E.A. (1999) Solubility parameter values in bandrup, in *Polymer Handbook*, 4th edn (eds E.H. Immergut and E.A. Gulke), John Wiley & Sons Inc., Hoboken (NJ).
- Van Krevelen, D.W. (1990) *Properties of Polymers: Their Correlation with Chemical Structures Their Numerical Estimation and Prediction from Additive Group Contributions*, Elsevier, Amsterdam, Netherlands.
- Hansen, C.M. (2000) *Hansen Solubility Parameters: A User's Handbook*, CRC Press, Boca Raton, Florida.
- Coleman, M.M., Serman, C.J., Bhagwagar, D.E., and Painter, P.C. (1990) *Polymer*, **31**, 1187–1203.
- Jawalkar, S.S. and Aminabhavi, T.M. (2006) *Polymer*, **47**, 8061–8071.
- Martinez de Arenaza, I., Meaurio, E., Coto, B., and Sarasua, J. (2010) *Polymer*, **51**, 4431–4438.
- Meaurio, E., Zuza, E., and Sarasua, J.R. (2005) *Macromolecules*, **4**, 1207–1215.
- Meaurio, E. and Katime, I. (2005) *Macromolecules*, **290**, 1166–1175.



- 20 Li, D. and Brisson, J. (1998) *Polymer*, **39**, 793–800.
- 21 Gestoso, P. and Brisson, J. (2003) *Polymer*, **44**, 2321–2329.
- 22 Lejardi, A., Meaurio, E., Fernández, J., and Sarasua, J.R. (2011) *Macromolecules*, **44**, 7351–7363.
- 23 Eguiburu, J.L., Iruin, J.J., Fernandez-Berridi, M.J., and San Román, J. (1998) *Polymer*, **39**, 6891–6897.
- 24 Nijenhuis, A.J., Colstee, E., Grijpma, D.W., and Pennings, A.J. (1996) *Polymer*, **37**, 5849–5857.
- 25 Zhang, L., Goh, S.H., and Lee, S.Y. (1998) *J. Appl. Polym. Sci.*, **70**, 811–816.
- 26 Zhang, L., Goh, S.H., and Lee, S.Y. (1998) *Polymer*, **39**, 4841–4847.
- 27 Meaurio, E., Zuza, E., and Sarasua, J. (2005) *Macromolecules*, **38**, 9221–9228.
- 28 Zuza, E., Meaurio, E., Etxeberria, A., and Sarasua, J. (2006) *Macromol. Rapid Commun.*, **27**, 2026–2031.
- 29 Biros, J., Zeman, L., and Patterson, D. (1971) *Macromolecules*, **4**, 30–35.
- 30 Taimoori, M., Modarress, H., Saboury, A.A., and Moosavi-Movahedi, A.A. (2001) *Polym. Eng. Sci.*, **41**, 867–872.
- 31 Taimoori, M., Modarress, H., and Mansoori, G.A. (2000) *J. Appl. Polym. Sci.*, **78**, 1328–1340.
- 32 Coleman, M.M. and Painter, P.C. (1995) *Prog. Polym. Sci.*, **20**, 1–59.
- 33 Painter, P.C. and Coleman, M.M. (2000) Hydrogen bonding systems, in *Polymer Blends*, vol. 1, *Formulation* (eds D.R. Paul and C.B. Bucknall), Wiley Interscience, New York.
- 34 Coleman, M.M. and Painter, P.C. (1998) *Macromol. Chem. Phys.*, **199**, 1307–1314.
- 35 Hu, Y., Gamble, V., Painter, P.C., and Coleman, M.M. (2002) *Macromolecules*, **35**, 1289–1298.
- 36 Case, F.H. and Honeycutt, J.D. (1994) *Trends Polym. Sci.*, **2**, 259–266.
- 37 Mu, D., Huang, X., Lu, Z., and Sun, C. (2008) *Chem. Phys.*, **348**, 122–129.
- 38 Gestoso, P. and Brisson, J. (2001) *Comput. Theor. Polym. Sci.*, **11**, 263–271.
- 39 Kawahara, S., Sato, K., and Akiyama, S. (1994) *J. Polym. Sci., Part B: Polym. Phys.*, **32**, 15–20.
- 40 Angerman, H., Hadziioannou, G., and Brinke, G. (1994) *Phys. Rev. E.*, **50**, 3808–3813.
- 41 Nair, L.S. and Laurencin, C.T. (2007) *Prog. Polym. Sci.*, **32**, 762–798.
- 42 Lim, L., Auras, R., and Rubino, M. (2008) *Prog. Polym. Sci.*, **33**, 820–852.
- 43 Auras, R., Harte, B., and Selke, S. (2004) *Macromol. Biosci.*, **4**, 835–864.
- 44 Urayama, H., Moon, S., and Kimura, Y. (2003) *Macromol. Mater. Eng.*, **288**, 137–143.
- 45 Sarasua, J., Prud'homme, R., Wisniewski, M., Le Borgne, A., and Spassky, N. (1998) *Macromolecules*, **31**, 3895–3905.
- 46 Tsuji, H. and Ikada, Y. (1999) *Polymer*, **40**, 6699–6708.
- 47 Sarasua, J., Arraiza, A., Balerdi, P., and Maiza, I. (2005) *Polym. Eng. Sci.*, **45**, 745–753.
- 48 Sarasua, J., Arraiza, A., Balerdi, P., and Maiza, I. (2005) *J. Mater. Sci.*, **40**, 1855–1862.
- 49 Ikada, Y., Jamshidi, K., Tsuji, H., and Hyon, S. (1987) *Macromolecules*, **20**, 904–906.
- 50 Tsuji, H. and Ikada, Y. (1996) *Polymer*, **37**, 595–602.
- 51 Cha, Y. and Pitt, C.G. (1990) *Biomaterials*, **11**, 108–112.
- 52 Oyama, H.T., Tanaka, Y., and Kadosaka, A. (2009) *Polym. Degrad. Stab.*, **94**, 1419–1426.
- 53 Shinoda, H., Asou, Y., Kashima, T., Kato, T., Tseng, Y., and Yagi, T. (2003) *Polym. Degrad. Stab.*, **80**, 241–250.
- 54 Castillo, R.V. and Mueller, A.J. (2009) *Prog. Polym. Sci.*, **34**, 516–560.
- 55 Sheth, M., Kumar, R.A., Dave, V., Gross, R.A., and McCarthy, S.P. (1997) *J. Appl. Polym. Sci.*, **66**, 1495–1505.
- 56 Faucher, J.A., Koleske, J.V., Santee, E.R., Stratta, J.J., and Wilson, C.W. (1966) *J. Appl. Phys.*, **37**, 3962–3964.
- 57 Cai, Q., Bei, J., and Wang, S. (2002) *Polym. Adv. Technol.*, **13**, 534–540.
- 58 Younes, H. and Cohn, D. (1988) *Eur. Polym. J.*, **24**, 765–773.
- 59 Yang, J., Chen, H., You, J., and Hwang, J.C. (1997) *Polym. J.*, **29**, 657–662.
- 60 Jiang, W. and Schwendeman, S. (2001) *Pharm. Res.*, **18**, 878–885.

- 61 Hu, Y., Rogunova, M., Topolkaraev, V., Hiltner, A., and Baer, E. (2003) *Polymer*, **44**, 5701–5710.
- 62 Nakafuku, C. and Sakoda, M. (1993) *Polym. J.*, **25**, 909–917.
- 63 Lai, W.C., Liao, W.B., and Lin, T.T. (2004) *Polymer*, **45**, 3073–3080.
- 64 Hu, Y., Hu, Y.S., Topolkaraev, V., Hiltner, A., and Baer, E. (2003) *Polymer*, **44**, 5711–5720.
- 65 Pillin, I., Montrelay, N., and Grohens, Y. (2006) *Polymer*, **47**, 4676–4682.
- 66 Baiardo, M., Frisoni, G., Scandola, M., Rimelen, M., Lips, D., Ruffieux, K., and Wintermantel, E. (2003) *J. Appl. Polym. Sci.*, **90**, 1731–1738.
- 67 Ran, X., Jia, Z., Han, C., Yang, Y., and Dong, L. (2010) *J. Appl. Polym. Sci.*, **116**, 2050–2057.
- 68 Kim, K., Chin, I., Yoon, J., Kim, D., and Kim, S. (1996) *Polymer (Korea)*, **20**, 497–505.
- 69 Honarbakhsh, S. and Pourdeyhi, B. (2011) *J. Mater. Sci.*, **46**, 2874–2881.
- 70 Ghosh, S., Viana, J.C., Reis, R.L., and Mano, J.F. (2008) *Acta Biomater.*, **4**, 887–896.
- 71 Tsuji, H., Smith, R., Bonfield, W., and Ikada, Y. (2000) *J. Appl. Polym. Sci.*, **75**, 629–637.
- 72 Kim, K., Chin, I., Yoon, J., Choi, H., Lee, D., and Lee, K. (2001) *J. Appl. Polym. Sci.*, **82**, 3618–3626.
- 73 Tan, B., Lee, J., and Cooper, A.I. (2007) *Macromolecules*, **40**, 1945–1954.
- 74 Shuai, X., He, Y., Asakawa, N., and Inoue, Y. (2001) *J. Appl. Polym. Sci.*, **81**, 762–772.
- 75 Tsuji, H. and Muramatsu, H. (2001) *J. Appl. Polym. Sci.*, **81**, 2151–2160.
- 76 Gajria, A., Dave, V., Gross, R., and McCarthy, S. (1996) *Polymer*, **37**, 437–444.
- 77 Park, J.W. and Im, S.S. (2003) *Polymer*, **44**, 4341–4354.
- 78 Jin, H., Chin, I., Kim, M., Kim, S., and Yoon, J. (2000) *Eur. Polym. J.*, **36**, 165–169.
- 79 Yoon, J., Oh, S., Kim, M., Chin, I., and Kim, Y. (1999) *Polymer*, **40**, 2303–2312.
- 80 Katada, A., Buys, Y.F., Tominaga, Y., Asai, S., and Sumita, M. (2005) *Colloid Polym. Sci.*, **284**, 134–141.
- 81 Labet, M. and Thielemans, W. (2009) *Chem. Soc. Rev.*, **38**, 3484–3504.
- 82 Koleske, J.V. and Lundberg, R.D. (1969) *J. Polym. Sci., Part A-2: Polym. Phys.*, **7**, 795–807.
- 83 Chun, Y., Park, J., Sun, J., and Kim, W. (2000) *J. Polym. Sci., Part B: Polym. Phys.*, **38**, 2072–2076.
- 84 Chen, H., Wang, S., and Lin, T. (1998) *Macromolecules*, **31**, 8924–8930.
- 85 Bisso, G., Casarino, P., and Pedemonte, E. (1999) *Macromol. Chem. Phys.*, **200**, 376–383.
- 86 Princi, E. and Vicini, S. (2010) *J. Polym. Sci., Part B: Polym. Phys.*, **48**, 2129–2139.
- 87 Eastmond, G. (1999) *Adv. Polym. Sci.*, **149**, 59–223.
- 88 Coleman, M.M. and Moskala, E.J. (1983) *Polymer*, **24**, 251–257.
- 89 Sanchis, A., Prolongo, M., Salom, C., and Masegosa, R. (1998) *J. Polym. Sci., Part B: Polym. Phys.*, **36**, 95–104.
- 90 Lezczano, E.G., Prolongo, M.G., and Coll, C.S. (1995) *Polymer*, **36**, 565–573.
- 91 Lopez-Rodriguez, N., Lopez-Arraiza, A., Meaurio, E., and Sarasua, J.R. (2006) *Polym. Eng. Sci.*, **46**, 1299–1308.
- 92 Maglio, G., Malinconico, M., Migliozi, A., and Groeninckx, G. (2004) *Macromol. Chem. Phys.*, **205**, 946–950.
- 93 Dell'Erba, R., Groeninckx, G., Maglio, G., Malinconico, M., and Migliozi, A. (2001) *Polymer*, **42**, 7831–7840.
- 94 Tsuji, H. and Ikada, Y. (1996) *J. Appl. Polym. Sci.*, **60**, 2367–2375.
- 95 Yeh, J., Wu, C., Tsou, C., Chai, W., Chow, J., Huang, C., Chen, K., and Wu, C. (2009) *Polym. Plast. Technol. Eng.*, **48**, 571–578.
- 96 Broz, M., Van der Hart, D., and Washburn, N. (2003) *Biomaterials*, **24**, 4181–4190.
- 97 Tsuji, H. and Ikada, Y. (1998) *J. Appl. Polym. Sci.*, **67**, 405–415.
- 98 Hiljanen-Vainio, M., Varpomaa, P., Seppälä, J., and Törmälä, P. (1996) *Macromol. Chem. Phys.*, **197**, 1503–1523.
- 99 Tsuji, H. and Ikada, Y. (1996) *J. Appl. Polym. Sci.*, **60**, 2367–2375.
- 100 Lopez-Rodriguez, N., Lopez-Arraiza, A., Meaurio, E., and Sarasua, J.R. (2006) *Polym. Eng. Sci.*, **46**, 1299–1308.
- 101 Meredith, J. and Amis, E. (2000) *Macromol. Chem. Phys.*, **201**, 733–739.

- 102 Tsuji, H., Sawada, M., and Bouapao, L. (2009) *ACS Appl. Mater. Interfaces*, **1**, 1719–1730.
- 103 Tsuji, H., Yamada, T., Suzuki, M., and Itsuno, S. (2003) *Polym. Int.*, **52**, 269–275.
- 104 Wu, D., Zhang, Y., Zhang, M., and Zhou, W. (2008) *Eur. Polym. J.*, **44**, 2171–2183.
- 105 Na, Y.H., He, Y., Shuai, X., Kikkawa, Y., Doi, Y., and Inoue, Y. (2002) *Biomacromolecules*, **3**, 1179–1186.
- 106 Blümm, E. and Owen, A.J. (1995) *Polymer*, **36**, 4077–4081.
- 107 Koyama, N. and Doi, Y. (1997) *Polymer*, **38**, 1589–1593.
- 108 Yoon, J., Lee, W., Kim, K., Chin, I., Kim, M., and Kim, C. (2000) *Eur. Polym. J.*, **36**, 435–442.
- 109 Ohkoshi, I., Abe, H., and Doi, Y. (2000) *Polymer*, **41**, 5985–5992.
- 110 Zhang, L., Xiong, C., and Deng, X. (1996) *Polymer*, **37**, 235–241.
- 111 Zhang, J., Sato, H., Furukawa, T., Tsuji, H., Noda, I., and Ozaki, Y. (2006) *J. Phys. Chem. B*, **110**, 24463–24471.
- 112 Malinova, L. and Brozek, J. (2011) *J. Therm. Anal. Calorim.*, **103**, 653–660.
- 113 Gunaratne, L.M., Wasantha, K., and Shanks, R.A. (2008) *Polym. Eng. Sci.*, **48**, 1683–1692.
- 114 Focarete, M., Scandola, M., Dobrzynski, P., and Kowalczyk, M. (2002) *Macromolecules*, **35**, 8472–8477.
- 115 Koyama, N. and Doi, Y. (1996) *Macromolecules*, **29**, 5843–5851.
- 116 Zhang, L., Deng, X., Zhao, S., and Huang, Z. (1997) *J. Appl. Polym. Sci.*, **65**, 1849–1856.
- 117 Furukawa, T., Sato, H., Murakami, R., Zhang, J., Noda, I., Ochiai, S., and Ozaki, Y. (2007) *Polymer*, **38**, 1749–1755.
- 118 Furukawa, T., Sato, H., Murakami, R., Zhang, J., Noda, I., Ochiai, S., and Ozaki, Y. (2007) *Polymer*, **48**, 1749–1755.
- 119 Gross, S., Camozzo, D., Di Noto, V., Armelao, L., and Tondello, E. (2007) *Eur. Polym. J.*, **43**, 673–696.
- 120 Zhang, G., Zhang, J., Wang, S., and Shen, D. (2003) *J. Polym. Sci., Part B: Polym. Phys.*, **41**, 23–30.
- 121 Shirahase, T., Komatsu, Y., Tominaga, Y., Asai, S., and Sumita, M. (2006) *Polymer*, **47**, 4839–4844.
- 122 Li, S. and Woo, E.M. (2008) *Polym. Int.*, **57**, 1242–1251.
- 123 Li, S. and Woo, E.M. (2008) *J. Polym. Sci., Part B: Polym. Phys.*, **21**, 2355–2369.
- 124 Landry, M.R., Massa, D.J., Landry, C.J.T., Teegarden, D.M., Colby, R.H., Long, T.E., and Henriches, P.M. (1994) *J. Appl. Polym. Sci.*, **54**, 991–1011.
- 125 Wang, J., Cheung, M.K., and Mi, Y. (2002) *Polymer*, **43**, 1357–1364.
- 126 He, Y., Zhu, B., and Inoue, Y. (2004) *Prog. Polym. Sci.*, **29**, 1021–1051.
- 127 Kratochvíl, J., Šturcová, A., Sikora, A., and Dybal, J. (2009) *Eur. Polym. J.*, **45**, 1851–1856.
- 128 Chen, H., Liu, H., and Lin, J. (2000) *Macromolecules*, **33**, 4856–4860.
- 129 Bank, M., Leffingw, J., and Thies, C. (1971) *Macromolecules*, **4**, 43–8.
- 130 Choperena, A. and Painter, P. (2009) *Macromolecules*, **42**, 6159–6165.
- 131 Guo, L., Sato, H., Hashimoto, T., and Ozaki, Y. (2011) *Macromolecules*, **44**, 2229–2239.
- 132 Lee, L. and Woo, E. (2004) *Polym. Int.*, **53**, 1813–1820.
- 133 Wang, J., Cheung, M.K., and Mi, Y. (2002) *Polymer*, **43**, 1357–1364.
- 134 Wang, P., Liu, B., Li, L., and Zheng, S. (2008) *J. Macromol. Sci., Part B: Phys.*, **47**, 800–817.
- 135 Moskala, E.J., Varnell, D.F., and Coleman, M.M. (1985) *Polymer*, **26**, 228–234.
- 136 Xu, J. and Guo, B. (2010) *Biotechnol. J.*, **5**, 1149–1163.
- 137 Yokohara, T. and Yamaguchi, M. (2008) *Eur. Polym. J.*, **44**, 677–685.
- 138 Park, J.W. and Im, S.S. (2002) *J. Appl. Polym. Sci.*, **86**, 647–655.
- 139 Bhatia, A., Gupta, R.K., Bhaattacharya, S.N., and Choi, H.J. (2007) *Kor.-Austr. Rheol. J.*, **19**, 125–131.
- 140 Lee, S. and Lee, J. (2005) *Kor.-Austr. Rheol. J.*, **17**, 71–77.
- 141 Bhatia, A., Gupta, R.K., Bhaattacharya, S. N., and Choi, H.J. (2010) *Int. Polym. Proc.*, **25**, 5–14.
- 142 Shibata, M., Teramoto, N., and Inoue, Y. (2006) *Polymer*, **48**, 2768–2777.
- 143 Shibata, M., Inoue, Y., and Miyoshi, M. (2006) *Polymer*, **47**, 3557–3564.

- 144 Qiu, Z., Miao, L., and Yang, W. (2006) *J. Polym. Sci., Part B: Polym. Phys.*, **44**, 1556–1561.
- 145 Hirano, S., Nishikawa, Y., Terada, Y., Ikehara, T., and Nishi, T. (2002) *Polym. J.*, **34**, 85–88.
- 146 Lu, J., Qiu, Z., and Yang, W. (2007) *Polymer*, **48**, 4196–4204.
- 147 Woo, E.M., Hsieh, Y., Chen, W., Kuo, N., and Wang, L. (2010) *J. Polym. Sci., Part B: Polym. Phys.*, **48**, 1135–1147.
- 148 Peng, S., An, Y., Chen, C., Fei, B., Zhuang, Y., and Dong, L. (2003) *J Appl. Polym. Sci.*, **90**, 4054–4060.
- 149 Ning, W., Xingxiang, Z., Jiugao, Y., and Jianming, F. (2008) *Polym. Int.*, **57**, 1027–1035.
- 150 Ma, X., Yu, J., and Wang, N. (2006) *J. Polym. Sci., Part B: Polym. Phys.*, **44**, 94–101.
- 151 Moon, H.K., Choi, Y.S., Lee, J., Ha, C., Lee, W., and Gardella, J.A.Jr (2009) *Langmuir*, **25**, 4478–4483.
- 152 Biresaw, G. and Carriere, C.J. (2002) *J. Polym. Sci., Part B: Polym. Phys.*, **40**, 2248–2258.
- 153 Sarazin, P. and Favis, B. (2003) *Biomacromolecules*, **4**, 1669–1679.
- 154 Mohamed, A., Gordon, S.H., and Biresaw, G. (2007) *J. Appl. Polym. Sci.*, **106**, 1689–1696.
- 155 Zuza, E., Lejardi, A., Ugartemendia, J.M., Monasterio, N., Meaurio, E., and Sarasua, J.R. (2008) *Macromol. Chem. Phys.*, **209**, 2423–2433.
- 156 Biresaw, G. and Carriere, C. (2004) *Composites, Part A: Appl. Sci. Manuf.*, **35**, 313–320.
- 157 Felker, F.C. and Biresaw, G. (2007) *J. Biobased Mater. Bioenergy*, **1**, 401–408.
- 158 Yuan, Z. and Favis, B.D. (2004) *Biomaterials*, **25**, 2161–2170.
- 159 Feng, F. and Ye, L. (2010) *J. Macromol. Sci., Part B: Phys.*, **49**, 1117–1127.
- 160 Feng, F. and Ye, L. (2011) *J. Appl. Polym. Sci.*, **119**, 2778–2783.
- 161 Chen, H., Pyda, M., and Cebe, P. (2009) *Thermochim. Acta*, **492**, 61–66.
- 162 Lin, Y., Zhang, K., Dong, Z., Dong, L., and Li, Y. (2007) *Macromolecules*, **40**, 6257–6267.
- 163 Zhang, W., Zhang, Y., and Chen, Y. (2008) *Iran. Polym. J.*, **17**, 891–898.
- 164 Okamoto, K., Ichikawa, T., Yokohara, T., and Yamaguchi, M. (2009) *Eur. Polym. J.*, **45**, 2304–2312.
- 165 Xu, C., Luo, X., Lin, X., Zhuo, X., and Liang, L. (2009) *Polymer*, **50**, 3698–3705.
- 166 Alina, S. (2011) *Prog. Polym. Sci.*, **36**, 1254–1276.
- 167 Aroguz, A.Z., Engin, H.H., and Baysal, B. M. (2007) *Eur. Polym. J.*, **43**, 403–409.
- 168 He, Y., Li, J., Uyama, H., Kobayashi, S., and Inoue, Y. (2001) *J. Polym. Sci., Part B*, **39**, 2898–2905.
- 169 Kuo, S., Chan, S., and Chang, F. (2003) *Macromolecules*, **36**, 6653–6661.
- 170 Woo, E.M. and Mandal, T.K. (1999) *Macromol. Rapid Commun.*, **20**, 46–49.
- 171 Mandal, T.K. and Woo, E.M. (1999) *Polym. J.*, **31**, 226–232.
- 172 Yasin, M. and Tighe, B.J. (1992) *Biomaterials*, **13**, 9–16.
- 173 Hubbell, D.S. and Cooper, S.L. (1977) *J. Appl. Polym. Sci.*, **21**, 3035–3061.
- 174 Li, Y. and Jungnickel, B. (1993) *Polymer*, **34**, 9–15.
- 175 Greco, P. and Martuscelli, E. (1989) *Polymer*, **30**, 1475–1483.
- 176 Kaito, A. (2006) *Polymer*, **47**, 3548–3556.
- 177 Avella, M. and Martuscelli, E. (1988) *Polymer*, **29**, 1731–1737.
- 178 Scandola, M., Ceccorulli, G., and Pizzoli, M. (1992) *Macromolecules*, **25**, 6441–6446.
- 179 Maekawa, M., Pearce, R., Marchessault, R. H., and Manley, R.S.J. (1999) *Polymer*, **40**, 1501–1505.
- 180 Iriondo, P., Iruin, J.J., and Fernandez-Berridi, M.J. (1995) *Polymer*, **36**, 3235–3237.
- 181 Paglia, E.D., Beltrame, P.L., Canetti, M., Seves, A., Marcandalli, B., and Martuscelli, E. (1993) *Polymer*, **34**, 996–1001.
- 182 Al-Salah, H. (1998) *Polym. Bull.*, **41**, 593–600.
- 183 Iriondo, P., Iruin, J.J., and Fernandez-Berridi, M.J. (1996) *Macromolecules*, **29**, 5605–5610.
- 184 Xing, P., Ai, X., Dong, L., and Feng, Z. (1998) *Macromolecules*, **31**, 6898–6907.
- 185 Abe, H., Matsubara, I., Doi, Y., Hori, Y., and Yamaguchi, A. (1994) *Macromolecules*, **27**, 6018–6025.
- 186 Lotti, N., Pizzoli, M., Ceccorulli, G., and Scandola, M. (1993) *Polymer*, **34**, 4935–4940.

- 187 Azuma, Y., Yoshie, N., Sakurai, M., Inoue, Y., and Chujo, R. (1992) *Polymer*, **33**, 4763–4767.
- 188 Lisuardi, A., Schoenberg, A., Gada, M., Gross, R.A., and McCarthy, S.P. (1992) *PSME Preprints*, **67**, 298–300.
- 189 Yang, K.K., Wang, X.L., and Wang, Y.Z. (2002) *J. Macromol. Sci. Polym. Rev.*, **C42**, 373–398.
- 190 Zeng, J., Zhu, Q., Li, Y., Qiu, Z., and Wang, Y. (2010) *J. Phys. Chem. B*, **114**, 14827–14833.
- 191 Dias, M., Moraes Antunes, M.C., Santos, A.R. Jr, and Felisberti, M.I. (2008) *J. Mater. Sci. - Mater. Med.*, **19**, 3535–3544.
- 192 Pezzin, A.P.T., van Ekenstein, G.O.R.A., Zavaglia, C.A.C., ten Brinke, G., and Deuk, E.A.R. (2003) *J. Appl. Polym. Sci.*, **88**, 2744–2755.
- 193 Bai, W., Zhang, Z., Li, Q., Chen, D., Chen, H., Zhao, N., and Xiong, C. (2009) *Polym. Int.*, **58**, 183–189.
- 194 Zhou, Z.X., Wang, X.L., Wang, Y.Z., Yang, K.K., Chen, S.C., Wu, G., and Li, J. (2006) *Polym. Int.*, **55**, 383–390.
- 195 Hernandez-Montero, N., Meaurio, E., Elmiloudi, K., and Sarasua, J.R. (2012) *Eur. Polym. J.*, **48**, 1455–1465.
- 196 Rocha, G., Gross, R., and McCarthy, S. (1992) *Polym. Prepr. (Am. Chem. Soc., Div. Polym. Chem.)*, **33**, 454–456.
- 197 Dickers, K.J., Huatan, H., and Cameron, R.E. (2003) *J. Appl. Polym. Sci.*, **89**, 2937–2939.
- 198 Thomas, S.E. (1998) *Polymer*, **39**, 4741–4749.
- 199 Smith, R. (2005) *Biodegradable Polymers for Industrial Applications*, Woodhead Publishing Limited, England.
- 200 Auras, R. (2010) *Poly(lactic acid): Synthesis, Structures, Properties, Processing and Applications*, Wiley & Sons, Hoboken, N.J.
- 201 Bastioli, C. and Knovel, L. (2005) *Handbook of Biodegradable Polymers*, Rapra Technology, Shawbury, p. 534.
- 202 Vroman, I. and Tighzert, L. (2009) *Materials*, **2**, 307–344.
- 203 Reis, R.L., Neves, N.M., Mano, J.F., Gomes, M.E., Marques, A.P., and Azevedo, H.S. (2008) *Natural-Based Polymers for Biomedical Applications*, Woodhead Publishing Limited and Maney Publishing Limited, England.
- 204 Mao, L., Imam, S., Gordon, S., Cinelli, P., and Chiellini, E. (2000) *J. Polym. Environ.*, **8**, 205–211.
- 205 Bastioli, C. (1998) *Polym. Degrad. Stab.*, **59**, 263–272.
- 206 Bastioli, C., Belloti, V., Camia, M., Delgiudice, L., and Ralli, S. (1994) Starch/vinyl-alcohol copolymer interactions, in *Biodegradable Plastics and Polymers*, (eds Y. Doi and F. Fukuda), Elsevier Science, Amsterdam, pp. 200–213.
- 207 Amass, W., Amass, A., and Tighe, B. (1998) *Polym. Int.*, **47**, 89–144.
- 208 Graaf, R.A.D. and Janssen, L.P.B.M. (2001) *Polym. Eng. Sci.*, **41**, 584–594.
- 209 Martin, O. and Averous, L. (2001) *Polymer*, **42**, 6209–6219.
- 210 Ke, T. and Sun, X. (2000) *Cereal Chem.*, **77**, 761–768.
- 211 Godbole, S., Gote, S., Latkar, M., and Chakrabarti, T. (2003) *Bioresour. Technol.*, **86**, 33–37.
- 212 Gordon, S.H., Imam, S.H., Shogren, R.L., Govind, N.S., and Greene, R.V. (2000) *J. Appl. Polym. Sci.*, **76**, 1767–1776.
- 213 Ramsay, B.A., Langlade, V., Carreau, P.J., and Ramsay, J.A. (1993) *Appl. Environ. Microbiol.*, **59**, 1242–1246.
- 214 Mani, R. and Bhattacharya, M. (2001) *Eur. Polym. J.*, **37**, 515–526.
- 215 Meyers, M.A., Chen, P.Y., Lin, A.Y.M., and Seki, Y. (2008) *Prog. Mater. Sci.*, **53**, 1–206.
- 216 Masson, J.F. and Manley, R.S.J. (1992) *Macromolecules*, **25**, 589–592.
- 217 Masson, J.F. and Manley, R.S.J. (1991) *Macromolecules*, **24**, 6670–6679.
- 218 Lee, Y.M., Kim, S.H., and Kim, S.J. (1996) *Polymer*, **37**, 5897–5905.
- 219 Hasegawa, M., Isogai, A., Kuga, S., and Onabe, F. (1994) *Polymer*, **35**, 83–987.
- 220 Nudga, L.A., Petrova, V.A., Bochek, A.M., Kalyuzhnaya, L.M., Alekseev, V.L., Evmenenko, G.A., and Petropavlovskii, G.A. (1999) *Polym. Sci., Ser. A*, **41**, 1137–1142.
- 221 Nudga, L.A., Petrova, V.A., Sergeeva, S.N., and Bochek, A.M. (2003) *Polym. Sci., Ser. A*, **45**, 551–554.
- 222 Buchanan, C.M., Gedon, S.C., White, A.W., and Wood, M.D. (1993) *Macromolecules*, **26**, 2963–2967.
- 223 Rinaudo, M. (2006) *Prog. Polym. Sci. (Oxford)*, **31**, 603–632.

- 224 Pal, K., Behera, B., Roy, S., Sekhar Ray, S., and Thakur, G. (2013) *Soft Mater.*, **11**, 125–142.
- 225 Struszczyk, M.H. (2002) *Polimery*, **47**, 396–403.
- 226 Struszczyk, M.H. (2002) *Polimery*, **47**, 316–325.
- 227 Terbojevich, M., Cosani, A., Conio, G., Marsano, E., and Bianchi, E. (1991) *Carbohydr. Res.*, **209**, 251–260.
- 228 Rogovina, S.Z. and Vikhoreva, G.A. (2006) *Glycoconj. J.*, **23**, 611–618.
- 229 Karavas, E., Georgarakis, E., and Bikiaris, D. (2006) *J. Therm. Anal. Calorim.*, **84**, 125–133.
- 230 Khoo, C.G.L., Frantzich, S., Rosinski, A., Sjöström, M., and Hoogstraate, J. (2003) *Eur. J. Pharm. Biopharm.*, **55**, 47–56.
- 231 Suyatma, N.E., Copinet, A., Tighzert, L., and Coma, V. (2004) *J. Polym. Environ.*, **12**, 1–6.
- 232 Dufresne, A., Cavaillé, J., Dupeyre, D., Garcia-Ramirez, M., and Romero, J. (1999) *Polymer*, **40**, 1657–1666.
- 233 Peesan, M., Supaphol, P., and Rujiravanit, R. (2005) *Carbohydr. Polym.*, **60**, 343–350.
- 234 Sarasam, A. and Madihally, S.V. (2005) *Biomaterials*, **26**, 5500–5508.
- 235 Wu, Y., Yu, S., Mi, F., Wu, C., Shyu, S., Peng, C., and Chao, A. (2004) *Carbohydr. Polym.*, **57**, 435–440.
- 236 Fernandes, S.C.M., Freire, C.S.R., Silvestre, A.J.D., Pascoal Neto, C., and Gandini, A. (2011) *Polym. Int.*, **60**, 875–882.
- 237 Fan, L., Du, Y., Zhang, B., Yang, J., Zhou, J., and Kennedy, J.F. (2006) *Carbohydr. Polym.*, **65**, 447–452.
- 238 Wittaya-Areekul, S. and Prahsarn, C. (2006) *Int. J. Pharm.*, **313**, 123–128.
- 239 Miyahara, T., Murai, A., Tanaka, T., Shiozawa, S., and Kameyama, M. (1982) *J. Gerontol.*, **37**, 651–655.
- 240 Sionkowska, A. (2003) *Eur. Polym. J.*, **39**, 2135–2140.
- 241 Sionkowska, A., Skopinska-Wisniewska, J., and Wisniewski, M. (2009) *J. Mol. Liq.*, **145**, 135–138.
- 242 Yang, X., Yuan, M., Li, W., and Zhang, G. Y. (2004) *J. Appl. Polym. Sci.*, **94**, 1670–1675.
- 243 Sionkowska, A., Wisniewski, M., Skopinska, J., Kennedy, C.J., and Wess, T. J. (2004) *Biomaterials*, **25**, 795–801.
- 244 Taravel, M.N. and Domard, A. (1995) *Biomaterials*, **16**, 865–871.
- 245 McClure, M.J., Sell, S.A., Simpson, D.G., Walpoth, B.H., and Bowlin, G.L. (2010) *Acta Biomater.*, **6**, 2422–2433.
- 246 Zhang, L., Xiong, C., and Deng, X. (1996) *Polymer*, **37**, 235–241.
- 247 Tsuji, H. and Muramatsu, H. (2001) *Polym. Degrad. Stab.*, **71**, 403–413.
- 248 Qiu, Z., Ikehara, T., and Nishi, T. (2003) *Polymer*, **44**, 3101–3106.
- 249 López-Rodríguez, N., López-Arraiza, A., Meaurio, E., and Sarasua, J.R. (2006) *Polym. Eng. Sci.*, **46**, 1299.
- 250 Vogel, C., Wessel, E., and Siesler, H.W. (2008) *Macromolecules*, **41**, 2975–2977.
- 251 Xiao, H., Lu, W., and Yeh, J. (2009) *J. Appl. Polym. Sci.*, **112**, 3754–3763.
- 252 Stoclet, G., Seguela, R., and Lefebvre, J. (2011) *Polymer*, **52**, 1417–1425.

### 3

## Thermodynamics and Morphology and Compatibilization of Polymer Blends

Zdeněk Starý

### 3.1

#### Introduction

The tempting idea to prepare novel materials by mixing different polymers appeared just at the start of the “polymer era,” many decades ago. The first documented polymer blend was most likely a mixture of natural rubber and gutta-percha, prepared by Thomas Hancock during the mid-1800s [1]. Indeed, the blending of two or more polymers can be an effective and relatively cheap method of preparing materials with enhanced or new end-use properties – at least, in theory. Subsequently, various research groups began to realize that the simple mixing of polymers very often provides materials that have inferior mechanical properties and are unacceptable for practical applications. The reason for this is the limited miscibility of different polymers as a result of the unfavorable thermodynamics of mixing; in fact, miscibility is generally an exception rather than a rule, and most polymer blends are immiscible. Between these two extreme cases, however, can be found a variety of partially miscible polymer blends.

The most important feature of partially miscible and immiscible polymer blends is a phase separation leading to a heterogeneous structure. As phase-separated systems display often weak interfacial adhesion – which is the reason for their insufficient mechanical properties – the interface becomes the weak point of the polymer blends. Yet, methods are available which enable this deficiency to be overcome, such that the heterogeneous structure can be tuned to provide the major advantages of multiphase polymer blends. Whereas, the properties of miscible blends are generally an average of those of the neat components, the properties of phase-separated systems are governed also by their phase structure; hence, they can exhibit new unique properties or property profiles that cannot be achieved by using pure materials. Generally, in order to

obtain a heterogeneous polymer blend with required properties, it is necessary to face two main challenges:

- 1) A modification of the interface between immiscible blends components. As noted above, the weak interfacial adhesion can be enhanced by using so-called *compatibilization methods*, and these will be discussed later in the chapter.
- 2) An understanding of the relationships between the processing parameters and the final blend morphology. The choice of suitable processing parameters, such as blend compositions, the flow field applied and the corresponding flow characteristics of the components to name but a few, is a key factor when designing polymer blends with tailored properties. Taking into account the complex flow fields encountered in mixing devices, and the non-Newtonian behavior of the blend components, this task is extremely complicated and has not yet been resolved satisfactorily.

In this chapter, the basic thermodynamic considerations regarding polymer miscibility will first be described, followed by a discussion of the phase behavior in heterogeneous polymer blends, and of the properties of the interfaces and interphases involved. The morphology of polymer blends and its development during processing will then be outlined, after which details of the most common compatibilization concepts will be summarized. However, before discussing these topics in detail, it is important to define the terms used:

- A polymer blend is considered *miscible* when its structure is homogeneous down to the molecular level – that is, the domain size is comparable with the dimensions of the statistical segment of polymer chains.
- *Miscibility* is defined from the thermodynamic of mixing; *partially miscible* blends exhibit homogeneous structures only over a certain (limited) range of concentrations; outside this concentration range, phase separation occurs and the phases are richer in terms of one of the blend components.
- *Immiscible* polymer blends show heterogeneous structures and the separated phases consist of pure components. In contrast to these, the often-used term *compatible* blend should be avoided, at least on a scientific level, as it is non-specific and refers only to the useful mechanical properties of the system, or to sufficient interfacial adhesion.
- The *interface* is defined as a boundary between the phases; that is, in the case of polymer blends between polymer solids or melts, but strictly speaking it is a two-dimensional object with zero thickness. However, especially in the case of partially miscible or compatibilized blends, a layer between the phases with features (composition, structure, etc.) that differ distinctly from those of bulk blend phases can be identified. This region is called the *interphase*, although it does not fulfill the thermodynamic requirement for a phase as a region of a system separated from other phases by a sharp boundary. The thickness of the interphase can be estimated using either microscopy or diffraction methods, and may vary from 2 to 60 nm.



### 3.2

#### Thermodynamics of Polymer Blends

A thermodynamic equilibrium corresponds to the minimum of Gibbs free energy of a system. Thus, each physical or chemical spontaneous process – that is, a process heading towards thermodynamic equilibrium – must fulfill the basic requirement that the change in Gibbs free energy must be less than zero. In the case of mixing, it is convenient to express this change as the *Gibbs energy of mixing* ( $\Delta G_m$ ), which is a combination of the enthalpy of mixing ( $\Delta H_m$ ) and the entropy of mixing ( $\Delta S_m$ ):

$$\Delta G_m = \Delta H_m - T\Delta S_m \quad (3.1)$$

The enthalpy of mixing  $\Delta H_m$  is the heat consumed ( $\Delta H_m > 0$ ) or generated ( $\Delta H_m < 0$ ) during the mixing, at constant pressure. If the mixing is exothermic, then the enthalpic term will drive the system towards miscibility. As the entropy provides a measure of disorder or randomness, and the systems always incline to a uniform distribution of energy,  $\Delta S_m$  is always positive and therefore the entropic term is favorable for mixing.

#### 3.2.1

##### Enthalpy of Mixing

As noted above, the contribution of the enthalpic term to the Gibbs energy of mixing can be either positive or negative. To support miscibility – that is, to bring  $\Delta G_m$  to negative values – the heat must be liberated during the mixing ( $\Delta H_m < 0$ ). This means that the newly formed interactions between components have to be energetically poorer compared to the interactions between molecules or segments of pure components. Calculation of the enthalpy of mixing is carried out on the basis of the regular solution theory using the lattice approach. Assuming a binary mixture, the exchange energy  $w_{12}$  can be defined as:

$$w_{12} = \frac{1}{2}(\varepsilon_{11} + \varepsilon_{22}) - \varepsilon_{12} \quad (3.2)$$

where  $\varepsilon_{ij}$  is the energy of contact between components  $i$  and  $j$ . By using Eq. (3.2), the enthalpy of mixing can be expressed as follows:

$$\Delta H_m = \frac{V}{v_r} z w_{12} \varphi_1 \varphi_2 \quad (3.3)$$

where  $V$  is the total volume of the system,  $v_r$  is the volume of the interacting unit (molecule or segment),  $z$  is the coordination number (i.e., the number of neighbors of each interacting unit), and  $\varphi_i$  is the volume fraction of the components.

Now, the Flory–Huggins interaction parameter,  $\chi_{12}$ , as defined below, is usually employed. This can be determined experimentally using the solubility parameter concept [2,3], which is described later:

$$\chi_{12} = \frac{z w_{12}}{k T} \quad (3.4)$$

The interaction parameter is dimensionless and, in principle, it characterizes the change of enthalpy for each interacting molecule or segment. In polymer blends,  $\chi_{12}$  was found to depend not only on temperature but also on the composition and molecular weight of the components. Inserting Eq. (3.4) into Eq. (3.3), another expression for  $\Delta H_m$  is obtained:

$$\Delta H_m = k T V \frac{\chi_{12}}{v_r} \varphi_1 \varphi_2 \quad (3.5)$$

The interaction parameter is accessible through the determination of Hildebrand solubility parameters  $\delta_i$  of the blend components [3], using the following calculation:

$$(\delta_1 - \delta_2)^2 = \chi_{12} k T / v_r \quad (3.6)$$

The solubility parameter,  $\delta_i$ , is defined as the square-root of a cohesive energy density, which is the energy needed to vaporize 1 mole of a liquid at zero pressure. For polymers,  $\delta$  can be estimated from the swelling of a lightly crosslinked polymer or from intrinsic viscosity measurements in different solvents with known  $\delta$ -values. The solubility parameter of the polymer is then considered as the  $\delta$  of the solvent in which the highest swelling ratio was reached, or as the  $\delta$  of the solvent which yielded the most viscous solution. Another possibility is to use one of the group contribution approaches [4–7]. In this case, the final solubility parameter of the polymer is calculated as a sum of molar attraction constants of functional groups of repeating unit, and thus it can be determined from knowledge of the polymer chemical structure only. It should be noted that combining Eqs (3.5) and (3.6) always leads to zero or a positive mixing enthalpy. The solubility parameter approach is thus relevant only for systems with weak interactions, such as polyolefin blends, whereas for systems with strong specific interactions between components – which are so important to obtain miscibility – other approaches must be employed. Some practical guidelines of how to predict the miscibility of polymers are provided in Ref. [8].

### 3.2.2

#### Entropy of Mixing

The entropy of mixing is an important quantity, as the entropic term always supports the formation of a homogeneous mixture (Eq. (3.1)). The entropy characterizes the degree of disorder in the system, and can be determined using the lattice

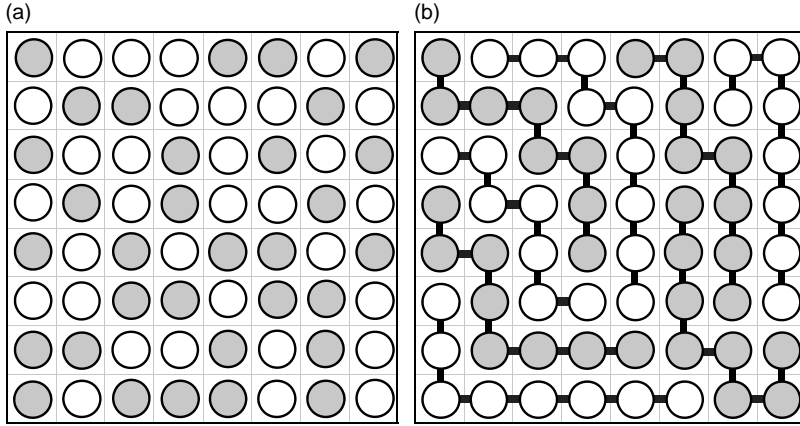


**Figure 3.1** Schematic representation of spatial arrangements of molecules in a binary mixture of (a) low-molecular-weight components and (b) a polymer blend.

approach introduced by Huggins [9] and Flory [10]. In the simplest case, imagine a lattice consisting of cells with equal volume and regularly distributed in space. As the entropy of pure components is assumed to be zero, the entropy of mixing can be determined from the Boltzmann relationship:

$$\Delta S_m = k \ln \Omega \quad (3.7)$$

where  $\Omega$  is the total number of possible distinguishable space arrangements of  $N$  molecules in the lattice (Figure 3.1). For a binary mixture consisting of  $N_1$  molecules of the first component and  $N_2$  molecules of the second component, the following relationship holds:

$$\Omega = \frac{N!}{N_1!N_2!} \quad (3.8)$$

Using Sterling's approximation ( $\ln N! = N \ln N - N$ ) and inserting Eq. (3.8) into Eq. (3.7), the entropy of mixing can be written as:

$$\Delta S_m = -k(N_1 \ln x_1 + N_2 \ln x_2) \quad (3.9)$$

where  $x_1$  and  $x_2$  are the molar fractions of the components. Until now, it has been assumed that the molecule sizes of both components are equal, and that one cell is occupied by one molecule, which is reasonable for compounds of low molecular weight. However, this assumption is not applicable to systems containing polymers, as their long macromolecules are much larger than a cell volume and thus one molecule will occupy more cells in the lattice (Figure 3.1). For polymer

systems, the parameter  $r_i$  can be defined which characterizes the number of segments of polymer chain having a volume equal to the volume of the cell ( $V_{cell}$ ):

$$r_i = \frac{V_i}{V_{cell}} = \frac{V_i N}{V} \quad (3.10)$$

where  $V_i$  is the volume of a macromolecule and  $N$  is the total number of cells in the system. Assuming that one cell is occupied by one monomer unit, then  $r_i$  is the degree of polymerization. In polymer systems where the number of molecules is not equal to the number of cells occupied by a component, the molar fractions in Eq. (3.9) are substituted by the volume fractions,  $\varphi_i$ :

$$\varphi_i = \frac{N_i V_i}{V} \quad (3.11)$$

After this substitution, and using Eqs (3.10) or (3.11), one of the commonly used expressions is obtained for the entropy of mixing in polymer systems:

$$\Delta S_m = -k V \left( \frac{\varphi_1}{V_1} \ln \varphi_1 + \frac{\varphi_2}{V_2} \ln \varphi_2 \right) \quad \text{or} \quad \Delta S_m = -k N \left( \frac{\varphi_1}{r_1} \ln \varphi_1 + \frac{\varphi_2}{r_2} \ln \varphi_2 \right) \quad (3.12)$$

The one problem of this approach appears in the case of two polymers with considerably different chemical structures – that is, with monomer units of unequal size. It is then necessary to choose repeating units such that these occupy the same volume for both polymers. A detailed discussion of the lattice approach and alternative derivations of entropy of mixing are provided in Ref. [11].

### 3.2.3

#### Flory–Huggins Theory

The above-discussed derivations of enthalpy and entropy of mixing are indeed just the parts of the theory that enable the determination of free energy of mixing in polymer systems. This theory, developed and published independently by Huggins [9] and a few months later by Flory [10] some 70 years ago, remains – despite its drawbacks – a cornerstone of the thermodynamics of polymer mixing. Combining the expressions for enthalpy (Eq. (3.5)) and entropy (Eq. (3.12)) of mixing, the key equation of the Flory–Huggins theory is obtained:

$$\Delta G_m = k T V \left( \frac{\varphi_1}{V_1} \ln \varphi_1 + \frac{\varphi_2}{V_2} \ln \varphi_2 + \frac{\chi_{12}}{v_r} \varphi_1 \varphi_2 \right) \quad (3.13)$$

or assuming  $v_r = V_{cell}$

$$\Delta G_m = k T N \left( \frac{\varphi_1}{r_1} \ln \varphi_1 + \frac{\varphi_2}{r_2} \ln \varphi_2 + \chi_{12} \varphi_1 \varphi_2 \right) \quad (3.14)$$

where  $v_r$  is the volume of a chain segment and  $V_i$  is the volume of a macromolecule. Substituting the Boltzmann constant  $k$  by universal gas constant  $R$  in Eq. (3.13), these molecular volumes change into the molar volumes of chain segment and respective polymers.

First, the two logarithmic entropic terms are negative and, therefore, are favorable for mixing; however, their contribution to the overall free energy of mixing is very small (or even negligible) in the case of polymer blends. As the molecular weight of the macromolecules increases, however, the number of possible spatial arrangements in the lattice decreases (see Figure 3.1), which leads to a low entropy of mixing. This can be seen also in Eq. (3.13) directly. The molar volumes of polymers are several orders of magnitude higher compared to those of low-molecular-weight compounds, and thus the values of both logarithmic terms are very low. Following on from that, the term driving the system towards miscibility is the enthalpic contribution, which must be negative in order to obtain a negative free energy of mixing.

The mixing is exothermic ( $\Delta H_m < 0$ ) only when strong specific interactions occur between the blend components. As already noted by Flory [12], this only occurs among polymers with polar substituents interacting with each other. The most common specific interaction that can be found in polymer blends is hydrogen bonding. In this case, when a hydrogen bound to an electronegative partner serves as a proton donor and interacts with a proton acceptor or electron donor group. It should be noted that some functional groups, such as hydroxyl, carboxyl, urethane or amide, have the ability to interact as proton donors and simultaneously as proton acceptors, which leads to a self-association of the molecules. Hydrogen bonding was identified as being responsible for the miscibility of blends of poly( $\epsilon$ -caprolactone)/PVC [13], poly(4-vinylphenol) with polymethacrylates [14,15], polyvinylacetate [16] and polyethers [17] or PVC/PBT [18] and many others. The strength of these interactions can be demonstrated on blends of polyacrylic acid (PAA) and polyethylene oxide (PEO) [19,20]. Whereas, both of these polymers are soluble in water, they form a stable complex that is insoluble in water when blended. A comprehensive review of hydrogen bonding in polymer blends is available in Ref. [21]. Besides hydrogen bonding, other types of specific interaction can cause miscibility in polymer blends. For example, dipole–dipole interactions were detected in miscible systems of PEO with PMMA [22,23] or with PVAc [24] and in blends of polyvinylidene fluoride with different polymethacrylates [25]. The blends of polyamides with different ionomers were found to be miscible due to ion interactions [26]. The doping of hydrogen-bonded blends with metal ions can also increase the strength of the interactions, and thus enhance the miscibility of the blends [27]. In the PS/PPO blend (one of the few commercially available miscible blends), the interactions between the  $\pi$ -orbitals of PS and the methyl groups of PPO were proposed as a reason for their miscibility [28].

The specific interactions are not random; rather, they are formed between specific segments of the polymer chains, and therefore the specific interactions will impact also on the spatial arrangement of the blend – that is, they

will also influence the entropy of the final blend. Following on from that point, the Flory–Huggins interaction parameter  $\chi_{12}$  is not purely enthalpic but involves also an entropic contribution in systems with specific interactions. As the role of the specific interactions decreases with increasing temperature, miscible polymer blends always display a lower critical solution temperature (LCST), unless this is not preceded by a thermal decomposition of the components.

The one deficiency of the Flory–Huggins theory is its inability to predict the LCST behavior – that is, phase separation during heating. Two main reasons have been identified for this failure. First, as noted above, the original Flory–Huggins theory was derived only for systems with weak dispersive interactions. To overcome this deficiency, Painter, Park and Coleman developed a so-called *association model* (for a summary, see Ref. [8]) where an additional term describing the change of free energy due to specific interactions is added to the basic Flory–Huggins equation. This term takes the equilibrium between nonbonded, selfassociated and interassociated functional groups into account, and it can be determined from a detailed analysis of the Fourier transform infrared (FTIR) spectrum of the blend. Second, the Flory–Huggins theory assumes an incompressibility of the blend components. However, if the polymers show distinctively different “equation-of-state” or “pVT” behavior – that is, the thermal expansion coefficients of the pure polymers differ significantly – then the existence of two separated lattices is preferred. This leads to a decrease in the entropy of the blend, and phase separation may occur at elevated temperatures. In other words, the original Flory–Huggins theory does not take into account the free volume of polymers and the changes during mixing into account, as it assumes that all sites in the lattice are fully occupied by polymer segments. However, these drawbacks can be overcome by using a generalization of Flory–Huggins theory, the so-called *lattice fluid model*, which takes the compressibility effects into account [29,30]. For a comprehensive description of the lattice fluid model and other equation-of-state models, see Refs [11,31].

### 3.3

#### Phase Behavior of Polymer Blends

As discussed above, polymer blends are often heterogeneous systems consisting of multiple phases. The system is in a thermodynamic equilibrium if the chemical potentials of the components  $\mu_i$  are equal in all phases. The chemical potential is defined as a change in the Gibbs energy of the system induced by the addition of one molecule of component  $i$ , while the pressure, temperature and number of other molecules are kept constant (Eq. (3.15)):

$$\mu_i = \left( \frac{\partial G}{\partial n_i} \right)_{T,p,n_j} \quad (3.15)$$

## 3.3.1

## Phase Diagrams

In order to determine the phase behavior of heterogeneous polymer blends, phase diagrams are usually constructed in terms of the interaction parameter  $\chi_{12}$  and the composition or temperature and composition. Figure 3.2a represents the dependence of  $\Delta G_m$  on  $\varphi_1$  as computed from the Flory–Huggins equation (Eq. (3.14)) for a symmetric binary blend ( $r_1 = r_2 = r$ ). The curves are shown for different values of  $\chi_{12}r$ , which is the only relevant parameter in the Flory–Huggins equation. For exothermic or adiabatic mixing ( $\chi_{12}r \leq 0$ ),  $\Delta G_m = f(\varphi_1)$  is always negative with a minimum at  $\varphi_1 = 0.5$ , which means that miscibility will occur over the whole concentration range (this is not shown in Figure 3.2). In the case of endothermic mixing – that is, when values of  $\chi_{12}$  are positive – a change can be observed in the shape of the curves. For  $\chi_{12}r$  above a certain critical value, a maximum rather than a minimum emerges at  $\varphi_1 = 0.5$ , although  $\Delta G_m$  is still negative. Such systems can be denominated as *partially miscible*. For very high positive  $\chi_{12}r$  values,  $\Delta G_m$  is higher than zero over the whole composition range and the blend is immiscible. For polymer blends with different degrees of polymerization of the components ( $r_1 \neq r_2$ ), the concentration dependence of  $\Delta G_m$  loses its symmetry and the positions of the extremes are shifted (Figure 3.2b).

In the case of partially miscible systems, the mixing of pure components would lead to a homogeneous blend as  $\Delta G_m < 0$  (point O in Figure 3.2b). However, there is a possibility of reducing the Gibbs energy of the system further by decomposition to two mixed phases A and B that are rich in components 1 or 2. These phases are in thermodynamic equilibrium (Eq. (3.15)), and therefore their exact composition  $\varphi_1^A$  and  $\varphi_1^B$  can be estimated from the position of the points with the common tangent. The relative amount of the phases  $\varphi^A$  and  $\varphi^B$  can be determined graphically using a lever rule (Eq. (3.16)), and the overall  $\Delta G_m$  from the linear additive rule (Eq. (3.17)):

$$\frac{\varphi^A}{\varphi^B} = \frac{|BC|}{|AC|} \quad (3.16)$$

$$\Delta G_m = \varphi^A \Delta G_m^A + \varphi^B \Delta G_m^B \quad (3.17)$$

In the range of  $\chi_{12}r$ , where the concentration dependence of  $\Delta G_m$  exhibits two minima, the final result of the mixing depends on the blend composition. For low and high values of  $\varphi_1$ , miscibility is observed, whereas in the central region – in the so-called *miscibility gap* – a partially miscible blend is obtained. Generally, the following condition must be fulfilled in order for a blend to be miscible over the whole concentration range:

$$\frac{\partial^2 \Delta G_m}{\partial \varphi_1^2} > 0 \quad (3.18)$$

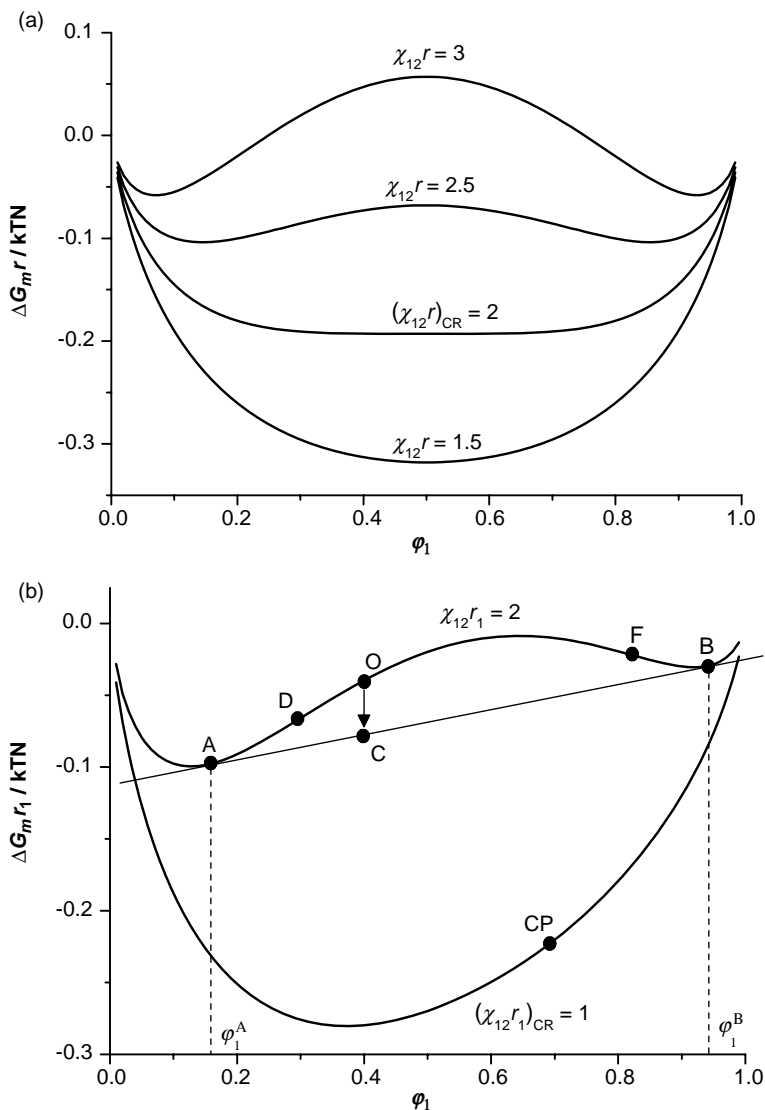


**Figure 3.2** Gibbs energy of mixing for binary polymer system as a function of its composition. (a) Symmetric blend; (b) Asymmetric blend with  $r_2/r_1 = 5$ .

A region in which a one-phase blend is always stable for any composition, and a region in which two mixed phases are more stable than a homogeneous system, are divided by the critical point (CP). This is defined mathematically as the point at which the second and third derivatives of the Gibbs free energy with respect to the polymer volume fraction are zero. Applying these conditions to the Flory–Huggins equation (Eq. (3.14)), it is possible to define the



critical value of the Flory–Huggins interaction parameter  $\chi_{12,CR}$  and the location of critical point  $\varphi_{1,CR}$ :

$$\chi_{12,CR} = 0.5 \left( \frac{1}{\sqrt{r_1}} + \frac{1}{\sqrt{r_2}} \right)^2 \quad (3.19)$$

$$\varphi_{1,CR} = \frac{\sqrt{r_2}}{\sqrt{r_1} + \sqrt{r_2}} \quad (3.20)$$

For a symmetrical blend the  $\chi_{12,CR}$  has the value of  $2/r$ , and the critical point is located directly at  $\varphi_1 = 0.5$ .

The basic features of the phase behavior of polymer blends can be inferred from Figure 3.2. With increasing lengths of polymer chains (i.e., with higher  $r$ -values),  $\Delta G_m$  rises and the blend tends towards phase separation. The same trend is observed with respect to the Flory–Huggins interaction parameter  $\chi_{12}$ . For endothermic mixing, where  $\chi_{12}$  is inversely proportional to the temperature, a decrease in temperature is unfavorable for miscibility and the system shows an upper critical solution temperature (UCST). This behavior was observed for example in blends of polystyrene and polybutadiene with low molecular weights. In the opposite case of exothermic mixing, with specific interactions between polymers,  $\chi_{12}$  increases with temperature and a lower critical solution temperature (LCST) behavior is observed. A typical example of such a system that has been extensively studied is the blend of polystyrene and poly(vinylmethylether).

Using Figure 3.2 and the corresponding equations, it is possible to construct a phase diagram of a binary polymer blend in terms of  $\chi_{12}r_1$  and  $\varphi_1$  or, with the knowledge of temperature dependence of  $\chi_{12}$ , in terms of  $T$  and  $\varphi_1$ . Figure 3.3

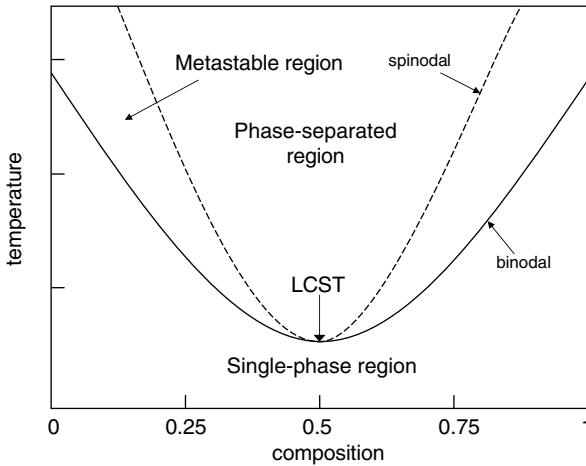


**Figure 3.3** Phase diagram of a binary symmetric polymer blend with low critical solution temperature.

shows such a phase diagram for a symmetric binary blend with LCST typical of miscible polymer systems with specific interactions. The limits of miscibility are denoted by the *binodal curve*, which is determined by the points of common tangent to the Gibbs energy curve, where the chemical potentials of the two coexisting phases are equal (points A and B in Figure 3.2b). Outside the binodal, the single phase system is thermodynamically stable, but if the stable system is transferred inside the binodal – typically by increasing the temperature – phase separation occurs. The mathematical determination of the binodal is not trivial and can be found in Ref. [11]. Nevertheless, the points on the binodal can be estimated experimentally by using a cloud point analysis – that is, by measuring light scattering at different temperatures (e.g., see Refs [32,33]) or from rheological measurements [34,35].

The second important curve is the *spinodal*, which denotes the limits of metastability of the system. The spinodal is given by inflexion points of the Gibbs energy curve at which the second derivative of  $\Delta G_m$  with respect to composition is zero (points D and F in Figure 3.2b). Inside the spinodal, the system is unstable to all concentration fluctuations, and the blend separates spontaneously into coexisting phases via a process known as *spinodal decomposition*. Between the spinodal and binodal there is a metastable region (between the points A and D, F and B) where the single phase structure is stable to small spontaneous local concentration fluctuations. In this region, phase separation occurs by a mechanism known as *nucleation and growth*. The spinodal is also experimentally accessible by applying time-resolved light-scattering measurements [36].

Practical polymer blends usually consist of polymers with different degrees of polymerization ( $r_1 \neq r_2$ ). Following on from the discussion above, the phase diagram is not symmetric in such cases and the extreme points of binodal and spinodal are shifted towards lower concentrations of the polymer with higher  $r$ -values. The phase behavior of the polymer blends becomes more complicated if the molecular weight distributions of the polymers are taken into account. In polydisperse blends, the critical point is no longer positioned at the minimum, but it is shifted in the direction of the component with a higher index of polydispersity IP, which is defined as the ratio of  $z$ -average and weight average of  $r$  (Figure 3.4a). Molecular fractionation may also occur during the phase separation, which means that the polymer chains with a low molecular weight become concentrated in one of the equilibrium phases, whereas the high-molecular-weight tail is located preferentially in the second phase. The distribution of the polymer chains before and after phase separation is shown schematically in Figure 3.4b.

### 3.3.2

#### Phase Separation

The occurrence of two different phase-separation mechanisms – namely, spinodal decomposition and nucleation and growth – becomes evident from a consideration of the shape of the  $\Delta G_m$  curve as a function of  $\varphi_1$ . The initial stage of phase separation is connected with concentration fluctuations. It can be shown that the

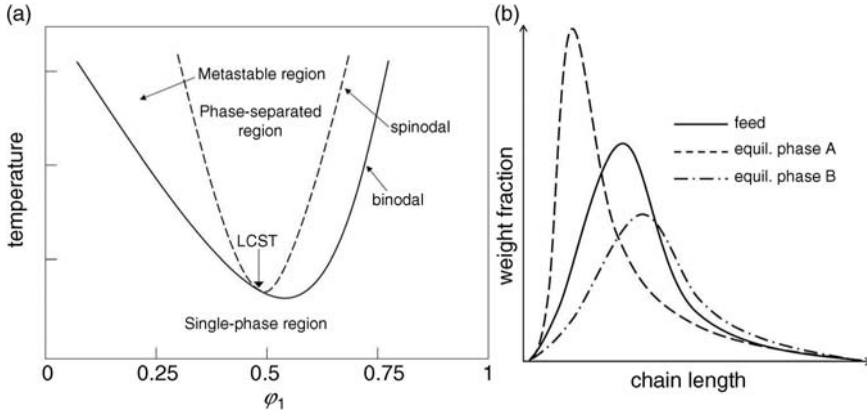


**Figure 3.4** The phase behavior of blends of polydisperse polymers. (a) Phase diagram of a polydisperse blend ( $IP_1 < IP_2$ ); (b) Molecular fractionation during phase separation.

change in Gibbs energy induced by the local concentration fluctuation  $\delta G$  is proportional to the second derivative of  $\Delta G_m$ :

$$\delta G \sim \frac{\partial^2 \Delta G_m}{\partial \phi_1^2} \quad (3.21)$$

This means that in the regions where the  $\Delta G_m$  curve is convex (between points A and D, F and B), the concentration fluctuations lead to an increase in Gibbs energy. However, this is not favorable and the system tends to suppress these fluctuations and thus preserve its homogeneous character. In contrast, when the  $\Delta G_m(\phi_1)$  is a concave function (between D and F), the Gibbs energy decreases with any fluctuation in concentration. Moreover, the amplitude of these fluctuations grows until the equilibrium composition is reached, as shown schematically in Figure 3.5; the system then undergoes phase separation immediately in the

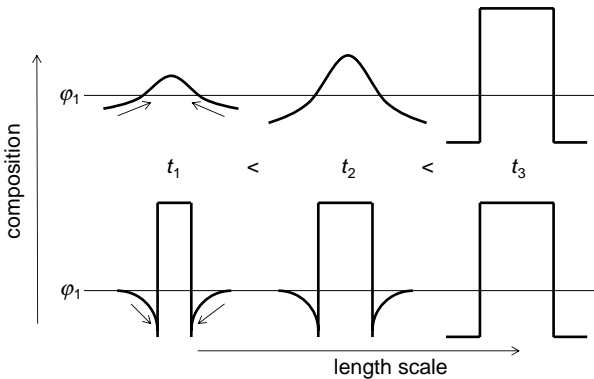


**Figure 3.5** Schematic representation of phase separation mechanisms: spinodal decomposition (top) and nucleation and growth (bottom). The last stage at time  $t_3$  displays an equilibrium state.

whole volume by spinodal decomposition. The arrows in Figure 3.5 indicate the direction of diffusion of the polymer chains. During spinodal decomposition the macromolecules migrate to the regions of high concentrations and, therefore, the diffusion coefficient is considered negative in this case. The resulting morphology of the phase-separated blend exhibits a high degree of cocontinuity, at least in the initial stages of spinodal decomposition. In the initial stages the kinetics of spinodal decomposition is given by the diffusion of macromolecules only, and can be described by Cahn–Hilliard theory [37] which predicts the exponential growth of the amplitude of concentration fluctuations and the existence of one dominant fluctuation wavelength. When the fluctuations produce phases with compositions near to the equilibrium, the growth of the fluctuation amplitude decelerates and the kinetics changes considerably. At this late stage the interfacial effects play a dominant role and a coarsening of the cocontinuous structure takes place, and can even change in the dispersed structure. This morphology development is driven by a reduction of the surface energy, and is also largely influenced by the amount of the newly formed equilibrium phases  $\varphi^A$  and  $\varphi^B$  and their viscosities. A comprehensive review of spinodal decomposition and its kinetics is provided in Ref. [38].

In the case of phase separation by nucleation and growth, small local fluctuations decay again. The system retains its one-phase character until a large fluctuation appears, which leads directly to the formation of a nucleus with equilibrium composition. If the nucleus is of a sufficient size it starts to grow as the polymer chains diffuse to the surface of the nucleus, enclosed by a layer with a reduced concentration of a given polymer (Figure 3.5). Therefore, in contrast to the spinodal decomposition, the diffusion coefficients are positive. Another crucial difference from spinodal decomposition is the presence of an activation barrier. Similar to the crystallization, a newly formed nucleus must have a certain critical size to be stable. The reason for this is that the surface free energy of the nucleus contributes to an increase in the overall Gibbs energy of the system, which is thermodynamically unfavorable. Therefore, the nucleus must be so large that the decrease in Gibbs energy due to the phase separation (cf. Figure 3.2b) overrules the effect of the surface free energy. The activation barrier of nucleation approaches infinity at the binodal, and decreases with the distance from the binodal when moving to the spinodal, where the spinodal decomposition sets in. However, the spinodal denotes no sharp transition between the two phase separation regimes. In the vicinity of the spinodal, both processes can occur simultaneously or nucleation and growth can disappear already before reaching the spinodal, due to a very low nucleation barrier. Analogous to the crystallization, the presence of nucleating agents makes the nucleation step significantly easier as this lowers the activation barrier. Generally, the rate of nucleation is very low and, therefore undercooling or overheating – depending on whether the system shows UCST or LCST behavior – is necessary to study this process at reasonable rates. If the blend undergoes phase separation by nucleation and growth, the final phase structure is the droplet-matrix type. In the case of a large amount of the

dispersed phase, further morphology changes will occur, and structure coarsening by coalescence or Ostwald ripening cannot be excluded.

### 3.3.3

#### Interfaces in Polymer Blends

The mechanical performance of heterogeneous polymer blends is influenced to a great extent by the properties of interfaces. As discussed above, the majority of polymer pairs are immiscible for thermodynamic reasons. From a thermodynamic point of view, the Flory–Huggins interaction parameter  $\chi_{12}$  can be seen as a measure of repelling forces between the polymers. For immiscible blends with rather high positive values of  $\chi_{12}$ , the attractive forces between phases are very low. Following on, the interfacial adhesion is insufficient to ensure the transfer of stresses from one phase to another such that, when a crack develops, it will follow the line of least resistance and run preferentially along the interface. This feature is often employed in the visualization of immiscible blend structures with scanning electron microscopy, when the fractured surfaces are observed. As an example, Figure 3.6a shows the morphology of a polystyrene/polyethylene (PS/PE) blend where the PE particles can be clearly seen dispersed in the PS matrix, along with the typical features of an immiscible polymer system such as sharp and smooth interfaces, holes remaining where particles have fallen out of the matrix, and/or a very broad distribution of dispersed particle sizes. A weak interfacial adhesion is then seen as a reason for any inferior mechanical properties of the immiscible polymer blends. In order to enhance the mechanical characteristics, a compatibilizer is often incorporated; when this is successful and the compatibilizer is located preferentially at the interface it can lead to an increased cohesion between the phases. It is then possible to distinguish only a few particles with blurred interfaces on the fracture surface, which implies that the fracture path has not followed the interfaces preferentially (Figure 3.6b). Although quite often, no interactions are considered at the interface in immiscible systems, a detailed microscopic

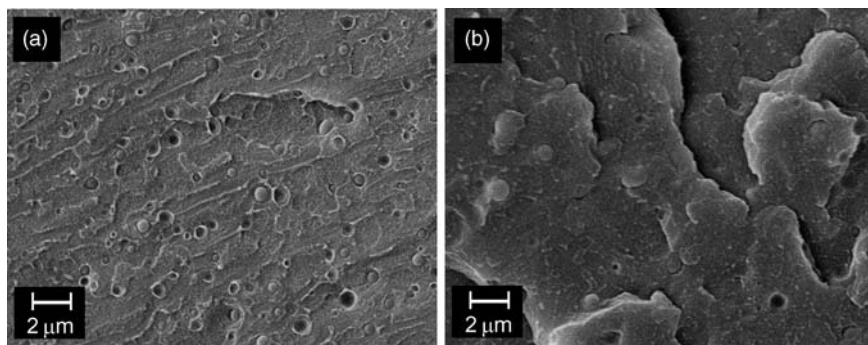


**Figure 3.6** Fracture surfaces of the PS/PE 95/5 (wt%). (a) Without compatibilizer; (b) With 1 wt.% of styrene-butadiene-styrene block copolymer as a compatibilizer. Reproduced with permission from Ref. [122]; © 2012, Elsevier.

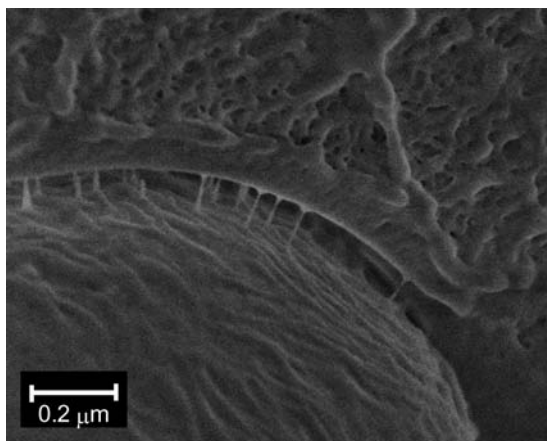


**Figure 3.7** PS/PE interface at high magnification showing thin fibers connecting the phases.

analysis can reveal thin fibers connecting the phases, and thus also a certain degree of adhesion (Figure 3.7).

An understanding of the interface formation and its properties is an important issue in order to achieve polymer blends with desired property profiles. Unfortunately, the properties of the interface are generally neither easy to determine experimentally nor easy to predict on a theoretical basis, for several reasons. First, the composition of the interfacial layers can differ significantly from the composition of the bulk phases. It is well known that the chain ends tend to concentrate on the surface of the phase. Consequently, as the chain-end mobility and usually also the chemical structure differ from those of the remainder of the chain, this effect can alter the interfacial tension between the blend components [39]. Moreover, low-molecular-weight fractions in polydisperse systems can also become concentrated at the interface [40], while the effect of other low-molecular-weight species (e.g., antidegradants or plasticizers which are often used as additives in polymer blends) on the interfacial properties are usually unknown. A second reason is that the achievement of a state of thermodynamic equilibrium during mixing is not commonplace in polymer systems with a very low diffusivity of macromolecules.

The basic theoretical description of the polymer–polymer interface was introduced by Helfand and Tagami [41–43]. Using a self-consistent field approach, these authors derived a segmental density  $\rho_1$  profile across the interface (Eq. (3.22)), as shown in Figure 3.8 for a system of polymers with an infinite number of segments.

$$\rho_1 = 0.5 + 0.5 \tanh\left(\frac{x\sqrt{6\chi_{12}}}{b}\right) \quad (3.22)$$

In Eq. (3.22),  $x$  represents the distance from the interface in the perpendicular direction, while  $b$  is the segmental length which is assumed to be the same for both polymers.

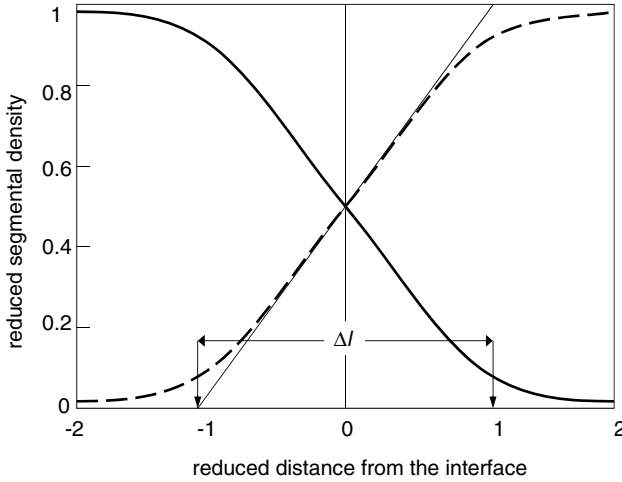


**Figure 3.8** Segmental density profile across the interface in polymer blends.

The interfacial thickness  $\Delta l$  is defined as:

$$\Delta l = \frac{2b}{\sqrt{6\chi_{12}}} \quad (3.23)$$

Additionally, the interfacial tension  $\Gamma_{12}$  can be estimated as a function of the interaction parameter and segmental length according to Eq. (3.24), where  $\rho_0$  is the density (assumed equal for both polymers):

$$\Gamma_{12} = b \rho_0 k T \sqrt{\frac{\chi_{12}}{6}} \quad (3.24)$$

From the above equations it is clear that, with decreasing interaction parameter  $\chi_{12}$ , the density profile becomes flatter and the interfacial thickness increases with the square-root of  $\chi_{12}$ . When  $\chi_{12}$  approaches zero,  $\Delta l$  goes to infinity, that is, the interface can no longer be distinguished and a single-phase system is formed. The basic Helfand–Tagami model was then extended by Broseta *et al.* [44] for the interface of polymers with defined chain lengths:

$$\Delta l = \frac{2b}{\sqrt{6\chi_{12}}} \left[ 1 + \frac{\ln 2}{\chi_{12}} \left( \frac{1}{r_1} + \frac{1}{r_2} \right) \right] \quad (3.25)$$

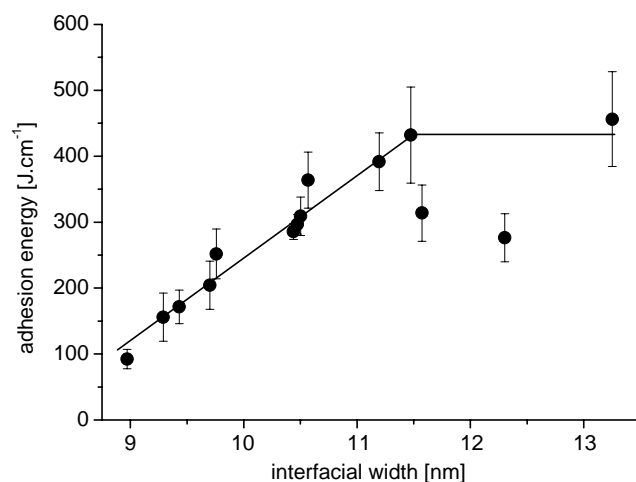
Comparing Eqs (3.23) and (3.25), it can be shown that the interface becomes broader in systems with low-molecular-weight components [45]. The experimentally estimated interfacial thicknesses [45–48] were found to be in reasonable agreement with the Helfand–Tagami and Broseta predictions. The distribution of the chain segments for systems containing at the interface a block copolymer as a compatibilizer, was derived by Noolandi [49]. Typical values of the interfacial thickness in different polymer blends are summarized in Table 3.1.

**Table 3.1** Typical values of the interfacial thickness in different polymer blends.

Blend	Interfacial thickness (nm)	Reference(s)
Immiscible blends	2–4	46
Immiscible blends with block copolymer	5–15	48,49
Homopolymer/copolymer blends	30	47
Reactively compatibilized blends	30–60	50
Partially miscible blends	Up to 300	51

As noted above, the lack of interactions or entanglements at the interface is responsible for the often unacceptable mechanical properties of heterogeneous polymer blends. Therefore, an increase in the number of interactions or entanglements at the interface, accompanied by a broadening of the interface, should lead to an enhancement of the adhesion of phases. This was proved experimentally by Schnell *et al.* [52] in systems of polystyrene and poly-*p*-methylstyrene. In this case, the number of entanglements between the sheets of polymers was varied by changing the annealing conditions, and the interfacial adhesion was then determined by fracture toughness measurements. As can be seen in Figure 3.9, the fracture toughness characterized by adhesion energy increases with the interfacial thickness until it reaches a plateau value.

The addition of a block copolymer acting as a compatibilizer represents another possibility of inducing linkages between the bulk phases. In the simplest case, it is assumed that the block copolymer is anchored in both phases, and that its blocks are miscible with the main components of the blend. If the molecular weight of

**Figure 3.9** Adhesion energy of different samples of PS/PpMS plotted as a function of the interfacial width. Reproduced with permission from Ref. [52]; © 1998, American Chemical Society.



the blocks is sufficient to form entanglements with the chains of bulk phases, a reinforcement of the interface occurs and a considerable increase in interfacial adhesion can be expected.

The properties of the interface in polymer blends can be investigated by applying different measuring techniques. The values of interfacial tension can be estimated by pendant drop or embedded fiber measurements. The former is an equilibrium measurement, and as such has several drawbacks with respect to high-molecular-weight materials. Due to the high viscosity of polymer melts, long times are required to achieve the equilibrium state and the materials can suffer from thermal degradation. This danger is less crucial in the latter case, because it is a dynamic method. However, neither technique can provide information regarding interfacial thickness or segmental density profile. The interfacial thickness can be determined by using ellipsometry, but this requires the polymers to have different refraction indices. Small-angle X-ray scattering and small-angle neutron scattering can each provide values of interfacial thickness and segmental profile. However, such information is extracted from the region of Porod scattering, where the signal is generally very low compared to background. Probably the most versatile techniques for interface characterization are neutron or X-ray reflectometry, both of which provide very good resolution (typically on the order of 0.2 nm), and both interfacial thickness and segmental profiles are obtained. Whereas, the application of X-ray reflectometry is limited due to small differences in the electron densities of organic polymers, neutron reflectometry can be applied to all polymer systems where one component can be deuterated. The interface can also be observed directly by using transmission electron microscopy in conjunction with an appropriate staining agent or element-specific detection. A concise overview of the methods suitable for investigating polymer–polymer interfaces is provided in Ref. [53].

### 3.4

#### Morphology of Polymer Blends

Polymer blends combine the properties of their components, and they can also possess unique properties that cannot be achieved by use of the neat polymers only. The major advantage of the polymer blends is the possibility to control their end-use properties over a wide range, according to the requirements for specific applications. As multiphase materials, the properties of polymer blends are considerably influenced by their phase structure. The final morphology of a polymer blend prepared by melt mixing is a result of the complex relationships of inner and outer parameters. Besides the chemical structure and rheological properties of pure components or blend composition as inner parameters, applied flow field or temperature as outer factors influence the morphology development to great extent. Therefore, by changing the composition of the blend or processing conditions it is possible to obtain materials with morphologies of different types and/or degrees of fineness.

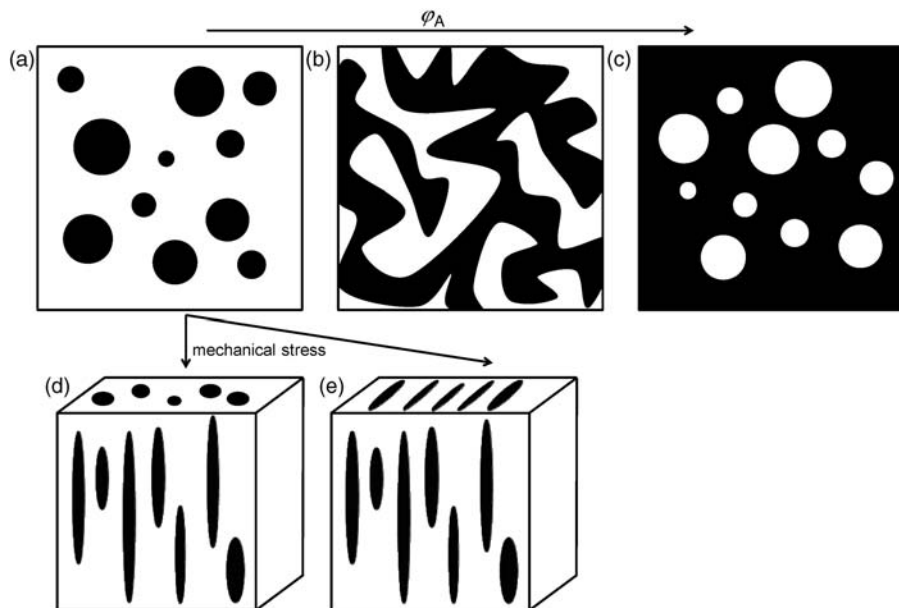


**Figure 3.10** Basic types of phase structures in polymer blends.

Generally, the vast majority of polymer blends can be classified as a blend with either a dispersed or cocontinuous morphology, as shown schematically in Figure 3.10. If the amount of component A is low, it forms a dispersed particles surrounded by a matrix of component B (Figure 3.10a). Increasing the amount of phase A, the size of the dispersed domains grows and approaching the threshold of geometric percolation the first continuous structures appear. The morphology is considered cocontinuous when both of the phases are fully continuous (Figure 3.10b). With a further increase in the concentration of A, the structures of phase B disintegrate and finally the phases invert and A forms the matrix of the blend and B the dispersed phase (Figure 3.10c). In order to minimize the free surface energy of the system, the dispersed particles tend to achieve a spherical shape. However, many anisotropic particle shapes, such as ellipsoids, fibrils or platelets, can be observed in polymer blends (Figure 3.10d and e), as the final morphology is often quenched immediately after melt processing. Thus, any particles deformed by the shear and/or elongational stresses applied in the mixing devices are solidified before they can regain an energetically favorable spherical shape. For monodisperse spherical particles, the critical concentration for percolation – that is, the limit where first continuous structures can be expected – is 15.6 vol.%, but in the case of anisotropic particles this limit is shifted to even lower values.

Several attempts have been made to predict this limit of cocontinuity. A simple relationship was identified experimentally by Avgeropoulos *et al.* [54], who showed that the composition at which a phase inversion occurs and a cocontinuous

morphology is formed is related to the ratio of torques of the neat components  $T_A$  and  $T_B$ , measured in an internal mixer:

$$\frac{T_A}{T_B} = \frac{\varphi_A}{\varphi_B} \quad (3.26)$$

This simple approach was found to be more accurate than models that used the shear viscosity ratio for blends with a viscosity ratio not far from unity [55], as the torque reflects to some extent also the effects of melt elasticity and elongational flow component. Lyngaae-Jorgensen and Utracki developed a model which predicts the range of cocontinuity, and not only the phase inversion point [56,57]. This model, which is based on the percolation theory, relates the degree of cocontinuity  $\Phi_A$ , which can be determined experimentally from extraction experiments, to the volume fraction of the given blend component  $\varphi_A$  (Eq. (3.27)).

$$\phi_A = k(\varphi_A - \varphi_{CR})^{0.45} \quad (3.27)$$

The  $\varphi_{CR}$  is the critical concentration characterizing the onset of cocontinuity, and it depends on the shape of the dispersed particles ( $\varphi_{CR} = 0.156$  for mono-disperse spheres and  $\varphi_{CR} < 0.156$  for anisotropic particles);  $k$  is an empirical parameter.

Generally, the range of cocontinuity is dependent on the viscosity (torque) ratio. In blends with a viscosity ratio near unity, a fully cocontinuous structure appears around 50:50 composition; otherwise, the component with a lower viscosity tends to form a continuous phase and the range of cocontinuity is shifted to the lower amounts of less-viscous component (Figure 3.11). A second important parameter determining the formation of cocontinuous structure is the interfacial tension. With increasing interfacial tension, the minor phase forms more spherical

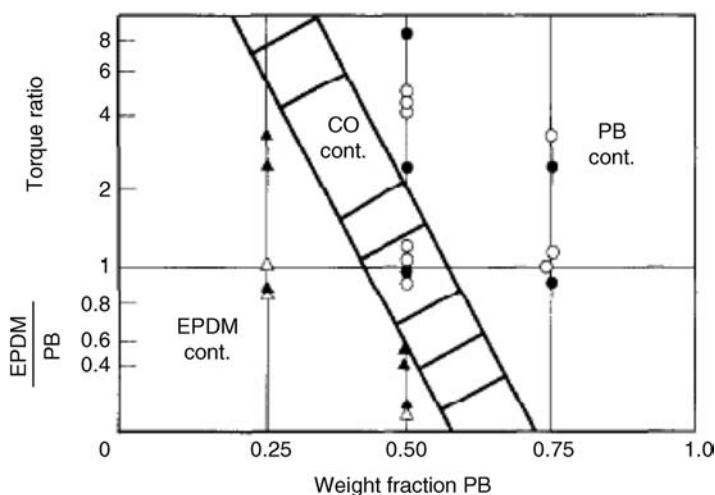


**Figure 3.11** Type of final morphology of EPDM/PB blends with different torque ratios. Reproduced with permission from Ref. [54]; © 1976, American Chemical Society.

domains which results in a higher  $\varphi_{CR}$  and thus in a higher percolation threshold and a narrower range of cocontinuity [58,59].

An exhaustive overview of the literature covering cocontinuous morphology, its formation and properties, is available in the review of Pötschke and Paul [60].

### 3.4.1

#### Morphology Development During Melt Processing

The vast majority of polymer blends is produced by melt-mixing from powders or pellets of pure components. In the initial stage of mixing the original, typically millimeter-sized solid particles are heated and sheared, so that the material melts and the size of the domains decreases into the micro- or even nanorange. The morphology development in this early mixing stage was studied extensively by Scott and Macosko [61–63], who found that the pellets in contact with the hot walls of a processing device are exposed to high shear stresses and disintegrate into thin sheets or ribbons. Subsequently, as the thickness of these sheets decreases in the micrometer range, the interfacial forces become important and holes are formed in the sheets (Figure 3.12a). These lacey structures then break up into irregularly shaped particles, which in turn break up further or relax into near-spherical particles (Figure 3.12b). This mechanism leads to a rapid decrease in the dispersed particle sizes during the first few minutes of mixing.

At this stage a processing phase inversion can occur, depending on the softening temperatures of the polymers used. If the minor component softens earlier, it initially forms a continuous phase; then, as the major component becomes liquid and the structure of the minor component disintegrates, a phase inversion takes place so that the major component forms a matrix surrounding the dispersed particles of the minor phase [64,65]. The rate of phase inversion was found to be markedly influenced by the viscosity ratio ( $p = \eta_{\text{minor}}/\eta_{\text{major}}$ ) of the components [66]. Whereas, for blends with  $p > 0.1$  the phase inversion occurred within the first minute of mixing, for blends with  $p < 0.1$  the time to phase inversion was increased with the decreasing viscosity ratio; for example, for a blend with  $p = 0.003$  the time taken was more than 10 min.

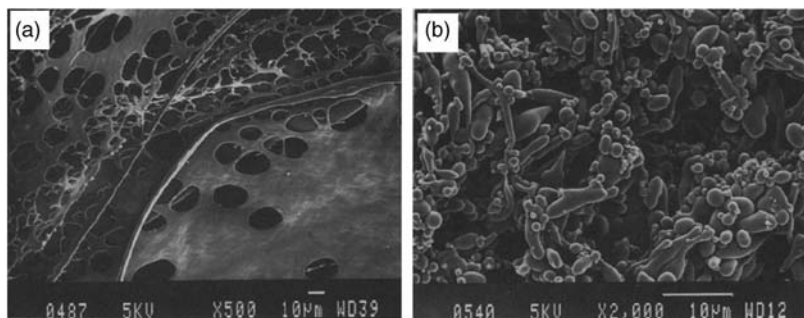


**Figure 3.12** Phase structures observed in PS/PA 80/20 (wt%) blends prepared in an internal mixer after selective dissolution of PS matrix. (a) After 60 s of mixing; (b) After 90 s of mixing. Reproduced with permission from Ref. [61]; © 1991, Springer.

After the initial stage of mixing the domain size decreases only slightly such that, after some time (usually 5–10 min), the phase structure no longer shows any changes. In this time interval – termed *steady-state mixing* – the morphology is stable until thermal degradation alters the rheological properties of polymers considerably. Whereas, the stability of the dispersed morphologies during mixing is generally accepted, the stability of cocontinuous structures remains an issue of debate. Based on the extensive studies of Lee and Han [67,68] or Chuai [69], it was concluded that the cocontinuous morphology is simply a transitory morphological state, through which one dispersed morphology is transformed into another. However, the results of Sarazin and Favis [70] support the concept of a stable steady-state cocontinuous morphology, as they observed no considerable changes in the cocontinuous morphology of PCL/PS 50/50 blends, even after 120 min of mixing. Thus it seems that the steady-state cocontinuous morphology can be obtained only in a very narrow composition range, if at all.

The morphology development during mixing is a result of the competition between droplet deformation and break-up on one side, and droplet coalescence on the other side [71–73]. In steady-state mixing these two processes are in dynamic equilibrium, and this determines the final shape and size of the phase domains. A prediction of the final morphology – that is, the shape, size and spatial arrangement of the phases – is a difficult task because its development is a consequence of complex relationships between the viscosity and elasticity of the components, the processing conditions (type of deformation, deformation rate, time of deformation), the chemical structure of the components and, of course, the blend composition. The deformation of a liquid droplet dispersed in a liquid matrix under a flow can be described using two dimensionless parameters, the capillary number ( $Ca$ ) and the viscosity ratio ( $p$ ) [74,75]. Generally,  $Ca$  is the ratio of the hydrodynamic stress applied to the droplet which forces the drop to deform, and the interfacial stress which tends to preserve the spherical shape of the droplet in order to minimize its surface energy.

$$Ca = \frac{\eta_m \dot{\gamma} d}{2 \Gamma_{12}} \quad (3.28)$$

In Eq. (3.28)  $\eta_m$  is the matrix viscosity,  $\dot{\gamma}$  the shear rate,  $d$  the particle diameter, and  $\Gamma_{12}$  the interfacial tension.

If the hydrodynamic stress is sufficiently high,  $Ca$  exceeds a certain value known as the critical capillary number,  $Ca_{CR}$ . Under these conditions no stable shape can persist in the flow, and the droplet deforms continually until it breaks into daughter droplets. These can undergo consequent deformations and break-ups until the droplets are so small that the interfacial stress overrules the hydrodynamic stress. At  $Ca < Ca_{CR}$  the droplets are deformed into a shape which is stable in the flow and can be also predicted by the theory of Maffettone and Minale [76]. On the other hand, at very high values of  $Ca$  ( $Ca \gg Ca_{CR}$ ), a quick affine deformation of the droplets occurs and long cylindrical threads are formed which are rather stable in the flow and decay only at very high deformations or even just after the cessation of flow [77,78].

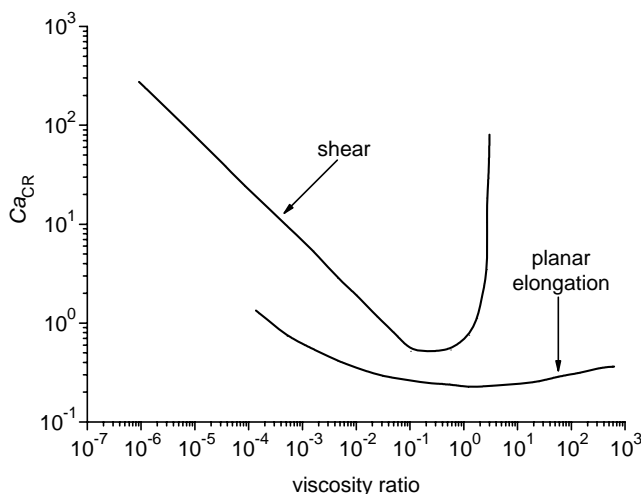


**Figure 3.13** Critical capillary number as a function of viscosity ratio in Newtonian systems. Reproduced with permission from [79]; © 1982, Taylor & Francis.

The value of  $Ca_{CR}$  depends on the viscosity ratio of the blend components. This dependence was determined experimentally by Grace [79] on Newtonian systems in shear and planar elongational flow (Figure 3.13). Subsequently, it was shown, in agreement with the theories of Taylor and Cox [74,75], that elongational flow is more efficient in droplet deformation and break-up than simple shear flow, and that no droplet break-up is possible in systems with  $p > 4$  under shear. This is because the dispersed particles cannot rotate during elongation, and circulation of the material inside the droplets is also disabled. Both mentioned processes lead to an energy dissipation and, therefore, to a reduction of the effective hydrodynamic stress at the interface. In shear at  $p > 4$  these effects dominate the droplets behaviour and the stress needed to reach the critical capillary number goes to infinity.

However, polymer blends of interest for practical application are almost always non-Newtonian systems. The viscoelasticity of the blend components can have significant effects on drop deformation and break-up, and can also affect the value of  $Ca_{CR}$  [80]. Indeed, the  $Ca_{CR}$  for viscoelastic drops in a Newtonian matrix was found to be higher compared to that in the corresponding Newtonian case [81]. In accordance with that, droplet deformation increases with the increasing elasticity of the matrix and decreases with the increasing elasticity of the droplet [82–84]. In contrast to these findings, others have shown that the viscoelasticity of the matrix hinders break-up of a Newtonian drop [85,86]. Recently, the behavior of dispersed droplets in confined conditions (i.e., near solid walls) was investigated and distinct differences were observed in comparison to bulk conditions [87]. Whereas, for blends with more viscous drops ( $p > 1$ ) the values of  $Ca_{CR}$  were decreased, for blends with  $p < 1$  the opposite effect was observed. Regardless of the viscosity ratio, the confinement stabilized the droplets against break-up, which means that break-up occurred at a higher total deformation than by droplets in the bulk.

The basic theories of droplet deformation postulated by Taylor [74] and Cox [75] were derived for Newtonian liquids and neglected any hydrodynamic interactions between neighboring droplets. Moreover, they are valid only in the range of small deformations – that is, droplet break-up is not taken into account. Not surprisingly, deviations were reported for real polymer blends with viscoelastic properties [80–86] or higher amounts of the dispersed phase [88]. Nevertheless, these theories using  $Ca$  and  $p$  as the main parameters remain a cornerstone for qualitative predictions of morphology development in polymer blends. Taylor's theory enables a quantitative determination of droplet shape in two limiting cases: (i) at low  $Ca$ -values, when a drop reaches its equilibrium deformation; and (ii) at very high  $Ca$ -values, when the effect of interfacial tension can be neglected and an affine deformation of the particles occurs. In the region of moderate  $Ca$  values, when hydrodynamic and interfacial stresses contest for the final droplet shape and break-up can occur, no quantitative description of droplet deformation is available, even for Newtonian fluids.

If the  $Ca_{CR}$  is exceeded and the total deformation of the droplet is sufficiently high, it can break into smaller particles. At moderate values of  $Ca$ , the droplet breaks up usually into two daughter droplets according to a stepwise mechanism termed *necking* (Figure 3.14). The critical deformation necessary for break-up also depends on  $p$ , as found experimentally by Stone *et al.* [89].

At very high  $Ca$ -values, highly elongated thin fibrils are formed. As the aspect ratio of the particles increases, the interfacial instabilities become important, and the development of these instabilities in Newtonian systems was described by Tomotika [90]. The theory states that there are very small sinusoidal disturbances (also called Rayleigh instabilities) on the surface of the fibril, but only those distortions with wavelengths larger than the circumference of the fibril grow. For a given  $p$ -value there is one dominant wavelength which grows fastest, and this distortion will break up the fibril into a line of droplets (Figure 3.14). This so-called Rayleigh break-up is often used to determine interfacial tension by the *breaking-thread method*. The original theory of Tomotika, which was derived for quiescent conditions, was then extended for linear flows [91,92]. In this case, as the fibril is

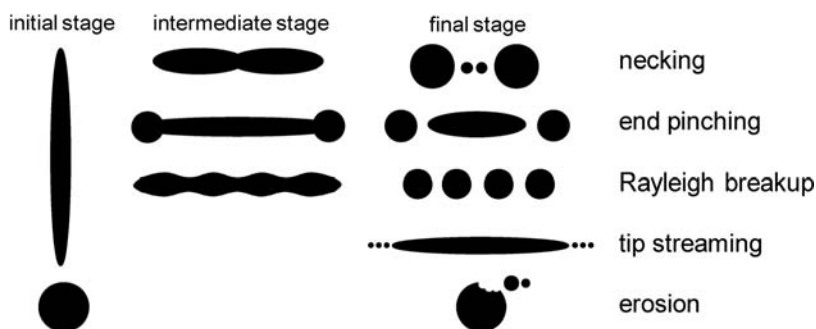


Figure 3.14 Different droplet break-up mechanisms observed in polymer blends under flow.

stretched the wavelength of distortions increases which leads to the fact that the break up times of fibrils are higher in flows compared to quiescent conditions.

Another break-up mechanism termed *end pinching* was observed experimentally during the pioneer studies of Taylor [74] and Grace [79], and typically occurs after sudden changes in flow. Initially, the deformed particle is transformed into a dumbbell shape, after which two droplets are formed at the ends which, as a consequence, are torn off (Figure 3.14). End pinching is explained as a consequence of an interfacial tension gradient along the drop surface with different curvature [93], and a raised fluid motion produced by internal pressure gradients leads to break-up. As the break-up by this mechanism is connected with a relatively high transport of mass inside the drop, the total deformations required for break-up are lower in systems with a lower viscosity ratio.

The formation of small satellite droplets was observed with all three of the above-mentioned mechanisms [79,80,93]. The droplets (as shown schematically in Figure 3.14) formed by necking were substantially smaller than the main daughter droplets. Tjahjadi *et al.* [94] found that the number of satellite droplets increases with the decreasing viscosity of the dispersed phase.

The tip streaming mechanism causes very fine droplets to be released from the tips of deformed droplets (Figure 3.14). This type of break-up can be observed in systems with low-viscosity droplets – that is, when  $p < 0.1$ , or in blends containing surfactants or compatibilizers [95,96]. These species can be dragged towards the tips by the flow of the surrounding matrix, and this results in a local decrease of interfacial tension at the tips. This causes the tip region to be preferentially deformed in a very thin body which breaks up easily via either necking or Rayleigh break-up.

The final break-up mechanism is specific, as it does not require deformation of the mother droplet. Lin *et al.* [97] observed a release of thin ribbons and streams of droplets from the surface of the mother droplet, and termed the mechanism *surface erosion*. Surprisingly, this type of break-up was confirmed also in blends with  $p > 4$  – that is, in systems where Taylor theory and many experimental studies have claimed that droplet break-up under shear is not possible.

The second process influencing blend morphology is a coalescence of the dispersed particles. This phenomenon must be taken into account even in blends containing a few volume percent of the dispersed phase. In contrast to droplet break-up, coalescence leads to an increase in droplet size and a coarsening of the phase structure. Flow-induced coalescence is a consequence of the collision of droplets having different velocities. When two droplets approach each other, they begin to deform due to the axial force, and at the same time the matrix film between the particles is squeezed out. If the critical distance between the particles is reached, the matrix film ruptures and the droplets merge. The theoretical description of flow-induced coalescence is rather complicated even for Newtonian systems, with the assumption of a collision of two spherical droplets [98]. For real polymer blends with viscoelastic properties, where multiple collisions of nonspherical particles occur, the appropriate theoretical treatment is missing.



## 3.4.2

**Stability of Blend Morphology**

The phase structures of polymer blends leaving the mixing device are usually far from thermodynamic equilibrium. The general tendency of a polymer blend with a nonzero interfacial tension is to minimize the interfacial area; consequently, the morphologies induced by melt mixing are usually unstable and can undergo considerable changes during the course of further processing or annealing.

In order to decrease the interfacial area in blends with a dispersed morphology, two approaches are possible. The first approach involves a shape relaxation of the deformed particles that may occur as the latter tend to acquire a spherical shape. Nevertheless, highly stretched particles can simultaneously undergo further break-ups after the cessation of flow, and this process is concurrent to shape relaxation [99]. A second approach to reducing the total surface energy of the system is for the droplets to become fused; this will lead to a coarsening of the blend's phase structure.

Shape relaxation is the dominant process for droplets with an aspect ratio less than 10 [80]. The relaxation time of the droplet can be estimated using Mafetone–Minale [76] or Palierne [100] theory. The shape relaxation process can generally be divided into two stages [101,102]. The first stage involves a shape change from an extended droplet towards an ellipsoid, and is associated with a relatively slow decay of the droplet length. The second stage is a relatively fast retraction of the ellipsoid to a sphere. Whereas, the viscoelasticity of the droplet was found to have no significant effect on shape relaxation, the matrix viscoelasticity retards the droplet retraction [103]. Similarly, confinement of the droplet also leads to a deceleration of the shape relaxation [103].

With regards to the coarsening of dispersed morphologies, two main mechanisms are present in molten polymer blends, namely Ostwald ripening and coalescence [104]. During the course of Ostwald ripening, small droplets dissolve and large droplets grow [105,106] due to a concentration gradient of the minor component dissolved in the matrix, which is related to droplet diameter. A negative gradient exists near the surface of small droplets, whereas a positive gradient exists near large droplets; as a result there is a diffusive transfer of macromolecules from small to large droplets.

Coalescence in quiescent blends containing spherical dispersed droplets can be induced by interdroplet molecular forces, namely van der Waals forces and/or Brownian motion. An approximate theory of the molecular forces and Brownian motion-driven coalescence was derived [107] which considers the interaction of a droplet only with its nearest neighbor. Furthermore, it considers the system as monodispersed, and also treats the Brownian motion in a very approximate manner. The theory was derived for Newtonian droplets in a Newtonian matrix, and for Newtonian droplets in a viscoelastic matrix described by the Maxwell model. Coalescence in viscoelastic matrix was shown to be more rapid than in the Newtonian matrix with the same viscosity.

However, the difference between the rate of coalescence in the Newtonian and viscoelastic matrices was not pronounced.

An analysis of the theory of Ostwald ripening showed that the rate of growing of average droplet size should decrease with interfacial tension. On the other hand, the theory of molecular forces-induced coalescence predicts an increase in the rate of droplet growth with interfacial tension. An analysis of the experimental data showed that the rate of phase structure coarsening strongly increased with increasing interfacial tension [104], and therefore it is apparent that Ostwald ripening can contribute substantially to phase structure coarsening only in systems with a low interfacial tension. For blends with moderate and high interfacial tensions, coalescence is a decisive mechanism of structure coarsening, and in both cases theory predicts that droplet size during coarsening grows in line with the third-power of time.

Due to their high surface area, cocontinuous morphologies are very susceptible to additional changes after melt mixing. In a limit case, the cocontinuous structure can disintegrate completely and be transformed into a dispersed morphology, although this normally occurs only in blends with an asymmetric composition where the minor phase forms a network with long and thin threads connecting the knots. Such threads can then break up or retract to the knots during annealing, causing the cocontinuous structures to disappear [108]. In symmetric polymer blends (50/50 composition), the dimensions of phase domains increase with the time of annealing, but the cocontinuous nature persists. The rate of coarsening was found to be constant over time; that is, the size of domains grows linearly with time, it increases with interfacial tension and decreases with the viscosities of the components [108,109]. Recently, a second coarsening regime was observed that occurred at very late times of annealing but which proceeded considerably more slowly [110,111]. López-Barrón and Macosko developed a model that was able to describe both stages of coarsening by taking into account the tendency of the system to eliminate energetically unfavorable sharp curvatures of the interface [112].

### 3.5

#### **Compatibilization of Polymer Blends**

Compatibilization can be defined as a process leading to an increase in interfacial adhesion between the components of an immiscible polymer blend and, thus, to enhance the mechanical properties of the blend. This goal is usually achieved by the incorporation of compatibilizers, which are macromolecular species located preferentially at the interface. Two important objectives of compatibilizers in the blending process are: (i) to decrease the domain size; and (ii) to stabilize the morphology induced by blend processing. Polymers with a blocky structure, where each of the constituent blocks is miscible or compatible with one blend component, are commonly used as compatibilizers [113,114]. In the ideal case, each block of a compatibilizer penetrates the parent phase and forms entanglements

with the chains of bulk polymers, such that the interfacial adhesion is enhanced. From this point of view, an efficient compatibilizer should have just two blocks with a high molecular weight. However, these are exactly the properties which support the micelle formation of block copolymers and, thus, decrease the amount of the compatibilizer that can operate effectively at the interface. Moreover, kinetic criteria must be taken into account, as the high molecular weight of the compatibilizer impedes its diffusion to the interface. Therefore, the molecular architecture of the compatibilizer – that is, the number and length of the blocks – considerably affects not only the compatibilization efficiency but also, as a consequence, the morphology of the final blend [115].

### 3.5.1

#### Morphology Development in Compatibilized Blends

The presence of a compatibilizer at the interface has a considerable effect on the behavior of dispersed droplets in the flow because it can lower the interfacial tension, which makes droplet deformation and break-up easier. Distinct differences were found in the behavior of compatibilized droplets with respect to the viscosity ratio [116]. Typically, when the viscosity of the dispersed phase was higher than the viscosity of the matrix, the droplets were stabilized by the addition of a block copolymer; that is, they were less deformed than the uncompatibilized droplets. In the opposite case of a more viscous matrix, the droplets inclined to higher deformations and to asymmetric break-ups [117,118].

Other effects can also be observed in compatibilized blends. Due to the flow of the matrix surrounding the dispersed droplets, the compatibilizer can be conveyed towards the tips of the droplets, which makes the behavior of the droplets more complex [119]. An inhomogeneous distribution of the compatibilizer leads to the concentration gradient at the interface which causes so-called *Marangoni stress* that tries to equalize the compatibilizer concentration on the droplet surface (Figure 3.15). It is supposed that the formation of the concentration gradient is easier in the systems with a  $p$ -value below unity [120]. As the Marangoni stress

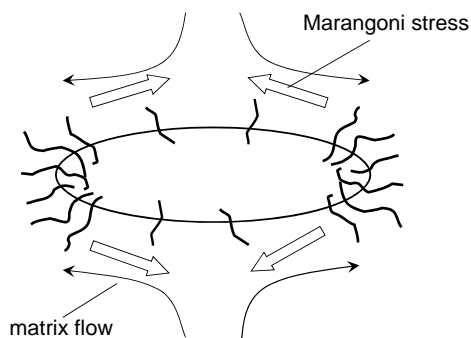


**Figure 3.15** Scheme of the effect of Marangoni stress induced by inhomogeneous distribution of the compatibilizer at the interface.

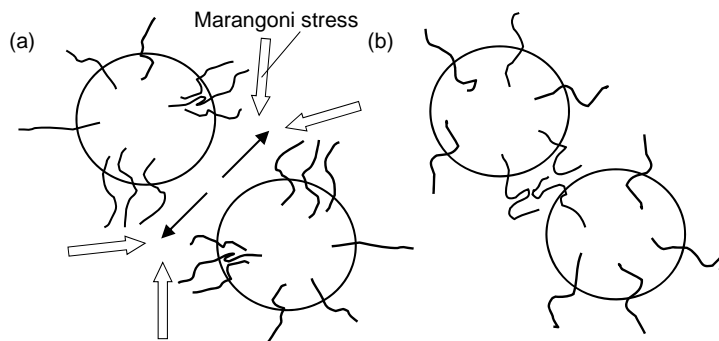


**Figure 3.16** Schematic representation of two possible mechanisms of the coalescence suppression in compatibilized polymer blends. (a) Due to Marangoni stress; (b) Due to steric repulsion. Adapted from Ref. [128]; © 2001, Elsevier.

counteracts the hydrodynamic stress, it can stabilize the droplet and prevent it from undergoing neck formation; this will postpone droplet break-up to higher deformations or even prevent any further deformation of the droplet [121,122]. After the cessation of flow, when the hydrodynamic stress falls to zero, the Marangoni stress accelerates the retraction of deformed droplets to spheres [122].

The second phenomenon induced by the incorporation of a compatibilizer is a suppression of the coalescence during flow, and also under quiescent conditions. Two mechanisms have been proposed to explain this effect. The first mechanism involves the Marangoni stress which prevents drainage of the matrix film between approaching droplets (Figure 3.16) [121,123,124]. The second mechanism was proposed by Macosko *et al.* [125,126], and claims that there is a repulsive force between the droplets resulting from a compression of the block copolymer chains at the surface of the approaching droplets (Figure 3.16). In both cases, the droplets cannot overcome the critical distance that is necessary for rupture of the matrix film and the consequent fusion of droplets. The above-mentioned studies provide opposing solutions to the question as to which of the mechanisms is decisive. A theoretical analysis and a concise review of this problem are available in Refs [127,128]. Although the exact mechanism of the coalescence suppression is unknown, this effect is assumed to be a key factor in the refinement and stabilization of blend structure, and the support of the droplet break-up plays only a minor role [128].

Although the exact explanation and theoretical description of the compatibilizers activity remains an open field of research, the morphology changes induced by effective compatibilization are qualitatively the same. The efficiency of a compatibilizer can be determined from emulsification curves showing the size of the dispersed particles as a function of compatibilizer concentration [129,130].

With increasing concentration, the compatibilizer is deposited at the interface and the dispersed particle size decreases. However, when the interface is

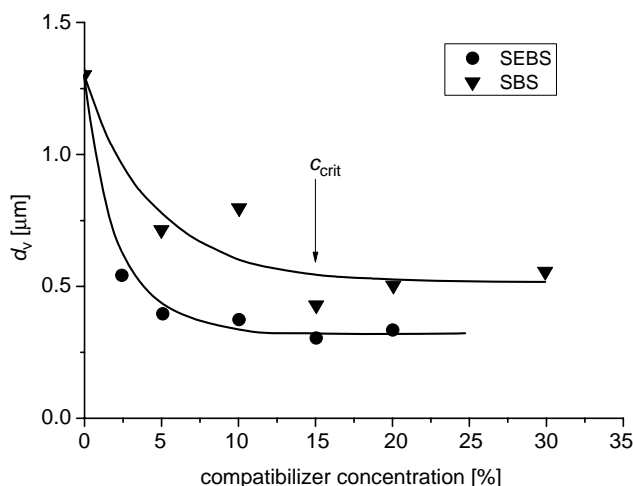


**Figure 3.17** Influence of compatibilizer concentration (based on volume of dispersed phase) on dispersed particle size in PS/EPR 90/10 (vol.%) modified by unsaturated SBS and saturated SEBS triblock copolymers. Reproduced with permission from Ref. [130]; © 1998, Elsevier.

saturated ( $c_{\text{crit}}$ ) the compatibilizer begins to form micelles in the bulk phases and thus the particle size is no longer affected. The data in Figure 3.17 illustrate that the chemical structure of the compatibilizer has a considerable effect on its efficiency, and consequently an optimal structure must be sought for each particular case.

In the case of cocontinuous morphologies, a few general tendencies can be observed with regards to the influence of the compatibilizer. The compatibilized cocontinuous structures are formed at higher concentrations of the minor phase compared to the uncompatibilized systems [58,131]; in addition, the range of cocontinuity is significantly narrowed by the addition of a compatibilizer. Both of these effects can be explained by a suppression of coalescence in compatibilized blends [132]. Nevertheless, the already-formed, compatibilized cocontinuous structures are more stable, they usually do not transform to a dispersed morphology and are more resistant against coarsening during the annealing.

### 3.5.2

#### Compatibilization Techniques

The two most common compatibilization techniques of additive and reactive compatibilization differ in the origin of the compatibilizer. In the former case, the preprepared compatibilizer is added to the blend and has to diffuse to the interface during mixing. In reactive compatibilization, the compatibilizer is generated *in situ* directly at the interface by a chemical reaction of one or both blend

components with additional reactive species. In both cases, on completion of the mixing the blend contains particles that are covered by either block or graft copolymer, ensuring an enhanced interfacial adhesion. Then, when the fracture path runs along the interface it must either pull out or cleave the macromolecules of the compatibilizer that are anchored in the bulk phases [133]. In order to reinforce the interface successfully the molecular weight of the blocks should be greater than the critical molecular weight which is necessary for entanglement formation [134]. Moreover, there is an optimum chain density at the interface because when the compatibilizer is present at high concentrations it can form its own phase, which can reduce resistance against crack propagation [135].

### 3.5.2.1 Addition of Preprepared Copolymer

The incorporation of a preprepared block or graft copolymer represents an easy means of compatibilizing an immiscible polymer blend. However, the efficiency of the compatibilizer involves a complex interplay between the rheology and structure of the blend components and the compatibilizer itself. Many attempts have been made to provide an understanding of the relationships between the molecular structure of block copolymers (the number and length of blocks) and their compatibilization efficiency for a certain polymer pair, but these have led to contradictory results. It follows from some studies [136,137] that diblock copolymers are more efficient than triblocks and multiblocks, but other studies have arrived at the opposite conclusion [138,139]. Some studies have shown that copolymers with block lengths comparable to the lengths of the related blend components are the most efficient [137], while others [140,141] have concluded that copolymers with substantially shorter blocks can show a high efficiency. Fortelný *et al.* performed a comprehensive systematic study on the compatibilization efficiency of a set of model styrene–butadiene–styrene copolymers, with different numbers and lengths of blocks in blends of PS with various polyolefins [142,143 and references therein]. The compatibilization efficiency of a block copolymer was found to depend not only on its molecular structure and interaction parameters, but also on the ratio of the blend components and on the processing conditions. A pronounced migration of copolymers between the interface and bulk phases observed during blend annealing showed that the distribution of a copolymer between the interface and bulk phases in a steady flow and in the quiescent state is not the same, and it cannot be predicted by equilibrium thermodynamics. The tendency of the block copolymers to form their own phase can be suppressed by the synthesis of tapered block copolymers without any sharp transition in the chemical composition of the blocks. Such copolymers are preferentially localized at the interface and display a higher compatibilization efficiency than the usual block copolymers [144].

Statistical copolymers of monomers that are the same as or miscible with blend components also often show a positive effect on the fineness of the phase structure and mechanical properties of immiscible polymer blends. However, they are unable to effectively suppress the coarsening of the phase structure during further processing [145].

### 3.5.2.2 Addition of Reactive Polymer

Block or graft copolymers can be generated also directly *in situ* by the addition of an appropriate reactive polymer. The latter has a backbone that is miscible or compatible with the first nonreactive component, and carries end or pendant groups capable of reacting with a second blend component. This approach is suitable for blends containing a polycondensate having naturally reactive end groups. The main advantage of this method is that the compatibilizer is formed only at the interface. Moreover, the viscosity of the reactive polymer is lower compared to the respective preprepared copolymer, and therefore diffusion of the reactive polymer to the interface is faster. This is a crucial point, as a sufficient amount of copolymer must be formed during processing times that usually are less than 5 min. As the concentration of end groups of high-molecular-weight polycondensate is limited, polymers carrying pendant reactive groups are preferred as precursors to grafted copolymers in order to ensure a sufficient rate of copolymer formation. Nevertheless, if the blend component is pendant-reactive, it is important to be aware that a large amount of pendant-reactive precursor could lead to the formation of crosslinked structures which may have a deleterious effect on the processability of the blend.

Typical precursors used in reactive compatibilization are polymers containing maleic anhydride (MA) grafted onto polyolefins or as a comonomer in styrenic polymers. MA can react with amine end groups of polyamides, as well as with the hydroxyl groups of polyesters. Thus, PP-g-MA was used successfully to compatibilize PP/PA6 [146] or PP/PET blends [147]. Similarly, PA/ABS or PA/SAN blends were compatibilized by the addition of styrene-MA copolymers [148,149]. Another functional group often employed is the epoxide group; for example, glycidyl methacrylate can be grafted directly onto polyolefins in the presence of a peroxide initiator. Such graft copolymers display a higher compatibilization efficiency compared to analogous MA-grafted copolymers [150,151].

If both blend components are nonreactive, it is necessary to add two reactive polymers which provide – after reaction at the interface – an effective compatibilizer. Thus, the interfacial adhesion in PP/PE blends was enhanced by the addition of PP-g-MA and poly(ethen-co-vinylalcohol) [152] or in PP/PS blends using PP carrying oxazoline groups and carboxyl-terminated PS [153].

Although the addition of a reactive polymer represents a major route for the compatibilization of immiscible blends on an industrial level, the exact mechanism and kinetics of the interfacial reactions remain uncertain. The reasons for this are the different reaction rates for the same functional groups on different polymers, and the effects of flow in a mixing device which can significantly accelerate the interfacial reaction, most likely due to convection as well as to the creation of a fresh interface [154].

### 3.5.2.3 Addition of Reactive Low-Molecular-Weight Compounds

An alternative compatibilization strategy is to add one or more low-molecular-weight compounds which can react with both blend components. Typical examples of these are peroxides and/or bifunctional compounds. Although the

incorporation of an organic peroxide into an immiscible blend appears attractive because it is cheap and simple to perform, a major disadvantage is that the selectivity of the radical reactions is very low. For example, in PP/PE blends the addition of a peroxide led to the formation of only very limited amounts of graft copolymers at the interface. On the other hand, the reactions can also occur in bulk phases, notably crosslinking in PE and chain scission in PP [155]. These processes alter the rheology of the components during mixing which makes the control of blend properties very difficult, if not impossible. Despite these apparent drawbacks, however, this simple compatibilization procedure has found applications in the upgrading of polymer waste mixtures [156].

In order to form block copolymers in blends of polycondensates, it is possible to use bisepoxides that react with the end groups of the blend components. A combination of peroxide and unsaturated bifunctional components (MA, triallylisocyanurate, low-molecular-weight unsaturated rubber) was reported to induce copolymer formation in PS/PE and polyolefins blends [157–159].

#### 3.5.2.4 Other Compatibilization Techniques

For blends of polycondensates, the interchange reactions can occur during melt mixing [160] and may lead to miscible systems; this situation is undesirable as the amorphous product has lost the beneficial properties of both blend components. Therefore, processing should be led in such a way that only a small amount of block copolymer is formed. This requires relatively low processing temperatures, short residence times in the melt, and only traces of a catalyst (if any).

Both, block and grafted copolymers can also be produced by solid-state shear pulverization [161], whereby polymer powders are exposed to high shear stresses below their  $T_g$  or  $T_m$ , leading to the cleavage of covalent bonds. The polymer radicals then recombine during consequent melt mixing and form compatibilization-effective copolymers.

Recently, much attention has been paid to the possibility of controlling morphology development in immiscible polymer blends by the addition of interfacially active nanoparticles. In fact, it was found that some nanoparticles could refine and stabilize the morphology, whereas the addition of others leads to an increase in the dispersed particle size [162]. Generally, the optimization of this approach seems to be much more difficult compared to the incorporation of block or graft copolymers. One probable reason for this is that the polymer–filler interactions at the interface are weaker than in the case of copolymers anchored in the respective polymer phases. A critical comprehensive review on this topic was produced by Fenouillot *et al.* [163].

## References

- 1 Hancock, T. (1857) *Personal Narrative of the Origin and Progress of the Caoutchouc or India-rubber Manufacture in England*, Longman, Brown, Green, Longmans & Roberts, London.
- 2 Scatchard, G. (1931) *Chem. Rev.*, 7, 321.



- 3 Hildebrand, J.H. and Scott, R.L. (1964) *The Solubility of Nonelectrolytes*, Dover, New York.
- 4 Small, P.A. (1953) *J. Appl. Chem.*, **3**, 71.
- 5 Hoy, K.L. (1970) *J. Paint. Technol.*, **42**, 76.
- 6 van Krevelen, D.W. (1972) *Properties of Polymers: Correlations with Chemical Structure*, Elsevier, Amsterdam.
- 7 Coleman, M.M., Serman, C.J., Bhagwagar, D.E., and Painter, P.C. (1990) *Polymer*, **31** (7), 1187.
- 8 Coleman, M.M., Graf, J.F., and Painter, P.C. (1991) *Specific Interactions and Miscibility of Polymer Blends*, Technomic, Lancaster.
- 9 Huggins, M.L. (1941) *J. Chem. Phys.*, **9** (5), 440.
- 10 Flory, P.J. (1941) *J. Chem. Phys.*, **9** (8), 660.
- 11 van Dijk, M.A. and Wakker, A. (1997) *Concepts of Polymer Thermodynamics*, Technomic, Lancaster.
- 12 Flory, P.J. (1953) *Principles of Polymer Physics*, Cornell University Press, Ithaca.
- 13 Olabisi, O. (1975) *Macromolecules*, **8**, 316.
- 14 Zhang, S., Jin, X., Painter, P.C., and Runt, J. (2002) *Macromolecules*, **35** (9), 3636.
- 15 Pomposo, J.A., Cortázar, M., and Calahorra, E. (1994) *Macromolecules*, **27** (1), 252.
- 16 Zhang, S., Painter, P.C., and Runt, J. (2002) *Macromolecules*, **35** (22), 8478.
- 17 Pedrosa, P., Pomposo, J.A., Calahorra, E., and Cortazar, M. (1994) *Macromolecules*, **27** (1), 102.
- 18 Robeson, L.M. (1978) *J. Polym. Sci. Polym. Lett. Ed.*, **16** (6), 261.
- 19 Miyoshi, T., Takegoshi, K., and Hikichi, K. (1997) *Polymer*, **38**, 2315.
- 20 Lu, X. and Weiss, R.A. (1995) *Macromolecules*, **28**, 3022.
- 21 He, Y., Zhu, B., and Inoue, Y. (2004) *Prog. Polym. Sci.*, **29**, 1021.
- 22 Chow, T.S. (1990) *Macromolecules*, **23**, 333.
- 23 Straka, J., Schmidt, P., Dybal, J., Schneider, B., and Špěváček, J. (1995) *Polymer*, **36**, 1147.
- 24 Kalfoglou, N.K., Sotiropoulou, D.D., and Margartis, A.G. (1988) *Eur. Polym. J.*, **24**, 389.
- 25 Paul, D.R., Barlow, J.W., Bernstein, R.E., and Wahrmund, D.C. (1978) *Polym. Eng. Sci.*, **18** (16), 1225.
- 26 Molnár, A. and Eisenberg, A. (1993) *Polymer*, **34** (9), 1918.
- 27 Rakkapao, N., Vao-Soongnern, V., Masubuchi, Y., and Watanabe, H. (2011) *Polymer*, **52** (12), 2618.
- 28 Djordjevic, M.B. and Porter, R.S. (1983) *Polym. Eng. Sci.*, **23**, 650.
- 29 Sanchez, I.C. and Lacombe, R.H. (1978) *Macromolecules*, **11**, 1145.
- 30 Panayiotou, C.G. (1987) *Macromolecules*, **20**, 861.
- 31 Sanchez, I.C. and Stone, M.T. (2000) Statistical thermodynamics of polymer solutions and blends, in *Polymer Blends Volume 1: Formulation* (eds D.R. Paul and C.B. Barlow), John Wiley & Sons, New York.
- 32 Roe, J.R. and Zin, W.C. (1980) *Macromolecules*, **13**, 1221.
- 33 Hashimoto, T., Itakura, M., and Hasegawa, H. (1986) *J. Chem. Phys.*, **85**, 6118.
- 34 Kapnistos, M., Hinrichs, A., Vlassopoulos, D., Anastasiadis, S.H., Stammer, A., and Wolf, B.A. (1996) *Macromolecules*, **29**, 7155.
- 35 Niu, Y.H. and Wang, Z.G. (2006) *Macromolecules*, **39**, 4175.
- 36 Hashimoto, T., Kumaki, J., and Kawai, K. (1983) *Macromolecules*, **16**, 641.
- 37 Cahn, J.W. (1965) *J. Chem. Phys.*, **42**, 93.
- 38 Binder, K. and Fratzl, P. (2001) Spinodal decomposition, in *Phase Transformations in Materials* (ed. G. Kostorz), Wiley-VCH Verlag, Weinheim.
- 39 Fleischer, C.A., Morales, A.R., and Koberstein, J.T. (1994) *Macromolecules*, **27**, 379.
- 40 Reiter, J., Zifferer, G., and Olaj, O.F. (1990) *Macromolecules*, **23**, 224.
- 41 Helfand, E. and Tagami, Y. (1971) *J. Chem. Phys.*, **9**, 741.
- 42 Helfand, E. and Tagami, Y. (1971) *J. Chem. Phys.*, **56**, 3592.
- 43 Helfand, E. and Sapse, A.M. (1975) *J. Chem. Phys.*, **62**, 1327.
- 44 Broseta, D., Fredrickson, G.H., Helfand, E., and Leibler, N. (1990) *Macromolecules*, **23**, 132.
- 45 Sferrazza, M., Xiao, C., Bucknall, D.G., and Jones, R.A.L. (2001) *J. Phys. Condens. Matter*, **13**, 10269.

- 46 Fernandez, M.L., Higgins, J.S., Penfold, J., Ward, R.C., Shackleton, J., and Walsh, D.J. (1998) *Polymer*, **29**, 1923.
- 47 Schubert, D.W., Abetz, V., Stamm, M., Hack, T., and Siol, W. (1995) *Macromolecules*, **28**, 2519.
- 48 Shull, K.R., Kramer, E.J., Hadziioannou, G., and Tang, W. (1990) *Macromolecules*, **23**, 4780.
- 49 Noolandi, J. and Hong, K.M. (1982) *Macromolecules*, **15**, 482.
- 50 Yukioka, S. and Inoue, T. (1994) *Polymer*, **35**, 1182.
- 51 Kressler, J., Higashida, N., Inoue, T., Heckmann, W., and Seitz, F. (1993) *Macromolecules*, **26**, 2090.
- 52 Schnell, R., Stamm, M., and Creton, C. (1998) *Macromolecules*, **31**, 2284.
- 53 Stamm, M. and Schubert, D.W. (1995) *Annu. Rev. Mater. Sci.*, **25**, 325.
- 54 Avgeropoulos, G.N., Weissert, F.C., Biddison, P.H., and Boehm, G.G.A. (1976) *Rubber Chem. Technol.*, **49**, 93.
- 55 Mekhilef, N. and Verhoogt, H. (1996) *Polymer*, **37** (18), 4069.
- 56 Lyngaae-Jørgensen, J. and Utracki, L.A. (1991) *Makromol. Chem. Macromol. Symp.*, **48/49**, 189.
- 57 Lyngaae-Jørgensen, J., Rasmussen, K.L., Chtcherbakova, E.A., and Utracki, L.A. (1999) *Polym. Eng. Sci.*, **39** (6), 1060.
- 58 Li, J., Ma, P.L., and Favis, B.D. (2002) *Macromolecules*, **35**, 2005.
- 59 Marin, N. and Favis, B.D. (2002) *Polymer*, **43**, 4723.
- 60 Pötschke, P. and Paul, D.R. (2003) *J. Macromol. Sci., Part C: Polym. Rev.*, **43** (1), 87.
- 61 Scott, C.E. and Macosko, C.W. (1991) *Polym. Bull.*, **26**, 341.
- 62 Scott, C.E. and Macosko, C.W. (1995) *Polymer*, **36** (3), 461.
- 63 Macosko, C.W., Guégan, P., Khandpur, A.K., Nakayama, A., Marechal, P., and Inoue, T. (1996) *Macromolecules*, **29**, 5590.
- 64 Shih, C.K. (1995) *Polym. Eng. Sci.*, **35** (21), 1688.
- 65 Sundararaj, U. and Macosko, C.W. (1996) *Polym. Eng. Sci.*, **36** (13), 1769.
- 66 Scott, C.E. and Young, S.K. (1996) *Polym. Eng. Sci.*, **36** (12), 1666.
- 67 Lee, J.K. and Han, C.D. (1999) *Polymer*, **40**, 6277.
- 68 Lee, J.K. and Han, C.D. (2000) *Polymer*, **41**, 1799.
- 69 Chuai, C.Z., Almdal, K., and Lyngaae-Jørgensen, J. (2003) *Polymer*, **44**, 481.
- 70 Sarazin, P. and Favis, B.D. (2007) *J. Polym. Sci., Part B: Polym. Phys.*, **45**, 864.
- 71 Utracki, L.A. and Shi, Z.H. (1992) *Polym. Eng. Sci.*, **32**, 1824–1833.
- 72 Janssen, J.M.H. and Meijer, H.E.H. (1995) *Polym. Eng. Sci.*, **35**, 1766–1780.
- 73 Fortelný, I., Kovář, J., and Stephan, M. (1996) *J. Elastomers Plast.*, **28**, 106–139.
- 74 Taylor, G.I. (1932) *Proc. Roy. Soc.*, **138**, 41.
- 75 Cox, R.G. (1969) *J. Fluid Mech.*, **37**, 601.
- 76 Maffettone, P.L. and Minale, M. (1998) *J. Non-Newtonian Fluid Mech.*, **78**, 227.
- 77 Janssen, J.M.H. (1993) Dynamics of liquid–liquid mixing. PhD Thesis, Eindhoven University of Technology.
- 78 Elemans, P.H.M., Bos, H.L., Janssen, J.M.H., and Meijer, H.E.H. (1993) *Chem. Eng. Sci.*, **48**, 267.
- 79 Grace, H.P. (1982) *Chem. Eng. Commun.*, **14**, 225.
- 80 Tucker, C.L. and Moldenaers, P. (2002) *Annu. Rev. Fluid Mech.*, **34**, 177.
- 81 de Bruijn, R.A. (1989) Deformation and breakup of drops in simple shear flows. PhD Thesis, Eindhoven University of Technology.
- 82 Levitt, L., Macosko, C.W., and Pearson, S.D. (1996) *Polym. Eng. Sci.*, **36**, 1647.
- 83 Mighri, F., Ajji, A., and Carreau, P.J. (1997) *J. Rheol.*, **41**, 421.
- 84 Lerdwijitjarud, W., Larson, R.G., and Sirivat, A. (2003) *J. Rheol.*, **47**, 37.
- 85 Guido, S., Simeone, M., and Greco, F. (2003) *J. Non-Newtonian Fluid Mech.*, **114**, 65.
- 86 Sibillo, V., Simeone, M., and Guido, S. (2004) *Rheol. Acta*, **43**, 449.
- 87 Janssen, P.J.A., Vananroye, A., Van Puyvelde, P., Moldenaers, P., and Anderson, P.D. (2010) *J. Rheol.*, **54**, 1047.
- 88 Caserta, S., Reynaud, S., Simeone, M., and Guido, S. (2007) *J. Rheol.*, **51**, 761.
- 89 Stone, H.A., Bentley, B.J., and Leal, L.G. (1986) *J. Fluid Mech.*, **173**, 131.
- 90 Tomotika, S. (1935) *Proc. R. Soc. Lond. Ser. A*, **150**, 322.
- 91 Mikami, T., Cox, R.G., and Mason, R.G. (1975) *Int. J. Multiphase Flow*, **2**, 113.
- 92 Khakhar, D. and Ottino, J.M. (1987) *Int. J. Multiphase Flow*, **13**, 71.
- 93 Stone, H.A. (1994) *Annu. Rev. Fluid Mech.*, **26**, 65.

- 94 Tjahjadi, M., Stone, H.A., and Ottino, J.M. (1992) *J. Fluid Mech.*, **243**, 297.
- 95 de Bruijn, R.A. (1993) *Chem. Eng. Sci.*, **48**, 227.
- 96 Eggleston, C., Tsai, T., and Stebe, K. (2001) *Phys. Rev. Lett.*, **87** (4), 483021.
- 97 Lin, B., Sundararaj, U., Mighri, F., and Huneault, M.A. (2003) *Polym. Eng. Sci.*, **43** (4), 891.
- 98 Wang, H., Zinchenko, A.K., and Davis, R. H. (1994) *J. Fluid Mech.*, **265**, 161.
- 99 Starý, Z., Musialek, M., and Münstedt, H. (2011) *Macromol. Mater. Eng.*, **296**, 414.
- 100 Palierne, J.F. (1990) *Rheol. Acta*, **29**, 204, erratum *Rheol. Acta* (1991), **30**, 497.
- 101 Hayashi, R., Takahashi, M., Yamane, H., Jinnai, H., and Watanabe, H. (2001) *Polymer*, **42**, 757.
- 102 Assighaou, S. and Benyahia, L. (2008) *Phys. Rev. E*, **77**, 0363051.
- 103 Cardinaels, R. and Moldenaers, P. (2010) *J. Polym. Sci., Part B: Polym. Phys.*, **48**, 1372.
- 104 Fortelný, I., Živný, A., and Jůza, J. (1999) *J. Polym. Sci., Part B: Polym. Phys.*, **37**, 181.
- 105 Crist, B. and Nesarikar, A.R. (1995) *Macromolecules*, **28**, 890.
- 106 Stachurski, Z.H., Edward, G.H., Yin, M., and Long, Y. (1996) *Macromolecules*, **29**, 2131.
- 107 Fortelný, I. and Živný, A. (1998) *Polymer*, **39**, 2669.
- 108 Veenstra, H., Van Damm, J., and Posthuma de Boer, A. (2000) *Polymer*, **41**, 3037.
- 109 Scholten, E., Sagis, L.M.C., and van der Linden, E. (2005) *Macromolecules*, **38**, 3515.
- 110 Pyun, A., Bell, J.R., Won, K.H., Weon, B.M., Seol, S.K., Je, J.H., and Macosko, C.W. (2007) *Macromolecules*, **40**, 2029.
- 111 Omonov, T.S., Harrats, C., Groeninckx, G., and Moldenaers, P. (2007) *Polymer*, **48**, 5289.
- 112 López-Barrón, C.R. and Macosko, C.W. (2010) *Soft Matter*, **6**, 2637.
- 113 Koning, C., Van Duin, M., Pagnoulle, Ch., and Jerome, R. (1998) *Prog. Polym. Sci.*, **23**, 707.
- 114 Ruzette, A.V. and Leibler, L. (2005) *Nat. Mater.*, **4** (1), 19.
- 115 Starý, Z., Fortelný, I., Kruliš, Z., and Šlouf, M. (2008) *J. Appl. Polym. Sci.*, **107**, 174.
- 116 Hu, Y.T., Pine, D.J., and Leal, L.G. (2000) *Phys. Fluids*, **12**, 484.
- 117 de Bruijn, R.A. (1993) *Chem. Eng. Sci.*, **48**, 277.
- 118 Levitt, L. and Macosko, C.W. (1999) *Macromolecules*, **32**, 6270.
- 119 Pawar, Y. and Stebe, K. (1996) *Phys. Fluids*, **8**, 1738.
- 120 Bazhlekoy, I.B., Anderson, P.D., and Meijer, H.E.H. (2006) *J. Colloid Interface Sci.*, **298**, 369.
- 121 Van Puyvelde, P., Velankar, S., Mewis, J., and Moldenaers, P. (2002) *Polym. Eng. Sci.*, **42** (10), 1956.
- 122 Starý, Z., Pemsel, T., Baldrian, J., and Münstedt, H. (2012) *Polymer*, **53** (9), 1881.
- 123 Milner, S.T. and Xi, H. (1996) *J. Rheol.*, **40**, 663.
- 124 Ramic, A.J., Stehlin, J.C., Hudson, S.D., Jamieson, A.M., and Manas-Zloczower, I. (2000) *Macromolecules*, **33**, 371.
- 125 Sundaraj, U. and Macosko, C.W. (1995) *Macromolecules*, **28**, 2647.
- 126 Lyu, S.P., Jones, T.D., Bates, F.S., and Macosko, C.W. (2002) *Macromolecules*, **35**, 7845.
- 127 Fortelný, I. (2004) *Eur. Polym. J.*, **40**, 2161.
- 128 Van Puyvelde, P., Velankar, S., and Moldenaers, P. (2001) *Curr. Opin. Colloid Interface Sci.*, **6**, 457.
- 129 Matos, M., Favis, B.D., and Lomellini, P. (1995) *Polymer*, **36**, 3899.
- 130 Cigana, P. and Favis, B.D. (1998) *Polymer*, **39**, 3373.
- 131 Dedecker, K. and Groeninckx, G. (1998) *Polymer*, **39**, 4993.
- 132 Tol, R.T., Groeninckx, G., Vinckier, I., Moldenaers, P., and Mewis, J. (2004) *Polymer*, **45**, 2587.
- 133 Creton, C., Kramer, E.J., Hui, C.Y., and Brown, H.R. (1992) *Macromolecules*, **25**, 3075.
- 134 Creton, C., Kramer, E.J., and Hadziioannou, G. (1991) *Macromolecules*, **24**, 1846.
- 135 Washiyama, J., Creton, C., Kramer, E.J., Xiao, F., and Hui, C.Y. (1993) *Macromolecules*, **26**, 6011.
- 136 Fayt, R., Jerome, R., and Teysie, P. (1989) *J. Polym. Sci., Part B: Polym. Phys.*, **29**, 945.
- 137 Xu, G. and Lim, S. (1996) *Polymer*, **37**, 421.
- 138 Kroeze, E., ten Brinke, G., and Hadziioannou, G. (1997) *Polym. Bull.*, **38**, 203.
- 139 Horák, Z., Fořt, V., Hlavatá, D., Lednický, F., and Večerka, F. (1996) *Polymer*, **37**, 65.

- 140 Radonjić, G., Musil, V., and Šmit, I. (1999) *J. Appl. Polym. Sci.*, **72**, 291.
- 141 Hlavatá, D., Horák, Z., Hromádková, J., Lednický, F., and Pleska, A. (1999) *J. Polym. Sci., Part B: Polym. Phys.*, **37**, 1647.
- 142 Fortelný, I., Šlouf, M., Sikora, A., Hlavatá, D., Hašová, V., Mikešová, J., and Jacob, C. (2006) *J. Appl. Polym. Sci.*, **100**, 2803.
- 143 Hlavatá, D., Hromádková, J., Fortelný, I., Hašová, V., and Pulda, J. (2004) *J. Appl. Polym. Sci.*, **92**, 2431.
- 144 Harrats, C., Fayt, R., and Jerome, R. (2002) *Polymer*, **43**, 863.
- 145 Guo, H.F., Packisiram, S., Mani, R.S., Aronson, C.L., Gvozdic, N.V., and Meier, D.J. (1998) *Polymer*, **39**, 2495.
- 146 Shi, D., Ke, Z., Yang, J., Gao, Y., Wu, J., and Yin, J. (2002) *Macromolecules*, **35**, 8005.
- 147 Yoon, K.H., Lee, H.W., and Park, O.O. (1998) *J. Appl. Polym. Sci.*, **70**, 389.
- 148 Takeda, Y. and Paul, D.R. (1992) *J. Polym. Sci., Part B: Polym. Phys.*, **30**, 1273.
- 149 Sailer, C. and Handge, U.A. (2008) *Macromolecules*, **41**, 4258.
- 150 Loyens, W. and Groeninckx, G. (2002) *Macromol. Chem. Phys.*, **203**, 1702.
- 151 Pracella, M., Chionna, D., Pawlak, A., and Galeski, A. (2005) *J. Appl. Polym. Sci.*, **98**, 2201.
- 152 Tselios, Ch., Bikiaris, D., Maslis, V., and Panayiotou, C. (1998) *Polymer*, **39**, 6807.
- 153 Pötschke, P., Malz, H., and Pionteck, J. (2000) *Macromol. Symp.*, **149**, 231.
- 154 Macosko, C.W., Jeon, H.K., and Hoyer, T.R. (2005) *Prog. Polym. Sci.*, **30**, 939.
- 155 Braun, D., Richter, S., Hellmann, G.P., and Rätzsch, M. (1998) *J. Appl. Polym. Sci.*, **68**, 2019.
- 156 Vivier, T. and Xanthos, M. (1994) *J. Appl. Polym. Sci.*, **54**, 569.
- 157 Xanthos, M., Greci, J., Patel, S.H., Patel, A., Jacob, C., Dey, S., and Dagli, S.S. (1995) *Polym. Compos.*, **16**, 204.
- 158 Teh, J.W. and Rudin, A. (1992) *Polym. Eng. Sci.*, **32**, 1678.
- 159 Kruliš, Z., Kokta, B.V., Horák, Z., Michálková, D., and Fortelný, I. (2001) *Macromol. Mater. Eng.*, **286**, 156.
- 160 Porter, R.S. and Wang, L.H. (1992) *Polymer*, **33**, 2019.
- 161 Nesarikar, A.R., Carr, S.H., Khait, K., and Mirabella, F.M. (1997) *J. Appl. Polym. Sci.*, **63**, 1179.
- 162 Thareja, P., Moritz, K., and Velankar, S.S. (2010) *Rheol. Acta*, **49**, 285.
- 163 Fenouillot, F., Cassagnau, P., and Majesté, J.-C. (2009) *Polymer*, **50**, 1333.

## Further Reading

### Thermodynamics and Miscibility of Polymer Blends

- Olabisi, O., Robeson, L.M., and Shaw, M.T. (1979) *Polymer-Polymer Miscibility*, Academic Press, New York.
- Utracki, L.A. (1989) *Polymer Alloys and Blends. Thermodynamics and Rheology*, Hanser Publishers, Munich, Vienna, New York.
- Utracki, L.A. (2002) *Polymer Blends Handbook*, Kluwer Academic Publishers, Dordrecht, (including a list of miscible polymer systems).
- Enders, S. and Wolf, B. (eds) (2011) *Polymer Thermodynamics*, Springer Verlag, Berlin, Heidelberg.

### Phase Behavior of Polymer Blends

- Koningsveld, R., Stockmayer, W.H., and Nies, E. (2001) *Polymer Phase Diagrams: A Text Book*, Oxford University Press, Oxford.
- Yokoyama, H. (2006) Polymer-polymer interfaces: Theoretical, experimental and adhesion aspects, in *Micro- and Nanostructured Multiphase Polymer Blend Systems: Phase Morphology and Interfaces* (eds C. Harrats, S. Thomas, and G. Groeninckx), Taylor and Francis, Boca Raton.

## Morphology Development During Melt Mixing

- Fortelný, I. (2006) Theoretical aspects of phase morphology development, in *Micro- and Nanostructured Multiphase Polymer Blend Systems: Phase Morphology and Interfaces* (eds C. Harrats, S. Thomas, and G. Groeninckx), Taylor and Francis, Boca Raton.
- Favis, B.D. (2000) Factors influencing the morphology of immiscible polymer blends in melt processing, in *Polymer Blends Volume 1: Formulation* (eds D.R. Paul and C. B. Barlow), John Wiley & Sons, New York.

## Compatibilization

- Datta, S. and Lohse, D.J. (1996) *Polymeric Compatibilizers: Uses and Benefits in Polymer Blends*, Hanser Verlag, Munich.
- Robeson, L.M. (2007) *Polymer Blends: A Comprehensive Review*, Hanser, Munich.
- Koning, C., Van Duin, M., Pagnoulle, C., and Jerome, R. (1998) *Prog. Polym. Sci.*, **23**, 707.



## 4

# Characterization of Polymer Blends: Rheological Studies

Yingfeng Yu

### 4.1

#### Introduction

The rheological properties of polymer systems are of fundamental importance for both scientific studies and industrial applications, as they are closely related to the viscoelasticity, morphology evolution, chemical reactions, and processing properties of polymer systems, including neat polymer, polymer solutions, or polymer blends which may also have state transitions of different characters. Generally, three types of polymer blends exist: (i) thermoplastic (linear polymer)-thermoplastic polymer blends; (ii) thermoplastic-thermosetting polymer blends; and (iii) polymer-filler blends. Each type has been studied extensively, using combinations of rheology and other property characterization.

For polymer melts and polymer solutions, numerous excellent reviews [1–5] have provided detailed descriptions of the concepts, test methods and rheological transitions in these systems. The rheological behaviors of thermoplastic blends, including both homopolymers and block copolymers, have also been extensively reviewed [6]. In the case of thermosetting blends, the majority of the information related to rheological studies has been reported in journals. Consequently, after a brief introduction of some of the concepts related to these studies, recent developments in thermosetting blend systems will be reviewed in the following sections.

#### 4.1.1

##### General Description of Thermoset Rheological Behaviors

The rheological analysis of thermosetting resins, including unsaturated polyester, epoxy, and urethane, began during the 1970s. As the curing or polymerization of thermosets is always conducted via chemical reactions in the presence of an initiator(s) or a catalyst(s), investigations into the rheological behavior of thermosets is referred to as “chemorheology” [7]. By using combinations of differential scanning calorimetry (DSC), Fourier transform infrared (FTIR) spectroscopy, dielectric measurements, and rheokinetic measurements, the chemorheology of the different types of thermosets have been investigated. In particular, studies of the curing

reaction kinetics of individual thermosetting polymers have attracted much attention [8–17].

Unlike linear polymers, thermosetting resins are initially ordinary low-molecular-weight monomers or oligomers; the curing of a thermosetting reactive “prepolymer” usually involves the transformation of oligomers from a liquid to a solid state as a result of the formation of a polymer network, either via a chemical reaction or via polymerization of the reactive groups of the system [8]. For neat thermosetting resins, the simplest model of the curing process assumes a single reaction mechanism and no phase separation.

Clearly, the chemorheology of thermoset blends is much more complex than the rheology of thermoplastics, because the curing reaction, phase separation, state transition and rheological behavior of thermosets are inseparable. A good representation of the rheological behavior of thermosetting blends must include the rheological properties ( $\eta$ ,  $N_1$ ,  $G'$  and  $G''$ ), the extent of the cure reaction  $\alpha$ , the state transitions (e.g., gelation, vitrification), and the morphology evolution of the blend systems. Furthermore, variations in the test conditions of thermosetting blends, such as shear rate and strain mode, cause the rheological behavior of thermosetting blends to be much more complicated than for ordinary thermoplastic systems. Hence, a brief introduction to neat thermosetting resins will help to provide an understanding of the sequence of events that occurs in blend systems.

#### 4.1.2

##### Thermosetting Resins: Gelation, Vitrification, and Viscoelasticity

The *gel point* is normally used to distinguish this process into two stages. Growth and branching of the polymer chains occur before the gel point, when the reactive system is soluble and fusible. However, after the gel time an infinite network of polymer chains appears and develops, such that the reactive system loses its solubility and fusibility; as a consequence, the final reactions take place in the solid state.

Generally, two rheologically active kinetic transitions occur during isothermal curing, namely gelation and vitrification. Three types of isothermal behavior occur if [9]: (i) the curing temperature ( $T_{\text{cure}}$ ) is higher than the  $T_g$  of full-cured thermosets ( $T_{g\infty}$ ), when only gelation is observed; (ii) if  $T_{\text{cure}}$  is lower than the  $T_g$  of thermosets at the gel point ( $T_{gg}$ ), only vitrification is observed, while if  $T_{g\infty} > T_{\text{cure}} > T_{gg}$ , both gelation and vitrification are observed. It should be noted that the term TTT (Time-Temperature-Transformation) isothermal cure diagram is always used to provide an intellectual framework for understanding and comparing the cure and physical property changes of thermosetting systems [18].

In Figure 4.1, the curing process is shown for an ordinary epoxy/amine system. Initially, the  $G'$  modulus is parallel to the time axis, after which the modulus increases exponentially versus time, where the gel process takes place. Finally, the modulus increases more rapidly, at which point a wide dispersion of the measurements is obtained, indicating vitrification.



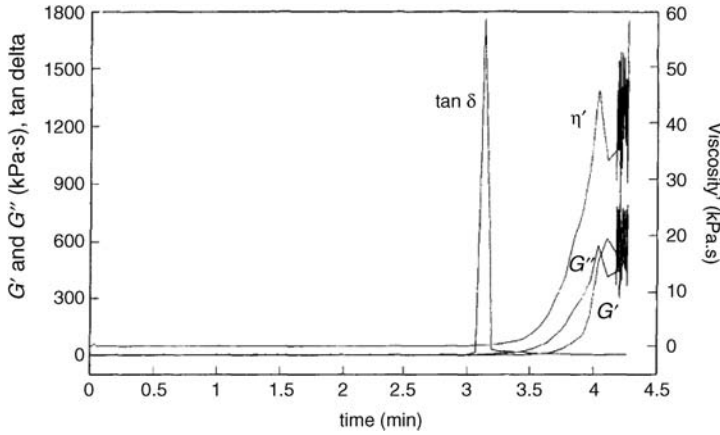


**Figure 4.1** Storage modulus ( $G'$ ), loss modulus ( $G''$ ), dynamic viscosity ( $\eta'$ ) and  $\tan \delta$  versus cure time for an epoxy/amine system. Reproduced with permission from Ref. [19]; © 1999, Elsevier.

The gel time has been determined according to different criteria as [10]:

- 1) The criterion of maximum peak in  $\tan \delta$ , based on the point where there is a maximum difference between the elastic and viscous behaviors of the system.
- 2) The criterion corresponding to the crossover between the  $G'$  and  $G''$  curves: at this point, the system presents not only an elastic but also viscous behavior, storing a similar amount of energy to the energy that is dissipated.
- 3) The criterion of the tangent line to the  $G'$  curve: this point corresponds to the crossing between the baseline ( $G' = 0$ ) and the tangent drawn at the  $G'$  curve when  $G'$  reaches a value close to 100 kPa.s.
- 4) The criterion of viscosity: at this point the real dynamic viscosity  $\nu'$  reaches several determined values (1000, 2000, and 5000 Pa.s).

For a given thermosetting system, the chemical conversion obtained at the gel time is considered to be constant [8]. Therefore, the gel time ( $t_g$ ) can be related to the apparent kinetic constant of the reaction, which is related to the temperature by an Arrhenius relationship [19]:

$$t_g = A_0 \cdot \frac{1}{k} \quad (4.1)$$

where  $k$  is the apparent kinetic constant of the reaction and  $A_0$  is the magnifier,

$$k = k_0 \cdot e^{-\frac{E_a}{RT}} \quad (4.2)$$

therefore

$$\ln t_g = A'_0 + \frac{E_a}{RT} \quad (4.3)$$

where  $E_a$  is the apparent activation energy,  $T$  is the curing temperature, and  $R$  is the gas constant. A linear relationship exists between  $\ln t_g$  and the inverse of temperature for isothermal curing reactions, and from the slope of this relationship the apparent activation energy can be obtained, which reflects the chain mobility and entanglement during the process.

For the quantitative viscosity data treatment obtained from thermosetting systems cured under isothermal conditions, most of the methods are based mainly on the Williams–Landel–Ferry (WLF) equation [2]:

$$\log \alpha_T = -C_1 \times \frac{T - T_s}{C_2 + (T - T_s)} \quad (4.4)$$

where  $\alpha_T$  is the shift factor,  $T_s$  is a temperature of reference, and  $C_1$  and  $C_2$  are two universal constants with values of 17.44 and 5.16, respectively, only if  $T_s$  is the  $T_g$  of the material. This equation was considered exclusively to observe the dynamic-mechanical relaxation times on the zone  $T_g$  to  $T_g + 50^\circ\text{C}$ .

Tajima and Crozier [15,16] first reported that, at any stage of the reaction, the temperature dependency of the viscosity for an epoxy/amine system can be described as:

$$\log \eta(T) = \log \eta(T_s) - \frac{26.8 \times (T - T_s)}{13.4 + (T - T_s)} \quad (4.5)$$

where the parameters  $T_s$  and  $\eta(T_s)$  vary with the degree of reaction for an epoxy-amine system, which at the same time is determined by the amine concentration.

Therefore, viscosity data can be treated by fitting to empirical equations where the temperature and the conversion dependency of the viscosity is separated into two independent terms:

$$\eta(T, \alpha) = \eta(T) * \eta(\alpha) \quad (4.6)$$

Assuming that the kinetic of the reaction in the liquid state is the order  $n=1$  before the gel time (not diffusion control), taking into account that  $\eta(\alpha)$  is related to the degree of entanglement and that, for a fixed temperature,  $\eta(T)$  can be considered as a constant,  $\eta_0$  [19]:

$$\ln \eta = \ln \eta_0 + k \cdot t \quad (4.7)$$

where  $\eta$  is the viscosity as a function of the temperature and the conversion “ $\alpha$ ”;  $\eta_0$  is the viscosity at  $t=0$ , and  $k$  is the apparent kinetic constant.

Another model for high curing conversion was proposed by Roller [20]:

$$\ln \eta = \ln \eta_\infty + E_\eta/RT + \int_0^t k_\infty \exp(E_k/RT) dt \quad (4.8)$$

where  $\eta$  is the viscosity at time  $t$  and at temperature  $T$ ,  $\eta_\infty$  is the viscosity at very high temperature ( $T_\infty$ ),  $E_\eta$  is the flow activation energy,  $R$  is the universal gas constant,  $k_\infty$  is the rate constant for cure reactions at  $T_\infty$  and  $E_k$  is the activation energy for the cure reaction. By using this viscosity-dependent empirical model,

Loen [19,21,22] and others [17,23] predicted the change of complex viscosity ( $\eta^*$ ) with time in different thermosets, such as vinyl ester resin [22], epoxy-phenolic [21], and other epoxy systems.

#### 4.1.3

##### Methods of Rheological Measurement

Generally, two different types of measurement are applied to determine the linear viscoelastic behavior, namely static (or equilibrium) and dynamic mechanical measurements. Static tests involve the imposition of a step change in stress and the observation of any subsequent development in time of the strain, whereas dynamic tests involve the application of a harmonically varying strain. In ordinary thermoplastic polymer systems, test conditions such as strain or frequency must be in the linear range; otherwise, the results will be dependent on the experimental details rather than on the material under test.

The thermosetting blends require very complicated restrictions, and the limitations and advantages of each type of measurement technique have been reviewed by Halley and Mackay [7]. At this point, only a brief summary is provided:

- First, as the curing kinetics is always obtained under isothermal conditions, rheological testing under other conditions is rather difficult (though some dynamic temperature tests have been conducted).
- Second, the exothermic curing reaction releases heat and alters the isothermal conditions; as a result, it is essential that the test samples have a large surface-to-volume ratio to ensure heat transfer.
- Third, the morphology transitions of thermosetting blends require low strain/stress or shear rates in order to avoid any measurement influence on the phase separation.

In the isothermal steady shear tests, the viscosity ( $\eta$ ) is measured as a function of steady shear rate ( $\dot{\gamma}$ ) over a range of curing time (conversions). Common shear rates encountered in the processing of thermosetting resins extend from  $1 \text{ s}^{-1}$  to  $10\,000 \text{ s}^{-1}$ . The isothermal dynamic frequency sweeps measure the complex viscosity ( $\eta^*$ ) as a function of the dynamic oscillation rate ( $\omega$ ) at constant temperature. In order to ensure that the curing reaction undergoes only minor changes during a round of sweep, it is necessary that the sweeps are conducted within a limited time for ordinary curing systems, or in slow-curing systems.

The complex viscosity can be related to the steady shear viscosity ( $\eta$ ) via the empirical Cox–Merz rule, which states that the shear rate-dependence of the steady-state viscosity,  $\eta(\dot{\gamma})$ , is equivalent to the frequency dependence of the complex viscosity,

$$\eta(\dot{\gamma}) = |\eta^*(\omega)|_{\omega=\dot{\gamma}} = \sqrt{[(G'/\omega)^2 + (G''/\omega)^2]}_{\omega=\dot{\gamma}} \quad (4.9)$$

where  $G'$  and  $G''$  are the storage and loss moduli, respectively.

## 4.2

### Thermosetting Blend Systems with Rubbers and Thermoplastics

Thermosetting networks tend to have a characteristic low resistance to brittle fracture, and therefore the modification of these materials with rubbers, thermoplastics, core-shell particles, block copolymers and fillers has posed a significant challenge during the past few decades. The cured modified thermosetting resins generally have two types of morphology, namely homogeneous or heterogeneous. As the homogeneous systems always show limited property improvements, most studies have been focused on heterogeneous systems.

For blends with phase separations, the modifiers are initially soluble in the mixture of prepolymers of thermosets, although several structural transitions may take place during the curing process. As polymerization occurs, the solubility of the modifiers is continuously decreased due to the unfavorable variation of the entropy of mixing from chain growth of thermosetting resins. The variation of the enthalpy of mixing from either chemical reaction or polymerization of monomers may also contribute to the decrease in solubility. At a particular conversion, the demixing of a phase that is rich in the modifiers will begin to take place.

#### 4.2.1

##### Phase Separation and Rheological Behavior of Rubber-Modified Systems

The modification of thermosetting resins by rubbers and thermoplastics was initiated by Bucknall [24–26], Inoue [27–29], Pascault and Williams [30–33], and Kyu [34,35], among others. Unlike thermoplastic blends, the complicated phase evolutions of coexisting phases of thermoplastic or rubber in a reactive thermoset precursor are changing continuously with the reaction time. Consequently, studies of the phase mechanism became the primary target for understanding the mechanical property changes that occurred in these types of material at an early stage. Certain similarities have been identified between thermoplastic blends and thermoset blends, notably that phase separation proceeds by either nucleation and growth (NG) or spinodal decomposition (SD). Depending on the composition location of blends at either meta-stable or unstable regions during the early stage of phase decomposition, thermosetting blends show a much more complicated evolution of morphology, as evidenced by experiments involving light scattering, optical microscopy (OM) and scanning electron microscopy (SEM) [28,29,34–42].

As the structure–property relationship was more involved during the early stages of these studies, rheological measurements were always applied as an auxiliary method. An example was that of Pucciariello *et al.* [43], who used a rheological method to monitor the gel time of rubber-modified epoxy resins.

Kwak *et al.* [44] used an isothermal steady shear test to monitor the copolymerization of siloxane-containing oligomers and diglycidylether of bisphenol A (DGEBA) epoxy. The gel time of the blends was obtained from values of the storage modulus ( $G'$ ) and loss modulus ( $G''$ ). Based on the concept of Eq. (4.3),

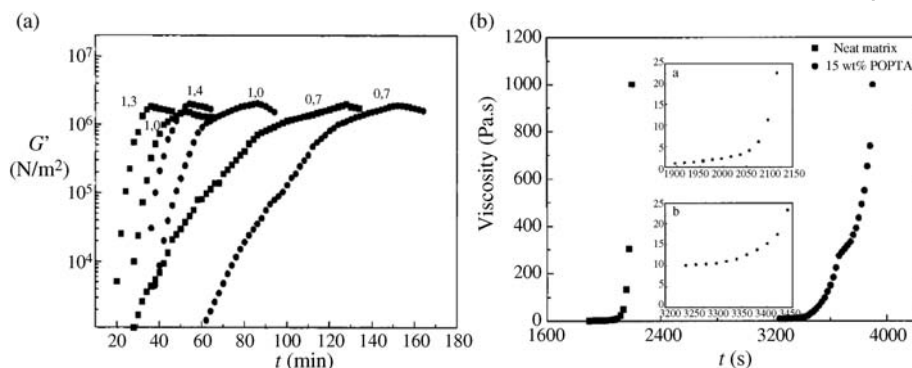


**Figure 4.2** Loss modulus, viscosity versus curing time profiles for unmodified (■) and 15 wt% POPTA-modified (●) mixtures with several stoichiometries. Reproduced with permission from Ref. [45]; © 2000, John Wiley & Sons.

the crosslinking activation energies were determined from the Arrhenius plot, based on gel times and reaction temperatures.

Mondragon *et al.* [45] were the first to conduct a systematic study of rubber-modified systems, in which a liquid elastomer poly(oxypropylentriamine) (POPTA) was used to modify a DGEBA epoxy. Based on the concept that the relative concentrations of both the epoxy monomer and the hardeners may differ from that in the initial formulation (which leads to a departure from stoichiometry), these authors studied the kinetics and rheology of systems with different ratios of epoxies to hardeners.

Figure 4.2 shows the rheological results of the dynamic loss modulus  $G''$  and viscosity of neat and 15 wt% POPTA-modified DGEBA cured with 4,4'-diamino-3,3'-dimethyl dicyclohexyl methane at several stoichiometric ratios at 80 °C. Vitrification was identified as the maximum in  $G''$  due to the rigidity of the forming network, which leveled off with increasing time. The viscosity,  $G''$ , and gel time results showed that the addition of a rubber modifier produced a clear delay in the occurrence of gelation and vitrification phenomena. In other words, the rubber POPTA showed a dilution effect only in the chemorheology of curing, and this behavior was seen to be independent of not only the matrix stoichiometry but also the molecular weight of the neat resin.

As the carboxyl-terminated copolymer of butadiene and acrylonitrile (CTBN), liquid rubber is widely used as a rubber modifier for epoxy resin. When Calabrese and Valenza [46] studied the effect of CTBN inclusion on the chemorheological behavior of an anhydride-cured epoxy system, the carboxyl-terminated groups of the CTBN rubber showed a catalytic effect on the epoxy-anhydride reaction. Consequently, at a fixed temperature the gel time was decreased in line with the increase in CTBN rubber content; in other words, the presence of a rubbery phase induced a higher rate of gel formation during the early stages of reactions, and of vitrification at a later stage. The rheological data obtained fitted well with the ordinary neat epoxy empirical chemorheological model.

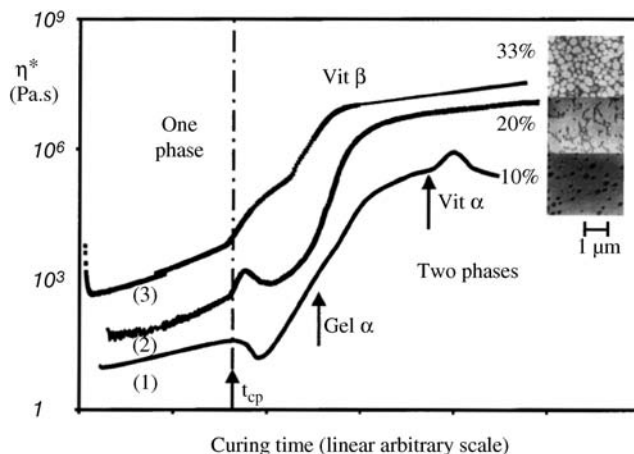


**Figure 4.3** Influence of morphology on the rheological behavior of epoxy resins with different content of thermoplastics (polyetherimide). showing the final morphologies of the cured blends. Reproduced with permission from Ref. [49]; © 1999, American Chemical Society. Transmission electron microscopy images

#### 4.2.2

##### Phase Separation and Rheological Behavior of Thermoplastic-Modified Systems

Compared to rubber, thermoplastic-modified systems show a much more complicated phase separation and structure evolution, and consequently very few studies were initially undertaken related to phase separation and rheological behavior. Examples of these studies included Pethrick *et al.* [47,48], who applied a curemeter to monitor the pot life and gel time of thermoplastic-modified epoxy systems. In 1999, Bonnet and Pascault *et al.* [49] were the first to conduct a study of the relationship between rheological behavior and thermoplastic concentration in polyetherimide-modified epoxy-amine systems. By using an isothermal steady shear test with parallel plates at low deformation (1%), these authors showed that the rheological behavior at phase separation was greatly dependent on the initial concentration of thermoplastics.

The evolution of viscosity with regards to blend composition is shown in Figure 4.3. Viscosity was shown to correspond well with the three types of typical phase structure, namely phase dispersion, bicontinuous and phase-inversion morphology in thermoplastic-modified thermoset systems. Before phase separation, the homogeneous mixture behaved as a semidilute polymer solution, and the viscosity increased in line with the poly(ether imide) concentration. However, on phase decomposition,  $\eta^*$  was shown to increase or decrease abruptly, depending on the morphology variation.

For a low-thermoplastic-concentration system with phase dispersion structure, the phase separation process was followed by a rapid decrease in viscosity, which was induced by the initially dissolved highly viscous thermoplastic component

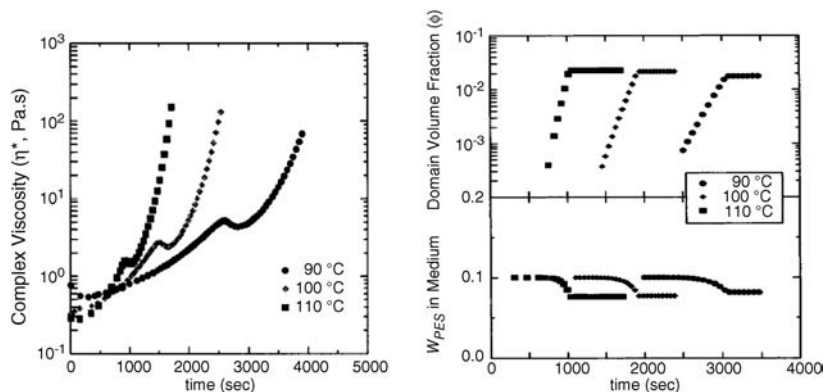


**Figure 4.4** Changes of the complex viscosity, volume fraction and weight percent of PES in the DGEBA/DDM/PES mixture with 10 wt% PES at different isothermal curing

temperatures as a function of curing time. Reproduced with permission from Ref. [50]; © 2000, American Chemical Society.

separating from the thermoset-rich matrix. In contrast, when thermoplastic concentration was high enough to ensure a continuous thermoplastic-rich phase up to the end of the phase separation process (with final phase-inversion structure), the onset of phase separation was accompanied by a gradual increase in viscosity.

Whilst the composition with a final bicontinuous phase structure showed a more complex rheological behavior, the initial increase in viscosity at the start of the phase separation process was also due to the formation of a continuous thermoplastic-rich phase structure. However, a decrease of  $\eta^*$  was observed shortly afterwards following destruction of the continuous thermoplastic-rich phase structure and the reappearance of an epoxy-rich matrix.

This type of viscosity change with curing and phase separation was also investigated by other research groups. For example, Kim *et al.* [50] studied the rheological behavior of a polyethersulfone (PES)-modified epoxy resin (diglycidyl ether of bisphenol A) cured with 4,4'-diaminodiphenylmethane at different temperatures. The system with low thermoplastic concentration and dispersion phase structure, which is always assumed to follow nucleation and growth mechanisms, had been found to follow an SD mechanism due to the appearance of periodical light-scattering profiles [29,51]; this was specially studied using a combination of light-scattering and rheological methods.

The evolution of viscosity, volume fraction and weight percent of PES during the curing process is shown in Figure 4.4. The volume fraction of PES was calculated from the measured domain size, which in turn was obtained by comparing the domain correlation lengths obtained from light-scattering studies with the scanning electron microscopy (SEM) images of fully cured samples, and the number of domains per unit volume ( $N$ ), where  $\phi = 4\pi r^3 N/3$ .

The dispersion structure of PES would apparently affect the rheological behavior of the blend due to transition from a homogeneous state to a heterogeneous state.

Consequently, two major factors affect the rheological properties of the mixture during phase separation: (i) the change of composition in the epoxy-rich matrix; and (ii) the variation of viscoelastic behavior of the phase-separated blend. The authors employed a two-phase suspension model as proposed by Graebbling and Palierne [52] to explain the effect of viscoelastic behavior on the phase-separated mixture:

$$G^*(\omega) = G_{\text{med}}^*(\omega) \frac{1 + 3\phi H(\omega)}{1 - 2\phi H(\omega)} = i\omega\eta^*(\omega) \quad (4.10)$$

where

$$H = \frac{4\left(\frac{\alpha}{r}\right)(2G_{\text{med}}^* + 5G_{\text{PES}}^*) + (G_{\text{PES}}^* - G_{\text{med}}^*)(16G_{\text{med}}^* + 19G_{\text{PES}}^*)}{4\left(\frac{\alpha}{r}\right)(G_{\text{med}}^* + G_{\text{PES}}^*) + (2G_{\text{PES}}^* + 3G_{\text{med}}^*)(16G_{\text{med}}^* + 19G_{\text{PES}}^*)}$$

where  $\omega$  is the angular frequency of oscillatory shear,  $i$  is  $\sqrt{-1}$ ,  $\phi$  is the domain volume fraction in the phase-separated mixture,  $r$  is the average domain radius, and  $G_{\text{med}}^*$  and  $G_{\text{PES}}^*$  are the complex shear modulus of the medium and PES, respectively.  $\alpha$  is the interfacial tension between the epoxy-rich matrix and the PES-rich particle, which is assumed to be independent of local shear and interfacial area change. Typical values of the interfacial tension are  $10^{-3}$  to about  $10^{-2} \text{ N m}^{-1}$  for blends of molten polymers.

To simplify, the elastic effect in the rheological behaviors of both the matrix and the domain is negated. As the  $T_g$  of PES is much higher than the experimental temperatures, and the PES viscosity is too high to measure, the viscosity ratio of the PES particle to the epoxy-rich medium ( $\eta_{\text{PES}}/\eta_{\text{med}}$ ) is large enough that the zero-shear viscosity of the mixture from Eq. (4.10) is reduced to the well-known Einstein relation:

$$\eta^* = \eta_0 \approx \eta_{\text{med}} \left(1 + \frac{5}{2}\phi\right) \quad (4.11)$$

The viscosity of the epoxy-rich medium ( $\eta_{\text{med}}$ ) can be estimated from the measured complex viscosity, and the domain volume fraction given in Figure 4.3.

The viscoelastic effect of the PES particles on phase separation was estimated with the Maxwell model:

$$G_{\text{PES}}^* = \frac{i\omega\eta_{\text{PES}}}{1 + i\omega\tau_{\text{PES}}} \quad (4.12)$$

where  $\tau_{\text{PES}}$  is the characteristic relaxation time for the PES domain and  $\omega$  is the angular frequency of oscillatory shear. Therefore, with Eqs (4.10) and (4.12), the authors calculated the viscosity change by testing the shear and interfacial tension effects on the complex viscosity with two extreme cases of oscillatory shear ( $\omega\tau_{\text{PES}} = 0$  and  $\infty$ ) and three values of interfacial tension ( $0$ ,  $10^{-3}$ , and  $1 \text{ N m}^{-1}$ ). The result showed that the viscosity profiles of the epoxy-rich medium, when calculated with different frequencies and interfacial tensions, almost overlap the profile shown in Figure 4.3. This implies that the viscoelastic effect of the PES



domain and the effects of shear and interfacial tension are almost negligible in the studied system.

Tribut *et al.* [53] further studied and modeled the rheological behavior of a polystyrene (PS)-modified DGEBA-aromatic amine system of different morphology. The model contained four contributions to the viscoelastic behavior: progressive deplastification of the polystyrene matrix involving a modification of the glass transition and thus of free volume; dilution of the network of entanglements of the matrix by the not-yet converted low-molecular-weight molecules; emulsion behavior after the separation of the epoxy-rich phase; and finally interparticular interactions being assimilated to a mechanical percolation.

In another case, Yu *et al.* [54] studied the rheological behavior of binary and ternary systems of polyethersulfone- and polyetherimide-modified epoxy systems by using an isothermal steady shear test with parallel plates. The study results showed that the molecular weight of the thermoplastics had an influence on the morphology of the modified systems, which further affected the viscosity change during curing. However, the ternary systems showed minimal differences on the viscosity-morphology relationship; in other words, the fluctuation of viscosity is derived mainly from the phase structure change.

In these studies the authors provided a good correlation of the onset of phase separation time by employing light-scattering and rheological studies. Notably, the modulus of conservation  $G'$ , the modulus of loss  $G''$ , and  $\tan \delta$  variation were seen to have a close relationship with the phase separation, gelation, and morphology change. Although a twofold crossover of  $G'$  and  $G''$  was observed in the phase inversion system, the authors did not provide any explanation.

When Cassagnau *et al.* [55] studied the effects of stoichiometry on phase separation and shear rate on the morphology in a PS-modified epoxy-amine system, the amine was shown to diffuse faster than the epoxy, which led to nonstoichiometry of the reactive functions across the sample. Yet, when the blend was polymerized under shear, the kinetic of the reaction remained unchanged, regardless the level of shear. The morphologies were significantly different, however, which highlighted the importance of the coalescence and droplet deformation phenomena. Spherical droplets were observed at a low shear rate of  $0.15 \text{ s}^{-1}$ , while elongated droplets and fibers were found at higher rates of  $1.5$  and  $15 \text{ s}^{-1}$ .

Clearly, these early rheological studies of thermoplastic-modified thermosets were based mainly on traditional phase separation theory, and were focused on phase structure-viscosity changes; indeed, most of them omitted the special effect of the thermoplastic phase on viscoelasticity and gelation. Although isothermal steady shear sweeps are widely applied, a lack of dynamic frequency sweeps the measurements.

#### 4.2.3

##### Viscoelastic Properties of the Blends

As the morphologic evolution of thermoplastic-modified thermosetting cannot be explained using classic phase-separation theory, Yu, Gan and Li *et al.* [56–61]

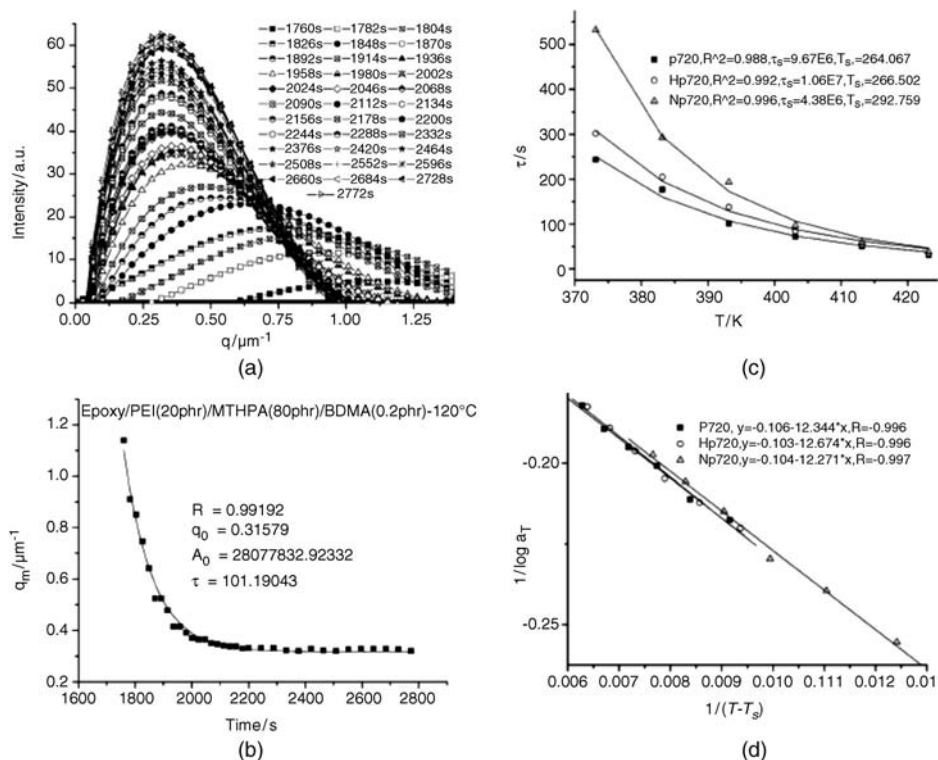


**Figure 4.5** Light-scattering results of viscoelastic phase separation of polyetherimide modified epoxy-anhydride systems. (a) Intensity versus  $q_m$  at different times; (b) Exponential decay of  $q_m$  versus time; (c) Relaxation time

of phase separation plotted by fitting WLF equation; (d) Linear fitting of shift factor for systems with different amounts of accelerators. Reproduced with permission from Ref. [56]; © 2003, American Chemical Society.

introduced the concept of a viscoelastic phase separation theory [62–64] into thermosetting systems, and undertook considerable research in this area. In this theory, there exists a dynamic asymmetry between the two components that is induced by a large difference either in size or  $T_g$ . Even the minority phase transiently forms a continuous structure, and rather than interface tension a viscoelastic relaxation of the slow part (thermoplastics) dominates the phase structure evolution. Results of light-scattering studies revealed that the WLF equation was well used to describe the phase separation behavior (as shown in Figure 4.5).

Therefore, relaxation of the thermoplastic plays a very important role as long as the thermosetting phase has unblocked its chain mobility. Yu *et al.* [59] examined the viscoelastic phase separation of a PES-modified DGEBA-anhydride system by comparative use of rheological methods, light scattering, and differential scanning calorimetry (DSC). In this blend, the onset and offset of phase separation occurred much earlier than gelation, where the curing conversion was between 0.09 and 0.35 depending on the curing temperature. Phase separation was seen to be

controlled by the viscoelastic relaxation of the PES chain, much like demixing in a polymer solution system.

Correspondingly, a quick blocking of phase separation by chain-polymerization would result in a finer phase structure at an earlier stage. By using imidazole as the curing agent, an increase in the curing temperature led to a rapid increase in curing rate while the viscosity was enlarged sharply at a low conversion of 6~8% [58]. Thus, the relaxation time for a thermoplastic molecule in a viscous medium is directly proportional to the viscosity, according to Debye:

$$\tau = \frac{4\pi\alpha^3\eta}{kT} \quad (4.13)$$

where  $\eta$  is the viscosity of the medium,  $\alpha$  is the molecular radius,  $k$  is Boltzmann's constant, and  $T$  is the absolute curing temperature. Based on this expression, the quick increase in viscosity causes a major enlargement of the characteristic relaxation time of chain disentanglement of thermoplastics during the early stages of phase separation. As a result, the morphology would not appear to change from the early stage of phase separation to the end of the process.

In a polyesterimide (PEtI)-modified DGEBA-anhydride system, where the phase separation process evolved much earlier than the gel time, by considering the viscoelastic relaxation of the phase-separation behavior Yu *et al.* [65] were the first to observe an exponential growth of complex viscosity during phase separation (as shown in Figure 4.6).

$$\eta^*(t) = \eta_0^* + A_0 \exp(t/\tau_\eta) \quad (4.14)$$

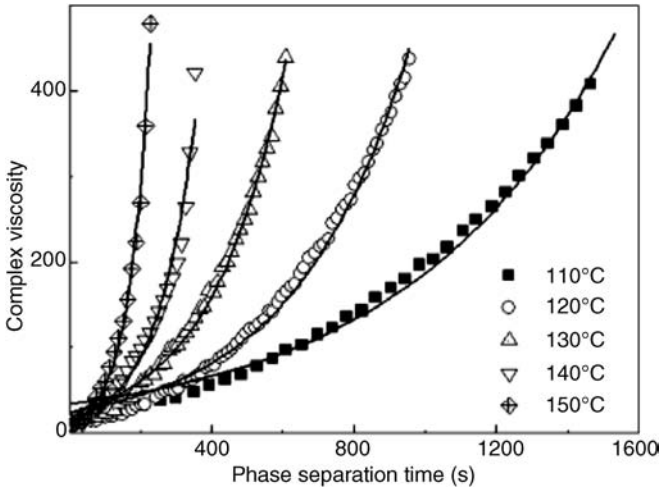


**Figure 4.6** Complex viscosity evolution during phase separation in 20 phr PEtI- modified DGEBA-anhydride systems cured at different temperatures. Dots correspond to the

experimental data, and lines correspond to exponential growth simulation. Reproduced with permission from Ref. [65]; © 2006, Springer.

where  $A_0$  is the magnifier, and  $\tau_\eta$  is the relaxation time. Much like the relaxation time from light-scattering of light intensity and  $q_m$ , the rheological results can also be well fitted to the WLF equation.

In a system with a phase inversion structure, the complex viscosity of a blend system can be described by the Einstein equation (Eq. (4.11)). During viscoelastic phase separation, in which the interfacial tension plays a minor effect, the change in curing conversion is quite low and the viscosity difference between thermoplastics-rich matrix and dispersed thermoset-rich (low conversion and molecular weight) is very large and increases with the phase-separation process. When the viscosity of the dispersed thermoset-rich phase was neglected, the viscosity of the blend can be simplified as that of the thermoplastic-rich phase.

A thermoplastics-rich phase could be taken as a polymer solution and its viscosity determined by the free volume; this scheme was employed by Kelley and Bueche [66] to predict the viscosity of a concentrated (entangled) polymer solution, using the neat polymer (thermoplastics) as the reference. Then

$$\frac{\eta}{\eta_p} = \phi_p^4 \exp \left( \frac{1}{\phi_p + f_p + \phi_L f_L} - \frac{1}{f_p} \right) \quad (4.15)$$

where the free volumes of the polymer and liquid (thermosets) are  $f_p = 0.025 + 4.8 \times 10^{-4}(T - T_{gp})$  and  $F_L = 0.025 + \alpha_L(T - T_{gL})$ , respectively.  $\alpha_L$  is the difference between the expansion coefficient of the liquid above and that of below the  $T_g$ . The  $T_g$ -values of the polymer and the solvent are  $T_{gp}$  and  $T_{gL}$ , respectively. By substituting an exponent decay of phase separation and concentration into Eq. (4.15), it is possible to obtain the exponent growth of viscosity as  $\eta \propto e^{t/\tau}$ . Thus, the viscosity would be related to the relaxation time  $\tau$ ; that is, the diffusion of epoxy monomers/growing chains from thermoplastic-rich would result in an exponent decay of thermoplastic concentration during phase separation, which give an exponent growth of complex viscosity.

While examining other thermoplastic-modified epoxy systems (ABS-modified DBEBA/DDS system), Jyotishkumar and Thomas *et al.* [67] recently found that this type of exponential growth of viscosity has connections with the thermoplastic content. By comparing the ABS content from 3.6% to 12.9%, the reference relaxation time  $\tau_s$  values obtained from the stimulation of WLF equation were found to increases with the ABS content. It is believed that a lower viscosity of the epoxy/DDS in a small content of the ABS-modified systems would favor the polymer chains flowing.

The effect of the molecular weight of the thermoplastic on viscoelastic phase separation and rheological behavior was also studied in an epoxy/cyanate ester resin modified with different amounts of PES of three different molecular weights [68]. The results showed that the character relaxation time  $\tau_\eta$  of viscosity increases quickly with PES concentration (same molecular weight), whereas for the same content of PES,  $\tau_\eta$  first increases when the PES molecular weight is at a lower range, but then levels at higher molecular weight values. It was further shown

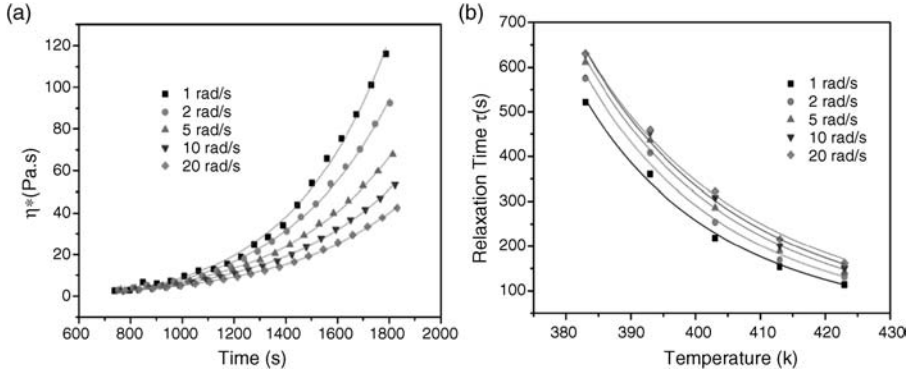


**Figure 4.7** (a)  $\eta^*$  evolution at 120 °C during a phase separation process in a 20 wt% PES-modified epoxy system at different frequencies. Symbols correspond to the experimental data, and lines correspond to results simulated by Eq. (4.14); (b) WLF fitting of relaxation time  $\tau_\eta$

versus temperature at different frequencies.

Symbols correspond to experimental data, and lines correspond to results simulated by WLF equation. Reproduced with permission from Ref. [69]; © 2008, American Chemical Society.

that a higher viscosity of the blends, as the result of large concentrations of thermoplastics, would hinder the viscoelastic phase separation process.

Unlike previous steady shear tests, Yu *et al.* [69] conducted a dynamic multifrequency isothermal rheological study using a PES-modified DGEBA-anhydride system with different PES molecular weights. At the same concentration of 20% PES, the relaxation time  $\tau_\eta$  obtained by exponential growth fitting decreased with the increase in PES molecular weight, at the same curing temperature and oscillatory shear frequency. The reference temperature ( $T_s$ ) values obtained from the fitting result of the WLF equation was seen to increase in line with the PES molecular weight.

The exponential growth in viscosity was shown to depend strictly on frequency. The data in Figure 4.7 show that the non-Newtonian behavior and exponential growth of complex viscosity at all frequencies were maintained in all 20 wt% systems with various molecular weights of PES (one type of PES is shown as an example). The relaxation times obtained from the viscosity exponential growth fitted very well to the WLF equation, for all frequencies.

The reference relaxation times  $\tau_s$  of the same blend, obtained from simulation of the WLF equation, were increased with frequency. Taking into consideration the frequency dependence of molecular motion

$$\log \omega = a - \frac{b}{\tau} \quad (4.16)$$

where  $\omega$  is the test frequency,  $\tau$  is the characteristic relaxation time from the simulation with WLF equation, and  $a$  and  $b$  are parameters, the authors were able to linear-fit  $\tau_s$  to the test frequency and obtain a correlation coefficient of  $-0.996$ . In other words, at a moderate frequency range, the phase separation process shows a

linear viscoelastic response due to a negligible change in the viscosity of the thermosetting-rich phase during phase decomposition.

#### 4.2.4

##### Gelation Behaviors of the Blends

From the steady shear sweeps, the gel time of blends from epoxy crosslinking was identified as a crossover of either  $G'$  and  $G''$ , or the maximum peak in  $\tan\delta$ ; Jyotishkumar *et al.* [67] calculated the apparent activation energy ( $E_a$ ) of gelation based on Eq. (4.3). The  $E_a$  values of neat epoxy and thermoplastic-modified systems were all close to  $65 \text{ kJ mol}^{-1}$ , which was quite similar to that of ordinary epoxy resin and rubber-modified systems. Clearly, in these systems the phase separation had been completed before gelation of the epoxy resin, and so had a limited effect on the chain mobility of epoxy during gelation.

Nonetheless, Yu *et al.* [70] noted that three types of phase separation behavior could be identified related to gelation, namely the onset and offset of phase separation occurring far before gelation, occurring close to gelation, and phase separation being blocked by gelation. At similar volume fractions of thermoplastics, the former type had the lowest continuous thermoplastics-rich phase structure, the latter type had the largest, and both types may have two maximum peaks in  $\tan\delta$ .

Using a combination of light-scattering, OM, DSC and dynamic shear sweeps, Yu *et al.* [69–74] identified two types of gelation among thermoplastics-modified thermosetting systems. The first of these corresponded to the end of phase separation, and the second to the chemical crosslinking of thermosetting resins.

As the first gelation may relate to physical gels, the critical gel theory proposed by Winter and Chambon [75] was reintroduced to explain such double-gelation behavior. At the gel point, the stress relaxation behavior of the network follows a power law [76]:

$$G(t) = St^{-n} \quad (4.17)$$

where  $S$ , the strength of the gel, is related to the mobility of the crosslinked chain segments, and depends on the flexibility of the molecular chains and the crosslinking density at gel point. The relaxation exponent  $n$  (physically restricted for  $0 < n < 1$ ) is a viscoelastic parameter that is related to the geometry of clusters existing at the gel point. By studying the flexibility and viscoelasticity of the gel, it is possible to obtain a better understanding of the mechanical property of the resin material.

From Eq. (4.17), the frequency dependence of the dynamic shear modulus at gel point was deduced as [77]:

$$G'(\omega) = G''(\omega)/\tan(n\pi/2) = \Gamma(1-n)\cos(n\pi/2)S\omega^n \quad (4.18)$$

Thus, the gel point can only be accurately determined under special conditions, using the crossover point of  $G'$  and  $G''$ . These conditions are that stress relaxation in the gelation follows a power law, and the exponent  $n$  must be exactly 0.5. For most network systems, however, although stress relaxation at gel point also

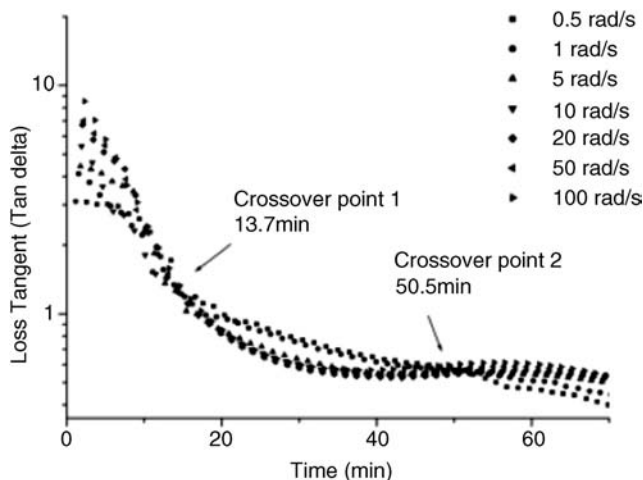


**Figure 4.8** Multifrequency shear test of  $\tan\delta$  versus curing time for a PES-modified bismaleimide resin at 165 °C. Reproduced with permission from Ref. [71]; © 2006, John Wiley & Sons, Inc..

follows a power law, the relaxation exponent  $n$  is not 0.5 and the gel point clearly does not coincide with the  $G'$  and  $G''$  crossover in such cases. Therefore, the general definition of the gel point is the time when the loss tangent  $\tan\delta$  becomes independent of frequency because:

$$\tan\delta = G''/G' = \tan(n\pi/2) \quad (4.19)$$

Figure 4.8 shows a plot of double  $\tan\delta$  versus curing time during the multifrequency shear testing of a PES-modified bismaleimide resin. The second gel point – the chemical crosslinking point – was fitted by the gel time versus temperatures, as in Eq. (4.3), to calculate the activation energy. All had values of about 95 kJ mol<sup>-1</sup> [71], which is typical for a bismaleimide resin.

When analyzing the two gelations, the relaxation exponent  $n$  is determined from the slope when plotting  $\log G'$  and  $\log G''$  versus  $\log\omega$ ; the gel strength  $S$  can then be calculated from the interception of  $\log G'$  and  $\log G''$  versus  $\log\omega$ , according to Eq. (4.18). The values of  $n$  are slightly decreased with the increase in PES content, but are located in the range of 0.62–0.68 for first gel and 0.30–0.42 for second gel. A reduction of the relaxation exponent with increasing polymer content in the semidilute regime was believed due to an increased entanglement density. The gel strength  $S$  was seen to increase with PES content for both the first and second structural transition, which implies a reduction in chain mobility with high PES concentrations.

The effect of thermoplastic molecular weight and curing rate on gelation behavior has also been studied [70]. By using modified DGEBA-anhydride systems with three different molecular weight-types of PES (20 wt%) and different amounts of

amine accelerator, the relaxation exponent  $n$  was found to be increased, while the gel strength  $S$  decreased in line with the increase in PES molecular weight, no matter what amount of accelerator had been added.

As the initial morphology during phase separation tends to be a phase-inversion structure in dynamic asymmetry systems [63], a faster phase separation in high-molecular-weight PES systems would result in a greater elastic deformation of the PES-rich phase. Thus, with the same PES content, PES-continuous structures are more easily obtained for higher-molecular-weight PES systems, due to the greater difference in both molecular weight and chain mobility between the thermoplastics phase and the slightly cured thermoset phase. At the same time, a faster phase separation and a larger elastic deformation in the higher-molecular-weight PES systems would also result in a sharper increase in blend viscosity. This could be explained by the greater sensitivity of higher-molecular-weight PES to the solution concentration and the curing of epoxy.

Therefore, in the case of higher-molecular-weight PES systems, a quicker structural transition would result in a PES-rich gel with a lower molecular weight of epoxy particles and a smaller cluster size. This, in turn, would lead to a decrease in gel strength and an increase of the relaxation exponent.

The cure rate has a relatively small effect on gelation behavior, as relaxation exponents at the two gel points will decrease slightly with an increase of the cure rate. The physical gel strength is known to vary depending on the PES system present, and the chemical gel strength is increased remarkably as a higher degree of the crosslinking is achieved from the amine-catalyzed ring-opening polymerization of epoxy and anhydride.

### 4.3

#### Thermosetting Systems with Nanostructures

The addition of nanostructured modifiers provides thermosets with special mechanical properties or functionality. Among such modifiers, the two types most widely used are block copolymers and nanoparticles (or fillers).

Block copolymers have long been applied to modify thermosets, since the first reports made by Bates [78]. The rheology of the order–disorder transition of diblock copolymers in epoxy monomers was first studied by Fine *et al.* [79], who suggested that a solid-like to a liquid-like transition would correspond to such a structural transition due to the solubility changes that occur around the transition. Subsequently, Serrano *et al.* [80] examined the rheological behavior of an epoxidized styrene-butadiene linear diblock copolymer-modified epoxy with nanostructures. An increase in the magnitude of both the viscosity and the moduli was detected for the block copolymer-modified blends just before gelation, associated with the reaction-induced microphase separation (RIPS).

Nanoparticle-modified thermosets are known to differ greatly from neat thermosetting resins. With the effects of fillers on the chemorheology of thermosetting resins having been studied for decades [7], rheological models are today basically



similar to neat thermosets (as introduced in Section 4.1.2), based on the WLF equation or power law [81]. In fact, the early studies on nanoparticles (such as carbon black and silica) suggested that the elastic modulus of a resin could be expressed in terms of the filler concentration and the modulus of the matrix, and that the gel time would be reduced as the filler concentration increased [82]. Alternatively, the filler can affect the reaction kinetics; carbon-black fillers have long been known to increase the reaction rate via kinetic rate constants, while silica fillers affect reaction rates through activation energies [83].

One of most important properties of nanoparticle-filled systems is that interconnected aggregates of nanoparticles at high concentrations form a three-dimensional network of flocs that extends throughout the volume of the suspension as a “physical gel” [84]. When large-amplitude oscillatory preshear is applied to these systems, the network linkages are disrupted and this results in the formation of isolated flocs. Restoration of the network after preshear has been investigated by applying small-amplitude oscillations to observe the development of an elastic modulus ( $G'$ ) with time.

Highly anisotropic nanometric fillers such as layered silicates (e.g., montmorillonite; MMT) can greatly improve the thermomechanical and barrier properties of thermosets, if the silicate layers are individually dispersed (exfoliated) within the polymer matrix. The rheology of epoxy silicate suspensions has been shown to depend on the amount of silicate exposed to the polymer, and this is influenced by silicate dispersion, silicate content, as well as the physico-chemical interactions between the monomer and the silicate surface [85]. If the silicate concentration is kept constant, the primary factor that determines the viscosity of an epoxy prepolymer/layered silicate will be the silicate delamination, and therefore the rheological properties will be related to the distortion or deformation of the nanodispersions. Moraru [86] noted that the suspensions which showed the highest yield stress and moduli were those which demonstrated the worst dispersion state at the nanometric scale. In contrast, the gel strength increases gradually with structure changes, which is linked to the dispersion state, changing from a well-dispersed state to a flocculated state and to the aggregated state.

Solar *et al.* [87] applied oscillatory measurements to study the durability of nanodispersions in a DGEBA epoxy resin with an organophilic MMT (Nanofil 919) in the presence of vibration or external stress. The dependence of rheological properties on the intercalated/exfoliated structures and the surface characteristics between the polymer chains and clays were then monitored. An increase in both the  $G'$  and  $G''$  moduli was detected as the concentration of nanoclay was increased. A transition from a liquid-like behavior ( $G'' > G'$  at low temperatures) to a solid-like behavior ( $G' > G''$  at higher temperatures) was also observed, due to the formation of a percolated structure of interconnected tactoids through hydrophobic interactions (as shown in Figure 4.9). This transition was seen to shift to a lower temperature as the nanoparticle content was increased.

Chen *et al.* [88] studied the interlayer expansion mechanism of MMT in epoxy resins by using time-resolved, high-temperature X-ray diffraction (XRD), DSC and isothermal rheological analyses, and found that the interlayer expansion

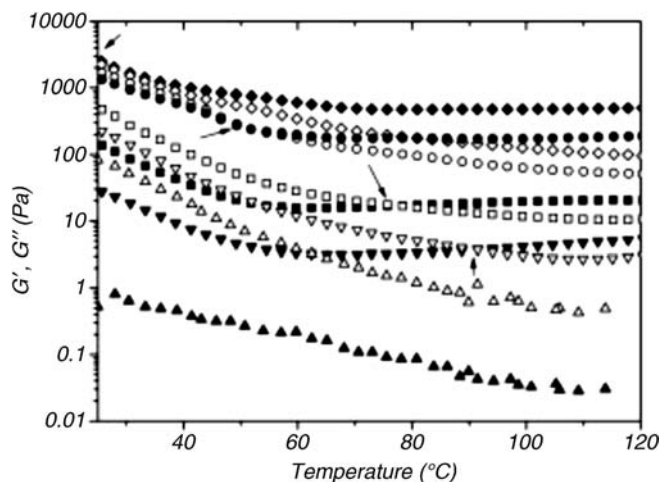


**Figure 4.9** Temperature-dependence of  $G'$  (filled symbols) and  $G''$  (empty symbols) at  $10 \text{ rad s}^{-1}$  for epoxy/Nanofil dispersions at different clay loadings: 0 per 100 parts of resin (phr) ( $\blacktriangle$ ), 1 phr ( $\blacktriangledown$ ), 2 phr ( $\blacksquare$ ), 5 phr ( $\blacklozenge$ ), and 7 phr ( $\diamond$ ). Reproduced with permission from Ref. [87]; © 2008, John Wiley & Sons, Inc.

mechanism could be separated into three stages. The chemorheology of MMT-modified epoxy, compared to the XRD data, is shown in Figure 4.10. After an initial interlayer expansion induced by intragallery polymerization, the second interlayer expansion stage was accompanied by a rapid increase in the storage modulus. The rate of interlayer expansion decreased as the storage modulus

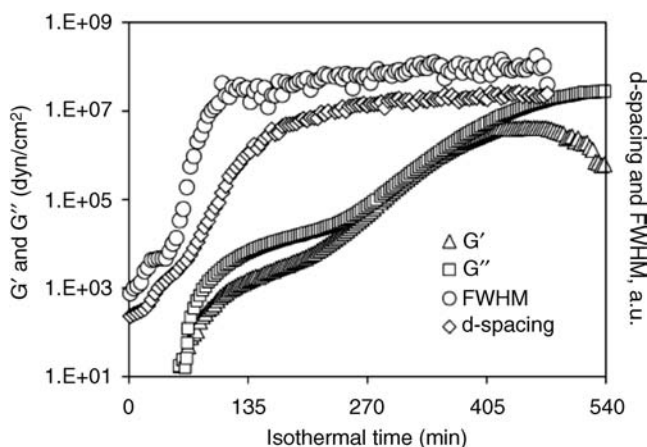


**Figure 4.10** Isothermal rheological study of 10 wt% MMT-modified epoxy resins. Changes in  $d_{001}$ , full-width half-maximum (FWHM) of the primary diffraction peak, plotted for comparison. Reproduced with permission from Ref. [88]; © 2002, Elsevier.

began to reach its first plateau between  $1 \times 10^3$  and  $1 \times 10^5 \text{ dyn cm}^{-2}$ , which was most likely due to the onset of extragallery gelation. As the curing reaction proceeded, the storage modulus began to increase rapidly again and approached a second plateau ( $1 \times 10^7 \text{ dyn cm}^{-2}$ ) due to vitrification of the polymer matrix. The interlayer spacing stopped expanding during this process, possibly when the modulus of the extragallery polymer became equal to or exceeded the modulus of the intragallery polymer.

When Dean *et al.* [89] studied the chemorheology of MMT/epoxy nanocomposites by performing isothermal steady shear sweeps, the intergallery diffusion before curing was found to be essential for exfoliation, while the gel time was shortened and the viscosity was increased in line with the MMT content. The activation energy obtained by plotting the logarithm of the gel time versus  $1/T$  (Eq. (4.3)) for the neat resin and nanocomposite showed that the activation energy associated with interlayer expansion was less, and could in fact be a necessary requirement for obtaining exfoliated samples.

The chemorheology of other nanofillers such as sepiolite [90] and nanofibers [91], when used to modify epoxy systems, was also studied, and all showed (more or less) a similarity to that of the MMT-modified systems.

Recently, numerous research groups have shown that nanofillers can have dramatic effects on the morphology and properties of either rubber- or thermoplastic-modified epoxy systems [92–95]. Although such rheology studies are still in progress, it is expected that any differences in viscoelastic behavior would further influence the phase separation process, and so have serious effects on the rheological behavior.

#### 4.4

#### Conclusions

The rheological properties of polymer blends – and especially of thermosetting polymer blends – share a close relationship to the morphology and reactions involved. Moreover, these properties can cause changes in shear or strain conditions that may lead to dramatic variations in the phase structure and other properties of polymer blends. The time-temperature superposition principle (WLF-type equations) and power laws have been widely applied to the linear viscoelastic behavior of both neat polymers and blends, despite the fact that they may reflect different types of structure transitions for either thermoplastic or thermosetting resins.

#### References

- 1 Dubin, P., Bock, J., and Thies, C. (1994) *Macromolecular Complexes in Chemistry and Biology*, Springer-Verlag Berlin, New York.
- 2 Ferry, J.D. (1980) *Viscoelastic Properties of Polymers*, 3rd edn, John Wiley & Sons Inc., New York.

- 3 Han, C.D. (1976) *Rheology in Polymer Processing*, Academic Press, New York.
- 4 Nielsen, L.E. (1977) *Polymer Rheology*, Marcel Dekker, New York.
- 5 Shenoy, A.V. and Saini, D.R. (1996) *Thermoplastic Melt Rheology and Processing*, Marcel Dekker, New York.
- 6 Han, C.D. (2007) *Rheology and Processing of Polymeric Materials*, Oxford University Press, New York.
- 7 Halley, P.J. and Mackay, M.E. (1996) Chemorheology of thermosets – An overview. *Polym. Eng. Sci.*, **36** (5), 593–609.
- 8 Babayevs, P.G. and Gillham, J.K. (1973) Epoxy thermosetting systems – dynamic mechanical analysis of reactions of aromatic diamines with diglycidyl ether of bisphenol-A. *J. Appl. Polym. Sci.*, **17** (7), 2067–2088.
- 9 Gillham, J.K., Benci, J.A., and Noshay, A. (1974) Isothermal transitions of a thermosetting system. *J. Polym. Sci. Polym. Symp.*, **46** (1), 279–289.
- 10 Gillham, J.K., Benci, J.A., and Noshay, A. (1974) Isothermal transitions of a thermosetting system. *J. Appl. Polym. Sci.*, **18** (4), 951–961.
- 11 Buchman, A. and Katz, D. (1979) Chemorheology of crosslinked epoxy-resins subjected to large strains. *Polym. Eng. Sci.*, **19** (13), 923–928.
- 12 Chang, D.H. and Lem, K.W. (1983) Chemorheology of thermosetting resins .1. The chemorheology and curing kinetics of unsaturated polyester resin. *J. Appl. Polym. Sci.*, **28** (10), 3155–3183.
- 13 Lem, K.W. and Chang, D.H. (1983) Chemorheology of thermosetting resins .2. Effect of particulates on the chemorheology and curing kinetics of unsaturated polyester resin. *J. Appl. Polym. Sci.*, **28** (10), 3185–3206.
- 14 Lem, K.W. and Chang, D.H. (1983) Chemorheology of thermosetting resins .3. effect of low-profile additive on the chemorheology and curing kinetics of unsaturated polyester resin. *J. Appl. Polym. Sci.*, **28** (10), 3207–3225.
- 15 Tajima, Y.A. and Crozier, D. (1983) Thermokinetic modeling of an epoxy-resin. 1. Chemoviscosity. *Polym. Eng. Sci.*, **23** (4), 186–190.
- 16 Tajima, Y.A. and Crozier, D.G. (1986) Chemorheology of an amine-cured epoxy-resin. *Polym. Eng. Sci.*, **26** (6), 427–431.
- 17 Hsieh, T.H., Wang, T.L., Ho, K.S., and Wang, Y.Z. (2000) Chemorheological analysis of an epoxy-novolac molding compound. *Polym. Eng. Sci.*, **40** (2), 418–429.
- 18 Aronhime, M.T. and Gillham, J.K. (1986) Time-temperature-transformation (TTT) cure diagram of thermosetting polymeric systems. *Adv. Polym. Sci.*, **78**, 83–113.
- 19 Laza, J.M., Julian, C.A., Larrauri, E., Rodriguez, M., and Leon, L.M. (1999) Thermal scanning rheometer analysis of curing kinetic of an epoxy resin: 2. An amine as curing agent. *Polymer*, **40** (1), 35–45.
- 20 Roller, M.B. (1986) Rheology of curing thermosets: a review. *Polym. Eng. Sci.*, **26** (6), 432–440.
- 21 Laza, J.M., Vilas, J.L., Mijangos, F., Rodriguez, M., and Leon, L.M. (2005) Analysis of the crosslinking process of epoxy-phenolic mixtures by thermal scanning rheometry. *J. Appl. Polym. Sci.*, **98** (2), 818–824.
- 22 Martin, J.S., Laza, J.M., Morras, M.L., Rodriguez, M., and Leon, L.M. (2000) Study of the curing process of a vinyl ester resin by means of TSR and DMTA. *Polymer*, **41** (11), 4203–4211.
- 23 Theriault, R.P., Osswald, T.A., and Castro, J.M. (1999) A numerical model of the viscosity of an epoxy prepreg resin system. *Polym. Compos.*, **20** (5), 628–633.
- 24 Bucknall, C.B. and Partridge, I.K. (1983) Phase-separation in epoxy-resins containing polyethersulfone. *Polymer*, **24** (5), 639–644.
- 25 Bucknall, C.B., Partridge, I.K., and Phillips, M.J. (1991) Morphology and properties of thermoset blends made from unsaturated polyester resin, poly(vinyl acetate) and styrene. *Polymer*, **32** (5), 786–790.
- 26 Maistros, G.M., Block, H., Bucknall, C.B., and Partridge, I.K. (1992) Dielectric monitoring of phase-separation during cure of blends of epoxy-resin with carboxyl-terminated poly(butadiene-co-acrylonitrile). *Polymer*, **33** (21), 4470–4478.
- 27 Yamanaka, K., Takagi, Y., and Inoue, T. (1989) Reaction-induced phase-separation

- in rubber-modified epoxy-resins. *Polymer*, **30** (10), 1839–1884.
- 28 Yamanaka, K. and Inoue, T. (1990) Phase-separation mechanism of rubber-modified epoxy. *J. Mater. Sci.*, **25** (1A), 241–245.
  - 29 Inoue, T. (1995) Reaction-induced phase-decomposition in polymer blends. *Prog. Polym. Sci.*, **20** (1), 119–153.
  - 30 Moschiar, S.M., Riccardi, C.C., Williams, R.J.J., Verchere, D., Sautereau, H., and Pascault, J.P. (1991) Rubber-modified epoxies .3. Analysis of experimental trends through a phase-separation model. *J. Appl. Polym. Sci.*, **42** (3), 717–735.
  - 31 Verchere, D., Pascault, J.P., Sautereau, H., Moschiar, S.M., Riccardi, C.C., and Williams, R.J.J. (1991) Rubber-modified epoxies .2. Influence of the cure schedule and rubber concentration on the generated morphology. *J. Appl. Polym. Sci.*, **42** (3), 701–716.
  - 32 Grillet, A.C., Galy, J., and Pascault, J.P. (1992) Influence of a 2-step process and of different cure schedules on the generated morphology of a rubber-modified epoxy system based on aromatic diamines. *Polymer*, **33** (1), 34–43.
  - 33 Riccardi, C.C. and Williams, R.J.J. (1992) Influence of prepolymerization on gelation of diepoxide diamine systems. *Polymer*, **33** (1), 44–51.
  - 34 Lee, H.S. and Kyu, T. (1990) Phase-separation dynamics of rubber epoxy mixtures. *Macromolecules*, **23** (2), 459–464.
  - 35 Kim, J.Y., Cho, C.H., Palffymuhoray, P., Mustafa, M., and Kyu, T. (1993) Polymerization-induced phase-separation in a liquid-crystal-polymer mixture. *Phys. Rev. Lett.*, **71** (14), 2232–2235.
  - 36 Guo, Q.P., Peng, X.S., and Wang, Z.J. (1991) The miscibility and morphology of epoxy-resin poly(ethylene oxide) blends. *Polymer*, **32** (1), 53–57.
  - 37 Chen, J.P. and Lee, Y.D. (1995) A real-time study of the phase-separation process during polymerization of rubber-modified epoxy. *Polymer*, **36** (1), 55–65.
  - 38 Pascault, J.P. (1995) Rubber-modified and thermoplastic-modified polymer networks – phase-separation process induced by polymerization and polycondensation. *Macromol. Symp.*, **93**, 43–51.
  - 39 Kyu, T. and Lee, J.H. (1996) Nucleation initiated spinodal decomposition in a polymerizing system. *Phys. Rev. Lett.*, **76** (20), 3746–3749.
  - 40 Chan, P.K. and Rey, A.D. (1997) Polymerization-induced phase separation. 2. Morphological analysis. *Macromolecules*, **30** (7), 2135–2143.
  - 41 Bagheri, R., Marouf, B.T., and Pearson, R.A. (2009) Rubber-toughened epoxies: A critical review. *Polym. Rev.*, **49** (3), 201–225.
  - 42 Girard-Reydet, E., Sautereau, H., Pascault, J.P., Keates, P., Navard, P., Thollet, G., and Vigier, G. (1998) Reaction-induced phase separation mechanisms in modified thermosets. *Polymer*, **39** (11), 2269–2279.
  - 43 Pucciariello, R., Villani, V., Bianchi, N., and Braglia, R. (1991) Relationship between gelation and morphology of rubber-modified epoxy-resins. *Polym. Int.*, **26** (2), 69–73.
  - 44 Kwak, G.H., Park, J.H., Kim, K.S., and Park, S.J. (1999) Rheological properties and cure kinetics of siloxane-modified epoxy resins. *Polym.-Korea*, **23** (3), 427–433.
  - 45 Aizpurua, B., Franco, M., Corcuera, M.A., Riccardi, C.C., and Mondragon, I. (2000) Chemorheology and ultimate behavior of epoxy-amine mixtures modified with a liquid oligomer. *J. Appl. Polym. Sci.*, **76** (8), 1269–1279.
  - 46 Calabrese, L. and Valenza, A. (2003) Effect of CTBN rubber inclusions on the curing kinetic of DGEBA-DGEBF epoxy resin. *Eur. Polym. J.*, **39** (7), 1355–1363.
  - 47 Mackinnon, A.J., Jenkins, S.D., McGrail, P.T., and Pethrick, R.A. (1992) A dielectric, mechanical, rheological, and electron-microscopy study of cure and properties of a thermoplastic-modified epoxy-resin. *Macromolecules*, **25** (13), 3492–3499.
  - 48 Mackinnon, A.J., Jenkins, S.D., McGrail, P.T., and Pethrick, R.A. (1993) Dielectric, mechanical and rheological studies of phase-separation and cure of a thermoplastic modified epoxy-resin - incorporation of reactively terminated polysulfones. *Polymer*, **34** (15), 3252–3263.
  - 49 Bonnet, A., Pascault, J.P., Sautereau, H., and Camberlin, Y. (1999) Epoxy-diamine thermoset/thermoplastic blends. 2. Rheological behavior before and after phase

- separation. *Macromolecules*, **32** (25), 8524–8530.
- 50 Kim, H. and Char, K. (2000) Effect of phase separation on rheological properties during the isothermal curing of epoxy toughened with thermoplastic polymer. *Ind. Eng. Chem. Res.*, **39** (4), 955–959.
  - 51 Cahn, J.W. (1965) Phase separation by spinodal decomposition in isotropic systems. *J. Chem. Phys.*, **42** (1), 93–98.
  - 52 Graebbling, D., Muller, R., and Paliarne, J.F. (1993) Linear viscoelastic behavior of some incompatible polymer blends in the melt. Interpretation of data with a model of emulsion of viscoelastic liquids. *Macromolecules*, **26** (2), 320–329.
  - 53 Tribut, L., Fenouillot, F., Carrot, C., and Pascault, J.P. (2007) Rheological behavior of thermoset/thermoplastic blends during isothermal curing: Experiments and modeling. *Polymer*, **48** (22), 6639–6647.
  - 54 Yu, Y.F., Zhang, Z.C., Gan, W.J., Wang, M.H., and Li, S.J. (2003) Effect of polyethersulfone on the mechanical and rheological properties of polyetherimide-modified epoxy systems. *Ind. Eng. Chem. Res.*, **42** (14), 3250–3256.
  - 55 Cassagnau, P. and Fenouillot, F. (2004) Rheological study of mixing in molten polymers: 2-mixing of reactive systems. *Polymer*, **45** (23), 8031–8040.
  - 56 Gan, W.J., Yu, Y.F., Wang, M.H., Tao, Q.S., and Li, S.J. (2003) Viscoelastic effects on the phase separation in thermoplastics-modified epoxy resin. *Macromolecules*, **36** (20), 7746–7751.
  - 57 Tao, Q.S., Gan, W.J., Yu, Y.F., Wang, M.H., Tang, X.L., and Li, S.J. (2004) Viscoelastic effects on the phase separation in thermoplastics modified cyanate ester resin. *Polymer*, **45** (10), 3505–3510.
  - 58 Wang, M.H., Yu, Y.F., Wu, X.G., and Li, S.J. (2004) Polymerization induced phase separation in poly(ether imide)-modified epoxy resin cured with imidazole. *Polymer*, **45** (4), 1253–1259.
  - 59 Yu, Y.F., Wang, M.H., Gan, W.J., Tao, Q.S., and Li, S.J. (2004) Polymerization-induced viscoelastic phase separation in polyethersulfone-modified epoxy systems. *J. Phys. Chem. B*, **108** (20), 6208–6215.
  - 60 Liu, X., Yu, Y.F., and Li, S.J. (2006) Viscoelastic phase separation in polyethersulfone modified bismaleimide resin. *Eur. Polym. J.*, **42** (4), 835–842.
  - 61 Zhan, G.Z., Yu, Y.F., Tang, X.L., Tao, Q.S., and Li, S.J. (2006) Further study of the viscoelastic phase separation of cyanate ester modified with poly(ether imide). *J. Polym. Sci., Part B: Polym. Phys.*, **44** (3), 517–523.
  - 62 Tanaka, H. (1993) Unusual phase-separation in a polymer-solution caused by asymmetric molecular-dynamics. *Phys. Rev. Lett.*, **71** (19), 3158–3161.
  - 63 Tanaka, H. (2000) Viscoelastic phase separation. *J. Phys. Condens. Matter*, **12** (15), R207–R264.
  - 64 Tanaka, H. (2009) Formation of network and cellular structures by viscoelastic phase separation. *Adv. Mater.*, **21** (18), 1872–1880.
  - 65 Yu, Y.F., Wang, M.H., Gan, W.J., and Li, S.J. (2006) Phase separation and rheological behavior in thermoplastic modified epoxy systems. *Colloid Polym. Sci.*, **284** (10), 1185–1190.
  - 66 Kelley, F.N. and Bueche, F. (1961) Viscosity and glass temperature relations for polymer - diluent systems. *J. Polym. Sci.*, **50** (154), 549–556.
  - 67 Jyotishkumar, P., Pionteck, J., Ozdilek, C., Moldenaers, P., Cvelbar, U., Mozetic, M., and Thomas, S. (2011) Rheology and pressure-volume-temperature behavior of the thermoplastic poly (acrylonitrile-butadiene-styrene)-modified epoxy-DDS system during reaction induced phase separation. *Soft Matter*, **7** (16), 7248–7256.
  - 68 Zhan, G.Z., Hu, S., Yu, Y.F., Li, S.J., and Tang, X.L. (2009) The study on poly(ether sulfone) modified cyanate ester resin and epoxy resin curing blends. *J. Appl. Polym. Sci.*, **113** (1), 60–70.
  - 69 Yu, Y.F., Wang, M.H., Foix, D., and Li, S.J. (2008) Rheological study of epoxy systems blended with poly(ether sulfone) of different molecular weights. *Ind. Eng. Chem. Res.*, **47** (23), 9361–9369.
  - 70 Liu, Y., Zhong, X.H., and Yu, Y.F. (2010) Gelation behavior of thermoplastic-modified epoxy systems during polymerization-induced phase separation. *Colloid Polym. Sci.*, **288** (16-17), 1561–1570.
  - 71 Liu, X.Y., Zhan, G.Z., Yu, Y.F., and Li, S.J. (2006) Rheological study on structural transition in polyethersulfone-modified

- bismaleimide resin during isothermal curing. *J. Polym. Sci., Part B: Polym. Phys.*, **44** (21), 3102–3108.
- 72 Gan, W.J., Zhan, G.Z., Wang, M.G., Yu, Y. F., Xu, Y.Z., and Li, S.J. (2007) Rheological behaviors and structural transitions in a polyethersulfone-modified epoxy system during phase separation. *Colloid Polym. Sci.*, **285** (15), 1727–1731.
  - 73 Liu, X.Y., Yu, Y.F., Wang, M.H., Zhao, L., Li, L., and Li, S.J. (2007) Study on the polyethersulfone/bismaleimide blends: morphology and rheology during isothermal curing. *J. Mater. Sci.*, **42** (6), 2150–2156.
  - 74 Wang, M.H., Yu, Y.F., and Li, S.J. (2007) Polymerization-induced phase separation in polyethersulfone modified epoxy resin systems: effect of curing reaction mechanism. *Sci. China Ser. B*, **50** (4), 554–561.
  - 75 Winter, H.H. and Chambon, F. (1986) Analysis of linear viscoelasticity of a crosslinking polymer at the gel point. *J. Rheol.*, **30** (2), 367–382.
  - 76 Scanlan, J.C. and Winter, H.H. (1991) Composition dependence of the viscoelasticity of end-linked poly (dimethylsiloxane) at the gel point. *Macromolecules*, **24** (1), 47–54.
  - 77 Lairez, D., Adam, M., Emery, J.R., and Durand, D. (1992) Rheological behavior of an epoxy/amine system near the gel point. *Macromolecules*, **25** (1), 286–289.
  - 78 Hillmyer, M.A., Lipic, P.M., Hajduk, D.A., Almdal, K., and Bates, F.S. (1997) Self-assembly and polymerization of epoxy resin amphiphilic block copolymer nanocomposites. *J. Am. Chem. Soc.*, **119** (11), 2749–2750.
  - 79 Fine, T., Lortie, F., David, L., and Pascault, J.P. (2005) Structures and rheological properties of reactive solutions of block copolymers. Part I. Diblock copolymers in a liquid epoxy monomer. *Polymer*, **46** (17), 6605–6613.
  - 80 Serrano, E., Tercjak, A., Ocando, C., Larranaga, M., Parellada, M.D., Corona-Galvan, S., Mecerreyes, D., Zafeiropoulos, N.E., Stamm, M., and Mondragon, I. (2007) Curing behavior and final properties of nanostructured thermosetting systems modified with epoxidized styrene-butadiene linear diblock copolymers. *Macromol. Chem. Phys.*, **208** (21), 2281–2292.
  - 81 Spoelstra, A.B., Peters, G.W.M., and Meijer, H.E.H. (1996) Chemorheology of a highly filled epoxy compound. *Polym. Eng. Sci.*, **36** (16), 2153–2162.
  - 82 Ng, H. and Manas-Zloczower, I. (1993) Chemorheology of unfilled and filled epoxy-resins. *Polym. Eng. Sci.*, **33** (4), 211–216.
  - 83 Dutta, A. and Ryan, M.E. (1979) Effect of fillers on kinetics of epoxy cure. *J. Appl. Polym. Sci.*, **24** (3), 635–649.
  - 84 Kosinski, L. and Caruthers, J. (1985) Rheological properties of poly (dimethylsiloxane) filled with fumed silica: II. Stress relaxation and stress growth. *J. Non-Newtonian Fluid Mech.*, **17** (1), 69–89.
  - 85 Le Pluart, L., Duchet, J., Sautereau, H., Halley, P., and Gerard, J.F. (2004) Rheological properties of organoclay suspensions in epoxy network precursors. *Appl. Clay Sci.*, **25** (3–4), 207–219.
  - 86 Moraru, V.N. (2001) Structure formation of alkylammonium montmorillonites in organic media. *Appl. Clay Sci.*, **19** (1–6), 11–26.
  - 87 Solar, L., Nohales, A., Munoz-Espi, R., Lopez, D., and Gomez, C.M. (2008) Viscoelastic behavior of epoxy prepolymer/ organophilic montmorillonite dispersions. *J. Polym. Sci., Part B: Polym. Phys.*, **46** (17), 1837–1844.
  - 88 Chen, J.S., Poliks, M.D., Ober, C.K., Zhang, Y., Wiesner, U., and Giannelis, E. (2002) Study of the interlayer expansion mechanism and thermal-mechanical properties of surface-initiated epoxy nanocomposites. *Polymer*, **43** (18), 4895–4904.
  - 89 Dean, D., Walker, R., Theodore, M., Hampton, E., and Nyairo, E. (2005) Chemorheology and properties of epoxy/ layered silicate nanocomposites. *Polymer*, **46** (9), 3014–3021.
  - 90 Franchini, E., Galy, J., and Gerard, J.F. (2009) Sepiolite-based epoxy nanocomposites: Relation between processing, rheology, and morphology. *J. Colloid Interface Sci.*, **329** (1), 38–47.
  - 91 Zhamu, A., Jana, S., Salehi-Khojin, A., Kolodka, E., Gan, Y.X., and Zhong, W.H. (2007) Chemorheology of reactive graphitic

- nanofiber-reinforced epoxy as a composite matrix. *Compos. Interfaces*, **14** (3), 177–198.
- 92 Hore, M.J.A. and Laradji, M. (2008) Prospects of nanorods as an emulsifying agent of immiscible blends. *J. Chem. Phys.*, **128** (5), 054901.
- 93 Soule, E.R., Borrajo, J., and Williams, R.J.J. (2007) Thermodynamic analysis of a polymerization-induced phase separation in nanoparticle-monomer-polymer blends. *Macromolecules*, **40** (22), 8082–8086.
- 94 Zhong, X., Liu, Y., Su, H., Zhan, G., Yu, Y., and Gan, W. (2011) Enhanced viscoelastic effect of mesoscopic fillers in phase separation. *Soft Matter*, **7** (7), 3642–3650.
- 95 Liu, Y., Zhong, X.H., Zhan, G.Z., Yu, Y.F., and Jin, J.Y. (2012) Effect of mesoscopic fillers on the polymerization induced viscoelastic phase separation at near- and off-critical compositions. *J. Phys. Chem. B*, **116** (12), 3671–3682.



## 5

## Characterization of Phase Behavior in Polymer Blends by Light Scattering

Petr Svoboda

## 5.1

### Introduction

The field of polymer science and technology has undergone an enormous expansion over the past several decades, primarily through chemical diversity. First, there was the development of new polymers from a seemingly endless variety of monomers. Next, random copolymerization was used as an effective technique for tailoring or modifying polymers. Later, more controlled block-and-graft copolymerization was introduced [1,2].

The pace of developing new molecules has not stopped, but it has slowed considerably as new chemistry is expensive and takes a long time to commercialize. Polymer blending or alloying has become an alternate route to new products and for problem-solving [3].

Improving mechanical properties such as toughness usually serve as the main reasons for the development of novel thermoplastic alloys and blends [4]. Other reasons for blending two or more polymers together include: (i) to improve the polymer's processability, especially for the high-temperature polyaromatic thermoplastics; (ii) to enhance the physical and mechanical properties of the blend, making them more desirable than those of the individual polymers in the blend; and (iii) to meet the market force (cost dilution). Most products succeed because of a beneficial combination or balance of properties rather than because of any single characteristic. In addition, a material must have a favorable benefit-to-cost relation if it is to be selected over other materials for a particular application. One key technical issue is whether the blend will exhibit additive properties, or not. In many cases properties are well below additive, while in others they may be above additivity. The property relationships exhibited by blends depend critically on the correct control of their phase behavior [3].

Basically, polymer blends are divided into two large groups: *miscible* on the molecular level; and *immiscible*. Among commercial products based on miscible blends can be mentioned, for example, polystyrene (PS)–poly(phenylene oxide) (PPO), poly(vinylidene fluoride) (PVDF)–poly(methyl methacrylate) (PMMA),

PVDF-PEMA, and poly(vinyl chloride) (PVC)-nitrile rubber. The immiscible blends include applications such as rubber blends in tires, impact-modified plastics, and coextruded film and fibers [1].

Miscible blends are homogeneous to the polymer segmental level. Single-phase blends are usually optically transparent, and most physical properties will be at least as good as the composition-weighted average of the pure components. At the very early stages of polymer science it was concluded that miscibility among polymer-polymer pairs was a rare exception. However, research conducted over the past decade has proven this rule to be somewhat overstated [3], and polymer miscibility has actually become a major area of research in many industrial and academic laboratories [2].

One interesting phenomenon in the field of miscible blends is the phase separation that is usually brought about by variations in temperature, pressure, and/or the composition of the mixture [2]. The two major classes of phase transition in a dense phase are: (i) liquid-solid phase transition; and (ii) liquid-liquid phase transition. The first of these transitions is exemplified by the vitrification of one or all of the chemically different equilibrium liquid phases, and by crystallization of one or all of the chemically different equilibrium liquid phases. In the second transition, the final stage of the system is dictated by the combined effects of the thermodynamics of the system (i.e., the extension, location, and nature of the miscibility gap in the temperature-composition behavior) and the flow properties of the different polymers. While the mechanism of liquid-solid phase separation is generally the classic one of nucleation and growth, for liquid-liquid the mechanism depends on the stage of the thermodynamic stability of the system. In one region, nucleation and growth predominate, whereas in another spinodal decomposition is the mechanism of the phase transformation [2]. The liquid-liquid phase separation in the temperature versus blend composition plane was named LCST (lower critical solution temperature) and UCST (upper critical solution temperature) [1].

## 5.2

### **Amorphous/Crystalline Polymer Blends**

Polymer blends containing a crystallizable component have attracted many scientists, both from basic research and applied research laboratories. This is probably due to the fact that the majority of commercially used thermoplastic blends and alloys contain at least one crystallizable material [5]. In order to obtain the desired product properties, it is often very important to control the crystallization process. For instance, in certain applications it is useful to have amorphous polyester (e.g., PET, as a package material), whereas for other applications a higher degree of crystallinity is necessary (e.g., as a fiber material). In amorphous/crystalline polymer blends the crystallization behavior is often strongly influenced by the amorphous component. Usually, the crystallization rate of the crystalline polymer is reduced by the amorphous polymer. In most systems this is caused by an increase

of the glass transition temperature ( $T_g$ ) of the amorphous phase. Examples of this behavior are blends of PMMA/PVDF, poly( $\epsilon$ -caprolactone) (PCL)/PVC, PCL/poly(styrene-*co*-acrylonitrile) (SAN), PVDF/poly(ethyl acrylate) and PMMA/poly(ethylene oxide)(PEO). In contrast it was reported recently that, in a single-phase mixture of an aramid and polyethersulfone (PES), crystallization of the aramid occurs on a reasonable timescale whereas crystallization cannot be observed in the neat aramid. This increase in the crystallization rate may be caused partially by a lowering of the  $T_g$  in the system because PES has a lower  $T_g$  than the aramid. However, the main contribution should be made by dissociation of the aramid–aramid interactions, such as strong hydrogen bonds [6].

Another interesting development in the field of crystalline polymer blends was initiated by the Toyota Motor Corporation, which recently introduced a “super-olefin polymer.” This material was designed on a lamellar level (on a nanometer scale), and it has been speculated that this material is a blend of low-molecular-weight poly(propylene)(PP) with a new olefinic copolymer. This material, which has excellent hardness and toughness, as well as good flow properties, was designed to replace the expensive reaction injection molding (RIM) polyurethane [3].

### 5.3

#### Light Scattering

Light scattering is a powerful analytical tool that can be used to investigate various aspects of miscible and immiscible polymer blends. Recently, significant progress has been made in developing the instrumentation for light scattering. A schematic diagram of a time-resolved light-scattering apparatus based on a moving photodiode is shown in Figure 5.1a, and photometer with a 46-photodiode array system is shown on Figure 5.1b. Using a highly sensitive charge-coupled device (CCD) camera system, it is possible to carry out time-resolved measurements of a two-dimensional scattering pattern (see Figure 5.1c). Light scattering under  $V_v$  geometry (vertical polarizer with vertical analyzer) describes very well the two-phase structure, while  $H_v$  geometry (horizontal polarizer with vertical analyzer) focuses mainly on crystallization. An example of the modulated structures observed by  $V_v$  light scattering is shown in Figure 5.2, while Figure 5.3 shows an example of  $H_v$  scattering development in time during crystallization.

Light scattering occurs when light is incident on a heterogeneous material. The intensity of scattering,  $I(q)$ , is linked to inhomogeneity, or the scattering contrast, due to fluctuations in density, concentration, or orientation;  $I(q)$  is customarily expressed through a Fourier inversion as [7]

$$I(q) = I_0 \nu \langle \eta^2 \rangle \int \gamma(r) \exp\{-i(\vec{q} \cdot \vec{r})\} d^3r \quad (5.1)$$

where  $I_0$  is the incident light,  $\nu$  is the illumination volume,  $r$  is the distance between scattering units, and  $q$  is the scattering wave number, defined as

$$q = (4\pi/\lambda) \sin(\theta/2) \quad (5.2)$$

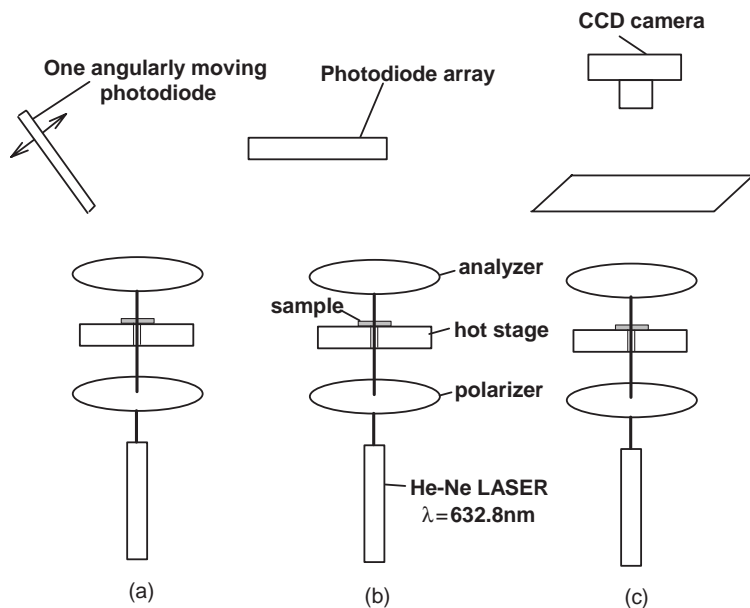


**Figure 5.1** Light-scattering apparatus. (a) Based on moving photodiode; (b) Based on photodiode array; (c) Based on CCD camera.

Here,  $\lambda$  and  $\theta$  are the wavelength of light and the scattering angle measured in the medium, respectively.  $\gamma(r)$  is the correlation function, defined as

$$\gamma(r) = \frac{\langle \eta_1(r) \eta_2(r) \rangle}{\langle \eta^2 \rangle} \quad (5.3)$$

where  $\eta_i = n_i - n_0$  is the fluctuation representing the contrast of the refractive indices of component  $i$  ( $= 1$  or  $2$ ) [5,6]. The static scattering technique is extensively used for cloud-point determination to define the phase diagram, and also as time-resolved light scattering to study phase-separation dynamics in polymer blends.

## 5.4

### Cloud-Point Determination

One of the main characteristics of phase separation in polymer blends is the cloudy appearance of the materials. This cloudiness is a consequence of light scattering due to the inhomogeneity of the phase-separated blend structure. Hence, a cloud-point determination method, based on the static light-scattering phenomenon, has been employed customarily to locate the position of the

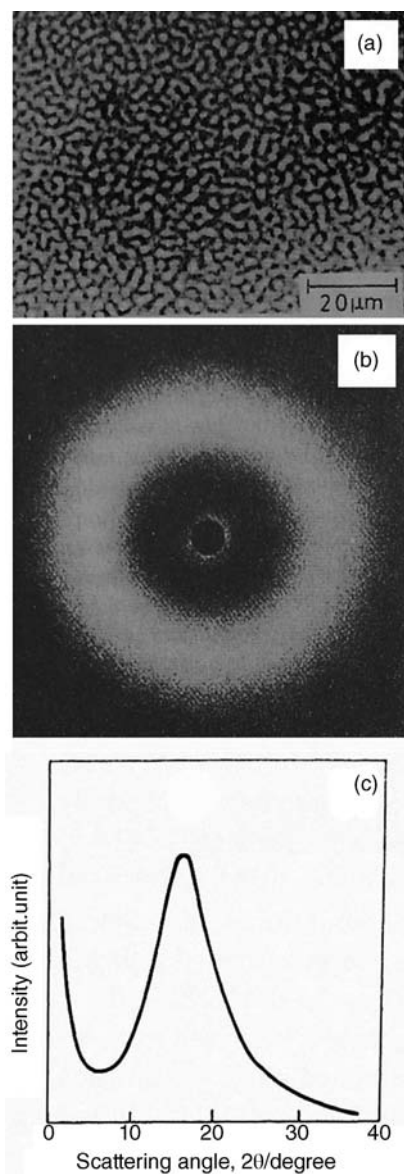


**Figure 5.2** (a) Modulated structure; (b)  $V_v$  light-scattering pattern; (c) One-dimensional  $V_v$  scattering intensity profile.

phase boundary (or the coexistence curve) of a binary polymer blend. The static light-scattering apparatus used in the cloud-point determination includes a laser light source (a randomly polarized He–Ne laser), a goniometer for angular rotation, and a photomultiplier (or photodiode) detector. The scattered

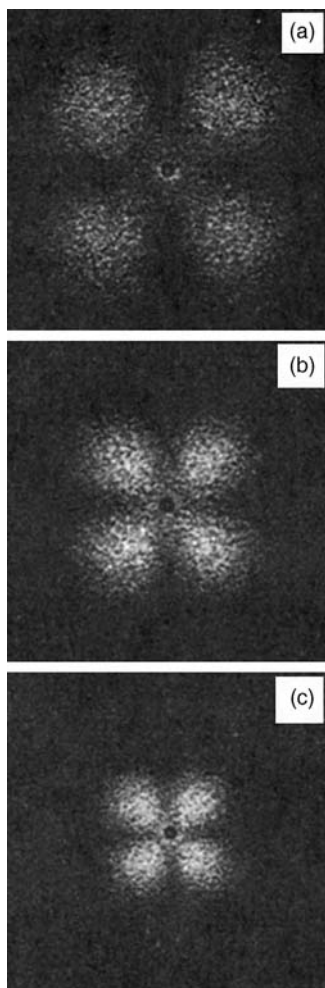


**Figure 5.3**  $H_v$  light-scattering profile during continuing crystallization.

intensity is customarily measured at a given scattering angle, typically in the range of  $20\text{--}40^\circ$ , depending on the length scale (size) of the heterogeneity. The temperature at which the scattered intensity changes abruptly is called the cloud-point. In the case for which the scattering shows a strong angular dependence, a one-dimensional silicon-diode-array detector may be used to monitor the change in the scattering curve. The cloud-point measurement can be performed at various rates (see the example in Figure 5.4), after which the position of LCST is extrapolated to a zero heating rate (see the example in Figure 5.5).

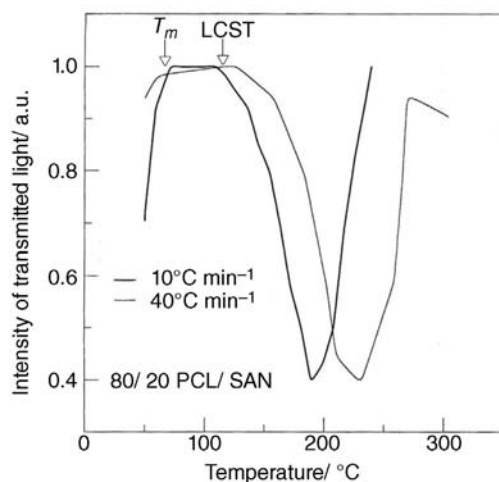


**Figure 5.4** Transmitted light intensity versus temperature in thermo-optical analysis at two heating rates ( $10$  and  $40\text{ }^{\circ}\text{C min}^{-1}$ ) for 80/20 PCL/SAN sample.

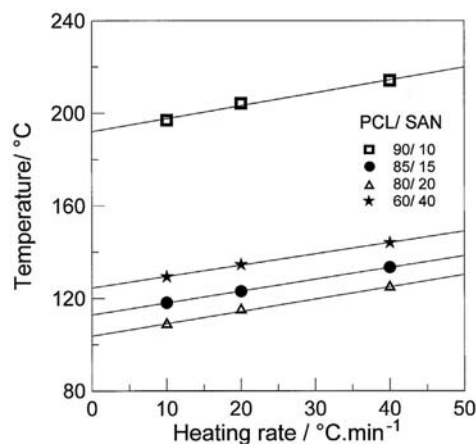


**Figure 5.5** Evaluation of LCST phase boundary by extrapolating to zero heating rate.

## 5.5

### Time-Resolved Light Scattering

#### 5.5.1

##### Immiscible Blends

The technique of static light scattering can be applied to studies of the dynamic phenomena of polymer phase transitions by simultaneous acquisition of the angular dependence of the scattering pattern in one or two dimensions at relatively

short time intervals. Such an approach, termed *time-resolved light scattering*, measures the temporal evolution of the static structure factor, or scattered intensity, during polymer–polymer phase separation or homogenization. The temporal change in the scattered intensity may be described as

$$I(q, t) = I_0(q, t) \int \langle \eta_1(r, t) \eta_2(r, t) \rangle \exp\{-i(q \cdot r)\} dr^3 \quad (5.4)$$

For irregular two-phase materials, the scattering theory goes back to the fundamental work of Debye and Bueche [8]. The theory provides a relation between the intensity distribution of scattered light and the statistical parameters that describe the two-phase structure. The intensity of scattered light from the irregular two-phase material usually decreases monotonically with increasing scattering angle,  $\theta$ . The decreasing function is described by

$$I(q)^{-1/2} = (1 + \xi^2 q^2) \cdot (8\pi \langle \eta^2 \rangle \xi^3)^{-1/2} \quad (5.5)$$

The correlation distance  $\xi$  can be obtained from the slope and the intercept in the Debye–Bueche plot,  $I(q)^{-1/2}$  versus  $q^2$ . Once the value of  $\xi$  is known, the other morphological parameters, such as the specific interfacial area  $S_{sp}$  and the mean radius of dispersed particles  $R$ , are obtained from the relationships

$$S_{sp} = 4\phi(1 - \phi)\xi^{-1} \quad (5.6)$$

$$R = 3\phi S_{sp}^{-1} \quad (5.7)$$

where  $\phi$  is the volume fraction of the dispersed phase. Values of  $R$  obtained from light scattering have been compared with transmission electron microscopy (TEM) data for ABS and blends of a block copolymer with a homopolymer, and good agreement was reported [9].

### 5.5.2

#### Spinodal Decomposition

In 1965, Cahn [10] laid a basis for the mathematical treatment of spinodal decomposition, starting with an expression for the free energy of an inhomogeneous solution, the composition of which always differed only slightly from the average composition, and with small composition gradients.

$$F = \int [f(c) + \kappa(\nabla c)^2] dV \quad (5.8)$$

Here,  $f(c)$  is the free-energy density of homogeneous material of composition  $c$ , and  $\kappa(\nabla c)^2$  is the additional free-energy density if the material is in a gradient in composition. In the development of the theory it became convenient to consider the Fourier components of the composition rather than the composition. Because of the orthogonality of the Fourier components,  $\Delta F$  is the sum of contributions from each Fourier component separately.



The kinetics of the initial stages of phase separation can be obtained by solving the diffusion equation. It is necessary to define a mobility  $M$  which is (minus) the ratio of diffusional flux to the gradient in chemical potential

$$J_B = -J_A = M\nabla(\mu_A - \mu_B) \quad (5.9)$$

Simple thermodynamic considerations show that  $M$  must be positive if diffusion which results spontaneously from the chemical potential gradient is to result in a decrease in free energy. One obtains  $\mu_A - \mu_B$  from the variational derivative of  $F$  in Eq. (5.8),

$$\mu_A - \mu_B = \left( \frac{\delta F}{\delta c_A} \right) = \left( \frac{\partial f}{\partial c_A} \right) - 2\kappa \nabla^2 c_A + \text{terms higher in order and degree} \quad (5.10)$$

It is possible to discard the higher-order terms if we are only interested in the initial stages. By substituting Eq. (5.10) into Eq. (5.9) and taking the divergence, and keeping only first-degree terms, the following diffusion equation is obtained:

$$\frac{\partial c}{\partial t} = M \left( \frac{\partial^2 f}{\partial c^2} \right) \nabla^2 c - 2M\kappa \nabla^4 c \quad (5.11)$$

Since the coefficient of  $\nabla^2 c$  may be identified with a diffusion coefficient, it can be seen that at the spinodal the diffusion coefficient changes sign. The solution to Eq. (5.11) is

$$c - c_0 = e^{[R(\beta)t]} \cos(\beta \mathbf{r}) \quad (5.12)$$

where  $\beta$  is the wavenumber and  $R(\beta)$  is given by

$$R(\beta) = -M \left( \frac{\partial^2 f}{\partial c^2} \right) \beta^2 - 2M\kappa \beta^4 \quad (5.13)$$

Cahn has developed his model for small molecules in metallurgy, and these equations have been slightly modified for polymer blends. Today,  $g$  is used instead of  $f$ , and  $q$  instead of  $\beta$ . Light scattering became popular in the quantitative evaluation of spinodal decomposition in polymer blends. Here, in the initial stage of phase separation (or phase dissolution), the intensity of the scattered light ( $I$ ) is expected to increase (or decrease) exponentially with time  $t$ .

$$I_{V_V}(q, t) \propto e^{2R(q)t} \quad (5.14)$$

where  $R(q)$  is the growth rate (or decay rate) of concentration fluctuation at the scattering vector  $q$  (see Eq. (5.2)).

Today,  $R(q)$  is given by (essentially the same as Eq. (5.13) in 1965)

$$R(q) = -Mq^2 \left( \frac{\partial^2 g}{\partial c^2} + 2\kappa q^2 \right) \quad (5.15)$$

where  $M$  is the mobility,  $g$  is the free-energy density of the blend with composition  $c$ , and  $\kappa$  is the gradient energy coefficient.

The existence of a scattering peak that is moving to lower values of angle suggests that demixing proceeds via a spinodal decomposition (SD) mechanism.

The SD process in *near-critical* mixtures can be divided into an early stage, an intermediate stage, and a late stage [11]. In the early stage, the time evolution of the concentration fluctuations can be approximated by the linearized theory. The characteristic wavenumber  $q_m(t, T)$ , which is related to the domain spacing  $\Lambda_m(t, T)$ ,

$$\Lambda_m(t) = \frac{2\pi}{q_m(t)} \quad (5.16)$$

of the dominant mode of the concentration fluctuations at time  $t$  and phase-separation temperature  $T$  is independent of  $t$ . The intensity of the Fourier mode of the fluctuations with wavenumber  $q$ ,  $I(q, t, T)$ , grows exponentially with time.

The intermediate stage is characterized by a decrease of  $q_m(t, T)$  as well as a further increase in the intensity due to a nonlinear nature in the time evolution of the concentration fluctuations.

In the late stage, the two phases reach equilibrium composition and the interface between the two phases narrows to equilibrium thickness. The domains, however,  $\Lambda_m(t, T)$  are still increasing in order to lower the interfacial free energy of the system [11].

In order to observe the whole process of SD it is convenient to plot the position of the maximum  $q_m$  and intensity at the maximum  $I_m$  as a function of time in a double-logarithmic plot. In this way, it is possible to divide the SD process into three stages. In the early stage, the position of the maximum  $q_m$  stays almost constant, while in the intermediate and late stages, a scaling analysis is used. Binder and Stauffer [11] proposed scaling rules, assuming that clusters aggregate by a diffusion process and coalesce into larger clusters, and described the self-similar growth of the structure by the time evolution of  $q_m(t, T)$  and  $I_m(t, T)$  as

$$q_m(t, T) \sim t^{-\alpha} \quad (5.17)$$

and

$$I_m(t, T) \sim t^\beta \quad (5.18)$$

In the intermediate stage, a relation  $\beta > 3\alpha$  is observed. The late stage is reached when  $\beta = 3\alpha$ , at which time the two phases attain equilibrium compositions, and self-similar growth of the structure can be observed.

- 1) In the early stage, there is no increase in wavelength  $\Lambda_m$ , ( $q_m$  stays constant) concentration fluctuations  $\Delta\phi(\tau)$  are increasing and the slope of the line ( $\alpha$ ) is 0.
- 2) In the intermediate stage, both the amplitude of the concentration fluctuations  $\Delta\phi(t)$  and wavelength  $\Lambda_m(t)$  of the fluctuations grow with time, and the position of maximum  $q_m$  is decreasing to lower angles, the slope of the line  $\alpha$  is gradually increasing. Because  $\beta$  is almost a constant,  $\beta/\alpha$  will gradually decrease until it reaches a value of 3.

- 3) In the late stage, where the value  $\Delta\phi$  reaches an equilibrium value,  $\Delta\phi_e$  determined by the coexistence curve and the phase separation temperature, only  $\Lambda_m$  grows with time. The ratio  $\beta/\alpha = 3$ .

Cahn began by describing the Gibbs free energy of fluctuating system by a sum of the local free energy of mixing and the square of concentration gradient term. The gradient term remains in Eq. (5.15) as the second term. The first term of Eq. (5.15) is the second derivative of  $g$ , which is the thermodynamic driving force for fluctuation growth (i.e., the degree of instability of homogeneously mixed state). The second term of Eq. (5.15) suggests that a very sharp gradient with large  $q$  (short wavelength of fluctuation) suppresses the fluctuation growth. In contrast, the fluctuation with small  $q$  (long wavelength) grows slowly, because the molecules should diffuse long distance for the fluctuation growth. Then, there should exist a peak of rate constant  $R(q)$  at a particular  $q$ .

One can estimate the growth (or decay) rate  $R(q)$  of concentration fluctuations from the initial slope of a  $\ln(I_{Vv})$  versus  $t$  plot for different angles (or  $q$  values).

After such detailed analysis, it is possible to calculate the  $R(q)/q^2$  versus  $q^2$  plot for various temperatures. The apparent diffusion coefficient  $D_{app}$  is defined by

$$D_{app} = -M \left( \frac{\partial^2 g}{\partial c^2} \right) \quad (5.19)$$

and can be obtained from  $R(q)/q^2$  versus  $q^2$  plot as the intercept of the  $R(q)/q^2$  axis.

The apparent diffusion coefficient  $D_{app}$  obtained in this way was positive for phase dissolution, and negative for phase separation.

### 5.5.3

#### Crystallization by $H_v$ Light Scattering

$H_v$  light scattering is a powerful technique for the investigation of crystallization in polymer blends. Compared to optical microscopy, where the choice always has to be made from a limited number of spherulites,  $H_v$  light scattering provides information about the whole system.

The observed scattering patterns can be the four-leaf-clover type. The clover patterns become smaller with time of crystallization, and the average radius of the spherulites  $R_{Hv}$  can be calculated from the position of the maximum in scattering intensity,  $\theta_m$ , by using this equation [12]:

$$4.09 = 4\pi(R_{Hv}/\lambda)\sin(\theta_m/2) \quad (5.20)$$

In order to discuss the time variation of the internal spherulitic structure, it is convenient to employ the scattering profiles at an azimuthal angle  $45^\circ$  using a reduced scattering angle  $w$  [13].

$$w = \left( \frac{2\pi}{\lambda} \right) R_{Hv} \sin \theta \quad (5.21)$$

By using  $w$ , the scattering profiles are corrected to the reduced profiles with the peak maximum at  $w = 4$ . The sharpness of the peaks is different for different samples. An increased radial disorder leads to an increased relative  $I_{Hv}$  scattered intensity at angles larger than that of the maximum. To compare quantitatively the order inside the spherulite, it is convenient to define a so-called order parameter ( $Pr$ ):

$$Pr = \frac{I(4)}{I(x)} \quad (5.22)$$

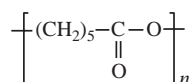
where  $I(4)$  represents intensity at  $w = 4$  and  $I(x)$  is the intensity at  $w = x$ . In the literature, two values of  $x$  were used, namely 8 and 15.

#### 5.5.4

##### Model Blend of Poly( $\epsilon$ -Caprolactone) (PCL) and Poly(Styrene-co-Acrylonitrile) (SAN)

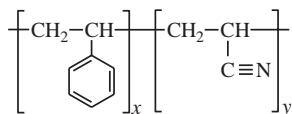
Miscible polymer blends containing one crystallizable component are interesting from a scientific as well as an industrial point of view. Occasionally, the LCST behavior occurs and blend starts to demix at certain elevated temperature by the SD mechanism. In this case, a highly interconnected two-phase morphology ("SD structure") develops, where the periodic distance of the SD structure will depend on the temperature and time of SD. By quenching the blend having SD structure below the melting point, the SD structure may be partly preserved by pinning, associated with a formation of crystal lamellae of the crystallizable component [1]. The spinodal decomposition of polymer blends was very well studied by Hashimoto *et al.* [14–18]. Crystallization connected with phase separation (many times by SD) has attracted the attention of many research groups [19–21].

In these studies, two polymers were used, namely poly( $\epsilon$ -caprolactone) (PCL) and poly(styrene-co-acrylonitrile) (SAN). PCL is linear, semicrystalline aliphatic polyester with the chemical structure:



PCL became available commercially following efforts at Union Carbide to identify synthetic polymers that could be degraded by microorganisms. The high solubility of PCL, its low melting point (59–64 °C), and its exceptional ability to form blends has stimulated research on its application as a biomaterial. PCL degrades at a slower pace than poly(lactic acid) (PLA), and can therefore be used in drug-delivery devices that remain active for over one year. The Capronor system, a one-year implantable contraceptive device, has become commercially available in Europe and in the United States. The toxicology of PCL has been extensively studied as a part of the evaluation of Capronor. Based on a large number of tests,  $\epsilon$ -caprolactone and PCL are currently regarded as nontoxic and tissue-compatible materials. PCL is currently being investigated as a part of wound dressing, and in Europe it is already in clinical use as a degradable staple (for wound closure) [22].

The next polymer to be investigated was a copolymer of styrene and acrylonitrile (SAN), with the following chemical structure:



Industrially produced SAN usually contains 15–35 wt% of acrylonitrile, and is prepared by radical polymerization. Compared to the polystyrene homopolymer, SAN copolymers have a higher softening point, an improved impact strength, and a higher resistance to hydrocarbons and oils because of the polar nature of the acrylonitrile (very polar  $\text{C}\equiv\text{N}$  group in contrast to the nonpolar benzene group). The higher the acrylonitrile content, the greater the heat and chemical resistance, impact strength, toughness, scratch resistance and barrier properties. SAN is frequently used in households as well as in industry.

Studies of blends of PCL and SAN have provided the rare opportunity of investigating various types of phase behavior such as phase separation, phase dissolution and crystallization, and many research groups have examined this blend [23–25]. Both, PCL and SAN are miscible only when SAN contains 8~28 wt% of acrylonitrile, and near to the borders of this “miscibility window,” LCST behavior is observed. For this study, SAN with 27.5 wt% AN was selected. The PCL/SAN-27.5 blend exhibited LCST behavior depending on the blend composition, but in this study attention was focused mainly on a blend having a critical composition of PCL/SAN (80/20).

In this part, the critical blend underwent phase separation at a fixed temperature above LCST for various times, yielding different periodic distances of SD structure. The phase-separated blend was subsequently quenched to various temperatures below the melting point ( $T_m$ ) of PCL and then isothermally annealed. The kinetics of structure development during isothermal annealing was analyzed quantitatively by light scattering, and the developed structure was observed using TEM. The development of a phase-separated structure above LCST and following crystallization was also observed using optical microscopy.

### 5.5.5

#### Samples Preparation

The PCL used in these studies (PCL-767;  $M_w = 40\,400 \text{ g mol}^{-1}$ ,  $M_w/M_n = 2.61$ ) was obtained from the Union Carbide Corporation. Copolymers of styrene and acrylonitrile (SAN) were synthesized at  $60^\circ\text{C}$  using ethylbenzene as a solvent and azoisobutyronitrile (AIBN), at a concentration of  $0.02 \text{ mol l}^{-1}$  as the initiator. The conversion was less than 5%. The acrylonitrile content in SAN was in range 10–35 wt%. SAN containing 27.5 wt% acrylonitrile (briefly, SAN-27.5) exhibited an interesting phase behavior and was studied extensively; the molecular weight data acquired were  $M_w = 169\,000 \text{ g mol}^{-1}$ ,  $M_w/M_n = 2.09$ . The blends were prepared by casting a 5 wt% solution of both polymers in 1,2-dichloroethane onto a cover

glass; the solvent was evaporated at room temperature and the samples were then dried for several days in a vacuum oven at 60 °C.

Phase separation and phase dissolution of the blend are described in the following section [26].

#### 5.5.6

#### Phase Separation and Phase Dissolution in Poly( $\epsilon$ -Caprolactone)/Poly(Styrene-co-Acrylonitrile) Blend

The phase diagram of the PCL/SAN-27.5 blend is shown in Figure 5.6. All specimens of PCL/SAN-27.5 blends were optically clear, and no structure was observed microscopically at 80 °C (i.e., above the melting temperature of PCL). When the specimens were heated above LCST, however, they became opaque and a two-phase structure was observed.

The blend was first annealed below LCST in one-phase region (point A in Figure 5.6). The sample was then transferred onto another hot stage to various temperatures set above LCST (point B), and annealed isothermally. Phase separation proceeded to various levels depending on the temperature and duration of annealing at point B. Finally, the phase-separated sample was quenched to various phase dissolution temperatures (50–115 °C) below LCST (point C).

In Figure 5.7, the structural development in 80/20 PCL/SAN-27.5 after the temperature jump from 80 to 130 °C is shown. Initially, no structure was seen, but after 5 min a two-phase structure with a unique periodicity and phase connectivity was detected. The contrast of the structure became higher with the time of annealing (30 min), after which the structure became coarser and larger with time (60, 90, and 120 min).

Figure 5.8 shows a typical example of the change in scattering profile with annealing (demixing) time  $t$  at 130 °C. Here, the scattered light intensity  $I_{V_V}$  is shown as a function of the scattering vector  $q$  (see Eq. (5.2)). At  $t = 0$  min, the scattering intensity is very weak and the profile has hardly any angle dependence,

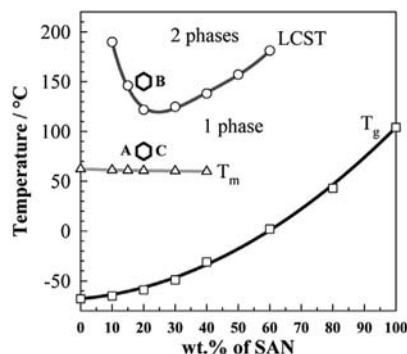
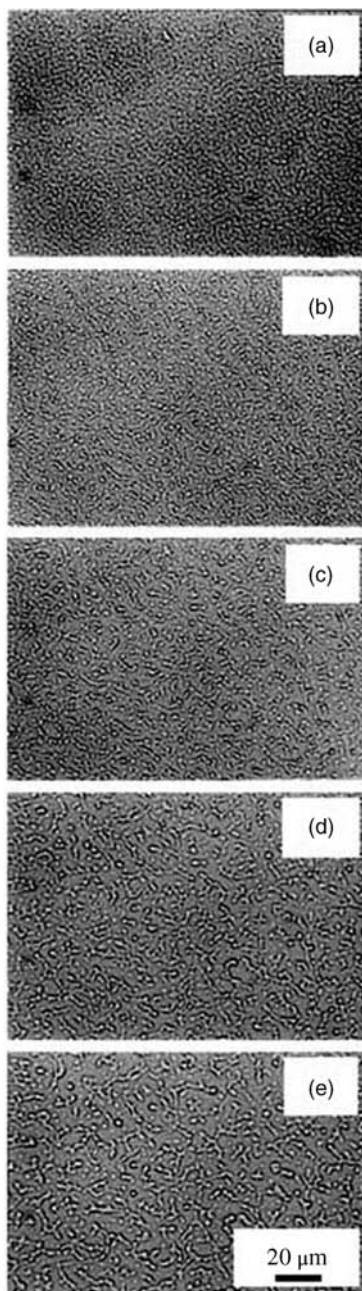
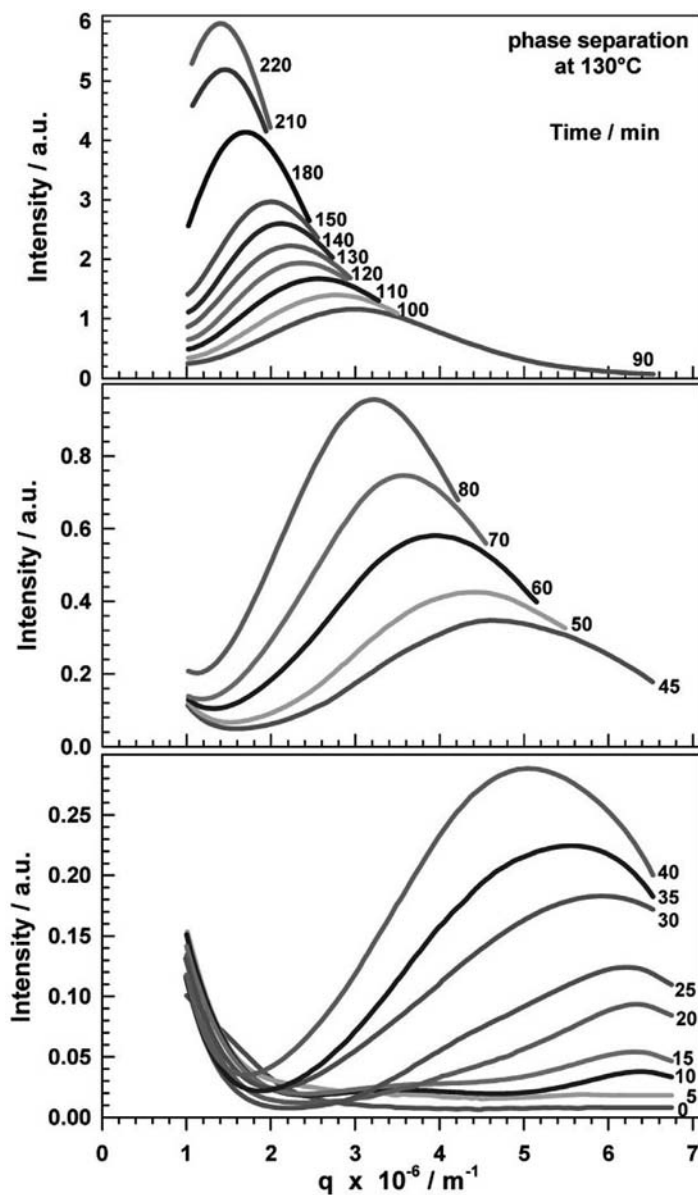


Figure 5.6 Phase diagram of PCL/SAN-27.5 blend.



**Figure 5.7** Optical micrographs of PCL/SAN-27.5 (80/20) blend showing phase separation at constant temperature 130 °C developing in time. (a) 5 min; (b) 30 min; (c) 60 min; (d) 90 min; (e) 120 min.



**Figure 5.8** Change of light-scattering  $V_v$  profile of PCL/SAN-27.5 (80/20) blend during isothermal phase separation at 130 °C.

which suggests a homogeneous mixture. This mixture begins to phase-separate when annealed at 130 °C, as shown by the increase in the scattering intensity. The existence of a scattering peak that is moving to lower values of angle suggests that demixing proceeds via a SD mechanism.



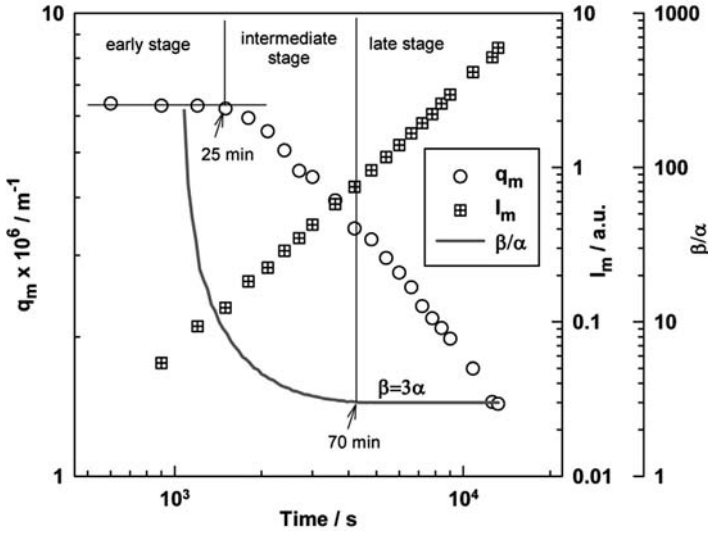


**Figure 5.9** Time evolution of the characteristic wavenumber at maximum  $q_m$ , intensity at maximum  $I_m$  and  $\beta/\alpha$  ratio for PCL/SAN-27.5 (80/20) blend during isothermal phase separation at 130 °C.

According to Eqs (5.17) and (5.18), the duration of the early stage was between 0 and 25 min (see Figure 5.9), the intermediate stage was 25–70 min, and the late stage 70–220 min.

The variation of  $\Lambda_m$  over time for PCL/SAN-27.5 (80/20) blends at two different temperatures of 130 and 150 °C is plotted in Figure 5.10. The values of  $\Lambda_m$  can be

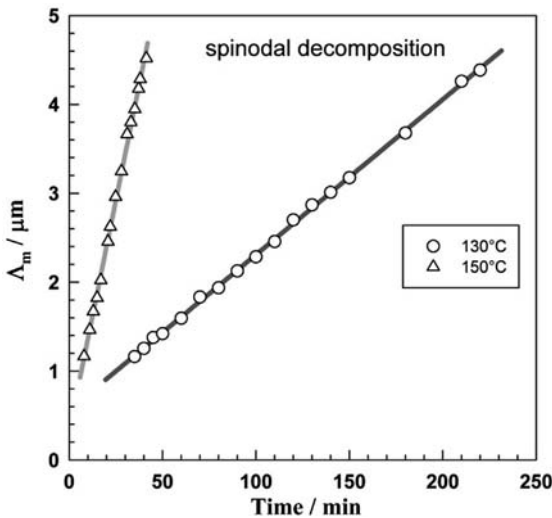


**Figure 5.10** Wavelength of concentration fluctuations  $\Lambda_m$  (from  $V_v$  scattering) versus time for PCL/SAN-27.5 (80/20) blend. Samples were heated to 80 °C for 1 min (one-phase region) and then transferred to another hot stage at 130 °C or 150 °C (two-phase region).

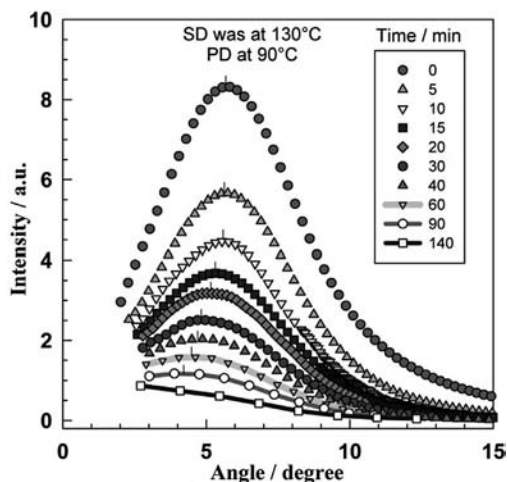


**Figure 5.11** Change of light-scattering profile of PCL/SAN-27.5 (80/20) blend during isothermal phase dissolution at 90 °C after phase separation at 130 °C for 220 min.

used for designing the desired size of domains and, indeed, this plot was used to prepare two different samples with apparently the same wavelength of the concentration fluctuations  $\Lambda_m$  being about 4.3  $\mu\text{m}$ . The first sample was prepared by SD at 130 °C for 220 min, and the second sample at 150 °C for 38 min. These two, supposedly identical, samples were then subjected to phase dissolution (PD) at 90 °C.

The results are shown in Figures 5.11 and 5.12. The light-scattering instrument was set to measure precisely the intensity at smaller angles (compared to Figure 5.10). It should be noted that the initial peak at 0 min was slightly broader

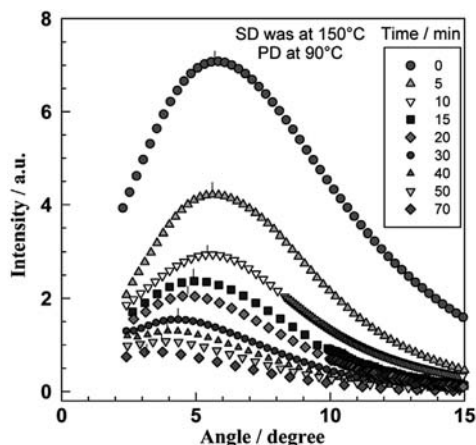


**Figure 5.12** Change of light-scattering profile of PCL/SAN-27.5 (80/20) blend during isothermal phase dissolution at 90 °C after phase separation at 150 °C for 38 min.

in the case of the sample phase-separated at 150 °C compared to that separated at 130 °C. This indicated a quite narrow particle size distribution of the phase-separated structure created at 130 °C, and the coexistence of larger and smaller particles created at 150 °C.

In both cases, the light-scattering peak was decreasing and the position of the maximum shifting towards the lower angle. There are several possible interpretations of this shift of the peak maximum in Figures 5.11 and 5.12, one of which is the faster decay of the high- $q$  Fourier components in the concentration pattern. Only the slower components with long wavelengths (small  $q$ ) survive for longer times. This results in an effective peak shift towards small  $q$  (small angles) during the dissolution process.

This is shown schematically in Figure 5.13, for particles 1 and 2. While the large particle #1 survives up to Figure 5.13c, particle #2 in Figure 5.13c is already dissolved. Light scattering at the late stage of phase dissolution detects only the

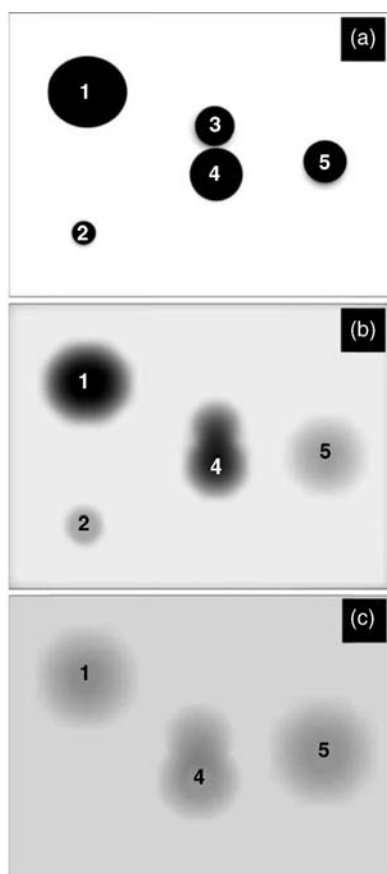


**Figure 5.13** Model of phase dissolution development in time derived from the light-scattering data shown in Figures 5.6 and 5.7.

remaining particle #1. Another possible interpretation of the peak shift towards a smaller angle would be a coalescence of close particles #3 and #4. Actual growth of the particles during phase dissolution is also possible, as was observed directly using TEM by Okada [27], and calculated by Cheng, using a model [28]. This is shown schematically by particle #5. In this particular PCL/SAN (80/20) system, the particles were formed by the SAN-rich phase. SAN has rather high  $T_g$  (ca. 103 °C), while for PCL  $T_g = -66$  °C and  $T_m \cong 60$  °C. The molecular weight of SAN ( $M_w = 169\,000\text{ g mol}^{-1}$ ) is also higher compared to PCL ( $M_w = 40\,400\text{ g mol}^{-1}$ ). The above-mentioned facts might contribute to a much higher mobility of PCL compared to SAN at the PD temperature (90 °C). Thus, it is possible that PCL molecules diffuse into SAN particles faster than the SAN molecules are leaving, and this would result in a swelling of the SAN particles.

With regards to phase separation, the existence of a scattering peak that is moving to lower values of the scattering angle (as shown in Figure 5.8) indicates that demixing proceeds via a SD mechanism.

As noted above, and described by Eq. (5.14), during the early stage of SD the intensity should increase exponentially with time, and this was indeed observed (see Figure 5.14). By using natural logarithms of intensity, the plot will yield straight lines during the initial stage, after which the growth (or decay) rate  $R(q)$  of concentration fluctuations can be estimated from the initial slope of a  $\ln(I_{vv})$  versus  $t$  plot (shown in Figure 5.16 for phase separation, and in Figure 5.15 for phase dissolution) for different angles (or  $q$  values).

After such detailed analysis, it is possible to calculate the  $R(q)/q^2$  versus  $q^2$  plot, as it is shown in Figure 5.16 for SD and Figure 5.17 for PD, for various temperatures. The apparent diffusion coefficient  $D_{app}$  is defined by Eq. (5.19), and can be

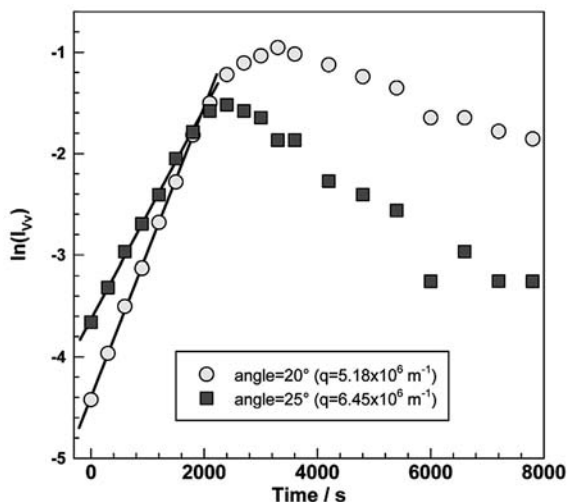


**Figure 5.14** Change of  $\ln(I_{vv})$  in time during spinodal decomposition at 130 °C (from light scattering). Evaluation of slopes for various angles.

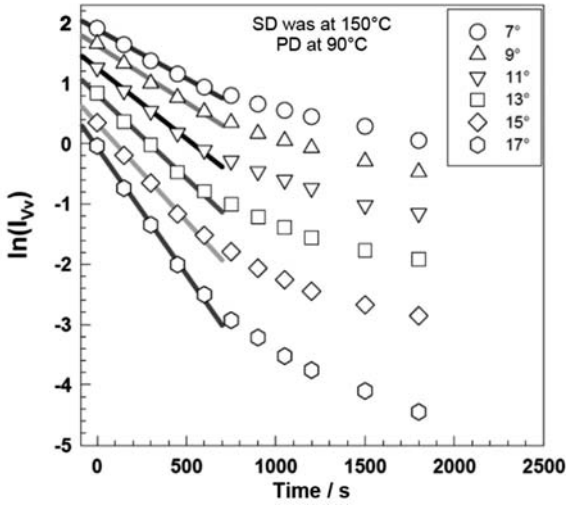


Figure 5.15 Change of  $\ln(I_{vv})$  in time during phase dissolution at 90 °C (from light scattering). Evaluation of slopes for various angles.

obtained from the  $R(q)/q^2$  versus  $q^2$  plot as the intercept of the  $R(q)/q^2$  axis in Figures 5.16 and 5.17.

The apparent diffusion coefficient  $D_{app}$  obtained in this way was positive for phase dissolution, and negative for phase separation. It is interesting to compare the absolute values of  $D_{app}$  for SD and PD in one plot (see Figure 5.18).

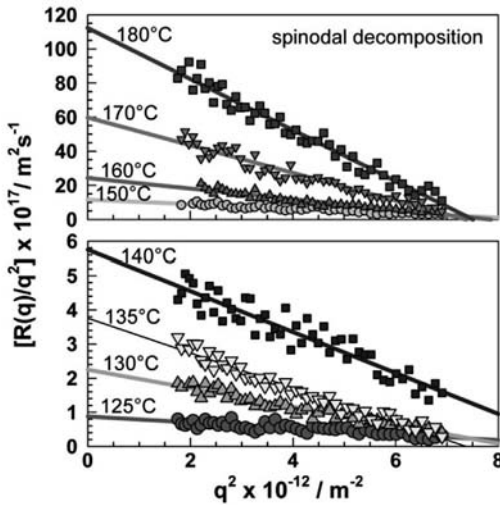


Figure 5.16 Plot of  $R(q)/q^2$  versus  $q^2$  of PCL/SAN-27.5 (80/20) blend: spinodal decomposition at 125–180 °C.  $R(q)$  values were obtained by an analysis of the slopes shown in Figure 5.10.

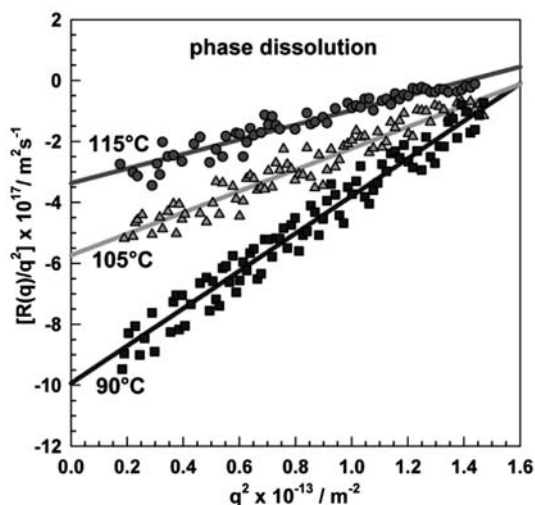


Figure 5.17 Plot of  $R(q)/q^2$  versus  $q^2$  of PCL/SAN-27.5 (80/20) blend; phase dissolution at 90, 105, and 115 °C after previous spinodal decomposition at 150 °C for 15 min.

The  $D_{app}$  for phase dissolution was found to have values between 3 and  $11 \times 10^{-17} \text{ m}^2 \text{ s}^{-1}$  over the temperature range of 50 to 115 °C. Closer to LCST, the values decrease; they are also low in the range of 50–65 °C. The diffusion should be slower at a lower temperature due to a lower mobility. In the present case, the presence of a virtual UCST of about 40 °C, as was found earlier for similar

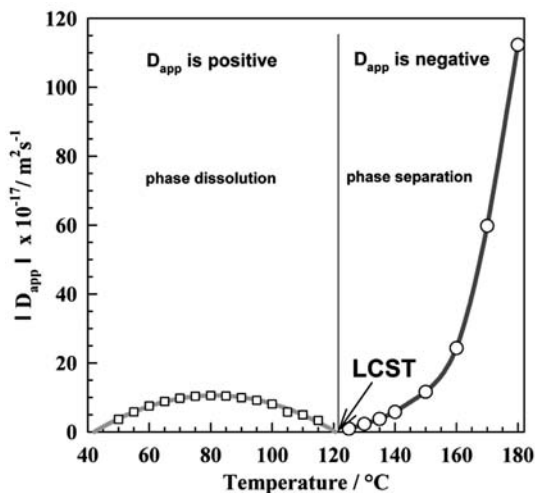


Figure 5.18 Apparent diffusion coefficient for phase dissolution (squares) and phase separation (circles) as a function of annealing temperature. The lower critical solution temperature (LCST) is shown by the arrow.

systems [29], should cause the decrease in  $D_{app}$ . Comparable values of  $D_{app}$  for phase separation (but of opposite sign, i.e., negative values) were found in the temperature range of 125 to 150 °C. By further increasing the temperature the SD would proceed much more quickly, an example being value of  $D_{app}$  at 180 °C which was more than 10-fold higher than the fastest phase dissolution. From the exponential-like curve, it could be assumed that this difference would most likely be even higher (perhaps 100-fold or even 1000-fold) if the temperature were to be increased to, for example, 200–220 °C.

#### 5.5.7

#### Crystallization Kinetics by Optical Microscopy and by $H_v$ Light Scattering

The specimens were forced to undergo demixing into different levels, which was evaluated quantitatively by using the  $V_v$  light-scattering technique described above, and then crystallized by quenching to a temperature below  $T_m$ . The starting point of the kinetics analysis was the crystallization of PCL/SAN-27.5 (80/20) from the homogeneous state (one phase), achieved by annealing the sample at 100 °C for 1 min. After annealing, the sample was transferred to another hot stage at 40 °C, where the time development of spherulites was observed using optical microscopy. An example of the growth of spherulites over time is shown in Figure 5.19 (a plot of the spherulite radius versus time of crystallization is shown in Figure 5.21). As the size and shape of spherulites differed slightly, values for about three spherulites were averaged. Typically, a linear dependence was always obtained, with the slope of the line being equivalent to the spherulite growth rate,  $G$ .

The samples were also forced to undergo SD to different levels, represented by different times of SD at 150°, and then quenched to a crystallization temperature of 40 °C. An example of spherulite growth from these phase-separated structures is shown in Figure 5.20. The first observation led to the conclusion that, after SD, the number of small spherulites would be higher, implying a greater number of nucleation centers. The size of the spherulites was clearly larger than the size of the domains, which meant that crystallization had proceeded via the PCL-rich matrix, somehow ignoring the obstacles represented in this case by SAN-rich domains. Quantitative and more detailed conclusions are difficult to draw using only optical microscopy, and consequently both light-scattering and TEM imaging were applied for this purpose (as will be described later). The variations in spherulite radius are plotted in Figure 5.21. where, again, the growth was linear with time. The growth rate appeared to be accelerated by SD, in that the further SD proceeded the faster was the crystallization. Although crystallization did not proceed in SAN-rich domains, it was not stopped at the SAN-rich borders, due to the interconnectivity of the PCL-rich phase; rather, it proceeded in the PCL-rich phase. As shown in Figure 5.22, the crystallization kinetics was accelerated during the early and middle stages of SD. With increasing SD time, the crystallization kinetics  $G$  increases; the reason for this is an increased concentration of PCL in the PCL-rich regions. On the other hand,  $G$  is almost constant with demixing time in the late stage of SD, mainly because there was no further evolution of

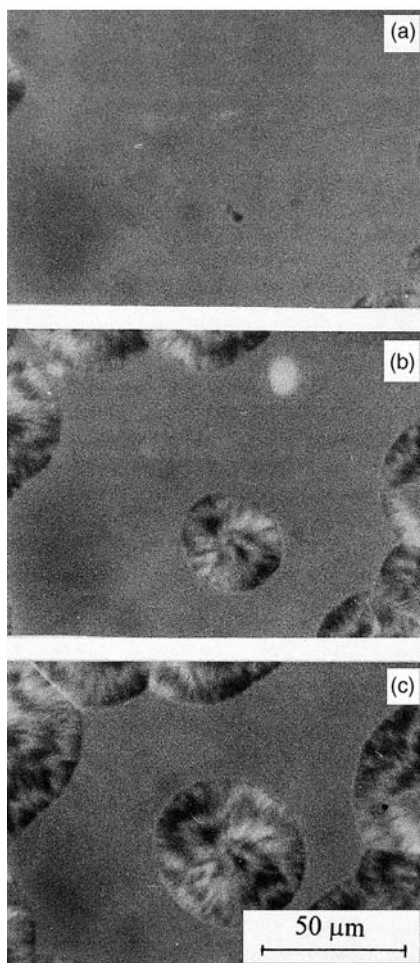


**Figure 5.19** Optical micrographs of PCL/SAN-27.5 (80/20) blend that was heated in the one-phase region (100 °C for 1 min) and then quenched to the crystallization temperature (40 °C). Spherulite growth times: (a) 14 min; (b) 26 min; (c) 34 min.

concentration fluctuations at the late stage of SD (only  $\Lambda_m$  increases in line with the demixing time).

One other interesting phenomenon is the ordering of the PCL lamellae inside spherulites. However, a greater understanding of this situation can be acquired by applying  $H_v$  light scattering in association with TEM imaging.

$H_v$  light scattering represents a powerful technique for investigating crystallization in polymer blends. The main advantage of the technique is that, compared to optical microscopy – for which only a limited number of spherulites can be chosen –  $H_v$  light scattering can provide information on the whole system.



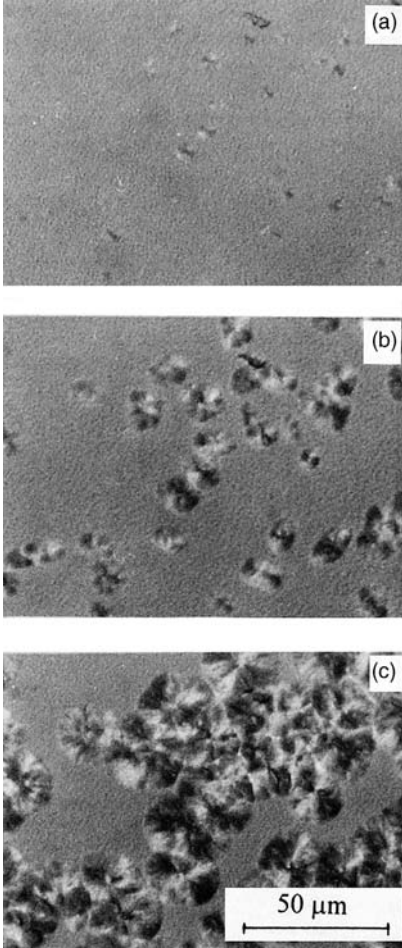


**Figure 5.20** Optical micrographs of PCL/SAN-27.5 (80/20) blend that was heated in the one-phase region ( $100^{\circ}\text{C}$  for 1 min), phase-separated for 40 min at  $150^{\circ}\text{C}$ , and then finally crystallized at  $40^{\circ}\text{C}$ . Time of development: (a) 2 min; (b) 4 min; (c) 8 min.

For this study, a crystallization temperature of  $40^{\circ}\text{C}$  was chosen. The observed scattering patterns were of the four-leaf-clover type similar to that shown in Figure 5.3, but the clover patterns became smaller with time of crystallization. Figure 5.23 shows the one-dimensional  $H_v$  scattering profiles at an azimuthal angle of  $45^{\circ}$  for a sample crystallized after 20 min of SD. The average radius of the spherulites  $R_{Hv}$  can be calculated from the position of the maximum in scattering intensity,  $\theta_m$ , by using Eq. (5.20). In order to discuss the time variation of the internal spherulitic structure, it is convenient to employ the scattering profiles at an azimuthal angle  $45^{\circ}$  using a reduced scattering angle,  $w$  (see Eq. (5.21)). By using  $w$ , the scattering profiles are corrected to the reduced profiles with the peak maximum at  $w=4$ , as shown in Figure 5.24. The sharpness of the peaks is different for the samples with different

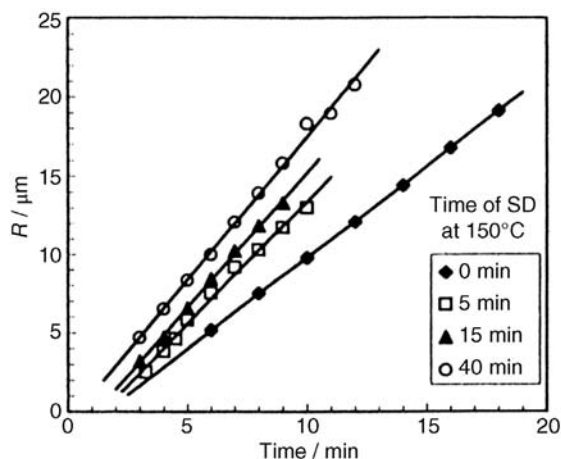


**Figure 5.21** Variation of spherulite radius  $R$  with crystallization time for PCL/SAN-27.5 (80/20) at 40°C by optical microscopy. Comparison is made for sample crystallized from the one-phase region (0 min) with samples that have undergone different times of spinodal decomposition (SD) at 150°C.

times of SD. An increased radial disorder leads to an increased relative  $I_{Hv}$  scattered intensity at angles larger than that of the maximum. In order to compare quantitatively the order inside the spherulite, it is convenient to define a so-called order parameter ( $Pr$ ) (see Eq. (5.22)); the situation is shown schematically in Figure 5.24, while how  $Pr$  changes during crystallization is shown in Figure 5.25. At the start of crystallization, ordering inside the spherulite is higher, but it then decreases and

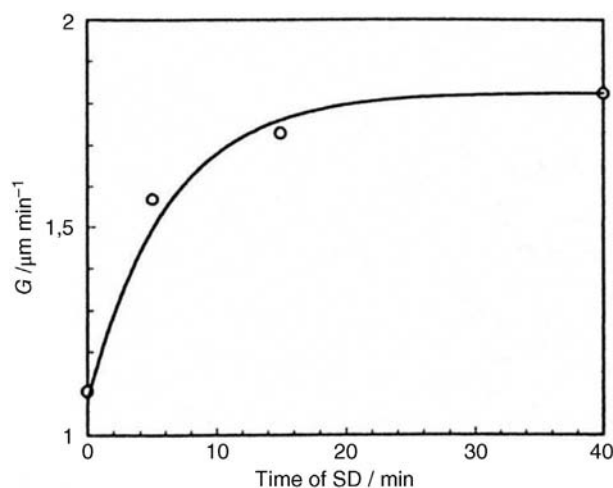


**Figure 5.22** Growth rate ( $G$ ) of spherulites at 40°C versus time of spinodal decomposition (SD) at 150°C.

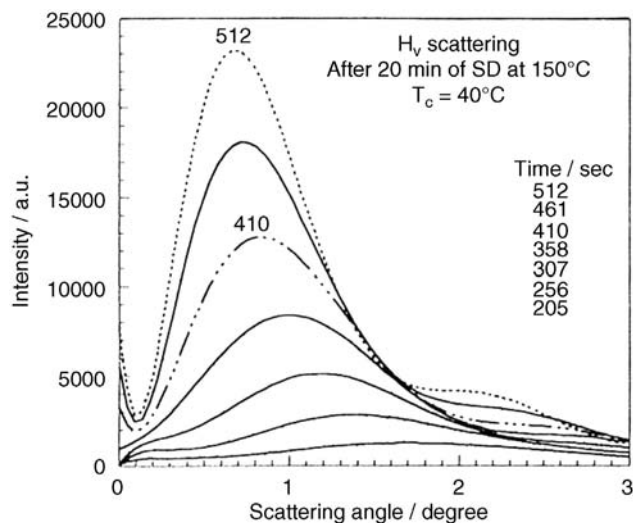


**Figure 5.23** Change of  $H_v$  scattering profiles with time after quenching the PCL/SAN-27.5 (80/20) blend to 40°C after 20 min of spinodal decomposition at 150°C. Azimuthal angle  $\mu = 45^\circ$ .

remains at an almost constant level. This behavior was observed for the sample crystallized from the homogeneous phase, and also for samples crystallized after different times of SD.

The explanation for this phenomenon is that, at the start of crystallization, the lamellae of PCL grow from the center of the spherulite in a radial direction, such that  $Pr$  is high. However, after a short time branching begins in regions where the PCL concentration is lower, and this causes a decrease in  $Pr$ . The radial growth

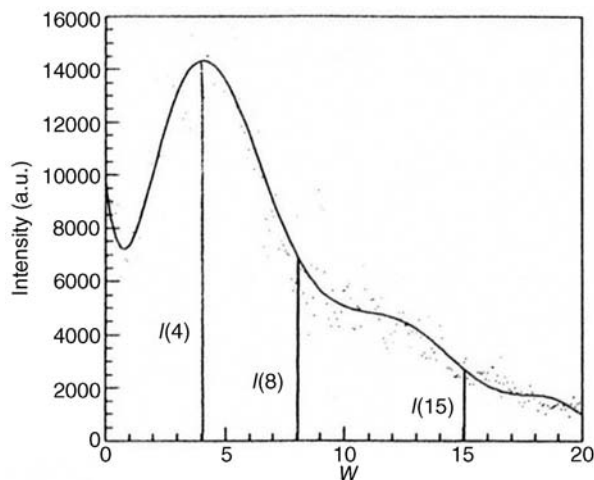


**Figure 5.24** Schematic picture of determination of order parameter  $I(4)/I(8)$  and  $I(4)/I(15)$ .

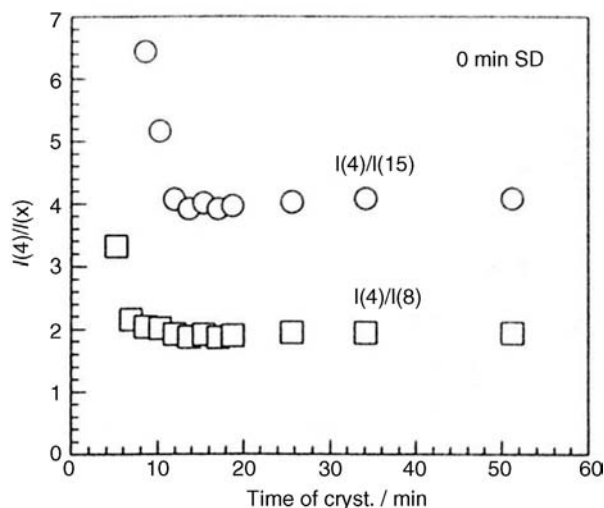


**Figure 5.25** Order parameter versus time of crystallization at 40 °C for (80/20) blend quenched from homogeneous state (100 °C for 1 min).

and branching then reach an equilibrium, so that  $Pr$  becomes constant; this constant value was used to compare samples crystallized from different stages of SD (as shown in Figure 5.26).

In Figure 5.26, two values of  $Pr - I(4)/I(8)$  and  $I(4)/I(15)$  – are plotted as a function of time of SD at 150 °C. All samples were crystallized at a constant temperature

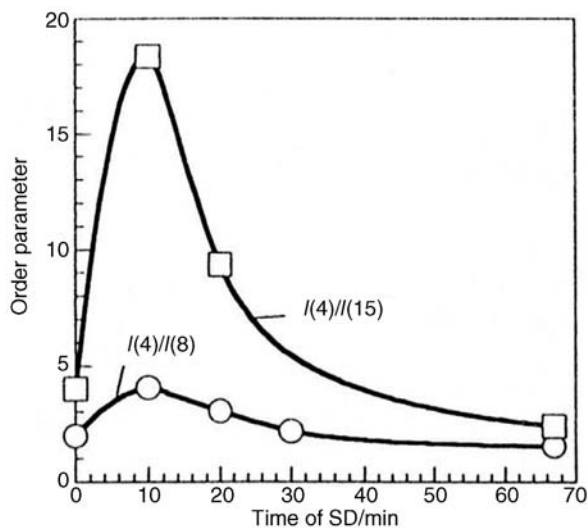


**Figure 5.26** Order parameter versus time of spinodal decomposition (SD) at 150 °C.

of 40 °C. Regardless of which  $Pr$  is considered, an interesting phenomenon emerged whereby,  $Pr$  initially increased (in about 10 min) but then slowly decreased with increasing time of SD. By using the  $V_v$  light-scattering analysis at 150 °C, it is possible to identify a change from the middle to late stages of SD at about 10 min. From the data in Figure 5.26, it is apparent that ordering of the spherulites is increased for samples crystallized after SD in the early and middle stages. However, by the late stage  $Pr$  decreases continually with increasing time of SD.

In order to better understand this phenomenon, however, it was necessary to perform a TEM analysis, for which the following samples were chosen. All samples had the same blend composition PCL/SAN-27.5 (80/20) and were crystallized at 40 °C for 14 h after a different prior history. The first sample (Figure 5.27) was crystallized from the homogeneous phase attained by annealing the sample at 80 °C for 1 min. In this case, the lamellae were short and oriented in many directions, in contrast to the radial growth of spherulites. It appeared that the SAN was partly segregated from the growing front, and partly remained in an amorphous mixture with PCL between the PCL lamellae. As  $RuO_4$  “stains” benzene rings (i.e., SAN), the broad dark region might represent areas where the concentration of SAN had increased due to segregation during crystallization. On many occasions the lamellae terminate in these areas and begin to grow in new directions, which could explain the low  $Pr$  value.

Three additional samples with different degrees of phase separation (Figure 5.28, 5 min; Figure 5.29, 15 min; Figure 5.30, 40 min) were also examined, and a clear two-phase system could be seen in all three cases. In Figure 5.28, which represents 5 min of SD (middle stage), the lamellae are highly oriented in one direction, which corresponds to a high  $Pr$ . An interesting phenomenon in this case is that the lamellae grow through the SAN-rich areas (dark) without any change of direction; moreover, the number of lamellae in these areas is, as expected, smaller because of the lower concentration of PCL in these SAN-rich areas. In Figure 5.29, the system phase had been separated for 15 min before

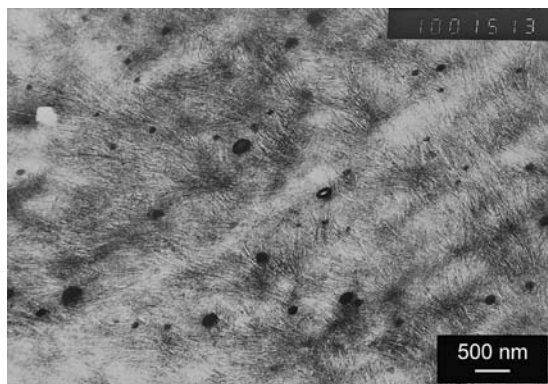


**Figure 5.27** TEM image of PCL/SAN-27.5 (80/20) sample crystallized at 40 °C for 14 h after this history: 80 °C for 1 min.

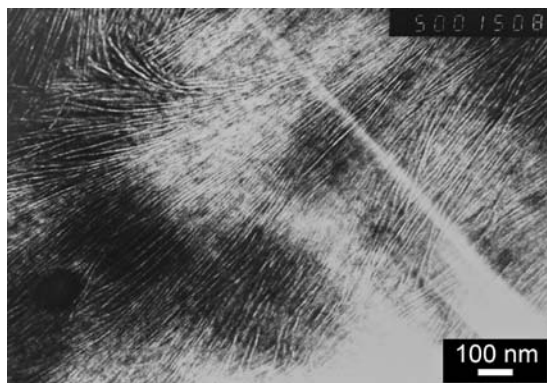


**Figure 5.28** TEM image of PCL/SAN-27.5 (80/20) sample crystallized at 40 °C for 14 h after this history: 100 °C for 1 min, 150 °C for 5 min.

crystallization (late stage), and the concentration inside the SAN-rich domains had already reached an equilibrium value. The difference here is the size of the SAN-rich domains, which are larger. As the PCL concentration inside the SAN-rich domains crosses the critical level that would allow crystallization, the lamellae are unable to penetrate these domains, probably due to a mobility effect. The  $T_g$  of these domains is probably higher than the crystallization temperature, and the mixture of PCL and SAN becomes frozen inside these domains. The alignment of lamellae in the PCL-rich matrix is rather high, which corresponds with a high  $Pr$ -value. The growth of spherulite continues through the bridges between the SAN-rich domains.

The last sample (Figure 5.30) had undergone 40 min of SD (again, the late stage), and the size of the domains had gradually increased. The difference compared to Figure 5.29 is that the alignment of lamellae is much worse, with

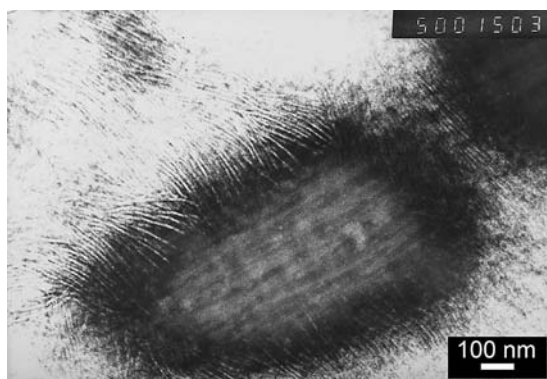


**Figure 5.29** TEM image of PCL/SAN-27.5 (80/20) sample crystallized at 40 °C for 14 h after this history: 100 °C for 1 min, 150 °C for 15 min.

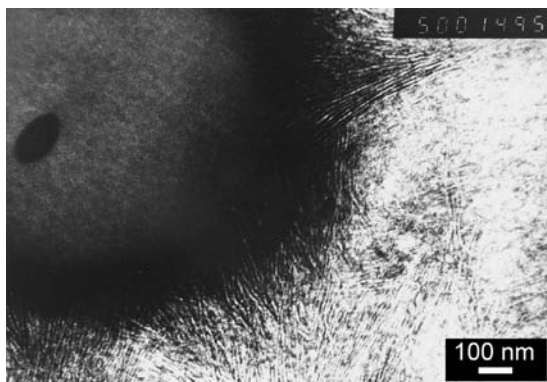


**Figure 5.30** TEM image of PCL/SAN-27.5 (80/20) sample crystallized at 40 °C for 14 h after this history: 100 °C for 1 min, 150 °C for 40 min.

lamellae growing in all directions, which corresponds to a lower  $Pr$ -value. In both cases (Figures 5.29 and 5.30), the surface of the SAN-rich domain is darker, which suggests that the SAN concentration in this interface is higher than that inside the domain. This situation could be explained by the crystallization of almost all the PCL from this area, while the SAN remained. Inside the domains, the concentration of amorphous PCL was higher than at the surface of the domains.

In the SAN-rich phase, the crystallization growth rate is much slower (crystallization may even be prevented by the mobility effect) than in the PCL-rich phase. This is due to an increasing  $T_g$  of the blend when the SAN content is increasing (the  $T_g$  of pure PCL is ca.  $-60^\circ$ , while that of SAN is ca.  $105^\circ\text{C}$ ). However, as the PCL-rich phase is highly interconnected, the lamellae will grow much faster in this phase, somehow ignoring the slow SAN-rich domains. At this blend composition (PCL/SAN 80/20), the growth of large spherulites is not prevented by SD; rather, due to the formation of a PCL-rich phase during SD, the SAN concentration in this phase will gradually decrease to an equilibrium value; as a consequence, the  $T_g$  of the phase will decrease, resulting ultimately in a higher rate of crystallization.

The PCL/SAN-27.5 blend provided an excellent opportunity to investigate phase dissolution kinetics and to add some experimental data (that are still quite rare) to this subject. First, attention was focused on phase separation above LCST (at  $122^\circ\text{C}$ ), and examined this qualitatively with optical microscopy (at  $130^\circ\text{C}$ ) and then quantitatively by light scattering at various temperatures ( $125$ – $180^\circ\text{C}$ ). The SD mechanism of phase separation was confirmed by a detailed data analysis based on Cahn–Hilliard theory. Second, the phase-separated structure was quenched to various temperatures below LCST ( $50$ – $115^\circ\text{C}$ ) to study phase dissolution. The latter was affected by the temperature of previously performed SD and, based on light-scattering data, a model of phase dissolution mechanism was created. Several possible interpretations exist to explain the shift in the peak maximum during phase dissolution, one of which is a faster decay of the high- $q$

Fourier components in the concentration pattern. Only those slower components with long wavelengths (small  $q$ ) will survive for longer times, and this results in an effective peak shift towards small  $q$  (small angles) during the dissolution process. Again, for PD it was possible to use linearized theory to obtain an apparent diffusion coefficient  $D_{app}$ . Finally, when the  $D_{app}$  values were compared for SD and PD, the fastest PD was seen to be about 10-fold slower than the fastest SD over a measured temperature range.

By using optical microscopy, the crystallization kinetics was observed for samples crystallized after decomposition into different stages of SD. A major acceleration of the crystallization kinetics was observed for samples that had undergone SD in the early and middle stages. This can be explained by a gradual change of concentration in the PCL-rich domains. However, during the late stage the concentration reaches an equilibrium value and the crystallization kinetics reach almost constant level.

The  $H_v$  light-scattering technique enabled a quantitative evaluation of the ordering of PCL lamellae inside the spherulites which, in the present case, were always bigger than in the phase-separated domains. The results of this analysis indicated that the radial ordering of lamellae would be increased for samples crystallized after SD to the early and middle stages, but this would gradually decrease in the case of samples separated to the late stage of SD.

The TEM images explained the rather surprising results of the previous analysis. In samples crystallized from the homogeneous phase the ordering of lamellae was rather poor, and SAN was probably partly segregated during crystallization. However, when the amount of segregated SAN exceeded a certain level the lamellae began to grow in new directions. For samples crystallized after separation to the middle stage of SD, ordering of the lamellae was much higher, and they grew through the SAN-rich areas without changing direction. For samples crystallized after SD to the late stage, the PCL lamellae could not penetrate the SAN-rich domains, and crystallization was halted at the borders of the SAN-rich domains. As the PCL-rich phase is interconnected, crystallization can proceed through bridges between SAN-rich domains; lamellae growth would then continue by branching which, of course, would decrease the radial ordering of lamellae inside the spherulite. Notably, the more decomposition proceeded, the less ordered were the lamellae.

#### 5.5.8

#### Competition of Phase Dissolution and Crystallization

The variation of  $\Lambda_m$  in time for PCL/SAN-27.5 blends at a temperature of 150 °C is plotted in Figure 5.10. Here, the values of  $\Lambda_m$  can be used to design the desired size of domains.

Initially, the early stage of SD was chosen to observe differences in structure after annealing isothermally below  $T_m$  at three different temperatures. TEM images of the annealed samples are shown in Figure 5.31 and, depending on the annealing temperature ( $T_a$ ), the final structures were very different. In Figure 5.31a



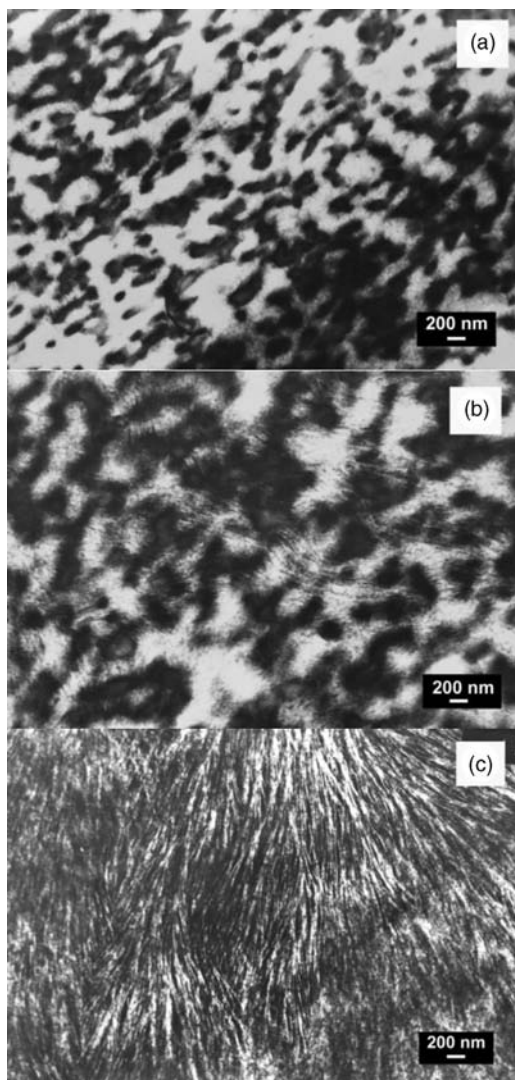


**Figure 5.31** TEM images of PCL/SAN-27.5 (80/20) blend after SD at 150 °C for 3 min, followed by annealing at lower temperatures. (a) 40 °C; (b) 45 °C; (c) 51 °C.

( $T_a = 40\text{ }^{\circ}\text{C}$ ), an SD structure with a periodic distance of  $0.4\text{ }\mu\text{m}$  was preserved. However, after annealing at a higher temperature ( $T_a = 45\text{ }^{\circ}\text{C}$ ) the structure had a longer periodic distance (Figure 5.31b); also evident was the presence of a gray gradient between the dark and bright regions, which suggested an appreciable progress of PD. In Figure 5.31c, a completely different structure of the sample annealed at a higher temperature, close to the  $T_m$  of PCL ( $T_a = 51\text{ }^{\circ}\text{C}$ ) for a long time (three days), could be seen. In this case, the SD structure had completely

disappeared, which suggested that PD had been completed and crystallization had proceeded in the single-phase mixture.

The results in Figure 5.31 suggest that both PD and crystallization occur at low temperatures, below  $T_m$  ( $<LCST$ ). This point was justified by TEM observations of a specimen after a longer period of SD, chosen to achieve a higher degree of SD (Figure 5.32). A typical SD structure was apparent at lower magnification (Figure 5.32a); however, at higher magnification of the same structure (Figure 5.32b), the dark region (due to  $RuO_4$  “staining” of the phenyl ring) could be assigned to the SAN-rich region, the bright matrix to the PCL-rich region, and thin bright stripes to the PCL crystal lamellae. The lamellae were seen clearly only at the edge of SAN-rich domains. Taken together, these results may suggest that the core of the domain would be a single-phase mixture vitrified without crystallization, probably resulting from the lower mobility of the PCL chains in the high- $T_g$  region of high SAN content. Contrast between the stripes would become weaker at the outer edge, and be too faint to be clearly visualized in the matrix. Bearing in mind that this striped pattern results from a deep staining of SAN segregated between the PCL lamellae, the gradient of stripes may correspond to a concentration gradient that is created by PD before crystallization.

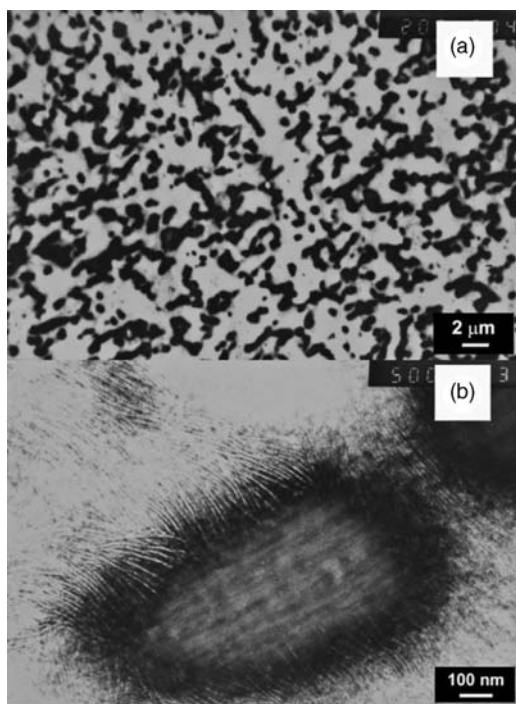


**Figure 5.32** TEM images of PCL/SAN-27.5 (80/20) blend after SD at 150 °C for 15 min, followed by annealing at 40 °C for 14 h.; (a) Low magnification ( $\times 2000$ ); (b) High magnification ( $\times 50\,000$ ).

A quantitative discussion of the competition of crystallization and PD was made possible by an analysis of the light-scattering data.  $V_v$  scattering is sensitive to both PD and crystallization, whereas  $H_v$  detects only crystallization. In order to discuss the kinetics, it is convenient to use the invariant  $Q$ , that is, the integrated scattering intensity [30]

$$Q = \int_0^{\infty} I(q) q^2 dq \quad (5.23)$$

where  $q$  is the scattering vector mentioned above, and  $I(q)$  is the intensity of scattered light at  $q$ . The  $H_v$  invariant  $Q_{H_v}$  is described by the mean-square optical anisotropy  $\langle \delta^2 \rangle$  (proportional to volume fraction of spherulites) and  $Q_{V_v}$  is ascribed to both  $\langle \delta^2 \rangle$ , and the mean-square density fluctuation  $\langle \eta^2 \rangle$ . The results are shown in Figure 5.33. Here, the specimen underwent first a phase separation at 150 °C for 3 min, followed by a temperature drop to two lower temperatures: 33 °C and 46 °C. In case of 33 °C (Figure 5.33a), both  $H_v$  and  $V_v$  invariants increased rapidly, implying that the crystallization takes place very quickly but that

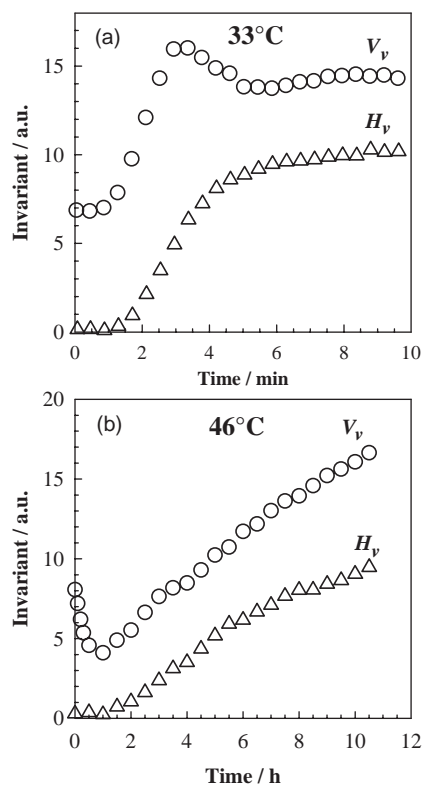


**Figure 5.33**  $V_v$  and  $H_v$  invariants of blend decomposed at 150 °C for 3 min, as a function of time after temperature drop to: (a) 33 °C and (b) 46 °C.

PD barely proceeds. The PD was most likely prevented by the rapid formation of crystal lamellae. In contrast, at 46 °C (Figure 5.33b), there was a decrease in the  $V_v$  invariant at an early stage, followed by slow increases in  $V_v$  and  $H_v$  (note that the x-axis in Figure 5.33b is in hours, while that in Figure 5.33a is in minutes). This suggests that PD initially occurs, rendering a one-phase mixture, and then crystallization follows. Thus, crystallization prevails over PD at low temperatures (Figure 5.33a), while dissolution proceeds followed by crystallization at high temperatures (close to  $T_m$ ; see Figure 5.33b). Which of these processes ultimately occurs will depend most likely on the crystallization temperature.

Such competition may also depend on the degree of SD before the temperature drop. In Figure 5.34, four samples were phase-separated to different levels of SD depending on the period of SD time at 150 °C. All samples showed a decrease in  $V_v$  invariant from the start, implying the progress of PD, followed by increases in both  $V_v$  and  $H_v$  invariants, implying subsequent crystallization. The longer the SD time, the later was the onset of  $V_v$  invariant growth, whereas the onset of  $H_v$  invariant was seen after about 2 h for all samples. These results suggest that the situation for the samples after short SD periods (3 and 15 min) is similar to that

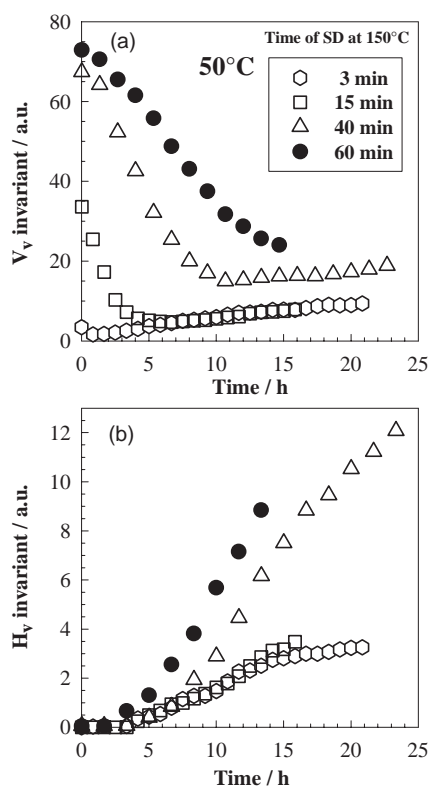


**Figure 5.34** Change in invariant with time after temperature drop to 50 °C, after different times of SD at 150 °C (3, 15, 40 and 60 min). (a)  $V_v$ ; (b)  $H_v$ .

in Figure 5.33b; that is, PD proceeds, followed by crystallization. In contrast, when samples are phase-separated for longer periods (40 and 60 min), it is clear that PD and crystallization are competing. In the former cases (short SD time), there was no significant difference in the increase of  $H_v$  invariant, which probably suggests that crystallization occurs in a single-phase mixture after the completion of PD in both samples. In the latter cases (long SD time), crystallization can proceed quickly in a well-demixed PCL-rich phase (with low SAN concentration as impurity). A longer SD time may yield a lower SAN content in the PCL-rich region, and hence crystallization should be faster (compare  $\Delta$  and  $\bullet$  in Figure 5.34b); however, the dissolution should be slower (compare  $\Delta$  and  $\bullet$  in Figure 5.34a), as the SD has already reached the later stage of SD, yielding a longer spacing of SD structure and a higher SAN content in SAN-rich regions (with the higher  $T_g$ ).

From the increase in  $H_v$  invariant with time (see Figure 5.35) after a temperature drop from 150 °C, it is possible to estimate the rate of crystallization; for example,  $\tau_{1/2}^{-1}$ , where  $\tau_{1/2}$  is the time required to reach half of the invariant's maximum level. The rate of crystallization described by  $\tau_{1/2}^{-1}$  as a function of crystallization temperature is plotted in Figure 5.36; notably, crystallization is faster at lower temperatures.

The two rate-related constants  $\tau^{-1/2}$  and  $D_{app}$  are plotted in Figure 5.37 as functions of temperature ( $T_a$ ). The apparent diffusion coefficient  $D_{app}$  curve exhibits a maximum at about 80 °C, but at LCST (122 °C) the  $D_{app}$  is thought to have a zero value. At a lower temperature, the thermodynamic driving force for PD should be stronger, and so a faster PD is expected. At much lower temperatures, chain mobility should be decreased when approaching  $T_g$ . Another possibility for a decrease in  $D_{app}$  with decreasing temperature is the presence of a virtual UCST, at which  $D_{app}$  should be zero. Nevertheless, there is a certain temperature range (44–50 °C), over which the competition between crystallization and PED can be clearly seen. For the results shown in Figure 5.33a, PD does not occur at low temperature (30 °C), and the rapid crystallization will suppress dissolution. However, the

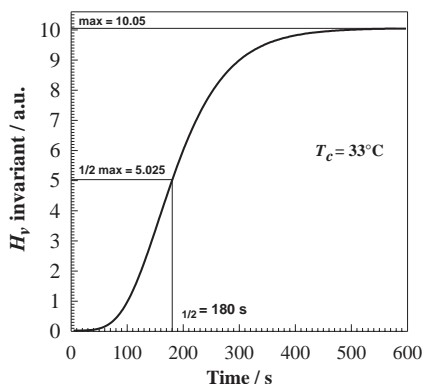


**Figure 5.35** Change of  $H_v$  invariant in time at 33 °C. Evaluation of  $\tau_{1/2}$ , the half-time of crystallization, as a time necessary to reach one-half of the maximum height of the  $H_v$  invariant.

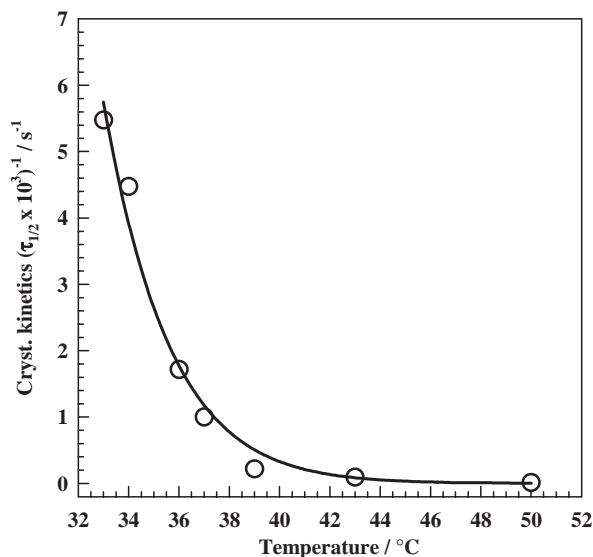


**Figure 5.36** Half-time of crystallization  $\tau_{1/2}$  as a function of the crystallization temperature.

possible existence of a virtual UCST could also make PD impossible, for thermodynamic reasons. Such behavior has been observed in the past for a PCL/SAN-26.4 blend with a virtual UCST of about 35 °C [29].

The results of optical microscopy observations, TEM imaging and light scattering, mainly for samples phase-separated at an early stage of SD, are summarized in Table 5.1. At high temperatures, very long induction period (many hours) were observed before crystallization commenced, providing sufficient time for PD to be completed. At low temperatures, however, the crystallization was very fast (a few minutes) and the SD structure was pinned by the growing spherulites. Only at intermediate temperatures was it possible to observe competition between the two processes.

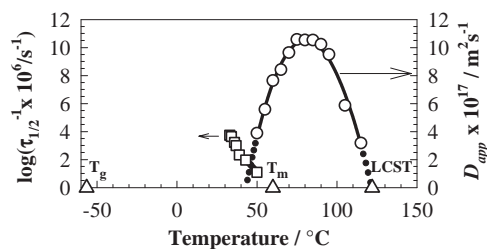


**Figure 5.37** Crystallization rate constant  $\tau_{1/2}^{-1}$  (□) and the apparent diffusion coefficient for dissolution as a function of annealing temperature (○). Triangles show  $T_g$ ,  $T_m$ , and LCST temperatures.

**Table 5.1** Three temperature ranges: summary.

Temperature range 1 (30–43 °C)	Temperature range 2 (44–50 °C)	Temperature range 3 (51–55 °C)
Very fast crystallization $G = 100\text{--}3000 \mu\text{m h}^{-1}$ $2\text{--}50 \mu\text{m min}^{-1}$	Slower crystallization $G = 1\text{--}50 \mu\text{m h}^{-1}$ $0.1\text{--}1 \mu\text{m min}^{-1}$	Extremely slow crystallization $G = 0.1\text{--}1 \mu\text{m h}^{-1}$
Phase dissolution is very slow $0.1\text{--}1 \mu\text{m h}^{-1}$	Phase dissolution is a little faster, around $1 \mu\text{m h}^{-1}$	Phase dissolution is faster, around $1\text{--}21 \mu\text{m h}^{-1}$
Crystallization is faster than phase dissolution, and crystals pin the phase-separated structure so that phase dissolution cannot occur	Phase dissolution is competing with crystallization	Extremely long induction period of crystallization; Before crystallization starts, phase dissolution finishes
Main process: crystallization	Competition	First phase dissolution, second crystallization

A PCL/SAN-27.5 blend provided an excellent and rare opportunity to investigate the competition of PD and crystallization below the  $T_m$  of PCL. Selecting different times of annealing above LCST allowed the starting SD structure to be set up. Based on results of TEM imaging and light-scattering analyses, crystallization at lower temperatures ( $<44^\circ\text{C}$ ) was much faster than the PD, while the SD structure was pinned by the rapidly growing PCL crystal lamellae. Above  $50^\circ\text{C}$ , however, crystallization was very slow and PD was completed before crystallization started. At intermediate temperatures, PD was seen to compete with the crystallization.

The less-decomposed sample dissolved more quickly, before crystallization began, whereas the highly decomposed sample dissolved partially and the SD structure was fixed by the growing crystal lamellae. A detailed study of PD kinetics using light scattering also suggested the existence of a virtual UCST phase boundary (ca.  $40^\circ\text{C}$ ), below which temperature PD would be impossible.

## 5.6

### Determination of Virtual UCST Behavior

The scattering of light caused by crystalline polymers arises in part from fluctuations in the average refractive index, and in part from fluctuations in the orientation of anisotropic entities [31]. These contributions can be quantitatively separated by applying polarized light. The contribution from anisotropic fluctuations can be detected in a  $H_v$  configuration, while contributions of density (refractive index) and orientation fluctuations are detected by a  $V_v$  configuration [30]. Time-resolved scattering profiles obtained for  $V_v$  and  $H_v$  optical alignments are

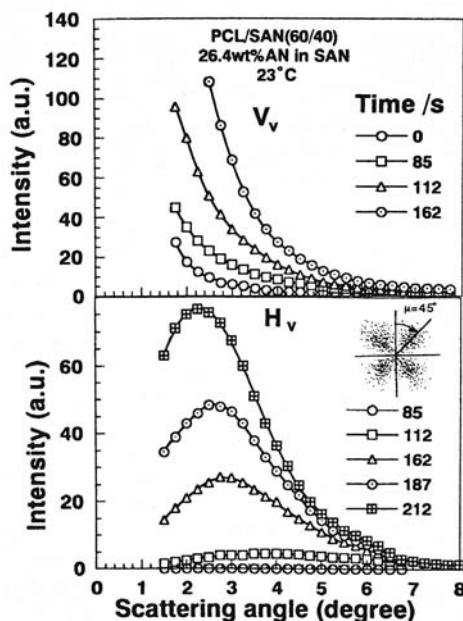


Figure 5.38 Change of  $V_v$  and  $H_v$  scattering profiles with time after quenching the PCL/SAN-26.4 (60/40) blend to 23 °C;  $H_v$  profiles are at the azimuthal angle  $\mu = 45^\circ$ .

shown in Figure 5.38. There is a significant change in the  $V_v$  profile from the start of the measurement (0 s) until 85 s, whereas the  $H_v$  profile remains at a zero level until 100 s, after which a significant increase in intensity occurs; hence, whilst the  $H_v$  profile does not change for a certain period of time, the  $V_v$  scattering increases rapidly. This implies that density fluctuations caused by two isotropic phases precede the evolution of optical anisotropy. In other words, before crystallization starts, a liquid–liquid phase separation occurs—that is, the sample seems to be crystallized below the UCST in the two-phase region.

For the quantitative evaluation of kinetics of crystallization and liquid–liquid phase separation, it is convenient to use the invariant  $Q$ , that is, the integrated scattering intensity [30] (see Eq. (5.23))

The time variations of the invariants  $Q_{Hv}$  and  $Q_{Vv}$  are plotted in Figure 5.39. The values of both invariants increase with the time of annealing;  $Q_{Hv}$  begins to increase after a certain time lag when  $Q_{Vv}$  has already reached a relatively higher level. The rapid increase in  $Q_{Vv}$  and the slow increase in  $Q_{Hv}$  after the time lag may suggest that liquid–liquid phase separation precedes crystallization. In other words, the crystallization temperature locates below the UCST, and crystallization begins when phase separation has proceeded to a certain level.

It is also possible to discuss the location of the UCST from the relative increase in  $Q_{Vv}$ , normalized by that of  $Q_{Hv}$ . The initial slope of the time variation of  $Q_{Hv}$  (the straight line tangent in Figure 5.39),  $Q_{Hv}/dt$ , is thought to represent the rate



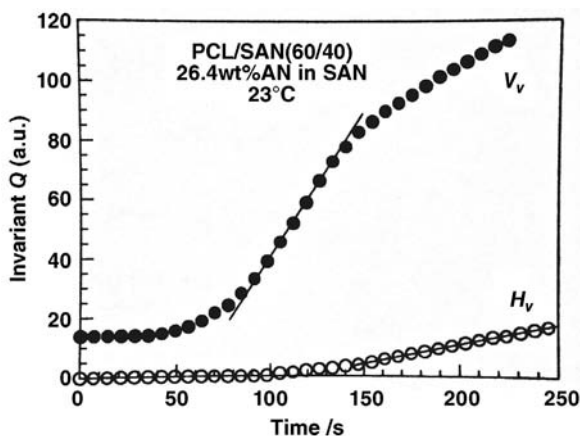


Figure 5.39 Time-dependence of  $V_v$  and  $H_v$  invariants for PCL/SAN-26.4 (60/40).

of crystallization [32] for systems without phase separation, while  $Q_{Vv}/dt$  is composed of two rates below the UCST-(1) crystallization and (2) liquid-liquid phase separation. The ratio  $(Q_{Vv}/dt)/(Q_{Hv}/dt)$  is a relative measure of the rate of the crystallization and phase separation. For neat PCL, the ratio remains constant (ca. 1) for all measured temperatures. However, a totally different situation arises after quenching the blend (Figure 5.40), when a clear discontinuity appears. At lower temperatures, the ratio exhibits a relatively large value of about 7, after which a sharp decrease occurs to about 1, and this remains constant at higher temperatures. Thus, the temperature at which the ratio deviates from 1 is the spinodal temperature ( $T_s$ ); the implication here is that above  $T_s$  only crystallization takes

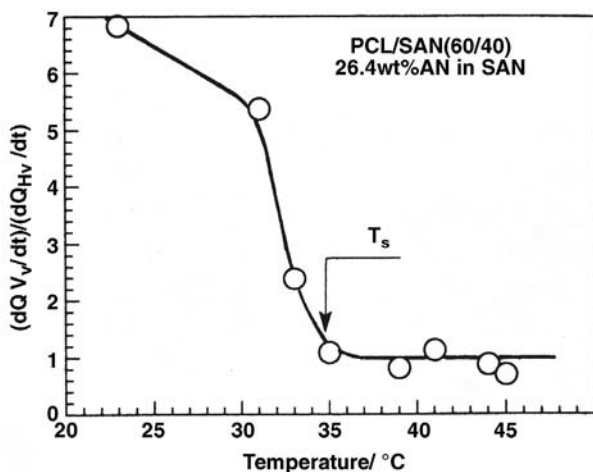
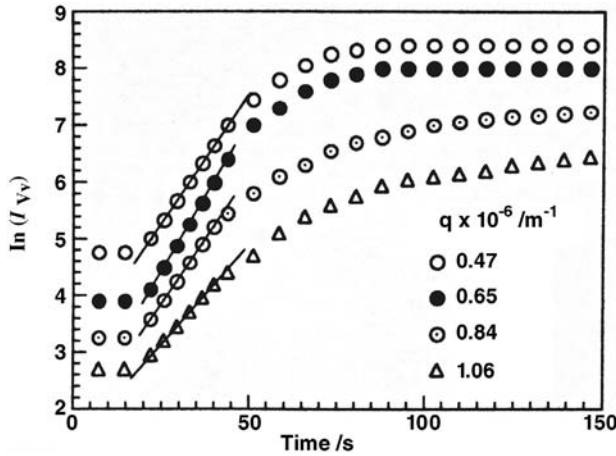


Figure 5.40 Temperature-dependence of the relative value  $(dQ_{Vv}/dt)/(dQ_{Hv}/dt)$ .



**Figure 5.41** Time-dependence of the scattered light intensity of different scattering vectors  $q$  after temperature drop to 25 °C for PCL/SAN-12.4 (60/40) blend.

place, whereas below  $T_s$  liquid–liquid phase separation proceeds, suggesting a UCST-type of phase behavior.

For further analysis of the liquid–liquid phase separation, it should be noted that at the very early stage the contribution of crystallization to the overall  $V_v$  scattering is almost zero (see Figures 5.38 and 5.39). Consequently, it is possible to discuss the details of liquid–liquid phase separation by the initial time variation of  $I_{V_v}$ , at a time window before the onset of crystallization. Below the UCST, the linear theory of SD [10] can be applied for data analysis. In the initial stage of phase separation, the intensity of the scattered light ( $I$ ) will vary exponentially with time  $t$  (see Eq. (5.14)). It is possible to estimate the growth rate  $R(q)$  for fluctuations from the initial slope of a  $\ln I$  versus  $t$  plot (Figure 5.41) for different values of  $q$ . Figure 5.42 shows the  $R(q)$  spectrum for different temperatures; for temperatures below the UCST the curves exhibit a maximum at  $q_m$ . The position of the maximum changes in line with the distance from  $T_s$ ; the dependence of  $q_m$  on the difference between the spinodal and annealing temperatures can be easily deduced.

Equation (5.24) is obtained from Eq. (5.15) in the case that  $[dR(q)/dq]$  is set to zero

$$q_m^2 = - \frac{\left( \frac{\partial^2 f}{\partial c^2} \right)}{4\kappa} \quad (5.24)$$

de Gennes theory for the SD of incompressible mixtures [33] leads to

$$\frac{\partial^2 f}{\partial c^2} = \frac{\chi - \chi_s}{\chi_s} \quad (5.25)$$

where  $\chi$  is the Flory–Huggins interaction parameter and  $\chi_s$  is the interaction parameter at the spinodal. Furthermore, it was shown that [15]

$$\frac{\chi - \chi_s}{\chi_s} \propto |T - T_s| \quad (5.26)$$

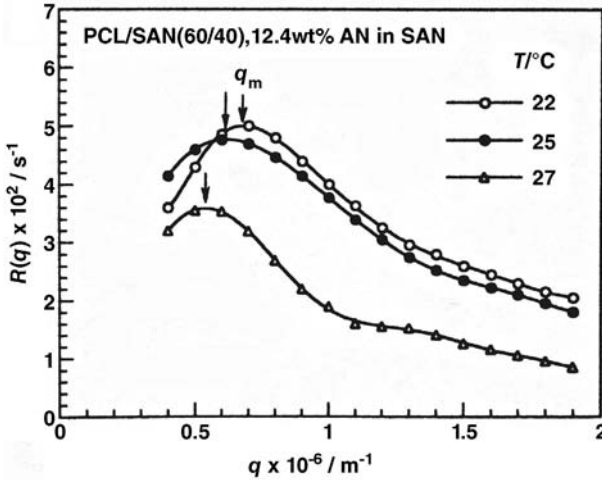


Figure 5.42 Dependence of  $R(q)$  on  $q$  for different temperatures.

From Eqs (5.24)–(5.26), it follows that

$$q_m^2 \propto |T - T_s| \quad (5.27)$$

It also follows that at the spinodal ( $T = T_s$ )

$$\left( \frac{\partial^2 f}{\partial c^2} \right)_{T,p} = q_m^2 = 0 \quad (5.28)$$

Thus, the temperature-dependence of  $q_m^2$  can be used to obtain  $T_s$ , as shown in Figure 5.43. When Eqs (5.7) and (5.8) were applied,  $T_s$  was taken as the intercept from the extrapolation of the straight line to  $q_m^2 = 0$ .

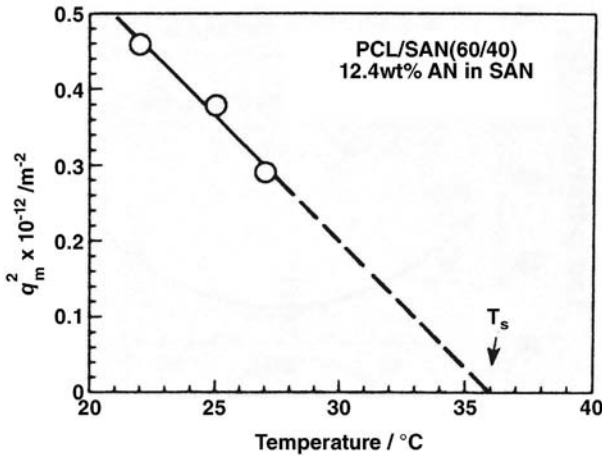
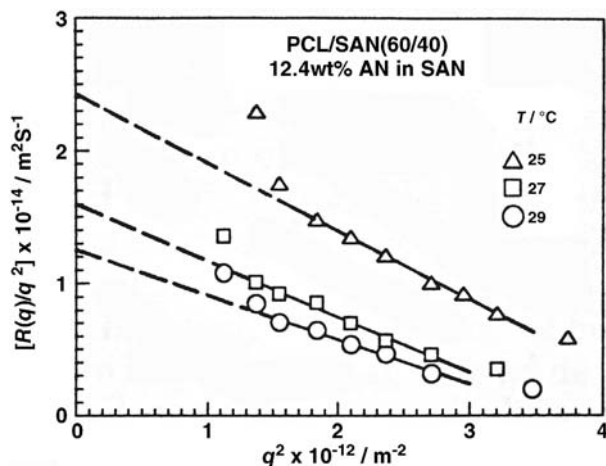


Figure 5.43 Temperature-dependence of  $q_m^2$  of a PCL/SAN-12.4 (60/40) blend.



**Figure 5.44** Plot of  $R(q)/q^2$  versus  $q^2$  for different temperatures of a PCL/SAN-12.4 (60/40) blend.

Furthermore, the spinodal temperature can be obtained from the temperature-dependence of the apparent diffusion constant ( $D_{app}$ ), which is defined by Eq. (5.19).

By using Eqs (5.15) and (5.19),  $D_{app}$  can be obtained from  $R(q)/q^2$  versus  $q^2$  plots as the intercept of the  $R(q)/q^2$  axis, as shown in Figure 5.44. Since  $M \propto T$ , according to the Stokes–Einstein equation, and because of Eqs (5.25) and (5.26), the temperature-dependence of  $D_{app}$  in the vicinity of the spinodal is given by

$$D_{app} \propto T|T - T_s| \quad (5.29)$$

The spinodal temperature can be obtained from the  $D_{app}/T$  versus  $T$  plot as the intercept of the straight line with the temperature axes (Figure 5.45), because at the spinodal temperature  $D_{app}$  is 0.

The spinodal temperatures were obtained for a fixed blend ratio (PCL/SAN 60/40) and three different copolymer compositions by using three different methods, as discussed above. All obtained values of  $T_s$  were plotted as a function of the copolymer composition (Figure 5.46), creating a UCST border of PCL/SAN blends. It is reasonable that the curve has a minimum because, according to thermodynamic calculations, the miscibility window might be a “closed” area under some circumstances [34]. An experimentally obtained LCST border and a calculated miscibility loop are also shown in Figure 5.46 [29].

TEM was applied in order to support the light-scattering methods used to determine UCST behavior. Figure 5.47a and b show TEM images of a sample crystallized at 46 °C, above the virtual UCST. A TEM image of the same sample quenched to 24 °C, below the UCST, is shown in Figure 5.47c, where the white regions are PCL-rich and the black regions are SAN-rich (the black is produced by  $\text{RuO}_4$ -staining of the phenyl ring). In Figure 5.47a and b, the white lamellae of PCL can be seen very clearly, and between them the amorphous region composed

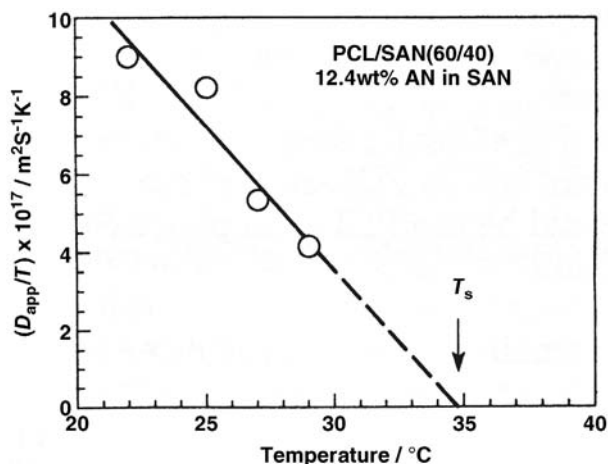


Figure 5.45 Temperature dependence of  $D_{app}/T$  for a PCL/SAN-12.4 (60/40) blend.

of a PCL/SAN mixture. This implies that crystallization of the blend had occurred above the UCST, from a homogeneous mixture. A completely different structure can be seen in Figure 5.47c, where SAN-rich domains (dark regions of ca.  $0.1 \mu\text{m}$ ) can be clearly distinguished from the continuous PCL-rich phase (which appears as a white background and contains large amounts of amorphous and crystalline PCL). The PCL lamellae cannot be detected because the amount of SAN present may be too small to provide an effective staining contrast. This structure proposes that crystallization had occurred after liquid–liquid phase separation had achieved a certain level, with the sample having been quenched below the UCST.

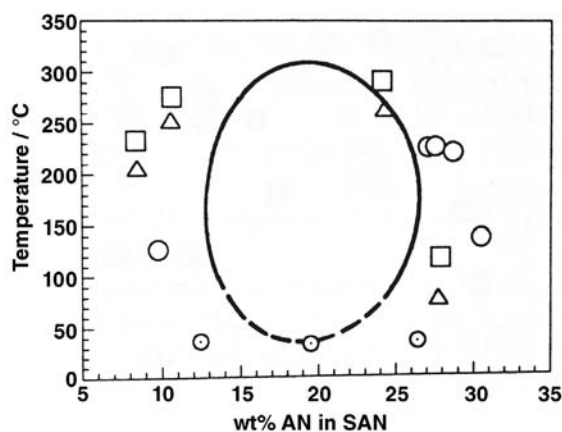
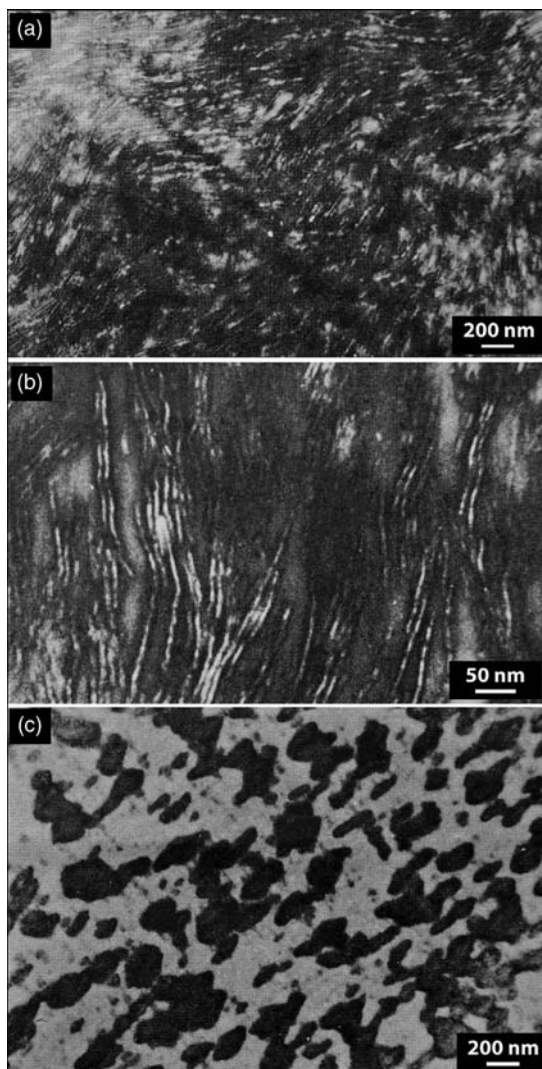


Figure 5.46 Miscibility loop of PCL/SAN blends.



**Figure 5.47** (a, b) TEM images of a PCL/SAN-12.4 (60/40) sample quenched to 46 °C (above UCST) with two different magnifications; (c) The same sample quenched to 24 °C (below UCST).

#### 5.6.1

##### Evaluation of Particle Size in Immiscible Blends

Light scattering is a very convenient method for evaluating particle size according to Eqs (5.5)–(5.7). It is also possible to visualize structure development over time, as shown in Figure 5.48, where coarsening proceeds over a period of time at elevated temperatures [35]. In the present studies a very interesting foam-like structure was discovered when a PCL/SAN (70/30) blend was prepared by precipitation

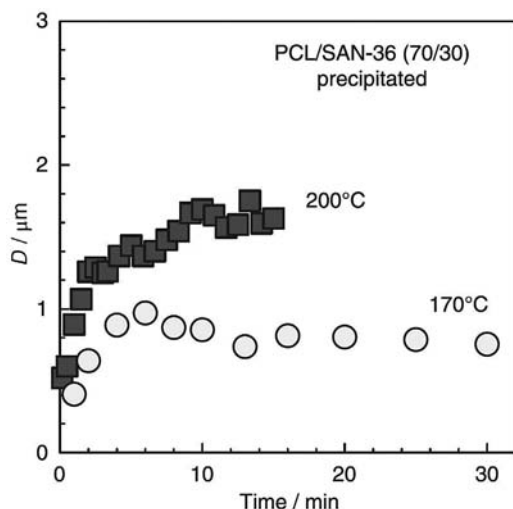


**Figure 5.48** Time variation of the average particle size,  $D$ , of a PCL/SAN (70/30) blend prepared by precipitation into methanol, by light scattering, during static annealing at 200 °C and at 170 °C.

into methanol, during static annealing at 200 °C. Notably, the SAN (at 30% content) formed only thin walls.

At this point, the possibility should also be mentioned of phase separation via a nucleation and growth mechanism [36].

## Acknowledgments

These studies have been supported by the Operational Programme Research and Development for Innovations, cofunded by the European Regional Development Fund (ERDF) and the national budget of Czech Republic within the framework of the Center of Polymer Systems project (reg. number: CZ.1.05/2.1.00/03.0111).

## References

- 1 Paul, D.A. and Newman, S. (eds) (1978) *Polymer Blends*, Academic Press, New York.
- 2 Olabisi, O., Robeson, L.M., and Shaw, M.T. (1979) *Polymer-Polymer Miscibility*, Academic Press, New York.
- 3 Choy, C.L. and Shin, F.G. (eds) (1994) *Proceedings of the International Symposium on Polymer Alloys and Composites*, Hong Kong Polytechnic, Hong Kong.
- 4 Folkes, M.J. and Hope, P.S. (eds) (1993) *Polymer Blends and Alloys*, Blackie Academic and Professional, London.
- 5 Nadkarni, V.M. and Jog, J.P. (1991) *Two-Phase Polymer Systems* (ed. L.A. Utracki), Hanser, Munich, p. 213.
- 6 Matsuura, M., Saito, H., Nakata, S., Imai, Y., and Inoue, T. (1992) Aramid poly(ether sulfone) blend-crystallization accelerated by the presence of amorphous polymer. *Polymer*, **33** (15), 3210–3214.

- 7 Paul, D.R. and Bucknall, C.B. (eds) (2000) *Polymer Blends*, John Wiley & Sons, Inc., New York, p. 319.
- 8 Debye, P. and Bueche, A.M. (1949) Scattering by an inhomogeneous solid. *J. Appl. Phys.*, **20**, 518–525.
- 9 Moritani, M., Inoue, T., Motegi, M., and Kawai, H. (1970) Light scattering from a 2-phase polymer system – scattering from a spherical domain structure and its explanation in terms of heterogeneity parameters. *Macromolecules*, **3**, 433.
- 10 Cahn, J.W. (1965) Phase separation by spinodal decomposition in isotropic systems. *J. Chem. Phys.*, **42** (1), 93–99.
- 11 Binder, K. and Stauffer, D. (1974) Theory for the slowing down of the relaxation and spinodal decomposition of binary mixtures. *Phys. Rev. Lett.*, **33** (17), 1006–1009.
- 12 Stein, R.S. and Rhodes, M.B. (1960) Photographic light scattering by polyethylene films. *J. Appl. Phys.*, **31**, 1873–1884.
- 13 Yoon, D.Y. and Stein, R.S. (1974) Lattice theory of light-scattering from disordered spherulites. *J. Polym. Sci., Polym. Phys. Ed.*, **12**, 763–784.
- 14 Hashimoto, T., Tsukahara, Y., and Kawai, H. (1981) Dynamic small-angle X-ray scattering studies on diffusion of macromolecules in bulk. 2. Principle and preliminary experimental results. *Macromolecules*, **14** (3), 708–715.
- 15 Hashimoto, T., Kumaki, J., and Kawai, H. (1983) Time-resolved light scattering studies on kinetics of phase separation and phase dissolution of polymer blends. 1. Kinetics of phase separation of a binary mixture of polystyrene and poly(vinyl methyl ether). *Macromolecules*, **16** (4), 641–648.
- 16 Inaba, N., Sato, K., Suzuki, S., and Hashimoto, T. (1986) Morphology control of binary polymer mixtures by spinodal decomposition and crystallization. 1. Principle of method and preliminary results on PP/EPR. *Macromolecules*, **19** (6), 1690–1695.
- 17 Nakai, A., Shiwaku, T., Hasegawa, H., and Hashimoto, T. (1986) Spinodal decomposition of polymer mixtures with a thermotropic liquid crystalline polymer as one component. *Macromolecules*, **19** (12), 3008–3010.
- 18 Inaba, N., Yamada, T., Suzuki, S., and Hashimoto, T. (1988) Morphology control of binary polymer mixtures by spinodal decomposition and crystallization. 2. Further studies on polypropylene and ethylene-propylene random copolymer. *Macromolecules*, **21** (2), 407–414.
- 19 Chuang, W.T., Jeng, U.S., Hong, P.D., Sheu, H.S., Lai, Y.H., and Shih, K.S. (2007) Dynamic interplay between phase separation and crystallization in a poly( $\epsilon$ -caprolactone)/poly(ethylene glycol) oligomer blend. *Polymer*, **48** (10), 2919–2927.
- 20 Okada, K., Watanabe, K., Toda, A., Sasaki, S., Inoue, K., and Hikosaka, M. (2007) Supercooling ( $\Delta T$ ) dependence of nano-nucleation of PE by SAXS and proposal of a new nucleation theory. *Polymer*, **48** (4), 1116–1126.
- 21 Wang, H. (2006) SANS study of the early stages of crystallization in polyethylene solutions. *Polymer*, **47** (14), 4897–4900.
- 22 Ratner, B.D., Hoffman, A.S., Schoen, F.J., and Lemons, E.J. (2004) *Biomaterials Science*, Elsevier Academic Press, New York.
- 23 Madbouly, S.A. and Ougizawa, T. (2004) Isothermal crystallization of poly( $\epsilon$ -caprolactone) in blend with poly(styrene-co-acrylonitrile): Influence of phase separation process. *Macromol. Chem. Phys.*, **205** (14), 1923–1931.
- 24 Kiersnowski, A. and Piglowski, J. (2004) Polymer-layered silicate nanocomposites based on poly( $\epsilon$ -caprolactone). *Eur. Polym. J.*, **40** (6), 1199–1207.
- 25 Su, C.C. and Lin, J.H. (2004) Ringed spherulites in ternary polymer blends of poly( $\epsilon$ -caprolactone), poly(styrene-co-acrylonitrile), and polymethacrylate. *Colloid Polym. Sci.*, **283** (2), 182–193.
- 26 Svoboda, P., Svobodova, D., Slobodian, P., Merinska, D., Iizuka, Y., Ougizawa, T., and Inoue, T. (2009) Phase separation and phase dissolution in poly( $\epsilon$ -caprolactone)/poly(styrene-co-acrylonitrile) blend. *Eur. Polym. J.*, **45** (8), 2434–2442.
- 27 Okada, M., Tao, J., and Nose, T. (2002) Attenuation of concentration fluctuations after a quench to a temperature in the



- single-phase region. *Polymer*, **43** (2), 329–335.
- 28 Cheng, M.H. and Nauman, E.B. (2003) Non-linear diffusion with concentration-driven flows in miscible systems. *Polymer*, **44** (21), 6707–6712.
  - 29 Svoboda, P., Kressler, J., Chiba, T., and Inoue, T. (1994) Light-scattering and TEM analyses of virtual upper critical solution temperature behavior in PCL/SAN Blends. *Macromolecules*, **27**, 1154–1159.
  - 30 Koberstein, J., Russell, T.P., and Stein, R.S. (1979) Total integrated light-scattering intensity from polymeric solids. *J. Polym. Sci., Polym. Phys. Ed.*, **17** (10), 1719–1730.
  - 31 Stein, R.S., Erhard, P.F., Clough, S.B., and Adams, G. (1966) Scattering of light by films having nonrandom orientation fluctuations. *J. Appl. Phys.*, **37**, 3980.
  - 32 Tomura, H., Saito, H., and Inoue, T. (1992) Light-scattering analysis of upper critical solution temperature behavior in a poly(vinylidene fluoride) poly(methyl methacrylate) blend. *Macromolecules*, **25**, 1611–1614.
  - 33 De Gennes, P.-G. (1971) Reptation of a polymer chain in the presence of fixed obstacles. *J. Chem. Phys.*, **55**, 572.
  - 34 Kammer, H.W., Inoue, T., and Ougizawa, T. (1989) Upper and lower critical solution temperature behavior in polymer blends and its thermodynamic interpretation. *Polymer*, **30**, 888–892.
  - 35 Jelinkova, L., Svoboda, P., Saha, P., and Inoue, T. (2012) Kinetics of coarsening in immiscible poly( $\epsilon$ -caprolactone)/poly(styrene-co-acrylonitrile) blends. *Polym. J.*, **44**, 155–161.
  - 36 Utracki, L.A. (1989) *Polymer Alloys and Blends, Thermodynamics and Rheology*, Hanser, Munich.



## 6

## Characterization of Polymer Blends by X-Ray Scattering: SAXS and WAXS

*Jitendra Sharma*

## 6.1

### Introduction

The X-ray scattering techniques that have in the past been used conventionally in solid-state physics are beginning to experience a wider applicability in soft matter research. By virtue of length scale accessibility, X-ray scattering embraces systems such as polymer melts, blends and solutions, as well as complex fluids such as microemulsions, colloidal dispersions and micellar solutions. Structural information over approximately three decade of length scales – 1 nm, 10 nm, and 100 nm – can easily be obtained using X-scattering at wide-, small-, and ultra-small-angles, respectively. Among these techniques, two complementary approaches – namely, wide-angle X-ray scattering (WAXS) and small-angle X-ray scattering (SAXS) – are today used extensively for studies of polymer blends. With regards to the description of WAXS, it should be emphasized here that workers in the field interchangeably use three different terms – WAXS, XRD (X-ray diffraction), and WAXD (wide-angle X-ray diffraction).

The interaction of X-rays with matter, in general, results in two different types of event/phenomena: (i) scattering by the individual electrons; and (ii) interference among the scattered waves. While the term *scattering* refers only to the former, *diffraction* is a combination of both. Strictly speaking, WAXS refers only to the first event (i.e., scattering), whereas XRD refers to both events (scattering and diffraction). When the pattern of interest is diffuse, or contains a diffuse component (as in the case of semi-crystalline polymers), or is situated in the region of small angles, the term “scattering” is used exclusively, even if it also involves a contribution from interference. Previously, the term XRD has often been used for cases when the sample is fully crystalline – that is, so regular as to concentrate the scattered X-rays around sharply defined scattering directions in the form of narrow crystalline peaks (as in WAXS from semi-crystalline polymers). Thus, when referring to the description of polymer blends and related text, WAXS would be a far more acceptable and general term.

WAXS is a diffraction experiment that consists primarily of scanning large diffraction angles to cover a wide range of scattering variables down to very small length scale (from  $\sim 1$  nm to a few nanometers, which corresponds roughly to the size of chemical bonds) or  $d$ -spacing of unit cells in crystalline polymers. As such, the crystallinity of polymers can easily be determined by comparing the area under crystalline peaks to the total scattered intensity in a WAXS scan [1]. It is therefore, an important tool for the structural characterization and determination of the degree and state of crystallization in polymer melts and blends.

SAXS, on the other hand, probes structural order or length scales larger than the unit cell ( $\sim 10$  nm) in polymers. With advances in instrumentation (e.g., high-speed detectors) and computational methods, combined with the advent of modern synchrotron radiation facilities (i.e., intense X-ray source) and enhanced capabilities for faster data collection, processing and analysis, these techniques offer distinct advantages in terms of structural investigations at higher spatial resolution and smaller time scales (suitable for the *in-situ* examination of processes such as crystallization and melting).

Similar to XRD and nuclear magnetic resonance (NMR) measurements, X-ray scattering experiments with polymer blends also require a few milligrams of purified material as the sample. More recently, both WAXS and SAXS have proven to be relevant as robust characterization tools for the structural analysis of soft matter systems [1–7]. In principle, SAXS functions in much the same way as XRD, even allowing some instruments to employ both techniques when using same X-ray source, but with two different cameras. For both types of measurement, a flat surface of the sample is illuminated by a narrow beam of well-collimated monochromatic X-rays as a radiation source. The sample is then either rotated (or tilted) over a range of angles with respect to the beam, so as to produce a linear scan (as shown in Figure 6.1a) similar to those used in classical XRD set-ups (using the Bragg–Brentano configuration). Such symmetrical-reflection geometry or a two-dimensional detector (as shown in Figure 6.1b) is then used to capture the entire scattering pattern simultaneously in one action, which is useful for

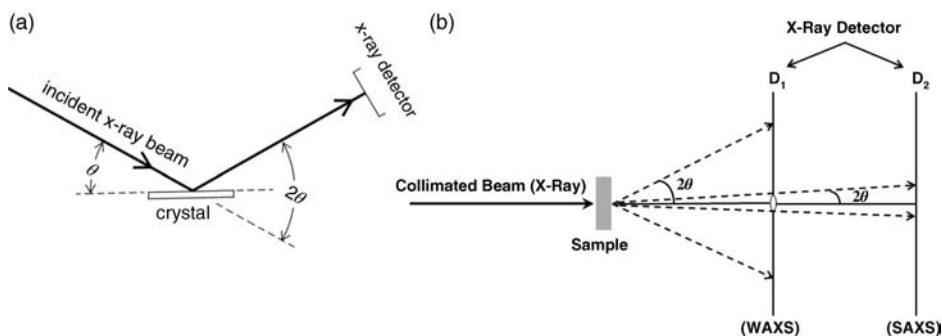


**Figure 6.1** Schematic of experimental X-ray set-up. (a) In reflection-mode for XRD (common with the Bragg–Brentano type configuration) and GISAXS; (b) In transmission-mode for WAXS (or XRD) and SAXS.

both WAXS (or XRD) and SAXS measurements in symmetrical-transmission geometry. A configuration of the former type (i.e., reflection-mode) is also common with grazing-incidence small-angle X-ray scattering (GISAX), while the latter (i.e., transmission-mode geometry) is exploited at synchrotron X-ray source facilities for simultaneous SAXS/WAXS measurements. The main difference between SAXS and WAXS measurements on an instrument is due to the detector being placed either close to (for the wider angles involved in WAXS) or at a distance far away (for the smaller angles needed in SAXS) from the sample. Both, SAXS/WAXS and crystallography involve the scattering/diffraction of a highly collimated beam of X-rays that is scattered/diffracted by the sample and measured at an angle of  $2\theta$  with respect to the direct beam. For simultaneous WAXS/SAXS measurements, the first detector (WAXS) would leave a space close to the center to allow the diffracted intensity at lower angles to be detected by a second detector (SAXS) far away from the first, so as to fulfil the criterion:  $2\theta(\text{SAXS}) \ll 2\theta(\text{WAXS})$ .

For an X-ray of wavelength,  $\lambda$ , diffracted at an angle  $\theta$  by planes of lattice separated by a distance  $d$  apart, it follows from Bragg's law (Figure 6.2) that:

$$m\lambda = 2d \sin \theta \quad (6.1)$$

where  $m$  is the order of diffraction and for a first-order diffraction ( $m = 1$ ),

$$d \sin \theta = \frac{\lambda}{2} \quad (6.2)$$

This imposes the limit of resolution; that is, the minimum distance ( $d_{\min}$ ) at which two particles/atoms can be distinguished, for an X-ray to be

$$d_{\min} = \frac{\lambda}{2} \quad (6.3)$$

However, in actual macromolecular systems, experimentally measured (via SAXS) values (1–5 nm or more) are much higher than those predicted theoretically in

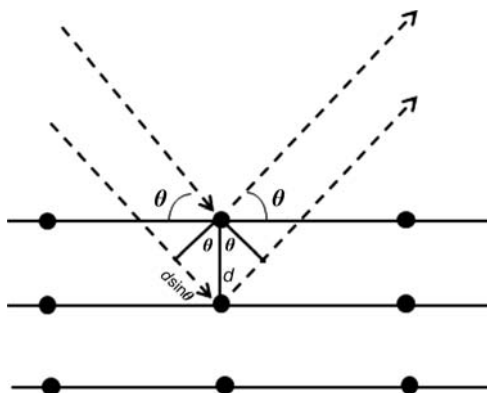


Figure 6.2 Diffraction of X-rays from planes of lattice separated by distance  $d$ .

Eq. (6.3). This is because sizes of the crystals of macromolecules are generally high with the added complexity of the presence of internal disorder in the system. In the reciprocal space ( $s$ ), Eq. (6.2) may be rewritten as:

$$s = \frac{1}{d} = \frac{2 \sin \theta}{\lambda} \quad (6.4)$$

Here,  $s$  is modulus of the scattering wave vector, and is an important experimental parameter (this point is discussed later in the text).

### 6.1.1

#### Development of SAXS Techniques for Polymers

Following the discovery of X-rays by Röntgen and subsequent developments in crystallography around 1915, there was a significant delay in developing SAXS as a fully fledged blown-out technique for studying polymers [8]. The reason for this can largely be ascribed to the experimental difficulties encountered in measuring X-ray scattering at small angles, coupled with the non-availability of an intense X-ray source (i.e., difficulties due to the low intensity of X-rays produced from conventional sources). As noted by Chu and Hsiao [9] in their review of SAXS on polymers, scattered intensity measurements at angles close to the incident X-ray beam was one of the primary experimental difficulties encountered by the early investigators in the field. To measure a  $d$ -spacing of 10 nm with the Cu K $\alpha$  line of 0.154 nm, the required scattering angle is 0.880 (or a Bragg angle of 0.440). Similarly, a 100 nm periodicity measurement would require one-tenth of this scattering angle (i.e., 0.0880). For a probing order of  $d = 1000$  nm (the order of structural hierarchies in macromolecular systems), scattering measurements at  $\theta = 0.0088^\circ$  (32 s or 0.16 mrad) must be carried out 16 mm away from the incident beam, with the sample placed 100 m away from the detector in order to reduce background or stray X-rays at small angles and to minimize parasitic scattering contributions.

### 6.1.2

#### Instrumentation and the Synchrotron Advantage

With high power density and a small divergence of the incident beam, synchrotron X-rays offer improved tools for monitoring *in-situ* processes (following cryo- or heat treatment) such as crystallization, and the subsequent structural changes that occur in semi-crystalline polymers. Thus, the availability of synchrotron X-ray sources has enabled precise time-resolved SAXS/WAXS measurements to be made, using fast detectors.

With conventional X-ray sources, a Kratky-type of SAXS instrument with a “block” collimation system [10] (see Figure 6.3) is often used [11]. For flux optimization and resolution (of the X-ray beam), such instruments have used a slit geometry for collimation and a simple filter for monochromatization. However, these instruments suffer from the disadvantage that, due to anisotropy resolution

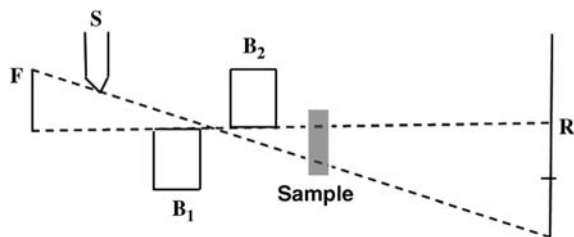


**Figure 6.3** Schematic of “block” collimation system in a Kratky-camera. Here, S is the entrance slit, B<sub>1</sub> and B<sub>2</sub> are the two collimating blocks, R is the plane of detection, and F is a focal plane.

function, they are not suitable for studying all types of polymeric/colloidal system. A pin-hole configuration is often used in the X-ray source of high-power rotating anodes and synchrotron facilities, while Bragg scattering from a single crystal is used for monochromatization. Detectors of various types, notably area-sensitive detectors, gas-proportional detectors and image plate detectors, including charge-coupled devices (CCDs), are used for recording scattered X-rays.

## 6.2

### Basics of X-Ray Scattering

Scattering is a process that involves the deviation of a beam of radiation or particles from its initial trajectory by the inhomogeneities in the medium which it traverses. Thus, scattering experiments are easy to conceptualize and require only a source, a sample, and a detector (see Figure 6.1). Solution scattering is relatively easier to perform as it does not require special sample processing such as crystallization or cryo-cooling. For aqueous solutions of macromolecules, the scattering arises from the inhomogeneities due to solute particles. The interaction of X-rays with (the electrons of) atoms in the irradiated volume gives rise to scattered radiations. As X-rays interact largely with electrons, it is rather convenient to treat objects as a continuous distribution of scattering density (electron density in case of X-rays) and not just discrete atoms.

#### 6.2.1

##### Elastic Scattering of Electromagnetic Radiation by Single Electron

To understand the scattering of electromagnetic radiation from a single electron, it can be assumed that a monochromatic plane wave linearly polarized along the  $x$ -axis with electric field  $E(t) = E_0 e^{i\omega t}$  is scattered elastically by an electron placed at the origin of the Cartesian coordinate system. For an observer located at distance  $r$  from the origin, the electric field of the resultant wave is given by:

$$E(r, t) = E(t) \frac{e^2}{mc^2} \frac{\sin \Psi}{r} \frac{\omega^2}{\omega_0^2 - \omega^2} \quad (6.5)$$

where  $\Psi$  is the angle between the direction of polarization and the observer's line of sight. Clearly, there exists a linear relationship between the fields of the scattered intensity and the incident waves. The three pre-factors are:

- 1) A constant, which is numerically equal to the classical electron radius,  $r_0$ .
- 2) A geometric factor for the projection of incident electric field in a direction perpendicular to the observer's line of sight.
- 3) A frequency factor containing the natural frequency  $\omega_0$  of the undamped oscillator (representing the motion of electron).

For visible light ( $\lambda \approx 5000 \text{ \AA}$ ), the frequency factor reduces to  $\omega^2/\omega_0^2$  as  $\omega \ll \omega_0$ . This is known as Rayleigh scattering, wherein the scattered intensity at  $r$  is in phase with the incident wave and proportional to  $\omega^2$ . Light scattering (elastic or quasi-elastic) is an ideal probe to extract information about intermolecular interactions in solution within this domain, but very little information on the structural details can be extracted (owing to the long wavelength of light), except in the case of larger entities.

In the case of X-rays ( $\lambda \approx 1 \text{ \AA}$ ),  $\omega_0 \ll \omega$ , The resultant frequency factor becomes equal to  $-1$  as the phase of scattered wave is  $\pi$  shifted and the amplitude of the scattered wave becomes independent of frequency. The phenomenon is called *Thompson scattering*. Equation (6.5), thus reduces to

$$E(r, t) = -E(t)r_0 \frac{\sin \Psi}{r} \quad (6.6)$$

As seen in Figure 6.4, the differential scattering cross-section given by

$$\frac{d\sigma}{d\Omega} = \frac{\text{number of scattered particles per solid angle per second}}{\text{incident flux}} = \frac{J}{J_0} \quad (6.7)$$

where  $J_0$  and  $J$  are the incident and scattered flux density, respectively.

Like crystallography, SAXS is also based on the elastic (Thompson) scattering of photons by electrons of the macromolecular entities. As the monochromatic beam of X-rays hits the object, the electrons of its atoms (except for heavy atoms, which play no role in small-angle scattering) resonate with the frequency of X-rays and become sources of coherent secondary waves. The intensity of the secondary waves is given by the *Thompson formula*:

$$I(2\theta) = r_0^2 \frac{1 + \cos^2(2\theta)}{2} \frac{1}{r^2} I_0 \quad (6.8)$$

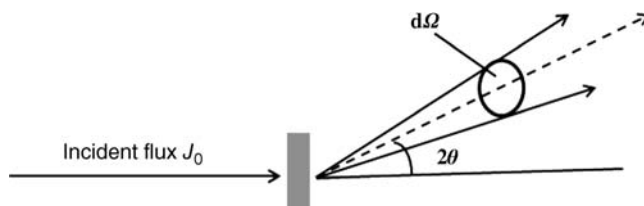


**Figure 6.4** Incident (plane wave) and scattered flux (spherical wave) in the X-ray scattering.



where  $r$  is the distance of the object from the point of registration,  $I_0$  is the intensity of the incident beam, and  $r_0$  is the classical electron radius (and  $r_0^2 = 7.95 \times 10^{-26} \text{ cm}^2$ )

$$r_0 = \frac{e^2}{mc^2} = 0.282 \times 10^{-12} \text{ cm} \quad (6.9)$$

and

$$\frac{d\sigma}{d\Omega} = r_0^2 \frac{1 + \cos^2(2\theta)}{2} \frac{1}{r^2} \quad (6.10)$$

At small angles,  $\cos(2\theta) \cong 1$ . And, so

$$\frac{d\sigma}{d\Omega} \cong r_0^2 = 7.95 \times 10^{-26} \text{ cm}^2 \quad (6.11)$$

which is equal to square of the modulus of scattering length,

$$|b|^2 = \frac{d\sigma}{d\Omega} \quad (6.12)$$

therefore, the scattering length of a single electron will be

$$b_e = r_0 \sqrt{\frac{1 + \cos^2(2\theta)}{2}} \quad (6.13)$$

As per definition, the scattering factor,  $f$ , of an object is simply the ratio of scattering amplitude of the object/atom to that of an electron under identical conditions. The scattering factor of an electron, therefore, always equals unity, that is,  $f_e = 1$ .

### 6.2.2

#### Scattering by Assembly of Electrons: Scattering Geometry and Interference

Figure 6.5 shows the scattering geometry from the two-point center of an assembled matter. Neglecting the insignificant incoherent (Compton) scattering at

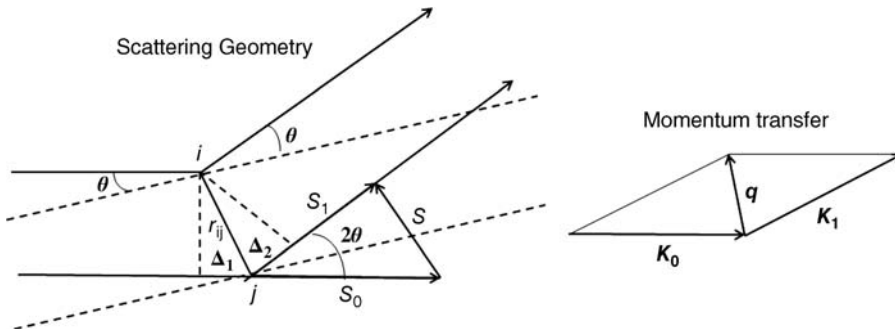


**Figure 6.5** Scattering from two-point center of matter, and the corresponding momentum transfer (at right).

small angles, the resultant scattered intensity can be obtained by taking the absolute value of the square of sum of amplitudes contributed by the superimposing coherent (Thompson) scattered waves that differ only in phase,  $\phi$  (depending on the position of electron in space), but not amplitude. If the directions of the incident and scattered rays are given by the unit vectors  $\vec{S}_0$  and  $\vec{S}_1$ , respectively, then the phase difference of point  $i$  and  $j$  (defined by the vector  $r_{ij}$  with respect to the origin) may be calculated as follows:

$$\text{Path difference, } \Delta = \Delta_1 + \Delta_2 = -\vec{S}_0 \cdot r_{ij} + \vec{S}_1 \cdot r_{ij} \quad (6.14)$$

$$= (\vec{S}_1 - \vec{S}_0) \cdot r_{ij} = \vec{S} \cdot r_{ij} \quad (6.15)$$

The phase difference will be

$$\text{Phase change, } \Delta\phi = \frac{2\pi}{\lambda} \times \Delta = \frac{2\pi}{\lambda} \vec{S} \cdot r_{ij} \quad (6.16)$$

The corresponding momentum transfer,  $q$ , is expressed in terms of the incident and scattered wave vectors,  $\vec{k}_0 \left( = \frac{2\pi}{\lambda} \vec{S}_0 \right)$  and  $\vec{k}_1 \left( = \frac{2\pi}{\lambda} \vec{S}_1 \right)$ , respectively, as

$$\vec{q} = \vec{k}_1 - \vec{k}_0 \text{ and } |\vec{k}_0| = |\vec{k}_1| = \frac{2\pi}{\lambda} \quad (6.17)$$

The phase change in terms of momentum transfer is therefore

$$\Delta\phi = \vec{q} \cdot r_{ij} \quad (6.18)$$

From the Figure 6.5, it can easily be seen that the magnitude of  $\vec{S}$  is

$$|\vec{S}| = |(\vec{S}_1 - \vec{S}_0)| = 2 \sin \theta \quad (6.19)$$

Therefore, the magnitude of wave vector  $q$  is similar to  $s$  (modulus of the scattering vector), and using Eq. (6.19), is given by

$$|q| = q = 2\pi s = \left( \frac{4\pi}{\lambda} \right) \sin \theta \quad (6.20)$$

which could be linked to the space between lattice planes  $d$ , using Eq. (6.4)

$$d = \frac{2\pi}{q} \quad (6.21)$$

and thus provides the link between real space distance and the reciprocal space.

### 6.2.3

#### Scattered Intensity

The amplitude of the incident X-ray (as shown in Figures 6.3 and 6.4), consisting of electromagnetic waves, may be represented by a plane wave:

$$A(\vec{r}, t) = A_0 \exp(i\omega t - i\vec{k} \cdot \vec{r}) \quad (6.22)$$

The wave amplitude of X-ray scattered ( $E' = E'_0 e^{i(\omega t + \phi_0)} e^{i\mathbf{q} \cdot \mathbf{r}_j}$ ) from an electron  $j$  at the position  $\mathbf{r}_j$  (with respect to an arbitrary origin) is

$$A_j(\vec{q}) = f_e \exp(i\vec{q} \cdot \vec{r}_j) \quad (6.23)$$

So, the total amplitude of scattered waves (of X-rays) from two such electrons at positions  $\mathbf{r}_i$  and  $\mathbf{r}_j$ , respectively, will simply be given by the sum of the two amplitudes

$$\begin{aligned} A^{tot}(\vec{q}) &= A_i(\vec{q}) + A_j(\vec{q}) = f_e \exp(i\vec{q} \cdot \vec{r}_j) + f_e \exp(i\vec{q} \cdot \vec{r}_i) \\ &= f_e \exp(i\vec{q} \cdot \vec{r}_j) \{1 + \exp[i\vec{q} \cdot (\vec{r}_i - \vec{r}_j)]\} \end{aligned} \quad (6.24)$$

$$= f_e \exp(i\vec{q} \cdot \vec{r}_j) \{1 + \exp i\vec{q} \cdot \vec{r}_{ij}\} \quad (6.25)$$

Since experimental detectors measure the intensity  $I(q)$  and not amplitude  $A^{tot}(\vec{q})$ . The intensity is obtained by taking a product of the amplitude  $A^{tot}(\vec{q})$  with its complex conjugate. Therefore, intensity of scattered radiation at the detector is given by:

$$I(\vec{q}) = |A^{tot}(\vec{q})|^2 \quad (6.26)$$

Following the same analogy for a collection of  $N$  electrons, the scattered intensity will be

$$I(\vec{q}) = |A_j(\vec{q})|^2 = \left| \sum_{j=1}^N f_e \exp(-i\vec{q} \cdot \vec{r}_j) \right|^2 \equiv F^2(\vec{q}) \quad (6.27)$$

Following which, the scattered wave amplitude due to collection of  $N$  electrons located at  $\mathbf{r}_i$  may be defined using the Fourier series of the distribution

$$F(\vec{q}) = \sum_{j=1}^N f_e \exp(-i\vec{q} \cdot \vec{r}_j) \quad (6.28)$$

If the scatterers take all orientations (e.g., in a gas or solution), the total intensity will be obtained by taking an ensemble average over all orientations and the phase factor is spherically averaged to give

$$\langle I(q) \rangle = \langle I(\vec{q}) \rangle_{\Omega} \quad \text{and} \quad \langle \exp(-i\vec{q} \cdot \vec{r}_j) \rangle_{\Omega} = \frac{\sin(qr)}{qr} \quad (6.29)$$

Using Eq. (6.29) in Eq. (6.28), the scattering factor or the atomic form factor for an atom with radial electron density  $\rho(r)$  is simply obtained by replacing summation with integral, following which

$$F(q) = 4\pi \int \rho(r) r^2 \frac{\sin(qr)}{qr} dr \quad (6.30)$$

Clearly,  $F(0) = Z$ , gives the total number of electrons in the atom. For small-angle scattering ( $2\theta < 5^\circ$ ), the angular dependence of the scattering factor  $F(q)$  may be

neglected for lighter elements as it remains constant with a value nearly equal to  $F(0)$ .

Using Eq. (6.30), the scattered intensity reduces to

$$I(q) = 4\pi \int_0^\infty \gamma_0(r) \frac{\sin(qr)}{qr} r^2 dr, \quad (6.31)$$

where

$$P(r) = \gamma_0(r) r^2, \quad (6.32)$$

is the pair distance distribution function and gives the histogram of all the intra-particle distances. Hence,

$$I(q) = 4\pi \int_0^\infty P(r) \frac{\sin(qr)}{qr} dr, \quad (6.33)$$

For a homogenous sample, the scattering profile can easily be derived from the pair-distribution function,  $P(r)$ , and is expressed as

$$I(q) = 4\pi \int_0^{D_{\max}} P(r) \frac{\sin(qr)}{qr} dr, \quad (6.34)$$

where,  $D_{\max}$  is the maximum linear dimension of the scattering particle.

### 6.3

#### Small- and Wide-Angle X-Ray Scattering (SAXS and WAXS)

Depending on the available experimental conditions such as sample-to-detector distance, and the X-ray wavelength, the diffraction pattern of the sample under investigation can be measured as intensity versus either the  $s$ -vector ( $s = (2 \sin \theta)/\lambda$ ) or the  $q$ -vector ( $q = 2\pi s$ ) or versus  $2\theta$ , which is the angle of scattering/diffraction. In terms of  $2\theta$ , a diffraction experiment involving  $2\theta > 1^\circ$  is generally referred to as wide-angle X-ray scattering/diffraction (WAXS/WAXD), those with  $1^\circ > 2\theta > 0.3^\circ$  are described as medium-angle X-ray scattering (MAXS), and those with  $2\theta < 0.3^\circ$  fall into the category of SAXS. The representation of intensity versus wave vector ( $s$  or  $q$ ) is useful for small-angle scattering (SAS) measurements as it allows the diffraction patterns to be recorded in terms of a parameter ( $s$  or  $q$ ) that can easily be compared irrespective of the source of radiation (light, neutron and X-ray, etc.) used in the experiment. According to Bragg's law, the  $s$  or  $q$  values (i.e.,  $s^*$  or  $q^*$ ) at which a peak in the intensity is observed, corresponds to  $d = \frac{1}{s^*} = 2\pi/q^*$ , the distance of separation between diffracting crystalline planes. Thus, the real-space dimension and the magnitude of measured  $s$ -vector or  $q$ -vector are inversely related to each other. Therefore, larger structural features such as crystallinity/periodicity are generally measured in a SAXS experiment, whereas smaller features involving chain (homopolymer)/microdomain (block copolymers) ordering are investigated using WAXS. Besides the contribution from instrumental factors, any deviation from perfect ordering in

the system leads to a broadening of the diffraction peaks (observed at these angles). Even for a disordered phase, it is possible to observe peaks (albeit they are substantially broadened) in the wide-angle regime. While the positions of such peaks reflect the distance of short range order in an amorphous phase, the area under the peak provides an estimate of the amount/fraction of such phase in the material. Hence both, SAXS and WAXS, hold great promise for the structural analysis of different building blocks in soft matter systems.

In solid systems with regularly positioned macromolecules, the waves reinforce/interfere to produce typical diffraction peaks (XRD) that allow the collection of crystallographic information relating to the system. In addition, from the observed intensities of the diffraction peaks it is possible to easily reconstruct the three-dimensional electron density  $\rho(r)$  and the high-resolution crystal structure of the system [12]. However, in SAXS studies of macromolecular solutions, the molecules move freely and are randomly oriented, and hence no peaks or low-intensity peaks with only poor resolution are observed. However, despite the loss of information on the details of orientation, SAXS offers an estimation of the magnitude of inter-atomic distances and overall structural parameters, and hence a low-resolution shape of the particle from the observed data. Consequently, SAXS is today considered as an established technique for the investigation of non-periodic structures (e.g., scattering media such as macromolecules in solution or inhomogeneities in solid matrix) with dimensions ranging from about 1 nm to several hundred nanometers. Several excellent reviews and textbooks are available describing the fundamentals of X-ray small-angle scattering [11–18].

## 6.4

### Polymer Blend Morphology

A typical crystalline material often consists of crystalline planes separated by distances of the order 0.1 to 1 nm. Soft condensed matter, in particular, comprises a wide variety of complex materials/fluids marked by the presence of hierarchical structural arrangement ranging from 10 to 100 nm. In terms of thermodynamics, the phase behavior of polymer blends is governed by the minimization of the free energy arising from the balance between the entropy and enthalpy of the system. To a first approximation, they are evaluated on the basis of the molecular weight (defined by the degree of polymerization), and the Flory–Huggins interaction parameter  $\chi$ , which describes the interaction between the different chain segments.

#### 6.4.1

##### Blends of Homopolymers

Semi-crystalline polymers often manifest a lamellar morphology consisting of stacks of laminar crystals with a characteristic thickness of  $l_c$ , intercalated by an amorphous region represented by a length scale,  $l_a$ . Polymer blends that consists

of two (binary) or more (ternary, etc.) polymers may have at least one or more crystalline/semi-crystalline components. A binary polymer blend ( $A/B$ , where “ $A$ ” is a crystallizable polymer component while “ $B$ ” is amorphous) may simply have crystals of “ $A$ ” dispersed in the amorphous phase “ $B$ ” or, in a yet another scenario, the growth of spherulites of “ $A$ ,” consisting of both lamellar crystalline and amorphous regions, might have taken place in the matrix of “ $B$ ” (the amorphous component). In the latter case, the amorphous “ $B$ ” may be located in the interspherulitic region, interfibrillar regions, interlamellar regions or a complex combination of these [19–22]. All such semi-crystalline polymers or their blends are manifested by two characteristic lengths,  $l_c$  and  $l_a$ , wherein  $L$  (or  $L_p$ ) =  $l_a + l_c$  defines a long period which is on the order of 10 nm.

The different characteristic length scales so defined in a semi-crystalline polymer or a blend consisting of at least one crystallizable component are thus accessible in X-ray scattering experiments and are probed by varying the scattering angle (SAXS or WAXD) that depends on the available sample to detector distance of the instrumental set-up.

#### 6.4.1.1 Structural Characterization: SAXS Data

Important morphological parameters such as the long period ( $L$ ), crystal thickness ( $l_c$ ), and amorphous layer thickness ( $l_a$ ) of semi-crystalline polymer melts and blends can be determined using SAXS via two different approaches. In the first approach, standard models such as the Hosemann–Tsvankin [23] and the Vonk–Kortleve [24,25] for lamellar stacks are fitted to data obtained for the SAXS profile. The second approach is based on performing a Fourier transform for the SAXS profile to produce a one-dimensional correlation function,  $\gamma(z)$  (which is Fourier transform of the measured  $I(q)$  in SAXS) or an interphase distribution function (IDF) in real space.

In scattering measurements, structural information from a three-dimensional (3D) system is often recorded in two-dimensional (2D) form, and hence an  $I(q)$  versus  $q$  data does not offer an ideal representation to extract meaningful structural details of the system. To resolve this issue, the data are multiplied by  $q^2$ , which is termed the “Lorentz-correction.”

**Correlation Function (CF) Method** This Lorentz-corrected SAXS profile ( $Iq^2$  versus  $q$ ) is used to calculate the one-dimensional (1D) correlation function,  $\gamma(z)$ , given by

$$\gamma(z) = \frac{1}{Q} \int_0^\infty I(q) q^2 \cos(qz) dq \quad (6.35)$$

where  $q = (4\pi/\lambda)\sin(\theta)$  when  $\theta$  is the scattering angle and  $z$  represents the direction perpendicular to the surfaces of lamellae along which the electron density is measured, and  $Q$  (the normalization factor) is the scattering invariant defined by

$$Q = \int_0^\infty I(q) q^2 dq = \gamma(0) \quad (6.36)$$

**Interphase Distribution Function (IDF) Method** The IDF,  $g_1(z)$ , is equal to the second derivative of the correlation function,  $\gamma(z)$ , and is given by

$$g_1(z) = \gamma''(z) \quad (6.37)$$

Thus, the morphological parameters can be deduced from the simple geometric analysis of  $\gamma(z)$  and  $g_1(z)$  and by locating their maxima and minima.

However, due to experimental limitations, only a limited/finite  $q$ -range is accessible/measured, and hence extrapolation of measured intensity data to both a low- and a high- $q$  region is necessary before the Fourier transform. The Debye–Bueche model [26,27] defined by

$$I(q) = \frac{I(0)}{(1 + a_0^2 q^2)^2} \quad (6.38)$$

is used conveniently to fit the limited  $q$ -range data for an extrapolated zero- $q$  intensity estimate. Here,  $I(0)$  represents the intensity at zero- $q$  and  $a_0$  is the correlation length. The slope and intercept of a straight-line curve fit to the plot of  $I(q)^{-1/2}$  versus  $q^2$  readily gives these two parameters. Similarly, the high- $q$  data can be extrapolated using the Porod–Ruland model [28], where the tail of the curve (at high- $q$ ) is fitted with a function expressed as a superimposition of positive and negative deviations from Porod's law [29–31]:

$$I(q) = K_p \frac{\exp(-\sigma^2 q^2)}{q^4} + I_b \quad (6.39)$$

where  $K_p$  is the Porod constant,  $I_b$  is the background intensity caused by thermal density fluctuations, and  $\sigma$  is a parameter (characterizing a sigmoidal electron-density in the layer) related to the thickness of the crystal-amorphous interface (i.e., the transition layer). These parameters ( $K_p$ ,  $\sigma$  and  $I_b$ ) are thus obtained from the curve fitting of intensity profile at large- $q$  region.

Figure 6.6a shows the Lorentz-corrected SAXS profiles of miscible polymer blends of homopolymer poly(vinylidene fluoride) (PVF<sub>2</sub>) with varying compositions (10–30 wt%) of poly(1,4-butylene adipate) (PBA) in the semicrystalline/semicrystalline state (20 °C) [32]. From the Lorentz-corrected SAXS profile ( $Iq^2$  versus  $q$ ) of the blends, the long period or the interlamellar spacing of PVF<sub>2</sub> in the blend can be estimated using Bragg's law ( $L = 2\pi/q^*$ , where  $q^*$  is the first peak in the low- $q$  region). For other parameters ( $l_c$  and  $l_a$ ), use can be made of the correlation function (after the low- and high- $q$  extrapolation of the intensity versus wave-vector SAXS data) through the following equations [33,34]:

$$\chi_{cl}(1 - \chi_{cl}) = Z_1 \quad (6.40)$$

where “ $Z_1$ ” on the  $Z$ -axis is the position of first intercept of the correlation function and  $\chi_{cl}$  is the *linear crystallinity* within the lamellar structure; this is so (“linear”) defined to distinguish it from volume/bulk crystallinity in the sample, owing to the fact that it does not account for the presence of extended domains (of matrix material) outside the scattering entities. By definition, the linear

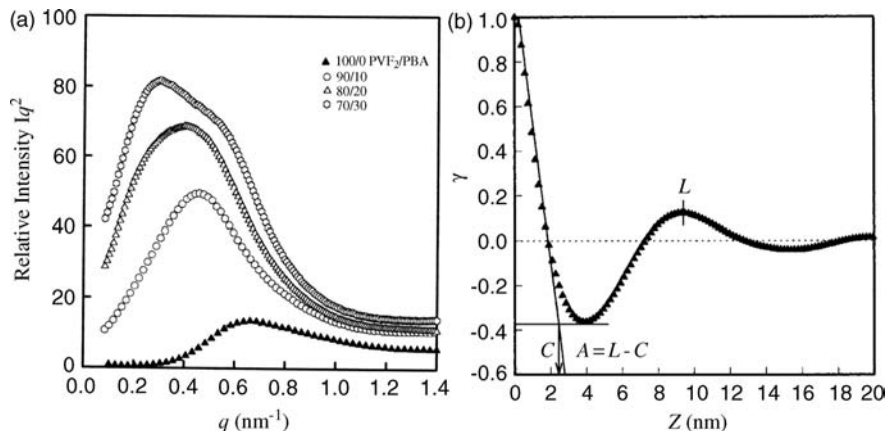


**Figure 6.6** (a) Plot of Lorentz-corrected SAXS profiles of miscible polymer blends of PVF<sub>2</sub> with PBA (10–30 wt%) in the semicrystalline/semicrystalline state (20 °C); (b) Deduction of Long Period ( $L$ ), Crystalline-phase thickness

( $C$  or  $l_c$ ), and amorphous phase thickness ( $A$  or  $l_a$ ) =  $L - l_c$  from correlation function of pure PVF<sub>2</sub> homopolymer. Reproduced with permission from Ref. [32]; © 1997, American Chemical Society.

crystallinity is obtained from the relationship:

$$\chi_{cl} = l_c / L \quad (6.41)$$

where the values of long period ( $L$ ) and crystalline-phase thickness ( $l_c$ ) are estimated from the first maxima of the correlation function and intercept of the initial slope and its intercept with the baseline (drawn through the point of first minima parallel to the  $z$ -axis) and follows the relationship:

$$l_a = (1 - \chi_{cl})L \quad \text{or} \quad l_a = L - l_c \quad (6.42)$$

Figure 6.6b depicts the deduction of relevant parameters ( $L$ ,  $l_c$  and  $l_a$ ) for pure homopolymer PVF<sub>2</sub> using the correlation function method [32] which satisfies Eqs (6.40)–(6.42). However, the values of  $\chi_{cl}$  and  $(1 - \chi_{cl})$  so determined cannot be uniquely assigned to the crystalline and amorphous phases (they could also be opposite). Being quadratic, Eq. (6.40) has two solutions (one is  $\chi_{cl}$  corresponding to  $l_c$  and other linked to  $l_a$ ), with the constraint that their sum is equal to 1. However, based on the analysis presented so far, the two different lengths ( $l_c$  and  $l_a$ ) obtained from the initial slope and first minima in the correlation function method, it is unclear whether the opposite (i.e.,  $l_c$  could be  $l_a$  and vice-versa) is untrue (based on these data alone), which is interestingly an aspect of the Babinet principle. An experimental determination of unique  $\chi_{cl}$  could be made if the value for the volume fraction of bulk crystallinity ( $\phi_c$ ) is known from measurements such as WAXS/XRD (see below) or differential scanning calorimetry (DSC) [19]. Otherwise, according to Wang *et al.* [34], the longer length (thickness) obtained from a high value of  $\chi_{cl}$  ( $> 0.5$ ) gives  $l_c$ , while the shorter length ( $l_a$ ) is simply obtained by applying the formula,  $l_a = L - l_c$ . In the case of a lower value of linear



crystallinity,  $\chi_{cl} (< 0.5)$ , the values of obtained  $l_c$  and  $l_a$  are simply exchanged. The volume fraction of lamellar stacks,  $\phi_s$ , in sample is given by

$$\phi_s = \phi_c / \chi_{cl} \quad (6.43)$$

which links the linear crystallinity,  $\chi_{cl}$ , to the bulk crystallinity,  $\phi_c$  (measured by density or thermal analysis), and is valid when the spherulites are volume filling. Since  $\phi_s$  is always less than equal to unity, the bulk crystallinity cannot be higher than the linear crystallinity. The volume fraction of the bulk crystallinity ( $\phi_c$ ) can also be estimated from the index of crystallinity ( $\chi_c$ ) obtained from WAXD/XRD via [35]

$$\phi_c = \frac{\chi_c / d_c}{\chi_c / d_c + (1 - \chi_c) / d_a} \quad (6.44)$$

where  $d_c$  and  $d_a$  are the mass densities of the crystalline and amorphous phase, respectively.

However, the results of recent studies by Cruz *et al.* [36] have suggested that the positions of the first minima and first maxima in the 1D correlation function may be perturbed by a broad size distribution of lamellae. Therefore, an alternative approach via the IDF calculation defined in Eq. (6.37) may be adopted to derive the morphological parameters in polymer blends, as shown in Figure 6.7a and b.

Figure 6.7a depicts the IDF profile from different compositions of melt-miscible crystalline/amorphous blends of PCL/PVC (i.e., polycaprolactone (PCL)/poly(vinyl chloride)). The maxima and minima in the obtained IDF profile, and their deconvolution, provides an estimate of the long period,  $L$  (negative peak) and the thickness of crystalline ( $l_c$ ) and amorphous layers ( $l_a$ ) as either  $l_1$  and  $l_2$  or vice-versa, as shown in Figure 6.7b. The entire IDF profile has been fitted to the superimposition of three peak contributions: two positive peaks (corresponding to  $l_c$  and  $l_a$ ) and one negative peak ( $L$ ), assuming their Gaussian distribution.

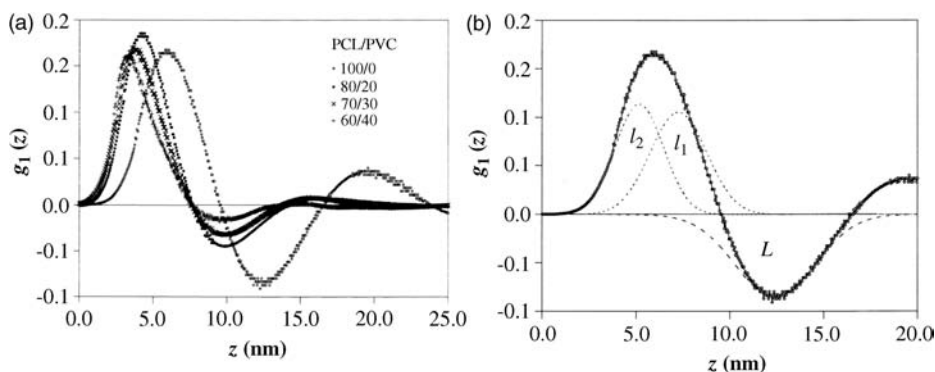


**Figure 6.7** (a) The interphase distribution function (IDF) for the listed compositions of PCL/PVC blends; (b) Morphological parameters obtained from the deconvolution of the

obtained maxima and minima in the IDF. Reproduced with permission from Ref. [20]; © 1998, American Chemical Society.

### 6.4.1.2 Crystallinity: WAXS Data

**Degree of Crystallinity** The index of crystallinity ( $\chi_c$ ) is evaluated from WAXS data by taking the ratio of crystalline diffraction area to the total diffraction area of the diffraction profile, and is given by

$$\chi_c = \frac{\text{Crystalline diffraction area}}{\text{Total diffraction area}} = \frac{A_{\text{cry}}}{A_{\text{cry}} + A_{\text{am}}} \quad (6.45)$$

After appropriate background corrections,  $A_{\text{am}}$ , represents the area of the amorphous halo, whereas  $A_{\text{cry}}$  is the total area under all Bragg peaks in a WAXS profile. For the purpose, the entire WAXS profile obtained experimentally can be fitted using a peak-fitting program after assigning narrow peaks for Bragg reflections and one or more broader peaks for the amorphous halo. The number and positions of Bragg peaks so obtained provides information about the number of crystallographically distinguishable phases present in the system.

**Size of Crystals** During crystallization measurements, the intensity varies over several orders from the initial amorphous halo to Bragg peaks. Intensity dynamic range and spatial resolution are critical in WAXS. An estimate of the size (at sub-micron level) of crystallite linked to broadening of peaks in diffraction pattern can be obtained using the Scherrer equation:

$$\tau = \frac{K_{1/2} \lambda}{\beta \cos \theta} \quad (6.46)$$

where  $\tau$  is the mean size of the crystallite,  $\beta$  is the full-width at half-maximum (FWHM) of the Bragg peak (in radians),  $K_{1/2}$  is the Scherrer constant (the value of which will depend on the shape of the crystallite), and  $\theta$  is the angular position of the scattering plane.

Data recoded from WAXS measurements are often exploited for the analysis of different types of phase (e.g.,  $\alpha$ ,  $\beta$ , or  $\gamma$ ) present in the constituent phase of a polymer system. For example, the different phases in the blends (iPP1/iPP2) of isotactic polypropylene (iPP) with varying degrees of stereoregularity are identified from their WAXS profile (see Figure 6.8). Accordingly, all the iPP1/iPP2 blends with indicated compositions presented in their WAXS profiles are crystallized in  $\alpha$  or  $\gamma$  forms, or in the distorted form ( $\alpha/\gamma$  form) intermediate to the  $\alpha$  and  $\gamma$ .

### 6.4.2

#### Blends of Block Copolymers

In block copolymers (BCPs), the frustration of chains offered by the covalent connectivity of the blocks prevents them from undergoing macrophase separation on a large scale, and this induces a microphase separation of the blocks resulting in the formation 10–100 nm scale periodic structures with different shapes and geometries (depending on the fraction  $f$  of the component copolymers and the product  $\chi N$ ) viz., lamellar, hexagonal closed pack (HCP), body-centered cubic

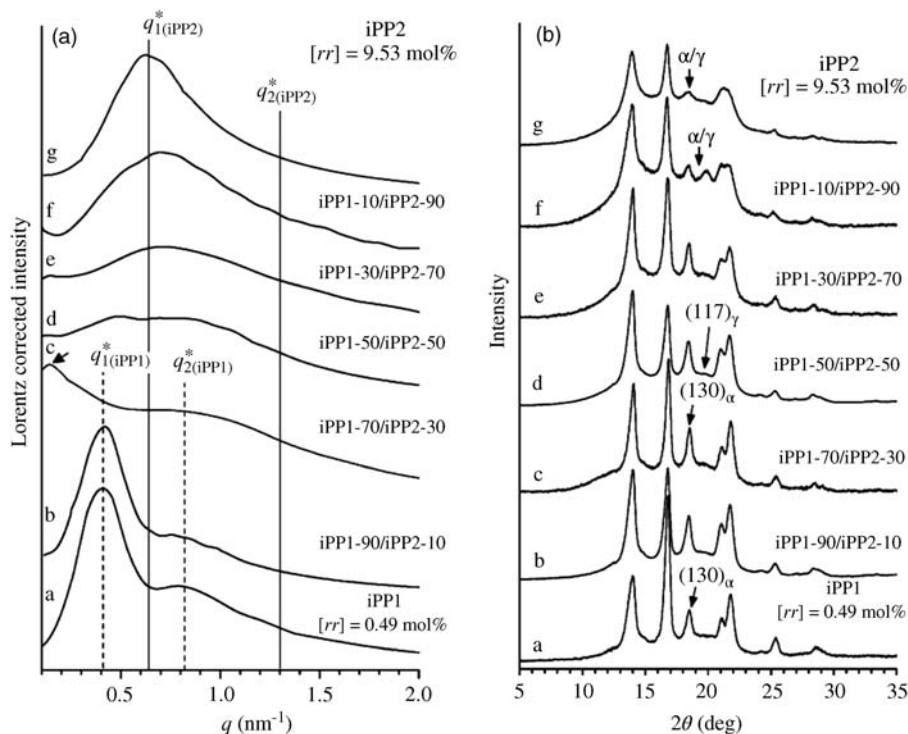


**Figure 6.8** (a) Lorentz-corrected SAXS profiles and (b) corresponding WAXS profiles of polymer blends (iPP1/iPP2) of isotactic polypropylene (iPP) with varying degrees of stereoregularity (with indicated compositions),

wherein iPP1 has a greater degree of stereoregularity than iPP2. Reproduced with permission from Ref. [35]; © 2010, American Chemical Society.

(BCC), and gyroid. Blending such BCPs with homopolymers has resulted in interesting changes in their structure and morphology [37,38].

Both, SAXS and SANS are powerful tools for investigating microphase separation and/or the periodic structures in BCPs. The selection of radiation for the study depends primarily on the choice of polymers, which determines the contrast [39]. For example, nonpolar systems such as PS–polydiene, which are governed by relatively large  $\chi$  parameters, exhibit a sizeable electron density difference between components and thus provide a good X-ray contrast. On the other hand, choosing structurally similar polymers such as isomers increases the block compatibility [40,41] and thus eliminates the X-ray contrast, rendering SANS more suitable for investigations of structures. Figure 6.9 shows the SAXS scattering profile for a neat diblock copolymer poly(4-vinylphenol-*b*-styrene) (PVPh-*b*-PS) in the diagram, and when it is blended with the homopolymer poly(4-vinylpyridine) (P4VP), designated as HS and HS/V, respectively (in the diagram). As the volume fraction of P4VP was increased from 6% to 13%, 15%, 22%, 29% and 71%, the HS/V blends

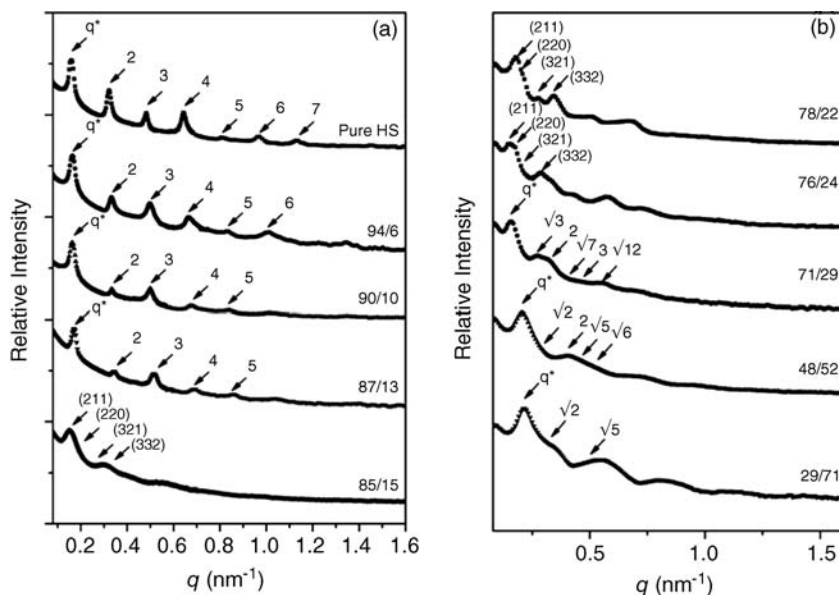


**Figure 6.9** SAXS profile of pure HS and its blends (HS/V) with varying compositions mentioned over each curve in the diagrams. (a) HS/V blend compositions (94/6, 90/10, 87/13, 85/15); (b) HS/V blend compositions (78/22, 76/24, 71/29, 48/52, and 29/71). The

arrows in the diagram shows the peak ratios (relative to the first peak position marked as  $q^*$ ) or reflections planes for the corresponding ordered structures. Reproduced with permission from Ref. [38]; © 2010, American Chemical Society.

underwent a series of order-order phase transitions from the lamellar, gyroid, hexagonally packed cylinder, to BCC structures [38].

Binary blends of crystalline-amorphous diblock copolymers are interesting systems to study, and are also a good substitute for miscible crystalline/crystalline homopolymer blends with a large asymmetry in the rate of crystallization (over a given range of temperatures) [42]. Here, the components of the binary blend consisted of diblock copolymers of poly( $\epsilon$ -caprolactone)-*block*-polybutadiene copolymer (henceforth referred to as the PCL-*b*-PB copolymer) with a large asymmetry in the rate of crystallization for the crystallizable block (PCL). The crystallization of such a neat diblock copolymer is marked by the transformation of the microdomain structure into a lamellar morphology – that is, alternating structures of crystalline and amorphous layers [43].

The morphology of alternate crystalline and amorphous layers in PCL-*b*-PB copolymers is more complicated, however, than of those found in the case of miscible crystalline/crystalline homopolymer blends (with a large crystallization rate asymmetry). In the case of the former, a covalent connectivity of the amorphous and crystalline blocks prevented a macrophase separation or complete rejection of the amorphous blocks from the crystalline region/blocks. The SAXS curves obtained during the melting (or crystallization) transformations in the PCL-*b*-PB

copolymers often showed two well-separated characteristic peaks corresponding to the microdomain structure (at high- $s$ ) of dimension  $D$  (the repeating distance of the microdomain structure), and lamellar morphology (at low- $s$ ) of dimension  $L$  (long spacing of lamellar morphology) prevailing in the system. However, late stage melting of the copolymer was marked by a combined bimodal distribution of the diffraction peaks, as shown in Figure 6.10. The contribution of each peak can be separated computationally from the combined curve by approximating individual peaks with the phenomenological functions of Gaussian  $I_G(s)$ , and Lorentzian  $I_L(s)$ , while the combined curve is approximated by *pseudo-Voigt* function  $I_V(s)$  expressed as a linear combination of the former two in the ratio  $\eta:1 - \eta$  and defined as follows:

$$I_G(s) = \frac{2A\sqrt{\ln 2}}{\sqrt{\pi}W} \exp \left[ -\frac{4 \ln 2}{W^2} (s - s_{\max})^2 \right] \quad (6.47)$$

$$I_L(s) = \frac{2A}{\pi W} \left[ 1 + \frac{4}{W^2} (s - s_{\max})^2 \right]^{-1} \quad (6.48)$$

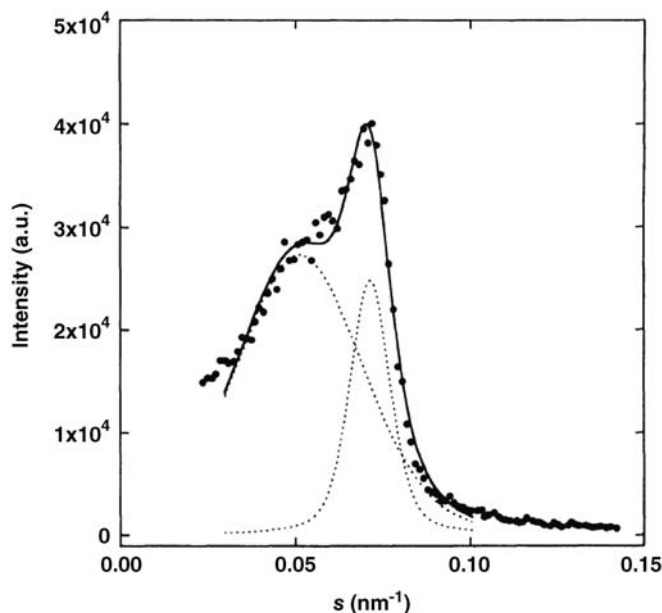


**Figure 6.10** Experimental SAXS peaks obtained from late-stage melting of poly( $\epsilon$ -caprolactone)-*block*-polybutadiene copolymers. The solid line in the figure depicts the best-fit curve which is a sum of two *pseudo-Voigt* functions represented by the broken curves (in the diagram),

and belongs to two different scattering peaks arising from microdomain structure (at high- $s$ ) and the lamellar morphology (at low- $s$ ), respectively. Reproduced with permission from Ref. [43]; © 1998, American Chemical Society.

and

$$I_V(s) = \eta I_G(s) + (1 - \eta) I_L(s) \quad (6.49)$$

where  $W$  is the FWHM of the peak,  $s_{\max}$  is the maximum of  $s$ , and  $A$  is proportional to the peak area. Whereas, Eqs (6.47)–(6.49), presented here to study the late-stage melting behavior peaks of PCL-*b*-PB copolymers are only empirical in nature and follow no theoretical basis for the same, it would not be out of place to mention that Eq. (6.48) is generally applicable for analyzing and resolving SAXS peaks arising from the lamellar morphology and microstructure domains when they are very close, and even during the crystallization of binary blends of PCL-*b*-PB copolymers [42].

### 6.4.3

#### Time-Resolved Studies: Kinetics of Crystallization and Melting

Understanding the mechanism of polymer crystallization is not only important from the point of view of fundamental physics, but also stipulates its need in industrial applications. Structural features associated with the nucleation and growth of crystals in synthetic polymers helps to optimize their manufacturing and processing conditions. Polymers undergo crystallization through chain folding and subsequent ordering, mostly into a lamellar morphology of the folded chains (as discussed earlier). However, there is no unified theory to describe satisfactorily which situation is universally applicable to all polymeric systems. To date, several structural models of polymer crystals have been proposed. Initially, the fringed micelle model assumed that polymer crystals would consist of partly crystalline and partly amorphous domains; hence, this was termed the semi-crystalline model. Within the crystal, ordered arrays (known as crystallite) are separated from each other by an amorphous domain. Another model that closely followed the fringed micelle model was termed the folded chain lamellar model. Accordingly, the crystalline region takes the form of thin platelets or thin lamellae (crystallites) which carry polymer chains that are aligned perpendicular to the flat surface of the platelets and fold repeatedly. Later, an adjacent re-entry model and a switch-board model were also proposed. Owing to such arguments, an understanding of the kinetics and structural pathways of melt crystallization and the melting of polymers becomes even more important. Currently, one of the most widely accepted theories for the kinetics of isothermal crystallization is due to Avrami, and is given by the equation:

$$X(t) = 1 - e^{-Kt^n} \quad (6.50)$$

where  $X(t)$  is the extent of crystallization at time  $t$ ,  $K$  is the overall crystallization rate constant which contains contribution from both nucleation and growth, and  $n$  is known as the Avrami exponent. Depending on the presence or absence of a pre-existing seed nuclei, nucleation is classified as either primary nucleation

(homogeneous) or secondary nucleation (heterogeneous). The Avrami exponent may be expressed as

$$n = n_d + n_n \quad (6.51)$$

where  $n_d$  is the dimensionality of growing crystals and has integer values of 1, 2, or 3. Values of 2 and 3 are found commonly in polymers and are due to 2D lamellar aggregates and 3D aggregates of radial lamellae (spherulites), respectively.  $n_n$  represents the time dependence of nucleation, and can have values of either 0 (instantaneous or heterogeneous nucleation) or 1 (sporadic or homogeneous nucleation). Since nucleation sometimes lies in between completely instantaneous to completely homogeneous, a non-integer Avrami exponent is also possible.

Despite intense research in the field, the kinetics/mechanism of crystallization remains poorly understood. Whereas, traditional studies with X-rays involved the investigations of and information relating to ordered regions, a more detailed understanding of the mechanism requires information regarding the time evolution of both the crystalline and amorphous phases simultaneously during the transformations. However, with the advent of synchrotron sources enabling a faster data collection, mapping the path of isothermal crystallization, or the reverse phenomenon of melting in semi-crystalline polymers and blends over a temperature range of 10°C close to the melting transition, using SAXS/WAXS, have become even more easier and widespread. Time-resolved SAXS measurements using synchrotron sources (often referred to as SR-SAXS) have emerged as a robust tool for studying the kinetics of crystallization and melting in polymeric systems. Simultaneous information concerning the morphology and key structural features of polymer melting or crystallization can be obtained using either SAXS (for lamellar crystal arrangements) and/or WAXS (for polymer chain ordering) measurements.

In conventional X-ray scattering studies, the parameters of interest for monitoring these processes (i.e., changes in morphology) involved crystallinity ( $\chi_c$  or  $X_c$ ), long period ( $L$  or  $L_p$ ), and the SAXS integrated intensity or the invariant  $Q$ . These measurements are often combined with simultaneous optical microscopy/spectroscopy and thermal property measurements aimed at identifying the different regions of nucleation and growth of crystallization in semi-crystalline homopolymer and diblock copolymer blends during such transitions. A number of experiments employing simultaneous SAXS and calorimetric measurements have been reported on polymeric systems, namely both syndiotactic [44,45] and isotactic [46–48] polypropylene, and polyethylene and its copolymers [49–57]. The characteristic features observed in SAXS measurements of the melting process include: (i) a gradual decrease in the integrated intensity from the semi-crystalline microstructure as the melting temperature ( $T_m$ ) is approached and vanishes completely at  $T_m$ ; (ii) the interference maximum shifts towards lower angles at temperatures close to  $T_m$  (during heating); and (iii) the intensity of interference maximum becomes less prominent simultaneously, and the overall pattern gradually evolves towards that of single particle scattering with a maximum at zero angles. These SAXS signatures are generally reversed in the case of crystallization.

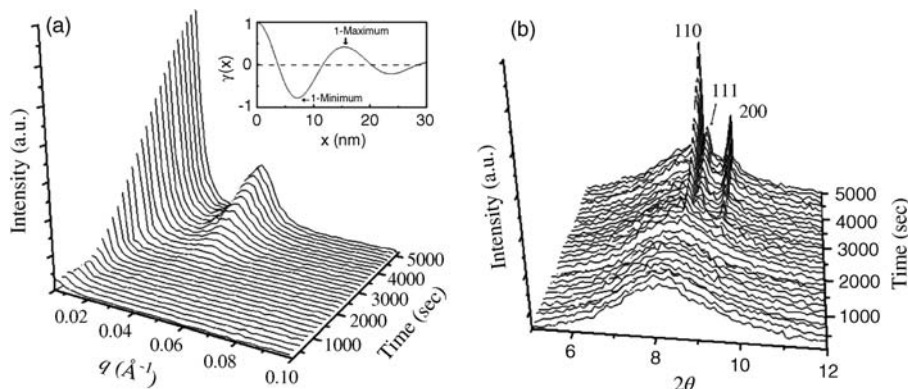


**Figure 6.11** Time evolution of (a) SAXS and (b) WAXS profiles for the isothermal crystallization of PCL/PEG blend at 48 °C. The inset in panel (a) shows the correlation function estimated from the SAXS data at evolution time of 4100 s after quenching. Adapted from Ref. [58].

The competition between liquid–liquid phase separation (LLPS) and early-stage crystallization plays a significant role in determining the final structure and morphology of semicrystalline/amorphous polymer blends, as described by Chuang *et al.* (see Ref. [58] and references therein). Such coupling between LLPS and crystallization may cause the polymer blend to become kinetically trapped in a non-equilibrium state, leading to structures and morphology that may affect the properties of the blend. Such experiments have challenged the classical view of understanding crystallization as a mere two-stage process of nucleation followed by a growth mechanism. Figure 6.11 shows the typical SAXS and WAXS profiles obtained from isothermal crystallization of poly( $\epsilon$ -caprolactone)/poly(ethylene glycol) blends (henceforth referred as PCL/PEG blends) at 48 °C (when the sample temperature fell rapidly from 160 °C to 48 °C), below the  $T_m$  of PCL (62 °C). In the SAXS data, a detectable broad halo appears after 2000 s in the vicinity of  $q = 0.031 \text{ \AA}^{-1}$  which gradually develops into a sharp peak after 4500 s, signifying the formation of well-defined lamellar stacks. Shifting of the peak with time to larger  $q$ -values indicates the condensing of these stacks as crystallization proceeds. The inset in Figure 6.11a shows the plot of correlation function,  $\gamma(x)$ , estimated from the SAXS data after 4100 s of crystallization. The values of the long period  $L = 15.4 \text{ nm}$  (first maxima of the correlation function), thickness ( $l_1 = 7.1 \text{ nm}$ ) of the thinner and thicker ( $l_2 = L - l_1 = 8.3 \text{ nm}$ ) phase of the lamellar stacks are estimated from the correlation function using the method described earlier. These values suggested a corresponding value of linear crystallinity as either 0.46 ( $X_1 = l_1/L$ ) or 0.54 ( $X_2 = l_2/L$ ). In line with DSC predictions (bulk crystallinity,  $\phi_c \approx 0.47$ ),  $l_1$  is assigned to amorphous layer thickness,  $l_a$ , while  $l_2$  is associated with the thickness of the crystalline layers,  $l_c$ . The estimated values of the parameters  $L$ ,  $l_a$ ,  $l_c$  and SAXS invariant  $Q$ , and their evolution at different times of crystallization, are depicted in Figure 6.12, along with crystallinity,  $X_c$  (from WAXS) and  $X_{c \text{ DSC}}$  (from DSC). The results suggested that PCL/PEG blend crystallization is a



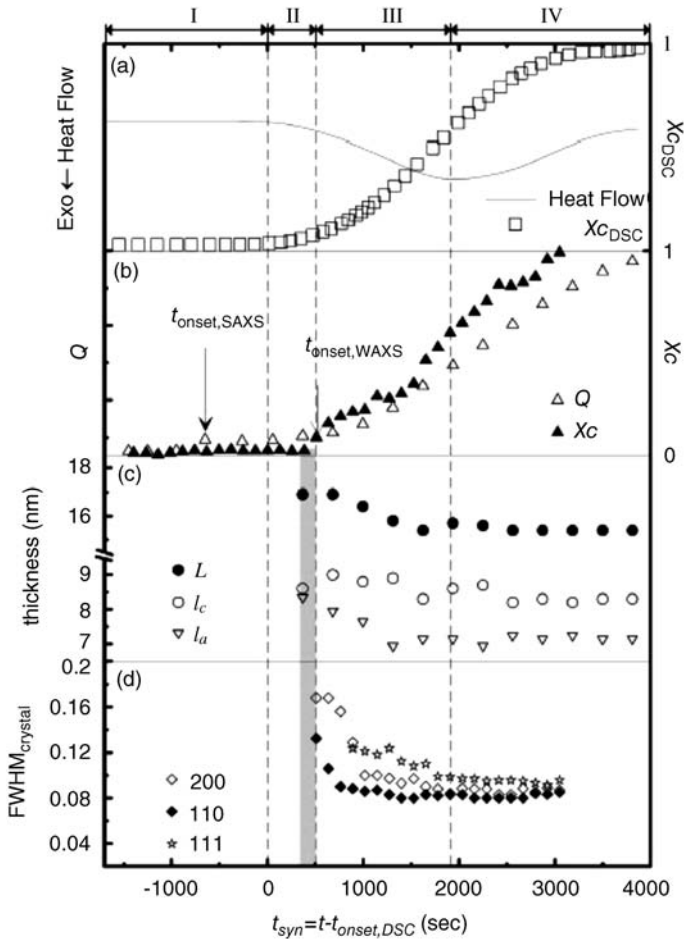


**Figure 6.12** Time evolution of the parameters  $L$ ,  $l_a$ ,  $l_c$  and the SAXS invariant,  $Q$ , along with crystallinity,  $X_c$  (from WAXS) and  $X_{c,DSC}$  (from DSC) for the isothermal crystallization of PCL/PEG blend. The four stages of structural evolution are also marked in the figure. Adapted from Ref. [58].

four-stage process consisting of induction (I), nucleation (II), growth (III), and late stage (IV), as shown in the figure.

## 6.5

### Conclusions

This chapter has provided a brief presentation of the underlying theories, and the analytical tools and techniques used to characterize polymer blends by X-ray scattering (SAXS and WAXS). The text was not aimed at reviewing the studies conducted with all types of polymer blends – that is, miscible versus immiscible

blends, or any combinations thereof with semicrystalline/semicrystalline, semi-crystalline/amorphous and amorphous/amorphous components – specific examples have been given to explain the concept and tools involved for analyzing the experimental data. Data analysis in the field of scattering is mostly limited by the availability of specific models, the information is obtained in the reciprocal space, and as such their conversion to useful real space information remains a major challenge in the field. For example, the challenges posed by a need to improve the optics of SAXS instrumentation, the loss of information caused by smearing/de-smearing and background correction procedures, and the conversion of 3D data to two dimensions, as are obtained in such experiments, calls for an intense research effort. The results of recent studies [59,60] have confirmed that significant improvements in the quality of structural information from the oriented part of the scattering can be achieved through image reconstruction (via the automatic processing of SAXS images), followed by computation of the chord distribution function (CDF), and through WAXS image processing in the microfibrillar composites produced from oriented polymer blends.

Finally, the advent of synchrotron-mediated (intense) sources of X-rays has led to dramatic improvements in the study of dynamics and transient processes such as crystallization in polymer blends. Moreover, the capability of measuring nano-scale dimensions via small-angle scattering will have great potential for future investigations of nanostructured materials and devices.

## References

- 1 Alexander, L.E. (1969) *X-Ray Diffraction Methods in Polymer Science*, John Wiley & Sons, New York.
- 2 Baltá-Calleja, F.J. and Vonk, C.G. (1989) *X-Ray Scattering of Synthetic Polymers*, Elsevier.
- 3 Cebe, P., Hsiao, B.S., and Lohse, D.J. (eds) (1999) *Scattering from Polymers*, ACS Symposium Series 739, American Chemical Society, Washington, DC.
- 4 Jones, R. and Jones, R.A.L. (2002) *Soft Condensed Matter*, Oxford University Press, Oxford.
- 5 Strobl, G. (1996) *The Physics of Polymers*, Springer, Berlin.
- 6 Nogales, A., Broza, G., Roslaniec, Z., Schulte, K., Šics, I., Hsiao, B.S., Sanz, A., García-Gutiérrez, M.C., Rueda, D.R., Domingo, C., and Ezquerro, T.A. (2004) Low percolation threshold in nanocomposites based on oxidized single wall carbon nanotubes and poly(butylene terephthalate). *Macromolecules*, **37**, 7669–7672.
- 7 Rueda, D.R., García-Gutiérrez, M.C., Nogales, A., Capitán, M.J., Ezquerro, T.A., Labrador, A., Fraga, E., Beltrán, D., Juanhuix, J., Herranz, J.F., and Bordas, J. (2006) Versatile wide angle diffraction setup for simultaneous wide and small angle X-ray scattering measurements with synchrotron radiation. *Rev. Sci. Instrum.*, **77**, 033904.
- 8 Guinier, A. and Fournet, G. (1955) *Small Angle Scattering of X-Rays*, Wiley, New York.
- 9 Chu, B. and Hsiao, B.S. (2001) Small-angle X-ray scattering of polymers. *Chem. Rev.*, **101**, 1727–1761.
- 10 Kratky, O. and Stabinger, H. (1984) X-ray small-angle camera with block collimation. *Colloid Polym. Sci.*, **262**, 345–360.
- 11 Glatter, O. and Kratky, O. (eds) (1982) *Small Angle X-ray Scattering*, Academic Press, New York.

- 12 Blundell, T.L. and Johnson, L.N. (1976) *Protein Crystallography*, Academic Press, New York.
- 13 Feigin, L.A. and Svergun, D.I. (1987) *Structure Analysis by Small-Angle X-Ray and Neutron Scattering*, Plenum Press, New York.
- 14 Koch, M.H., Vachette, P., and Svergun, D.I. (2003) Small-angle scattering: A view on the properties, structures and structural changes of biological macromolecules in solution. *Q. Rev. Biophys.*, **36**, 147–227.
- 15 Putnam, C.D., Hammel, M., Hura, G.L., and Tainer, J.A. (2007) X-ray solution scattering (SAXS) combined with crystallography and computation: Defining accurate macromolecular structures, conformations and assemblies in solution. *Q. Rev. Biophys.*, **40**, 191–285.
- 16 Svergun, D.I. (2007) Small-angle scattering studies of macromolecular solutions. *J. Appl. Crystallogr.*, **40**, S10–S17.
- 17 Svergun, D.I. and Koch, M.H.J. (2003) Small-angle scattering studies of biological macromolecules. *Rep. Prog. Phys.*, **66**, 1735–1782.
- 18 Tsuruta, H. and Irving, T. (2008) Experimental approaches for solution X-ray scattering and fiber diffraction. *Curr. Opin. Struct. Biol.*, **18**, 601–608.
- 19 Talibuddin, S., Wu, L., Runt, J., and Lin, J. S. (1996) Microstructure of melt-miscible, semicrystalline polymer blends. *Macromolecules*, **29**, 7527–7535.
- 20 Chen, H.L., Li, L.J., and Lin, T.L. (1998) Formation of segregation morphology in crystalline/amorphous polymer blends: Molecular weight effect. *Macromolecules*, **31**, 2255.
- 21 Chen, H.L. and Hsiao, M.S. (1998) Morphological structure induced by combined crystallization and liquid-liquid demixing in poly(ethylene terephthalate)/poly(ether imide) blends. *Macromolecules*, **31**, 6579.
- 22 Yeh, F., Hsiao, B.S., Chu, B., Sauer, B.B., and Flexman, E.A. (1999) Effect of miscible diluent on the lamellar morphology of poly(oxyethylene) blends. *J. Polym. Sci., Polym. Phys. Ed.*, **37**, 3115–3122.
- 23 Hosemann, R. and Bagchi, S.N. (1962) *Direct Analysis of Diffraction by Matter*, North-Holland, Amsterdam.
- 24 Vonk, C.G. (1982) in *Small-Angle X-ray Scattering* (eds O. Glatter and O. Kratky), Academic Press, New York.
- 25 Vonk, C.G. and Kortleve, G. (1967) X-ray small-angle scattering of bulk polyethylene. *Kolloid Z. Z. Polym.*, **220**, 19.
- 26 Debye, P. and Bueche, A.M. (1949) Scattering by an inhomogeneous solid. *J. Appl. Phys.*, **20**, 518.
- 27 Debye, P., Anderson, R., and Brumberger, H. (1957) Scattering by an inhomogeneous solid. II. The correlation function and its application. *J. Appl. Phys.*, **28** (6), 679.
- 28 Ruland, W. (1971) Small-angle scattering of two-phase systems: Determination and significance of systematic deviations from Porod's law. *J. Appl. Crystallogr.*, **4**, 70–73.
- 29 Porod, G. (1951) The small-angle X-ray scattering from densely packed colloidal systems. *Kolloid-Zeitschrift*, **124**, 83–114.
- 30 Porod, G. (1952) Die Röntgenkleinwinkelstreuung von dichtgepackten kolloiden Systemen. II. Teil. *Kolloid-Zeitschrift*, **125**, 51–57.
- 31 Porod, G. (1952) Die Röntgenkleinwinkelstreuung von dichtgepackten kolloiden Systemen. II. Teil. *Kolloid-Zeitschrift*, **125**, 108–122.
- 32 Liu, Li-Zhi, Chu, Benjamin, Penning, J.P., and Manley, R. St. John (1997) A synchrotron SAXS study of miscible blends of semicrystalline poly(vinylidene fluoride) and semicrystalline poly(1,4-butylene adipate). *Macromolecules*, **30**, 4398–4404.
- 33 Verma, R., Marand, H., and Hsiao, B. (1996) Morphological changes during secondary crystallization and subsequent melting in poly(ether ether ketone) as studied by real time small angle X-ray scattering. *Macromolecules*, **29**, 7767–7775.
- 34 Wang, W., Schultz, J.M., and Hsiao, B.S. (1997) Dynamic study of microstructures during crystallization and melting of PEEK/PEKK blend. *Macromolecules*, **30**, 4544–4550.
- 35 Auriemma, F., deBallesteros, O.R., and De Rosa, C. (2010) Theoretical investigation of nano-scale organization in blends of semicrystalline/semicrystalline polymers by small angle X-ray scattering. *Macromolecules*, **43**, 9787–9801.
- 36 Santa Cruz, C.S., Stribeck, N., Zahmann, H.G., and Baltá-Calleja, F. (1991) Novel

- aspects in the structure of poly(ethylene terephthalate) as revealed by means of small angle x-ray scattering. *J. Macromolecules*, **24**, 5980.
- 37 Floudas, G., Hadjichristidis, N., Stamm, M., Likhhtman, A.E., and Semenov, A.N. (1997) Microphase separation in block copolymer/homopolymer blends: Theory and experiment. *J. Chem. Phys.*, **106**, 3318–3328.
  - 38 Chen, Shih-Chien, Kuo, Shiao-Wei, Jeng, U-Ser, Su, Chun-Jen, and Chang, Feng-Chih (2010) On modulating the phase behavior of block copolymer/homopolymer blends via hydrogen bonding. *Macromolecules*, **43**, 1083–1092.
  - 39 Bates, F.S. (1990) Block copolymer thermodynamics: Theory and experiment. *Annu. Rev. Phys. Chem.*, **41**, 525–557.
  - 40 Cohen, R.E. and Wilfong, D.E. (1982) Properties of block copolymers and homopolymer blends comprised of 1,2-polybutadiene and 1,4-polybutadiene. *Macromolecules*, **15**, 370–375.
  - 41 Bates, F.S., Bair, H.E., and Hartney, M.A. (1984) Block copolymers near the microphase separation transition. 1. Preparation and physical characterization of model system. *Macromolecules*, **17**, 1987.
  - 42 Tanimoto, S., Ito, K., Sasaki, S., Takeshita, H., and Nojima, S. (2002) Crystallization process in binary blends of poly ( $\epsilon$ -caprolactone)-*block*-polybutadiene copolymers. *Polym. J.*, **34**, 593–600.
  - 43 Nojima, S., Kanda, Y., and Sasaki, S. (1998) Time-resolved small-angle X-ray studies on the melting behavior of poly ( $\epsilon$ -caprolactone)-*block*-polybutadiene copolymers. *Polym. J.*, **30**, 628–634.
  - 44 Schmidtke, J., Strobl, G., and Thurn-Albrecht, T. (1997) A four-state scheme for treating polymer crystallization and melting suggested by calorimetric and small angle X-ray scattering experiments on syndiotactic polypropylene. *Macromolecules*, **30**, 5804–5821.
  - 45 Hauser, G., Schmidtke, J., and Strobl, G. (1998) The role of *co*-units in polymer crystallization and melting: New insights from studies on syndiotactic poly(propene-*co*-octene). *Macromolecules*, **31**, 6250–6258.
  - 46 Ryan, A.J., Stanford, J.L., Bras, W., and Nye, T.M.W. (1997) A synchrotron X-ray study of melting and recrystallization in isotactic polypropylene. *Polymer*, **38**, 759–768.
  - 47 Iijima, M. and Strobl, G. (2000) Isothermal crystallization and melting of isotactic polypropylene analyzed by time- and temperature-dependent small-angle X-ray scattering experiments. *Macromolecules*, **33**, 5204–5214.
  - 48 Dai, P.S., Cebe, P., Capel, M., Alamo, R.G., and Mandelkern, L. (2000) Simultaneous in-situ SAXS and WAXS study of crystallization and melting behavior of metallocene isotactic poly(propylene), in *Scattering from Polymers. Characterization by X-Rays, Neutrons and Light* (eds P. Cebe, B.S. Hsiao, and D.J. Lohse), ACS Symposium Series 739, American Chemical Society, Washington, DC, pp. 152–165.
  - 49 Fulcher, K.U., Brown, D.S., and Wetton, R.E. (1972) Morphological changes during the melting of bulk-crystallized polymers. *J. Polym. Sci. Part C: Polym. Symp.*, **38**, 315.
  - 50 Schultz, J.M., Fischer, E.W., Schaumburg, O., and Zachmann, H.G. (1980) Small-angle X-ray studies of melting. *J. Polym. Sci. Polym. Phys. Ed.*, **18**, 239–245.
  - 51 Strobl, G.R., Schneider, M.J., and Voight-Martin, I.G. (1980) Model of partial crystallization and melting derived from small-angle X-ray scattering and electron microscopic studies on low-density polyethylene. *J. Polym. Sci. Polym. Phys. Ed.*, **18**, 1361–1381.
  - 52 Vonk, C.G. and Koga, Y. (1985) An X-ray diffraction study of nonlinear polyethylene. II. Small-angle scattering observations near the melting point. *J. Polym. Sci. Polym. Phys. Ed.*, **23**, 2539–2548.
  - 53 Tanabe, Y., Strobl, G.R., and Fischer, E.W. (1986) Surface melting in melt-crystallized linear polyethylene. *Polymer*, **27**, 1147.
  - 54 Schouterden, P., Vandermarliere, M., Riekkel, C., Koch, M.H.J., Groeninckx, G., and Raynaers, H. (1989) Characterization of the morphological changes in linear low-density polyethylene during the melting process using synchrotron radiation. *Macromolecules*, **22**, 237–244.
  - 55 Albrecht, T. and Strobl, G. (1995) Temperature-dependent crystalline-amorphous structures in linear

- polyethylene - surface melting and the thickness of the amorphous layers. *Macromolecules*, **28**, 5827–5833.
- 56 Goderis, B., Reynaers, H., Koch, H.M.J., and Mathot, V.B.F. (1999) Use of SAXS and linear correlation functions for the determination of the crystallinity and morphology of semi-crystalline polymers. Application to linear polyethylene. *J. Polym. Sci. Part B: Polym. Phys.*, **37**, 1715–1738.
- 57 Goderis, B., Peeters, M., Mathot, V.B.F., Koch, M.H.J., Bras, W., Ryan, A.J., and Reynaers, H. (2000) Morphology of homogeneous copolymers of ethylene and 1-octene. III. Structural changes during heating as revealed by time-resolved SAXS and WAXD. *J. Polym. Sci. Part B: Polym. Phys.*, **38**, 1975–1991.
- 58 Chuang, W., Jeng, U., Sheu, H., and Hong, P. (2006) Competition between phase separation and crystallization in PCL/PEG polymer blend captured by synchronized SAXS, WAXS and DSC. *Macromol. Res.*, **14**, 45–51.
- 59 Stribeck, N. and Fakirov, S. (2001) Three-dimensional chord distribution function SAXS analysis of 48 the strained domain structure of a poly(ether ester) thermoplastic elastomer. *Macromolecules*, **34**, 7758–7761.
- 60 Barbi, V., Funari, S.S., Gehrke, R., Scharnagl, N., and Stribeck, N. (2003) Nanostructure of Nafion membrane material as a function of mechanical load studied by SAXS. *Polymer*, **44**, 4853–4861.



## 7

# Characterization of Polymer Blends and Block Copolymers by Neutron Scattering: Miscibility and Nanoscale Morphology

Kell Mortensen

## 7.1

### Introduction

The interaction between materials and radiation takes a variety of forms, including absorption and fluorescence, refraction, scattering and reflection. These types of interaction are all tightly related in terms of physical quantities. In this chapter, attention will be focused on the scattering term, when used to determine materials' properties such as miscibility and nanoscale structure. The method relies on the wave-character of the radiation; this is the case whether using electromagnetic beams of light or X-rays with oscillating electric and magnetic fields, or particle radiation such as neutrons or electrons. In the latter cases, it is the de Broglie wave character of the particles that is the relevant quantity.

Insight into structural properties using scattering techniques appears as a result of the interference between radiation that is scattered from different sites in the sample. A simple illustration is given in the Young interference experiment, shown in Figure 7.1, where the radiation of plane waves propagate through two slits, making an interference pattern that depend on the separation distance between the two slits, and the wavelength of the radiation.

## 7.2

### Small-Angle Scattering

The principle of small-angle scattering is illustrated schematically in Figures 7.2 and 7.4. A sample is placed in a collimated, monochromatic beam and the scattered beam is monitored. The detected scattering pattern reflects the structural properties of the sample. Small-angle scattering by X-rays (SAXS) or by neutrons (SANS) are ideal techniques for studying structures on the length scale of 1 to 500 nm, that is, nanoscale structural properties such as macromolecules, nanoparticles or molecular density fluctuations. Neutron sources for SANS experiments may be either continuous (typical for reactor sources) or pulsed (typical for spallation sources). For the pulsed sources, the demand for a monochromatic beam

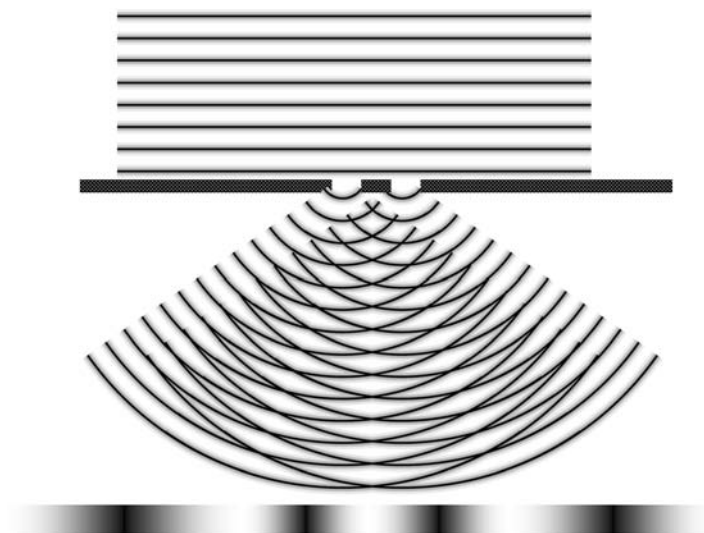


**Figure 7.1** Experiments using scattering methods rely on interference between wave-like radiation, here illustrated schematically in Young's two-slit experiment.

can be obtained using the time-profile of the elastic scattered beam, or the beam can be monochromatized as required in the reactor case. SAXS instruments may be either laboratory instruments based on an irradiated anode source, or located at synchrotron facilities.

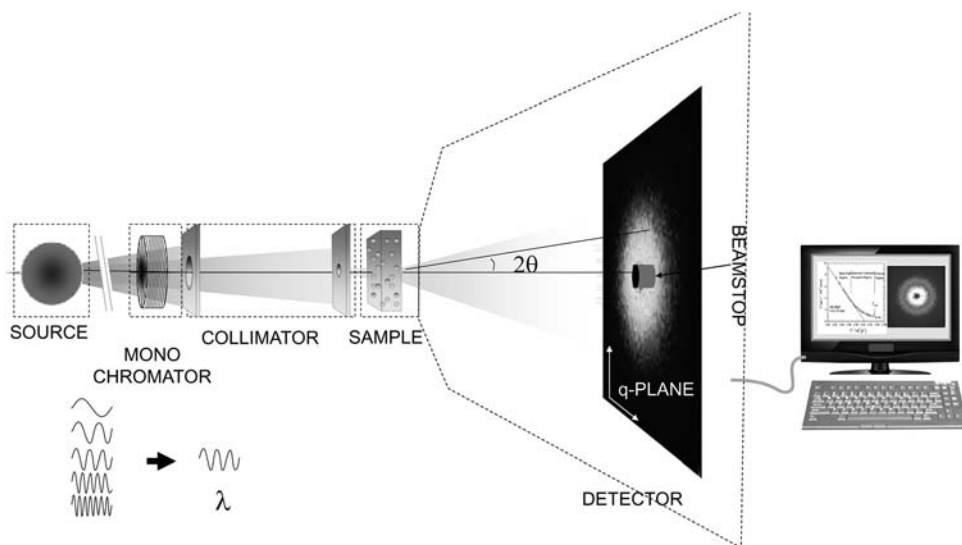


**Figure 7.2** Illustration of small-angle scattering.



The scattered beam is, beyond trivial factors such as incoming flux, transmission and geometric factors, proportional to two terms: (i) a contrast factor reflecting the ability of individual atoms to interact with the radiation; and (ii) the structure factor resulting from interference effects of scattering originating from different sites in the sample, providing information on structural properties.

Reflectometry is somewhat related to small-angle scattering, especially grazing-incidence reflectometry. Simple reflectometry measures the reflected beam from a surface or interface of the sample investigated.

### 7.2.1

#### Contrast

In order to measure structural properties, there must be difference between the ability to scatter radiation from the characteristic elements to be studied. There must also be a contrast, as seen by the applied radiation.

Neutrons are probably best known as elementary particles that comprise the nuclei of atoms. Typical nuclei contain approximately similar numbers of protons and neutrons. The free neutron has, as any particle, an associated wavelength determined by the mass,  $m_n$ , and the velocity,  $v_n$ , according to the de Broglie relation:

$$\lambda_n = \frac{h}{m_n v_n}$$

where  $h$  is Planck's constant. At ambient temperatures,  $T = 300$  K,  $v_n = \sqrt{k_B T / m_n} \approx 3000$  m s<sup>-1</sup> giving the thermal neutron wavelength:  $\lambda_n = 1.4$  Å. This value, which is of the same order of magnitude as that of X-radiation, makes neutrons effective as structural probes on the nanometer length scale.

The interaction between neutrons and matter is complex, and includes magnetic terms as the neutron itself is magnetic. The interaction between a neutron and a nuclei can generally not be calculated *ab initio*, but is given in tables based on experimental values of scattering lengths and scattering cross-sections. The interaction between the electrons and the neutron is primarily via the magnetic moment. The magnetic interaction makes neutron scattering ideal for studying magnetic structures and fluctuations.

For nonmagnetic materials, the magnetic moments of the nuclei are completely uncorrelated. The magnetic scattering is therefore not coherent, but gives rise to an isotropic incoherent background that may be quite large for some materials. An important example here is hydrogen <sup>1</sup>H, which has a large incoherent scattering contribution. Oxygen <sup>16</sup>O and carbon <sup>12</sup>C, on the other hand, are examples of elements that produce very little incoherent background due to the vanishing magnetic moment in these nuclei.

The nonmagnetic interaction gives rise to coherent scattering, where interference effects are effective. This is the part of the scattering that provides insight into the structural properties. The interaction with neutrons not only depends on the atomic number within the periodic system; indeed, different

**Table 7.1** Scattering length and incoherent scattering cross-section of typical nuclei of soft matter materials. Nuclei with no index represent natural, mixed isotopes [<http://www.ncnr.nist.gov/resources/n-lengths>].

Nuclei	Coherent scattering length	Incoherent cross-section
	$b$	$\sigma_{ic}$
H	$-0.3739 \times 10^{-12}$ cm	$80.26 \times 10^{-24}$ cm <sup>2</sup>
<sup>1</sup> H	$-0.3741 \times 10^{-12}$ cm	$80.27 \times 10^{-24}$ cm <sup>2</sup>
<sup>2</sup> H = D	$0.6671 \times 10^{-12}$ cm	$2.05 \times 10^{-24}$ cm <sup>2</sup>
C	$0.6646 \times 10^{-12}$ cm	$0.001 \times 10^{-24}$ cm <sup>2</sup>
N	$0.936 \times 10^{-12}$ cm	$0.5 \times 10^{-24}$ cm <sup>2</sup>
O	$0.5803 \times 10^{-12}$ cm	$0.0 \times 10^{-24}$ cm <sup>2</sup>
Si	$0.4149 \times 10^{-12}$ cm	$0.004 \times 10^{-24}$ cm <sup>2</sup>

isotopes of the same atom may have significantly different abilities to scatter neutrons, and even different signs in the related scattering length,  $b$ . A most important example of this is hydrogen, where the most common <sup>1</sup>H isotope (H) and the heavy hydrogen counterpart, <sup>2</sup>H, deuterium (D) have significant different scattering lengths:  $b_H = -0.3739 \times 10^{-12}$  cm and  $b_D = 0.6671 \times 10^{-12}$  cm. The scattering lengths and incoherent scattering cross-sections for selected isotopes are listed in Table 7.1.

Chemically, the two hydrogen isotopes are similar, and specific structural identities can thereby be highlighted by replacing H with D at given chemical sites; specific units can be “colored” to make them visible in the neutron beam.

Important examples using deuterium labeling include polymer melts, where individual polymer coils can be highlighted by mixing similar polymers with respectively H and D atoms in the chain; this is illustrated in Figure 7.3.

The characteristics of small-angle scattering does not allow atomic resolution. It is desirable, therefore, to substitute the nuclear scattering lengths,  $b$ , with a continuous *scattering length density* function,  $\rho$ , which averages the  $b$ -values over an appropriate volume  $V$ , which should be small compared to the instrumental resolution.  $\rho$  is thus defined as

$$\rho = \frac{1}{V} \sum_V b_i = \frac{N_A \delta}{M_V} \sum_V b_i \quad (7.1)$$

which is summed over the nuclear  $b_i$ -values within the volume  $V$ .  $N_A$  is Avogadro’s number,  $\delta$  the mass density, and  $M_V$  the molar mass corresponding to the chosen volume. For a liquid, one would typically calculate  $\rho$  based on the sum over a single solvent molecule, while for a polymer it would be that of the monomer unit.

For X-rays, the interaction between radiation and matter is primarily via interaction between the electrons and the oscillatory electric field of the electromagnetic beam.  $E = E_0 \cos(\omega t)$ . An electron will, in the X-ray beam, be accelerated by the oscillating electric field; an accelerated charged particle, on the other hand, will

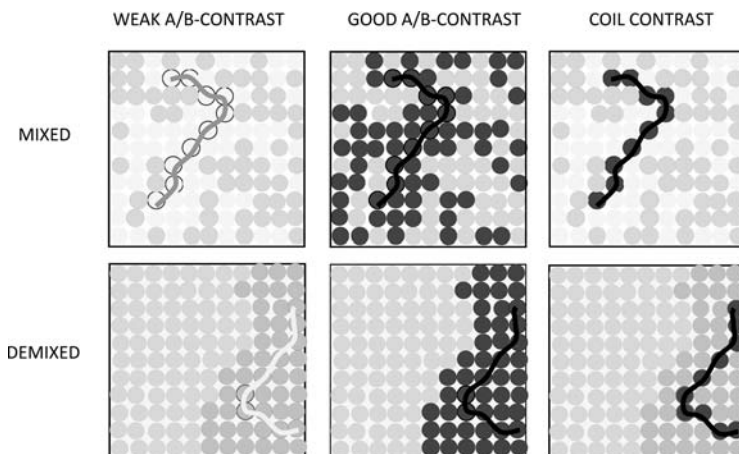


**Figure 7.3** Neutron scattering contrasts of polymer blend, illustrating good and weak contrast. The weak contrast examples illustrate the contrast within typical polymer blends. The good contrast example illustrates how contrast between the A and B-polymers can be

enhanced using D-labeling. The coil contrast example shows how “single” coils can be labeled to study the conformation of individual polymer chains in the mixed and in the demixed states. The units may be interpreted as the Kuhn-length of the polymer chain.

irradiate radiation itself with frequency equal to the accelerating field. The result is X-ray irradiated from the electron:

$$\mathbf{E}_{\text{rad}} \propto -\frac{e^2}{m_e c^2} \frac{\mathbf{E}}{r} \quad (7.2)$$

The pre-factor in Eq. (7.2) is the scattering length,  $b$ , for an individual electron, that is,

$$b_e = -\frac{e^2}{m_e c^2} = 0.282 \times 10^{-4} \text{ \AA} \quad (7.3)$$

with the dimension of length.  $b_e$  of the electron is also called the Thompson scattering length. To obtain the scattering of an atom, it is necessary to integrate over all electrons in the atom which, for small angles (small  $q$ ) approach  $b_e$  times the number of electrons, that is,

$$b_{\text{atom}} \approx b_e \cdot Z.$$

Different polymers have typically rather similar electron densities, giving only weak X-ray contrasts. Neutron scattering is therefore usually superior for studying the thermodynamics of polymer blends, using specific deuterium labeling.

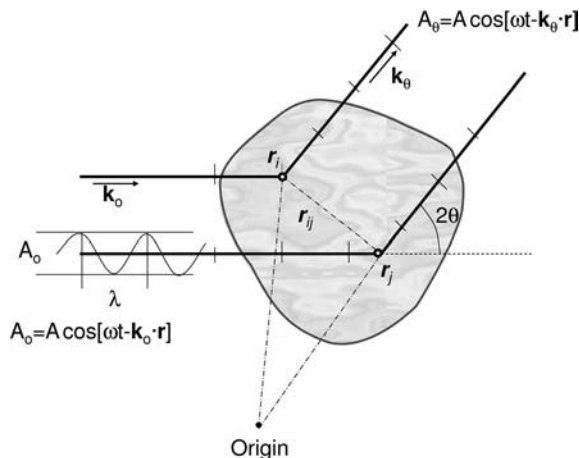


Figure 7.4 Phase difference for scattering from different sites into given angle  $2\theta$ .

### 7.2.2

#### Scattering Function

Figure 7.4 describes schematically the radiation scattered into a given angle  $2\theta$  from two sites in the sample,  $\mathbf{R}_i$  and  $\mathbf{R}_j$ . The incoming radiation is characterized by the wavelength  $\lambda$  and direction given by wave vector  $\mathbf{k}_o$ .

The elastically scattered wave has the same wavelength, and we consider the term scattered into a given angle  $2\theta$  defined by the scattered wave vector  $\mathbf{k}_\theta$ . The phase difference  $\Delta\phi$  between radiation origination from the two sites  $\mathbf{R}_i$  and  $\mathbf{R}_j$  is, from the figure, seen to be  $2\pi/\lambda$  times the path length difference, which may be expressed as

$$\Delta\phi = \mathbf{r}_{ij} \cdot (\mathbf{k}_\theta - \mathbf{k}_o) = \mathbf{r}_{ij} \cdot \mathbf{q} \quad (7.4)$$

where  $\mathbf{r}_{ij} = \mathbf{R}_i - \mathbf{R}_j$ , and  $\mathbf{q} \equiv (\mathbf{k}_\theta - \mathbf{k}_o)$  is the *scattering vector*. The numerical value of  $\mathbf{q}$  is

$$q = |\mathbf{q}| = \frac{4\pi}{\lambda} \sin\theta \quad (7.5)$$

The radiation is for light, X-ray and neutrons expressed in terms of a plane wave with amplitude oscillating in time ( $t$ ) and space ( $\mathbf{R}$ ) which, using complex notation, is expressed as

$$A(\mathbf{R}, t) = A_o \exp[i(\omega t - \mathbf{k} \cdot \mathbf{R})] \quad (7.6)$$

where the real part of Eq. (7.6) reflects the physical value. The radiation scattered from various sites may vary, thus reflecting the ability for different atoms to interact with the beam. The probability that the plane wave is scattered from a given site  $\mathbf{R}_i$  of the sample is defined in terms of the scattering length density,  $\rho$ , as discussed above.

The amplitude of the radiation at a site  $\mathbf{R}$  and time  $t$  scattered from a point  $\mathbf{R}_i$  into the angle  $2\theta$  (i.e., with wave vector  $\mathbf{k}_\theta$  and momentum transfer  $\mathbf{q}$ ) depends on the ability to scatter at the site  $\mathbf{R}_i$  ( $\rho(\mathbf{R}_i)$ ) and the phase is given by the specific scattering site  $\Delta\phi_i = \mathbf{R}_i \cdot \mathbf{q}$ :

$$\begin{aligned} A(\mathbf{q})_{\mathbf{R}_i} &= A_o \rho(\mathbf{R}_i) \exp[i(\omega t - \Delta\phi_i - \mathbf{k}_\theta \cdot \mathbf{R})] \\ &= A_o \rho(\mathbf{R}_i) \exp[-i(\mathbf{q} \cdot \mathbf{R}_i)] \exp[i(\omega t - \mathbf{k}_\theta \cdot \mathbf{R})] \end{aligned} \quad (7.7)$$

The phase-factor  $\exp[i\mathbf{q} \cdot \mathbf{R}_i]$  explicitly gives the phase relative to that of the non-interacting beam. The total radiation amplitude scattered into a given scattering vector  $\mathbf{k}_\theta$ , that is, a scattering momentum  $\mathbf{q}$ , is the simple sum over all sites in the sample:

$$A(\mathbf{q}) = \sum_{\mathbf{R}_i} A(\mathbf{q})_{\mathbf{R}_i} = A_o \sum_{\text{sample}} \rho(\mathbf{R}_i) \exp[-i(\mathbf{q} \cdot \mathbf{R}_i)] \exp[i(\omega t - \mathbf{k}_\theta \cdot \mathbf{R})] \quad (7.8)$$

Now, it is only possibly to measure beam-intensity, but not the direct in time and space oscillating wave. The intensity is equal to the numerically squared value of  $|A(\mathbf{q})|$  or, in complex numbers, the product of  $A(\mathbf{q})$  and the complex conjugated  $A(\mathbf{q})^*$ . Moreover, we measure the ensemble average, thus giving:

$$\tilde{I}(\mathbf{q}) = I_o \sum_i \sum_j \langle \rho(\mathbf{R}_i) \rho(\mathbf{R}_j) \exp[-i(\mathbf{q} \cdot \mathbf{r}_{ij})] \rangle \quad (7.9)$$

with  $A_o^2 = I_o$  equal to the intensity of the incoming beam, and where  $\langle \dots \rangle$  denotes ensemble average. Now, let us normalize with respect to  $I_o$ , giving the scattering function:

$$I(\mathbf{q}) = \sum_i \sum_j \langle \rho(\mathbf{R}_i) \rho(\mathbf{R}_j) \exp[-i(\mathbf{q} \cdot \mathbf{r}_{ij})] \rangle \quad (7.10)$$

Let us further substitute the summations with integrals using that  $\rho(\mathbf{R})$  can be treated as a continuous function. The scattering function Eq. (7.10) can then be reformulated into integral-form, expressed as

$$\begin{aligned} I(\mathbf{q}) &= \int_{\mathbf{R}_i} \int_{\mathbf{R}_j} \langle \rho(\mathbf{R}_i) \rho(\mathbf{R}_j) \rangle \exp[-i\mathbf{q} \cdot \mathbf{r}_{ij}] d\mathbf{R}_j d\mathbf{R}_i \\ &= \int_{\mathbf{R}} \int_{\mathbf{r}} \langle \rho(\mathbf{R}) \rho(\mathbf{R} + \mathbf{r}) \rangle \exp[-i\mathbf{q} \cdot \mathbf{r}] d\mathbf{r} d\mathbf{R} \end{aligned} \quad (7.11)$$

where  $\mathbf{R}_i$  and  $\mathbf{R}_j$  are substituted with respectively  $\mathbf{R}$  and  $\mathbf{R} + \mathbf{r}$ . The averaged correlation function  $\langle \rho(\mathbf{R}) \rho(\mathbf{R} + \mathbf{r}) \rangle$  does not depend on the specific sites  $\mathbf{R}$  and  $\mathbf{R} + \mathbf{r}$ , but only on the distance  $\mathbf{r}$ . The  $\mathbf{R}$ -integral of Eq. (7.11) can thus be eliminated, thereby giving

$$\begin{aligned} I(\mathbf{q}) &= V \cdot \int \langle \rho(\mathbf{R}) \rho(\mathbf{R} + \mathbf{r}) \rangle \exp[-i\mathbf{q} \cdot \mathbf{r}] d\mathbf{r} \\ &= V \cdot \int \gamma(\mathbf{r}) \exp[-i\mathbf{q} \cdot \mathbf{r}] d\mathbf{r} \end{aligned} \quad (7.12)$$

with the correlation function  $\gamma(\mathbf{r}) \equiv \langle \rho(\mathbf{R}) \rho(\mathbf{R} + \mathbf{r}) \rangle$ . We thus see that, mathematically, the scattering function is the Fourier transform of the ensemble-averaged correlation function  $\gamma(\mathbf{r})$  correlating densities separated by distances  $\mathbf{r}$ . For an isolated polymer chain, the correlation function describes the probability of finding segments of the chain separated by a distance  $\mathbf{r}$ . In experimental systems this

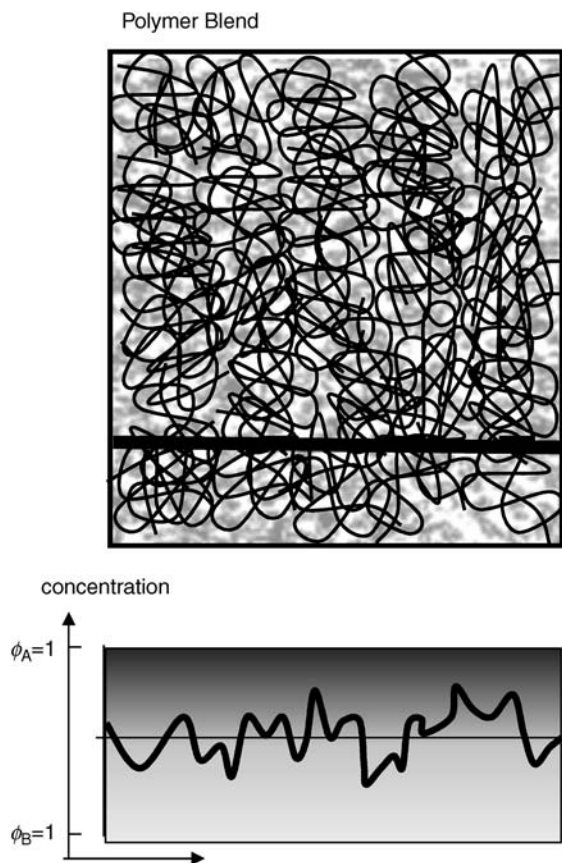


**Figure 7.5** Composition fluctuations in a polymer blend illustrated by blends of black and grey chains.

may be polymer chains in dilute solution, or few labeled chains in an environment of nonlabeled (see Figure 7.3). In polymer blends, the correlation function describes the spatial correlation of concentration fluctuations, as illustrated in Figure 7.5.

### 7.2.3

#### Gaussian Chain

The conformation of ideal polymer chains corresponds to that of a *random walk*. The mutual distance between segments within the chain obey Gaussian statistics [1]. The size of polymer chains is often given in terms of the *end-to-end distance*,  $R_o$ , or the *radius of gyration*,  $R_g$ . The radius of gyration is experimentally accessible from scattering experiments.

The end-to-end vector is given by

$$\mathbf{R}_o = \sum_{i=1}^N \mathbf{R}_i \quad (7.13)$$

where  $N$  is the number of Kuhn-segments (proportional to the degree of polymerization) and  $\mathbf{R}_i$  is the vector of the  $i$ -th segment. For an isotropic collection of chains the average end-to-end vector must be zero:  $\langle \mathbf{R}_o \rangle = 0$ . The mean-square end-to-end distance, on the other hand, is non-zero:

$$\langle \mathbf{R}_o^2 \rangle = \sum_{i=1}^N \sum_{j=1}^N \langle \mathbf{R}_i \cdot \mathbf{R}_j \rangle = Na^2 \quad (7.14)$$

where  $a$  is the segment length:  $a = |\mathbf{R}_i|$ . The center of mass of the coil is

$$\mathbf{R}_c = \frac{1}{N} \sum_{i=1}^N \mathbf{R}_i, \quad (7.15)$$

and the radius of gyration,  $R_g$ , is by definition given as

$$R_g^2 = \frac{1}{N} \sum_{i=1}^N \langle (\mathbf{R}_i - \mathbf{R}_c)^2 \rangle \quad (7.16)$$

which with Eq. (7.15) inserted gives

$$R_g^2 = \frac{1}{2N^2} \sum_{i=1}^N \sum_{j=1}^N \langle (\mathbf{R}_i - \mathbf{R}_j)^2 \rangle \quad (7.17)$$

Gaussian polymer coils obey the relation (see e.g., Doi, [1])

$$\langle (\mathbf{R}_j - \mathbf{R}_i)^2 \rangle = a^2 |j - i| \quad (7.18)$$

The radius of gyration is therefore

$$R_g^2 = \frac{1}{2N^2} \sum_{i=1}^N \sum_{j=1}^N |j - i| a^2 \quad (7.19)$$

For large  $N$  we may replace the sum with integrals, getting

$$R_g^2 = \frac{a^2}{2N^2} \int_0^N \int_0^N |j - i| di = \frac{1}{6} Na^2 = \frac{1}{6} \langle \mathbf{R}_o^2 \rangle \quad (7.20)$$

Gaussian chains are characterized by the distribution function of the two segments separated by  $n$  segments (see e.g., Ref. [1]):

$$P(\mathbf{r}, n) = \left( \frac{3}{2\pi na^2} \right)^{3/2} \exp \left[ -\frac{3\mathbf{r}^2}{2na^2} \right] \quad (7.21)$$

Inserting this into the expression for the correlation function in the scattering function, we get the *form factor* of a Gaussian polymer chain equal the Debye function,  $g_D$ :

$$P(\mathbf{q}) = g_D(\mathbf{q}, R_g) = \frac{2}{x^2} (e^{-x} - 1 + x), \quad x = R_g^2 q^2 \quad (7.22)$$

## 7.3

## Thermodynamics of Polymer Blends and Solutions. Flory–Huggins Theory

The phase behavior of polymer blends and solutions is, like any other mixtures, governed by enthalpic interactions between the different units and entropic effects, as described in thermodynamics [1]. The stable phase is determined from the minimum in free energy.

Flory and Huggins proposed a simple theory to calculate the free energy [2]. This theory will be presented based on the lattice model, assuming that polymer segments all occupy equal unit volume (see Figure 7.6). Assume that we have an ensemble of  $\Omega$  lattice sites available, of which  $n_A$  of the polymer chains are A coils, each characterized having  $N_A$  segments, that is, a volume fraction equal  $\phi_A = n_A N_A / \Omega$ . Correspondingly, there are  $n_B$  coils of polymer B, each with  $N_B$  segments, corresponding to a volume fraction  $\phi_B = n_B N_B / \Omega$ . Note that an incompressible material is assumed, corresponding to  $\phi_A + \phi_B = 1$ . The partition function of the system is given by

$$\mathcal{Z} = \sum_i \exp[-E_i/k_B T], \quad (7.23)$$

where  $E_i$  is the energy associated to a given configuration,  $i$ , of the A- and B-polymers. In the Flory–Huggins model,  $\mathcal{Z}$  is calculated in a *mean-field approach* where the site-dependent energy  $E_i$  is replaced with a mean value  $\bar{E}$ , and the number of configurations available for respectively the  $n_A$  and the  $n_B$  polymer chains are taken into account by a prefactor  $W$ . The partition function  $\mathcal{Z}$  then becomes

$$\mathcal{Z} \simeq W \exp(-\bar{E}/k_B T) \quad (7.24)$$

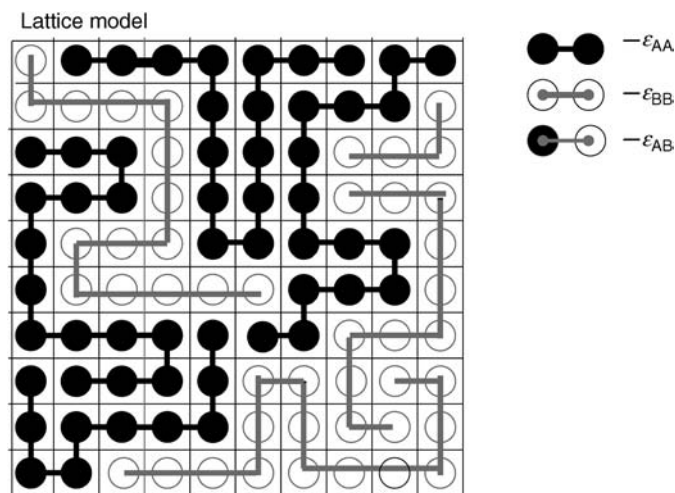


Figure 7.6 The lattice model for a polymer blend.



With the Helmholtz free energy

$$F = -k_B T \ln(Z) = -TS + U, \quad (7.25)$$

where  $S$  is the entropy and  $U$  the enthalpy; we thus get the result

$$F = -k_B T \ln(W) + \bar{E} \quad (7.26)$$

It can be seen thereby that  $W$  represents the entropy of the system:  $k_B \ln W = S$ , while  $\bar{E}$  is the enthalpic energy.

The average energy in the mixed state is calculated based on the average number of neighboring sites of respectively A and B segments (see Figure 7.6). The enthalpic interaction energy associated with these pairs will be denoted respectively  $-\varepsilon_{AA}$ ,  $-\varepsilon_{BB}$  and  $-\varepsilon_{AB}$ . The average energy  $\bar{E}$  can then be written as

$$\bar{E}_{\text{mixed}} = -\Omega z \left[ \frac{1}{2} \varepsilon_{AA} \phi_A^2 + \frac{1}{2} \varepsilon_{BB} \phi_B^2 + \varepsilon_{AB} \phi_A \phi_B \right] \quad (7.27)$$

where  $z$  is the number of nearest neighbors. The corresponding energy of the demixed state is the simple sum of the  $\varepsilon_{AA}$ -energy of the  $\phi_A \Omega_A$ -sites and  $\varepsilon_{BB}$ -energies of the  $\phi_B \Omega_B$ -sites,

$$\bar{E}_{\text{demixed}} = -\Omega z (\phi_A \varepsilon_{AA}/2 + \phi_B \varepsilon_{BB}/2). \quad (7.28)$$

The change in average enthalpic energy upon mixing is thereby

$$\Delta \bar{E} = \bar{E}_{\text{mixed}} - \bar{E}_{\text{demixed}} = \chi \phi_A \phi_B k_B T \quad (7.29)$$

where we have used that  $\phi_B = 1 - \phi_A$  and where  $\chi$  is the Flory–Huggins interaction parameter

$$\chi \equiv -\frac{1}{k_B T} \frac{z}{2} (\varepsilon_{AA} + \varepsilon_{BB} - 2\varepsilon_{AB}) \quad (7.30)$$

The ensemble configuration term  $W$ , and thereby the entropy, is calculated assuming that each chain can be placed randomly on the lattice, independent of each other. In the homogeneous state, each polymer chain has then

$$w_A(\text{mixed}) = w_B(\text{mixed}) = \Omega \quad (7.31)$$

possible positions of center of mass (translational states), while in the demixed state, the A- and B-polymers have respectively

$$w_A(\text{demixed}) = N_A n_A = \phi_A \Omega \quad \text{and} \quad w_B(\text{demixed}) = N_B n_B = \phi_B \Omega \quad (7.32)$$

possible states. The entropy change by mixing,  $\Delta s = k_B \ln w(\text{mixed}) - k_B \ln w(\text{demixed})$  is thus

$$\Delta s_i = k_B \ln(\Omega) - k_B \ln(\phi_i \Omega) = -k_B \ln \phi_i, \quad i = A \text{ or } B \quad (7.33)$$

for each of the two polymer systems. Since the volume fractions are less than 1, Eq. (7.33) tells us that the entropy change  $\Delta s_A$  and  $\Delta s_B$  upon mixing is always positive; that is, the entropy term of the free energy drag the system toward mixing. To calculate the total entropy of mixing,  $\Delta \tilde{S}$ , the entropy contribution from

each polymer molecule  $\Delta s_A$  and  $\Delta s_B$  is summed:

$$\Delta \tilde{S}_{mix} = n_A \Delta s_A + n_B \Delta s_B = -k_B n_A \ln \phi_A - k_B n_B \ln \phi_B \quad (7.34)$$

Substituting  $n_A = \phi_A \Omega / N_A$  and  $n_B = \phi_B \Omega / N_B$ , and dividing by the number of lattice sites, we get the change of entropy per unit volume:

$$\Delta S_{mix} = -k_B \left[ \frac{\phi_A}{N_A} \ln \phi_A + \frac{\phi_B}{N_B} \ln \phi_B \right] \quad (7.35)$$

The Helmholtz free energy of mixing is the sum of entropic and enthalpic contribution according to

$$F_m = -T\Delta S + \Delta \bar{E} \quad (7.36)$$

which, using Eqs (7.29) and (7.35), is rewritten into the Flory–Huggins formula

$$F_m(\phi) = k_B T \left[ \frac{\phi_A}{N_A} \ln \phi_A + \frac{\phi_B}{N_B} \ln \phi_B + \chi \phi_A \phi_B \right] \quad (7.37)$$

For classical, low-molar-mass liquids (corresponding to  $N_A$  and  $N_B$  equal to 1 in Eq. (7.37)), the driving force for mixing is typically the gain in entropy. For polymer blends, the large molecular sizes (large  $N$ -values) markedly reduce the entropic gain. The result is the general statement, that typical polymers do not mix. Only when the enthalpic forces under special circumstances effectively becomes very small, will the entropy cause polymers to mix.

Whether a system of two polymers, A and B remains phase-separated or will mix can be predicted from the  $\phi$  dependence of the free energy function,  $F_m(\phi)$ . Suppose that the free energy function  $F_m$  has a U-shaped  $\phi$ -dependence, and consider a sample with polymer A concentration equal to  $\phi$ . If the blend tend to demix into concentrations  $\phi_1$  and  $\phi_2$  it will have the free energy,  $F_{demix}$ , this being the concentration-weighted average of the energies in the two concentrations  $\phi_1$  and  $\phi_2$ . With the U-shaped  $\phi$ -dependence of  $F_m$ , the demixed energy will be larger than the mixed, and the system equilibrium is in the mixed state. If the  $\phi$ -dependence of the free energy of mixing  $F_m$ , on the other hand is  $\cap$ -shaped, the free energy of the phase separated state is lower than that of the mixed, and the thermodynamic stable state is phase separated. Thermodynamically, the free energy has a U-shaped  $\phi$ -dependence of  $F_m$  nearby the two *binodal* points ( $B1$  and  $B2$ ), which can be shown to fulfill the relation

$$\left. \frac{\partial F_m}{\partial \phi} \right|_{\phi_{B1}} = \left. \frac{\partial F_m}{\partial \phi} \right|_{\phi_{B2}} \quad (7.38)$$

Thus, for phase-separated systems, the concentrations  $\phi_{B1}$  and  $\phi_{B2}$  of the two thermodynamic stable phases are uniquely determined by the points of common tangent. The inflection points separating U- from  $\cap$ -shaped  $F(\phi)$  will accordingly represent an *instability* points, the so-called *spinodal points* given by the condition

$$\left. \frac{\partial^2 F_m}{\partial \phi^2} \right|_{\phi_{S1}} = \left. \frac{\partial^2 F_m}{\partial \phi^2} \right|_{\phi_{S2}} = 0 \quad (7.39)$$

Systems with concentrations between the two spinodal points will be unstable and decompose spontaneously. Polymer mixtures with overall concentrations between the binodal and the spinodal, will be metastable, and decompose following a nucleation-and-growth mechanism. For polymer blends with concentrations “outside” the two binodals, the system is mixed in a thermodynamically stable single phase.

The free energy function depends generally on temperature – that is, the binodal and spinodal concentrations varies on changing temperature. At a given temperature, the two binodals and the two spinodals all meet at one point in the concentration–temperature phase-diagram. This is the *critical point* given by

$$\frac{\partial^3 F_m}{\partial \phi^3} = 0 \quad (7.40)$$

For a symmetric polymer blend,  $N_A = N_B = N$ , the equations above lead to a critical point given by relation

$$\chi_c N = 2 \quad (7.41)$$

## 7.4

### The Scattering Function and Thermodynamics

In the preceding chapter we have, based on the Flory–Huggins theory, discussed the basis for the phase behavior of polymer blends. Miscible polymer blends and polymer solutions have, even in the mixed one-phase system, spatial variations in the polymer concentration. These *concentration fluctuations* reflect the thermodynamic parameters of the free energy, as described in the Flory–Huggins model.

In a real polymer material, the fluctuations are not limited to chemical composition fluctuations. Thermal density fluctuations will generally also be present and can be measured. According to the fluctuation–dissipation theorem, these fluctuations are characterized by the material compressibility  $\partial \ln V / \partial P$ , where  $V$  is the volume and  $P$  the pressure [3]. In neutron scattering experiments using labeled chains (see Figure 7.3), the thermal fluctuations are negligible as compared to composition fluctuations. We will, for simplicity, neglect thermal density fluctuations and assume a constant segment density; that is, in the lattice model (Figure 7.6) we assume that every lattice site is filled with polymer *segments* imposed by the constraint

$$\phi_A(\mathbf{R}) + \phi_B(\mathbf{R}) = 1 \quad (7.42)$$

satisfied for all sites  $\mathbf{R}$ . The concentration fluctuations can be measured directly by scattering methods; hence, scattering experiments can provide insight into the thermodynamics of polymer systems.

The ensemble-averaged concentrations  $\phi_A = \langle \phi_A(\mathbf{R}) \rangle$  and  $\phi_B = \langle \phi_B(\mathbf{R}) \rangle$  must fulfill the same relation  $\phi_A + \phi_B = 1$ . The fluctuation terms are advantageously described by the deviation of the segment density from average at each lattice site;

rather than the concentrations themselves:

$$\begin{aligned}\delta\phi_A(\mathbf{R}) &= \phi_A(\mathbf{R}) - \phi_A \\ \delta\phi_B(\mathbf{R}) &= \phi_B(\mathbf{R}) - \phi_B\end{aligned}\quad (7.43)$$

With the density constraint the fluctuation  $\delta\phi_A$  and  $\delta\phi_B$  terms holds:

$$\delta\phi_A(\mathbf{R}) + \delta\phi_B(\mathbf{R}) = 0 \quad (7.44)$$

The product

$$\delta\phi_i(\mathbf{R})\delta\phi_j(\mathbf{R} + \mathbf{r}) \quad i = A, B; \quad j = A, B. \quad (7.45)$$

characterizing the spatially correlated fluctuations is a unique measure of the thermodynamics. Equation (7.45) describes the correlation between segments  $i$  in a position  $\mathbf{R}$  with those of species  $j$  in position  $\mathbf{R} + \mathbf{r}$ .

Usually, these correlations would be expected to have a relatively short range, since distant segments will be completely independent. The products in Eq. (7.45) will accordingly be nonzero only for relatively small values of  $\mathbf{r}$ .

The thermodynamics of the system is described in terms of the ensemble average,  $\gamma_{ij}(\mathbf{r})$ , of the spatially correlated fluctuations:

$$\gamma_{ij}(\mathbf{r}) = \langle \delta\phi_i(\mathbf{R})\delta\phi_j(\mathbf{R} + \mathbf{r}) \rangle \quad i = A, B; \quad j = A, B. \quad (7.46)$$

where  $\langle \dots \rangle$  denotes the ensemble average. With  $\delta\phi_A = -\delta\phi_B$ , it follows that

$$\gamma_{AA}(\mathbf{r}) = \gamma_{BB}(\mathbf{r}) = -\gamma_{AB}(\mathbf{r}) = -\gamma_{BA}(\mathbf{r}), \quad (7.47)$$

which leads to the important and very simple result: The concentration fluctuations of an incompressible two component system are characterized by a *single correlation function*  $\gamma(\mathbf{r})$  which, by definition, will be associated with the self-correlation function:

$$\gamma(\mathbf{r}) \equiv \gamma_{AA}(\mathbf{r}). \quad (7.48)$$

The correlation function is, as mentioned above, tightly related to the thermodynamics of the system. Furthermore, the Fourier transform of the spatial correlation functions can be measured directly in neutron scattering experiments, as outlined in Eq. (7.12). This will be discussed further below.

#### 7.4.1

##### The Forward Scattering

The experimentally accessible correlation function,  $\gamma_{ij}(\mathbf{r}) = \langle \phi_i(\mathbf{R})\phi_j(\mathbf{R} + \mathbf{r}) \rangle$ , can be expressed in terms of thermodynamic parameters. In order to calculate the correlation functions  $\gamma_{ij}(\mathbf{r})$ , we follow basically the route of de Gennes [4] and Doi [1], using the fact that the correlation function can be shown to express the proportionality constant when using *linear response theory* to treat energy changes.

To find the thermodynamic relationship to the correlation function, we start to calculate the response on the total energy upon perturbing individual segments with a weak external potential. Let us assume that the potentials  $u_A(\mathbf{R})$  and  $u_B(\mathbf{R})$

act on, respectively, A and B segments in site  $\mathbf{R}$ . The resulting change in the system's potential energy is then

$$U_e = \int [u_A(\mathbf{R})\phi_A(\mathbf{R}) + u_B(\mathbf{R})\phi_B(\mathbf{R})]d\mathbf{R} \quad (7.49)$$

where the subscript e denotes “external” and where we have used a continuous description of the ensemble ( $\int_{\mathbf{R}}$ ) rather than the lattice representation ( $\sum_{\mathbf{R}}$ ). The  $u_A$  and  $u_B$  external potentials acting on individual sites will cause local deviation from average composition; that is, generally we may expect that  $\phi_A(\mathbf{R})$  is not equal to  $\phi_A$  and  $\phi_B(\mathbf{R})$  is not equal to  $\phi_B$ . With  $U_o$  being the intrinsic energy of the system, the equilibrium average can be written as

$$\overline{\delta\phi_A(\mathbf{R})} = \frac{\int \delta\phi_A(\mathbf{R}) \exp[-(U_o + U_e)/(k_B T)] d\mathbf{r}}{\int \exp[-(U_o + U_e)/k_B T] d\mathbf{r}} \quad (7.50)$$

according to statistical mechanics ([5]). We rewrite the formula into the form

$$\overline{\delta\phi_A(\mathbf{R})} = \frac{\langle \delta\phi_A(\mathbf{R}) \exp[-U_e/(k_B T)] \rangle}{\langle \exp[-U_e/(k_B T)] \rangle} \quad (7.51)$$

where  $\langle \dots \rangle \equiv \int (\dots) e^{-U_o/k_B T} d\mathbf{r} / \int e^{-U_o/k_B T} d\mathbf{r}$  denotes the equilibrium average without external fields. For weak external fields,  $U_e/k_B T \ll 1$  we can make the approximations

$$\exp(-U_e/(k_B T)) \approx 1 - U_e/(k_B T) \quad \text{and} \quad \frac{1}{1 - U_e/(k_B T)} \approx 1 + U_e/(k_B T)$$

making Eq. (7.51) into the form

$$\overline{\delta\phi_A(\mathbf{R})} \approx \langle \delta\phi_A(\mathbf{R}) \rangle (1 + \langle U_e/k_B T \rangle) - \langle \delta\phi_A U_e/k_B T \rangle \quad (7.52)$$

to first order in  $U_e/(k_B T)$ . The first term in Eq. (7.52) vanishes, as the equilibrium average of  $\delta\phi_A(\mathbf{R})$  by definition is zero without external fields. With Eq. (7.49) it thus follows from Eq. (7.52) that

$$\overline{\delta\phi_A(\mathbf{R})} \approx -\frac{1}{k_B T} \langle \delta\phi_A(\mathbf{R}) U_e \rangle$$

which, when using the expression for  $U_o$  can be rewritten into

$$\begin{aligned} \overline{\delta\phi_A(\mathbf{R})} \approx & -\frac{1}{k_B T} \langle \delta\phi_A(\mathbf{R}) \int [\phi_A u_A(\mathbf{R} + \mathbf{r}) + \phi_B u_B(\mathbf{R} + \mathbf{r})] d\mathbf{r} + \\ & \delta\phi_A(\mathbf{R}) \int [\delta\phi_A(\mathbf{R} + \mathbf{r}) u_A(\mathbf{R} + \mathbf{r}) + \delta\phi_B(\mathbf{R} + \mathbf{r}) u_B(\mathbf{R} + \mathbf{r})] d(\mathbf{R} + \mathbf{r}) \rangle \end{aligned} \quad (7.53)$$

Assuming that the potentials  $u_A(\mathbf{R})$  and  $u_B(\mathbf{R})$  varies little over the length scale of fluctuations, the first term vanished due to mean zero of  $\delta\phi_A(\mathbf{R})$ . The fluctuation term then becomes

$$\overline{\delta\phi_A(\mathbf{R})} = -\frac{1}{k_B T} \left[ \int \langle \delta\phi_A(\mathbf{R}) \delta\phi_A(\mathbf{R} + \mathbf{r}) \rangle u_A(\mathbf{R} + \mathbf{r}) d\mathbf{r} + \int \langle \delta\phi_A(\mathbf{R}) \delta\phi_B(\mathbf{R} + \mathbf{r}) \rangle u_B(\mathbf{R} + \mathbf{r}) d\mathbf{r} \right] \quad (7.54)$$

The result Eq. (7.54), originally derived by de Gennes [4], is most important. It expresses the *linear response theory* that the thermal averaged local concentration fluctuations depends linearly on the fields acting on any other sites, with proportionality constants equal the spatial correlation functions  $\gamma_{AA}(\mathbf{r})$  and  $\gamma_{AB}(\mathbf{r})$ , as defined in Eq. (7.46). Using further that  $\delta\phi_B(\mathbf{R}) = -\delta\phi_A(\mathbf{R})$ , Eq. (7.54) may be rewritten into

$$\begin{aligned}\overline{\delta\phi_A}(\mathbf{R}) &= -\frac{1}{k_B T} \int \langle \delta\phi_A(\mathbf{R}) \delta\phi_A(\mathbf{R} + \mathbf{r}) \rangle [u_A(\mathbf{R} + \mathbf{r}) - u_B(\mathbf{R} + \mathbf{r})] d\mathbf{r} \\ &= -\frac{1}{k_B T} \int \gamma(\mathbf{r}) [u_A(\mathbf{R} + \mathbf{r}) - u_B(\mathbf{R} + \mathbf{r})] d\mathbf{r}\end{aligned}\quad (7.55)$$

where the definition Eq. (7.48),  $\gamma \equiv \gamma_{AA}$ , is used.

The correlation function  $\gamma$  is expected to be of relative short range, that is,  $\gamma$  is likely non-zero only for  $\mathbf{r}$ -values up to some coil-diameters in the mixed phase. We will therefore, as above, assume that the spatial variation of  $u_A(\mathbf{R})$ ,  $u_B(\mathbf{R})$  is gradual, so that these potentials can be considered constant over the range where  $\gamma(\mathbf{r})$  has a nonzero value. In this case, Eq. (7.55) can be approximated as follows

$$\overline{\delta\phi_A}(\mathbf{R}) \simeq -\frac{1}{k_B T} [u_A(\mathbf{R}) - u_B(\mathbf{R})] \int \gamma(\mathbf{r}) d\mathbf{r} \quad (7.56)$$

The Fourier transform of  $\gamma(\mathbf{r})$  is the structure factor  $I(\mathbf{q})$  (Eq. (7.12)) given by

$$I(\mathbf{q}) = \int \gamma(\mathbf{r}) \exp[-i\mathbf{q} \cdot \mathbf{r}] d\mathbf{r}. \quad (7.57)$$

The integral in Eq. (7.56) can thereby be expressed in terms of the structure factor at zero  $\mathbf{q}$ -value, that is,

$$\overline{\delta\phi_A}(\mathbf{R}) = -\frac{1}{k_B T} I(0) [u_A(\mathbf{R}) - u_B(\mathbf{R})] \quad (7.58)$$

With  $u_A(\mathbf{R})$  and  $u_B(\mathbf{R})$  assumed to be almost constant, the deviation  $\overline{\delta\phi_A}(\mathbf{R})$  is determined from the condition of thermodynamic equilibrium as expressed by the chemical potentials  $\mu_A$  and  $\mu_B$ . In the absence of external fields, we have, according to thermodynamics:

$$\left( \frac{\partial F_m}{\partial \phi} \right) \bigg|_{\mathbf{r}} + [\mu_A(\mathbf{r}) - \mu_B(\mathbf{r})] = C \quad (7.59)$$

where  $C$  is a constant independent of concentration. With perturbations with the small external potentials,  $u_A(\mathbf{R})$  and  $u_B(\mathbf{R})$ , the local chemical potentials  $\mu_A(\mathbf{R})$  and  $\mu_B(\mathbf{R})$  will change by these respective values. The changes in the free-energy derivative is expressed in terms of the associated change in concentration

$$\Delta \left( \frac{\partial F_m}{\partial \phi} \right) \bigg|_{\mathbf{R}} \simeq \left( \frac{\partial^2 F_m}{\partial \phi^2} \right) \bigg|_{\mathbf{R}} \overline{\delta\phi}(\mathbf{R}) \quad (7.60)$$

assuming that the fluctuation-term  $\overline{\delta\phi}(\mathbf{R})$  is small. From these perturbations in respectively free energy and chemical potential, Eq. (7.59) thereby gives the

condition for thermodynamic equilibrium

$$\left(\frac{\partial^2 F_m}{\partial \phi^2}\right) \overline{\delta \phi}(\mathbf{R}) + [u_A(\mathbf{R}) - u_B(\mathbf{R})] = 0 \quad (7.61)$$

and thereby

$$\overline{\delta \phi}(\mathbf{R}) = -\left(\frac{\partial^2 F_m}{\partial \phi^2}\right)^{-1} [u_A(\mathbf{R}) - u_B(\mathbf{R})] \quad (7.62)$$

Combining Eq. (7.62) with Eq. (7.58) describes thereby the fluctuation correlation function in terms of thermodynamics

$$I(0) = \int \gamma(\mathbf{r}) d\mathbf{r} = k_B T \left(\frac{\partial^2 F_m}{\partial \phi^2}\right)^{-1}, \quad (7.63)$$

that is, the structure factor,  $I(0)$ , is directly related to the thermodynamics of the polymer blend. The spinodal point of polymer blends,  $\partial^2 F_m / \partial \phi^2 = 0$ , can thus be obtained experimentally by measuring the structure factor at  $\mathbf{q} = 0$ , and extract the temperature where the  $I^{-1}(\mathbf{0})$  approach zero (see Figure 7.7).

Figure 7.7 shows an experimental example of such studies, showing the forward scattering  $I(0)$  of a polymer blend of polystyrene (PS) and poly(vinylmethylether) (PVME) with a given concentration ( $\phi_{PS} = 0.32$ ) [6]. The forward scattering is obtained from experimental  $I(q)$  data extrapolating  $q \rightarrow 0$ . A number of equivalent data, obtained for various concentrations, may give the whole spinodal curve.

The coexistence curve, or the binodal, can also be obtained from the same scattering experiments, identifying the abrupt and (usually, due to the relative slow

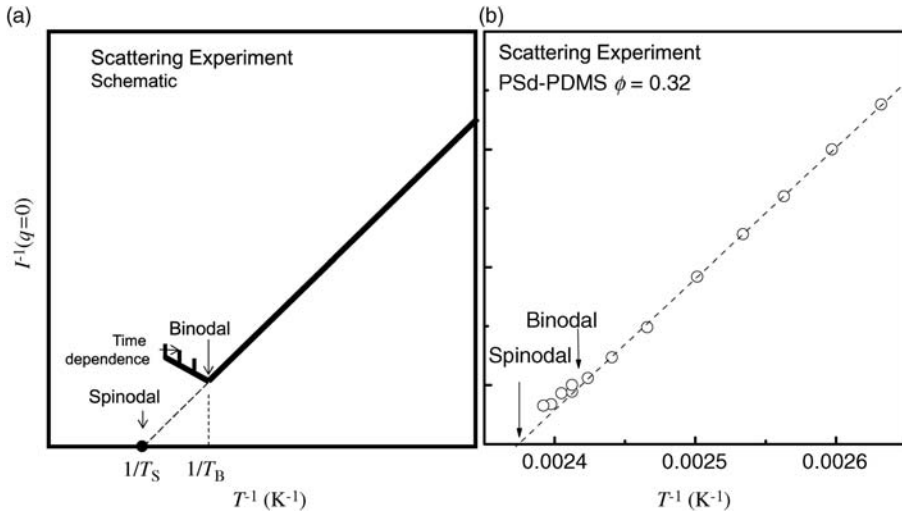


**Figure 7.7** Small-angle neutron scattering data  $I^{-1}(0)$  versus  $T^{-1}$  identifying the spinodal and the binodal temperatures. (a)  $I^{-1}(0)$  versus  $T^{-1}$  schematically; (b) An experimental example of a polymer blend of polystyrene (PS) and

poly(vinyl methylether) (PVME) giving the experimental spinodal and binodal values. The linear  $I^{-1}(0)$  versus  $T^{-1}$  is in accordance with the RPA result (Eq. (7.82)), with  $\chi \propto T^{-1}$ . Experimental data reproduced from Ref. [6].

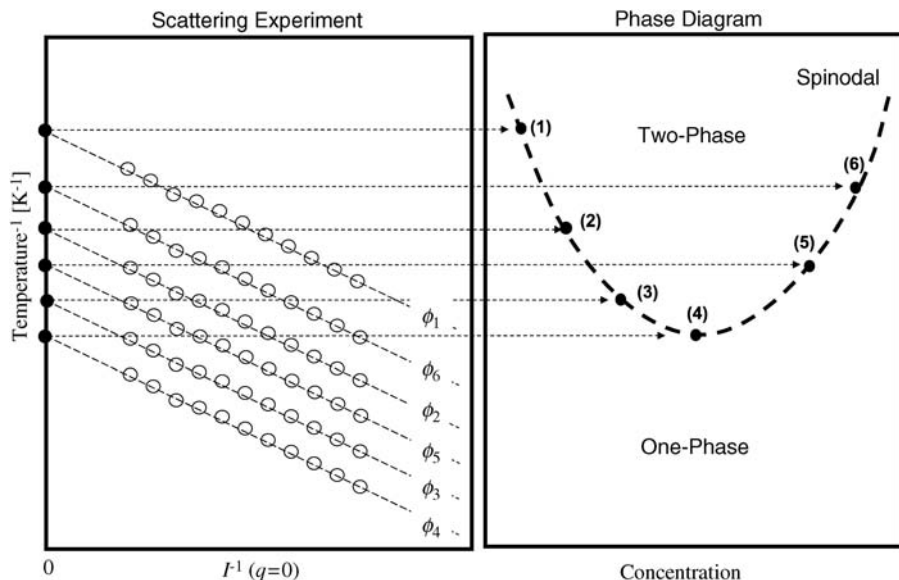


**Figure 7.8** By measuring the forward scattering  $I(q=0)$  it is possible experimentally to determine the spinodal curve (second derivative of free energy,  $\partial^2 F_m / \partial \phi^2$ , is zero) of the binary phase diagram, since  $\partial^2 F_m / \partial \phi^2 = I^{-1}(0)$ .

nucleation and growth mechanism) time-dependent deviation in the  $I^{-1}$  versus  $T^{-1}$  plot ( $T_B$  in the Figure 7.7).

By measuring the temperature dependence of  $I(0)$  for a variety of concentrations, as sketched in Figure 7.8, the spinodal phase boundary can be mapped out for polymer blends.

#### 7.4.2

##### Random Phase Approximation (RPA)

In the next section, an attempt will be made to evaluate further details on the composition fluctuations as related to the experimental scattering function,  $I(\mathbf{q})$ .

The calculations will be based on the result (see Eq. (7.55)) that the pair correlation function is expressed in terms of linear response theory. The calculations will further be made using a mean-field approximation principally where the excluded volume effects, the density constrain and the interactions between chains are taken into account as perturbations, expressed in terms of potential energies. This calculation is called the random phase approximation (RPA).

Initially, consider the case where polymers A and B are placed on the lattice at random, without any excluded volume effects or interaction energies. In this case, there is by definition no correlation in the positioning of polymers segments A and B, and the correlation term  $\langle \delta \phi_A(\mathbf{R}) \delta \phi_B(\mathbf{R} + \mathbf{r}) \rangle$  obviously equals zero. The correlations  $\langle \delta \phi_A(\mathbf{R}) \delta \phi_A(\mathbf{R} + \mathbf{r}) \rangle$  and  $\langle \delta \phi_B(\mathbf{R}) \delta \phi_B(\mathbf{R} + \mathbf{r}) \rangle$  between A – A and B – B



segments, on the other hand, are both finite since the segments of the polymers are linked together making up A and B polymer chains, respectively. If external fields  $u_A(\mathbf{R})$  and  $u_B(\mathbf{R})$  are applied to this system, the resulting change in the concentration  $\overline{\delta\phi_A}(\mathbf{R})$  is then responding with the change in fluctuations (Eq. (7.54))

$$\overline{\delta\phi_A}(\mathbf{R}) = -\frac{1}{k_B T} \int \gamma_{AA}^\circ(\mathbf{r}) u_A(\mathbf{R} + \mathbf{r}) d\mathbf{r} \quad (7.64)$$

where the response function is identical to the pair correlation function, as discussed above in Eq. (7.55). Now, in reality there are of course both enthalpic interactions between the chains and volume constraint. These terms will be taken into account as perturbations using a mean field approximation.

If the concentrations of A and B segments in position  $\mathbf{R}$  are respectively  $\overline{\phi_A}(\mathbf{R}) = \phi_A + \overline{\delta\phi_A}(\mathbf{R})$  and  $\overline{\phi_B}(\mathbf{R}) = \phi_B + \overline{\delta\phi_B}(\mathbf{R})$ , the enthalpic fields acting on the segments A and B are given by respectively,

$$\begin{aligned} w_A(\mathbf{R}) &= -z[\varepsilon_{AA}\overline{\phi_A}(\mathbf{R}) + \varepsilon_{AB}\overline{\phi_B}(\mathbf{R})] \quad \text{and} \\ w_B(\mathbf{R}) &= -z[\varepsilon_{BA}\overline{\phi_A}(\mathbf{R}) + \varepsilon_{BB}\overline{\phi_B}(\mathbf{R})] \end{aligned} \quad (7.65)$$

The conservation of volume condition:  $\phi_A(\mathbf{R}) + \phi_B(\mathbf{R}) = 1$ , will thermodynamically correspond to a force acting on each site, expressed as a potential,  $V(\mathbf{R})$ . The total energy  $U_{\text{excl}}$  representing the excluded volume effect is then calculated by integrating  $V(\mathbf{R})$  over volume:

$$U_{\text{excl}} \equiv \int V(\mathbf{R}) d\mathbf{R} = \int V(\mathbf{R}) [\phi_A(\mathbf{R}) + \phi_B(\mathbf{R})] d\mathbf{R} \quad (7.66)$$

where in the last equality we have replaced a factor 1 with the identical  $[\phi_A(\mathbf{R}) + \phi_B(\mathbf{R})]$  sum. The internal fields acting on segments A and B are the sums, respectively  $w_A + V$  and  $w_B + V$ . In the linear response theory  $\overline{\delta\phi_A}$  and  $\overline{\delta\phi_B}$  can thus be expressed as

$$\overline{\delta\phi_A}(\mathbf{R}) = \frac{1}{k_B T} \int \gamma_{AA}^\circ(\mathbf{R}) [u_A(\mathbf{R} + \mathbf{r}) + w_A(\mathbf{R} + \mathbf{r}) + V(\mathbf{R} + \mathbf{r})] d\mathbf{r} \quad (7.67)$$

$$\overline{\delta\phi_B}(\mathbf{R}) = \frac{1}{k_B T} \int \gamma_{BB}^\circ(\mathbf{R}) [u_B(\mathbf{R} + \mathbf{r}) + w_B(\mathbf{R} + \mathbf{r}) + V(\mathbf{R} + \mathbf{r})] d\mathbf{r} \quad (7.68)$$

The constraint  $\phi_A(\mathbf{R}) + \phi_B(\mathbf{R}) = 1$  gives, as discussed already above,

$$\overline{\delta\phi_A}(\mathbf{R}) + \overline{\delta\phi_B}(\mathbf{R}) = 0 \quad (7.69)$$

Equations (7.67)–(7.69) form a set of simultaneous equations for the unknowns  $\overline{\delta\phi_A}(\mathbf{R})$ ,  $\overline{\delta\phi_B}(\mathbf{R})$ , and  $V(\mathbf{R})$ . To solve these equations, we will use the Fourier transform of  $\delta\phi(\mathbf{R})$  and  $V(\mathbf{R})$ . In setting the formula Eq. (7.67) for the concentration fluctuation expressed in terms of the spatial correlation function, the Fourier transformed  $\overline{\delta\phi}(\mathbf{R})$  acquires the form

$$\begin{aligned} \overline{\delta\psi_A}(\mathbf{q}) &= \frac{1}{V} \int \overline{\delta\phi_A}(\mathbf{r}) \exp[i\mathbf{q} \cdot \mathbf{r}] d\mathbf{r} \\ &\simeq -\frac{1}{V} \frac{1}{k_B T} [u_A - u_B] \int \int \gamma(\mathbf{r}) \exp[i\mathbf{q} \cdot \mathbf{r}] d\mathbf{R} \quad d\mathbf{r} \\ &= -\frac{1}{k_B T} I(\mathbf{q}) [u_A - u_B], \end{aligned} \quad (7.70)$$

where we used the formula for the structure factor,  $I(\mathbf{q})$  (Eq. (7.12)).

After some mathematical rewritings, using the expression for the unperturbed structure factor of noninteracting polymer chains

$$I_{AA}^{\circ}(\mathbf{q}) = \int \gamma_{AA}^{\circ}(\mathbf{r}) e^{-i\mathbf{q}\cdot\mathbf{r}} d\mathbf{r}, \quad (7.71)$$

that  $w_A(\mathbf{R}) = -z[\varepsilon_{AA}\bar{\phi}_A(\mathbf{R}) + \varepsilon_{AB}\bar{\phi}_B(\mathbf{R})]$ , and that  $\vartheta(\mathbf{q})$  is the Fourier transform of the potential  $V(\mathbf{R})$ , we find

$$\bar{\delta\psi}_A(\mathbf{q}) = -\frac{1}{k_B T} I_{AA}^{\circ}(\mathbf{q}) [u_A - z[\varepsilon_{AA}\bar{\delta\psi}_A(\mathbf{q}) + \varepsilon_{AB}\bar{\delta\psi}_B(\mathbf{q})] + \vartheta(\mathbf{q})] \quad (7.72)$$

The corresponding expression for the Fourier transform  $\bar{\delta\psi}_B(\mathbf{q})$  of  $\bar{\delta\phi}_B(\mathbf{r})$  is

$$\bar{\delta\psi}_B(\mathbf{q}) = -\frac{1}{k_B T} I_{BB}^{\circ}(\mathbf{q}) [u_B - z[\varepsilon_{BA}\bar{\delta\psi}_A(\mathbf{q}) + \varepsilon_{BB}\bar{\delta\psi}_B(\mathbf{q})] + \vartheta(\mathbf{q})] \quad (7.73)$$

The sum,  $\bar{\delta\psi}_A(\mathbf{q}) + \bar{\delta\psi}_B(\mathbf{q})$ , of these two Fourier transforms is zero, according to

$$\bar{\delta\psi}_A(\mathbf{q}) + \bar{\delta\psi}_B(\mathbf{q}) = \int [\bar{\delta\phi}_A(\mathbf{r}) + \bar{\delta\phi}_B(\mathbf{r})] e^{i\mathbf{q}\cdot\mathbf{r}} d\mathbf{r} = 0 \quad (7.74)$$

Solving the three Eqs (7.72)–(7.74) with the three unknowns  $\bar{\delta\psi}_A$ ,  $\bar{\delta\psi}_B$  and  $\vartheta$  give

$$\bar{\delta\psi}_A(\mathbf{q}) = -\frac{1}{k_B T} \left[ \frac{1}{I_{AA}^{\circ}(\mathbf{q})} + \frac{1}{I_{BB}^{\circ}(\mathbf{q})} - 2\chi \right]^{-1} (u_A - u_B) \quad (7.75)$$

Here,  $\chi = z/(2k_B T)[\varepsilon_{AA} + \varepsilon_{BB} - 2\varepsilon_{AB}]$  is the Flory–Huggins interaction parameter defined above (Eq. (7.30)). From Eq. (7.70) the structure factor  $I(\mathbf{q})$  is thereby given by the rather simple expression

$$\frac{1}{I(\mathbf{q})} = \frac{1}{I_{AA}^{\circ}(\mathbf{q})} + \frac{1}{I_{BB}^{\circ}(\mathbf{q})} - 2\chi \quad (7.76)$$

Equation (7.76) may be rewritten into the more general RPA form,

$$I(\mathbf{q}) = \frac{N}{F_{\text{blend}}(\mathbf{q}) - 2\chi N} \quad (7.77)$$

where the function  $F(\mathbf{q})$  for blends is given by

$$F_{\text{blend}}(\mathbf{q}) = \frac{1}{N} \left[ \frac{1}{I_{AA}^{\circ}(\mathbf{q})} + \frac{1}{I_{BB}^{\circ}(\mathbf{q})} \right] = \frac{1}{N} \frac{I_{AA}^{\circ}(\mathbf{q}) + I_{BB}^{\circ}(\mathbf{q})}{I_{AA}^{\circ}(\mathbf{q}) I_{BB}^{\circ}(\mathbf{q})} \quad (7.78)$$

with the “average” degree of polymerization,  $N$ , defined as

$$N = \frac{N_A N_B}{N_A + N_B} \quad (7.79)$$

The individual polymer coils obey Gaussian statistics with the associated Debye-function (Eq. (7.22)) giving the bare structure factors, that is,

$$I^{\circ}(\mathbf{q}) = \phi N g_D(q, N), \quad (7.80)$$

Using further the approximation

$$g_D(x) = 2/(x^4) \cdot [\exp(-x^2) - 1 + x^2] \approx 1 - \frac{1}{3}x^2 \approx \frac{1}{1 + \frac{1}{3}x^2} \quad (7.81)$$

the RPA expression, Eq. (7.76) becomes

$$\frac{1}{I(\mathbf{q})} = \frac{1 + q^2 R_A^2/3}{\phi_A N_A} + \frac{1 + q^2 R_B^2/3}{\phi_B N_B} - 2\chi \quad (7.82)$$

which we rewrite into

$$I^{-1}(\mathbf{q}) = \left[ \frac{1}{\phi_A N_A} + \frac{1}{\phi_B N_B} - 2\chi \right] + \left[ \frac{R_A^2}{3\phi_A N_A} + \frac{R_B^2}{3\phi_B N_B} \right] q^2 \quad (7.83)$$

that is, the scattering function has the simple Lorentzian (Ornstein–Zernike) form:

$$I^{-1}(\mathbf{q}) = I^{-1}(0)[1 + \xi^2 q^2] \quad (7.84)$$

where

$$I^{-1}(0) = \frac{1}{\phi_A N_A} + \frac{1}{\phi_B N_B} - 2\chi \quad (7.85)$$

is the forward scattering already discussed above, relating directly to the thermodynamics of the system. The correlation length  $\xi$

$$\xi = \left[ \frac{R_A^2}{3\phi_A N_A} + \frac{R_B^2}{3\phi_B N_B} \right]^{1/2} \sqrt{I(0)} \quad (7.86)$$

describes the spatial extend of the fluctuations. We see that the RPA theory expresses thermodynamic properties of polymer blends, as described within the Flory–Huggins model, in terms of experimental accessible parameters. Measurements of the scattering function as a function of composition and temperatures provide both the spinodal phase boundary, and the temperature and concentration dependent Flory–Huggins interaction parameter ( $\chi$ ). The Flory–Huggins model describes the enthalpic interactions in terms of temperature independent neighboring interactions  $\varepsilon_{ij}$ , giving a  $T^{-1}$ -dependent  $\chi$ -parameter. The mean field treatment thus predict the following scaling for forward scattering and correlation length:

$$I(0) \propto T^{-1} \quad \text{and} \quad \xi \propto T^{-1/2} \quad (7.87)$$

as already used in Figures 7.7 and 7.8. Figures 7.9 and 7.10 shows experimental scattering functions for two polymer systems: a polystyrene/poly(vinyl

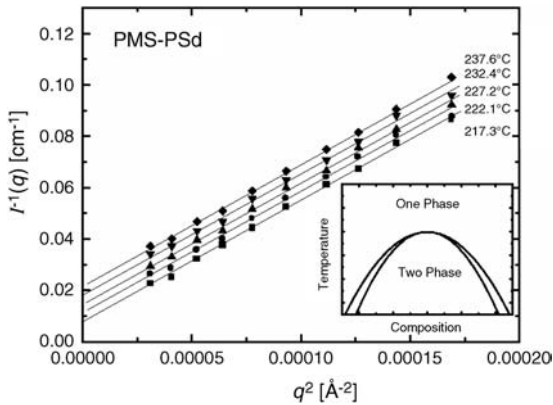


**Figure 7.9** Small-angle neutron scattering experiments of polymer blends of polystyrene (PS) and poly(methylstyrene) (PMS) showing the agreement with the RPA-result:  $I^{-1}(q)$  linear in  $q^2$ . The inset shows schematically the phase diagram, which for the PS/PMS system

is of the UCST-type. The PS polymers are deuterated (PSd) in order to obtain contrast between the two polymers in the neutron scattering experiment. Experimental data reproduced from Ref. [7].

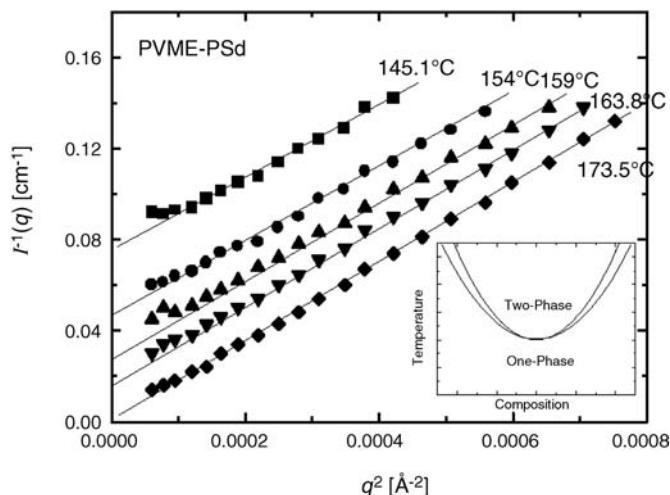


**Figure 7.10** Small-angle neutron scattering experiments of polymer blends of polystyrene (PS) and poly(vinylmethylether) (PVME) showing the agreement with the RPA-result:  $I^{-1}(q)$  linear in  $q^2$ . The insert shows schematically the phase diagram, which for the PS/PVME system

is of the LCST-type. The PS polymers are deuterated (PSd) in order to obtain contrast between the two polymers in the neutron scattering experiment. Experimental data reproduced from Ref. [7].

methylether) blend and a polystyrene/poly(methylstyrene) blend, plotted as  $I^{-1}$  versus  $q^2$ . The results are in agreement with the RPA result Eq. (7.82) and exhibit the expected linear relationships based on Flory–Huggins thermodynamics and mean-field random phase approximation. It may be noted that for the PS/PMS system, the  $I^{-1}(0)$ -parameter decreases upon lowering the temperature (i.e.,  $I(0)$  increases) implying that the system is mixed at high temperature and demixed at low temperature, an upper critical solution temperature (UCST) system. The PVME/PS system is opposite, having a lower critical solution temperature (LCST).

The  $\chi$ -parameter is, according to the definition (Eq. (7.30)), assumed to be purely enthalpic and short-ranged. It reflects segmental nearest neighbor interactions, which are likely to be dominated by dipole–dipole interactions. Experimentally determined  $\chi$ -values appear to be more complex; only high-molar-mass polymers have effectively a segmental  $\chi$ -parameter where end-effects are negligible, and the temperature-dependence is seldom pure  $T^{-1}$ . In spite of such difficulties, the mean-field random phase approximation and Flory–Huggins theory provide an excellent basis for analyzing polymer thermodynamics.

#### 7.4.3

##### Beyond Mean Field

The RPA method is based on a completely random organization of the polymer chains where the effects of interactions are estimated using a perturbation calculation. Such mean field calculations are only valid as long as the length scale of the fluctuations are small compared to characteristic lengths of the system (the

Ginzburg criteria). In a region close to the critical point,  $T_c$ , thermal composition fluctuations may significantly renormalize the thermodynamics. In polymers, relevant length scales separating valid mean-field from non-mean-field characteristics may be the correlation length of fluctuations  $\xi$  as compared to the polymer segmental length  $b$  (the lattice site). For correlation lengths  $\xi$  larger than the lattice sites, random positioning is no longer consistent, and more advanced theories that self-consistently include the effect of thermal composition fluctuations are needed.

The thermal composition fluctuations tend to stabilize the “disordered” phase, giving rise to a renormalized critical temperature. The relation between the mean-field value  $T_c^{\text{MF}}$  and the real  $T_c$  is expressed by the Ginzburg relation [8]:

$$T_c^{\text{mf}} = T_c / (1 - G), \quad (7.88)$$

where  $G$  is the Ginzburg number. In a plot showing the inverse forward scattering  $I^{-1}(0)$  versus reciprocal reduced temperature,  $\tau^{-1}$ , the Ginzburg number clearly appear as the crossover temperature from linear (mean field) to nonlinear characteristics. Here, the reduced temperature is defined as  $\tau = |1 - T_c/T|$ . For critical composition  $\phi = \phi_c$ , analogous to those of Figures 7.7 and 7.8, one will find deviation from linear relationship. Polymer blends behave like classical fluids showing a three-dimensional Ising-type of scaling behavior [9,10], that is,

$$I(0) \propto \left( \frac{|T_c - T|}{T} \right)^{-\gamma} \quad \text{with } \gamma = 1.24 \quad (7.89)$$

as  $T$  approaches  $T_c$ . An experimental example is provided in Figure 7.11, showing critical scattering of the polymer blend of polystyrene and polybutadiene (dPB/PS) [11,12].

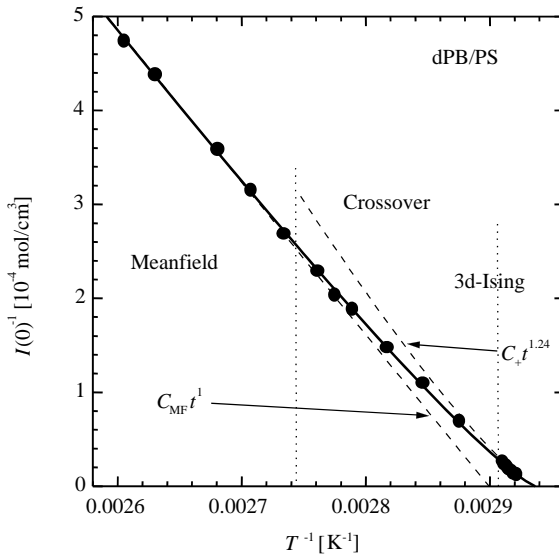


**Figure 7.11** Inverse forward scattering  $I^{-1}(0)$  versus inverse temperature for a mixture of dPB and PS of near critical composition. The solid line represents the best fit using the

crossover function while the dotted lines show the asymptotic mean-field and 3d-Ising laws, respectively. Adapted from Ref. [12].

Experimentally determined susceptibility,  $I(0)$  versus  $T$ , like that shown in Figure 7.11, can effectively be analyzed by applying a single function describing  $I(0)$  within the whole one-phase regime. Based on an  $\varepsilon$ -expansion model, one may develop a function that describes the experimental data very well [13], as seen in Figure 7.11. The parameters of the *crossover function* are the Ginzburg number, the critical temperature, and the critical exponents.

The experimental example shown in Figure 7.11 indicates clearly that the validity of the mean-field Flory–Huggins model for binary polymer blends is somewhat limited. The relevant temperature regime of most miscible polymer blends are in fact in the crossover range rather than in the mean-field, as originally anticipated. Experiments have shown that the deviation from mean-field characteristics, as expressed by the Ginzburg number, is markedly dependent on the degree of polymerization. The temperature range of non-meanfield characteristics scale as

$$|T_{\text{mf}} - T_c| \propto N^{-\alpha}, \quad (7.90)$$

with the exponent  $\alpha$  of the order of 1 to 2 [14], but approaching a low- $N$  value that is up to two orders of magnitude larger than that of classical liquids. The latter is the reason that most polymers in reality obey non-meanfield characteristics. Only for polymer blends with  $N$ -values larger than approximately 1000 can one find mean-field characteristics even very close to the critical point.

## 7.5

### Block Copolymers

Polymers are, by definition, molecules composed by a large number of small chemical units, the monomers. Above, we have discussed A- and B-*homopolymers*, assuming that all A-polymers are composed of the same single A-monomer, and B-polymers by another specific B-monomer. Such chemical equality is often the situation in synthetic polymers, as for example polyethylene purely composed of  $-\text{CH}_2-$  ethylene monomers. Many natural polymers, on the other hand, are composed of several different monomers; example of these include proteins, which are polymeric chains composed of different amino acids; such polymers are termed *copolymers*.

One important class of synthetic copolymers is composed of two different monomers which, in the general discussion, will be abbreviated A and B. The A and B segments may be positioned randomly within the chain, or in “blocks” of respectively A and B. Diblock copolymers composed of two linear polymer blocks linked covalently together are the most simple of this class. Diblock copolymers are closely related to blends of homopolymers; both systems are composed of two linear polymer chains, but the covalent bond between the A- and the B-blocks has of course significant implications on the physical properties.

Polymers of different chemistry are generally not miscible, as discussed above. The A- and B-molecules of an AB-diblock copolymer melt will therefore tend to cluster into domains rich in respectively A and B units. In opposition to polymer

blends, the bond between the A and B blocks prevents macroscopic phase separation. The clustering of block copolymers is therefore restricted to the nanometer length scale of the polymer blocks: they form a *micro phase-separated* state.

In diblock copolymer melts, the free energy of a micro-phase-separated state can be shown to favor ordered domain structures where the mutual organization of A- and B-domains form regular lattices. The equilibrium structure depends on the relative size of the respective polymer blocks, the overall polymer size and the temperature (or rather the product  $\chi N$  of the Flory–Huggins interaction parameter and the degree of polymerization).

The phenomenological theory of block copolymers is quite analogous to that of polymer blends, discussed above. The thermodynamic properties are also here determined as an interplay between configurational entropy and enthalpic contributions according to the Flory–Huggins model of the Gibbs free energy (see Section 7.3; see also Ref. [15]). It should be emphasized however that, thermodynamically, block copolymer melts are single-component system, independent of any local structural features.

Let us consider an AB-diblock copolymer with volume fraction  $f$  of A-segments and  $(1 - f)$  of B-segments. With the total diblock degree of polymerization (or rather number of Kuhn segments)  $N$ , each chain will have

$$\begin{aligned} N_A &= fN && \text{A-segments} \\ N_B &= (1 - f)N && \text{B-segments} \end{aligned} \quad (7.91)$$

As in the development of the RPA equations for polymer blends, we will assume a uniform mixing of the A- and B-blocks, and consider the response on the spatial distribution function of A- and B-segments as a response when external fields  $u_A(\mathbf{R})$  and  $u_B(\mathbf{R})$  are applied to the system.

In the blend of homopolymers A and B, the random positioning implied that the correlation functions  $\gamma_{AB} = \gamma_{BA} = 0$ . In block copolymers, two A and B blocks are covalently bound, and the  $\gamma_{AB}$ -correlation term in Eq. (7.64) will accordingly not vanish. Following the arguments relating to Eqs (7.67) and (7.68) we will, when including the AB-cross terms, obtain

$$\begin{aligned} \overline{\delta\psi_A}(\mathbf{q}) &= -\frac{1}{k_B T} [I_{AA}^\circ(\mathbf{q})u_A^{\text{eff}} + I_{AB}^\circ(\mathbf{q})u_B^{\text{eff}}] \\ \overline{\delta\psi_B}(\mathbf{q}) &= -\frac{1}{k_B T} [I_{AB}^\circ(\mathbf{q})u_A^{\text{eff}} + I_{BB}^\circ(\mathbf{q})u_B^{\text{eff}}] \end{aligned} \quad (7.92)$$

where we have defined

$$\begin{aligned} u_A^{\text{eff}} &= u_A - z[\varepsilon_{AA}\overline{\delta\psi_A}(\mathbf{q}) + \varepsilon_{AB}\overline{\delta\psi_B}(\mathbf{q})] + V \\ u_B^{\text{eff}} &= u_B - z[\varepsilon_{AB}\overline{\delta\psi_A}(\mathbf{q}) + \varepsilon_{BB}\overline{\delta\psi_B}(\mathbf{q})] + V \end{aligned} \quad (7.93)$$

Combining this with the  $\overline{\delta\psi_A} + \overline{\delta\psi_B} = 0$  restriction, we can in analogy with derivation for blends in Section 7.4.2, solve the equations for diblock copolymers and get the result:

$$\overline{\delta\psi_A}(\mathbf{q}) = \frac{1}{k_B T} \left[ \frac{I_{AA}^\circ(\mathbf{q}) + I_{BB}^\circ(\mathbf{q}) + 2I_{AB}^\circ(\mathbf{q})}{I_{AA}^\circ(\mathbf{q})I_{BB}^\circ(\mathbf{q}) - (I_{AB}^\circ(\mathbf{q}))^2} - 2\chi \right]^{-1} (u_A - u_B) \quad (7.94)$$

which, in analogy with Eq. (7.77), may be rewritten into the form

$$\overline{\delta\psi_A}(\mathbf{q}) = \frac{1}{k_B T} \frac{N}{F_{\text{diblock}}(\mathbf{q}) - 2\chi N} (u_A - u_B) \quad (7.95)$$

with

$$F_{\text{diblock}}(\mathbf{q}) = \frac{1}{N} \frac{I_{AA}^\circ(\mathbf{q}) + I_{BB}^\circ(\mathbf{q}) + 2I_{AB}^\circ(\mathbf{q})}{I_{AA}^\circ(\mathbf{q})I_{BB}^\circ(\mathbf{q}) - (I_{AB}^\circ(\mathbf{q}))^2} \quad (7.96)$$

which is similar to the corresponding F-function for polymer blends (Eq. (7.78)), except for the AB-cross-terms. We will assume that the diblock copolymer in the homogeneous state obeys Gaussian statistics similar to the linear homopolymers discussed above (Eq. (7.22)). The partial structure factor  $I_{AA}^\circ$  of the individual block copolymer can then be expressed as

$$I_{AA}^\circ(\mathbf{q}) = \frac{1}{N} \int_0^{N_A} \int_0^{N_A} \exp\left[-\frac{b^2}{6}|n-m|\right] dn dm = Nh(f, N, q) \quad (7.97)$$

where  $h(f, N, q)$  is a generalized Debye-function given by

$$h(f, N, q) = \frac{2}{x^2} [fx + e^{-fx} - 1] \quad \text{with} \quad x = q^2 R_g^2 \quad (7.98)$$

A corresponding calculation gives the partial structure factor  $I_{BB}$

$$I_{BB}^\circ(\mathbf{q}) = Nh(1-f, N, q) \quad (7.99)$$

The partial structure factor  $I_{AB}$  for the diblock copolymer is correspondingly

$$I_{AB}^\circ(\mathbf{q}) = \frac{1}{N} \int_0^{N_A} \int_{N_A}^N \exp\left[-\frac{b^2}{6}|n-m|\right] dn dm$$

giving

$$I_{AB}^\circ(\mathbf{q}) = \frac{N}{2} [h(1, N, q) - h(f, N, q) - h(1-f, N, q)] \quad (7.100)$$

Substituting these results into Eq. (7.94) gives the RPA-structure factor for a diblock copolymer melt

$$I(\mathbf{q}) = \frac{N}{F_{\text{diblock}}(f, N, \mathbf{q}) - 2\chi N} \quad (7.101)$$

which has the same form as that of the blend given in Eq. (7.77), but with another F-function:

$$F_{\text{diblock}}(f, N, \mathbf{q}) = \frac{h(1, N, \mathbf{q})}{h(f, N, \mathbf{q})h(1-f, N, \mathbf{q}) - \frac{1}{4}[h(1, N, \mathbf{q}) - h(f, N, \mathbf{q}) - h(1-f, N, \mathbf{q})]} \quad (7.102)$$

The structure factor Eq. (7.101) with  $F$  given by Eq. (7.102) was originally derived by Leibler [15]. The structure factor approaches zero for both  $q \rightarrow 0$  and  $q \rightarrow \infty$ , and has a distinct maximum at a  $q^*$ -value reflecting the overall size of the copolymer, and which can be calculated from the derivative:  $dI(q)/dq = 0$ . For



symmetric block copolymers,  $f = 0.5$ , this gives

$$q^* \simeq 1.945/R_g \quad (7.103)$$

The scattering function at  $q = q^*$ ,  $I(q^*)$ , markedly depends on the interaction parameter  $\chi$ , and diverges according to Eq. (7.101) at the critical value  $\chi_c$ :

$$\chi_c \equiv \frac{F(f, N, q_c)}{2N}, \quad (7.104)$$

which with  $\chi \sim 1/T$  corresponds to a critical temperature  $T_c$ . Beyond  $T_c$  the block-copolymer system is unstable and will phase-separate on the length scale of the polymer coils: so-called micro-phase separation. The critical temperature  $T_c$  corresponds to the spinodal point for polymer blends.

Figure 7.12 shows examples of experimental  $I(q)$  as measured at different temperature and fits using the analytical Leibler function. The experimental data are indeed fitted very well by the structure factor of the RPA theory. The solid curves shown in the figure represents best fits convoluted by the experimental resolution function. In the insert is shown the effect of instrumental smearing. In typical data analysis, both the polymer radius of gyration  $R_g$  and the Flory–Huggins interaction parameter  $\chi$  are used as adjustable parameters.

Plotting the inverse of the peak-value,  $I^{-1}(q^*)$ , as a function of reciprocal temperature,  $T^{-1}$  (or interaction parameter  $\chi$ ) one should, according to the mean-field treatment, obtain a straight line in analogy with the  $I^{-1}(0)$ -susceptibility of blends, Eq. (7.87), which approaches zero at the critical point, here the spinodal temperature. For symmetric block copolymers,  $f = 0.5$ , Eqs (7.101) and (7.102) lead to the critical value,  $\chi_c N$ :

$$\chi_c N = 10.495, \quad (7.105)$$

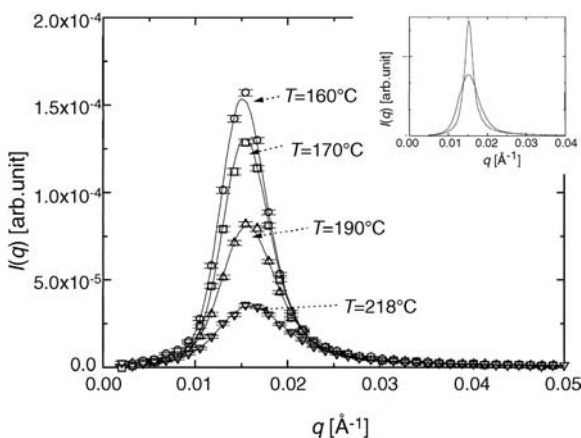


**Figure 7.12** Example of experimental scattering function of a diblock copolymer, and fits using the meanfield RPA theory (solid line). The fits represent the model function including

instrumental smearing. The effect of smearing is shown in the insert, giving the resulting Leibler function at 160 °C, with and without smearing.

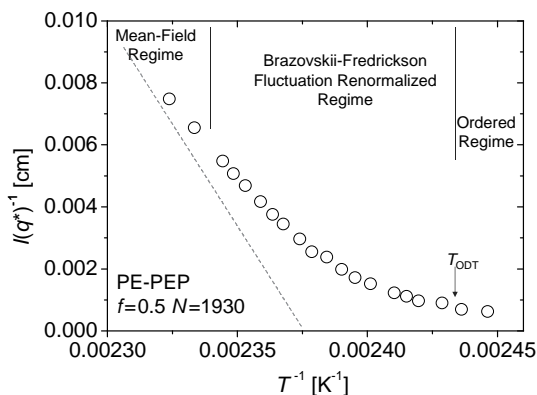


**Figure 7.13** Experimental susceptibility given by the maximum value of the scattering function:  $I^{-1}(q^*)$  plotted versus inverse temperature. The data illustrates the marked influence in the fluctuation renormalization near the  $T_{\text{ODT}}$ . The figure shows data of a symmetric PE-PEP diblock copolymer with  $N = 1930$ . Experimental data adapted from Ref. [17].

which may be compared with the corresponding critical value of symmetric,  $N_A = N_B$  binary blends (Eq. (7.41)):  $\chi_c N = 2$ .

The mean-field theory of Leibler agrees very well with experimental observations based on X-ray and neutron scattering when obtained relatively far from the microphase separation temperature (MST). In the vicinity of the MST, however, mean-field treatment is less accurate. Both, Leibler and Fredrickson and Helfand noted that the effective Hamiltonian appropriate for diblock copolymers is in the Brazovskii-universality class [15,16]. Based on the Hartree treatment used in the Brazovskii theory, Fredrickson and Helfand found that the structure factor can still be written as the mean-field expression Eq. (7.101), but with renormalized values  $\tilde{\chi}$  and  $\tilde{N}$  [16]. The fluctuation renormalization makes the order parameter  $I^{-1}(q^*)$  nonlinear in  $\chi$ , and thereby nonlinear in  $T^{-1}$ . This is shown in the experimental example given in Figure 7.13.

### 7.5.1

#### Ordered Phases

Until now, we have discussed the disordered phase in some detail, but have not really mentioned phase behavior beyond the point where the order-parameter diverges. In fact, block copolymers do not reach the critical point, but rather undergo a weak first-order phase transition into a mesoscopic ordered structure. A significant amount of the attention paid to block copolymers in recent years has been concerned with these self-assembled microstructures. Various geometries occur, depending on the volume fraction,  $f$ , the mismatch in entropic stretching energy of the different blocks, and the degree of fluctuations as manifested through the degree of polymerization,  $N$  [18].

Most theoretical models that have been proposed are effectively based on hard core interactions by implementing the incompressibility constraint where the

average segment concentration is forced to be uniform. The remaining interactions are assumed to be local. The thermodynamic stable phases are determined by minimizing the free energy density for a given  $\chi N$ -value. With this approach, Leibler determined the stability of the classical ordered structures and the condition for mesophase transitions. In the symmetric  $f = 0.5$  case, the transition should be of second order, going from the disordered directly to the lamellar structure. For  $f \neq 0.5$ , the transition is weakly first order. In the very near vicinity of the disordered phase, the minority component forms spherical micellar domains that are arranged on a bcc lattice with the matrix consisting of the majority component. Upon a further decrease in  $T$  (increase in  $\chi N$ ), the mean-field RPA predicts a first-order transition to the hexagonal-ordered phase, where cylinders are formed by the minority component. Finally, after an even further decrease in  $T$ , a first-order transition to the lamellar structure is predicted.

Leibler's studies can be mapped onto the Brazovskii Hamiltonian, allowing calculations beyond mean-field [16]. The effect of fluctuation renormalization is not only to shift the phase boundaries to larger  $\chi N$ -values, but also to change the second-order critical point to a line of first-order transition between the disordered and the lamellar phase. In addition, the fluctuation renormalization causes a direct transition from the disordered phase to the hexagonal rod phase. The cubic bcc phase is substantially limited to highly asymmetric block copolymer architectures, but this depends on the overall degree of polymerization. Matsen and Bates used self-consistent field theory to show the bicontinuous  $Ia\bar{3}d$ -symmetric gyroid structure near the order-disorder transition regime located between the hexagonal and lamellar phases [19].

The experimental challenge related to the ordered block copolymer structures concerns the unique crystallographic identification of the phases, and also verification of the stability of an apparent observed ordered nanostructure. Since the characteristic dynamics of high-molar-mass polymer systems is often very slow, it is very difficult to conclude that an observed ordered phase is thermodynamically stable. A crystallographic description of the ordered structure has, in principle, to be solved much like the investigation of any classic crystal, but the large length scale and the amorphous building units will, of course, provide a number of special features.

Small-angle X-ray and neutron scattering has been used to solve the ordered microstructures of block copolymers. By identifying the sequence of Bragg-reflections, the ordered structure can be identified according to standard crystallographic tables. The relative intensity of the different Bragg-peaks can further be used to obtain information beyond just the ordering symmetry. Typical block copolymer samples show, however, usually only rather weak higher-order reflections; this is both a result of relative low coherence of many ordered phases, paracrystallinity, and due to the intrinsic structural characteristics. The building blocks of the block copolymer have sizes comparable to the lattice distance, causing major reductions in the intensity of the high-order reflections. Moreover, the concentration profile – and thereby the profile of the scattering contrast – has near the order-disorder transition close to sinusoidal profile. With the scattering function being the Fourier transform of the contrast profile, such a sinusoidal profile will give a significant intensity only in the first harmonics.

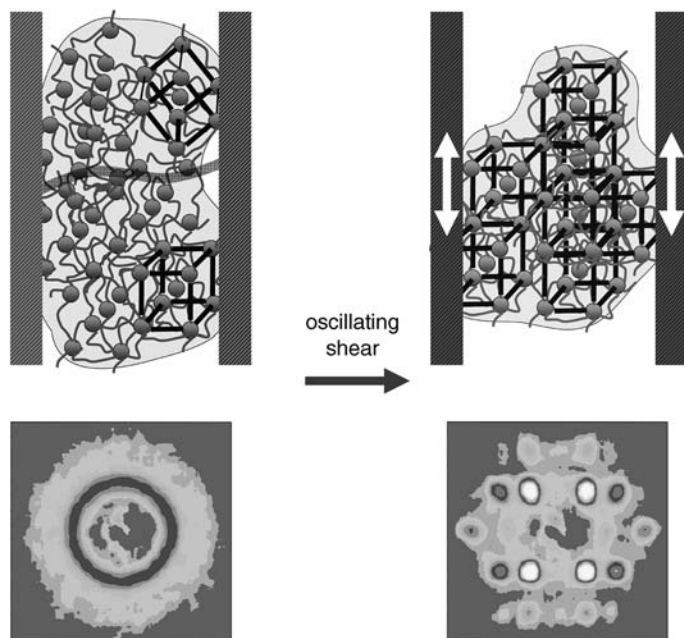


**Figure 7.14** Schematic illustration of shearing a block copolymer into single domain texture, and the corresponding SANS scattering pattern.

Insight into structures can be significantly improved if the polymer sample is first transformed into a single-domain texture, and this may be achieved by applying an appropriate field. *Shear* has, in particular, been proven to be excellent for determining field-induced bulk orientation, and the shear set-up and corresponding experimental SANS pattern are shown in Figure 7.14. Specific domain-orientations may even be controlled by using appropriate shear amplitude and frequency [20]. This is shown in the experimental shear-diagram in Figure 7.15, which illustrates the characteristic texture of a polystyrene–poly(ethylene propylene)–polystyrene block copolymer network.

SANS experiments with shear-aligned samples have been used to reveal the block copolymer *phase diagram*. As each diblock copolymer is, from a thermodynamic aspect, principally a one-component system, it may be formulated as a diagram of ordered microstructures given as a function of the volume fraction of the block copolymer component,  $f$ , and the product of the degree of polymerization ( $N$ ) and the interaction parameter ( $\chi$ ) (which is proportional to the reciprocal temperature) [18,21]. Beyond the classical phases, these experimental diagrams show lamellar, hexagonal and bcc, as well as bicontinuous  $Ia\bar{3}d$ , and modulated lamellar structures. An example of an experimental block-copolymer phase diagram, as obtained from SANS studies of a large variety of synthesized polystyrene–polyisoprene diblock copolymers, is shown in Figure 7.16 [18,21]. Examples of experimental scattering patterns revealing the different ordered phases are provided in Figures 7.14 and 7.15.

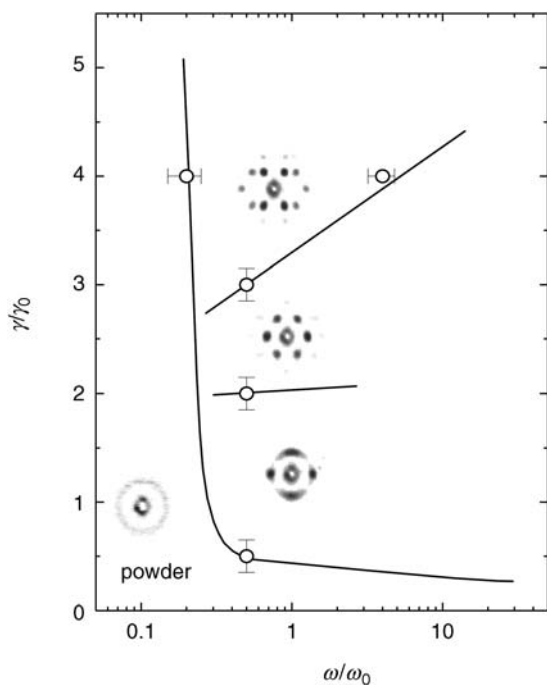


**Figure 7.15** The texture of ordered diblock copolymers can be controlled in great detail applying shear with given shear-amplitude  $\gamma$  and shear-frequency  $\omega$ . Adapted from Ref. [20].

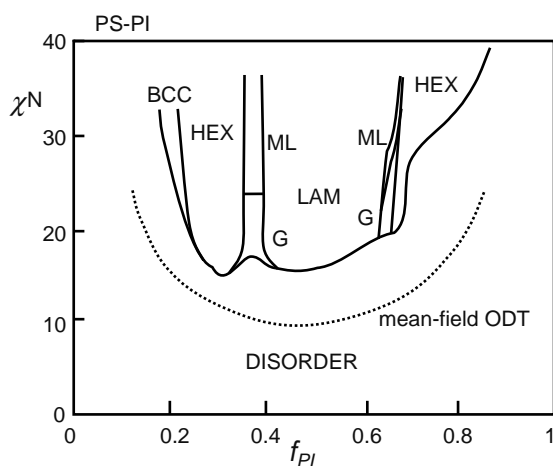


**Figure 7.16** Experimental phase diagram of a diblock copolymer melt: polystyrene–polyisoprene (PS-PI) [21], showing disordered regime and five ordered microstructures:

lamellar (LAM); hexagonally ordered cylinders (HEX); bodycentered cubic (BCC); modulated lamellar (ML); bicontinuous gyroid phase (G) [20].

## References

- 1 Doi, M. (1996) *Introduction to Polymer Physics*, Clarendon Press, Oxford.
- 2 Flory, P. (1953) *Principles of Polymer Chemistry*, Cornell University Press, New York.
- 3 Higgins, J. and Beno, H. (1994) *Polymers and Neutron Scattering*, Clarendon Press, Oxford.
- 4 deGennes, P. (1970) Theory of x-ray scattering by liquid macromolecules with heavy atom label. *Le J. Phys-Paris*, **31**, 235–238.
- 5 Landau, L. and Lifshitz, E. (1980) *Statistical Physics*, Pergamon Press, New York.
- 6 Schwahn, D., Mortensen, K., Springer, T., Yee-Madeira, H., and Thomas, R. (1987) Investigation of the phase diagram and critical fluctuations of the system polyvinylmethylether and d-polystyrene with neutron small angle scattering. *J. Chem. Phys.*, **87**, 6078–6087.
- 7 Brereton, M., Fischer, E., Herkt-Maetzky, C., and Mortensen, K. (1987) Neutron scattering from a series of compatible polymer blends: Significance of the  $\chi_f$  parameter. *J. Chem. Phys.*, **87**, 6144–6149.
- 8 Goldenfeldt, N. (1992) *Lectures on Phase Transitions and the Renormalization Group*, vol. **85**, Frontiers in Physics, Addison-Wesley, New York.
- 9 Schwahn, D., Mortensen, K., and Yee-Madeira, H. (1987) Mean-field and Ising critical behavior of a polymer blend. *Phys. Rev. Lett.*, **58**, 1544–1546.
- 10 Bates, F.S., Rosedale, J.H., Stepanek, P., Lodge, T.P., Wiltzius, P., Fredrickson, G.H., and Hjelm, R.P. (1990) Static and dynamic crossover in a critical polymer mixture. *Phys. Rev. Lett.*, **65**, 1893–1896.
- 11 Frielinghaus, H., Schwahn, D., Mortensen, K., Willner, L., and Almdal, K. (1997) Pressure and temperature effects in homopolymer blends and diblock copolymers. *J. Appl. Crystallogr.*, **30**, 696–701.
- 12 Schwahn, D. and Mortensen, K. (2000) Thermal Composition Fluctuations in Polymer Blends studied with Small-Angle Neutron Scattering, in *Scattering in Polymeric and Colloidal Systems*, (eds W. Brown and K. Mortensen), Gordon & Breach Science Publ., Amsterdam, The Netherlands, pp. 371–412.
- 13 Anisimov, M., Kiselev, S., Sengers, J., and Tang, S. (1992) Crossover approach to global critical phenomena in fluids. *Physica A: Statistical Mechanics and Its Applications*, **188**, 487–525.
- 14 Schwahn, D., Meier, G., Mortensen, K., and Janssen, S. (1994) On the n-scaling of the Ginzburg number and the critical amplitudes in various compatible polymer blends. *J. Phys. II (France)*, **4**, 837–848.
- 15 Leibler, L. (1980) *Macromolecules*, **13**, 1602–1617.
- 16 Fredrickson, G.H. and Helfand, E. (1987) Fluctuation effects in the theory of microphase separation in block copolymers. *J. Chem. Phys.*, **87** (1), 697–705.
- 17 Rosedale, J.H., Bates, F.S., Almdal, K., Mortensen, K., and Wignall, G.D. (1995) Order and disorder in symmetric diblock copolymer melts. *Macromolecules*, **28**, 1429–1443.
- 18 Bates, F., Schulz, M., Khandpur, A., Förster, S., Rosedale, J., Almdal, K., and Mortensen, K. (1994) Fluctuations, conformational asymmetry and block-copolymer phase-behavior. *Faraday Discuss.*, **98**, 7–18.
- 19 Matsen, M. and Bates, F. (1996) Unifying weak- and strong-segregation block copolymer theories. *Macromolecules*, **29**, 1091–1098.
- 20 Mortensen, K. (2004) Three-dimensional crystallographic determination of the body-centered-cubic morphologies of shear-aligned block copolymer systems. *J. Polym. Sci., Part B: Polym. Phys.*, **42**, 3095–3101.
- 21 Khandpur, A., Förster, S., Bates, F., Hamley, I., Ryan, A., Bras, W., Almdal, K., and Mortensen, K. (1995) Polyisoprene-polystyrene diblock copolymer phase diagram near the order-disorder transition. *Macromolecules*, **28**, 8796–8806.

## 8

# Ultrasound in Polymer Blends

*Sangmook Lee and Jae Wook Lee*

### 8.1

#### Introduction

Recently, many engineers working in the field of polymer blends have shown interest in ultrasound as a characterization tool for quality control and as an energy source for the compatibilization of immiscible polymer blends and nanocomposites [1–7]. Ultrasound is the name given to sound waves having frequencies higher than those to which the human ear can respond. The uses of ultrasound within a large frequency range may be divided broadly into two areas, as shown in Figure 8.1 [8].

The first area involves low-amplitude propagation, which is commonly referred to as high-frequency ultrasound. Typically, high-frequency ultrasound is used to measure the velocity and absorption coefficient of waves in the 1–10 MHz range. Typically, it is used for diagnostic scanning, in chemical analyses, for characterizing and monitoring the composition of polymer blends, for measuring extrusion flow instabilities, and for monitoring injection-molding processes [9–18].

The second area involves high-energy (low-frequency) waves, and is known as low-power ultrasound. In this case, the waves are in the 20–100 kHz range and are used for cleaning, plastic welding and, more recently, to effect chemical reactivity [19–26]. Low-power ultrasound has great acoustic energy that is capable of inducing cavitation in liquids. When polymers undergo sonication during melt processing the polymer chains are subjected to extremely large shear forces, intense local heating, a high pressure with a very short lifetime, and are also stretched severely by microbubbles that first form and then collapse [27,28] (Figure 8.2). If the energy is sufficiently large it can cause the bonds in the chain to be broken [27,29]. In the case of polymers, low-power ultrasound can be used for polymer chain modification, for the compatibilization of immiscible blends, and for dispersing nanoparticles in polymer melts [30–37]. In many cases the mechanical properties of the materials show no signs of deterioration, despite a lowering of both the molecular weight and viscosity.

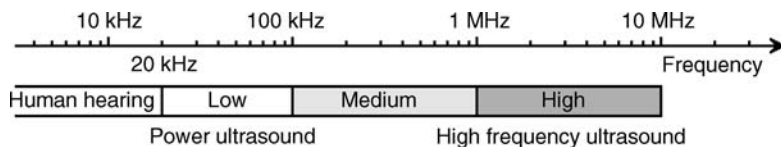


Figure 8.1 The frequency range of ultrasound.

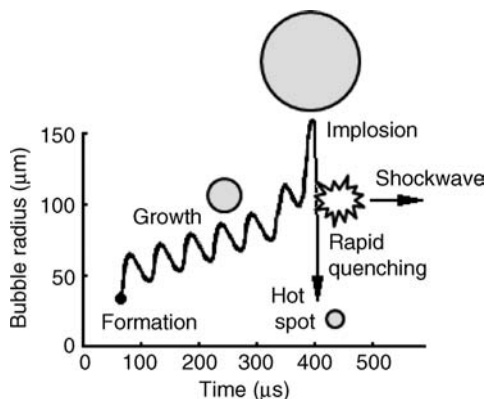


Figure 8.2 Graphical representation of the lifetime of a cavitation bubble.

## 8.2

### High-Frequency Ultrasound

Low-power or high-frequency ultrasound was used to characterize polymer blends by indirect contact with the polymers. According to the measuring state, the applications of high-frequency ultrasound can be described as either static characterization (static method) or in-line monitoring (dynamic method).

#### 8.2.1

##### Static Characterization

Various sophisticated instrumental methods have been developed to characterize polymer blends and compatibility, including thermal, microscopy, spectroscopy and other processing techniques. Recently, ultrasound has also been applied extensively to the study of polymer blend properties in both solutions and solids. The ultrasonic velocity and attenuation by the interaction of the propagating wave were used to investigate the various physical properties of the polymer blends, including density, compatibility, molecular orientation, and phase inversion.

##### 8.2.1.1 Miscibility of Solution Blends

Varada Rajulu *et al.* [13] carried out miscibility studies of polystyrene/poly(vinyl pyrrolidone) (PS/PVP) and poly(methyl methacrylate)/poly(vinylpyrrolidone)



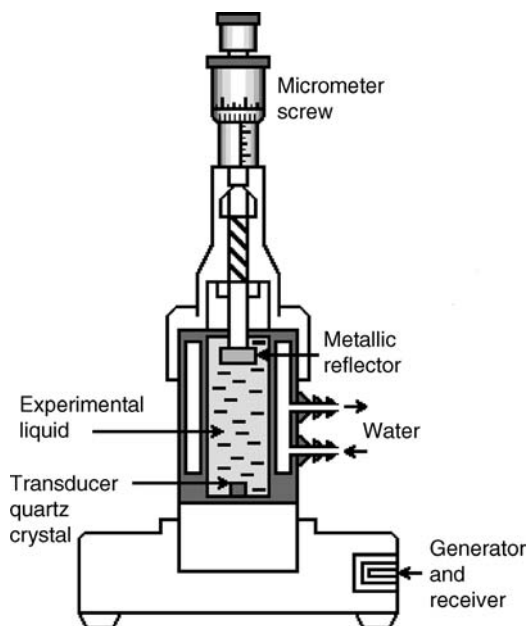


Figure 8.3 Schematic representation of an ultrasonic interferometer [13].

(PMMA/PVP) in a cosolvent of dimethyl formamide and cyclohexanone in various blend compositions by using ultrasonic interferometry, as shown in Figure 8.3. The ultrasonic velocity was calculated directly as:

$$\text{Ultrasonic velocity } (v) = \text{wavelength } (\lambda) \times \text{frequency } (f)$$

The interaction parameters suggested by Sun *et al.* [38] were obtained using viscosity data to determine the miscibility. The ultrasonic velocity of the blend solutions as a function of PVP content is shown in Figure 8.4. For PS/PVP blends, there was an almost insignificant effect of the blend ratio on ultrasonic velocity, which indicated the presence of only one phase. In contrast, the PMMA/PVP blends showed a nonlinearity that indicated the presence of two phases. In the case of the blend system of cellulose acetate/PMMA [39], the nonlinear behavior of ultrasonic velocity with blend composition was due to the blend's immiscible nature. Singh and Singh [40] also attributed the linear variation of the ultrasonic velocity of PMMA/poly(vinyl acetate) with blend composition to the miscible nature of the blend. Singh *et al.* [41] noted that both the ultrasonic velocity and density with blend composition were linear for miscible blends but nonlinear (S-shaped) for immiscible blends, respectively.

Pandey *et al.* [14] characterized the compatibility of immiscible binary blends of acrylonitrile-*co*-butadiene rubber (NBR) and ethylene propylenediene rubber (EPDM) by using ultrasonic interferometry. Variations in the ultrasonic velocity of solution blends at room temperature with respect to the varied blend ratios, as

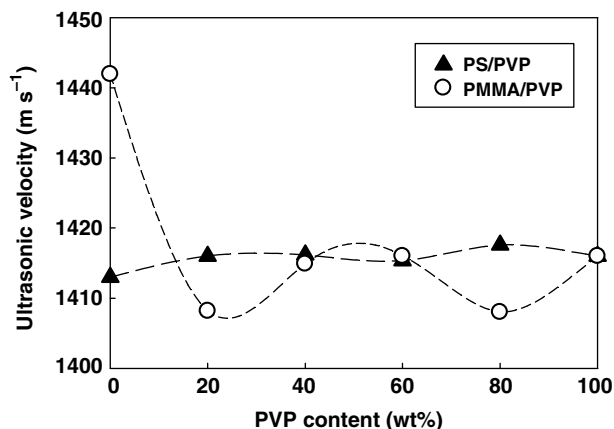


**Figure 8.4** Ultrasonic velocity versus PVP content (wt%) for PS/PVP and PMMA/PVP blends in a cosolvent (dimethyl formamide and cyclohexanone) at 30 °C [13].

well as after the addition of either chlorinated polyethylene (CM) or chlorosulfonated polyethylene (CSM) as a compatibilizer, are shown in Figure 8.5. In the absence of the compatibilizer the ultrasonic velocity was seen to vary in an apparently sinusoidal fashion as the blend ratio was varied. An alternate rise-and-fall-type of propagation of the ultrasonic wave was due to immiscibility between the NBR and EPDM phases. Singh and Singh [40] and Sidkey *et al.* [42] have each reported similar observations. However, the addition of a compatibilizer resulted in a marked increase in the ultrasonic velocity and a significant change in the shape of the graph produced.

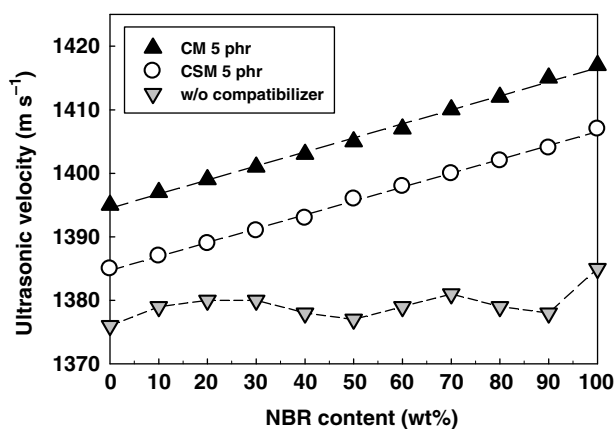


**Figure 8.5** Ultrasonic velocity versus NBR content for NBR/EPDM blends [14].

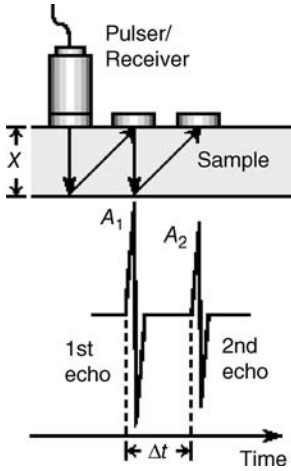


Figure 8.6 Schematic representation of ultrasound propagation [15]. See text for details.

#### 8.2.1.2 Compatibility

Recently, the most commonly used method has been the pulse–echo technique. In this case, a short sinusoidal electrical wave is first used to activate the ultrasonic transducer; the latter then projects sound waves into the sample, with which it is in firm contact. One advantage of the pulse–echo technique is that the sound velocity and attenuation can be measured simultaneously. As shown in Figure 8.6, the incident wave is generated from the transducer when it is in direct contact with the plate specimen, transmitted into the sample of thickness  $X$ , and then reflected back and forth at the two surfaces. In this way, a series of echo signals can be obtained as the ultrasound is reflected between the two surfaces, although the amplitudes of the echo signals will gradually be decreased with time due to ultrasonic attenuation. By using an oscilloscope, direct measurements of the time required for the pulses to travel twice the length of the specimen, and also the amplitude of the pulses are possible. This, in turn, allows an immediate calculation of the ultrasonic wave velocity,  $v$ , and the attenuation,  $\alpha$ , as given in the following equations:

$$v = \frac{2X}{\Delta t} \alpha = \frac{20 \log(A_1/A_2)}{2X}$$

where  $X$  is the sample thickness,  $\Delta t$  is the time interval, and  $A_1$  and  $A_2$  are the amplitudes at peak 1 and at peak 2, respectively.

Sidkey *et al.* [15] measured the longitudinal ultrasonic velocity and ultrasonic attenuation of four blend systems – namely Adiprene CM/NBR, Adiprene CM/natural rubber (NR), Adiprene E/NR, and Adiprene E/NBR – at room temperature, using the pulse–echo technique. The relationship between the measured ultrasonic absorption and temperature and the glass transition temperature ( $T_g$ ) of the

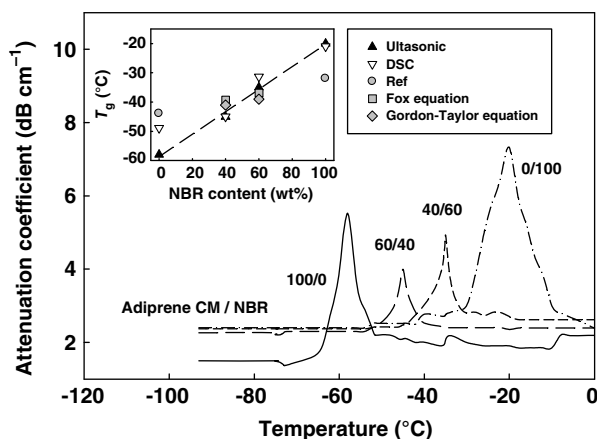


**Figure 8.7** Variation of attenuation coefficient of Adiprene CM/NBR blends with temperature [15].

Adiprene CM/NBR blends is shown in Figure 8.7. The absorption was of a relaxational nature and was not due to scattering of the dispersed phase. The presence of only one single transition temperature peak for all blend compositions indicated very clearly that this blend system was compatible. The  $T_g$ -values of neat rubbers, Adiprene CM and NBR were provided in Refs [43–46], while those for the blends were calculated on a theoretical basis using the Fox equation [47] and the Gordon–Taylor equation [48]. The  $T_g$ -values calculated theoretically from both the Fox and Gordon–Taylor equations were very close to the values obtained experimentally. The presence of a single transition temperature observed in differential scanning calorimetry (DSC) thermograms and ultrasonic attenuation–temperature relationships was a decisive confirmation of the formation of one single phase and the compatibility behavior of the blend [43,49], whereas two transition temperatures were taken as an evidence of phase separation and incompatibility of the blend.

### 8.2.1.3 Density

Afifi and Sayed [16] obtained the ultrasonic velocities for the propagation of longitudinal and transverse ultrasonic waves in epoxidized natural rubber/ethylene propylene diene monomer (ENR/EPDM) blends at a frequency of 2 MHz using the pulse–echo method; the density of the rubber blend was also measured. The results of the two ultrasonic wave velocities (longitudinal and shear), as well as the density of the ENR/EPDM blend samples at different compositions, were plotted (see Figure 8.8). As the EPDM content was increased, the densities of the samples increased, whereas both the longitudinal and shear ultrasonic velocities increased up to about 60–80 wt% but then decreased again. These data suggested that the increase in ultrasonic velocity up to a maximum was due to the occurrence of a strong specific intermolecular interaction within the components of the

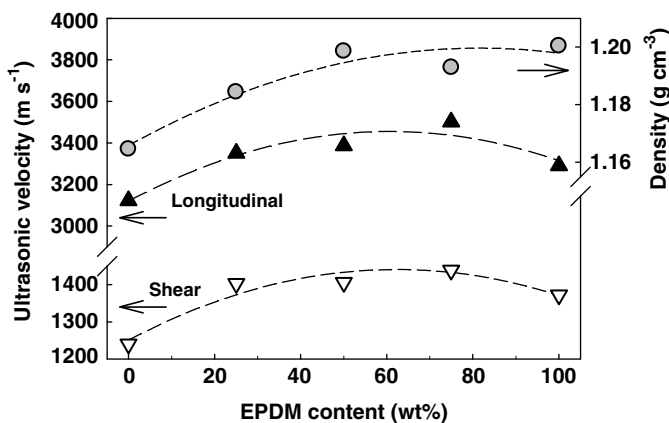


**Figure 8.8** Variation of ultrasonic velocity (longitudinal and shear) and density for ENR/EPDM blends as a function of EPDM content [16].

ENR/EPDM system. This behavior also indicated a good miscibility between two rubber components. It has been also been suggested that a linear relation between ultrasonic velocity and composition could be interpreted as a sign of the presence of single-phase morphology [50–53].

#### 8.2.1.4 Phase Inversion

He *et al.* [17] investigated the morphology of polymer blends by ultrasonic attenuation and velocity, together with scanning electron microscopy (SEM) observations. It has long been known that EPDM elastomer is immiscible with polystyrene (PS) over the entire range of concentrations [54]. However, by employing SEM observations these authors confirmed that the phase inversion of EPDM/PS blends occurred at about 46–56 vol% of the PS content. The nonlinear relationship of ultrasonic attenuation and velocity with the composition of EPDM/PS blends is shown in Figure 8.9. In this case, the attenuation increased steadily up to about 36 vol% PS content, but then rose dramatically to 56 vol% PS. Unfortunately, the peak could not be observed with the present measuring system because of the poor signal-to-noise ratio (SNR) of the reflected waves. Although, in the region of 56–100 vol% PS content the attenuation fell sharply again with increasing PS content, when the PS content was increased so too did the ultrasonic velocity, showing an inflection at about 53 vol% PS that corresponded to the phase inversion observed using SEM. Based on the relationship between ultrasonic velocity and composition, it was suggested that the nonlinear behavior indicated the multi-phase nature of the EPDM/PS blends, and that the inflection point simply corresponded to the phase inversion. A discontinuity of ultrasonic attenuation was always observed when phase inversion occurred. However, for miscible polymer blend systems there was only a linear change of ultrasonic attenuation and velocity, without any discontinuity or inflection. Hence, it was suggested that the

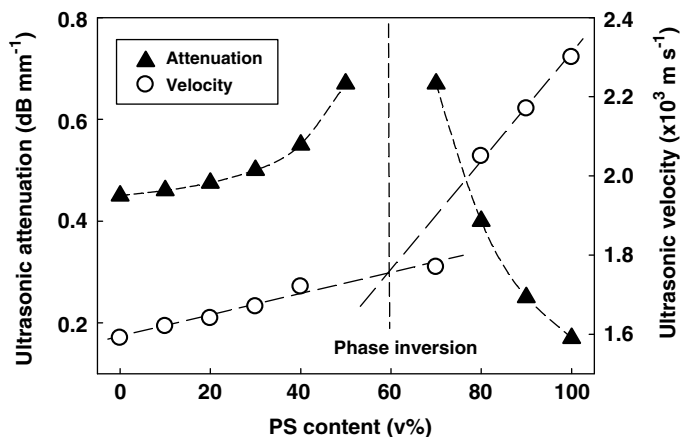


**Figure 8.9** Variation of ultrasonic attenuation and velocity for EPDM/PS blends as a function of PS content [17].

discontinuity of ultrasonic attenuation might serve as a useful tool to rapidly determine the phase inversion of immiscible polymer blends.

#### 8.2.1.5 Molecular Orientation

As the mechanical properties of the final product often depend on the orientation of the polymer chain, it is very important to characterize the orientation of the polymer chain both quickly and accurately in nondestructive fashion. When Edwards and Thomas [55] used the propagation velocity of an ultrasonic shear wave to detect anisotropic behavior in the mechanical properties of a solid, the results obtained indicated that this method was quite sensitive for semicrystalline polymers but much less effective for amorphous polymers.

He *et al.* [18] used a normal incident shear wave, which travels at different velocities in anisotropic media, to explore the orientation structure of high-density polyethylene (HDPE)/isotactic polypropylene (i-PP) blends obtained by dynamic packing injection molding, as shown in Figure 8.10. The sample with a highly oriented structure was obtained by introducing the shear stress field to the cooling melt during the packing stage by two reversibly moving pistons. The pulser/receiver, which consisted of a normal incident shear wave transducer, was added to their previous set-up [17], as shown in Figure 8.11. The shear wave had two characteristic velocities—parallel and vertical to the flow direction, respectively—when an ultrasonic wave was propagated in anisotropic media. From a practical standpoint, however, use of the corresponding echo times,  $t_p$  and  $t_v$ , was more convenient than to use the velocity to reflect the orientation. The larger the echo time difference ( $\Delta t = t_v - t_p$ ), the higher was the degree of orientation. A comparison of the ultrasonic results and two-dimensional wide-angle X-ray scattering (2D-WAXS) data is shown in Figure 8.12. With increasing i-PP content, the variation of echo time difference,  $\Delta t$ , for the ultrasonic method was always similar to that of

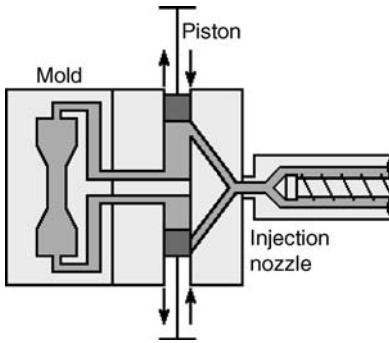


Figure 8.10 Schematic diagram of the device used for dynamic packing injection molding [18].

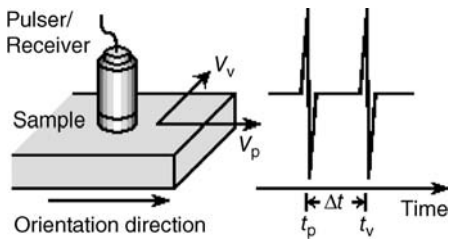


Figure 8.11 Schematic diagram of normal incident shear wave propagation in uniaxial oriented media [18].

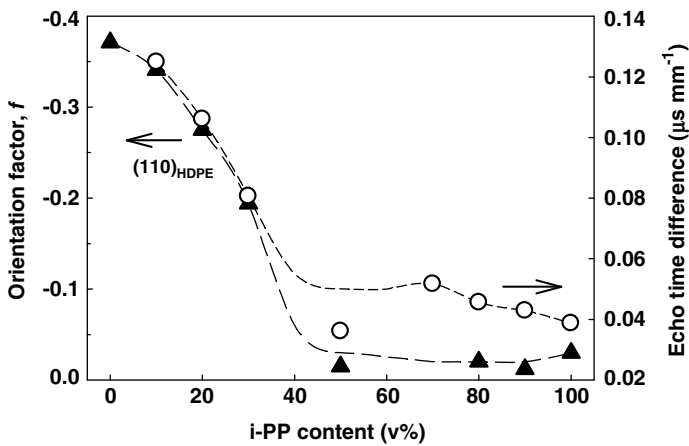


Figure 8.12 Comparison of ultrasonic results and 2D-WAXS results in terms of orientation measurement for HDPE/iPP blends [18].

the crystalline orientation factor,  $f$  (reflection of the (110)<sub>HDPE</sub> plane) for 2D-WAX, especially in the region of low i-PP content.

### 8.2.2

#### In-Line Monitoring

Whilst off-line techniques such as calorimetry and microscopy are time-consuming and tend to yield insufficient data points to allow for a detailed analysis, in-line methods are faster by comparison but have not yet been found sufficiently reliable owing to the noisy analog signals that they produce. However, recent developments in high-speed sensing and digitalizing technologies have led to in-line monitoring being possible. Indeed, ultrasound may be used as a powerful tool for the in-line monitoring of polymer processing, without direct contact being made with the fluids.

##### 8.2.2.1 Morphology

It is well known that the mechanical properties of polymer blends are determined by their composition, domain size, and domain size distribution. The ability to monitor and control the morphology of immiscible polymer blends is very important. For example, Epstein and Carhart [56] used a Newtonian model for emulsions and derived relationships for the attenuation as a function of blend composition, domain size,  $R$ , and frequency,  $f$ . A longitudinal wave propagating in the matrix approaching an interface with a domain of the second fluid will give rise to reflected, transmitted shear and thermal waves, while excess attenuation can be determined as a linear function of the composition. A similar approach was also described elsewhere [57].

Verdier and Piau [12] applied ultrasound with a multiple scattering model to investigate the morphology of immiscible polyamide 6 (PA6/polypropylene (PP) blends in real time. As the composition of the blends and types of surfactant were changed, the blends gave rise to different acoustic responses during real flow through a capillary. An ultrasonic measuring cell built below a capillary rheometer used to measure ultrasonic velocity and attenuation is shown Figure 8.13. In this case, the fluid is first passed through a slit in a steel block held at constant temperature by convection, and then through a contraction. The pulser/receiver was fixed on one side of the steel block, and measured the signal that returned from the steel and the polymer blends in melt state at constant temperature. The method of separation of echoes was used such that, after transferring the data to the computer, the time difference ( $t_2 - t_1$ ) and amplitude ratio ( $V_1/V_2$ ) could be determined. The attenuation  $\alpha$  and ultrasonic velocity  $v$  obtained from a preliminary test with an oil-in-water emulsion system agreed well with the results of McClements and Povey [58]. Figure 8.14 shows  $\alpha$  and  $v$  for values of  $Rf^{1/2}$  and for concentrations corresponding to the total approximate volume fraction of PA6 and PP. The total excess attenuation was dominated by the viscosity; the attenuation depended heavily on the radius, whereas the velocity of propagation varied only slightly as a function of the domain size. Hence, it was possible to deduce the



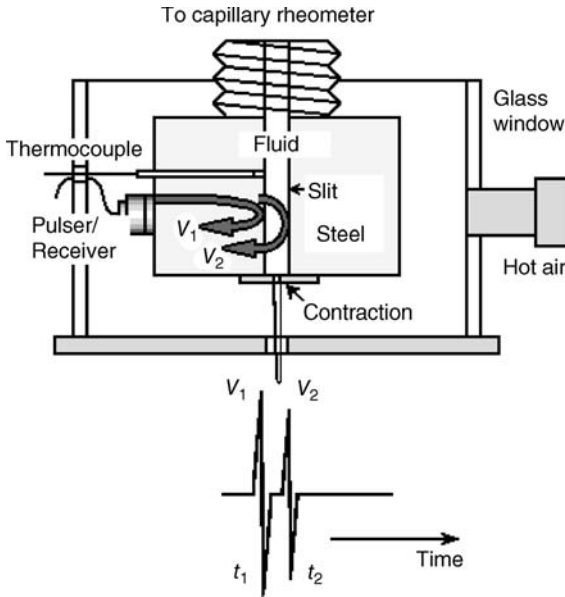


Figure 8.13 Schematic of ultrasonic cell geometry and different echoes [12].

concentration from the velocity of propagation measurements, and the mean domain size from attenuation measurements at the same volume fraction.

Ultrasonic devices can also be used very effectively as powerful tools for in-line monitoring of the composition of polymer blends, residence time distribution, injection-molding processes, temperature, polymer orientation, and flow instabilities. Franca *et al.* [59] demonstrated the sensitivity of ultrasonic waves

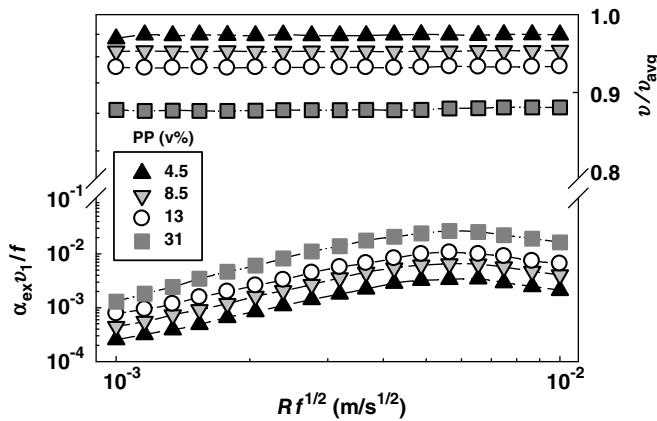


Figure 8.14 Reduced theoretical excess attenuation and velocity of PA6/PP blends [12].

to different concentrations of polystyrene and polyethylene as the feed was switched from one polymer to the other during a twin-screw extrusion. Lee *et al.* [9] measured the residence time distribution at the die exit of a corotating twin-screw extruder by using a slit die attached to a steel buffer rod. When Chen *et al.* [60] adopted a clad rod-type ultrasonic sensor to measure the melt temperature during extrusion, in real time, the temperature measured ultrasonically agreed well with that obtained using a commercial thermocouple. Edwards and Thomas [61] also investigated the on-line measurement of polymer orientation, by using ultrasonic technology.

### 8.3

#### Power Ultrasound

High-power or low-frequency ultrasound with sufficient acoustic energy to break polymer chains was used for nanoparticle dispersion and polymer compatibilization, and also for polymer modifications such as grafting reaction and molecular weight control. The applications of power ultrasound on three typical polymer processing methods— injection molding, batch melt mixing and extrusion—are introduced in the following subsections.

#### 8.3.1

##### Injection Molding

When power ultrasound oscillation was introduced to polymer melts, the mobility of the polymer molecules was increased such that, many of the common problems encountered in polymer processing could be resolved. For example, in the case of injection molding, ultrasonic oscillations were applied to improve molecular diffusion across the weld line so as to enhance the weld line strength.

##### 8.3.1.1 Weld Line Strength Improvement

Lu *et al.* [62] investigated the effect of ultrasonic oscillations on the weld line strength of injection-molded PS and PS/HDPE blends by using two different sonication methods. Details of the injection molding set-up, equipped with an ultrasonic device, are shown in Figure 8.15. It has been reported that the dramatic decrease in weld line strength of immiscible polymer blends was due to the morphology of the dispersed phase at the weld line being much more complicated than that of the neat polymer [63–68]. Compared to the tensile strength of PS and PS/HDPE (90/10) blends, the weld line strength of PS (23–27 MPa) was much higher than that of PS/HDPE (3–6 MPa), and was more pronounced at a higher melt temperature (see Figure 8.16). This was due to the ultrasonic oscillations promoting molecular diffusion across the interface in the weld line region, with a resultant improvement in weld line strength. Sonication performed after injection mold filling was also found to be more effective than if it was continued during the entire injection molding process.

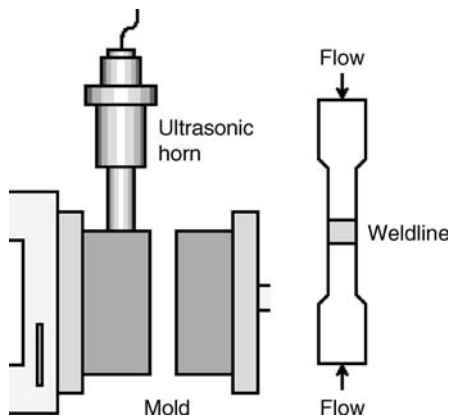


Figure 8.15 Schematic of injection molding machine equipped with an ultrasonic device [62].

### 8.3.2

#### Batch Melt Mixing

A variety of blending techniques have been used to improve particular properties that a polymer might not possess, or are lacking. Although some of the blends were found to be immiscible, which resulted in poor mechanical properties, recent attempts to overcome this problem involved the application of ultrasound irradiation to the immiscible polymer blend pairs during melt mixing, using a mixer fitted with a sonication device.

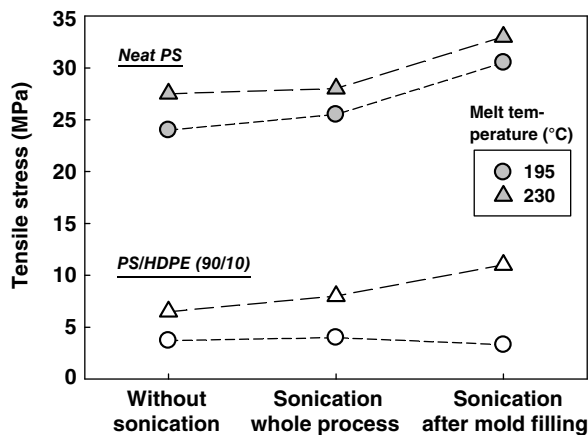


Figure 8.16 Tensile stress of injection molded PS and PS/HDPE (90/10) blend at two different sonication modes and melt temperatures [62].

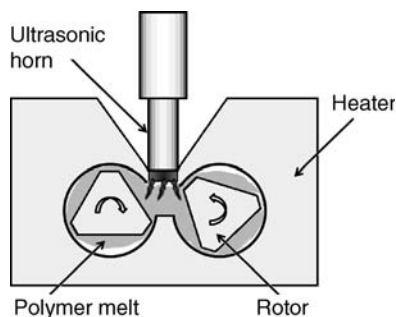


Figure 8.17 Schematic of melt mixer equipped with an ultrasonic device [1].

### 8.3.2.1 Compatibilization

Lee *et al.* [1] investigated the effect of ultrasound irradiation on a blend of poly(lactic acid) (PLA) and poly(butylene adipate-co-terephthalate) (PBAT). Blends of PLA/PBAT(50/50) (PBAT50) were prepared in a melt mixer equipped with an ultrasonic device (see Figure 8.17), and the thermal, rheological and mechanical properties, the morphology, and biodegradability of the sonicated blends were analyzed. A plot of  $T_g$ -values of PBAT50 obtained from  $\tan \delta$  peaks of the dynamic mechanical analyzer against sonication time is shown in Figure 8.18. Interestingly, as the sonication time increased, the difference between the  $T_g$ -values of the PLA and PBAT phases became narrower, were narrowest at about 11 sonication, and then became wider again. This suggested that an optimum energy input by ultrasound exists to increase the compatibility of the blend system. Generally, the addition of a low-molecular-weight component to immiscible blends results in a

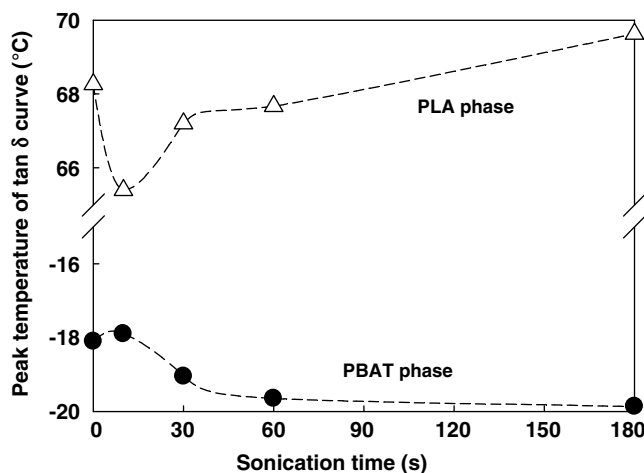
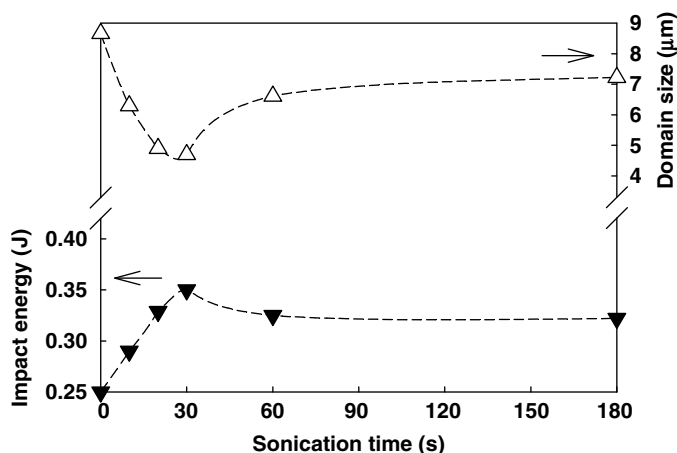


Figure 8.18 Effect of ultrasonic irradiation on the compatibility of PLA/PBAT (50/50) blends [1].



**Figure 8.19** Impact energy and domain size versus sonication time for PLA/PBAT (50/50) blends [1].

decreasing viscosity, due to a plasticizing action by the added component [69]. However, the viscosity of the sonicated blends was increased by ultrasound irradiation, owing to strong interactions, such as transesterification. Some of PLA blends were found to be immiscible, and this resulted in poor mechanical properties [70]. The impact strength and domain size of PBAT50 as a function of sonication time is shown in Figure 8.19. In this case, as the sonication time was increased the impact strength was also increased due to deformation of the compatibilized phase (which consumed excess energy) up to about 30 s sonication, but soon decreased again. In contrast, the average domain size obtained via SEM observations was decreased up to 30 s sonication; this effect may have been due to the ultrasound supplying sufficient energy to the PBAT50 system to initiate a reaction (e.g., transesterification) that would improve adhesion and reduce interfacial tension between the two phases. In the case of blends sonicated for more than 30 s, however, the PBAT domains were poorly distributed and larger, again due to their flocculation [71,72], and this resulted in a poor impact strength. Plochocki *et al.* [73] also observed a minimum dispersed phase size in line with compatibilizer amounts in a blend system of low-density polyethylene/PS. Subsequent atomic force microscopy (AFM) data showed the surface of the sonicated PBAT50 to be smoother than that of the untreated blend, after a minimum 20 s sonication.

### 8.3.3

#### Extrusion

During recent decades, extrusion has been one of the most important processes in the plastics industry. However, as industrial requirements have become increasingly diversified, the need for products with properties tailored for specific applications has increased. Some of these materials could be produced using an

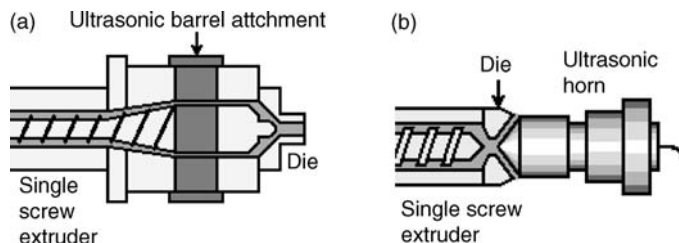


**Figure 8.20** Schematic drawings of (a) barrel and (b) coaxial ultrasonic reactors [74].

extruder fitted with a sonication device, in which the location and design of ultrasonic horns could differ according to purpose.

### 8.3.3.1 Molecular Weight Control

Isayev and Hong [74] found that *in-situ* copolymer formation and the compatibilization of immiscible polymer blends would occur during ultrasonic-assisted extrusion in the melt state. In this case, HDPE and PP were first mixed with an equal amount of uncured rubbers using a twin-screw extruder, extruded, and sonicated at 20 kHz using an ultrasonic barrel attachment (see Figure 8.20a) [75]. A 50/50 natural rubber/styrene butadiene rubber (NR/SBR) blend was prepared on a two-roll mill, after which the blend was treated ultrasonically in a single-screw extruder with a coaxial ultrasonic die attachment provided with one water-cooled horn (see Figure 8.20b) [76]. The horn oscillated longitudinally with a frequency of 20 kHz, and the residence times were on the order of seconds. The mechanical performance of the plastic/rubber and rubber/rubber blends subjected to ultrasonic treatment was significantly enhanced compared to those of identical blends not sonicated. The molecular weights and molecular weight distributions of the untreated and ultrasonicated NR/SBR (50/50) blends are shown in Figure 8.21. Clearly, as the ultrasonic amplitude was increased, both a low-molecular-weight tail and a high-molecular-weight tail were generated. Although the number average molecular weights ( $M_n$ ) became lower, the weight average molecular weight ( $M_w$ ) became higher and thus the polydispersity index (PDI) was broadened remarkably. The generation of a high-molecular-weight tail was also strong evidence that the NR and SBR components in the blends had undergone a chemical transformation during ultrasonic treatment of the NR/SBR blends, leading to the possible *in-situ* formation of the NR/SBR copolymer.

### 8.3.3.2 Tensile Properties Enhancement

Oh *et al.* [77] prepared immiscible PP/NR (50/50) blends by using a twin-screw extruder, and then passed the blends through an ultrasonic reactor consisting of a plastic extruder followed by a slit die. Two water-cooled horns with 20 kHz frequency were placed in the middle of the slit die (see Figure 8.22). The stress-strain curves shown in Figure 8.23 indicated that the sonicated blend samples had a higher tensile strength and elongation to break when compared to untreated

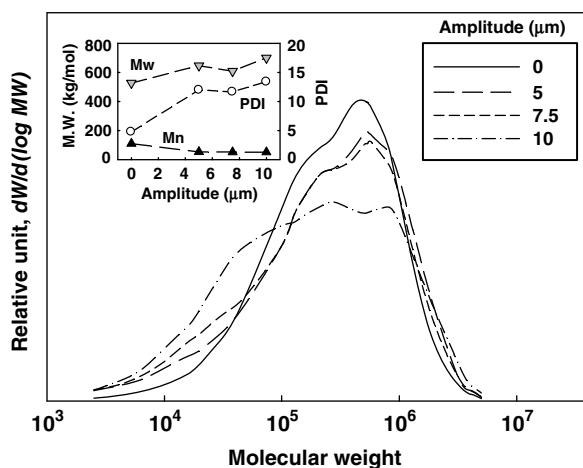


**Figure 8.21** Molecular weight distribution of untreated and ultrasonically treated NR/SBR (50/50) blends [74].

blends. The primary products of the sonochemical cleavage of polymers are macromolecular radicals [78]. Specifically, the cleavage of C—C bonds in main-chain polymers during ultrasonication during the devulcanization of rubber [76] and in polymer melt extrusion [79] led to the formation of polymer radicals [80,81] of each blend component. Subsequently, the macroradicals formed can undergo a rapid recombination, leading to the *in-situ* formation of a copolymer during ultrasonication; indeed, such an *in-situ*-formed copolymer may be the main reason for the improved mechanical properties of the sonicated blends. However, the ultrasonic treatment of blends with two horns induced a greater degree of degradation of the polymer blends, which overcame the positive effect of compatibilization.

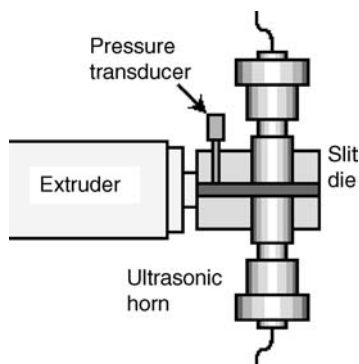


**Figure 8.22** Schematic drawing of the ultrasonic reactor with a slit die with positions of horns [77].

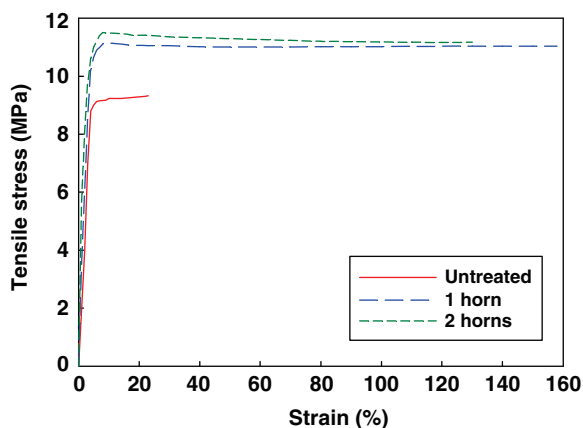


**Figure 8.23** The stress–strain curves for PP/NR (50/50) blends untreated and sonicated (gap 4 mm; flow rate  $0.63 \text{ g s}^{-1}$ ; amplitude  $10 \mu\text{m}$ ) [77].

### 8.3.3.3 Compatibilization

Feng and Isayev [82,83] treated dynamically vulcanized PP/EPDM blends using high-intensity ultrasonic waves during extrusion (as shown in Figure 8.22). The tensile properties of dynamically vulcanized PP/EPDM (50/50) blends, after ultrasonication at different amplitudes with one horn, are shown in Figure 8.24. As the amplitude was increased, the tensile strength and elongation to break of the unvulcanized blends remained almost constant, whereas those of the vulcanized blends had higher values, increased until about  $8 \mu\text{m}$  amplitude, and soon decreased again. During ultrasonication of the blends, long polymer chain radicals

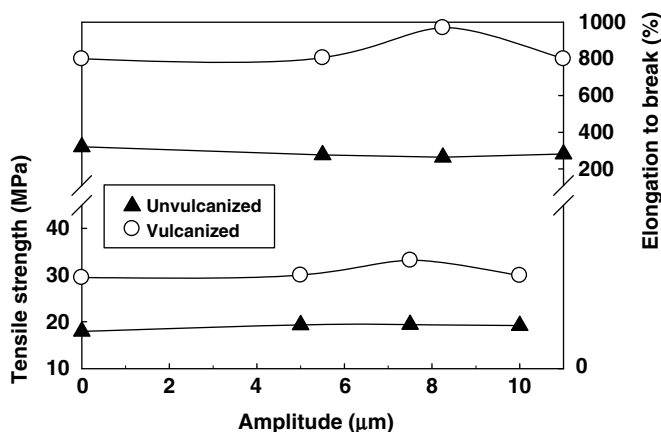


**Figure 8.24** Tensile strength and elongation to break versus ultrasonic amplitude for PP/EPDM (50/50) blends treated by one horn at a gap of 4 mm and a flow rate of  $0.63 \text{ g s}^{-1}$  [82].



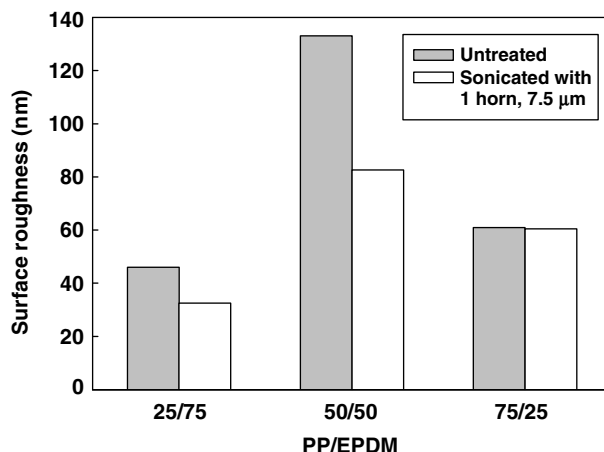


**Figure 8.25** Surface roughness versus blend composition of compression-molded samples of PP/EPDM blends untreated and treated by one horn at a gap size of 2 mm and a flow rate of  $0.63 \text{ g s}^{-1}$  [83].

generated from the breakage of long polymer chains may combine and form copolymers. It was suggested that the copolymers formed would reduce the interfacial tension between the two polymers and improve the tensile properties, much like a typical compatibilization in polymer blends. The root mean square (RMS) surface roughness of untreated and sonicated PP/EPDM blends at different blend ratios, visualized using AFM, are shown in Figure 8.25. The surface roughness of sonicated blends was less than that of untreated blends, among which PP/EPDM (50/50) had the most pronounced roughness. This was related to the blend's morphology, its stability, and the difference in the thermal expansion coefficients of PP and EPDM. Apparently, copolymers which are formed at the interface during the ultrasonication of blends will improve interfacial adhesion, which would in turn restrict the thermal expansion so that the sonicated blends would have a smoother surface. The Fourier transform infrared (FT-IR) spectra of PP, EPDM, untreated and sonicated PP/EPDM (50/50) blends are shown in Figure 8.26. Although the band at  $720 \text{ cm}^{-1}$  associated with the ethylene sequence of EPDM [84,85] was clearly observed, no such peak was visible in PP and the untreated blend after extraction. Yet, despite being extracted, the sonicated blend still exhibited the peak related to the ethylene sequence of EPDM, which indicated the existence of a copolymer in the sonicated blend.

#### 8.3.3.4 Rheological Modification

From the dynamic viscoelastic properties, valuable information about the compatibility and phase separation of polymer blends [86–91] can be obtained, based on their sensitivity to variations in the morphology of blends. Some emulsion models for polymer blends [92–97] have been used to estimate the interfacial tension of HDPE/PS (80/20) blends. Chen *et al.* [98] used the linear rheological properties of

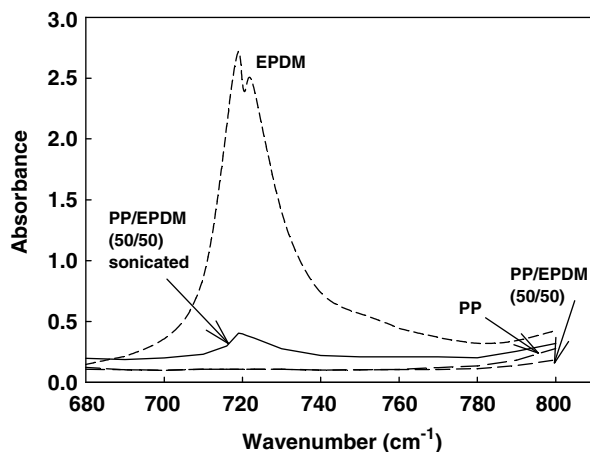


**Figure 8.26** FT-IR spectra of PP, EPDM, and PP/EPDM (50/50) blends untreated and sonicated by one horn at a gap size of 4 mm and a flow rate of  $0.63 \text{ g s}^{-1}$  [83].

HDPE, PS, and HDPE/PS (80/20) blends to characterize their structural development during extrusion in the presence of ultrasonic oscillations. The extruder set-up, equipped with a capillary die and an ultrasonic device, is shown in Figure 8.27. The slopes of  $\log G'$  versus  $\log G''$  for HDPE/PS (80/20) blends in the low-frequency region (i.e., long relaxation time) and an emulsion model were used to characterize the ultrasonic enhancement of the compatibility of the blends. The results showed that ultrasonic oscillations could reduce the interfacial tension and enhance the compatibility of the blends, and this was consistent with the data provided by Chen *et al.* [99].

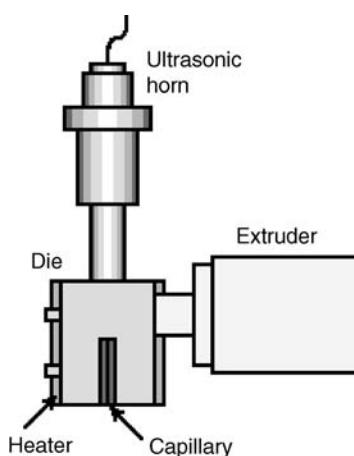


**Figure 8.27** Schematic of extruder equipped with an ultrasonic device [98].

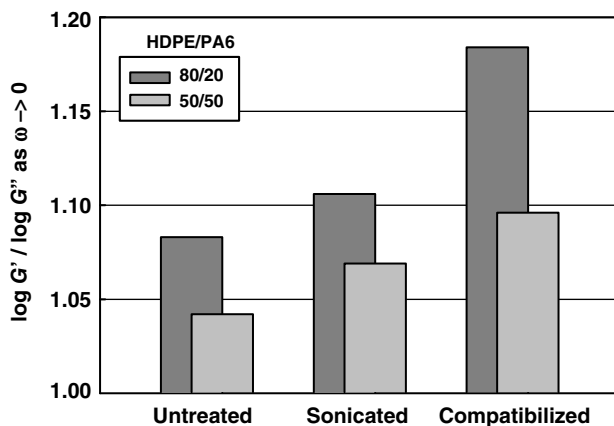


Figure 8.28 Effect of ultrasonic irradiation on slope in the low-frequency region at 235 °C [100].

Li *et al.* [100] studied the blends of HDPE and PA6 prepared by ultrasonic extrusion. The extruder set-up, equipped with a capillary die and an ultrasonic device, is shown in Figure 8.27. Ultrasonic irradiation led to the degradation of polymers and *in-situ* compatibilization of blends, as confirmed by variations in complex viscosity, storage modulus and loss modulus. The relationship between storage modulus and loss modulus indicated the effect of ultrasonic irradiation on the compatibility of HDPE/PA6 blends. Theoretically, in the linear viscoelastic region ( $\omega \rightarrow 0$ ), the  $G'$  and  $G''$  of compatible polymer blends have the following relationship:

$$\log G' \propto \log G''$$

For incompatible blends, the slope of  $\log G'$  versus  $\log G''$  plots in the terminal region was less than 2. The slopes of the sonicated and compatibilized samples were higher than that of untreated samples in the linear viscoelastic region (see Figure 8.28), which meant that the compatibility could be enhanced by ultrasonic irradiation as well as by a compatibilizer. Palierne [97] has developed a model that can predict the linear viscoelastic behavior of a polymer emulsion, by considering the droplet size in a matrix and the interfacial tension between the components. From this model the unknown interfacial tension between the matrix and the dispersed phase could be estimated, and the predicted values decreased by ultrasonic irradiation due to ultrasonic compatibilization.

#### 8.3.3.5 Morphology Control

Li *et al.* [101] introduced high-power ultrasound into PS/EPDM (80/20) blend melts during extrusion. The structure and properties of sonicated PS/EPDM blends were investigated by measuring the mechanical and rheological properties and morphology. In general, when a compatibilizer was added to a completely incompatible polymer blend, the disperse phase tended to become spherical and

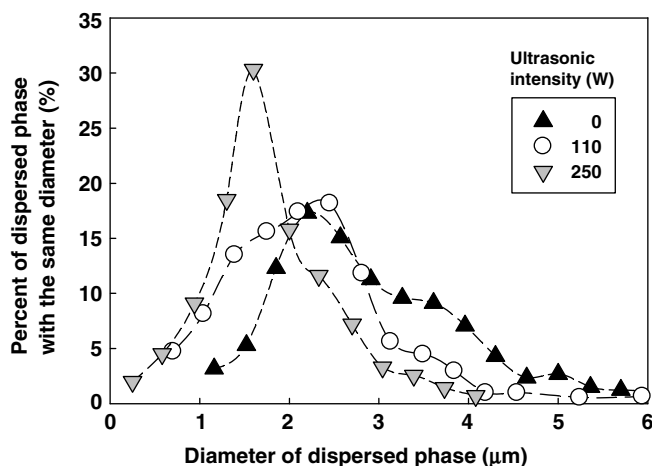
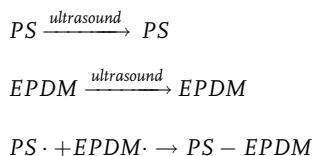


Figure 8.29 Differential particle size distribution of the dispersed phase in PS/EPDM blends [101].

the particle size was reduced [102]. Similar changes could be seen in the SEM images. It was shown that, with an increase in ultrasonic intensity from 0 to 250 W, the average domain sizes of the blends was decreased and their size distribution tended to be narrower (Figure 8.29). This indicated that ultrasonic irradiation could improve the compatibility of PS/EPDM blends due to the formation of a copolymer of PS and EPDM at the interface by the combination of different macroradicals:



In order to confirm this mechanism, ultraviolet (UV) spectra of the blends were recorded, as depicted in Figure 8.30. The ultrasonically treated samples showed an absorption peak at 250 nm that was related to the benzene chromophore of PS. These UV spectra confirmed the formation of copolymer in PS/EPDM blends extruded in the presence of ultrasonic irradiation, which could lead to an improvement in compatibility.

#### 8.3.3.6 Die Swell Reduction

Li *et al.* [103] studied the die swell behaviors of PS, EPDM, and PS/EPDM (80/20) by using a special ultrasonic oscillation extrusion system developed in their laboratory. These authors investigated the effects of ultrasonic intensity and screw speed on die pressure, volume flow rate and apparent viscosity of polymers, as well as die swell. During extrusion, the apparent viscosities of the blends depended not

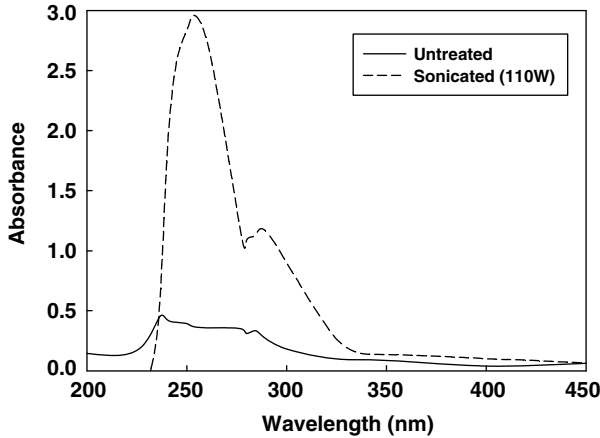


Figure 8.30 UV absorbance spectra of PS/EPDM (80/20) blends [101].

only on the shear rate but also on the ultrasonic intensity (see Figure 8.31). As the ultrasonic intensity was increased, both the viscosity and die swell ratio were decreased. In contrast, as the screw speed was increased the viscosity was decreased, but the die swell ratio was increased. This dependence of the apparent viscosity on ultrasonic intensity was suggested as being due to the degradation of polymer chains during ultrasonic extrusion [104–106]. However, based on the results of high-pressure capillary rheometry experiments, Li *et al.* [103] concluded that decreases in the apparent viscosities of polymer melts during ultrasonic extrusion could not be related to ultrasonic degradation; rather, degradation was

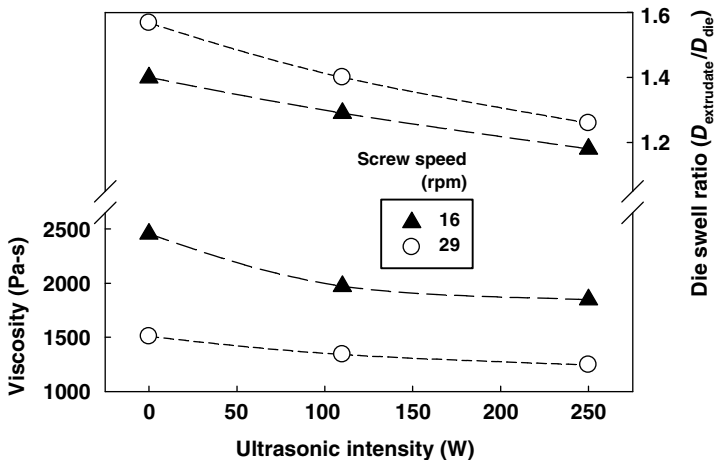


Figure 8.31 Dependences of viscosity and die swell ratio of PS/EPDM (80/20) blends melt on ultrasonic intensity at different screw speeds [103].

attributed to the fact that ultrasound of high frequency and low amplitude made the polymer molecules easy to move. In order to enhance polymer extrusion productivity, an increase in the screw speed would lead to an increase in both die pressure and the melt fracture of polymer melts. Die swelling of the extrudate was caused by deformation of polymer in the die and a relaxation of melt molecules at the exit of the die. Consequently, with increasing ultrasonic intensity or decreasing screw speed, the die swell ratio was decreased. In this case it was proposed that the ultrasonic irradiation had enhanced the molecular motion, causing the molecules to slip, thereby decreasing both the deformation of molecules and the die swell ratio.

#### 8.4

##### Summary

In this chapter, the applications of ultrasound to polymer blends have been reviewed, with low-power or high-frequency ultrasound being used to measure both velocity and absorption coefficients. Such measurements were allocated to two groups: (i) static characterization, including ultrasonic interferometry and pulse–echo techniques; and (ii) dynamic characterization, such as in-line monitoring. By using ultrasonic interferometry, the miscibility of solution blends of PS/PVP and PMMA/PVP could be determined according to whether the ultrasonic velocity as a function of blend composition was linear, or not. For solid samples, pulse–echo techniques—which have the advantage of simultaneous measurement of sound velocity and attenuation—were used to investigate the compatibility of polymer blends. By using this technique, the density of rubber blends (e.g., ENR/EPDM) as well as their compatibility, could be obtained by monitoring the ultrasonic velocities of propagation of longitudinal and transverse ultrasonic waves. The morphology of immiscible EPDM/PS blends was also investigated using ultrasonic attenuation and velocity, together with SEM observations. It was suggested that the discontinuity of ultrasonic attenuation might serve as a useful tool for rapidly determining the phase inversion of immiscible polymer blends. When a normal incident shear wave was used to explore the molecular orientation of HDPE/i-PP blends obtained by dynamic packing injection molding, the larger the echo time difference the greater was the degree of orientation. These results were comparable with those obtained using X-ray scattering; indeed, ultrasound with a multiple scattering model was applied to monitor (in-line) the morphology of immiscible PA6/PP blends during capillary flow, in real time. Subsequently, based on the different acoustic responses according to changes in morphology, the domain size could be deduced.

In contrast, high-power or low-frequency ultrasound can be used to compatibilize immiscible polymer pairs by the high shear and degradation of the polymer chains. Moreover, in many cases there was no deterioration in mechanical properties, despite a lowering of both the molecular weight and viscosity. Dramatic improvements in the weld line strength of immiscible PS/HDPE blends were

identified when power ultrasound was applied during injection molding; this effect was thought to result from the ultrasonic oscillations promoting molecular diffusion across the interface in the weld line region. An optimum ultrasonic energy input was identified to increase the compatibility of PLA/PBAT blends prepared using a melt mixer equipped with an ultrasonic device. In this case, the molecular weight of NR/SBR blends could be controlled by using a single-screw extruder fitted with a coaxial ultrasonic die attachment. The immiscible PP/NR blends prepared by slit die extrusion with sonication showed a higher tensile strength and elongation to break than did the neat blends, due to the formation of macroradicals. Ultrasonic-extruded PP/EPDM blends that were dynamically vulcanized showed improved mechanical properties and lower degrees of surface roughness (as measured with AFM). It was apparent that the enhanced compatibility was due to copolymer formation at the interface during ultrasonication, which in turn improved the interfacial adhesion, as confirmed using FT-IR analysis. Valuable information was also obtained regarding the compatibility and phase separation of polymer blends by monitoring the dynamic viscoelastic properties of the HDPE/PS and HDPE/PA6 blends that had been ultrasonic-extruded with a capillary die. The unknown interfacial tension between the matrix and the dispersed phase was estimated using an emulsion model. Domain size reductions of the extruded PS/EPDM blends were observed in SEM images with increasing ultrasonic intensity, while formation of the copolymer was confirmed with UV analysis. With increasing ultrasonic intensity, the die swell ratio of the PS/EPDM blends was decreased due to an enhanced molecular motion and slip.

Ultrasound is an expanding area of research which continues to thrive on the basis of outstanding laboratory results. Recently, attention has been increasingly focused on the applications of ultrasound as the frequency effects are further exploited, the mechanism is studied in greater detail, and appropriate equipment is designed and developed. Among these promising applications can be included the characterization of polymer blends, polymer modifications, property enhancement, and the monitoring of polymer processing. Clearly, ultrasound—with its many benefits—will be investigated and employed in a wide variety of polymer blend applications in the future.

## References

- 1 Lee, S., Lee, Y., and Lee, J.W. (2007) Effect of ultrasound on the properties of biodegradable polymer blends of poly (lactic acid) with poly(butylene adipate-co-terephthalate). *Macromol. Res.*, **15**, 44–50.
- 2 Hong, I.-K. and Lee, S. (2013) Properties of ultrasound-assisted blends of poly (ethylene terephthalate) with polycarbonate. *J. Ind. Eng. Chem.*, **19**, 87–93.
- 3 Choi, M., Kim, Y., Kim, J., and Kim, H. (2008) Rheological properties and thermal degradation behaviors of sonochemically treated polycarbonate/polysiloxane blends. *Kor.-Aust. Rheol. J.*, **20**, 245–251.
- 4 Ahn, Y., Kim, H., and Lee, J.W. (2010) Ultrasound assisted batch-processing of EVA-organoclay nanocomposites. *Korean J. Chem. Eng.*, **27**, 723–728.

- 5 Isayev, A.I., Kumar, R., and Lewis, T.M. (2009) Ultrasound assisted twin screw extrusion of polymer-nanocomposites containing carbon nanotubes. *Polymer*, **50**, 250–260.
- 6 Zhu, S.H., Penlidis, A., Tzoganakis, C., and Ginzel, E. (2012) Ultrasonic properties and morphology of devulcanized rubber blends. *J. Appl. Polym. Sci.*, **124**, 2062–2070.
- 7 Swain, S.K., Prusty, G., and Das, R. (2012) Sonochemical compatibility of polyvinyl alcohol/polyacrylic acid blend in aqueous solution. *J. Macromol. Sci. Part B: Phys.*, **51**, 580–589.
- 8 Ley, S.V. and Low, C.M.R. (1989) *Ultrasound in Synthesis*, Springer-Verlag, Berlin, Heidelberg, p. 2.
- 9 Lee, S.M., Park, J.C., Lee, S.M., Ahn, Y.J., and Lee, J.W. (2005) In-line measurement of residence time distribution in twin-screw extruder using non-destructive ultrasound. *Kor.-Aust. Rheol. J.*, **17**, 87–95.
- 10 Kim, J.G., Kim, H., Kim, H.S., and Lee, J.W. (2004) Investigation of pressure-volume-temperature relationship by ultrasonic technique and its application for the quality prediction of injection molded parts. *Kor.-Aust. Rheol. J.*, **16**, 163–168.
- 11 Truell, R., Elbaumand, C., and Chick, B. (1969) *Ultrasonic Methods in Solid State Physics*, Academic Press, New York, London.
- 12 Verdier, C. and Piau, M. (1996) Analysis of the morphology of polymer blends using ultrasound. *J. Phys. D: Appl. Phys.*, **29**, 1454–1461.
- 13 Rajulu, A.V., and Reddy, R.L., and Siddaramaiah, J. (1998) Ultrasonic, refractometric, and viscosity studies of some polymer blends in solution. *J. Appl. Polym. Sci.*, **70**, 1823–1827.
- 14 Pandey, K.N., Setua, D.K., and Mathur, G. N. (2005) Determination of the compatibility of NBR-EPDM blends by an ultrasonic technique, modulated DSC, dynamic mechanical analysis, and atomic force microscopy. *Polym. Eng. Sci.*, **45**, 1265–1276.
- 15 Sidkey, M.A., Yehia, A.A., Abd El Malak, N.A., and Gaafar, M.S. (2002) Compatibility studies on some rubber blend systems by ultrasonic techniques. *Mater. Chem. Phys.*, **74**, 23–32.
- 16 Afifi, H.A. and Sayed, A.M.E. (2003) Ultrasonic properties of ENR-EPDM rubber blends. *Polym. Bull.*, **83**, 115–122.
- 17 He, B., Yang, Y., Zou, H., Zhang, Q., and Fu, Q. (2005) Fast determination of phase inversion in polymer blends using ultrasonic technique. *Polymer*, **46**, 7624–7631.
- 18 He, B., Yuan, X., Yang, H., Tan, H., Qian, L., Zhang, Q., and Fu, Q. (2006) Ultrasonic measurement of orientation in HDPE/iPP blends obtained by dynamic packing injection molding. *Polymer*, **47**, 2448–2454.
- 19 Kim, K.Y., Nam, G.J., Lee, S.M., and Lee, J.W. (2006) Rheological properties of polypropylene modified by high-intensity ultrasonic waves. *J. Appl. Polym. Sci.*, **99**, 2132–2137.
- 20 Ryu, J.G., Kim, H., Kim, M.H., and Lee, J.W. (2004) Morphology and mechanical properties of LDPE/PS blends prepared by ultrasound-assisted melt mixing. *Kor.-Aust. Rheol. J.*, **16**, 147–152.
- 21 Kim, H., Ryu, J.G., and Lee, J.W. (2002) Evolution of phase morphology and in-situ compatibilization of polymer blends during ultrasound-assisted melt mixing. *Kor.-Aust. Rheol. J.*, **14**, 121–128.
- 22 Kim, H., Lee, H., and Lee, J.W. (2007) Rheological properties of branched polycarbonate prepared by an ultrasound-assisted intensive mixer. *Kor.-Aust. Rheol. J.*, **19**, 1–5.
- 23 Kim, K.Y., Nam, G.J., Lee, S.M., and Lee, J.W. (2006) Rheological properties of polypropylene modified by high-intensity ultrasonic waves. *J. Appl. Polym. Sci.*, **99**, 2132–2137.
- 24 Kim, H. and Lee, J.W. (2002) Effect of ultrasonic wave on the degradation of polypropylene melt and morphology of its blend with polystyrene. *Polymer*, **43**, 2585–2589.
- 25 Sohn, C.H., Shim, D.C., and Lee, J.W. (2007) Effects of high-intensity ultrasound and supercritical nitrogen on PP-MA reactive extrusion. *Macromol. Symp.*, **249–250**, 580–585.
- 26 Kim, H., Yang, H., and Lee, J.W. (2005) Effect of viscosity ratio and AN content on



- the compatibilization of PC-SAN blends during ultrasound-assisted melt mixing. *Kor.-Aust. Rheol. J.*, **17**, 165–170.
- 27 Elias, L., Fenouillot, F., Majeste, J.C., Alcouffe, P., and Cassagnau, P. (2008) Immiscible polymer blends stabilized with nano-silica particles: rheology and effective interfacial tension. *Polymer*, **49**, 4378–4385.
  - 28 Hwang, T.Y., Kim, H.J., Ahnand, Y., and Lee, J.W. (2010) Influence of twin screw extrusion processing condition on the properties of polypropylene/multi-walled carbon nanotube nanocomposites. *Kor.-Aust. Rheol. J.*, **22**, 141–148.
  - 29 Steinmann, S., Gronschiand, W., and Friedrich, C. (2002) Influence of selective filling on rheological properties and phase inversion of two-phase polymer blends. *Polymer*, **43**, 4467–4477.
  - 30 Zhu, L. and Xanthos, M. (2004) Effects of process conditions and mixing protocols on structure of extruded polypropylene nanocomposites. *J. Appl. Polym. Sci.*, **93**, 1891–1899.
  - 31 Dennis, H.R., Hunter, D.L., Chang, D., Kim, S., White, J.L., Cho, J.W., and Paul, D.R. (2001) Effect of melt processing conditions on the extent of exfoliation in organoclay-based nanocomposites. *Polymer*, **42**, 9513–9522.
  - 32 Ryu, J.G., Kim, H., and Lee, J.W. (2004) Characterization of polystyrene/polyethylene/clay nanocomposites prepared by ultrasound-assisted mixing process. *Polym. Eng. Sci.*, **44**, 1198–1204.
  - 33 Park, J.-E., Saikawa, M., Atobe, M., and Fuchigami, T. (2006) Highly-regulated nanocoatings of polymer films on carbon nanofibers using ultrasonic irradiation. *Chem. Commun.*, **2006**, 2708–2710.
  - 34 Hwang, T.Y., Kim, H.J., Ahn, Y., and Lee, J.W. (2010) Influence of twin screw extrusion processing condition on the properties of polypropylene/multi-walled carbon nanotube nanocomposites. *Kor.-Aust. Rheol. J.*, **22**, 141–148.
  - 35 Ryu, J.G., Lee, P.S., Kim, H., and Lee, J.W. (2001) Ultrasonic degradation of polypropylene and its application for the development of PP based copolymer and nanocomposite. *Kor.-Aust. Rheol. J.*, **13**, 61–65.
  - 36 Ryu, J.G., Park, S.W., Kim, H., and Lee, J.W. (2004) Power ultrasound effects for in situ compatibilization of polymer-clay nanocomposites. *Mater. Sci. Eng. C*, **24**, 285–288.
  - 37 Kim, K.Y., Ju, D.U., Nam, G.J., and Lee, J.W. (2007) Ultrasonic effects on PP/PS/clay nanocomposites during continuous melt compounding process. *Macromol. Symp.*, **249–250**, 283–288.
  - 38 Sun, Z., Wangand, W., and Fung, Z. (1992) Criterion of polymer-polymer miscibility determined by viscometry. *Eur. Polym. J.*, **28**, 1259–1261.
  - 39 Rajulu, A.V., Reddy, R.L., and Reddy, R.N.V. (1998) Ultrasonic and viscometric investigation of cellulose acetate/poly (methyl methacrylate) blends in solution. *Acustica*, **84**, 577–579.
  - 40 Singh, Y.P. and Singh, R.P. (1983) Compatibility studies on solutions of polymer blends by viscometric and ultrasonic techniques. *Eur. Polym. J.*, **19**, 535–541.
  - 41 Singh, Y.P., Das, S., Maiti, S., and Singh, R.P. (1981) Miscibility of poly(vinyl chloride)/poly(vinyl acetate) blend in chlorobenzene. *J. Pure Appl. Ultrason.*, **3**, 1–3.
  - 42 Sidkey, M.A., Abd El Fattah, A.M., Yehia, A.A., and Abd El All, N.S. (1991) Ultrasonic investigation of some rubber blends. *J. Appl. Polym. Sci.*, **43**, 1441–1449.
  - 43 Zerjal, B., Jelcic, Z., and Malavasic, T. (1996) Miscibility in thermoplastic polyurethane elastomer/poly (styrene-co-acrylonitrile) blends. *Eur. Polym. J.*, **32**, 1351–1354.
  - 44 Brandrup, J.E. (1960) *Polymer Hand Book*, John Wiley & Sons, New York.
  - 45 Pohl, M.M., Dany, R., Mix, R., Gahde, J., and Hinrichsen, G. (1996) Miscibility of a liquid crystalline polyurethane with common segmented polyurethanes. *Polymer*, **37**, 2173–2177.
  - 46 Ferry, A., Jacobson, P., Van Heumen, J.D., and Stevens, J.R. (1996) Raman, infra-red and d.s.c. studies of lithium coordination in a thermoplastic polyurethane. *Polymer*, **37**, 737–744.
  - 47 Fox, T.G. (1956) Influence of diluent and of copolymer composition on the glass

- temperature of a polymer system. *Bull. Am. Phys. Soc.*, **1**, 123–125.
- 48 Gordon, M. and Taylor, J.S. (1952) Ideal copolymers and the second-order transitions of synthetic rubbers. I. non-crystalline copolymers. *J. Appl. Chem.*, **2**, 493–500.
  - 49 Song, M., Hammiche, A., Pollock, H.M., Hourston, D.J., and Reading, M. (1995) Modulated differential scanning calorimetry. 1. A study of the glass transition behavior of blends of poly (methyl methacrylate) and poly(styrene-co-acrylonitrile). *Polymer*, **36**, 3313–3316.
  - 50 Hourstonand, D.J. and Hughes, I.D. (1977) Poly(vinylidene fluoride)-poly (methylmethacrylate) blends. *Polymer*, **18**, 1175–1178.
  - 51 Hourston, D.J. and Hughes, I.D. (1979) Dynamic mechanical and sonic velocity behavior of polystyrene-poly(vinylmethyl ether) blends. *Polymer*, **19**, 1181–1185.
  - 52 Singh, Y.P. and Singh, R.P. (1983) Compatibility studies on solid polyblends of poly(methyl methacrylate) with poly (vinyl acetate) and polystyrene by ultrasonic technique. *J. Eur. Polym.*, **19**, 529–533.
  - 53 Singh, Y.P. and Singh, R.P. (1983) Compatibility studies on solutions of polymer blends by viscometric and ultrasonic techniques. *J. Eur. Polym.*, **19**, 535–541.
  - 54 Sheng, J., Hu, J., Yuan, X.-B., Han, Y.-P., Li, F.-K., and Bian, D.-C. (1998) The study of polystyrene blends: The relationship of phases and structure in blends of polystyrene with ethylene-propylene diene monomer rubber and its grafted copolymer. *J. Appl. Polym. Sci.*, **70**, 805–810.
  - 55 Edwards, R. and Thomas, C. (2001) On-line measurement of polymer orientation using ultrasonic technology. *Polym. Eng. Sci.*, **41**, 1644–1653.
  - 56 Epstein, P.S. and Carhart, R.R. (1953) The absorption of sound in suspensions and emulsions. I. Water fog in air. *J. Acoust. Soc. Am.*, **25**, 553–565.
  - 57 Allegra, J.R. and Hawley, S.A. (1972) Attenuation of sound in suspensions and emulsions: theory and experiments. *J. Acoust. Soc. Am.*, **51**, 1545–1564.
  - 58 McClement, D.J. and Povey, M.J.W. (1989) Scattering of ultrasound by emulsions. *J. Phys. D: Appl. Phys.*, **22**, 38–47.
  - 59 Franca, D.R., Jen, C.-K., Nguyen, K.T., and Gendron, R. (2000) Ultrasonic in-line monitoring of polymer extrusion. *Polym. Eng. Sci.*, **40**, 82–94.
  - 60 Chen, T.-F., Nguyen, K.T., Wen, S.-S.L., and Jen, C.-K. (1999) Temperature measurement of polymer extrusion by ultrasonic techniques. *Meas. Sci. Technol.*, **10**, 139–145.
  - 61 Edwards, R. and Thomas, C. (2001) On-line measurement of polymer orientation using ultrasonic technology. *Polym. Eng. Sci.*, **41**, 1644–1653.
  - 62 Lu, C., Yu, X., and Guo, S. (2005) Ultrasonic improvement of weld line strength of injection-molded polystyrene and polystyrene/polyethylene blend parts. *Polym. Eng. Sci.*, **45**, 1666–1672.
  - 63 Brahimi, B., Ait-Kadi, A., and Ajjji, A. (1994) Weld lines and mechanical properties of injection molded polyethylene/polystyrene/copolymer blends. *Polym. Eng. Sci.*, **34**, 1202–1210.
  - 64 Jarus, D., Summers, J.W., Hiltner, A., and Baer, E. (2000) Weld line strength of poly (vinyl chloride)/polyethylene blends. *Polymer*, **41**, 3057–3068.
  - 65 Kim, J.K., Park, S.H., O, H.T., and Jeon, H.K. (2001) The effect of weld-lines on the morphology and mechanical properties of amorphous polyamide/poly(ethylene-ran-propylene) blend with various amounts of an in situ compatibilizer. *Polymer*, **42**, 2209–2221.
  - 66 Mekhilef, N., Ait-Kadi, A., and Ajjji, A. (1995) Weld lines in injection-moulded immiscible blends: model predictions and experimental results. *Polymer*, **36**, 2033–2042.
  - 67 Fellahi, S., Favis, B.D., and Fisa, B. (1996) Morphology stability in injection-moulded high-density polyethylene/polyamide-6 blends. *Polymer*, **37**, 2615–2626.
  - 68 Guo, S. and Ait-Kadi, A. (2002) A study on weld line morphology and mechanical strength of injection molded polystyrene/ poly(methyl methacrylate) blends. *J. Appl. Polym. Sci.*, **84**, 1856–1865.
  - 69 Utracki, L.A. (1989) *Polymer Blends and Alloys*, Hanser, New York.

- 70 Lee, S. and Lee, J.W. (2005) Characterization and processing of biodegradable polymer blends of poly (lactic acid) with poly(butylene succinate adipate). *Kor.-Aust. Rheol. J.*, **17**, 71–77.
- 71 Piirma, I. (1992) *Polymeric Surfactants*, Marcel Dekker, New York.
- 72 Seo, Y., Hong, S.M., Hwang, S.S., Park, T.S., Kim, K.U., Lee, S., and Lee, J.W. (1995) Compatibilizing effect of a poly(ester imide) on the properties of the blends of poly(ether imide) and a thermotropic liquid crystalline polymer. 2. Morphology and mechanical properties of the in situ composite system. *Polymer*, **36**, 525–534.
- 73 Plochocki, A.P., Dagli, S.S., and Andrews, R.D. (1990) The interface in binary mixtures of polymers containing a corresponding block copolymer: Effects of industrial mixing processes and of coalescence. *Polym. Eng. Sci.*, **30**, 741–752.
- 74 Isayev, A.I. and Hong, C.K. (2003) Novel ultrasonic process for *in-situ* copolymer formation and compatibilization of immiscible polymers. *Polym. Eng. Sci.*, **43**, 91–101.
- 75 Yun, J., Oh, J.S., and Isayev, A.I. (2001) Ultrasonic devulcanization reactors for recycling of GRT: comparative study. *Rubber Chem. Technol.*, **74**, 317–330.
- 76 Isayev, A.I., Chen, J., and Tukachinsky, A. (1995) Novel ultrasonic technology for devulcanization of waste rubbers. *Rubber Chem. Technol.*, **68**, 267–280.
- 77 Oh, J.S., Isayeva, A.I., and Rogunova, M.A. (2003) Continuous ultrasonic process for *in situ* compatibilization of polypropylene/natural rubber blends. *Polymer*, **44**, 2337–2349.
- 78 Basedow, A.M. and Ebert, K.H. (1977) Ultrasonic degradation of polymers in solution. *Adv. Polym. Sci.*, **22**, 83–148.
- 79 Isayev, A.I., Wong, C.M., and Zeng, X. (1990) Effect of oscillations during extrusion on rheology and mechanical properties of polymers. *Adv. Polym. Technol.*, **10**, 31–45.
- 80 Casale, A. and Porter, R.S. (1977) *Polymer Stress Reactions*, Academic Press, New York.
- 81 Baramboim, N.K. (1964) *Mechanochemistry of Polymers*, Maclaren, London.
- 82 Feng, W. and Isayev, A.I. (2004) *In-situ* ultrasonic compatibilization of unvulcanized and dynamically vulcanized PP/EPDM blends. *Polym. Eng. Sci.*, **44**, 2019–2028.
- 83 Feng, W. and Isayev, A.I. (2004) *In-situ* compatibilization of PP/EPDM blends during ultrasound aided extrusion. *Polymer*, **45**, 1207–1216.
- 84 Hummel, O. and Scholl, F. (1982) *Infrared Analysis of Polymers, Resins and Additives*, Hanser, Munich.
- 85 Koenig, J.L. (1999) *Spectroscopy of Polymers*, 2nd edn, Elsevier, New York.
- 86 Han, C.D. and Kim, J. (1987) Rheological technique for determining the order-disorder transition of block copolymers. *J. Polym. Sci. Part B: Polym. Phys.*, **25**, 1741–1764.
- 87 Han, C.D., Kim, J., and Kim, J.K. (1989) Determination of the order-disorder transition temperature of block copolymers. *Macromolecules*, **22**, 383–394.
- 88 Han, C.D. and Kim, J.K. (1993) On the use of time-temperature superposition in multicomponent/multiphase polymer systems. *Polymer*, **12**, 2533–2539.
- 89 Utracki, L.A. (1990) *Polymer Alloys and Blends*, Hanser, Munich, p. 13.
- 90 Yanovsky, Y.G. (1993) *Polymer Rheology: Theory and Practice*, Chapman & Hall, London, p. 517.
- 91 Qiang, Z., Masaoki, T., and Toshiro, M. (1999) Relationship between breakdown of time-temperature superposition principle and phase-separation for PMMA/ $\alpha$ -MSAN blends. *Chem. J. Chin. Univ.*, **20**, 969–973.
- 92 Friedrich, C., Gleinser, W., Korat, E., Maier, D., and Weese, J. (1995) Comparison of sphere-size distributions obtained from rheology and transmission electron microscopy in PMMA/PS blends. *J. Rheol.*, **39**, 1411–1425.
- 93 Graebbling, D., Muller, R., and Palierne, J.F. (1993) Linear viscoelastic behavior of some incompatible polymer blends in the melt. Interpretation of data with a model of emulsion of viscoelastic liquids. *Macromolecules*, **26**, 320–329.
- 94 Gramespacher, H. and Meissner, J. (1992) Interfacial tension between polymer melts measured by shear oscillations of their blends. *J. Rheol.*, **36**, 1127–1141.

- 95 Bousmina, M. and Muller, R. (1993) Linear viscoelasticity in the melt of impact PMMA. Influence of concentration and aggregation of dispersed rubber particles. *J. Rheol.*, **37**, 663–679.
- 96 Bousmina, M., Bataille, P., Sapieha, S., and Schreiber, H.P. (1995) Comparing the effect of corona treatment and block copolymer addition on rheological properties of polystyrene/polyethylene blends. *J. Rheol.*, **39**, 499–517.
- 97 Paliarne, J.F. (1990) Linear rheology of viscoelastic emulsions with interfacial tension. *Rheol. Acta*, **29**, 204–214.
- 98 Chen, G., Guo, S., and Li, Y. (2004) Dynamic rheological properties of high-density polyethylene/polystyrene blends extruded in the presence of ultrasonic oscillations. *J. Appl. Polym. Sci.*, **92**, 3153–3158.
- 99 Chen, G., Guo, S., and Li, H. (2002) Ultrasonic improvement of the compatibility and rheological behavior of high-density polyethylene/polystyrene blends. *J. Appl. Polym. Sci.*, **86**, 23–32.
- 100 Li, J., Liang, M., Guo, S., Kuthanova, V., and Hausnerova, B. (2005) Linear viscoelastic properties of high-density polyethylene/polyamide-6 blends extruded in the presence of ultrasonic oscillations. *J. Polym. Sci.: Part B: Polym. Phys.*, **43**, 1260–1269.
- 101 Li, J., Guo, S., Slezak, R., and Hausnerova, B. (2005) In situ compatibilization of PS/EPDM blends during ultrasonic extrusion. *Macromol. Chem. Phys.*, **206**, 2429–2439.
- 102 Seo, Y., Hong, S.M., Hwang, S.S., Park, T.S., Kim, K.U., Lee, S., and Lee, J. (1995) Compatibilizing effect of a poly(ester imide) on the properties of the blends of poly(ether imide) and a thermotropic liquid crystalline polymer: 1. Compatibilizer synthesis and thermal and rheological properties of the in situ composite system. *Polymer*, **36**, 515–523.
- 103 Li, J., Guo, S., and Liang, M. (2006) Effects of ultrasonic oscillation on processing behaviors of PS, EPDM, and PS/EPDM blend. *J. Appl. Polym. Sci.*, **100**, 1856–1863.
- 104 Chen, G., Guo, S., and Li, H. (2002) Ultrasonic improvement of rheological behavior of polystyrene. *J. Appl. Polym. Sci.*, **84**, 2451–2460.
- 105 Wu, H., Guo, S., Chen, G., Lin, J., Chen, W., and Wang, H. (2003) Ultrasonic oscillations effect on rheological and processing properties of metallocene-catalyzed linear low density polyethylene. *J. Appl. Polym. Sci.*, **90**, 1873–1878.
- 106 Guo, S., Li, Y., Chen, G., and Li, H. (2003) Ultrasonic improvement of rheological and processing behaviour of LLDPE during extrusion. *Polym. Int.*, **52**, 68–73.

## 9

### Characterization of Polymer Blends: Ellipsometry

Éva Kiss

#### 9.1

##### Ellipsometry

##### 9.1.1

##### Principles of Ellipsometry

Ellipsometry is a high-precision optical characterization technique, the potential of which has not yet been sufficiently exploited in polymer science. It is a rapid and nondestructive experimental method for the analysis of surfaces and thin films. Besides the determination of film thickness with high sensitivity ( $\sim 0.1$  nm), optical parameters related to material properties can also be evaluated [1]. The facts that ellipsometric measurements can be performed under any ambient conditions, and require no special sample preparation procedures, provide a definite advantage over other surface science techniques [2–4].

The reflection of polarized incident light from a surface or a film changes the polarization state of that light. In ellipsometry, this change is measured through the two ellipsometric angles,  $\psi$  and  $\Delta$ ; the former is the amplitude ratio and the latter is the phase difference, between the parallel (p) and perpendicular (s) components of the electric field vector of the light wave [5]. The ellipsometry configuration is shown in Figure 9.1.

In spectroscopic ellipsometry,  $(\psi, \Delta)$  spectra are measured by changing the wavelength of light. In general, the spectroscopic ellipsometry measurement is carried out in the ultraviolet (UV)-visible region, although measurements in the infrared (IR) region have also been performed.

The  $\psi$  and  $\Delta$  measured from ellipsometry are defined from the ratio ( $\rho$ ) of reflection coefficients for p- and s-polarization ( $r_p, r_s$ ):

$$\rho = r_p/r_s = \tan(\psi)e^{i\Delta}$$

This is the principal equation of ellipsometry, where the reflection coefficients are a function of the complex refractive indices ( $N$ ) of the materials, the film

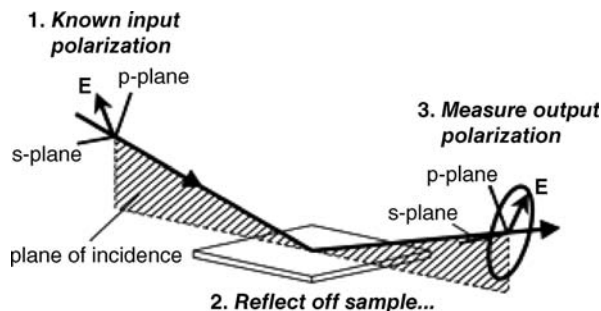


**Figure 9.1** Typical ellipsometry configuration, where linearly polarized light is reflected from the sample surface and the polarization change is measured to determine the sample response.

thickness ( $d$ ), and also the angle of incidence ( $\theta_o$ ). Considering a thin film on a solid support:

$$\rho = f(N_o, N_1, N_2, d, \theta_o)$$

where  $N_o$ ,  $N_1$  and  $N_2$  denote the complex refractive indices of air, thin film and substrate, respectively, the complex refractive index will be composed of optical constants such as the refractive index ( $n$ ) and extinction coefficient ( $k$ ):

$$N = n - i k$$

The spot size of a light beam in ellipsometry is typically several millimeters, which results in a low spatial *resolution*. In order to improve lateral resolution imaging ellipsometry has been developed which combines the high vertical resolution of conventional ellipsometry with a lateral resolution in the micrometer range.

### 9.1.2

#### Thickness and Optical Properties of Layers on Solid Supports

The *film thickness* is determined by measuring the interference between light reflecting from the surface and light traveling through the film. Interference involves both amplitude and phase information; the phase information is very sensitive to films down to submonolayer thickness. If the material absorbs light, then the thickness measurements made by optical instruments will be limited to thin, semi-opaque layers. However, this limitation can be circumvented by targeting measurements to a spectral region with a lower absorption. For example, an organic film may strongly absorb both UV and IR light, but will remain transparent at mid-visible wavelength [6].

The construction of an *optical model* is required for data analysis to extract physical properties, including the optical constants and film thickness of the sample. The model is an idealized representation of a given sample that allows the expected optical properties of the film to be calculated; the calculated values are then compared to experimental data. Finding the best match between the model

and the experiment is typically achieved through regression; generally, an estimator such as the mean squared error (MSE) will be used to quantify the difference between the curves. The unknown parameters are allowed to vary until the minimum MSE is reached [6].

The *complex dielectric function*,  $\varepsilon = \varepsilon_1 - i\varepsilon_2$ , which describes the material properties is connected to the complex refractive index  $N$  for discussing optical propagation through  $\varepsilon = N^2$ , with  $\varepsilon_1 = n^2 - k^2$  and  $\varepsilon_2 = 2nk$ . For absorbing media,  $k$  and  $\varepsilon_2$  are positive. Ellipsometry allows direct measurements to be made of the refractive index ( $n$ ) and the extinction coefficient ( $k$ ).

Any material has a dielectric function that is unique to that material or, more specifically, which is a unique function of wavelength. If the material is a composite of two or more substances, then the dielectric response of the composite will be determined by the dielectric functions of the components and their spatial distribution [7]. When the characteristic length scale of the inhomogeneities is smaller than the wavelength of the light that constitutes the probing beam, and is large enough to retain their dielectric identity, then the material can be treated as a *macroscopically homogeneous effective medium* [8]. In that case, the optical properties of the composite can be analyzed using *effective-medium* theory for both composition and microstructure.

This possibility is extremely useful for the structural characterization of polymer blends. The optical properties of the polymer layer can be described by a so-called *effective dielectric function*, which is a suitable average of the dielectric functions of the two components. Three averaging effective medium approximation (EMA)s – the linear, Maxwell–Garnett and Bruggeman EMAs – are widely used for this purpose [9]. These approximations differ in their spectral densities for a given volume fraction.

#### 9.1.2.1 Linear EMA

The linear EMA is a simple linear interpolation between the constituent optical constants; this EMA is not highly accurate, but is often used for graded layers to reduce the calculation time:  $\varepsilon = f_A \varepsilon_A + f_B \varepsilon_B$

#### 9.1.2.2 Maxwell–Garnett EMA

The Maxwell–Garnett EMA [10] is developed for very diluted collections of small particles (in dipole approximation):

$$f_A \frac{\tilde{\varepsilon}_A - \tilde{\varepsilon}}{\tilde{\varepsilon}_A + 2\tilde{\varepsilon}} = f_B \frac{\tilde{\varepsilon}_B - \tilde{\varepsilon}}{\tilde{\varepsilon}_B + 2\tilde{\varepsilon}}$$

where  $\tilde{\varepsilon}$  is the effective complex dielectric function of the mixture,  $f_A$  is the host medium volume fraction and is equal to  $1 - f_B$ , where  $f_B$  is the volume fraction of the particles.  $\tilde{\varepsilon}_A$  and  $\tilde{\varepsilon}_B$  are the complex dielectric functions of the host and the inclusion material. For very small fraction of material B,  $f_A \approx 1$ . This approximation contains one resonance, namely the dipole resonance, which occurs in the case of low volume fractions. For higher-volume fractions the resonance shifts to smaller frequencies due to electric interactions of the particles.

### 9.1.2.3 Bruggeman EMA

The most often applied effective medium model is the Bruggeman formula: [11]

$$f_A \frac{\tilde{\epsilon}_A - \tilde{\epsilon}}{\tilde{\epsilon}_A + 2\tilde{\epsilon}} + f_B \frac{\tilde{\epsilon}_B - \tilde{\epsilon}}{\tilde{\epsilon}_B + 2\tilde{\epsilon}} = 0$$

In this theory, the film is regarded as an array of two components. By isolating a single grain of one component, of complex dielectric constant  $\tilde{\epsilon}_A$ , the remainder of the film is regarded as a homogeneous medium of complex dielectric constant  $\tilde{\epsilon}$ . The chosen grain is assumed to be spherical in shape. The calculation is then repeated with a spherical grain of the second component of complex dielectric constant  $\tilde{\epsilon}_B$  embedded in the same homogeneous medium. At low volume fractions, the Bruggeman formula approaches that of Maxwell. The Bruggeman characteristics with increasing volume fraction are quite reasonable, the isolated particles become closer and closer as the density increases, and finally a connected network due to aggregation is built up. This qualitative behavior makes the Bruggeman formula a good choice in many cases.

It is well known that the Bruggeman EMA formula is derived by considering one of the constituents as a small sphere. A deviation from such an assumption required a modification the formula to include depolarization factor. Typically, a value of 0.333 is used as a default value in the EMA layer, which assumes a spherical shape of the inclusion. The other two extremes are 0, for a needle-like or columnar microstructure, and 1 for flat disks or a laminar microstructure. This type of transition was found for polyaniline/poly(methylmethacrylate) blend films presenting with a spherical-like microstructure at low sample concentration, whereas at relatively high concentrations the depolarization factor shifted to values closer to 1. This indicated the formation of flat microstructures due to aggregation of the polyaniline particles [8].

Porous systems [12–14] and microscopically rough surfaces [8,12] can also be considered as heterogeneous materials, being a mixture of bulk and air.

A *dispersion* relationship describes the optical constant shape versus wavelength. The adjustable parameters of the dispersion relationship allow the overall optical constant shape to match the experimental results. For transparent materials, the most often used refractive index ( $n$ ) wavelength ( $\lambda$ ) relationship is the Cauchy function, which has three adjustable parameters, namely  $n_0$ ,  $A$ , and  $B$ :

$$n(\lambda) = n_0 + \frac{A}{\lambda^2} + \frac{B}{\lambda^4}$$

Absorbing materials will often have a transparent wavelength region that can be modeled with the Cauchy function, but the absorbing region must account for both real and imaginary optical constants. Many dispersion relationships use oscillator theory to describe absorption for various materials; these include the Lorenz, Harmonic and Gaussian oscillators. Kramers–Kronig consistency is used to calculate the shape of the real component after the imaginary behavior is described by the oscillator [6].

Based on measurements in the UV-visible region, the interband transitions (band structures) can be characterized. As the band structure generally varies



according to the surface temperature, alloy composition, phase structure and crystal grain size, these properties can also be determined from the spectral analysis of the optical constants [5].

### 9.1.3

#### **Depth Profiling**

For inhomogeneous films, the few-layer model is used as a first approximation to describe the depth profile [2,14–19]. Either a linear [20] or an exponential decay [21] of the properties along the direction of film normal are also supposed. By benefiting from the increasing operating speed of computers, inhomogeneous films can be treated by dividing the film into either several independent sublayers or a large number of interdependent sublayers in order to calculate the ellipsometric spectra.

### 9.1.4

#### **Sample Preparation**

Polymer films for ellipsometric investigation are usually deposited on to a solid substrate by spin-coating. The substrate, which generally is a silicon wafer, is carefully cleaned by sonication in organic solvents and bidistilled water. After drying in a vacuum oven, the wafer is exposed to UV light/ozone or purified further by oxygen plasma treatment to remove any traces of possible contamination. Glass microscopy slides with a rough black rare surface have also been used as the substrate in some cases.

The components of the polymer blend are dissolved in a common volatile solvent. The concentration of the polymers, the selection of solvent and also the experimental parameters of the spin-coating process can be used to control the thickness of the sample layer. The substrate is spin-coated with a portion of a suitably filtered solution of the polymer, and then dried in a vacuum (typically for several hours) to remove any residual solvent. It should be noted that any further processes that might be applied, such as thermal or vapor annealing treatments, may influence the structure of the films.

Multilayer samples can be formed by subsequent spin-casting on a precoated layer, or by a combination of spin-coating with other techniques such as self-assembly or vapor deposition. One special method developed to prepare self-supporting polymeric bilayers employed a floating-on-water and pick-up technique [22,23].

### 9.1.5

#### **Types of Instrument and Measurements**

Historically, the most important type of instrument has been the classical null ellipsometer, although today this has been superseded by the automatic spectroscopic ellipsometer (SE), which can take measurements over a wide range of

wavelengths and also allows variation of the angle of incidence. The most recent technique to be used is referred to as variable angle spectroscopic ellipsometry (VASE) [24,25]). Detailed descriptions of the various types of ellipsometry, ranging from the simple polarizer-compensator-sample-analyzer (PCSA) ellipsometer to a multichannel system in which an array of detector elements is used to capture a full ellipsometric spectrum in a relatively short time scale (e.g., every 15 ms to 1 s), are available in the *Handbook of Ellipsometry* [26].

#### 9.1.5.1 Spectroscopic Ellipsometry, Real-Time Measurement

Spectroscopic ellipsometry measurements are carried out in the UV-visible region, though measurements in the IR region have also been performed [19,27,28]. Both, infrared spectroscopic ellipsometry (IRSE) and infrared variable angle spectroscopic ellipsometry (IR-VASE) have been used extensively to characterize semiconductor and organic thin films [29,30]. IRSE is widely applied for quantifying the molecular orientation of organic and inorganic monolayers, and was recently evaluated for studying polymer interfaces and interdiffusion as a complementary method to neutron reflectivity (NR) and X-ray reflectivity (XR) [31,32]. IRSE was selected for this purpose because most polymer materials possess very strong and distinct absorption bands, in the mid-IR spectral region. These absorption bands, which correspond to the imaginary part of the refractive index, can provide large optical contrasts among different polymer species. This feature provides IRSE with a unique advantage, because most organic polymer systems have similar electron densities or neutron scattering length densities, and cannot be distinguished by using XR or NR measurements.

Rapid advances in computer technology during the past decades have made possible the automation of ellipsometry instruments and data analysis [5]. Developments in spectroscopic ellipsometry, based on rapid data collection, can offer the real-time characterization of dynamic behavior of thin layers [33,34], including the evaluation of structural changes, phase separation, or the swelling of polymer films [17].

## 9.2

### Applications in the Characterization of Polymer Blend Films

In order to improve a given polymer's properties, or to achieve a special functional behavior, it is relatively easy to add another type of polymer and to form a blend. Such blending can also be used to control the basic properties of the polymers, without sacrificing the many attractive properties of each component [35,36]. The many new products which have been created in this way have attracted widespread interest and commercial utilization [37,38].

#### 9.2.1

##### Phase Separation in Thin Polymer Blend Films

The interaction parameters between the two components determine the nature and the width of the interface between two *immiscible* components [16,39], or they

may affect the physical and mechanical properties of *miscible* systems. An enhancement of compatibility is generally intended to improve the mechanical properties [40], but in many cases phase separation in the polymer mixture can be successfully exploited for pattern formation or for the preparation of designed porous systems. When using both approaches, it is necessary to detect and understand in detail the occurrence of phase separation under equilibrium conditions and also the kinetics of the process.

The miscibility of polymer blends can be predicted experimentally by using several techniques, including electron microscopy and time-resolved light scattering. Other techniques, such as small-angle neutron scattering, ellipsometry and NR allow the determination of interaction parameters in both miscible and immiscible systems.

### 9.2.2

#### Analysis of Interfacial Thickness and Interfacial Reaction

Phase separation involves the *formation of interfaces* between domains with different compositions, whilst *compatibilization* affects the interfacial structure and composition. Both of these processes can be investigated efficiently by using ellipsometry which, as a *surface-sensitive optical technique*, fits in well with the geometry of the interfaces. One major advantage of ellipsometry [16] is that it is easy to operate, especially when compared to NR which, despite having an excellent depth of resolution (ca. 0.2 nm), requires deuterated samples and large-scale apparatus.

Ellipsometry is a powerful tool [16] for measuring the interfacial thickness between two polymers, whether in the case of immiscible or miscible polymer blends. In the case of miscible blends, investigations of changes in interfacial thickness with time at a fixed temperature allow the calculation of mutual diffusion coefficients [22]. In contrast, for immiscible blends the Flory–Huggins interaction parameter  $\chi$  can be deduced by measuring the interfacial thickness in an equilibrium state, and using the theory of Helfand [41] and its extended version [42].

Besides using ellipsometry to determine the thickness of the interface and to characterize the interfacial reaction, it is also possible to reveal phase morphologies, as well as the distribution, size and shape of phases with different optical properties.

The importance of ellipsometric investigations is emphasized by the widespread application of thin-film technologies in various fields such micro- or nanoelectronics, and in biomaterials where knowledge of the properties of polymers or polymer-containing films is required within a confined geometry.

#### 9.2.2.1 Miscibility

The generally accepted criterion of polymer miscibility is the detection of a single glass transition temperature ( $T_g$ ), the value of which is intermediate between those corresponding to two-component polymers. The variable temperature ellipsometric technique has been used widely to determine  $T_g$  in thin polymer films by

detecting volumetric changes as a function of temperature between the glassy and rubbery states; similar investigations of polymer blends have been introduced more recently [43–45].

Studies of  $T_g$  in thin polymer films have revealed that this parameter depends on the film thickness, and that such dependence increased as the film thickness decreased [43]. In the case where the interaction between a polymer and a substrate is insufficient to affect glass transition, then  $T_g$  will usually decrease with decreasing thickness. This was found valid for films of varying blends of poly(2,6-dimethyl-1,4-phenylene oxide) (PPO) and polystyrene (PS). Thin films of different thicknesses were prepared by spin-coating toluene solutions of various concentrations at 0, 30, 50, and 70% PPO weight contents. A single-wavelength null-type ellipsometer was then used to continuously monitor the ellipsometric angles ( $\psi$ ,  $\delta$ ) while the sample was heated or cooled at a constant rate of  $2 \text{ K min}^{-1}$ . As the thickness of the films or the PPO content increased, the measured  $T_g$  of the thin films also increased (Figure 9.2).

It was concluded that, as with bulk blend systems, PPO and PS are miscible at all compositions; confirmation was also provided that molecular miscibility is not affected by film thickness down to 20 nm [43].

Subsequently, further studies shed light on the importance of identifying the optical parameters [46] in studies of phase separation. When curing a thermoset/thermoplastic blend, triglycidyl *p*-aminophenol (epoxy)/poly(ether sulfone) (PES), the originally homogeneous mixture became phase-separated via various

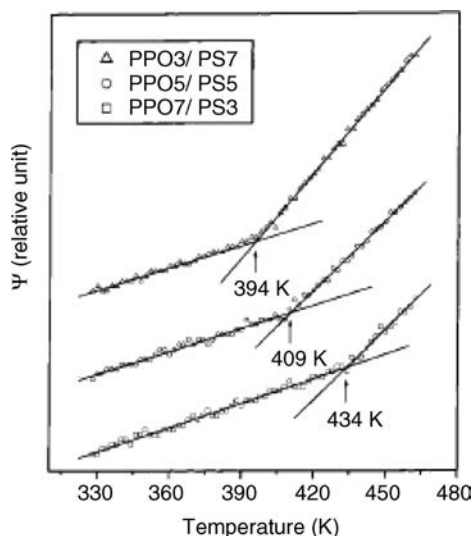


**Figure 9.2** Typical ellipsometric cooling scan for PPO and PS blend thin films. The thicknesses of PPO3/PS7, PPO5/PS5, and PPO7/PS3 are 477, 464, and 457 Å, respectively. The vertical arrow indicates  $T_g$  for the film. The

angle of incidence of radiation is  $70^\circ$ , and its wavelength is  $6328 \text{ Å}$ . These data points are obtained every minute during the cooling process at a rate of  $-2 \text{ K min}^{-1}$  [43].

transformations triggered by a reaction with the curing agent 4,4'-diaminodiphenylsulfone (DDS). The structure formation was followed by detecting increased light scattering; however, as the curing reaction proceeded a decay in intensity suggested that phase dissolution had occurred at the late stage of curing. An ellipsometric determination of the refractive indices of the epoxy components, and their changes with reaction, revealed the reason for this unexpected finding. When the refractive index of the epoxy/DDS mixture was measured during isothermal curing, a strong increase was observed; however, as the refractive indices of fully cured epoxy and the other polymer component (PES) were identical, the optical contrast vanished. This matching led to a weak light scattering of the heterogeneous system formed when the blend was cured.

The interfacial thickness,  $\lambda$ , of immiscible polymer pairs was described on the basis of Helfand theory [41] by the following equation [42]

$$\lambda = \frac{2b}{\sqrt{6\chi_{AB}}} \left[ 1 + \frac{\ln 2}{\chi_{AB}} \left( \frac{1}{N_A} + \frac{1}{N_B} \right) \right]$$

where  $b$  is a Kuhn's segment length,  $\chi_{AB}$  is the Flory-Huggins interaction parameter to show the degree of affinity or miscibility between A and B polymers, and  $N_i$  is the number of segments per chain [40]. According to that relation, the thicker interfacial layer corresponds to the more compatible blend possessing a lower interaction parameter. The thin interfacial layer on the other hand, is the sign of limited interfacial mixing due to a high  $\chi_{AB}$  value.

The miscibility of poly(styrene-co-acrylonitrile) (SAN) with PS or polycarbonate (PC) was investigated using ellipsometry, by measuring the thickness of the interfacial layer between the films of the two polymers [16,39]. The bilayer film was prepared on a solid substrate, and the ellipsometric parameters were detected as a function of temperature in the range of 180 to 215 °C. The calculations of interfacial thickness were based on a four-layer model, taking into account the air(1)–SAN(2)–interface(3)–PC(4) layers [23]. The temperature dependence of the refractive indices of neat SAN ( $n_2$ ) and PC films ( $n_4$ ) were previously measured using ellipsometry. This model implies that the refractive index at the interface is approximated to being uniform, and equals  $n_3 = (n_2 + n_4)/2$ . Although this step-wise approximation does not show precisely the real interface which has the concentration gradient, the values of interfacial thickness obtained were thus compared with those obtained by other methods, and good agreement was obtained [16].

Both, the temperature and copolymer composition (AN content) dependence of the interfacial thickness in the equilibrium state indicated a maximum that defined the compositional and thermal conditions for the highest interaction characterized by the lowest  $\chi_{AB}$  value.

Equilibrium interfacial thickness at 180 °C shows a maximum as a function of the copolymer composition at 25% AN content for PC/SAN film, which allows the most compatible polymer pair to be defined. There was a correlation between the compatibility (interfacial layer thickness) and the degree of dispersion in bulk, since the

finest phase dispersion of the SAN particles was observed at AN = 25 wt% for PC/SAN = 70/30, using scanning electron microscopy (SEM).

#### 9.2.2.2 Reactive Compatibilization

Additional material that is able to tune the interfacial properties can contribute to the improvement of mechanical properties of a phase-separated polymer blend. The application of a carefully selected or designed block copolymer influences not only the structure of the interface but also the distribution of dispersed domains in the matrix phase. According to the Ostwald–Buzágh principle of continuity [47], block copolymers with blocks miscible with one of the homopolymer domains localize at the interface between immiscible homopolymers, thus decreasing the interfacial tension (e.g., Ref. [48]) and stabilizing the minor blend phase against coalescence [49]. The entanglement of the two block copolymer sequences with the homopolymer phases across the interface led to a significant enhancement of the adhesion between the homopolymers. However, the possible chemical coupling to the polymer molecules forming the appropriate phases further enhances the strength of the interface. The aim of reactive processing developed is in line with that approach is to form reactive coupling polymers *in situ* during mixing of the blend components [40].

In order to be able to modify and control the interfacial interactions in the above-described manner, it is extremely important to monitor the structure of the interfacial layer. Ellipsometry was used [15,40,50,51] to detect the procedure and influence of reactive compatibilization on polymer blends. In an early study, the reactive blending of polypropylene (PP) with amorphous polyamide (aPA) was carried out using maleic anhydride-grafted PP (MAH-gPP) as a reactive PP [50]. The emulsifying effect of the *in situ*-formed PP-aPA graft copolymer was indicated by finer particles and a better stability of the dispersed phase obtained in bulk. In accordance with these findings, ellipsometry showed that the interface established in the reactive system was rather thick (ca. 40 nm), indicating an improved compatibility.

Polyamide was the subject of another reactive compatibilization experiment with PS [15], in which a reactive copolymer poly(styrene-*co*-maleic anhydride) (SMA) miscible with PS was applied in the blend. An ellipsometric analysis of the interfacial layer during annealing revealed the optimum amount of SMA to produce the thickest interfacial layer (45 nm) with maximum compatibility. The interfacial thickness was related to the interfacial adhesion measured by fracture toughness  $G_a$  [40] in a reactive polysulfone-polyamide (PSU-aPA) system. Block ( $\omega$ , end-grafted) or grafted (g) copolymers were formed between the amine groups of aPA and maleinic anhydride-functionalized PSU. The development of a thick interfacial layer was followed using ellipsometry. The effects of the functional groups incorporated in the PSU on interfacial thickness are summarized in Figure 9.3. A drastic increase in the interfacial thickness was observed at the two  $T_g$ -values of the component polymers in any system; for example, at 97 °C (aPA) and 165 °C (PSU), demonstrating the important contribution of molecular dynamics to form *in situ* copolymers at the interface.

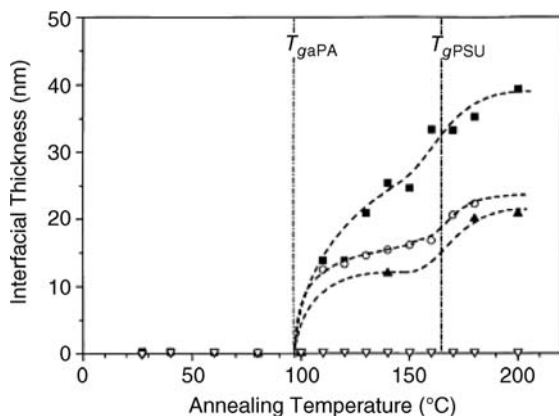


**Figure 9.3** Temperature dependence of interfacial thickness in differently functionalized PSU-aPA systems. ■, MAH-grafted PSU; ○, COOH-grafted PSU; ▲, end-grafted PSU; ▽, nonfunctional PSU. The concentration of the functional group was chosen at about  $90 \mu\text{mol g}^{-1}$  [40].

Considering the possible mechanism of fracture at the nonreactive interface of annealed immiscible polymers, it is reasonable to estimate higher fracture toughness,  $G_a$  at higher interfacial thickness,  $\lambda$ , where the polymer chains are interdiffused:  $G_a \sim \lambda^2$ . Although at the reactive interface more factors are involved, the experimental  $G_a$  values showed a similar dependence on layer thickness. It is noteworthy, however, that the fracture toughness is significantly increased by forming the reactive interface compared to a nonreactive blend.

### 9.2.3

#### Morphology, Roughness, and Pattern Formation in Nanolayers

The phase separation of a polymer blend might lead to a special morphology in thin polymer films, and patterning can occur during spin-coating or upon annealing. In the case of thin films, the presence of a film interface can have a dramatic effect on phase separation morphology. The preferred interaction of one component of the polymer blend with the solid substrate results in the formation of a wetting layer which directs the lamellar phase separation. The effect of an additional  $\text{SiO}_x$  capping layer on the PS-PMMA blend film was investigated on the morphology of phase separation [52]. A series of multilayer films were prepared, and ellipsometry was used for the exact determination of layer thicknesses. Depending on the thickness of the capping layer, a transition was found from lateral to lamellar phase separation which was explained by a comparison of the interfacial free energies of phase formation and the elastic bending of the capping layer.

Phase separation in thin films of a similar system (PS-PMMA), but under quite different conditions, was reported recently [53]. During the spin-casting process, specular reflectivity and off-specular scattering data were recorded and *ex situ* optical and atomic force microscopy (AFM), NR and ellipsometry were used to

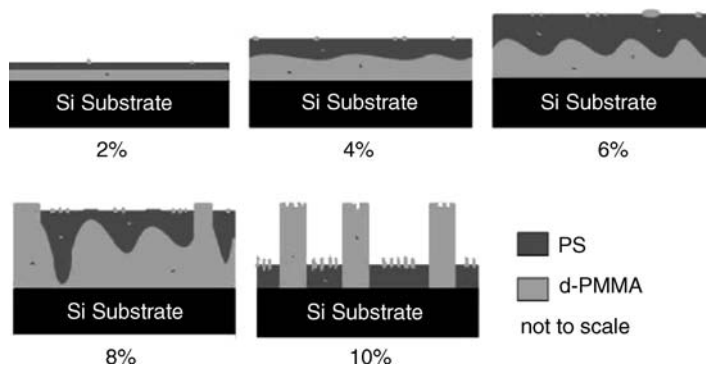


**Figure 9.4** A schematic diagram of the final structures in the samples prepared at different polymer concentrations [53].

characterize the film morphologies. Ellipsometry was used to determine the film thickness averaged over the ellipsometer beam area (an ellipse of ca.  $3 \text{ mm} \times 8 \text{ mm}$ ). A spectroscopic ellipsometer (J.A. Woolham; M2000 V; 370–1000 nm) was used to conduct these measurements, and the data were fitted using a Cauchy model. The ellipsometry results provided an averaged thickness over the beam area of  $\sim 10 \text{ mm}^2$ . The determined thickness values were in the range of 70 to 700 nm, and steadily increased with solution concentration. The film thicknesses established from the AFM step height data were in reasonable agreement with values obtained with ellipsometry. For the 8% and 10% samples, where the height variation was very large across this area, it was expected that the error margins of the ellipsometry results would be large, and therefore those values were less reliable. A schematic diagram of the different structures formed in each of the different solution concentrations is shown in Figure 9.4.

The results showed that it is possible to selectively control the film morphology by altering the solution concentration used. Low-concentration polymer solutions favored the formation of flat inplane phase-separated bilayers, whilst at intermediate concentrations the films formed consisted of an in-plane phase-separated bilayer with an undulating interface; some secondary phase-separated pockets rich in d-PMMA in the PS-rich layer, and vice versa, were also observed. The use of high-concentration solutions resulted in laterally phase-separated regions with sharp interfaces.

Polymer phase separation was combined with self-assembly and photopatterning to obtain porous silica film with hierarchical porosity [13]. Patternable nanoporous silica thin films with pore sizes on multiple length scales were fabricated using preformed block copolymer/homopolymer blend films as templates. The polymer system was a mixture of poly(hydroxystyrene) (PHOSt) and an amphiphilic block copolymer (Pluronic F127 or Brij78) doped with a photoacid generator. This provided three length scales in the material; one from self-assembly of the amphiphilic molecule ( $< 10 \text{ nm}$ ), another from the polymer–polymer phase separation (50–200 nm), and finally photopatterning provided a “device level”



structure (1–100  $\mu\text{m}$ ). An acid-catalyzed (generated by UV exposure of the photo-acid) reactive modification of the polymer blend film converted part of the organic template to a silica network through exposure to precursor vapors. The impact of the polymer blend composition on the structure of the porous silica films was examined with the structure of the porous silica films determined using X-ray diffraction (XRD), SEM, transmission electron microscopy (TEM), spectroscopic ellipsometry (SE), and ellipsometric porosimetry (EP).

The optical properties and thickness of the films were quantified using spectroscopic ellipsometry (M-2000, J.A. Woollam). Film porosity was calculated from the Bruggemann effective medium approximation (BEMA) model [11,54], assuming that only two phases existed: amorphous silica and voids. The refractive index of the film was determined and directly translated into the film porosity, knowing the refractive index of the wall framework. The wall was assumed to be solely amorphous silica with a reported refractive index of 1.458. The film porosity calculated was found to be in the range of 50–60%.

Ellipsometric porosimetry was performed using toluene as a probe molecule to provide information regarding pore size distribution. The films were exposed to controlled relative pressures of toluene, and the change in refractive index during the vapor adsorption/desorption provided detailed information regarding pore filling [55]. In order to estimate the pore size distribution (PSD), adsorption/desorption curves were fitted, after which the Kelvin equation was applied. As a result, a pore size distribution was obtained which demonstrated the presence of nanopores in the silica films (Figure 9.5).

It was concluded that simple variations in processing parameters would allow the pore morphology to be tuned to create high-surface-area materials with

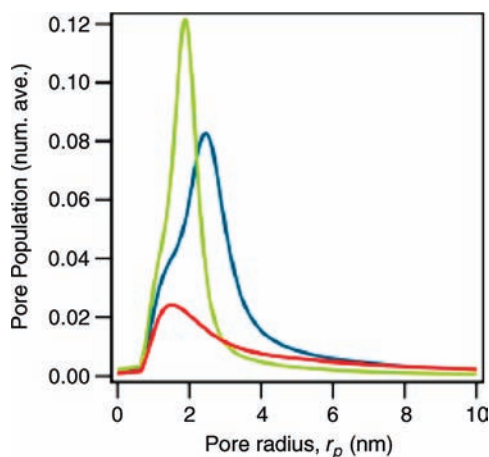


**Figure 9.5** Pore size distribution of the porous silica film estimated from desorption isotherm for toluene using the Kelvin equation. The template is a blend of Brij78 and PHOSt with 10% CGI1311 cast from ethanol: PGMEA (1 : 1

molar ratio). The weight ratio of Brij78 to PHOSt significantly impacted the morphology for 28 wt% PHOSt and 72 wt% Brij78 (blue), 17 wt% PHOSt and 83 wt% Brij78 (green) and 5 wt% PHOSt and 95 wt% Brij78 (red) [55].

structures on the order of 1 nm, 100 nm and micrometers from self-assembly, phase separation, and lithographic patterning, respectively.

#### 9.2.4

##### Biomaterial Surfaces

Polymers continue to attract much attention with regards to biomedical applications, due mainly to the great versatility in their physical and chemical properties. Chemical inertness, optical transparency, elasticity and biodegradability are just some of the advantageous features of polymeric materials that make them suitable for a variety of functional purposes in medicine and pharmacy. The blending of polymers is a promising approach in surface modification to enhance their biocompatibility, in improving functional (e.g., optical or imaging) properties, and in the development of advanced drug-delivery systems.

#### 9.2.5

##### Surface Modification, Adsorption from Solution

Interfacial interactions affecting the surface biocompatibility can be studied on thin films which are suitable model systems to be investigated by ellipsometry. A biodegradable polyester poly(lactic-co-glycolic acid) copolymer (PLGA) was blended with a poly(ethylene oxide)-containing block copolymer (Pluronic) to increase the hydrophilicity and hence the biocompatibility of the system [56]. PLGA thin films with various thicknesses on a solid support were characterized by ellipsometry during contact with aqueous solution.

The thickness of the blend layer varied during its contact with aqueous solution, depending on the composition (Figure 9.6). The thickness of the pure PLGA film presented a slight increase, while the thickness of blend films decreased significantly (by a few percent in 20 min) and in proportion to the Pluronic content.

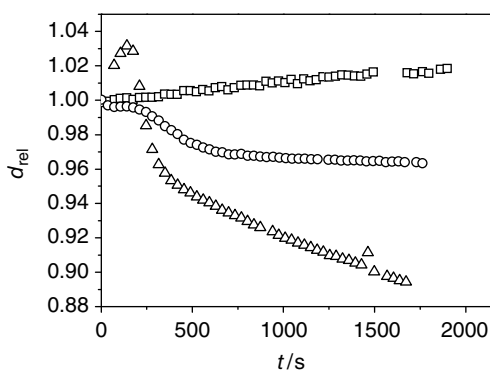


**Figure 9.6** Relative change of layer thickness,  $d_{\text{rel}}$ , during the contact with phosphate buffer for PLGA (□) and PLGA+Pluronic blend films with Pluronic concentration of 3.8% (w/w) (○) and 9.1% (w/w) (△). The initial thickness of the layers was 90 nm [56].

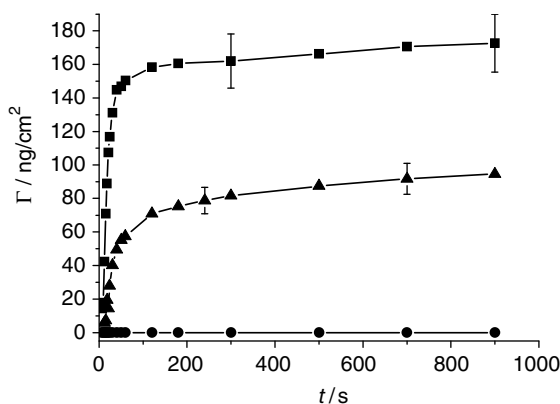


**Figure 9.7** Adsorbed amount of protein ( $\Gamma$  ng cm $^{-2}$ ) from 1.2 g l $^{-1}$  bovine serum albumin solution on PLGA films with 0% (■), 3.8% (▲), and 9.1% (w/w) (●) Pluronic concentration [56].

Protein-adsorption behavior was also investigated by *in situ* spectroscopic ellipsometry using a rotating compensator apparatus [56]. A fixed angle of incidence of 75° was used over a spectrum range of 191 to 1690 nm. The refractive indices of the polymer and the adsorbed protein layer as transparent materials were described using the Cauchy relationship. The thickness ( $d$ ) and refractive index ( $n$ ) of the adsorbed protein determined were used to calculate the surface concentration of protein ( $\Gamma$ ) using De Feijter's formula:

$$\Gamma = \frac{d \cdot (n - n_w)}{a}$$

where  $d$  is the thickness,  $n_w$  is the refractive index of the liquid medium, and  $a$  is the refractive index increment, which is approximated to 0.183 cm $^3$  g $^{-1}$  at a wavelength of 632.8 nm.

The degree of protein adsorption showed a good correlation with the hydrophilicity, and surface composition (Figure 9.7). Whilst improvements in resistance to protein adsorption are known to enhance biocompatibility [57,58], the most striking observation was that the layer thickness had a major impact on the interfacial characteristics of the polymer blend films in the investigated regime (20–200 nm). Thick layers presented a high permanent hydrophilicity and a great resistance to protein adsorption, while the thin layer proved to be less hydrophilic in the protein-adsorption experiment. Such behavior was considered due to swelling of the polymer film by water, combined with a partial dissolution of the water-soluble Pluronic from the layer. A constant supply of Pluronic from the deeper regions of the blends might compensate for its dissolution from the surface layer in the case of thicker films.

#### 9.2.5.1 Biomaterial Blends

Matrix-assisted pulsed laser evaporation (MAPLE) was used successfully to prepare thin films of a similar blend of PLGA with poly(ethylene glycol) (PEG), with

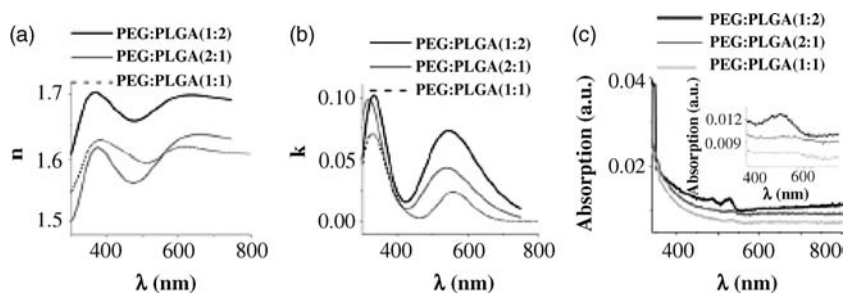


**Figure 9.8** (a) Refractive indices ( $n$ ) versus wavelength ( $\lambda$ ) and (b) extinction coefficients ( $k$ ) versus wavelength for the indicated polymeric films, as determined by SE; (c) UV-visible absorption spectra of the same samples [59].

a view to their being used for controlled drug delivery in ophthalmology [59]. The influence of the blending ratios on the characteristics of the films was revealed using AFM, Fourier transform infrared (FTIR) spectroscopy, and ellipsometry. The ratios in which the two polymers were blended were found to have a significant impact on the morphology, chemical structure and optical characteristics of the polymeric films. The roughness of the films was affected by the ratio of each polymer within the blend; the films were smoother when the blends had a higher PEG content. The optical constants of the polymeric films, which directly affect the quality of the device in special applications such as ocular use, were assessed using SE. A higher content of PEG within the blends resulted in films with lower refractive indices. The SE results were validated using AFM and UV-visible spectrophotometry (Figure 9.8).

Polymer blending was utilized as a strategy to increase the radio-opacity of a new biodegradable polymer [18]. Tyrosine-derived polycarbonates are used in a wide range of biomaterial applications such as cardiovascular stents, tissue engineering scaffolds, nanospheres for drug delivery, and thin film coatings. Their performance, however, in *in-vitro* and *in-vivo* imaging techniques requires improvement, for example by the incorporation of iodine. Hence, an iodinated derivative of desaminotyrosyl ethyl tyrosine polycarbonate [p(I<sub>2</sub>-DTE carbonate)] was blended with p(DTE carbonate) at various concentrations to estimate the effect of composition and layer thickness on the mechanical properties of the polymer film. Several discrete blend films were measured using a method based on surface wrinkling. This technique involves the formation of a polymer film on a solid substrate following a float transfer to a poly(dimethylsiloxane) (PDMS) substrate applying an intermediate release layer of poly(acrylic acid) (PAA). For that reason, the layer system to determine the thicknesses is quite complex, and four-phase (Si, native oxide, film, air as well as air, PDMS, film, air) or five-phase (Si, native oxide, PAA, film, air) models were used to analyze the data obtained by variable angle spectroscopic

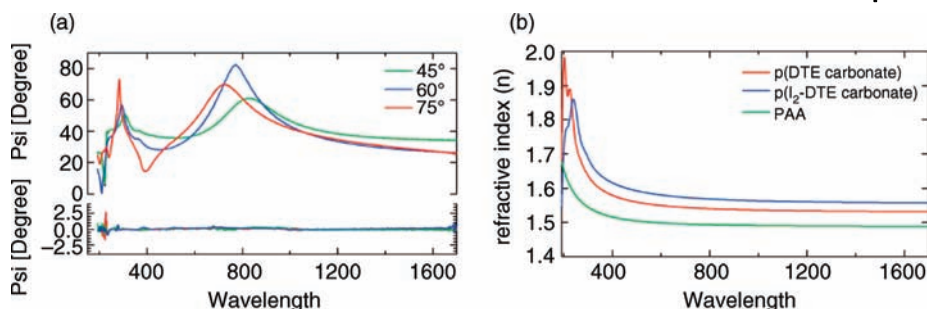


**Figure 9.9** (a) Ellipsometric parameter  $\psi$  ( $\psi$ ) and the respective fits (black line) to model in which PAA layer is assumed to be partially swept away during flow coating. Best fit p(DTE carbonate) thickness is 140 nm; the residual PAA layer thickness is 9 nm; (b) Refractive indices of the polymers [18].

ellipsometry in the range of 190 to 1700 nm. A comparison of the pre- and post-transferred film thicknesses showed no considerable differences, except for the indication that a significant amount of PAA was dissolved or was swept aside during the flow-coating process (Figure 9.9). It was concluded that the elastic modulus of thin films was not influenced by film thickness and blend composition over a 30 to 200 nm thickness range, which is an important region for coatings and delivery systems in biomedical applications.

#### 9.2.5.2 Distribution and Release of Drugs

Polymeric materials have proven effective for the controlled delivery of drugs, both in terms of the ability to program the kinetics of release and the ability to target the location of delivery. Ellipsometry, in being sensitive to the composition through the complex refractive index, is a powerful technique to detect the loading and release of drug components from a polymer layer. The drug content of a thin poly(lactic acid) film was determined using SE [60]; the ellipsometric data at high wavelengths ( $>500$  nm) were then used to obtain the film thickness, assuming that the films were transparent in this region (extinction coefficient,  $k=0$ ) and the dispersion in refractive index ( $n$ ) could be approximated with a two-parameter Cauchy function. The wavelength-dependent optical constants  $n$  and  $k$  were then calculated across the whole wavelength range (195 to 1700 nm) through a direct inversion of the ellipsometric data. It was assumed that the optical constants for films with an intermediate codeine drug loading were a linear combination of those of the pure PLA, and that the film had the highest codeine content. This confirmed that the fraction of codeine in the film scaled linearly with the fraction in solution. As a result of ellipsometric analysis, a good correlation was found between the solution composition, or drug loading, and the relative composition of the films generated.

Recent studies have shown that the performances of polymers used for controlled drug delivery as coating of pellets or tablets may be much improved by

blending [14,59,61]. The most attractive feature is that the polymer blends degrade differently and exhibit different drug-release properties compared to single polymers, thus offering the possibility to fine-tune the drug-release rates as a function of blend composition [62].

One polymeric delivery system that has received significant attention over the past decade has been the drug-eluting coronary stent, where the drug is dispersed within a thin biodegradable polymer film on the metal stent. As the polymer degrades, the drug is intended to be released to the local tissues [14,63]. Polymer blends offer an interesting potential as coating materials, with major advantages that include a facilitated adjustment of desired drug-release patterns, improved film-forming characteristics and storage stability, as well as mechanical and adhesive properties.

The release profile is mainly determined by the structure and morphology of the polymer blend. The important consequences of the different film-formation mechanisms for drug release are presented schematically in Figure 9.10.

A structural difference also exists in the dry form of blend films. In the case of films prepared using an aqueous dispersion the chains are less entangled and this facilitates a rapid swelling and high drug mobility; this manifests as a quick release facility in comparison to the more dense blend of film that is formed from organic solutions.

The porous structure, the void volume and the surface roughness of a film can all be effectively studied using ellipsometry, as the refractive index is a function of the material's density, composition, and morphology. For the structure of a

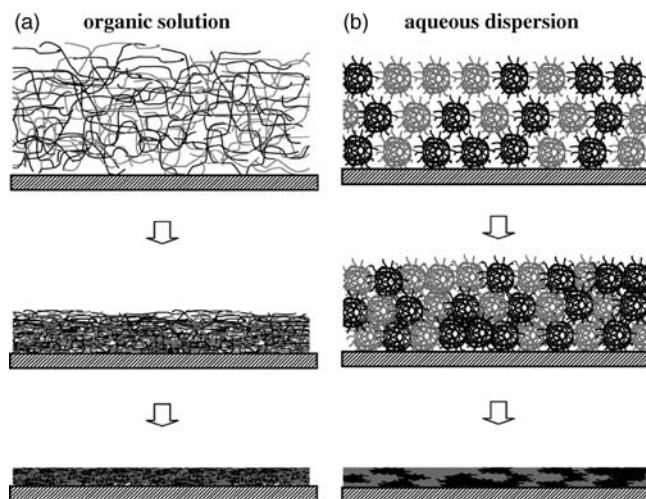


**Figure 9.10** Schematic presentation of film-formation mechanisms in systems containing two types of polymer, prepared from: (a) organic polymer solutions; (b) aqueous polymer dispersions [64].

polymer blend film prepared via dispersion, a model was constructed that involved two layers [65]. One layer corresponded to the polymer film with a certain porosity, while the other layer on top was the rough surface, composed of polymer and air at a given volume ratio (50–50%).

If the size of the voids is below the wavelength of light, then the refractive index of a layer will depend on the volume fraction of voids, as predicted in an effective medium approximation (EMA). Given that  $n_p$  is the refractive index of the fully dense polymer at a certain wavelength (measured independently), and that  $n_v$  is the refractive index of air voids ( $n_v = 1.00$ ), it is possible to calculate the void concentration from a measurement of the index,  $n$ , of a composite film consisting of polymer and voids. According to an EMA model, the volume fraction of voids,  $f_v$ , is

$$f_v = \frac{n^2 - n_p^2}{n^2 + 2n_p^2} \frac{n_v^2 + 2n_p^2}{n_v^2 - n_p^2}$$

The two fitting parameters – surface roughness and void concentration – can be determined independently with certainty via the fitting procedure. If aqueous polymer dispersions with different particle sizes are blended, an optimal particle packing (with minimal void volume) is achieved when the small particles form a continuous phase surrounding the large particles.

#### 9.2.6

##### Composite Layers for Organic Solar Cells

Organic thin film photovoltaic devices based on conjugated molecules and polymers have been shown to be highly efficient [66]. The high conversion efficiencies of light to current are the result of an efficient absorption of light and charge generation inside the devices. The efficiency is considerably enhanced when a single active conjugated polymer layer is replaced by heterojunctions (bilayers) with molecules having a high electron affinity and a low ionization potential. *Fullerene* proved to be suitable for this role as electron acceptor [67,68]. The structure of a sandwich-type thin film photovoltaic device, with the main functional components, is presented in Figure 9.11.

The donor–acceptor heterojunction is built up from poly(3-(4'-(1'',4'',7''-trioxaoctyl)phenyl)thiophene) (PEOPT) and C60. The device consisted of poly(3,4-ethylenedioxythiophene) (PEDOT) and poly(styrenesulfonate) (PSS) (PEDOT-PSS) layers spin-coated onto an indium tin oxide (ITO)/glass substrate as the hole-collecting electrode, and Al as the electron-collecting electrode. The PEDOT-PSS layer is used because the injection/collection conditions for electrons/holes are better, and this results in improved current–voltage characteristics for the device.

A significant improvement was achieved compared to the layered structure when the heterojunction was realized in bulk (involving a large interfacial area) by

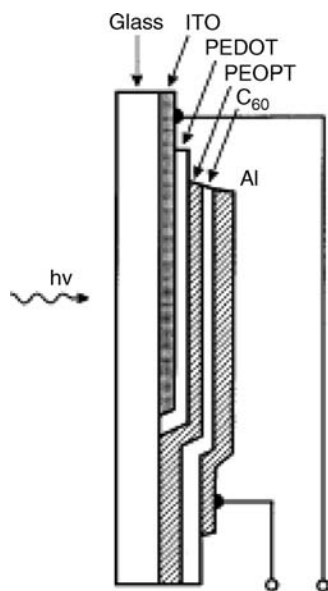


**Figure 9.11** Schematic presentation of the thin-film photovoltaic device structure: glass/ITO/PEDOT/PEOPT/C<sub>60</sub>/Al [66].

preparing a blend of the two components. The most frequently used blending component is a fullerene derivative: [6,6]-phenyl C<sub>61</sub> butyric acid methyl ester (PCBM). The most likely reason for such higher efficiency is that the blend provides optimum conditions for charge transfer and transport, due to its nanoscale heterogeneity. The mechanism to generate the photocurrent involves the creation of bound electron–hole pairs (excitons) by the absorption of light in the active parts of the devices. Charge generation occurs as a result of dissociation of the excitons, and by interaction of the excitons with interfaces, impurities, or defects. Thus, the high degree of dispersion – and hence the incorporation of dissociation sites – provides a beneficial performance for devices made from blends.

As the molecular-scale heterogeneity of the active layer greatly influences the power conversion efficiency, it is fundamentally important to identify and control the structural and optical properties and their relation to the function of a photovoltaic device. Ellipsometry is especially useful in determining the complex index of refraction and layer thickness, as well as structural details in thin-film geometry [69–72]. This information is needed to calculate the internal optical electric field distribution and the resulting photocurrent action spectra with respect to the efficiency of thin-film devices [66].

Although the above blends, when applied in organic photovoltaic devices, are not – strictly-speaking – a mixture of two or more polymers, their characterization by ellipsometry is analogous to that of polymer blend systems, and offers



excellent examples to demonstrate the potential of this technique in structural investigations.

As a basic study, modeling of the photocurrent action spectrum in thin-film organic photovoltaic devices was reported [66] with the use of complex indices of refraction and layer thickness of the materials determined with SE.

Composite films of P3HT/PCBM (poly[3-hexylthiophene-2,5-diyl] and [6,6]-phenyl C61 butyric acid methyl ester), which are widely used as the active layer in plastic solar cells [69,70], presented an increased performance when annealed above 100 °C [73]. When comparing the structural and optical properties of such films, using XRD and SE, the increased crystallinity of P3HT was found to be responsible for the increased optical absorption in the visible region. In combination with an enhancement of hole mobility, this would lead to a higher power conversion efficiency of annealed P3HT/PCBM solar cells.

Subsequently, SE and AFM were used to characterize the properties of P3HT/PCBM blend films commonly used in organic solar cells [71]. These studies focused on the effects of solvent and the composition ratio of the polymer and fullerene components used to prepare the blend film, and the various morphologies and surface roughnesses that resulted. The SE data obtained were analyzed with and without a surface roughness correction to examine how the morphology would affect the optical properties. Generally, a smoother film would be formed from a less-volatile solvent, although the different solubilities of P3HT and PCBM also affected both the surface roughness and phase separation during film formation. As a consequence, it proved reasonable to use various annealing procedures after film formation to achieve a more defined and controlled phase distribution in the active layer of a solar cell.

Morphology formation has also recently been characterized in fine detail [20,74] to reveal the effects of various treatments, including the choice of solvent, the rate of drying, thermal annealing and vapor annealing. All of these techniques were shown to lead to a common arrangement of the components, which consisted of a vertically and laterally phase-separated blend of crystalline P3HT and PCBM. Variable-angle SE, as a well-established noninvasive technique, was used to retrieve the optical constants of thin films, as well as the concentration–depth profiles of composite films [7,26,75].

The model that best represents the experimental data for all of these samples consists of two layers: a blend of P3HT and PCBM, the relative concentrations of which vary with depth, beneath a mixed PCBM–air layer. The top layer accounts for the PCBM crystalline domains that are observed to protrude from the film. The vertical distribution of the PCBM component in the blend film is shown schematically (Figure 9.12) and also as a concentration profile (Figure 9.13), before and after thermal annealing of the P3HT:PCMB 1:1 blend layer.

According to model fits to these data, the untreated film had a composition that varied from a PCBM-rich region close to the substrate to a P3HT-rich region near the free (air) surface (Figure 9.13). A similar vertical distribution of the polymer

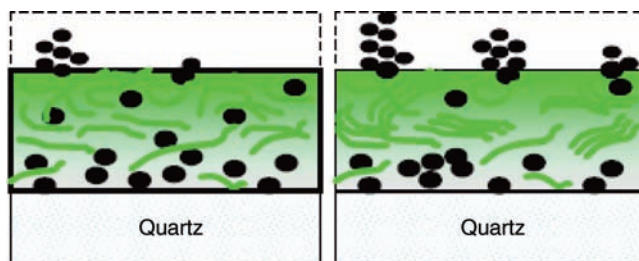
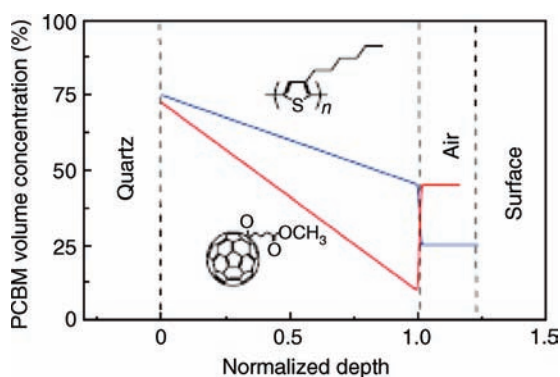


**Figure 9.12** Schematic representations of the model used to fit the ellipsometry data, showing typical PCBM distributions before and after vapor or thermal annealing [20].

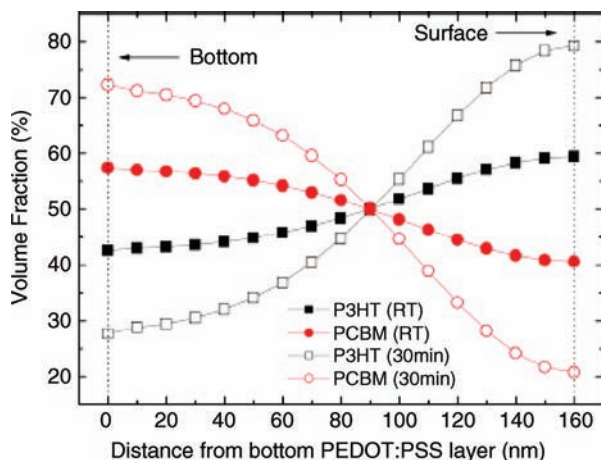
and fullerene derivative was obtained by others, although it was approximated by an exponential gradient model [21].

Figure 9.14 shows the evolution of the calculated volume fractions of P3HT and PCBM in the bottom and top regions of the blend film, with annealing time. The spin-coating process leads to blend films that are characterized by P3HT-enriched top regions and PCBM-enriched bottom regions. Thermal annealing above the polymer's  $T_g$  provides the macromolecules with an appropriate mobility to rearrange and reach a more thermodynamically favorable demixed state; this leads to an enhanced segregation of PCBM molecules toward the bottom regions.

Segregation of the electron-donor material (P3HT) towards the anode interface (ITO), and of the electron-acceptor material (PCBM) towards the cathode (Al) interface, would be expected to be beneficial for solar cell performance. The change in vertical distribution observed after thermal annealing contributes to this type of separation by the diffusion of PCBM molecules towards the nanoscopic PCBM domains. At the same time, the gradient of PCBM concentration



**Figure 9.13** PCBM concentration profiles obtained from analysis of ellipsometric data for P3HT:PCBM blend films spin-coated on fused silica before (blue) and after (red) thermal annealing [20].



**Figure 9.14** Evolution of the volume fractions of the P3HT and PCBM films from the bottom interface with PEDOT:PSS to the top regions of two representative blend films. Filled points indicate annealed samples; Hollow points indicate samples annealed at 140 °C for 30 min [21].

throughout the film is further increased (Figure 9.14). The analysis developed in these investigations for probing the structure of blend films is very powerful, and may also show the effect of the substrate on the distribution of components due to specific interactions (Figure 9.15).

These results show clearly that the direction of vertical segregation can be controlled by the surface energy of the substrate, which in turn makes surface

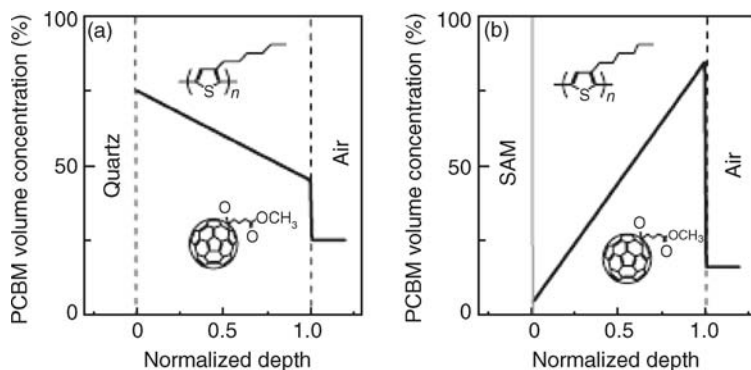


**Figure 9.15** PCBM concentration profiles obtained from analysis of ellipsometric data for P3HT:PCBM blend films spin-coated (a) on fused silica and (b) on a Si wafer

(with native oxide) precoated with a hydrophobic, self-assembled hexamethyldisilazane monolayer [20].

modification an easy way of directing phase separation. When considering the performance of organic solar cells, the detailed structural information obtained allows the conclusion to be drawn that an optimum distribution must be accomplished as the intimate intermixing of components is desirable for efficient exciton dissociation, whilst a certain degree of segregation of the two components is beneficial for efficient charge transport.

As noted in the above-described examples, SE is especially useful when probing the distribution of various components normal to the surface of the blend film, and is critically important for device efficiency. However, the lateral structural details can only be resolved at nanoscale level by using imaging ellipsometry [76]. The active layer materials used in organic photovoltaic cells often self-assemble into highly ordered morphologies, and the bicontinuous interpenetrating network of donor/acceptor domains with ordered structures would be expected to have an enhanced performance [77]. Such films demonstrate a significant optical anisotropy, and this was taken into consideration recently when constructing thin layers of organic solar cells [78]. As a result of numerous analytical and numerical calculations, the orientation of polymer domains in organic photovoltaic cells was shown to correlate with an increased light absorption.

### 9.3

#### Concluding Remarks

Ellipsometry is an especially versatile optical technique that has applications in many different fields, ranging from microelectronics and semiconductors (e.g., for characterizing oxides or photoresists on silicon wafers) to biology. In principle, ellipsometry enables the determination of thicknesses ranging from about 1 nm to about the wavelength of the incident light, and also of the composition of layers in multilayer thin films, especially if experiments are performed over a range of incident beam wavelengths or angles of incidence. Ellipsometry is an easily performed, noncontact and nondestructive technique that can handle samples under any ambient conditions (e.g., temperature, liquid). Although, to date, the potential of this sensitive technique in the field of polymer science has not yet been fully realized, it can provide unequaled capabilities for thin-film metrology, providing valuable information on phase separation, morphology, nanoporosity, adhesive and adsorption properties that may be related to drug-carrier systems, reinforced composite or solar cells. New developments – including measurements over a wide range of wavelengths and in real-time – will provide further encouragement for the future use of ellipsometry.

#### Acknowledgments

G. Gyulai and Cs. B. Péntzes are acknowledged for their valuable assistance in the preparation of the manuscript.

## References

- 1 Kim, M.S., Khang, G., and Lee, H.B. (2008) *Prog. Polym. Sci.*, **33**, 138.
- 2 Walsh, C.B. and Franes, E.I. (1999) *Thin Solid Films*, **347**, 167.
- 3 Fried, M., Lohner, T., and Petrik, P. (2001) Ellipsometric characterization of thin films, in *Handbook of Surfaces and Interfaces of Materials*, vol. 4 (ed. H.S. Nalwa), Academic Press, pp. 335–367.
- 4 Azzam, R.M.A. (2010) Ellipsometry, in *Handbook of Optics*, 3rd edn, vol. 1 (ed. in-chief M. Baas), McGraw-Hill, New York, pp. 16.1–16.25.
- 5 Fujiwara, H. (2007) *Spectroscopic Ellipsometry Principles and Application*, John Wiley & Sons, Ltd, Chichester.
- 6 Woollam, J.A. (2000) Ellipsometry, variable angle spectroscopic, in *Wiley Encyclopedia of Electrical and Electronics Engineering*, John Wiley & Sons, New York, pp. 109–116.
- 7 Fried, M., Petrik, P., Lohner, T., Khánh, N.Q., Polgár, O., and Gyulai, J. (2004) *Thin Solid Films*, **455**, 404.
- 8 Al-Attar, H.A. and Telfah, A.Dh. (2004) *Opt. Commun.*, **229**, 263.
- 9 Jellison, G.E. Jr (1993) *Thin Solid Films*, **23**, 416.
- 10 Garnett, J.C.M. (1904) *Philos. Trans. R. Soc. London*, **203**, 385.
- 11 Bruggeman, D.A.G. (1935) *Ann. Phys.*, **24**, 636.
- 12 Fian, A., Haase, A., Stadlober, B., Jakopic, G., Matsko, N.B., Grogger, W., and Leising, G. (2008) *Anal. Bioanal. Chem.*, **390**, 1455.
- 13 Song, L., Wu, Q., and Vogt, B.D. (2008) *J. Colloid Interface Sci.*, **328**, 374.
- 14 Siepmann, F., Siepmann, J., Walther, M., MacRae, R.J., and Bodmeier, R. (2008) *J. Controlled Release*, **125**, 1.
- 15 Dedecker, K., Groeninckx, G., and Inoue, T. (1998) *Polymer*, **39**, 5001.
- 16 Li, H., Yang, Y., Fujitsuka, R., Ougizawa, T., and Inoue, T. (1999) *Polymer*, **40**, 927.
- 17 Zudans, I., Heineman, W.R., and Seliskar, C.J. (2004) *Thin Solid Films*, **455–456**, 710.
- 18 Aamer, K.A., Stafford, C.M., Richter, L.J., Kohn, J., and Becker, M.L. (2009) *Macromolecules*, **42**, 1212.
- 19 Kang, S., Prabhu, V.M., Soles, C.L., Lin, E. K., and Wu, W. (2009) *Macromolecules*, **42**, 5296.
- 20 Campoy-Quiles, M., Ferenczi, T., Agostinelli, T., Etchegoin, P.G., Kim, Y., Anthopoulos, T.D., Stavrinou, P.N., Bradley, D.D.C., and Nelson, J. (2008) *Nat. Mater.*, **7**, 158.
- 21 Karagiannidis, P.G., Georgiou, D., Pitsalidis, C., Laskarakis, A., and Logothetidis, S. (2011) *Mater. Chem. Phys.*, **129**, 1207.
- 22 Yukioka, S. and Inoue, T. (1991) *Polym. Commun.*, **32**, 17.
- 23 Yukioka, S., Nagoto, K., and Inoue, T. (1992) *Polymer*, **33**, 1171.
- 24 Woollam, J.A. and Snyder, P.G. (1990) *Mater. Sci. Eng., B: Solid-State Mater. Adv. Techn.*, **B5** (2), 279.
- 25 Jenkins, T.E. (1999) *J. Phys. D: Appl. Phys.*, **32** (9), R45.
- 26 Tompkins, H.G. and Irene, E.A. (eds) (2005) *Handbook of Ellipsometry*, William Andrew Publishing, Norwich, New York.
- 27 Vedam, K. (1998) *Thin Solid Films*, **313–314**, 1.
- 28 Stehle, J.L. and Piel, J.P. (2009) *Appl. Surface Sci.*, **256**, S72.
- 29 den Boer, J.H.W.G. (1995) Spectroscopic infrared ellipsometry: components, calibration, and application. PhD thesis, Eindhoven University of Technology, The Netherlands.
- 30 Drevillon, B. (1998) *Thin Solid Films*, **313–314**, 625.
- 31 Duckworth, P., Richardson, H., Carelli, C., and Keddie, J.L. (2005) *Surf. Interface Anal.*, **37**, 33.
- 32 Nikonenko, N.A., Hinrichs, K., Korte, E., Pionteck, J., and Eichhorn, K.J. (2004) *Macromolecules*, **37**, 8661.
- 33 Collins, R.W. (1990) *Rev. Sci. Instrum.*, **61**, 2029.
- 34 Hilfiker, J.N. (2011) In situ spectroscopic ellipsometry (SE) for characterization of thin film growth, in *In Situ Characterization of Thin Film Growth* (eds G. Koster and G. Rijnders), Woodhead Publishers, Cambridge, pp. 99–151.
- 35 Inoue, T. and Kyu, T. (2000) Optical characterization: Light scattering, birefringence, and ellipsometry, in *Polymer Blends* (eds D.R. Paul and C.B. Bucknall), Wiley & Sons, Ltd, Chichester, pp. 319–347.

- 36 Pukánszky, B. (2005) *Eur. Polymer J.*, **41**, 645.
- 37 Schulze, U., Fónagy, T., Komber, H., Pompe, G., Pionteck, J., and Iván, B. (2003) *Macromolecules*, **36**, 4719.
- 38 Földes, E. and Pukánszky, B. (2005) *J. Colloid Interface Sci.*, **283**, 79.
- 39 Hanafy, G.M., Madbouly, S.A., Ougizawa, T., and Inoue, T. (2004) *Polymer*, **45**, 6879.
- 40 Koriyama, H., Oyama, H.T., i Ougizawa, T., Inoue, T., Weber, M., and Koch, E. (1999) *Polymer*, **40**, 6381.
- 41 Helfand, T. and Tagami, Y. (1972) *J. Chem. Phys.*, **56**, 3592.
- 42 Broseta, D., Fredrickson, G.H., Helfand, E., and Leibler, L. (1990) *Macromolecules*, **23**, 132.
- 43 Kim, J.H., Jang, J., Lee, D.-Y., and Zin, W.-C. (2002) *Macromolecules*, **35**, 311.
- 44 Hamon, L., Grohens, Y., and Holl, Y. (2003) *Langmuir*, **19**, 10399.
- 45 Ao, Z.M. and Jiang, Q. (2006) *Langmuir*, **22**, 1241.
- 46 Kim, B.S., Chiba, T., and Inoue, T. (1995) *Polymer*, **36**, 67.
- 47 von Buzágh, A. (1937) *Colloid Systems. A Survey of the Phenomena of Modern Colloid Physics and Chemistry*, The Technical Press Ltd, London.
- 48 Cho, D., Jalbert, C.J., and Koberstein, J.T. (2000) *Macromolecules*, **33**, 5245.
- 49 Lyu, S., Jones, T.D., Bates, F.S., and Macosko, C.W. (2002) *Macromolecules*, **35**, 7845.
- 50 Li, H., Chiba, T., Higashida, N., Yang, Y., and Inoue, T. (1997) *Polymer*, **38**, 3921.
- 51 Hu, W., Brown, H.R., Koberstein, J.T., Bhatia, R., Lingelser, J.-P., and Gallot, Y. (2006) *C. R. Chimie*, **9**, 45.
- 52 Dalnoki-Veress, K., Forrest, J.A., and Dutcher, J.R. (1998) *Phys. Rev. E*, **57**, 5811.
- 53 Dunbar, A.D.F., Mokarian-Tabari, P., Parnell, A.J., Martin, S.J., Skoda, M.W.A., and Jones, R.A.L. (2010) *Eur. Phys. J. E: Soft Matter*, **31**, 369.
- 54 Boissiere, C., Grosso, D., Lepoutre, S., Nicole, L., Bruneau, A.B., and Sanchez, C. (2005) *Langmuir*, **21**, 12362.
- 55 Baklanov, M.R., Mogilnikov, K.P., Polovinkin, V.G., and Dultsev, F.N. (2000) *J. Vac. Sci. Technol. B*, **18**, 1385.
- 56 Gyulai, G., Péntzes, Cs.B., Mohai, M., Lohner, T., Petrik, P., Kurunczi, S., and Kiss, É. (2011) *J. Colloid Interface Sci.*, **362**, 600.
- 57 Gölander, C.-G. and Kiss, É. (1988) *J. Colloid Interface Sci.*, **121**, 240.
- 58 Kiss, É., Dravetzky, K., Hill, K., Kutnyánszky, E., and Varga, A. (2008) *J. Colloid Interface Sci.*, **325**, 337.
- 59 Paun, I.A., Ion, V., Moldovan, A., and Dinescu, M. (2011) *Appl. Surf. Sci.*, **257**, 5259.
- 60 Rafati, A., Davies, M.C., Shard, A.G., Hutton, S., Mishra, G., and Alexander, M. R. (2009) *J. Controlled Release*, **138**, 40.
- 61 Chim, C.H., Cho, K.Y., Choi, E.J., and Park, J.K. (2000) *J. Appl. Polym. Sci.*, **77**, 226.
- 62 Amighi, K. and Moes, A.J. (1995) *Drug Dev. Ind. Pharm.*, **21**, 2355.
- 63 Braun, R.M., Cheng, J., Parsonage, E.E., Moeller, J., and Winograd, N. (2006) *Anal. Chem.*, **78**, 8347.
- 64 Lecomte, F., Siepmann, J., Walther, M., MacRae, R.J., and Bodmeier, R. (2004) *Pharm. Res.*, **21**, 882.
- 65 Tzitzinou, A., Keddie, J.L., Geurts, J.M., Peters, A.C.I.A., and Satguru, R. (2000) *Macromolecules*, **33**, 2695.
- 66 Pettersson, L.A.A., Roman, L.S., and Inganäs, O. (1999) *J. Appl. Phys.*, **86**, 487.
- 67 Datta, D., Tripathi, V., Gogoi, P., Banerjee, S., and Kumar, S. (2008) *Thin Solid Films*, **516**, 7237.
- 68 Sharma, S.S., Tripathi, B., Singh, M., Bhatnagar, D., and Vijay, Y.K. (2009) *Appl. Surf. Sci.*, **255**, 7070.
- 69 Slooff, L.H., Veenstra, S.C., Kroon, J.M., Moet, D.J.D., Sweelssen, J., and Koetse, M. M. (2007) *Appl. Phys. Lett.*, **90**, 143506.
- 70 Tvingstedt, K., Persson, N.-K., Inganäs, O., Rahachou, A., and Zozoulenko, I.V. (2007) *Appl. Phys. Lett.*, **91**, 113514.
- 71 Ng, A.M.C., Cheung, K.Y., Fung, M.K., Djurišić, A.B., and Chan, W.K. (2008) *Thin Solid Films*, **517**, 1047.
- 72 Ng, A., Li, C.H., Fung, M.K., Djurisić, A.B., Zapien, J.A., Chan, W.K., Cheung, K.Y., and Wong, W.-Y. (2010) *J. Phys. Chem. C*, **114**, 15094.
- 73 Erb, T., Zhokhavets, U., Hoppe, H., Gobsch, G., Al-Ibrahim, M., and Ambacher, O. (2006) *Thin Solid Films*, **511–512**, 483.
- 74 Campoy-Quiles, M., Schmidt, M., Nassyrov, D., Peña, O., Goñi, A.R., Alonso, M.I., and

- Garriga, M. (2011) *Thin Solid Films*, **519**, 2678.
- 75 Zaumseil, P., Krüger, D., Kurps, R., Fursenko, O., and Formanek, P. (2004) *Solid State Phenom.*, **95–96**, 473.
- 76 Jin, G., Jansson, R., and Arwin, H. (1996) *Rev. Sci. Instrum.*, **67**, 2930.
- 77 Liu, F., Gu, Y., Jung, J.W., Jo, W.H., and Russell, T.P. (2012) *J. Polym. Sci. B: Polym. Phys.*, **50**, 1018.
- 78 Grote, R.R., Brown, S.J., Driscoll, J.B., Osgood, R.M., and Schuller, J.A. (2013) *Opt. Express*, **21**, A847.





## 10

### Inverse Gas Chromatography

*Kasylda Milczewska and Adam Voelkel*

#### 10.1

##### Concept and History of Inverse Gas Chromatography (IGC)

During the past 40 to 50 years, inverse gas chromatography (IGC) has developed into a widespread, popular, and fruitful technique for the physico-chemical characterization of various materials, as well for providing descriptions of the interactions between components in various systems. Indeed, during the past 20 year several reviews detailing the theoretical background of IGC, as well as its parameters, the interpretation of experimental data and applications have been produced [1–8].

In a typical IGC experiment, the apparatus used is similar to that used in conventional gas chromatography. The test solute, which has known properties, is injected at the inlet of the column, which may be either of two forms:

- A *packed column*, where the investigated material is loaded onto the column as solid particles or is supported on an inert material.
- A *capillary column*, where an annular film of the polymer is coated onto the column inner wall.

Because the stationary phase is the phase of interest (in contrast to conventional gas chromatography), this process is termed inverse gas chromatography. The physico-chemical properties of the examined material are deduced from the retention data of a series of carefully selected test solutes [7].

The application of IGC to studies of polymeric systems was initiated in 1969 by Smidsrød and Guillet [9], who showed that gas chromatography could be used to demonstrate several interesting properties of the polymer. Nowadays, IGC is a useful and quite versatile technique for material characterization, because it can provide information on thermodynamic properties over a wide temperature range. To date, IGC has been used for the characterization of polymer blends [10], block copolymers [11,12], hyperbranched polymers [13], fillers [14], and other materials [15–17].

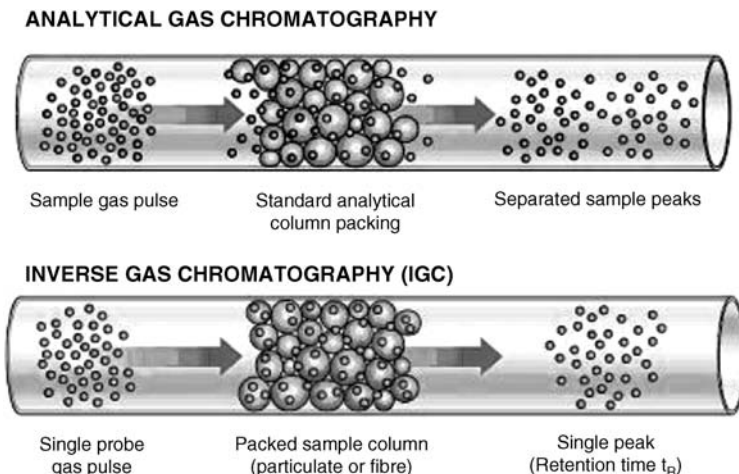


**Figure 10.1** Analytical versus inverse gas chromatography. [[http://en.wikipedia.org/wiki/File:Inverse\\_and\\_analytical\\_gas\\_chromatography.JPG](http://en.wikipedia.org/wiki/File:Inverse_and_analytical_gas_chromatography.JPG) - filelinks 29-02-2012].

## 10.2

### Theoretical Background

The principles of IGC, as a gas-phase technique used to characterize the surface and bulk properties of solid materials, are very simple as the process is the reverse of conventional gas chromatography. Typically, an empty cylindrical column is uniformly packed with the solid material of interest, normally a powder, fiber, or film. A pulse or constant concentration of gas is then injected down the column at a fixed carrier gas flow rate, and the retention behavior of the pulse or concentration front is measured with a detector (Figure 10.1). The retention of a solvent or “probe” molecule on the material is recorded and the measurement is made effectively at an infinite dilution of the probe. A range of thermodynamic parameters can then be calculated. A major advantage of IGC is that it is readily applicable to mixtures of two or more polymers.

The retention of the test solutes is expressed as the corrected retention time ( $t'_R$ ):

$$t'_R = t_R - t_M \quad (10.1)$$

where  $t_R$  is the measured retention time and  $t_M$  is the gas hold-up time, calculated using the Grobler–Balazs procedure [18].

For physico-chemical calculations, the retention data are often presented as the specific retention volume  $V_g$  ( $\text{cm}^3 \text{g}^{-1}$ ):

$$V_g = \frac{3}{2} \cdot \frac{t'_R \cdot j \cdot F_c \cdot 273.15}{m_w \cdot T} \quad (10.2)$$

where  $F_c$  is the flow rate of carrier gas measured at room temperature,  $T$  is the temperature of the experiment,  $m_w$  is the mass of the stationary phase, and  $j$  is the James–Martin coefficient, which is used to correct for the gas carrier compressibility and is defined as follows:

$$j = \frac{3}{2} \cdot \left[ \frac{\left(\frac{P_i}{P_o}\right)^2 - 1}{\left(\frac{P_i}{P_o}\right)^3 - 1} \right] \quad (10.3)$$

where  $P_i$  and  $P_o$  are the inlet and outlet pressures, respectively.

It is worth noting two points with regards to the background of IGC:

- It is possible to work at a finite concentration of test solutes (FC-IGC) or in the region of an infinitive dilution (ID-IGC).
- Retention of the test solute may be result of a pure adsorption equilibrium, or of a mixed retention mechanism, such as bulk sorption and adsorption on existing interfaces. The first mechanism is obvious during the examination of solid materials (adsorbents, fibers, polymers below  $T_g$ ), while the second mechanism might be important when a rubbery polymer (above  $T_g$ ), polymer blends or oils are characterized.

Nastasovic and Onija [19] presented the advantages and drawbacks of the IGC over traditionally used methods when determining the glass transition temperature ( $T_g$ ). The precision and accuracy of  $T_g$  determination is influenced by: (i) the inert support type; (ii) the coating thickness; (iii) the sorbate type; and (iv) the flow rate. The report of Nastasovic and Onija is, and the references cited therein, should be taken into account when examining polymer properties by means of IGC below and above  $T_g$ .

Solute equilibrium conditions between the mobile and stationary phases are achieved at zero surface coverage of the surface. The chromatogram must be symmetric and the maximum of the chromatographic peak should be independent of the amount of retained adsorbate [20]. The concentration of adsorbate in the gas phase is minimal, and the sorption process is derived from real adsorbate–adsorbent interactions. The adsorbate might be considered as an ideal gas both in the gas phase and in the adsorbed state. At infinite dilution, the net retention volume ( $V_N$ ) is related to the concentration of adsorbate in the gas phase  $c$ , as follows:

$$V_N = \frac{q}{c} \cdot S \quad (10.4)$$

where  $S$  is the specific surface area of the examined material and  $q$  is the adsorbate concentration in the stationary phase.

In the region of higher solute concentration (finite concentration area) the isotherm is not linear and the net retention volume will be related to the mole fraction of the adsorbate in the gas phase  $y_0$ :

$$V_N = S(1 - jy_0) \cdot \frac{dq}{dc} \quad (10.5)$$

The application of Eq. (10.5) allows the relation between the shape of the chromatographic peak and the slope of the adsorption isotherm to be determined.

### 10.3

#### Thermodynamic Aspects: Parameters Used for Polymer Blend Characterization

The term “miscibility of polymers” relates to the possibility of an interpenetration of components at the molecular level [21–23]. The numerical expression of the energy required to achieve miscibility is the Gibbs free energy of mixing  $\Delta G_{mix}$ :

$$\Delta G_{mix} = \Delta H_{mix} - T \cdot \Delta S_{mix} \quad (10.6)$$

where  $\Delta H_{mix}$  is the enthalpy of mixing and the entropy of mixing ( $\Delta S_{mix}$ ) is:

$$\frac{\Delta S_{mix}}{RT} = n_1 \ln \phi_1 + n_2 \ln \phi_2 \quad (10.7)$$

where  $n$  is the number of moles in the mix and  $\phi$  is the mole fraction of components 1 and 2.

Two components are mutually miscible if the mixing free energy:

$$\Delta G_{mix} < 0 \quad (10.8)$$

and

$$\left( \frac{\partial^2 \Delta G_{mix}}{\partial \phi^2} \right)_{p,T} > 0 \quad (10.9)$$

Spontaneous mixing occurs when  $\Delta G_{mix}$  is negative. Exothermic mixtures ( $\Delta G_{mix} < 0$ ) will mix spontaneously, whereas for endothermic mixtures miscibility will occur only at high temperatures. A plot of  $\Delta G_{mix}$  versus  $\phi$  is a convex function of the mixture composition, and is represented by a bimodal or spinodal phase with a lower critical solution temperature (LCST) or an upper critical solution temperature (UCST).

Equation-of-state theory, as developed by Flory and coworkers, can be used to explain phase separation – that is, LCST behaviour – by considering the effect of volume changes on mixing [22]. In the case of most miscible blends, the miscibility stems from specific interactions, although it may also result from reductions in unfavorable specific interactions between groups of the same polymer [21,22,24].

## 10.3.1

**Flory–Huggins Interaction Parameter for Polymer–Test Solute Systems**

The properties of polymer blends are determined mainly by the miscibility of the components and structure. Usually, thermodynamic miscibility and homogeneity can be attained when the free energy of mixing is negative. The classical thermodynamics of binary polymer–solvent systems was developed independently by Flory [25] and Huggins [26], and is based on the well-known *lattice model*. A quantitative calculation of the entropy of mixing led to the introduction of a dimensionless value, the so-called Flory–Huggins interaction parameter,  $\chi$ . The latter is an important factor of miscibility of polymer blends and solutions, and has been considered as a Gibbs free energy parameter. According to such an assumption, the interaction parameter  $\chi$  can be separated into enthalpic  $\chi_H$  and entropic  $\chi_S$  components [27].  $\chi_S$  was found to be positive and typically should be between 0.2 and 0.6; in polymer solution the term is sometimes also related to the reciprocal of the coordination number. For complete miscibility between polymer and solvent,  $\chi$  should be  $<0.5$  and, since the entropic term is about 0.3,  $\chi_H$  must be very small:

$$\chi = \chi_H + \chi_S \quad (10.10)$$

The Flory–Huggins interaction parameter, which indicates the interaction of a vapor-phase probe at infinite dilution with a polymer,  $\chi_{12}^\infty$ , can be related to the specific retention volume of probes,  $V_g$ , by the following equation:

$$\chi_{12}^\infty = \ln \left( \frac{273.15 \cdot R}{p_1^o \cdot V_g \cdot M_1} \right) - \frac{p_1^o}{R \cdot T} \cdot (B_{11} - V_1^o) + \ln \left( \frac{\rho_1}{\rho_2} \right) - \left( 1 - \frac{V_1^o}{V_2^o} \right) \quad (10.11)$$

where 1 denotes the solute and 2 denotes the examined material,  $M_1$  is the molecular weight of the solute,  $p_1^o$  is the saturated vapor pressure of the solute,  $B_{11}$  is the second virial coefficient of the solute,  $V_i^o$  is the molar volume,  $\rho_i$  is the density, and  $R$  is the gas constant.

The vapor pressure  $p_1^o$  is calculated from the Antoine equation [11], while the second virial coefficients  $B_{11}$  are computed using the following equation [28,29]:

$$B_{11} = \frac{9 \cdot R \cdot T_c}{128 \cdot P_c} \cdot \left[ 1 - 6 \cdot \left( \frac{T_c}{T} \right)^2 \right] \cdot 10^6 \quad (10.12)$$

where  $T_c$  and  $P_c$  are the critical temperature and critical pressure of the solute, respectively.

When  $\ln \left( \frac{\rho_1}{\rho_2} \right) \rightarrow 0$  and  $\left( \frac{V_1^o}{V_2^o} \right) \rightarrow 0$ , Eq. (10.11) can be simplified to [11,30–32]:

$$\chi_{12}^\infty = \ln \left( \frac{273.15 \cdot R \cdot v_2}{p_1^o \cdot V_g \cdot V_1^o} \right) - \frac{p_1^o}{R \cdot T} \cdot (B_{11} - V_1^o) - 1 \quad (10.13)$$

where  $v_2$  is the specific volume of the stationary phase.

For the case of the mixture (polymer-filler composition), subscripts 2 and 3 are used to represent the first and second mixtures' components, and Eq. (10.11) can be rearranged as [33,34]:

$$\chi_{1m}^{\infty} = \ln \left( \frac{273.15 \cdot R}{p_1^{\circ} \cdot V_g \cdot M_1} \right) - \frac{p_1^{\circ}}{R \cdot T} \cdot (B_{11} - V_1^{\circ}) + \ln \left( \frac{\rho_1}{\rho_m} \right) - \left( 1 - \frac{V_1^{\circ}}{V_2^{\circ}} \right) \cdot \varphi_2 - \left( 1 - \frac{V_1^{\circ}}{V_3^{\circ}} \right) \cdot \varphi_3 \quad (10.14)$$

$$\varphi_2 = \frac{w_2 \cdot \nu_2}{w_2 \cdot \nu_2 + w_3 \cdot \nu_3} \quad \varphi_3 = \frac{w_3 \cdot \nu_3}{w_2 \cdot \nu_2 + w_3 \cdot \nu_3} \quad (10.15)$$

where  $\varphi_2$  and  $\varphi_3$  are the volume fractions of the polymer and filler, and the index  $m$  denotes the mixture.

When  $\chi < 0.5$ , the liquid probe is generally characterized as a good solvent for the polymer, whereas  $\chi > 0.5$  indicates a poor solvent which use may lead to phase separation. In the case of a polymer blend, the parameter  $\chi$  can still be defined, and miscibility generally occurs when  $\chi < 0$  because the high molar volume of both components will diminish the combinatorial entropy [35].

Many authors use Eq. (10.13) also to calculate the Flory–Huggins parameter  $\chi_{12}^{\infty}$  for blends or compositions.

The uncertainty of the basic physico-chemical data used in the calculation of IGC-derived parameters inevitably implies an error of estimation of IGC parameters which may, in several cases, exceed 10%.

Voelkel and Fall [29] indicated that the significant variation in second virial coefficient data collected from different sources will affect the final result; that is, the value of physico-chemical parameters describing the properties of polymer systems. Conder and Young [36] indicated that the permissible uncertainty when estimating the second virial coefficient of the solute should be  $\pm 10\%$  (at 20–50 °C).

The second virial coefficient  $B_{11}$  has been determined using a variety of methods, as discussed earlier [37]; values have also been tabulated for limited group of compounds in handbooks (e.g., Ref. [38]).

The Flory–Huggins solute-polymer interaction parameter may be also calculated from activity coefficients [16,39]. In the case of pure solvents the equation is:

$$\chi_{12}^{\infty} = \ln \Omega_1^{\infty} + \ln \frac{\rho_1}{\rho_2} - \left( 1 - \frac{V_1^{\circ}}{V_2^{\circ}} \right) \quad (10.16)$$

$$\ln \Omega_1^{\infty} \equiv \ln \frac{a_1}{w_1} = \ln \left( \frac{273.15 \cdot R}{p_1^{\circ} \cdot V_g \cdot V_1^{\circ}} \right) - \frac{p_1^{\circ}}{R \cdot T} \cdot (B_{11} - V_1^{\circ}) \quad (10.17)$$

where  $a_1$  and  $w_1$  are the activity and weight fraction coefficients of the solute in the polymer phase, respectively.

When the polymer is a mixture of two polymers (mixed stationary phases) the Eq. (10.16) becomes [39]:

$$\chi_{1m}^{\infty} = \ln \Omega_1^{\infty} + \ln \frac{\rho_1}{\rho_m} - \left(1 - \frac{V_1^0}{V_2^0}\right) \cdot \varphi_2 - \left(1 - \frac{V_1^0}{V_3^0}\right) \cdot \varphi_3 \quad (10.18)$$

where  $\rho_m$  is the density of the mixture of polymers. As  $V_2^0$  and  $V_3^0$  are much larger than  $V_1^0$ , the use of Eq. (10.18) is greatly simplified:

$$\chi_{1m}^{\infty} = \ln \Omega_1^{\infty} + \ln \frac{\rho_1}{\rho_m} - 1 \quad (10.19)$$

The dependence of  $\chi_{12}^{\infty}$  on the chemical nature of the solutes is evident and is due to the interaction of solutes with the polymer surface [40].  $\chi_{12}^{\infty}$  values can be interpreted that the strength of specific interactions of these solutes ranges from a somewhat exothermic nature to an endothermic nature.

### 10.3.2

#### Flory–Huggins Interaction Parameter for “Multiple” Systems

By applying the Flory–Huggins equations of polymer solutions to a ternary system with two polymers and one probe, the interaction parameter  $\chi_{1m}^{\infty}$  can be related to the probe–polymer interaction parameters ( $\chi_{12}^{\infty}$  and  $\chi_{13}^{\infty}$ ) and the polymer–polymer interaction parameter ( $\chi_{23}$ ) by the following equation [41]:

$$\chi'_{23} = \frac{1}{\varphi_2 \cdot \varphi_3} \cdot (\chi_{12}^{\infty} \cdot \varphi_2 + \chi_{13}^{\infty} \cdot \varphi_3 - \chi_{1m}^{\infty}) \quad (10.20)$$

where  $\varphi_i$  is the volume fraction of appropriate polymer. Because the molar volumes of polymers may not be accurately known, it is a common practice of IGC studies to define a probe-normalized interaction parameter [41,42]:

$$\chi'_{23} = \chi_{23} \cdot \left(\frac{V_1}{V_2}\right) \quad (10.21)$$

The advantage of using  $\chi'_{23}$  is that it can be directly related to the specific retention volumes by the formula:

$$\chi'_{23} = \frac{\chi_{23}^{\infty} \cdot V_1}{V_2} = \frac{1}{\varphi_2 \cdot \varphi_3} \cdot \left( \ln \frac{V_{g,m}}{w_2 \cdot v_2 + w_3 \cdot v_3} - \varphi_2 \cdot \ln \frac{V_{g,2}}{v_2} - \varphi_3 \cdot \ln \frac{V_{g,3}}{v_3} \right) \quad (10.22)$$

This parameter is also called the “apparent” polymer–polymer interaction parameter ( $\chi_{23}^{app}$ ) [43].

In order to obtain  $\chi'_{23}$  for a polymer blend, by utilizing IGC,  $\chi_{12}^{\infty}$  and  $\chi_{13}^{\infty}$  must be known. Consequently, three columns are usually prepared – two for homopolymers and a third prepared from a blend of the two samples used earlier. These columns should be studied under identical conditions of column temperature, carrier gas flow rate and inlet pressure of the carrier gas, and with the same solutes (probes) [8].

By using Eq. (10.22), the contact energy parameter,  $B_{23}$ , as another indicator of the miscibility of the polymer pair can be calculated [44]:

$$B_{23} = \left( \frac{R \cdot T}{V_1 \cdot \varphi_2 \cdot \varphi_3} \right) \frac{1}{\varphi_2 \cdot \varphi_3} \cdot \left( \ln \frac{V_{g,m}}{w_2 \cdot \nu_2 + w_3 \cdot \nu_3} - \varphi_2 \cdot \ln \frac{V_{g,2}}{\nu_2} - \varphi_3 \cdot \ln \frac{V_{g,3}}{\nu_3} \right) \quad (10.23)$$

where  $B_{23}$  determines the miscibility of the blend, with the negative value being necessary for mixing and related to the Flory–Huggins interaction parameter  $\chi'_{23}$  by the following equation:

$$B_{23} = R \cdot T_m^o \cdot \left( \frac{\chi'_{23}}{V_3} \right) \quad (10.24)$$

where  $V_3$  is the molar volume of diluent polymer, and  $T_m^o$  is the equilibrium melting point of the polymer in the blend [8].

This method for calculating the Flory–Huggins  $\chi'_{23}$  parameter was used successfully in the analysis of polymers filled with inorganic fillers [45,46].

#### 10.4

##### Procedures Used in IGC Experiments Leading to the Determination of Polymer Blend Characteristics

The values of  $\chi'_{23}$  estimated by IGC have been found to depend on the chemical nature of the solutes, and various IGC research groups have attributed such dependency on deficiencies of the Flory–Huggins theory. The variation of the  $\chi'_{23}$  values from the probe was described as the  $\Delta\chi$  effect, and Prolongo *et al.* [47] were among those who recognized that the equation of state does not yield true polymer–polymer parameters for polymer blend systems. Hence, they attempted to correct for this dependency by recognizing the different types of interactions. Shi and Schreiber [48] also attempted to obtain the true polymer–polymer interaction coefficient and reviewed various experimental results from independent sources. Ultimately, Shi and Schreiber suggested that the surface and bulk compositions in multicomponent polymer systems (blends) generally differed, and that the partitioning of vapor-phase molecules between components of the surface layer of a solid would most likely be nonrandom. Rather, they suggested – and tested experimentally – a procedure that involved IGC for establishing the true surface composition of a polymer blend system. In this case, the surface concentration of one polymer in the blend was found always to exceed the bulk composition (wt% ratio), and that this difference varied greatly with the choice of vapor solute used.

Olabisi [49] reported that the dependence of the value of Flory–Huggins parameter  $\chi'_{23}$  on the solute could be attributed to the nonrandom distribution of the solute in the stationary phase, owing to its preferential affinity for one of the components. In other words, the nonrandom distribution of the solute in the stationary phase owed its preferential affinity to one of the components. As selective



solutes are not sensitive to the three varieties of intramolecular contact in the polymer mixture (A–A, A–B, B–B) in proportion to concentration, it would be expected that a better measure of the polymer–polymer interaction would most likely be obtained with less-selective solvents.

Lezcano, Prolongo and Coll [50] suggested that probes should be selected which gave similar interactions ( $\chi_{12}^{\infty} = \chi_{13}^{\infty}$ ) with each component (polymer).

When Zhao and Choi [51] also discussed the solvent-dependence of  $\chi'_{23}$ , they found that the problem had essentially originated from an incorrect choice of reference volumes used when calculating the binary interaction parameter between various solvents and the pure polymers, and their blends. Traditionally, in Flory–Huggins theory the molar volume of the solvent ( $V_1$ ) is taken as the reference volume ( $V_0$ ). This problem is valid for ternary systems, and differences in the values of the  $\chi$  parameter originate from the lattice size used. Zhao and Choi [51] have proposed the use of a “common reference volume,” calculating  $\chi'_{23}$  from the equation:

$$\left(\frac{V_0}{V_1}\right) \cdot \chi_{1m} = \varphi_2 \cdot \left(\frac{V_0}{V_1}\right) \cdot \chi_{12} + \varphi_3 \cdot \left(\frac{V_0}{V_1}\right) \cdot \chi_{13} - \varphi_2 \cdot \varphi_3 \cdot \left(\frac{V_0}{V_2}\right) \cdot ZC\chi'_{23} \quad (10.25)$$

where  $V_0$  is volume of the segment of polymer used.

Plotting  $\chi_{1m}$  versus  $(\varphi_2 \cdot \chi_{12} + \varphi_3 \cdot \chi_{13})$  (Eq. (10.18)) gives a straight line with a slope 1 and an intercept of  $-\varphi_2 \cdot \varphi_3 \cdot ZC\chi'_{23}$ , where  $ZC\chi'_{23}$  denotes  $\chi'_{23}$  determined using Zhao–Choi procedure [52].

Recently, J.-C. Huang [53] suggested the rearrangement of Eq. (10.25) into the following form:

$$\frac{\chi_{1m}}{V_1} = \left( \frac{\varphi_2 \cdot \chi_{12} + \varphi_3 \cdot \chi_{13}}{V_1} \right) - \varphi_2 \cdot \varphi_3 \cdot \left( \frac{\chi'_{23}}{V_2} \right) \quad (10.26)$$

The polymer–polymer interaction term can be determined from the intercept at  $\varphi_2 \cdot \chi_{12} + \varphi_3 \cdot \chi_{13} = 0$ .

Su and Patterson [54] also observed the  $\Delta\chi$  effect, and suggested that it becomes relevant only when the difference between  $\chi_{13}^{\infty}$  and  $\chi_{12}^{\infty}$  is very large. Furthermore, the effect is more apparent for higher concentrations of the preferred (non-glassy) polymer. Thus, Su and Patterson suggested calculating the critical  $\chi'_{23}$  values from the equation:

$$\chi'_{23(critical)} = \frac{1}{2} \left[ \left( \frac{V_1}{V_2} \right)^{\frac{1}{2}} + \left( \frac{V_1}{V_3} \right)^{\frac{1}{2}} \right]^2 \quad (10.27)$$

where  $V_2$  and  $V_3$  reflect different molar volumes.

Other authors [54] noted that Eq. (10.27) should still give a reasonable approximate value of this interaction parameter, which appeared to be extremely small.

When  $\chi$  values are determined for a given polymer or other nonvolatile component of a polymer system, and for a series of vapors for which solubility parameter values are known, the IGC method provides a unique approach to determining the solubility parameter,  $\delta_T$ , for the polymer phase. The method is based on the principle that the Flory–Huggins interaction parameter,  $\chi$ , can be related to  $\delta_T$  by combining the Hildebrand–Scatchard solution theory with the Flory–Huggins theory [21]:

$$\chi = \frac{V_1}{RT} \cdot (\delta_1 - \delta_2)^2 \quad (10.28)$$

Here,  $V_1$  is the molar volume of the probe and  $\delta_1$  and  $\delta_2$  are the solubility parameters of the probe and stationary phase, respectively.

The necessary relationship, between  $\chi$  and solubility parameters, states that:

$$\frac{\delta_1^2}{R \cdot T} - \frac{\chi}{V_1} = \frac{2 \cdot \delta_2}{R \cdot T} \delta_1 - \left( \frac{\delta_2^2}{R \cdot T} + \frac{\chi_s}{V_1} \right) \quad (10.29)$$

where  $\delta_1$  is the solubility parameter of component 1 and  $\delta_2$  is the solubility parameter of component 2,  $V_1$  is the molar volume of the probe, and  $\chi_s$  is the entropic contribution to  $\chi$ . A plot of the left-hand side of Eq. (10.29) versus  $\delta_1$  should lead to a straight line, with  $\delta_2$  obtained from its slope.

## 10.5

### Application of Chemometric Methods

Heberger *et al.* [55] used principal component analysis (PCA) to reduce the amount of test solutes when calculating Flory–Huggins parameters  $\chi'_{23}$ . Subsequently, PCA became a popular technique in data analysis for pattern recognition and dimension reduction, as it can reveal several underlying components, and may also help to explain the vast majority of variance among the data [56,57]. PCA is particularly useful for classifying stationary phases [58,59], polarity [56], and interaction parameters [57]. Detailed descriptions of PCA are available in standard chemometric books and reviews [58,59]. Notably, the method should facilitate the solution of problems connected with the solute dependence of the  $\chi'_{23}$  parameter.

Values of the Flory–Huggins  $\chi'_{23}$  parameter expressing the magnitude of interactions between the polymer matrix and filler depend heavily on the type of test solute being used in IGC experiments. This causes problems when analyzing the influence of the type and amount of filler on the magnitude of these interactions; however, such an analysis is clearly possible by using PCA.

The collection of retention data for all test solutes is time-consuming, and it would be very useful to select only those test solutes that carried statistically valid information, to apply these species to IGC experiments, and then to use the retention data in calculations of  $\chi'_{23}$  with the Zhao–Choi procedure. Today, PCA has

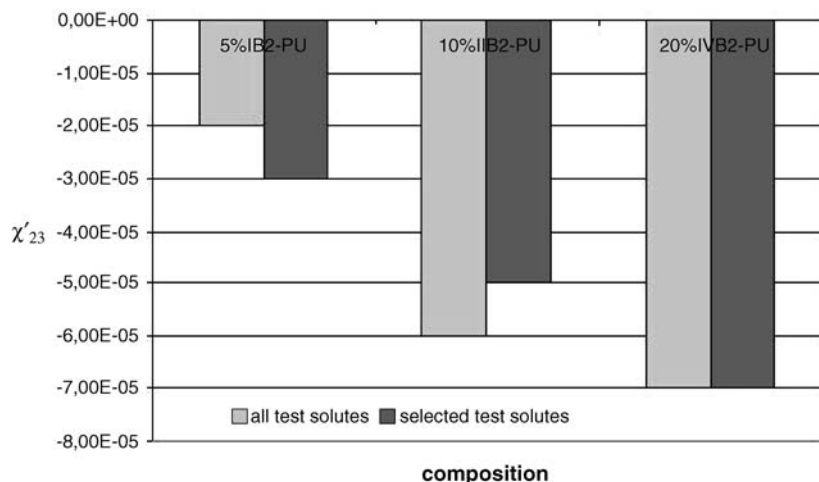


**Figure 10.2** Comparison of  $\chi'_{23}$  calculated by the Zhao–Choi procedure before and after PCA selection of test solutes for polyurethane (PU). Reproduced with permission from Ref. [55]; © 2006, Elsevier.

enabled a significant reduction in the number of test solutes required for correct determination of the Flory–Huggins parameter. Indeed, values of the Flory–Huggins parameter  $\chi'_{23}$  calculated before and after PCA analysis are comparable. As shown in Figure 10.2, in the case of PU (polyurethane)-B2 compositions, the corrected values were lower or higher than those found for all test solutes, but they indicate the presence or absence of interaction.

## 10.6

### Transport Properties of Polymeric Mixtures

A knowledge of mass transfer properties is important for various manufacturing operations of polymers such as polymerization, drying, vacuum/gas stripping, and devolatilization. The activity coefficients and diffusivities of small molecules in polymeric systems might be conventionally determined by gravimetric sorption/desorption experiments. Regrettably, however, these techniques are difficult when applied to systems with extremely small amounts of solvent, or at temperatures close to  $T_g$ . These experiments might be also time consuming if the value of diffusivity is small. Subsequently, IGC was found to be a reliable and fast technique for determining activity coefficients and diffusivities, especially at high polymer concentrations. Indeed, IGC-based measurements can be completed in a relatively short time, and it is feasible to measure the diffusion coefficient at a level of  $10^{-13} \text{ cm}^2 \text{ s}^{-1}$  [60,61].

Capillary column IGC was used to determine the diffusivity, solubility and transport properties of various test solutes in polymers and polymeric mixtures. These

experiments might be carried out at finite concentration and infinite dilution. Faridi *et al.* [62] demonstrated the validity of IGC in comparison with gravimetric sorption methods. The procedure was introduced by Pawlisch *et al.* [63,64], and later fruitfully developed by Danner and coworkers [62,65–69]. Tihminlioglu and Danner [65] presented an equation that enabled the determination of parameters expressing the transport properties of the system:

$$\frac{CL}{C_o u} = \exp\left(\frac{1}{2\Gamma}\right) \times \exp\left[-\left(\frac{1}{4\Gamma^2} + \frac{S}{\Gamma} + \frac{2\sqrt{S}}{\alpha\beta\Gamma}\right) \tanh(\beta\sqrt{S})\right] \quad (10.30)$$

where:

$$\Gamma = \frac{D_g}{uL} \quad \alpha = \frac{R}{K(1-\gamma)\tau} \quad \beta^2 = \frac{\tau^2}{D_p t_c}$$

where  $\tau$  is the thickness of the polymer film,  $K$  is equal to  $dC'/dC$ ,  $S$  is the Laplace operator, and  $D_g$  and  $D_p$  are the gas-phase and polymer-phase diffusion coefficients, respectively. The elution profile is a function of three parameters  $\alpha$ ,  $\beta$ , and  $\Gamma$ , where  $\alpha$  is inversely related to the partition coefficient,  $\beta$  is inversely related to the polymer diffusion coefficient, and  $\Gamma$  depends on the gas-phase diffusion coefficient.  $\gamma$  is the true mole fraction obtained after correction for gas-phase non-ideality and compressibility effects [68,70].

Equation (10.30) is an extension of an equation introduced by Pawlisch [63,64], by addition of the  $(1-\gamma)$  term in the  $\alpha$  parameter [36]. This expresses the change in velocity with concentration (sorption effect); the  $\gamma$  parameter is equal to zero at infinite dilution.

The Pawlisch model [63] was applied, for example, to calculate the partition coefficient and diffusion coefficients of a series of solvents in PMMA-*co*-BMA (poly(methyl methacrylate-*co*-butyl methacrylate)) at infinite dilution [66]. Values of  $K$  and  $D_p$  that best fitted the experimental data were found, and the model predicted perfectly the system behavior. The Vrentas–Duda free volume theory was found to correctly correlate diffusion data above  $T_g$ .

Zhang *et al.* [71] employed a packed-column IGC technique to determine the activity coefficients and diffusivities of small molecules in phenol resins. For this, they applied the Romdhane–Danner approach for data analysis, and the Braun–Guillet approach to determine the thickness of the polymer layer on the support. Subsequently, the authors reported that the IGC-derived diffusivity data were consistent with the theoretical data obtained from the Romdhane–Danner approach, and might be further used to predict the temperature- and concentration-dependence of diffusivity by the free volume theory.

Cava *et al.* [72] applied the IGC technique to examine the effect of moisture on the transport properties of several low-molecular-weight alcohols through high-barrier copolymers. The application of Romdhane–Danner methods allowed an estimation of the diffusion coefficient  $D_p$  at different humidity conditions, that is, at various values of relative humidity (%RH). The sorption of water by the

material being examined caused increases in the partition and diffusion coefficients of the alcohols in the case of the copolymer. The values of partition coefficient for larger molecules were the most sensitive, but for  $D_p$  the effect was opposite, with diffusion through the water-conditioned sample being faster for smaller alcohol molecules. An abrupt increment of  $D_p$  for all the samples was observed between 35% and 47% RH, but this was attributed to a water-induced plasticization of the copolymer.

Zhao *et al.* [73] used the van Deemter equation to determine the infinite dilution diffusion coefficient for several *n*-alkanes in crosslinked silicone rubber. The infinite diffusion coefficient was calculated from:

$$D^\infty = \frac{8d_p^2}{\pi^2 C} \cdot \frac{k}{(1+k)^2} \quad (10.31)$$

where  $d_p$  denotes the thickness of the stationary phase (the examined material), and  $k$  is the retention coefficient. The thickness of the polymer coated onto the support was calculated from:

$$d_p = \frac{w_p \rho_d d_d}{6 \rho_p w_d} \quad (10.32)$$

where  $w_p$  and  $\rho_p$  denote the mass and density of polymer, respectively, while  $w_d$ ,  $\rho_d$  and  $d_d$  are the mass, density, and average diameter of the support. The constant  $C$  is related to column characteristics through the well-known van Deemter equation [74]. The authors proved that the diffusion coefficient would depend on the temperature of the experiment, the molecular weight of the solvent, and the concentration of crosslinking agent.

Hamdan *et al.* [75,76] developed and applied a model for the accurate measurement of polymer-phase diffusion coefficients in polymer-solvent systems. A general model was developed which took into account the effect of Taylor dispersion on pulse dispersal in IGC experiments. It was shown that, close to the glass temperature of the polymers, the Taylor dispersion had a negligible effect over a wide range of  $\gamma$  (the concentration of the solute in the gas phase). Hence, it was concluded that, for high values of  $D_p$ , higher L/R (length/radius of the capillary column) ratios than were earlier anticipated should be used to minimize the Taylor dispersion effect. It must be noted that the Hamdan *et al.* model should be used at low  $\gamma$  and  $\beta$  values (related to  $D_p$  by Eq. (10.9) in Ref. [76]), when the Taylor dispersion effect has a significant effect on the elution profiles.

R.Y.M. Huang *et al.* [77] designed a new rectangular thin-channel column dedicated to IGC experiments for determining the partition and diffusion coefficients of small molecules in polymer membranes. The main advantages of this column are the ease of preparation of stationary phase (thin polymer layer), the uniform distribution of polymer thickness, and repeated use. Huang and coworkers used the column to determine diffusion and partition coefficients of ethanol and propanol-1 in cellulose diacetate and sulfonated poly(ether ether ketone).

## 10.7

**Usefulness of IGC: Applications of IGC-Derived Parameters in the Characterization of Various Systems**

Since the first use of Flory–Huggins theory, many authors have applied the interaction parameters  $\chi_{12}^{\infty}$  and  $\chi'_{23}$  for the characterization of polymer systems.

When Olabisi [49] used IGC to study polymer–polymer miscibility in the molten state, he used the  $\chi'_{23}$  parameter to examine miscibility in poly( $\epsilon$ -caprolactone)-poly(vinyl chloride) (PCL-PVC) blends. Although the values of  $\chi'_{23}$  were seen to vary with the probe, all those obtained were negative, which meant that the polymers had been well mixed.

At this point, mention should be made of the reversed-flow gas chromatography technique, a version of IGC that has been applied successfully to the measurement of activity coefficients in polymer solutions [78], and also for determining Flory–Huggins interaction parameters and solubility parameters in polymer–solvent systems [79].

Zhao and Choi [51] measured the Flory–Huggins interaction parameters of two well-known immiscible binary polyolefin blends consisting of high-density polyethylene (HDPE) and isotactic polypropylene (i-PP), and of HDPE and atactic polystyrene (a-PS). These blends were studied at three different concentrations over a temperature range of 170 to 230 °C. The authors proposed the use of a single common reference volume to obtain solvent-independent  $\chi'_{23}$  values. The interaction parameters obtained were in the range of 0.04 to 0.13 for the HDPE/i-PP blends, and 0.04 to 0.19 for the HDPE/a-PS blends, which was consistent with values obtained with neutron reflectivity measurements. The  $\chi'_{23}$  values obtained indicated that both blends were immiscible in the melt state, which was in good agreement with findings of other groups.

In another study, J.-C. Huang [12] tested two copolymer systems of poly(vinyl acetate); poly(dimethylsiloxane) and the copolymers as mixtures of two homopolymers. When two components are thermodynamically unfavorable in terms of their miscibility, their interaction parameters will be positive; hence, for polymer mixtures a small but positive  $\chi'_{23}$  could indicate an immiscible system. Huang also showed that a difference in interaction energy between the functional groups of solutes and solvent mixtures could lead to an apparent solvent solubility parameter that was different from the volume average of the components. An equation was derived to relate the probe dependency with deviation of the solubility parameter. By plotting  $\varphi_2\varphi_3RT(\chi_{23}/V_2)$  versus the solubility parameter of solutes, a straight line could be obtained with a slope that was proportional to the deviation of the solvent solubility parameter. The plot was shown to yield negative slopes for miscible polymer blends, but when there was an unfavorable interaction between two solvents an opposite situation would be observed.

Milczewska and Voelkel used IGC to study polymer compositions and interactions between polymer and filler. For this, they determined Flory–Huggins parameters  $\chi_{12}^{\infty}$  and  $\chi'_{23}$  for various compositions with inorganic fillers, and tested the procedure proposed by Zhao-Choi to calculate the solvent-independent  $\chi'_{23}$

parameter. The results obtained from the “classical equation” and modified Zhao-Choi were compared [46]. Subsequently, the authors used the Zhao-Choi procedure for compositions of polybutadiene-urethane oligomer filled with modified silica [80]; poly(ether urethane)/modified carbonate silicate fillers [52]; and polyethylene with modified silica fillers [81], among others. The values of  $\chi'_{23}$  for almost all of the examined systems were below 0.5, and indicated strong interactions between the components. An application of the procedure proposed by Zhao-Choi allowed the  $\Delta\chi$  effect to be eliminated.

Galdamez *et al.* [67] have determined polymer-solvent interactions, as well as partition and diffusion coefficients for various solutes in poly(styrene-*co*-acrylonitrile). For this, they used the results of thermodynamic investigations to determine the degree of compatibility between poly(styrene-*co*-acrylonitrile), and found aromatic solvents to be the most suitable for the examined copolymer. The values of partition coefficients depended slightly on the presence of acrylonitrile groups, but the diffusion coefficients of the migrating species were decreased systematically. The same authors also highlighted the possibility of using IGC to examine multi-component systems. Similar results were reported by Galdamez *et al.* [66] for mixtures of tetrahydrofuran and cyclohexane in PVAc. Taken together, these results can be seen as an important extension of IGC applications to the examination of “real” systems.

## 10.8

### Advantages and Drawbacks of IGC

The usefulness and applicability of IGC techniques have been stressed on many occasions. Charmas and Leboda [20] noted that “. . . IGC is an excellent, quick and precise method for obtaining data . . .”. However, it might lead to correct or incorrect results, depending on the model applied, experimental data evaluation and selection, the careful selection of physico-chemical data for both solvents and materials examined (e.g., the density of the polymer) and, finally, the correct calculation procedures. It may also be worth mentioning the suggestion of Santos and Guthrie [21]: “All of these approaches have valuable advantages and relevant drawbacks. Thus, it is recommended the simultaneous use of several alternative approaches in order to corroborate the experimental results, analyses and theoretical predictions”.

Today, the reduced number of test molecules with known and reliable physico-chemical parameters, as noted by Ansari and Price [82], imposes serious limitations in the ability to select adequate probe substances. This might be due to a high activity of the examined material and a nonreversible adsorption of the test solute onto the material being examined. Thielmann *et al.* [83] also stressed that high-concentration pulse measurements are often difficult due to problems with kinetics. Likewise, in the case of a strong interaction (chemisorption), the total molecules adsorbed cannot be eluted at temperatures under which the experiments are conducted.

There remain problems also with the collection of experimental data at high-concentration intervals, and at very high concentrations the behavior of the interaction parameter of polymer–solvent systems tends to be unsatisfactory [84]. Another source of error might be the nonuniform coating of the stationary phase on the support, as well as nonuniform packing throughout the column [76].

The results obtained using IGC methods are very often different from those obtained using, for example, contact angle measurements of liquids [85,86]. However, the tendency for these values to change, perhaps due to modifications of the material, is at least consistent.

## References

- Lloyd, D.R., Ward, T.S., and Schreiber, H.P. (eds) (1989) *Inverse Gas Chromatography of Polymers and Other Materials*, ACS Symposium Series 391, American Chemical Society, Washington, DC.
- Belgacem, M.N. and Gandini, A. (1999) IGC as a tool to characterize dispersive and acid-base properties of the surface of fibers and powders, in *Interfacial Phenomena in Chromatography* (ed. E. Pefferkorn), Marcel Dekker, New York, pp. 41–124.
- Voelkel, A. (1991) Inverse gas chromatography: characterization of polymers, fibers, modified silicas, and surfactants. *Crit. Rev. Anal. Chem.*, **22**, 411–439.
- Thielmann, F. (2004) Introduction into the characterization of porous materials by inverse gas chromatography. *J. Chromatogr. A*, **1037**, 115–123.
- Voelkel, A. (1996) Inverse gas chromatography in examination of acid-base and some other properties of solids, in *Adsorption on New and Modified Inorganic* (eds A. Dąbrowski and V.A. Tertykh), Elsevier, Amsterdam, pp. 465–477.
- Sun, C. and Berg, J.C. (2003) A review of the different techniques for solid surface acid–base characterization. *Adv. Colloid Interface Sci.*, **105**, 151–175.
- Voelkel, A., Strzemiecka, B., Adamska, K., Milczewska, K., and Batko, K. (2009) Surface and bulk characteristics of polymers by means of inverse gas chromatography, in *Polymeric Materials* (eds A. Nastasovic and S. Jovanovic), Research Signpost, pp. 71–102.
- Wu, R., Que, D., and Al-Saigh, Z.Y. (2007) Surface and thermodynamic characterization of conducting polymers by inverse gas chromatography II. Polyaniline and its blend. *J. Chromatogr. A*, **1146**, 93–102.
- Smidsrød, O. and Guillet, J.E. (1969) Study of polymer-solute interactions by gas chromatography. *Macromolecules*, **2** (3), 272–277.
- Al-Ghamdi, A. and Al-Saigh, Z.Y. (2000) SEBS triblock copolymer–solvent interaction parameters from inverse gas chromatography measurement. *J. Polym. Sci., Part B: Polym. Phys.*, **38**, 1155–1166.
- Zou, Q.C., Zhang, S.L., Wang, S.M., and Wu, L.M. (2006) Investigation of thermodynamic properties of poly (methylethacrylate-co-n-butylacrylate-co-cyclopentyl styryl-polyhedral oligomeric silsesquioxane) by inverse gas chromatography. *J. Chromatogr. A*, **1129**, 255–261.
- Huang, J.-C. (2011) Probe dependency of segmental interaction parameters in copolymers by inverse gas chromatography. *J. Appl. Polym. Sci.*, **119**, 719–725.
- Domańska, U. and Żolek-Tryznowska, Z. (2010) Measurements of mass-fraction activity coefficient at infinite dilution of aliphatic and aromatic hydrocarbons, thiophene, alcohols, water, ethers, and ketones in hyperbranched polymer, Boltorn H2004, using inverse gas chromatography. *J. Chem. Thermodyn.*, **42**, 363–370.
- Milczewska, K. and Voelkel, A. (2002) Characterization of the interactions in polymer–filler systems by inverse gas



- chromatography. *J. Chromatogr. A*, **969**, 255–259.
- 15 Tümssek, F., Börekçi, M., Yazıcı, D.T., and Aşkın, A. (2011) Examination of polystyrene by inverse GC: Part 2. Above glass transition temperature. *Chromatographia*, **73**, 117–122.
- 16 Ovejero, G., Pérez, P., Romero, M.D., Díaz, I., and Díez, E. (2009) SEBS triblock copolymer–solvent interaction parameters from inverse gas chromatography measurement. *Eur. Polym. J.*, **45**, 590–594.
- 17 Fall, J., Milczewska, K., and Voelkel, A. (2001) Characterization of mineral oil/polyester, mineral oil/poly- $\alpha$ -olefin mixtures by inverse gas chromatography. *J. Mater. Chem.*, **11**, 1042–1046.
- 18 Grobler, A. and Báizis, G. (1974) Computer program for a statistical calculation of retention indices. *J. Chromatogr. Sci.*, **12**, 57–58.
- 19 Nastasovic, A. and Onija, A.E. (2008) Determination of glass temperature of polymers by inverse gas chromatography. *J. Chromatogr. A*, **1195**, 1–15.
- 20 Charmas, B. and Leboda, R. (2000) Effect of surface heterogeneity on adsorption on solid surfaces. Application of inverse gas chromatography in the studies of energetic heterogeneity of adsorbents. *J. Chromatogr. A*, **886**, 133–152.
- 21 Santos, J.M.R.C.A. and Guthrie, J.T. (2005) Analysis of interactions in multicomponent polymeric systems: The key-role of inverse gas chromatography. *Mater. Sci. Eng.*, **R50**, 79–107.
- 22 Utracki, L.A., Walsh, D.J., and Weiss, R.A. (eds) (1989) *Multiphase Polymers: Blends and Ionomers*, American Chemical Society, pp. 1–35.
- 23 Rätzsch, M., Haudel, G., Pompe, G., and Meyer, E. (1990) Interaction between polymers. *J. Macromol. Sci. Chem.*, **A27**, 1631–1655.
- 24 Lee, M.H., Fleischer, C.A., Morales, A.R., Koberstein, J.T., and Koningsveld, R. (2001) The effect of end groups on thermodynamics of immiscible polymer blends. 2. Cloud point curves. *Polymer*, **42**, 9163–9172.
- 25 Flory, P.J. (1942) Thermodynamics of high polymer solutions. *J. Chem. Phys.*, **10**, 51–61.
- 26 Huggins, M.L. (1942) Theory of solutions of high polymers. *J. Am. Chem. Soc.*, **64**, 1712–1719.
- 27 Barton, A.F.M. (2000) *CRC Handbook of Solubility Parameter and Other Cohesion Parameters*, CRC Press, Boca Raton, FL.
- 28 Voelkel, A. and Janas, J. (1993) Solubility parameters of broad and narrow distributed oxyethylates of fatty alcohols. *J. Chromatogr. A*, **645**, 141–151.
- 29 Voelkel, A. and Fall, J. (1995) Influence of prediction method of the second virial coefficient on inverse gas chromatographic parameters. *J. Chromatogr. A*, **721**, 139–145.
- 30 Al-Saigh, Z.Y. (1999) Inverse gas chromatographic characterization of poly(ethylene oxide). *Polymer*, **40**, 3479–3485.
- 31 Kozłowska, M.K., Domańska, U., Lempert, M., and Rogalski, M. (2005) Determination of thermodynamic properties of isotactic poly(1-butene) at infinite dilution using density and inverse gas chromatography. *J. Chromatogr. A*, **1068**, 297–305.
- 32 Huang, J.-C. (2006) Anomalous solubility parameter and probe dependency of polymer–polymer interaction parameter in inverse gas chromatography. *Eur. Polym. J.*, **42**, 1000–1007.
- 33 Milczewska, K., Voelkel, A., and Jęczalik, J. (2001) Characterization of the interactions in polymer/silica systems by inverse gas chromatography. *Macromol. Symp.*, **169**, 45–55.
- 34 Milczewska, K., Voelkel, A., and Jęczalik, J. (2003) The use of Flory-Huggins parameters to characterization of polymer/filler interactions. *Macromol. Symp.*, **194**, 305–311.
- 35 Huang, J.-C. (2009) Multiparameter solution model and evaluation of polymer–polymer miscibility using inverse gas chromatography data. *J. Appl. Polym. Sci.*, **113**, 4085–4091.
- 36 Conder, J.R. and Young, C.L. (1979) *Physicochemical Measurements by Gas Chromatography*, John Wiley & Sons, Chichester.
- 37 Voelkel, A., Strzemińska, B., Adamska, K., and Milczewska, K. (2009) Inverse gas chromatography as a source of physicochemical data. *J. Chromatogr. A*, **1216**, 1551–1566.

- 38 Dymond, J.H. and Smith, E.B. (1980) *The Virial Coefficients of Pure Gases and Mixtures*, Clarendon Press, Oxford.
- 39 Fernandez-Sanchez, E., Fernandez-Torres, A., Garcia-Dominguez, J.A., Santiuste, J.M., and Pertierra-Rimada, E. (1988) Solubility parameters of gas chromatographic mixed stationary phases. *J. Chromatogr.*, **457**, 55–71.
- 40 Al-Saigh, Z.Y. and Munk, P. (1984) Study of polymer-polymer interaction coefficients in polymer blends using inverse gas chromatography. *Macromolecules*, **17** (4), 803–809.
- 41 Huang, J.-C. (2003) Determination of polymer-polymer interaction parameters using inverse gas chromatography. *J. Appl. Polym. Sci.*, **90**, 671–680.
- 42 Huang, J.-C. (2004) Concentration dependency of interaction parameter between PVC and plasticizers using inverse gas chromatography. *J. Appl. Polym. Sci.*, **91**, 146–156.
- 43 Ourdani, S. and Amrani, F. (2002) Study of the miscibility of poly(styrene-co-4-vinylbenzoic acid) with poly(ethyl methacrylate) or with poly(ethyl methacrylate-co-(2-N,N-dimethylaminoethyl) methacrylate) by inverse gas chromatography. *J. Chromatogr. A*, **969**, 287–299.
- 44 Al-Saigh, Z.Y. (1997) Inverse gas chromatography for the characterization of polymer blends. *Int. J. Polym. Anal. Charact.*, **3**, 249–291.
- 45 Milczewska, K. (2001) Charakterystyka oddziaływań polimer-napełniacz metodą odwróconej chromatografii gazowej. PhD thesis, Poznan University of Technology, Poznan (in Polish).
- 46 Milczewska, K. and Voelkel, A. (2006) The use of Flory-Huggins parameters as a measure of interactions in polymer-filler systems. *J. Polym. Sci., Part B: Polym. Phys.*, **44**, 1853–1862.
- 47 Prolongo, M.G., Masegosa, R.M., and Horta, A. (1989) Polymer-polymer interaction parameter in the presence of a solvent. *Macromolecules*, **22** (11), 4346–4351.
- 48 Shi, Z.H. and Schreiber, H.P. (1991) On the application of inverse gas chromatography to interactions in mixed stationary phases. *Macromolecules*, **24** (12), 3522–3527.
- 49 Olabisi, O. (1975) Polymer compatibility by gas-liquid chromatography. *Macromolecules*, **8**, 316–322.
- 50 Lezcano, E.G., Prolongo, M.G., and Coll, C.S. (1995) Characterization of the interactions in the poly(4-hydroxystyrene)/poly( $\epsilon$ -caprolactone) system by inverse gas chromatography. *Polymer*, **36** (3), 565–573.
- 51 Zhao, L. and Choi, P. (2002) Measurement of solvent-independent polymer-polymer Flory-Huggins interaction parameters with the use of non-random partitioning solvents in inverse gas chromatography. *Polymer*, **43**, 6677–6681.
- 52 Milczewska, K. and Voelkel, A. (2008) Use of Flory-Huggins parameters in the characterization of polymer-filler compositions. *J. Appl. Polym. Sci.*, **107**, 2877–2882.
- 53 Huang, J.-C. and Deanin, R.D. (2004) Concentration dependency of interaction parameter between PVC and plasticizers using inverse gas chromatography. *J. Appl. Polym. Sci.*, **91**, 146–156.
- 54 Su, C.S. and Patterson, D. (1977) Determination by gas-liquid chromatography of the polystyrene-poly(vinyl methyl ether) interaction. *Macromolecules*, **10**, 708–710.
- 55 Voelkel, A., Milczewska, K., and Héberger, K. (2006) Inverse gas chromatographic and chemometric tools for determination of interactions between the components of polymeric composition. *Anal. Chim. Acta*, **559**, 221–226.
- 56 Héberger, K. (1999) Evaluation of polarity indicators and stationary phases by principal component analysis in gas-liquid chromatography. *Chemom. Intell. Lab. Syst.*, **47**, 41–49.
- 57 Héberger, K., Milczewska, K., and Voelkel, A. (2001) Principal component analysis of polarity and interaction parameters in inverse gas chromatography. *J. Chromatogr. Sci.*, **39**, 375–384.
- 58 Malinowski, E.R. (1991) *Factor Analysis in Chemistry*, 2nd edn, John Wiley & Sons, New York.
- 59 Wold, S., Esbensen, K., and Geladi, P. (1987) Principal component analysis. *Chemom. Intell. Lab. Syst.*, **2**, 37–52.

- 60 Arnould, D. and Laurence, R.I. (1989) Solute diffusion in polymers by capillary inverse gas chromatography, in *Inverse Gas Chromatography* (eds D.R. Lloyd, T.C. Ward, H.P. Schreiber), American Chemical Society, Washington, DC, pp. 87–120.
- 61 Surana, R.K., Danner, R.P., Tihminlioglu, F., and Duda, J.L. (1997) Evaluation of inverse gas chromatography for prediction and measurement of diffusion coefficients. *J. Polym. Sci., Part B: J. Polym. Phys.*, **35**, 1233–1240.
- 62 Faridi, N., Romdhane, H., Danner, R.P., and Duda, J.L. (1994) Diffusion and sorption in ethylene-propylene copolymers: Comparison of experimental methods. *Ind. Eng. Chem. Res.*, **33** (10), 2483–2491.
- 63 Pawlisch, C.A., Bric, J.R., and Laurence, R.L. (1987) Solute diffusion in polymers. 1. The use of capillary column inverse gas chromatography. *Macromolecules*, **20** (7), 1564–1578.
- 64 Pawlisch, C.A., Macris, A., and Laurence, R.L. (1988) Solute diffusion in polymers. 2. Fourier estimation of capillary column inverse gas chromatography data. *Macromolecules*, **21** (6), 1685–1698.
- 65 Tihminlioglu, F. and Danner, R.P. (1999) Application of inverse gas chromatography to the measurement of diffusion and phase equilibria in polyacrylate–solvent systems. *J. Chromatogr. A*, **845**, 93–101.
- 66 Galdamez, J.R., Danner, R.P., and Duda, J.L. (2007) Application of mass spectrometer-inverse gas chromatography to study polymer–solvent diffusivity and solubility. *J. Chromatogr. A*, **1157**, 399–407.
- 67 Galdamez, J.R., Kernion, S.J., Duda, J.L., and Danner, R.P. (2008) Determination of thermodynamic and transport properties of a polystyrene-co-acrylonitrile copolymer by infinite and finite concentration IGC. *Polymer*, **49** (12), 2873–2879.
- 68 Scicolone, J., Davis, P.K., Danner, R.P., and Duda, J.L. (2006) Solubility and diffusivity of solvents by packed column inverse gas chromatography. *Polymer*, **47**, 5364–5370.
- 69 Tihminlioglu, F., Surana, R.K., Danner, R.P., and Duda, J.L. (1997) Finite concentration inverse gas chromatography: Diffusion and partition measurements. *J. Polym. Sci., Part B: Polym. Phys.*, **35**, 1279–1290.
- 70 Eser, H. and Tihminlioglu, F. (2005) Solubility and diffusivity of solvents and nonsolvents in poly(methyl methacrylate co butyl methacrylate). *Fluid Phase Equilib.*, **237**, 68–76.
- 71 Zhang, S., Tsuboi, A., Nakata, H., and Ishikawa, T. (2002) Activity coefficients and diffusivities of solvents in polymers. *Fluid Phase Equilib.*, **194–197**, 1179–1189.
- 72 Cava, D., Lagaron, J.M., Martinez-Gimenez, F., and Gavara, R. (2007) Inverse gas chromatography study on the effect of humidity on the mass transport of alcohols in an ethylene-vinyl alcohol copolymer near the glass transition temperature. *J. Chromatogr. A*, **1175**, 267–274.
- 73 Zhao, C., Li, J., Jiang, Z., and Chen, C. (2006) Measurement of the infinite dilution diffusion coefficients of small molecule solvents in silicone rubber by inverse gas chromatography. *Eur. Polym. J.*, **42**, 615–624.
- 74 Van Deemter, J.J. and Inderweg, F.J. (1956) Longitudinal diffusion and resistance to mass transfer as causes of nonideality in chromatography. *Chem. Eng. Sci.*, **5**, 271–289.
- 75 Hamdan, E., Milthorpe, J.F., and Lai, J.C.S. (2005) New approach for evaluation of capillary column inverse gas chromatography. *J. Chromatogr. A*, **1078**, 144–151.
- 76 Hamdan, E., Milthorpe, J.F., and Lai, J.C.S. (2005) The influence of nonuniform coating and Taylor dispersion on the evaluation of capillary column inverse gas chromatography. *J. Chromatogr. A*, **1091**, 137–144.
- 77 Huang, R.Y.M., Shao, P., Nawawil, G., Feng, X., and Burns, C.M. (2001) Measurements of partition, diffusion coefficients of solvents in polymer membranes using rectangular thin-channel column inverse gas chromatography (RTCCIGC). *J. Membr. Sci.*, **188**, 205–218.
- 78 Agathonos, P. and Karaiskakis, G. (1988) Measurement of activity coefficients in polymer solutions by the reversed-flow technique. *Chromatographia*, **25**, 453–454.
- 79 Agathonos, P. and Karaiskakis, G. (1989) Thermodynamic study of polymer solvent systems by reversed-flow gas

- chromatography. *J. Appl. Polym. Sci.*, **37**, 2237–2250.
- 80 Milczewska, K. and Voelkel, A. (2006) Chromatograficzne badanie oddziaływań w układach polimerowych. *Przemysł Chemiczny*, **85**, 953–955 (in Polish).
  - 81 Milczewska, K. and Voelkel, A. (2008) The use of Flory–Huggins parameters in characterization of polymer–filler compositions. *Mater. Sci. Forum*, **587–588**, 667–671.
  - 82 Ansari, D.M. and Price, G.J. (2004) Correlation of mechanical properties of clay filled polyamide mouldings with chromatographically measured surface energies. *Polymer*, **45** (11), 3663–3670.
  - 83 Thielmann, F., Butler, D.A., and Williams, D.R. (2001) Characterization of porous materials by finite concentration inverse gas chromatography. *Colloids Surf. A: Phys. Eng. Asp.*, **187–188**, 267–272.
  - 84 Etxabarren, C., Iriarte, M., Uriarte, C., Etxeberria, A., and Iruin, J.J. (2002) Polymer–solvent interaction parameters in polymer solutions at high polymer concentrations. *J. Chromatogr. A*, **969**, 245–254.
  - 85 Ahfat, N.M., Buckton, G., Burrows, R., and Ticehurst, M.D. (2000) An exploration of inter-relationships between contact angle, inverse phase gas chromatography and triboelectric charging data. *Eur. J. Pharm. Sci.*, **9**, 271–276.
  - 86 Garnier, G. and Glasser, W.G. (1994) Measurement of the surface free energy of amorphous cellulose by alkane adsorption: A critical evaluation of inverse gas chromatography (IGC). *J. Adhesion*, **46**, 165–180.

## 11

### Thermal Analysis in Polymer Blends

Ramesh T. Subramaniam and R. Shanti Rajantharan

#### 11.1

##### Introduction to Polymer Blends

Polymer blending is a technique of interest that has captured the attention of numerous research groups since the twentieth century to the present day. Pioneering studies in the development of high-performance polymer electrolytes has mainly been focused on the use of single types of preformed polymers, such as poly(ethylene oxide) (PEO), poly(methyl methacrylate) (PMMA), and poly(vinyl chloride) (PVC). However, as the properties of the homopolymer-based electrolytes were unable to support the applications of high-conducting electronic devices in many ways, an alternative approach was sought which involved the blending of two or more preformed polymers of different natures to form an ionic conducting matrix [1,2].

During subsequent years, the conducting matrix underwent development by employing copolymers synthesized from mixtures of monomers, and consequently the formulation of brand new polymers via the polymerization process captured the attention of many research groups. Unfortunately, however, most synthetic efforts cannot guarantee the creation of polymers that will meet the entire needs of research groups in terms of electrical, structural, mechanical, and thermal properties.

The polymerization process is not straightforward, and cannot be easily be performed without a full knowledge of the field of polymer synthesis. Indeed, a large number of contributing factors must be considered before attempting to synthesize copolymers, that include: (i) the type of monomers and compositions to be used; (ii) selection of the medium; (iii) the temperature of the synthesizing process; and (iv) the time required for synthesis to be completed. The problem persists however that, although excellent formulations can be prepared by optimizing the conditions of synthesis, the synthesized polymers may not possess all of the desired properties.

Thus, the technique of *polymer blending* has been developed as a more convincing and practicable method to create high-performance polymer electrolytes membrane with known properties. Moreover, the polymer blends will possess

properties that are complementary to those of the individual component homopolymers. The blending technique may also have significant effects on improvements in the thermal properties of polymer electrolytes [3], while at the same time achieving all of the desired physical properties within a compositional regime.

#### 11.1.1

##### **The Principle of Polymer Blending**

Polymer blends are the intimate mixtures formed between different types of commercially available polymers with no covalent bond connecting the individual component polymers [4,5]. This type of mixture is formed either by melt-mixing or via a simple solution-blending technique. The property profile of a polymer blend is complementary to the useful characteristics of each component polymers, and superior to those of its single homopolymers.

The polymer blends can be further categorized as two types: homogeneous and heterogeneous blends. The polymer blend mixtures may appear in either homogeneous or heterogeneous phase on a microscopic scale, but should not exhibit any obvious inhomogeneity on the macroscopic scale [4,6]. The observation of these two different types of blended nature is related solely to the factors of miscibility and compatibility between the interacting component homopolymers.

Most of the polymer blending formulations are of the heterogeneous type, but several are homogeneous. The heterogeneous blends are immiscible and exhibit symptoms of polymer segregation as result of the incompatibility between the added components of homopolymers. However, those components of homopolymers that are miscible on mixing are identified as being compatible with each other and hence appear as a homogeneous solution. Some examples of heterogeneous polymer blends include:

- poly(methyl methacrylate)/poly(butadiene) (PMMA/PB)
- poly(vinyl chloride)/poly(methyl methacrylate) (PVC/PMMA)
- poly(styrene)/poly(ethylene) (PS/PE).

The polymer blends listed below represent examples of homogeneous type:

- poly(vinyl chloride)/poly(ethylene-co-vinyl acetate) (PVC/EVA)
- poly(methyl methacrylate)/poly(vinylidene fluoride) (PMMA/PVDF)
- poly(phenylene oxide)/poly(styrene) (PPO/PS).

A low degree of compatibility between the mixed components of homopolymers is a serious problem that is encountered in polymer blends. Consequently, compatibilizers are being increasingly incorporated into blend polymer solutions to provide a better miscibility of one component of the homopolymer in another polymer type. This reduces the tendency for any possible undesirable processes to take place in the polymer blends, such as the separation of phases, delamination, agglomeration or skinning and, ultimately, physical failure [4].

## 11.2 Experimental

A total of four different types of polymer electrolyte systems are formulated in this section. In System 1, the starting materials of PVC and poly(ethylene oxide) (PEO) were purchased from Fluka and Aldrich, respectively, while in System 2 a type of doping salt, lithium triflate ( $\text{LiCF}_3\text{SO}_3$ ; purchased from Aldrich) was added to the PVC/PEO blends. In System 3, the matrix of PVC/PEO- $\text{LiCF}_3\text{SO}_3$  was plasticized with two different types of plasticizer, namely dibutyl phthalate (DBP) and ethylene carbonate (EC), obtained from Aldrich and Fluka, respectively. In System 4, the formulation of composite polymer electrolyte was developed using a fumed silica ( $\text{SiO}_2$ ) powder with a particle size of 10–30 nm, as supplied by Wacker Chemie. Each of the above-mentioned formulations is prepared by dissolving the starting materials in tetrahydrofuran (THF; from J.T. Baker).

The four different types of formulated system, including the preparation method, are described in detail in the following subsections. All samples obtained from the four formulations presented in thin-film form, using a solution-casting technique.

### 11.2.1

#### System 1: PVC/PEO Blends

Of all the types of halogenated polymers, PVC is the most extensively studied. Some of PVC's excellent properties in terms of electrical and mechanical superiority have led to its wide range of use in the development of synthetic types of polymer electrolytes. Unfortunately, a lack of thermal properties has proved to be a barrier that has limited the use of PVC in energy-based applications that involve high-temperature processing. In order to improve the thermal profile of PVC, the homopolymer component is blended with another type of homopolymer that possesses a good thermal resistance towards heat, at a very high temperature. This blending technique is highly effective due to the excellent miscibility of PVC with various important types of homopolymer component [7–9].

Before blending a selective type of polymer component with PVC, it is important to take note of the thermal profile of the respective polymer component. In this studies, the thermal properties of PVC are improved by blending it with PEO, which begins to decompose at a very high temperature of 420 °C. The high heat resistivity of PEO has proved it to be the best type of homopolymer component for blending with PVC, as such blending not only suppresses the extreme heat sensitivity of PVC but also creates a matrix for high-temperature applications.

PEO was the first of the host polymers to be investigated for the development of polymer electrolyte systems, and these early findings led to recent studies of applications requiring very high-conducting systems that could be attributed to the highly crystalline nature of PEO. Indeed, the development of polymer electrolyte matrices utilizing PEO remains the focus of many research groups, owing to the polymer's water-soluble nature, high solvating power with metal ions, good

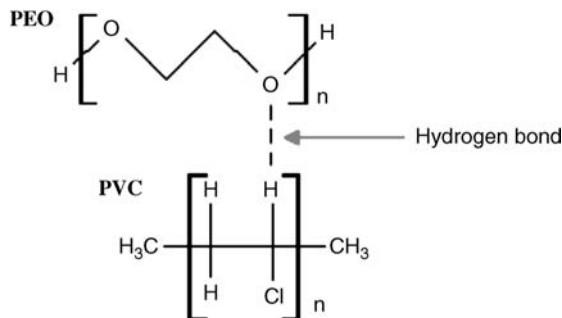


**Figure 11.1** Interpolymer hydrogen bonding between PEO and PVC.

processability, superior mechanical properties, and good thermal resistance. Thus, the blending of PVC with PEO has also been identified as an alternative approach to suppressing the limitations of PEO while sustaining its good properties.

The blending of PVC with PEO results in the formulation of a semicrystalline PVC/PEO matrix with improved properties that are complementary with the characteristics of each of the homopolymers. Some of the properties possessed by PVC and PEO that have set barriers for their individual use in the preparation of polymer electrolytes, have been identified as being suppressed in the PVC/PEO blend. This makes the matrix well-suited to applications in electronic devices, owing to its improved electrical, mechanical, and thermal characteristics.

This blending mixture is of the homogeneous type, and the miscibility of the blending mixture results from a compatibility between PVC and PEO, via hydrogen bond formation between the  $\alpha$ -hydrogen atoms in the weak proton-donating PVC with the proton-accepting ether oxygen in PEO [10–13]. A symmetry diagram of the formation of hydrogen bonds between PVC and PEO is shown in Figure 11.1.

The preparation of a homogeneous blend in System 1 is achieved by mixing the individual components of the homopolymer solutions, with PVC and PEO being dissolved separately in THF as solvent. The mixture is then stirred overnight to achieve maximum compatibility between the PVC and PEO, and this results in a homogeneous viscous blending solution. The latter can then be processed into a free-standing thin film by evaporating the THF solvent inside the desiccator, applying the technique of solvent casting.

The properties possessed by the PVC/PEO blend alone are insufficient to support its application in electronic devices, especially in terms of thermal resistance. Consequently, several different types of additive can be incorporated into the polymer blend for the purpose of formulating a matrix with a better thermal profile.

### 11.2.2

#### **System 2: PVC/PEO:LiCF<sub>3</sub>SO<sub>3</sub> Blends**

In System 2, the thermal properties of the PVC/PEO blend are tailored by the addition of LiCF<sub>3</sub>SO<sub>3</sub>, which is dissolved separately in THF prior to its addition to



the PVC/PEO blend solution mixture. The solution mixture is then stirred overnight to obtain complete miscibility of  $\text{LiCF}_3\text{SO}_3$  in the PVC/PEO blend solution. The solution mixture is then cast onto a Petri dish so as to obtain free-standing thin films, using a solvent casting technique. In these studies, two different proportions (20 and 50 wt%) of  $\text{LiCF}_3\text{SO}_3$  were incorporated into the PVC/PEO blend matrix, and their effects on the thermal properties of the matrix were evaluated.

### 11.2.3

#### **System 3: PVC/PEO- $\text{LiCF}_3\text{SO}_3$ -DBP:EC Blends**

In System 3, a mixed plasticizer solution of DBP and EC was added into the PVC/PEO- $\text{LiCF}_3\text{SO}_3$  matrix. The addition of an appropriate plasticizer into the PVC/PEO- $\text{LiCF}_3\text{SO}_3$  blend leads to the production of a matrix which is physically softer and more flexible. These features help to improve the electrical properties of the formulated matrix, although a negative aspect to this is that the matrix loses some of its thermal resistance properties (this point is discussed later in the chapter). The mechanically free-standing thin films for this formulation are prepared from blended solutions containing 10 wt% and 30 wt% EC, while the DBP content is held constant. This mixture solution is stirred overnight before carrying out the solution-casting procedure.

### 11.2.4

#### **System 4: PVC/PEO- $\text{LiCF}_3\text{SO}_3$ -DBP-EC: $\text{SiO}_2$ Blends**

In System 4, efforts were made to improve the thermal profile of the PVC/PEO- $\text{LiCF}_3\text{SO}_3$ -DBP:EC blend by incorporating  $\text{SiO}_2$  particles into the matrix. In this case the heat-stabilized  $\text{SiO}_2$  particles were suspended directly into the blend solution, which was stirred overnight at room temperature to achieve a homogeneous, viscous mixture. When the suspension was poured into a Petri dish and allowed to evaporate slowly inside a desiccator, the final product was a mechanically stable, free-standing thin film.

## 11.3

### **Instrumentation**

The characteristics of the developed polymer electrolytes were focused essentially on their thermal properties, with assessments made using a thermogravimetric analysis (TGA) technique (Rheometric Scientific TGA 1000 instrument). When the developed samples are subjected to this analytical technique, certain aspects must be considered, including: (i) the weight of the tested sample(s); (ii) the testing temperature range; (iii) the gaseous environment; and (iv) the heating rate.

## 11.3.1

**Sample Weight**

The first point to be considered is the weight of the tested sample. In TGA, the measurements are performed on a suitable dimension of cutting sections of polymer electrolyte films. For comparative studies, the weight of the sample cutting sections should fall within the range of 3–5 mg, and should be consistent among samples being compared. Indeed, if the weights of the samples to be compared are allowed to vary, then the thermal property data cannot be compared between samples. In the present system, all samples subjected to thermal analysis weighed approximately 5 mg.

## 11.3.2

**Testing Temperature Range**

Temperature is another important parameter to be considered before conducting the TGA. Different type of sample will have different testing temperature ranges, and normally the specific temperature range is identified by using either of two methods. The first method involves running the analysis from minimum to maximum temperatures and then narrowing down the temperature range where peaks are likely to be observed. The analysis is rerun at the narrowed temperature range. The second method is more reliable and practicable, whereby the testing temperature range of the samples is obtained from the literature or from previous investigations. The temperature may vary from 10 °C up to 550 °C, depending on the type of instrument used. The correct temperature range can only be identified by understanding the nature of the samples. Some samples can be oxidized at a lower temperature (perhaps as low as 200 °C), while some can resist up to a highest temperature of 450 °C. In the present study the influence of temperature on the thermal properties of the developed thin film samples was evaluated at between 10 °C and 320 °C.

## 11.3.3

**Gas Environment**

The appropriate selection of gas environment prior to TGA is crucial. Although few choices of gaseous environment are available (e.g., nitrogen, oxygen, helium), a correct gas selection must be made depending on the type of information that is intended to be collected from the sample. With studies accounting for a total weight loss of samples with temperature the analysis must be carried out under inert conditions; in this case a nitrogen atmosphere is preferable. This type of study cannot be executed under an oxygen environment due to the possible occurrence of secondary reactions. In this case, the observed weight loss might not be attributed solely to the decomposition of the sample of interest; rather, such loss may partly have resulted from the decomposition of secondary reaction products. In the present studies, all analyses were conducted under a nitrogen atmosphere.

## 11.3.4

**Heating Rate**

The heating rate is another prominent factor for discussion, the most commonly used rate being  $10^{\circ}\text{C min}^{-1}$ . The sample should not be heated from one temperature to another very rapidly, as some of the informative phenomena that occur during the temperature rise could go undetected. However, heating the sample at a lower rate is not advisable either, especially when the TGA is being carried out over a broader temperature scale, attributed to a longer experimental completion time. A lower heating rate can also be used very effectively when the analysis is performed over a shorter temperature range, when even small changes can be clearly observed. Typically, a heating rate of  $10^{\circ}\text{C min}^{-1}$  is used, due mainly to the limited experimental time that is generally available.

## 11.4

**Thermal Analysis**

The thermal analysis of polymers is based on changes in the thermal properties of a polymer sample as its temperature is increased when it is subjected to continuous heating. These properties of polymer electrolytes are especially important from an industrial point of view.

## 11.4.1

**Information Obtained from TGA**

In TGA, information on the heat-resistivity and thermal stability of a sample is obtained as a function of that sample being progressively subjected to heat. The heat-resistivity of a sample is based on its decomposition temperature ( $T_d$ ), whereas the thermal stability is obtained by calculating the sample's total weight loss. The heat-resistivity of a polymer indicates the ability of the chains in the polymer electrolyte matrix to sustain their original form when subjected to continuous heating. When the decomposition temperature is exceeded the sample will become heat-sensitive and undergo structural deformation, forming oxides; this will result in a weight loss and, in turn, will indicate the sample's thermal stability. An example of how the decomposition temperatures and percentage total weight loss are obtained, using the TGA thermogram of pure PVC, is shown in Figure 11.2.

## 11.4.2

**Thermal Process**

In TGA, two different types of degradation mechanism involving polymer electrolytes are observed, namely *dehydration* and *decomposition*. The dehydration process occurs at a temperature of  $100^{\circ}\text{C}$ , which corresponds to the evaporation of

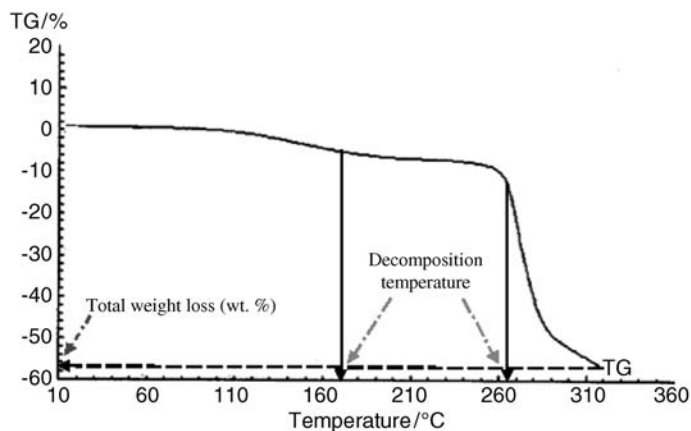


**Figure 11.2** The labeled TGA thermogram of pure PVC.

residual solvent and moisture [14]. However, any further increase in the temperature above 100 °C will lead to a depolymerization process, in which a radical loss in the sample's weight will be observed. Further subjecting the sample to heat, above its maximum  $T_d$ , will result in carbonization and ash formation [15].

#### 11.4.3

##### The Value of the TGA Information

Knowledge of the thermal properties of developed polymer electrolytes are important before determining their major applications, which mainly involve the fabrication of high-conducting electrochemical devices. These characteristics are due to the nature of the device, which may undergo self-heating when mobile ions are transported through and flow from the anode to the cathode. In time, the point at which heating occurs will become enlarged on heavy usage, and this can result in an explosion if the polymer continues to be used for excessive working periods. These effects highlight the need to monitor the safety aspects of electrochemical device usage at higher temperatures.

The importance of identifying the thermal properties of each developed system becomes apparent from the many reports on this subject. Studies have also been conducted on the thermal properties of polymer electrolytes composed of polymer blend matrices in the presence of a highly heat-stabilized component polymer. The latter type of formulation was found to have a better thermal profile when compared to homopolymer-type-based electrolytes.

A pioneering study conducted by Varughese and coworkers [16] revealed that the thermal properties of PVC are improved when it is blended with an appropriate amount of epoxidized natural rubber (ENR). The blending of ENR potentially inhibits the formation of chlorine free radicals as the PVC decomposes, thus eliminating the evolution of HCl that may promote chain dehydrochlorination.

Detailed studies on the influence of an increasing ENR content on the thermal stability of PVC/ENR blends have also been reported. Other evidence was obtained by Calandrelli and coworkers [17], who improved the thermal properties of the aromatic polyoxadiazole by blending it with a secondary homopolymer component, polyamide.

The thermal degradation of blends based on PVC, PMMA and PS was also monitored [4]. Recent studies of PMMA systems by Ramesh and coworkers showed that the low thermal resistance of PMMA was suppressed when it was blended with PVC [18], and suggested that the PMMA/PVC blend matrix is more heat-stable than a matrix formed by the PMMA homopolymer alone.

## 11.5

### Results and Discussion: Thermal Analysis

In TGA studies, an initial weight loss is generally observed to start above room temperature (ca. 70 °C), which corresponds to the desorption of residual solvent or moisture [15]. This process was not observed in any of the TGA curves of the tested samples up to 100 °C, which indicated that the thin films appeared to be dry. Whilst this process was omitted in the present studies, the contributing factors that induced a weight loss of the tested samples (starting at >100 °C) was considered by referring to the TGA curves in Figures 11.3 to 11.10.

#### 11.5.1

##### Pure PVC

The TGA curve of pure PVC film (see Figure 11.3) indicates that pure PVC undergoes degradation via a two-step process. The initial degradation process is seen to start above 110 °C and continue up to 220 °C. The most prominent degradation

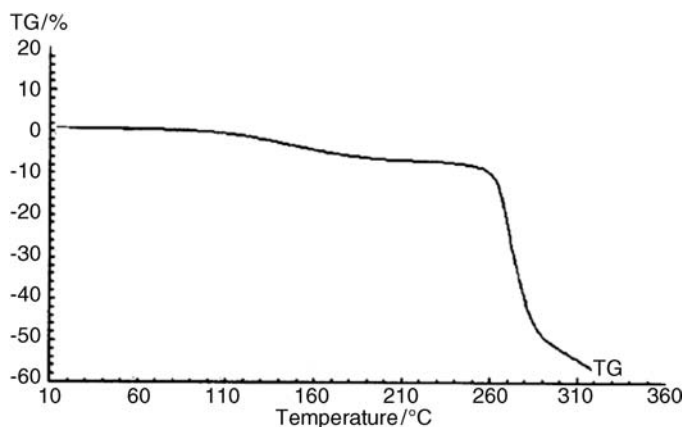


Figure 11.3 Thermogravimetric curve of pure PVC.

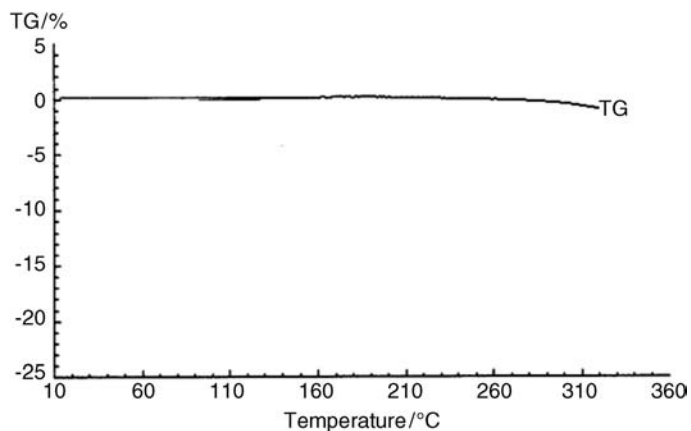


Figure 11.4 Thermogravimetric curve of pure PEO.

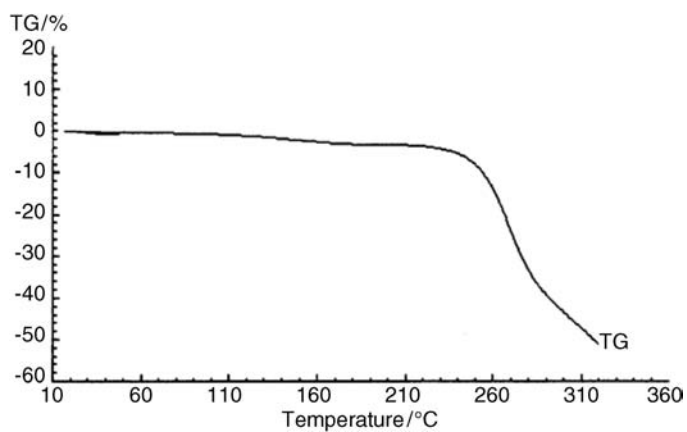


Figure 11.5 Thermogravimetric curve of PVC/PEO blend.

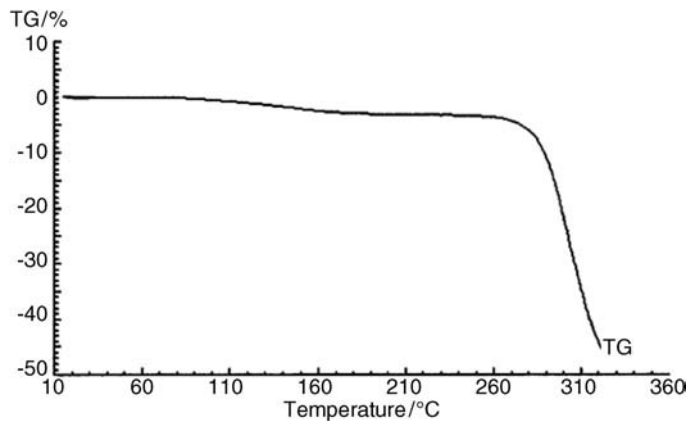


Figure 11.6 Thermogravimetric curve of PVC/PEO:LiCF<sub>3</sub>SO<sub>3</sub> (80 wt%:20 wt%).

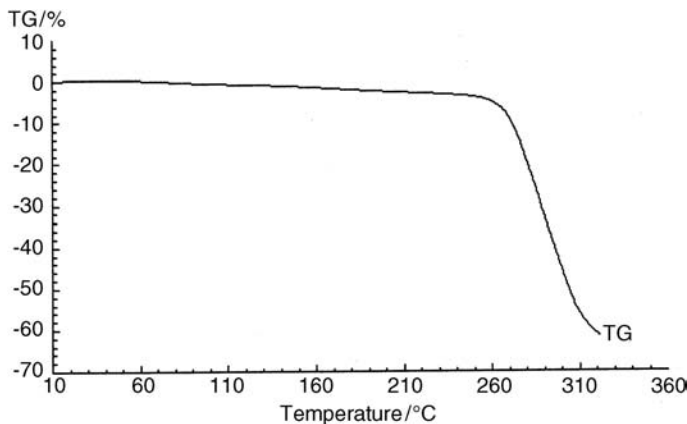


Figure 11.7 Thermogravimetric curve of PVC-PEO:LiCF<sub>3</sub>SO<sub>3</sub> (50 wt%:50 wt%).

occurs at about 170 °C, as evidenced by the observed slump in the TGA curve at that temperature, which induces a weight loss. The degradation process is initiated by the formation of free radicals of chlorine (Cl•), with the degradation product being obtained on the combustion of PVC [4]. As the temperature rises above 260 °C, the free radicals abstract the hydrogen atoms of the methylene group in PVC so that hydrogen chloride gas (HCl) is formed [4,19]. The HCl then catalyzes the dehydrochlorination reaction [18], leading to the production of polyene sequences with lengths ranging from six to 14 conjugated double bonds to a maximum of 30 units. The occurrence of the dehydrochlorination reaction is represented in Scheme 11.1.

The dehydrochlorination reaction may occur via either a radical or ionic mechanism, or it might even occur simultaneously following more than one

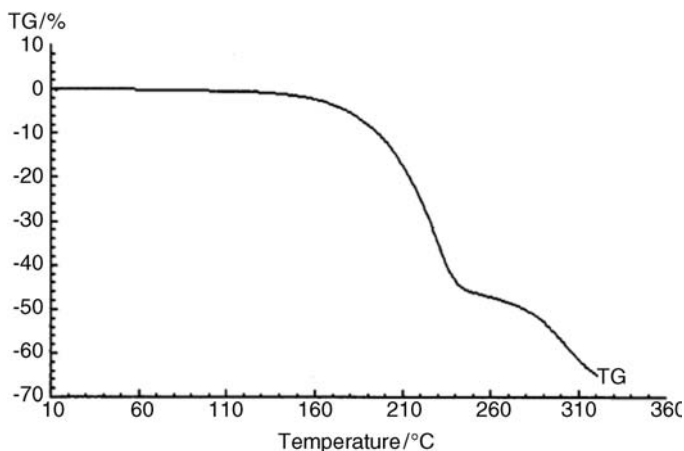
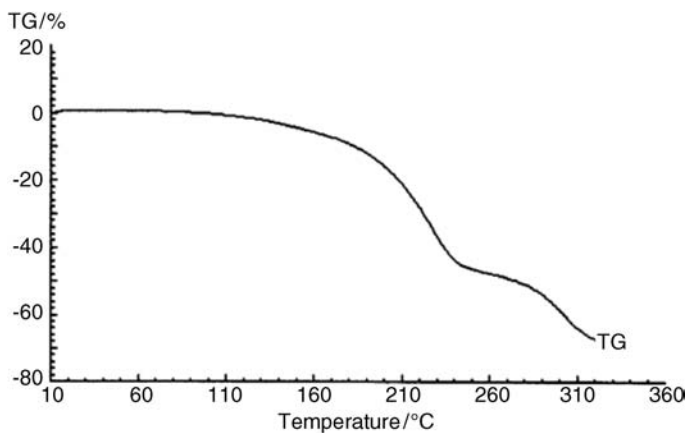
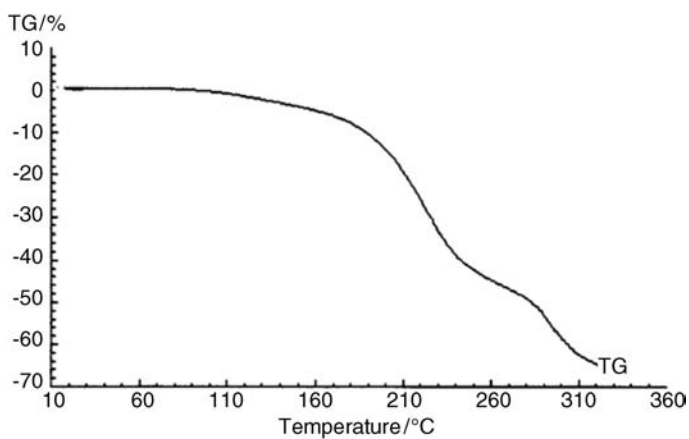


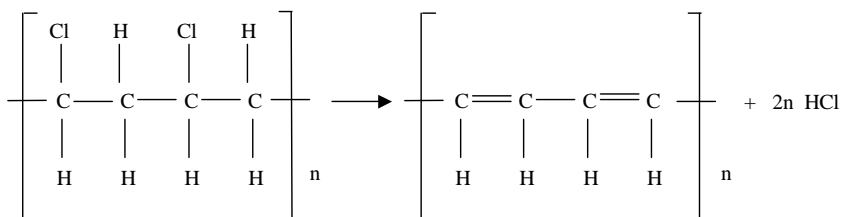
Figure 11.8 Thermogravimetric curve of PVC-PEO-LiCF<sub>3</sub>SO<sub>3</sub>-DBP:EC (90 wt%:10 wt%).



**Figure 11.9** Thermogravimetric curve of PVC-PEO-LiCF<sub>3</sub>SO<sub>3</sub>-DBP:EC (70 wt%:30 wt%).



**Figure 11.10** Thermogravimetric curve of PVC-PEO-LiCF<sub>3</sub>SO<sub>3</sub>-DBP-EC:SiO<sub>2</sub>.



**Scheme 11.1** Details of the dehydrochlorination reaction.



mechanism. The decomposition process generates a byproduct of the components of monomers and oligomers that are sufficiently small in terms of molecular weight to be easily volatilized from the PVC matrix when subjected to continuous heating [20]. This led to a dramatic increase in weight loss by PVC above a temperature of 260 °C as the result of a second decomposition process. The exclusion of HCl gas is another contributory factor for the observed increase in total weight loss. The total weight loss exhibited by pure PVC up to a final tested temperature of 320 °C was 57.3 wt%.

The total weight loss can also be calculated by using Scheme 11.1; the loss was calculated as 58.4 wt% when considering the molar mass ratio between the product (73 ng for 2 n HCl) and the reactant (125 ng). This value is very close to the value obtained from the pure PVC thermogram in Figure 11.1 (57.3 wt%). Thus, it can be concluded that the weight loss of pure PVC with temperature is due mainly to the release of HCl gas.

### 11.5.2

#### Pure PEO

The TGA curve of pure PEO is shown in Figure 11.4. In theory, the thermal decomposition of pure PEO occurs in a one-step process at temperatures >420 °C [21], which is beyond the temperature range of the present study. Thus, no change in the weight percentage of the sample was observed up to 320 °C.

The change in weight is only accountable when a depolymerization process occurs as the result of radical formation in the macromolecule. Therefore, it seems that no free radicals are formed over the temperature range studied that would induce the degradation of pure PEO. Based on the TGA results of pure PVC and PEO, it was concluded that pure PEO is thermally more stable than pure PVC.

### 11.5.3

#### System 1: PVC/PEO Blends

The TGA curve of a PVC/PEO blend is shown in Figure 11.5. This blend was seen to experience a total weight loss of 51.5 wt%, and to have an improved thermal stability compared to pure PVC. These data help to explain the choice of polymer blending technique used when developing high-thermal resistance matrices containing PVC polymers. The thermal properties of the PVC-based formulations were also shown to be improved when blended with poly(isobornyl acrylate) (PIBA), as reported by Kok *et al.* [22].

Many blending solutions have been formulated in the presence of PEO, owing to its high thermal resistivity towards the heat. As noted by Caykara *et al.* [23], the thermal properties of homopolymeric sodium alginate (NaAlg) are improved when it is blended with PEO; indeed, the thermal properties (i.e., heat resistance) of the blended formulation were seen to be similar to those of pure PEO. Alternative combinations of the PEO blend were reported by Kanis *et al.* [24], who showed

that the thermal profile of PEO (which always increases the thermal profile of other homopolymers) was improved by blending with a type of polymer called carbopol, which is more thermally stable than PEO. The resultant delay in thermal degradation demonstrated the efficacy of carbopol in increasing the thermal stability of PEO.

The improvement in thermal stability of the PVC/PEO blend was due to the resistance of PVC to undergo the dehydrochlorination reaction – a process that, in PVC, is observed to start at  $>110^{\circ}\text{C}$ . This process is retarded due to an absence of released free  $\text{Cl}^{\bullet}$  radicals to catalyze the chain dehydrochlorination of the PVC phase; rather, these radicals migrate into the PEO phase and generate  $\text{PEO}^{\bullet}$  macroradicals by abstracting the hydrogen atoms in PEO [4]. The PEO chains can then undergo chain scission at sites adjacent to the macroradicals' center, without undergoing the stages of depolymerization. As a result, the formation of low-molecular-weight volatile components would be suppressed and a reduction in weight loss observed on its volatilization. The free radicals which normally would contribute to a degradation of the polymer via chain dehydrochlorination would be stabilized. A reduction in the release of free  $\text{Cl}^{\bullet}$  radicals in the blend can be proved, via a decreased slump in the TGA curve of the blend at temperatures ranging from  $110^{\circ}\text{C}$  to  $190^{\circ}\text{C}$ .

The second decomposition temperature of the blend is approximately  $245^{\circ}\text{C}$ ; this value was seen to be lower than that obtained in pure PVC and pure PEO. The reduction in the second decomposition temperature was attributed to the presence of a high amorphous phase concentration in the PVC/PEO matrix. The atoms present in the PVC/PEO blend are diffused far into the amorphous phase and are bonded together by weaker interactions; consequently, only a small amount of heat would be sufficient to disrupt or break these loosely held atoms. This is suggested as being the reason for the observed reduction in second decomposition temperature of the blend when compared to neat PVC and PEO.

#### 11.5.4

#### System 2: PVC/PEO:LiCF<sub>3</sub>SO<sub>3</sub> Blends

The TGA curves of the PVC/PEO:LiCF<sub>3</sub>SO<sub>3</sub> matrix with the LiCF<sub>3</sub>SO<sub>3</sub> content of 20 wt% and 50 wt% are shown in Figures 11.6 and 11.7, respectively. In the following subsections, changes in the thermal properties of the PVC/PEO blend after the addition of LiCF<sub>3</sub>SO<sub>3</sub> are examined in comparison with Figure 11.5, and the variations with increasing contents of LiCF<sub>3</sub>SO<sub>3</sub> are also discussed.

The data in Figures 11.5 and 11.6 show clearly that the initial addition of LiCF<sub>3</sub>SO<sub>3</sub> to the PVC/PEO blend provides improvements in both heat-resistivity and thermal stability. Displacement of the second decomposition temperature from an approximate value of  $245^{\circ}\text{C}$  in the PVC/PEO blend to  $280^{\circ}\text{C}$  in the blend containing 20 wt% LiCF<sub>3</sub>SO<sub>3</sub> illustrates the enhanced heat-resistivity. This displacement to a higher temperature was attributed to the presence of an organic group in LiCF<sub>3</sub>SO<sub>3</sub>, which undergoes decomposition at the higher temperature and indicates the non-heat-sensitive nature of the sample. Consequently, fewer

components would become detached from the matrix when it is subjected to increasing heat. This resulted in total weight loss reductions of 51.5 wt% and 45.8 wt% in the PVC/PEO blend and in the matrix containing 20 wt%  $\text{LiCF}_3\text{SO}_3$ , respectively, illustrating an enhancement in thermal stability.

A comparative study on the thermal properties of PVC/PEO: $\text{LiCF}_3\text{SO}_3$  with different doping of  $\text{LiCF}_3\text{SO}_3$  was made based on the data of Figures 11.6 and 11.7. The decomposition temperature of the sample was found to decrease slightly in line with increases in  $\text{LiCF}_3\text{SO}_3$  content, from about 280 °C to 270 °C. This effect was attributed to a destabilization defect on the polymer host imposed by the high  $\text{LiCF}_3\text{SO}_3$  concentration.

The results of various studies on the effect of the guest ionic species content on polymer stability have been interpreted as a consequence of the interaction between guest ions and polymeric solvent, which weakens the bonding in the macromolecular backbone and makes it less resistant towards thermal degradation. In other words, the sample with the highest  $\text{LiCF}_3\text{SO}_3$  content can be termed heat-sensitive. This interpretation further supports the suggestion that the interaction between the guest salt and the host polymer is linked to increases in salt content.

As the sample with a high  $\text{LiCF}_3\text{SO}_3$  content is heat-sensitive, a major increase in total weight loss would also be expected. Indeed, the increased weight loss was calculated to range from 45.8 wt% to 61.3 wt% as the  $\text{LiCF}_3\text{SO}_3$  content was increased from 20 wt% to 50 wt%. These data indicate that the addition of increasing amounts of  $\text{LiCF}_3\text{SO}_3$  to the PVC/PEO: $\text{LiCF}_3\text{SO}_3$  blend lead caused its thermal stability to undergo stepwise decreases in line with the  $\text{LiCF}_3\text{SO}_3$  concentration. These results were in accordance with previous findings observed with PEO-based electrolytes [25], where the onset of degradation was dependent on the electrolyte composition, confirming that the salt does indeed have a destabilizing influence on the polymer hosts.

#### 11.5.5

##### **System 3: PVC/PEO- $\text{LiCF}_3\text{SO}_3$ -DBP:EC Blends**

The effects of increasing EC content on the thermal properties of PVC/PEO- $\text{LiCF}_3\text{SO}_3$ -DBP:EC are shown in Figures 11.8 and 11.9, where the EC contents are 10 wt% and 30 wt%, respectively. The plasticized matrix began to decompose at a very low temperature, with the first decomposition occurring at about 170 °C. This effect was caused by a high degree of volatilization of the plasticizer, which escaped from the matrix when the latter was subjected to only low heat levels.

The second decomposition temperature occurred at 245 °C, and was due to an increase in the amorphous nature of the matrix when plasticized with increasing EC contents [15]. This increase in the amorphous region provided a greater availability of loosely bonded atoms, which easily decomposed under minimum heating. Thus, the sample increasingly lost its heat-resistivity as the EC doping level was raised. This led to increases in total weight loss, of 64.8 wt% and 70.4 wt%, respectively, in samples containing 10 wt% and 30 wt% of EC. Thus, it was

concluded that increases in EC plasticization would reduce both the heat-resistivity and thermal stability of the matrix [26].

Similar reductions in the thermal stability of samples were reported by Ramesh *et al.* [27] when, in the presence of EC, the matrix began to lose its heat-resistivity. In another study the matrix was reported to have lost its heat-resistive nature upon the incorporation of EC [28]. Clearly, the thermal properties of polymer electrolytes are reduced when plasticizers are incorporated into the matrix.

#### 11.5.6

##### **System 4: PVC-PEO-LiCF<sub>3</sub>SO<sub>3</sub>-DBP-EC:SiO<sub>2</sub> Blends**

The addition of SiO<sub>2</sub> has a significant effect on the thermal properties of PVC/PEO-LiCF<sub>3</sub>SO<sub>3</sub>-DBP-EC:SiO<sub>2</sub>, as shown by the TGA curve in Figure 11.10. The degradation process in this system is found to start at a temperature of approximately 170 °C, which is attributed to decomposition of the plasticizers. The second decomposition takes place at about 245 °C and correlates to decomposition of the matrix that is highly amorphous in nature.

The change in total weight loss upon the addition of SiO<sub>2</sub> is marked, decreasing from 70.4 wt% (noncomposite sample) to 64.8 wt% (composite sample). This reduction is indicative of improvements in the thermal stability of composite thin films, and may be attributed to the elimination of the initial decomposition that produces Cl• free radicals in the presence of SiO<sub>2</sub> particles [29]. This, in turn, will inhibit the depolymerization process producing low-molecular-weight volatile compounds, such that lesser components will be volatilized and the weight loss will be minimized. A second reason for the lesser availability of volatile compounds is the strong acid–base interaction between the lithium cation (Li<sup>+</sup>) (from the lithium salt) and the oxygen atom (in the SiO<sub>2</sub> particle). Improvements in thermal stability were also observed when titanium oxide (TiO<sub>2</sub>) was incorporated into the matrix formulated by Rajendran *et al.* [30]. Clearly, the thermal profile of a polymer electrolyte can be improved by blending it with any type of filler compound.

## 11.6

### **Conclusion**

PVC/PEO blend-based polymer electrolytes were prepared using a solution-casting method. By using TGA, the thermal profile of pure PVC was shown to be improved when blended with a highly heat-stabilized PEO; this was achieved by retarding the release of free Cl• radicals that catalyzed chain dehydrochlorination. The thermal properties of the PVC/PEO blend were improved by an initial addition of LiCF<sub>3</sub>SO<sub>3</sub>; however, when the LiCF<sub>3</sub>SO<sub>3</sub> content was further increased the matrix began to lose its thermal resistance. These reductions in thermal properties were induced by a weakening of the bonds within the macromolecule backbone in the presence of a high LiCF<sub>3</sub>SO<sub>3</sub> content. The thermal properties of PVC/PEO:

$\text{LiCF}_3\text{SO}_3$  were seen to decrease when increasing amounts of EC were incorporated into the mixed plasticizer solution containing DBP. As a consequence, the plasticized matrix became more heat-sensitive due to the presence of high concentrations of amorphous phase within the blended polymer matrix. These improvements in the thermal properties of plasticized matrices were achieved by the addition of heat-stabilized  $\text{SiO}_2$  particles, the presence of which eliminated the initiation process producing  $\text{Cl}^\bullet$  free radicals and consequently inhibiting depolymerization processes; thus, fewer low-molecular-weight compounds are likely to be present and volatilized. This formulation may be well suited to applications of high-temperature solid-state cells.

## References

- 1 Morita, M., Tanaka, H., Ishikawa, M., and Matsuda, Y. (1996) Effects of crown ethers on the electrochemical properties of polymeric solid electrolytes consisting of poly(ethylene oxide)-grafted poly(methyl methacrylates). *Solid State Ionics*, **86–88**, 401–405.
- 2 Kim, D.W. and Sun, Y.K. (2001) Electrochemical characterization of gel polymer electrolytes prepared with porous membranes. *J. Power Sources*, **102**, 41–45.
- 3 Rajendran, S., Kannan, R., and Mahendran, O. (2001) Ionic conductivity studies in PMMA–PEO hybrid polymer electrolytes with lithium salts. *J. Power Sources*, **96**, 406–410.
- 4 Pospisil, J., Horak, Z., Krulis, Z., Nespurek, S., and Kuroda, S.-i. (1999) Degradation and aging of polymer blends I. Thermomechanical and thermal degradation. *Polym. Degrad. Stabil.*, **65**, 405–414.
- 5 Ramesh, S., Liew, C.-W., Morris, E., and Durairaj, R. (2010) Effect of PVC on ionic conductivity, crystallographic structural, morphological and thermal characterizations in PMMA-PVC blend-based polymer electrolytes. *Thermochim. Acta*, **511**, 140–146.
- 6 Fox, D.W. and Allen, R.B. (1991) *High Performance Polymers and Composites* (ed. J. I. Kroschwitz), J. Wiley & Sons, New York, pp. 65–82.
- 7 El-Hibri, M.J. and Munk, P. (1988) Marker retention in inverse gas chromatography experiments on polymers. *Macromolecules*, **21**, 264–266.
- 8 Huang, X.D. and Goh, S.H. (2002) Miscibility of  $\text{C}_{60}$ -end-capped poly(ethylene oxide) with poly(vinyl chloride). *Polymer*, **43**, 1417–1421.
- 9 Lai, C.H., Paul, D.R., and Barlow, J.W. (1988) Group contribution methods for predicting polymer–polymer miscibility from heats of mixing of liquids. 1. Comparison of the modified Guggenheim quasi-chemical (MGQ) and UNIQUAC models. *Macromolecules*, **21**, 2492–2502.
- 10 Katime, I.A., Anasagasti, M.S., Peleteiro, M.C., and Valenciano, R. (1987) Compatibility of poly(ethylene oxide)/poly(vinyl chloride) blends by differential scanning calorimetry. *Eur. Polym. J.*, **23**, 907–911.
- 11 Marco, C., Gomez, M.A., Fatou, J.G., Etxeberria, A., Elorza, M.M., and Iruin, J.J. (1993) Miscibility of poly(vinyl chloride)/poly(ethylene oxide) blends – I. Thermal properties and solid state  $^{13}\text{C}$ -NMR study. *Eur. Polym. J.*, **29**, 1477–1481.
- 12 Kaczmarek, H. and Szalla, A. (2006) Photochemical transformation in poly(acrylic acid)/poly(ethylene oxide) complexes. *J. Photochem. Photobiol. B: Chem.*, **180**, 46–53.
- 13 Mauro da Silva Neiro, S., Cardosa Dragunski, D., Forti Rubira, A., and Curti Muniz, E. (2000) Miscibility of PVC/PEO blends by viscometric, microscopic and thermal analyses. *Eur. Polym. J.*, **36**, 583–589.

- 14 Mohamad, A.A. and Arof, A.K. (2007) Plasticized alkaline solid polymer electrolyte system. *Mater. Lett.*, **61**, 3096–3099.
- 15 Mano, J.F., Koniarova, D., and Reis, R.L. (2003) Thermal properties of thermoplastic starch/synthetic polymer blends with potential biomedical capability. *J. Mater. Sci.-Mater. Med.*, **14**, 127–135.
- 16 Varughese, K.T. (1988) Poly(vinyl chloride)/epoxidised natural rubber miscible blends: Thermal and flame behavior. *Kautsch. Gummi Kunstst.*, **41**, 1114–1117.
- 17 Calandrelli, L., Immirzi, B., Malinconico, M., Martuscelli, E., and Riva, F. (1992) Structural and thermal investigations on aromatic polyoxadiazole/polyamide 6 blends. *Makromol. Chem.*, **193**, 669–679.
- 18 Ramesh, S., Liew, C.-W., and Ramesh, K. (2011) Evaluation and investigation on the effect of ionic liquid onto PMMA-PVC gel polymer blend electrolytes. *J. Non-Cryst. Solids*, **357**, 2132–2138.
- 19 Lizymol, P.P., Thomas, S., and Jayabalan, M. (1997) Effect of dehydrochlorination of PVC on miscibility and phase separation of binary and ternary blends of poly(vinyl chloride), poly(ethylene-co-vinyl acetate) and poly(styrene-co-acrylonitrile). *Polym. Int.*, **44**, 23–39.
- 20 Mano, V., Felisberti, M.I., Matencio, T., and Paoli, M.A.D. (1996) Thermal, mechanical and electrochemical behavior of poly(vinyl chloride)/polypyrrole blends (PVC/PPy). *Polymer*, **37**, 5165–5170.
- 21 Chowdari, B.V.R., Huq, R., and Farrington, G.C. (1992) Studies of plasticized-polymer electrolytes containing mixed Zn (II) and Li (I). *Electrochim. Acta*, **37**, 1667–1670.
- 22 Kok, M., Demirelli, K., and Aydogdu, Y. (2008) Thermophysical properties of blend of poly(vinyl chloride) with poly(isobornyl acrylate). *Int. J. Sci. Technol.*, **3**, 37–42.
- 23 Caykara, T., Demirci, S., Eroglu, M.S., and Guven, O. (2005) Poly(ethylene oxide) and its blends with sodium alginate. *Polymer*, **46**, 10750–10757.
- 24 Kanis, L.A., Viel, F.C., Crespo, J.S., Bertolino, J.R., Pires, A.T.N., and Soldi, V. (2000) Study of poly(ethylene oxide)/carbopol blends through thermal analysis and infrared spectroscopy. *Polymer*, **41**, 3303–3309.
- 25 Smith, M.J., Silva, M.M., Cerqueira, S., and MacCallum, J.R. (2001) Preparation and characterization of a lithium ion conducting electrolyte based on poly(trimethylene carbonate). *Solid State Ionics*, **140**, 345–351.
- 26 Ramesh, S. and Arof, A.K. (2001) Structural, thermal and electrochemical cell characteristics of poly(vinyl chloride)-based polymer electrolytes. *J. Power Sources*, **99**, 41–47.
- 27 Ramesh, S., The, G.B., Louh, R.-F., Hou, Y.K., Sin, P.Y., and Yi, L.J. (2009) Preparation and characterization of plasticized high molecular weight PVC-based polymer electrolytes. *Sadhana*, **35**, 87–95.
- 28 Ibrahim, S. and Johan, M.R. (2012) Thermolysis and conductivity studies of poly(ethylene oxide) (PEO)-based polymer electrolytes doped with carbon nanotubes. *Int. J. Electrochem. Sci.*, **7**, 2596–2615.
- 29 Garcia, N., Corrales, T., Guzman, J., and Tieblo, P. (2007) Understanding the role of nanosilica particle surfaces in the thermal degradation of nanosilica-poly(methyl methacrylate) solution-blended nanocomposites: From low to high silica concentration. *Polym. Degrad. Stabil.*, **92**, 635–643.
- 30 Rajendran, S., Ravi Shanker Babu, and Sivakumar, P. (2008) Investigations on PVC/PAN composite polymer electrolytes. *J. Membr. Sci.*, **315**, 67–73.

## 12

**Dynamic Mechanical Thermal Analysis of Polymer Blends**

*José-David Badía, Laura Santonja-Blasco, Alfonso Martínez-Felipe,  
and Amparo Ribes-Greus*

The development and commercialization of polymer blends involves the need to provide materials with a balance of properties that is not affordable via common polymers, without investing in the creation of new macromolecules [1]. In order to offer a wide variety of performance conditions, polymer blends must show toughness, rigidity, stiffness and thermal resistance, as well as flexibility, low cost and environment-friendly production. Potential applications include electrolytes for membranes [2–7], packaging [8–18], controlled-released drug carriers [19], high-tech fabrics [20], roofing [21], green consumables as mobile phones [22], and many others. Polymer blends may perform under a variety of service conditions (e.g., vibrations, damping, acoustics) that may induce small stresses ( $\sigma$ ) which provoke small strains ( $\varepsilon$ ) in their structure; this, in turn, may have a degrading impact [23–28] on the cooperative motions responsible for the macromolecular dynamics of the blends. The viscoelasticity of the polymer blend components plays an important part in their performance under external mechanical solicitations. In this chapter, the potential of dynamical mechanical thermal analysis (DMTA) is assessed by focusing on ability of the technique to offer information not only on the viscoelastic performance of polymer blends in terms of mechanical moduli, but also in terms of miscibility, segmental dynamics, and the effect of plasticizers and crosslinkers. It should be noted that, although the viscoelasticity and rheology of polymers are intimately related, only nonflowing situations are described in this chapter. It should also be noted that the bibliography provided corresponds to studies on polymer blends that are known to be physical mixtures of polymers in dissolution, or in melts, in contrast to the definitions of copolymers and polymer composites [29].

## 12.1

**Dynamic Mechanical Thermal Analysis (DMTA)**

The technique of DMTA is devoted to assessing the viscoelastic response of a material submitted to a mechanical solicitation, as a function of temperature and

frequency [30]. DMTA allows the study of molecular-level thermal transitions at different segmental scales by characterizing the evolution of macromolecular relaxation times with temperature [31]. A brief description of DMTA, with details of its theoretical basis, are provided in the following subsection.

### 12.1.1

#### The DMTA Analyzers

A general schematic of the primary components of a DMTA instrument is shown in Figure 12.1. The majority of DMTA analyzers include: (i) a displacement sensor, such as a linear variable differential transformer (LVDT), which measures the changes in voltage that occur as the instrument probe moves through a magnetic core; (ii) a temperature control system or furnace; (iii) a linear drive motor for probe loading, which provides a load for the applied force; (iv) a drive shaft support and control system that acts as a guide for the force from the motor to the sample; and (v) clamps which hold the sample being tested in place.

Analyzers are available for both strain (displacement) and stress (force) control. On the one hand, under strain control, the probe is displaced and the resulting stress of the sample is measured by implementing a force balance transducer, which utilizes different shafts. The advantages of strain control include a better short-term response for materials of low viscosity, which allows experiments of stress relaxation to be performed with relative ease. On the other hand, under stress control a set force is applied while several other experimental conditions (temperature, frequency, or time) are varied. Although stress control analyses are

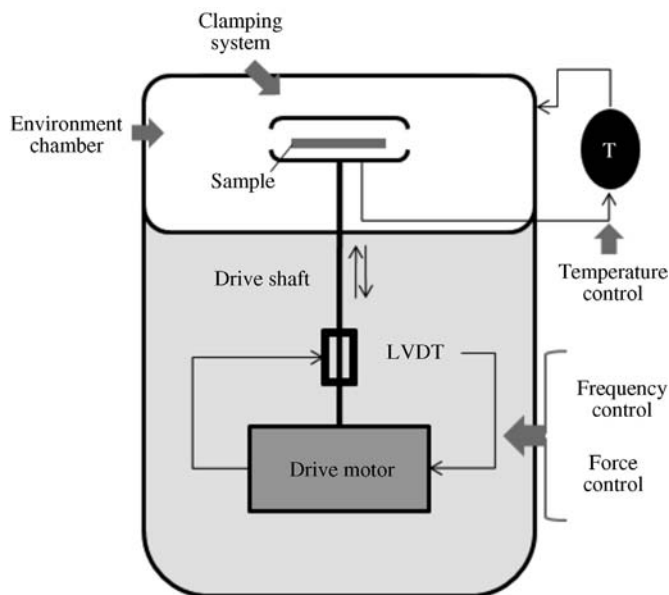


**Figure 12.1** Schematic representation of a DMTA device.



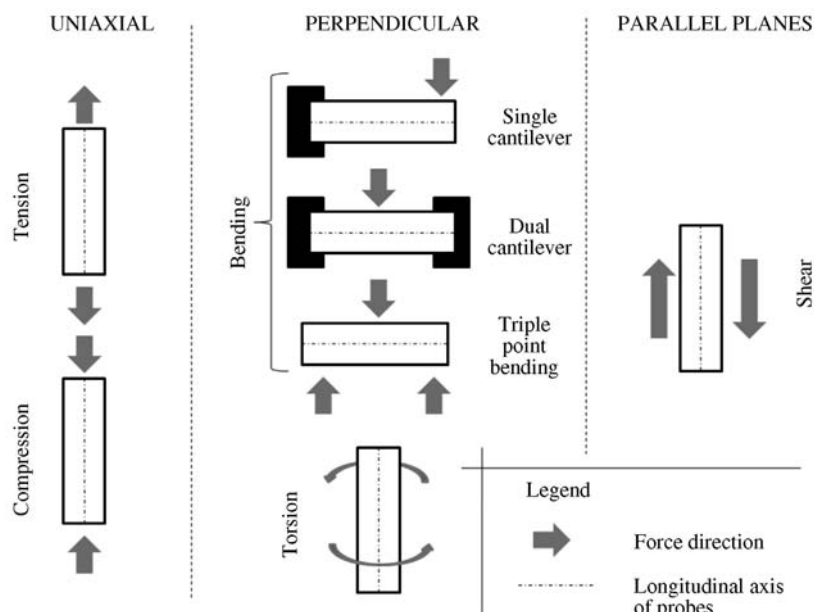


Figure 12.2 DMTA geometries of experimental testing.

typically less expensive to conduct than strain control analyses (because only one shaft is needed), they are more difficult to perform. The main advantages of stress control analysis are that the sample structure is less likely to be destroyed, such that the relaxation times can be used and longer creep studies performed. The spatial resolution is another variable that must be taken into account. Usually, the resolution of LVDTs approaches 1 : 200 000, which means that the system can be used to measure nanometric displacements [32]; however, in order to assure reliable measurements of 1 nm the maximum displacement of the DMTA must be set at 200  $\mu\text{m}$ . This factor would be especially relevant when testing for miscibility.

According to the service conditions at which the polymer blends may perform, or depending on the probe geometry, different deformation modes can be applied, as shown in Figure 12.2. With regards to the distribution of applied forces to the longest dimension of probes, uniaxial modes cover tension and compression experiments. Perpendicular modes gather torsion and bending experiments, the latter with three geometries, according on the clamping used: single cantilever; dual cantilever; or triple-point bending. Finally, the shear mode induces contrary forces in parallel planes. With regards to the probe geometry, bars are usually measured by bending or torsion, films by shear and tension, fibers by tension, and foams, elastomers and even viscous liquids by compression.

Depending on the commercial trademark, the DMTA analyzers can offer different ranges of temperature and frequency ranges. In general terms, currently available analyzers have can perform between  $-150$  and  $600^\circ\text{C}$ , in multifrequency

mode, from 0.001 to 300 Hz [32–34], although a more reduced range is advisable in order to obtain more consolidated experimental results. If, in contrast, larger ranges are required – in terms of both time-scale and/or temperature-scale – this can be achieved indirectly by performing several isothermal DMTA experiments over a frequency range and then applying the time–temperature superposition theory [31].

### 12.1.2

#### Using DMTA to Analyze the Viscoelastic Behavior of Polymers

The classical theory of elasticity describes the mechanical properties of elastic solids, where the stress  $\sigma$  is proportional to strain  $\varepsilon$  in small deformations. Such a response of stress is independent of strain rate, with a constant  $E$ , known as Young's modulus.

$$\sigma = E \cdot \varepsilon \quad (12.1)$$

On the other hand, the classical theory of hydrodynamics describes the properties of viscous fluids, for which the response of stress is dependent on strain rate, where the constant of proportionality is known as viscosity  $\eta$ .

$$\sigma = \eta \cdot \frac{d\varepsilon}{dt} \quad (12.2)$$

Polymers, when subjected to an external action (thermal, mechanical, magnetic, etc.), react by developing processes in their structures which have the property of not instantly adapting to a new equilibrium. These processes occur in characteristic times, known as relaxation times  $\tau$ . It should also be noted that the response of a polymer depends on both the time and temperature of application.

Macromolecular segments have ability to absorb energy by a segmental rearrangement that involves changes in the lengths and angles of bonds, both at the main macromolecular polymer chain, as well as at the secondary and branching segments; this movement or rearrangement is termed “creep.” Polymers remain solid even when these parts of their chains are rearranging in order to accompany the stress, and as this occurs it creates a back-stress in the material. Thus, when the back-stress has the same magnitude as the applied stress, the material will no longer creep. However, when the original stress is removed the accumulated back-stresses will cause the polymer to return to its original form. Usually, part of the material will creep – hence the prefix “visco-” – while part of the material recovers – hence the suffix “-elasticity.”

Apart from relaxation and creep experiments, two major types of test mode can be used to monitor the viscoelastic properties of polymers, namely temperature sweep and frequency sweep tests. These experiments are usually performed at short strains (<0.5% of active length) so as to be within the linear region when a sinusoidal stress  $\sigma$  (Eq. (12.3)) (i.e., force per area unit) is applied to a viscoelastic material; the resultant strain  $\varepsilon$  (i.e., unitary relative geometric displacement) appears out-of-phase (Eq. (12.4)), with the angle  $\delta$  being  $\omega$  the angular frequency

of the oscillation:

$$\sigma(t) = \sigma_0 \cdot \cos(i(\omega \cdot t)) \quad (12.3)$$

$$\varepsilon(t) = \varepsilon_0 \cdot \cos(i(\omega \cdot t + \delta)) \quad (12.4)$$

From trigonometric relationships and separating into “in-phase totally elastic response” and “out-of-phase totally viscous response,” and dividing stress by strain, it is possible to arrive at the expressions of complex modulus (Eq. (12.5)), and loss factor (Eq. (12.6)):

$$E^* = \frac{\sigma(t)}{\varepsilon(t)} = E_0 \cdot (\cos \delta + i \sin \delta) = E' + i E'' \quad (12.5)$$

$$\tan \delta = \frac{E''}{E'} \quad (12.6)$$

The real part of  $E^*$ ,  $E'$ , is termed as the “storage modulus,” and represents the energy that is absorbed and released elastically during the deformation. On the other hand, the imaginary part of  $E^*$ ,  $E''$ , is termed as the “loss modulus” and represents the amount of energy absorbed due to internal motions in the material.

### 12.1.3

#### Description of DMTA Results: The Viscoelastic Spectra

The macromolecular rearrangements and motions that occur during DMTA experiments, due to the viscoelastic character of polymer blends, can be either primary (e.g., glass–rubber relaxation) or secondary (due to segmental motions of side groups or local motions in the backbone, such as stretching or bending). One of the main advantages of DMTA is that it is particularly sensitive to secondary transitions. The main parameter is the glass–rubber relaxation temperature,  $T_\omega$  which is usually related to the calorimetric glass transition temperature,  $T_g$ . However, despite both parameters being expressions of the same physical phenomenon – that is, a massive cooperative relaxation of polymer segments from rigid to mobile states – they only coincide under specific experimental conditions [31]. In the following sections this temperature will be referred to as  $T_\omega$ , since it is more appropriate for viscoelastic experiments. Figure 12.3 shows the  $E'$  responses of a DMTA test for ideal polymers in which different sections can be distinguished, as follows.

##### 12.1.3.1 The Glassy State

At temperatures below  $T_\omega$  the material is in glassy state and only small increases in free volume due to molecular motions can modify the moduli:  $E'$  is slightly decreased along with small increases in  $E''$ . In this region,  $\omega \cdot \tau \gg 1$ ; that is, the applied oscillatory deformation is faster than the relaxation time of the side-group polymer segments, and consequently the material shows a rigid behavior.

In this range, small peaks can appear in the loss modulus  $E''$  evolution; these peaks are associated with secondary transitions in the glassy-state, referred to as

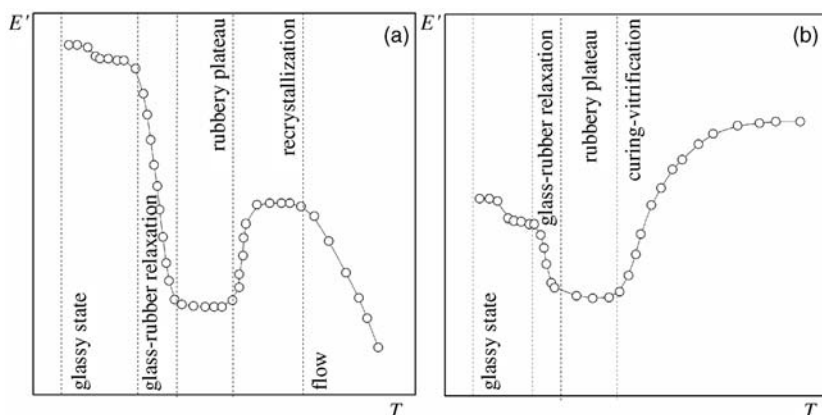


**Figure 12.3** DMTA response for ideal (a) thermoplastic and (b) thermoset polymers.

“local-scale motions,” such as the rotations and oscillations of side groups and oscillations and partial rotations of the blend backbone. The peaks and their transitions are usually labeled in decreasing temperature order as  $T_\beta$ ,  $T_\gamma$ ,  $T_\delta$ , and so on. These transitions can be related to different material properties in the glassy state, such as peel-strength in paints [33], toughness [35], or acoustical and vibration damping [34]. The use of dielectric methods, as well as solid-state NMR, helps to complete the study of those groups responsible for these small macromolecular motions [31].

The plot of the influence of modifying the frequency of analysis  $f$  versus the reciprocal of the peak temperatures of  $E''$  or  $\tan \delta$ , for all experiments at all frequencies, displays different behaviors for sub- $T_\alpha$  transitions and the glass–rubber relaxation, as shown in Figure 12.4. Typically, a linear behavior is found for sub- $T_\alpha$  transitions, which can be analyzed using an Arrhenius model (Eq. (12.7)), from which the apparent activation energy  $Ea$  can be obtained, as shown in Eq. (12.8), where  $\tau_0$  is a time reference scale (in seconds), and  $R$  is the ideal gas constant ( $8.31 \text{ J K}^{-1} \text{ mol}^{-1}$ ).

$$\tau(T) = \tau_0 \cdot \exp\left(\frac{Ea}{R \cdot T}\right) \quad (12.7)$$

$$Ea = R \cdot \frac{d \ln \tau}{d(1/T)} \quad (12.8)$$

Monitoring the evolution of  $Ea$  can serve as a reliable indicator of molecular rearrangement due to the degradation of polymers [23,24]. In this sense, blends of low-density polyethylene (LDPE) and a starch-based commercial biodegradable material commonly used as an additive, Mater-Bi AF05 H, were studied after a period of annealing and biodegradation in soil [18]. The changes in  $Ea$  observed in the blended samples indicated that degradation of the blends was due mainly to the presence of Mater-Bi, the carbonated chains of which seemed to act by hindering the uniform growth of crystallites in LDPE, thus promoting a broader

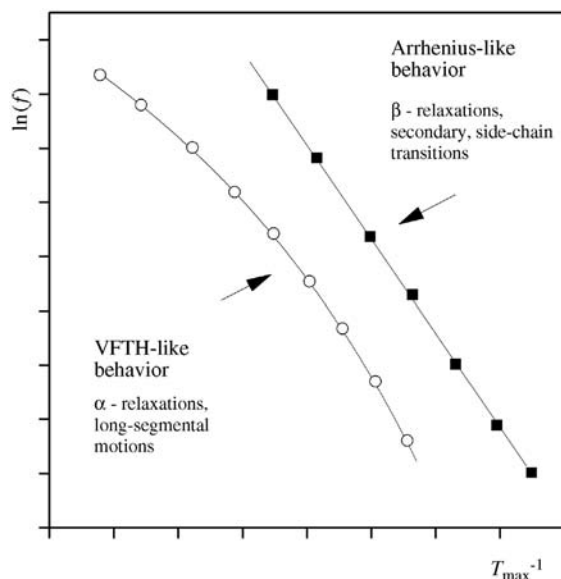


**Figure 12.4** Arrhenius plots for sub- $T_g$  (fitted to Arrhenius equation) and glass–rubber relaxation (fitted to VFTH equation).

distribution of crystallites within the LDPE. Over a range of exposure times in soil, the changes observed in relaxation indicated degradation of the Mater-Bi, as the spectra of the blended samples tended to resemble those of pure polyethylene.

### 12.1.3.2 The Glass–Rubber Relaxation

Due to the increase in temperature, the glass–rubber relaxation (also termed  $\alpha$ -relaxation) involves large-scale polymer segments and produces significant changes in the material's performance. The temperature that defines this region can be calculated by different conventions: onset or peak of  $E''$ ; onset or peak of  $\tan\delta$ ; and/or onset or inflection of  $E'$  drop. The method should be specified in order to compare results. In addition, if a small jump is seen just before the  $\alpha$ -relaxation this is due to internal rearrangements to relieve stresses due to a sub- $T_g$  thermal history that is mainly induced by processing and storage conditions.

The glass–rubber relaxation occurs when  $\omega \cdot \tau \sim 1$ ; that is, when the reciprocal of angular frequency approaches the relaxation time of the polymer segments, and thus, the major internal rearrangement (i.e., highest  $E''$ ) is obtained. A crankshaft cooperative segmental motion of the backbone is then produced which increments the large-scale mobility and a rubbery-state flow of the blend. In general terms, the ratio between unrelaxed ( $E'$  at  $T < T_g$ ) and relaxed ( $E'$  at  $T > T_g$ ) moduli is notably higher for the glass–rubber relaxation than for sub- $T_g$  transitions.

It was shown in Figure 12.4 that, in the case of glass–rubber relaxation, the linearity of the plot of peak  $E''$  or the peak of  $\tan \delta$  versus the reciprocal of the peak temperature, was lost. Consequently, the Vogel–Fulcher–Tamman–Hesse

(Eq. 12.9) [36–39] is applied where  $B$  (K) and  $T_{\text{VFTH}}$  (K) are positive parameters specific to the material. It has been shown that  $T_{\text{VFTH}}$  is identified with the Kauzmann temperature  $T_K$ , which represents the configurational ground-state temperature at which the viscosity diverges and the excess configurational entropy vanishes [40,41]; typically, this appears 40–60 K below  $T_g$ . It is common to rewrite the parameter  $B$  as  $B = D \cdot T_{\text{VFTH}}$ , where  $D$  is a dimensional factor termed “fragility” or “strength parameter.” Qualitatively,  $D$  is related to the topology of the theoretical potential energy surface of the system, where fragile systems ( $D \leq 6$ ) present a high density of energy minima, in contrast to strong systems ( $D \geq 15$ ) which present a lower density. The activation energy can thus be obtained from Eq. (12.10):

$$\tau(T) = \tau_0 \cdot \exp\left(\frac{B}{T - T_{\text{VFTH}}}\right) = \tau_0 \cdot \exp\left(\frac{D \cdot T_{\text{VFTH}}}{T - T_{\text{VFTH}}}\right) \quad (12.9)$$

$$Ea = R \cdot \frac{d \ln \tau}{d(1/T)} = \frac{R \cdot B}{\left(1 - \frac{T_{\text{VFTH}}}{T}\right)^2} \quad (12.10)$$

Some examples of the analysis of the apparent activation energy  $Ea$  of blends can be found in the literature. When evolution of the  $Ea$  of liquid *cis*-polyisoprene/*trans*-polyisoprene (CPI/TPI) blends was analyzed using the VFTH model [41], the  $Ea$  for pure TPI was observed to be higher than that of TPI/CPI blends. Moreover, as the concentration of TPI decreased, then the  $Ea$  also decreased; this was ascribed to the fact that in glass–rubber relaxation the motion of molecules is governed by the crosslink density. As the decrease in TPI content caused a decrease in crosslink density, this in turn enhanced the motion of chains, and consequently less  $Ea$  was required to promote segmental cooperative movements.

### 12.1.3.3 Rubbery Plateau

Above  $T_g$  the material remains in a rubbery state, and at this point  $E'' \rightarrow 0$  due to  $\omega \cdot \tau \ll 1$ ; that is, the applied oscillatory deformation is far slower than the cooperative segmental movements, and thus the internal reorganizations elastically absorb the solicitation. Thus,  $E'$  shows a constant value that may be related to the molecular weight between entanglements or crosslinks [42]. The influence of physical fillers may play a role in the  $E'$ -values during the rubbery plateau, as will be shown later.

### 12.1.3.4 Recrystallization or Curing

Although it is not common, some polymers show a remarkable cold-crystallization during heating scans in thermal analytical techniques [25], due to the polymer segments acquiring the necessary mobility to rearrange into crystalline domains. This results in an increase of  $E'$  but no remarkable change in  $E''$ , as the regime is still in  $\omega \cdot \tau \ll 1$ . Rather, it might be due to the effect of short chains or particles acting as nucleants for the formation of crystalline regions. However, this effect should be taken into account when designing polymer blends.

In thermosetting systems, the increase in temperature will increment the number of crosslinks, and this in turn will increase the storage modulus of the polymer blend; this is shown schematically in Figure 12.3b.

### 12.1.3.5 Flowing

At temperatures just below melting, the material will start to flow in a liquid-like manner, causing a dramatic reduction in the moduli. Thus, it is advisable to design experiments in the correct fashion by defining a final temperature that is safe enough to avoid spreading and to prevent the polymer blend from sticking to the probe of the DMTA analyzer.

### 12.1.4

#### Modeling the Viscoelastic Behavior

The complex modulus components  $E'$  and  $E''$  are frequently modeled in the frequency domain by means of the so-called Cole–Cole [43] plot, that is,  $E'' = f(E')$ , and application of the Havriliak–Negami model [44], provided that there is no overlapping between  $\alpha$  and  $\beta$  relaxations:

$$E^* = E_\infty - \frac{E_\infty - E_0}{[1 + (i\omega\tau^{1-a})]^b} \quad (12.11)$$

where  $E_\infty$  and  $E_0$  are the unrelaxed and the relaxed moduli, respectively,  $i$  is the square-root of  $(-1)$ ,  $\omega$  is the angular frequency – that is  $(2\pi \cdot f)^{-1}$ , where  $f$  is the linear frequency – and  $a$  and  $b$  are constants.

The Kohlrausch–Williams–Watts model [45,46] can also be used in the time domain, by means of Eq. (12.12):

$$E^* = (E_\infty - E_0) \cdot \exp\left(-\frac{t}{\tau}\right)^k + E_0 \quad (12.12)$$

where  $k$  is a constant.

Although the modeling of viscoelastic behavior in the frequency and time domains is very interesting from a scientific point of view, it is beyond the scope of this chapter, which is focused more on the technological applications of DMTA. A summary of the main frequency-domain models is shown in Table 12.1, and further information on this subject is available elsewhere [31].

## 12.2

### Miscibility Studies

Miscibility can be understood in terms of the homogeneity of polymer blend segments at the molecular level. Variations in  $T_\alpha$  are indicative of the miscibility of polymer blends, as shown in Figure 12.5 for an ideal polymer blend in terms of loss modulus, with the following options:

- i) Homogeneous miscibility, when the  $T_\alpha$  of the polymer blend lies between the  $T_\alpha$ -values of the pure polymers.

**Table 12.1** Theoretical models to explain the viscoelastic behavior of polymer and polymer blends.

Model	Equation	Reference
Debye	$E^* = E_\infty + \frac{E_0 - E_\infty}{1 + i\omega\tau}$ $E' = E_\infty + \frac{(E_0 - E_\infty)}{1 + \omega^2\tau^2}$ $E'' = (E_\infty - E_0) \frac{\omega\tau}{1 + \omega^2\tau^2}$	[47]
Cole-Cole	$E^* = E_\infty + \frac{E_0 - E_\infty}{1 + (i\omega\tau)^{1-\alpha}} \quad 0 < \alpha < 1$	[43]
Fuoss-Kirkwood		[48]
Davidson-Cole	$E^* = E_\infty + \frac{E_0 - E_\infty}{(1 + i\omega\tau)^\beta} \quad 0 < \beta < 1$	[49]
Havriliak-Negami	$E^* = E_\infty + \frac{E_0 - E_\infty}{\left[1 + (i\omega\tau)^{1-\alpha}\right]^\beta} \quad 0 < \alpha < 1; \quad 0 < \beta < 1$	[44]
Lunkenheimer-Pimenov-Dressel-Schiener-Schneider-Loidl	$E'' = a \frac{(\omega\tau_0)^\alpha}{1 + (\omega\tau_0)^{\alpha+\beta}} \quad 0 < \alpha, \beta < 1, \alpha + \beta < 1$	[50]
Friedrich-Braun	$E^* = \frac{E_0 E_\infty (1 + (i\omega\tau)^c)}{(E_0 - E_\infty) \left[ E_\infty (1 + (i\omega\tau)^c) + (E_0 - E_\infty)(i\omega\tau)^d \right]}$ $d > c$	[51]
Biparabolic model	$E^* = E_0 - \frac{E_0 - E_\infty}{1 + \delta' (i\omega\tau')^{-k} + (i\omega\tau')^{-h}}$ $1 > h > k > 0$ $\delta' = \delta \left( \frac{E_0}{E_\infty} \right)^{\frac{k}{h}-1}; \tau' = \tau \left( \frac{E_0}{E_\infty} \right)^{\frac{1}{h}}$	[52]

- ii) Heterogeneous miscibility, when the  $T_\alpha$  of the pure polymers is modified with respect to that of the polymer blend, but presents certain phenomena such as a significant broadening of the glass-rubber transition.
- iii) Partial miscibility, when one of the components modifies its  $T_\alpha$  but that of the other component(s) remain(s) almost unaltered.
- iv) Immiscibility, when the  $T_\alpha$  of the pure components is the same as for the polymer blend.

### 12.2.1

#### Binary Systems

Some examples of miscibility can be highlighted. For example, thermosetting polymer blends composed of bisphenol A-based benzoxazine (BA-a) and cyanate



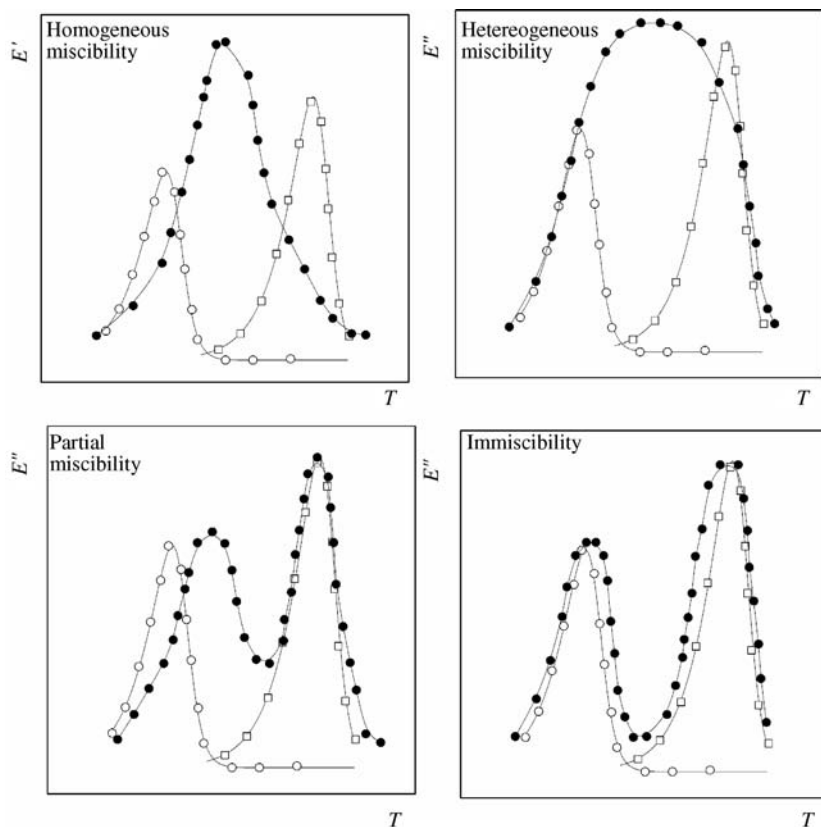


**Figure 12.5** Miscibility of polymer blends by examination of the glass–rubber relaxation temperature. Hollow and full symbols differentiate initial (individual polymers) and final (polymer blend) situations.

ester (BACY) were prepared via the co-curing of benzoxazine with cyanate ester [53]. In this case only a single peak was revealed, that could be associated with a single glass–rubber relaxation between those of the two homopolymers. A single  $T_g$  of the blends was found between those of the component polymers, which implied a near-homogeneous matrix; this improved not only the modulus of the blend but also its thermal stability. Other studies performed on liquid *cis*-polyisoprene/*trans*-polyisoprene (CPI/TPI) blends exhibited a single glass–rubber relaxation which also indicated the miscibility and better compatibility of these blends for industrial applications [41]. In contrast, poly(ethylene-*co*-vinyl alcohol) and poly(methyl methacrylate) blends were shown to be immiscible, independent of the ethylene vinyl alcohol (EVOH) and blend composition [54].

During recent years, polymer blends derived from renewable resources [55] have attracted much scientific, technological and commercial interest, due to the provision of “green” replacements for the commonly used petroleum-based polymeric materials. In this sense, when the compatibilization of melt-mixed

polylactide/polyhydroxyalkanoate (PLA/PHBV) blends was investigated in dynamic mode [12], the results highlighted the important role of the interfaces between PLA and PHBV and the peculiar behavior in terms of the viscosity of some mixtures at low frequencies. At medium and high frequencies, the mixture dynamic viscosity followed the mixing law. Others investigated the compatibility of binary blends of poly(lactic acid) and glycidyl methacrylate grafted poly(ethylene octane) (PLA/mPEO) [56]. All of the binary blend compositions exhibited two distinct glass–rubber relaxation temperatures that corresponded to the mPOE-rich and PLA-rich phases, respectively. These peaks approached each other with increasing mPOE content, indicating the partial compatibility of PLA/mPOE blends, which was ascribed to the reaction between epoxy groups of the mPOE and the carboxyl end-groups of PLA.

### 12.2.2

#### Ternary Systems

Although the miscibility of blends usually relates to binary systems, miscibility in ternary blends may show a different behavior for different components. A general blend of A/B, when blended with a third polymer C, may show variations in  $T_{\alpha_A}$  but not for  $T_{\alpha_B}$ , thus demonstrating the different degrees of miscibility between A and C, and immiscibility for B and C. This is the case for mixtures of polyarylate (PAR) with liquid-crystalline copolyesters of *p*-hydroxybenzoate–poly(ethylene terephthalate) (PET), which showed variations of the  $T_{\alpha_{PAR}}$  with blend composition, and no variation of  $T_{\alpha_{PET}}$ , showing no miscibility of PAR in PET [57]. These observations may be interesting if the coupling of immiscible polymers is being considered, as this can be achieved by using a mutually miscible third polymer, as shown elsewhere [58,59].

### 12.2.3

#### Influence of Type of Processing

The type of process used may have a direct influence on the final composition of the blend. For example, in mixtures of LDPE and linear low-density polyethylene (LLDPE), it was shown [60] that during quenching the two phases appeared clearly separated, whereas during a slow annealing process the blend was partially compatible. It is interesting to note that the processability of polymers can be improved by blend mixing, as shown for the rubber toughening of poly(ether imide) (PEI) by the addition of poly(butylene terephthalate) (PBT) [61]. The  $\tan \delta$  of the PEI–PBT 80/20 blend showed a single peak at about 177 °C, this being the temperature intermediate to those of the neat components (221 and 66 °C, respectively), and indicating the presence of a single miscibilized amorphous phase. This decrease in  $T_{\alpha}$  of the PEI matrix after the addition of 20% PBT indicated that the processability could be improved, by allowing the mixing temperature to be reduced from the usual 340 °C for neat PEI to 290 °C for the blend. This concept was also used successfully to mix PEI–PBT/mPEO blends, thereby avoiding

significant mPEO thermal degradation because similar processing temperatures were used to process blends such as PET/mPEO [62] (275 °C), PA66/mSEBS [63] (280 °C) and PSU/mPEO [64] (290 °C). Other studies showed that the addition of LDPE to LLDPE not only facilitated the extrusion process but also improved the optical properties of the blown film [65].

Blends that are initially immiscible or partially miscible and which have been modified to increase compatibility are also referred to as “polymer alloys” [29]. One interesting approach to homogenizing initially immiscible materials may involve thermal treatment, and along this line the effect of annealing on the miscibility and phase behavior of poly(trimethylene terephthalate) (PTT) and bisphenol A polycarbonate (PC) blends was examined [66]. These blends, which exhibited a heterogeneous phase-separated morphology and two well-spaced glass–rubber relaxation temperatures, were submitted to an annealing process at 260 °C during 2 h. Subsequently, a single  $T_g$  was shown as a clear effect of homogenization. It was also noted that the original semicrystalline morphology could be transformed into an amorphous nature by extending the annealing period.

#### 12.2.4

#### **Recovering Plastic Waste by Polymer Blending**

Blending can also be an effective strategy for recovering polymer-based waste. In this sense, the introduction of styrene-based polymers to prepare polymer blends from recycled poly(vinyl chloride) was studied to test the potential for recovering PVC from disposed credit cards [67]. The incorporation of styrene/acrylonitrile (SAN) to the recycled PVC improved the mechanical properties, but a strong reduction in the ductile properties was reported; this was attributed to the fragile nature of the SAN itself and the lack of total miscibility among the components. In the case of acrylonitrile/butadiene/styrene (ABS) blends, an enhancement of the ductile properties was noted, and assigned to the butadiene segments.

#### 12.2.5

#### **Influence of Nanoparticles**

The use of nanoparticles such as nanoclays or carbon nanotubes (CNTs) has been shown to play a role in the partial miscibility of blends. For example, nanoclays can be used as both coupling agents and reinforcing agents in polychloroprene/ethylene–propylene–diene–monomer rubber (PCR/EPDM rubber) blends [68]. In one case, the addition of nanoclays reduced the interfacial energy between the phases by accumulating at the interfaces; this permitted a finer intercalation–exfoliation process during mixing and vulcanization, and also provided a strong reinforcement to the rubber blends. In particular, the incorporation of <9 wt% nanoclay increased the dynamic storage modulus of the blend above the glass–rubber relaxation region, from ~2 MPa to ~54 MPa. Chemically treated fillers can also act as coupling agents for previously immiscible polymer blends, as was the

case with blends of poly(etherimide)/liquid crystalline polymer (PEI/LCP), filled with multiwalled CNTs (MWCNTs), modified with polycarbosilane-derived b-SiC particles (SiC-MWCNTs) [69]. Whereas, the blending of LCP with PEI decreased the  $E'$ -value of the binary blend compared to pure PEI (due to incompatibility between the two matrices), the incorporation of MWCNTs into the PEI/LCP blend system enhanced the  $E'$ -value. However, in the presence of SiC-MWCNTs the  $E'$ -value of PEI/LCP showed a remarkable improvement compared to the values for pure PEI, PL, and LCP. A remarkable finding was that the  $E'$  curve of the binary blend showed a two-step drop, as compared to a one-step drop for the pure components (PEI and LCP). Further reports were made of similar contributions by nanoclays in improving the miscibility of thermoplastic polyurethane (TPU)/polypropylene (PP) blends coupled with maleic anhydride-grafted polypropylene (MA-g-PP) [70]. The incorporation of unmodified MWCNTs into the binary blend also showed a two-step drop in  $E'$ , but the SiC-MWCNT-filled system depicted a single-step drop demonstrating the improvement in compatibility of the PEI/LCP blends. In this sense, other studies of the effect of MWCNTs on polycarbonate/liquid crystalline polymer (PC/LCP) blends [71] proved that, by increasing the MWCNT loading, the maximum of  $\tan\delta$  was decreased, highlighting the reduction of any dampening effect by the addition of MWCNT. This suggested that some interfacial adhesion existed between PC and LCP, and that this was increased in the presence of a higher MWCNT content and resulted in a better stress transfer between PC and LCP. The same type of observation was made in the case of wood fiber-reinforced polyhydroxybutyrate-co-valerate composites [72].

#### 12.2.6

##### The Study of the Rubbery Plateau as an Indicator of Miscibility

The study of the rubbery plateau also provides information on the effects of some additives on the miscibility of blends. The morphologic development of polystyrene (PS)/polyamide (PA6) blends in which titanium dioxide ( $\text{TiO}_2$ ) nanoparticles were localized preferentially in the PA6 domains was investigated [73]. For the blend without nanoparticles, the  $E'$  curve showed a similar shape as for neat PS, which suggested that PA6 was separately dispersed in the PS matrix to form a matrix-droplet structure. However, by adding a large amount of  $\text{TiO}_2$  nanoparticles a significant rubbery plateau of PS appeared at  $T > T_\alpha$ . Moreover, an increase in the  $\text{TiO}_2$  content not only led to a higher  $E'$  at the rubbery plateau but also extended its temperature range, thus demonstrating an improvement in co-continuity for the  $\text{TiO}_2$ -filled PS/PA6 system. The results of other studies [68] also showed that the reinforcement and migration of nanoclay in polychloroprene/ethylene-propylene–diene-monomer (PCR/EPDM) rubber blends played a role in the compatibilization of incompatible rubber blends, thus offering new routes to the design of novel rubber-based technical products for a diversity of applications. Considerable increases in the  $E'$  of the rubbery plateau were found in these cases.

**Table 12.2** Compositional rules based on the study of the glass–rubber relaxation temperature ( $C_p$ : heat capacity obtained by differential scanning calorimetry;  $a$ ,  $k$ , and  $q$  are adjustable parameters).

Author	Equation	Reference
Fox	$\frac{1}{T_g} = \frac{w_1}{T_{g1}} + \frac{w_2}{T_{g2}}$	[75]
Gordon–Taylor	$T_g = \frac{w_1 \cdot T_{g1} + k \cdot w_2 \cdot T_{g2}}{w_1 + k \cdot T_{g2}}$ $k = \frac{\Delta\alpha_2 \cdot V_2}{\Delta\alpha_1 \cdot V_1}$	[76]
Couchman–Karasz	$\ln T_g = \frac{\sum_i w_i \cdot \Delta C p_i \cdot \ln T_{gi}}{\sum_i w_i \cdot \Delta C p_i}$	[77]
Kwei	$T_g = \frac{w_1 \cdot T_{g1} + k \cdot w_2 \cdot T_{g2}}{w_1 + k \cdot T_{g2}} + q \cdot w_1 \cdot w_2$	[78]

### 12.2.7

#### Theoretical Approaches to Calculating the Glass–Rubber Relaxation Temperature

The  $T_\alpha$  of polymer blends can be related to the blend composition by different equations, as shown in Table 12.2. The  $T_\alpha$  of miscible blends of poly(*p*-dioxanone) with poly(vinyl phenol) (PPDO/PVPh) [74], as studied using the Fox [75], Gordon–Taylor [76], Couchman–Karasz [77] and Kwei [78] models, showed that the experimental data lay below the Fox equation, suggesting that the free volume of the blends was larger than predicted, assuming free volume additivity. On the other hand, the Gordon–Taylor and the simplified Kwei equations fitted the experimental  $T_\alpha$  values appropriately. Other studies have shown that the  $T_\alpha$  of SAN/PMMA blends was also effectively approached by the Gordon–Taylor relationship [79,80].

## 12.3

### Segmental Dynamics, Fragility Index, and Free-Volume

Studies of the loss modulus  $E''$  by means of DMTA provides important information regarding the dynamics involved throughout the glass transition of these materials. The strong–fragile glass concept formerly proposed by Angell [81] relates to the variation of viscosity with temperature, and can be explained under two border limits. A fragile glass-former experiences a dramatic loss of properties (rheological, mechanical) throughout a specific short temperature interval, such as the glass–rubber relaxation, whereas a strong glass-former maintains its properties without any significant changes [82,83]. Whilst, on the one hand, the  $\tau(T)$  of a strong glass-forming behavior can be expressed by the Arrhenius law (Eq. (12.7)),

on the other hand a fragile glass-forming polymer would deviate from the thermally activated Arrhenius behavior, as usually occurs with linear polymeric materials, as shown in Figure 12.4. As noted above, this effect can be explained by a Vogel–Fulcher–Tamman–Hesse model (Eq. (12.9)), whereby the so-called fragility index  $m$  permits an assessment of the deviation of  $\tau(T)$  from the Arrhenius behavior of polymers. The index is defined as the characteristic slope of the fragility plot  $\log \tau$  versus  $T_\alpha \cdot T^{-1}$ , and varies between two limiting values of 16 and  $\geq 200$  for strong and fragile glass-formers, respectively [84,85].

$$m = \left. \frac{d \log(\tau)}{d(T_g/T)} \right|_{T=T_g} = \frac{B \cdot T}{\ln(10) \cdot (T_g - T_{VFTH})^2} \quad (12.13)$$

considering the  $T_g = T_\alpha$  corresponding to experiments at  $\tau \sim 100\text{--}200$  s. In this case,  $m$  can be assimilated to the average energy barrier related to the segmental cooperation, which has to be overcome to reach a minimum energy state after the  $\alpha$  transition.

Kunal *et al.* [86] performed several studies to relate the dynamic fragility of several families of polymers to their substituents, in terms of steric hindrances and chemical interactions, and some examples are also available for polymer blends. The effect of adding a high-molecular-weight epoxy (HMWE) monomer to a low-molecular-weight epoxy (LMWE) on the fracture toughness properties of the epoxydic blend was considered in terms of the degree of crosslinking and density heterogeneity [87]. Subsequent DMTA studies confirmed that the density heterogeneity in the blends was gradually increased with the amount of HMWE, which in turn reduced the dynamic fragility and improved the fracture toughness. Other reports were focused on the segmental dynamics of two phase-separated, reactively prepared PS blends, namely unsaturated polyester resin (UPR) and high-impact polystyrene (HIPS), in order to compare the roles of stiff and rigid inclusions on the fragility of PS [88]. The dynamic fragility of the UPR system was mildly greater than that of the HIPS system. This can be explained in terms of segmental motions, restricted by networks crosslinks in the case of the UPR systems.

The effectiveness of blending can be also assessed from the point of view of segmental mobility, by measuring either the free-volume coefficient or the thermal expansion coefficient in the rubbery state. This can be considered not only as an indicator of the degree of miscibility, with its consequent viscoelastic performance, but also as a technological parameter for applications where the transport properties are crucial, as in the case of membranes for gasoline [89]. The free-volume coefficient can be drawn from an analysis of the  $E''$  spectra, taking into account the empirical expression formulated by Doolittle and Doolittle [90], where the relaxation times of the viscoelastic mechanism were found to behave as follows:

$$\tau(T) = CT_1 \cdot \exp\left(\frac{CT_2}{\phi \cdot T}\right) \quad (12.14)$$

where  $\phi$  is the free-volume coefficient given by  $\phi = (v - v_0) \cdot v^{-1}$ , with  $v$  and  $v_0$  being total and occupied specific volumes, respectively, and  $CT_1$  and  $CT_2$  are both constant parameters, where the latter is close to the unity. In comparison with the VFTH equation, this equates to:

$$\phi = \frac{(T - T_{\text{VFTH}})}{B} \quad (12.15)$$

In this sense, the steric hindrance induced by poly(ethylene oxide) (PEO) on poly(methyl methacrylate) (PMMA) in PMMA/PEO blends [91] showed an increase in free volume that controlled the segmental dynamics. Other reports noted the effects of blending cis-polyisoprene (CPI) with trans-polyisoprene when, the higher the CPI content the softer was the blend. When a blend with a lower CPI content was subjected to a low temperature, the free volume of the molecules of chains in the blend was decreased [41]. Thus, in line with the calculations of apparent activation energies, more  $E_a$  was required to make the transition from a rubbery phase to a glassy phase. Likewise, the peel-strength of rubbers, especially ethylene-propylene-diene-based (EPDM) rubbers, following the addition of two different resins, namely hydrocarbon (HC) and coumaroneindene (CI), was studied in terms of miscibility and free volume [92]. The HC tackifier was shown to be fully compatible with vulcanized EPDM, whereas the CI tackifier became heterogeneous with EPDM of low-weight proportions. For all HC-blended systems, a single  $T_\alpha$  indicated phase miscibility which, when displaced to higher values, indicated a reduction in free volume available for local segmental motions. It was concluded that the peel strength of the blended rubber would be increased incrementally in line with the concentration of the HC tackifier.

## 12.4

### Effects of Plasticizers and Chemical and Physical Crosslinks

The variables that affect dynamic mechanical behavior include important factors such as the level of crosslinking, the presence of a plasticizer, or phase separation. Moreover, each factor may occur in either block or segmented copolymers, in polymer blends, and in semicrystalline systems. In general terms, crosslinking tends to increase the magnitude of the glass-rubber relaxation and loss behavior; however, occasionally the relaxation is caused to broaden, as might be expected due to an influence on the spreading of relaxation times caused by cooperative backbone motions. In contrast, the addition of a plasticizer tends to reduce the glass-rubber relaxation temperature and often broadens the loss response, though different plasticizers may behave in quite different ways in terms of the extent of such loss. This permits a degree of control on the thermal range over which damping occurs. Antiplasticizers can, in fact, depress or eliminate one or more of the sub- $T_\alpha$  loss responses by limiting the mobility of the corresponding molecular group responsible for that transition. A representation of the effects of plasticizers

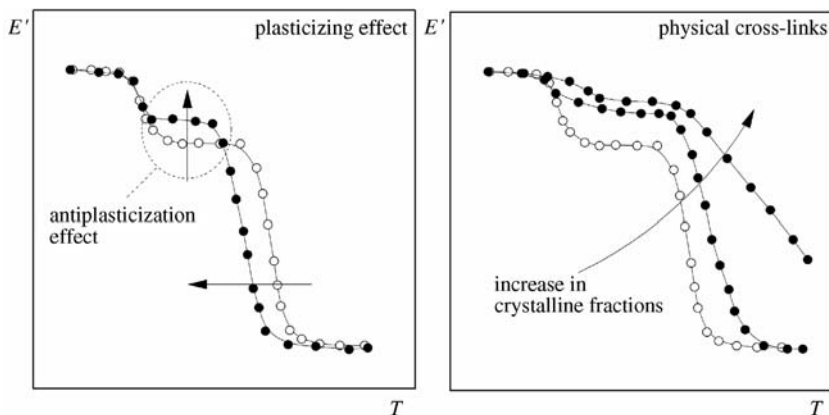


**Figure 12.6** Schematic representation of the effects of plasticizers and crosslinkers on the storage modulus curve. Hollow and full symbols differentiate initial (polymer blend) and final (influence of plasticizer or crosslinker) situations.

and crosslinkers on the storage modulus curve on an ideal polymer blend is shown schematically in Figure 12.6.

#### 12.4.1

##### **Influence of Plasticizers on Viscoelastic Performance of Polymer Blends**

Some examples of the effects of plasticizers on the viscoelastic response of polymer blends are available in the literature [93–97]. Currently, within the field of packaging, very many studies have been conducted with new polymeric materials derived from renewable resources. For example, the effect of citric acid acting as a plasticizer was investigated on polylactide/thermoplastic wheat flour (wheat flour/PLA) blends [93]. This led to the creation of highly deformable materials, all with a significant degree of toughness that was due mainly to the PLA contribution, and which provided an interesting compromise between brittle PLA and highly ductile glycerol-plasticized wheat flour. Other studies were initiated to investigate compatibility between hydrophilic starch granules and hydrophobic PLA, glycerol, formamide and water, each of which were assessed as plasticizers for starch so as to enhance the dispersion and interfacial affinity of thermoplastic starch (TPS)/PLA blends [94]. Studies of the variation of  $\tan\delta$  showed formamide to be a much more effective plasticizer for starch than was glycerol, after having excluded water from the blend. Along the same lines, the effect of amphiphilic additives (e.g., Tween 60, linoleic acid, and zein) on thermoplastic starch/poly(lactic acid) (TPS/PLA) was analyzed using monofrequency compression DMTA testing [95]. The blends showed a lower  $T_{\alpha}$ , due to the plasticizing effect, which in turn facilitated the processability, flowability and extensibility of these blends. Linoleic acid proved to be a more effective additive for enhancing the flowability of the TPS/PLA blends than did either Tween 60 or zein.



Current investigations are aimed at providing polymers derived from renewable resources but with electroactive properties. For example, an ionic liquid (1-butyl-3-methyl imidazolium chloride; BMIM-Cl) was used as a plasticizer in starch, zein and their blends, and compared to glycerol, as a classical plasticizer of starch [96]. For the blends, the temperature of the two relaxations associated with the starch-rich and zein-rich phases was decreased with increasing zein content, this effect being assigned to the migration of glycerol and/or water from the zein phase to the starch phase. Subsequent DMTA testing showed that a compatibilization of starch/zein blends took place in the presence of BMIM-Cl, whereas those plasticized by glycerol were incompatible. Interestingly, these results opened up new perspectives for the use of bioplastics as solid electrolytes, as these materials are electrically conductive due to the presence of the ionic liquid [97].

#### 12.4.2

##### **Influence of Chemical and Physical Crosslinkers on the Viscoelastic Performance of Polymer Blends**

Physical crosslinks can be introduced into polymer segments by various means. For example, they can be crystalline fractions inherent to any of the blend components, or they may be formed after homogenization of the polymer blend, due to physical entanglements or strain-induced crystallization (i.e., orientation). The addition of fillers has also been widely used to increase the stiffness of polymer blends, while post-blending processes to induce covalent chemical crosslinking can also be effective in this respect.

As some of the polymers present in blends may present with a degree of crystallinity, it is important to understand exactly how the crystalline domains can affect the viscoelastic behavior of the blend. When processing polymer blends it is essential to conduct any operations very carefully in order to prevent or improve the development of crystalline phases according to the desired performance for a certain application. Under service conditions the main effects of crystallinity occur below the glass–rubber relaxation temperature, when not only is the storage modulus enhanced as major but the influence of the semicrystalline polymer present in the blend, due to the physical crosslinking effect induced by crystallites. For example, numerous studies to demonstrate the effects of the morphology and crystallization processing of LDPE-LLDPE blends by means of Ziegler–Natta initiators [98–103] showed that the crystallization speed has a clear influence on the segregation of crystals and cocrystallization of the blends [102]. Another example involved studies of the influence of crystallinity of polyamide 11 (PA11) into polylactide/polyamide11 blends (PLA/PA11), using monofrequency DMTA tests [104]. At  $T < T_{\alpha}$  for both polymers, the stiffness of PA11 was somewhat lower than that of PLA, while the  $E'$ -value of the blends roughly obeyed a linear mixing rule. Due to the closeness of the two polymer moduli, the morphological changes that occurred with blend composition had very weak effect on the  $E'$  of the blends. However, when passing  $T_{\alpha}$  the crystalline phase of PA11 preserved a reinforcing effect in spite of the fall in temperature accounted for by both components alone.

Drawing can also introduce physical crosslinks via the formation of crystalline phases that improve the performance of blends. For instance, microfibrillar composites (MFCs) were prepared using different draw/stretch ratios from polypropylene/polyethylene terephthalate (PP/PET) blends [105]. The oriented PET fibrils in the stretched blend were found to have a greater nucleating effect for the crystallization of PP than did the spherical PET particles in the neat blend and randomly oriented short PET fibrils in the MFC, thus improving the storage modulus.

The concept of reinforcement is widely applied not only in the rubber sector but also in the recovery of plastics. Elastomeric blends of *trans*-polyisoprene and liquid *cis*-polyisoprene (TPI/CPI) showed a considerable shift in glass–rubber relaxation temperature towards higher values, and this effect was ascribed to the increasing crystallinity with the decrease in TPI content [41]. In fact, TPI has a rigid structure whereas CPI has a loose viscous structure; thus, when CPI was added at the cost of TPI in the TPI/CPI blends the material converged towards a rubbery elastic phase. The effect of dynamic vulcanization on the mechanical and fatigue properties of ground tire rubber, styrene-butadiene rubber and their combination on polypropylene (PP/GTR and PP/SBR/GTR) blends was also studied [106]. The values of  $E'$  at  $T < T_g$  increased as the amount of GTR in the blend was increased, due to an increased crosslink density of the rubber phase and also to the presence of greater amounts of filler. When the dynamic mechanical properties of recycled high-density polyethylene and poly(vinyl alcohol) (rHDPE/PVA) blends were studied in tension mode [107], a reduction in the relaxation temperature of the amorphous domains of the PVA was demonstrated that was most likely due to degradation of the material during processing. Increasing the amount of PVA in the blend composition led to a higher values of loss modulus in the blends; notably, this behavior was associated with the molecular rigidity of the PVA.

It must be noted that some additives can play a different role, and in this sense the coupling of a poly(etherimide)/thermotropic liquid crystalline polymer (PEI/LCP) blend was characterized in terms of the addition of amino-phenol, allyl-phenol and diethylether-substituted polyphosphazene, using monofrequency DMTA tests [108]. The highest increase in  $E'$  was provided by the amino-phenol compound, due to an improved interfacial bonding between the matrix phase and the dispersed phase, conferred by H-bonding between the amine group of the polyphosphazene and the carbonyl group of the LCP. In contrast, the effect of the diethylether-unsubstituted polyphosphazene provoked a greater flexibility, reducing the  $T_g$  of the PEI/LCP blend.

### 12.4.3

#### Strategies to Tune the Heat Distortion Temperature by Polymer Blending

The heat distortion temperature (HDT), which is also referred to as the deflection temperature under load (DTUL), is usually presented in the datasheet of a material in order to rapidly estimate its thermal resistance capabilities under certain

conditions. The HDT consists of a monotonously triple-point bending, under constant load and in a controlled-temperature chamber. The temperature at which the probe is deflected by more than 0.25 mm is recorded as the HDT [109].

The application of DMTA can also provide HDT values, the main advantage being an ability to offer a span of HDTs for different loads, simply by applying a monofrequency DMTA analysis with the same heating rate as in HDT tests. In one study [110], the relationship between experiments with polymer blends having different degrees of miscibility, as well as the effect of fiber reinforcement and the increase of crystallinity in the blend matrixes, were demonstrated. In brief, if the ordinate of the storage modulus spectrum is entered with the value of the theoretical modulus  $E$  that will apply in a HDT analysis then, for common prismatic probes, Eq. (12.16) can be used to determine the modulus  $E$ , where  $\sigma_{\max}$ ,  $L$  and  $\Delta d$  are the maximum stress, the distance between supports applicable by HDT, and the deflection at which HDT is registered (0.25 mm), respectively. Figure 12.7 shows a calculation of the HDT for two polymer blends with different values of  $T_{\alpha}$ . Clearly, if increasing the HDT of a polymer is focused, then a good criterion would be to blend it with another polymer with a higher  $T_{\alpha}$ , that would displace the HDT to a higher temperature. In amorphous blends this option was shown to be more effective than adding fillers, as HDT is connected directly to the  $T_{\alpha}$ . This was shown to be an interesting option for semicrystalline polymers, which usually have a high melting temperature but a low  $T_{\alpha}$ . As shown in Figure 12.7, the addition of fillers may considerably increase the HDT. Another interesting design strategy would be to combine semicrystalline polymers (which confer strength to the blend) with amorphous polymers (which provide processability). This is the case for nylon-PPE blends [111], which have been used in automobiles to create

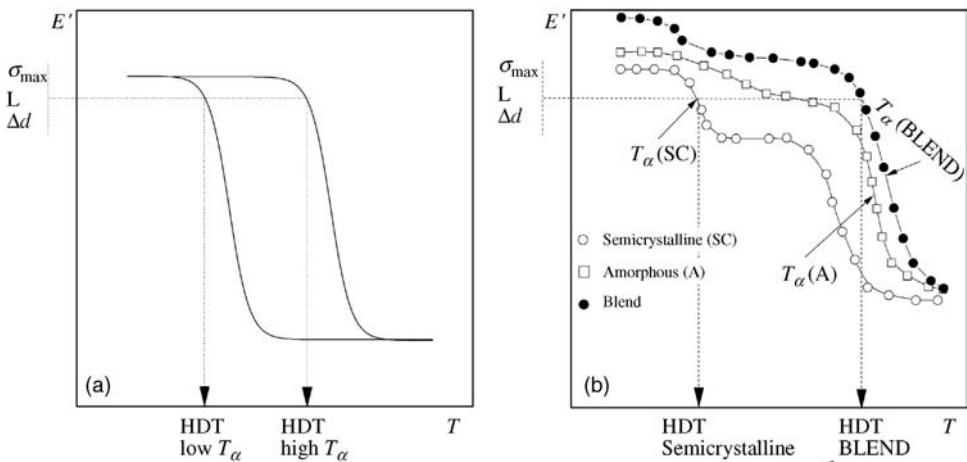


**Figure 12.7** (a) Differences between polymers with low HDT (dashed line) and high HDT (full line); (b) Schematic representation of the effects of blending on the HDT values. Hollow and full symbols differentiate initial (individual polymers) and final (polymer blends) situations.

external components that need to be painted and baked at high temperatures, but without softening.

$$E = \sigma_{\max} \cdot \frac{L^2}{6 \cdot \Delta d} \quad (12.16)$$

Some examples can be highlighted at this point. When the influence of chlorinated polyethylene (CPE) content on the properties of poly(vinyl chloride) (PVC)/poly ( $\alpha$ -methylstyrene-acrylonitrile) ( $\alpha$ -MSAN) blends (70/30) was investigated [112], the addition of CPE was seen to contribute to improvements in toughness but played a negative role in terms of strength and modulus. Indeed, the HDT values remained essentially unchanged over all of the blend compositions, a property attributed to the greater rigidity of PVC/ $\alpha$ -MSAN matrix compared to PVC. It was also shown that the incorporation of CPE could increase the impact strength, without sacrificing any heat resistance.

Other research groups have focused attention on different binary and ternary blends of PP, grafted-PP with acrylic acid (PP-g-AA), and ethylene-vinyl acetate (EVA) and their reinforcement by organoclays [113]. The incorporation of 40 wt% EVA into PP led to a decrease in the HDT, according to an increase of flexibility and toughness due to incorporation of the elastomeric phase. In contrast, the addition of organoclays to a PP/EVA blend led to a slight increase in both modulus and HDT.

In the case of organoclay-based nanocomposites, the extent of enhancement of  $E'$  and HDT have been reported as indicators of the aspect ratio of the organoclay particles dispersed in the polymer blend matrix and, therefore, reflect the state of exfoliation or dispersion of the organoclay [114,115]. In this sense, the reinforcement by montmorillonite (MMT) of nylon 6 improved the HDT of the nanocomposites, due primarily to a combination of the high modulus and aspect ratio of MMT, rather than to changes in the polymer matrix caused by the clay platelets [114]. Other blends of nylon, modified by maleated ethylene-propylene rubber (EPR-g-MA) plus glass fibers, showed that either octyl or anhydride treatment would produce improved HDTs relative to either nylon 6 or nylon 6/EPR-g-MA blends [116]. In the case of poly(hydroxyl butyrate-co-valerate) (PHBV) reinforced with wood fibers [72], an improvement of 24 °C in HDT was shown. The improvement in HDT by enhancing the fiber content was due not only to reinforcement by the fiber, which had a higher HDT than the polymer matrix, but also to an increase in the degree of crystallinity in PHBV due to the addition of wood fibers, the surface of which had served as nucleating sites.

## 12.5

### Summary

The technique of DMTA is devoted to assessing the viscoelastic responses of materials submitted to mechanical solicitations, as a function of both temperature and frequency. Polymer blends may perform under conditions which induce

stress-strain mechanical solicitations that may impact on the cooperative motions responsible for their viscoelastic performance. The application of DMTA not only allows investigations of thermal transitions to be made at different segmental scales by characterizing the evolution of macromolecular relaxation times with temperature, but also relates these effects to the technological parameters that are vital in a variety of industrial sectors. In this chapter, the application of DMTA to study polymer blends has been approached from both scientific and technical points of view, with attention focused especially on the theoretical basis of viscoelastic theory, on studies of segmental dynamics, free volume and dynamic fragility, on miscibility, and on the effects of adding plasticizers and chemical or physical crosslinkers to polymer blends.

## References

- 1 Hale, A. and Bair, H.A. (1997) Polymer blends and block copolymers, in *Thermal Characterization of Polymeric Materials*, 2nd edn (ed. E.A. Turi), Academic Press, New York.
- 2 Yave, W., Car, A., Peinemann, K.V., Shaikh, M.Q., Rätzke, K., and Faupel, F. (2009) Gas permeability and free volume in poly(amide-b-ethylene oxide)/polyethylene glycol blend membranes. *J. Membr. Sci.*, **339**, 177–183.
- 3 Al Minnath, M., Unnikrishnan, G., and Purushothaman, E. (2011) Transport studies of thermoplastic polyurethane/natural rubber (TPU/NR) blends. *J. Membr. Sci.*, **379**, 361–369.
- 4 Appetecchi, G.B., Kim, G.T., Montanino, M., Carewska, M., Marcilla, R., Mecerreyes, D., and DeMeatza, I. (2010) Ternary polymer electrolytes containing pyrrolidinium-based polymeric ionic liquids for lithium batteries. *J. Power Sources*, **1195**, 3668–3675.
- 5 Arranz-Andres, J., Lorenzo, V., de la Orden, M.U., Pérez, E., and Cerrada, M.L. (2011) Tailoring transport properties in blends based on olefinic and liquid crystalline polymers. *J. Membr. Sci.*, **377**, 141–150.
- 6 Rajendran, S. and Shanti Bama, V. (2010) A study on the effect of various plasticizers in poly(vinyl acetate)-poly(methyl methacrylate) based gel electrolytes. *J. Non-Cryst. Solids*, **356**, 2764–2768.
- 7 Zhu, M., Qian, J., Zhao, Q., An, Q., and Li, J. (2010) Preparation method and pervaporation performance of polyelectrolyte complex/PVA blend membranes for dehydration of isopropanol. *J. Membr. Sci.*, **361**, 182–190.
- 8 Morris, B.A. (2009) Polymer blending for packaging applications, in *Multilayer Flexible Packaging* (ed. J.R. Wagner), Elsevier Inc.
- 9 Bitinis, N., Verdejo, R., Cassagnau, P., and López-Manchado, M.A. (2011) Structure and properties of polylactide/natural rubber blends. *Mater. Chem. Phys.*, **129**, 823–831.
- 10 Bocchini, S., Battagazzore, D., and Frache, A. (2010) Poly(butylsuccinate-co-adipate)-thermoplastic starch nanocomposite blends. *Carbohydr. Polym.*, **82**, 802–808.
- 11 Coltelli, M.B., Bronco, S., and Chineza, C. (2010) The effect of free radical reactions on structure and properties of poly(lactic acid) (PLA) based blends. *Polym. Degrad. Stabil.*, **95**, 332–341.
- 12 Gerard, T. and Budtova, T. (2012) Morphology and molten-state rheology of polylactide and polyhydroxyalkanoate blends. *Eur. Polym. J.*, **48**, 110–1117.
- 13 González-Gutiérrez, J., Partal, P., García-Morales, M., and Gallegos, C. (2011) Effect of processing on the viscoelastic, tensile and optical properties of alumen/starch-based bioplastics. *Carbohydr. Polym.*, **84**, 308–315.

- 14 Meng, B., Deng, J., Liu, Q., Wu, Z., and Yang, W. (2012) Transparent and ductile poly(lactic acid)/poly(butyl acrylate) (PBA) blends: Structure and properties. *Eur. Polym. J.*, **48**, 127–135.
- 15 Mir, S., Yasin, T., Halley, P.J., Siddiqi, H. M., and Nicholson, T. (2011) Thermal, rheological, mechanical and morphological behavior of HDPE/chitosan blend. *Carbohydr. Polym.*, **83**, 414–421.
- 16 Sarazin, P., Li, G., Orts, W.L., and Favis, B. D. (2008) Binary and ternary blends of polylactide, polycaprolactone and thermoplastic starch. *Polymer*, **49**, 599–609.
- 17 Tang, X. and Alavi, S. (2011) Recent advances in starch, polyvinyl alcohol based polymer blends, nanocomposites and their biodegradability. *Carbohydr. Polym.*, **85**, 7–16.
- 18 Vallés-Lluch, A., Contat-Rodrigo, L., and Ribes-Greus, A. (2002) Degradation studies of LDPE-Mater-Bi blends annealed and aged in soil. *J. Appl. Polym. Sci.*, **86**, 405–413.
- 19 Aldana, A.A., González, A., Strumia, M. C., and Martinelli, M. (2012) Preparation and characterization of chitosan/genipin/poly(*N*-vinyl-2-pyrrolidone) films for controlled release drugs. *Mater. Chem. Phys.*, **134**, 317–324.
- 20 Del Gaudio, C., Ercolari, E., Nanni, F., and Bianco, A. (2011) Assessment of poly( $\alpha$ -caprolactone)/poly(3-hydroxybutyrate-co-3-hydroxyvalerate) blends processed by solvent casting and electrospinning. *Mater. Sci. Eng. A*, **528**, 1764–1772.
- 21 Navarro, F.J., Partal, P., Martínez-Bosa, F.J., and Gallegos, C. (2010) Novel recycled polyethylene/ground tire rubber/bitumen blends for use in roofing applications: Thermo-mechanical properties. *Polym. Test.*, **29**, 588–595.
- 22 Lee, J.B., Lee, Y.K., Choi, G.D., Na, S.W., Park, T.S., and Kim, W.N. (2011) Compatibilizing effects for improving mechanical properties of biodegradable poly(lactic acid) and polycarbonate blends. *Polym. Degrad. Stabil.*, **96**, 553–560.
- 23 Badia, J.D., Strömberg, E., Karlsson, S., and Ribes-Greus, A. (2012) Material valorisation of amorphous polylactide. Influence of thermo-mechanical degradation on the morphology, segmental dynamics, thermal and mechanical performance. *Polym. Degrad. Stabil.*, **97**, 670–678.
- 24 Badia, J.D., Strömberg, E., Karlsson, S., and Ribes-Greus, A. (2012) The role of crystalline, mobile amorphous and rigid amorphous fractions in the performance of recycled poly(ethylene terephthalate) (PET). *Polym. Degrad. Stabil.*, **97**, 98–107.
- 25 Santonja-Blasco, L., Moriana, R., Badia, J. D., and Ribes-Greus, A. (2010) Thermal analysis applied to the characterization of degradation in soil of polylactide: I. Calorimetric and viscoelastic analyses. *Polym. Degrad. Stabil.*, **95**, 2192–2199.
- 26 De JuanoArbona, V.S. and Ribes-Greus, A. (2009) Effect of photooxidative ageing at natural conditions on dynamic mechanical properties of PE-LD/PE-LLD blends. *Polimery/Polymers*, **54**, 250–254.
- 27 Badia, J.D., Vilaplana, F., Karlsson, S., and Ribes-Greus, A. (2009) Thermal analysis as a quality tool for assessing the influence of thermo-mechanical degradation on recycled poly(ethylene terephthalate). *Polym. Test.*, **28**, 169–175.
- 28 Wang, K., Addiego, F., Bahlouli, N., Ahzi, S., Rémond, Y., Toniazoo, V., and Muller, R. (2012) Analysis of thermomechanical reprocessing effects on polypropylene/ethylene octene copolymer blends. *Polym. Degrad. Stabil.*, **97**, 1475–1484.
- 29 Utracki, L.A. (1990) *Polymer Alloys and Blends. Thermodynamics and Rheology*, Hanser Publishers.
- 30 Turi, E.A. (ed) (1997) *Thermal Characterization of Polymeric Materials*, 2nd edn, Academic Press, New York.
- 31 Riande, E., Díaz-Calleja, R., Prolongo, M.G., Masegosa, R.M., and Salom, C. (2000) *Polymer Viscoelasticity. Stress and Strain in Practice*, Marcel Dekker Inc., N.Y., Basel.
- 32 Brown, M.E. (2001) *Introduction to Thermal Analysis: Techniques and Applications*, Springer.
- 33 Menard, K.P. (2008) *Dynamical Mechanical Analysis, a Practical Introduction*, CRC Press, Boca Ratón, US, p. 101.
- 34 Arnold, F.E. Jr, Bruno, K.R., Shen, D., Eashoo, M., Lee, C.J., Harris, F.W., and Cheng, S.Z.D. (1993) The origin of  $\beta$  relaxations in segmented rigid-rod

- polyimide and copolyimide films. *Polym. Sci. Eng.*, **33**, 1373–1380.
- 35 Nelson, F.C. (1994) Vibration isolation: A review, I. Sinusoidal and random excitations. *Shock. Vib. Digest*, **1** (5), 485–493.
  - 36 Vogel, H. (1921) The temperature dependence law of the viscosity of fluids. *Phys. Z.*, **22**, 645–646.
  - 37 Fulcher, G.S. (1925) Analysis of recent measurements of the viscosity of glasses. *J. Am. Ceram. Soc.*, **8**, 339–355.
  - 38 Tammann, G. and Hesse, G. (1926) The dependence of viscosity upon temperature of supercooled liquids. *Z. Anorg. Allg. Chem.*, **156**, 245–257.
  - 39 Bohmer, R. and Angell, C.A. (1994) *Disorder Effects on Relaxational Processes* (eds R. Richert and A. Blumen), Springer, Berlin.
  - 40 Scherer, G.W. (1990) Theories of relaxation. *J. Non-Cryst. Solids*, **123**, 75–89.
  - 41 Baboo, M., Dixit, M., Sharma, K., and Saxena, N.S. (2010) Activation energy and thermo-mechanical properties of *trans*-polyisoprene and liquid *cis*-polyisoprene blends. *Thermochim. Acta*, **502**, 47–50.
  - 42 Macosko, C. (1994) *Rheology*, VCH, New York.
  - 43 Cole, K.S. and Cole, R.H. (1941) Dispersion and adsorption in dielectrics. *J. Chem. Phys.*, **9**, 341–351.
  - 44 Havriliak, S. and Negami, S. (1967) A complex plane representation of dielectric and mechanical relaxation processes in some polymers. *Polymer*, **8**, 161–210.
  - 45 Kohlrausch, R. (1854) Theorie des elektrischen Rückstandes in der Leidner Flasche. *Ann. Phys. und Chemie (Poggendorff)*, **91**, 56–82, 179–213.
  - 46 Williams, G. and Watts, D.C. (1970) Non-symmetrical dielectric relaxation behavior arising from a simple empirical decay function. *Trans. Faraday Soc.*, **66**, 80–85.
  - 47 Debye, P. (1929) *Polar Molecules*, Chem. Catalog Co., New York.
  - 48 Fuoss, R.M. and Kirkwood, J.G. (1941) Electrical properties of solids. VIII. Dipole moments in polyvinyl chloride-diphenyl system. *J. Am. Chem. Soc.*, **63**, 385–394.
  - 49 Davidson, P.W. and Cole, R.M. (1950) Dielectric relaxation in glycerine. *J. Chem. Phys.*, **18**, 1417.
  - 50 Lunkenheimer, P., Pimenov, A., Dressel, M., Schiener, B., Schneider, U., and Loidl, A. (1997) Broadband dielectric spectroscopy on glass-forming liquids. *Prog. Theor. Phys. Suppl.*, **126**, 123–131.
  - 51 Friedrich, Chr. and Braun, H. (1992) Generalized Cole-Cole behavior and its rheological relevance. *Rheol. Acta*, **31**, 309–322.
  - 52 Diaz-Calleja, R., Sanchis, M.J., and Mostos, J. (1996) Biparabolic model to represent dielectric relaxation data. *Polymer*, **37**, 4003–4008.
  - 53 Kumar, K.S.S., Nair, C.P.R., and Ninan, K.N. (2009) Investigations on the cure chemistry and polymer properties of benzoxazine-cyanate ester blends. *Eur. Polym. J.*, **45**, 494–502.
  - 54 de Lima, J.A. and Felisberti, M.I. (2008) Poly(ethylene-co-vinyl alcohol) and poly(methyl methacrylate) blends: Phase behavior and morphology. *Eur. Polym. J.*, **44**, 1140–1148.
  - 55 Yu, L., Dean, K., and Li, L. (2006) Polymer blends and composites from renewable resources. *Prog. Polym. Sci.*, **31**, 576–602.
  - 56 Su, Z., Li, Q., Liu, Y., Hu, G., H., and Wu, C. (2009) Compatibility and phase structure of binary blends of poly(lactic acid) and glycidyl methacrylate grafted poly(ethylene octane). *Eur. Polym. J.*, **45**, 2428–2433.
  - 57 Wang, L.H. and Porter, S. (1993) Miscibility of a polyarylate with a liquid crystalline copolyester. *J. Polym. Sci. Part B: Polym. Phys.*, **31**, 1067–1073.
  - 58 Kwei, T.K., Frisch, H.L., Radigan, W., and Vogel, S. (1977) Ternary polymer mixtures. *Macromolecules*, **10**, 157–160.
  - 59 Machado, J.M. and Lee, C.S. (1994) Compatibilization of immiscible blends with a mutually miscible third polymer. *Polym. Eng. Sci.*, **34**, 59–68.
  - 60 Sáenz De Juano Arbona, V. (2008) Contribución al estudio de la degradación ambiental de poliolefinas fotoestabilizadas. Doctoral thesis, Universitat Politècnica de València. Available at: <http://hdl.handle.net/10251/2909>.
  - 61 Zabaleta, A., González, I., Eguizábal, J.I., and Nazábal, J. (2009) Rubber toughening of poly(ether imide) by modification with

- poly(butylene terephthalate). *Eur. Polym. J.*, **45**, 466–473.
- 62 Guericca-Echevarria, G., Eguiazabal, J.I., and Nazabal, J. (2006) Structure and mechanical properties of compatibilized poly(ethylene terephthalate)/poly(ethylene octene) blends. *Polym. Eng. Sci.*, **46**, 172–180.
  - 63 Oshinski, A.J., Keskkula, H., and Paul, D.R. (1992) Rubber toughening of polyamides with functionalized block copolymers. 2. Nylon-6,6. *Polymer*, **33**, 284–293.
  - 64 Guericca-Echevarria, G., Eguiazabal, J.I., and Nazabal, J. (2005) Supertoughness in poly sulfone/poly(ethylene-octene) blends. *Macromol. Mater. Eng.*, **290**, 38–44.
  - 65 Schlund, B. and Utracki, L.A. (1987) Linear low density polyethylenes and their blends: Part 1. Molecular characterization. *J. Polym. Eng. Sci.*, **27**, 359–366.
  - 66 Aravind, I., Elchhorn, K.J., Komber, H., Jenichen, D., Zafeiropoulos, N.E., Ahn, K.H., Grohens, Y., Stamm, M., and Thomas, S. (2009) A study on reaction-induced miscibility of poly(trimethylene terephthalate)/polycarbonate blends. *J. Phys. Chem. B*, **113**, 1569–1578.
  - 67 Garcia, D., Balart, R., Parres, F., and López, J. (2007) Characterization of blends of poly(vinyl chloride) waste for building applications. *J. Mater. Sci.*, **42**, 10143–10151.
  - 68 Das, A., Mahaling, R.N., Stöckelhuber, K. W., and Heinrich, G. (2011) Reinforcement and migration of nanoclay in polychloroprene/ethylene–propylene–diene-monomer rubber blends. *Compos. Sci. Technol.*, **71**, 276–281.
  - 69 Nayak, G.Ch., Rajasekar, R., and Das, C.K. (2010) Effect of SiC coated MWCNTs on the thermal and mechanical properties of PEI/LCP blend. *Composites Part A*, **41**, 1662–1667.
  - 70 Kannan, M., Bhagawan, S.S., Jose, T., Thomas, S., and Joseph, K. (2010) Effect of sequence of nanoclay addition in TPU/PP blends: thermomechanical properties. *J. Mater. Sci.*, **45**, 1078–1085.
  - 71 Mukherjee, M., Das, T., Rajasekar, R., Bose, S., Kumar, S., and Das, C.K. (2009) Improvement of the properties of PC/LCP blends in the presence of carbon nanotubes. *Composites Part A*, **40**, 1291–1298.
  - 72 Singh, S. and Mohanty, A.K. (2007) Wood fiber reinforced bacterial bioplastic composites: Fabrication and performance evaluation. *Compos. Sci. Technol.*, **67**, 1753–1763.
  - 73 Cai, X., Li, B., Pan, Y., and Wu, G. (2012) Morphology evolution of immiscible polymer blends as directed by nanoparticle self-agglomeration. *Polymer*, **53**, 259–266.
  - 74 Hernández-Montero, N., Meaurio, E., Elmiloudi, K., and Sarasua, J.R. (2012) Novel miscible blends of poly(p-dioxanone) with poly(vinyl phenol). *Eur. Polym. J.*, **48**, 1455–1465.
  - 75 Fox, T.G. (1956) Influence of diluent and of copolymer composition on the glass temperature of a polymer system. *Bull. Am. Phys. Soc.*, **123**.
  - 76 Gordon, M. and Taylor, J.S. (1952) Ideal copolymers and the second-order transitions of synthetic rubbers in non-crystalline copolymers. *J. Appl. Chem.*, **2**, 493–500.
  - 77 Couchman, P.R. and Karasz, F.E. (1978) A classical thermodynamic discussion of the effect of composition on glass transition temperatures. *Macromolecules*, **11**, 117–119.
  - 78 Kwei, T.K. (1984) The effect of hydrogen bonding on the glass transition temperatures of polymer mixtures. *J. Polym. Sci., Polymer Chem. Ed.*, **22**, 307–313.
  - 79 Tiwari, R.R. and Natarajan, U. (2011) Effect of blend composition and organoclay loading on the nanocomposite structure and properties of miscible poly(methyl methacrylate)/poly(styrene-co-acrylonitrile) blends. *Polym. Eng. Sci.*, **51**, 979–991.
  - 80 Kim, E., Kramer, E.J., Wu, W.C., and Garrett, P.D. (1994) Diffusion in blends of poly(methyl methacrylate) and poly(styrene-co-acrylonitrile). *Polymer*, **35**, 5706–5715.
  - 81 Angell, C.A. (1991) Relaxation in liquids, polymers and plastic crystals – strong/fragile patterns and problems. *J. Non-Cryst. Solids*, **13**, 131–133.



- 82 Godard, M.E. and Saiter, J.M. (1998) Fragility and non-linearity in polymethyl ( $\alpha$ -n-alkyl) acrylates. *J. Non-Cryst. Solids*, **235**, 635–639.
- 83 Saiter, A., Hess, M., D'Souza, N.A., and Saiter, J.M. (2002) Entropy and fragility in vitreous polymers. *Polymer*, **43**, 7497–7504.
- 84 Bohmer, R., Angell, C.A., Richert, R., and Blumen, A. (eds) (1994) *Disorder Effects on Relaxational Processes*, Springer, Berlin.
- 85 Vilgis, T.A. (1993) Strong and fragile glasses: a powerful classification and its consequences. *Phys. Rev. B*, **47**, 2882–2885.
- 86 Kunal, K., Robertson, C.G., Pawlus, S., Hahn, S.F., and Sokolov, A.P. (2008) Role of chemical structure in fragility of polymers: A qualitative picture. *Macromolecules*, **41**, 7232–7238.
- 87 Haris, A., Adachi, T., Araki, W., and Hayashi, Y. (2007) Fracture toughness of epoxy resins containing blends of monomers with different molecular weights. *Key Eng. Mater.*, **345–346**, 1511–1514.
- 88 Qazvini, N.T. and Mohammadi, N. (2007) Segmental dynamics of reactively prepared polystyrene blends: unsaturated polyester resin versus high impact polystyrene. *J. Appl. Polym. Sci.*, **106**, 498–504.
- 89 Cui, L., Yeh, J.T., Wang, K., Tsai, F.C., and Fu, Q. (2009) Relation of free volume and barrier properties in the miscible blends of poly(vinyl alcohol) and nylon 6-clay nanocomposites film. *J. Membr. Sci.*, **327**, 226–233.
- 90 Doolittle, A.K. (1951) Studies in Newtonian flow. II. The dependence of the viscosity of liquids on free-space. *J. Appl. Phys.*, **22**, 1471–1475.
- 91 Shang, S.Y., Fang, Z.P., and Zhu, Z.G. (2009) Relaxation study of Poly (methylmethacrylate) in miscible blends with poly(ethylene oxide) by low-frequency anelastic spectroscopy. *Physica B*, **404**, 1200–1203.
- 92 Basak, G., Bandyopadhyay, A., and Bhowmick, A.K. (2010) Effect of tackifier compatibility and blend viscoelasticity on peel strength behavior of vulcanized EPDM rubber co-cured with unvulcanized rubber. *Int. J. Adhes. Adhes.*, **30**, 489–499.
- 93 Chabrat, E., Abdillahi, H., Rouilly, A., and Rigal, L. (2012) Influence of citric acid and water on thermoplastic wheat flour/poly (lactic acid) blends. I: Thermal, mechanical and morphological properties. *Ind. Crop. Prod.*, **37**, 238–246.
- 94 Wang, N., Yu, J., Chang, P., and Ma, X. (2008) Influence of formamide and water on the properties of thermoplastic starch/poly(lactic acid) blends. *Carbohydr. Polym.*, **71**, 109–118.
- 95 Yokesahachart, C. and Yoksan, R. (2011) Effect of amphiphilic molecules on characteristics and tensile properties of thermoplastic starch and its blends with poly(lactic acid). *Carbohydr. Polym.*, **83**, 22–31.
- 96 Leroy, E., Jacquet, P., Coativy, G., Reguerre, A.I., and Lourdin, D. (2012) Compatibilization of starch–zein melt processed blends by an ionic liquid used as plasticizer. *Carbohydr. Polym.*, **89**, 955–963.
- 97 Sankri, A., Arhaliass, A., Dez, I., Gaumont, A.C., Grohens, Y., Lourdin, D., Pillin, I., Rolland-Sabaté, A., and Leroy, E. (2010) Thermoplastic starch plasticized by an ionic liquid. *Carbohydr. Polym.*, **82**, 256–263.
- 98 Müller, A.J., Balsamo, V., and Rosales, C.M. (1992) On the miscibility and mechanical compatibility of low density and linear low density polyethylene blends. *Polym. Networks Blends*, **2**, 215.
- 99 Hill, M.J. and Puig, C.C. (1997) Liquid-liquid phase separation in blends of a linear low-density polyethylene with a low-density polyethylene. *J. Appl. Polym. Sci.*, **65**, 1921–1931.
- 100 Kyu, T., Hu, S.R., and Stein, R.S. (1987) Characterization and properties of polyethylene blends II. Linear low-density with conventional low-density polyethylene. *J. Polym. Sci. Part B: Polym. Phys.*, **25**, 89–103.
- 101 Joskowicz, P.L., Muñoz, A., Barrera, J., and Müller, A. (1995) Calorimetric study of blends of low density polyethylene (LDPE) and linear low density polyethylene (LLDPE) temperature rising elution fractionation (TREF) fractions. *J. Macromol. Sci. Phys.*, **196**, 385–398.

- 102 Tsukame, T., Ehara, Y., Shimizu, Y., Kutsuzawa, M., Saitoh, H., and Shibasaki, Y. (1997) Characterization of microstructure of polyethylenes by differential scanning calorimetry. *Thermochim. Acta*, **299**, 27.
- 103 Prasad, A. (1998) A quantitative analysis of low density polyethylene and linear low density polyethylene blends by differential scanning calorimetry and Fourier transform infrared spectroscopy methods. *J. Polym. Eng. Sci.*, **38**, 1716–1728.
- 104 Stoclet, G., Seguela, R., and Lefebvre, J.M. (2011) Morphology, thermal behavior and mechanical properties of binary blends of compatible biosourced polymers: Polylactide/polyamide11. *Polymer*, **52**, 1417–1425.
- 105 Jayanarayanan, K., Jose, T., Thomas, S., and Joseph, K. (2009) Effect of draw ratio on the microstructure, thermal, tensile and dynamic rheological properties of in-situ microfibrillar composites. *Eur. Polym. J.*, **45**, 1738–1747.
- 106 Maglioli, M., Sirqueira, A.S., and Soares, B.G. (2010) The effect of dynamic vulcanization on the mechanical, dynamic mechanical and fatigue properties of TPV based on polypropylene and ground tire rubber. *Polym. Test.*, **29**, 840–848.
- 107 Brandalise, R.N., Zeni, M., Martins, J.D.N., and Forte, M.M.C. (2009) Morphology, mechanical and dynamic mechanical properties of recycled high density polyethylene and poly(vinyl alcohol) blends. *Polym. Bull.*, **62**, 33–43.
- 108 Bose, S., Pramanik, N., Das, C.K., Ranjan, A., and Saxena, A.K. (2010) Synthesis and effect of polyphosphazenes on the thermal, mechanical and morphological properties of poly(etherimide)/thermotropic liquid crystalline polymer blend. *Mater. Des.*, **31**, 1148–1155.
- 109 ISO 75-1: (2004) Plastics – Determination of temperature of deflection under load – Part 1: General test method.
- 110 Scobbo, J.J. (2000) Thermomechanical performance of polymer blends, in *Polymer Blends*, vol. 2 (eds D.R. Paul and C.B. Bucknall), John Wiley & Sons, New York.
- 111 Wu, J.Y., Lee, W.C., Kuo, W.F., Kao, H.C., Lee, M.S., and Lin, J.L. (1995) Effects of molecular weights and compatibilizing agents on the morphology and properties of blends containing polypropylene and nylon-6. *Adv. Polym. Technol.*, **14**, 47–57.
- 112 Zhang, Z., Chen, S., Zhang, J., Li, B., and Jin, X. (2010) Influence of chlorinated polyethylene on poly(vinyl chloride)/poly( $\alpha$ -methylstyrene-acrylonitrile) blends: Mechanical properties, morphology and thermal properties. *Polym. Test.*, **29**, 995–1001.
- 113 Martins, C.G., Larocca, N.M., Paul, D.R., and Pessan, L.A. (2009) Nanocomposites formed from polypropylene/EVA blends. *Polymer*, **50**, 1743–1754.
- 114 Fornes, T.D. and Paul, D.R. (2003) Modeling properties of nylon 6/clay nanocomposites using composite theories. *Polymer*, **44** (17), 4993–5013.
- 115 Balakrishnan, S., Start, P.R., Raghavan, D., and Hudson, S.D. (2005) The influence of clay and elastomer concentration on the morphology and fracture energy of preformed acrylic rubber dispersed clayfilled epoxy nanocomposites. *Polymer*, **46** (251), 11255–11262.
- 116 Laura, D.M., Keskkula, H., Barlow, J.W., and Paul, D.R. (2002) Effect of glass fiber surface chemistry on the mechanical properties of glass fiber-reinforced, rubber-toughened nylon 6. *Polymer*, **43**, 4673–4687.

## 13

# Thermomechanical Analysis and Processing of Polymer Blends

*Suchart Siengchin*

### 13.1

#### Introduction

Combinations of standard polymers can help in the development of new materials; indeed, the blending of polymers represents a technological approach to providing materials with a full set of desirable and specific properties. During the past few decades there has been a growing interest in polymer blends for the following reasons:

- The quest for new materials.
- The successful use of these blends in the automotive industry and various other engineering applications.
- Improved processing capabilities, product uniformity, and the ability to make quick changes to the formulations.

The reasonable performances of polymer blends has attracted economic interest in a variety of industries. The method by which polymer blends are characterized is very important from the point of their utility and added value. Such characterization may also help to provide an understanding of the behavior of any new materials developed using these polymers, including polymer blends. The characterization of polymer blends is also very important if the user industries need to define suitable quality aspects in order to obtain products that are of consistent quality. This would be especially important when the quality criteria depend on the proposed application of the blend. A careful examination of the various properties of a polymer blend not only provides details of its chemical composition and constituents, but would also be valuable for predicting the types of possible application. Knowledge of the blend structure and of its observed properties would also be helpful when developing appropriate modifications of polymer blends for various applications. Accordingly, the main aim of this chapter is to provide a systematic examination of the toughness characteristics of polymer blends, using novel methods. Additional aims are to show that the concepts of latex and online

manufacture of blends are feasible, and to study the structure–thermomechanical relationships of the blends that have been produced.

## 13.2

### Polymer Toughness

The applications of a semicrystalline polymer are often limited by the high level of crystallinity, accompanied by brittleness and low-impact resistance [1,2]. However, this problem can be overcome by blending the thermoplastic with an elastomeric modifier, which in turn will also improve the polymer's toughness. Many research groups have documented the effects of the various parameters of these modifiers on the polymer's toughness response, including rubber particle size [3,4], rubber concentration [3,5] and interparticle distance [6,7]. These studies have revealed that the rubber concentration should be above a critical level in terms of its particle size. In order to improve the toughness of a polymer, the interparticle distance should fall below a critical value that depends on the volume fraction and the particle size of the rubbers. In this case, the stress fields of neighboring particles will overlap such that a larger volume fraction of the matrix will support an average load that is greater than the applied load. As a consequence of this, multiple localized plastic deformations will be initiated in the plastic zone ahead of the crack tip. A typical rubber loading is up to 10 wt%, while the particle sizes required to provide an effective toughening should range between 100 nm and 10  $\mu\text{m}$ . Although particles in excess of 100 nm will produce an adequate stress concentration effect, smaller particles are unable to store sufficient elastic energy. Rubber particles with diameters  $>10\mu\text{m}$  have been found to be relatively inefficient, though they may be effective for bridging cracks.

Polyoxymethylene (POM) demonstrates a variety of outstanding properties, including easy processing, high stiffness and tensile strength, high heat deflection temperature, and solvent resistance. Consequently, POM is used widely, especially in the automotive and electronic sectors. To date, POM has been combined with polyurethane (PU), ethylenepropylene-dieneterpolymer, and other rubbery materials to improve its toughness [8,9]. Currently, POM/PU blends that exhibit high-impact strength and good thermal stability are well established in the market. The PU additive is mostly a thermoplastic version that is incorporated into POM via melt compounding.

The toughening of polyamide-6 (PA-6) has also been well studied; indeed, the incorporation of rubber particles into PA has recently attracted increasing interest due to the excellent impact properties that are created. The toughening of PAs via melt compounding with various rubbers (e.g., ethylene–propylene copolymer, ethylene–propylene–dieneterpolymer, styrene–ethylene/butadiene–styrene–with and without various functional groups for improved compatibility with PA) is recognized as a state-of-the-art procedure [10–12]. Hydrogenated nitrile rubber (HNBR), as one of the most stable rubbers, has also been applied as a toughener in PAs [13]. In fact, HNBR is the preferred component for temperature- and

oil-resistant thermoplastic elastomers of the blend type, which often contain PAs [14,15].

### 13.3

#### Thermomechanical Analysis and Manufacture of Polymer Blends

Knowledge of both the thermal and mechanical properties of a polymer blend is important in order for the material to achieve its highest potential. Thermomechanical analysis reveals the temperature and energy changes associated with structural changes in a polymer blend, and hence the blend's suitability for many applications. In fact, the evaluation of thermomechanical properties, such as modulus versus temperature, is used to monitor the quality of the polymer blend for an intended application. In general, the thermomechanical analytical methods employed will vary from laboratory to laboratory. Typically, dynamic mechanical thermal analysis (DMTA), short-time creep (performed at various temperatures) and thermogravimetric analysis (TGA) are used to evaluate the various properties of a polymer blend. Details of such applicability and of other investigations with polymer blends are provided in the following subsections.

During the past few decades, the thermomechanical properties of polymer blends have been studied extensively by many research groups. For example, Wong *et al.* [16] investigated the empirical results obtained from TGA analysis to offer a convenient means to estimate the overall crystallinity percentage of a polymer blend system. These authors found that the effect of temperature on the induction time of PP/PE blends could be explained by considering the trend of the Arrhenius equation. When Fernández-Berridi *et al.* [17] conducted a high-resolution TGA of the elastomer composition of SBR/NR in tire formulations, satisfactory results were obtained for the rapid quantitative determination of elastomer blends used in tires. A detailed survey of TGAs conducted in atmospheres of both nitrogen and air was presented by Mourad *et al.* [18,19], who showed that the variations in decomposition temperature with low-density polyethylene (LDPE) and isotactic polypropylene (i-PP) blend ratios and aging time were analogous in both dynamic nitrogen and air atmospheres. The thermomechanical properties revealed that the LDPE/i-PP blends are partially miscible/compatible, and that the resulting blends were not fully homogeneous [19]. The effect of glycidyl methacrylate (GMA) on the thermal and mechanical properties of biodegradable PLA/PBAT blend was studied by Kumar *et al.* [20]. In both TGA and DMA, the results showed improved thermal properties as compared with virgin PLA. The results with DMA revealed an increase in damping factor, thus confirming the strong interface between PLA and PBAT blends in the presence of GMA.

Over the past few years, many attempts have been made to improve the thermomechanical properties of polymers by blending. Nonetheless, there remains a need for additional studies to widen the scope of knowledge of blending processes and the thermomechanical behavior of the related polymer blends. Although many studies have addressed the issue of creep polymers, investigations of the

short- and long-term creep behaviors of polymer blends are lacking. Hence, the present study was conducted to predict long-term creep behavior, based on short-term creep results of polymer blend systems.

### 13.3.1

#### Theoretical Background

##### 13.3.1.1 Dynamic Mechanical Thermal Analysis (DMTA)

The dynamic loading of materials by oscillating deformations (or stresses) has become an increasingly popular method of rheological measurement. One advantage of dynamic measurements is that periodic signals can be measured with great accuracy. As nonperiodic disturbances can be easily eliminated by filtering, Dynamic Mechanical Thermal Analysis is a quite common method to provide a better understanding of some of the additional complications that arise due to the time- and temperature-dependence of the modulus of viscoelastic materials. Usually, the material's viscoelastic behavior can be determined by measuring the storage modulus and the loss modulus over a wide range of frequencies and temperatures. The storage modulus is proportional to the degree of elasticity of the system, while the loss modulus is proportional to the dissipation or loss of energy as heat in a cycle deformation, and to a certain degree reflects the viscosity of the system [21]. A schematic of a dynamic experiment, illustrating graphically the nature of the two sinusoidal signals against time, is shown in Figure 13.1.

Consider the application of a sinusoidal strain, which can be presented by:

$$\varepsilon(t) = \varepsilon_0 \sin \omega t \quad (13.1)$$

where  $\varepsilon_0$  is the maximum amplitude of the strain,  $\omega$  is the angular frequency, and  $t$  is time.

The phase of the strain is set arbitrarily at zero, which can be done without any loss of generality (perfectly elastic). The resulting stress  $\sigma(t)$  is given by:

$$\sigma(t) = \sigma_0 \sin(\omega t + \delta) \quad (13.2)$$

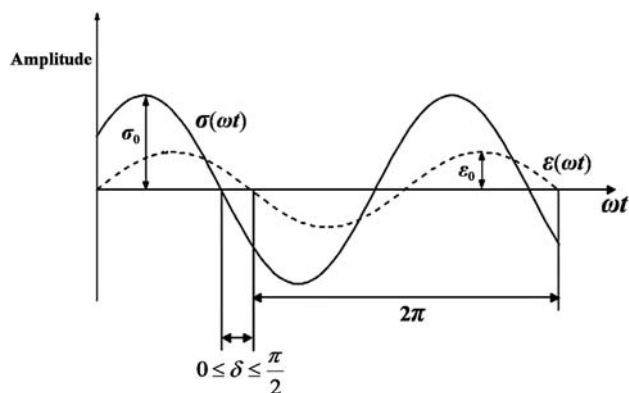


**Figure 13.1** Schematic of the dynamic mechanical experiment.

A complex Young's modulus ( $E^*$ ) reflects the contribution of both storage ( $E'$ ) and loss ( $E''$ ) components to the stiffness of material, as follows:

$$E^* = \frac{\sigma_0}{\varepsilon_0} = E' + iE'' \quad (13.3)$$

According to schematic of DMTA, the modulus at these two points can be calculated from Eqs. (13.2) and (13.3). The storage modulus ( $E'$ ) gives directly:

$$E' = E^* \cos \delta \quad (13.4)$$

and in terms of the loss modulus ( $E''$ ):

$$E' = E^* \sin \delta \quad (13.5)$$

The ratio of the loss modulus to the storage modulus is the tangent of the phase angle shift  $\delta$  between the stress and strain vectors, thus:

$$\tan \delta = \frac{E''}{E'} \quad (13.6)$$

#### 13.3.1.2 Creep Response

Polymer blends used for structural applications of practical interest may exhibit a viscoelastic behavior that has a profound influence on their performance. Viscoelasticity is of particular interest in materials science and engineering, as it is causally linked to a variety of microphysical processes and can be used as an experimental probe of those processes as a function of temperature. The viscoelastic behavior of polymer blends can usually be characterized in a creep test (where the creep strain is measured in time under a constant load) at different temperatures. In order to describe the creep results, phenomenological models composed of spring and dashpot elements are frequently used (cf. Figure 13.2). A spring element (elastic) behaves exactly like a metal spring, stretching instantly when a stress is applied, maintaining the stress indefinitely, and returning to its original dimension at the instant the stress is removed. In a dashpot (viscous) under stress, the plunger moves through the fluid at a rate that is proportional to the stress. In a creep experiment, the stress is kept constant and the change in deformation of the polymer as a function of time is recorded.

In the linear viscoelastic range, the parameters of this series do not depend on the level of the applied load.

For creep under applied constant stress  $\sigma_0$ , the material response is:

$$D(t) = \frac{\varepsilon(t)}{\sigma_0} \quad (13.7)$$

where  $D(t)$  is the viscoelastic creep compliance and  $\varepsilon(t)$  is creep strain at time,  $t$ .

In the nonlinear range the dependence on the level of the applied load can be expressed by multiplying the linear parameters by so-called nonlinearity factors which, of course, are load-, time- and temperature-dependent [22,23]. The

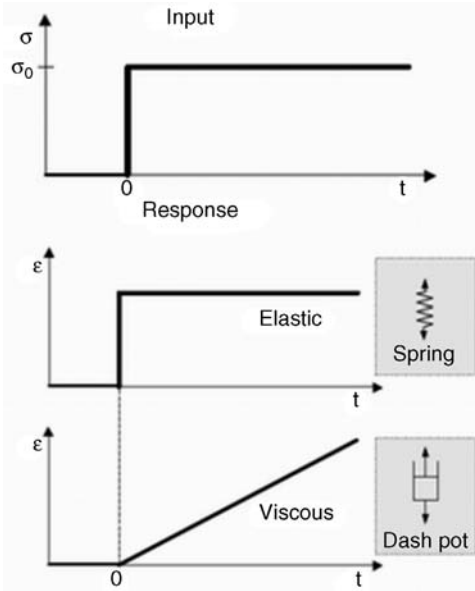


**Figure 13.2** Behavior of a Hookian spring and a Newtonian dashpot under excitation of constant load.

nonlinear creep compliance is given by:

$$D(t, \sigma(t), T) = \frac{\varepsilon(t, \sigma(t), T)}{\sigma_0} \quad (13.8)$$

where  $\sigma(t)$  is the real stress at time  $t$ , and  $T$  is temperature. This equation can be simplified as:

$$\varepsilon(t, \sigma(t), T) = \varepsilon(t, \sigma_0, T) = \varepsilon(t, T)c\sigma_0 \quad (13.9)$$

Thus, the following equation can be also expressed in terms of creep compliance:

$$D(t, \sigma(t), T) = D(t, \sigma_0, T) = c\varepsilon(t, T) \quad (13.10)$$

where  $c$  is a constant. In the above equation, creep compliance is only a function of the time and temperature.

**Time–Temperature Superposition** In order to predict the long-term creep behavior based on short-term creep measurements, it is generally assumed that the polymer does not change its structure with time, and consequently the time–temperature superposition (TTS) principle can be adopted. TTS has been used to obtain the master curves for creep compliance against time. According to TTS, the creep at a given temperature ( $T_0$ ) is related to the creep at another temperature



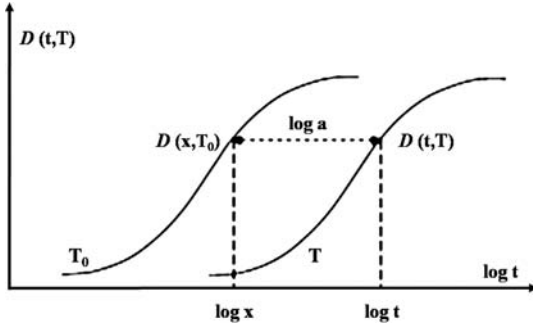


Figure 13.3 Scheme of the shift process according to TTS.

( $T$ ) by considering the shift factor ( $a_T$ ) along the time scale ( $t$ ):

$$D(t, T_0) = \frac{D(t, T)}{a_T} \quad (13.11)$$

To illustrate the shifting process more clearly, two individual creep curves are considered in Figure 13.3. The creep curves obtained at different temperatures are superposed by horizontal shifting along a logarithmic time scale.

The shift factors can be correlated with temperature via the Williams–Landel–Ferry (WLF) or the Arrhenius equations [24,25]:

$$\log(a_T) = \frac{-C_1(T - T_0)}{C_2 + (T - T_0)} \quad (13.12)$$

where  $C_1$  and  $C_2$  are constants and  $T_0$  is the reference temperature.

From the temperature dependence of the shift factor, the activation energy ( $\Delta H$ ) can be deduced from the following Arrhenius equation [26,27]:

$$\ln a_T = \frac{\Delta H}{R} \left( \frac{1}{T} - \frac{1}{T_0} \right) \quad (13.13)$$

where  $R$  is the universal gas constant.

#### 13.3.1.3 Thermogravimetric Analysis

The technique of thermogravimetric analysis (TGA), which is used for thermomechanical analysis, is one of the most widely used methods due to its rapidity of operation and a lesser need for sample manipulation compared to other conventional analyses. TGA is defined as a continuous process that involves the measurement of mass variation as a function of temperature or of time, at a constant temperature and/or heating rate. The construction of a thermogravimetric balance is shown schematically in Figure 13.4.

#### 13.3.2

#### Latex and Online-Manufacturing Concept of Polymer Blends

The blending of polymers is an economic method for developing new polymeric materials. Ultimately, the final properties of the blend will depend on the

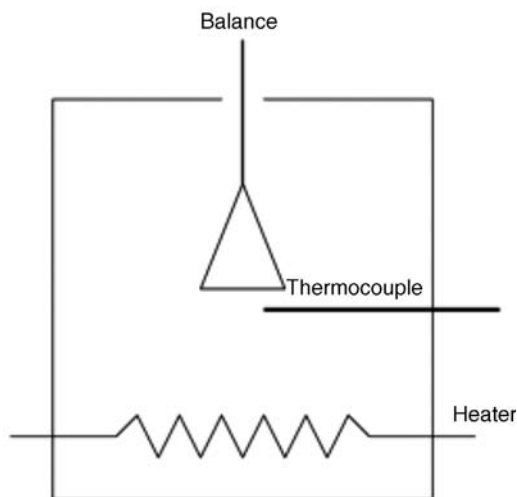


**Figure 13.4** The schematic construction of a thermogravimetric balance.

properties of its polymeric components and its composition, but mainly on the miscibility of the polymers. In contrast, the rheological properties strongly dictate the choice of processing conditions, which in turn greatly influence the morphology and therefore the mechanical/physical properties of the finished product. In order to prepare polymeric polymer blends, a variety of methods have been followed, including *in-situ* polymerization, melt-blending and solution techniques. It should be noted that one of the main aspects for many applications is a uniformity of the blend, so that the properties obtained are uniform throughout the material. *In-situ* polymerization is a challenge in this respect, as it allows the chemistry to be adjusted in order to optimize the suitably functionalized polymer components. Unfortunately, this process is cumbersome and also costly, but if the modification of the polymer material can be eliminated then the procedure might be simplified and the production costs substantially reduced compared to state-of-the-art processes. The use of conventional melt-compounding techniques to prepare polymer blends is usually more practical and economical than *in-situ* polymerization, and common polymer processing equipment such as extruders and internal mixers are best-suited for that purpose. This blending process is somewhat similar to compounding. In a polymer blend the constituent polymers are usually present in significant weight or volume proportions with respect to each other.

The latex compounding technique represents an alternative approach to the preparation of blend materials. Latex compounding is a promising method when compared, for example, to the *in-situ* polymerization and solution techniques that are used to produce polymer blends. Today, the procedure is becoming increasingly important as many simple polymers are available in latex form, and latex can be introduced into the polymer melt during compounding in line. In an

aqueous polymer latex, the microscopic solid polymer particles are suspended in water; Figure 13.5a and b shows a transmission electron microscopy image of PS latex and an atomic force microscopy image of a POM/PU blend, respectively. In this case, the mean particle size is about 200 nm and the particles are present over a very narrow distribution. The main advantage of the latex compounding process is that expensive chemical modifications of the polymer blend can be avoided. In addition, polymer-containing lattices can be injected into the melt during continuous melt-compounding.

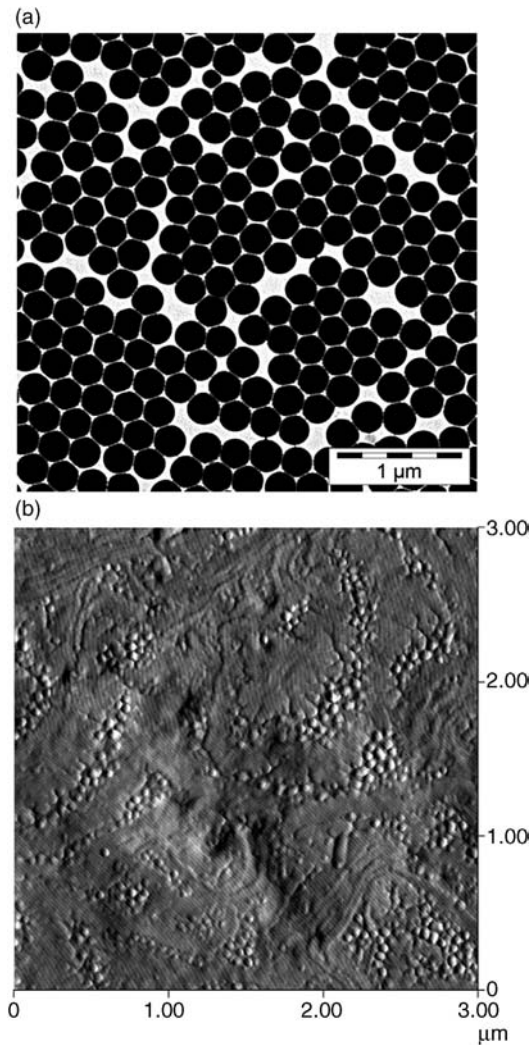


**Figure 13.5** (a) Transmission electron microscopy image of the PS latex; (b) Atomic force microscopy image of the POM/PU blend.

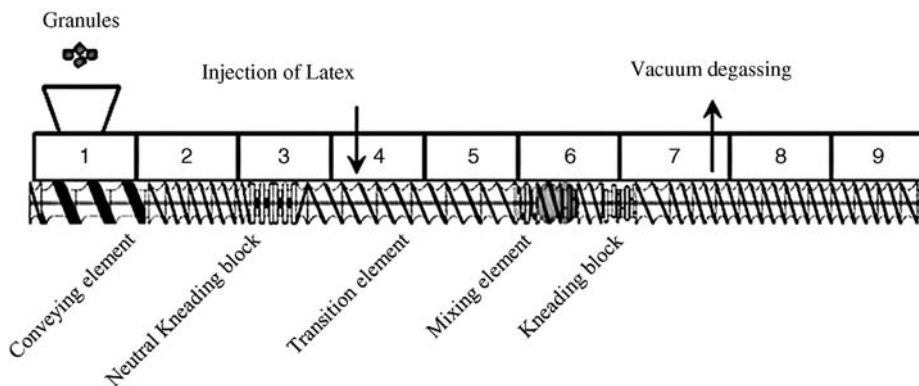


**Figure 13.6** Online extrusion compounding of a polymer blend.

This latex technique is also highly suited to the online extrusion compounding of tough polymer blends. By using this online melt-compounding method, different toughened thermoplastics-based blend systems can be produced continuously in a twin-screw extruder. For blending, a conventional mixing screw with a specific design was used [28]. Thermoplastics-based blend systems were developed so that the sum totals could be set to a specified mass flow rate. The rubber latex could then be injected into the extruder, using a pump, and the extrusion temperature selected to process a range of material systems from the hopper to the die for blends. The polymer pellets were charged into the feeder in the first zone of the extruder, after which the toughened thermoplastics-based blend was prepared using a pump; the rubber latex was then injected into the melting zone of the extruder. The water was eventually degassed in the transport zone of the screw and evaporation completed using a vacuum pump (see Figure 13.6). One additional benefit of this proposed online extrusion melt-compounding is that thermoplastics with extra toughening (including the use of nanofillers) can be produced via a very effective process that is both simple to operate and cost-efficient.

### 13.3.3

#### Materials Systems Studied

The present studies have addressed the toughening of thermoplastics via a latex and online melt-compounding technique. Accordingly, a PU latex with 50 wt% dry content (Aralen U 550), with particle sizes ranging from 100 to 1000 nm (according to the suppliers' information), was kindly supplied by Polymer Latex GmbH (Marl, Germany). Granulated POM (Hostaform C 9021; Ticona GmbH, Frankfurt, Germany) was used as the polymeric matrix for all composite systems. The volumetric melt flow rate (MVR at 190 °C/2.16 kg) was 0.8 cm<sup>3</sup> min<sup>-1</sup>. POM is fairly stable against hydrolysis, and at the same time requires relatively low processing temperatures. PU (10 wt%) was selected as the toughening agent for POM, and

used in its latex form. It should be noted that the mean size of the rubber lattices was closely matched to that of the conventional toughening agents and impact modifiers. HNBR latex with a 40 wt% dry rubber content (Zetpol ZLX-A; Zeon Corporation, Tokyo, Japan) was also used as an impact modifier in the PA-6; the HNBR content of the PA-6 blend was set at 10 wt%, while HNBR latex was provided as an aqueous dispersion of submicron-sized rubber particles. Granulated PA-6 (Ultramid<sup>®</sup> BS 700; BASF, Ludwigshafen, Germany) of density  $1.15 \text{ g cm}^{-3}$  and melting point  $220^\circ\text{C}$  was selected as the polymeric matrix for all composite systems. The blend composition was produced by melt-blending PA-6 with HNBR that had been obtained after drying the corresponding latex.

### 13.4

#### Results and Discussion

##### 13.4.1

##### POM/PU Blend

Scanning electron microscopy images of the fracture surfaces of tensile-loaded specimens provided further insight into the dispersion state of the PU particles in the POM matrix. This was due to the larger field of view for SEM compared to TEM. The PU rubber particles were also seen to be well-dispersed in the POM matrix (Figure 13.7a and b). The mean diameter of the PU particles was between 700 and 900 nm, which closely matched the initial size of the PU particles in the corresponding latex. The above-mentioned results support the effective dispersion of rubber particles on the nanoscale range when using the latex online extrusion technique. It should be noted that the dispersed PU particle size in a POM/PU blend that had been produced discontinuously was clearly larger when compared to the present techniques. Although, this technique is not straightforward for POM, the processing conditions did not result in a prominent thermal degradation of POM. This claim is based on an inspection of the fracture surfaces of the specimens where no formaldehyde-caused bubbles were seen.

The storage modulus ( $E'$ ) and mechanical loss factor ( $\tan\delta$ ) as a function of temperature for the POM and POM/PU blends are depicted in Figure 13.8. As can be seen, the storage modulus  $E'$  of POM systems decreases with increasing temperature, whereas the stiffness of the POM/PU blend was less than that of the POM, due to the rubbery character of the incorporated PU. With regards to the relaxation processes, it is well known that pure POM exhibits three transitions [29–31]. The relaxation transition ( $\gamma$ ) located at about  $-60^\circ\text{C}$  is assigned to the glass transition temperature ( $T_g$ ). The two peaks observed at ambient temperature ( $\beta$ -relaxation) and about  $130^\circ\text{C}$  ( $\alpha$ -relaxation), respectively, are usually assigned to the motions of long molecular segments in disordered and well-ordered crystalline phases, respectively [30]. The addition of PU results in a further relaxation, located at about  $-50^\circ\text{C}$ , representing the  $T_g$  of the PU. It should be noted that the incorporation of PU decreases the intensity of both the  $\alpha$ - and  $\beta$ -relaxations to lower

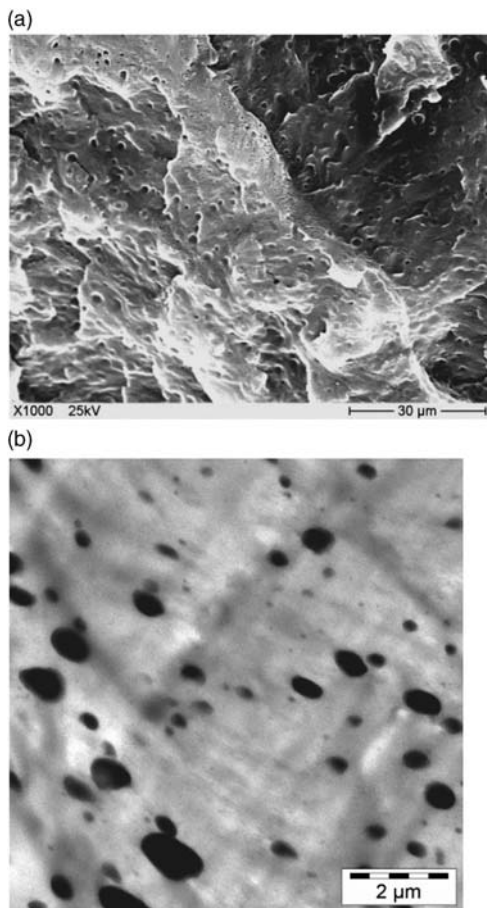


**Figure 13.7** (a) Scanning electron microscopy image of the fracture surfaces; (b) Transmission electron microscopy image of the POM/PU blend.

temperatures (ca. 5 °C), with the most prominent change being noted for the  $\beta$ -relaxation. The intensity of the  $\beta$ -peak was further increased when part of the PU was present.

The effects of increased temperature on the creep response of POM and POM/PU blend are shown in Figure 13.9a and b. The addition of PU to the POM matrix resulted in a considerable increase in creep compliance, as might be expected owing to such rubber modification at all test temperatures. Although, in all POM systems, creep is sensitive to temperature a more interesting observation is the relative change in transient creep compared to instantaneous creep as the temperature rises. Notably it was observed that, at ambient temperature, creep was assigned to the motions of long molecular segments of POM in both disordered and well-ordered crystalline phases; subsequently, creep remained unchanged at low values of creep strain, followed by a creep strain plateau that

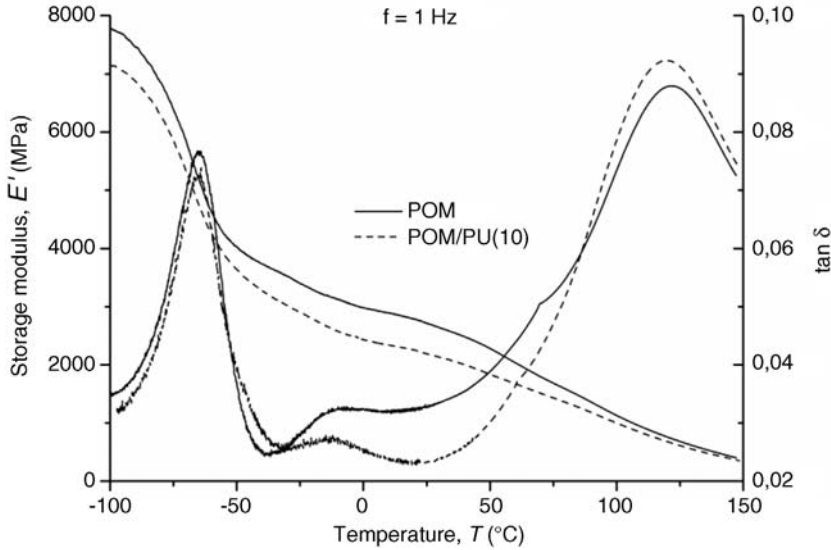


Figure 13.8  $E'$  versus  $T$  and  $\tan \delta$  versus  $T$  traces for POM and the POM/PU blend.

was time-independent. Not unexpectedly, the molecular mobility was highly thermally activated at high temperature and acquired a rubbery status that was time-dependent. In particular, the accelerating movement of the amorphous chains was once more increased with increasing time.

The creep data, measured as a function of both time and temperature ( $T = -50 \dots 80^\circ\text{C}$ ), have been utilized to create creep master curves by adopting the TTS principle. Creep at other temperatures can be estimated by considering the shift factor ( $a_T$ ) along the time scale ( $t$ ) (cf. Eq. (13.11)). The modeling of creep behaviors is important from both fundamental and applications-driven perspectives. The Findley power law model has been proposed in order to evaluate the creep behavior of polymer blends and to predict the long-term deformation based on short-term experimental data. An empirical description for the creep compliance versus time is given by the Findley power law [32]:

$$D_F = D_{F0} + D_{F1} * t^n \quad (13.14)$$

where  $n$  is a stress-independent constant,  $D_{F0}$  is the time-independent compliance, and  $D_{F1}$  is the coefficient of the time-dependent compliance term.

The constructed master curves, along with their Findley fits, are shown in Figure 13.10. Whilst the rubber particles caused a marked increase in creep, the POM systems experienced prominent creep due to the incorporation of PU in the POM/PU blend. The data in Figure 13.10 show also that the power law model fits very well to the creep data for all system for up to 3000 h, or at least until a given threshold. Although the authors observed the power law to be in good agreement with experimental results up until a given time, for longer time durations the calculated data may have shown a considerable deviation from the experimental

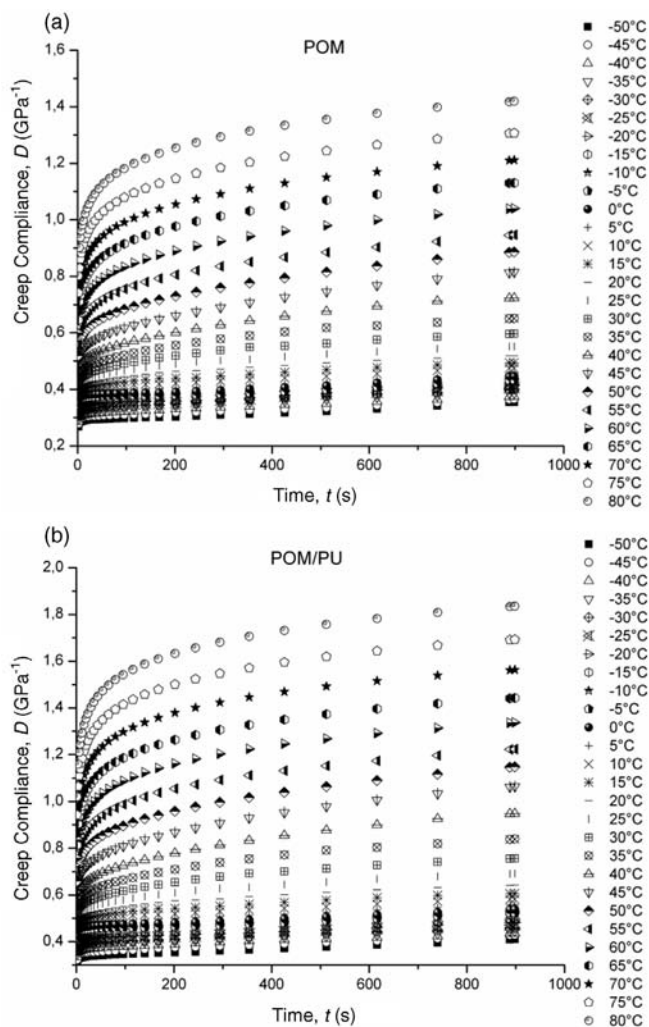


**Figure 13.9** Effect of temperature on the tensile creep of (a) POM and (b) the POM/PU blend.

results. It should be noted that the master curves constructed from short-term creep data at high temperatures may not follow the expected creep behavior, due mostly to the increasing mobility of the polymer chains.

It has been reported that the addition of PU may result in a synergistic effect in the thermo-oxidative stability of the POM matrix [8], in accordance with the TGA-based observations shown in Figure 13.11, where thermal degradation of the neat POM clearly occurs as a one-step procedure representing depolymerization. Whereas, the resistance to thermo-oxidative degradation by incorporating PU is less than that of POM, subsequent TGA investigations revealed very similar data relating to the thermal stability of POM-based systems between the nitrogen and



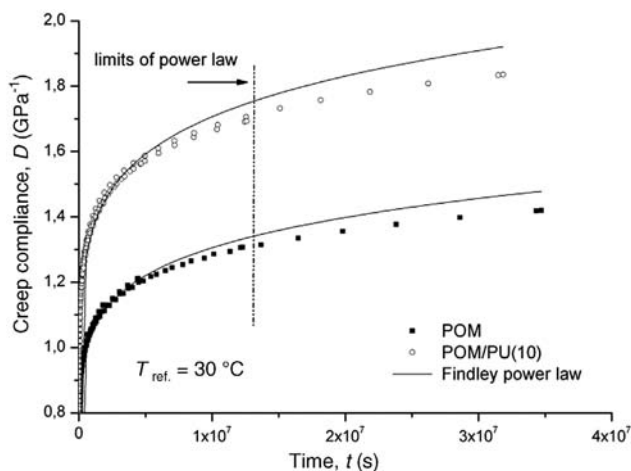


**Figure 13.10** Creep master curves constructed by considering  $T_{\text{ref}} = 30\text{ }^{\circ}\text{C}$  for POM and the POM/PU blend.

oxygen flows (not reported here). Recently, TGA was used to investigate the degradation properties of these blends in terms of the effect of thermally aged polyethylene/polypropylene blends [33]. In this case, variations in decomposition temperature for the PE/PP blends, and of the aging times in dynamic nitrogen and air atmospheres, were analogous.

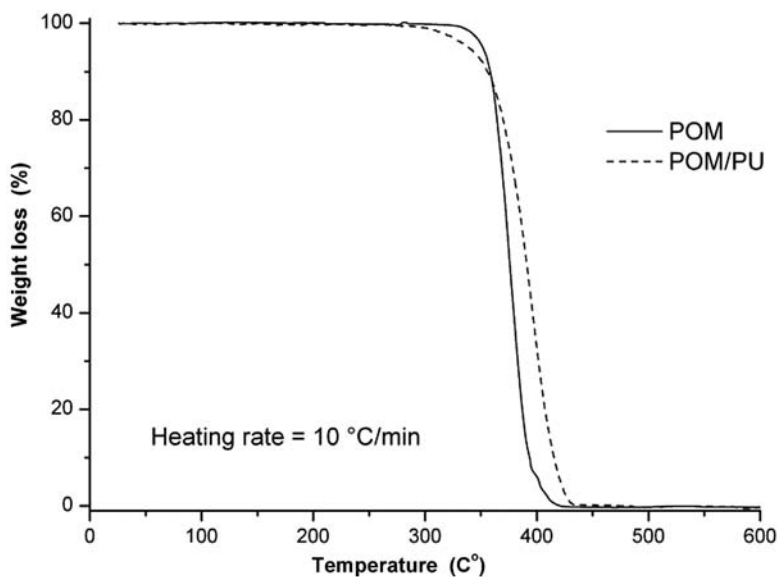


**Figure 13.11** Weight loss versus temperature for POM and the POM/PU blend.

## 13.4.2

**PA-6/HNBR Blend**

DMTA spectra in the form of storage modulus ( $E'$ ) and loss factor ( $\tan\delta$ ) as a function of temperature were plotted and are shown in Figure 13.12a and b. These data show that the blend with HNBR exhibits a markedly lower stiffness than the PA-6, at least below the  $T_g$  of PA-6; this effect is due to the rubbery characteristics of the incorporated HNBR. The plots in Figure 13.12b reveal the  $T_g$  of PA-6 to be ca. 50 °C, with a strong secondary transition at about -50 °C. The latter peak ( $\beta$ -relaxation) is usually attributed to the mobility of nonhydrogen-bonded amide groups on adjacent chains [34]. The incorporation of HNBR yielded an additional maximum at -18 °C ( $T_g$  of HNBR) in the  $\tan\delta$  versus  $T$  curves. The increment in  $\tan\delta$  caused by adding HNBR is due to an increased chain flexibility, most likely in the interphase regions. It should be noted that the HNBR particles are dispersed on the microscale and rather coarsely in the PA-6 matrix, due to the incompatibility between PA-6 and HNBR.

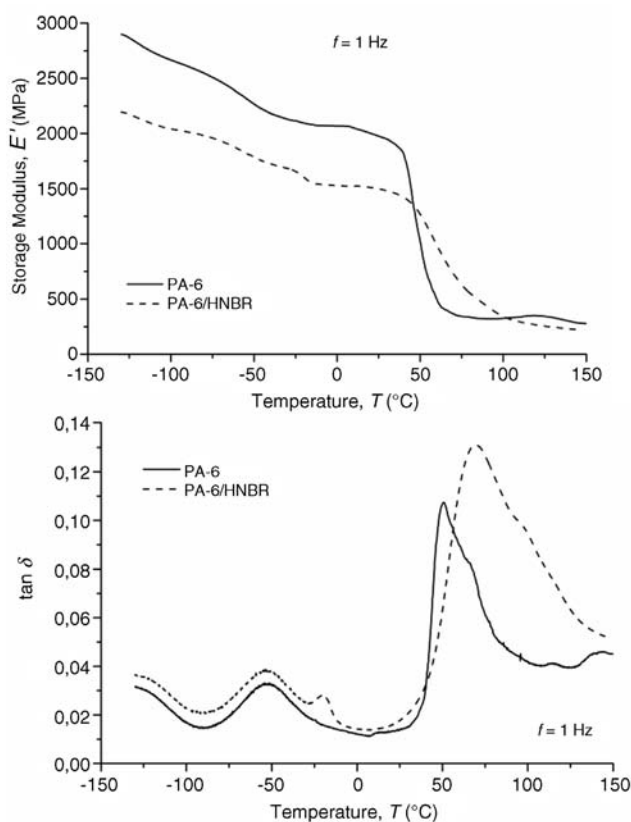


**Figure 13.12** (a)  $E'$  versus  $T$  and (b)  $\tan \delta$  versus  $T$  traces for PA-6 and the PA-6/HNBR blend.

The effects of increased temperature on the creep response of neat PA-6 and a PA-6/HNBR blend are shown in Figure 13.13a and b. A creep rate can be quantified as the time derivative ( $dD/dt$ ) of the creep compliance curve. The creep rate and creep compliance indicate the temperature-active softening of the PA-6 matrix as a result of the highly increased mobility of polymer chains under the same applied load. As might be expected, the incorporation of HNBR increased the creep compliance and creep rate at all test temperatures. The effect on creep can be explained based on the morphology of the PA-6/HNBR blend. When considering the external mechanical loading, including changes at the lamellar level in a semi-crystalline polymer, the first lamellae rotation and separation occur when the amorphous molecules have been fully stretched. These rotation and separation mechanisms, the occurrence of which depends on the relative orientation of the lamellae with respect to loading, are also operational in the linear viscoelastic (i.e., creep) range. In this case, the HNBR particles act as stress concentrators due to the large difference in  $E$ -moduli between PA-6 and HNBR. This stress-concentrating effect supports a stretching of the amorphous chains, while lamellae separation and rotation are also favored via the tie-molecules. The ultimate outcomes are increases in both creep and creep rate (cf. Figure 13.13c).

The related parameters—that is,  $D_{F0}$ ,  $D_{F1}$  and  $n$ —were deduced from the best fits applied to the experimental data (cf. Eq. (13.14)). The related master curves, viz. creep compliance as a function of time, selecting  $T_{\text{ref}} = 30^\circ\text{C}$  as a reference temperature, are depicted in Figure 13.14. The power law adequately describes the incorporation of HNBR, which increases the tensile creep compliance compared to PA-6. The parameters of the Findley power law (cf. Eq. (13.14)) are listed in Table 13.1. It can be seen that this power law fits very well to the creep data for all systems up to about 1500 h. It should also be noted that the master curves constructed from short-term creep data at high temperatures may not follow traditional creep behavior, due to the highly increased mobility of the polymer chains. Thus, the power law seems adequate for predicting the creep behavior of polymers within a given time interval. Recent results achieved with PA-66- and polyoxymethylene (POM)-based systems showed that the power law function describes the experimental results correctly up until a given time threshold, but for a longer time duration the calculated data may show considerable deviation from the experimental data [28,35].

The effect of testing temperature on the force-versus-time curve is shown for the PA-6/HNBR blend in Figure 13.15. Notably, with increasing temperature the time to fracture was increased, as also was the peak force. The largest change in fracture time occurred between room temperature (RT) and  $T = 80^\circ\text{C}$ , due to the fact that the  $T_g$  of PA-6 had been surpassed at the latter testing temperature. In the first approximation, it can be assumed that the maximum load in the fractograms increases with increasing testing temperature; accordingly, a similar increase would be expected in  $K_d$ . The temperature dependence of the fracture toughness and energy is depicted in Figure 13.16a and b, respectively, from which it can be seen (Figure 13.16a) that the incorporation of HNBR causes a marked improvement in the fracture toughness of the PA-6. The large scatter in the  $K_d$  data of

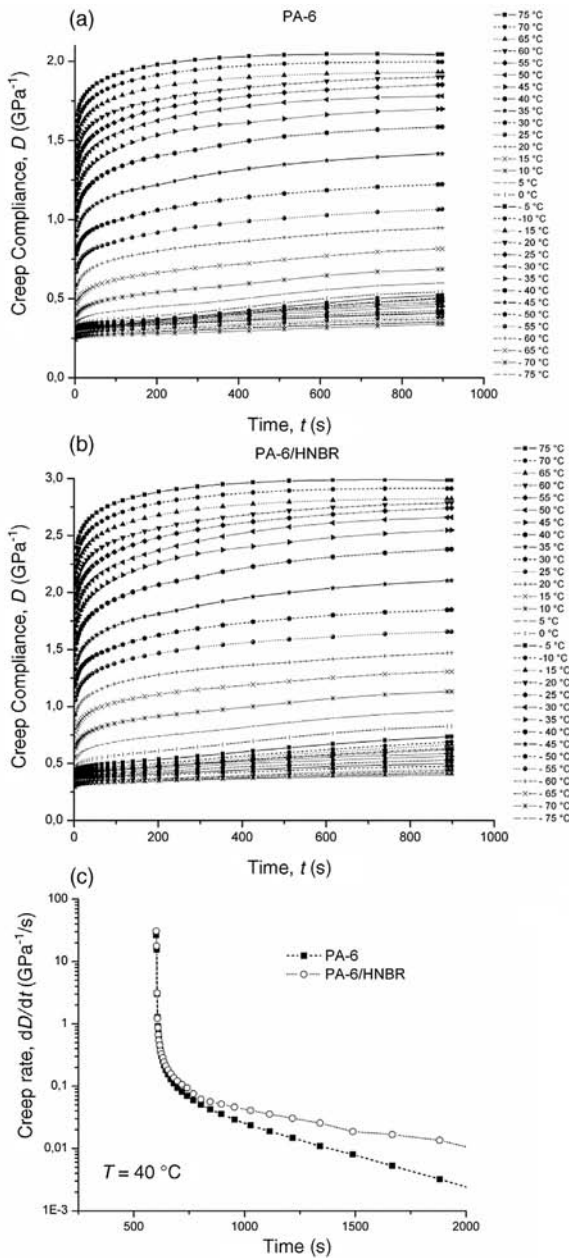


**Figure 13.13** Effect of temperature on the tensile creep. (a) PA-6; (b) PA-6/HNBR blend; (c) Creep rate versus time traces.

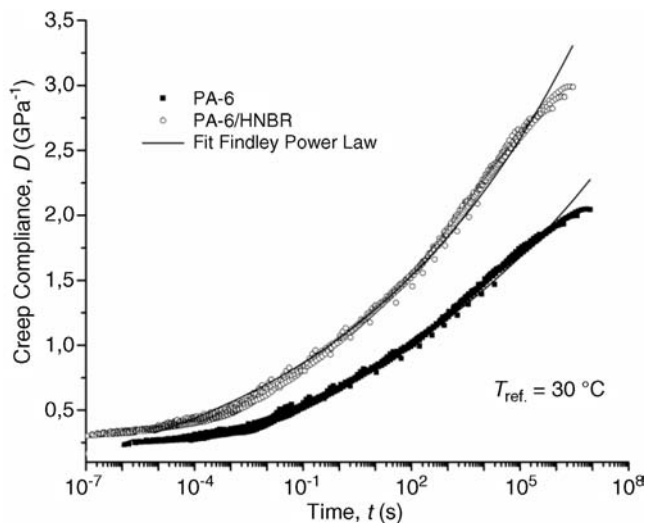


**Figure 13.14** Creep master curves (compliance versus time) constructed by considering the TTS and selecting  $T_{ref}=30\text{ }^{\circ}\text{C}$ , and their fitting by the Findley power law equation.

**Table 13.1** Fitting parameters of the Findley power law.

Sample designation	$D_{F0}\text{ (GPa}^{-1}\text{)}$	$D_{F1}\text{ (GPa}^{-1}\text{ s}^{1/n}\text{)}$	$n$
PA-6	0.232	1.058	0.057
PA-6/HNBR	0.284	1.352	0.066

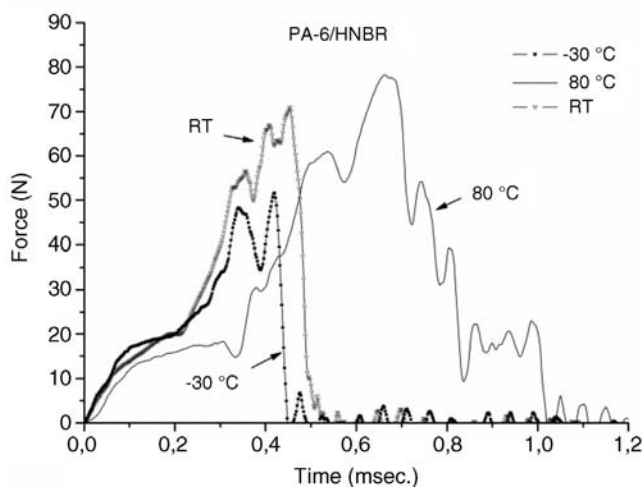


**Figure 13.15** Characteristic force–time curves registered on notched specimens of PA-6/HNBR at different testing temperatures.

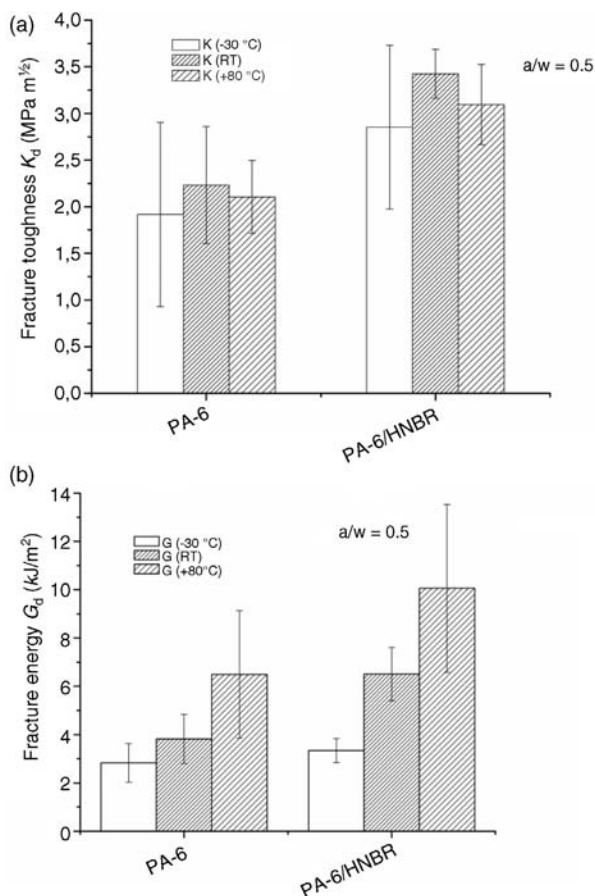


**Figure 13.16** (a) Fracture toughness and (b) energy of PA-6 and the PA-6/HNBR blend at different testing temperatures.

PA-6 at  $T = -30\text{ }^{\circ}\text{C}$  was not reduced by HNBR, as the  $T_g$  of the latter was slightly above this testing temperature. Clearly, the incorporation of HNBR improves the  $G_d$ , though prominently only at RT and above (see Figure 13.16b). As noted above, this effect is due to the rather high  $T_g$  of HNBR (ca.  $-25\text{ }^{\circ}\text{C}$  according to Ref. [36]). It should also be noted that the crazing and shear yielding act as a major energy-absorption mechanism in PA-6/HNBR.

### 13.5

#### Summary

The aim of this chapter was to develop the toughening of polymers via novel methods that allow the creation of both microblends and nanoblends. Latex is effectively a stable aqueous dispersion of fine rubber particles within the

submicron–micron range, with the relative particle size distribution depending heavily on how the latex is manufactured. The mean rubber particle sizes in the latexes are exactly as required for improving the toughness and impact modification of thermoplastics, and for this purpose polyoxymethylene (POM) and polyamide-6 (PA-6) matrices were both used. Polyurethane (PU) and hydrogenated nitrile rubber (HNBR) may also be selected and used as toughening agents. The dispersion of the blends was characterized by using transmission and scanning electron microcopies, while their thermomechanical properties were investigated using DMTA (for creep, performed at various temperatures) and TGA. The dispersed rubber particle size was closely matched to that of the usual toughening agents and impact modifiers. The impact resistance of PA-6 was greatly enhanced by the addition of HNBR rubber, while online extrusion compounding to produce polymer blends containing rubber particles to impart toughness offers a general method of modifying these properties. It is essential, however, that the toughened properties are optimized by incorporating various ratios of rubber content and concentrations.

### 13.5.1

#### Greek Symbols

- $\varepsilon, \varepsilon_0$  = Strain-, amplitude of the strain  
 $\sigma$  = Stress  
 $\sigma_0$  = Applied constant stress  
 $\omega$  = Angular frequency  
 $\delta$  = Phase angle shift

#### Acknowledgment

The author is grateful to King Mongkut's University of Technology North Bangkok for providing the opportunity of working in an outstanding environment from both scientific and technical points of view.

#### References

- 1 Plummer, C.J.G., Menu, P., Cudré-Mauroux, N., and Kausch, H.-H. (1995) The effect of crystallization conditions on the properties of polyoxymethylene. *J. Appl. Polym. Sci.*, **55** (3), 489–500.
- 2 Xu, W. and He, P. (2001) Isothermal crystallization behavior of polyoxymethylene with and without nucleating agents. *J. Appl. Polym. Sci.*, **80** (2), 304–310.
- 3 Borggreve, R.J.M., Gaymans, R.J., and Schuijjer, J. (1987) Impact behaviour of nylon/rubber blends: 5. Influence of the mechanical properties of the elastomer. *Polymer*, **30** (1), 71–77.
- 4 Margolina, A. and Wu, S. (1988) Percolation model for brittle-tough transition in nylon/rubber blends. *Polymer*, **29** (12), 2170–2173.
- 5 Baldi, F., Bignotti, F., Tieghi, G., and Riccò, T. (2006) Rubber toughening of

- polyamide6/organoclay nanocomposites obtained by melt blending. *J. Appl. Polym. Sci.*, **99** (6), 3406–3416.
- 6 Wu, S. (1988) A generalized criterion for rubber toughening: The critical matrix ligament thickness. *J. Appl. Polym. Sci.*, **35** (2), 549–561.
  - 7 Jiang, W., Yuan, Q., An, L., and Jiang, B. (2002) Effect of cavitations on brittle-ductile transition of particle toughened thermoplastic. *Polym. Commun.*, **43** (4), 1555–1558.
  - 8 Mehrabzadeh, M. and Rezaie, D. (2002) Impact modification of polyacetal by thermoplastic elastomer polyurethane. *J. Appl. Polym. Sci.*, **84** (14), 2573–2582.
  - 9 Chiang, W.-Y. and Lo, M.-S. (1988) Properties of copolymer-type polyacetal/polyurethane blends. *J. Appl. Polym. Sci.*, **36** (7), 1685–1700.
  - 10 Paul, D.R. and Bucknall, C.B. (eds) (2000) *Polymer Blends: Formulation and Performance*, vol. 2, John Wiley & Sons, Ltd, New York.
  - 11 Wahit, M.U., Hassan, A., Mohd Ishak, Z. A., and Czigány, T. (2009) Ethylene-octene copolymer (POE) toughened polyamide 6/ polypropylene nanocomposites: Effect of POE maleation. *eXPRESS Polym. Lett.*, **3** (5), 309–319.
  - 12 Bárány, T., Czigány, T., and Karger-Kocsis, J. (2010) Application of the essential work of fracture (EWF) concept for polymers, related blends and composites: A review. *Prog. Polym. Sci.*, **35** (10), 1257–1287.
  - 13 Ramezani-Dakheel, H. and Garmabi, H. (2010) A systematic study on notched impact strength of super-toughened polyamide 6 nanocomposites using response surface methodology. *J. Appl. Polym. Sci.*, **118** (2), 969–979.
  - 14 Das, P.K., Ambatkar, S.U., Sarma, K.S.S., Sabharwal, S., and Banerji, M.S. (2006) Electron beam processing of nylon 6 and hydrogenated nitrile rubber (HNBR) blends: 1. Development of high strength heat- and oil-resistant thermoplastic elastomers. *Polym. Int.*, **55** (1), 118–123.
  - 15 Das, P.K., Ambatkar, S.U., Sarma, K.S.S., Sabharwal, S., and Banerji, M.S. (2006) Electron-beam processing of nylon 6 and HNBR blends. Part II: development of high strength, heat- and oil-resistant thermoplastic elastomers. *Polym. Int.*, **55** (6), 688–693.
  - 16 Wong, A.C.-Y. and Lam, F. (2002) Study of selected thermal characteristics of polypropylene/polyethylene binary blends using DSC and TGA. *Polym. Test.*, **21** (6), 691–696.
  - 17 Fernández-Berridi, M.J., González, N., Mugica, A., and Bernicot, C. (2006) Pyrolysis-FTIR and TGA techniques as tools in the characterization of blends of natural rubber and SBR. *Thermochim. Acta*, **444** (1), 65–70.
  - 18 Mourad, A.H., Akkad, R., Ahmad, S., and Tarek, M. (2009) Characterization of thermally treated and untreated polyethylene–polypropylene blends. *Macromol. Eng.*, **34** (1), 1–5.
  - 19 Mourad, A.H. (2010) Thermo-mechanical characteristics of thermally aged polyethylene/polypropylene blends. *Mater. Des.*, **31** (2), 918–929.
  - 20 Kumar, M., Mohanty, S., Nayak, S.K., and Rahail-Parvaiz, M. (2010) Effect of glycidyl methacrylate (GMA) on the thermal, mechanical and morphological property of biodegradable PLA/PBAT blend and its nanocomposites. *Bioresour. Technol.*, **101** (21), 8406–8415.
  - 21 Shaw, M.T. and MacKnight, W.J. (eds) (2005) *Introduction to Polymer Viscoelasticity*, John Wiley & Sons, New York.
  - 22 Schapery, R.A. (1969) On the characterization of nonlinear viscoelastic materials. *Polym. Eng. Sci.*, **9** (4), 295–310.
  - 23 Brueller, O.S. (1987) On the nonlinear characterization of the long term behaviour of polymeric materials. *Polym. Eng. Sci.*, **27** (2), 144–148.
  - 24 Ferry, J.D. (1980) *Viscoelastic Properties of Polymers*, Wiley, New York.
  - 25 Palade, L.I., Verney, V., and Attane, P. (1995) Time-temperature superposition and linear viscoelasticity of polybutadienes. *Macromolecules*, **28** (21), 7051–7057.
  - 26 Williams, M.L., Landel, R.F., and Ferry, J.D. (1955) The temperature dependence of relaxation mechanisms in amorphous polymers and other glass-forming liquids. *J. Am. Chem. Soc.*, **77**, 3701–3706.
  - 27 Ward, I.M. (1979) Chapter 7, in *Mechanical Properties of Solid Polymers*, John Wiley & Sons, Inc., New York.



- 28 Siengchin, S., Karger-Kocsis, J., and Thomann, R. (2008) Nanofilled and/or toughened POM composites produced by water-mediated melt compounding: Structure and mechanical properties. *eXPRESS Polym. Lett.*, **2** (10), 746–756.
- 29 Horrion, J., Cartasegna, S., and Agarwal, P.K. (1996) Morphology, thermal, and mechanical properties of polyacetal/ionomer blends. *Polym. Eng. Sci.*, **36** (16), 2061–2068.
- 30 Kaito, A., Nakayama, K., and Kanetsuna, H. (1986) Roller drawing of polyoxymethylene. *J. Appl. Polym. Sci.*, **32** (2), 3499–3513.
- 31 Højfors, R.J., Baer, E., and Geil, P.H. (1977) Dynamic-mechanical study of molecular motions in solid polyoxymethylene copolymer from 4 to 315 °K. *J. Macromol. Sci. B*, **3**, 323–348.
- 32 Findley, W.N., Lai, J.S., and Onaran, K. (1989) *Creep and Relaxation of Nonlinear Viscoelastic Materials*, Dover Publications, Inc., New York.
- 33 Abdel-Hamid, I. (2010) Mourad thermo-mechanical characteristics of thermally aged polyethylene/polypropylene blends. *Mater. Des.*, **31** (2), 918–929.
- 34 Araújo, E.M., Hage, E., and Carvalho, A.J.F. (2004) Thermal properties of nylon6/ABS polymer blends: compatibilizer effect. *J. Mater. Sci.*, **39** (4), 1173–1178.
- 35 Starkova, O., Yang, J.L., and Zhang, Z. (2007) Application of time-stress superposition to nonlinear creep of polyamide 66 filled with nanoparticles of various sizes. *Compos. Sci. Technol.*, **67** (13), 2691–2698.
- 36 Xu, D., Karger-Kocsis, J., and Schlarb, A.K. (2009) Friction and wear of HNBR with different fillers under dry rolling and sliding conditions. *eXPRESS Polym. Lett.*, **3** (2), 126–136.



## 14

### Water Sorption and Solvent Sorption Behavior

*Fatemeh Sabzi*

#### 14.1

##### Introduction

Miscibility in polymer blends is currently an area of intense interest because of scientific inquiry about its causes and the potential technological utility of this physical approach to “new” polymeric materials. Because of their high molecular weights, the combinatorial entropy of mixing of two polymers is quite small and, thus, the usual source of a free energy driving force for mixing is virtually absent. For this reason, miscibility between two polymers was once thought to be quite rare. However, it is now recognized that an exothermic heat of mixing suffices to create thermodynamic conditions for miscibility, and that this possibility is not as rare as was once thought, particularly when the two polymers have molecular structures of complementing dissimilarity which permit specific interactions. Based on this simple notion, many miscible blends have been discovered during the past decade, and new systems are being identified at a rapid rate. Consequently, much interest has arisen about the property relationships exhibited by such mixtures and, in turn, there is a serious need for techniques to characterize the interactions between components of the blend. These two questions are somewhat interrelated since, to a degree, the strength of the interactions responsible for miscibility will influence the physical properties of the blend.

In this chapter, an extensive study of miscibility is presented by solvent sorption methods, utilizing solvent probes to ascertain interactions existing in polymer blends. These methods employ the Flory–Huggins equation for the activity of the probe  $a_1$ , in the polymer blend [1]:

$$\ln a_1 = \ln \varphi_1 + (1 - \varphi_1) + (\chi_{12}\varphi_2 + \chi_{13}\varphi_3)(1 - \varphi_1) - \chi'_{23}\varphi_2\varphi_3$$

where 1 = probe and 2,3 represent the polymers in the blend. The interaction parameter of the probe and blend,  $\chi_{1b}$ , is affected by the interaction parameter of the blend  $\chi'_{23}$  as noted in:

$$\chi_{1b} = \chi_{12}\varphi_2 + \chi_{13}\varphi_3 - \chi'_{23}\varphi_2\varphi_3$$

This equation notes that the interaction between the probe and the blend is also a function of the interaction energy between the blend components. Thus, the pair interaction parameters for components of multicomponent polymer blends can be determined by analyzing the sorption isotherms of the common solvent. For instance, the isotherms of water vapor sorption by poly(vinyl pyrrolidone) (PVP)-poly(ethylene glycol) (PEG) and PVP-PEG-poly(acrylic acid) (PAA) blends with different compositions have been used to calculate the PVP-PAA, PVP-PEG, and PAA-PEG pair interaction parameters [2]. The calculated values are all negative and in good agreement with each other. Although  $\chi'_{23}$  yields useful information concerning the compatibility of polymer blends, this value should nevertheless be regarded with caution. In a previous study [3], a theoretical discussion was presented regarding the Flory–Huggins interaction parameter for several random copolymer–solvent systems, along with their corresponding homopolymer pairs. The data on  $\chi_{1b}$  used for an approximate estimation of the  $\chi'_{23}$  interaction parameter for the limiting case of zero solvent concentration. The  $\chi'_{23}$  for polyacrylonitrile (PAN)-poly(*cis*-1,4-butadiene) (*cis*-Bu) is more negative in pentane than in hexane or acetonitrile. Clearly, it seems that the solvent used for the study affects the value of  $\chi'_{23}$ .

The present study adds some insight into the interactions between two polymers but, more importantly, illustrates the type of property behavior that can be expected from miscible or immiscible – but compatible – blends which exhibit macroscopically uniform physical properties. The solubility, diffusivity and permeability behavior of numerous series of blends have been evaluated between 1974 and 2012. Whether or not a single phase exists depends on the chemical structure, molar mass distribution, and molecular architecture of the components present. Water, organic solvents and gases have been used as probes in sorption experiments and transport processes incorporating pervaporation, vapor, and gas permeation.

## 14.2

### Water Sorption

#### 14.2.1

##### Chitosan Blends

Chitosan, the alkaline N-deacetylated derivative of chitin, is one of the most abundant naturally occurring polysaccharides, and has been proven to be biologically renewable, biodegradable, biocompatible, nonantigenic, nontoxic, and biofunctional. Unfortunately, the rapid degradation and low hygroscopic mechanical property of chitosan limit its use, but to overcome this limitation chitosan generally has been blended with other polymers. The resultant blended chitosan-based materials were shown to exhibit combinations of properties that could not be obtained by the individual polymers. As the molecular chains of chitosan are rigid, an improvement of the selectivity of chitosan membranes by manipulating its

chain flexibility represents a promising approach for producing polymeric packaging films. One important role of a packaging material is to reduce the exchange of water between a product and the environment. Hence, the sorption data are useful for selecting a suitable packaging material that has desirable water vapor barrier properties.

When chitosan-poly (vinyl alcohol) (PVA) blend films were prepared, their water sorption and permeability were found to increase with increases of sorbitol and sucrose contents as plasticizers [4]. In another study [5], gravimetric investigations were conducted of the kinetics of water sorption from air of various water activities by chitosan with different degrees of deacetylation (and molecular weights) and chitosan/PVA blends. An analysis of the results presented showed a clear effect of the deacetylation degree of chitosan and the presence of PVA in chitosan blends on the water sorption rate. The character of the sorption curves, the calculated values of diffusion coefficients of water vapor and the micropore volumes have each shown that the higher chitosan deacetylation (and lower molecular weight,  $M_w$ ), the lower the sorption of water vapor. This observed effect can be explained by a rising ordering of the molecular chains leading to an increase in the structural packing in chitosan. A modification of the chitosan structure in miscible blends with PVA has been reflected in reductions of their sorptive properties, which depend on the weight fraction of PVA and water activity. The lower PVA the content in the blends, the higher sorption ability is found. A good compatibility of the components, resulting from the presence of hydrogen bonds between specific groups (hydroxyl, amide) of chitosan and the PVA chains, causes an increase in molecular packing and thus a decrease in pore volume and the rate of water diffusion. The modification of chitosan with other polymers, such as hydroxyl propyl cellulose (HPC), poly(ethylene oxide) (PEO) and jellified starch, demonstrated the same water sorption behavior and miscibility of their components [6].

In the case when chitosan and PVA form interpenetrating polymer networks (IPNs) [7], it is believed that an IPN with a greater PVA content will have a more compact complex structure than other hydrogels, and a lower swelling ratio. When studies on the moisture sorption characteristics of chitosan/PEO were carried out [8], by applying the same reason for the chitosan/PVA blend behavior the slope of the isotherm curves of sorption was found to increase with an increase in chitosan content. The concentration-dependence of the thermodynamic functions of mixing chitosan with PVA and PEO was determined by Grebennikov *et al.* [9] and Rashidova *et al.* [10]. Subsequently, the identification of negative Gibbs free energies for both systems containing up to 30 wt% PVA and PEO suggested the formation of homogeneous structures.

A novel type of asymmetric blend membrane using a superfine chitosan powder (SCP) and biomedical polyurethane (PU) was prepared, and the variation of water absorption of different SCP/PU membranes investigated [11]. Chitosan chains contain abundant hydrophilic  $-\text{OH}$  and  $-\text{NH}_2$  groups which easily absorb water molecules; hence, as the SCP ratio was increased the membranes were able to absorb more water and reach a higher equilibrium water absorption percentage. The other factor that affects water absorption is membrane structure. In this case,

as the SCP/PU ratio changes the porosity variation of the membranes was inconsistent with that of membrane water absorption. As the SCP content was increased from 0 wt% to 30 wt%, both the water absorption percentage and water vapor transmission rate (WVTR) were found to increase, and this was attributed to improvements in the porosity and hydrophilicity of the blend membrane. However, when the SCP content was further increased to 50 wt% and 70 wt%, the porosities of the blend membranes began to reduce, thus depressing the diffusion rate of the water vapor, whereas the water absorption of the blend membranes remained enhanced. Consequently, the WVTR of the blend membranes still increased in line with the SCP content. In addition, when the SCP content is very high the  $-\text{OH}$  and  $-\text{NH}_2$  groups of the chitosan chains can interact with  $-\text{C}=\text{O}$  and  $-\text{NH}-$  groups in the PU chains, by hydrogen bonding. The interaction of the PU chains is then weakened and the amorphous region increases, which in turn contributes to the permeation of water vapor. Taken together, these findings suggested that the SCP content was a major factor influencing the water absorption of blend membranes, and that a decrease in porosity had a negligible effect on such absorption.

#### 14.2.2

##### **PVP/Polysulfone Blend**

Miscible polymer blends offer a physical method for tailoring properties to obtain combinations that may be more desirable than those of either component polymer. The water sorption and transport behavior of miscible polymer blends have been examined in several studies. For example, Schult and Paul [12] investigated the water sorption and transport properties of homogeneous blends of PVP, a water-soluble polymer that is miscible with a relatively hydrophobic bisphenol A polysulfone (PSF) over the entire composition range. Unfortunately this study was restricted to blends containing  $\leq 40\%$  PVP, since blends containing  $>40\%$  PVP would phase-separate when exposed to high water vapor activities. Such phase-separation is driven by the fact that one polymer wishes to swell or dissolve in water, while the other does not.

Equilibrium sorption isotherms were measured for various blend compositions at  $40^\circ\text{C}$  as a function of water vapor activity, as shown in Figure 14.1 [12]. Similar results were obtained at 30 and  $50^\circ\text{C}$  [13]. Water uptake was increases at all activities with increasing PVP content, although at high activities the concentration of water in the film showed a significant upturn or swelling behavior. This effect became more exaggerated at high PVP compositions.

Two possible interpretations of this situation were: (i) plasticization of the polymer by the penetrant; or (ii) clustering of the penetrant. These two phenomena can be distinguished by the behavior of the diffusion coefficient. Typically, plasticization results in an increase in the diffusion coefficient with activity due to increased segmental polymer mobility caused by the penetrant. In contrast, when clustering occurs the effective diameter of the diffusing entity is increased, which in turn decreases the penetrant mobility or diffusion coefficient.

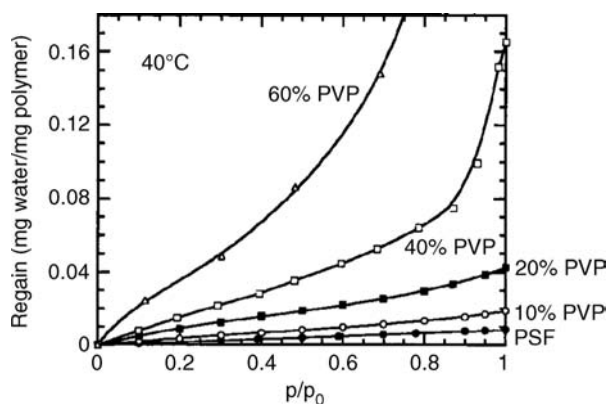


Figure 14.1 Equilibrium water vapor sorption isotherms versus activity at 40 °C.

The diffusion coefficients of blends containing 0%, 10%, 20% and 40% PVP as a function of water vapor activity are shown in Figure 14.2. The reduction in the absolute magnitude of the diffusion coefficient, as PVP is added to PSF, may be explained by the concurrent decrease in the fractional free volume. For the blend containing 40% PVP the diffusion coefficient increased with activity and was greater than that of PSF at high activities. This behavior most likely reflects the strong tendency of sorbed water to plasticize the blend, which overshadows the influence of the decrease in the free volume of the dry polymer. The permeability coefficients for blends containing up to 20% PVP are generally lower than those for PSF, because the decrease in diffusion coefficient is greater than the increase in equilibrium water solubility. In contrast, for a blend containing 40% PVP the permeability coefficients are larger and more dependent on activity than those for

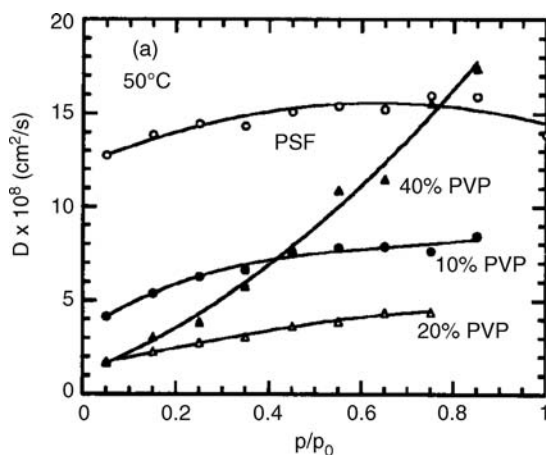


Figure 14.2 Water vapor diffusion coefficient versus activity at 40 °C.

PSF, owing to the very high water solubility and strong plasticization effect on the diffusion coefficient.

### 14.2.3

#### PEOX Blends

In a similar study, Schult and Paul [14] examined the water sorption and transport properties of a series of miscible blends of hydrophilic poly(ethyloxazoline) (PEOX) and the relatively hydrophobic poly(ethersulfone) (PES) at 40 °C. Similar results were obtained at 30 and 50 °C [13], and the study was restricted to blends containing 20% PEOX, or less. Similar to the PVP/PSF blends, the equilibrium water sorption was increased with an increasing hydrophilic polymer content of PEOX/PES. The equilibrium water uptake for pure PES was greater than that of pure PSF, owing to the higher relative content of the sulfone unit. For a given blend composition, the increase in the concentration of water sorbed relative to that of the pure hydrophobic polymer was greater for PVP/PSF blends than for PEOX/PES blends.

The addition of PEOX to PES causes the water vapor diffusion coefficient to decrease in absolute magnitude, but to increase more strongly with activity. This behavior reflects the increased water sorption and the resultant tendency for materials containing PEOX to be plasticized, and overshadows the effect of the decrease in the free volume of dry polymer. The permeability coefficients for blends containing 10% and 20% PEOX were lower than those for PES, because the decrease in the diffusion coefficient was larger than the increase in the equilibrium water solubility.

Blends of water-soluble PEOX with a series of hydrophobic styrene–acrylonitrile (SAN) copolymers of varying AN content were also immersed in water to determine the kinetics of water swelling and the extent of PEOX extraction [15]. Copolymers containing 25% and 40% by weight of AN formed miscible blends with PEOX, whereas those containing higher and lower amounts of AN formed immiscible mixtures with PEOX. The sorption of large amounts of water by PEOX induced a microphase separation of the two miscible polymers to form microdomains of SAN in which, evidently, segments of PEOX were entrapped to form physical crosslinks that precluded disintegration of the sample and extraction of the PEOX, the phase of which was highly swollen by the sorbed water.

### 14.2.4

#### PES/PEO Blend

Water sorption isotherms have been determined for PES, PEO, and 95/5, 90/10, 80/20, 70/30 and 60/40 PES/PEO blends at 30, 40, and 50 °C [16]. The level of sorption for the PES/PEO blends is similar up to activities of approximately 0.6. However, for water vapor activities <0.6 the affinity for water of PEO is not high enough to allow for crystallinity. As the activity of vapor is increased, the sorption rises steeply around activities of 0.7–0.8. Clearly, some highly favorable interaction



occurs at these higher activities, most likely through the formation of PEO/water complexes sufficient to overcome constraints imposed by crystallites and cause an eventual dissolution of the polymer. This behavior is reflected in the isotherms for blends containing more than 10% PEO, and may indicate the presence of incipient or induced PEO nuclei with properties approaching that of bulk PEO; the interaction of water with these small domains, if present, would eventually be restricted by the surrounding PES continuum. Sorption isotherms have been not obtained for blends containing more than 40% PEO, as there was evidence of some degree of crystallization of the PEO component at higher fractions. An analysis of the equilibrium sorption isotherms provided information regarding polymer–polymer interaction,  $\chi'_{23}$ , with negative values of  $\chi'_{23}$  indicating the miscibility of two components in the range of compositions examined.

#### 14.2.5

##### Phenoxy Blends

The transport and sorption of water in miscible PES/Phenoxy blends has been studied at 40 °C as a function of blend composition [17]. The isotherms are essentially linear over much of the activity range. The highest values of sorption, diffusion and permeation have been observed for PES with a volume percent of 100, and the lowest values for pure phenoxy. The intermediate compositions show decreasing values with decreases in PES content. In an earlier study of this system [18], the isotherms for the pure components and blends were reported to be practically coincident, except for activities  $>0.7$  where the sorption at a given activity was increased significantly with the phenoxy content of the blend. The differences in sample preparation or incomplete removal of solvent may be responsible for these discrepancies.

Miscible 80/20 and 90/10 wt% blends of poly(*n*-vinyl pyrrolidone) (PVP) and phenoxy polymer were also swollen with 73–85% water to produce rubbery hydrogels [19]. A ternary phase diagram was calculated assuming athermal mixing between PVP–H<sub>2</sub>O and PVP and the known endothermic interaction between H<sub>2</sub>O–phenoxy. Phase separation into a phenoxy phase containing minimal H<sub>2</sub>O and PVP and a water-swollen PVP phase was predicted in accordance with experimental results. Phase separation was suspected as forming first an interconnected phenoxy phase that was later dispersed by swelling forces transmitted through PVP tie chains.

#### 14.2.6

##### Poly(ethylene terephthalate) (PET) Nanocomposites

The incorporation of impermeable clay particles into PET (which is a semi-crystalline polymer) can improve the barrier properties of PET nanocomposites towards gases and water vapor. This, in turn, results in outstanding property improvements in terms of a decreasing water permeability for food packaging and an increasing flame resistance. When a new system of saturated polyesters

and their nanocomposites synthesized from glycolized poly(ethylene terephthalate) (GPET) with various compositions was investigated for the sorption and diffusion in water [20], the swelling of the saturated polyester was seen to decrease in line with increases in GPET content. Typically, a sample containing 50% GPET showed minimum swelling, whereas a neat sample (without GPET) showed maximum swelling. The sorption, diffusion and permeability coefficients for all samples showed a decrease that was in line with increases in GPET content, indicating that the solvent assimilation or the ability to absorb solvent had decreased with the incorporation of rigid bulky groups (e.g., an aromatic ring) into the chain, causing the polymer to become stiffer and have a reduced flexibility. These data confirmed the good compatibility of the nanoclay and polymer matrix. The sorption curves of samples with varying montmorillonite clay contents showed maximum and minimum swellings for samples with 5% and 4% clay contents. However, this effect may have been due to an accumulation of clay at the interface that reduced the barrier properties of the nanocomposite.

As the temperature is increased, the polymer chain shows a higher segmental mobility and the swelling rate is also increased. However, the nanocomposite sample with 4% clay showed a reverse order, with maximum swelling at low temperatures and minimum swelling at high temperatures. Layered nanofillers have a platelet-like structure that is evenly distributed into the polymer matrix, creating multiple parallel layers that force the solvent molecules to flow through the polymer via a tortuous path, forming complex barriers to the solvent molecules.

#### 14.2.7

##### **PMMA/HHIS and PMMA/HS**

Modified polystyrenes containing *p*-(hexafluoro-2-hydroxyisopropyl) (HHIS) [21] and *p*-hydroxystyrene (HS) [22] groups as hydrogen-bond donors were blended with (poly(methyl methacrylate) (PMMA) as acceptors. The two poly(styrene-*co*-*p*-hydroxystyrene) (PHS) copolymers used contained 5 and 15 mol% of HS units, respectively, while water vapor was used as a diffusional probe to study segmental mobility in the hydrogen-bonded polymer blends. Although, both the HHIS and HS groups had strong affinities for hydrogen bonding with the carbonyl groups of PMMA, which resulted in miscible blends, the phenol groups had a greater tendency towards self-association. The excess volumes of mixing were negative for the PHS-5 blends. Whereas, negative excess volumes appeared to be the norm for miscible blends, the volume of mixing for the PHS-15 blends changed from a slightly negative value to a positive value as the PHS content was increased from 25% to 75%. Similar trends were found for the blends of HHIS copolymers, with the excess volumes becoming more positive when the proportion of hydroxyl groups in the styrene copolymer was increased. Central to the interpretation here is the assumption that the volume shrinkage expected from the formation of a hydrogen bond between a free hydroxyl group and a carbonyl group would be diminished to some extent by the poor packaging of styrene and methyl methacrylate segments in the immediate neighborhood of the interacting sites, and

consequently the net volume shrinkage would be small. However, the dissociation of the self-associated hydroxyl groups was accompanied by a volume increase. If the establishment of an  $\text{OH} \cdots \text{O}=\text{C}$  bond cannot overcome the volume increase caused by the break-up of self-association and poor chain packing, then the excess volume would become positive.

The sorption isotherms showed that the PHS-5 copolymer absorbed less water vapor than did PMMA, whilst the PHS-15 copolymer (with more polar hydroxyl groups) absorbed more water vapor than did PHS-5, but still less than did PMMA. In both blends the vapor solubility was decreased with increasing amounts of the copolymer. It is well known that, in relatively nonpolar polymers, there is a tendency for the sorbed water molecules to associate or form clusters. Composed predominantly of styrene units, the PHS-5 polymer is relatively nonpolar and the tendency for the sorbed water molecules to form clusters is greatest. The cluster function is much smaller for PMMA, when the clustering values in the blend are decreased with decreasing amounts of PHS-5. The clustering of sorbed water molecules is reduced in PHS-15, which contains a larger proportion of polar groups than PHS-5, to a point that it is almost indistinguishable from the clustering in PMMA.

The diffusivity values of PHS-5 blends far exceed the average values of the component polymers; the blends have almost the same diffusion coefficients as PMMA, while PHS-5 has the lowest value, and it appears that negative excess volumes of mixing and clustered water molecules causing partial immobilization are responsible for this behavior. In contrast, in PHS-15 blends the positive excess volume of mixing seems to nullify the restrictive effect of hydrogen bonding, such that the diffusivity is equal to the average value for each blend. In the case of HHIS blends [21], the positive excess volumes found for several pairs were believed to be the result of poor chain packing of styrene and methyl methacrylate. In fact, for several blends the diffusion coefficients were higher than the average values for the component polymers.

#### 14.2.8

##### PVC/EVAc

Marais *et al.* [23] focused their attention on using copolymers and blends as selective packaging materials that exhibited high  $\text{H}_2\text{O}/\text{CO}_2$  and  $\text{CO}_2/\text{O}_2$  selectivities; these would provide a better preservation of foods by decreasing the respiratory intensity and anaerobic fermentation rate through controlling the permeabilities of oxygen, carbon dioxide and water. Investigations were made into the transport properties of water, pure carbon dioxide and oxygen through miscible binary blends of poly(ethylene-*co*-vinylacetate) (EVAc) with PVC. The main benefit of mixing PVC into EVAc copolymers is the possibility of introducing a glassy polymer that is known to be compatible with rubbery EVAc series, and which would provide a barrier to gas permeation and thereby improve gas selectivity by changing the permeability, diffusivity and solubility. Usually, glassy polymers are recognized as being more selective than rubbery permeable polymers, and subsequent

investigations have been made with a range of EVAc copolymers including EVAc<sub>19</sub> (19% w/w VAc), EVAc<sub>50</sub> (50% w/w VAc) and EVAc<sub>70</sub> (70% w/w VAc), as well as blends of EVAc<sub>19</sub>/PVC (13% w/w VAc), EVAc<sub>50</sub>/PVC (29% w/w VAc) and EVAc<sub>70</sub>/PVC (35% w/w VAc).

As can be seen in Figure 14.3a, the water permeability increases steadily with the VAc content, as would be expected when the average number of polar groups (carboxyl) in the copolymer is increased. In the case of blends, this number is not the predominant factor, however. The unexpected decrease in the permeability coefficient for EVAc<sub>70</sub>/PVC appeared to be linked to the addition of PVC, a glassy

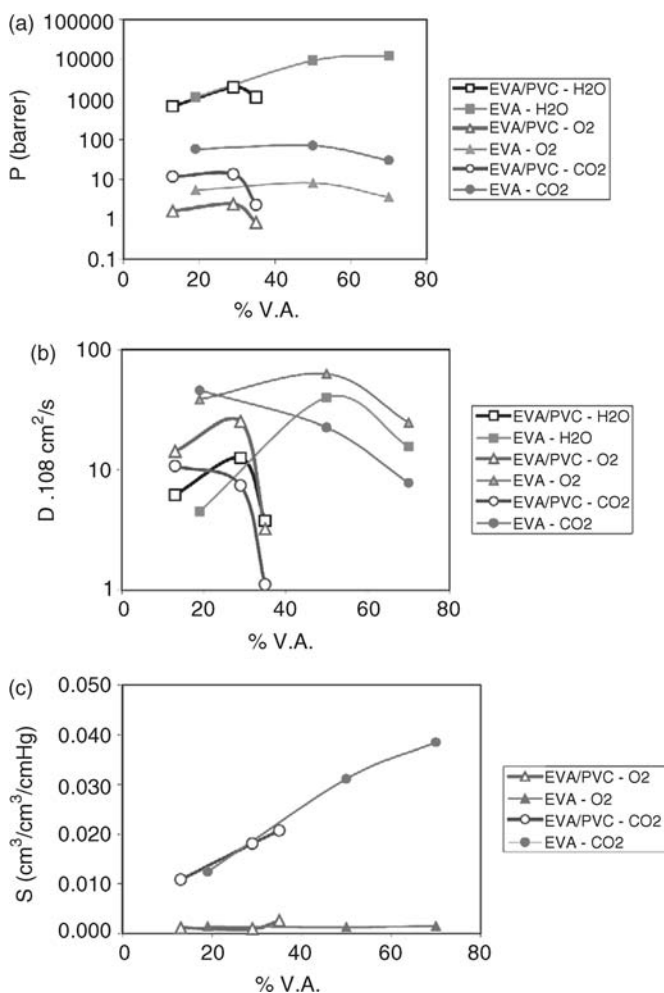


**Figure 14.3** Transport parameters for water, oxygen and carbon dioxide with EVA series and EVA/PVC blends. (a) Permeability coefficients; (b) Diffusivity coefficients; (c) Solubility coefficients.

polymer that is able to interact with the acetate groups of EVAc. However, in order to have a better approach to the water permeability it is necessary to examine the diffusivity data (Figure 14.3b). In comparison with the EVAc series, the lower overall water diffusivity in the EVAc/PVC blends can be explained by the very low intrinsic free volume of PVC and largest density of material or the small chain segment mobility caused by hydrogen-bond interactions between hydrogen atoms and Cl-substituted carbon of PVC with VAc carbonyls. For the EVAc<sub>x</sub> series and EVAc<sub>x</sub>/PVC blends, the same behavior was observed when the polar group content was increased. This variation can be explained by the fact that, for a high VAc content, the amounts of amorphous phase and the associated amount of polar groups are sufficiently large to govern the diffusion process. The presence of VAc units reduces the crystallinity of the polymer material, which in turn enhances diffusivity by decreasing the tortuosity of the diffusion path. In contrast, the polar and bulky acetyl groups also reduce chain segment mobility; the latter reduction in mobility is enhanced by the addition of PVC, which interacts with VAc groups in the blends.

In terms of water solubility, the amount of water sorbed by the blend was very low, despite the polar character of PVC; notably it was only half that of the pure EVAc<sub>x</sub> film of equivalent overall VAc content. It would appear that the interaction between the two polymers leads to a reduction in the number of polar groups available to interact with water.

Similar to water permeation in EVA/PVC blends, the VAc content is not the predominant factor and the permeability coefficients for O<sub>2</sub> and CO<sub>2</sub> do not depend on the increase in the average number of polar groups. Assuming that gases (as small permeants) have practically no affinity with polymeric materials, and their sorption coefficient varies moderately with their chemical composition, then the diffusivity will be mainly governed by the structure of the material. On the one hand, polar and bulky acetyl groups reduce the chain segment mobility, whereas on the other hand the presence of VAc units also reduces the crystallinity of the polymer material, thus enhancing diffusivity by decreasing the tortuosity of the diffusion path. In the case of solubility, as there are no polar interactions between oxygen molecules and polymer groups, the sorption coefficient for O<sub>2</sub> would be much lower than that for CO<sub>2</sub>, and would vary randomly with the VAc content. In the case of CO<sub>2</sub> the sorption coefficient would increase in line with the VAc content of the copolymer. The blending of EVAc with glassy PVC would lead to a reduction in the sorption coefficient.

The selectivity to water ( $\alpha_{\text{H}_2\text{O}/\text{O}_2}$  and  $\alpha_{\text{H}_2\text{O}/\text{CO}_2}$ ) increased with the VAc content in EVAc copolymers and in EVAc/PVC blends, and was highest for the copolymer EVAc<sub>70</sub>. The CO<sub>2</sub>/O<sub>2</sub> selectivity was lowest for the blend of EVAc<sub>70</sub> with PVC. Nevertheless, it is interesting to note that for water selectivity with equivalent VAc content, the EVAc/PVC blends are better than EVAc copolymers, whereas for the gas the selectivity was practically unchanged. These results can be explained (at least in part) by the intrinsic properties of PVC, which offers high water and low gas selectivities.

## 14.2.9

**PBI/PI**

The miscibility of a polybenzimidazole {poly[2,2'-(*m*-phenylene)-5,5'-bibenzimidazole]} (PBI) and a polyimide {poly[2,2'-bis(4-(3,4-dicarboxyphenoxy)phenyl)propane-*m*-phenylenediimine]} (PI) was studied over the entire composition range [24]. The relationships between composition and the diffusion coefficients of water and 1,2,4-trichlorobenzene (TCB) indicated that the specific free volume of PBI/PI blends decreased with polymer–polymer interaction due to hydrogen bonding between the N—H groups of PBI and the carbonyl groups of PI. The water sorption of PBI was relatively high, while that of PI was small. The equilibrium uptake of TCB was always lower than water, and was higher in PBI than in PI. The vapor absorption of the blends was lower at each composition than might be expected by the rule of additivity, or by considering the limiting case of a simple physical combination of pure PBI and PI phases, which was attributed to the specific interaction of the two polymers. The polymer–polymer interaction parameter,  $\chi'_{23}$  calculated from the equilibrium water and TCB vapor uptake, were positive and shown to depend on the composition. The results obtained from the water absorption provided increasing values of  $\chi'_{23}$  with an increasing PI content of the blend. Below 0.6 PI fraction, the change was slower than above, when the increase in the interaction parameter became considerable. The  $\chi'_{23}$  values calculated from TCB uptake showed smaller changes as a function of composition, though a sudden increase was observed between 0.4 and 0.6 PI content. Considering that the equilibrium vapor sorption of PBI is much higher than that of PI for both solvents, it can be assumed that the solvent uptake of the blends would be a consequence of interactions only with PBI, and PI can be considered as a neutral component. In addition, the calculated  $\chi_{12}$ - and  $\chi_{13}$ -values were found to be independent of composition, which proves the validity of this assumption. In summarizing these results it can be deduced that PBI and PI do not form thermodynamically homogeneous blends, in spite of intermolecular hydrogen bonding. The formation of an heterogeneous structure can be attributed to the stiffness and self-association of the polymer chains. A phase inversion takes place between 0.4 and 0.6.

## 14.2.10

**PP/EVA**

Among oxygen-sensitive food-packaging applications, several materials have been developed that provide a high-barrier to gas diffusion; unfortunately, however, some of these are easily plasticized by moisture and consequently are more often blended with hydrophobic polymers. The water sorption and diffusion properties of poly(ethylene-*co*-vinyl alcohol) (EVA) and its polypropylene (PP) blends of increasing EVA content are, therefore, of considerable interest from both fundamental and practical points of view [25].

The water sorption isotherms of all PP/EVA blends are shown in Figure 14.4. With regards to the EVA content, differences in water uptake are apparent

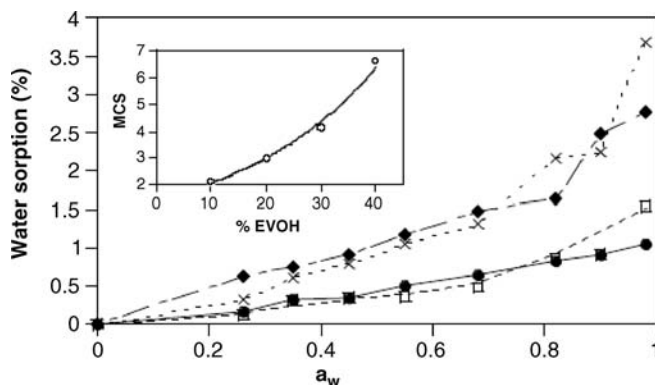


**Figure 14.4** Sorption isotherm of PP/EVOH blends in terms of water sorbed amount (%) as a function of EVOH content at 25 °C. ●, 90/10; □, 80/20; ◆, 70/30; ×, 60/40. The inset shows the mean cluster size (MCS) versus EVOH content.

between the 90/10 and 80/20 blends on the one hand, and between the 70/30 and 60/40 blends on the other hand, though these differences are only strongly accentuated as the water activity rises. The reason why these blends fail to show any clearly ranked differences in water uptake at low water activities lies in their morphologies. When plasticization is negligible (as shown in Figure 14.5), water uptake is the result of a balance between the number of hydrophilic sites and the existing free volume. The mean cluster size (MCS; shown in Figure 14.4 as an inset) increases exponentially with increasing blend hydrophilicity.

The water-solubility coefficients of the PP/EVA films, and values for pure PP and EVA for comparison, have been included in Figure 14.5. As expected, the percentage water uptake increases linearly with the EVA content, owing to the increasing number of OH groups within the polymer matrix that are able to develop strong hydrogen bonds with the water molecules. The degree of plasticization increases linearly with EVA content up to 30%, but tends to stabilize for the highest concentration. Moreover, even in the latter blends this parameter is significantly smaller than that of the EVA copolymer; this is due to the EVA phase being confined in isolated spherical domains within the hydrophobic PP phase, which in turn prevents the EVA fraction swelling.

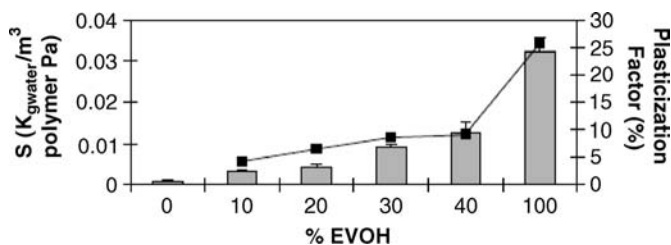


**Figure 14.5** Water solubility coefficients ( $S$ ) (bars) and plasticization factors (lines) of the EVOH amorphous fraction in PP/EVOH films at 25 °C and 0.98 water activity.

In terms of diffusivity, the  $D$ -values diminish linearly from 10% to 30% EVA. It appears that a higher number of interacting sites and a greater cluster size contribute to a further reduction in the effective diffusivity on increasing EVA content. This factor alone does not explain the slightly higher diffusion coefficient of the 40% EVA sample, however. Rather, the effect is related to the greater void space around EVA spheres, which causes the plasticized interface to become a preferential pathway for moisture diffusion. In the case of pure EVA, the diffusion coefficients are at least one order of magnitude smaller with respect to 70/30 PP/EVA blends at lower water activities. The reasons for this are the faster free volume blocking (due to the greater number of hydrophilic sites) and differences in the initial free volume owing to the high inter- and intra-chain self-association in EVA copolymers. Because of the well-known plasticization process that the EVA copolymer undergoes, the  $D$ -values become superimposable with those of the 70/30 blends at very high water activities.

#### 14.2.11

##### PVA/P(AA-AMPS)

Blend membranes of poly(vinyl alcohol)/(acrylic acid-*co*-2-acrylamido-2-methylpropylsulfonic acid) (P(AA-AMPS)) were constructed to analyze the effects of polymer blend ratio on the sorption and diffusion properties of penetrant molecules, by applying molecular simulations. The sorption and diffusion of water/propylene was calculated respectively, using grand canonical Monte Carlo (GCMC) and molecular dynamics (MD) simulations [26]. The calculated amount of propylene adsorbed in the PVA and PVA-P(AA-AMPS) blends was zero, notably because the interaction between propylene and the polymer, and also its large molecular size, made it difficult for propylene to be adsorbed. Although increasing the P(AA-AMPS) content of the membrane caused the water uptake to be increased to 51 wt%, a further increase in P(AA-AMPS) content caused the water sorption to be decreased. These simulated results showed the same changing trends as the experimental study [27]. As the acetate and sulfonic groups in the P(AA-AMPS) chains had a stronger interaction with water than with hydroxyl groups in the PVA chains, the incorporation of P(AA-AMPS), with a high density of acetic acid and sulfonic groups, would increase the interaction between the blend membranes and water, and thus enhance the water uptake. However, as the P(AA-AMPS) content was increased, there was a sharp decrease in the free volume that led to a decrease in the number of adsorbed sites. Consequently, the water uptake was decreased at higher P(AA-AMPS) contents.

The simulated results of water diffusion in the PVA and PVA-P(AA-AMPS) blend membranes showed that the diffusion coefficients of water would decrease in line with increases in P(AA-AMPS) content. The main factors determining the diffusion of water in the membrane are the free volume properties, chain mobility, and polymer–water interactions. With an increase in P(AA-AMPS) content the diffusion coefficients of water continue to decrease, despite the chain mobility



being increased slightly. Consequently, the greater polymer–water interactions and the decreased free volume would probably play a more important role than would chain mobility. Notably, for these membranes the water diffusion coefficients assessed by simulation showed the same trend as did the experimental measurements [27].

#### 14.2.12

##### **PVP/PEG**

Treatment of the water state in hydrogels represents a major challenge if the effect of sorbed water is obscured or hidden by a strong specific interaction between the polymeric components of the composite. This is exactly the case for a compatible blend based on a stoichiometric hydrogen-bonded complex formed by mixing high-molecular-weight poly(*N*-vinylpyrrolidone) (PVP) with the short-chain poly(ethylene glycol) (PEG) [28]. PEG, which bears two hydrogen donor hydroxyl groups at both ends of short chains, has been shown to form hydrogen bonds with the proton-accepting carbonyl units of significantly longer PVP macromolecules. In this way, the flexible PEG chains can serve as a comparatively long H-bonded crosslink, thus creating a free volume between the cohesively interacting PVP macromolecule and the plasticizing glassy PVP, because of the free volume formation and greater molecular mobility of the PEG compared to the PVP chain segments. Water is not a compatibilizer in the PVP-PEG systems, but rather offers serious competition to PEG for hydrogen bonding with PVP. The hydrogen bonding of the PEG hydroxyl groups to the carbonyl groups in the PVP units is thought to occur directly through water molecules associated with the PVP carbonyls, thus increasing water mobility. However, whereas water sorption has a dramatic effect on the state of crystalline excess PEG in blends, the state of the amorphous phase – which is constituted by the PVP–PEG hydrogen-bonded complex – is essentially unaffected by hydration.

#### 14.2.13

##### **iPHB/aPHB and iPHB/PECH**

Poly(hydroxyalkanoates) (PHA) comprise a family of biopolymers that recently has attracted much attention, due to their full biodegradability, biocompatibility and natural origin. The most well-studied but easily produced member of this family is poly(3-hydroxybutyrate) (iPHB), an isotactic which serves as a carbon and energy storage material. In efforts to improve the properties of iPHB, it has been blended with a miscible second polymer, intended as a polymeric toughener that does not impair the biodegradability of the original iPHB. Thus, only iPHB-rich blends containing up to 40% atactic PHB (aPHB) or poly(epichlorohydrin) (PECH) have been considered, for which the carbon dioxide and water vapor transport properties were studied [29].

CO<sub>2</sub> sorption was increased with the amount of aPHB added to bacterial iPHB. This was an expected behavior as the effect of aPHB is to decrease the overall crystallinity of the blend in such a manner that more amorphous polymer is available to the CO<sub>2</sub> molecules for sorption, assuming zero gas solubility in the crystalline phase. However, the behavior of the iPHB/PECH system was less straightforward, given that the blend isotherms appear to overlap with that of iPHB. It is worth noting that, in this case, the situation is complicated due to the superposition of the effects of the blend composition and the crystallinity degree. The apparent CO<sub>2</sub> solubility in the iPHB/aPHB blends is clearly higher than in iPHB/PECH blends. In contrast, the behavior of the diffusion coefficients is opposite to this, being higher for the iPHB/PECH system. This is consistent with a higher mobility of the amorphous phase in this blend, leading to a facilitated transport of CO<sub>2</sub> molecules through the polymeric media. Interestingly, the trends made evident by solubility and diffusion coefficients tended to compensate in such a manner that both systems showed virtually the same permeability to carbon dioxide at each composition. The interaction energy density for the polymer pair calculated from sorption measurement gave a value of  $-0.60 \text{ cal cm}^{-3}$  at 30 °C. This result was clearly different from those reported for other types of experimental measurement, and confirmed the concentration- or temperature-dependence of this parameter.

The dependence of water sorption isotherms on blend composition follows the same trend as CO<sub>2</sub>. The diffusion coefficient for iPHB/aPHB blends tended to be slightly higher than those for the iPHB/PECH system, as opposed to the observed behavior for carbon dioxide. The upward curvature of the sorption isotherms, together with a decrease in the diffusion coefficients with activity, is usually indicative of the clustering phenomenon. This means that there is a tendency for the sorbed water molecules to associate or to form clusters, due to the pre-eminence of water–water over water–polymer interactions.

#### 14.2.14

##### Epoxy Resin/PEI

The fragile nature of epoxy resins can be improved by the introduction of a second component that is capable of phase separation, such as rubbers and thermoplastic polymers. The excellent properties of epoxy materials are greatly affected by absorbed water, and thus their potential applications are confined. Consequently, water sorption behavior in polyetherimide-modified diglycidyl ether bisphenol-A/4,4'-diaminodiphenyl sulfone (DGEBA/DDS) systems has been investigated by Li *et al.* [30]. Increasing the polyetherimide fraction in the blends has the effect of reducing water uptake, while the fractional free volume is seen to decrease with the increasing polyetherimide fraction. Pure epoxy resins show the highest uptake and lowest diffusion coefficient; this is due to the numerous hydrophilic groups (e.g., hydroxyl and amine) that couple strongly with water molecules (by hydrogen bonding), causing them to locate mainly in the epoxy resin and impede water diffusion.

## 14.2.15

**PMMA/PEO**

The equilibrium sorption and transport of water vapor in poly(ethylene oxide)/poly(methylmethacrylate) (PEO/PMMA) blends has been investigated in order to determine which parameters govern the morphology and scale of component compatibility in films of semi-crystalline polymers, together with problems related to the number and composition of the amorphous phases [31]. Blends are either immiscible or (most probably) partly miscible in the amorphous phase; the exceptions are the 10/90 and 20/80 PEO/PMMA blends, which are miscible as the PMMA phase contains a small part of the PEO component. A decay in permeability has been observed when passing from the more-permeable PEO-rich films to blend films that are rich in the least-permeable PMMA. The sorption equilibrium has been determined only for PEO and 90/10 and 80/20 PEO/PMMA blends, mainly because the quantity of sorbed water is too small in blends that contain a greater PMMA content. However, the sorption equilibrium was seen to decrease with increasing PMMA content, as the number of hydrophobic sites was increased. The clustering function value was larger for the more hydrophobic PMMA than for PEO, and was increases in line with PMMA content in the blend; this confirmed the decreasing trend in the diffusion coefficient with PMMA content. These results were subsequently compared with data obtained for blends prepared from amorphous PMMA and a semicrystalline biodegradable polybutylene succinate-adipate polyester (BIONOLLE 3000) [32]. Again, although the permeability was decreased by PMMA content, the slope was much less important than had been reported for the PEO/PMMA blend. At this point it is important to remember that the crystallinity of pure PEO is much higher than that of BIONOLLE. Furthermore, the crystallinity of PEO in the blend was strongly decreased as the PMMA content was increased, whereas the crystallinity of BIONOLLE was quite independent of the PMMA content.

It is interesting to add that, by preparing interpenetrating polymer network (IPN) hydrogels from PEO and PMMA polymers [33], the equilibrium water content of the hydrogel would increase with increasing PEO content. This effect was attributed to the hydrophilicity of PEO and hydrophilic functional groups capable of hydrogen bonding, such as  $-\text{CONH}$  and  $-\text{CONH}_2$ . With an increase in the hydrophilic content of the IPN hydrogels, the diffusion coefficient values were found to increase as the result of a greater penetration of water into the hydrogels.

In another study, diethyl ether was used as a probe to investigate the local structure in blends of PEO/PMMA [34]. Typically, the diffusion values decrease as a sign of the tortuous pathway observed in heterogeneous systems, where there are regions that support rapid diffusion and regions that support slow diffusion, or act as barriers. In this blend, PEO is known to undergo a rapid segmental motion typical of a rubbery state, whereas the segmental motion of PMMA is slower by many orders of magnitude. Mobile PEO would provide a pathway for the diffusion of structurally similar diethyl ether, whereas the solid-like PMMA would act as a barrier.

### 14.3

#### Pervaporation

##### 14.3.1

#### THF/Water Mixtures

Srinivasa *et al.* [35] studied the performance of PVA membranes that are used for dehydrating tetrahydrofuran (THF) and water mixtures, by blending the polymer with poly(ethyleneimine) (PEI). The blend membrane was crosslinked with glutaraldehyde (GA) in order to reduce swelling and increase the structural strength. The interactions included hydrogen bonding between hydrogen ions of the hydroxyl groups of PVA and nitrogen ions of the amine groups of PEI, as well as covalent crosslinking induced by the addition of GA. Although both PVA and PEI are soluble in water, their blend is not. In fact, the PVA/PEI blend membrane is highly hydrophilic in nature and absorbs water preferentially owing to extensive intra- and intermolecular hydrogen bonding. Comparatively, the sorption percentage was greater for the PVA/PEI membrane than for a GA-crosslinked PVA/PEI membrane, due to the compact nature of the membrane after crosslinking. Unfortunately, an increased swelling has a negative impact on membrane selectivity, as the swollen and plasticized upstream membrane layer allows some THF molecules to escape into the permeate side, along with water.

In order to acquire a more detailed picture of the molecular transport phenomenon, Srinivasa *et al.* [36] performed sorption gravimetric experiments to monitor how varying the blend ratios would affect the swelling, diffusion and permeability coefficients of the above-mentioned system. At lower PVA concentrations, the membrane swells appreciably due to the presence of  $\text{—NH}_2$  groups of the relatively more hydrophilic PEI. A higher concentration of PVA caused an increased interaction between the amino groups of PEI and the hydroxyl groups of PVA, and this resulted in a lesser degree of swelling. The decrease in diffusion coefficient and increase in PVA content could be attributed to reductions of the free volume and inter-segmental spacing in the polymer network. It is clear that permeability – which is the net effect of sorption and diffusion – decreases in line with the PVA content, thus allowing a lower degree of water transfer across the membrane.

In another study, Sunitha *et al.* [37] described the experimental pervaporative dehydration of THF, using a blend membrane of PVA/PVP with different blend ratios. The polymers are perfectly miscible via hydrogen-bond interactions between the carbonyl groups of the cationic PVP and the hydroxyl groups of the neutral PVA. The results showed that a high selectivity and promising permeability could be achieved with a 9 : 1 blending ratio of the PVA/PVP membrane. However, on increasing the PVP concentration the affinity towards water was increased and selectivity decreased, due to enhancements in hydrophilicity and the membrane free volume.

Novel IPN membranes were prepared by crosslinking PVA with GA and PVP with 4,4'-diazostilbene-2,2'-disulfonic acid, disodium salt (DAS), and then used to separate THF/water and THF/methanol mixtures by pervaporation [38]. It is

interesting to note that the permeation flux increases in line with the PVP content in the membrane at about 80 wt%, without any loss of selectivity attributed to the disappearance of PVA crystallinity. The absence of any further increase in the permeation flux for PVP contents >80% was seen to be related to the crosslinking of both polymer components, and the membrane was unable to swell any further. This IPN membrane would be best-suited for the dehydration of THF, as it is much less fragile than a pure PVP membrane, although when PVA/PVP IPN membranes were used to separate a THF/methanol mixture the membranes appeared to be less selective. Moreover, the selectivity was decreased when the PVP content was increased. The sharp decrease in membrane selectivity at a PVP content of about 20 wt% was attributed to the fact that PVP shows not only a lower affinity towards methanol compared to water, but that it also exhibits hydrogen-bond interactions with PVA and blocks PVA crystallization. As a result, the THF molecules can penetrate more easily into the membrane, which in turn leads to a lower membrane selectivity.

#### 14.3.2

##### **Acetic Acid/Water Mixture**

In industrial unit operations, waste water is almost always contaminated with acetic acid, the separation of which is difficult by conventional distillation, due to the close relative volatilities of the two compounds. In contrast, pervaporation (PV) – which involves dehydration using hydrophilic blend membranes – represents an attractive alternative. In order to obtain a better PV performance, a novel mixed-blend membrane was developed using a suitable graft copolymer such as hydroxyl ethylcellulose and acrylamide (HEC-g-AAM) with a hydrophilic sodium alginate (NaAlg) polymer [39]. The degree of membrane swelling was increased in line with the increasing HEC-g-AAM content. However, as the amount of graft-copolymer was increased the blend membrane became more hydrophilic than NaAlg itself, an effect which further increased the free volume and resulted in a tenfold increase in flux. Consequently, selectivity must also be increased by the same ratio – that is, the higher the grafting ratio, the higher would be the selectivity. Although difficult to achieve, this type of simultaneous enhancement in flux and selectivity supports the increased selective permeation of water molecules through the swollen membrane at higher grafting ratios.

#### 14.3.3

##### **Ethanol/Water Mixture**

Ethanol is a renewable fuel that can be produced from biomass by fermentation, and PV has proved to be a viable technology to supplement the distillation of ethanol for purification purposes. In order to dehydrate such organic solvents, hydrophilic membranes were prepared by blending sericin and PVA, followed by chemical crosslinking with dimethylolurea (DMU) [40]. DMU appears to be an appropriate crosslinking agent, as the crosslinking occurs primarily through the

hydroxyl functionality of the polymers; this would leave the amino groups in sericin free to interact with water, thus improving the dehydration performance. Although each of the membranes investigated were able to selectively permeate water, the chemically crosslinked sericin/PVA blend was generally superior to membranes made from either sericin or PVA alone. For all of the above-mentioned membranes, a high selectivity appeared to be accompanied by a relatively low permeability. When comparing the permeation flux of the two sericin/PVA-DMU1 and sericin/PVA-DMU5 membranes, it became clear that a more intense chemical crosslinking using a larger amount of DMU would restrain membrane swelling and lead to a lower permeation flux.

#### 14.3.4

##### **DMF/Water Mixtures**

The separation of aqueous dimethylformamide (DMF) solutions has been studied over the concentration range of 0 to 100 wt%, using sodium alginate (NaAlg)/PVP blend membranes [41]. By adding PVP, the permeation flux was increased while the separation factor decreases. An increase in operating temperature was also found to increase the permeation flux, but to decrease the separation factor. A blend ratio of 75/25 (NaAlg/PVP, w/w) was preferred for the remainder of the study, due to acceptable flux and separation factors. When Aminabhavi and Naik [42] grafted PVA with acrylamide to separate water/DMF mixtures, the membranes proved to be more selective for water than DMF; moreover, while the separation factor was increased with grafting, the permeation flux did not change to any considerable extent. In another study performed by Kurkuri and Aminabhavi [43], the grafting of PVA with polyacrylonitrile caused the flux to decrease but the selectivity to increase. When Das *et al.* [44] crosslinked polyurethane urea/polymethylmethacrylate (PMMA) IPN membranes for the PV separation of DMF/water solutions they showed that, as the PMMA content was increased, the DMF flux and separation factor values were also increased due to the presence of more polar groups in PMMA.

#### 14.3.5

##### **1,4-Dioxane/Water**

A blend membrane of PVA with PEI was developed for the dehydration of 1,4-dioxane [45]. Although PVA and PEI are both water-soluble, their blend exhibited swelling but was insoluble in water. Such non-solubility may be due to the formation of a weak force of interactions, resulting in blending of the two homopolymers. The PVA/PEI blend membrane is highly hydrophilic in nature, and preferentially absorbs water owing to extensive intra- and inter-molecular hydrogen bonding and dipole–dipole interactions between water and the functional groups of the PVA/PEI membrane, such as amine and hydroxyl. On increasing the PVA content of PVA/PEI blend membranes, the sorption percentage would be decreased and this would result in a reduction in flux and a rise in selectivity. A

higher concentration of PVA would cause an increased interaction between the amino groups of PEI and the hydroxyl groups of PVA. Increased interactions would also reduce the degree of swelling, which would in turn lower the free volume of the polymer due to the close proximity of the chains. This would enable the preferential permeation of water molecules that are smaller in size and therefore would diffuse more rapidly than dioxane molecules.

## 14.4

### Vapor Permeation

#### 14.4.1

##### Chitosan/CPA

Safronov *et al.* [46] performed a thermodynamic investigation of the compatibility in binary blends of chitosan with ter-copolymamide 6/66/610 (CPA) under ambient conditions, based on the dissolution of the individual polymers and their blends of different composition in formic acid. The chitosan-rich blends were characterized by large and negative values of the enthalpy of mixing that provided a high polymer compatibility and negative values of Gibbs free energy of mixing. The first possible reason for this might be a specific hydrogen-bonding between the  $-\text{OH}$  and  $-\text{NH}_2$  groups in chitosan and  $-\text{CO}-\text{NH}-$  fragments in CPA. Subsequently, such interaction would lead to structuring in the blend, which would in turn give rise to negative values of entropy of mixing. A second possible reason might relate to the specific thermodynamic features of polymer glassy structures. When used in the present study, chitosan was amorphous and existed in a glassy state under ambient conditions; however, as CPA has a flexible chain it might be considered as a form of plasticizer, and this would result in large negative values of enthalpy of mixing. The entropy of mixing in this case would also be negative.

In CPA-rich blends, both the enthalpy and entropy of mixing are positive and, as a result, the Gibbs free energy of mixing (which is the difference between a relatively large enthalpy term and a smaller entropy term) would also become positive. The process may be similar to the isothermal fusion of CPA crystallites present in its structure under the influence of chitosan, which acts as a macromolecular solvent in the blend. The need for CPA fusion is an obstacle to its compatibility with chitosan, and the blends would tend to phase-separate, at least potentially.

#### 14.4.2

##### Natural Rubber Blends

The diffusion and transport properties of polymers were found to depend heavily on the additives and type of crosslinking. Usually, fillers are added to rubbers in order to cheapen the product and also to improve their properties. Thomas and others have investigated the transport properties of aromatic solvents such as

benzene, toluene and *p*-xylene through micron-sized [47] and nanostructured [48] filler-reinforced natural rubbers (NRs), carboxylated styrene-butadiene rubber (XSBR), and their 70/30 blend latex membranes. As a result of differences in polarity, the two components were seen to be thermodynamically immiscible and the affinity of the two phases towards the filler was different. The addition of a filler would reduce the availability of spaces and restrict the mobility of chain segments. Thus, the activation energy needed for the diffusion of penetrant molecules would be higher than that of a pristine polymer. As the filler concentration increased, the solvent uptake at equilibrium would decrease in the case of both NR and XSBR. For XSBR, the uptake would decrease constantly in line with filler loading, but this can be explained in terms of the polymer–filler interaction due to the polarity of XSBR. This system exhibits a lower diffusivity value due to the restricted chain mobility caused by the high cohesive energy density of XSBR. In NR, however, the solvent uptake appeared to level off at higher loadings, probably due to a poor rubber–filler interaction. The NR chain segments are more flexible and show higher diffusivity values; however, in the case of the NR/XSBR blend system the uneven distribution of filler in two immiscible phases resulted in a rather complex behavior, whereby solvent uptake and diffusivity were first decreased when a filler was added, but then showed remarkable increases at higher filler loadings.

An analysis of the transport of chlorinated [49] and aromatic [50] hydrocarbons through a Nylon/ethylene-propylene rubber (EPR) blend was investigated by Thomas *et al.* The permeation coefficient of Nylon is small compared to that of pure EPR, while the various blend compositions would have intermediate values. While the crystalline Nylon phase decreased in line with the increasing volume fraction of EPR, the sorption coefficient increased and so did the permeation coefficient; taken together, these observations supported the hetero-phase structure. As the Nylon/EPR blend is incompatible with poor physical and chemical interactions across the phase boundaries, this system requires compatibilization in order to reduce the interfacial energy between the phases. Nylon was compatibilized with EPR via the introduction of a compatibilizer precursor (EPR-g-MA) that was physically miscible with the second phase but had a chemical functionality (MA group) that was able to react with the amino end group of Nylon, so as to form a graft copolymer at the interface [49]. As a consequence the permeability was sharply increased when EPR-g-MA concentrations were increased to the critical micelle concentration (an effect attributed to a total surface area enhancement), but were then decreased. Only minimal changes were observed in permeation coefficient values at higher compatibilizer concentrations.

Similar to the Nylon/EPR system, the effect of compatibilization on transport properties can be seen in natural rubber/acrylonitrile-butadiene rubber (NR/NBR) blends compatibilized with poly(ethylene-co-vinyl acetate) (EVAc) [51]. In this case, the penetrant used was benzene. Subsequently, it was noted that the solvent uptake tendency of compatibilized samples was lower, while a greater time lag and minimum values for permeation and diffusion coefficients were exhibited compared to the uncompatibilized blend. The polar CN- end of NBR



was thought to interact with the polar part ( $-\text{OCOCH}_3$ ) of the EVAc phase, and its nonpolar part with the nonpolar NR phase; in this way, miscibility of the blend components would be increased while the interfacial tension between NR and NBR would be reduced. It appeared that the crystalline nature of EVAc would offer a greater resistance to solvent uptake, and a similar trend was found in NR/EVAc composites [52].

It has been established previously that the permeability of heterogeneous rubber–rubber blends is intermediate between that of the component polymers. This effect is remarkable with regards to the diffusion and permeation of substituted benzenes (notably benzene, toluene and *p*-xylene) through blends of NR/NBR [53], thermoplastic polyurethane (NR/TPU) [54], and polystyrene (NR/PS) [55]. Pure NR with flexible chains will easily adjust, with solvent ingress showing the highest degree of solvent uptake. However, based on the inherent solvent-resistant behavior of NBR, semicrystalline TPU and PS, the level of solvent uptake and the intrinsic diffusion coefficient would each be expected to decrease in line with the fall in rubber content and the increase in chain stiffness. The trend in the transport behavior of blends of NR and epoxidized natural rubber (ENR) epoxy-prene with 25 mol% epoxidation (and with pentane, hexane, heptane and octane as penetrants) was also in accordance with the above-described data [56]. In this case, the epoxy group and the polar nature of the ENR chains hindered chain flexibility. The same blend membranes were also evaluated for the selective separation of chlorinated hydrocarbons from acetone [57]. In this case, it was noted that the degree of swelling was increased in line with the volume fraction of ENR, and achieved a maximum for neat ENR-25 due to the polar nature of the ENR network and the greater hydrogen-bonding efficiency of acetone compared to chlorinated hydrocarbons. Therefore, by increasing the amount of ENR, the permeability (which is sorption multiplied by diffusion) is first increased and then decreases. The permeability of NR/ENR 70/30 and NR/ENR30/70 is then lower, compared to that of NR/ENR 50/50.

Siddaramaiah *et al.* reported details of the sorption and diffusion of aromatic liquids consisting of nitro, bromo, and chlorobenzene [58] and some aldehydes and ketones [59] into NR blends with bromo-butyl rubber (BIIR), chloro-butyl rubber (CIIR), neoprene, ethylene propylene diene terpolymer (EPDM), polybutadiene (PB), and styrene butadiene rubber (SBR). The maximum mass uptake of chlorobenzene and bromobenzene by all blends was in the order: NR/BIIR > NR/CIIR > NR/neoprene > NR/EPDM > NR/polybutadiene > NR/SBR. This may be due to the presence of polar groups such as bromide and chloride in BIIR, CIIR and neoprene. All of the penetrants showed relatively low sorption values for NR/EPDM, although these may have been attributed to the blend's tightly packed structure, such that it exhibited both the toughness of plastic and the elasticity of the gum elastomer phase. This intrinsic property of EPDM might restrict the free movement of penetrant molecules, leading to lower values of sorption. The same research groups also attempted to examine the sorption and diffusion behavior of structurally different EPDM blends, such as EPDM/NR, EPDM/BIIR, and EPDM/SBR, using aliphatic chlorinated hydrocarbon penetrants [60]. However, because

of the presence of the halogen atom in BIIR, which shows a greater interaction towards chlorinated hydrocarbons, the EPDM/BIIR exhibited a higher mass uptake compared to the other two blends.

#### 14.4.3

##### **NBR Blends**

The transport characteristics of styrene butadiene rubber/acrylonitrile–butadiene rubber (SBR/NBR) blends have been studied using  $\text{CH}_2\text{Cl}_2$ ,  $\text{CHCl}_3$ , and  $\text{CCl}_4$  as penetrants [61]. There is a regular reduction in solvent uptake, diffusion and permeation coefficients in  $\text{CH}_2\text{Cl}_2$  and  $\text{CHCl}_3$ , and an increase in these parameters when  $\text{CCl}_4$  was used with an increase in SBR content in the blend. This could be explained in terms of the polarity of the solvents:  $\text{CCl}_4$ , being nonpolar, interacts more with blends that contain larger amounts of SBR (nonpolar), whereas  $\text{CH}_2\text{Cl}_2$  and  $\text{CHCl}_3$  are polar and interact more with blends containing larger amounts of NBR (polar).

A similar trend of decreasing equilibrium uptake with crystalline EVAc and PP content increasing was observed, respectively, in the sorption of methyl-substituted benzenes through crosslinked nitrile rubber/poly(ethylene-*co*-vinyl acetate) (NBR/EVAc) [62] and acrylonitrile-*co*-butadiene rubber/polypropylene (NBR/PP) blend membranes [63]. The two crosslinking systems used in this investigation were sulfur and peroxide; the peroxide-cured system had a lower solvent uptake than the sulfur-cured system, as the peroxide-cured samples had rigid C—C bonds and higher crosslink density, whereas the sulfur-cured samples had more flexible and long S—S bonds and a lower crosslink density.

An ethylene propylene diene monomer/poly (ethylene-*co*-vinyl acetate) (EPDM/EVAc) blend has also been proven to exhibit the above observations in systems with benzene, toluene and xylene as probe molecules [64]. The reduction in solvent uptake was prominent when the EVAc content was increased, and the compositions became less rubbery or more plastic-like due to the semicrystalline nature of EVAc. The liquid sorption characteristics of sulfur- and peroxide-crosslinked 40/60 EPDM/EVAc blends can be explained by the nature of the S—S and C—C chemical bonds.

The separation of hexane–acetone mixtures through high-density polyethylene/ethylene propylene diene monomer (HDPE/EPDM) blend membranes was linked to the polymer blend concept when developing membrane materials for PV [65]. The flux was lowest for the 100/0 HDPE/EPDM membranes, but was slowly increased in line with increases in the weight % of EPDM present, although EPDM did have a retarding effect on selectivity. Because of their close solubility parameter values, there was a strong interaction between EPDM and hexane. Such interaction effectively increased the frequency and amplitude of the rubber chain motions, which in turn allowed the permeate molecules to pass easily through the membrane. As a result, the permeation rate was increased and the selectivity decreased. The swelling ratio and permeation rate were highest for blends vulcanized with sulfur, but lowest for those treated with peroxide. However, the reverse of this situation was observed with regards to selectivity.

The barrier properties of 70/30 acrylonitrile–butadiene rubber/ethylene propylene diene monomer rubber (NBR/EPDM) vulcanizates, when loaded with carbon black fillers [e.g., ISAF (intermediate super-abrasion furnace), HAF (high-abrasion furnace) and SRF (semi-reinforcing furnace)] and using benzene, toluene and xylene as penetrants, have been examined with reference to the type of filler employed [66]. The filled samples were found to exhibit a better resistance to uptake of the three organic solvents when compared to the respective unfilled blends for any given blend ratio. With regards to the three types of carbon black used, solvent uptake was in the order: SRF- > HAF- > ISAF-filled samples. The reason for this order was attributed to the better filler reinforcements and enhanced crosslink densities of the matrix as the size of the carbon black particles used was decreased. A similar behavior was also identified for NR/EVA composites [52].

#### 14.4.4

##### LCP Blends

The sorption of toluene, CCl<sub>4</sub> and THF by blends of PP and a thermotropic liquid crystal polymer (LCP), poly(ethylene terephthalate/*p*-hydroxybenzoic acid) copolyester (Rodrun 5000) have been studied, as have the effects of solvent presence on the blend's structural properties [67]. At the initial stage of the sorption curve, and for whichever solvent was used, sorption uptake was faster and more extensive as the Rodrun content was increased, despite the very low permeability of the latter. These results also indicated that microcracking had occurred as a consequence of sorption, and that this was in addition to the microcracking induced by the presence of Rodrun. A combination of a lack of solvent uptake in Rodrun, a lack of a nonoccupied volume change in PP as a result of solvent presence, and the irreversible nature of the process in the blend provided support for the existence of this additional microcracking. Plasticization was also believed to occur due to debonding of the dispersed Rodrun phase.

The transport properties of incompatible blends of poly(ethylene terephthalate) (PET) and a blend composed of 40 mol% PET and 60 mol% Rodrun 3000 were investigated, using dichloromethane as permeant [68]. Blends submitted to physical aging showed a decrease in permeability of a proportion that was increased in line with the amount of LC phase present, and by a larger contribution that was derived from the polymeric matrix. This decrease in permeability was essentially attributed to a lowering of sorption, as the diffusional behavior of the different samples was the same.

Data relating to the diffusivity and solubility of methanol in blends of polyether-sulfone (PES) and a type of LCP, poly(hydroxyl-benzoic acid (73 mol%)-*co*-hydroxynaphthoic acid (27 mol%)) have been reported by Wiberg *et al.* [69]. Samples were taken from injection-molded and compression-molded specimens over a wide range of compositions. The solubility of methanol was proportional to the PES content. Values beyond 40% LCP were not available because of the low methanol diffusion in blends with a high LCP content; consequently, the LCP phase

constitutes an impenetrable obstacle to methanol diffusion. The methanol solubility was seen to be independent of whether the LCP phase was febrile (injection-molded) or continuous (compression-molded). Methanol transport in PES may be referred to as a “concentration-dependent diffusion”; that is, there was a substantial increase in the free volume associated with sorption, but this was not sufficient to induce a transformation of the glassy polymer to a rubbery state. The extensive solubility of methanol in PES caused a nonuniform swelling and the formation of microcracks. The zero-concentration diffusivity of the blends decreased strongly in line with the increasing LCP content.

#### 14.4.5

##### **PU/PDMS**

The main aim of elucidating the sorption behavior and diffusion coefficients of pure toluene and methanol in blends incorporating various levels of polyurethane (PU) into rubbery poly(dimethylsiloxane) (PDMS) is to optimize the transport properties [70]. Previously, it has been shown that the solubility of methanol increases while that of toluene decreases in line with the PU content of the blends, and this results in lower values of selectivity with higher PU contents. These data suggest that the declining diffusivity of both solvents in PU-rich membranes can be explained by a lower fractional free volume due to the mobility confinement arising from the higher hard-segment level contribution of PU. The diffusion selectivity in the polymer blends preferentially favored toluene diffusion, and toluene also exhibited a higher solubility in the membranes. The adsorbed toluene molecules may loosen the hard-segment structure and cause chain relaxation, promoting toluene diffusion to a greater extent than for methanol.

#### 14.4.6

##### **EEA-CB**

In order to understand the phenomena behind resistance variations in the conductive polymer composites (CPCs) due to solvent diffusion, Feller *et al.* [71] have performed sorption experiments with poly(ethylene-co-ethyl acrylate)-carbon black (EEA-CB) and EEA films in the presence of toluene. One main point here was to determine the influence of CB in the diffusion process. The first results showed that, whichever polymer was used, the diffusion coefficient increased with toluene activity, which indicated plasticization of the material by the solvent. However, it was interesting to note that the plasticization phenomenon was reduced when fillers were introduced into the polymer matrix. It also appeared that the toluene diffusivity was about twofold lower in EEA-CB than in EEA, which was certainly due to a hindrance effect of the carbon black particles. In other words, the decrease in toluene solubility was the result of a tortuosity effect due to the morphology of CPC with a dispersion of CB particles, which acted as barrier components and increased the path for toluene molecules inside the composite.

Moreover, it seemed that the presence of CB in contact with solvent molecules led to an organizing effect in the CPC, allowing more cohesion in the polymer matrix and suggesting the presence of strong interactions between EEA chains and CB resulting from an adsorption process.

#### 14.4.7

##### **PVC/EVAc**

Today, PVC is one of the most widely industrialized materials used to create PV membranes to separate benzene/cyclohexane mixtures, with a proven high sorption selectivity for benzene; however, a pure PVC membrane does not have a high permeation flux in a low benzene content. Therefore, PVC is modified by blending with low-molecular-weight EVAc in the region of compatibility with  $W_{\text{EVAc}} < 0.2$ , where the sum of dispersion forces between the alkyl, ester and chlorinated units, dipole–dipole interaction among ester molecules, and hydrogen-bonding interaction between the carbonyl groups in EVAc and the CHCl groups in PVC is positive. There is, however, considerable disagreement regarding the influence of VAc content on blend compatibility [72]. The degree of swelling (DS) values for all blend membranes in the benzene/cyclohexane mixture were lower than in benzene, and pure PVC had almost no swelling. This indicated that PVC is good against cyclohexane, but that the addition of a small amount of EVAc to the PVC could cause a very large increase in the equilibrium DS of the blend membrane. In contrast, the permeation flux was increased as the  $W_{\text{EVAc}}$  content of the blend was increased, while the value of the separation factor was lowered.

#### 14.4.8

##### **PHB/PEO and PHB/PMMA**

The miscibility behaviors of poly-D(–)(3-hydroxybutyrate) (PHB)/poly(ethylene oxide) (PEO) and PHB/poly(methyl methacrylate) (PMMA) blends have been studied using a chloroform vapor sorption technique [73]. The addition of PEO, which has been reported to be miscible with both PHB and PMMA, did not enhance the compatibility of PHB and PMMA. Polymer–polymer interaction parameters monitored by using the chloroform vapor sorption technique were found to be negative for PHB/PEO, but positive for PHB/PMMA systems. However, the interaction parameters of both systems were changed significantly depending on their composition.

#### 14.4.9

##### **PVA/PAA**

The PV properties of homogeneous membranes prepared from a polymer blend of PVA with poly(acrylic acid) (PAA) have been investigated using methanol–toluene and ethanol–toluene liquid mixtures [74]. The PV flux was decreased and selectivity increased gradually for all feed mixtures with different compositions as

the PVA content in the blends was increased. Notably, the higher the rigid PVA content, the less was the membrane swollen.

## 14.5

### Gas Permeation

#### 14.5.1

##### PVA/PEI/PEG

The results of various studies have shown alkanolamines to be important carriers for the selective removal of CO<sub>2</sub>. For example, Matsuyama *et al.* [75] prepared a polyethyleneimine/poly(vinyl alcohol) (PEI/PVA) blend membrane and investigated its CO<sub>2</sub>/N<sub>2</sub> separation performance. PEI contains both primary and second amino groups, exhibits an extended hydrogen-bonding with PVA so as to reduce the latter's crystallinity and promote miscibility. When Hamouda *et al.* [76,77] investigated the sorption behavior and the permeability of PVA/PEI/PEG membranes for pure CO<sub>2</sub> and N<sub>2</sub>, the compact organization of the polymer crystallites prevented any sorption of the permeant molecules in their structure. This caused molecular diffusion in the remaining amorphous phase to be much slower, by creating impermeable obstacles on the diffusion pathways. Clearly, an inverse relationship exists between the PVA crystallinity and the gas permeability of the blend. The PVA crystallinity would pass through a minimum at the content of maximum permeability and selectivity with the PEI content. In contrast, PEG does not show an extremely high performance, but would be partially associated with PVA in its amorphous form by hydrogen bonding; however, the main part of the PEG would be separated into a PEG-rich dispersed phase that would cause a reduction in the selectivity of the membrane.

#### 14.5.2

##### PS/PC

The CO<sub>2</sub> sorption isotherms of samples of polystyrene/polycarbonate (PS/PC) blends with different compositions have been obtained as a function of the polymer blend composition [78]. Basically, the polymer blend system studied was heterogeneous (i.e., phase-separated), although a small amount of polystyrene was found to be partly miscible with polycarbonate and this would most likely disrupt the crystallization of polycarbonate, especially at the higher polystyrene content. The relationship between the extent of CO<sub>2</sub> sorption by the PS/PC polymer blend and the PC composition was seen to obey an increasing trend. The CO<sub>2</sub> sorption behavior of the PS/PC blend system could be explained by a simple additive rule corrected for the degree of crystallinity of the PC component, such that the effect of the partly miscible region in this system on sorption behavior would be almost negligible. This finding suggested that the amount of this miscible region was small and that the interaction in the PS/PC blend was weak.

## 14.5.3

**PS/PPO**

The sorption and permeation of CO<sub>2</sub> gas in miscible blends of poly(phenylene oxide) (PPO) and PS has been measured over the entire range of blend compositions [79]. The sorption curves for blends lie intermediate to those for the pure components, as seen for mixtures of polycarbonates and a copolyester formed from 1,4-cyclohexanedimethanol and a mixture of terephthalic and isophthalic acids [80] and an increasing PPO content. This trend suggested that CO<sub>2</sub> would be bound more strongly in the blends than in pure PS. The magnitude of the heat of mixing was exothermic, and the  $\chi'_{23}$  found in this way was  $-1.08$ . It was interesting to note that PPO is much more permeable to CO<sub>2</sub> than is PS. The permeability and diffusion coefficients for the blends fell between the extremes for the pure component polymers; however, this relationship was far from additive either on an arithmetic or logarithmic scale, as has been found for the polycarbonate-copolyester blends. The negative departure from such additive expressions is apparently general for miscible blend systems interpreted in terms of a free volume model, and showed that a part – but not all – of this departure may be attributed to the volume contraction that was exhibited by the PPO–PS system and expected for mixtures with an exothermic heat of mixing. However, such an observed behavior may have practical value when good barrier properties are an issue.

The compatibility of PS and PPO may also be explained in part by the near-equal solubility parameters of the two polymers [81]. PS and PPO pack more closely when blended than is possible for either homopolymer in the pure state, and this suggestion is supported by permeation measurements which showed that hexane molecules have a lower permeability in PS/PPO polymer blended films than in films of either of the two homopolymers. This apparent increase in the packing of PS and PPO in the blends suggests that an intimate molecular mixing of the two homopolymers occurs in the blends.

## 14.5.4

**PS/PTMPS**

The gas permeability of O<sub>2</sub> and CO<sub>2</sub> was studied for various polymer blend membranes of polystyrene (PS) and poly[1,1,1-tris(trimethylsiloxy)methacrylate propylsilane (PTMPS) [82]. In order to improve the compatibility of these polymer blends, the effect of adding the graft copolymer was also investigated. The gas permeability of various composition polymer-blend membranes increased rapidly with an increasing content of PTMPS in the polymer blend. In the polymer blend membranes containing the graft copolymer, the gas permeability decreased in line with increases in the graft copolymer content and then reached a near-constant value, when the PTMPS content remained constant. This result was attributed to a decrease in the interstices at the phase boundaries, owing to improvements in the compatibility of the component polymers.

## 14.5.5

**Matrimid/PSF**

The permeation rates of He, H<sub>2</sub>, CO<sub>2</sub>, N<sub>2</sub> and O<sub>2</sub> have been reported for a series of miscible polysulfone–polyimide (PSF-PI) blend membranes [83]. For gases which do not interact with the polymer matrix, such as He, H<sub>2</sub>, N<sub>2</sub> and O<sub>2</sub>, the permeability coefficients were seen to vary monotonically between the values of the two pure component polymers. In the case of CO<sub>2</sub>, permeability through the blend membranes was in all cases lower than that for the pure polymers. This behavior was attributed to a strong interaction between CO<sub>2</sub> and polyimide in the blend membranes, or to possible polymer matrix densification and consolidation caused by CO<sub>2</sub> permeation at high pressures. Regardless of the absolute value of CO<sub>2</sub> permeability in the blends, the plasticization phenomena of PSF/PI membranes were of major importance, with pure PSF and PI polymers showing different CO<sub>2</sub> permeation characteristics. In PSF, the CO<sub>2</sub> permeability varied in accordance with predictions of the dual sorption theory, whereas the CO<sub>2</sub> permeability in PI decreased initially with increasing pressure and, after a short leveling at a critical pressure (which was well predicted by the dual-mode theory) it increased again. The pressure where CO<sub>2</sub> permeability reached its lowest value and the respective curve showed an inflection point is termed the critical pressure of plasticization. The plasticization pressure was seen to shift to higher pressures with increasing PSF content, while the plasticized polyimide exhibited a substantially higher permeability, due to polymer matrix swelling, though its permselective efficiency was diminished to rubbery polymer levels. The extent of plasticization of the PSF/PI blend membranes was analogous to the PI weight content.

He permeation is also very sensitive to local concentration fluctuations, and thus can be used as a probe for the phase state in polymer blends [84]. In the above-mentioned system, the PSF-rich blend exhibited partial miscibility below the  $T_g$  whereas, after annealing, the PSF- and PI-rich domains phase separated; this resulted in a reduction of the permeability coefficient and showed that PI controls the absolute permeability values. It was concluded that transport in a phase-separated Matrimid/PSF is dominated by the polyimide over a wide concentration range. Assuming that the plasticization behavior may also be dominated by the polyimide, it must be concluded that only the homogeneous blend such as Matrimid/P84 would be less susceptible to plasticization.

## 14.5.6

**Matrimid/P84**

The high plasticization tendency of Matrimid can be stabilized by blending with copolyimide P84, which is hardly affected by the sorbed molecules [85]. The CO<sub>2</sub> concentration in the P84 film was lower than in the Matrimid/P84 and Matrimid film at corresponding pressures. It was unclear why the sorption isotherms of the Matrimid film and the blend coincided. The permeability coefficients of the blend were found to lie between the values of the homopolymers. On the basis of the



film densities, it was concluded that blending Matrimid with P84 would result in a densification of the polymer matrix, and hence a reduction in the free volume. Densification of the polymer matrix resulted in lower permeability values. The plasticization pressure of the Matrimid/P84 blend was shifted to higher feed pressures with increasing P84 content. The diffusion coefficients of the blend corresponded with the diffusion coefficients of P84, which was lower compared to that of Matrimid. This explained the lower permeability of the blend compared to Matrimid, as the concentration in the blend was comparable to Matrimid; hence, Matrimid blended with P84 would result in a decrease in diffusivity. The selectivity of the blends lay between the values of homopolymers; the selectivity of P84 was greatest, and decreased in line with the increasing Matrimid content.

#### 14.5.7

##### **Matrimid/PBI**

Gas separation in systems containing  $H_2/N_2$ ,  $CO_2/CH_4$  and  $H_2/CO_2$  has been evaluated by blending the high-performance polymers Matrimid and polybenzimidazole (PBI) [86]. The blend membrane was completely miscible through strong hydrogen bonding interaction among the functional groups, which in turn caused an increase in chain packing density and hindrance in the segmental mobility of the polymer chains. Thus, a general decline could be observed in gas permeability with increases in PBI concentration. The consequence of this behavior was the melioration in selectivity of selected gas pairs.

An attractive performance for the separation of  $H_2/N_2$ ,  $N_2/CH_4$ ,  $CO_2/CH_4$ ,  $O_2/N_2$  and  $H_2/CO_2$  gas pairs has been also obtained by tuning the PBI content in homogeneous Matrimid/PBI blend carbon membranes [87]. Carbon membranes are basically formed through the pyrolysis of polymeric materials, and exhibit a much larger permeability and permselectivity compared to their corresponding precursors. When gas permeability and selectivity were evaluated for three different compositions, a large difference was clearly apparent in the permeability values of the samples; essentially, the higher PBI content brought about a lower permeability, whereas selectivity was only enhanced for the  $H_2/N_2$ ,  $O_2/N_2$  and  $H_2/CO_2$  pairs. A gradual reduction in the PBI content of precursors could provide a carbon membrane with enhanced  $N_2/CH_4$  and  $CO_2/CH_4$  selectivities. One interesting property of the carbon membranes developed for separating  $N_2$  and  $CO_2$  from  $CH_4$  was due to the prominent effect of diffusivity selectivity than of solubility selectivity. The possession of such an enhanced diffusivity selectivity would indicate the formation of finely tuned pores in the microstructure of carbon membranes that could either constrict or retard the transport of large molecules such as  $CH_4$ .

#### 14.5.8

##### **CA/PMMA**

The  $He$ ,  $O_2$  and  $N_2$  gas-transport properties of cellulose acetate (CA), poly(methyl-methacrylate) (PMMA) and CA/PMMA blends of several compositions have been

measured at 35 °C [88]. Consistent with the lower absolute permeability, PMMA exhibited exceptionally high He/N<sub>2</sub> and He/O<sub>2</sub> gas separation factors that would make PMMA-based membranes most attractive for helium extraction and purification. PMMA was also more selective for CO<sub>2</sub>/CH<sub>4</sub> separation than either PS or bischloral polycarbonate (BCPC) [89]. In spite of the tendency for the MMA moiety to invoke plasticization by CO<sub>2</sub>, PMMA proved to be considerably less permeable than either PS or BCPC. The permeability of these blends also fell between the values of the homopolymers.

#### 14.5.9

##### **PU/PMMA**

The effect of blend composition on the permeability, diffusivity and solubility of CO<sub>2</sub>, H<sub>2</sub>, O<sub>2</sub>, CH<sub>4</sub> and N<sub>2</sub> has been investigated using phase-separated polyurethane/poly(methylmethacrylate) (PU/PMMA) blend membranes [90]. The diffusion process in homogeneous blends was seen to be strongly influenced by the interaction between the polymers, whereas in heterogeneous blends the permeability was much more dependent on the degree of heterogeneity. The permeability of all gases was decreased as the PMMA concentration in the blend was increased, due to a decrease in the volume available for molecule diffusion. Addition of the vitreous component PMMA hampered diffusion of the gas molecules, because the transport occurred better through the elastomeric PU phase. For H<sub>2</sub>/N<sub>2</sub> and O<sub>2</sub>/N<sub>2</sub> gas pairs, the addition of PMMA increased both the diffusion selectivity and permselectivity. In the case of CO<sub>2</sub>/CH<sub>4</sub> and CO<sub>2</sub>/N<sub>2</sub> pairs, the behavior of diffusion selectivity did not follow a general tendency; this may be understood as a complex effect of CO<sub>2</sub> plasticization on the mobility of the polymeric chains, which depends on the blend composition and varies in relation to the gas pair being evaluated.

#### 14.5.10

##### **EVA-45/H-48**

The sorption and permeation of CO<sub>2</sub> and CH<sub>4</sub> have been studied for blends of ethylene-vinyl acetate copolymer (EVA-45) and chlorinated polyethylene (H-48) [91]. A small negative  $\chi'_{23}$  obtained from sorption experiments introduced the blend as miscible, while the permeability and diffusion coefficients were decreasing functions of the H-48 volume fraction. The results of steady-state diffusion coefficients suggested a small negative value of activation energy for diffusion. Although, in general, positive activation energy values are expected for miscible blends, the small negative values reported here may reflect interference associated with an imperfect mixing of the components.

#### 14.5.11

##### **PS/PVME**

A similar behavior as above was observed for propane diffusion in miscible blends of polystyrene and poly(vinyl methyl ether) (PVME) in the rubbery state [92]. The

small value of selectivity indicated a weak ability to discriminate on the basis of molecular size and shape. This behavior is typical of rubbery polymers. The relatively low value of selectivity highlighted the reason why few rubbery polymers have found applications as gas-separation membranes. The sorption of CO<sub>2</sub> in PS/PVME blend also exhibited a negative deviation from semi-logarithmic additivity rule as a sign of a single-phase blend [93].

#### 14.5.12

##### **TLCP/PET**

The alteration of CO<sub>2</sub>, N<sub>2</sub> and O<sub>2</sub> transport properties of the PET matrix due to the presence of the TLCP phase has been evaluated by Motta *et al.* [94]. The addition of TLCP increased the barrier properties of PET; indeed, blending PET with only 2% (w/w) TLCP decreased the permeability down to about 30% with respect to pure PET, and this was attributed essentially to an extraordinarily low gas solubility. The nonlinear relationship between the logarithm of the permeability and blend composition suggested that the system is incompatible. The ordered domains of the nematic mesophase, with their efficient chain packing, formed impenetrable barriers to the molecules of gases. The impermeable regions also imposed a more tortuous path on the steady-state permeation of the penetrant across the polymer film, which in turn reduced the space available for diffusion and led to the penetrant taking a longer path in order to circumnavigate the impermeable regions.

#### 14.5.13

##### **CELL/PVA**

The relationship between the gas-transport properties and composition of semi-crystalline binary blends of cellulose (CELL) and PVA has been assessed by following the kinetics of CO<sub>2</sub> sorption [95]. The blends are thermodynamically miscible with  $\chi'_{23} = -0.985$ , consistent with the presence of favorable interactions due to hydrogen bonding between the two different polymers. As sorption takes place only in the amorphous regions, the absolute level of CO<sub>2</sub> equilibrium sorption is relatively low with the highest value for pure CELL. The sorption curves for the blends lie intermediate to those for the pure components. Accordingly, both the diffusion coefficient and permeability were increased in line with the CELL content, with little or no pressure dependency.

#### 14.5.14

##### **Trogamid Blends**

Studies of the free volume in blends of an amorphous polyamide (Trogamid) with three additives, namely of 4,4'-(hexafluoroisopropanilidene) diphenol (HFBA), 1,5-dihydroxynaphthalene (Ndiol) and poly(4-vinylphenol) (PVPh), each of which can act as an antiplasticizer, have been performed by monitoring CO<sub>2</sub> transport

properties [96]. Results obtained with the HFBA blend showed an increase in both free volume and  $D$ , indicating that the addition of this compound produced a plasticization of Trogamid. In general, the permeability stayed constant but the solubility was slightly diminished because the gas-polymer interaction was weaker than the additive-polymer interaction. In the case of blends with Ndiol, a decrease in transport magnitudes was appreciated as a consequence of reducing the hole size and antiplasticization effects. Finally, for polymeric blends of Trogamid with PVPh, the  $\text{CO}_2$  transport properties were hardly affected by the presence of a second component. In fact, this situation was seen as logical when considering that the specific volume of both polymers, and subsequently the free volume, did not vary by much either.

#### 14.5.15

##### **TPX/Siloxane**

The effects of composition on the homogeneity, gas permeability and selectivity of oxygen/nitrogen of poly(4-methyl-pentent-1) (TPX) and siloxane blend membranes have been studied [97]. The results showed that the gas permeability had been significantly improved without any loss of selectivity compared to pure TPX membrane, for blended membranes containing less than 20 wt% siloxane. As the proportion of siloxane increased, however, the blend showed phase separation and an increased permeability and decreased selectivity for oxygen and nitrogen. It also appeared that, the lower the siloxane content, the greater was the homogeneity shown.

#### 14.5.16

##### **PTMSMMA/3-Methylsulfolane**

The performances and characteristics of a series of poly(trimethylsilylmethyl methacrylate) (PTMSMMA) membranes blended with low 3-methylsulfolane relative to selectivity have been studied through the determination of  $\text{CO}_2$  permeability [98]. The PTMSMMA blend membranes changed from a glassy to a near-rubbery state, while the solubility and permeability of  $\text{CO}_2$  became lower with an increasing 3-methylsulfolane content due to a decrease in the volume of the microvoids. This increase in diffusivity of  $\text{CO}_2$  was attributed to an increased mobility of the polymer chains. The ideal separation factor for  $\text{CO}_2$  over  $\text{N}_2$  could not be improved satisfactorily through blending with a low 3-methylsulfolane content, but it did exhibit very much higher levels of permeability and selectivity with a high 3-methylsulfolane content.

#### 14.5.17

##### **BCPC/PMMA**

The miscibility of PMMA with bisphenol chloral polycarbonate (BCPC) has been studied using gas-permeation experiments [99]. Gas permeability coefficients for

He, H<sub>2</sub>, O<sub>2</sub>, Ar, N<sub>2</sub>, CH<sub>4</sub> and CO<sub>2</sub> are lower than those calculated from the semi-logarithmic additivity rule, indicating that PMMA is miscible with BCPC over the whole blend composition range. These permeation results can be interpreted in terms of the free volume contraction which has been proposed to describe gas transport behavior in polymer mixtures. Similar observations for the miscible blends of polycarbonate with a copolyester formed from 1,4-cyclohexanedimethanol and a mixture of terephthalic and isophthalic acids have been made using CO<sub>2</sub> [100]. Negative deviations of both permeability and diffusion coefficients from simple additivity relations have been observed, and interpreted qualitatively to have resulted from the decrease in volume when the blends were mixed.

## 14.6

### Conclusions

The aim of this chapter was to provide a comprehensive review of the type of water sorption and solvent sorption behavior that can be expected from miscible or immiscible, but compatible, polymer blends. It was concluded that miscibility depends on the molecular structures of the polymers, their morphologies and the blend composition, as well as the processes of the blends. Several blends also exist which, despite intermolecular hydrogen bonding, do not form thermodynamically homogeneous blends due to the stiffness and self-association of the polymer chains.

The data obtained also suggest that the declining diffusivity of solvents in membrane can be explained by a lower fractional free volume due to the mobility confinement arising from polymer–polymer interactions due to hydrogen bonding between donor and acceptor groups, or from chain segment crystallinity. However, as the temperature increases the polymer chain showed a higher segmental mobility and the swelling rate was increased. A plasticization phenomenon that depends on the blend composition and solvent activity may also affect polymer chain mobility.

### References

- 1 Flory, P.J. (1953) Chapter 12, in *Principles of Polymer Chemistry*, Cornell University Press, Ithaca.
- 2 Shcherbina, A.A., Gerasimov, V.K., and Chalykh, A.E. (2004) Determination of pair interaction parameters for multicomponent polymer blends. *Russian Chem. Bull. Int. Ed.*, **53**, 2601–2603.
- 3 Sabzi, F. and Boushehri, A. (2006) Compatibility of polymer blends. I. Copolymers with organic solvents. *J. Appl. Polym. Sci.*, **101**, 492–498.
- 4 Arvanitoyannis, I., Kolokuris, I., Nakayama, A., Yamamoto, N., and Aiba, S. (1997) Physico-chemical studies of chitosan-polyvinyl alcohol blends plasticized with sorbitol and sucrose. *Carbohydr. Polym.*, **34**, 9–19.
- 5 Mucha, M., Ludwiczak, S., and Kawinska, M. (2005) Kinetics of water sorption by chitosan and its blends with poly(vinyl alcohol). *Carbohydr. Polym.*, **62**, 42–49.
- 6 Ludwiczak, S. and Mucha, M. (2010) Modeling of water sorption isotherms of

- chitosan blends. *Carbohydr. Polym.*, **79**, 34–39.
- 7 Kim, S.J., Park, S.J., and Kim, S.I. (2003) Swelling behavior of interpenetrating polymer network hydrogels composed of poly(vinyl alcohol) and chitosan. *React. Funct. Polym.*, **55**, 53–59.
  - 8 Jagadish, R.S., Rastogi, N.K., and Raj, B. (2010) Moisture sorption characteristics of chitosan/polyethylene oxide blended films. *J. Polym. Environ.*, **18**, 266–276.
  - 9 Grebennikov, S.F., Vnuchkin, A.V., and Sashina, E.S. (2010) Thermodynamic features of mixing of chitosan with polyvinyl alcohol and polyethylene oxide. *Russian J. Appl. Chem.*, **83**, 1189–1195.
  - 10 Rashidova, S.Sh., Voropaeva, N.L., Nikonovich, G.V., Burkhanova, N.D., Yugay, S.M., Pulatova, H.P., Ibragimov, I. Sh., and Ruban, I.N. (2004) The structure and physicochemical properties of mixtures of water-soluble polymers. *Chromatographia*, **59**, 521–524.
  - 11 Zuo, D.Y., Tao, Y.Z., Chen, Y.B., and Xu, W.L. (2009) Preparation and characterization of blend membranes of polyurethane and superfine chitosan powder. *Polym. Bull.*, **62**, 713–725.
  - 12 Schult, K.A. and Paul, D.R. (1997) Water sorption and transport in blends of poly(vinyl pyrrolidone) and polysulfone. *J. Polym. Sci. Part B: Polym. Phys.*, **35**, 655–674.
  - 13 Schult, K.A. (1996) Water sorption and transport in a series of polysulfones. PhD dissertation, The University of Texas at Austin.
  - 14 Schult, K.A. and Paul, D.R. (1997) Water sorption and transport in blends of polyethyloxazoline and polyethersulfone. *J. Polym. Sci. Part B: Polym. Phys.*, **35**, 993–1007.
  - 15 Pfenning, L.G., Keskkula, H., and Paul, D. R. (1986) Water extraction of polyethyloxazoline from miscible and immiscible polymer blends. *J. Appl. Polym. Sci.*, **32**, 3657–3673.
  - 16 Singh, V.B., Barrie, J.A., and Walsh, D.J. (1986) Sorption of water in polyethersulfone/poly(ethylene oxide) blends. *J. Appl. Polym. Sci.*, **31**, 295–299.
  - 17 Swinyard, B.T., Sagoo, P.S., Barrie, J.A., and Ash, R. (1990) The transport and sorption of water in polyethersulphone, polysulphone, and polyethersulphone/phenoxy blends. *J. Appl. Polym. Sci.*, **41**, 2479–2485.
  - 18 Singh, V.B. and Walsh, D.J. (1986) The miscibility of polyethersulfone with phenoxy resin. <http://www.tandfonline.com/doi/abs/10.1080/00222348608248032>. *J. Macromol. Sci. Phys.*, **25**, 65–87.
  - 19 Tsang, C.J., Clark, J.C., Wellingshoff, S.T., and Miller, W.G. (1991) Structure–property relationships in poly(*n*-vinyl pyrrolidone)-phenoxy-water gels. *J. Polym. Sci. Part B: Polym. Phys.*, **29**, 247–259.
  - 20 Katoch, S., Sharma, V., and Kundu, P.P. (2010) Water sorption and diffusion through saturated polyester and their nanocomposites synthesized from glycolized PET waste with varied composition. *Chem. Eng. Sci.*, **65**, 4378–4387.
  - 21 Gsell, T.C., Pearce, E.M., and Kwei, T.K. (1991) Miscibility and segmental mobility in hydrogen-bonded polymer blends. *Polymer*, **32**, 1663–1672.
  - 22 Hsu, W.P., Li, R.J., Myerson, A.S., and Kwei, T.K. (1993) Sorption and diffusion of water vapor in hydrogen-bonded polymer blends. *Polymer*, **34**, 597–603.
  - 23 Marais, S., Bureau, E., Gouanvé, F., Ben Salem, E., Hirata, Y., Andrio, A., Cabot, C., and Atmani, H. (2004) Transport of water and gases through EVA/PVC blend films: permeation and DSC investigations. *Polym. Test.*, **23**, 475–486.
  - 24 Földes, E., Fekete, E., Karasz, F.E., and Pukánszky, B. (2000) Interaction, miscibility and phase inversion in PBI/PI blends. *Polymer*, **41**, 975–983.
  - 25 Lasagabáster, A., José Abad, M., Barral, L., Ares, A., and Bouza, R. (2009) Application of FTIR spectroscopy to determine transport properties and water-polymer interactions in polypropylene (PP)/poly(ethylene-co-vinyl alcohol) (EVA) blend films: effect of poly(ethylene-co-vinyl alcohol) content and water activity. *Polymer*, **50**, 2981–2989.
  - 26 Pan, F., Ma, J., Cui, L., and Jiang, Z. (2009) Water vapor/propylene sorption and diffusion behavior in PVA-P(AA-AMPS) blend membranes by GCMC and

- MD simulation. *Chem. Eng. Sci.*, **64**, 5192–5197.
- 27 Pan, F.S., Jia, H.P., Jiang, Z.Y., Zheng, X. H., Wang, J.T., and Cui, L. (2008) P(AA-AMPS)-PVA/Polysulfone composite hollow fiber membranes for propylene dehumidification. *J. Membr. Sci.*, **323**, 395–403.
  - 28 Feldstein, M.M., Kuptsov, S.A., Shandryuk, G.A., Platé, N.A., and Chalykh, A.E. (2000) Coherence of thermal transition in poly(N-vinyl pyrrolidone)-poly(ethylene glycol) compatible blends. 3. Impact of sorbed water upon phase behavior. *Polymer*, **41**, 5349–5359.
  - 29 Miguel, O., Egiburu, J.L., and Iruin, J.J. (2001) Blends of bacterial poly(3-hydroxybutyrate) with synthetic poly(3-hydroxybutyrate) and poly (epichlorohydrin): transport properties of carbon dioxide and water vapour. *Polymer*, **42**, 953–962.
  - 30 Li, L., Liu, M., and Li, S. (2004) Morphology effect on water sorption behavior in a thermoplastic modified epoxy resin system. *Polymer*, **45**, 2837–2842.
  - 31 Elberaichi, A., Daro, A., and David, C. (1999) Water vapour transport in polyethylene oxide/polymethylmethacrylate blends. *Eur. Polym. J.*, **35**, 1217–1228.
  - 32 Elberaichi, A. and David, C. (2001) Phase behavior and water vapor transport in BIONOLLE/polymethylmethacrylate blends. *Eur. Polym. J.*, **37**, 19–24.
  - 33 Kim, S.J., Lee, C.K., Kim, I.Y., An, K.H., and Kim, S.I. (2003) Preparation and characterizations of interpenetrating polymer network hydrogels of poly (ethylene oxide) and poly(methyl methacrylate). *J. Appl. Polym. Sci.*, **89**, 258–262.
  - 34 Cao, H., Lin, G., and Jones, A.A. (2004) Anomalous penetrant diffusion as a probe of the local structure in a blend of poly (ethylene oxide) and poly (methylmethacrylate). *J. Polym. Sci. Part B: Polym. Phys.*, **42**, 1053–1067.
  - 35 Srinivasa Rao, P., Sridhar, S., and Krishnaiah, A. (2006) Dehydration of tetrahydrofuran by pervaporation using crosslinked PVA/PEI blend membranes. *J. Appl. Polym. Sci.*, **102**, 1152–1161.
  - 36 Srinivasa Rao, P., Sridhar, S., Wey, M.Y., and Krishnaiah, A. (2007) Pervaporation performance and transport phenomenon of PVA blend membranes for the separation of THF/water azeotropic mixtures. *Polym. Bull.*, **59**, 289–298.
  - 37 Sunitha, K., Ravi Kumar, Y.V.L., and Sridhar, S. (2009) Effect of PVP loading on pervaporation performance of poly(vinyl alcohol) membranes for THF/water mixtures. *J. Mater. Sci.*, **44**, 6280–6285.
  - 38 Lu, J., Nguyen, Q., Zhou, J., and Ping, Z. H. (2003) Poly(vinyl alcohol)/poly(vinyl pyrrolidone) interpenetrating polymer network: synthesis and pervaporation properties. *J. Appl. Polym. Sci.*, **89**, 2808–2814.
  - 39 Krishna Rao, K.S.V., Vijaya Kumar Naidu, B., Subha, M.C.S., Sairam, M., Mallikarjuna, N.N., and Aminabhavi, T.M. (2006) Novel carbohydrate polymeric blend membranes in pervaporation dehydration of acetic acid. *Carbohydr. Polym.*, **66**, 345–351.
  - 40 Gimenes, M.L., Liu, L., and Feng, X. (2007) Sericin/poly(vinyl alcohol) blend membranes for pervaporation separation of ethanol/water mixtures. *J. Membr. Sci.*, **295**, 71–79.
  - 41 Solak, E.K., Asman, G., Çamurlu, P., and Şanlı, O. (2008) Sorption, diffusion, and pervaporation characteristics of dimethylformamide/water mixtures using sodium alginate/polyvinyl pyrrolidone blend membrane. *Vacuum*, **82**, 579–587.
  - 42 Aminabhavi, T.M. and Naik, H.G. (2002) Pervaporation separation of water/dimethylformamide mixtures using poly (vinyl alcohol)-g-polyarylamide copolymeric membranes. *J. Appl. Polym. Sci.*, **83**, 273–282.
  - 43 Kurkuri, M.D. and Aminabhavi, T.M. (2004) Polyacrylonitrile-g-Poly(vinyl alcohol) membranes for the pervaporation separation of dimethylformamide and water mixtures. *J. Appl. Polym. Sci.*, **91**, 4091–4097.
  - 44 Das, S., Banthia, A.K., and Adhikari, B. (2006) Pervaporation separation of DMF from water using a crosslinked

- polyurethane urea-PMMA IPN membrane. *Desalination*, **197**, 106–116.
- 45 Srinivasa Rao, P., Smitha, B., Sridhar, S., and Krishnaiah, A. (2006) Effect of blending ratio on pervaporative separation of 1,4-dioxane/water mixtures through PVA–PEI membranes. *Vacuum*, **81**, 299–306.
  - 46 Safronov, A.P., Suvorova, A.I., Tyukova, I. S., and Smirnova, Y.A. (2007) Opposite trends in thermodynamic compatibility between copolyamide and chitosan in their binary blend. *J. Polym. Sci. Part B: Polym. Phys.*, **45**, 2603–2613.
  - 47 Stephen, R., Joseph, K., Oommen, Z., and Thomas, S. (2007) Molecular transport of aromatic solvents through microcomposites of natural rubber (NR), carboxylated styrene butadiene rubber (XSBR) and their blends. *Compos. Sci. Technol.*, **67**, 1187–1194.
  - 48 Stephen, R., Varghese, S., Joseph, K., Oommen, Z., and Thomas, S. (2006) Diffusion and transport through nanocomposites of natural rubber (NR), carboxylated styrene butadiene rubber (XSBR) and their blends. *J. Membr. Sci.*, **282**, 162–170.
  - 49 George, S.C., Ninan, K.N., Geuskens, G., and Thomas, S. (2004) Permeation of chlorinated hydrocarbons through nylon 6/ethylene-propylene rubber blends. *J. Appl. Polym. Sci.*, **91**, 3756–3764.
  - 50 George, S.C., Groeninckx, G., Ninan, K. N., and Thomas, S. (2000) Molecular transport of aromatic hydrocarbons through nylon 6/ethylene-propylene rubber blends: relationship between phase morphology and transport characteristics. *J. Polym. Sci. Part B: Polym. Phys.*, **38**, 2136–2153.
  - 51 Kumari, P., Radhakrishnan, C.K., George, S., and Unnikrishnan, G. (2008) Mechanical and sorption properties of poly(ethylene-co-vinyl acetate)(EVA) compatibilized acrylonitrile butadiene rubber/natural rubber blend system. *J. Polym. Res.*, **15**, 97–106.
  - 52 Sujith, A. and Unnikrishnan, G. (2005) Barrier properties of natural rubber/ethylene vinyl acetate/carbon black composites. *J. Mater. Sci.*, **40**, 4625–4640.
  - 53 Mathai, A.E., Singh, R.P., and Thomas, S. (2002) Transport of substituted benzenes through nitrile rubber/natural rubber blend membranes. *J. Membr. Sci.*, **202**, 35–54.
  - 54 Al Minnath, M., Unnikrishnan, G., and Purushothaman, E. (2011) Transport studies of thermoplastic polyurethane/natural rubber (TPU/NR) blends. *J. Membr. Sci.*, **379**, 361–369.
  - 55 Mathew, A.P., Packirisamy, S., Stephen, R., and Thomas, S. (2002) Transport of aromatic solvents through natural rubber/polystyrene (NR/PS). *J. Membr. Sci.*, **201**, 213–227.
  - 56 Johnson, T. and Thomas, S. (1999) Natural rubber/epoxidised natural rubber-25 blends: morphology, transport phenomena and mechanical properties. *J. Mater. Sci.*, **34**, 3221–3239.
  - 57 Johnson, T. and Thomas, S. (1999) Pervaporation of acetone-chlorinated hydrocarbon mixtures through polymer blend membranes of natural rubber and epoxidized natural rubber. *J. Appl. Polym. Sci.*, **71**, 2365–2379.
  - 58 Siddaramaiah Roopa, S. and Premakumar, U. (1998) Sorption and diffusion of aromatic penetrants into natural rubber blends. *Polymer*, **39**, 3925–3931.
  - 59 Siddaramaiah Roopa, S., Premakumar, U., and Varadarajulu, A. (1998) Sorption and diffusion of aldehydes and ketones into natural rubber blends. *J. Appl. Polym. Sci.*, **67**, 101–112.
  - 60 Siddaramaiah Roopa, S. and Guruprasad, K.H. (2003) Interaction of crosslinked ethylene-propylene-dieneterpolymer blends with chlorinated organic penetrants. *J. Appl. Polym. Sci.*, **88**, 1366–1375.
  - 61 Habeeb Rahiman, K. and Unnikrishnan, G. (2006) The behavior of styrene butadiene rubber/acrylonitrile butadiene rubber blends in the presence of chlorinated hydrocarbons. *J. Polym. Res.*, **13**, 297–314.
  - 62 Joseph, A., Mathai, A.E., and Thomas, S. (2003) Sorption and diffusion of methyl substituted benzenes through cross-linked nitrile rubber/poly(ethylene-co-vinyl acetate) blend membranes. *J. Membr. Sci.*, **220**, 13–30.



- 63 George, S.C., Varughese, K.T., and Thomas, S. (2000) Molecular transport of aromatic solvents in isotactic polypropylene/acrylonitrile-co-butadiene rubber blends. *Polymer*, **41**, 579–594.
- 64 George, S., Kumari, P., and Unnikrishnan, G.P. (2010) Influence of static and dynamic crosslinking techniques on the transport properties of ethylene propylene diene monomer rubber/poly (ethylene-co-vinyl acetate) blends. *J. Polym. Res.*, **17**, 161–169.
- 65 Anil Kumar, P.V., Anil Kumar, S., Varughese, K.T., and Thomas, S. (2012) Separation of n-hexane/acetone mixtures by pervaporation using high density polyethylene/ethylene propylene diene terpolymer rubber blend membranes. *J. Hazard. Mater.*, **199–200**, 336–342.
- 66 Manoj, K.C., Kumari, P., Rajesh, C., and Unnikrishnan, G. (2010) Aromatic liquid transport through filled EPDM/NBR blends. *J. Polym. Res.*, **17**, 1–9.
- 67 Guerrica-Echevarría, G., Eguiazábal, J.I., and Nazábal, J. (2000) Solvent sorption effects on the structure and properties of PP/Rodrun blends. *J. Polym. Sci. Part B: Polym. Phys.*, **38**, 1090–1100.
- 68 Gorrasí, G., Incarnato, L., Di Maio, L., Acierno, D., and Vittoria, V. (1997) Transport properties of poly(ethylene terephthalate)/Rodrun 3000 blends. *J. Macromol. Sci. Part B*, **36**, 643–653.
- 69 Wiberg, G., Hedenqvist, M.S., Boyd, R.H., and Gedde, U.W. (1998) Transport properties of methanol in blends of a liquid crystalline copolyester and polyethersulfone. *Polym. Eng. Sci.*, **38**, 1640–1648.
- 70 Lue, S.J., Ou, J.S., Chen, S.L., Hung, W.S., Hu, C.C., Jean, Y.C., and Lai, J.Y. (2010) Tailoring permeant sorption and diffusion properties with blended polyurethane/poly(dimethylsiloxane) (PU/PDMS) membranes. *J. Membr. Sci.*, **356**, 78–87.
- 71 Feller, J.F., Langevin, D., and Marais, S. (2004) Influence of processing conditions on sensitivity of conductive polymer composites to organic solvent vapours. *Synthetic Metals*, **144**, 81–88.
- 72 An, Q.F., Qian, J.W., Sun, H.B., Wang, L. N., Zhang, L., and Chen, H.L. (2003) Compatibility of PVC/EVA blends and the pervaporation of their blend membranes for benzene/cyclohexane mixtures. *J. Membr. Sci.*, **222**, 113–122.
- 73 Yoon, J.S., Choi, C.S., Maing, S.J., Choi, H.J., Lee, H.S., and Choi, S.J. (1993) Miscibility of poly-D(–)(3-hydroxybutyrate) in poly(ethylene oxide) and poly(methyl methacrylate). *Eur. Polym. J.*, **29**, 1359–1364.
- 74 Park, H.C., Meertens, R.M., Mulder, M.H. V., and Smolders, C.A. (1994) Pervaporation of alcohol-toluene mixtures through polymer blend membranes of poly(acrylic acid) and poly(vinyl alcohol). *J. Membr. Sci.*, **90**, 265–274.
- 75 Matsuyama, H., Terada, A., Nakagawara, T., Kitamura, Y., and Teramoto, M. (1999) Facilitated transport of CO<sub>2</sub> through polyethyleneimine/poly(vinyl alcohol) blend membrane. *J. Membr. Sci.*, **163**, 221–227.
- 76 Hamouda, S.B. and Roudesli, S. (2008) Transport properties of PVA/PEI/PEG composite membranes: sorption and permeation characterizations. *Cent. Eur. J. Chem.*, **61**, 634–640.
- 77 Hamouda, S.B., Nguyen, Q.T., Langevin, D., and Roudesli, S. (2010) Poly (vinylalcohol)/poly(ethyleneglycol)/poly (ethyleneimine) blend membranes – structure and CO<sub>2</sub> facilitated transport. *C. R. Chimie*, **13**, 372–379.
- 78 Kato, s., Tsujita, Y., Yoshimizu, H., Kinoshita, T., and Higgins, J.S. (1997) Characterization and CO<sub>2</sub> sorption behaviour of polystyrene/ polycarbonate blend system. *Polymer*, **38**, 2807–2811.
- 79 Morel, G. and Paul, D.R. (1982) CO<sub>2</sub> sorption and transport in miscible poly (phenyleneoxide)/polystyrene blends. *J. Membr. Sci.*, **10**, 273–282.
- 80 Masi, P., Paul, D.R., and Barlow, J.W. (1982) Gas sorption and transport in a copolyester and its blend with polycarbonate. *J. Polym. Sci. Part B: Polym. Phys.*, **20**, 15–26.
- 81 Jacques, C.H.M. and Hopfenberg, H.B. (1974) Vapor and liquid equilibria in glassy polyblends of polystyrene and poly (2,6-dimethyl-1,4-phenylene oxide). Part I. *Polym. Eng. Sci.*, **14**, 441–448.

- 82 Kang, Y., Araki, K., Iwamoto, K., and Senō, M. (1982) Preparation and gas permeability of polymer blend membranes of polystyrene and poly[1,1,1-tris(trimethylsiloxy)methacrylate propylsilane]. *J. Appl. Polym. Sci.*, **27**, 2025–2032.
- 83 Kapantaidakis, G.C., Kaldis, S.P., Dabou, X.S., and Sakellariopoulos, G.P. (1996) Gas permeation through PSF-PI miscible blend membranes. *J. Membr. Sci.*, **110**, 239–247.
- 84 Kapantaidakis, G.C., Kaldis, S.P., Sakellariopoulos, G.P., Chira, E., Loppinet, B., and Floudas, G. (1999) Interrelation between phase state and gas permeation in polysulfone/polyimide blend membranes. *J. Polym. Sci. Part B: Polym. Phys.*, **37**, 2788–2798, 8.
- 85 Bos, A., Pünt, I., Strathmann, H., and Wessling, M. (2001) Suppression of gas separation membrane plasticization by homogeneous polymer blending. *AIChE J.*, **47**, 1088–1093.
- 86 Hosseini, S.S., Teoh, M.M., and Chung, T. S. (2008) Hydrogen separation and purification in membranes of miscible polymer blends with interpenetration networks. *Polymer*, **49**, 1594–1603.
- 87 Hosseini, S.S. and Chung, T.S. (2009) Carbon membranes from blends of PBI and polyimides for  $N_2/CH_4$  and  $CO_2/CH_4$  separation and hydrogen purification. *J. Membr. Sci.*, **328**, 174–185.
- 88 Bikson, B., Nelson, J.K., and Muruganandam, N. (1994) Composite cellulose acetate/poly(methyl methacrylate) blend gas separation membranes. *J. Membr. Sci.*, **94**, 313–328.
- 89 Raymond, P.C., Koros, W.J., and Paul, D. R. (1993) Comparison of mixed and pure gas permeation characteristics for  $CO_2$  and  $CH_4$  in copolymers and blends containing methyl methacrylate units. *J. Membr. Sci.*, **77**, 49–57.
- 90 Sales, J.A., Patrício, P.S.O., Machado, J.C., Silva, G.G., and Windmüller, D. (2008) Systematic investigation of the effects of temperature and pressure on gas transport through polyurethane/poly(methylmethacrylate) phase-separated blends. *J. Membr. Sci.*, **310**, 129–140.
- 91 Barrie, J.A. and Webb, W.D. (1989) Gas transport in miscible blends of ethylene-vinyl acetate copolymer and chlorinated polyethylene. *Polymer*, **30**, 327–332.
- 92 Spencer, H.G. and Yavorsky, J.A. (1983) Solubility and diffusion of propane in blends of polystyrene and poly(vinyl methyl ether) at  $T > T_g$ . *J. Appl. Polym. Sci.*, **28**, 2937–2946.
- 93 Ramachandra Rao, V.S. and Watkins, J.J. (2000) Phase separation in polystyrene-poly(vinyl methyl ether) blends diluted with compressed carbon dioxide. *Macromolecules*, **33**, 5143–5152.
- 94 Motta, O., Di Maio, L., Incarnato, L., and Acierio, D. (1996) Transport and mechanical properties of PET/Rodrun 3000 blown films. *Polymer*, **37**, 2373–2377.
- 95 Pate1, K. and St John Manley, R. (1995) Carbon dioxide sorption and transport in miscible cellulose/poly(vinyl alcohol) blends. *Macromolecules*, **28**, 5793–5798.
- 96 Garcia, A., Iriarte, M., Uriarte, C., and Etxeberria, A. (2006) Study of the relationship between transport properties and free volume based in polyamide blends. *J. Membr. Sci.*, **284**, 173–179.
- 97 Lai, J.Y., Wu, G.J., and Shyu, S.S. (1987) TPX/siloxane blend membrane for oxygen enrichment. *J. Appl. Polym. Sci.*, **34**, 559–569.
- 98 Li, J., Tachihara, K., Nagai, K., Nakagawa, T., and Wang, S. (1996) Selective permeation of sour gases through polymeric membranes modified by sulfolanes. I. Study of selective permeation of  $CO_2$  through modified polymeric membranes determined on different systems. *J. Appl. Polym. Sci.*, **60**, 1645–1654.
- 99 Chiou, J.S. and Paul, D.R. (1987) Gas permeation in miscible blends of poly(methylmethacrylate) with bisphenol chloral polycarbonate. *J. Appl. Polym. Sci.*, **33**, 2935–2953.
- 100 Masi, P., Paul, D.R., and Barlow, J.W. (1982) Gas sorption and transport in a copolyester and its blend with polycarbonate. *J. Polym. Sci. Part B: Polym. Phys.*, **20**, 15–26.

## 15

### Modeling and Simulation

*Yingrui Shang and David Kazmer*

#### 15.1

##### Introduction

##### 15.1.1

##### Numerical Models for Polymer Blends

Polymer blends and composites have been widely used as engineering and functional materials [1–3]. Immiscible and partially miscible blends, including polymers, are also involved in many common application processes such as evaporation, injection, or extrusion. During recent years, computer simulation has become an important tool in the polymer sciences, complementing both analytical theory and experiment. This interest is due both to the many fundamental scientific questions that polymer systems pose, and to the importance of polymeric materials in technology. Computer modeling and numerical simulation can help research groups and engineers to study the thermodynamics, miscibility, morphology and interfaces of polymer blends. Some of the properties of these polymer blends can be characterized by the same experimental measures as for homogeneous materials, including mechanical properties, strain and stress curves, or viscosity. Although certain aspects of the blends are not observable *in situ*, it is possible to employ methods such as scanning electron microscopy, transmission electron microscopy, or atomic force microscopy to observe the structure and morphology of polymer blends on the nanometer scale. However, these methods can only replicate partial images of the system. In the meantime, although small-angle X-ray diffraction can be used to provide statistical information on the structures of blends, detailed local structural information at the micro/meso level of the blends remains vague.

When compared to experimental assessment methods, simulation methods are capable of providing detailed illustrations of the structural features at the scale of macromolecules, lattices, or even atoms. Moreover, the simulation methods have provided tools for in-line investigations of the evolution and formation of multiphase polymeric structures during a variety of processes such as annealing and spin coating. Numerical simulations allow the modeling and investigation of

phenomena with varying material properties and process states, allowing the quantitative assessment of process dynamics, feasibility, and sensitivities.

Whilst it would be rather difficult to provide a comprehensive and detailed description of all types of numerical simulation methods on polymer blends, different models can be applied depending on the topic under discussion.

The volume of fluid (VOF) method represents a category of numerical techniques used to trace the free surface of the fluid or the interface of two types of adjacent fluids. The fluids or mixture are described with a mesh grid, which is either stationary or moves with the flow front or interfaces in a prescribed manner. The interfaces of the different components in each mesh grid are then calculated for each step. Hence, the VOF technique is an advection method which describes only the flow front and must be adapted to other constitutive equations (e.g., Navier–Stokes) to describe the physics in the motion of the flow.

In the VOF method, the volume fraction of fluid A,  $C_A$ , is defined as the integral of indicator function of fluid A in each mesh grid (control volume). Obviously,

$$C_A \in [0, 1] \quad (15.1)$$

and the volume fraction of fluid B,  $C_B = 1 - C_A$ .

Taking  $h = dx = dy = dz$  as the size of one mesh grid in each dimension, the whole domain can be divided into  $n^3$  small control volumes. Therefore, if  $C_{A,i,j,k}$  denotes the volume fraction of fluid A in the  $i, j, k$ th grid,

$$C_{A,i,j,k} h^3 = V_{A,i,j,k} \quad (15.2)$$

where  $V_{A,i,j,k}$  denotes the volume of fluid A in the  $i, j, k$ th control volume, while the multiphase fluid flows in space  $\mathbf{R}^3$  with velocity  $\mathbf{v}$ . In an incompressible fluid without consideration for chemical reactions and the diffusion of one type of fluid to another, the movement of fluid (flow) is the only cause of a change in the volume fraction, which can be denoted as follows:

$$\frac{\partial C}{\partial t} + \mathbf{v} \cdot \nabla C = 0 \quad (15.3)$$

The interface segments are then determined based on the volume fraction in each control volume. In the VOF method, the interface is usually simulated as linear segments or planers in control volumes. In this way, the VOF method conserves the volume of the fluid and describes the interfaces within the multiphase flow. Once the interface has been determined, the pressure and velocity can be updated with constitutive equations. The evolution of the topology can represent multiphase phenomena, such as breaking up and joint of the flow front.

Figure 15.1 shows a schema comparing the real fluid configuration, where Figure 15.1c shows the simple line interface calculation (SLIC) VOF and Figure 15.1d the piecewise linear interface calculation (PLIC) VOF (the latter is also referred to as Youngs' method). From these data it can be seen that, in the SLIC VOF method, the interfaces are implemented as segments parallel to the  $x$  or  $y$  axis. Although the SLIC method is advantageous in terms of simplicity and

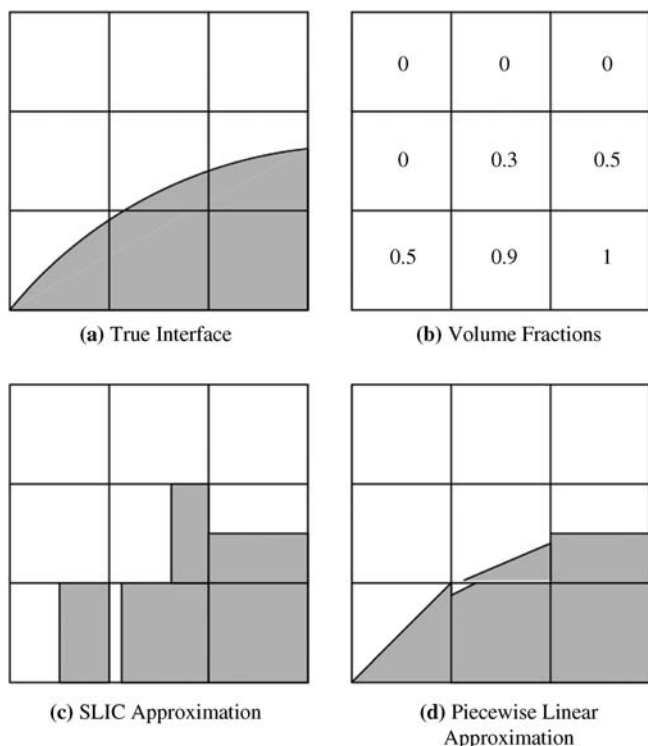


**Figure 15.1** Interface reconstructions of fluid shown by: (a) actual configuration; (b) volume fraction; (c) representation with simple line interface calculation (SLIC); and (d) piecewise linear interface calculation (PLIC) [12].

computation time and has an acceptable reliability, the PLIC method is superior to the SLIC method in terms of accuracy and flexibility [4].

The VOF methods are popular for interface tracking and predicting the morphologic development of blends because they are easy to implement and can be extended from a two-dimensional (2D) model to three-dimensional (3D) model. In the past, VOF methods have been implemented more and discussed in greater detail by fluid physicists than by polymer scientists, and an historic overview of VOF methods has been produced by Scardovelli and Zaleski [5]. An alternative review of numerical interface tracking methods was prepared by Hyman [6], while numerous other reviews have been made of VOF simulations of specific fluid–fluid or fluid–gas morphologies [4,7–9]. Other reviews of VOF methods are available elsewhere [10,11]. Generally, for VOF methods the composition gradient between the two components is not considered, and only a sharp interface or the midline of the interface can be calculated using a VOF-type method.

Molecular dynamics (MD) modeling refers to a category of simulation methods that focus on the particles in an ensemble (e.g., molecules and atoms) and calculate the movements of those particles in an established force field (the force field

is a vector field that describes the forces applied to particles). Examples of elements that contribute to the force field may include Van de Waals forces, dielectric fields of charged particles, chemical bonds, and magnetic fields. Subsequently, the velocity and acceleration of the particles can be calculated from the force field, while macroscopic properties such as pressure and temperature can be obtained by summation of the state of the particles. By providing the length scale of the domain scales concerned, a fully atomistic or molecular description of a macroscopic system remains beyond the capabilities of current computations. While the MD simulation of polymers benefits investigations of the configurations of very long polymer chains or meso-scale features. Another critical issue of MD modeling on polymeric systems is the long balance time, given the complexity of the very long polymer chains. In fact, it is necessary to employ an acceleration method to identify the possible metastable states that occur during molecular movements, and then to employ Monte Carlo methods to determine the next configuration, based on their probabilities [13,14]. Binder and Paul have provided a comprehensive review on the recent development of algorithms in the Monte Carlo sampling of polymer systems [15]. A coarse-grained particle-based simulation of polymer system can be adapted to illustrate the morphology of polymer blend in less detail [16–19]. Muller and Binder [19] showed that, when investigating the morphology of polymer blends, there is no need for a polymeric model containing details at the atomic level; rather, it is sufficient to use a coarse-grained model such as bond fluctuation on a lattice model [20–22]. Recently, Detcheverry *et al.* adapted the local density function normally used in a phase-field model to calculate the interaction energy in a Monte Carlo simulation of a coarse-grained polymer system [17]; however, the challenge remains to simulate the phase structure in a large domain.

The morphologic evolution of a polymer blends depend on the free energy of the system, which can be treated as a function of the local composition. The Cahn–Hilliard equation [23,24] can be used to describe the free energy of an inhomogeneous mixture, whereas for a polymer blend the local free energy is measured using the Flory–Huggins-type equation. In contrast to the VOF model, the domain interfaces in the Cahn–Hilliard model are represented by the composition gradient, while the thicknesses of the interfaces are influenced by the nature of the blend, which is more practical in the case of a polymeric blend system. Likewise, in many cases the morphology and influences of the interfaces are involved, rather than the microscopic configurations of the macromolecules.

In this chapter, attention will be focused on applications of the Cahn–Hilliard equation on the numerical simulation of an inhomogeneous polymer blend. The numerical model of a binary polymer system and a polymer–polymer–solvent system will be reviewed as examples to illustrate the application of such modeling methodologies. Attention will be paid in particular to a diffusion-controlled system with no mechanical flow, and the effects of substrate patterning will be taken into consideration to highlight the influences of external attraction during the phase separation of polymer blends. The results of the numerical simulation will then be verified using realistic experimental results, on a quantitative basis.

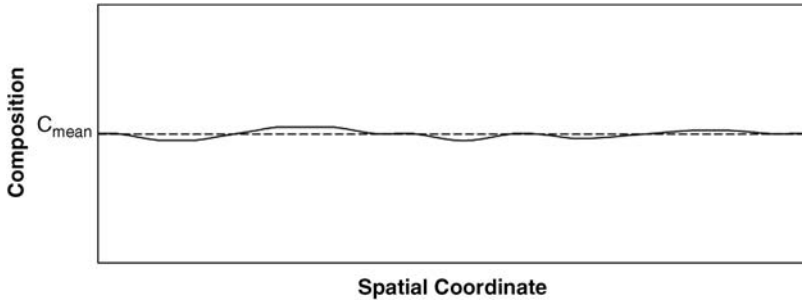


**Figure 15.2** The minimal fluctuation of composition in space.

### 15.1.2

#### Spinodal Decomposition

Due to the high enthalpy of mixing, different types of polymers are usually immiscible in a multiphase system. When the system is quenched in the spinodal region, phase separation will occur if small composition fluctuations exist in the mixture. A system with small fluctuation domains is usually referred to as being metastable, as shown in Figure 15.2. The spinodal decomposition actually represents the system in a very unstable state, and phase separation can be initiated without visible nucleation. In contrast, in a binodal decomposition, phase separation must be initiated with small domains with sharp composition changes, as shown in Figure 15.3. Phase separation initiated by major composition changes in the small domains is termed nucleation.

Mathematically, the condition for spinodal decomposition can be determined by the equation [25],

$$\frac{\partial^2 f}{\partial C^2} < 0 \quad (15.4)$$

where  $f$  is the mixing free energy of the system and  $C$  is the composition of one type of polymer in the mixture.

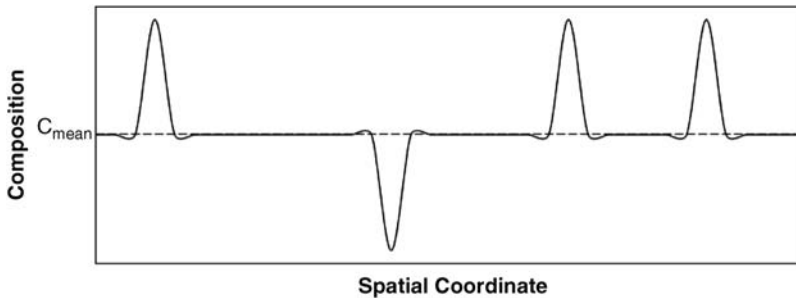


**Figure 15.3** The nucleation of an unstable phase.

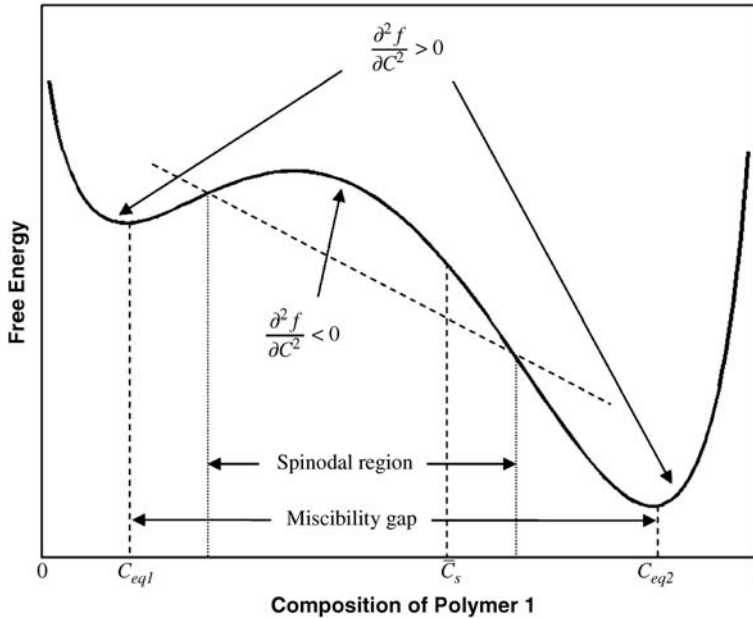


Figure 15.4 The free energy of a binary mixture.

The free energy profile of a binary system is plotted in Figure 15.4. In the spinodal region, the second derivative of the free energy with respect to the composition is negative. When considering an average composition of  $\bar{C}_s$  in the spinodal region, with arbitrarily small fluctuations in composition, it is clear that the free energy will decrease when one polymer is concentrated at the expense of the other. In the binodal region, when  $\frac{\partial^2 f}{\partial C^2} > 0$ , the free energy will increase as one type of polymer agglomerates from infinitesimal composition fluctuations. In order for the phase separation to be initialized in a binodal region, a sharp composition change should be present in the domain to lower the free energy. As shown in Figure 15.5,  $\bar{C}_b$  is an average composition in a binodal region, while  $C_l$  represents the composition that is significantly different to  $\bar{C}_b$ , with a smaller free energy level. Phase separation initiated by abrupt composition fluctuations in small domains in a binodal decomposition is termed nucleation.

The phase diagram of a typical binary immiscible system is shown in Figure 15.6, where the spinodal and binodal lines are depicted; these two lines can be calculated from the mixing free energy. The spinodal line of a binary system can be calculated from Eq. (15.4), whilst for a ternary system the spinodal line can be calculated from the mixing free energy from the equation as follows:

$$\frac{\partial^2 f}{\partial C_1^2} \frac{\partial^2 f}{\partial C_2^2} = \frac{\partial^2 f}{\partial C_1 \partial C_2} \quad (15.5)$$



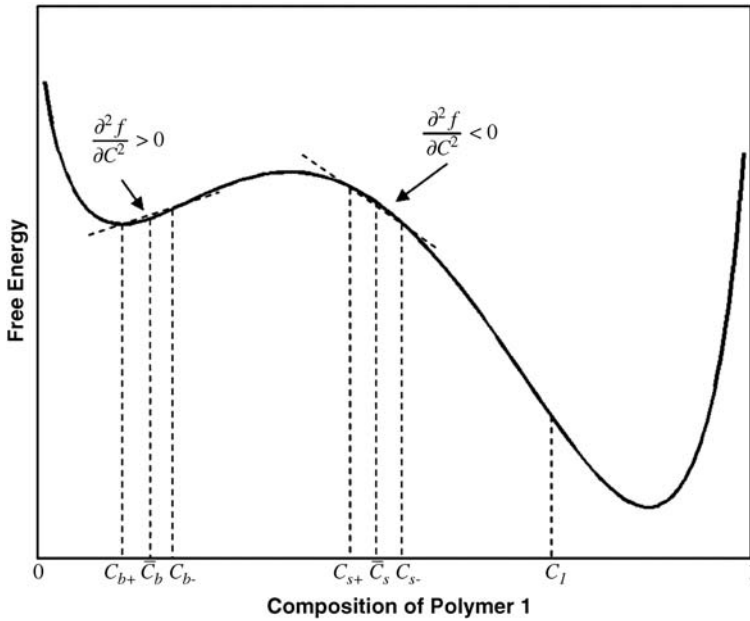


Figure 15.5 Spinodal decomposition and binodal decomposition.

where  $C_1$  and  $C_2$  represent the compositions of the two polymers. In a ternary system, it should be noted that  $C_1 + C_2 + C_3 = 1$ , where  $C_3$  is the composition of the third component which, in the present study, is the solvent.

In polymer blends, if two phases exist at equilibrium, the chemical potential of each component in the two phases should be the same. In a binary

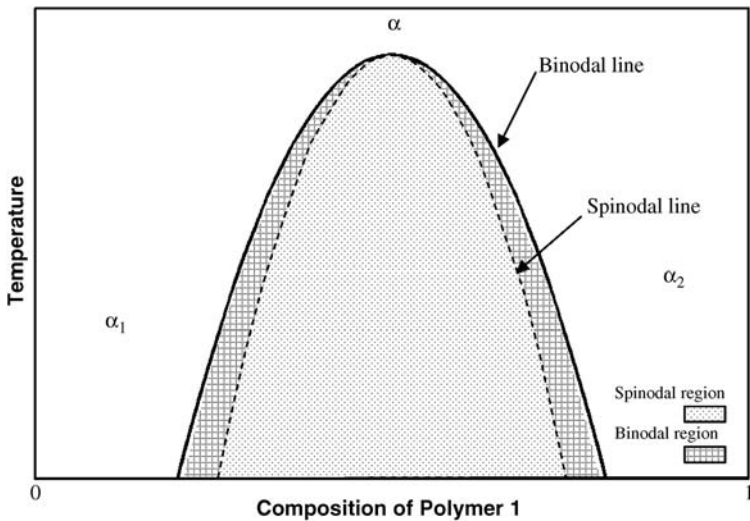


Figure 15.6 The phase diagram of a binary system.

system, the binodal line can be calculated simply based on the following condition:

$$\mu' = \mu'' \quad (15.6)$$

where  $\mu$  represents the chemical potential, and the prime and double primes represent the chemical potential in the two phases. In a ternary blend, the criteria can be represented as:

$$\begin{aligned} \mu'_1 &= \mu''_1 \\ \mu'_2 &= \mu''_2 \end{aligned} \quad (15.7)$$

where the subscripts 1 and 2 represent polymers 1 and 2. Calculation of the binodal line in a ternary system involves solving two nonlinear partial equations for four unknown variables. By applying the free energy equation into Eq. (15.7), these four variables are based on the compositions of three components. However, by applying the material conservation rule another unknown variable can be eliminated, and therefore this equation can, in theory, be solved (although in practice this is not very easy). A detailed discussion on the construction of ternary phase diagrams can be found elsewhere [26–30].

### 15.1.3

#### Cahn–Hilliard Equation

The free energy profile during the phase separation in a inhomogeneous mixture is described by the Cahn–Hilliard equation [23,24,31,32]:

$$F(C_1, C_2, C_3) = \int_V \left\{ f(C_1, C_2, C_3) + \sum_{i=1,2,3} [\kappa_i (\nabla C_i)^2] \right\} dV \quad (15.8)$$

where  $f$  is the local free energy density of homogeneous material,  $\phi_i$  is the lattice volume fraction of component  $i$ , and  $\kappa_i$  is the gradient energy coefficient for the component  $i$ . The total free energy of the system is composed by two items, as shown in Eq. (15.8). The first item is the local free energy, and the second item is the composition gradient contribution to the free energy.

The local free energy was presented with variety of mathematical models in different studies, such as the double-well model. A well Flory–Huggins equation can be adapted for a polymer blend; the ternary Flory–Huggins equation is as follows [33]:

$$f(C_1, C_2, C_3) = \frac{RT}{v_{site}} \left( \frac{C_1}{m_1} \ln C_1 + \frac{C_2}{m_2} \ln C_2 + C_3 \ln C_3 \right. \\ \left. + \chi_{12} C_1 C_2 + \chi_{13} C_1 C_3 + \chi_{23} C_2 C_3 \right) \quad (15.9)$$

where  $R$  is the ideal gas constant,  $T$  is the absolute temperature,  $v_{site}$  is the lattice site volume in the Flory–Huggins model,  $m_i$  is the degree of polymerization of component  $i$ , and  $C_i$  is the composition for the component  $i$ .

The Flory–Huggins-type of free energy is well known and has been studied extensively for polymer blends [34], although it was initially derived for small-molecular solutions. The primary drawback of the Flory–Huggins model for

polymer blends is that the macromolecules are assumed to be strings of small molecules, or even monomers, and each monomer occupies one lattice site. The entropy of the system is determined by the relative positions of the monomers. This clearly ignores the differences between the monomers in one polymer chain, and extra entropy from the connections of monomers within one macromolecule is therefore omitted in Flory–Huggins-type free energy. The effects of the entanglement are also ignored by this model. Nevertheless, Flory–Huggins-type free energy is selected, given the complexity of accurately measuring the local free energy, and the simplicity of numerical simulation within a reasonable computation time.

The gradient energy coefficient,  $\kappa$ , determines the influence of the composition gradient to the total free energy of the domain. The value of  $\kappa$  is difficult to measure experimentally. Although efforts have been made by Saxena and Caneba [35] to estimate the gradient energy coefficient in a ternary polymer system from experimental methods, few results have been reported for specific conditions. Initially, the value of  $\kappa$  can be estimated by the interaction distance between molecules [36]:

$$\kappa = \frac{RTa^2}{3v_{site}} \quad (15.10)$$

where  $a$  is the monomer size. A modified equation to calculate  $\kappa$ , taking into consideration the effects of the composition, has been reported by Gennes *et al.* [37]:

$$\kappa_i = \frac{RTa^2}{36v_{site}C_i} \quad (15.11)$$

where the subscript  $i$  represents component  $i$ .

The mobility is estimated from the diffusivity of the polymers. The mobility of polymer blends with long chains can be estimated by the equation as follows [37]:

$$M_i = \frac{C_i}{m_i} \frac{D_m N_e v_{site}}{RT} \quad (15.12)$$

where  $m_i$  is the degree of polymerization as stated before,  $D_m$  is the diffusivity of the monomer, and  $N_e$  is the effective number of monomers per entanglement length. Because of the scarce experimental data for  $N_e$ , a more generalized form was employed for the present study:

$$M = \frac{Dv_{site}}{RT} \quad (15.13)$$

#### 15.1.4

##### Numerical Method

According to Eq. (15.8), the time evolution of the local composition can be derived as:

$$\begin{aligned} \frac{\partial C_i}{\partial t} = & M_{ii} \nabla^2 \left[ \frac{\partial f}{\partial C_i} - \frac{\partial f}{\partial C_3} - 2\kappa_{ii} \nabla^2 C_i - 2\kappa_{ij} \nabla^2 C_j \right] \\ & + M_{ij} \nabla^2 \left[ \frac{\partial f}{\partial C_j} - \frac{\partial f}{\partial C_3} - 2\kappa_{ji} \nabla^2 C_i - 2\kappa_{jj} \nabla^2 C_j \right] \end{aligned} \quad (15.14)$$

where the subscripts  $i$  and  $j$  represent components 1 and 2, and

$$\begin{aligned} M_{ii} &= (1 - \langle C_i \rangle)^2 M_i + \langle C_i \rangle^2 \sum_{j \neq i} M_j \quad i = 1, 2; j = 1, 2, 3 \\ M_{ij} &= - \sum_{i \neq j} [(1 - \langle C_i \rangle) \langle C_j \rangle] M_i + \langle C_1 \rangle \langle C_2 \rangle M_3 \quad i = 1, 2; j = 1, 2 \end{aligned} \quad (15.15)$$

where  $\langle C_i \rangle$  is the average composition of component  $i$ . To simplify the derived equation, Eq. (15.14),  $\kappa_{ii} = \kappa_i + \kappa_3$ , and  $\kappa_{12} = \kappa_{21} = \kappa_3$ , where  $\kappa_i$  is the gradient energy coefficient. These equations provide a system of nonlinear fourth-order parabolic partial differential equations, and are difficult to solve with ordinary numerical methods. When using an ordinary finite difference method, the time step must be very small to obtain a stable result, and therefore the computation time will be extremely long before a significant real-time length can be achieved. Consequently, the spectral method was employed in the present study to solve the partial differential equation. The spectral method, using fast Fourier transform or discrete cosine transform are widely employed to solve the Cahn–Hilliard equation [38–40]. Spectral methods are viewed as a major development among weighted residuals discretization methods [41], the key elements of which are the trial functions, which approximate the target function. The trial functions often take the form of truncated serial expansions of the original function. The details of numerical treatments for different systems are introduced in Sections 15.2.2 and 15.3.3.

## 15.2

### Numerical Simulation of Phase Separation of Immiscible Polymer Blends on a Heterogeneously Functionalized Substrate

When investigating a binary polymer blend system, if the polymer mixture is quenched into an immiscible state then the stable blend will separate into A-rich and B-rich domains, and coarsen with time. In the present study, the system was assumed to be diffusion-controlled and there was no predominant dynamic mass flow. Rather, the composition profile was determined by the free energy minimization, as stated above.

In the aforementioned free energy model of polymer blends, the local free energy is a function of the composition and the temperature. The free energy penalty for the composition gradient is a function of the composition, the temperature, and the gradient of the composition. Other effects such as external pressure, temperature variations and contacting substrate may also be taken into consideration in specific systems. In this example, a functionalized substrate surface with different attraction forces to the two types of polymer is applied to one side of the polymer blend, while the other side is kept as a free surface. The surface energy is specified as a function of the coordinates and added to the total free energy to represent the contribution by the functionalized substrate. In practice, the application of a functionalized substrate is used to control the topology of the phase separation towards an ordered structure.

Polymers demonstrate viscoelastic properties in different states, and therefore on certain occasions it may be necessary for the numerical model to involve elastic energy during phase separation. In this example, the numerical simulation is carried out with and without this part of free energy. The elastic energy of the domain can be added to the total free energy in the model. In summary, both 2D and 3D numerical models are introduced to investigate template-directed polymer self-assembly with a binary polymer blend.

### 15.2.1

#### Fundamentals

According to Cahn [24,31], the mass flux,  $J$ , in the mixture can be denoted as:

$$J = -M \cdot \nabla \mu \quad (15.16)$$

where  $M$  is mobility and  $\mu$  is the chemical potential of the polymer blends. In order to determine the chemical potential, the expression of the total free energy must be determined. According to Cahn and Hilliard [23], the free energy,  $F$ , of a binary system can be written as:

$$F(C) = \int_V \{f + f_e + \kappa(\nabla C)^2\} dV \quad (15.17)$$

where  $C$  is the mole fraction of one polymer component,  $f$  is the local free-energy density of the homogeneous material,  $f_e$  is the elastic energy density, and  $\kappa$  is the gradient energy coefficient. Thus, the item  $\kappa(\nabla C)^2$  is the additional free energy density if the material is in a composition gradient. Consecutively, the chemical potential  $\mu$  is:

$$\mu = \frac{\partial f}{\partial C} + \frac{\partial f_e}{\partial C} - 2\kappa \nabla^2 C \quad (15.18)$$

The mobility of the diffusion model is non-negative and evaluated as a positive constant in this study. By substituting the chemical potential expression into the equation for the mass flux, the evolution of the composition can be written as the function of local composition:

$$\frac{dC}{dt} = \nabla^2 \cdot \left[ M \left( \frac{\partial f}{\partial C} + \frac{\partial f_e}{\partial C} - \kappa \nabla^2 C \right) \right] \quad (15.19)$$

The free energy variation on the heterogeneously functionalized substrate is simulated by a free energy term,  $f_s$ , which is also a function of the composition and the coordinates,  $\mathbf{r}$ . The surface free energy is added to the total free energy on the surface of the substrate:

$$F(C) = \int_V \{f + f_e + \kappa(\nabla C)^2\} dV + \int_S f_s(C, \mathbf{r}) dS \quad (15.20)$$

The term represents the thermal noise in the phase separation, and may be added to the free energy, as indicated in the studies of Shou and Chakrabarti [42].

However, in this study the thermal fluctuations are neglected as they are negligible for quenches far away from the critical points and/or spinodal lines [43,44].

The Flory–Huggins-type free energy is used as the bulk free energy density [33]. A binary Flory–Huggins free energy reads as follows:

$$f = \frac{RT}{v_{site}} \left( \frac{C_A}{m_A} \ln C_A + \frac{C_B}{m_B} \ln C_B + \chi_{AB} C_A C_B \right) \quad (15.21)$$

where  $C_i$  is the volume fraction of component  $i$ ,  $m_i$  is the degree of polymerization of component  $i$ ,  $T$  is the temperature (in K),  $R$  is the ideal gas constant,  $\chi_{AB}$  is the Flory–Huggins interaction parameter between the two components (which is dependent on temperature), and  $v_{site}$  is the molar volume of the reference site in the Flory–Huggins lattice model.

The elasticity is assumed isotropic in the domain. According to Vegard's law [45], the stress-free strain is isotropic and depends linearly on the composition:

$$e_{ij}^0 = \eta(C - C_0)\delta_{ij} \quad (15.22)$$

where  $e_{ij}^0$  is the stress-free strain,  $C_0$  is the average composition of the domain,  $\delta_{ij}$  is the Kronecker delta function, and  $\eta$  is the compositional expansion coefficient which is expected to be independent of the composition and the composition gradient [46].

According to the linear elasticity, the stress,  $\sigma_{ij}$  is linear with the change of the strain by Hook's law:

$$\sigma_{ij} = c_{ijkl}(e_{kl} - e_{kl}^0) \quad (15.23)$$

where  $c_{ijkl}$  represents the isothermal elastic tensor, which is independent of both position and composition. The elastic energy then can be expressed as follows, with no external anisotropic elastic applied:

$$f_e = \frac{1}{2} c_{ijkl} (e_{ij} - e_{ij}^0)(e_{kl} - e_{kl}^0) \quad (15.24)$$

The total strain can be evaluated by the local displacement,  $\mathbf{u}$  [47].

$$e_{ij} = \frac{1}{2} \left( \frac{\partial u_i}{\partial r_j} + \frac{\partial u_j}{\partial r_i} \right) \quad (15.25)$$

The displacement of the reference lattice is then solved by the elastic equilibrium. Given the fast relaxation time compared to the rate of morphology evolution, it can be assumed that the system is in elastic equilibrium [48]:

$$\frac{\partial \sigma_{ij}}{\partial r_j} = 0 \quad (15.26)$$

### 15.2.2

#### Numerical Method

The Cahn–Hilliard equation is known for its difficulty in solving due to its non-linearity and the biharmonic term. The cosine transform method is applied to the

spatial discretization:

$$\frac{d\hat{C}}{dt} = M\lambda \left( \left\{ \frac{\partial f}{\partial C} + \frac{\partial f_e}{\partial C} \right\} - \kappa\lambda\hat{C} \right) \quad (15.27)$$

where  $\hat{C}$  and  $\left\{ \frac{\partial f}{\partial C} + \frac{\partial f_e}{\partial C} \right\}$  represent the Fourier transform of the composition and the summation of the first derivation of bulk free energy density and surface free energy both with the respect of the composition.  $\lambda$  is the approximation of discrete Laplacian operator in the transform space [49]:

$$\lambda(\mathbf{k}) = \frac{2 \sum_i \cos(2\pi k_i) - \sum_i 2}{(\Delta x)^2} \quad (15.28)$$

Here, the vector  $\mathbf{k}$  denotes the discretized spatial element position in all dimensions. Numerically,  $k_i = n_i/N_i$ , where  $n_i$  is the element in the  $i$ th dimension and  $N_i$  represents the number of elements in the  $i$ th dimension.  $\Delta x$  is the spatial step in the numerical modeling.

By this means, the partial differential equation is transferred into an ordinary differential equation in the discrete cosine space. A semi-implicit method is used to trade-off the stability, computing time, and accuracy [39,40]. In order to remove the shortcomings with the small time-step size associated with the explicit Euler scheme to achieve convergence, the linear fourth-order operators can be treated implicitly while the nonlinear terms can be treated explicitly. The resulting first-order semi-implicit Fourier scheme is:

$$(1 + M\Delta t\kappa\lambda)\hat{C}^{n+1} = \hat{C}^n - M\Delta t\lambda \left\{ \frac{\Delta f(C^n)}{\Delta C} + \frac{\Delta f_e(C^n)}{\Delta C} \right\} \quad (15.29)$$

A second-order Adams–Bashforth method [50] was also used for the explicit treatment of the nonlinear term (the sum of the bulk free energy density and template surface free energy differentials). The equation can be discretized into the form,

$$(3 + 2M\Delta t\kappa\lambda^2)\hat{C}^{n+1} = 4\hat{C}^n - \hat{C}^{n-1} + 2M\Delta t\lambda \left( 2 \left\{ \frac{\partial f(C^n)}{\partial C} + \frac{\partial f_e(C^n)}{\partial C} \right\} - \left\{ \frac{\partial f(C^{n-1})}{\partial C} + \frac{\partial f_e(C^{n-1})}{\partial C} \right\} \right) \quad (15.30)$$

When the initial condition and the time length are selected, the composition profile of the domain for the second time step can be calculated with Eq. (15.29). Subsequently, the third and following time steps can be calculated with Eq. (15.30).

For simplicity and generality, the equations are dimensionalized. The scaling dimensions and time are chosen as follows:

$$\bar{L}^2 = \frac{\kappa v_{site}}{RT} \quad (15.31)$$

$$\bar{t} = \frac{\bar{L}^2 v_{site}}{M_C RT} \quad (15.32)$$

**Table 15.1** Characteristic terms for nondimensionalization.

Characteristic length	$\bar{L}^2 = \frac{\kappa v_{site}}{RT}$
Characteristic time	$\bar{t} = \frac{\bar{L}^2 v_{site}}{M_c RT}$
Characteristic free energy	$\bar{f} = \frac{RT}{v_{site}} f$
Characteristic gradient energy coefficient	$\bar{\kappa} = \frac{RT \bar{L}^2}{v_{site}}$
Characteristic mobility	$\bar{M} = \frac{M_c}{\bar{L}^2}$

The other parameters are treated accordingly. The factors for nondimensionalization are listed in Table 15.1.

### 15.2.3

#### Implementation

Another difficulty in the numerical simulation of polymer systems is the measurement of parameter values. Whilst such values may be readily available for small-molecule materials, the monomers and functional groups exhibit different properties in polymers, not to mention the differences in polymerization and polydispersity. The parameters are thus selected in a flexible and practical manner, according to the corresponding experiment conditions and the literature. The temperature is 363 K (90 °C), the degree of polymerization of polymers A and B are 447 and 915, respectively, and the interaction parameter,  $\chi_{AB}$ , in the Flory–Huggins-type free energy is evaluated by an empirical function of the temperature as follows:

$$\chi_{AB} = -a + \frac{b}{T} \quad (15.33)$$

where  $a$  and  $b$  are constants which are independent of temperature, with  $a$  equal to 0.032 and  $b$  equal to 48.2 according to Kressler *et al.* [51]. In order for the phase separation to occur, the critical value of the interaction parameter can be calculated from the degree of polymerization of the polymers:

$$\chi_c = \frac{1}{2} \left( \frac{1}{\sqrt{m_A}} + \frac{1}{\sqrt{m_B}} \right)^2 = 0.00323 \quad (15.34)$$

The gradient energy coefficient,  $\kappa$ , is selected as 6.9e-11 J m<sup>-1</sup> [52] for a generic polymer material, while the diffusivity,  $D = 1\text{e-}20 \text{ m}^2 \text{ s}^{-1}$ , is chosen as a typical value for polymers. The mobility of the system can then be evaluated, using the relationship [53]:

$$M = \frac{D v_{site}}{RT} \quad (15.35)$$



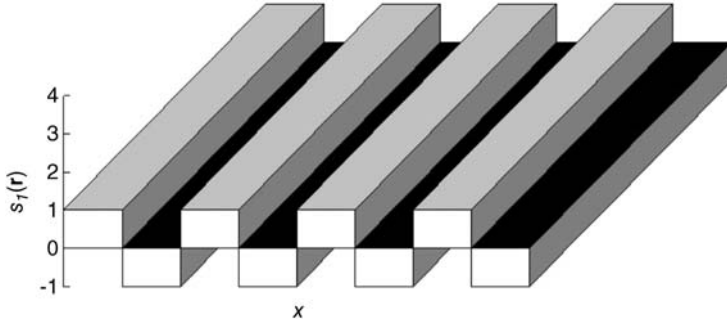


Figure 15.7 The spatial variation of surface free energy factor.

where  $D$  is the diffusivity, and  $v_{site}$  is usually chosen as the molar volume of water,  $1.8 \times 10^{-3} \text{ m}^3 \text{ mol}^{-1}$ ; thus,  $M = 5.98 \times 10^{-29} \text{ (J} \cdot \text{s)}^{-1}$ . In the simulation, the nondimensionalized mobility is 1.

In the elastic model, the reference composition is chosen according to the initial condition. The compositional expansion coefficient is chosen as  $\eta = 0.02$  [21].

The attraction force of the surface to the polymer is a short-range force which can only affect the domain near the substrate surface. The surface energy is linear to the local composition [54]:

$$f_s(C, \mathbf{r}) = s_0(\mathbf{r}) + s_1(\mathbf{r})(C - C_{ref}) \quad (15.36)$$

where  $s_0(\mathbf{r})$  and  $s_1(\mathbf{r})$  are surface attraction parameters that represent the functionalization of the substrate, and  $C_{ref}$  is the reference composition. For nondimensionalization,  $C_{ref}$  and  $s_0(\mathbf{r})$  are chosen to be 0. For example, as can be seen in Figure 15.7, the functionalized substrate energy factor  $s_1(\mathbf{r})$  is alternating across the  $x$  direction of the substrate in an effort to develop a corresponding alternating strip pattern in the self-assembling polymer near the substrate.

#### 15.2.4

#### Results and Discussion

To ensure that phase separation is induced spontaneously, the second derivative of the local free energy with respect to the composition should be negative [55]:

$$\frac{\partial^2 f}{\partial C^2} < 0 \quad (15.37)$$

To meet this requirement, the shape of the free energy must be tuned by temperature to quench the mixture into a miscibility gap. A process of phase separation initiated from a random composition distribution is shown in Figure 15.8. The effect of the functionalized substrate attraction is excluded; however, it can be seen that in the case without consideration of the elastic energy, the patterns evolve rapidly during the early stages of the phase separation, while the gradient in the interface of the two phases increases very quickly.

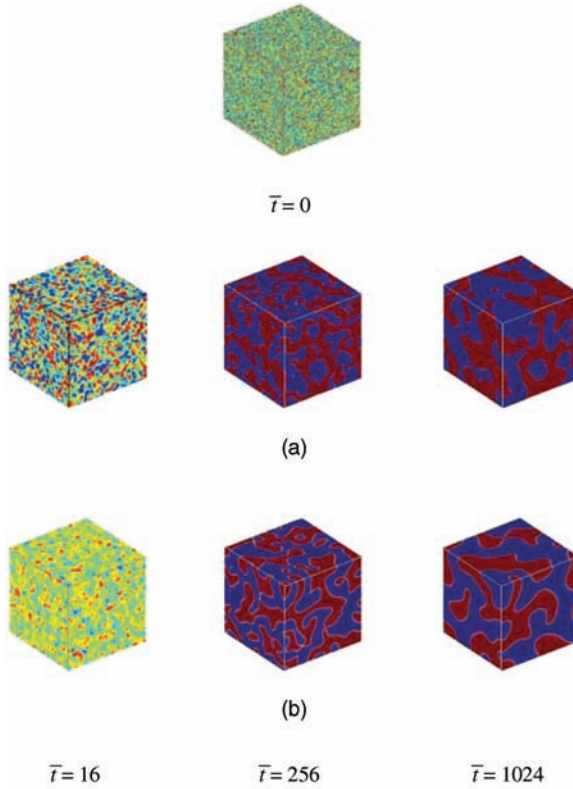


**Figure 15.8** Evolution of phase separation in a  $128 \times 128 \times 128$  three-dimensional domain without a patterned substrate. (a) Without elastic energy; (b) With isotropic elastic energy.

The situation when considering isotropic elastic energy initiates at a slower pace, with the slower rate of evolution being due to an elastic energy term increase when the local composition differs from the average value of the whole domain. The rapid change in local composition during the early stage exaggerates the effects of the elastic energy and thus slows down the decomposition. When the system nears a steady state the change in local composition slows, the impact of the isotropic elastic energy is hardly distinguishable, and a much longer time is required to observe any significant changes in the pattern.

In order to achieve an optimal polymer self-assembly replicating the pre-designed substrate, the characteristic length of the domain,  $R(t)$ , should match the pattern strip length,  $l_p$ . The characteristic length is then measured with respect to time. In numerical modeling the domain growth is studied by evaluating the pair-correlation functions  $g_i$ , where the subscripts  $i$  and  $j$  represent the directions in the domain [25].

$$g_i(d, t) = \frac{1}{N_j} \sum_{k_j=1}^{N_j} g_{i,k_j}(d, t) \quad (15.38)$$

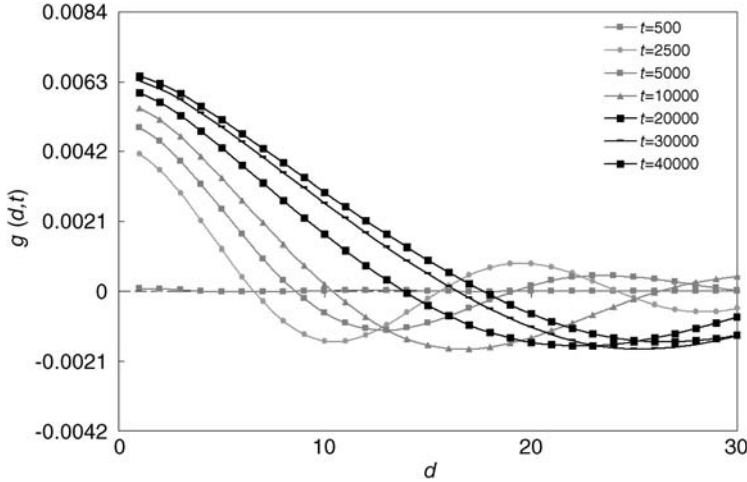


**Figure 15.9** Evaluation of the pair-correlation function  $g_i(d, t)$  in a 2D phase separation model without elastic energy.

where  $g_{i,ki}$  is defined as

$$g_{i,k_j}(d, t) = \langle \psi(\mathbf{k} = (k_i, k_j), t) \psi(\mathbf{k} = (k_i, k_j + d), t) \rangle \quad (15.39)$$

where  $\psi$  is the order parameter which equals the composition difference of the two polymers in the element  $\mathbf{k}$ , and  $d$  is a positive variable and varies from 1 to  $k_i$ . The angle brackets denote the average value of the expression inside the brackets over all the lattice points. The characteristic length in the  $i$ th dimension,  $R_i(t)$ , is the first zero value of  $g_i(d, t)$ .

The interface of the polymer and the patterned substrate is the focus of this study. For improved model fidelity, the characteristic length is measured using a 2D model of  $128 \times 128$  elements instead of a 3D model. Phase separation takes place on a neutral substrate, and the effect of the elastic field is included. In theory, when spinodal decomposition has occurred in the binary polymer mixture the average characteristic lengths are the same in all directions.  $R(t)$  is measured in both  $x$  and  $y$  directions, and the average value is recorded. The values of  $g_i(d, t)$  without and with elastic energy are shown in Figures 15.9 and 15.10, respectively. It has been established previously that  $R(t)$  increases proportionally to  $t^{1/3}$  [56–58]. In the present study, the value of  $g_i(d, t)$  was plotted with  $t^{1/3}$  to observe this relationship. It can be seen from Figures 15.9 and 15.10 that the first zero values of the pair-correlation function increased with time;  $R(t)$  was then determined with first-order interpolation between the two points when the sign of the pair-correlation function changed, as can be seen in Figure 15.11.

In the double logarithmic plot in Figure 15.11, the  $R(t)$  value without elastic energy can be fitted in a straight line in the double logarithmic diagram with the  $x$ -axis set to be  $t$ . The  $R(t)$  value of the system with the consideration of isotropic energy effects takes longer to become stable than the system without elasticity

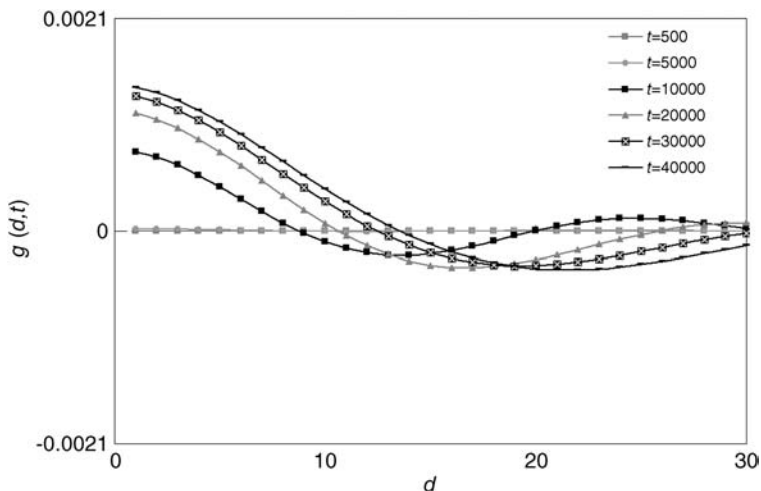


**Figure 15.10** Evaluation of the pair-correlation function  $g_i(d, t)$  in a 2D phase separation model with elastic energy.

effects, as can be seen in Figure 15.2. In the stable stage of an isotropic elastic system, the  $R(t)$ -value can also be fitted with a straight line in the double logarithmic diagram with respect to  $t$ . The fitting lines are in the form of  $\gamma = a + bx^n$ , where  $a$  and  $b$  are constants ( $a$  is equal to 0 in both cases). The exponents are 0.3567 and 0.3223, and  $b$  is equal to 0.4026 and 0.4480 for the nonelastic and elastic cases, respectively. These values are compatible with the observation that  $R(t)$  is proportional to  $t^{1/3}$  [25,28,29]. From the data in Figure 15.11 it can be seen

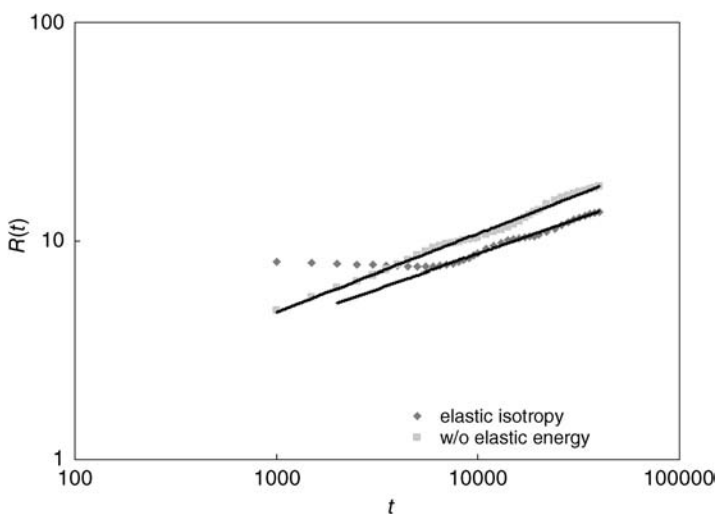


**Figure 15.11** The relationship between the characteristic length,  $R(t)$ , and time,  $t$ .

that  $R(t)$  increases faster in the case without elastic energy. The difference in the evolution rate of the two cases was also due to the elastic free energy term added to the local free energy, which slowed minimization of the free energy.

Clearly, the numerical simulation method has the major advantage that the results can be assessed quantitatively. Generally, the pattern of spinodal decomposition tends to replicate the pattern in the substrate with increasing time. Hence, in order to optimize the final pattern according to the substrate the characteristic length should be compatible with the pattern scale. The similarity of the final pattern to the pattern on the substrate is measured with respect to time. The compatibility of the final pattern with the patterns designed on the substrate can be measured by a factor,  $C_S$ :

$$C_S = \frac{1}{2} \langle |\psi(\mathbf{k}) - S_k| \rangle \quad (15.40)$$

where

$$S_k = \begin{cases} \frac{s_1(\mathbf{k})}{|s_1(\mathbf{k})|}, & s_1(\mathbf{k}) \neq 0, \\ 0, & s_1(\mathbf{k}) = 0 \end{cases} \quad (15.41)$$

and where  $s_1(\mathbf{k})$  is the parameter in the surface energy, which denotes the strength of the surface functionalization, and can be varied across the substrate surface.  $S_k$  is the qualitative representation of the substrate attraction. Clearly,

$$C_S \in [0, 1] \quad (15.42)$$

Hence, the greater the value of  $C_S$  the more compatible the resulting polymer morphology is to the functionalized substrate. If  $C_S$  is equal to 1, the resulting pattern absolutely replicates the substrate pattern, whereas if  $C_S$  is equal to 0 the random distribution of the phase separation is close to the substrate pattern. Phase separation can be simulated numerically in a  $128 \times 128$  elements 2D model on a heterogeneously functionalized substrate. The change in shape of the  $g(d, t)$  with time is depicted in Figures 15.12 and 15.13 (Figure 15.15 shows the  $R(t)$ -value across the direction perpendicular to the strips patterns on the substrate). It can be seen that, with the existence of functionalization on the substrate, the characteristic length,  $R(t)$ , in the  $x$  direction increases quickly in the early stage but slows beyond a critical value that is related to the dimension of the pattern strips. The system with isotropic elastic energy has smaller evolution rates but an earlier critical time than the phase separation without elastic energy; this effect is due to the longer initial time in the case without elastic energy, which can be seen in Figure 15.14. The  $x$ -axis is logarithmic according to  $t^{1/3}$  in Figures 15.14 and 15.15. When evolution has been initiated the characteristic length can be fitted into straight lines before and after the critical time, both in situations with and without elastic energy. The slope of the fitting line was decreased from 0.947 to 0.045 for the case without elastic energy, and from 0.491 to 0.046 for the case with elastic energy.

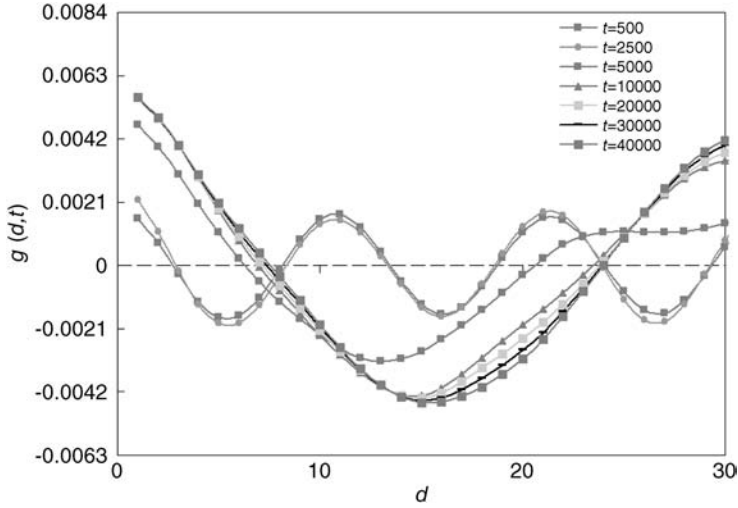


**Figure 15.12** Evaluation of the pair-correlation function  $g_i(d, t)$  in a 2D phase separation model without elastic energy on a heterogeneously functionalized substrate.

In Figure 15.15 the compatibility factor,  $C_S$  is also plotted with  $t^{1/3}$ . There is also a critical time during evolution of the compatibility factors; for example, the critical time for  $C_S$  was empirically identical to that of  $R(t)$  in Figure 15.15. The compatibility of the phase separation pattern with the substrate increased quickly before the critical time and became stable afterwards. The existence of a critical time in the evolution of the characteristic time and compatibility was due to an

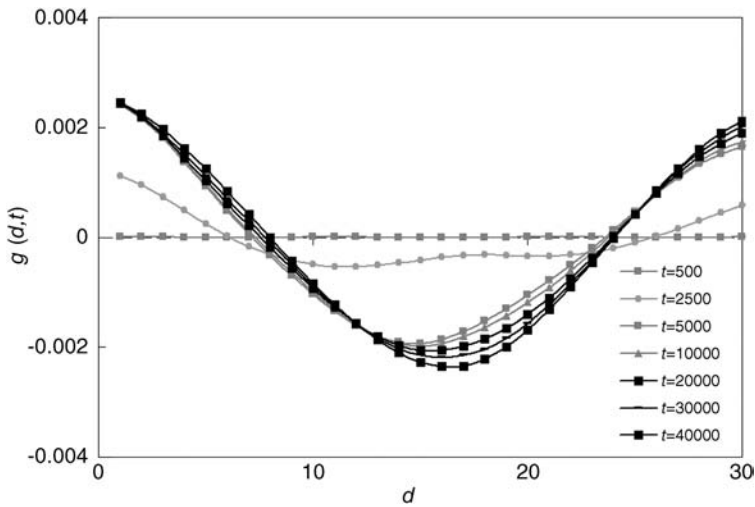


**Figure 15.13** Evaluation of the pair-correlation function  $g_i(d, t)$  in a 2D phase separation model with elastic energy on a heterogeneously functionalized substrate.

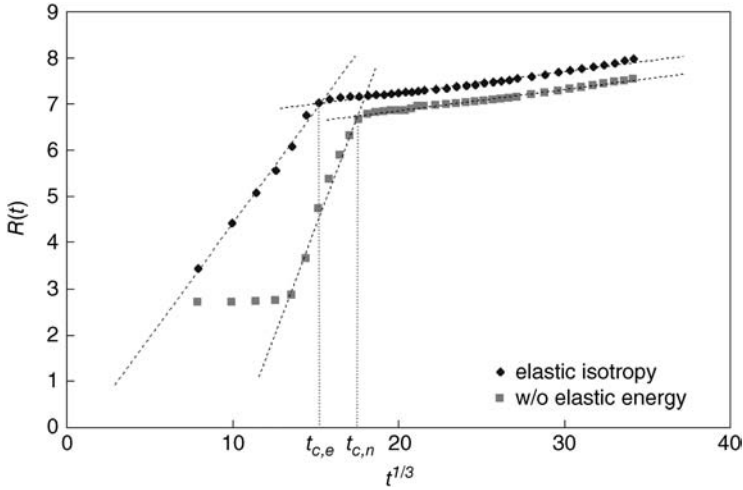


**Figure 15.14** The characteristic length in  $x$  direction (the direction perpendicular to the strips in the pattern).

effect of the pattern strips, whereby those strips in the  $x$  direction redefined the characteristic length other than the intrinsic value of the spinodal decomposition. However, when the resulting pattern from the phase separation covered the functionalized substrate as designed in general, the system reached its critical time, after which  $R(t)$  and  $C_S$  were both increased at a much slower pace. In practice, these results implied that the optimized annealing time should be close to the critical time, although a longer annealing time would not provide any significant help in refining the final pattern.

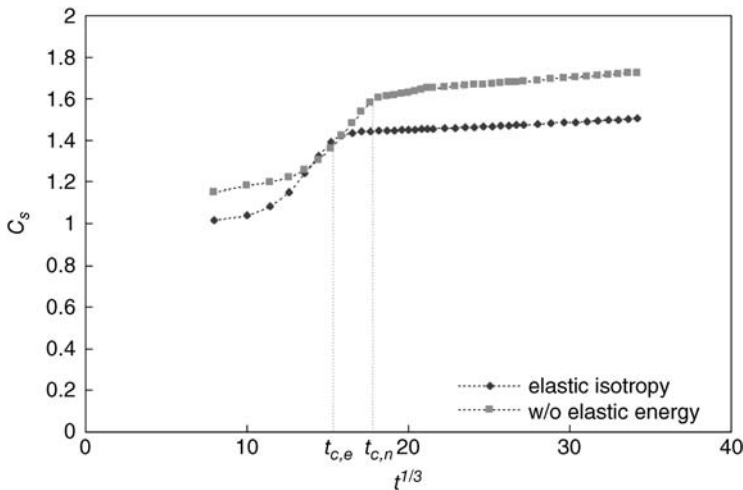


**Figure 15.15** The characteristic length in  $x$  direction (the direction perpendicular to the strips in the pattern).

It can be seen that the curve in the semi-logarithmic plot of  $C_S$  corresponds to that in the semi-logarithmic plot of  $R(t)$  for the phase separation patterns on a functionalized substrate. The critical time to enter the stable state, as shown in Figure 15.12, was almost the same as the critical time shown in Figure 15.11. The increase in  $C_S$  with respect to time after  $t_c$  can be fitted by a straight line in a semi-logarithmic axis; the slope of the fitting line was approximately 0.05. The trend shown in Figures 15.13 and 15.12 implied that the resultant pattern could be greatly refined according to the substrate by increasing the time. However, annealing for a time in excess of  $t_c$  would provide little help in optimizing the resultant pattern.

The lateral composition profile of phase decomposition with a patterned substrate can be observed in a 3D model, with a checkerboard structure being observed in the early stage of phase separation [59,60]. This effect was due to the alternating attraction factor,  $s_1(\mathbf{r})$ , on the strips, whereby the polymer close to the substrate was attracted and attached to the respective area on the substrate, while the neighboring region in the domain to the depth direction was concentrated on the other type of polymer. This effect was seen to start from the interface with the substrate and to decay through the thickness direction to the domain. As the spinodal decomposition developed in the bulk domain, the random phase separation would overcome the checkerboard effect. The attraction force on the substrate must be strong enough to sustain the effect from the bulk domain. The influence of the attraction factor is currently under investigation.

Spinodal decomposition with a heterogeneously functionalized pattern is shown in Figure 15.16 (though the initial state is the same as shown in Figure 15.8),

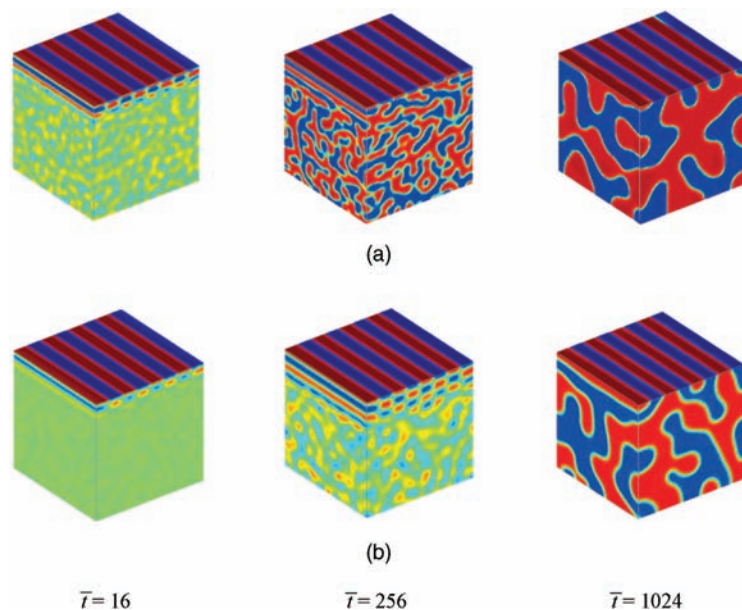


**Figure 15.16** Effect of heterogeneously functionalized pattern on phase decomposition. (a) Without elastic energy; (b) With isotropic elastic energy.



where the checkerboard structure in the lateral direction is seen to decay faster in the case without elastic energy. The impact of the substrate functionalization cannot propagate into the depth of the polymer blends; however, as the attraction force applies only to the substrate surface the checkerboard structure in the domain will be replaced by a bicontinuous structure.

The lateral composition profile with the patterned substrate can be investigated using the function,

$$h(z) = \frac{1}{k_1 k_2} \sum_{k_1} \sum_{k_2} \psi(\mathbf{k}) \cdot S_k \Big|_z \quad (15.43)$$

which represents the average order parameter  $\psi$  on the plane  $k_3 = z$ . In addition,  $k_1, k_2$ , and  $k_3$  represent the elements in the first, second, and third directions, respectively, with  $k_3$  in the direction perpendicular to the substrate. Changes in  $h(z)$  with time are shown in Figure 15.17. Clearly, the strength of the composition wave can be seen to decrease from the substrate surface in the depth direction, while the involvement of elastic energy retards the decomposition process in a lateral direction. The composition wave from the substrate propagates more slowly in the case that includes the isotropic elastic energy, due to the decreased driving force that was previously noted by Cahn [31]. The composition waves shown in Figure 15.17 cannot be observed in the phase separation with a substrate that is neutral to both polymers.

#### 15.2.5

##### Summary

Examples of 2D and 3D numerical simulations have been developed for the phase separation of a binary immiscible polymer blend. When the effects of isotropic elastic energy were investigated it was observed that, during the spinodal decomposition process, the characteristic length,  $R(t)$ , was proportional to  $t^{1/3}$ , and the involvement of an isotropic elastic energy resulted in a smaller slope in the  $R(t) \sim t^{1/3}$  diagram. The introduction of a patterned substrate with regular strips induced a critical time in  $R(t)$  in the direction perpendicular to the strips, and compatibility between the resultant pattern and the substrate pattern,  $C_S$ . The strips confined the increase in  $R(t)$  in a direction perpendicular to the strips. Although there remained a linear relationship between  $R(t)$  and  $t^{1/3}$  when the system had reached a critical time, the slope of the  $R(t) \sim t^{1/3}$  diagram was seen to decrease in the second stage.

The composition profile in depth direction was investigated using a 3D model, whereby a checkerboard structure was observed in the early stages of decomposition, but this decayed as the intrinsic value of  $R(t)$  in the bulk domain increased. The strip patterns were confined to the surface domain in the later stages of phase decomposition. A consideration of the isotropic elastic energy also caused a slower evolution in the depth direction.

The impact of these parameters will be investigated in future research, while the influences of the attraction force, composition, substrate pattern geography and

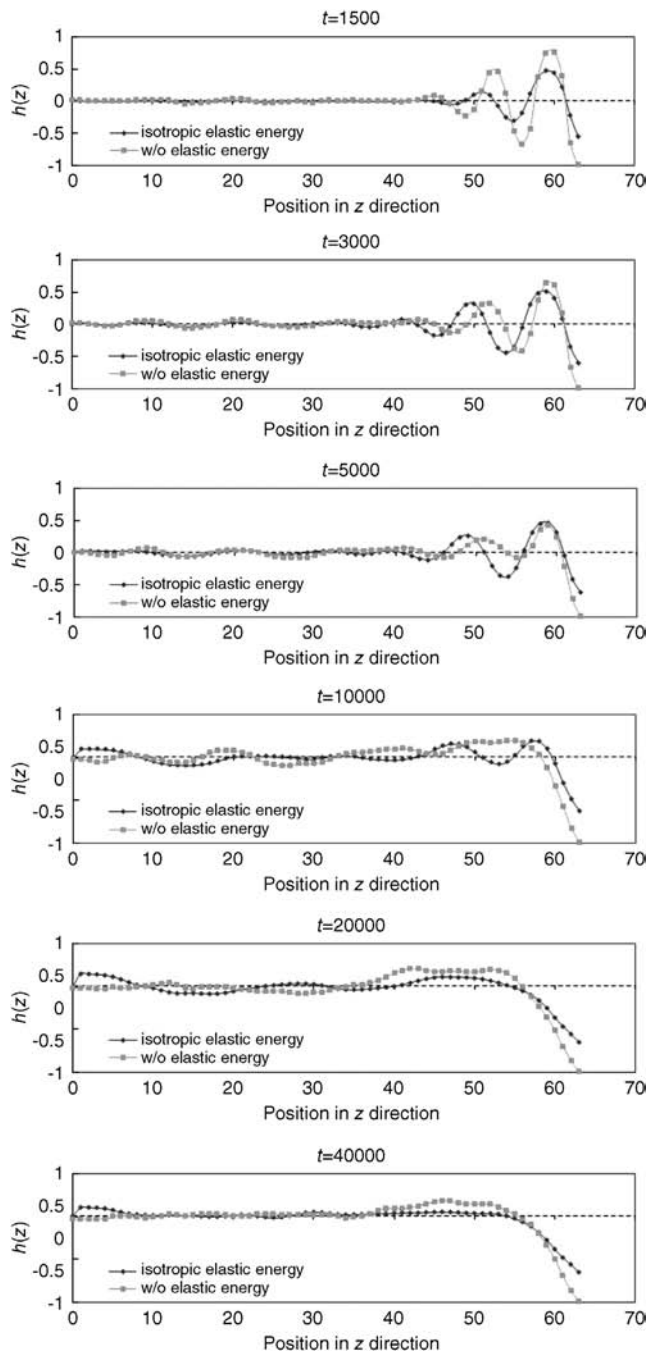


**Figure 15.17** Evolution of composition profile in the lateral direction with a patterned substrate.

other factors will be examined using numerical modeling. The numerical simulation will also be compared with experimental results to seek validation. A new polymer–polymer–solvent ternary model is also under development.

### 15.3

#### Numerical Simulation of the Self-Assembly of a Polymer–Polymer–Solvent Ternary System on a Heterogeneously Functionalized Substrate

##### 15.3.1

##### Introduction

In the past, polymer-based ternary systems have been the subjects of extensive study, with both Scott [29] and Hsu *et al.* [30] investigating the thermodynamic fundamentals of a polymer-based ternary system with Flory–Huggins-type free energy, as well as providing a method to calculate the binodal curve in ternary blends. A generalized numerical simulation for ternary phase separation was described by Chen [61], while Huang *et al.* established a numerical model for a polymer–polymer–solvent ternary system based on Flory–Huggins-type free energy and nonlinear diffusion equations [43]. Likewise, when He and Nauman investigated the influences of polymer chain length on phase separation, it was noted that the long chains of polymers would destabilize the blends and increase the quench depth [62]. Subsequently, numerical polymer–nonsolvent–solvent systems were established and studied by Altena *et al.* [63] and Zhou *et al.* [64], while Tong *et al.* developed a numerical model of a ternary phase separation with the consideration of chemical reaction dynamics [65].

In the following sections a polymer–polymer–solvent blend phase separation is investigated, with the respect to self-assembly on a heterogeneously functionalized substrate. The evolutionary mechanisms were studied by measuring the characteristic length, and the influence of different compositions was examined. The effects of a heterogeneously functionalized substrate were studied, and a discrete cosine transform spectral method was employed to solve the nonlinear partial differential equation. A semi-implicit method was used in the time evolution; this method was found to be efficient and unconditionally stable over large time steps [40] (see Section 15.1.4).

##### 15.3.2

##### Thermodynamics

During the process of phase separation in a mixture, the evolution of composition can be described by a continuity equation:

$$\frac{\partial C_i}{\partial t} = -\nabla J_{i,net} \quad (15.44)$$

where  $C_i$  represents the composition of the polymer  $i$ , and  $J_{i,net}$  denotes the net flux of component  $i$ . As the simple diffusion model described by Eq. (15.16) is

inadequate for a multiphase situation, the model developed by Kramer *et al.* [66] was employed in the present study as it was shown to agree better with experimental observations [67,68]. The mass flux of the nonlinear diffusion model can be written as:

$$J_{i,net} = J_i - C_i \sum_{j=1,2,3} J_j \quad (15.45)$$

Here, the chemical potential is determined by the expression of the free energy, while the total free energy of a ternary system,  $F$ , can be derived from the thermodynamic principles presented by Cahn and Hilliard [31,32], as can be seen in Eq. (15.8). The chemical potential of component  $i$  can then be derived [69]:

$$\mu_i = \frac{\partial F}{\partial C_i} = \frac{\partial f^*}{\partial C_i} - \nabla \left( \frac{\partial f^*}{\partial (\nabla C_i)} \right) \quad (15.46)$$

where  $f^*$  represents the nonhomogeneous free energy density, and is equal to  $f + \sum_{i=1,2,3} [\kappa_i (\nabla C_i)^2]$ . In an incompressible fluid,  $\sum_{i=1,2,3} C_i = 1$ , where  $C_1$  and  $C_2$  are regarded as independent variables and  $C_3 = 1 - C_1 - C_2$ . By substituting Eqs (15.45) and (15.46) into Eq. (15.44), the time evolution of the composition of component  $i$  can be represented as [37,43,70]:

$$\begin{aligned} \frac{\partial C_i}{\partial t} = & M_{ii} \left[ \frac{\partial f}{\partial C_i} - \frac{\partial f}{\partial C_3} - 2\kappa_{ii} \nabla^2 C_i - 2\kappa_{ij} \nabla^2 C_j \right] \\ & + M_{ij} \left[ \frac{\partial f}{\partial C_j} - \frac{\partial f}{\partial C_3} - 2\kappa_{ji} \nabla^2 C_i - 2\kappa_{jj} \nabla^2 C_j \right] \end{aligned} \quad (15.47)$$

where the subscripts  $i$  and  $j$  represent components 1 and 2, and

$$\begin{aligned} M_{ii} = & (1 - \bar{C}_i)^2 M_i + \bar{C}_i^2 \sum_{j \neq i} M_j \quad i = 1, 2; j = 1, 2, 3 \\ M_{ij} = & - \sum_{i \neq j} [(1 - \bar{C}_i) \bar{C}_j] M_i + \bar{C}_i \bar{C}_j M_3 \quad i = 1, 2; j = 1, 2 \end{aligned} \quad (15.48)$$

where  $\bar{C}_i$  is the average composition of component  $i$ . In order to simplify the solution of Eq. (15.47),  $\kappa_{ii} = \kappa_i + \kappa_3$ , and  $\kappa_{12} = \kappa_{21} = \kappa_3$ , where  $\kappa_i$  is the gradient energy coefficient.

The Flory-Huggins-type free energy is used as the bulk free energy density [33], which can be read as Eq. (15.9):

The free energy can be plotted in three dimensions, as depicted in Figure 15.18, where it can be seen that the free energy is minimized with intermediate concentrations of  $C_1$  and  $C_2$ , which would tend to drive diffusion from higher free-energy regions into lower free-energy regions.

In Figure 15.18, the interaction parameter of the two polymers,  $\chi_{12}$ , is chosen as 1 to show the immiscibility. The interaction parameters of polymers to the solvent,  $\chi_{13}$  and  $\chi_{23}$  are set to  $10^{-4}$  to represent the solubility of the polymers in the solvent. It can be seen that the free energy increases when the composition of the solvent decreases. On the surface of  $C_1 + C_2 = 1$ , and when there is no solvent in

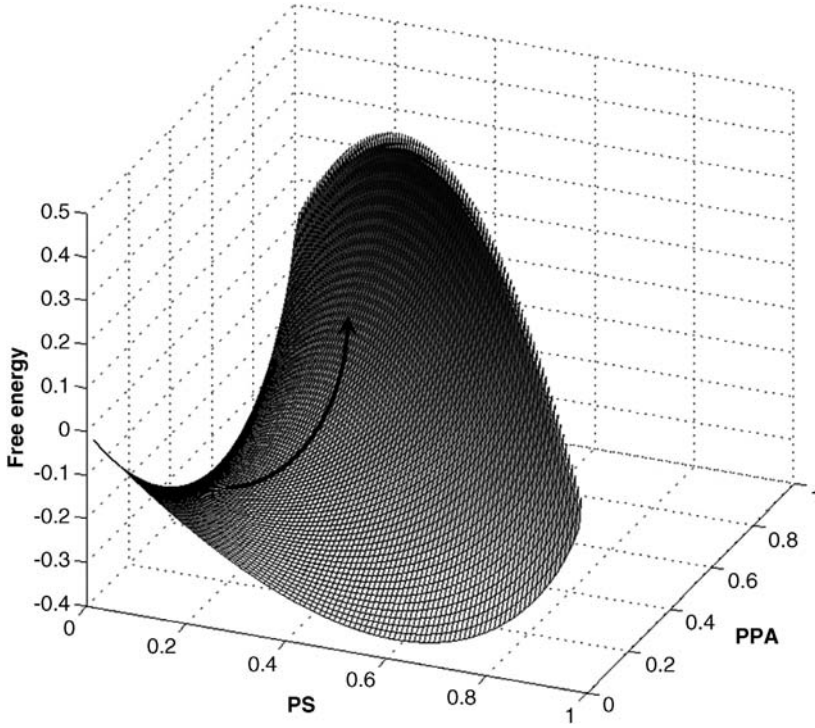


**Figure 15.18** The free energy of a polymer–polymer–solvent ternary mixture. PAA, poly(acrylic acid); PS, polystyrene.

the system, the free energy reflects the immiscible behavior of the two polymers. According to thermodynamics, the spinodal decomposition will occur when the system is quenched into the spinodal region in the phase diagram. The spinodal line in a ternary system can be calculated with the following equation [71]:

$$\frac{\partial^2 f}{\partial C_1^2} \frac{\partial^2 f}{\partial C_2^2} = \frac{\partial^2 f}{\partial C_1 \partial C_2} \quad (15.49)$$

The spinodal line in the ternary diagram can be calculated as shown in Figure 15.19. The initial conditions are marked in the phase diagram, as  $C_3$  to be 30%, 40%, 50%, 60%, and 70%, and  $C_1$  equal to  $C_2$ .

The heterogeneity of the functionalized substrate is implemented into the numerical model by an additional term,  $f_s$ , to the total free energy on the interface of the mixture and the substrate. Thus, an updated version of Eq. (15.9) can be read as

$$F(C_1, C_2, C_3) = \int_V \left\{ f(C_1, C_2, C_3) + \sum_{i=1,2,3} [\kappa_i (\nabla C_i)^2] \right\} dV + f_s(C_1, C_2, \mathbf{r}) \quad (15.50)$$

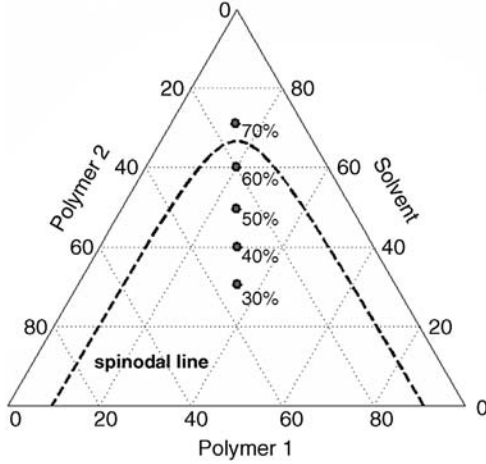


**Figure 15.19** The spinodal curve of the polymer–polymer–solvent system.

where  $\mathbf{r}$  is the coordinates vector on the mixture–substrate interface. Further details of this are discussed in the following section.

### 15.3.3

#### Numerical Method

The cosine spectral method was applied to the spatial coordinates. The evolution equations for a ternary system can then be transformed into the discrete cosine space as follows:

$$\begin{aligned} \frac{\partial \hat{C}_i}{\partial t} = & M_{ii} \left[ \left\{ \frac{\partial f}{\partial C_i} - \frac{\partial f}{\partial C_3} \right\} - 2\kappa_{ii}\lambda\hat{C}_i - 2\kappa_{ij}\lambda C_j \right] \\ & + M_{ij} \left[ \left\{ \frac{\partial f}{\partial C_j} - \frac{\partial f}{\partial C_3} \right\} - 2\kappa_{ji}\lambda\hat{C}_i - 2\kappa_{jj}\lambda C_j \right] \end{aligned} \quad (15.51)$$

where  $\hat{C}_i$  and  $\left\{ \frac{\partial f}{\partial C_i} - \frac{\partial f}{\partial C_3} \right\}$  represent the cosine transforms of  $C_i$  and  $\frac{\partial f}{\partial C_i} - \frac{\partial f}{\partial C_3}$ , respectively.  $\lambda$  is the approximation of discrete Laplacian operator in the transform space [49]:

$$\lambda(\mathbf{k}) = \frac{2 \sum_i \cos(2\pi k_i) - \sum_i 2}{(\Delta x)^2} \quad (15.52)$$

where  $\mathbf{k}$  denotes the discretized spatial position vector,  $k_i = \frac{n_i}{N_i}$  is the value of  $\mathbf{k}$  in the  $i$ th dimension,  $N_i$  represents the number of elements in the discrete space in the  $i$ th dimension, and  $\Delta x$  is the spatial step of the discretization. Similar to the methodology in the previous section, the linear fourth-order terms in Eq. (15.51) are treated implicitly and the nonlinear terms treated explicitly. The two ordinary differential equations with two unknowns are then solved to obtain the concentration for the next time step.

The parameters in the equation are nondimensionalized. The original values are divided by characteristic values to vanish the units, and the characteristic length and time are chosen as follows:

$$\begin{aligned} L_c^2 &= \frac{\kappa v_{site}}{RT} \\ t_c &= \frac{L_c^2 v_{site}}{M_c RT} \end{aligned} \quad (15.53)$$

where  $M_c$  is the characteristic mobility which is selected so that the value of the nondimensionalized mobility in the numerical simulation is 1. Other characteristic parameters can be derived from Eqs (15.47) and (15.53).

#### 15.3.4

##### Implementation

An immiscible polymer pair is implemented in this numerical modeling. The degree of polymerization was chosen as 100, according to experimental data. The interaction parameter,  $\chi_{ij}$ , in the Flory–Huggins free energy for polymers can be evaluated as a function of temperature in a binary case. In a ternary phase separation, the critical value of the interaction parameter for spinodal decomposition to occur between two polymers can be estimated as:

$$\chi_{12,c} = \frac{1}{2} \left( \frac{1}{\sqrt{m_1}} + \frac{1}{\sqrt{m_2}} \right)^2 \quad (15.54)$$

where  $\chi_{12}$  was chosen to be 0.08; this is greater than the critical value  $\chi_{12,c}$  and ensures that the initial values are quenched into the spinodal region [25].  $\chi_{13}$  and  $\chi_{23}$  are both set as 0.001, which represents a very good solubility of the polymers. The gradient energy coefficients were selected as  $\kappa_1 = \kappa_2 = \kappa_3 = 6.9 \times 10^{-11} \text{ J m}^{-1}$ , and the diffusivity,  $D = 1 \times 10^{-20} \text{ m}^2 \text{ s}^{-1}$ , which are common values for generic polymer blends [52,64]. The mobility of the system can be evaluated using the relationship [57]:

$$M_i = \frac{D v_{site}}{RT} \quad (15.55)$$

where the site volume of the lattice model in the Flory–Huggins free energy equation is usually selected as the volume of a water molecule. During modeling, the characteristic nondimensionalized mobility is 1.

The experimental functionalization is summarized in Table 15.2. Here, polystyrene/poly(acrylic acid) (PS/PAA) is the polymer pair, and the substrate is functionalized by  $-\text{NH}_2$  and ODT [72]. One type of functionalized surface will attract one type of polymer but meanwhile repel the other type of polymer to the same area of the substrate surface.

The additional term representing the surface energy on the blend–substrate interface is treated as a linear function with concentrations  $C_1$  and  $C_2$  [54,73]:

$$f_s(C_1, C_2, \mathbf{r}) = s_1(\mathbf{r})(C_1 - C_{1,ref}) + s_2(\mathbf{r})(C_2 - C_{2,ref}) + s_0(\mathbf{r}) \quad (15.56)$$

**Table 15.2** Functionalization in the experiments.

Polymer	Attracting/Repelling forces	Functionalization groups	
		NH <sub>2</sub>	ODT
PS	Hydrophobic	Repel	Attract
PAA	Negative static electrical force	Attract	Repel

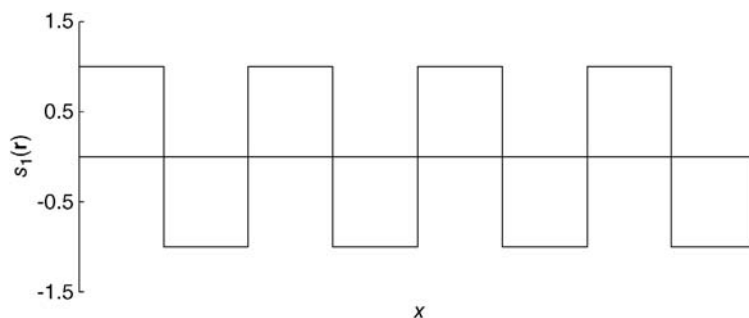
where  $s_0(\mathbf{r})$ ,  $s_1(\mathbf{r})$ , and  $s_2(\mathbf{r})$  are functions of the coordinate vector on the substrate, and  $C_{i,ref}$  are arbitrary reference compositions. For simplicity,  $C_{i,ref}$  are selected as 0, and  $s_0(\mathbf{r}) \equiv 0$ .  $s_1(\mathbf{r})$ , and  $s_2(\mathbf{r})$  are tuned so that there are alternating attraction forces to different type of polymers on the strips of the functionalized substrate, as can be seen in Figure 15.20. To qualitatively depict the functionalization of the substrate, the values of  $s_1$  and  $s_2$  are set to be alternating around zero across the  $x$  direction;  $s_1$  and  $s_2$  have opposite signs in all locations, representing the experimental condition that one type of functionalization on the surface will attract one polymer but repel the other.

A Matlab program with graphical user interface has been developed for the simulation of binary and ternary polymer systems. The users can easily edit the material properties and environment variables in the program, and the results are saved as images and data files in a designated folder. Analysis tools are also implemented in the Matlab program [74].

### 15.3.5

#### Results and Discussion

In this example, a 3D model was established to conduct the simulation with the mesh size of  $64 \times 128 \times 16$ . Similarly, the initial situation in modeling was a random distribution with small compositional differences in locations. According to the selected parameters, the system was initiated from average compositions of  $C_1 = 0.2$ ,  $C_2 = 0.2$ , and  $C_3 = 0.6$ , which is a relatively diluted solution. To isolate

**Figure 15.20** The spatial variation of the surface energy factor,  $s_1(\mathbf{r})$ .



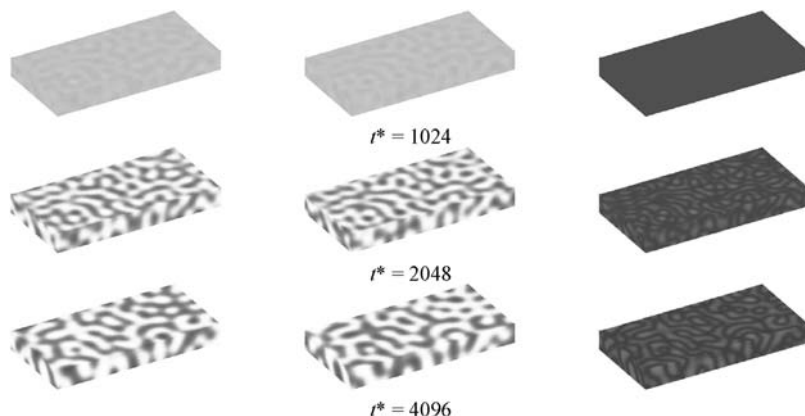


**Figure 15.21** Evolution of phase separation, showing: (a) PS; (b) PAA; and (c) solvent at different times for  $C_3 = 0.60$ .

the effects of the solvent composition, the compositions of polymers were set equal to each other, as in this case for the following simulations. The time evolution of the morphology for the system of  $C_3 = 0.60$  is shown in Figure 15.21.

The notation  $t^*$  represents the nondimensionalized time steps during the simulation, as defined in Eq. (15.53). In the figures, a darker color represents a higher concentration of one composition in the blends. It can be seen that the spinodal decomposition was induced from the random distribution, and as the two polymers are immiscible to each other they agglomerated into different domains. Clearly, for each polymer, as the time increased the maximum local composition increased and the characteristic domain size grew. Meanwhile, the solvent was miscible to both polymers thus it could be observed that during the early stages the solvent composition field tended to be uniform across the domain. However, since the polymers repelled each other and the peak values of the polymer compositions in different locations increased, small depressions appeared in the solvent composition field. During the later stage of the decomposition, the third component concentrated on the interface between two polymers and formed a thin layer. These phenomena were also observed by Huang *et al.* [34], whereby different type of polymers were seen to agglomerate separately and form an intersecting net structure.

The solvent in the blends can increase the mobility of the polymer molecules and decrease the interaction force between the macromolecules. From Figure 15.18, it can be seen that the solvent in an immiscible polymer pair can decrease the free energy level of the system and increase the miscibility of the two polymers. Therefore, the solvent concentration can influence the resultant pattern in the spinodal decomposition; indeed, the solvent concentration can be changed to investigate the influence of solvent composition on the morphology of phase separation. The morphology evolution of ternary systems with different solvent composition is shown in Figure 15.22; in this case the initial condition is the same,

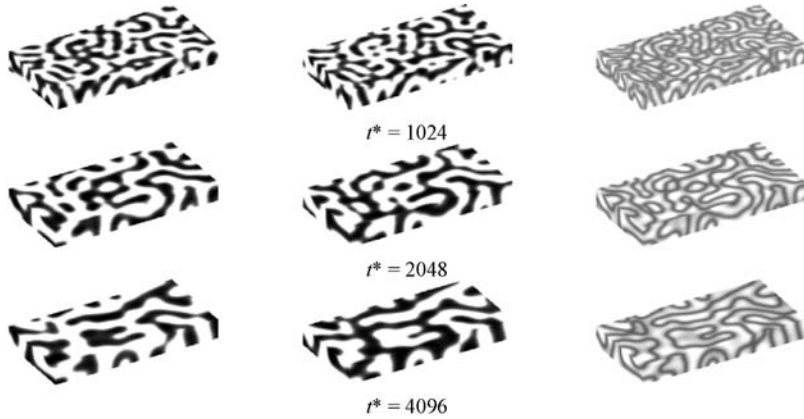


**Figure 15.22** Evolution of phase separation, showing: (a) PS; (b) PAA; and (c) solvent at different times for  $C_3 = 0.30$ .

except that the compositions are scaled according to the amount of solvent present.

It can be seen that the less solvent that is present in the blends the faster the phase separation is initiated and propagated. This behavior can be explained by the system being quenched more deeply into the miscibility gap by evaporation of the solvent, as can be seen in Figure 15.19; this phenomenon is also implied by the free energy depiction in Figure 15.18. Evaporation of the solvent will increase the total free energy level of the system, which in turn would make the polymer pair more likely to phase separate.

In order to quantitatively evaluate the morphology evolution, the characteristic lengths of the resultant patterns are measured from the composition profile. First, the pair-correlation function  $g_i$  is calculated with Eq. (15.57):

$$g_i = \frac{1}{N_j} \sum_{k_j=1}^{N_j} g_{i,k_j}(d, t) \quad (15.57)$$

where  $g_{i,k_j}(d, t)$  is defined as

$$g_{i,k_j}(d, t) = \langle \psi(\mathbf{k} = (k_i, k_j), t) \psi(\mathbf{k} = (k_i, k_j + d), t) \rangle \quad (15.58)$$

where  $\psi(\mathbf{k}, t)$  is the order parameter which equals the composition difference of the two polymers on the element  $\mathbf{k}$ , and  $d$  is a positive variable that varies from 1 to  $k_i$ . The angle brackets denote the average value of the expression inside the brackets over all the lattice nodes. The characteristic length in the  $i$ th dimension,  $R_i(t)$ , is the value of  $d$  when  $g_i$  first changes sign from positive to negative. The time evolution of the pair-correlation functions for systems with different solvent compositions can be seen in Figure 15.23, where it is apparent that a higher solvent concentration will result in a slower evolution of the domain size. In the system with a higher solvent concentration the maximum value of the

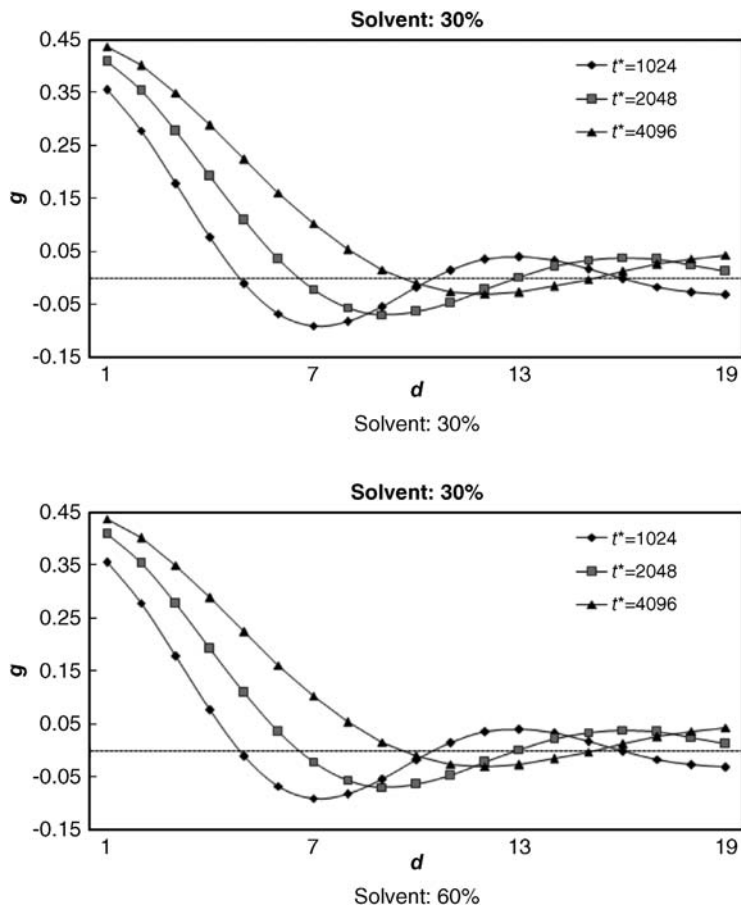


**Figure 15.23** The pair-correlation function,  $g_i$ , of the ternary system with different solvent compositions,  $t^* = 1024$ .

pair-correlation function is smaller than that in the system with a lower solvent concentration in which the polymers are less agglomerated. It can be seen that the first zero point of  $g_i$  increases with time.

The characteristic lengths are calculated from  $g_i$ . The comparison of the characteristic lengths,  $R(t)$ , of ternary systems with different solvent concentrations is shown in Figure 15.24.

When the  $R(t) \sim t$  relationship is plotted in a double logarithmic diagram, it can be observed that during the stable evolution the  $R(t) \sim t$  relationship can be fitted with a straight line. The index numbers of the fitting lines are 0.369 and 0.341, for the cases of  $C_3 = 0.60$  and  $C_3 = 0.30$ , respectively. These index numbers are close to that in the well-known relationship of  $R(t) \propto t^{\frac{1}{3}}$  reported elsewhere regarding numerical simulations and experiments [75,76]. The  $R(t)$  value of the condensed system is larger than that of the diluted system, and it is clear that with the

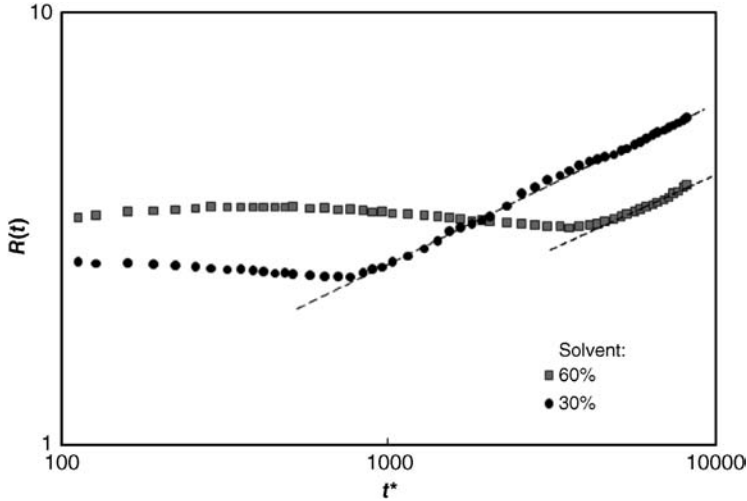


**Figure 15.24** The characteristic lengths of ternary phase separation.

decrease of the solvent the evolution rate is increased; this effect is due to a higher free energy level with less solvent in the system, as can be seen in Figure 15.18.

In order to investigate the influence of the heterogeneously functionalized substrate on the morphology evolution, the additional surface energy term,  $f_s$ , is added to the total free energy on the solution–substrate interface. In Eq. (15.56),  $|s_1|$  and  $|s_2|$  are set to be constantly  $1e-3$  on all positions and with alternating signs in the  $x$  direction, as shown in Figure 15.20. To measure the reproducibility of the result polymer surface pattern according to the substrate pattern, a parameter,  $C_s$ , is introduced:

$$C_s = \frac{1}{2} \langle |\psi(\mathbf{k}) - S_k| \rangle \quad (15.59)$$

and

$$S_k = \begin{cases} \frac{s_1(\mathbf{k})}{|s_1(\mathbf{k})|}, & s_1(\mathbf{k}) \neq 0, \\ 0, & s_1(\mathbf{k}) = 0 \end{cases} \quad (15.60)$$

where  $s_1(\mathbf{k})$  is the parameter in the surface energy expression for polymer 1, which denotes the strength of the surface attraction.  $S_k$  is the quantitative representation of the substrate attraction. Obviously,

$$C_s \in [0, 1] \quad (15.61)$$

The greater the value of  $C_s$ , the more compatible the resulting morphology is to the functionalized substrate. When  $C_s$  equals 1, it shows that the resultant pattern replicates the substrate pattern exactly. Meanwhile, when  $C_s$  is equal to 0.5 this represents a random phase separation, while  $C_s$  equal to 0 denotes a totally opposite phase pattern as desired by the substrate pattern.

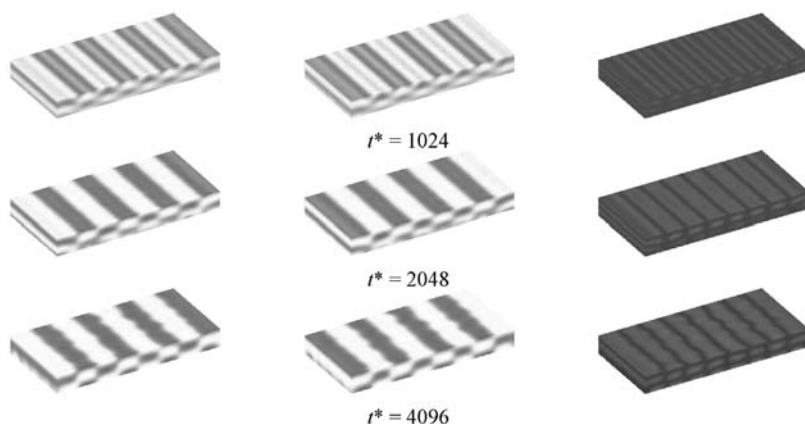


**Figure 15.25** Evolution of phase separation on a patterned substrate, showing: (a) PS; (b) PAA; and (c) solvent at different times for  $C_3 = 0.60$  and  $|s_1(\mathbf{k})| = 1e - 3$ .

The morphology evolution of ternary systems with different solvent concentrations are shown in Figures 15.25 and 15.26. An alternating composition profile can be observed near the substrate in the early stage of the decomposition in the case of  $C_3 = 0.60$ . The composition of the polymer alternates from the functionalized substrate into the depth, while the composition profile changes regularly in the depth direction and the direction parallel to the substrate and perpendicular to the strips. This checkerboard structure in the depth direction is similar to the situation in a binary case [77,78]. The pattern on the polymer surface next to the substrate replicates the substrate pattern very well in the early stages of the decomposition for varying solvent compositions. However, as the phase separation progresses, and when the internal thermodynamics force overcomes the surface

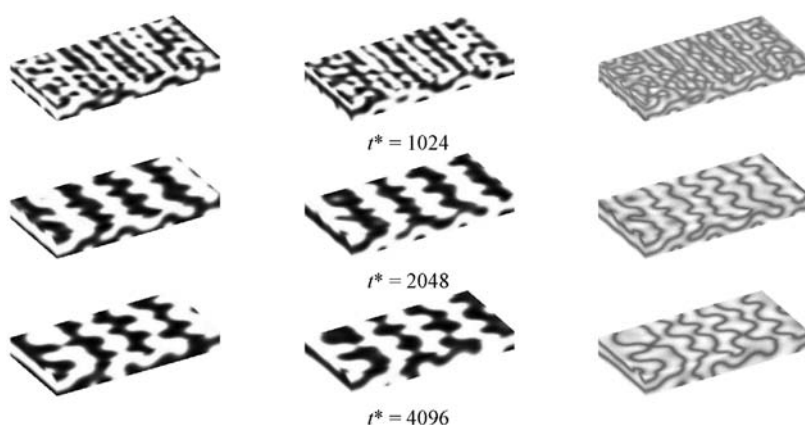


**Figure 15.26** Evolution of phase separation on a patterned substrate, showing: (a) PS; (b) PAA; and (c) solvent at different times for  $C_3 = 0.30$  and  $|s_1(\mathbf{k})| = 1e - 3$ .

attraction force, the polymer surface patterns for solutions with lower solvent concentrations are interrupted into unconnected sections aligned on the attracting strips. This was also observed by Keilhom in a binary numerical model [78], when the ternary blends on the surface tended to form a morphology with intrinsic characteristics similar to those of the bulk domain. With lower solvent concentrations (as shown in Figure 15.26), the intermolecular interaction is higher between the immiscible polymer pairs, and therefore the polymer pair tends to phase separate according to the thermodynamic force in the bulk domain, without significant assembly to the functionalized substrate.

When the ternary model with varying solvent concentrations was studied experimentally, the thickness of the polymer membrane was very thin compared to its width and length. As the solvent evaporates into air very rapidly, its composition is considered to be unchanged through the depth of the thin film. The decrease in average solvent composition was shown to obey the relationship [79]:

$$C_{3,t} = C_{3,0}e^{-\alpha t} \quad (15.62)$$

where  $C_{3,t}$  is the composition of the solvent in time  $t$ ,  $C_{3,0}$  is the initial solvent composition,  $\alpha$  is a constant, and  $t$  is time. According to the respective experimental conditions, the initial concentration of the solvent,  $C_{3,0}$  was set at 0.70. From Figure 15.19, it can be seen that during evaporation of the solvent the solution is quenched from the homogeneous region into the spinodal region, which is similar to the case of a spin-coating process in the experiment [72]. The thickness also decreased as the solvent was evaporated. The change in thickness due to solvent evaporation is shown in Figure 15.27, where the thickness,  $L_z$  is normalized by the initial value.

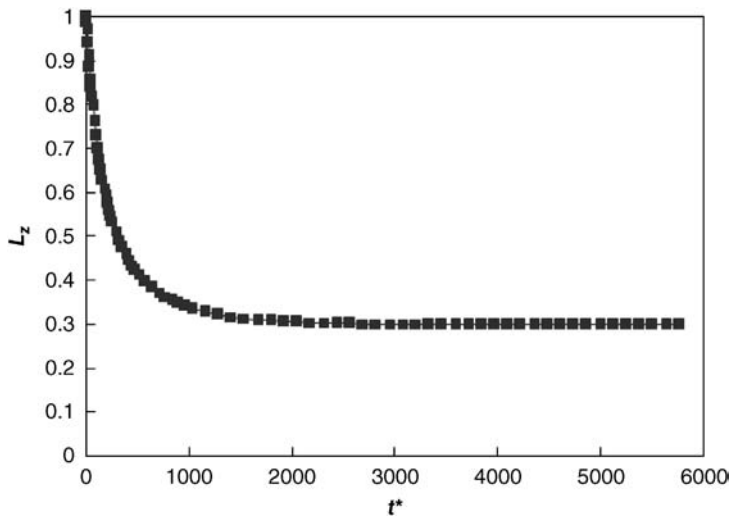


**Figure 15.27** Change of film thickness ( $L_z$ ) with time ( $t^*$ ).

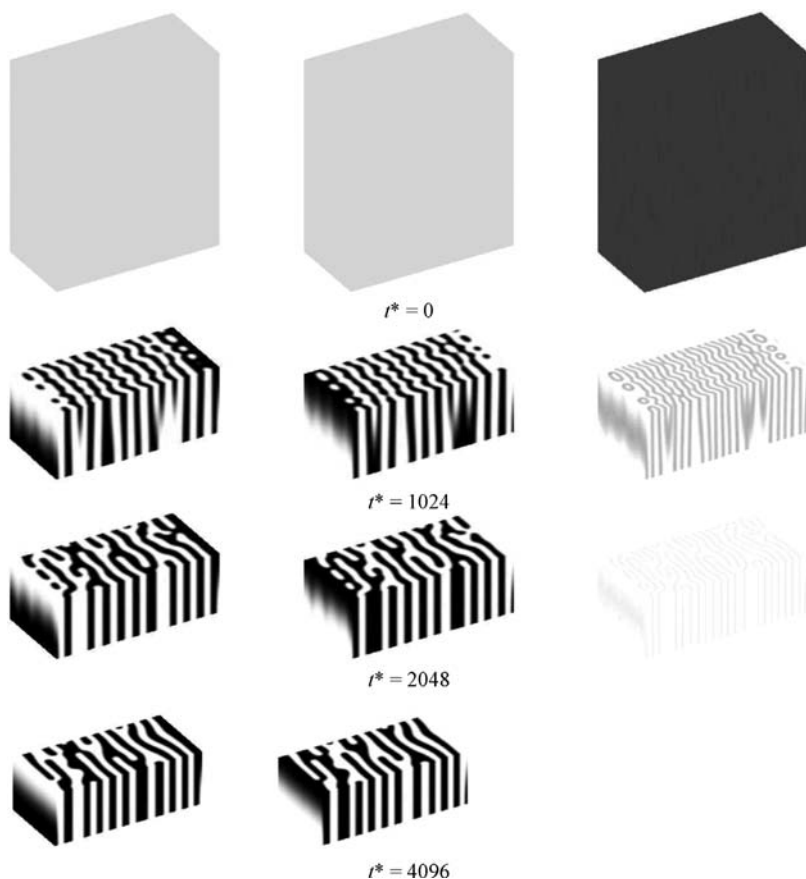


**Figure 15.28** Evolution of phase separation on a patterned substrate, showing: (a) PS; (b) PAA; and (c) solvent at different times for  $C_3 = 0.30$  and  $|s_1(\mathbf{k})| = 1e - 3$ . The thickness is scaled by a factor of 5.

The solvent composition and film thickness were both decreased rapidly during the early stage of evaporation and phase separation. However, in the later stages most of the solvent evaporated into the air, and  $C_3$  was close to 0.

The decrease in solvent with time influences the morphologic development. From data relating spinodal decomposition with solvent evaporation (see Figure 15.28) it can be seen that as the solvent evaporates the two polymers phase separate with a sharper interface. This effect was considered due to the low concentration, although as the film thickness was thin during the later stage of the evaporation the composition profile was almost the same in the depth direction.

The compatibility measurement,  $C_s$ , of the morphology at the solution–substrate interface, is plotted with the respect to time in Figure 15.29, and with respect to the thickness direction in Figure 15.30. It can be seen that there exists a critical time during the evolution of  $C_s$ , after which the mechanism of phase separation

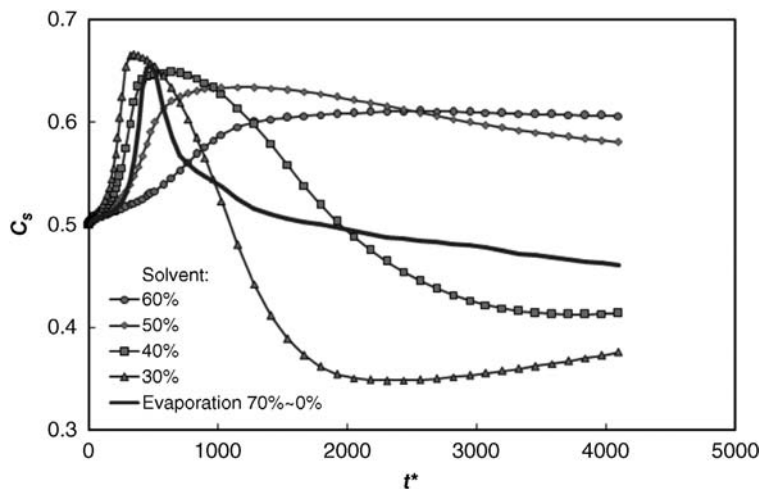


Figure 15.29 Compatibility,  $C_s$ , of the solution–substrate interface; evolution with time.

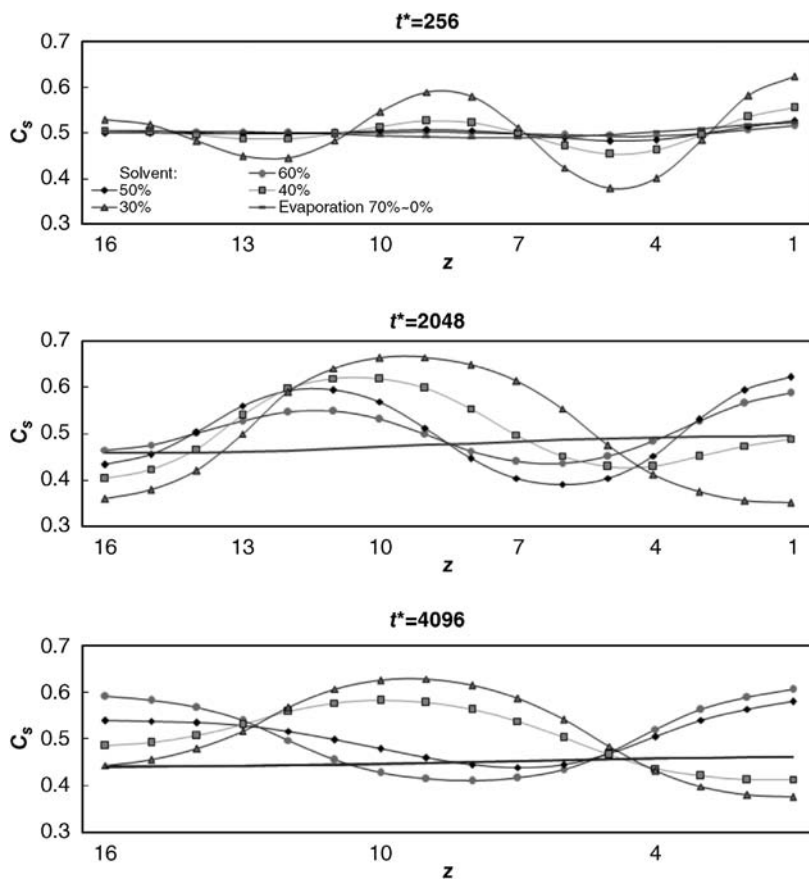


Figure 15.30 Compatibility,  $C_s$ ; variation with depth direction at (a)  $\times 256$ ; (b)  $\times 2048$ , and (c)  $\times 4096$ .



at the solution–substrate interface changes dramatically. The higher solvent concentration provides an earlier critical time, before which the surface compatibility of the condensed polymer solution increases at a faster rate than the diluted solution. After the critical time, the surface compatibility of system with  $C_3 = 0.60$  increases at a much slower rate compared to that before the critical time, whereas the surface compatibility in systems with  $C_3 = 0.50$ ,  $C_3 = 0.40$ , and  $C_3 = 0.30$  tends to decrease after the critical time. The  $C_s$  value on the surface of system with  $C_3 = 0.30$  decreases at the fastest rate and passes the  $C_s = 0.5$  level. The  $C_s$  value for  $C_3 = 0.30$  continues to decrease until it touches the lowest point, but then starts to increase at a very slow pace. In the system with solvent evaporation, the  $C_s$  value increases initially and then starts to decrease after a critical point, similar to that in the systems  $C_3 = 30\%$  and  $C_3 = 40\%$ , and without solvent evaporation effects. Though no obvious minima was observed during the evolution of  $C_s$  with time when solvent evaporation was considered.

Compatibility to the functionalized substrate of the morphology on the layers through the depth is plotted at different time spots. The depth of the film in the time spot concerned is divided by 16 nodes. In the case considering evaporation, there was no significant change in the value of  $C_s$  in the depth direction, but in cases with a constant solvent composition the compatibility alternated from the surface to the bulk domain, which indicates that the dominant polymer type had changed from the surface to the depth. This result was in accordance with the checkerboard structure in the depth direction. As stated above, the surface attraction can affect only the neighboring surface of the ternary blends, and the domain that is not connected to the substrate is influenced only indirectly. The influence of the functionalization decays very quickly into the depth from the substrate surface.

The depth composition profile can also be investigated via a quantity,  $h$ :

$$h(z) = \frac{1}{k_1 k_2} \sum_{k_1} \sum_{k_2} \psi(\mathbf{k}) \cdot S_k|_z \quad (15.63)$$

which evaluates the average of the order parameter,  $\psi(\mathbf{k})$ , on the plain  $k_3 = z$ . As indicated,  $k_1$ ,  $k_2$ , and  $k_3$  represent the elements in the first, second, and third direction, respectively, with  $k_3$  being the direction normal to the substrate surface. Equation (15.63) also considers the influence of the substrate functionalization on the composition profile. The  $h(z)$  values at different times can be seen in Figure 15.31.

To directly compare the order parameter in Figure 15.31,  $\psi(\mathbf{k}) = C_1(\mathbf{k}) - C_2(\mathbf{k})$ , the  $h(z)$  value of different composition systems has been scaled to maintain the similar magnitudes. As the two polymers are immiscible with each other, less solvent will result in a more unstable system and a faster evolution in the phase separation. It can be seen that the composition wave is initiated from the substrate and propagates into the depth direction with time. After scaling, the amplitude of the composition wave is still bigger for the condensed systems; growth of the wave is also faster when there is less solvent in the system. During the late stage

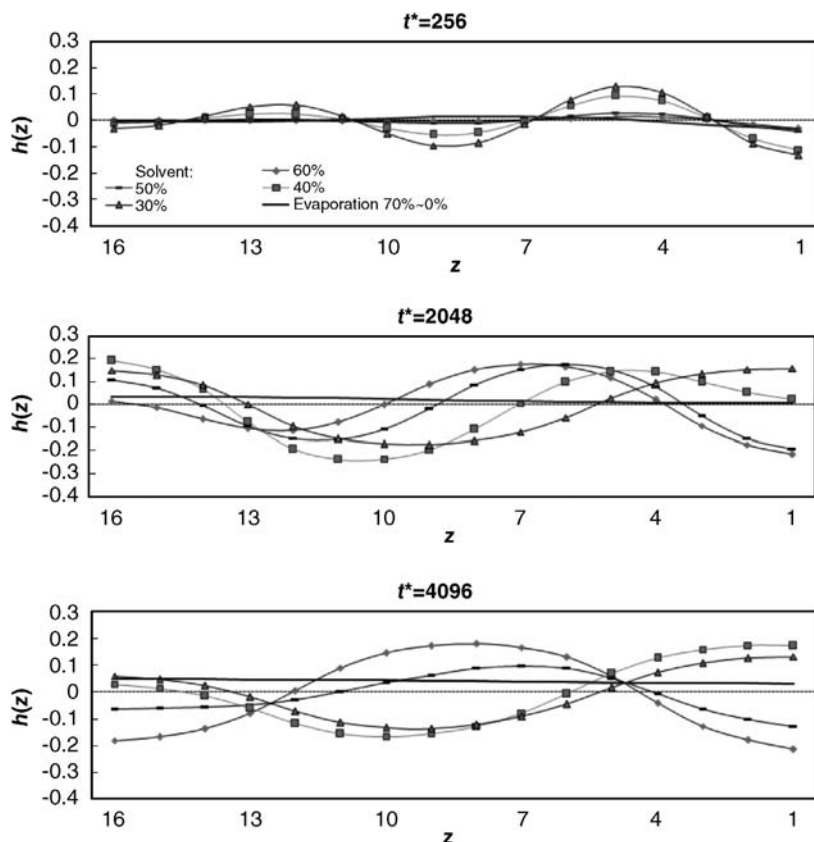


**Figure 15.31** The order parameter profile in the depth direction at (a)  $\times 256$ , (b)  $\times 2048$ , and (c)  $\times 4096$ .

of decomposition, the composition wavelength remains stable and in the condensed systems the composition wavelength decays with time. In the nondimensionalized time  $t^* = 4096$  the composition wave length in the most condensed system is decreased to a very small value, which means that there is no dominant species near the functionalized substrate surface.

### 15.3.6

#### Summary

Following the introduction of a 3D ternary numerical model, it can be seen that an expansion of the numerical model from binary to ternary involves alternations in basic physical equations. Yet, more interesting phenomena were also encountered in the ternary system; for example, the immiscible polymer pairs agglomerated into different locations and the solvent for each of the polymers was concentrated on the interface domain of the two polymers. The characteristic length,  $R(t)$ ,

followed the same rule of  $R(t) \propto t^{\frac{1}{3}}$  as in a polymer–polymer binary system, as shown in Section 15.3.5 [77]. The attraction forces of the heterogeneously functionalized substrates on different types of polymer are confined to the surface domain and decay very rapidly into the depth, and this can also be investigated in binary systems. Unlike the case of a 2D numerical system [77], the bulk domain has a significant influence on the surface pattern, as the phases separate at the solution–substrate interface according to the substrate patterns in the early stage. However, at the late stage of phase separation the surface morphology collapses into unconnected sections, the characteristic lengths of which obey the intrinsic values in the bulk domain. In a real experiment this implies a refined resultant pattern from a phase separation in a dilute solution rather than in a condensed solution. In the numerical simulation, evaporation of the solvent results in a sharper interface between the two polymer domains and a moderate decrease in the  $C_s$  value beyond the critical time, when compared to the case of a constant solvent concentration of 30%. The significant decrease in the thickness of the film caused a unified composition profile in the depth direction.

#### 15.4

##### **Verification of Numerical Simulation of the Self-Assembly of a Polymer–Polymer–Solvent Ternary System on a Heterogeneously Functionalized Substrate**

In this section an example is provided of the verification of numerical simulation with real experimental results. The AFM and TEM images are compared directly with the numerically simulated composition profiles, and an innovative methodology is applied to assess the nontrivial model parameters with simulation optimization.

The properties of the external surface can significantly alter phase separation in a thin polymer film. In extensive experimental investigations of the phase separation of polymer blends directed by patterned substrates [1,56,58,60,80–88] it was observed that the domain size evolved in a power law relation with time. The composition wave was normal to, and propagates inward from, the functionalized substrate. Likewise, processing parameters such as pattern size in the substrate were seen to affect refinement of the morphology.

The phase separation of a polymer–polymer–solvent solution with solvent evaporation was investigated using an established ternary model [77]. When Scott [29] and Hsu *et al.* [30] numerically studied the phase separation of a polymer-based ternary system with Flory–Huggins-type free energy, both groups employed similar methods to calculate the binodal curve in ternary blends. Chen [61] also provided a generalized numerical simulation for ternary blends, whereas later on Huang *et al.* established a numerical model for a polymer–polymer–solvent ternary system based on Flory–Huggins-type free energy and nonlinear diffusion equations [43]. Numerical polymer–nonsolvent–solvent systems have also been established and studied by Altena *et al.* [63] and Zhou *et al.* [64]. Tong *et al.* established a numerical model of a ternary phase separation with the consideration of

chemical reaction dynamics [65]. Subsequently, Tong and Nauman investigated the influences of polymer chain length on the phase separation, and showed that the long chains of polymers would destabilize the blends and increase the quench depth [62].

The numerical simulation was validated by comparison with experimental results obtained from a cooperating group [72]. The evolution mechanisms were studied both numerically and experimentally and the predicted morphology pattern of phase separation was compared quantitatively with the experimentally observed pattern. The effects of the processing parameters, including the composition of the polymers, the attracting factors and the rate of evaporation, were also investigated and compared in both the numerical simulation and in experiments.

#### 15.4.1

##### Experiment

A cooperating research group focused on developing a method for the nanomanufacture of highly ordered polymeric features by the direct assembly of polymer blends on chemically patterned surfaces [72]. Chemically heterogeneous patterns were prepared using a new method that combined electron-beam lithography and the self-assembly of alkanethiol monolayers. Three pattern periodicities (667, 1000, and 1333 nm) were employed to investigate these effects. The strip width ratios remained constant at 3/7; that is, the hydrophilic strips covered by 11-amino-1-undecanethiol hydrochloride (MUAM; 99% purity; Asemblon, Inc.) monolayers occupied 30% of the pattern periodicity, while their hydrophobic counterparts which were covered by 1-octadecanethiol (ODT; Aldrich Inc.) monolayers occupied the remaining 70%.

The basic experimental procedure was as follows: 1 wt% polymer blend solutions of PS (18 k molecular weight; Aldrich Inc.)/PAA (2 k molecular weight; Aldrich Inc.) with the 7/3 ratio in dimethylformamide was pipetted onto the template. After a 6-min period of quiescence, during which the humidity was maintained above 1.0% and the room temperature at 20 °C, the solutions were spin-coated onto the template surface using 3000 rpm spinning speed and 30 s endurance time. Two other spinning speeds (1000 rpm and 7000 rpm) were employed separately to investigate the influence of this parameter. The effects of two composition ratios of the PS/PAA blends (5/5 and 3/7) were also studied. Finally, the effect of the molecular weight of PAA was investigated by increasing it to 50 g mol<sup>-1</sup> and 450 g mol<sup>-1</sup>.

Subsequent field emission scanning electron microscopy (FESEM) images were obtained using a JEOL 7401 F microscope, while AFM topographic images of the initial morphologies of polymer blends were examined using scanned probe microscopy (Veeco NanoScopella; PSIA XE-150 mode; 40 N m<sup>-1</sup> tip spring constant) operating in noncontact mode. Fourier transform analyses were then performed using commercial AFM image analysis software (XEI, version 1.5; PSIA Corp.).

## 15.4.2

**Implementation**

The numerical model for polymer–polymer–solvent ternary system is provided in Section 15.3.3, while the parameters used in the simulation and some estimated values are listed in Table 15.4. Since, in the practical experiments, the conditions were more complicated than in the developed models, the values of the parameters were first estimated by fundamental theory and then tuned according to the experimental results.

The lattice volume fraction was chosen as the composition, as this (nonuniform) property is normally used in Flory–Huggins free energy. The relationship between the composition  $C_i$  and the mole fraction  $C_{m,i}$ , of component  $i$  is

$$C_i = \frac{m_i C_{m,i}}{\sum_{j=1,2} m_j C_{m,j} + C_{m,3}} \quad i = 1, 2$$

$$C_i = \frac{C_{m,i}}{\sum_{j=1,2} m_j C_{m,j} + C_{m,3}} \quad i = 3$$
(15.64)

In a ternary phase separation, the critical value of the interaction parameter for spinodal decomposition to occur between two polymers can be estimated as

$$\chi_{12,c} = \frac{1}{2} \left( \frac{1}{\sqrt{m_1}} + \frac{1}{\sqrt{m_2}} \right)^2$$
(15.65)

The Flory–Huggins interaction parameter is difficult to measure for a given system. The interaction parameters were selected so that there was a free energy barrier between the immiscible polymer pairs, as shown in Figure 15.9, where it can be seen that the free energy increases while the solvent concentration is decreasing.

The gradient energy coefficient can be calculated using the random phase approximation [37]:

$$\kappa_i = \left( \frac{RTa^2}{3v_{site}} \right) \quad i = 1, 2, 3$$
(15.66)

where  $a$  is the monomer size. The contribution of short-range van der Waals forces to  $\kappa_i$  is neglected in this study, since in polymers the short-range intermolecular force is  $\frac{1}{N}$  smaller than the intermolecular effects [23]. The gradient energy coefficients  $\kappa_{11}$  and  $\kappa_{22}$  are assumed to be equal in this simulation, which is supported by the studies of Caneba [35]. The diffusivity,  $D$ , was estimated as  $1 \times 10^{-13} \text{ m}^2\text{s}^{-1}$  for polymers and  $1 \times 10^{-10} \text{ m}^2\text{s}^{-1}$  for small-molecule solvents [64,89–92]. The mobility of the system can be evaluated with the relationship [57]:

$$M_i = \frac{Dv_{site}}{RT}$$
(15.67)

The experimental functionalization is summarized in Table 15.3. PS/PAA serves as the polymer pair while  $\text{NH}_2$  and ODT are used to functionalize the substrate

**Table 15.3** Functionalization in the experiments.

Polymer	Attracting/Repelling forces	Functionalization groups	
		NH <sub>2</sub>	ODT
PS	Hydrophobic	4.82 kJ m <sup>-2</sup>	-4.82 kJ m <sup>-2</sup>
PAA	Negative static electrical force	-4.82 kJ m <sup>-2</sup>	4.82 kJ m <sup>-2</sup>

[72]. One type of functionalized surface attracts one type of polymer but repels the other type of polymer to the same area of the substrate surface. The additional term representing the surface energy on the blend–substrate interface is treated as a linear function with concentrations  $C_1$  and  $C_2$  [54,73]:

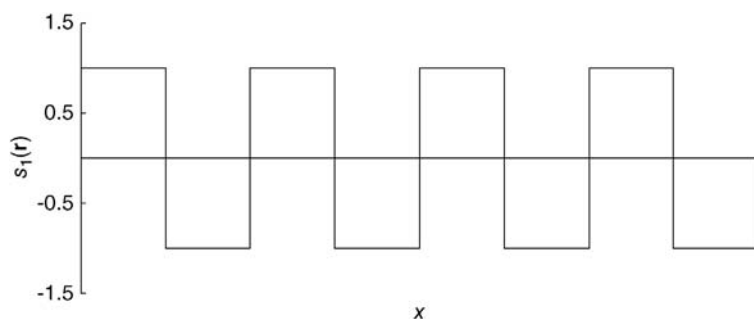
$$f_s(C_1, C_2, \mathbf{r}) = s_1(\mathbf{r})(C_1 - C_{1,ref}) + s_2(\mathbf{r})(C_2 - C_{2,ref}) + s_0(\mathbf{r}) \quad (15.68)$$

where  $s_0(\mathbf{r})$ ,  $s_1(\mathbf{r})$ , and  $s_2(\mathbf{r})$  are functions of the coordinate vector on the substrate.  $C_{i,ref}$  are arbitrary reference compositions. For simplicity,  $C_{i,ref}$  are selected as 0, and  $s_0(\mathbf{r}) \equiv 0$ .  $s_1(\mathbf{r})$ , and  $s_2(\mathbf{r})$  are tuned so that there are alternating attraction forces to the different types of polymers on the strips of the functionalized substrate, as can be seen in Figure 15.32. In order to qualitatively depict the functionalization of the substrate, the values of  $s_1$  and  $s_2$  are set with opposite signs to alternate around zero across the  $x$  direction. As such,  $s_1$  and  $s_2$  represent the experimental condition that one type of functionalization on the surface will attract one polymer and repel the other.

The effects of solvent evaporation were also studied. In these experiments the thickness of the polymer domain was very thin compared to its width and length. The solvent also evaporated into the air very quickly, and its concentration was considered to be unchanged through the depth of the thin film. The decrease in average solvent composition was shown to obey the relationship [79]:

$$C_{m,3,t} = C_{m,3,0}e^{-\alpha t} \quad (15.69)$$

where  $C_{m,3,t}$  is the mole fraction of the solvent in time  $t$ ,  $C_{m,3,0}$  is the initial solvent amount,  $\alpha$  is a constant, and  $t$  is time. From Figure 15.18 it can be seen that,

**Figure 15.32** The spatial variation of the surface energy factor,  $s_1(\mathbf{r})$ .

during evaporation of the solvent, the solution was quenched from the homogeneous region into the spinodal region, which was similar to the case in a spin-coating process in the experiment [72]. The thickness also decreased in line with evaporation of the solvent; the change in thickness due to solvent evaporation is shown Figure 15.27, such that the thickness,  $L_z$  is normalized by the initial value.

The amount of solvent and film thickness were both decreased rapidly during the early stages of evaporation and phase separation. At a later stage, most of the solvent had evaporated into the air and  $C_{m,3,t}$  was close to 0. The parameters of the simulation are listed in Table 15.4, where the descriptions of each parameter are also listed.

The parameters in the equation are nondimensionalized, and the original values are divided by characteristic values to vanish the units. The characteristic length and time are chosen as follows:

$$\begin{aligned} L_c^2 &= \frac{\kappa v_{site}}{RT} \\ t_c &= \frac{L_c^2 v_{site}}{M_c RT} \end{aligned} \quad (15.70)$$

where  $M_c$  is the characteristic mobility for nondimensionalization. Other characteristic parameters can be derived from Eqs (15.14) and (15.70), as listed in Table 15.5.

#### 15.4.3

#### Results and Discussion

A  $128 \times 64 \times 16$  finite element model in three dimensions was established to investigate the composition profile; the physical dimensions of the slab before nondimensionalization are listed in Table 15.4. The numerical simulation was conducted based on the experimental conditions. Some of the parameters were directly imported from the experimental condition, while some – such as the gradient energy coefficient and mobility – were difficult to measure. Those parameter values which were not directly obtainable were first estimated via the theories described in Section 15.4.2, and then benchmarked in the numerical simulation with the experimental results. For phase separation in a polymer–polymer–solvent ternary system, the solubility of the polymers in the solvent is much greater than that of the polymers in each other [94]. Consequently, the interaction parameters between the solvent and two polymers were set as 0, and the interaction parameter between two polymers can be estimated with the following equation [33]:

$$\chi_{12} = \frac{v_{site}(\delta_1 - \delta_2)^2}{RT} \quad (15.71)$$

where  $\delta_1$  and  $\delta_2$  are the solubility parameters of PS and PAA, respectively (the values of these are listed in Table 15.4). The interaction parameter,  $\chi_{12}$ , was calculated as 0.22, which also satisfied the requirement,  $\chi_{12} > \chi_c$ . The gradient energy coefficient,  $\kappa$ , affected the interface thickness and domain size of the resultant

**Table 15.4** Parameter values in the simulation.

Parameter	Value	Unit	Comments
$M_{w,1}$	18 100	$\text{g mol}^{-1}$	Molecular weight of PS.
$M_{w,2}$	2000, 50 000, 450 000	$\text{g mol}^{-1}$	Molecular weight of PAA, $M_{w,PAA}$ and $M_{w,PS}$ can alter the shape of the mixing free energy curve.
$DP_1$	27.78	1	Degree of polymerization of PS
$DP_2$	174.04	1	Degree of polymerization of PAA
$\delta_1$	19.09	$\text{MPa}^{-\frac{1}{2}}$	Solubility parameter of PS [93]
$\delta_2^{\text{a})}$	24.6	$\text{MPa}^{-\frac{1}{2}}$	Solubility parameter of PAA [94]
$\chi_{12,critical}$	0.0360	1	Critical Flory–Huggins interaction parameter between PS and PAA
$\chi_{12}$	0.221	1	Flory–Huggins interaction parameter between PS and PAA
$\chi_{13}$	0	1	Flory–Huggins interaction parameter between PS and DMF
$\chi_{23}$	0	1	Flory–Huggins interaction parameter between PAA and DMF. The Flory–Huggins interaction parameter determine the compatibility of the species.
$w_{polymer}$	3	%	Weight percentage of homopolymers in the solution
$w_1 : w_2$	30 : 70, 50 : 50, 70 : 30	%	Weight ratios of PS and PAA polymers
$w_{copolymer}$	10, 30	%	Weight percentages of copolymer based on the total weight of the polymers
$W_1 : W_2$	467 : 200, 700 : 300, 933 : 400	nm	Width of functionalized strips. $W_{PS}$ and $W_{PAA}$ represent the strips attractive to PS and PAA, respectively.
$t_e$	30	s	Time of evaporation
$D_3$	$5 \times 10^{-13}$	$\text{m}^2/\text{s}$	Diffusivity of PAA and PS monomers, and DMF
$ s_1 $	$4.82 \times 10^3$	$\text{J}/(\text{m}^2)$	Magnitude of the functionalized substrate surface energy for PS, the sign is alternating along the direction normal to the substrate pattern strips.
$ s_2 $	$4.82 \times 10^3$	$\text{J}/(\text{m}^2)$	Magnitude of the functionalized substrate surface energy for PAA, the sign of $s_2$ is opposite to $s_1$ .
$M_1, M_2, \text{ and } M_3$	$3.63 \times 10^{-21}$	$\text{m}^5/(\text{J} \cdot \text{s})$	Mobility of PS and PAA monomers, and DMF
$\nu_{site}$	$1.80 \times 10^{-5}$	$\text{m}^3$	Molar volume of the reference lattice
$a$	$6.3 \times 10^{-8}$	m	Monomer size [36]
$\kappa_1, \kappa_2, \text{ and } \kappa_3$	$1.821 \times 10^{-7}$	$\text{J m}^{-1}$	Gradient energy coefficients of PS and PAA monomers, and DMF
$L_x \times L_y \times L_z$	$4 \times 2 \times L_z$	$\mu\text{m}$	Real modeling dimensions, where $L_z$ changes during evaporation.

a) The value of solubility parameter for PAA is considered to be close to that of acrylic acid [95].



Table 15.5 Nondimensionalization of parameters.

Characteristic variable	Expression
$L_c^2$	$\frac{K\nu_{site}}{RT}$
$t_c$	$\frac{L_c^2\nu_{site}}{M_cRT}$
$f_c$	$\frac{RT}{\nu_{site}}$
$\kappa_c$	$\frac{RTL_c^2}{\nu_{site}}$
$M_c$	$M_{11}$

pattern in the numerical simulation. The mobility,  $M$ , which is determined by the diffusivity of the species, influenced the speed of the morphology evolution of the resultant pattern. The characteristic domain lengths of the resultant pattern in experiments conducted at a rotation speed  $<3000$  rpm were measured using AFM-topography images and Fourier transfer analysis. The  $5\text{ }\mu\text{m}$  AFM images and Fourier transform diagrams of different spin-coating rotation speeds are shown in Figure 15.33, where the radius of the intensified ring in the fast Fourier transform (FFT) image represents the inverse of the characteristic length of the original image. Therefore, in the FFT image the larger the radius of the intensified ring, the smaller the characteristic length in the original image.

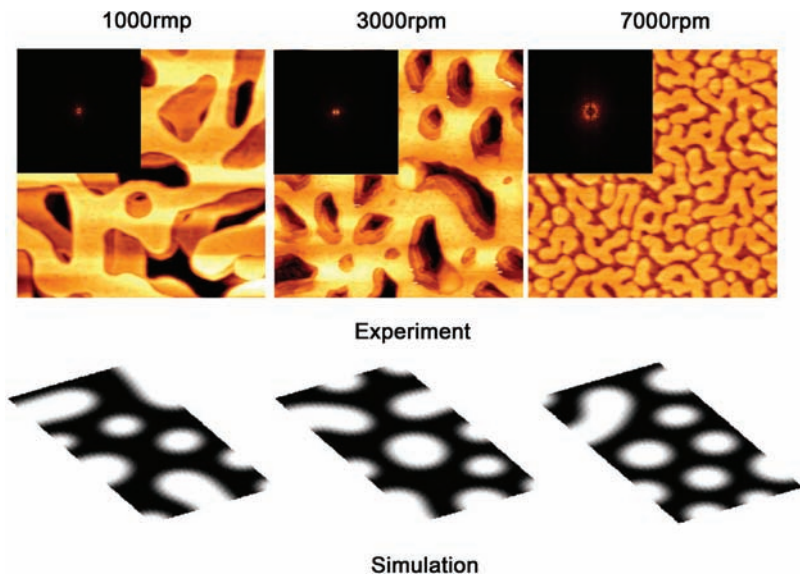
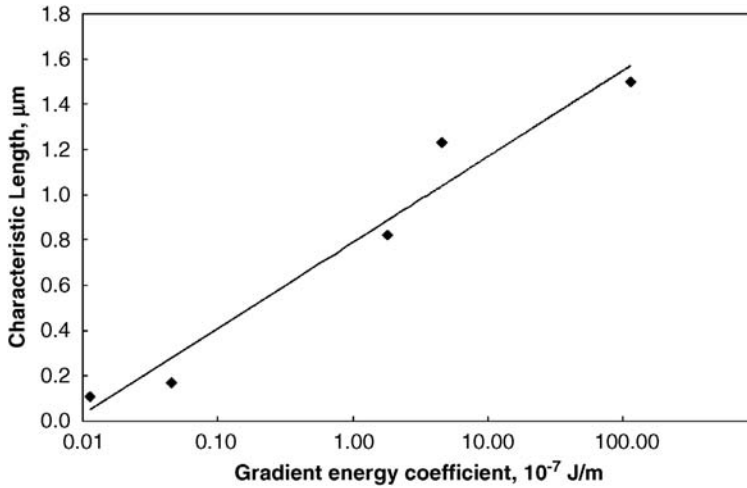
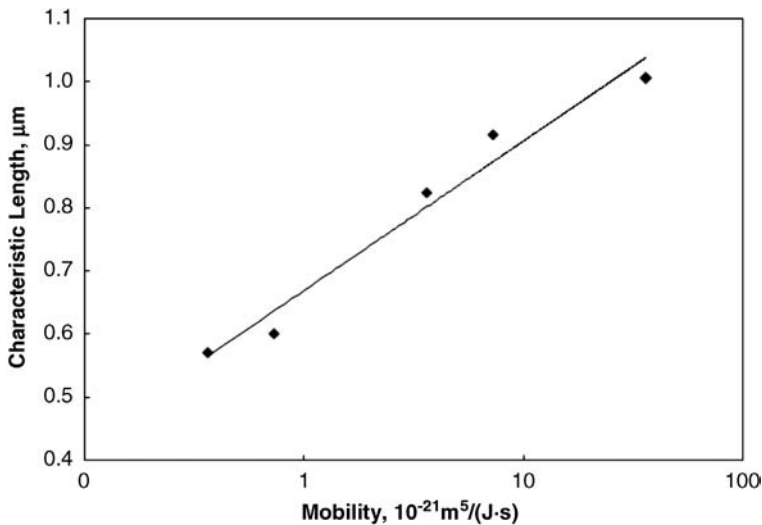


Figure 15.33 Atomic force microscopy images of experimental patterns and the Fourier transform diagrams for different speeds of rotation.



**Figure 15.34** Changes in characteristic length with gradient energy coefficient,  $\kappa_{12}$ , at 3000 rpm spin-coating rotation speed. The mobility was  $3.633 \times 10^{-21} \text{ m}^5/(\text{J} \cdot \text{s})$ .

The gradient energy coefficient,  $\kappa$ , and the mobility are two undetermined parameters. Although these can be estimated from the above-listed equations, they must be verified so that the characteristic lengths of the simulated pattern and the experiment pattern can match. When the numerical model is benchmarked in this system, the  $M$  and  $\kappa$  values are determined as  $3.633 \times 10^{-21} \text{ m}^5/(\text{J} \cdot \text{s})$  and  $1.821 \times 10^{-7} \text{ J/m}$ , respectively (see Table 15.4). The mobility and change in characteristic length with the gradient energy coefficient and mobility in the simulation result can be seen in Figures 15.34 and 15.35.



**Figure 15.35** Changes in characteristic length with mobility,  $M_{12}$ , at 3000 rpm spin-coating rotation speed. The gradient energy coefficient was  $1.821 \times 10^{-7} \text{ J/m}$ .

It was apparent that, when the other parameters were unchanged, the characteristic length of the domain increased with the increasing gradient energy coefficient. The gradient energy coefficient,  $\kappa$ , denotes the influence of the gradient to the free energy. As the system intrinsically minimizes the free energy, the larger the value of  $\kappa$ , the smaller will be the composition gradient and the smaller the interface area that the system is able to resist in a stable state. Therefore, the domain size tends to be larger with a smaller composition gradient and a thicker interface. Meanwhile, the higher the mobility,  $M$ , the faster the small molecules and the monomers can diffuse to the desired position, and the faster the domain pattern grows. Thus, the higher mobility of the system results in a higher domain size, while the other parameters remain constant.

Once the parameters have been determined, the phase separation and effects of solvent evaporation at different spin-coating rotation speeds can be investigated. Film thickness during spin-coating is measured at 3 s and 30 s for different rotation speeds. The thickness at 3 s was determined by dividing the weight increase on the template compared to the empty load relative to the respective area on the template. The final film thickness was measured using contact mode AFM immediately after the completed spin-coating stage (30 s). The polymer films were removed using a scalpel, and their thicknesses monitored from AFM topography images. The thickness data with time were substituted into Eq. (15.69). Thickness at 3 s, rather than the initial thickness, was selected for measurement because the most of the mass loss during the early stage of spin-coating is due to spin-off effects and not to evaporation. As the solvent evaporates quickly into air at the early stage, it can be assumed that the final film thickness is without any solvent; the initial thickness  $L_{z,0}$  and evaporation constant  $\alpha$  can then be estimated (the latter parameter increases with increasing spin-coating rotation speed).

Phase separation during spin-coating at different rotation speeds was also simulated according to the evaporation data in Table 15.6; the simulation patterns are also shown in Figure 15.33. Among views of the 3D model shown here, the top view is the free surface of the polymer film, which formed the focal point of the study. As the domain thickness is very thin, very little change occurs in the morphology through the thickness. It can be observed from the simulation patterns in Figure 15.33 that when the rotation speed decreases the characteristic length grows, and this matches the trend shown experimentally. A comparison of the characteristic length of the numerical simulation and experimental data is shown in Figure 15.36.

**Table 15.6** Estimation of the evaporation constant.

Rotation speed (rpm)	$L_{z,t=3s}$	$L_{z,t=30s}$	Initial thickness, $L_{z,t=0s}$	Evaporation constant, $\alpha$
1000	$1.819 \times 10^{-5}$ m	$1.572 \times 10^{-7}$ m	$1.949 \times 10^{-5}$ m	0.821
3000	$7.561 \times 10^{-7}$ m	$1.346 \times 10^{-7}$ m	$1.6863 \times 10^{-5}$ m	1.098
7000	$5.337 \times 10^{-7}$ m	$1.029 \times 10^{-7}$ m	$1.2893 \times 10^{-5}$ m	1.130

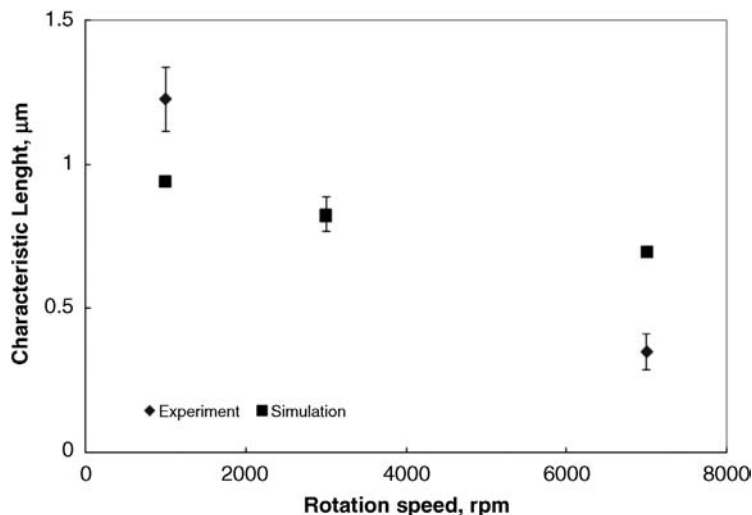


**Figure 15.36** Comparison of characteristic lengths of simulation and experimental patterns at different rotation speeds.

It can be seen from Figure 15.33 that, in the experimental results, the characteristic length decreases with increasing rotation speed, with a higher speed resulting in a smaller characteristic length. This trend was also simulated by the modeling results, as can be seen in the simulation results in Figures 15.33 and 15.36. As the rotation speed affects the rate of evaporation, a higher rotation speed in spin-coating will result in a faster evaporation of the solvent and thus a more rapid shrinking of the film in the thickness direction. As macromolecules move more slowly in a thinner film and solution with less solvent, the characteristic length of the pattern after slow-speed spin-coating will be larger than that after a fast-speed spin-coating.

The evolution of characteristic lengths for different rotation speeds in the numerical simulation is shown in Figure 15.37, where the characteristic length can be observed to have a peak value in the early stage. With most of the solvent escaping into the air, the morphology becomes stable and there is no obvious change in the characteristic length of the domain when the film has condensed (this point was also investigated in a previous study [96]).

Experimentally, the PS/PAA/solvent blend is spin-coated onto substrates with patterns of different geometric parameters. The composition ratio of the two polymers is also changed to investigate the influences on the resultant patterns in experiments. Typical SEM images of ternary phase separation with a PS:PAA weight ratio of 7:3 on different pattern strip widths are shown in Figure 15.38. These images show that the width ratio of the substrate pattern can alter the resultant morphology of the phase separation. Although the polymers are attracted to the respective areas on the substrate, the resultant patterns are not perfectly

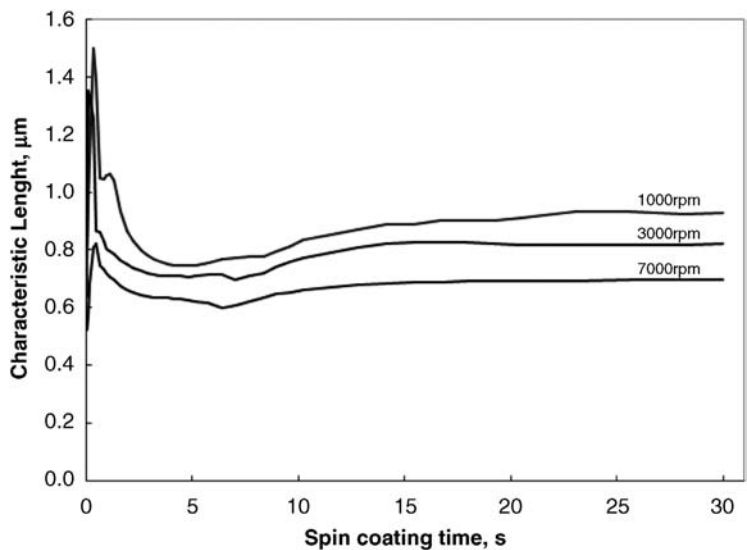


Figure 15.37 Evolution of characteristic lengths with time at different rotation speeds.

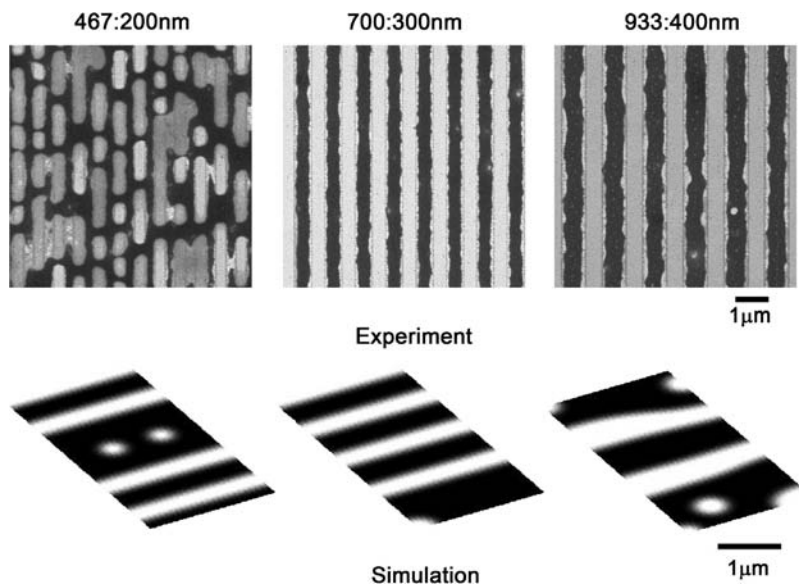


Figure 15.38 Phase separation of PS/PAA on different pattern strip widths functionalized with 1-octadecanethiol (ODT) and ( $\text{NH}_2$ ) according to Table 15.3 [72].

compatible with the desired shape. In order to investigate the quality of the phase separation according to the functionalized substrate patterns, a scaling factor,  $C_s$ , is introduced to determine quantitatively the compatibility of the morphology to the substrate patterns:

$$C_s = \frac{1}{2} \langle |\psi(\mathbf{k}) - S_k| \rangle \quad (15.72)$$

and,

$$S_k = \begin{cases} \frac{s_1(\mathbf{k})}{|s_1(\mathbf{k})|}, & s_1(\mathbf{k}) \neq 0 \\ 0, & s_1(\mathbf{k}) = 0 \end{cases} \quad (15.73)$$

where  $s_1(\mathbf{k})$  is the parameter in the surface energy expression for polymer 1, which denotes the strength of the surface attraction.  $S_k$  is the quantitative representation of the substrate attraction; then, clearly,

$$C_s \in [0, 1] \quad (15.74)$$

The greater the value of  $C_s$ , the more compatible is the resulting morphology with the functionalized substrate. For example, when  $C_s$  is equal to 1 the resulting pattern will replicate the substrate pattern exactly. However, if  $C_s$  is equal to 0.5 this represents a random phase separation, and  $C_s$  equal to 0 denotes a totally opposite phase pattern as desired by the substrate pattern. In order to measure the compatibility,  $C_s$ , of the SEM image, a template image representing the functionalized pattern on the substrate is applied to the original image, as shown in Figure 15.39.

The exact magnitude of the functionalization in a numerical simulation has yet to be determined. The absolute value of the surface energy term in Eq. (15.50) is changed and implemented in a series of numerical tests. The  $C_s$  values from numerical simulations with different values of  $f_s$  are plotted in Figure 15.40, where the composition ratio is PS : PAA = 70 : 30 and the pattern strip width ratio

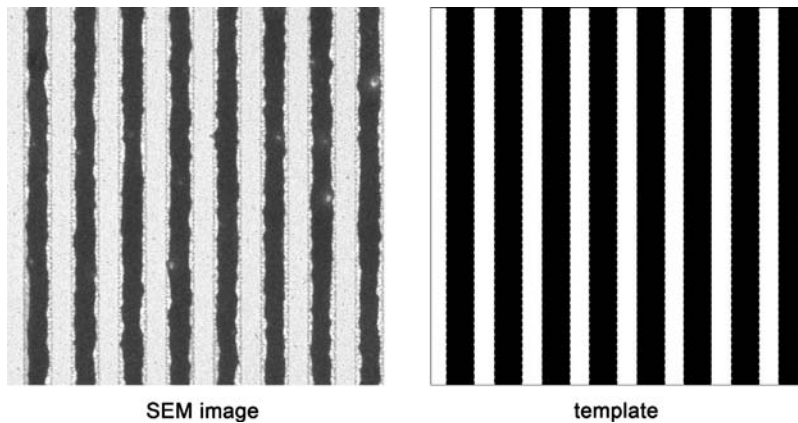


**Figure 15.39** Template image applied to the scanning electron microscopy image.

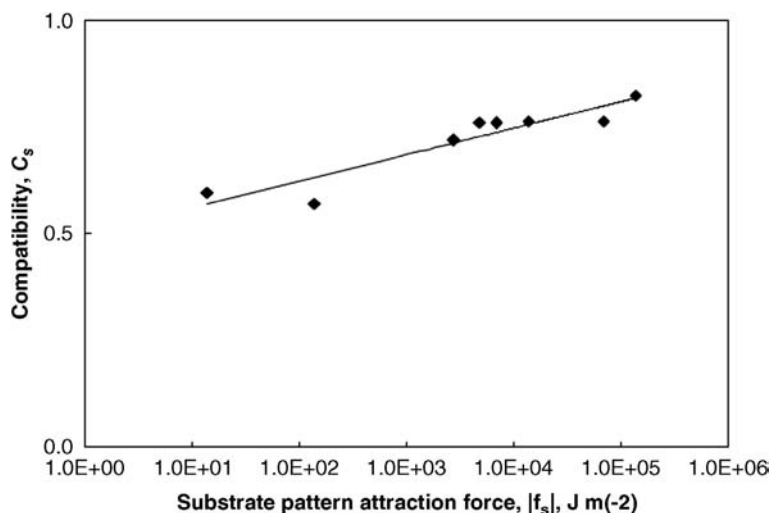


Figure 15.40 Effects of attraction force on compatibility,  $C_s$ .

is ODT:NH<sub>2</sub> = 700 : 300 nm. The  $x$ -axis value in this plot is the absolute value of  $f_s$ , as shown in Figure 15.32.

The compatibility of the morphology can be seen to increase with the value of  $|f_s|$  exponentially. However, by comparing this to the experimental results under different conditions the value of  $|f_s|$  is estimated as  $4.82 \times 10^3 \text{ J m}^{-2}$ .

The experimental and simulation resultant patterns are shown in Figure 15.38, where it can be seen that the ODT:NH<sub>2</sub> ratio of 700 : 400 nm results in the best compatibility in morphology when the weight ratio of PS : PAA is 7 : 3. It should be noted that, on a patterned substrate, the morphology evolution of the species in the solvent should be determined by the volume fraction of the two polymers rather than by the weight fraction. Generally, the  $C_s$  value is affected by the compatibility of the volume ratio of PS/PAA to the area ratio of ODT/NH<sub>2</sub> pattern strips. When the ODT/NH<sub>2</sub> strip width ratio is the same, the intrinsic characteristic length of the system should be close to the alternative strip width in order to obtain a refined pattern. In the experiment, the attraction force is also influenced by the effective functional groups in the polymer and the entanglement of the macromolecular chains. The  $C_s$  values from the simulation and experiments with the different strip widths are plotted in Figure 15.41.

It can be seen from the results shown in Figure 15.41 that the pattern strip width affects the  $C_s$  value of the phase separation. In different pattern strip widths, the  $C_s$  values can be compared as  $C_{s,933 \text{ nm}:400 \text{ nm}} > C_{s,700 \text{ nm}:300 \text{ nm}} > C_{s,467 \text{ nm}:200 \text{ nm}}$ , in both the experiments and modeling. However, the numerical simulation results are slightly less compatible with the substrate pattern than with the experimental results.

The SEM images of the phase-separated patterns with different PS : PAA weight ratios are shown in Figure 15.42. It can be seen that, in the modeled systems, the

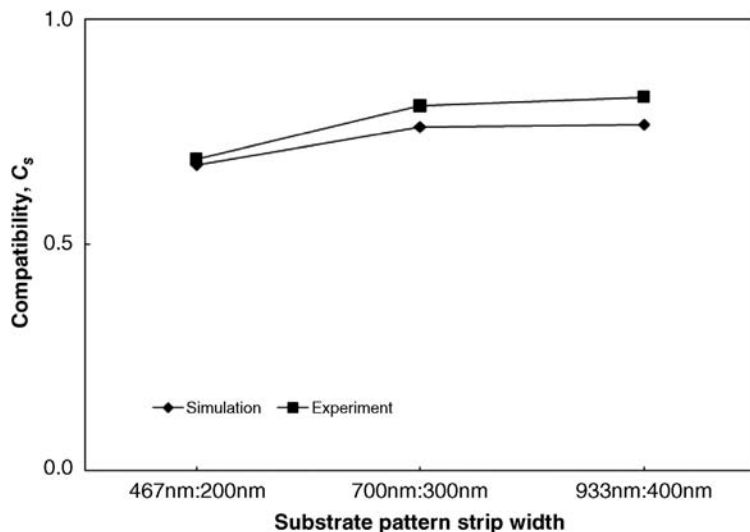


Figure 15.41 Changes if  $C_s$  with substrate pattern strip width.

solution with a weight ratio PS : PAA of 70 : 30 has the best compatibility with the desired pattern, and this also can be observed from the numerical simulation results shown in Figure 15.42, where the strip width ODT:  $\text{NH}_2$  is equal to 700 : 300 nm.

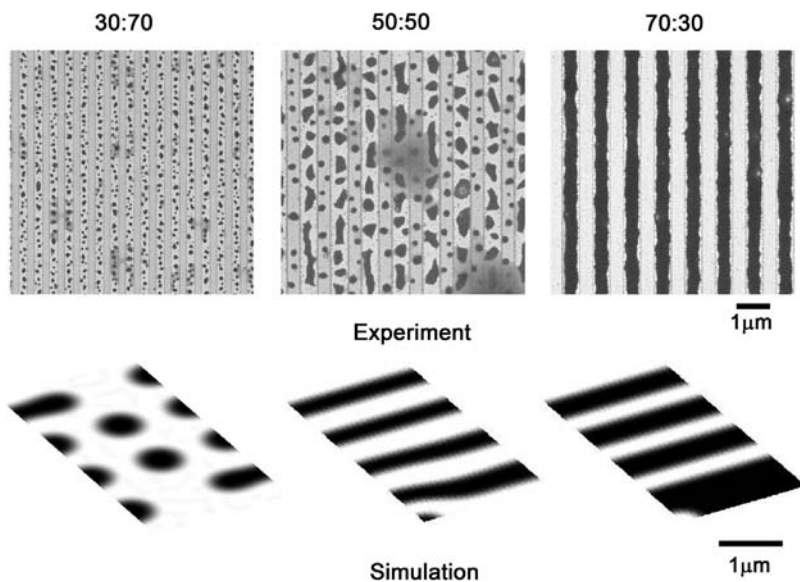
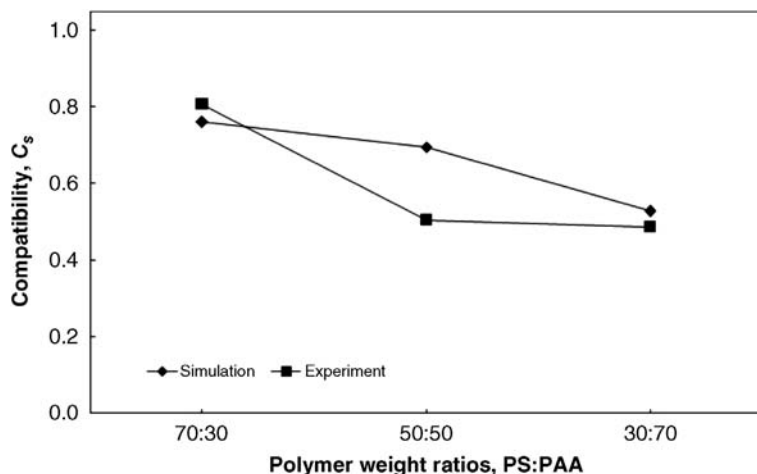


Figure 15.42 Scanning electron microscopy images of phase separation morphology in different polymer weight ratios (PS : PAA).





**Figure 15.43** Changes in  $C_s$  with polymer weight ratio.

The  $C_s$  values in the numerical simulation and the experiment results are plotted in Figure 15.43. The modeling results simulate the experiment results well on the trend of  $C_s$  with varying PS/PAA composition ratios, whereas the SEM image shows a better compatibility with the substrate pattern than with the simulation results.

The molecular weight of PAA has been changed to examine the effects of polymer molecular weight on the self-assembly on nanosized patterns. The Flory–Huggins-type local free energy can be affected by the molecular weights of the polymers, with the free energy barrier of two pure polymer phases being higher as the molecular weight was increased. Consequently, those polymers with higher molecular weights are less miscible with each other, and the phase separation will evolve more rapidly. A comparison of the experimental and simulated images with different PAA molecular weights is shown in Figure 15.44.

The more rapid evolution in the system with higher PAA molecular weights results in a larger characteristic length in the domain. The intrinsic characteristic length with PAA molecular weights of 50 k and 450 k mers no longer matches the alternative strip width, and therefore the compatibility will decrease in line with increases in PAA molecular weight. A comparison of the experimental and simulated results is shown in Figure 15.45.

#### 15.4.4

##### Summary

In this section, the Cahn–Hilliard numerical simulation of self-assembly with a polymer–polymer–solvent system was verified experimentally, and a real system of PS-PAA-DMF solvent was phase-separated during spin-coating. Some of the model parameters were derived directly from laboratory characterization. Due to

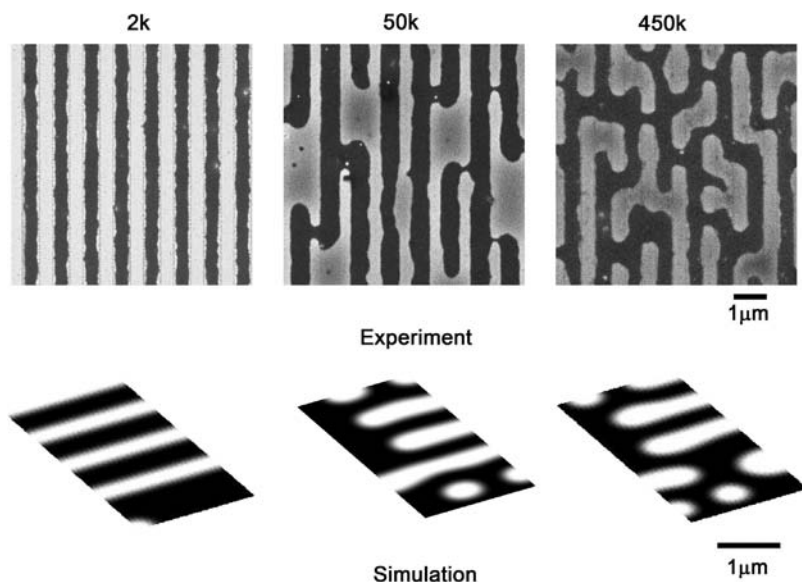


**Figure 15.44** Scanning electron microscopy images of phase separation morphology with different PAA molecular weights (in kDa).

uncertainties in mobility ( $M$ ) and gradient energy ( $\kappa$ ), a benchmarking method was developed to determine these parameters. Changes in the compatibility parameter ( $C_s$ ) with values of  $M$  and  $\kappa$  were investigated separately; subsequently, by comparing numerical and experimental results, values of  $M$  and  $\kappa$  were determined as  $3.63 \times 10^{-21} \text{ m}^5/(\text{J} \cdot \text{s})$  and  $1.821 \times 10^{-7} \text{ J m}^{-1}$ , respectively. An

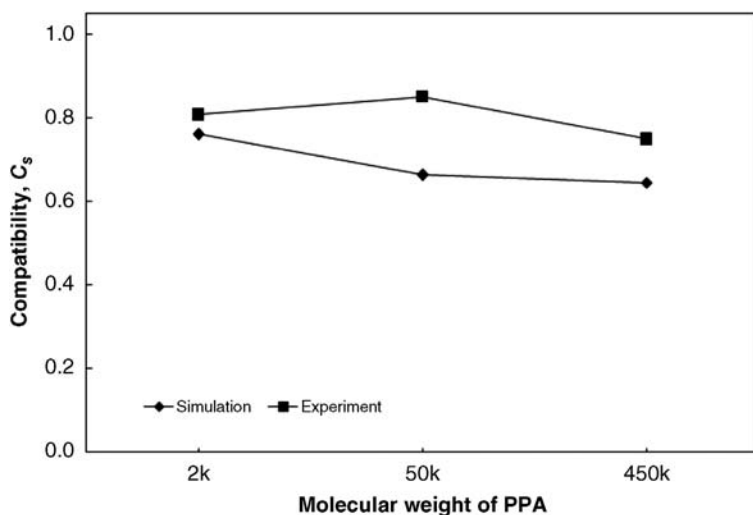


**Figure 15.45** Changes in  $C_s$  with different PAA molecular weights (in kDa).

ODT:  $\text{NH}_2$  heterogeneously functionalized patterned substrate was applied to the experimental blends during spin-coating. The magnitude of the surface energy term,  $f_s$ , was also determined by comparing simulated results with experimental results. The absolute value of  $f_s$  was determined as  $4.818 \times 10^3 \text{ J m}^{-1}$  in the present study.

The numerical simulation was consistent with experimental data with regards to influences of substrate pattern width, polymer weight ratio and polymer molecular weight of PAA. Both, experimental and simulated results showed that the intrinsic characteristic length should be compatible with the substrate pattern size for a refined phase separation pattern, according to the substrate pattern. Simulations also showed that the increase in polymer molecular weight can increase the speed of morphologic evolution. As the film thickness is very small the checkerboard structure of spinodal decomposition cannot be seen in these results, but they are present.

## 15.5

### Effects of Pattern Shapes and Block Copolymer

To investigate the effects of a more complicated pattern, a larger domain was simulated. The pattern on the substrate applied to the substrate surface is shown in Figure 15.46; the substrate pattern was designed to investigate the effects of different shapes, with the design containing characters of different sizes, squares, circles, and dead-end lines with triangles on the corners. The initial surface



Figure 15.46 The substrate pattern with complicated features.

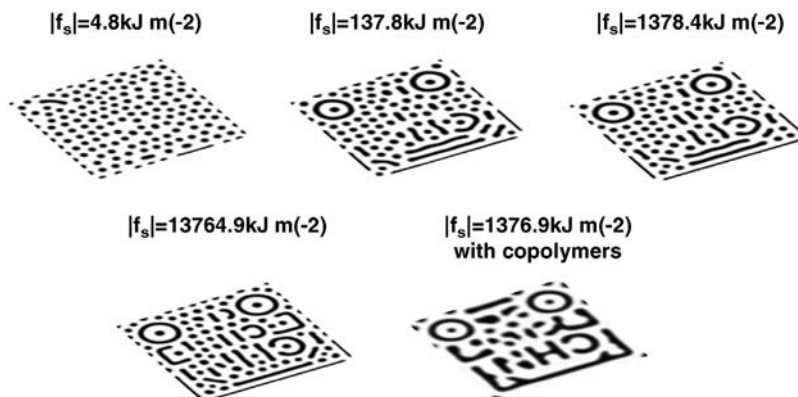


**Figure 15.47** The effects of attraction forces and the use of copolymers in self-assembly to complicated substrate patterns.

dimensions of the model were changed to  $12 \times 12 \mu\text{m}$ , and the initial thickness of the film was 1 mm (this shrank during solvent evaporation). The element in the modeling was  $384 \times 384 \times 16$ , and the average composition ratio of PS/PAA was changed to 38/62 to match the pattern. The resulting patterns from the simulation are shown in Figure 15.47.

It can be seen that, in a larger domain with complicated substrate patterns, the attraction factor must be increased to obtain a better replication. In general, the increase in attraction factor will in turn increase the refinement of the pattern according to the substrate pattern. However, as the substrate pattern has geometric features in different sizes, the attraction factor must be strong enough to force the intrinsic phase separation with unified characteristic lengths to match the substrate pattern in different sizes. This represents the main challenge to the replication of complicated patterns. It has been reported by Ming *et al.* [72] that the addition of a copolymer can improve the refinement of the final patterns in experiments. The reason for this is that the PAA-b-PS block copolymer will concentrate in the interface of the PS and PAA domains in the phase separation, thus decreasing the mixing free energy. Fundamentally, the addition of a block copolymer increased the miscibility of the two polymers. In order to simulate these phenomena, the Flory–Huggins interaction parameter is decreased from 0.22 to 0.1, so as to increase the miscibility of PS/PAA in the modeling. The resultant pattern is also shown in Figure 15.47, compared to cases without the addition of block copolymers; the images show that refinement of the phase-separated pattern is improved by the addition of a block copolymer.

The  $C_s$  values of the phase separation with complicated patterns are measured and plotted in Figure 15.48; these data show that the  $C_s$  value for the system with the block copolymer is 7.69E-01, which is higher than for the system without a block copolymer when the attraction forces are the same. The decrease in the Flory–Huggins interaction parameter increased miscibility of the polymers, which in turn decreased the miscibility gap of the polymers (as shown in Figure 15.4). At

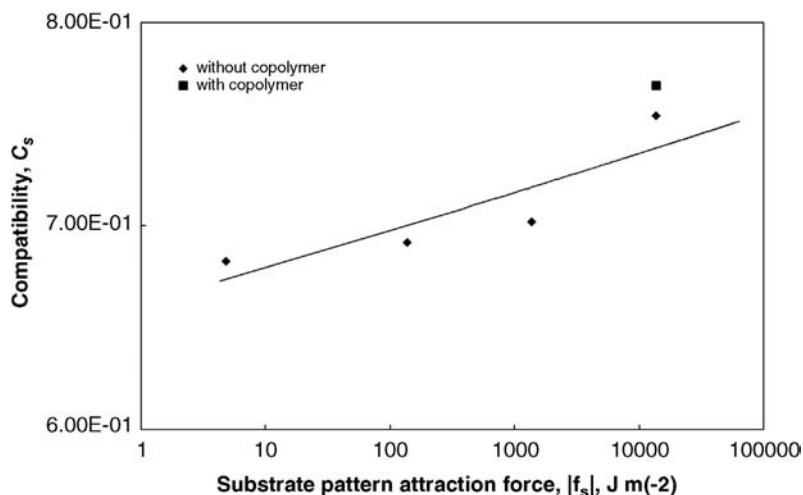


Figure 15.48 The effects of attraction forces on the compatibility index,  $C_s$ .

equilibrium, the two phases would be less concentrated in the different types of polymer, though this issue may need to be verified when the interaction parameter of the two polymers is changed.

## 15.6

### Conclusions

The numerical modeling methods for polymer blends have been reviewed in this chapter, with different categories such as volume-of-fluid, molecular dynamics and diffusion-controlled methods being introduced. Use of the Cahn–Hilliard method was emphasized for binary and ternary polymer systems with no obvious mechanical flux, while specific factors such as elastic energy and functionalized substrate were considered for purposes of comparison. The diffusion-controlled model described, using the Cahn–Hilliard equation as the constitutive equation, can be used to depict the gradient of the interface as well as the composition profile of partially miscible blends; hence, it is feasible to implement this equation in a polymer blend system. It should be noted that although these examples do not consider mechanical flux, additional constitutive equations (e.g., Navier–Stokes) can easily be added to this diffusion-controlled model.

Subsequently, a numerical model was introduced to simulate self-assembly by the phase separation of polymer blends on a heterogeneously functionalized substrate patterns. From thermodynamic principles, when polymer blends are quenched into the spinodal region in the phase diagram, phase separation can be initiated from small composition fluctuations in the blend. The Cahn–Hilliard equation is used to describe the energy profile in the domain with varying

compositions in different locations. According to Cahn and Hilliard, the total free energy in a blend consists of the local free energy and the free energy contributed by the composition gradient. In contrast, the Flory–Huggins equation was used to describe the local free energy term, which is a function of the composition and degrees of polymerization of two polymers.

The evolution of polymer composition in the spatial domain can be derived using the Cahn–Hilliard equation. In numerical simulations, the fourth-order nonlinear parabolic partial differential equations are solved using Fourier-spectral methods, while the partial differential equations are transferred by the discrete cosine transform into ordinary partial equations. The result is then transformed back with the inverse cosine transform to the ordinary space.

Thereafter, the mechanism of phase separation was investigated by numerical modeling. In the simulation, the characteristic length,  $R(t)$ , was obtained by measuring the pair-correlation function,  $g$ ; it was observed that  $Rt \propto t^{\frac{1}{3}}$ . In the case of strip patterns on the substrate, an  $R(t)$  value close to the intrinsic value on the substrate pattern would result in a better pattern after phase separation. Thus, a prediction of the evolution of  $R(t)$  with time might be used to design a good phase separation pattern according to the substrate pattern. In the case of substrate patterns, it was also shown that  $R(t)$  in the direction perpendicular to the substrate pattern strips were increased proportionally to  $t^{\frac{1}{3}}$  in the early stage, but that the rate of  $R(t)$  would decrease suddenly after a critical time,  $t_c$ . However, the increase in  $R(t)$  may be confined by the periodically changing length on the substrate pattern. When the inclusion of an elastic field into numerical modeling was investigated, this resulted in a slower evolution of phase separation, most likely due to addition of the free energy to the total free energy.

The ternary model was established to investigate the effects of a solvent in polymer blends during phase separation. In cases of constant solvent concentration it emerged that, the less solvent that was in solution, the slower was the evolution of the morphology in phase separation. This effect was due to the polymers being immiscible with each other, but both being miscible with the solvent. The addition of a solvent decreased the free energy level in the blend, which in turn slowed down the evolution of phase separation. The mechanism of phase separation with solvent evaporation was further complicated by dynamic solvent evaporation from the ternary system.

The numerical model with evaporation effects was verified experimentally. Whilst some of the parameters in the simulation were obtained under experimental conditions, there were three critical model parameters whose values were uncertain, namely mobility ( $M$ ), gradient energy coefficient ( $\kappa$ ), and the substrate pattern attraction factor ( $|f_s|$ ). In order to determine values for  $M$  and  $\kappa$ , the characteristic lengths of experiment patterns were measured using FFT analysis, and the two parameters were tuned in the numerical simulation by an inspection of results obtained from numerical modeling with the experiments. Having obtained values of  $M$  and  $\kappa$ ,  $|f_s|$  was determined by comparing the compatibility parameter,  $C_s$ , in numerical simulation and experiments. The numerical model could be verified from the experimental results by varying the parameters of substrate pattern

size, the composition ratio of the polymers, and their degrees of polymerization. Subsequently, the simulation results could be used to predict the trend in  $C_s$  values with changes in various other parameters.

## Acknowledgments

The authors appreciate the financial support provided by the National Science Foundation for this research (grant number NSF-0425826), and also the many investigators and research agencies that contributed to the chapter.

## References

- Walheim, S., Boltau, M., Mlynek, J., Krausck, G., and Steiner, U. (1997) Structure formation via polymer demixing in spin-cast films. *Macromolecules*, **30**, 4995–5003.
- Fink, Y., Winn, J.N., Fan, S., Chen, C., Michel, J., Joannopoulos, J.D., and Thomas, E.L. (1998) A dielectric omnidirectional reflector. *Science*, **282** (5394), 1679–1682.
- Mlynek, J., Walheim, S., Schaffer, E., and Steiner, U. (1999) Nanophase-separated polymer films as high-performance antireflection coatings. *Science*, **283**, 520–522.
- Deen, N.G., vanSint Annaland, M., and Kuipers, J.A.M. (2005) Numerical simulation of gas bubbles behaviour using a three-dimensional volume of fluid method. *Chem. Eng. Sci.*, **60**, 2999–3011.
- Scardovelli, R. and Zaleski, S. (1999) Direct numerical simulation of free-surface and interfacial flow. *Annu. Rev. Fluid Mech.*, **31**, 567–603.
- Hyman, J.M. (1984) Numerical methods for tracking interfaces. *Physica D*, **12**, 396–407.
- Rudman, M. (1997) Volume-tracking methods for interfacial flow calculations. *J. Numer. Meth. Fluids*, **24**, 671–691.
- Jeong, J.H. and Yang, D.Y. (1998) Finite element analysis of transient fluid flow with free surface using VOF (volume-of-fluid) method and adaptive grid. *Int. J. Numer. Methods Fluids*, **26**, 1127–1154.
- Tan, H.H., Zhao, Y., and Zhang, B. (2002) A high-resolution characteristics-based implicit dual time-stepping VOF method for free surface flow simulation on unstructured grids. *J. Comput. Phys.*, **183**, 233–273.
- Lafaurie, B., Nardone, C., Scardovelli, R., Zaleski, S., and Zanetti, G. (1994) Modelling merging and fragmentation in multiphase flows with surfers. *J. Comput. Phys.*, **113**, 137–147.
- Nadim, A., Gueyffier, D., Li, J., and Scardovelli, R. (1999) Volume-of-fluid interface tracking with smoothed surface stress methods for three-dimensional flows. *J. Comput. Phys.*, **152**, 423–456.
- Pilliod, J.E. Jr and Puckett, E.G. (2004) Second-order accurate volume-of-fluid algorithms for tracking material interfaces. *J. Comput. Phys.*, **199**, 465–502.
- Sorensen, M.R. and Voter, A.F. (2000) Temperature-accelerated dynamics for simulation of infrequent events. *J. Chem. Phys.*, **112**, 9599.
- Henkelman, G. and Jonsson, H. (2000) Improved tangent estimate in the nudged elastic band method for finding minimum energy paths and saddle points. *J. Chem. Phys.*, **113**, 9978.
- Binder, K. and Paul, W. (2008) Recent developments in Monte Carlo simulations of lattice models for polymer systems. *Macromolecules*, **41** (13), 4537–4550.
- Sun, D. and Guo, H. (2011) Influence of compositional gradient on the phase behavior of ternary symmetric homopolymer-copolymer blends: A Monte Carlo study. *Polymer*, **52**, 5922–5932.
- Detcheverry, F.A., Nealey, P.F., Pike, D.Q., Muller, M., and dePablo, J.J. (2009) Monte

- Carlo simulation of coarse grain polymeric systems. *Phys. Rev. Lett.*, **102**, 197801.
- 18 Müller, M., Pike, D.Q., and dePablo, J.J. (2011) Monte-Carlo simulation of ternary blends of block copolymers and homopolymers. *J. Chem. Phys.*, **135**, 114904.
  - 19 Muller, M. and Binde, K. (1995) Monte-Carlo simulation of ternary blends of block copolymers and homopolymers. *J. Chem. Soc., Faraday Trans.*, **91** (16), 2369–2379.
  - 20 Carmesin, I. and Kremer, K. (1988) The bond fluctuation method: A new effective algorithm for the dynamics of polymers in all spatial dimensions. *Macromolecules*, **21** (9), 2819–2823.
  - 21 Deutsch, H.P. and Binder, K. (1991) Interdiffusion and self-diffusion in polymer mixtures: A Monte Carlo study. *J. Chem. Phys.*, **94** (3), 459901.
  - 22 Malik, R., Hall, C.K., and Genzer, J. (2011) Phase separation dynamics for a polymer blend compatibilized by protein-like copolymers: A Monte Carlo simulation. *Macromolecules*, **44**, 8284–8293.
  - 23 Cahn, J.W. and Hilliard, J.E. (1958) Free energy of a nonuniform system. I. Interfacial free energy. *J. Chem. Phys.*, **28** (2), 258–267.
  - 24 Cahn, J.W. (1959) Free energy of a nonuniform system. II. Thermodynamic basis. *J. Chem. Phys.*, **30** (5), 1121–1124.
  - 25 Zhou, B. (2006) Simulation of Polymeric Membrane Formation in 2D and 3D. PhD thesis, Massachusetts Institute of Technology.
  - 26 Lin, F.-C., Lai, J.-Y., Lin, S.-F., and Wang, D.-M. (1997) Construction of ternary phase diagrams in nonsolvent/solvent/PMMA systems. *J. Polym. Sci. Pol. Phys.*, **44**, 1147–1160.
  - 27 Edmond, E. and Ogston, A.G. (1968) An approach to the study of phase separation in ternary aqueous systems. *Biochem. J.*, **109**, 569–576.
  - 28 Dely, J. and Bobak, A. (2006) Phase diagrams and multicritical points in the ternary mixed-spin alloy with a single-ion anisotropy. *Phys. Status Solidi C*, **3**, 187–190.
  - 29 Scott, R.L. (1949) The thermodynamics of high polymer solutions. V. Phase equilibria in the ternary system: Polymer 1-polymer 2-solvent. *J. Chem. Phys.*, **17** (3), 279–284.
  - 30 Hsu, C.C. and Prausnitz, J.M. (1973) Thermodynamics of polymer compatibility in ternary systems. *Macromolecules*, **7** (3), 320–324.
  - 31 Cahn, J.W. (1961) On spinodal decomposition. *Adv. Funct. Mater.*, **9**, 795–801.
  - 32 Cahn, J.W. (1965) Phase separation by spinodal decomposition in isotropic systems. *J. Chem. Phys.*, **42** (1), 93–99.
  - 33 Flory, P.J. (1953) *Principles of Polymer Chemistry*. Cornell University Press, Ithaca, New York.
  - 34 Huang, C., Olivera De La Cruz, M., and Voorhees, P.W. (1999) Interfacial adsorption in ternary alloys. *Acta Mater.*, **47** (17), 4449–4459.
  - 35 Saxena, R. and Caneba, G.T. (2002) Study of spinodal decomposition in a ternary polymer-solvent-nonsolvent system. *Polym. Eng. Sci.*, **42** (5), 1019–1031.
  - 36 Wise, S.M. (2003) Diffuse Interface Model for Microstructural Evolution of Stressed, Binary Thin Films on Patterned Substrates. PhD thesis, University of Virginia.
  - 37 deGennes, P.G. (1980) Dynamics of fluctuations and spinodal decomposition in polymer blends. *J. Chem. Phys.*, **72** (9), 4756–4763.
  - 38 Boyd, J.P. (2001) *Chebyshev and Fourier spectral methods: Second Revised Edition*, 2nd edn, Courier Dover Publications, N. Chelmsford, MA.
  - 39 Eyre, D.J. (1998) Unconditionally gradient stable time matching the Cahn–Hilliard equation. *Materials Research Society Symposium Proceedings*, Vol. 529. Materials Research Society.
  - 40 Eyre, D.J. (1998) An unconditionally stable one-step scheme for gradient systems. Available at: [www.math.utah.edu/~eyre/research/methods/stable.ps](http://www.math.utah.edu/~eyre/research/methods/stable.ps).
  - 41 Canuto, C., Hussaini, M.Y., Quarteroni, A., and Zang, T.A. (1987) *Spectral Methods in Fluid Dynamics*. Springer-Verlag, Berlin.
  - 42 Shou, Z. and Chakrabarti, A. (2001) Late stages of ordering of thin polymer films on chemically heterogeneous substrates: Energetics and metastability. *Polymer*, **42**, 6141–6152.
  - 43 Huang, C., Olvera de la Cruz, M., and Swift, B.W. (1995) Phase separation of ternary mixtures: Symmetric polymer blends. *Macromolecules*, **28**, 7996–8005.



- 44 Rogers, T.M., Elder, K.R., and Desai, R.C. (1998) Numerical study of the late stages of spinodal decomposition. *Phys. Rev. B*, **37** (16), 9638–9649.
- 45 Vegard, L. (1921) The constitution of mixed crystals and the space occupied by atoms. *Z. Phys.*, **5** (17), 17–26.
- 46 Denton, A.R. and Ashcroft, N.W. (1991) Vegard's law. *Phys. Rev. A*, **43** (6), 3161–3164.
- 47 Ag, K. (1983) *Theory of Structural Transformations in Solids*, Wiley, New York.
- 48 Seol, D.J., Hu, S.Y., Li, Y.L., Chen, J., Oh, K.H., and Chen, L.Q. (2003) Computer simulation of spinodal decomposition in constrained films. *Acta Mater.*, **51** (17), 5173–5185.
- 49 Copetti, M.L.M. and Elliot, C.M. (1990) Kinetics of phase decomposition process: Numerical solutions to Cahn–Hilliard equation. *Mater. Sci. Technol.*, **6**, 279–296.
- 50 Mauri, R., Shinnar, R., and Triantafyllou, G. (1996) Spinodal decomposition in binary mixtures. *Phys. Rev. E*, **53** (3), 2613–2623.
- 51 Kressler, J., Higashida, N., Shimomai, K., and Inoue, T. (1994) Temperature dependence of the interaction parameter between polystyrene and poly(methyl methacrylate). *Macromolecules*, **27**, 2448–2453.
- 52 Wise, S.M. and Johnson, W.C. (2003) Numerical simulations of pattern-directed phase decomposition in a stressed, binary thin film. *J. Appl. Phys.*, **94** (2), 889–898.
- 53 Wheeler, A.A., Boettinger, W.J., and McFadden, G.B. (1992) Phase-field model for isothermal phase transitions in binary alloys. *Phys. Rev. A*, **45** (10), 7424–7439.
- 54 Jones, R.A.L. (1993) Effect of long-range forces on surface enrichment in polymer blends. *Phys. Rev. E*, **47** (2), 1437–1440.
- 55 Goldburg, W.I., Shaw, C.-H., Huang, J.S., and Pilant, M.S. (1978) Spinodal decomposition in a binary liquid mixture. *J. Chem. Phys.*, **68** (2), 484.
- 56 Brown, G. and Chakrabarti, A. (1992) Surface-directed spinodal decomposition in a two-dimensional model. *Phys. Rev. A*, **46** (8), 4829–4835.
- 57 Wheeler, A.A., Boettinger, W.J., and McFadden, G.B. (1993) Phase-field model of solute trapping during solidification. *Phys. Rev. E*, **47** (3), 1893–1909.
- 58 Jones, R.A.L., Norton, L.J., and Kramer, E.J. (1991) Surface-directed spinodal decomposition. *Phys. Rev. Lett.*, **66** (10), 1326–1329.
- 59 Kielhorn, L. and Murthukumar, M. (1999) Spinodal decomposition of symmetric diblock copolymer/homopolymer blends at the Lifshitz point. *J. Chem. Phys.*, **110** (8), 4079–4089.
- 60 Karim, A., Douglas, J.F., Lee, B.P., Glotzer, S.C., Rogers, J.A., Jackman, R.J., Amis, E.J., and Whitesides, G.M. (1998) Phase separation of ultrathin polymer-blend films on patterned substrates. *Phys. Rev. E*, **57** (6), 6273–6276.
- 61 Chen, L.-Q. (1994) Computer simulation of spinodal decomposition in ternary systems. *Adv. Mater.*, **42** (10), 3503–3513.
- 62 He, D.Q. and Nauman, E.B. (1997) Spinodal decomposition with varying chain lengths and its application to designing polymer blends. *J. Polym. Sci. Polym. Phys.*, **35** (6), 897–907.
- 63 Altena, F.W. and Smolders, C.A. (1982) Calculation of liquid-liquid phase separation in a ternary system of a polymer in a mixture of a solvent and a nonsolvent. *Macromolecules*, **15**, 1491–1497.
- 64 Zhou, B. and Powell, A. (2006) Phase field simulations of liquid-liquid demixing during immersion precipitation of polymer membranes in 2D and 3D. *J. Membr. Sci.*, **268** (2), 150–164.
- 65 Tong, C., Zhang, H., and Yang, Y. (2002) Phase separation dynamics and reaction kinetics of ternary mixture coupled with interfacial chemical reaction. *J. Phys. Chem. B*, **106**, 7869–7877.
- 66 Kramer, E.J., Green, P., and Palmstrom, C. (1984) Interdiffusion and marker movements in concentrated polymer-polymer diffusion couples. *Polymer*, **25**, 473–480.
- 67 Composto, R.J., Kramer, E.J., and White, D. M. (1987) Fast macromolecules control mutual diffusion in polymer blends. *Nature*, **328**, 234–236.
- 68 Rhee, J. and Crist, B. (1991) Thermodynamics and phase separation in melt blends of polyethylene and model copolymers. *Macromolecules*, **24** (20), 5663–5669.
- 69 Balluffi, R.W., Allen, S.M., and Carter, W.C. (2006) *Kinetic Processes in Materials*, 1st edn,

- Wiley-Interscience, Cambridge, Massachusetts.
- 70 Battacharyya, S. and Abinandanan, T.A. (2003) A study of phase separation in ternary alloys. *Bull. Mater. Sci.*, **26**, 193–197.
  - 71 Altena, F.W. and Smolders, C.A. (1982) Calculation of liquid-liquid phase separation in a ternary system of a polymer in a mixture of a solvent and a nonsolvent. *Macromolecules*, **15**, 1491–1497.
  - 72 Wei, M., Fang, L., Lee, J., Somu, S., Xiong, X., Barry, C., Busnaina, A., and Mead, J. (2009) Directed assembly of polymer blends using nano-patterned templates. *Adv. Mater.*, **21**, 794–798.
  - 73 Johnson, W.C. and Wise, S.M. (2002) Phase decomposition of a binary thin film on a patterned substrate. *Appl. Phys. Lett.*, **81** (5), 919–921.
  - 74 Shang, Y. and Kazmer, D. (2012) A Matlab program for quantitative simulation of self-assembly of polymer blend films with nanoscaled features. *Int. J. Computer-Aided Eng. Technol.*, **4**, 181–192.
  - 75 Toral, R., Chakrabarti, A., and Gunton, J.D. (1988) Numerical study of the Cahn-Hilliard equation in three dimensions. *Phys. Rev. Lett.*, **60** (22), 2311–2314.
  - 76 Bray, A.J. (1994) Theory of phase-ordering kinetics. *Adv. Phys.*, **43** (3), 357–459.
  - 77 Shang, Y., Kazmer, D., Wei, M., Mead, J., and Carol, B. (2008) Numerical simulation of phase separation of immiscible polymer blends on a heterogeneously functionalized substrate. *J. Chem. Phys.*, **128**, 224909.
  - 78 Kielhom, L. and Muthukumar, M. (1999) Phase separation of polymer blend film near patterned surfaces. *J. Chem. Phys.*, **111** (5), 2259–2269.
  - 79 Bornside, D.E., Macosko, C.W., and Scriven, L.E. (1989) Spin coating: One-dimensional model. *J. Appl. Phys.*, **66** (11), 5185–5193.
  - 80 Jones, R.A.L., Kramer, E.J., Rafailovich, M. H., and Sokolov, J. (1989) Surface enrichment in an isotopic polymer blend. *Phys. Rev. Lett.*, **62** (3), 280–283.
  - 81 Puri, S. and Frisch, H.L. (1997) Surface-directed spinodal decomposition: Modelling and numerical simulations. *J. Phys. Condens. Matter*, **9**, 2109–2133.
  - 82 Seok, C. and Freed, K.F. (2000) Polymer melts and polymer solutions near patterned surfaces. *J. Chem. Phys.*, **112** (14), 6443.
  - 83 Winesett, D.A., Ade, H., Sokolov, J., Rafailovich, M., and Zhu, S. (2000) Substrate dependence of morphology in thin film polymer blends of polystyrene and poly(methyl methacrylate). *Polym. Int.*, **49** (5), 458–462.
  - 84 Venugopalt, G. and Krause, S. (1992) Development of phase morphologies of poly(methyl methacrylate)-polystyrene-toluene mixtures in electric fields. *Macromolecules*, **25** (18), 4626–4634.
  - 85 Wang, H. and Composto, R.J. (2002) Kinetics of surface and interfacial fluctuations in phase separating polymer blend films. *Macromolecules*, **35** (7), 2799–2809.
  - 86 Cyganik, P., Bernasik, A., Nudkowski, A., Bergues, B., Kowalski, K., Rysz, J., Lekki, J., Lekka, M., and Postawa, Z. (2001) Phase decomposition in polymer blend films cast on substrates patterned with self-assembled monolayers. *Vacuum*, **63**, 307–313.
  - 87 Cui, L., Zhang, Z., Li, X., and Han, Y. (2005) Surface-induced phase separation of binary polymer blends on the chemically patterned substrate. *Polym. Bull.*, **55**, 131–140.
  - 88 Boltau, M., Walheim, S., Mlynek, J., Krausch, G., and Steiner, U. (1998) Surface-induced structure formation of polymer blends on patterned substrates. *Nature*, **391**, 877–879.
  - 89 Bartels, C.R., Crist, B., and Graessley, W.W. (1984) Self-diffusion coefficient in melts of linear polymers: Chain length and temperature dependence for hydrogenated polybutadiene. *Macromolecules*, **17** (12), 2702–2708.
  - 90 Tsay, C.S. and McHugh, A.J. (1990) Mass-transfer modeling of asymmetric membrane formation by phase inversion. *J. Polym. Sci. Polym. Phys.*, **28** (8), 1327–1365.
  - 91 Chen, L.-P., Lin, D.-J., Shih, C.-H., Dwan, A.-H., and Gryte, C. (1999) Pvd membrane formation by diffusion-induced phase separation-morphology prediction based on phase behavior and mass transfer modeling. *J. Polym. Sci. Polym. Phys.*, **37** (16), 2079–2092.
  - 92 Kim, Y.D., Kim, J.Y., Lee, H.K., and Kim, S. C. (2001) A new modeling of asymmetric membrane formation in rapid mass transfer system. *J. Membr. Sci.*, **190** (1), 69–77.

- 93 Shvarts, A.G. (1956) *The Compatibility of High Polymers*, Kolliodn, Zh.
- 94 Brandrup, J., Immergut, E.H., Grulke, E.A., and Abe, A. (eds) (2003) *Polymer Handbook*, 4th edn, John Wiley & Sons, Hoboken, NJ.
- 95 Yu, Y., Zhang, L., and Eisenberg, A. (1998) Morphogenic effect of solvent on crew-cut aggregates of amphiphilic diblock copolymers. *Macromolecules*, **31** (4), 1144–1154.
- 96 Shang, Y., Kazmer, D., Wei, M., Barry, C., and Mead, J. (2009) Numerical simulation of the self-assembly of a polymer–polymer–solvent ternary system on a heterogeneously functionalized substrate. *Polym. Eng. Sci.*, **50** (12), 2329–2339.



## 16

# Optical Microscopy (Polarized, Interference, and Phase-Contrast Microscopy) and Confocal Microscopy

*Muruganathan Ramanathan and Seth B. Darling*

## 16.1

### Introduction

Optical microscopy (OM), which is also known as light microscopy or compound microscopy, is one of the oldest topographic morphology characterization techniques, dating back to the seventeenth century. Yet, even 400 years after its invention, OM remains a key characterization tool in a wide variety of disciplines including biology, mineralogy, crystallography, and materials sciences. Today, advanced OM is used as a common characterization technique in various stages of industrial processes including the manufacture, testing and/or failure analysis of metals, ceramics, foods, and polymers.

During recent decades, OM has played a significant role in the development of polymer-based materials and devices [1,2]. More recently, topographic characterization techniques have advanced beyond the resolution of visible light by the use of lasers or particles such as electrons, or of scanning probes to investigate structures down to atomic resolution. Despite these major advances in microscopic techniques, the role of OM is irreplaceable – especially when probing polymer morphologies and polymer blend morphologies that fall within length scales ranging from hundreds of nanometers to microns and even to millimeters [3]. Some examples of classic structures with a variety of length scales are depicted in Figure 16.1. These structures are obtained from a thin film of a metal-containing block copolymer – poly(styrene-*block*-ferrocenyldimethylsilane) – when it is subjected to hybrid annealing (thermal annealing followed by solvent annealing) [4]. The point here is that whereas OM plays an unprecedented role in identifying large fractal-like patterns, nanoscopic techniques such as atomic force microscopy (AFM) and transmission electron microscopy (TEM) are used to probe the fine structures within the large microscopic patterns. Clearly, OM is a complementary member of the “toolkit of polymer science.”

Advanced developments in optics and other components of OM have enabled more sophisticated variations in the technique, including bright-field, dark-field, polarization, interference and phase-contrast microscopies [5,6]. In the following

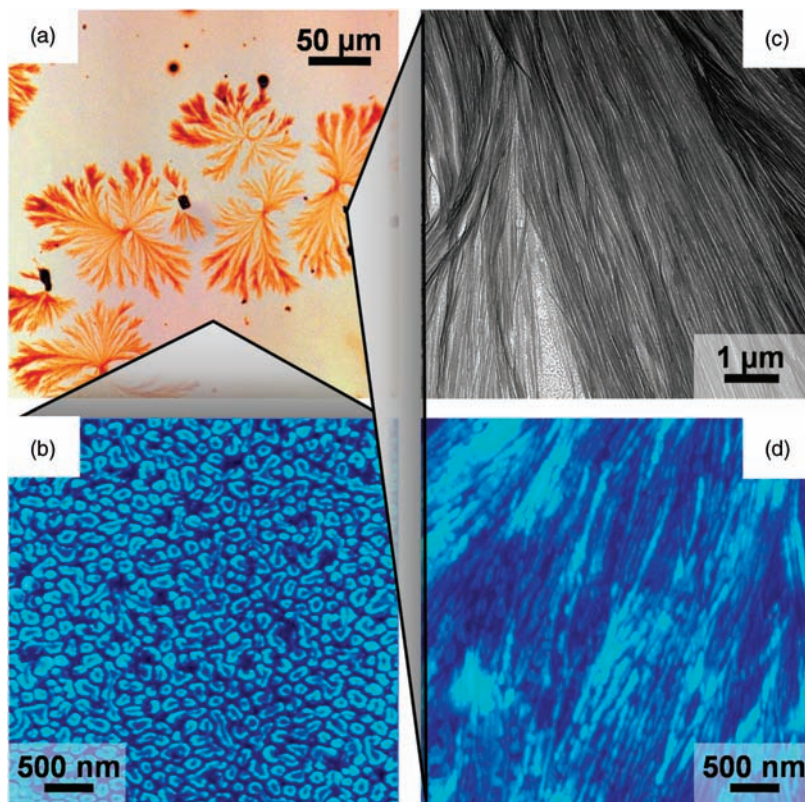


**Figure 16.1** Image showing the morphological information at different length scales on a dewetted polymeric thin film as characterized by (a) optical microscopy, (b) transmission electron microscopy, and (c,d) atomic force microscopy. Reprinted with permission from Ref. [4]; © 2009, Royal Society of Chemistry.

section, a brief overview is provided of the various microscopic techniques that are used in the characterization of polymer blend morphologies. Following a technical overview of some of the microscopic techniques employed, the topic of mesoscale morphologies in polymer blends is introduced. Finally, the microscopic characterization of various types of polymer–polymer blends is discussed in detail.

## 16.2

### Optical and Confocal Microscopy: A Brief Overview

Resolution, contrast and magnification are the three vital parameters of a microscope that overcome the limitations of the human eye as an instrument for the visual inspection of fine morphological details. In a conventional optical microscope, each individual point of the specimen is imaged by the objective lens, which determines the resolution of the optical system. Here, the resolution is

**Table 16.1** Optical microscopic techniques and their resolution limits.

Technique	Resolution
Light microscopy	~500 nm
Scanning near-field optical microscopy	~20 nm
Phase-measurement interferometric microscopy	1 $\mu\text{m}$ (lateral) and 0.6 nm (axial)
Laser scanning confocal microscopy	0.2 $\mu\text{m}$ (lateral) and 0.5 $\mu\text{m}$ (axial)

defined as the shortest distance between two points on a specimen that can be clearly distinguished by the image-processing system as separate entities. The numerical aperture (NA) determines this resolving power in conjunction with the wavelength of the light, which can be defined as  $r = 0.61 \lambda / \text{NA}$ , where  $r$  is the resolution and  $\lambda$  is the imaging wavelength [6,7]. Some of the most common optical microscopy techniques, and details of their resolution, are summarized in Table 16.1.

Perhaps the most common standard OM technique is bright-field imaging in transmittance mode [8]. Although, in this case, the absorbance of light by the sample provides the contrast, the issue of nonabsorbent samples that may be transparent and lack any contrast in this mode is often encountered. Fortunately, this problem has been overcome by employing various contrast-enhancing techniques, and the various illumination techniques and origins of contrast enhancement that cause minimal or no disruption to the specimen are summarized in Table 16.2.

In phase-contrast microscopy, the phase of the light is changed before it enters the specimen and is then recombined with light that has passed through the specimen, which results in an enhanced differentiation within a specimen [9,10]. This technique can be operated either in reflection or transmission mode. In polarization microscopy, polarized light (light which vibrates only in a single plane) is viewed under crossed polars; the polarization state of the light transmitted through or reflected from a specimen (birefringence) is detected by placing the sample between crossed polarizers [11]. In bright-field microscopy the intensity of the light is transmitted through the object, whereas in dark-field microscopy the light is scattered by the sample [12]. Fluorescence microscopy provides yet another contrast mechanism in which the specimen is usually stained with fluorescent dyes, if the samples are not autofluorescent. In this method, electrons are first excited by illumination and subsequently decay to the ground state; this causes the emission of photons of light that provide contrast enhancement [13,14].

**Table 16.2** Various illumination techniques and their contrast mechanisms.

Illumination mode	Contrast Mechanism
Bright-field	Absorption of light in the sample
Dark-field	Light scattered by the sample
Cross-polarized light	Rotation of polarized light through the sample
Phase contrast	Interference of different path length of light through the sample

Standard optical microscopic techniques are limited to optically thin specimens. An increased fluorophore density, a high refractive index contrast (which is a possible scenario in polymer blends) and attenuation due to the long optical path may each increase the optical density of the specimen, and this will render a sample extremely difficult (perhaps even impossible) to image using standard techniques [15]. In order to address this issue, confocal optical microscopy was developed, which combines the optical components of typical microscopy and scattering devices [16]. Although this technique is widely used in the biological sciences, the condensed matter physics community has recently started to use the technique to study the structure and dynamics of complex fluids.

Laser scanning confocal microscopy (LSCM) is an advanced version of confocal microscopy [17] in which the images are of a relatively high resolution and well-focused, mainly because the background is eliminated and the signal-to-noise ratio is optimal. In addition to these qualitative enhancements, LSCM permits a quantitative approach to the imaging of optical probes and also provides three-dimensional (3D) imaging and 3D image reconstruction capabilities [13]. These facilities are extremely useful with regards to the depth analysis of thick translucent samples, and also of layer-by-layer assemblies of polymeric materials and nanocomposites.

### 16.3

#### Mesoscale Morphologies in Polymer Blends: Spherulites and Microcrystallites

A polymer blend is generally defined as a combination of two or more polymers resulting from common processing steps; examples include the molten state mixing of two or more polymers and the casting of two or more polymers from a common solvent [18]. In earlier days, polymer blends were considered analogous to metal alloys and hence were referred to as “polymer alloys”; however, as knowledge of these systems has advanced in recent years this notion has now largely been rejected [19,20]. Depending on the nature of the polymers used in the blend, the blending can be either reactive or nonreactive [21]; the process can be further categorized as either miscible (homogeneous) or immiscible (heterogeneous) blends. In heterogeneous blends the glass transition temperature ( $T_g$ ) of every polymer involved in the blend is easily resolvable, whereas the homogeneous blend exhibits only one  $T_g$ -value [22,23]. Based on the interactions between the component polymers, immiscible polymer blends may be further differentiated as either compatible or noncompatible; typically, compatible polymer blends exhibit macroscopically uniform physical properties, whereas noncompatible blends differ in their macroscopic properties [19,24–26].

Polymer blends are interesting and highly important in terms of the ability to develop and control morphologies. For instance, by blending polymers with different physical, chemical or physico-chemical properties it is possible to develop a variety of morphologies that would differ from those exhibited by neat polymers. For instance, the blending of two amorphous polymers A and B, both of which are



colorless and transparent but demonstrate a difference in their refractive indexes of at least 0.003, has been shown to produce an opaque material. Although the neat polymers are transparent their blend is opaque, due to the fact that the size of phases exceeds 500 nm (i.e., the wavelength of visible light) [27].

Polymer blends provide a wide range of morphological structures, from coarse to fine. Both, optical and confocal microscopy have been used to characterize blend morphologies in sizes ranging from a few hundred nanometers to tens and hundreds of microns. Morphologies of this size range that encompasses both hundreds of nanometers and hundreds of microns are denoted as “mesoscale” morphologies [28]. The first set of mesoscale morphologies in polymeric blends was observed during the mid-twentieth century, when early studies in the field (conducted between the early 1950s and late 1980s) were largely devoted to a morphological understanding of polymer blends in which one or both polymers were crystallizable.

Spherulites are a common structural product of polymer crystallization from melts or concentrated solutions [29–31], and were the first microscopic structures ever to be observed, to be systematically studied, and to be reported in polymer blend films [32]. Spherulites can be obtained from a homopolymer as long as it is semicrystalline (highly ordered molecular structure with sharp melting point) [33,34]. In the case of polymeric blends, when one of the components is crystallizable its crystallization plays a dominant role in determining the morphology of the system. In contrast, in the case of amorphous blends the dominant factor in the formation of the morphology is the free energy of mixing of the components. In the blend the preference for a second component (amorphous or semicrystalline) may have a major effect on the final structure of the system [19,22,26].

Fully developed spherulites are usually microscopic and exhibit radial symmetry [19,35–38]; a schematic of a birefringent structure of a spherulite is shown in Figure 16.2 [28]. Nucleation and growth are the key mechanisms of spherulite formation [30,32,34,39,40]. Internal fluctuations in the system cause homogeneous

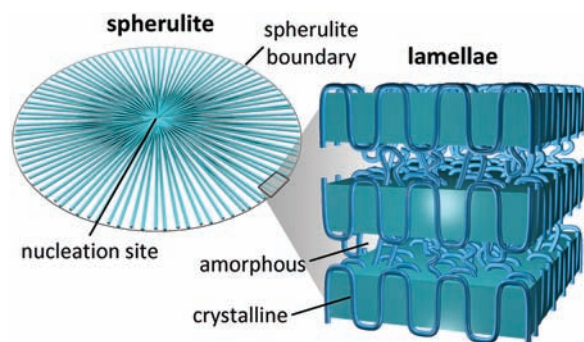


**Figure 16.2** Schematic representation of the birefringence structure of spherulites. The high-power image shows the helical chains stacked together in a well-ordered lattice of crystalline

lamellae and amorphous interlamellar links. The nucleation site of spherulization and its radial boundary are indicated. Reprinted with permission from Ref. [28]; © 2011, Elsevier.

nucleation, whereas foreign particles induce secondary nucleation. Gránásy and coworkers have provided a detailed mechanistic investigation of polycrystalline pattern formation, including the spherulization process [41–43].

## 16.4

### Optical Characterization of Mesoscale Morphologies in Polymer Blends

#### 16.4.1

##### Crystalline–Crystalline Blend

Spherulites from polymeric blends are frequently viewed using polarized optical microscopy (POM). The reason for such preferential use of the polarization mode is that the refractive index of spherulites in a radial direction differs from that in a tangential direction; this, in turn, leads to the development of a Maltese cross pattern of birefringent structures when viewed with polarized light between cross-polarizers [38]. A classic example showing the difference between polarization mode and standard reflection mode in microscopic studies on polymeric blend morphologies is shown in Figure 16.3 [44]; in Figure 16.3a–c the POM images of

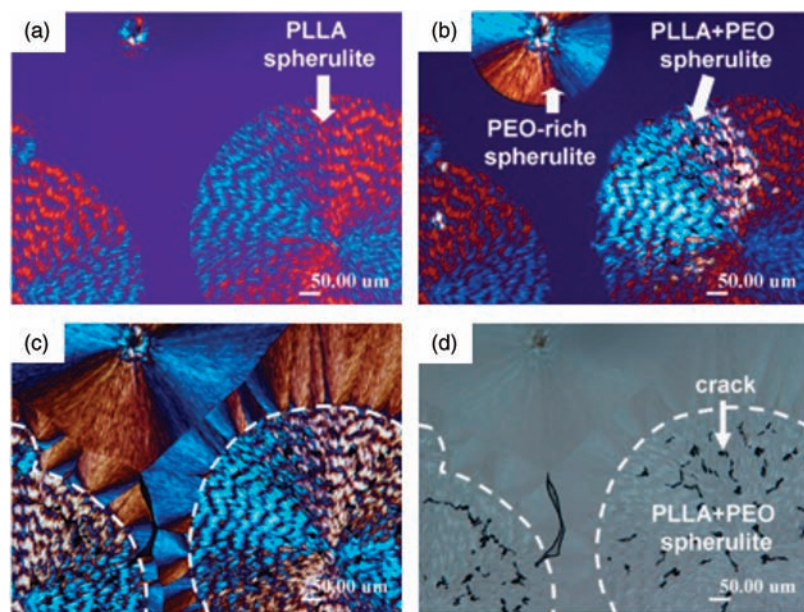


**Figure 16.3** POM images revealing the two types of spherulite and cracks in the PEO/PLLA (80/20) blend. The blend was crystallized at  $T_c = 110^\circ\text{C}$  and then cooled to ambient temperature and kept for (a) 9 s, (b) 12 s and (c)

21 s; (d) OM image of the sample in panel (c), showing cracks in the overlapping PEO/PLLA spherulites. Reprinted with permission from Ref. [44]; © 2011, Nature Publishing Group.

the spherulites show ring bands, whereas in Figure 16.3d an OM image shows cracks.

Both poly(ethylene oxide) (PEO) and poly(L-lactic acid) (PLLA) are crystalline polymers; consequently, either PEO or PLLA by themselves as single components can crystallize into spherulites. The blending of these two spherulite-forming polymers would result in an independent growth of spherulites of each polymer; moreover, these may impinge and overlap on each other, leading to complex interference and behavior between the cracks and ring bands. Woo *et al.* have blended these two polymers at various compositions in order to understand the correlation between the lamellar orientation in ring-banded spherulites and crack patterns in blends [44]. By examining the micrographs shown in Figure 16.3, it was possible to follow the evolution of the ring bands of PLLA spherulites in the first step (at crystallization temperature,  $T_c$ ) and of PEO spherulites in the second step (at ambient temperature) by using POM, although the cracks could not be clearly observed in the POM images. The cracks were clearly visible on the OM data, and by overlaying OM data on POM data it could be concluded that the cracks are formed along with the ring bands in the spherulites of the blend. POM can be used to help identify three distinct areas. First, when the blend was crystallized at  $T_c = 110^\circ\text{C}$ , the PLLA component showed characteristic zig-zag ring-bands (Figure 16.3a) with large inter-ring spacing in the spherulites. On cooling from  $T_c$  to ambient temperature, the PEO began to develop spherulites that eventually overlapped and impinged on the PLLA spherulites (Figure 16.3b and c). In Figure 16.3c and d, the same area was imaged using POM and OM modes, respectively. These micrographic investigations also helped to confirm that the cracks only appeared in the blend films when spherulites from two crystalline polymer overlapped; that is, no cracks were observed in either neat PEO spherulites or neat PLLA spherulites. Rather, cracks appeared in regimes where two different crystals were in contact with, were impinging, or were overlapping each other. As the spherulitic domains are randomly overlapped, the cracks were typically irregular.

OM has also been used to explore the compatibility and miscibility of amorphous–amorphous, amorphous–crystalline and crystalline–crystalline polymer blends. For example, Kalfoglou explored the compatibility of low-density polyethylene (LDPE) and poly( $\epsilon$ -caprolactone) (PCL) using OM in conjunction with dynamic mechanical and differential scanning calorimetry (DSC) techniques [25]. The results of this morphological examination revealed that, at low PCL concentrations and when the specimens were severely quenched, a uniform microspherulitic structure was formed. In contrast, Inoue and coworkers showed that blends of miscible crystalline/crystalline polymer would exhibit a wide variety of supra-molecular structures and mesoscale morphologies when compared to amorphous crystalline blend systems [3,45,46]. For instance, when the effects of a poly(vinylidene fluoride) (PVDF) component on the crystallization kinetics, crystalline structure, phase transition and morphology of polymorphic poly(butylene adipate) (PBA) in miscible PVDF/PBA binary blend were investigated by Yang *et al.* [45], the results indicated that the crystallization rate of PBA would be influenced

positively by PVDF at a lower PVDF concentration, but increasing the PVDF concentration would adversely affect the crystallization rate of PBA. Based on the POM images presented in Figure 16.4, it was found that at a lower PVDF concentration (<50%) a small amount of PVDF was distributed (as indicated by arrow) in the molten PBA (Figure 16.4a). Further decreasing the temperature of the system below the crystallization point of PBA revealed PVDF spherulites and a bright refringence of a large amount of PBA spherulites (Figure 16.4b). A lattice match analysis indicated that the PBA crystals are able to grow on the surface of the PVDF crystal, which acts as the nucleating agent via an epitaxial mechanism, although this trend was reversed when the PVDF concentration increased

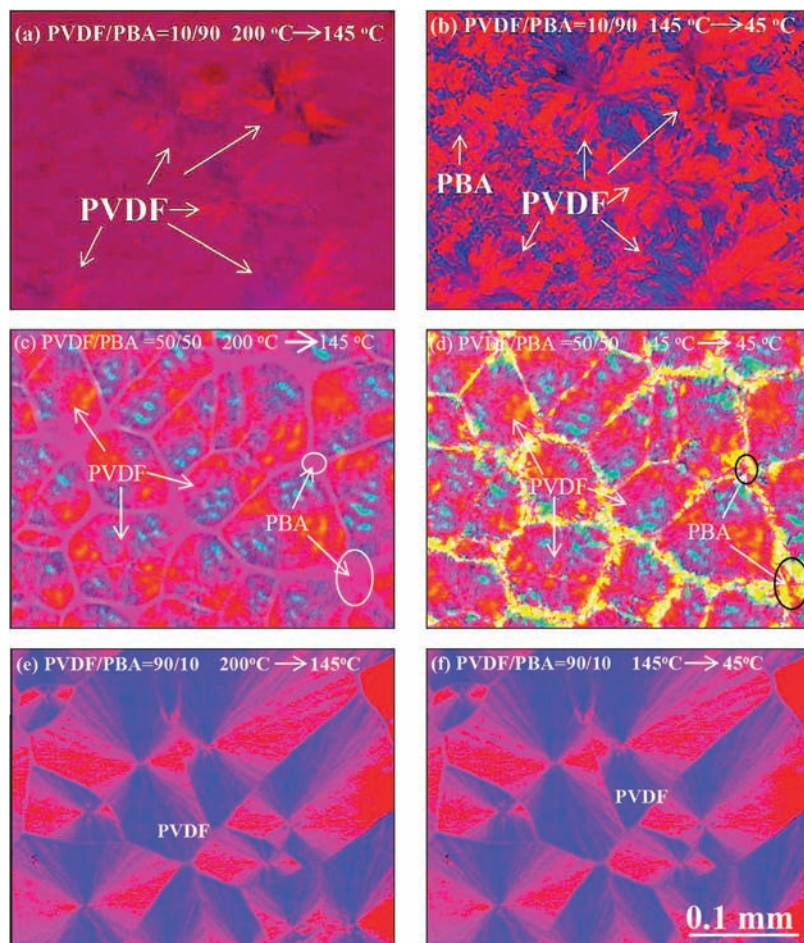


**Figure 16.4** POM images of the miscible crystalline/crystalline (PVDF/PBA) blend, showing ratio-dependent mesoscale morphologies. Cooling and quenching effects on these

morphologies are shown at the left and right, respectively. Reprinted with permission from Ref. [45]; © 2010, American Chemical Society.

beyond 50%. In Figure 16.4c, the PVDF was seen to be filled in the predominant region, as opposed to PBA, and this was further confirmed at lower temperatures, where the PBA is clearly seen to be restricted among the PVDF spherulites (Figure 16.4d). At very high PVDF concentrations, the PVDF spherulites were directly impinged and occupied almost the entire region (Figure 16.4e). As the PBA was completely entrapped in the interlamellar/interfibrillar region of the PVDF matrix, cooling of the system did not significantly change the microscopic morphology (Figure 16.4e). Similar results of ratio-dependent birefringence formation and the trapping/expulsion of a minor component were also seen when the miscible components of crystalline PVDF were blended with crystalline poly(butylene succinate) (PBS) [47].

#### 16.4.2

##### Crystalline–Amorphous Blend

The morphology of polymer blends that consist of one crystallizable component and one noncrystallizable amorphous compound has been studied in detail by several groups, with attention focused on various crystalline–amorphous combinations and compositions [48–50]. A single  $T_g$ -value always characterizes crystalline–amorphous blends, and is typically an intermediate value between that of the pure homopolymers; the exact  $T_g$  depends on the weight fraction of the two polymers, however. Highly crystalline polymers that have been studied in crystalline–amorphous blends include poly( $\epsilon$ -caprolactone) (PCL), poly(phenylene oxide) (PPO), poly(ethylene oxide) (PEO), poly(butylene terephthalate) (PBT), poly(ethyleneterephthalate) (PET), and high- and low-density polyethylene (HDPE and LDPE, respectively), whereas poly(vinyl chloride) (PVC) and poly(methyl methacrylate) (PMMA) are examples of amorphous polymers used for blending studies [51].

As a rule of thumb the crystalline–amorphous blend composition is soft (the behavior is more amorphous than crystalline) when the blend contains more than 70% of the amorphous component, but becomes rigid and crystalline when the weight fraction of the crystalline component exceeds 30% of the blend. Besides composition, aging of the blend also determines the compatibility of the two polymers. For instance, the crystallization rate and induction time for crystallization is critically dependent on the concentration of the components and aging [52]. Crystalline interactions have been shown to exist when PCL is blended with polyethylene and polypropylene, with  $\alpha$ -relaxation in polyethylene being affected in particular. However, because this effect is interrelated to motion in the polyethylene crystallites it was elucidated by assuming that the blend might be cocrystalline in nature.

PCL is one of the most widely studied crystalline polymers in blends, owing to its miscibility with many other polymers through hydrogen bonding, leading to miscible blends. Typically, the blending of PCL with amorphous polymers such as PVC destroys the crystallinity of PCL and leads to amorphous-like, soft compositions. Chen *et al.* used polarized-light OM to study changes in spherulization kinetics in crystalline PCL and amorphous polymer blend thin films [53]. Poly(*p*-

vinyl phenol) (PVPh), poly(benzyl methacrylate) (PBzMA) and poly(phenyl methacrylate) (PPhMA) are amorphous polymers that represent strong hydrogen-bonding and weak polar interactions, and hence high miscibility with PCL. When using these amorphous polymers as diluents, however, the spherulitic patterns of neat PCL undergo significant changes.

The Lauritzen–Hoffman (L-H) theory developed during the early 1960s describes the growth rate kinetics of polymer crystals [54], and several modifications have been suggested to this theory [54]. In a nutshell, the L-H model relates the lateral spreading rate with surface nucleation rate, which is highly temperature-dependent. Depending on the crystallization temperature, the L-H model distinguishes polymer crystal growth into three regimes, namely regimes I, II, and III [55,56]. The L-H plots in Figure 16.5 represent spherulitic morphologies and kinetic regime behaviors for neat PCL in comparison with 90/10 (w/w) blends of PCL/PVPh, PCL/PBzMA, and PCL/PPhMA [53]. For neat PCL (Figure 16.6a), the PCL displays a variety of Maltese cross, dendrite or ring-band patterns in spherulites that are melt-crystallized at the temperatures of regimes II and III. Regime growth transition from regime II to regime III is identified from this microscopic characterization, which signals a corresponding mesoscale pattern transition from

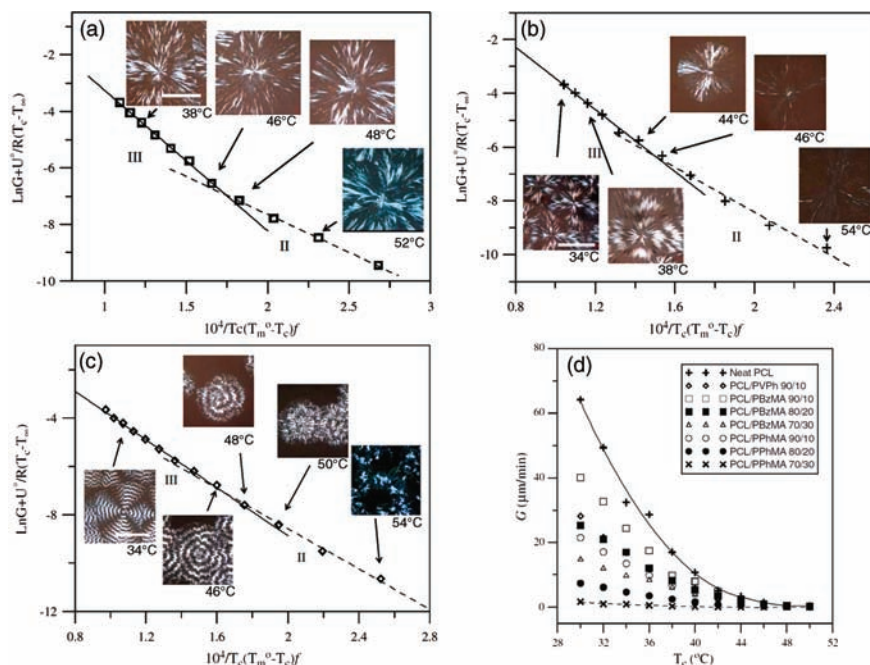


**Figure 16.5** Lauritzen–Hoffman plots showing spherulitic morphologies and kinetic regime behavior of crystalline/amorphous polymer blends in which the crystalline polymer was PCL and the amorphous polymer was varied.

(a) 90/10 PCL/PVPh blend; (b) PCL/PBzMA; (c) PCL/PPhMA; (d) The dependence of spherulite growth rate on crystallization temperature. Reprinted with permission from Ref. [53]; © 2008, Springer.



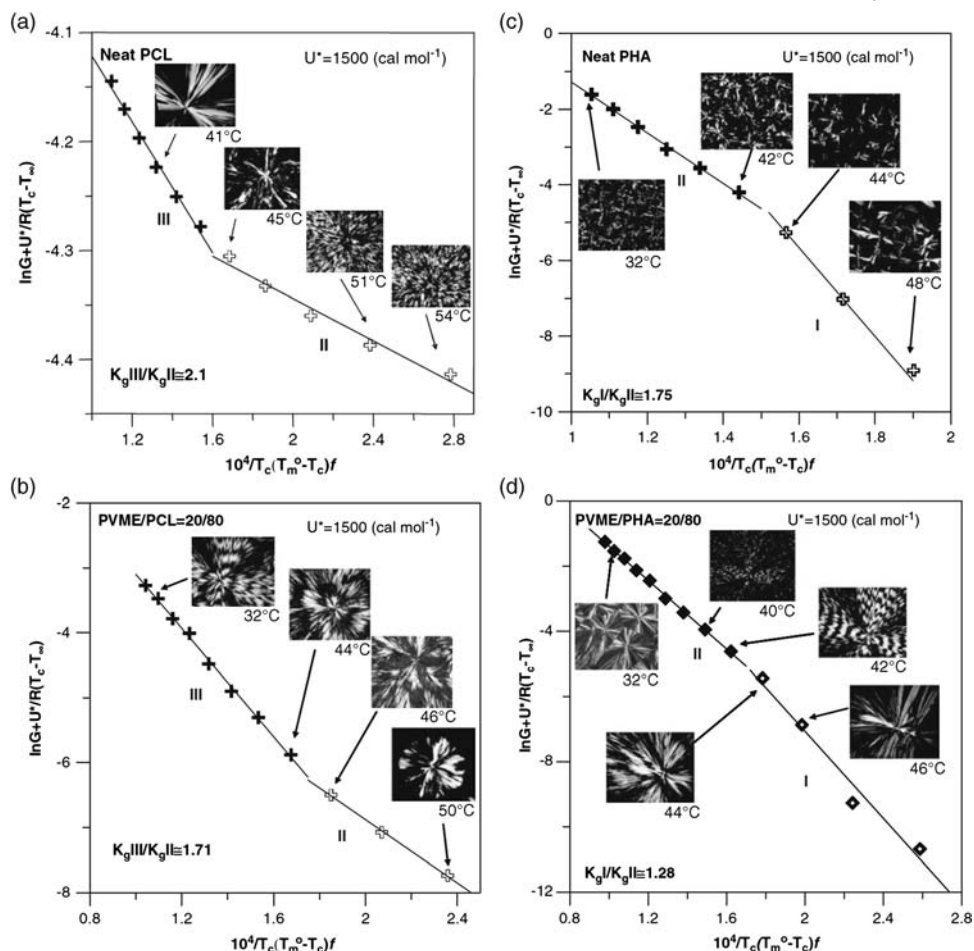


**Figure 16.6** Crystallization plots showing regime-II to regime-III transitions. (a and c) For neat and PVME/PCL blends; (b and d) For neat PHA and PVME/PHA blends. The POM images show spherulitic morphologies at different crystallization regimes. Reprinted with permission from Ref. [57]; © 2010, Nature Publishing Group.

Maltese cross (regime III) to dendritic (regime II). The blending of PCL with different amorphous polymers suppresses the growth rate and induces spherulitic patterns that are different from those in neat PCL.

Crystalline PCL polymer, when blended with different types of amorphous polymers, has exhibited variations in the interaction strength, although all amorphous polymers used in the blend are miscible with PCL, which influences the growth kinetics of the spherulites and ultimately produces morphologies that are significantly different one from another. Figure 16.5a–c represent 90/10 (w/w) blends of three amorphous polymers; the PCL/PVPh blend (Figure 16.5a) shows dendritic crystals with no ring bands. PPhMA and PBzMA differ in their chemical structure

only by a methylene unit, though microscopic investigations (as shown in Figure 16.5b and c) showed large differences in their crystallite structures. The PCL/PPhMA blend (Figure 16.5b) shows coil-like textures of ring bands, whereas the PCL/PBzMA blend (Figure 16.5c) shows zig-zag ring bands. It was suggested that this difference in ring-band textures may result from differences in interactions between PCL and PBzMA or PPhMA. As mentioned earlier, the inclusion of amorphous, miscible polymers has a direct influence on the growth kinetics of the PCL crystallites. In Figure 16.5d, the spherulite growth rates ( $G$ ) are shown to decrease as the crystallization temperature ( $T_c$ ) increases. The overall growth rate was suppressed as neat crystalline PCL was blended with any miscible, amorphous polymers. The types of amorphous polymer, and their ratio in the blend, are the determining factors of how strongly the spherulite growth rate will be suppressed.

When PCL is blended with non-hydrogen-bonding polymers, such as ether- or carbonyl-containing polymers, the blend can exhibit interesting yet peculiar phase behaviors. For example, in a detailed investigation of isomeric crystalline polyesters, PHA and PCL were each blended with amorphous poly(vinyl methyl ether) (PVME) [57]. Although PCL/PVME is a miscible blend, a lack of strong hydrogen bonding weakens the interaction between PVME and PCL. Both PCL and PHA are polyesters with isomeric structures, but the regime behavior of mesoscale crystalline morphologies was shown to be very different for the PCL/PVME and PCL/PHA blends [57]. The regime behaviors of neat PCL, PHA and their 80/20 (w/w) blend with PVME are compared in Figure 16.6. Neat PCL (Figure 16.6a) showed a regime II to regime III transition; microscopically this was observed as a Maltese cross-type to fluffy dendritic transition. In contrast, neat PHA (Figure 16.6c) showed a regime I to regime II transition, during which process there were no apparent microscopic structural changes – that is, Maltese cross patterns were observed in both regimes. However, on blending these neat polymers (PCL or PHA) with 20 wt% PVME the spherulitic morphology of the PVME/PCL or PVME/PHA blend underwent a dramatic change (as shown in Figure 16.6b and d, respectively), indicating that the amorphous and miscible diluent (PVME) had a critical role in the regime kinetics of the blends' morphologies. This situation may arise from an enhanced  $T_g$  of the blend and a depressed  $T_m$  of the crystalline component (PHA or PCL) of the mixture [57].

The crystallization temperature ( $T_c$ ) is another critical parameter that has a strong influence on the mesoscale morphologies seen in a polymer blend. The POM images of a PVME/PHA 20/80 blend shown in Figure 16.7 indicate that the spherulitic morphologies were distinctly different, even with moderate changes in  $T_c$ . When the  $T_c$  was  $\leq 38^\circ\text{C}$ , Maltese cross patterns (Figure 16.7a) were seen, whereas an increase of the  $T_c$  to  $42^\circ\text{C}$  and  $46^\circ\text{C}$  led to the creation of ring-banded spherulites and straight-stalk dendrites, respectively (Figure 16.7b and c). A  $T_c$  of  $48^\circ\text{C}$  or higher resulted in branching dendrites for the same blend composition, as seen in Figure 16.7d. These dramatic changes were attributed to a suppression of the growth rates, retarded by miscible PVME and  $T_c$ . These factors were proposed to affect the chain packing of crystalline components into large-dimension, single-crystal forms from bulk forms [57].



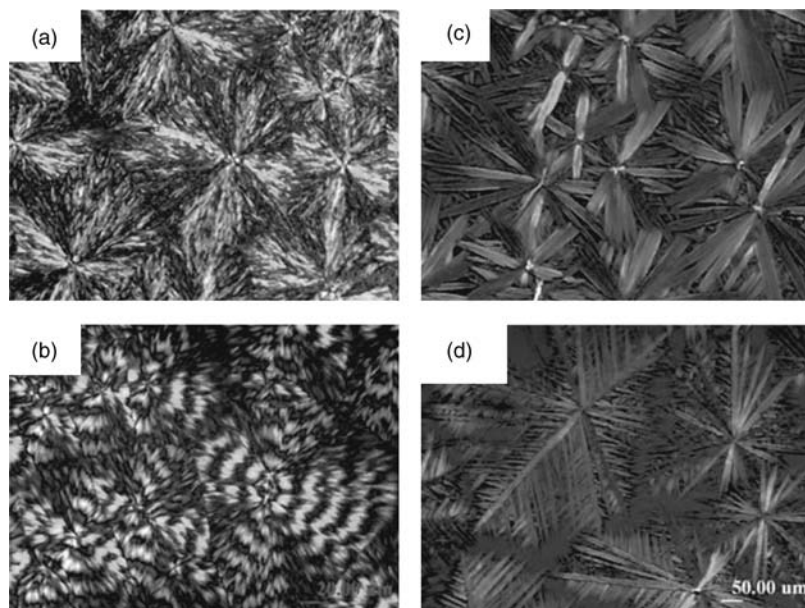


**Figure 16.7** POM images showing the effect of crystallization temperature on blend morphologies for the PVME/PHA (20/80) blend. (a) Maltese cross-type pattern at  $T_c \leq 38^\circ\text{C}$ ; (b) Ring-banded spherulites at  $T_c \leq 42^\circ\text{C}$ ; (c) Straight-stalk dendrites at  $T_c \leq 46^\circ\text{C}$  and branching dendrites at  $T_c \leq 48^\circ\text{C}$ . Reprinted with permission from Ref. [57]; © 2010, Nature Publishing Group.

### 16.4.3

#### Role of Polymer Tacticity on Polymer Blend Morphologies

The effect of tacticity (i.e., the stereochemical arrangement of the units in the main chain of a polymer) on the properties of polymers and polymer blends has long been recognized with such basic differences as in the  $T_g$ , miscibility, crystallization, and blend characterization, including their mesoscale morphologies. In general, isotactic polymers (where all substituents are located on the same side of the polymer backbone) are semicrystalline in nature, whereas atactic polymers (where all substituents are placed randomly along the backbone) are amorphous.

A ductile, semicrystalline isotactic polypropylene (iPP) blended with a brittle and amorphous atactic polystyrene (aPS) has been studied extensively, owing to its importance in the development of recyclable resins [58–61]. The morphology of this blend has been shown to reflect its final physico-mechanical properties. The rheological properties and mesoscale morphologies of these blends are determined by the blend composition, processing conditions and the compatibility of the isotactic and atactic mixtures. Blends of PCL/iPP, in the solid state and at compositions spanning the complete range, were characterized using dynamic mechanical, DSC and OM techniques [62]. Morphologic examinations revealed

**Table 16.3** Induction time and crystallization rate of the blends.

Sample	Induction time (min)	Crystallization rate ( $\mu\text{m min}^{-1}$ )
iPP + 10% PS	4	2.85
iPP + 20% PS	5	2.35
iPP + 30% PS	6	2.03
iPP + 10% PS + SEBS	6.5	1.98
iPP + 20% PS + SEBS	8	1.63
iPP + 30% PS + SEBS	10	1.22

iPP, isotactic polypropylene; PS, polystyrene; SEBS, styrene-*b*-ethylene-*co*-butylene-*b*-styrene.

Reprinted with permission from Ref. [58]; © 2011, John Wiley & Sons.

that increasing the PCL content caused a decrease in spherulitic size while enhancing the crystallinity. The size reduction of spherulites was shown to be associated with a limited miscibility of the amorphous phases when the blends were quenched, which also helped to enhance the crystallinity of iPP.

Borysiak [58] has investigated the influence of the aPS in the iPP matrix. Meso-scale  $\alpha$ -spherulites evolved in the iPP/aPS system at 140°C, where the crystallization time was shown to depend on the blend ratio, but increasing the aPS content increased the induction time (the time after which initiation of the development of spherulite structures is observed). In addition to the rate of development of spherulites, the final size of the spherulites was also affected by the iPP/aPS ratio, as shown in Table 16.3. As iPP and aPS are immiscible, blending these incompatible polymers will result in the formation of a continuous iPP phase and a dispersed aPS phase. Numerous studies have been conducted to compatibilize iPP/aPS blends, using either block or graft copolymers [63,64]. The effect of the compatibilization of poly(styrene-*b*-ethylene-*co*-butylene-*b*-styrene) grafted with maleic anhydride (SEBS-*g*-MA) block copolymer (BCP) in iPP/aPS blends on morphology induction time and growth rate are shown in Table 16.3. SEBS compatibilization led to a significant increase in the induction time [58]. For instance, iPP/20% aPS showed spherulitic structures after 5 min, which was increased to 8 min in the case of iPP/20% aPS/SEBS. Likewise, the crystal growth rate was decreased from  $2.35 \mu\text{m min}^{-1}$  to  $1.63 \mu\text{m min}^{-1}$ . This point was explained by considering that the added SEBS remarkably reduced the aPS phase size in contact with iPP, which weakened the nucleating abilities and delayed the induction time of SEBS-containing iPP/aPS blends. Moreover, the presence of the SEBS caused a deterioration in the nucleation ability of polypropylene.

Blends of two isotactic polymers, such as iPP with isotactic poly(butane-1) (iPB), have been investigated using not only OM but also electron microscopy and light scattering [65]. The results obtained indicated that iPP and iPB would form a miscible blend at ambient conditions, but that thermal treatment of this blend would induce a partial phase separation of those components exhibiting iPP-rich and iPB-rich phases. In this system, a higher temperature induced a stronger phase separation. When Bartczak *et al.* [65] compared the crystallization mechanism in pure iPP with that in an iPP/iPB blend, the heterogeneous primary nucleation in

blends was accordingly depressed when compared to neat iPP. The proposed mechanism for this difference was that, during the crystallization process, the less-active heterogeneities in blends lost their activity due to an increase in the energy barrier. Similarly, the rate of homogeneous nucleation was also decreased in the blends. In the case of very high undercooling, both iPP and iPB were crystallized at the same rate and developed spherulitic structures; consequently, at very high undercooling the total number of spherulites in a given area (as observed with OM) was much higher due to the fact that they contain both iPP spherulites and iPB spherulites. Understandably, with the same experimental conditions the neat iPP exhibited a relatively smaller number of spherulites.

#### 16.4.4

#### Crystallization Morphologies in Stereocomplexationable Chiral Blends

The stereoselective association or stereocomplexation of L and D enantiomeric polymer blends has been shown to provide several advantages over the parent components. For example, a blend of L- and D-poly(lactide) (PLLA and PDLA, respectively) exhibits a high mechanical performance and biodegradability [66,67]. These properties are orders of magnitude superior to those of neat PLLA or neat PDLA, exhibiting very high resistances to adverse conditions such as thermal and/or hydrolytic degradation [68,69]. Both, OM and POM have been used to clarify the crystallization kinetics and structure of the stereocomplexationable blends [70]. PLLA and PDLA are both isomeric forms of polylactides (PLAs), and can crystallize into  $\alpha$ ,  $\beta$  or  $\gamma$  forms, although the  $\alpha$  form is the most commonly obtained from melt or solution casting. That is, the mesoscale crystalline structures of PLA homopolymers (as observed with OM) are independent of processing routes such as thermal history and solvent–polymer interaction. In contrast, a stereocomplexed blend of PLLA and PDLA possesses very different physico-chemical characteristics from their parent components, such as higher melting temperatures, an elevated enthalpy of fusion and better mechanical properties. Likewise, the morphological patterns – such as inclusion of the helical conformation of the crystallites and spherulitic structures – are distinctly different [46,71,72]. The crystalline morphologies of PDLA/PLLA blends have been studied extensively with equimolecular-weight PDLA and PLLA [73–76]. The subsequent changes in properties and structures have been attributed to the stereoselective van der Waals forces between  $\text{CH}_3 \cdots \text{C}=\text{O}$  of PLLA and PDLA that facilitate the stereocomplexation.

Typically, Maltese cross patterns were observed for blends with equimolecular-weight components. In such blends, the kinetics of crystal (spherulite) formation depended on the  $T_m$  of the parent components, whereas the  $T_m$  was dependent on the chiral nature of lactic acid. If the  $T_m$  difference between the two polymers was small, then both PLLA and PDLA would crystallize simultaneously. However, as the  $T_m$  difference became larger the two crystalline components might crystallize sequentially, and there would be no simultaneous crystallization [69,73,74].

When Woo and Chang studied the crystallization of nonequimolar compositions of PDLA with low-molecular-weight PLLA (PDLA/LM<sub>w</sub>-PLLA) [77], either crystals

of the stereocomplexed crystallite or a mixture of stereocomplexed crystallites and homocrystallites was observed, depending on the blend ratio. POM images of the morphologies of neat PDLA and PDLA blended with various weight fractions of LM<sub>w</sub>-PLLA content and melt-crystallized at 120 °C are shown in Figure 16.8. In order to obtain a better understanding of the influence of stereocomplexation on the morphology, each sample was examined (using OM) as a function of temperature, blend composition and crystallization time. In these blends, when the temperature was decreased from the molten state, stereocomplexation became possible at a temperature above the crystallization of the homopolymers with a rearrangement of units of opposite configuration and the complexation of free adjacent units. The Maltese cross pattern structures of neat PDLA and neat

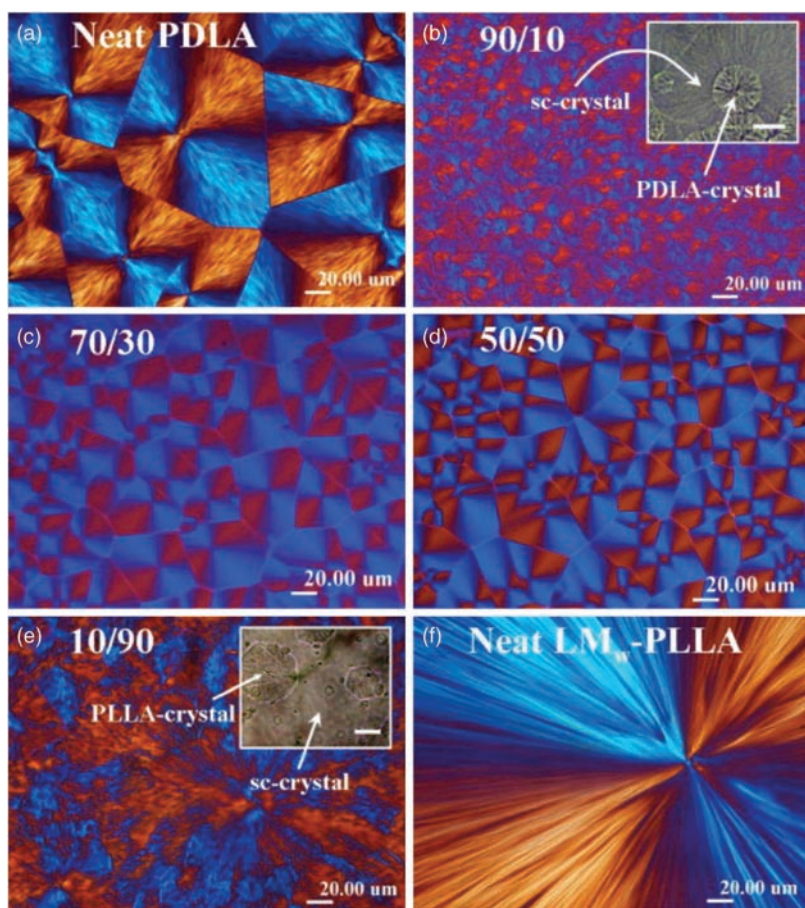


**Figure 16.8** POM images of PDLA/LM<sub>w</sub>-PLLA blends of various compositions melt-crystallized at 120 °C for 60 min. The insets show nonpolarizing OM images of the 90/10 and 10/90 blends, respectively, crystallized for 4 min. Reprinted with permission from Ref. [77]; © 2011, Elsevier.

LM<sub>w</sub>-PLLA are shown in Figure 16.8a and f, respectively. The  $T_m$  difference between these two isomeric polymers was at least 50 °C. Due to this large difference, the blend exhibited multistage crystallization depending on its composition; in general, a higher blend ratio would result in faster crystallization kinetics as the stereocomplex crystallites would be formed more rapidly than the homopolymer crystallites. POM images of blends crystallized at 120 °C for 4 min are shown in Figure 16.8b and e for 90/10 and 10/90 blend ratios, respectively. In these extreme compositions, the stereocrystallites are formed first, after which homopolymer crystallites are developed within the matrix of the stereochemical crystallites; these spherulitic crystallites then grow until they impinge with another homopolymer spherulite. Depending on the crystallization temperature and the crystallization time, transitions from an amorphous/amorphous mixture to a crystalline/amorphous, and later to crystalline/crystalline states, will be displayed.

Tsuji and Okumura used microscopy to compare the radial growth rate of spherulites from pure phases and blends of poly(L-2-hydroxybutyrate) (P(L2HB)) and poly(D-2-hydroxybutyrate) (P(D-2HB)) [78]. These are both biodegradable polymers with the structure of PLLA (PDLA), in which methyl groups are substituted with ethyl groups. The radial growth rate of spherulites ( $G$  in  $\mu\text{m min}^{-1}$ ) and the induction periods for spherulite growth ( $t_i$ ) of pure P(L-2HB), P(D-2HB) and their blends were estimated from polarized optical photomicrographs, as shown in Figure 16.9 [79]. Extrapolation of the spherulite radius plotted against crystallization time to a radius of 0 mm gave the  $t_i$  values. The  $G$ -value was notably sevenfold higher for the L and D blends ( $12 \mu\text{m min}^{-1}$ ) compared to the neat L and D polymers ( $1.6 \mu\text{m min}^{-1}$ ). This trend, seen in pure phases and blends of P(L-2HB), P(D-2HB), was consistent with the  $G$ -values reported for the PLLA/PDLA stereocomplexes [80]. A larger  $G$ -value for the blend indicated that the intermolecular interaction between L and D chains having opposite configurations in the molten state was higher than that between pure L or pure D chains with the same configurations. Consequently, the stereocomplex spherulites would grow much faster than the homocrystallites.

Tsuji and Ikada have shown that the melting temperature of racemic crystallites was independent of the size of the spherulites, but was decreased as the melt blend deviated from the equimolar mixing. This effect was ascribed to a disordered crystalline structure or to a smaller size of the respective crystallites where the disordered region of the spherulites was likely to contain small homocrystallites [73,76]. Tsuji reported the mesoscale morphological differences as a function of hydrolysis of the PLLA/PDLA (L/D) blend and homopolymer (L) films [78]. In this study, a stereocomplexed 1 : 1 blend and nonblended films with the thickness of about 25  $\mu\text{m}$  were used. The PLLA and PDLA used in this study had equal, medium molecular weights of  $1.5 \times 10^{-5} \text{ g mol}^{-1}$ . Before hydrolysis, the L film showed the presence of 100  $\mu\text{m}$  spherulites whereas the L/D blend film showed a large amount of microcrystallites but no well-defined spherulites (Figure 16.10). However, following hydrolysis for 30 months the image became darker in the L film and brighter in the L/D film; this suggested that the L film had been hydrolyzed preferentially at chains in the amorphous region that connected the

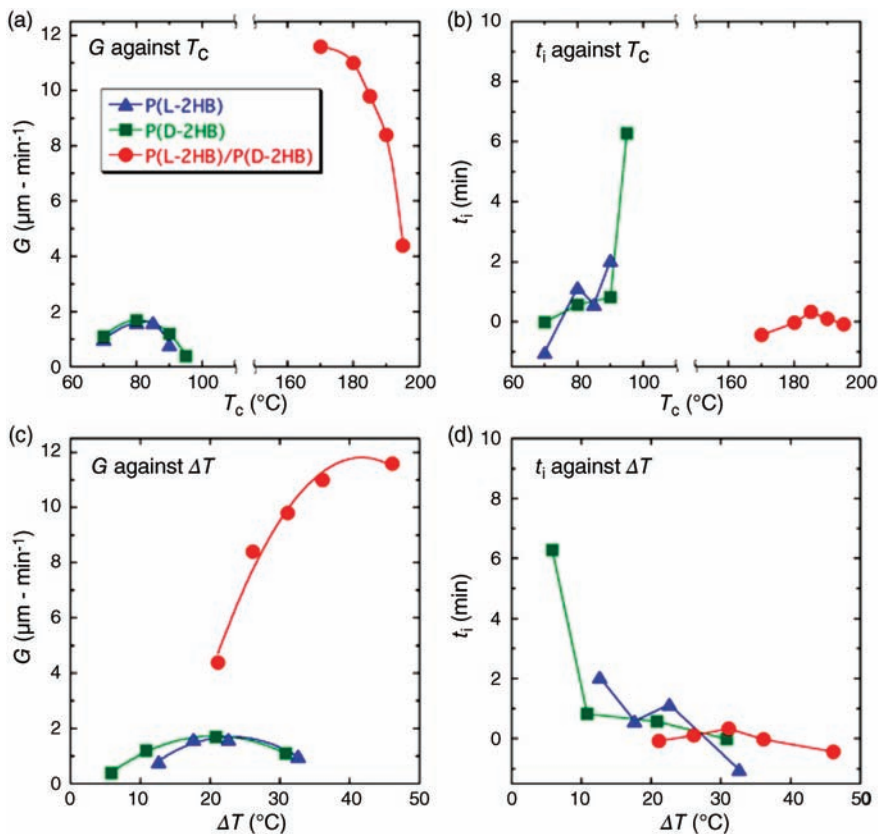


**Figure 16.9** Radial growth rates of spherulites and the induction periods for spherulite growth of pure phase and blends of stereocomplexationable polymers as estimated from the respective POM images. Reprinted with permission from Ref. [79]; © 2011, Nature Publishing Group.

crystalline lamellae in the spherulites, which in turn resulted in a reduced orientation of the lamellae.

#### 16.4.5

#### Mesoscale Morphologies in Conducting Polymer Blends

Polymers that are electrically conductive and composed of fully conjugated sequences of double bonds along macromolecular chains are termed intrinsically conducting polymers (ICPs) [81]. The electrical and optical properties of ICPs (in addition to their ease of synthesis and flexibility in processing) are attractive for modern technological applications, including biosensors, tissue engineering, neural probes, chemical and electrochemical sensors, and organic electronics [82–86]. In ICPs, the charge is transported along and between the polymer molecules via

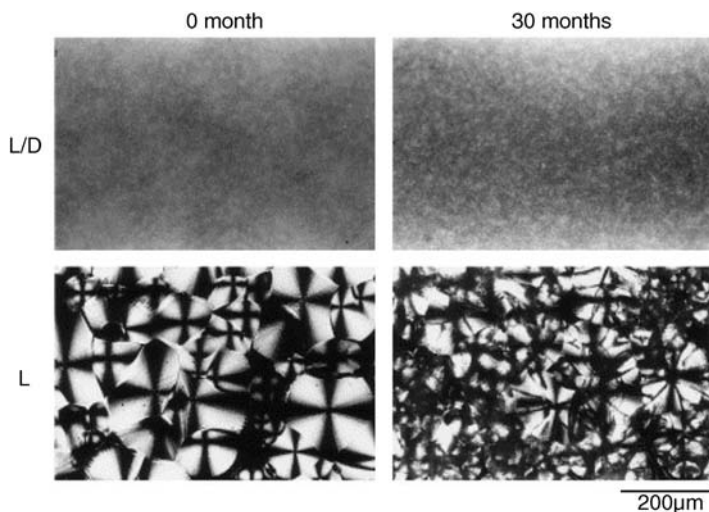


**Figure 16.10** POM images showing the effect of aging/hydrolysis on thin-film morphologies of L/D blend and L homopolymer films over a 30-month period. Reprinted with permission from Ref. [78]; © 2000, Elsevier.

generated charge carriers such as electrons and holes [87]. The bulk conductivity of these ICPs may be comparable to that of some metals. Typical examples of ICPs include polyacetylene, polythiophene, polyaniline (PAni) and polypyrrole, among which PAni has attracted significant attention due to the facts that its synthesis is straightforward and that it possesses good environmental stability and high electrical conductivity [88,89]. Despite these superior characteristics, all ICPs in general – and PAni in particular – suffer from poor processability and inadequate mechanical properties, which limits their commercial applications [88]. In order to overcome these problems, numerous strategies have been used, one of which is to blend ICPs with another insulating polymer that helps to overcome the mechanical and processability issues. PAni and other ICPs do not interact favorably with other insulating polymers, and remain immiscible where a phase-separation process restricts the formation of more integrated materials. Barra and coworkers have shown that this issue can be overcome by selecting a suitable dopant. For example, if PAni is doped with dodecylbenzene sulfonic acid (PAni.DBSA) it can be either melt-blended or solution-blended with conventional polymers so as to enable the fabrication of polymeric conducting blends with desired properties. In this case, the DBSA acts as a surfactant while its long alkyl chains increase the solubility of PAni.DBSA in solvents such as toluene and xylene; this in turn induces compatibility with polymer matrices having a similar structure [89].

Doped ICPs (e.g., PAni.DBSA) are sometimes blended with a thermoplastic elastomer such as thermoplastic polyurethane (TPU) in order to improve their mechanical properties and processability [90]. TPU exhibits a two-phase morphology in which a soft phase containing either polyesters or polyethers is reinforced by condensation with a hard domain that consists of an aromatic diisocyanate

extended with a short-chain diol. When Barra and coworkers examined the effect of PAni.DBSA addition on the morphology of TPU blends by using OM [88], a major finding was that the mode of casting was critical for the final morphology of the freestanding film, and this was reflected directly in its electrical conductivity and percolation threshold. Micrographs of PAni.DBSA/TPU blends at two different ratios (15/85 and 30/70) are shown in Figure 16.11, where the dark regions correspond to the dispersed PAni.DBSA phase. Solution-cast thin films of PAni.DBSA/TPU blends with 15/85 and 30/70 ratios, respectively, are shown in Figure 16.11a and c. The morphologies of blends prepared via an *in-situ* process are shown in Figure 16.11b and d for two different blend ratios. An increase in the PAni content from 15 to 30 wt% increased the conductive pathways in the solution-cast films. At 30 wt% the dispersed phase was better interconnected, which resulted in an enhanced electrical conductivity, from  $1.7 \times 10^{-6} \text{ S cm}^{-1}$  for 15 wt% PAni.DBSA to  $1.5 \times 10^{-2} \text{ S cm}^{-1}$  for 30 wt% PAni.DBSA. However, such a 10 000-fold increase in conductivity when doubling the doped ICP content was exhibited only when the blend was spun-cast. In contrast, the *in-situ* preparation method produced very different morphological characteristics at the same blend compositions as those attained by solution-casting. Micrographs of the interconnected phases for both blend compositions prepared via *in-situ* methods are

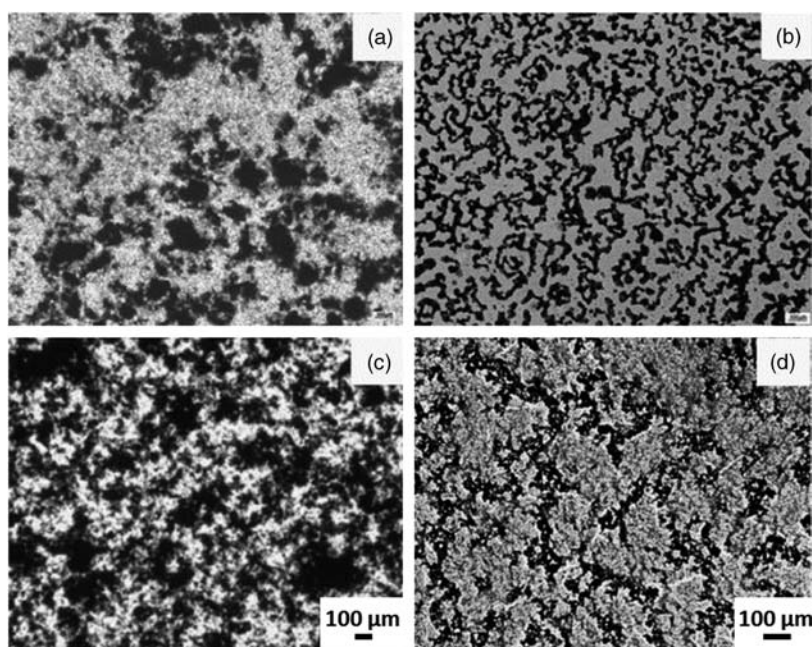


**Figure 16.11** OM images showing morphological differences in PAni.DBSA/TPU blends, depending on their mode of preparation. (a and c) Solution-cast blends; (b and d) “In-situ”-

processed blends at 15/85 and 30/70 (w/w), respectively. Reprinted with permission from Ref. [88]; © 2007, Elsevier.



shown in Figure 16.11b and d. In this case, the electrical conductivities were  $6.9 \times 10^{-5}$  and  $1.2 \times 10^{-1} \text{ S cm}^{-1}$  for the 15/85 and 30/70 blends, respectively, which was at least 10-fold higher than in the solution-cast films. The lower percolation threshold provided an explanation for the higher electrical conductivity of the PAni.DBSA/TPU blends obtained via “*in-situ*” processing, compared to the solution-casting process. These data confirmed that the *in-situ* blend preparation method would produce PAni.DBSA/TPU blends with enhanced compatibility, which would in turn result in a fine dispersion and vivid conducting pathways.

## 16.5

### Confocal Microscopy Characterization of Polymer Blends

In an effort to obtain superior axial imaging, laser scanning confocal microscopy (LSCM) has been applied to characterize polymer blends [91]. Several advantages emerge when using LSCM rather than conventional OM, which is limited in both its lateral (parallel to the focal plane) and axial (perpendicular to the focal plane) resolution. The large focal depth in a conventional light microscope causes the image to be smeared out, which limits the use of this technique for quantitative analysis. In LSCM, any “out-of-focus” information is excluded by focusing through a small aperture (a confocal pinhole) [92]. As a result, the confocal image arrives from a particular depth on the specimen, which enables observations to be made of the object at different optically sliced sections [93]. Morphological variations as a function of film depth can be seen in Figure 16.12 [94], which shows LSCM images obtained from a PMMA/PS blend in which the PMMA is labeled with 2-(4-nitro-2,1,3-benzoxadiazol-7-yl)aminoethyl (NBD) dye (bright spots). Whereas ordinary OM or fluorescence microscopy would provide information only for the top layer morphologies, the optical slicing capabilities of the LSCM enables imaging at 3 and  $6 \mu\text{m}$  beneath the top layer. Objects obtained at various optically sliced sections are then reconstructed into a three-dimensional (3D) image by using image-processing techniques [94].

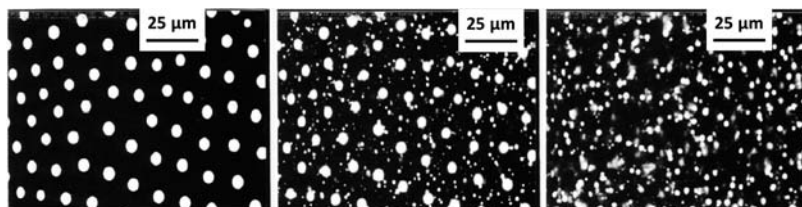


**Figure 16.12** LSCM images of solvent-cast 10:90 PMMA/PS blend film. The bright spots represent PMMA labeled with NBD dye, the dark areas represent PS. The morphologies shown are at the film surface (left), at  $3 \mu\text{m}$

beneath the surface (middle), and  $6 \mu\text{m}$  beneath the surface (right). Reprinted with permission from Ref. [94]; © 1994, American Chemical Society.

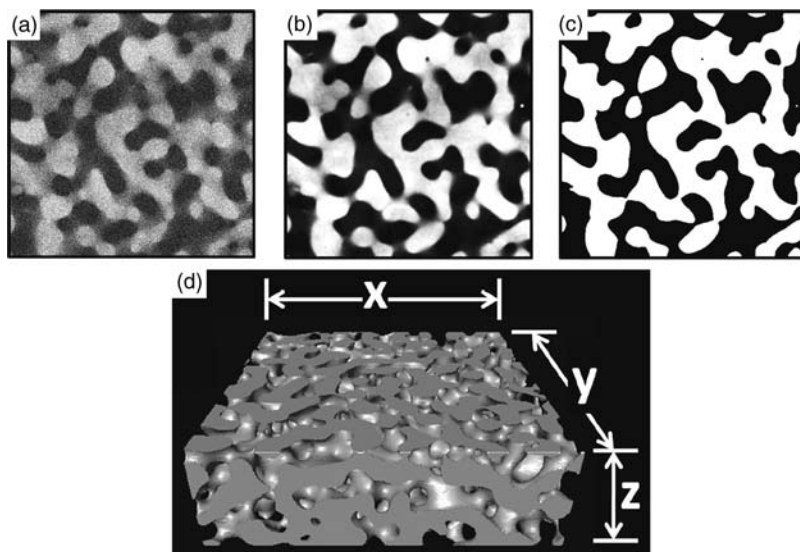


**Figure 16.13** LSCM image quality improvement and 3D reconstruction. (a) As-obtained LSCM image; (b) Image after deconvolution; (c) Image after thresholding; (d) An example of the rendered 3D micrographs showing the X-Y-Z dimensions of  $160 \times 160 \times 45 \mu\text{m}^2$ . Reprinted with permission from Ref. [23]; © 2009, American Chemical Society.

Lopez-Barron and Macosko have characterized the interface shape evolution in immiscible fluorescently labeled polystyrene and styrene-*ran*-acrylonitrile copolymer blend via 3D image analysis [23,95]. The LSCM images of these blends before image processing, after deconvolution and after thresholding, are shown in Figure 16.13, where the bright areas represent the fluorescently labeled PS polymer. Although noise and blurring are apparent in the 2D sliced image before processing, application of the deconvolution technique reduces the out-of-focus blurring. The as-obtained LSCM images were then further improved by thresholding them into binary images. The series of thresholded images are stacked into a single file to create a 3D image, as shown in Figure 16.13d. The availability of a third dimension in the reconstructed LSCM images is helpful in visualizing the true morphology; moreover, the 3D images provide information on the curvature of the interface.

Jinnai *et al.* have used multiple modes of LSCM to investigate the fine structures in bicontinuous phase-separated domains of a polymer blend consisting of poly(styrene-*ran*-butadiene) (SBR) and polybutadiene (PB) [91]. Although pure reflection LSCM images (as shown in Figure 16.14a) or pure fluorescence LSCM images (Figure 16.14b) exhibit such fine structures, it cannot be concluded whether these fine structures belong to the SBR or PB of the blend. A combination of reflection and fluorescence LSCM via superposition clearly revealed that fine structures exist only in the SBR-rich phase (as shown in Figure 16.14c).

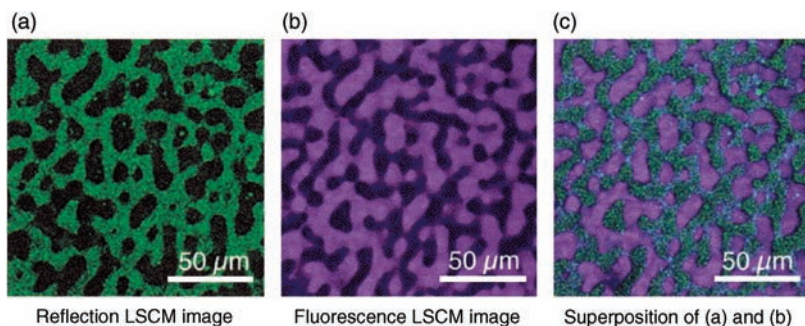


**Figure 16.14** LSCM images of poly(styrene-*ran*-butadiene) and polybutadiene blend imaged at 20  $\mu\text{m}$  beneath the top surface, using (a) reflecting and (b) fluorescence modes;

(c) Superposition of reflection LSCM and fluorescence LSCM images. Reprinted with permission from Ref. [96]; © 2001, American Chemical Society.

In LSCM, the contrast enhancement derives from the light emission of fluorescent dyes that have been added to the sample as labels or tracers. In polymer blends these labels or tracers are localized on a specific polymer, with organic molecules generally being used as dyes. Moffitt and coworkers [97,98] showed recently that polymer-coated, inorganic, semiconductor quantum dots (QDs) can also be used as fluorescent tracers for the LSCM imaging of phase morphology in polymer blends. Specifically, these authors used cadmium sulfide (CdS) QDs stabilized at the surface with PS-*b*-PAA block copolymers. In this case, the PAA is attached to the QDs, while the PS forms a brush-like layer. However, as the PS brush on the QDs interacts well with the PS in the PS/PMMA blend the QDs are well dispersed in the PS phase but completely excluded from the PMMA phase. This provides an excellent fluorescence contrast for the LSCM imaging of structures arising from phase separation between PS and PMMA (see Figure 16.15).

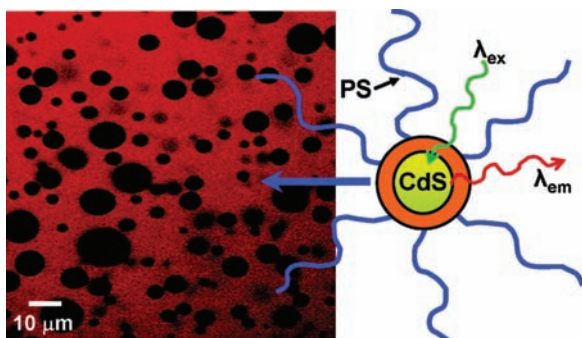


**Figure 16.15** LSCM image of a PS/PMMA blend, demonstrating inorganic QDs as effective tracers for the PS phase in fluorescence imaging of the blend structure. The bright regions represent the PS phase, and the dark

regions are phase-separated PMMA. The brightness for PS is provided by fluorescence emission from the CdS QDs. Reprinted with permission from Ref. [97]; © 2005, American Chemical Society.

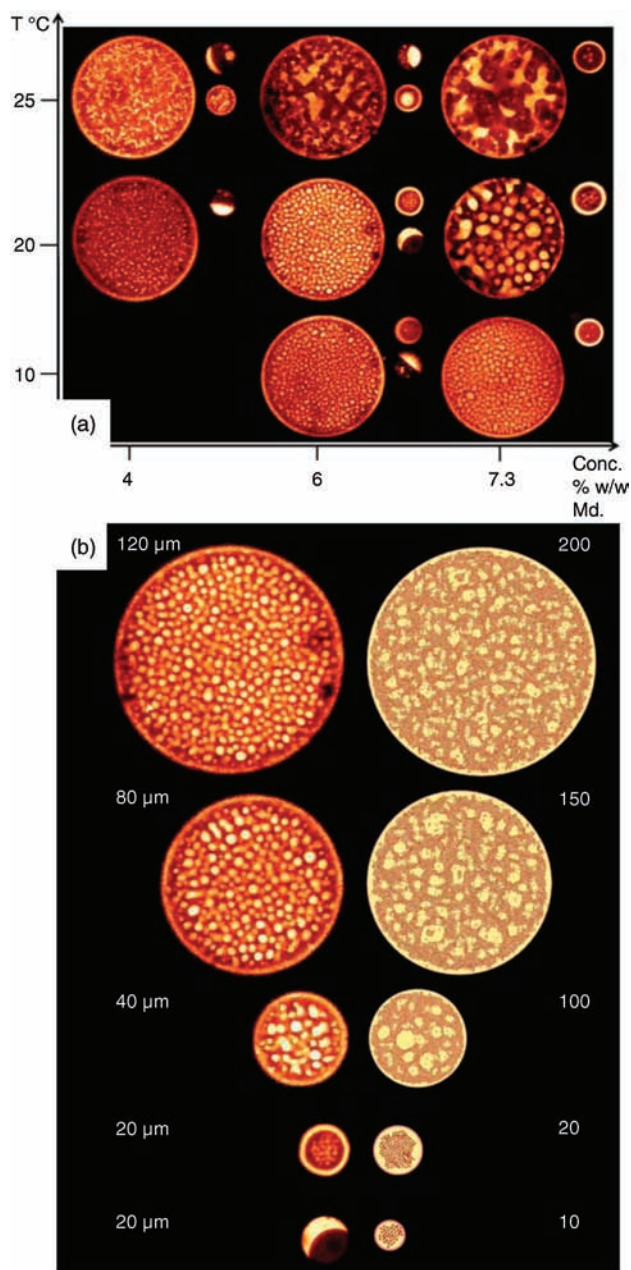


**Figure 16.16** LSCM images showing phase-separated morphologies of biopolymeric mixtures of gelatin and maltodextrin confined in emulsion droplets. The effect of confinement size on mesoscale morphologies is shown

(a) experimentally (LSCM images at bottom left) and (b) theoretically (simulation images at bottom right). Reprinted with permission from Ref. [100]; © 2010, Royal Society of Chemistry.

More importantly, the presence of the QDs does not alter the original phase separation morphology of the PS/PMMA blend, provided that their concentrations are kept relatively low.

Further, in the context of using confocal microscopy to characterize polymer blend films, Fransson *et al.* [99,100] have systematically studied the phase separation of biopolymeric blends in confined geometries using LSCM. The results obtained indicated that the morphology of a phase-separating and gelling biopolymer mixture of gelatin–maltodextrin was strongly affected by the presence of a confined geometry. Geometric confinement in the form of emulsion droplets of various sizes can be examined *in situ* using LSCM and subsequent image analysis (Figure 16.16a). For smaller droplets ( $<20\mu\text{m}$  diameter), two types of microstructure are observed using LSCM, namely surface-directed (maltodextrin shell and a gelatin core) and half-moon (gelatin and maltodextrin form two halves). For larger droplets ( $>20\mu\text{m}$  diameter), the morphology resembles the bulk morphology, which is a continuous gelatin phase with evenly distributed maltodextrin inclusions. An elastic Lennard–Jones (ELJ) model was used to predict the structures of this protein–polysaccharide blend under confinement [100]. The simulated microstructure obtained with the ELJ model was shown to be in excellent agreement with the experimental observations made using LSCM (as shown in Figure 16.16b).

## 16.6

### Summary

Polymer blends, when in thin-film form, exhibit morphologies at different length scales. A variety of OM techniques has been used to characterize the phase-separated structures (at the mesoscale level) that result from intermolecular/intramolecular interactions among the polymers involved in the blend. Besides providing information on morphological features at the mesoscale level, microscopic characterization is also a powerful aid in understanding the crystallization kinetics of polymer blends. Advances in microscopic techniques have provided the ability to observe 3D structural details at any given depth of polymer blend films. Moreover, optical slicing for 3D imaging is noninvasive to the sample and provides structural information that is influenced by neither the substrate nor the interface.

### Acknowledgments

Partial support from the Center for Nanophase Materials Sciences, which is sponsored at Oak Ridge National Laboratory by the Scientific User Facilities Division, Office of Basic Energy Sciences, US Department of Energy, is greatly acknowledged. These studies were also partly supported by the Center for Nanoscale Materials at Argonne National Laboratory by the US Department of Energy, Office of Science, Office of Basic Energy Sciences, under Contract No. DE-AC02-06CH11357.

## References

- 1 Sawyer, L.C., Grubb, D.T., and Meyers, G.F. (2008) Introduction to Polymer Morphology, in: *Polymer Microscopy*, Springer, New York, pp. 248–434.
- 2 Sawyer, L.C., Grubb, D.T., and Meyers, G.F. (2008) Application of Microscopy to Polymers, in: *Polymer Microscopy*, Springer, New York, pp. 1–25.
- 3 Inoue, T. (2003) Morphology of Polymer Blends, in: *Polymer Blends Handbook* (ed. L.A. Utracki), Springer, Netherlands, pp. 547–576.
- 4 Ramanathan, M. and Darling, S.B. (2009) Thickness-dependent hierarchical meso/nano scale morphologies of a metal-containing block copolymer thin film induced by hybrid annealing and their pattern transfer abilities. *Soft Matter*, 5, 4665–4671.
- 5 Herman, B. and Lemasters, J.J. (1993) *Optical Microscopy: Emerging Methods and Applications*, Academic Press, New York.
- 6 Davidson, M.W. and Abramowitz, M. (2002) *Encyclopedia of Imaging Science and Technology*, John Wiley & Sons, Inc. ISBN: 9780471443391; DOI: 10.1002/0471443395.
- 7 Abramowitz, M. (1987) *Contrast Methods in Microscopy: Transmitted Light*, Olympus America, Inc., New York.
- 8 Van der Voort, G.F. (2005) *Encyclopedia of Condensed Matter Physics* (eds F. Bassani, G.L. Liedl, and P. Wyder), Elsevier, Oxford, pp. 175–182.
- 9 Sheppard, C.J.R. (2005) *Encyclopedia of Modern Optics* (ed. B.D. Guenther), Elsevier, Oxford, pp. 103–111.
- 10 Evennett, P.J. and Hammond, C. (2005) *Encyclopedia of Analytical Science*, 2nd edn (eds P. Worsfold, A. Townshend, and C. Poole), Elsevier, Oxford, pp. 32–41.
- 11 Sheppard, C.J.R. (2005) *Encyclopedia of Modern Optics* (ed. B.D. Guenther), Elsevier, Oxford, pp. 61–69.
- 12 Novak, E. (2005) *Encyclopedia of Modern Optics* (ed. B.D. Guenther), Elsevier, Oxford, pp. 84–92.
- 13 Wilson, T. (2005) *Encyclopedia of Modern Optics* (ed. B.D. Guenther), Elsevier, Oxford, pp. 69–77.
- 14 Holgate, J.H. and Webb, J. (2003) *Encyclopedia of Food Sciences and Nutrition*, 2nd edn (ed. B. Caballero), Academic Press, Oxford, pp. 3917–3922.
- 15 Hammond, C. and Evennett, P.J. (2005) *Encyclopedia of Analytical Science*, 2nd edn (eds P. Worsfold, A. Townshend, and C. Poole), Elsevier, Oxford, pp. 100–106.
- 16 Solomon, M.J. and Kogan, M. (2005) *Encyclopedia of Condensed Matter Physics* (eds F. Bassani, G.L. Liedl, and P. Wyder), Elsevier, Oxford, pp. 229–235.
- 17 Halhuber, K. and Koenig, K. (2003) *Ann. Anat.*, 185, 1–20.
- 18 Work, W.J., Horie, M., Hess, M., and Stepto, R.F.T. (2004) *Pure Appl. Chem.*, 76, 1985–2007.
- 19 Martuscelli, E., Palumbo, R., and Kryszewski, M. (1979) *Joint Italian-Polish Seminar on Multicomponent Polymeric System* (eds E. Martuscelli, R. Palumbo, and M. Kryszewski), Plenum Press, Capri, Italy, p. 508.
- 20 Shonaike, O.G. and Simon, P.G. (1999) *Polymer Blends and Alloys* (eds O.G. Shonaike and P.G. Simon), Marcel Dekker, Inc., New York.
- 21 Baker, W., Scott, C., and Hu, G.H. (2001) *Reactive Polymer Blending*, Carl Hanser Verlag GmbH & Co. KG, Berlin.
- 22 Kulshreshtha, A.K. and Vasile, C. (2003) *Handbook of Polymer Blends and Composites*, Smithers Rapra Publishing, Shawbury, UK.
- 23 Lopez-Barron, C.R. and Macosko, C.W. (2009) *Langmuir*, 25, 9392–9404.
- 24 Robeson, L.M. (1982) *Polymer Compatibility and Incompatibility: Principles and Practices*, Harwood Academic Publishers, New York.
- 25 Kalfoglou, N.K. (1983) *J. Appl. Polym. Sci.*, 28, 2541–2551.
- 26 Olabisi, O., Robeson, L.M., and Shaw, M.T. (1979) *Polymer-Polymer Miscibility*, Academic Press, New York.
- 27 Koleske, J.V. (1978) *Polymer Blends*, Academic Press, New York.
- 28 Ramanathan, M. and Darling, S.B. (2011) *Prog. Polym. Sci.*, 36, 793–812.
- 29 Keller, A. (1955) *J. Polym. Sci.*, 17, 351–364.

- 30 Keller, A. (1955) *J. Polym. Sci.*, **17**, 291–308.
- 31 Keller, A. and Waring, J.R.S. (1955) *J. Polym. Sci.*, **17**, 447–472.
- 32 Shtukenberg, A.G., Punin, Y.O., Gunn, E., and Kahr, B. (2012) Spherulites. *Chem. Rev.*, **112** (3), 1805–1838.
- 33 Keller, A. (1955) *J. Polym. Sci.*, **15**, 31–49.
- 34 Keller, A. (1959) *J. Polym. Sci.*, **39**, 151–173.
- 35 Martuscelli, E., Pracella, M., and Wang, P.Y. (1984) *Polymer*, **25**, 1097–1106.
- 36 Masakazu, I. (1961) *J. Polym. Sci.*, **55**, 443–450.
- 37 Masakazu, I. (1962) *J. Polym. Sci.*, **60**, 81–89.
- 38 Yoshioka, T., Fujimura, T., Manabe, N., Yokota, Y., and Tsuji, M. (2007) *Polymer*, **48**, 5780–5787.
- 39 Fraser, P.P. (1959) *J. Polym. Sci.*, **37**, 71–89.
- 40 Fraser, P.P. and Ralph, W.K. (1962) *J. Polym. Sci.*, **57**, 395–403.
- 41 Granasy, L., Pusztai, T., Warren, J.A., Douglas, J.F., Borzsonyi, T., and Ferreira, V. (2003) *Nat. Mater.*, **2**, 92–96.
- 42 Granasy, L., Pusztai, T., Borzsonyi, T., Warren, J.A., and Douglas, J.F. (2004) *Nat. Mater.*, **3**, 645–650.
- 43 Granasy, L., Pusztai, T., Tegze, G., Warren, J.A., and Douglas, J.F. (2005) *Phys. Rev. E*, **72**, 011605.
- 44 Hsieh, Y.-T., Nurkhamidah, S., and Woo, E.M. (2011) *Polym. J.*, **43**, 762–769.
- 45 Yang, J., Pan, P., Hua, L., Zhu, B., Dong, T., and Inoue, Y. (2010) *Macromolecules*, **43**, 8610–8618.
- 46 Pan, P., Liang, Z., Zhu, B., Dong, T., and Inoue, Y. (2009) *Macromolecules*, **42**, 3374–3380.
- 47 Wang, T., Li, H., Wang, F., Schultz, J.M., and Yan, S. (2011) *Polym. Chem.*, **2**, 1688–1698.
- 48 Schulze, K., Kressler, J., and Kammer, H. W. (1993) *Polymer*, **34**, 3704–3709.
- 49 Defieuw, G., Groeninckx, G., and Reynaers, H. (1989) *Polymer*, **30**, 595–603.
- 50 Chiu, H.-J. (2007) *Polym. Eng. Sci.*, **47**, 2005–2011.
- 51 Robeson, L.M. (1984) *Polym. Eng. Sci.*, **24**, 587–597.
- 52 Katsumata, K., Saito, T., Yu, F., Nakamura, N., and Inoue, Y. (2011) *Polym. J.*, **43**, 484–492.
- 53 Chen, Y.-F. and Woo, E. (2008) *Colloid Polym. Sci.*, **286**, 917–926.
- 54 Frank, F.C. and Tosi, M. (1961) *Proc. R. Soc. Lond. A*, **263**, 323–339.
- 55 Hu, W. and Cai, T. (2008) *Macromolecules*, **41**, 2049–2061.
- 56 Cheng, S.Z.D. and Lotz, B. (2003) *Philos. Trans. Roy. Soc. A*, **361**, 517–537.
- 57 Woo, E.M., Chou, Y.-H., Chiang, W.-J., Chen, I.T., Huang, I.H., and Kuo, N.-T. (2010) *Polym. J.*, **42**, 391–400.
- 58 Borysiak, S. (2011) *Polym. Eng. Sci.*, **51**, 2505–2516.
- 59 Šmit, I. and Radonjić, G. (2000) *Polym. Eng. Sci.*, **40**, 2144–2160.
- 60 Li, Y.-y., Hu, S.-w., and Sheng, J. (2007) *Eur. Polym. J.*, **43**, 561–572.
- 61 Long, Y., Shanks, R.A., and Stachurski, Z.H. (1995) *Prog. Polym. Sci.*, **20**, 651–701.
- 62 Kalfoglou, N.K. (1985) *J. Appl. Polym. Sci.*, **30**, 1989–1997.
- 63 Santana, O.O. and Müller, A.J. (1994) *Polym. Bull.*, **32**, 471–477.
- 64 Hlavata, D. and Horak, Z. (1994) *Eur. Polym. J.*, **30**, 597–600.
- 65 Bartczak, Z., Galeski, A., and Pracella, M. (1994) *J. Appl. Polym. Sci.*, **54**, 1513–1524.
- 66 Zhang, X., Kotaki, M., Okubayashi, S., and Sukigara, S. (2010) *Acta Biomater.*, **6**, 123–129.
- 67 Quynh, T.M., Mitomo, H., Nagasawa, N., Wada, Y., Yoshii, F., and Tamada, M. (2007) *Eur. Polym. J.*, **43**, 1779–1785.
- 68 Kawai, F., Nakadai, K., Nishioka, E., Nakajima, H., Ohara, H., Masaki, K., and Iefuji, H. (2011) *Polym. Degrad. Stabil.*, **96**, 1342–1348.
- 69 Fan, Y., Nishida, H., Shirai, Y., Tokiwa, Y., and Endo, T. (2004) *Polym. Degrad. Stabil.*, **86**, 197–208.
- 70 Tsuji, H. (2003) *Biomaterials*, **24**, 537–547.
- 71 He, Y., Xu, Y., Wei, J., Fan, Z., and Li, S. (2008) *Polymer*, **49**, 5670–5675.
- 72 Karst, D. and Yang, Y. (2006) *Polymer*, **47**, 4845–4850.
- 73 Tsuji, H. and Ikada, Y. (1996) *Polymer*, **37**, 595–602.
- 74 Tsuji, H. (2002) *Polymer*, **43**, 1789–1796.
- 75 Brochu, S., Prud'homme, R.E., Barakat, I., and Jerome, R. (1995) *Macromolecules*, **28**, 5230–5239.
- 76 Tsuji, H. and Ikada, Y. (1993) *Macromolecules*, **26**, 6918–6926.

- 77 Woo, E.M. and Chang, L. (2011) *Polymer*, **52**, 6080–6089.
- 78 Tsuji, H. (2000) *Polymer*, **41**, 3621–3630.
- 79 Tsuji, H. and Okumura, A. (2011) *Polym. J.*, **43**, 317–324.
- 80 Tsuji, H. and Fukui, I. (2003) *Polymer*, **44**, 2891–2896.
- 81 Muller, D., Garcia, M., Salmoria, G.V., Pires, A.T.N., Paniago, R., and Barra, G.M.O. (2011) *J. Appl. Polym. Sci.*, **120**, 351–359.
- 82 Aldissi, M. (ed.) (1992) *Intrinsically Conducting Polymers: An Emerging Technology*, Kluwer Academic Publishers, Dordrecht, The Netherlands.
- 83 Guimard, N.K., Gomez, N., and Schmidt, C.E. (2007) *Prog. Polym. Sci.*, **32**, 876–921.
- 84 Zhang, F., Bijleveld, J., Perzon, E., Tvingstedt, K., Barrau, S., Inganas, O., and Andersson, M.R. (2008) High photovoltage achieved in low band gap polymer solar cells by adjusting energy levels of a polymer with the LUMOs of fullerene derivatives. *J. Mater. Chem.*, **18**, 5468–5474.
- 85 Wu, Y., Alici, G., Madden, J.D.W., Spinks, G.M., and Wallace, G.G. (2007) *Adv. Funct. Mater.*, **17**, 3216–3222.
- 86 Liu, J., Wang, Z., Xie, X., Cheng, H., Zhao, Y., and Qu, L. (2012) A rationally-designed synergetic polypyrrole/graphene bilayer actuator. *J. Mater. Chem.*, **22**, 4015–4020.
- 87 Anand, J., Palaniappan, S., and Sathyanarayana, D.N. (1998) *Prog. Polym. Sci.*, **23**, 993–1018.
- 88 Vicentini, D.S., Barra, G.M.O., Bertolino, J.R., and Pires, A.T.N. (2007) *Eur. Polym. J.*, **43**, 4565–4572.
- 89 Barra, G.M.O., Leyva, M.E., Soares, B.G., Mattoso, L.H., and Sens, M. (2001) *J. Appl. Polym. Sci.*, **82**, 114–123.
- 90 Barra, G.M.O., Matins, R.R., Kafer, K.A., Paniago, R., Vasques, C.T., and Pires, A.T. N. (2008) *Polym. Test.*, **27**, 886–892.
- 91 Jinnai, H., Nishikawa, Y., Koga, T., and Hashimoto, T. (1995) *Macromolecules*, **28**, 4782–4784.
- 92 Price, R.L. and Jerome, G.W. (2011) *Basic Confocal Microscopy* (eds R.L. Price and G. W. Jerome), Springer, New York.
- 93 Bell, J.R., Chang, K., Lopez-Barron, C.R., Macosko, C.W., and Morse, D.C. (2010) *Macromolecules*, **43**, 5024–5032.
- 94 Li, L., Sosnowski, S., Chaffey, C.E., Balke, S.T., and Winnik, M.A. (1994) *Langmuir*, **10**, 2495–2497.
- 95 Lopez-Barron, C.R. and Macosko, C.W. (2010) *Langmuir*, **26**, 14284–14293.
- 96 Jinnai, H., Yoshida, H., Kimishima, K., Funaki, Y., Hirokawa, Y., Ribbe, A.E., and Hashimoto, T. (2001) *Macromolecules*, **34**, 5186–5191.
- 97 Wang, C.W. and Moffitt, M.G. (2005) *Langmuir*, **21**, 2465–2473.
- 98 Guo, Y. and Moffitt, M.G. (2007) *Chem. Mater.*, **19**, 6581–6587.
- 99 Fransson, S., Lorean, N., Altskaär, A., and Hermansson, A.-M. (2009) *Biomacromolecules*, **10**, 1446–1453.
- 100 Fransson, S., Peleg, O., Lorén, N., Hermansson, A., and Kröger, M. (2010) *Soft Matter*, **6**, 2713–2722.



## 17

# Electron Microscopic Analysis of Multicomponent Polymers and Blends

Rameshwar Adhikari

### 17.1

#### Introduction and Overview

At this point it will not be necessary to provide details of polymer blends, nor of their fabrication routes and applications, as this entire book is devoted to such information. Indeed, a plethora of reference material describing different aspects of the materials science and engineering of polymer blends is available [1–11], with many references – both direct and indirect – being made to electron microscopy (EM) and/or atomic force microscopy (AFM) for such purpose. But this simply highlights the significance of microscopy in the characterization of multicomponent polymers, polymer blends, and their composites.

Polymer blends are characterized by rich variety of structural and functional diversities. The end-use properties of these materials are mainly determined by their morphology on different length scales, the latter being controlled by the molecular structure and chain architecture of the constituents, as well as the processing history of the compound at hand [12]. Therefore, it is of prime importance to understand and purposefully modify the structure of homopolymers, blends and composites on macroscopic, microscopic and molecular levels in order that materials having tailored property profiles can be designed [9,12]. Further, the construction of nanostructured polymers with specific mechanical and functional properties is an important facet of contemporary materials science and engineering. Today, there is a growing interest in the field of nanostructured polymeric materials, due to their promising mechanical and functional properties. Indeed, these materials have in recent years stimulated a great deal of interaction among physicists, chemists, biologists, and engineers such that, as a result, new techniques for the characterization of polymer blends have evolved and advanced. The development of new polymer blends with complex morphologies and properties has also triggered the advancement of new tools and techniques in both EM and AFM [10,13–23].

The mechanical properties of polymers are determined mainly by molecular parameters, as well as their structural details (morphology) and their response towards applied loads. Hence, in order to design polymeric materials possessing a

desired property profile it is essential to develop a suitable morphology aimed at specific micromechanical processes of deformation [24–29].

The different microscopic techniques available, ranging from optical microscopy (OM) to EM and scanning probe microscopy (SPM), play vital roles when characterizing the morphology of polymers on different length scales. These techniques are especially crucial when optimizing the properties of composites through structural characterization, which provides direct clues relating to the interfacial adhesion, shape, size, and distribution of the particles [11,30–44].

In this chapter an overview is presented of the application of EM to morphological studies of polymer blends, with special emphasis on sample preparation and comparative studies using AFM. A brief overview of sample preparation is first provided, followed by some typical characterizations of polymer blends, based on the present author's experience, research data, and information reported elsewhere. It should be noted that only the imaging of polymer blend structures will be described at this point, since the associated spectroscopic tools and chemical mapping are beyond the scope of the chapter.

## 17.2

### Sample Preparation Techniques

The quality of the results delivered by microscopy depends very much on the sample preparation step since, without great care being taken at this time, no conclusions can be drawn on polymer blend morphology that are free from error and/or artifacts. The principal sample preparation routes used for characterizing polymer morphology by EM involve thin films, cut surfaces, fractured surfaces, and etched surfaces.

#### 17.2.1

##### Thin-Film Preparation

Thin films for polymer microscopy (using both EM and AFM) can be prepared in a variety of ways:

- *Film by dropping:* This involves dropping the dilute polymer solution onto a substrate, followed by the subsequent drying and annealing if needed. The film thickness can be generally controlled by the concentration of polymer, but the film thickness will not be uniform.
- *Spin coating:* This involves subjecting a drop of the polymer solution taken onto a substrate to high-speed rotation. Drying and annealing of the films at elevated temperature may also be needed. The film thickness, which is more uniform than in the dropping technique, can be adjusted by changing the solution concentration and the speed of substrate rotation.
- *Dip coating:* This involves slowly drawing a substrate (e.g., a rectangular plate of smooth glass, mica or silicon wafer) that has been dipped into a polymer

solution. The film thickness can be controlled by varying the solution concentration and the film drawing speed.

- *Microtomy and ultramicrotomy:* This involves the sectioning of a bulk sample by means of a microtome or an ultramicrotome. If interest is focused on the morphology of an “as-processed” sample, the above three methods cannot be used because the morphology of interest is lost when the sample is dissolved in a solvent. This is generally the case when the structures of a nanocomposite prepared by different methods are to be compared, or an exact morphology developed during a particular processing route has to be evaluated. Microtomy and ultramicrotomy (sometimes equipped with cryodevices) are employed for the preparation of thin sections of nanocomposite materials. Generally, freshly prepared glass knives or diamond knives are used for this purpose.

As most of the polymeric materials are soft matter at room temperature, the specimens should be hardened before sectioning in order to avoid the local mechanical deformation of one or more of the components present in the blend. Treatment of the sample with high-energy radiations (e.g.,  $\gamma$  rays) or with a chemical staining agent (e.g., osmium tetroxide or ruthenium tetroxide) can help to harden the sample so that it can be sectioned at room temperature. More conveniently, the samples are sectioned at cryogenic temperatures using liquid nitrogen as a coolant. The sectioning temperature is generally below or close to the glass transition temperatures of all components in the blend.

The thickness of the films required for transmission electron microscopy (TEM) investigations should be in the range of 50 to 70 nm, whereas films of any thickness can be studied using either scanning electron microscopy (SEM) or/and AFM.

The ideal specimens for AFM operations are thin films prepared by solution-casting. In this case, the freshly prepared thin films (which range from a few tens of nanometers to a few microns in thickness) are cast from their solutions and can be most conveniently imaged using AFM. It should be noted that, if the film surface is not sufficiently flat, the substrate side of the film can be studied. However, it is important to be aware that the structures of the polymer blends in thin films in the presence of free air may be entirely different from those of bulk specimens, and hence no correlation can be made to the bulk specimen's properties.

### 17.2.2

#### Staining of Thin Sections

The mode of action of EM is based on the interaction of an electron beam with the atoms of the material under study, with contrast generally arising from the production of secondary or back-scattered electrons (in SEM) or the scattering of electrons by the specimen (in TEM). Thus, it is necessary to have a sufficient intrinsic atomic mass contrast and an appropriate surface topography for TEM and SEM investigations, respectively.

Polymers are comprised mainly of low-molar-mass elements such as carbon, hydrogen, and nitrogen, and consequently the atomic mass contrast is very low.

Therefore, when applying conventional TEM to heterophase polymers, the selective staining of one or more of the phases present in the polymer blends is required, using heavy-metal compounds (e.g., osmium tetroxide, ruthenium tetroxide, uranyl acetate) [45–48]. Such staining can be performed either on the bulk material prior to sectioning with an ultramicrotome, or on the films. As noted above, one advantage of staining the bulk sample is that it becomes hardened and can then be sectioned at room temperature.

### 17.2.3

#### **Etching of the Surface**

The free surfaces of samples are studied using SEM and AFM. The smooth specimen surfaces which are required for this purpose are prepared either by ultramicrotomy or by solution-casting procedures (e.g., spin-coating). The free surface can also be etched by reactive ions via a process known as reactive ion etching (RIE) [49–51], or by using chemicals as in the case of permanganic etching [52–55].

Permanganic etching is frequently used to prepare surfaces for SEM examinations, notably of semicrystalline polymers and their blends and composites. In this case the etchant attacks the polymers destructively and progressively removes the outer skin of the polymer, such that the loosely packed amorphous phase is preferentially etched out of the sample. This technique is especially useful for exposing the internal structural details of semicrystalline polymers.

The sample surfaces as received can either be dipped directly into the etchant solution, or the fresh surface for etching can be prepared by microtomy (or ultramicrotomy). The etching period may range from a few seconds to several minutes, depending on the nature of the material under investigation and the concentration of the etchant.

### 17.2.4

#### **Specimens for Fracture Behavior Analysis**

It is common practice in materials science studies of polymer blends to investigate the fracture surfaces (i.e., the surfaces produced after failure of the tensile or impact test specimens) by using SEM. In addition to studying the phase morphology of the blends, this also permits investigations to be made of the fracture behavior of blends, and to provide important clues as to the role of the interfacial structure on the blend's mechanical properties. In general, normally used specimen preparation techniques such as sputtering (or coating with conducting surfaces) are required for fracture surface analysis.

Details of the deformation micromechanisms of polymers can be investigated using different techniques. One of the most common approaches is to prepare specimens for TEM studies from the deformed sample taken from locations close to the fracture surface using an ultramicrotome, and this can be followed by the usual chemical and physical treatments. The thin films may also be stretched

outside the microscope and then examined using TEM. The thicknesses of the films may range from a few hundred nanometers to several microns.

During sample preparation, it should be borne in mind that etching of the sample surface is not obligatory for SEM and/or AFM investigations. Composite materials can be conveniently studied by SEM using the back-scattered electrons (BSE) imaging mode if the secondary electron (SE) mode does not provide sufficient phase information. In the case of AFM, the most important requirement is the flat surface is free from contamination and that there are sufficient differences in local mechanical properties (e.g., stiffness) between the components.

### 17.3

#### Morphological Characterization

The microscopic morphology of polymer blends results basically from the incompatibility of the components, while other factors that influence blend morphology include the processing conditions (e.g., application of shear forces, use of compatibilizer, cooling rate from the melt). Two types of morphology may be observed, namely cocontinuous and dispersed; the latter type is usually observed when one of the components is in a minority.

Both, EM and AFM can be used to determine the morphological details of polymer blends, including the shape, size and orientation of the particles, and the distances between the particles. These techniques reveal not only the polymer phase distribution but also many structural details of the components, and occasionally also of the interface between the polymers. Micromechanical deformation processes are revealed by studying deformed specimens using TEM, and in a very impressive fashion by using AFM. The morphologies of polymer blends presented in the following sections are categorized as blends of semicrystalline polymers, blends of amorphous polymers, and nanostructured copolymers and blends. Finally, some specialized techniques of microscopy and the application of new polymer blends, as well as the deformation behavior of selected polymer blends, will be introduced.

#### 17.3.1

##### Blends of Semicrystalline Polymers

The pioneering investigations of the morphology of polyethylene spherulite and lamellae were conducted by Bassett *et al.*, who studied blends of high-density and low-density polyethylene (weight ratio = 5/95) [56]. These blends were subjected to melt crystallization and then allowed to stretch to different draw ratios. The drawn specimens were cut open at 270 °C (using a glass knife and microtome), either parallel or transverse to the draw direction, and then etched prior to examination with SEM. Etching was continued for 1 h at room temperature with a 1% (w/v) solution of potassium permanganate in a 10:4:1 mixture (by volume) of sulfuric acid, 85%  $\alpha$ -phosphoric acid and water, respectively; this procedure removed a few millimeters from the cut surface. The etched specimens were then coated with gold prior to SEM examination.

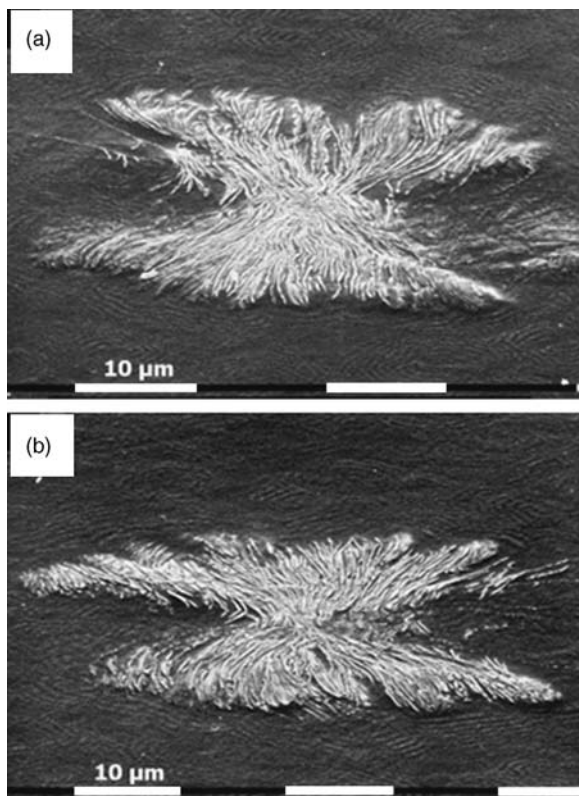


**Figure 17.1** Perpendicular sheaves of linear polyethylene drawn to 2 $\times$  extension at 100 °C at (a) 5 mm min<sup>-1</sup> and (b) 1000 mm min<sup>-1</sup>. The drawing direction is horizontal to the picture plane [56].

The morphology of the blend with a deformed high-density polyethylene (HDPE) spherulite drawn at 100 °C to a draw ratio of 2 with different speeds is shown in Figure 17.1 [56]. On careful examination of the micrographs, several interesting features were observed. The extent of internal lamellar deformation (i.e., the separation of lamellar bundles leading to the formation of kinked bands) was increased for the slightly higher draw ratio of 2.0, as shown first for parallel sheaves in Figure 17.1. The slow-drawn object in Figure 17.1a showed a paler contrast at its center and at its extremities, where the influence of the dominant lamellae survived in the grouping at the perimeter; the contrast was finely modulated throughout. At the higher draw rate (see Figure 17.1b), the same features were present but the contrast difference appeared larger than for the slow draw.

More importantly, the SEM images shown in Figure 17.1 provided an insight into the possibility of imaging individual spherulites in the blends of two different polyethylenes due to correct specimen preparation.

The second example of semicrystalline polymer blends involved the SEM imaging of a mixture of two different types of polyethylene, the surfaces of which were

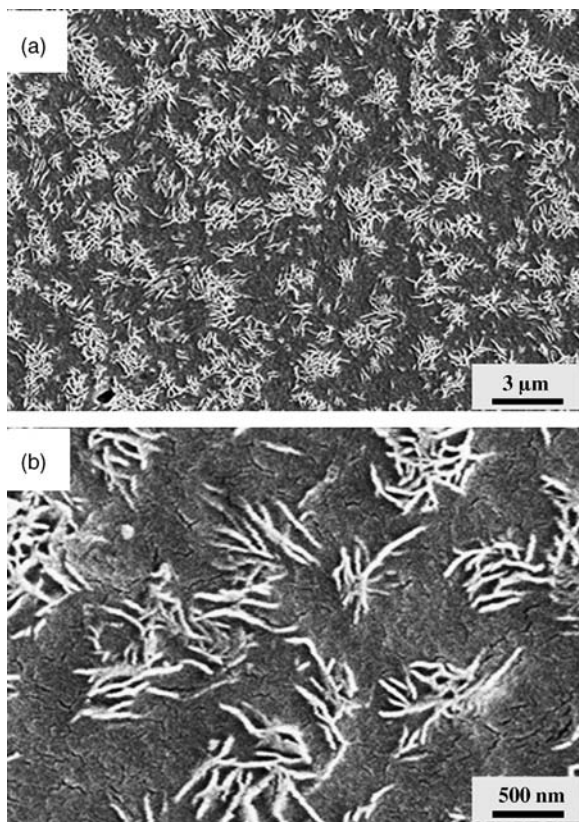


**Figure 17.2** SEM images of different magnifications showing the typical matrix/dispersed phase bulk morphology of HDPE/EOC (25/75) blend [57].

prepared in similar manner as the materials depicted in Figure 17.1. The sample surface for the SEM investigation was prepared according to a standard permanganic etching procedure that was described originally by Olley *et al.* [53,54] and further developed for specific multicomponent blends [52,55].

This technique was employed to visualize the morphology of polymer blends comprising HDPE and an ethylene/1-octene copolymer (EOC; Affinity<sup>TM</sup> EG 8150, a commercial product of the Dow Chemical Company) which had a relatively high 1-octene content [57]. The representative results are presented in Figure 17.2.

A strong tendency towards phase separation was observed for the different types of HDPE/EOC blend, irrespective of the blend composition. Among these blends, the HDPE/EOC system was found to incline most robustly towards segregation. As an example, the morphology of a blend containing 75 wt% EOC is shown in Figure 17.2.

The SEM images showed that the minority HDPE phase existed as isolated islands scattered in the matrix of the EOC. The HDPE lamellae appeared bright in the SEM images and extended to a length of several hundred nanometers,

acting as a filler for the matrix polymer. The formation of a spherulitic morphology, which is typical of HDPE, was thus strongly suppressed.

It should be noted that the investigated blend partners are characterized by differences in their melting points with, in general, the melting temperature being lowered with increasing 1-octene content [58]. The blends of HDPE with the copolymers showed two separate melting endotherms which corresponded to that of two pure components, and indicated that they had crystallized as separate entities in all of the blends [58]. For example, regardless of the composition, two melting points were observed around 400 K and 330 K in the HDPE/EOC blends. The presence of multiple melting points in the blends strongly supported the notion of demixing of the blend components [57].

When using TEM, the presence of long individual lamellar crystals with a very high aspect ratio was revealed in the EOC-rich blends [59] (see Figure 17.3). The growth of lamellae to exceptionally long dimensions was correlated with a wide gap in the melting temperatures of the polymers. However, on cooling the mixture from the melt, when the HDPE component solidified due to crystallization,

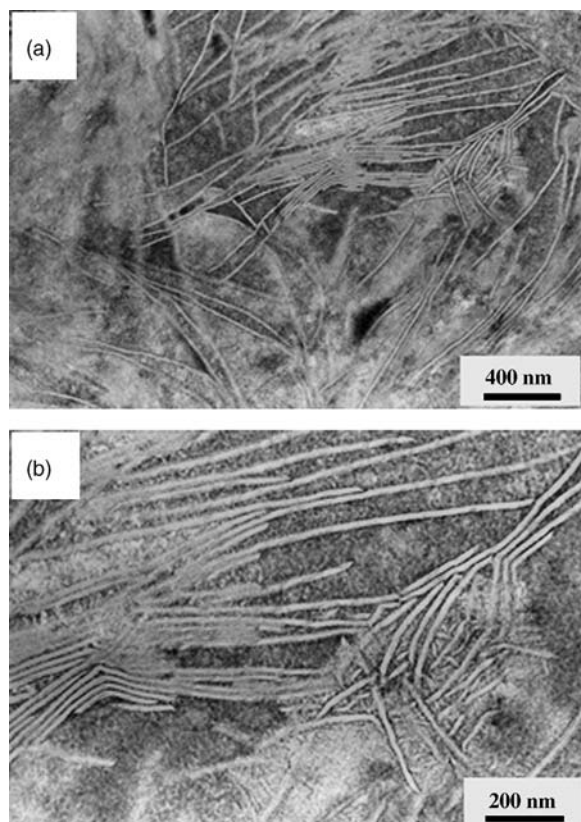


**Figure 17.3** Higher- (a) and lower- (b) magnification TEM images of HDPE/EOC (40/60) blend. The thin sections for the investigations were stained with RuO<sub>4</sub> vapor [59].



the surrounding EOC phase remained mobile (in a molten state) due to its much lower melting and crystallization temperatures. This situation enabled a rapid growth of the HDPE lamellae, which penetrated the EOC phase. This assumption was supported by the presence of a pointed, tip-like appearance of each lamella at the interface with the copolymer matrix [60,61]. Figure 17.3 also shows the lamellar arrangement of the crystals of HDPE which are embedded in the matrix of the composed micelle-like domains of the EOC. On careful observation of the matrix morphology, the latter can be observed as background structures [52].

Correct sample preparation is also crucial when studying the morphology of semicrystalline polymer blends using TEM. Typically, the blend is stained with ruthenium tetroxide ( $\text{RuO}_4$ ) vapor which, by virtue of its rapid diffusivity in the loosely packed amorphous regions of the sample, is deposited preferentially in the amorphous part of the blend. Consequently, in the TEM images the amorphous phase will appear dark and the crystalline phase bright.

The results produced via TEM investigations depend largely on various factors such as the thickness and uniformity of the sections, the staining agent concentration, the duration of staining process, and the selection of imaging parameters. Quantitative information can be obtained from the TEM images by using image-processing software, as is the case for the quantification of micrographs obtained using other techniques.

One quite reliable microscopic technique that requires no special sample preparation is that of AFM [22,62,63]. In particular, the phase-imaging mode in tapping mode AFM delivers important information regarding the structure and properties of heterogeneous semicrystalline polymer blends.

For the purpose of comparing results obtained via different techniques, an analysis should be made of the morphology of blends, using AFM and polymer combinations identical to those presented in Figures 17.2 and 17.3 (see Figures 17.4 and 17.5 below). The AFM phase images of HDPE/EOC blends with two different compositions are presented in Figure 17.4, where well-defined long lamellar crystals of HDPE phase can be seen to coexist with worm-like domains of much thinner crystals of the EOC phase that can easily be distinguished in the phase images. The sample for AFM imaging was prepared by annealing the polymer film surface between two freshly cleaved mica sheets close to melting point, and then slowing the rate of cooling to room temperature. Thus, the structure observed in Figure 17.4 represents that of the surface of the polymer blends and not that of the bulk. In order to analyze the bulk structure of the blends, the samples were sectioned (using an ultramicrotome) at about  $-120^\circ\text{C}$ , fixed to the AFM sample holder, and then scanned using tapping mode phase imaging under ambient conditions. The results obtained from one of these blends, using AFM, are presented in Figure 17.5, where the semicrystalline texture of the blend, with its unique arrangement of well-grown and long HDPE lamellar crystals, can be seen to coexist with the EOC phase. In the high-magnification AFM phase image (Figure 17.5b), ill-developed crystalline domains of the EOC phase were also clearly visible, appearing as a background structure in the polymer blend.

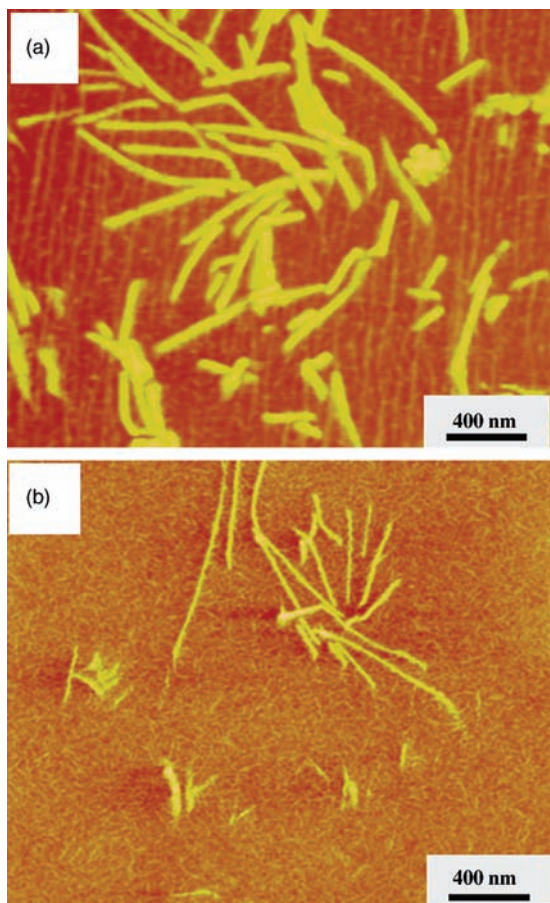


**Figure 17.4** Representative AFM phase micrographs of HDPE/EOC blend surfaces containing different weight fractions of EOC. (a) 50% EOC; (b) 75% EOC [57].

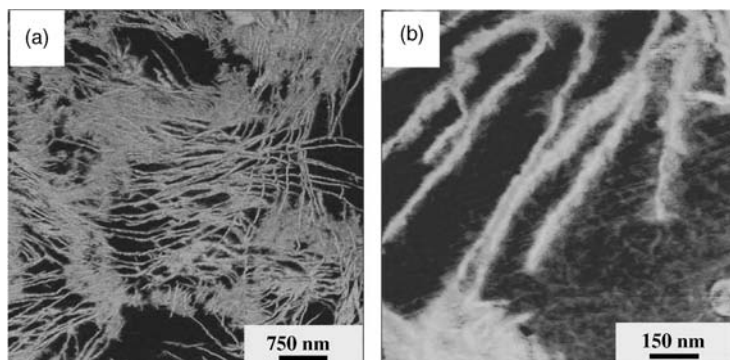


**Figure 17.5** AFM phase images of different magnifications obtained by scanning of cryo-ultramicrotomed surface of the HDPE/EOC (50/50) blend.

It should be borne in mind that the bulk morphology of the blend (Figure 17.5) was basically identical with the surface morphology of the blend (see Figure 17.4a), in terms of the arrangement of lamellar crystals and coexisting crystalline domains. However, in terms of the ratio of HDPE/EOC crystalline phase ratio, the morphology was completely different.

When discussing the contrast of the AFM phase images, one important aspect should not be disregarded; namely, that the contrast mechanism in AFM phase imaging is in fact coupled with a number of factors including experimental parameters [28].

In this section it was shown that, with correct sample preparation, a deeper and wider insight can be acquired into the morphology of blends comprising semicrystalline polymers by using different microscopic techniques (SEM, TEM, AFM) as complementary analytical tools. Quantitative information relating to lamellar dimensions, orientation and distribution, which are beyond the scope of this chapter, can be easily obtained using correct image-processing software.

### 17.3.2

#### **Blends of Amorphous Polymers**

With the morphology of blends of semicrystalline polymers having been discussed, some other blends that comprise amorphous polymers should now be examined. Since it is possible to create blends that consist of one or more of semicrystalline polymers and one or more amorphous polymers [9], two examples can now be introduced that illustrate the morphology of incompatible polymer blends, as investigated using two different techniques (viz., TEM and AFM). The micrographs shown in Figure 17.6 are of high-impact polystyrene (HIPS), a popular plastics material that is an excellent example of how multicomponent amorphous polymers can be investigated using different microscopic techniques. As in previous cases, the choice of imaging technique and corresponding sample preparation depended heavily on the type of morphological information being sought experimentally.

Figure 17.6a is a TEM image of an ultrathin section of the HIPS sample that had been stained with osmium tetroxide vapor [64]. The aim of such staining was to render the internal structure of the HIPS visible by selectively depositing a heavy-metal component in the butadiene-rich phase (or in the component with C=C unsaturated bonds). The image showed the typical “salami” structure of the sample, while the butadiene-rich phase and the “crazes” appeared as dark areas. This imaging was especially important because it provided information as to how the crazes evolved, “wandered,” and were eventually stopped by the presence of the “salami” particles.

TEM has also permitted the imaging of ultrathin sections of heterogeneous polymers by physically crosslinking the rubbery phase by gamma irradiation [65] (see Figure 17.6b) and using the Lorenz microscopy mode [66] (see Figure 17.6c) by virtue of inherent mass contrast. The same bulk morphology of the specimen could also be imaged in tapping mode AFM phase imaging, due to differences in the local mechanical properties of the components of the blend (see Figure 17.6d).

In order to further highlight the capabilities of tapping mode AFM imaging for the structural elucidation of polymer blends, the morphology of an acrylonitrile–

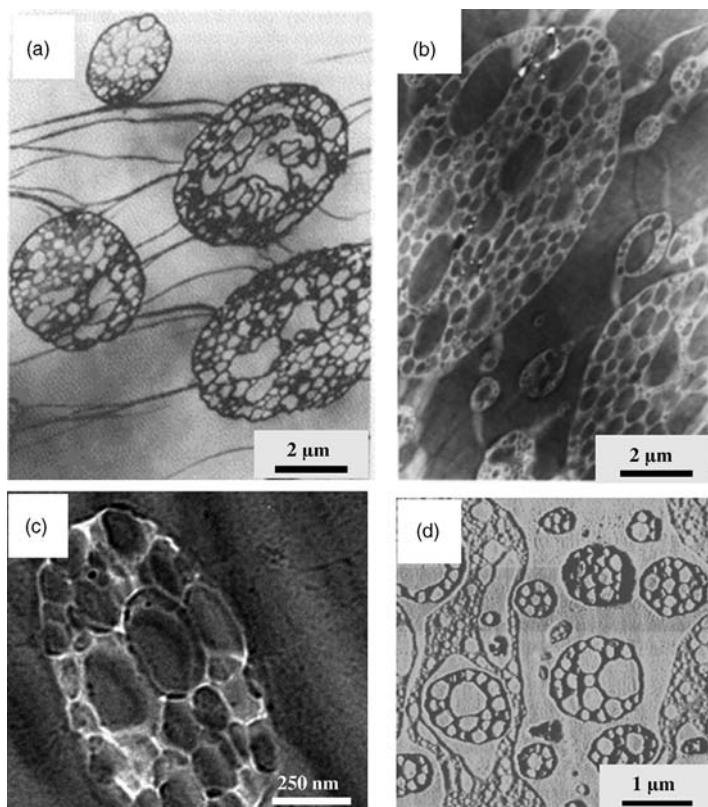


**Figure 17.6** Micrographs of HIPS samples imaged by using different microscopic techniques. (a) Craze in HIPS imaged using stained ultrathin sections by TEM [64];

(b) HIPS particles made visible by gamma irradiation with TEM [65]; (c) HIPS particle imaged using Lorenz microscopy [66]; (d) AFM phase imaging of the cut surface.

butadiene–styrene (ABS) copolymer is presented in Figure 17.7. The copolymer appeared practically as a blend of polystyrene particles embedded in a matrix of the styrene–acrylonitrile (SAN) copolymer. The adhesion between the particles and matrix was provided in this case by the presence of styrene copolymer chains at the matrix–particle interfacial region [2,9].

Figure 17.7a shows the AFM tapping mode topography or height image of the ABS copolymer, while Figure 17.7b shows the phase image of the same area. In the height image, around the particles' periphery, a thin layer of a bright-appearing ring was ascertained that was masked in the phase due to a high contrast between the particles and the matrix in the phase image (see Figure 17.7b). However, a closer examination of the phase image (Figure 17.7b) revealed both the presence of the ring and the heterogeneous texture of the particles themselves. These observations implied on the one hand the chemical heterogeneity of the particles, and on the other hand the formation of a thin, compatibilizing layer around the particles.

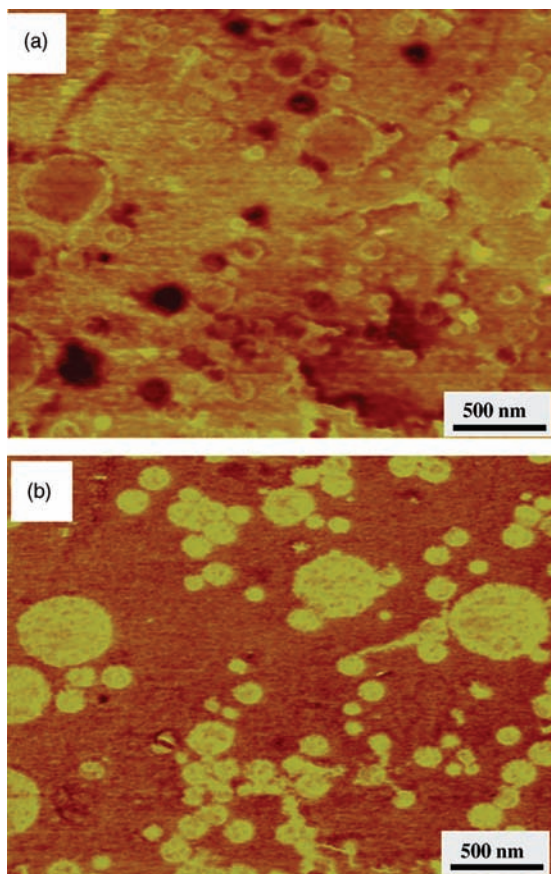


**Figure 17.7** AFM height (a) and phase (b) images of an ABS copolymer imaged on bulk cryo-ultramicrotomed surface.

Clearly, the height image does not provide much information regarding the morphology of samples under investigation; however, an analysis of the phase image may offer the possibility of determining the particle size and their distribution, as well as the distance between them. At first glance the material would appear to have a bimodal distribution of the particles, with their diameters centered at about 400 nm and 100 nm. Such a distribution of particles would be required to optimize the mechanical properties of these polymeric materials [67,68].

### 17.3.3

#### **Nanostructured Copolymers and Blends**

The blends discussed so far have had dimensions of phase separation ranging from several hundred nanometers to several micrometers, which are the characteristic features of classical polymer blends. Since the advent of nanotechnology,

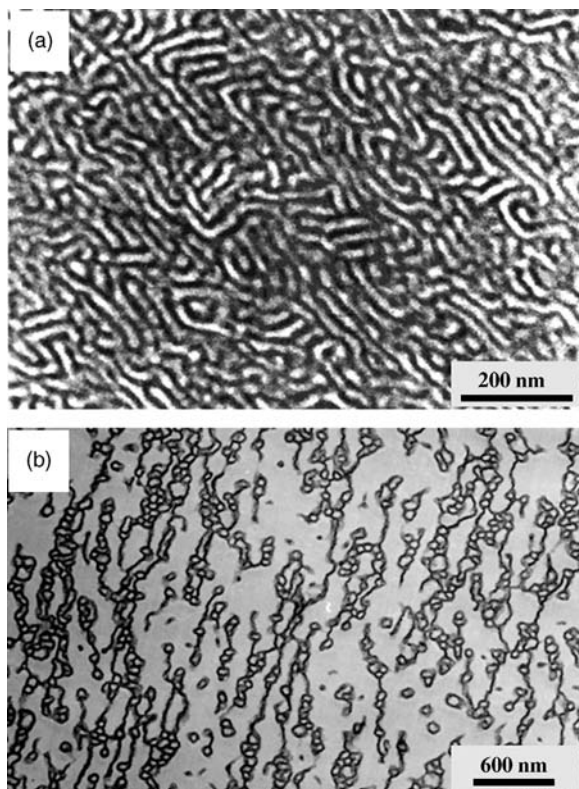


**Figure 17.8** TEM images of thin sections of (a) styrene/butadiene star block copolymer and (b) the blend of the star block copolymer with 80% by weight of general-purpose polystyrene [69].

there has been an increasing trend to incorporate nanosized particles into the polymer blends, or to generate a nanostructured morphology in the blends themselves. The morphology of some polymer blends that are characterized by their inherent nanostructured morphology that has evolved due to effects of molecular architecture, special compatibilization or to processing methods, are illustrated in the following subsections. Particular attention is paid to blends comprising block copolymers which are themselves nanostructured due to the chemical connectivity of different polymer chains via covalent linkages.

Figure 17.8a is the TEM image of a styrene/butadiene star block copolymer containing 74% (by volume) styrene. The nanostructured morphology arises from the fact that the constituents – that is, polystyrene (PS) and polybutadiene (PB) chains – are connected chemically by covalent bonds which do not permit a macroscopic segregation of the polymer chains. Due to the presence of a unique molecular architecture of the copolymer, the star block copolymer was found to show a cocontinuous arrangement of the nanostructures [69–72]. The star block copolymer specimen was treated with osmium tetroxide vapor prior to TEM imaging; such treatment

promotes the deposition of heavy-metal compounds in the butadiene domains, where unsaturated double bonds can react with the former.

A similar treatment allows a straightforward imaging of the nanostructures of the blend of the star block copolymer and general-purpose PS [73,74] (see Figure 17.8b). The block copolymer/PS weight ratio in the blend was 20/80, and the structures formed were the result of processing by compression molding. Under equilibrium conditions, these components would segregate macroscopically to yield a classic particle–matrix morphology with micro-sized particles [69].

The dark areas in Figure 17.8b represent the butadiene-rich component (due to staining by heavy-metal compounds) of the polymer blend, and the brighter areas the PS phase. Thus, the PS domains in the blend appear as the droplets surrounded by a rubbery phase; this typical arrangement has been referred to as “droplet morphology,” and is responsible for the observed greater toughness of the blends compared to corresponding blends with layered morphologies [75].

Block copolymers not only possess nanostructures in their blends with one of the corresponding homopolymers, but also induce nanostructures in the blends of other types of polymer, such as thermosetting resins [76–80]. Some examples reported recently by various research groups are described in the following examples.

Nanostructured blends of an epoxidized styrene/butadiene/styrene (SBS) tri-block copolymer with diglycidyl ether of bisphenol A (DGEBA) -based epoxy resins were recently reported by the groups of Thomas and Mondragon [76,77]. The nanostructured morphology of diaminodiphenyl-methane (DDM) cured blends of DGEBA and highly epoxidized SBS (eSBS; 90/10 weight ratio) is shown in Figure 17.9a [76]. This TEM image clarifies the nanostructured morphology in the blends with 47 mol% of eSBS. The spherical micelles with diameters of 20–30 nm were found to disperse in the continuous epoxy matrix containing epoxidized PB segments. The spherical micelles were generated with a core of incompatible PS domain, which was encircled by a shell of neat PB chains. The epoxidized PB chains were completely extended into the epoxy matrix because of the hydrogen-bonding interaction [76].

In a similar line of investigation, blends of epoxy resins with larger proportions of eSBS block copolymers were studied recently [77]. The morphological features observed on the cryo-ultramicrotomed face of the samples, using AFM, are presented in Figure 17.9b. This image shows the different orientations of the microdomains, as either parallel (flat-on) or perpendicular (edge-on) lamellae domains to the cut surface; notably, the parallel lamellae are characterized by a continuous phase. It was concluded that the nanostructures thus formed in the epoxy/eSBS (weight ratio 30/70) blend possessed lamellar nanostructures. It was further emphasized that the orientation of the lamellae microdomains – whether parallel or perpendicular to the cut surface – was similar to that observed in blends of different block copolymers [77].

Studies on epoxy resin-based nanostructured blends were focused mainly on the use of highly epoxidized block copolymers. Clearly, the extent of epoxidation can have a dramatic influence on the morphology of such blends; this phenomenon can be illustrated on the basis of TEM images collected from blends comprising the same

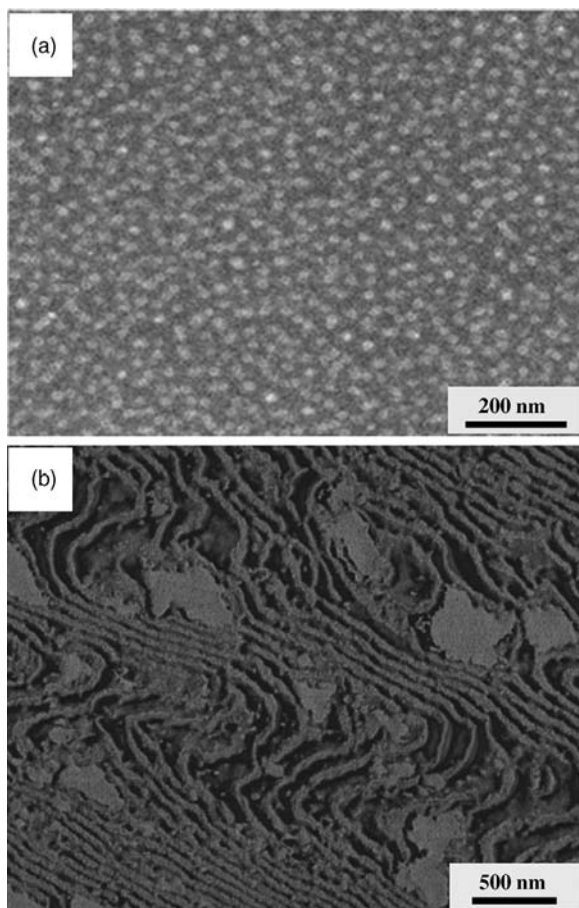


**Figure 17.9** (a) TEM image of a blend comprising 90 wt% epoxy resin and 10 wt% epoxidized (eSBS) block copolymer [76]; (b) AFM phase image of a similar blend comprising 30 wt% eSBS copolymer [77].

eSBS/epoxy weight ratio but differing in the extent of epoxidation of the butadiene units of the SBS triblock copolymer. The matrix used in this case was a methylene dianiline (MDA)-cured DGEBA-based epoxy resin, and the specimens were prepared using ultramicrotomy and stained with osmium tetroxide. The morphology of the blend containing 30 wt% eSBS with 25 wt% epoxidation is shown in Figure 17.10a. The TEM image shows the typical particle matrix morphology of the blend, with block copolymer domains as the matrix and epoxy resin particles as the dispersed phase; the segregation thus observed can be termed as a macrophase separation (R. Pandit, unpublished results). It is interesting to note that the block copolymer (i.e., the eSBS) formed a matrix even when present only as a minority phase.

The phase-separation behavior of the blend took a dramatic turn when the butadiene phase of the SBS copolymer was completely epoxidized (Figure 17.10b),



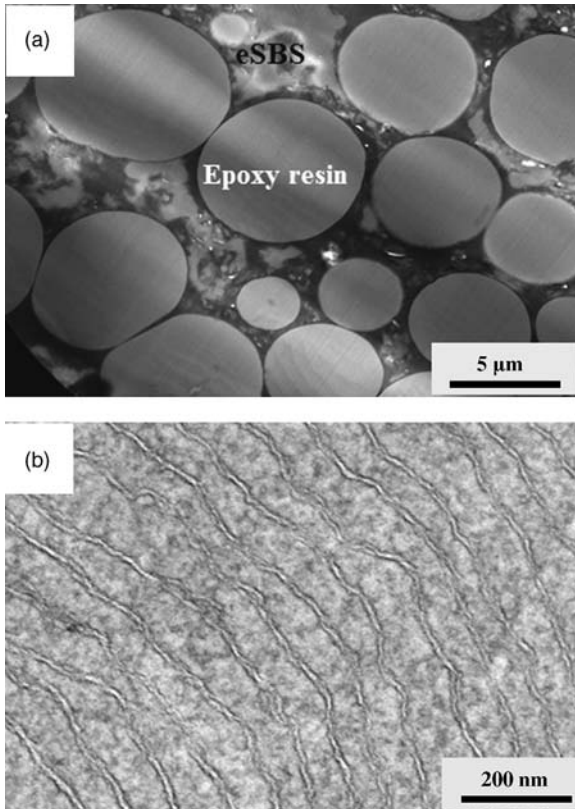


**Figure 17.10** TEM images of a blend comprising 70 wt% epoxy resin and 30 wt% epoxidized (eSBS) block copolymer. The degrees of epoxidation of the latter were 25 wt% (a) and 100% (b).

when the morphology changed into a completely microphase-separated form. The PS phase formed cylinders inside a cylinder of epoxidized block copolymer, with the double-walled cylinder embedded into the matrix of the epoxy resin.

## 17.4

### Special Techniques and Applications

Historically, EM has played important role in elucidating the structure and properties of various processing forms of classical polymer blends, composites fibers and biomedical objects. The microscopic analysis of certain special types of blend are examined in the following subsections.

A TEM image of the multilayered composite structure of a blend of polyethylene terephthalate (PET) and polycarbonate (PC) (PET/PC weight ratio 10/90) is shown in Figure 17.11a. The laminate structure of the blends was achieved by a special

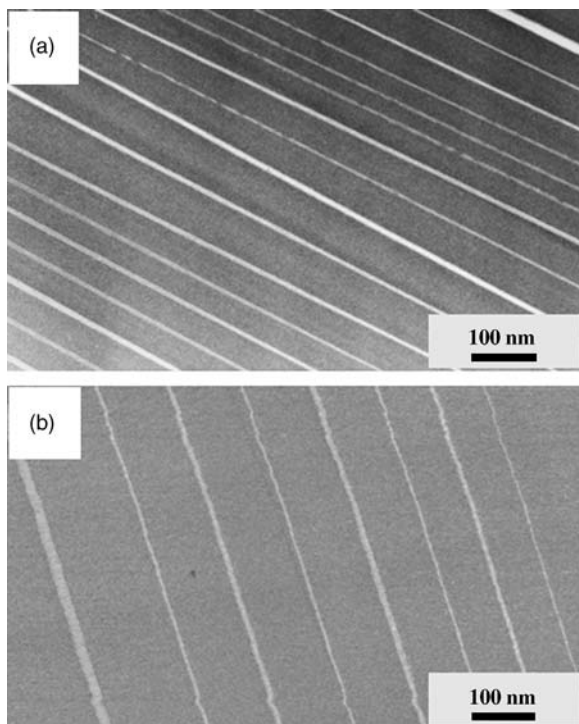


**Figure 17.11** (a) TEM image of a PET/PC (10/90 weight ratio) multilayered composite using  $\text{RuO}_4$  as staining agent; (b) AFM phase image of the same blend.

processing termed microlayer coextrusion [81–83], and the sections were stained with ruthenium tetroxide vapor prior to TEM imaging. The PC phase, owing to its lower density and hence preferential deposition of the staining agent, appeared darker in the TEM image (Figure 17.11a). The freshly ultramicrotomed face of the same sample was analyzed using AFM phase imaging in tapping mode (see Figure 17.11b). The results of both TEM and AFM investigations were comparable in terms of the size of the structures, which showed quite continuous and uniformly thick layers of the constituents in the blend.

It should be noted, however, that several attempts were required to stain the PC phase sufficiently for TEM imaging, whereas the difference in bulk mechanical properties between PET and PC was sufficient to obtain a sharp contrast in the AFM images, within minutes of microscope operation.

As another example of the special type of polymer blend studied with EM, the SEM images of a biopolymer-based compound are presented in Figure 17.12. Recently, the encapsulation of curcumin in submicrometer spray-dried chitosan/Tween 20 particles was evaluated using SEM imaging [84]. Tween 20 was a commercially available version of polyethylene glycol sorbitan monolaurate. The encapsulation of curcumin is important, as its optimal delivery in medicinal

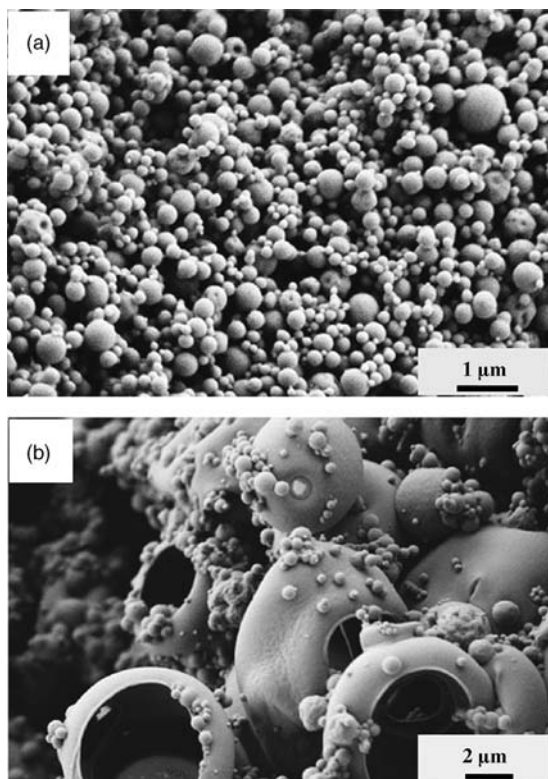


**Figure 17.12** SEM images of chitosan particles spray-dried with chitosan and Tween 20. (a) Low Tween 20 concentration; (b) High Tween 20 concentration [84].

applications requires a drug-delivery system that solubilizes curcumin and also prevents its degradation. Images of the particles produced, highlighting the effect of chitosan concentration on particle size, are shown in Figure 17.12. Moreover, as the proportion of Tween 20 was increased, the size of the particles was found also to increase drastically (cf. Figures 17.12a and b). An analysis of the particles with holes further confirmed that the vesicles were hollow, as would be required to serve as drug-delivery vehicles.

It should be noted that, whilst TEM and AFM may not be suited to the imaging of vesicular structures in drug-delivery systems, SEM may offer an excellent solution to the problem. In fact, environmental scanning electron microscopy (ESEM) provides an elegant approach to imaging the structures of biomedical materials at high resolution, and occasionally also under the physiological conditions encountered in body tissues [10].

During the past few decades, much progress has been made in the field of microscopic techniques based on spectroscopy. One such method is scanning transmission X-ray microscopy (STXM) which permits the nondestructive chemical mapping of heterogeneous polymers (including polymer alloys) through different specimen

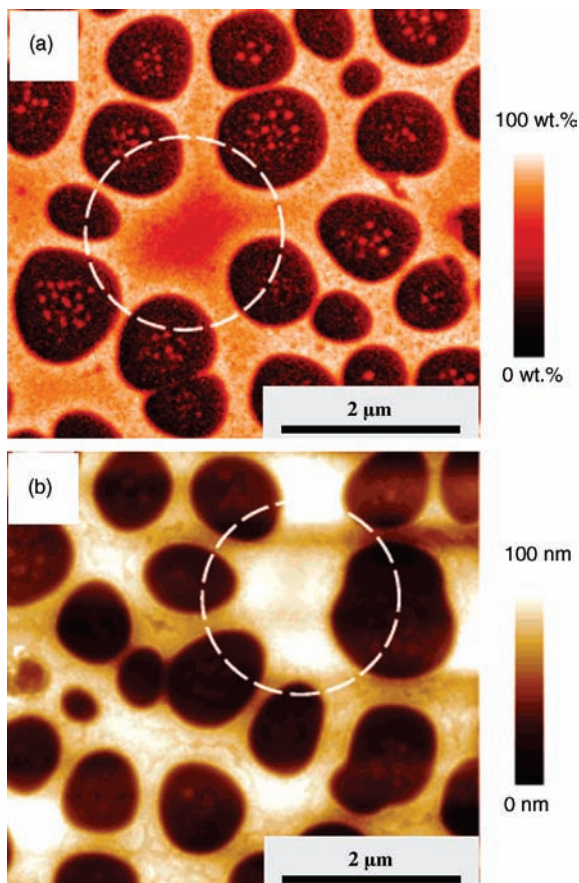


**Figure 17.13** Morphology of 150 nm-thick film of the TFB/F8BT blend. (a) STXM composition map of F8BT; (b) AFM image of the blend. The wider F8BT-rich areas that show little variation in surface features but a marked decrease in F8BT concentration are encircled [85].

thicknesses. Recently, the use of STXM allowed the quantitative chemical analysis of the bulk composition of spin-coated blends of poly(9,9-dioctylfluorene-*co*-*N*-(4-butylphenyl)diphenylamine) (TFB) and poly(9,9'-dioctylfluorene-*co*-benzothiadiazole) (F8BT), both of which are used in efficient polymer light-emitting diodes (LEDs). Subsequently, a combination of STXM with AFM permitted both the surface and subsurface structures of the blends to be revealed, as well as the enrichment of F8BT at the domain interface [85,86] (Figure 17.13). The matrix of the polymer is formed by F8BT phase in which the particles of the TFB particles are dispersed.

An STXM scan of the 150 nm-thick film (see Figure 17.13a) showed that F8BT depletion occurs only at regions more than 500 nm away from the interface. Interestingly, although TFB distribution within the F8BT region varied smoothly in these wider areas, in the narrower regions of the F8BT-rich phase of the film the

TFB was distributed unevenly. Unlike the F8BT-rich spots in the TFB-rich phase, which correlated with morphological features in the AFM images (see Figure 17.13b), the TFB-rich spots in the F8BT region did not match the surface structures seen with AFM. As STXM is sensitive to variations in bulk composition, this observation demonstrated the existence of subsurface structures in the F8BT-rich phase.

Thus, in the LED blend the AFM image provided only the structure of the surface, and no information on the bulk could be obtained. However, the subsurface information could easily be collected by employing the STXM technique.

## 17.5

### Deformation Studies on Polymer Blends

Knowledge of the deformation micromechanisms of polymers is an important aspect of the fields of materials science and engineering. Indeed, precise investigations of the processes of deformation and fracture have contributed a great deal to the construction of materials with tailored properties [87–89].

A glimpse of the contribution of EM to studies of the deformation behaviors of polymer combinations is provided in the following subsection, albeit limited to only some nanostructured blends. A first example is the analysis of the morphology of an SBS triblock copolymer with an original lamellar morphology [74] with glassy PS and rubbery PB layers. The lamellae were oriented via extrusion of the melt, and the extrudates subjected to tensile deformation, both parallel and perpendicular to the lamellae orientation direction. The deformation structured by perpendicular deformation is shown in Figure 17.14. The TEM specimens were taken from the deformed tensile bar, from an area close to the fracture surface, and stained with osmium tetroxide vapor. Thus, the deformation structures corresponded to the high-strain deformation of the lamellae.

On stretching the sample perpendicular to the lamellae orientation direction, the lamellae were found to be deformed by the formation of a “chevron” morphology or “fish bone” pattern. The long spacing was found to remain almost constant in the straight limbs of the chevron folds, but in the hinge regions the soft rubbery layers (the dark regions in the images) were more dilated than their glassy counterparts. Such deformation structures are commonly found in layered rocks that have been subjected to vertical strain for long periods of time [90]. The lamellar long period in the deformed sample did not change significantly, but there were regions of different periodicities in the deformed sample (see Figure 17.14). Stretching of the glassy PS layers, as well as the high dilation of the rubbery regions, was found to contribute to the high ductility of the lamellar block copolymer being examined [72,74,91,92].

The experiment performed to record the TEM images (as shown in Figure 17.14) was a type of post-mortem study that could also be performed with the aid of TEM, using a stretched, semi-thin section (i.e., a few microns thick) of the polymer. This study revealed the deformation structures that were more correlated to

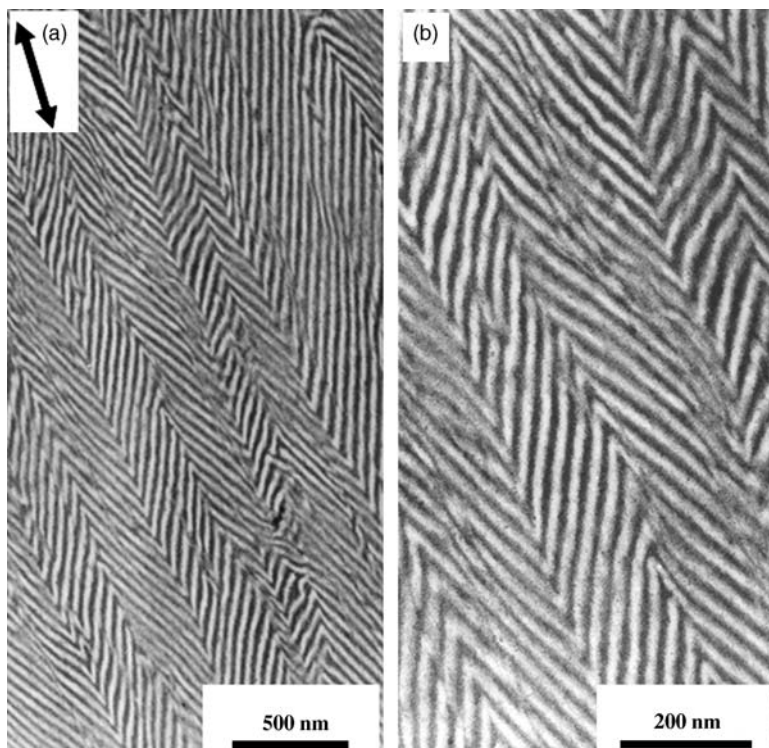


**Figure 17.14** (a) Lower- and (b) higher-magnification TEM images of a deformed lamellar SBS triblock copolymer, when the sample was stretched perpendicular to the lamellae orientation direction. The strain direction is shown by the arrow [74].

the bulk polymer deformation [93,94]. More direct information on these deformation micromechanisms can be obtained via *in-situ* deformation studies in polymer, blends, and composites [12,21,95,96].

A highly informative picture of the deformation phenomena in polymer blends can be obtained by simply studying the fracture surface of the specimens obtained after the macroscopic deformation mechanical tests, such as tensile and impact testing. These studies also provide information regarding bonding at the interfacial region and the extent of segregation of the components in the blends. For example, Figure 17.15 shows the SEM images of a blend comprising rubbery and thermoplastic polymers, where the first image shows a high elastomeric recovery and the second shows a large plastic deformation [97]. Both polymers were styrene/butadiene copolymers with different compositions.

The SEM images in Figure 17.15 show a typical “pits and hills” morphology. The “pits” are formed by the elastomeric polymer, which has also a relatively smooth texture due to the resilience of the rubbery chains, whereas the “hills” are rougher and are due to a greater plastic deformation. After plastic deformation the

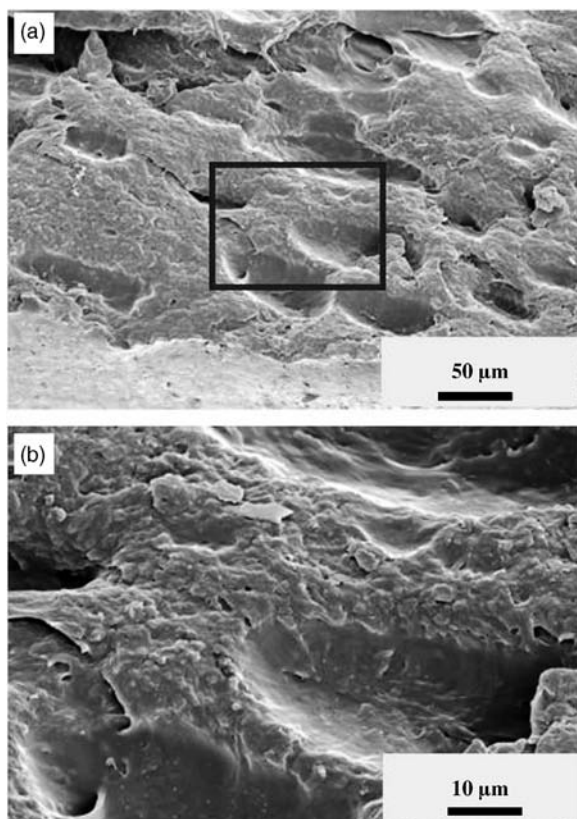


**Figure 17.15** (a) Lower- and (b) higher-magnification SEM images of tensile fracture surfaces of a blend comprising a thermoplastic polymer and an elastomer. Panel (b) is a high-magnification image of the boxed area in panel (a) [97].

thermoplastic remained rigid and consequently appeared as protrusions on the fracture surface [97].

Although thermosetting polymers such as epoxy resins have a long history and many potential applications, the issues related to their stiffness/toughness correlation have not yet been resolved. Whilst many attempts have been made in the past to increase the toughness of epoxy resins, the aim of the studies concerned with the fabrication of nanostructured morphologies (as shown in Figures 17.9 and 17.10) was to increase the toughness of these brittle materials.

The addition of a block copolymer to an epoxy resin matrix endows these materials with a greatly increased toughness. Direct evidence for this behavior has been found recently by studying the fracture surface morphologies of blends, using SEM (see Figure 17.16) [98]. Figure 17.16a shows the fracture surface morphology of the neat cured epoxy resin, where features that would be expected on the fracture of window glass – that is, flat and smooth surfaces with some steps

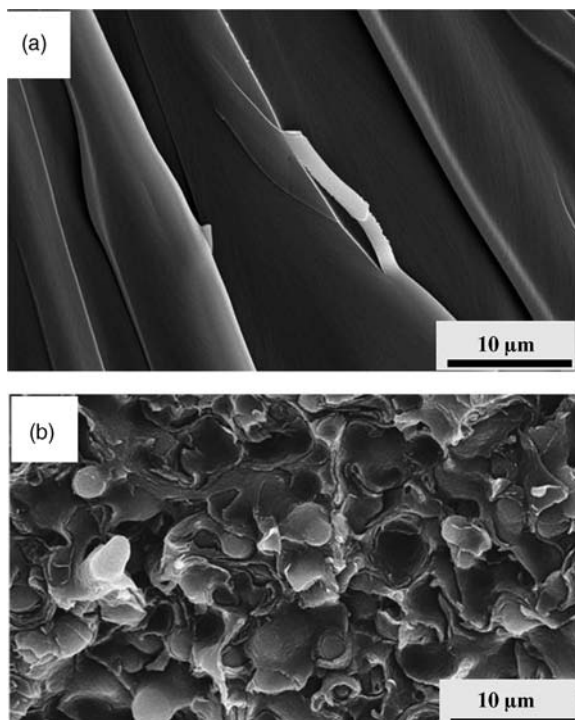


**Figure 17.16** SEM images of tensile cryofracture surfaces different polymers. (a) Neat cured DGEBA-based epoxy resin; (b) Blend comprising the resin and a small amount of eSBS [98].

showing fracture planes – can be observed. The same sample, after modification with small amounts of epoxidized block copolymer, showed a highly fibrillated morphology (Figure 17.16b) which was formed by a major plastic deformation of the matrix. The latter is a highly energy-absorbing process and contributes to the increased toughness of these materials [98].

## 17.6

### Concluding Notes

Electron microscopy, complemented by various other techniques (e.g., AFM, electron holography, STXM, micro- and nanoindentation techniques, energy filtering facilities in electron microscopes), has contributed– and will undoubtedly continue to contribute – to the comprehensive understanding of the morphology of polymer blends. In this chapter, the morphology of different types of polymer blends, when investigated by various microscopic techniques, was discussed with special reference to sample preparation and comparison among SEM, TEM, and AFM.



Sample preparation was shown to be a crucial issue for the error-free evaluation of the morphology of polymer blends. Whilst the selection of specimen preparation conditions and specific microscopic techniques depend largely on the nature of the problems at hand, the combination of two or more methods will certainly help in obtaining the most reliable picture of the blend morphologies.

One of the most important areas in which EM has delivered significant contributions has been the investigation of deformation behaviors of polymer blends, in particular with *in-situ* deformation tests. Post-mortem studies of specimens close to the fracture surface, or an evaluation of the deformed semi-thin section by means of TEM and an analysis of the fracture surfaces using SEM, may provide important clues as to the deformation micromechanisms of polymer blends.

## Acknowledgments

The author acknowledges the Alexander von Humboldt (AvH) Foundation for supporting several research visits to Germany. He also thanks Prof. Goerg H. Michler and his research group at Martin Luther University Halle-Wittenberg, Germany for their unconditional support to the author's research missions in the field of nanostructured polymers in Nepal.

## References

- 1 Kausch, H.H. (ed.) (1983) *Advances in Polymer Science: Cracking in Polymers*, vol. 52/53, Springer-Verlag, Berlin, Heidelberg.
- 2 Woodward, A.E. (1988) *Atlas of Polymer Morphology*, Hanser Publication, Munich, Vienna, New York.
- 3 Paul, D.R. and Bucknall, C.B. (eds) (2000) *Polymer Blends*, vol. I and II, John Wiley & Sons, New York.
- 4 Fakirov, S. (2002) *Handbook of Thermoplastic Polyesters: Homopolymers, Copolymers, Blends, and Composites*, Wiley-VCH, Weinheim, New York, Chichester.
- 5 Utracki, L.A. (1989) *Polymer Alloys and Blends*, Hanser Verlag, Munich.
- 6 Hamley, I. (1998) *The Physics of Block Copolymers*, Oxford Publishers, London.
- 7 Baltá-Calleja, F.J. and Fakirov, S. (2000) *The Microhardness of Polymers*, Cambridge University Press, Cambridge.
- 8 Michler, G.H. and Baltá-Calleja, F.J. (eds) (2005) *Mechanical Properties of Polymers based on Nanostructure and Morphology*, CRC Press, Boca Raton.
- 9 Michler, G.H. and Baltá-Calleja, F.J. (2012) *Nano- and Micromechanics of Polymers: Structure Modification and Improvement of Properties*, Hanser Verlag, Munich.
- 10 Michler, G.H. (ed.) (2008) *Electron Microscopy of in Polymers*, Springer-Verlag, Heidelberg.
- 11 Michler, G.H. and Lebek, W. (2004) *Ultramicrotomie in der Materialforschung*, Carl Hanser Verlag, Munich.
- 12 Michler, G.H. (1998) *Polym. Adv. Technol.*, **9**, 812.
- 13 Simon, P., Huhle, R., Lehmann, M., Lichte, H., Mönter, D., Bieber, T., Reschetilowski, W., Adhikari, R., and Michler, G.H. (2002) *Chem. Mater.*, **14**, 1505.
- 14 Michler, G.H., Adhikari, R., Lebek, W., Goerlitz, S., Weidisch, R., and Knoll, K. (2005) *J. Appl. Polym. Sci.*, **85**, 683.
- 15 Adhikari, R., Michler, G.H., Lebek, W., Goerlitz, S., Weidisch, R., and Knoll, K. (2002) *J. Appl. Polym. Sci.*, **85**, 701.
- 16 Adhikari, R., Henning, S., and Michler, G.H. (2002) *Macromol. Rapid Commun.*, **23**, 622.

- 17 Adhikari, R., Michler, G.H., Henning, S., Godehardt, R., Huy, T.A., Goerlitz, S., and Knoll, K. (2004) *J. Appl. Polym. Sci.*, **92**, 1219.
- 18 Jinnai, H., Tsuchiya, T., Motoki, S., Kaneko, T., Higuchi, T., and Takahara, A. (2013) *J. Electron Microsc.*, **62**, 243.
- 19 Ray, S.S. and Bandyopadhyay, J. (2010) *Microsc. Microanal.*, **16**, 1664.
- 20 Hindson, J.C., Saghi, Z., Hernandez-Garrido, J.-C., Midgley, P.A., and Greenham, N.C. (2011) *Nano Lett.*, **11**, 904.
- 21 Godehardt, R., Rudolf, S., Lebek, W., Goerlitz, S., Adhikari, R., Allert, E., Giesemann, J., and Michler, G.H. (1999) *J. Macromol. Sci.: Part B Phys.*, **38**, 817.
- 22 Vancso, J.G. and Schönherr, H. (2010) *Scanning Force Microscopy of Polymers*, Springer Laboratory, Springer-Verlag, Berlin.
- 23 Bamberg, E., Grippo, C.P., Wanakamol, P., Slocum, A.H., Boyce, M.C., and Thomas, E.L. (2006) *Precis. Eng.*, **30**, 71.
- 24 Vaia, R.A., Ishii, H., and Giannelis, E.P. (1993) *Chem. Mater.*, **5**, 1694.
- 25 Adhikari, R., Henning, S., and Michler, G.H. (2006) *Macromol. Symp.*, **233**, 26.
- 26 Gersappe, D. (2002) *Phys. Rev. Lett.*, **89**, 058301.
- 27 Michler, G.H. and Kausch, H.H. (2007) *J. Appl. Polym. Sci.*, **105**, 2577.
- 28 Godehardt, R., Lebek, W., Adhikari, R., Rosenthal, M., and Michler, G.H. (2004) *Eur. Polym. J.*, **40**, 917.
- 29 Kim, G.M., Lach, R., Michler, G.H., Poetschke, P., and Albrecht, K. (2006) *Nanotechnology*, **17**, 963.
- 30 Benetatos, N.M., Chan, C.D., and Winey, K.I. (2007) *Macromolecules*, **40**, 1081.
- 31 Sawyer, L.C. and Sawyer, L.C. (1996) *Polymer Microscopy*, 2nd edn, Chapman & Hall, London.
- 32 Niu, S. and Saraf, R.F. (2007) *Nanotechnology*, **18**, 125607.
- 33 Lee, S., Yoon, S.-M., Shin, H.-J., Joo, W.-J., Yi, D.K., Choi, J.-Y., Amarnath, C.A., and Paik, U. (2008) *Nanotechnology*, **19**, 075606.
- 34 Tsuchiya, K., Nagayasu, S., Okamoto, S., Hayakawa, T., Hihara, T., Yamamoto, K., Takumi, I., Hara, S., Hasegawa, H., Akasaka, S., and Kosikawa, N. (2008) *Opt. Express*, **16**, 5362.
- 35 Bai, Z., Yoonessi, M., Juhl, S.B., Drummy, L.F., Durstock, M.F., and Dang, T.D. (2008) *Macromolecules*, **41**, 9483.
- 36 Drummy, L.F., Wang, Y.C., Schoenmakers, R., May, K., Jackson, M., Koerner, H., Farmer, B.L., Mauryama, B., and Vaia, R.A. (2008) *Macromolecules*, **41**, 2135.
- 37 Drummy, L.F., Yang, J., and Martin, D.C. (2004) *Ultramicroscopy*, **99**, 247.
- 38 Walters, R.M., Taubert, A., Kim, J.-S., Winey, K.I., and Composto, R.J. (2008) *Macromolecules*, **41**, 9299.
- 39 Eloi, J.-C., Rider, D.A., Wang, J.-Y., Russell, T.P., and Manners, I. (2008) *Macromolecules*, **41**, 9474.
- 40 Garcia, I., Tercjak, A., Rueda, L., and Mondragon, I. (2008) *Macromolecules*, **41**, 9295.
- 41 Tada, Y., Akasaka, S., Yoshida, H., Hasegawa, H., Dobisz, E., Kercher, D., and Takenaka, M. (2008) *Macromolecules*, **41**, 9267.
- 42 Fu, B.X., Lee, A., and Haddad, T.S. (2004) *Macromolecules*, **37**, 5211.
- 43 Kirkmeyer, B.P., Weiss, R.A., and Winey, K.I. (2001) *J. Polym. Sci. Part B: Polym. Phys.*, **39**, 477.
- 44 Haggemueller, R., Fischer, J.E., and Winey, K.I. (2006) *Macromolecules*, **39**, 2964.
- 45 Trent, J.S., Scheinbeim, J.I., and Couchman, P.R. (1983) *Macromolecules*, **16**, 589.
- 46 Chen, S., Cao, T., and Jin, Y. (1987) *Polym. Commun.*, **28**, 314.
- 47 Kato, K. (1966) *J. Polym. Sci. Part B. Polym. Lett.*, **4**, 35.
- 48 Vitali, R. and Montani, E. (1980) *Polymer*, **21**, 1220.
- 49 Collins, S., Hamley, I.W., and Mykhaylyk, T. (2003) *Polymer*, **44**, 2403.
- 50 Lammertink, R.G.H., Hempenius, M.A., van den Enk, J.E., Chan, V.Z.-H., Thomas, E.L., and Vancso, G.J. (2000) *Adv. Mater.*, **12**, 98.
- 51 Park, M., Harrison, C., Chaikin, P.M., Register, R.A., and Adamson, D.H. (1997) *Science*, **276**, 1401.
- 52 Adhikari, R., Godehardt, R., Lebek, W., Michler, G., Radusch, H., and Baltá Calleja, F.J. (2005) *Polym. Adv. Technol.*, **16**, 156.
- 53 Olley, R.H. and Bassett, D.C. (1982) *Polymer*, **23**, 1707.
- 54 Olley, R.H., Bassett, D.C., Hine, P.J., and Ward, I.M. (1993) *J. Mater. Sci.*, **28**, 1107.

- 55 Henning, S., Adhikari, R., Michler, G.H., Baltá Calleja, F.J., and Karger-Kocsis, J. (2004) *Macromol. Symp.*, **214**, 157.
- 56 Lee, S.Y., Bassett, D.C., and Olley, R.H. (2003) *Polymer*, **44**, 5961.
- 57 Adhikari, R., Godehardt, R., Lebek, W., and Michler, G.H. (2007) *J. Appl. Polym. Sci.*, **103**, 1887.
- 58 Frangov, S. (2005) *Morphologie und Deformationsverhalten von Blends aus Polyethylen hoher Dichte und Ethylen-1-Octen-Copolymeren*, Shaker Verlag GmbH, Aachen.
- 59 Adhikari, R. (2012) *J. Nepal Chem. Soc.*, **30**, 5.
- 60 Bensason, S., Minick, J., Moet, A., Chum, S., Hiltner, A., and Baer, E. (1996) *J. Polym. Sci. Part B: Polym. Phys.*, **34**, 1301.
- 61 Subramaniam, C. (1999) Morphology, crystallization and melting behaviors of random copolymers of ethylene with 1-butene, 1-pentene and 1-hexene, PhD Thesis, Virginia Polytechnic Institute & State University.
- 62 Adhikari, R. and Michler, G.H. (2009) *J. Macromol. Sci., Polym. Rev.*, **49**, 141.
- 63 Adhikari, R. (2013) *Macromol. Symp.*, **327**, 10.
- 64 Dagli, G., Argon, A.S., and Cohen, R.E. (1995) *Polymer*, **36**, 2173.
- 65 Michler, G.H., Gruber, K., and Steinbach, H. (1982) *Acta Polym.*, **33**, 550.
- 66 Simon, P., Lichte, H., Drechsel, J., Formanek, P., Wahl, R., Mertig, M., Adhikari, R., and Michler, G.H. (2003) *Adv. Mater.*, **15**, 1485.
- 67 Laatsch, J., Kim, G.-M., Michler, G.H., Arndt, T., and Sufke, T. (1998) *Polym. Adv. Technol.*, **9**, 7716.
- 68 Michler, G.H. (1992) *Kunststoff-Mikromechanik: Morphologie, Deformations- und Bruchmechanismen*, Carl Hanser Verlag, Munich.
- 69 Adhikari, R., Buschnakowski, M., Lebek, W., Godehardt, R., Michler, G.H., Knoll, K., and Baltá Calleja, F.J. (2005) *Polym. Adv. Technol.*, **16**, 175.
- 70 Adhikari, R., Huy, T.A., Buschnakowski, M., Michler, G.H., and Knoll, K. (2004) *New J. Phys.*, **6**, 28 (1–20).
- 71 Adhikari, R., Buschnakowski, M., Henning, S., Huy, T.A., Godehardt, R., Lebek, W., Goerlitz, S., Lach, R., Michler, G.H., Geiger, K., and Knoll, K. (2004) *Macromol. Rapid Commun.*, **25**, 653.
- 72 Adhikari, R. and Michler, G.H. (2004) *Prog. Polym. Sci.*, **29**, 949.
- 73 Buschnakowski, M., Adhikari, R., Ilisch, S., Seydewitz, V., Godehardt, R., Lebek, W., Michler, G.H., Knoll, K., and Schade, C. (2006) *Macromol. Symp.*, **233**, 66.
- 74 Adhikari, R., Buschnakowski, M., Lebek, W., Godehardt, R., Michler, G.H., and Knoll, K. (2010) *Macromol. Symp.*, **294**, 45.
- 75 Henning, S., Adhikari, R., Borreck, S., Buschnakowski, M., and Michler, G.H. (2013) *Macromol. Symp.*, **327**, 85.
- 76 George, S.M., Puglia, D., Kenny, J.M., Jyotishkumar, P., and Thomas, S. (2012) *Polym. Eng. Sci.*, **52**, 2336.
- 77 Ocando, C., Fernández, R., Tercjak, A., Mondragon, I., and Eceiza, A. (2013) *Macromolecules*, **46**, 3444.
- 78 George, S., Puglia, D., Kenny, J.M., Causin, V., Parameswaranpillai, J., and Thomas, S. (2013) *Ind. Eng. Chem. Res.*, **52**, 9121.
- 79 Serrano, E., Larranaga, M., Remiro, P.M., Mondragon, I., Carrasco, P.M., Pomposo, J.A., and Mecerreyes, D. (2004) *Macromol. Chem. Phys.*, **205**, 987.
- 80 Serrano, E., Tercjak, A., Ocando, C., Larranaga, M., Parellada, M.D., Corona-Galvan, S., Mecerreyes, D., Zafeiropoulos, N.E., Stamm, M., and Mondragon, I. (2007) *Macromol. Chem. Phys.*, **208**, 2281.
- 81 Bernal-Lara1, T.E., Liu, R.Y.F., Hiltner, A., and Baer, E. (2005) *Polymer*, **46**, 3043.
- 82 Scholtyssek, S., Pfeifer, F., Seydewitz, V., Adhikari, R., Siesler, H.W., and Michler, G.H. (2012) *J. Appl. Polym. Sci.*, **126**, 1593.
- 83 Arabeche, K., Delbreilh, L., Adhikari, R., Michler, G.H., Hiltner, A., Baer, E., and Saiter, J.-M. (2012) *Polymer*, **53**, 1355.
- 84 O'Toole, M.G., Henderson, R.M., Soucy, P.A., Fasciotto, B.H., Hoblitzell, P.J., Keynton, R.S., Ehringer, W.D., and Gobin, A.S. (2012) *Biomacromolecules*, **13**, 2309.
- 85 Watts, B. and McNeill, C.R. (2010) *Macromol. Rapid Commun.*, **31**, 1706.
- 86 McNeill, C.R., Watts, B., Thomsen, L., Belcher, W.J., Greenham, N.C., and Dastoor, P.C. (2006) *Nano Lett.*, **6**, 1202.
- 87 Michler, G.H., Kausch, H.H., and Adhikari, R. (2006) *J. Macromol. Sci.: B-Phys.*, **45**, 727.
- 88 Michler, G.H. and Kausch-Blecken von Schmeling, H.-H. (2013) *Polymer*, **54**, 3131.

- 89 Grellmann, W. and Seidler, S. (eds) (2012) *Polymer Testing*, 2nd edn, Hanser Verlag, Munich.
- 90 Ramsay, J.G. (1974) *Geol. Soc. Am. Bull.*, **85**, 1741.
- 91 Cohen, Y., Albalak, R.J., Dair, B.J., Capel, M.S., and Thomas, E.L. (2000) *Macromolecules*, **33**, 6502.
- 92 Honeker, C.C. and Thomas, E.L. (2000) *Chem. Mater. Macromolecules*, **39**, 9407.
- 93 Ivankova, E.M., Michler, G.H., Hiltner, A., and Baer, E. (2004) *Macromol. Mater. Eng.*, **289**, 787.
- 94 Ivankova, E., Adhikari, R., Michler, G.H., Weidisch, R., and Knoll, K. (2003) *J. Polym. Sci.: Polym. Phys.*, **41**, 1157.
- 95 Garcia Gutierrez, M.C., Henning, S., and Michler, G.H. (2003) *J. Macromol. Sci. B: Phys.*, **42**, 95.
- 96 Qian, D. and Dickey, C. (2001) *J. Microsc.*, **204**, 39.
- 97 Adhikari, R., Lebek, W., Godehardt, R., Löschner, K., and Michler, G.H. (2004) *Kautschuk-Gummi-Kunststoffe*, **57**, 90.
- 98 Pandit, R., Michler, G.H., Lach, R., Grellmann, W., Saiter, J.M., Berkessel, A., and Adhikari, R. (2014) *Macromol. Symp.*, (in press).

## 18

# Characterization of Polymer Blends Using SIMS and NanoSIMS

Vanna Torrisi

### 18.1

#### Introduction

In this chapter, attention is focused on the surface chemical characterization of polymer blend and, in particular, on their spatially resolved molecular and elemental analysis.

The blending of polymers represents an effective means of producing materials that have properties which are unobtainable from single constituents. Thus, polymer blends are technologically extremely important, and for this reason their thermodynamic and bulk physico-mechanical properties have been extensively studied. Most polymer blends are immiscible or partially miscible and often form separated phases, which leads to a complex morphology in the bulk and at the surface. Hence, morphology studies incorporate one of the most active research topics in polymer blends [1,2]. In contrast, the results of various studies have shown that the surface and bulk chemical compositions of polymer blends are not the same, even though they are miscible in the bulk [3]. However, the surface composition and morphology of these blends have received relatively little attention.

Although, very often, the lower surface energy component tends to segregate to the surface, a number of other factors – such as solvent, specific interaction and crystallization – can also affect the blend's surface composition [4,5]. Consequently, whilst an understanding of the blend surface composition is of fundamental interest, it may not be easy to acquire. Implied is the simultaneous requirement for chemical speciation at both high lateral and depth resolution within the surface region.

In this chapter, the application of secondary ion mass spectrometry (SIMS) techniques, and in particular of time-of-flight secondary ion mass spectrometry (ToF-SIMS) and nanoscale secondary ion mass spectrometry (NanoSIMS), to polymer surface characterization is presented, with attention focused especially on polymer blends and interfaces.

Static secondary ion mass spectrometry (SSIMS) and ToF-SIMS have, in particular, become key surface-analysis techniques for organic and polymeric materials [6]. The main advantage of ToF-SIMS over other surface techniques is its capability to provide a high molecular specificity, a high spatial resolution, and a high sensitivity, which is ideal for elucidating the complex chemistry of polymer surfaces and interfaces. In particular, molecular structural information such as branching, saturation/unsaturation, chain conformation, functional groups, molecular weight distribution, end-groups and segmental length can be deduced from SIMS spectra [7].

With its ability to provide molecular information and submicron imaging resolution, ToF-SIMS is an ideally suitable analytical technique for the characterization of polymer blends. Indeed, it is the only technique that is able to provide both chemical composition and morphology information. The applications of ToF-SIMS to polymer blends cover the two main research areas cited above, namely surface composition and morphology.

In order to obtain more accurate spatial information on the polymer blend surface, a highly focused probe SIMS, namely NanoSIMS, can be used. Indeed, the lateral resolution (in the range of some tens of nanometers) of this technique would be expected to be sufficient for imaging the domains [8,9]. Due to dynamic SIMS conditions of the measurement, and to the limited thickness of the polymer blend thin films, it is possible to acquire only a few frames before reaching the substrate [10]. NanoSIMS has been used with some success to study the surface morphology and composition of thin-film polymer systems [8–10].

## 18.2

### Thin Films and Ultrathin Films of Polymer Blends

One of the current frontiers of the bottom-up strategies in nanotechnologies deals with the set-up of suitable techniques to obtain self-structuring organic ultrathin films – that is, molecular monolayers that are capable of “projecting” the desired structure design down to a molecularly defined lateral resolution. In this case, indeed, the homogeneity of coverage, sharpness and stability of the designed structures depend critically on the detailed interactions among molecules and, in the case of oligomers or polymers, among parts of the same molecule or among two or more polymers in a polymer blend [11].

Polymer blend thin films are interesting both for their technological applications (e.g., coatings) and from an academic point of view. By confining a polymer (blend) in a thin film, both the air–polymer and the polymer–substrate interface can (significantly) influence its physical properties, in comparison with those observed in bulk [12].

Two ToF-SIMS images of two polymer blends are shown in Figure 18.1, from which it is apparent that the addition of a small amount of poly(methyl methacrylate) (PMMA) to a polycarbonate (PC)/poly(vinylidene fluoride) (PVDF) blend can produce a significant change in the ToF-SIMS images. The preparation of thin

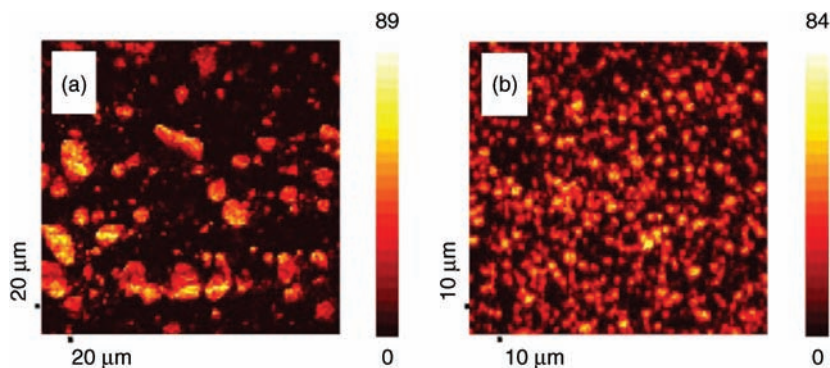


**Figure 18.1** ToF-SIMS  $F^-$  images obtained from (a) PC/PVDF (70/30) blend and (b) PC/PDVF/PMMA (70/25/5) blend. Reproduced with permission from Ref. [7].

and ultrathin films of polymer blends with ordered micro- and/or nanostructures has attracted increasing interest during recent years, and many methods have been devised to produce ordered arrays of various materials with sizes ranging from nanometers to micrometers. Among other techniques, both conventional (e.g., photolithography, extreme ultraviolet lithography) and nonconventional (e.g., embossing [13,14], soft lithography [15,16]) lithographic methods have been used. Recently, some inexpensive nonlithographical techniques such as phase separation [17], dewetting [18], air bubble [19], convection [20] and Langmuir–Blodgett (LB) [21] methods have appeared capable of providing other routes for obtaining patterns of polymeric materials [10,22].

Among these techniques, the LB method allows (at least in principle) the choice of to what extent the molecular interaction may operate at the air–water interface [10,22].

One very promising system for obtaining laterally structured organic monolayers involves applying the LB technique to polymer blends, including a “surface-active,” more-or-less hydrophilic component which can compete/interact with a “nonsurface-active,” more-or-less hydrophobic component. Hence, the LB technique prompts a differential organization of the two components, promoting relevant dephasing processes and producing a nanostructuring of the monolayers [23]. The advantage of this method is that it is possible to tune the shape of the structures obtained simply by changing the ratio between the two polymers [22]. The main result of this approach was that an effective chemical patterning could be obtained which consisted of distinct aggregates of the two components [22].

Spin-coating is the most widely used method for creating highly uniform, submicrometer-thick polymer films, and is applied extensively in industry for producing thin films of photoresists, sol–gel glasses and functional materials such as semiconducting polymers for use in polymer-based field-effect transistors, light-emitting diodes (LEDs) and photovoltaics. Whilst spinning a film of a single polymer generally produces a smooth, unstructured thin film, if a

mixture of polymers is used then the two polymers will usually phase separate. Many possible morphologies may result from this phase separation, which is a complex nonequilibrium process, the outcome of which is highly sensitive to the details of the solvent used and the precise spinning conditions employed. At one extreme, phase separation can take place exclusively in the direction perpendicular to the plane of the film, resulting in a self-stratified film [24,25]. Alternatively, phase separation can take place exclusively in the plane of the film, and this results in a laterally patterned film characterized by a length scale that depends in complex fashion on the processing history [1,26–33]. A schematic model describing film formation during the spin-coating process, and the final film morphology, are shown in Figure 18.2.

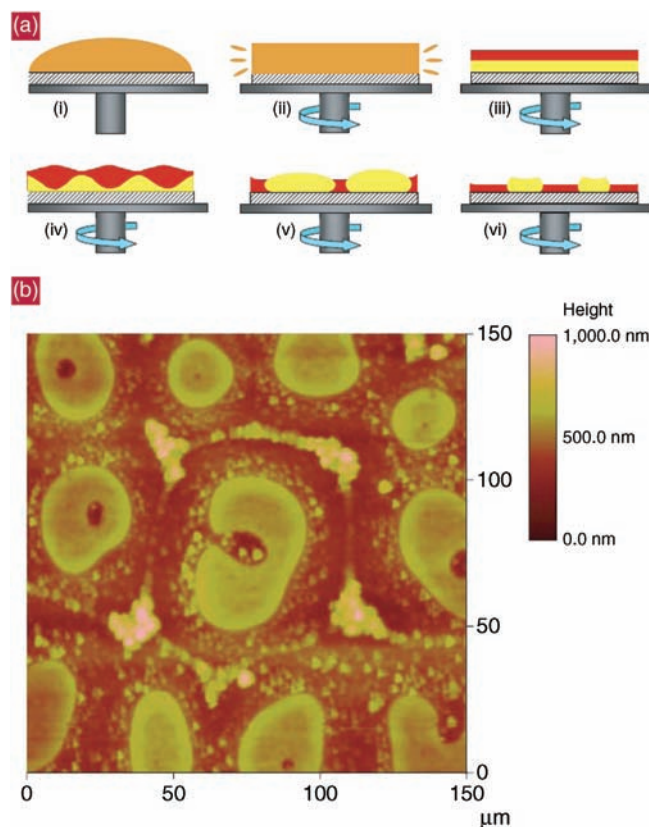


**Figure 18.2** Schematic model describing film formation during the spin-coating process, and the final film morphology. (a) After the initial spin-off stage where both polymer and solvent are removed (i), (ii), the film separates into two layers (iii) and the film thins owing to solvent evaporation only. The interface between the

polymers destabilizes (iv) and the film phase-separates laterally (v), (vi); (b) Atomic force microscopy image of the final morphology, imaged with a MultiMode SPM with a NanoscopeIIIa controller. Reproduced with permission from Ref. [33].



## 18.2.1

**Phase-Separation Phenomena**

Phase separation in bulk mixtures commonly leads to an isotropic, disordered morphology of the coexisting phases [34]. The presence of a surface can significantly alter the phase-separation process, however [35,36].

Phase separation can emerge spontaneously in thin films of polymer blend, and it is this thermodynamically driven phase-separation process that produces the patterning of thin polymer blend films. It can be induced by several parameters, each with critical values, including: (i) the ratio between the components [10,22]; (ii) the demixing temperature [12]; and (iii) the chemical nature of the solvent.

The complete demixing of a polystyrene (PS)/poly (2-vinylpyridine) (P2VP) polymer blend in an ultrathin film is shown in Figure 18.3.

The phase separation of thin polymer blend films can be also driven by substrate effects, including the effects of: (i) the substrate composition; (ii) the substrate functionalization; and/or (iii) the substrate structures. In particular, the self-assembly of polymer molecules on a substrate can be controlled by selectively modifying the chemistry of the substrate surface and/or the polymers to create patterned polymer films with tailored length scales.

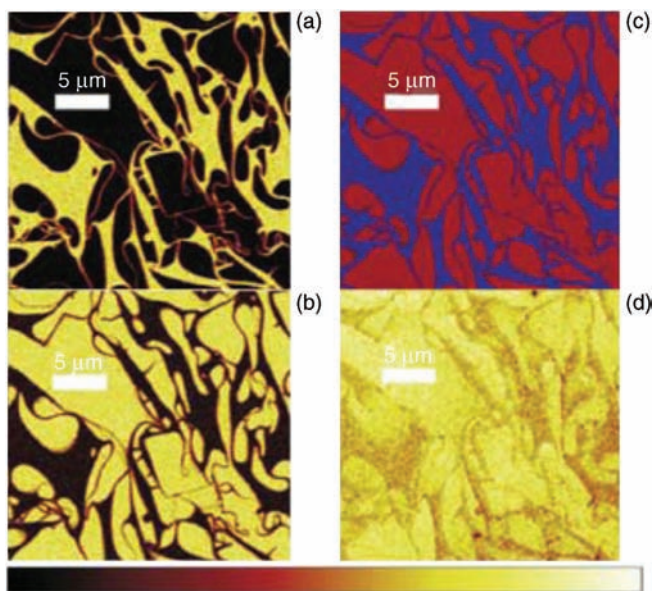


**Figure 18.3** ToF-SIMS chemical maps of the sum of the intensities of the most typical signals polystyrene (PS) (a) and the sum of the most typical signals of poly(2-vinylpyridine) (P2VP) (b); (c) Overlay image between the sum of the intensities of the most typical signals of

PS (blue) and the sum of the most typical intensities signals of P2VP (red). TIC, total ion current; (d) ToF-SIMS chemical maps refer to the film obtained by the 1/15 weight ratio P2VP-PS mixture. Reproduced with permission from Ref. [22].

In addition to the causes of phase separation, mention should also be made of the two mechanisms involved in phase separation, namely nucleation and growth and spinodal decomposition:

- *Nucleation and growth* is often associated with crystallization from solution. In the metastable region of the phase diagram, only nucleation and growth can occur, and this yields a phase-separated region that maintains a constant concentration and an increasing size with time.
- *Spinodal decomposition* occurs in the unstable region of the phase diagram, and results from low-amplitude concentration fluctuations that grow spontaneously into phase-separated regions. Spinodal decomposition yields a phase-separated region that exhibits a varying composition but a constant size (at early stage of the process) as time increases. In the intermediate stages of spinodal decomposition the periodicity of structure will start increasing as percolation of the network occurs, allowing liquid flow.

During the later stages of separation both processes can exhibit a coalescence of particles such that the morphology may become more coarse, depending on the surface forces and viscosity [37].

The phase-separation morphology [32,35,38–44] and dynamics [45–48] of thin polymer blend films have been studied extensively. The phase separation of spin-cast polymer blend films can occur during the spin-coating process for high-molecular-weight polymers [32,38,39], or upon annealing for low-molecular-weight polymers [35,40–44]. In the case of thin films, the presence of the film interfaces can have a dramatic effect on the phase-separation morphology. For example, the film interfaces can induce a spinodal decomposition [35] because of a preference of one of the constituent polymers for the film interfaces. The presence of a wetting layer can result in a lamellar phase separation morphology, which has been observed for a variety of polymer blend systems [40–42]. The film interfaces can also influence the phase-separation morphology produced during the spin-coating of very thin, high-molecular-weight polymer blends [38]. Some reports of phase-separation phenomena, whether substrate-induced, substrate composition-induced or patterning-induced, are outlined in the following subsections.

The spinodal decomposition process can be manipulated using surface patterns created by the microcontact printing (mCP) of functionalized molecules on the solid substrate supporting the blends.

The phase separation of ultrathin polymer-blend films of PS and polybutadiene on mCP-printed alkane thiol patterns with hydrophobic and hydrophilic end groups ( $-\text{CH}_3$  and  $-\text{COOH}$ ) has been investigated using atomic force microscopy (AFM). Simulations have suggested that the phase-separation morphology can be controlled through patterns that modulate the polymer–surface interaction, and the subsequently conducted experiment verified this concept. Length scale pattern control was found to be limited to a scale on the order of a few micrometers [49].

Many previous studies have considered the influence of confinement on the equilibrium phase separation temperature of thin films [50,51], and of spatial dimensionality on the kinetics of spinodal decomposition [52]. The latter study involved a combination of these factors, whereby an examination was made of the effect of finite film thickness on the kinetics of spinodal decomposition over a film thickness range where transition occurred from three-dimensional bulk-like to near two-dimensional kinetics. In particular, the 1000 Å thin polymer blend films of PS and polybutadiene on a silicon substrate were found to be sufficiently thick to exhibit phase-separation kinetics similar to those of bulk blends. The thinner film ( $L \approx 200$  Å) exhibited a different phase-separation kinetics, however [47].

The thin-film morphologies of poly(2,7-(9,9-di-*n*-octylfluorene)-*alt*-benzothiadiazole) (F8BT) and poly(2,7-(9,9-di-*n*-octylfluorene)-*alt*-(1,4-phenylene-((4-*sec*-butylphenyl)imino)-1,4-phenylene)) (TFB) blends produced by spin-casting showed distinctive microscale lateral phase separations. However, these phase-separated domains were not pure at the submicron length scale, and a nanoscale vertical phase segregation occurred in the thin blend films, with an enrichment of the lower surface energy component (TFB) at the air and substrate interfaces. Imaging of the spatial uniformity of electroluminescence emission on the microscopic scale indicated a spatially localized charge carrier recombination in LEDs fabricated with these blends [53].

A technique has been developed to study the process of phase separation in spin-cast films *in situ* as it occurs. In order to study the development of structure directly during the spin-coating process, time-resolved small-angle light scattering and light reflectivity were used. The results established the full sequence of processes that led to the final phase-separated thin film, and this permitted – at least in principle – the establishment of a full mechanistic understanding of the development of morphology in thin mixed polymer films. The results also demonstrated a route to the rational design of processing conditions, with the possibility of achieving desirable morphologies by self-assembly [33].

The phase evolution of a critical blend thin film of deuterated poly(methyl methacrylate) (dPMMA) and poly(styrene-*ran*-acrylonitrile) (SAN) was found to develop in three distinct stages. It has been observed during spinodal decomposition and symmetrically wetting that thin film polymer blends evolve via an early stage that is dominated by wetting and the formation of a trilayer structure, an intermediate stage involving 2D phase coarsening within the middle layer, a transition stage denoted by rupture of the middle layer and, finally, a late stage characterized by dewetting [54]. A distinct surface patterning in thin films of phase-separating binary polymer blends in which surface-directed spinodal waves are suppressed has also been observed [55].

Currently, AFM, neutron reflection (NR) spectroscopy and SIMS are used to examine phase separation in symmetrically segregating thin polymer blend films (ca. 1000 Å). Phase separation in the film leads to undulations of the liquid–air interface, provided that the film is sufficiently thin to suppress any surface-directed spinodal decomposition waves. Flattened droplets are formed at a very

late stage of the phase separation, and the aspect ratio of these droplets can be rationalized by an interfacial free energy minimization argument [55].

A poly(styrenesulfonate)-doped poly(3,4-ethylenedioxythiophene) (PEDOT-PSS) film, which had been spun-cast from a water suspension, was used in a certain polymer-emitting diode device configuration. The results of the measurements performed on this sample, combined with those of the studies outlined above, have indicated that several important parameters can affect device performance. PSS surface segregation has been identified, with phase segregation occurring on a single grain of PEDOT-PSS [56].

### 18.2.2

#### Technological Applications of Thin and Ultrathin Films of Polymer Blends

Polymer blend thin films are interesting both for their technological applications (e.g., coatings), and from an academic point of view [12].

The chemical pattern of thin films of polymer blends can be used for the highly specific and programmed assembly of nanostructures, or for the spatially resolved adhesion of biomolecules. Thus, chemically patterned films can be used as multi-sensing, spatially resolved surface or – if hydrophilic/hydrophobic patterns are to be exploited – for the spatially resolved adsorption/repulsion of proteins [57]. Indeed, patterned polymeric materials can be used (at least in principle) for a wide range of applications, including the prevention of etching [58], in molecular electronics [59–61], in optical devices [62–64], in biological [65] and chemical sensors [66–68], and in tissue engineering [69].

Today, important applications are emerging in which a better understanding and control of the process of phase separation in thin films would be highly desirable. Blends of semiconducting polymers can be used to create efficient photodiodes and photovoltaic devices, owing to the importance of interfaces in the localization and separation of excitons [70–74]. Similar considerations have also led to bilayer geometries becoming attractive for polymer photovoltaics [75]; in fact, it has been shown that such bilayer structures can be formed spontaneously during spin-coating, leading to the production of efficient devices [76–79].

The use of electroluminescent polymer blends as an active material has provided a new route to the fabrication of highly efficient organic devices [80–89]. In particular, polymer LEDs fabricated with F8BT blended with TFB as the emissive layer have shown significantly improved device performances (see Figure 18.4) [53,90–92].

Although micron-scale lateral phase separation has been observed in F8BT:TFB blend thin films, these phase-separated domains are not pure at the submicron length scale, and a nanoscale vertical phase segregation may occur with enrichment of the lower surface energy component (TFB) at both air and substrate interfaces. Imaging of the spatial uniformity of electroluminescence emission on the microscopic scale indicates a spatially localized charge-carrier recombination in LEDs fabricated with these blends [53].

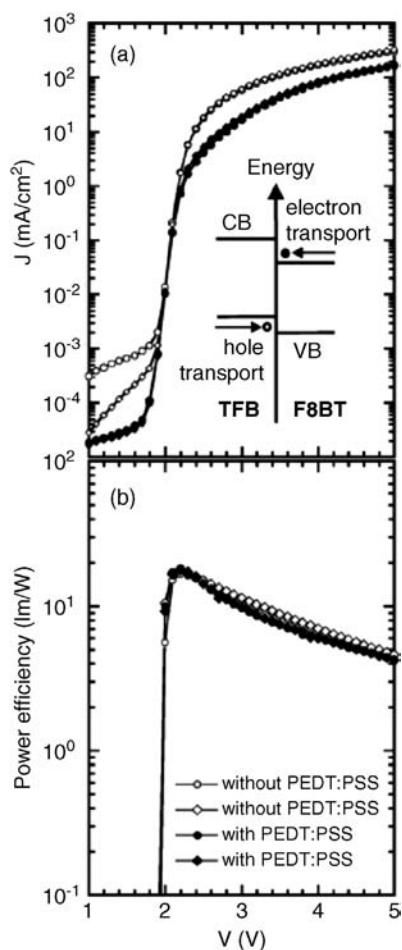


**Figure 18.4** (a) Current–voltage and (b) power efficiency voltage characteristics of the encapsulated ITO/F8BT:TFB blend (50:50, 80 nm)/Ca (5 nm)/Al (400 nm) LEDs with/without a PEDT:PSS (60 nm) layer (two of each). The inset shows a scheme for the heterojunction formed between F8BT and TFB. Energies for the top of the valence band (VB) with respect to the

vacuum level, estimated from cyclic voltammetry, were 5.33 eV (TFB) and 5.89 eV (F8BT). Electrons from F8BT and holes from TFB were transported, and exciton formation resulted from electron hole capture at the heterojunction. F8BT is a high-electron-mobility polymer; TFB is a high-hole-mobility polymer. Reproduced with permission from Ref. [53].

One application of polymer blend thin films is that of the so called “smart surfaces,” the properties of which are changed as a result of phase separation by thermal stimuli; an example is the patterning of polymer blend films by local heating. One recent proposal involved the use of a polymer blend film that was stable at the storage/working temperature but could be annealed in the two-phase region upon heating. For patterning, local heating might also be obtained by using an infrared laser [12].

## 18.2.3

**The Necessity of Compositional Information**

Today, it is accepted that ToF-SIMS and X-ray photoelectron spectroscopy (XPS) are the two most powerful surface analysis techniques for polymeric materials. In fact, ToF-SIMS has become increasingly popular for polymer surface analyses because it can provide not only detailed surface molecular information but also surface chemical imaging with submicron spatial resolution.

When studying the surface composition of polymer blends [93–106], ToF-SIMS can either be combined with XPS or used independently, since it has been proven very useful for elucidating the morphology and miscibility of these materials [107–109]. If combined with XPS, ToF-SIMS often provides very complementary information: typically, XPS will provide elemental and quantitative information, with chemical environment speciation, while ToF-SIMS yields molecular information but has a poor quantification due to matrix effects. Some divergence may exist, due mainly to the difference in sampling depth between the two techniques (5–10 nm for XPS, ca. 1 nm for ToF-SIMS), or to the fact that ToF-SIMS suffers from matrix effects. As the sampling depth of ToF-SIMS is less than that of XPS, the former procedure will provide the top-most surface composition and is more sensitive than XPS for detecting surface segregation when it occurs only at the top surface [100]. Unfortunately, however, it is not easy to deduce quantitative data from ToF-SIMS results, and it is for this reason that in most studies of polymer blends the SIMS relative peak intensities were (whenever possible) correlated with the surface composition by XPS, in attempts to understand the relationship between the SIMS intensities and surface composition. Results obtained for polymer blends involving hydrogen-bonding interactions [101–105] have shown that hydrogen-bonding, as the most important interaction in polymer blends, is one source of matrix effects [110]. For example, in a blend of poly(styrene-*co*-4-vinylphenol) and poly(styrene-*co*-4-vinylpyridine) [101], the phenol units form hydrogen-bonding with the pyridine units. Consequently, the pyridine fragments involving protonation are greatly enhanced as a result of the hydrogen-bonding, and such fragments are therefore unsuitable for SIMS quantitative analysis. Quantitative information can still be deduced, however, from other characteristic fragments that are unaffected by hydrogen-bonding [104,105,110]. In the case of other polymer blends, such as isotopic PS blends [99] or blends consisting of amorphous and semicrystalline polyethylene [97], XPS is totally impractical due to its lack of molecular specificity. In these cases, ToF-SIMS spectra (see Figure 18.5) have been used independently to quantify the blend surface composition [7].

In the case of the ethylene–trifluoroethylene copolymer (ETFE)/PMMA system, when using ToF-SIMS imaging it is possible to locate three regions: (i) a semicrystalline region containing mostly ETFE with a glass transition temperature ( $T_g$ ) close to that of pure ETFE; (ii) an amorphous region containing mostly PMMA with a  $T_g$  close to that of pure PMMA; and (iii) an amorphous region containing significant levels of ETFE and PMMA [111].

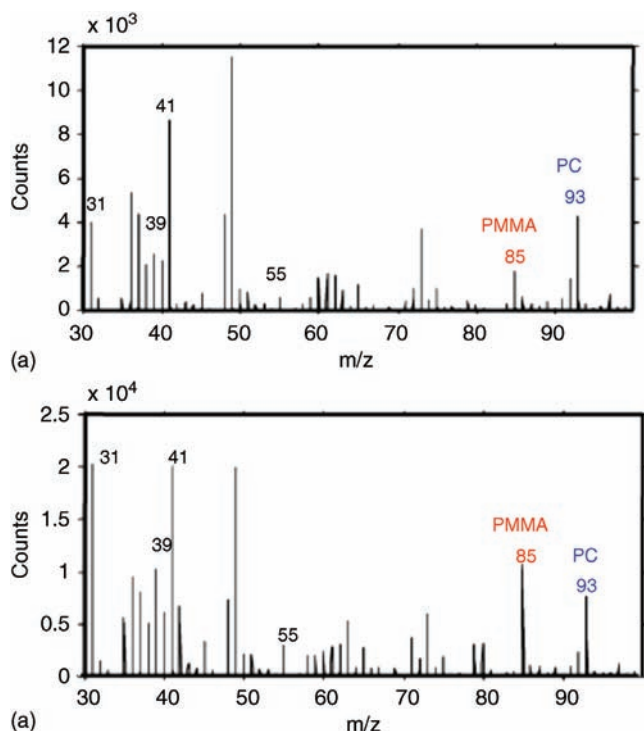


**Figure 18.5** Partial negative ToF-SIMS spectra for the PC side of the fractured laminate prepared at (a) 200 °C and (b) 240 °C. Reproduced with permission from Ref. [7].

### 18.3

#### SIMS: The Techniques and Outputs

The mode of action of SIMS is based on the fact that, under heavy particle bombardment, charged atomic and molecular species are ejected from the surface of a condensed phase (whether liquid or solid) [112]. During this bombardment by ions or neutral particles (which is generally in the energy range of 0.25 to 30 keV), surface particles are sputtered and the primary bombarding particle is implanted into the condensed phase. The primary ions penetrate into the solid surface to different depths (range of 1 to 10 nm) and transfer their kinetic energy through binary collisions to the atoms of the target. The target atoms are then displaced from their original sites and collide with other target atoms, which leads to the production of a collision cascade until the transferred energy is insufficient to cause atom displacement. Collision cascades that reach the surface may cause the ejection of sample material from the first atomic layers (sputtering process). Although most of these sputtered particles are neutral, some will be charged (secondary ions). Sputtering is one

of many processes that occur during this type of surface bombardment, which results in two general groups of events:

- Changes in the bombarded surface.
- Emission processes.

The impact of a primary particle on a surface causes energy and momentum transfer to a limited area around the point of particle impact, resulting in: (i) a change in the lattice structure; and (ii) a loss of surface material by sputtering.

The ion-bombardment-induced emission processes include electrons and photons, besides the emission of surface particles (atoms or molecules) in a charged or uncharged, and possibly excited, state. All of these emission products are emitted with a certain angular distribution.

The secondary ion emission includes all emitted ionized surface particles in the ground state and also in the excited state [112,113]. As virtually all secondary ions originate from the uppermost atomic layers of the bombarded surface, this represents one of the most important features of secondary ion mass spectrometry, namely its surface sensitivity.

One very important question in SIMS concerns the charge state of the emitted atomic or molecular particles, which is heavily dependent on the chemical environment of the sputtered species. In fact, by changing this chemical environment (e.g., from a pure metal to an oxide) the ionization probability of the same species (e.g., a metal atom) may be changed by several orders of magnitude (via matrix effects) [112].

The most commonly used primary ions are  $\text{Cs}^+$ ,  $\text{O}_2^+$ ,  $\text{Ar}^+$ ,  $\text{Xe}^+$  and  $\text{Ga}^+$ , as well as the more recently reported Bi and Au cluster ions ( $\text{Au}_n^{z+}$ ,  $\text{Bi}_n^{z+}$ ) and even  $\text{C}_{60}^+$  [114]. In comparison with the use of noble gas primary ions ( $\text{Ar}^+$  and  $\text{Xe}^+$ ), the use of  $\text{O}_2^+$  and  $\text{Cs}^+$  increases the ionization probability for species that tend to form cations and anions, respectively. Moreover,  $\text{Ga}^+$  is employed to obtain high lateral resolutions owing to the finely delivered focused beam [115]. Likewise,  $\text{C}_{60}^+$ , Bi and Au clusters have been recently used in order to increase the yield of molecular mass fragments for the analysis of polymers and biomolecules [116].

The secondary ions may be easily mass-separated using different types of mass analyzer and, depending on the analyzer used, many variations of SIMS technique can be distinguished. The mass analyzer forms an essential component of all mass spectrometers, its primary role being to separate sputtered atomic, molecular and cluster ions on the basis of their  $m/z$  ratio. This can be achieved by applying electric and/or magnetic fields (cyclotron frequency in the case of Fourier transform-ion cyclotron resonance; FT-ICR), thus effectively separating them in space.

Currently, at least four types of mass analyzer are used in mass spectrometry, namely ToF, magnetic/electric sector, quadrupole ion trap (see Figure 18.6), and FT-ICR. The ToF and magnetic/electric sector mass analyzers are most commonly used in mass spectrometry imaging, while FT-ICR analyzers have been applied only rarely to mass spectrometry imaging [117].



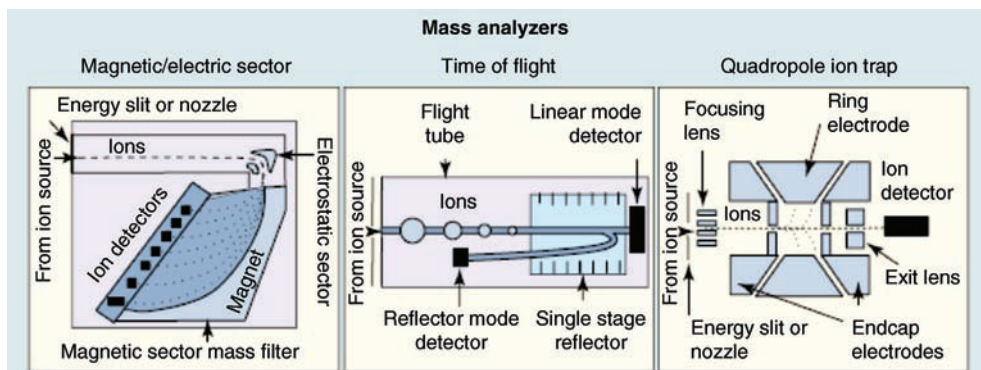


**Figure 18.6** Mass analyzers employed in imaging mass spectrometry research. A schematic representation of the NanoSIMS magnetic/electric sector mass analyzer is depicted in the left-hand panel ([http://www.cameca.fr/html/product\\_nanosims.html](http://www.cameca.fr/html/product_nanosims.html)). A ToF mass analyzer

is shown in the center panel, and illustrates both linear and reflectron modes of operation. A quadrupole ion trap is depicted in the right-hand panel. Reproduced with permission from Ref. [118].

Magnetic and electrostatic sector mass analyzers separate ions according to their  $m/z$  ratio by bending the flight trajectories of the ions with magnetic or electric fields applied perpendicularly to the ionbeam path. Ions with larger  $m/z$  values will be less affected than lighter ions and so will follow a longer, shallow trajectory. A single detector at each instrument setting can detect ions with only one  $m/z$  value, and must be adjusted for the detection of multiple analyte signals.

The ToF mass analyzer is the fastest, has a broad  $m/z$  range, is one of most sensitive mass spectrometry analyzers available, and is well-suited to imaging applications. In ToF mass analysis, gas-phase ions produced by a pulsed ion source are accelerated in a high vacuum by an electric field. After being accelerated, the ions enter a field-free region between the ion source and detector at a velocity related to their  $m/z$  ratio, with lower- $m/z$  ions reaching the detector earlier than higher- $m/z$  ions.

In the 3D quadrupole ion trap mass analyzer, radiofrequency (RF) voltages are applied to the ring electrode while the end-cap electrodes are typically kept at ground potential. Thus, ions with  $m/z$  above a selected value will be trapped inside the mass analyzer, while a continual increase in the RF amplitude applied to the ring electrode will result in the ejection of ions that pass through an opening in one of the end-cap electrodes, towards an ion detector; in this way, ions with a smaller  $m/z$  value will be ejected and detected first [118].

Many reviews have been produced on the subject of mass spectrometry and imaging, while two excellent books on SIMS are from Benninghoven [112] and Vickerman [119]. Reviews are also available on SIMS [120–125], imaging SIMS [126–130], biological SIMS [131–134], and SIMS of polymers [135]. Comparisons of the various microanalysis techniques using SIMS are also available [136,137]. In the following sections, attention is focused in particular on ToF-SIMS and NanoSIMS techniques.

## 18.3.1

**ToF-SIMS: The Technique**

ToF-SIMS is a surface-sensitive analytical method that uses a pulsed ion beam to remove molecules from the very outermost surface of the sample. The secondary ions are removed from the uppermost monolayers on the surface and then accelerated into a “flight tube”; their mass is determined by measuring the exact time at which they reach the detector. Three operational modes are available when using ToF-SIMS, namely surface spectrometry, surface imaging, and depth profiling.

The analytical capabilities of ToF-SIMS include:

- Mass resolution  $>10\,000$  amu. Ions with the same nominal mass (e.g., Si and  $C_2H_4$ , both with amu = 28) are easily distinguished one from another.
- Mass range of 0–10 000 amu; ions (positive or negative), isotopes, and molecular compounds (including polymers, organic compounds, and up to about amino acids) can be detected.
- Trace element detection limits in the ppm range.

At this point, a number of the critical and experimental issues associated with ToF-SIMS imaging will be discussed, and several recent applications of ToF-SIMS imaging to the study of polymer blend thin films [137] reviewed.

**18.3.1.1 Spectra, Profiling, and Imaging Mode**

ToF-SIMS may also be referred to as “static” SIMS because a low primary ion current ( $\sim 1 \times 10^{13}$  primary ions  $cm^{-2}$ ) is used to liberate ions, molecules and molecular clusters for analysis; it is also the method used to produce mass spectra and 2D chemical images. In contrast, “dynamic” SIMS is carried out using ion dosages well beyond the static limit, and is used to create 3D images and depth profiles. The ToF-SIMS spectrometer can be operated in dynamic mode, though by using an additional sputter gun and can be referred to as “dual beam mode.” Depth profiling with a vertical resolution between 0.1 and 30.0 nm has been achieved using primary ions [118].

As surface organic contamination generally covers any targeted trace elements in a sample, the use of a sputter gun (i.e., dynamic mode) is useful for a better detection and counting statistics for trace elements. In contrast, organic compounds are effectively destroyed by “dynamic” SIMS, such that no diagnostic information is obtained.

Under typical static operating conditions, the results of ToF-SIMS analyses include:

- A mass spectrum that surveys all atomic masses over a range of 0 to 10 000 amu.
- The rastered beam produces maps of any mass of interest on a submicron scale, and every pixel of a ToF-SIMS map represents a full mass spectrum. This

allows the analyst to produce maps retrospectively for any mass of interest, and to interrogate regions of interest (ROI) for their chemical composition via computer processing, once the dataset has been instrumentally acquired.

- Depth profiles are produced by removal of the surface layers by sputtering under the ion beam.

#### 18.3.1.2 ToF-SIMS: Spatially Resolved Molecular Information

The secondary ions can be detected in order to obtain the imaging of the surface by rastering a focused ion beam across the target [138]. This strategy places fewer restrictions on the nature of mass analyzers, and has become popular due to the development of the liquid metal ion gun (LMIG). The beam emanating from this ion source can be focused onto the target with a diameter of less than 20 nm, thus providing a very high lateral resolution of element-specific images [139]. In addition, the idea of imaging molecular species desorbed from a surface by a focused ion beam has come into play. This notion was made possible by the early discovery that molecular ions, as well as elemental ions, are seen in the mass spectrum if the primary ion dose is kept below certain limits [140]. In order to analyze a much larger mass range, ToF mass analyzers were implemented [141], and the resulting experimental configuration became known as ToF-SIMS imaging.

ToF-SIMS imaging exhibits remarkable characteristics. For example, by using a 25 keV Ga<sup>+</sup> or Bi<sup>+</sup> ion LMIG, these instruments can produce spatially resolved images of molecular species with molecular weights of up to several thousand Daltons and with a spatial resolution less than 100 nm [142].

Today, as the applications of molecular imaging experiments continue to expand, new variants of the experimental protocol promise further breakthroughs. For example, it is possible to improve the yield of molecular ions by using cluster ion beam sources rather than atomic ion sources [143,144]. Typically, a group of projectile atoms can more efficiently desorb labile molecules with less fragmentation than a single atomic ion [137].

**Lateral Resolution** Before discussing the requirements in more detail, it is worth introducing the concept of the duty cycle.

When considering a pulsed beam characterized by a pulse width  $t$  (ns) and a period  $\frac{1}{f}$  (where  $f$  is the repetition rate, s<sup>-1</sup>), the duty cycle ( $\delta$ ), defined by the time fraction during which the beam is on, is given by the following equation:

$$\delta = t \cdot f$$

Consequently, if  $t_m$  is defined as the time to erode the uppermost monolayer by a continuum beam:

$$t_m = \frac{d_s \cdot e \cdot A}{i \cdot Y}$$

where  $d_s$  is the atomic surface density (in cm<sup>-2</sup>),  $e$  is the electronic charge ( $1602 \times 10^{-19}$  Coulombs);  $A$  is the analyzed area (in cm<sup>2</sup>),  $I$  is the primary ion

current (in nA), and  $Y$  is the sputtering yield (dimensionless). The time ( $T$ ) to erode the uppermost monolayer by a pulsed beam characterized by a duty cycle  $\delta$  is given by:

$$T = \frac{t_m}{\delta} = \frac{t_m}{t \cdot f} = \frac{d_s \cdot e \cdot A}{i \cdot Y \cdot t \cdot f}$$

Some ToF-SIMS applications demand a high mass resolution, a high spatial resolution and a high secondary ion yield, in unison. A good example of this is in the imaging SIMS of biological structures, where it is necessary to identify the small-scale distribution of large molecules.

One approach is to use longer analysis beam pulses in conjunction with pulsed extraction, in order to optimize resolution in both space and mass. In this case, the switch-on of the extraction voltage will become the time reference.

In modern ToF instruments, a lateral resolution of  $<0.1 \mu\text{m}$  is a routine expectation, but to achieve this ions can only be accepted from a limited area of the source, and with a limited angular acceptance. Consequently, a source of high brightness is required, as is a low-energy spread, to minimize any chromatic aberration. The gallium and bismuth liquid and cluster (e.g.,  $\text{Bi}_n^+$  and  $\text{Au}_n^+$ ) ion guns offer high brightness and a reasonable energy spread.

The liquid metal ion source/extractor combination produces a divergent beam that apparently emerges from a point just behind the real position of the tip. The ion-optical column must collect this beam and perform the following operation on it:

- Focus it, with minimum aberrations from the lenses.
- Remove unwanted parts of the beam to optimize current at the required spot size.
- Chop it into pulses of the required length to enable the required mass resolution.
- Mass filter it (for certain types of beam).
- Remove neutrals.
- Scan it over the required area on the sample.
- Correct alignment and beam shape defects.

Whilst it is possible to focus a beam of ions extracted from a source using a single lens, the introduction of a second lens allows the production of a family of beams of different magnification. It also facilitates other ion-optical processes such as motionless pulsing.

In a typical ion column, the ions from the source are accelerated to full voltage and enter the first lens of the optical column; this can produce an intermediate focus or it may collimate the beam. The ions pass through most of the remaining ion-optical systems en route to a second lens, which focuses them onto the sample. The main determinants of spatial resolution in the ion-optical column are the lenses, the apertures, the pulsing unit, and the electrical supply to the column [137].

**ToF-SIMS Imaging of Polymer Blends** The study of polymer blend morphology using ToF-SIMS is inspired from the fact that the domain size of the dispersed phases in polymer blends is usually in the range of microns to tens-of-microns, which is above the spatial resolution of ToF-SIMS using a liquid metal ion gun source or cluster source, as well as  $\text{Bi}_n^+$  and  $\text{Au}_n^+$ . The main advantage of ToF-SIMS imaging over other techniques such as SEM, optical microscopy (OM) and AFM is its chemical capability. One important problem encountered with the latter three techniques in blend morphology studies is that, when the chemical nature of the blend components is partially identical or similar, it is very difficult to identify the phases. In the case of compatibilized blends, it is even more difficult to chemically identify and localize the compatibilizer from the rest of the blend with similar components from the rest of the blend, and also to determine its location when it has a similar chemical composition to the blend components. Such a problem can easily be resolved with ToF-SIMS by employing its molecular specificity capabilities. The abilities of ToF-SIMS imaging has indeed been well demonstrated in several polymer blend systems, including the morphology study of blends of poly(vinyl chloride) and PMMA [145], the morphology and miscibility study of blends of ETFE copolymer and PMMA [146], inter-diffusion study of blends of PMMA and PVDF [147], and studies on the compatibilization of immiscible blends [147,148]. The use of ToF-SIMS for studying the compatibilization of PC and PVDF has been also presented [149].

#### 18.3.1.3 Multivariate Analysis of ToF-SIMS Images

It has recently been seen that ToF-SIMS is generally a powerful technique for determining the spatial distribution of chemical species in polymer blends. However, imaging is difficult for a polymer blend such as polyethylene/polypropylene (PE/PP), in which the two polymers have very similar molecular structures and produce similar mass spectra. In addition, surface composition images are often difficult to extract because the intensity of the ion peaks depends not only on the surface composition but also on the surface topography and surface charge [150].

Figure 18.7 shows the loadings and scores on a PMMA-poly(ethyl methacrylate) (PEMA) polymer blend image.

Multivariate analysis (MVA) methods such as principal component analysis (PCA) and multivariate curve resolution (MCR) are all variants of factor analysis, which are widely employed in ToF-SIMS spectral processing and ToF-SIMS image processing [151–154]. Currently, the MVA methods are used to identify relationships between variables, and also between samples. In the case of ToF-SIMS image processing, the ion peak areas correspond to variables while the image pixels correspond to samples. In order to identify a small set of new variables which effectively describe the differences between the image pixels, it holds promise to resolve the above-described problems by increasing image contrast through a reduction of the topographic and charge-distribution effects, thus enabling the extraction of latent information and a more ready determination of the chemical components distribution. However, optimum procedures have not yet been

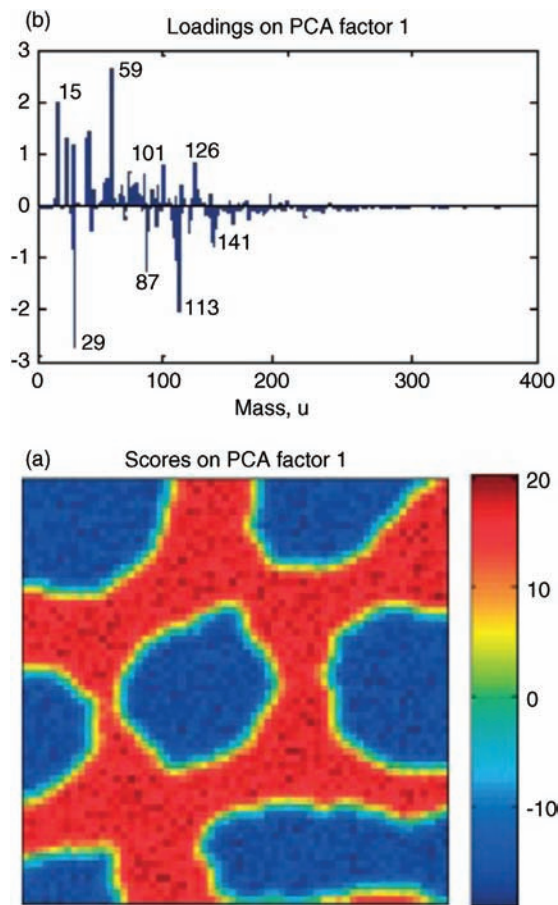


**Figure 18.7** PCA results obtained for the computer-simulated PMMA-PEMA polymer blend image, after Poisson scaling. (a) Loadings on PCA factor 1. PCA successfully distinguishes the two chemical phases. Positive peaks are

associated with PMMA, while negative peaks are associated with PEMA; (b) Scores on PCA factor 1. Reproduced with permission from Ref. [150].

established for applying MVA to ToF-SIMS data. In particular, it is unclear which MVA method and which preprocessing methods prior to MVA would be most effective for ToF-SIMS image analysis.

The distribution of two polymeric species in a blended-polymer film can be determined by applying PCA and MCR to ToF-SIMS imaging, together with preprocessing by pixel binning, normalization, and autoscaling to increase the image contrast by reducing topographic and charge-distribution effects. For example, the distribution of PE/PP was confirmed by MVA conducted on the image data over a static limit, while the MCR score with normalized-autoscaling was found to provide a distinct indication of the PE/PP distribution [150].

## 18.3.2

**NanoSIMS: The Technique**

NanoSIMS is nanoscale secondary ion mass spectrometry technique that allows precise, spatially explicit, elemental and isotopic analysis down to 50 nm resolution [155]. When working in dynamic conditions, NanoSIMS analysis is a destructive process that involves the continuous bombardment of a sample with an energetic ( $\sim 16$  keV) ion beam (either a  $\text{Cs}^+$  or  $\text{O}^+$  primary beam to enhance negative or positive ion formation, respectively), which results in sputtering of the upper sample surface and the consequent liberation of secondary ions.

The use of a reactive primary ion such as  $\text{Cs}^+$  in positive mode (when only negatively charged secondary ions can be detected) or  $\text{O}^+$  in negative mode (when only positively charged secondary ions can be detected) is required to increase the secondary ion yield of negative and positive ions, respectively.

The secondary ions are sorted on the basis of their energy in the instrument's electrostatic sector, before being dispersed in a mass spectrometer according to their  $m/z$  ratios. By acquiring a series of spatially referenced spectra, via a raster-scanning process, a map can be produced for almost any selected atomic mass, and information of isotopic ratios in the form of ROIs, line scans and depth profiles can be obtained. The system is maintained permanently under ultrahigh vacuum in order to prevent any atmospheric interference with the primary and secondary ions (typically  $10^{-10}$  Torr in the analysis chamber) [155].

**18.3.2.1 NanoSIMS: Ion Optical Set-Up**

The main conflict in the design of conventional ion optics in other SIMS systems is that the objective lens of the primary ion column must be as close as possible to the sample so as to produce a small and intense beam. However, the extraction optics must also be placed as close to the sample as possible in order to collect as many secondary ions as possible. The primary and secondary optics both have a physical size leading to a large working distance, and the optics are not in their optimum positions. The colinear optics of the NanoSIMS solves this problem by simultaneously focusing the primary ion beam and collecting most of the secondary ions. The coaxial optics has several advantages, including a shorter working distance, a smaller probe size, a higher collection efficiency (improved transmission), and a minimization of shadowing effects (normal incidence to the sample). The main disadvantages of this technique are that the primary and secondary ions must be of opposite polarity and equal energy. In a coaxial optic system, the secondary ions are extracted back through the primary ion beam diaphragm; this controls the lateral resolution but limits transmission – and thereby sensitivity – simultaneously.

**18.3.2.2 NanoSIMS: The Mass Spectrometer**

The NanoSIMS system uses a  $90^\circ$  spherical electrostatic sector and an asymmetric magnet. This type of mass spectrometer has reasonable transmission, unrivaled mass resolution ( $M/\Delta M > 104$ ), a high energy acceptance, and also preserves the

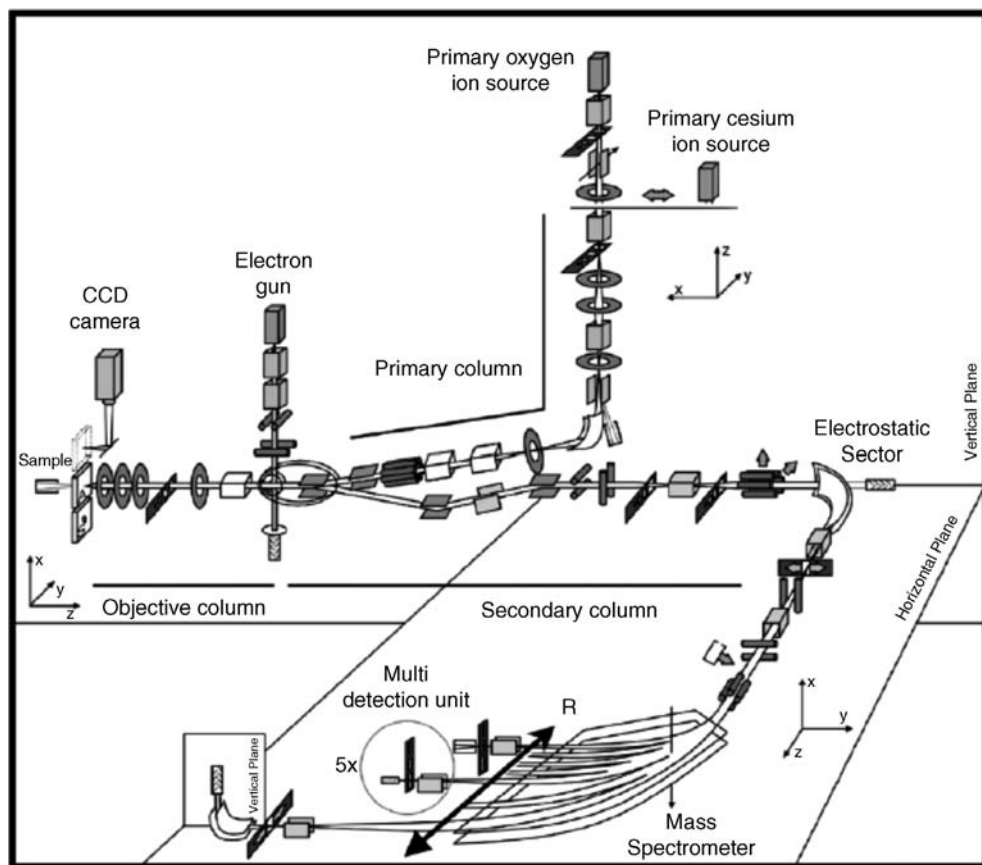


**Figure 18.8** Schematics of NanoSIMS ion optics. Figure kindly provided by Frank J. Stadermann, Washington University, St Louis, Missouri, USA; <http://presolar.wustl.edu/nanosims/schematic.html>. Reproduced with permission from Ref. [155].

lateral resolution which allows a high mass resolution with a small spot size. Following mass separation in the magnetic sector field, the secondary ions are detected using electron multipliers which can accurately measure low-intensity ion signals (higher-intensity signals can be measured using a Faraday cup). The NanoSIMS is equipped with four moveable detectors and one fixed detector, such that five secondary ions can be detected simultaneously (Figure 18.8). This multi-collection capability allows a more accurate reconstruction of the sample chemistry, as each ion image derives from exactly the same volume. It also ensures reliable isotopic measurements and image registration.

### 18.3.2.3 NanoSIMS: Highly Spatially Resolved Elemental Information

NanoSIMS has been optimized for high lateral resolution SIMS analysis. Indeed, NanoSIMS is the only dynamic SIMS system to allow simultaneously a high



lateral resolution (50 nm), a high mass resolution ( $M/\Delta M = 5000$ ) and a high sensitivity (ppb for some elements).

While the advantages of ToF-SIMS include the ability to acquire molecular and true isotopic surface information [152], these data cannot be acquired under conditions suitable for obtaining both high mass resolution (i.e., peak separation of elements with similar masses) and high spatial resolution with adequate signal transmission. In the ToF-SIMS instrument, any attempt at increasing mass resolution to ensure the separation of isobars or mass interferences would result in a loss of spatial resolution and signal transmission. Conversely, conditions designed to allow for increased signal transmission or improved spatial resolution would result in a decline in the operating mass resolution of the instrument. Cliff *et al.* [156] used very high-beam currents (600 pA) in order to obtain a sufficient mass resolution and signal, but this meant they could not achieve a high level of spatial resolution (100–200 nm). The main advantage of NanoSIMS over ToF-SIMS and other generations of SIMS is the ability of NanoSIMS to operate at a high mass resolution, while maintaining both excellent signal transmission (i.e., increased sensitivity) and high spatial resolution [155]. In particular, NanoSIMS has been used successfully to study the surface morphology and composition of thin-film polymer systems [8–10].

The controlled formation of microstructured, ultrathin layers of P2VP–PS mixtures can be accomplished by means of the horizontal precipitation Langmuir–Blodgett (HP-LB) method. Both, the shape and size of the observed structures will depend on the ratio of the two polymers in the blend, as evidenced using AFM [10]. In particular, conditions can be found that promote the formation of round-shaped structures with a relatively uniform size. Data produced with NanoSIMS chemical mapping has indicated that such structures are composed of PS (while P2VP forms the surrounding ultrathin matrix; see Figure 18.9), and explains the ToF-SIMS data in terms of the surface morphology of the film rather than of the surface enrichment of P2VP [10].

## 18.4

### 3D Imaging of Polymer Blends

With many breakthroughs in the lateral resolution of SIMS during recent years, new areas of research showing much promise have developed. Although the much improved lateral resolution of 50 nm of SIMS can effectively deliver more accurate 3D images, the traditional 3D reconstructions – which involve compiling previously acquired successive SIMS images into a 3D stack – do not represent the real localized chemical distribution of the sputtered volume. At this point, the advantages of combining topographical information obtained via AFM and chemical information acquired via SIMS, will be discussed. By taking into account the roughness evolution within the analyzed zone, 3D reconstructions become much more accurate and allow a much easier interpretation of the results [157].

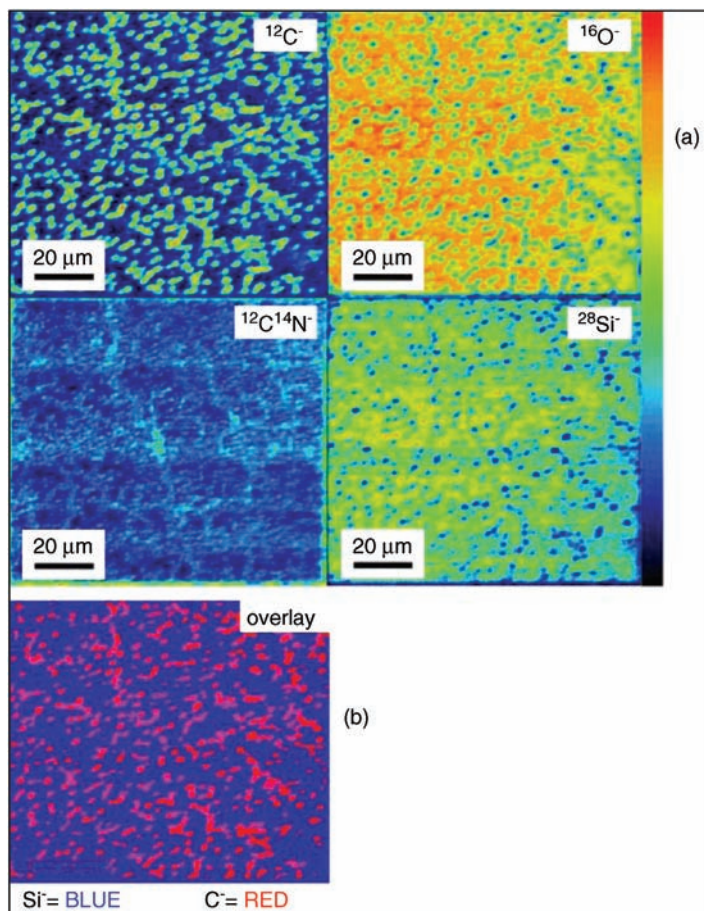


**Figure 18.9** Second frame of the NanoSIMS mass-resolved negative ion maps of a HP-LB film of P2VP/PS (1/4). Reproduced with permission from Ref. [10].

Since the earliest days of SIMS 3D imaging, 3D reconstructions have been carried out in order to better visualize the secondary ion signal distribution within the sputtered volume. The method involves acquiring several successive images and compiling them in a 3D stack; an example of such SIMS 3D imaging has been applied to an annealed PS/PMMA blend [158]. This method assumes that the sample surface is flat at the start of, and during, the sputtering process. Consequently, traditional 3D reconstructions may be inaccurate as they do not take into account the sample roughness initially, its evolution during sputtering, nor variations in erosion rate in the presence of different matrices [157].

By combining topographical information obtained from high-resolution AFM with chemical information obtained from SIMS, the 3D reconstructions became much more accurate (see Figure 18.10). To achieve this goal, the program “SAR-INA” (SPM Assisted Reconstruction of SIMS recorded nano-volumes), which is

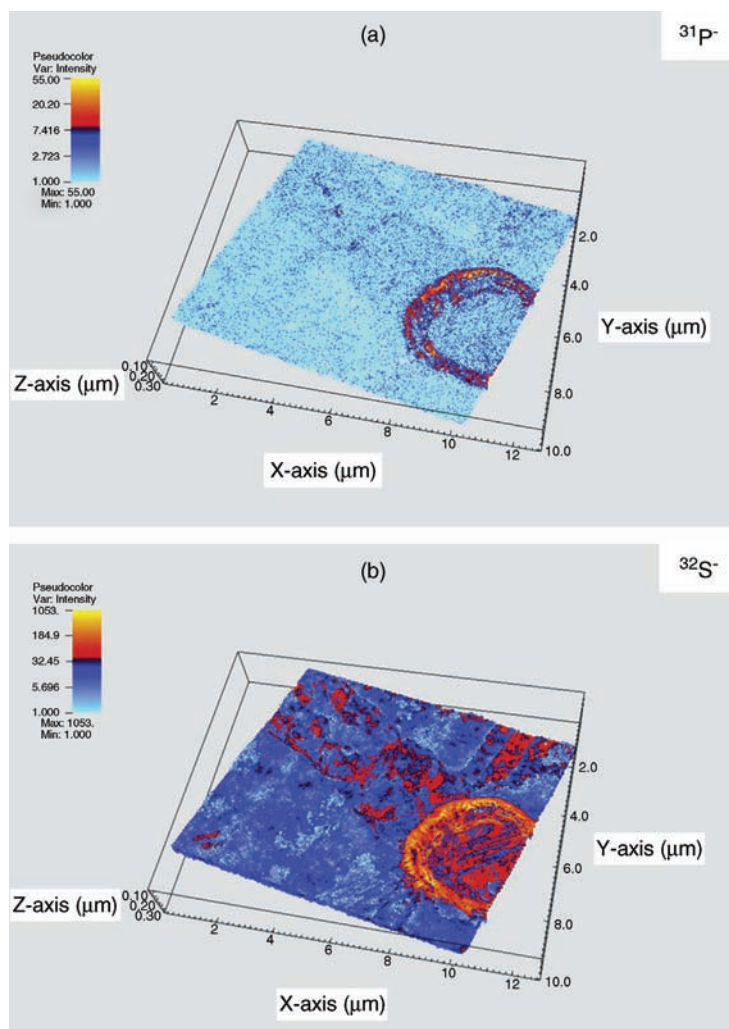


**Figure 18.10** 3D reconstruction of (a)  $^{31}\text{P}$ - and (b)  $^{32}\text{S}$ -contents in the *Anabaena* cyanobacterium, combining SIMS and AFM data using “SARINA” (sputter zone:  $10.4\ \mu\text{m} \times 8.7\ \mu\text{m}$ ).

In both images, the z-scale was magnified by a factor of 5, and the secondary ion counts were integrated over a depth of 20 nm. Reproduced with permission from Ref. [157].

based on the public domain image-processing software package “ImageJ” [159,160], was developed to combine these two types of information. This, in turn, allowed corrections to be made for sample roughness that were not taken into account in traditional 3D reconstruction methods. The generated z-position-corrected slices were realized using the program “Gnuplot” [161]. For volume rendering, the VisIt software developed at the Lawrence Livermore National Laboratory was used [162]. “SARINA” (SPM Assisted Reconstruction of SIMS recorded nano-volumes).

With regards to the poly(3-hexylthiophene) (P3HT)/[6,6]-phenyl- $C_{61}$ -butyric acid methyl ester (PCBM) blend, a major difference in sputter rate was noted and, as the crystalline part was sputtered much more slowly than the noncrystalline part, the step between both phases became increasingly apparent. As shown in Figure 18.10, the  $S^-$  secondary ion signal was mostly present at the crater bottom, whereas the hillock was very low in sulfur and a narrow, bright band remained on the steep slope. When the AFM-corrected reconstructions of the polymer blend were presented, given that the sputtering rate may have differed depending on pixel location, the AFM-corrected SIMS imaging allowed for a more accurate localization of the characteristic elements of a polymer in a polymer blend. Thus, these accurately spatially resolved reconstructions may prove to be very useful when interpreting the results of an analysis [157].

## 18.5

### Conclusions and Perspectives

In this chapter an overview has been provided of polymer blend thin films, of their phase-separation phenomena, and the applications related to such phenomena. The chapter underlines the importance of polymer blends and, in particular, of polymer blend thin films and their compositional characterization. An attempt was made to describe the most sensitive surface technique that allows molecular information and highly spatially resolved lateral information to be obtained. The technique employed was SIMS, which can be categorized as either static or dynamic. Various examples were reported of the surface characterization of polymer blend thin films, performed in particular using ToF-SIMS and NanoSIMS, and underlining the advantages of each technique. The technical characteristics of each techniques which guarantees the observed performance were also described. Clearly, whilst a multitechnique characterization is always beneficial in order to obtain a complete knowledge of a material's behavior, the spatially resolved molecular information provided by ToF-SIMS and the highly spatially resolved elemental information of SIMS, was absolutely necessary for polymer-blend thin films.

Research at the nanometer scale, aimed at creating novel materials and devices that can operate with a performance that is superior to that of conventional systems, is currently of great relevance in many branches of modern science and engineering. Such studies involve the monitoring, construction and control of systems based on engineered nanodevices and nanostructures. Today, the correct chemical characterization of nanosystems is crucial; moreover, in order to achieve a deeper understanding of complex biological processes, analytical tools with spatial resolution in the nanometer region are increasingly required. Analytical techniques based on mass spectrometry provide both elemental and molecular information, and their exceptional analytical features [163–165] will surely provide great advantages to analytical characterizations at the nanoscale. Today, mass spectrometry-based imaging elemental analyses are of interest not only in the

materials sciences and engineering; rather, the direct characterization of polymer-blend thin films at the nanoscale is extremely important in the life sciences and environmental chemistry.

One hopeful perspective in this field should be a new SIMS technique whereby the best characteristics of ToF-SIMS (the molecular information) and of NanoSIMS (the nanometer-scale resolution) are merged. Clearly, this combination technique should provide spatially resolved molecular information at the nanometer scale.

## References

- Li, X., Han, Y., and An, L. (2003) *Polymer*, **44**, 8155.
- Zong, Q., Li, Z., and Xie, X. (2004) *Macromol. Chem. Phys.*, **205**, 1116.
- Chan, C.-M. and Weng, L.T. (2000) *Rev. Chem. Eng.*, **16**, 341.
- Schmidt, J.J., Gardella, J.A., and Salvati, L. (1989) *Macromolecules*, **22**, 4489.
- You, J., Shi, T., Liao, Y., Li, X., Su, Z., and An, L. (2008) *Polymer*, **49**, 4456.
- Briggs, D. (1998) *Surface Analysis by XPS and Static SIMS*, Cambridge University Press, Cambridge, UK.
- Weng, L.-T. and Chan, C.-M. (2006) *Appl. Surf. Sci.*, **252**, 6570.
- Kailas, L., Audinot, J., Migeon, H., and Bertrand, P. (2006) *Compos. Interfaces*, **13**, 423.
- Kailas, L., Audinot, J., Migeon, H., and Bertrand, P. (2004) *Appl. Surf. Sci.*, **231–232**, 289.
- Torrise, V., Tuccitto, N., Delfanti, I., Audinot, J.N., Zhavnerko, G., Migeon, H.-N., and Licciardello, A. (2008) *Appl. Surf. Sci.*, **255**, 1006.
- Chai, J. and Buriak, J.M. (2008) *ACS Nano*, **2**, 489.
- Gotzen, N.-A., Huth, H., Schick, C., Van Assche, G., Neus, C., and Van Mele, B. (2010) *Polymer*, **51**, 647–654.
- Chou, S.Y., Krauss, P.R., and Renstrom, P.J. (1996) *Science*, **272**, 85.
- Chou, S.Y., Krauss, P.R., and Renstrom, P.J. (1995) *Appl. Phys. Lett.*, **67**, 3114.
- Xia, Y., Kim, E., Zhao, X.M., Rogers, J.A., Prentiss, M., and Whitesides, G.M. (1996) *Science*, **273**, 347.
- Kim, E., Xia, Y., and Whitesides, G.M. (1995) *Nature*, **376**, 581.
- Denekamp, C. and Feringa, B.L. (1998) *Adv. Mater.*, **10**, 1080.
- Luo, C.X., Xing, R.B., and Han, Y.C. (2004) *Surf. Sci.*, **552**, 139.
- Widawski, G., Rawiso, B., and François, B. (1994) *Nature*, **283**, 272.
- Mitov, Z. and Kamacheva, E. (1998) *Phys. Rev. Lett.*, **81**, 3427.
- Blodgett, K.B. and Langmuir, I. (1937) *Phys. Rev.*, **51**, 964.
- Torrise, V., Licciardello, A., and Marletta, G. (2010) *Mater. Sci. Eng. B*, **169**, 49.
- Paul, R., Karabiyik, U., Swift, M.C., and Esker, A.R. (2008) *Langmuir*, **24**, 5079.
- Geoghegan, M., Payne, R.S., Jones, R.A.L., Sakellariou, P., Clough, A.S., and Penfold, J. (1994) *Polymer*, **35**, 2019.
- Geoghegan, M. and Krausch, G. (2003) *Prog. Polym. Sci.*, **28**, 261.
- Prosycevas, I., Tamulevicius, S., and Guobiene, A. (2004) *Thin Solid Films*, **453**, 304.
- Dekeyser, C.M., Biltresse, S., Marchand-Brynaert, J., Rouxhet, P.G., and Dupont-Gillain, C.C. (2004) *Polymer*, **45**, 2211.
- Raczowska, J., Rysz, J., Budkowski, A., Lekki, J., Lekka, M., Bernasik, A., Kowalski, K., and Czuba, P. (2003) *Macromolecules*, **36**, 2419.
- Ton-That, C., Shard, A.G., and Bradley, R.H. (2002) *Polymer*, **43**, 4973.
- Muller-Buschbaum, P., Gutmann, J.S., and Stamm, M. (1999) *J. Macromol. Sci. - Phys. B*, **38**, 577.
- Ade, H., Winesett, D.A., Smith, A.P., Qu, S., Ge, S., Sokolov, J., and Rafailovich, M. (1999) *Europhys. Lett.*, **45**, 526.

- 32 Dalnoki-Veress, K., Forrest, J.A., Stevens, J.R., and Dutcher, J.R. (1997) *Physica A*, **239**, 87.
- 33 Heriot, S.Y. and Jones, R.A.L. (2005) *Nat. Mater.*, **4**, 782.
- 34 Gunton, J.D., San Miguel, M., and Sahni, P.S. (1983) *Phase Transitions and Critical Phenomena*, vol. 8 (eds C. Domb and J.L. Lebovitz), Academic, London, pp. 267–466.
- 35 Jones, R.A.L., Norton, L.J., Kramer, E.J., Bates, F.S., and Wiltzius, P. (1991) *Phys. Rev. Lett.*, **66**, 1326.
- 36 Krausch, G., Kramer, E.J., Rafailovich, M. H., and Sokolov, J. (1994) *Appl. Phys. Lett.*, **64**, 2655.
- 37 Robenson, L.M. (2007) *Polymer Blends: A Comprehensive Review*, Carl Hanser Verlag, Munich, pp. 27–28.
- 38 Dalnoki-Veress, K., Forrest, J.A., Stevens, J.R., and Dutcher, J.R. (1996) *J. Polym. Sci., Part B: Polym. Phys.*, **34**, 3017.
- 39 Walheim, S., Böltau, M., Mlynek, J., Krausch, G., and Steiner, U. (1997) *Macromolecules*, **30**, 4995.
- 40 Bruder, F. and Brenn, R. (1992) *Phys. Rev. Lett.*, **69**, 624.
- 41 Georghegan, M., Jones, R.A.L., Payne, R.S., Sakellariou, P., Clough, A.S., and Penfold, J. (1994) *Polymer*, **35**, 2019.
- 42 Georghegan, M., Jones, R.A.L., and Clough, A.S. (1995) *J. Chem. Phys.*, **103**, 2719.
- 43 Tanaka, K., Takahara, A., and Kajiyama, T. (1996) *Macromolecules*, **29**, 3232.
- 44 Karim, A., Slawacki, T.M., Kumar, S.K., Douglas, J.F., Satija, S.K., Han, C.C., Russell, T.P., Liu, Y., Overney, R.M., Sokolov, J., and Rafailovich, M.H. (1998) *Macromolecules*, **31**, 857.
- 45 Krausch, G., Dai, C.-A., Kramer, E.J., and Bates, F.S. (1994) *Ber. Bunsenges. Phys. Chem.*, **98**, 446.
- 46 Haas, C.K. and Torkelson, J.M. (1995) *Phys. Rev. Lett.*, **75**, 3134.
- 47 Sung, L., Karim, A., Douglas, J.F., and Han, C.C. (1996) *Phys. Rev. Lett.*, **76**, 4368.
- 48 Tanaka, H. (1996) *Phys. Rev. Lett.*, **76**, 787.
- 49 Karim, A., Douglas, J.F., Lee, B.P., Glotzer, S.C., Rogers, J.A., Jackman, R.J., Amis, E.J., and Whitesides, G.M. (1998) *Phys. Rev. E*, **57**, R6273.
- 50 Rouault, Y., Baschnagel, J., and Binder, K. (1995) *J. Stat. Phys.*, **80**, 1009.
- 51 Li, H., Paczuski, M., Kardar, M., and Huang, K. (1991) *Phys. Rev. B*, **44**, 8274.
- 52 Wu, Y., Alexander, F.J., Lookman, T., and Chen, S. (1995) *Phys. Rev. Lett.*, **74**, 3852.
- 53 Kim, J.-S., Ho, P.K.H., Murphy, C.E., and Friend, R.H. (2004) *Macromolecules*, **37**, 2861.
- 54 Wang, H. and Composto, R.J. (2000) *J. Chem. Phys.*, **113**, 10386.
- 55 Karim, A., Slawacki, T.M., Kumar, S.K., Douglas, J.F., Satija, S.K., Han, C.C., Russell, T.P., Liu, Y., Overney, R., Sokolov, J., and Rafailovich, M.H. (1998) *Macromolecules*, **31**, 857.
- 56 Greczynski, G., Kugler, Th., Keil, M., Osikowicz, W., Fahlman, M., and Salaneck, W.R. (2001) *J. Electron. Spectrosc.*, **121**, 1.
- 57 Zhang, F., Gates, R.J., Smentkowski, V.S., Natarajan, S., Gale, B.K., Watt, R.K., Asplund, M.C., and Linford, M.R. (2007) *J. Am. Chem. Soc.*, **129**, 9253.
- 58 Xia, Y., Mrksich, M., Kim, E., and Whitesides, G.M. (1995) *J. Am. Chem. Soc.*, **117**, 9576.
- 59 Burn, P.L., Kraft, A., Baigent, D.R., Bradley, D.D.C., Brown, A.R., Friend, R.H., Gymer, R.W., Holmes, A.B., and Jackson, R.W. (1993) *J. Am. Chem. Soc.*, **115**, 10117.
- 60 Dail, L., Griesse, G.H.J., Hang, X., Mau, A.W.H., Spurling, T.H., Yang, Y., and White, J.W. (1996) *Macromolecules*, **29**, 282.
- 61 Nishizawa, M., Shibuya, M., Sawaguchi, T., Matsue, T., and Uchida, I. (1991) *J. Phys. Chem.*, **95**, 9042.
- 62 Burn, P.L., Holmes, A.B., Kraft, A., Bradley, D.D.C., Brawn, A.R., Friend, R.H., and Gymer, R.W. (1992) *Nature*, **356**, 47.
- 63 Healey, B.G., Foran, S.E., and Walt, D.R. (1995) *Science*, **269**, 1078.
- 64 Xia, Y., Kim, E., Zhao, X.M., Rogers, J.A., Prentiss, M., and Whitesides, G.M. (1996) *Science*, **273**, 347.
- 65 Bohanon, T., Elender, G., Knoll, W., Koberle, P., Lee, J.S., Offenhausser, A., Ringsdorf, H., Sackmann, E., Simon, J., Tovar, G., and Winnik, F.M.J. (1996) *Biomater. Sci. Polymer. Ed.*, **8**, 19.

- 66 Bruening, M.L., Zhou, Y., Aguilar, G., Agee, R., Berbreiter, D.E., and Crooks, R.M. (1997) *Langmuir*, **13**, 770.
- 67 Liu, Y., Zhao, M., Beigbreiter, D.E., and Crooks, R.M. (1997) *J. Am. Chem. Soc.*, **119**, 8720.
- 68 Wells, M. and Crooks, R.M. (1996) *J. Am. Chem. Soc.*, **118**, 3988.
- 69 Langer, R. and Vacanti, J.P. (1993) *Science*, **260**, 920.
- 70 Halls, J.J.M., Walsh, C.A., Greenham, N.C., Marseglia, E.A., Friend, R.H., Moratti, S.C., and Holmes, A.B. (1995) *Nature*, **376**, 498.
- 71 Peumans, P., Uchida, S., and Forrest, S.R. (2003) *Nature*, **425**, 158.
- 72 Morteani, A.C., Dhoot, A.S., Kim, J.S., Silva, C., Greenham, N.C., Murphy, C., Moons, E., Cina, S., Burroughes, J.H., and Friend, R.H. (2003) *Adv. Mater.*, **15**, 1708.
- 73 Snaith, H.J. and Friend, R.H. (2004) *Thin Solid Films*, **451**, 567–571.
- 74 Moons, E. (2002) *J. Phys. C*, **14**, 12235.
- 75 Granstrom, M., Petritsch, K., Arias, A.C., Lux, A., Andersson, M.R., and Friend, R.H. (1998) *Nature*, **395**, 257.
- 76 Kim, J.S., Ho, P.K.H., Murphy, C.E., and Friend, R.H. (2004) *Macromolecules*, **37**, 2861.
- 77 Chappell, J., Jukes, P.C., Higgins, A.M., Thompson, R.L., O'Connor, S., Grizzi, I., Fletcher, R., O'Brien, J., Geoghegan, M., and Jones, R.A.L. (2003) *Nat. Mater.*, **2**, 616.
- 78 Corcoran, N., Arias, A.C., Kim, J.S., MacKenzie, J.D., and Friend, R.H. (2003) *Appl. Phys. Lett.*, **82**, 299.
- 79 Arias, A.C., Huck, W.T.S., Corcoran, N., Banach, M., Friend, R.H., and MacKenzie, J.D. (2002) *Appl. Phys. Lett.*, **80**, 1695.
- 80 Yu, G., Gao, J., Hummelen, J.C., Wudl, F., and Heeger, A.J. (1995) *Science*, **270**, 1789.
- 81 Halls, J.J.M., Walsh, C.A., Greenham, N.C., Marseglia, E.A., Friend, R.H., Moratti, S.C., and Holmes, A.B. (1995) *Nature (London)*, **376**, 498.
- 82 Halls, J.J.M., Arias, A.C., MacKenzie, J.D., Inbasekaran, M., Woo, E.P., and Friend, R.H. (2000) *Adv. Mater.*, **12**, 498.
- 83 Wilkinson, C.I., Lidzey, D.G., Palilis, L.C., Fletcher, R.B., Martin, S.J., Wang, X.H., and Bradley, D.D.C. (2001) *Appl. Phys. Lett.*, **79**, 171.
- 84 Morgado, J., Moons, E., Friend, R.H., and Cacialli, F. (2001) *Adv. Mater.*, **13**, 810.
- 85 Morgado, J., Friend, R.H., and Cacialli, F. (2002) *Appl. Phys. Lett.*, **80**, 2436.
- 86 Arias, A.C., Corcoran, N., Banach, M., Friend, R.H., MacKenzie, J.D., and Huck, W.T.S. (2002) *Appl. Phys. Lett.*, **80**, 1695.
- 87 Snaith, H.J., Arias, A.C., Morteani, A.C., Silva, C., and Friend, R.H. (2002) *Nano Lett.*, **2**, 1353.
- 88 Moons, E. (2002) *J. Phys.: Condens. Matter*, **14**, 12235.
- 89 Corcoran, N., Arias, A.C., Kim, J.S., MacKenzie, J.D., and Friend, R.H. (2003) *Appl. Phys. Lett.*, **82**, 299.
- 90 Morteani, A.C., Dhoot, A.S., Kim, J.S., Silva, C., Greenham, N.C., Friend, R.H., Murphy, C., Moons, E., Cina, S., and Burroughes, J. (2003) *Adv. Mater.*, **15**, 1708.
- 91 Cina, S., Baynes, N., Moons, E., Friend, R.H., Burroughes, J., Towns, C., Heeks, K., O'Dell, R., O'Connor, S., Athanassopoulou, N., and Soc., P. (2001) *Photo-Opt. Ins. (SPIE)*, **4279**, 221.
- 92 Kim, J.S., Ho, P.K.H., Murphy, C.E., Baynes, N., and Friend, R.H. (2002) *Adv. Mater.*, **14**, 206.
- 93 Bhatia, S.Q. and Burrell, M.C. (1990) *Surf. Interface Anal.*, **15**, 355.
- 94 Thompson, P.M. (1991) *Anal. Chem.*, **63**, 2447.
- 95 Lhoest, J.B., Bertrand, P., Weng, L.T., and Dewez, J.L. (1995) *Macromolecules*, **28**, 4631.
- 96 Affrossman, S., Bertrand, P., Hartshorne, M., Kiff, T., Leonard, D., Pethrick, R.A., and Richards, R.W. (1996) *Macromolecules*, **29**, 5432.
- 97 Brant, P., Karim, A., Douglas, J.F., and Bates, F.S. (1996) *Macromolecules*, **29**, 5628.
- 98 VandenEynde, X. and Bertrand, P. (1999) *Surf. Interface Anal.*, **27**, 157.
- 99 Takahara, A., Kawaguchi, D., Tanaka, K., Tozu, M., Hoshi, T., and Kaiyama, T. (2003) *Appl. Surf. Sci.*, **203**, 538.
- 100 Lei, Y.G., Cheung, Z.L., Ng, K.M., Li, L., Weng, L.T., and Chan, C.-M. (2003) *Polymer*, **44**, 3883.
- 101 Li, L., Chan, C.-M., Weng, L.T., Xiang, M.L., and Jiang, M. (1998) *Macromolecules*, **31**, 7248.

- 102 Zeng, X.M., Chan, C.-M., Weng, L.T., and Li, L. (2000) *Polymer*, **41**, 8821.
- 103 Liu, S.Y., Chan, C.-M., Weng, L.T., Li, L., and Jiang, L.M. (2002) *Macromolecules*, **35**, 5623.
- 104 Liu, S.Y., Chan, C.-M., Weng, L.T., and Jiang, M. (2004) *Anal. Chem.*, **76**, 5156.
- 105 Liu, S.Y., Chan, C.-M., Weng, L.T., and Jiang, M. (2004) *Polymer*, **49**, 4945.
- 106 Huang, H.L., Goh, S.H., Lai, D.M.Y., and Huan, C.H.A. (2004) *Appl. Surf. Sci.*, **227**, 373.
- 107 Weng, L.T., Smith, T.L., Feng, J., and Chan, C.-M. (1998) *Macromolecules*, **31**, 928.
- 108 Li, L., Chan, C.-M., and Weng, L.T. (1998) *Macromolecules*, **31**, 7248.
- 109 Briggs, D., Fletcher, I.W., Reichmaier, S., Agulo-Sanchez, J.L., and Short, R.D. (1996) *Surf. Interface Anal.*, **24**, 419.
- 110 Weng, L.T. and Chan, C.-M. (2003) *Appl. Surf. Sci.*, **203**, 532.
- 111 Weng, L.T., Smith, T.L., Feng, J., and Chan, C.-M. (1998) *Macromolecules*, **31**, 928–932.
- 112 Benninghoven, A., Rüdenauer, F.G., and Werner, H.W. (1987) *Secondary Ion Mass Spectrometry Basic Concepts, Instrumental Aspects, Applications and Trends*. John Wiley & Sons, New York.
- 113 Fernández, B., Costa, J.M., Pereiro, R., and Sanz-Medel, A. (2010) *Anal. Bioanal. Chem.*, **396**, 15–29.
- 114 Walker, A.V. (2008) *Anal. Chem.*, **80**, 8865.
- 115 Nygren, H., Malmberg, P., Kriegeskotte, C., and Arlinghaus, H.F. (2004) *FEBS Lett.*, **566**, 291.
- 116 Nygren, H. and Malmberg, P. (2007) *Trends Biotechnol.*, **25**, 499.
- 117 Behm, J.M., Hemminger, J.C., and Lykke, K.R. (1996) *Anal. Chem.*, **68**, 713.
- 118 Rubakhin, S.S., Jurchen, J.C., Monroe, E.B., and Sweedler, J.V. (2005) *Drug Discovery Today*, **10** (12), 823–827.
- 119 Vickerman, J.C., Brown, A., and Reed, N. M. (eds) (1989) *Secondary Ion Mass Spectrometry*, vol. 17, Clarendon Press, Oxford, UK.
- 120 Benninghoven, A., Hagenhoff, B., and Niehuis, E. (1993) *Anal. Chem.*, **65**, 630A.
- 121 Benninghoven, A. (1994) *Angew. Chem., Int. Ed. Engl.*, **33**, 1023.
- 122 Grasserbauer, M., Friedbacher, G., Hutter, H., and Stingeder, G. (1993) *Fres. J. Anal. Chem.*, **346**, 594.
- 123 Bertrand, P. and Weng, L.-T. (1996) *Mikrochim. Acta*, **13**, 167.
- 124 Benninghoven, A. (1994) *Surf. Sci.*, **299/300**, 246.
- 125 Brummel, C., Willey, K.F., Vickerman, J.C., and Winograd, N. (1995) *Int. J. Mass Spectrom. Ion Processes*, **143**, 257.
- 126 Odom, R.W. (1994) *Appl. Spectrosc. Rev.*, **29**, 67.
- 127 Winograd, N. (1993) *Anal. Chem.*, **65**, 622A.
- 128 Rüdenauer, F.G. (1994) *Anal. Chim. Acta*, **297**, 197.
- 129 Schueler, B.W. (1992) *Microsc. Microanal. Microstruct.*, **3**, 119.
- 130 Chabala, J.M., Soni, K.K., Li, J., Gavrilov, K.L., and Levi-Setti, R. (1995) *Int. J. Mass Spectrom. Ion Processes*, **143**, 191.
- 131 Fragu, P., Briancion, C., Fourré, C., Clerc, J., Jeusset, J., and Halpern, S. (1993) *Microbeam. Anal.*, **2**, 199.
- 132 Burns, M.S. (1982) *J. Microsc.*, **127**, 237.
- 133 Fragu, P., Clerc, J., Briancion, C., Fourré, C., Jeusset, J., and Halpern, S. (1994) *Micron*, **25**, 361.
- 134 Berry, J.P., Galle, P., Chassoux, D., Escaig, F., Linarez-Cruz, L.G., and Lespinats, G. (1992) *Biol. Cell*, **74**, 93.
- 135 Short, R.D., Ameen, A.P., Jackson, S.T., Pawson, D.J., O'Toole, L., and Ward, A.J. (1993) *Vacuum*, **44**, 1143.
- 136 Aller, A.J. (1992) *Appl. Spectrosc. Rev.*, **27**, 223.
- 137 Pacholski, M.L. and Winograd, N. (1999) *Chem. Rev.*, **99**, 2977.
- 138 Liebl, H. (1967) *J. Appl. Phys.*, **38**, 5277.
- 139 Levi-Setti, R., Wang, Y.L., and Crow, G. (1984) *J. Phys.*, **C9**, 197.
- 140 Benninghoven, A. (1973) *Surf. Sci.*, **35**, 427.
- 141 Chait, B.T. and Standing, K.G. (1981) *Int. J. Mass Spectrom. Ion Phys.*, **40**, 185.
- 142 Schwieters, J., Cramer, H.-G., Heller, T., Jürgens, U., Niehuis, E., Zehnpfenning, J., and Benninghoven, A. (1991) *J. Vac. Sci. Technol. A*, **9**, 2864.
- 143 Benguerba, M., Brunell, A., Della-Negra, S., Depauw, J., Joret, H., Le Beyec, Y., Blain, M.G., Schweikert, E.A., Ben Assayag, G.,



- and Sudraud, P. (1991) *Nucl. Instrum. Methods Phys. Res.*, **B62**, 8.
- 144 Andersen, H.H., Brunell, A., Della-Negra, S., Depauw, J., Jacquet, D., Le Beyec, Y., Chaumont, J., and Bernas, H. (1998) *Phys. Rev. Lett.*, **80**, 5433.
  - 145 Briggs, D., Fletcher, I.W., Reichlmaier, S., Agulo-Sanchez, J.L., and Short, R.D. (1996) *Surf. Interface Anal.*, **24**, 419.
  - 146 Weng, L.T., Smith, T.L., Feng, J., and Chan, C.-M. (1998) *Macromolecules*, **31**, 928.
  - 147 Feng, J.Y., Li, L., Chan, C.-M., and Weng, L.T. (2002) *Surf. Interface Anal.*, **33**, 455.
  - 148 Feng, J.Y., Weng, L.T., Li, L., and Chan, C.-M. (2000) *Surf. Interface Anal.*, **29**, 168.
  - 149 Zeng, X.M., Weng, L.T., Li, L., Chan, C.-M., Liu, S.Y., and Jiang, M. (2001) *Surf. Interface Anal.*, **31**, 421.
  - 150 Miyasaka, T., Ikemoto, T., and Kohno, T. (2008) *Appl. Surf. Sci.*, **255**, 1576.
  - 151 Pachuta, S.J. (2004) *Appl. Surf. Sci.*, **231–232**, 217.
  - 152 Ohlhausen, J.A.T., Keenan, M.R., Kotula, P.G., and Peebles, D.E. (2004) *Appl. Surf. Sci.*, **231–232**, 230.
  - 153 Wagner, M.S., Graham, D.J., and Castner, D.G. (2006) *Appl. Surf. Sci.*, **252**, 6575.
  - 154 Fletcher, J.S., Henderson, A., Jarvis, R.M., Lockyer, N.P., Vickman, J.C., and Goodacre, R. (2006) *Appl. Surf. Sci.*, **252**, 6869.
  - 155 Herrmann, A.M., Ritz, K., Nunan, N., Clode, P.L., Pett-Ridge, J., Kilburn, M.R., Murphy, D.V., O'Donnell, A.G., and Stockdale, E.A. (2007) *Soil Biol. Biochem.*, **39**, 1835.
  - 156 Cliff, J.B., Gaspar, D.J., Bottomley, P.J., and Myrold, D.D. (2002) *Appl. Environ. Microbiol.*, **68**, 4067.
  - 157 Fleming, Y., Wirtz, T., Gysin, U., Glatzel, T., Wegmann, U., Meyer, E., Maier, U., and Rychen, J. (2011) *Appl. Surf. Sci.*, **258**, 1322.
  - 158 Kailas, L., Nysten, B., Audinot, J.N., Migeon, H.N., and Bertrand, P. (2005) *Surf. Interface Anal.*, **37**, 435.
  - 159 Burger, W. and Burge, M.J. (2008) *Digital Image Processing - An Algorithmic Introduction using Java*. 1st edn, Springer, New York.
  - 160 Rasband, W. (2011) ImageJ: Image Processing and Analysis in Java. Available at: <http://imagej.nih.gov/ij/>.
  - 161 Janert, Ph.K. (2009) *Gnuplot in Action: Understanding Data with Graphs*, Manning Publications Co., Greenwich, CT, USA.
  - 162 VisIt Visualization Tool: Software that Provides Parallel Interactive Visualization (2011) Available at: <http://wci.llnl.gov/codes/visit/home.html>.
  - 163 Norris, J.L., Cornett, D.S., Mobley, J.A., Andersson, M., Seeley, E.H., Chaurand, P., and Caprioli, R.M. (2007) *Int. J. Mass. Spectrom.*, **260**, 212.
  - 164 Mas, S., Perez, R., Martinez-Pinna, R., Egido, J., and Vivanco, F. (2008) *Proteomics*, **8**, 3735.
  - 165 Becker, J.S., Zoriy, M., Wu, B., Matusch, A., and Becker, J.S. (2008) *J. Anal. At. Spectrom.*, **23**, 1275.



## 19

# Fluorescence Microscopy Techniques for the Structural Analysis of Polymer Materials

*Hiroyuki Aoki*

### 19.1

#### Introduction

As the morphology of phase separation in a polymer blend system greatly influences a variety of macroscopic properties (including viscoelastic behavior), the structure of polymer blends has been extensively studied using many different methods. In the structural analysis of polymer systems, real-space observations using microscopy have provided direct information concerning the system's morphology. Optical microscopy has long been used to obtain magnified images of a small object by using a set of lenses. As the basic concept of optical microscopy is very simple, it has been widely used in various fields of research. Optical microscopy can also be used to obtain images by employing a variety of contrast mechanisms, such as differential interference, phase contrast and polarization contrast.

By contrast, in fluorescence microscopy the image is formed by collecting the fluorescence emissions from a specimen. Because the fluorescence emitted from a specimen can provide many types of information, fluorescence microscopy has been used widely for the structural analysis of polymer blend systems.

In this chapter, the application of fluorescence imaging techniques to the structural analysis of polymer blend systems is discussed, and recent developments in fluorescence microscopy are described.

### 19.2

#### Fundamentals of Fluorescence Microscopy

Fluorescence is the light emitted upon the relaxation of an electronically excited molecule [1,2]. Figure 19.1a shows the energy diagram for the light absorption and emission processes. A molecule absorbs a photon with an energy corresponding to the difference between the energy levels in the ground ( $S_0$ ) and excited ( $S_1$ ) states. If an electron is excited to a higher energy level than  $S_1$ , the electron rapidly relaxes to the lowest level of  $S_1$  as the nonradiative transition. The excited electron

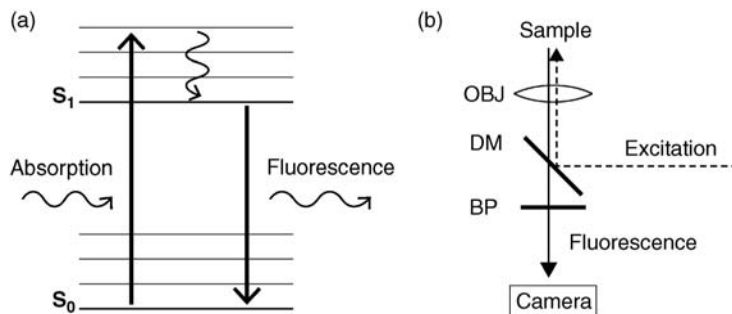


**Figure 19.1** (a) Energy diagram for the fluorescence emission; (b) Schematic illustration of a fluorescence microscope. OBJ, objective lens; DM, dichroic mirror; BP, band-pass filter.

in the  $S_1$  state then relaxes to the ground state by emitting a photon with energy equal to the gap between  $S_0$  and  $S_1$ . As shown clearly in Figure 19.1a, the energy of the fluorescence photon is less than that of the absorbed photon at the excitation; therefore, the wavelength of the fluorescence emission is longer than that of the absorbed light.

Fluorescence microscopy produces an image of the fluorescence emission from a sample, which is illuminated by light with a wavelength matched to the absorption band of the sample. Figure 19.1b shows the optical system of epifluorescence microscopy, where the illumination light is irradiated through an objective lens; the fluorescence signal is then collected by the same objective and focused onto an image plane through a dichroic mirror and an optical filter that passes only the fluorescence from the sample. Stray light of the illumination is minimized by selecting an appropriate optical filter. The fluorescent specimen can be brightly observed in a micrograph with low background noise. Moreover, currently available sensitive cameras can detect extremely weak fluorescence even from a single molecule. Fluorescence microscopy is suitable for analyzing the spatial distribution of fluorescent moieties with high contrast and sensitivity.

Confocal microscopy, another method used to obtain a fluorescence image, is a type of scanning microscopy technique that measures the signal from a single point illuminated with a focused light spot. A confocal microscope scans the light spot point-by-point to form an image [3,4], whereas, a conventional microscope forms a two-dimensional (2D) image of an object at once. Figure 19.2 shows a schematic image of a confocal microscope. Illumination from a light source is focused by an objective lens. The fluorescence signal from the illuminated point is collected and measured by a photodetector, such as a photomultiplier tube and a photodiode. In confocal microscopy, a pinhole is placed in front of the detector, which is optically conjugate to the focal point of the objective lens. The signal from the illuminated point is detected through the pinhole, whereas the stray light from an out-of-focus point is eliminated, as indicated by the dashed line in Figure 19.2. Therefore, confocal

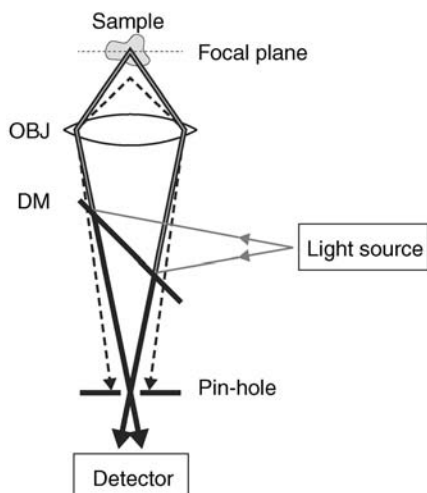


**Figure 19.2** Schematic illustration of a confocal microscope. The gray and black solid lines indicate the paths of the illumination and signal light, respectively. The dashed line indicates the signal from the sample out of the focal plane.

microscopy provides a high-contrast image provides at the focal plane. Depth-discriminated imaging allows three-dimensional (3D) observations. A 3D image over the entire specimen is reconstructed from a set of individual images sliced at different depth levels. The spatial resolution of confocal microscopy is about 200 nm and about 400 nm in the lateral and axial directions, respectively. The ability to perform 3D observations inside a bulk medium is effective for micrometer-order structural analysis of polymer blend systems.

In fluorescence microscopy measurements, it is obviously essential for the specimen to be fluorescent. In the case of polymer blend systems the structure of fluorescent polymers such as  $\pi$ -conjugated polymers can be directly observed. However, common synthetic polymers are transparent to visible light and are nonfluorescent. To observe such polymers, the component to be observed is labeled using a fluorescent dye. The simplest way to apply the fluorescent label is to disperse a low-molecular-weight dye in the blend system [5–8], whereby the dye molecules are selectively introduced to the domain of the polymer component by chemical interaction. For example, dye molecules with a carbonyl group are stabilized in the domain of poly(vinylpyridine) owing to the hydrogen bond between the hydroxyl and pyridine groups [8]. However, the labeling method involving the dispersion of a low-molecular-weight dye cannot be used for blend systems in which both components show similar interactions with the dye moiety. In order to avoid uncertainty regarding the labeled location, the fluorescent moiety is covalently attached to the polymer chain. The dye molecules are then introduced by: (i) polymerization with a monomer or an initiator having a fluorescent moiety [9–13]; and (ii) the reaction between a functional group in the fluorescent moiety and a reactive

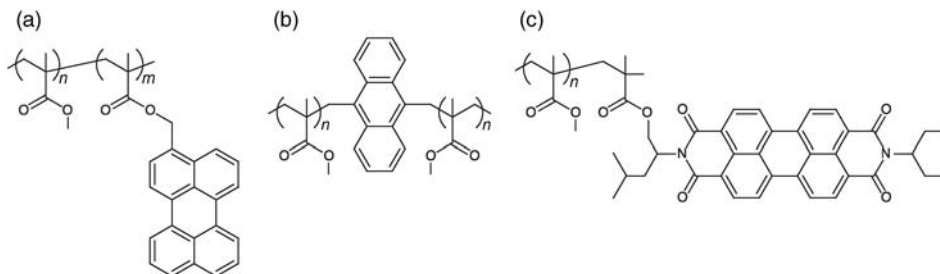


**Figure 19.3** Structure of fluorescence-labeled poly(methyl methacrylate)s, that are labeled at (a) the side chain, (b) the center segment, and (c) the chain end.

site on the polymer chain [14–16]. Examples of labeled polymers are shown in Figure 19.3. The side-chain-labeled poly(methyl methacrylate) (PMMA) in Figure 19.3a was prepared by the copolymerization of methacrylate and 3-perylenyl methacrylate, the center-labeled PMMA (Figure 19.3b) was prepared by termination of the living anion polymerization with bis-bromomethyl anthracene, and the end-labeled PMMA (Figure 19.3c) was synthesized by the atom transfer radical polymerization from an initiator containing a perylene diimide moiety. The covalent introduction of the dye moiety to the polymer chain allows the selective observation of individual components in a blend system.

### 19.3

#### Fluorescence Imaging of Polymer Blend Systems

Fluorescence microscopy can be used to identify the spatial distribution of individual components in a blend system by the selective fluorescence labeling of the specimen. Therefore, fluorescence imaging techniques have been widely used to study the domain structure at the length scale of micrometers [15–22]. In particular, without the use of confocal microscopy, it is difficult to obtain the detailed micrometer-order 3D data. The structural analysis in three dimensions for polymer blends is reviewed at this point.

##### 19.3.1

#### Real-Space Measurement of 3D Structure

It is well known that the properties and structures of the surface and interface are different from those in a bulk state. The 3D observations made using confocal microscopy are very useful for discussing the effects of the surface/interface on the phase-separation structure. Kumacheva *et al.* studied the morphology of the surface and bulk of a polystyrene (PS)/PMMA blend prepared by casting from a toluene solution [20]. The cross-sectional image of a PS/PMMA blend is shown in Figure 19.4, where the bright areas correspond to the PMMA domains. The depth-dependent phase-separation structure was

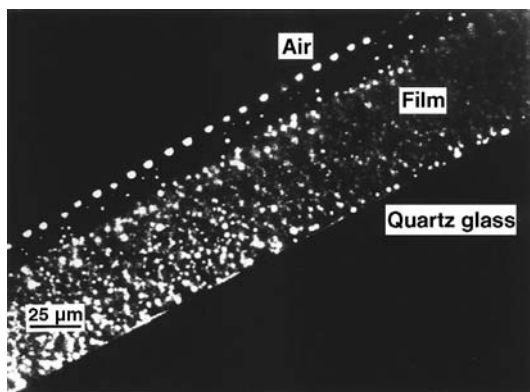


**Figure 19.4** Cross-sectional image of a PS/PMMA blend (9/1) film prepared by casting the solution in toluene at a slow evaporation rate. The bright domains correspond to the PMMA-rich phase labeled with NBD. Reprinted with permission from Ref. [20]; © 1997, American Chemical Society.

observed for the blend film prepared at a slow solvent evaporation rate: a depletion layer of PMMA was observed beneath the surface. During solvent evaporation, phase separation at the surface was enhanced and the PMMA chains were diffusively transferred from the liquid-like bulk to the surface, which resulted in a depletion layer free from the PMMA-rich domains. Thus, the 3D fluorescence observation provides invaluable information about structure formation in the solvent-casting process.

As confocal microscopy can be used to obtain a 3D image in a fast time scale (within a few minutes), it is suitable for studying the time evolution of the structural change. When studying structure growth the geometric parameters of the phase boundary, such as the interface area and curvature, are important physical quantities. Spinodal decomposition has been mainly studied in an inverse space by scattering methods; however, it is difficult to obtain all of the geometric parameters by using scattering techniques. On the other hand, real-space observations using fluorescence microscopy provide direct information about the geometry of the phase-separation structure. Jinnai *et al.* studied the spinodal decomposition of a binary blend by using confocal microscopy [15–17]. Figure 19.5 shows the time evolution of the phase-separation structure of a blend of polybutadiene (PB) and deuterated PB (DPB) [15], where the PB and DPB domains are indicated by bright and empty areas, respectively. This indicates that the size of the bicontinuous structure was increased with the elapsed time after the onset of phase separation, which in turn suggested that the late stage of spinodal decomposition had been observed. Quantitative analysis of the curvature of the phase boundary showed that a large portion of the interface was a hyperbolic surface, and that the time evolution of the interface was dynamically self-similar. Thus, fluorescence imaging can provide direct and invaluable information regarding the structure of polymer blend systems.

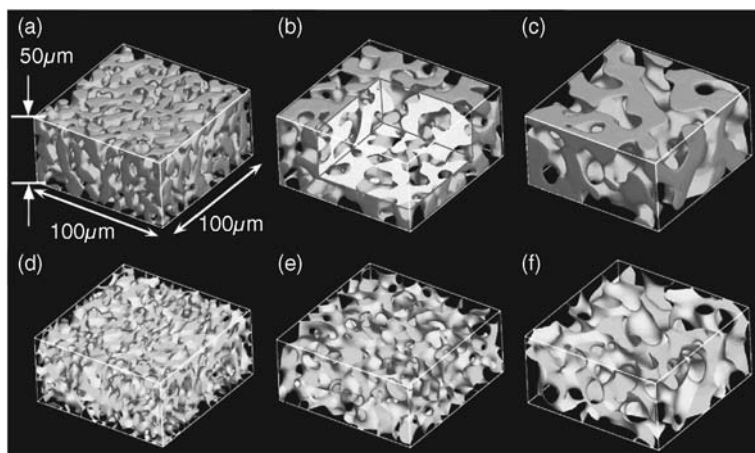


**Figure 19.5** Time evolution of bicontinuous structures in the PB/DPB blend at (a) 1675 min, (b) 2880 min, and (c) 4860 min after the onset of SD. Only the PB-rich phase labeled with anthracene is shown in the image; (d–f) The interfaces between two coexisting phases for the 3D volumes corresponding to (a–c), respectively. Reprinted with permission from Ref. [15]; © 2000, American Chemical Society.

### 19.3.2

#### Spectroscopic Information

The signal intensity in a fluorescence image corresponds to the density of the fluorescently labeled component. Fluorescence measurements can provide a variety of information through not only the intensity but also spectroscopy, because the fluorescence properties of a dye molecule are susceptible to the surrounding environment and the mobility of the molecule. For example, the viscosity and polarity around the dye molecule is estimated from the fluorescence spectrum and lifetime [23–27]. The phenomenon of fluorescence resonant energy transfer (FRET) is widely used to probe molecular interactions. The energy of an excited molecule transfers to another by dipole–dipole interaction among the molecules [28], and the rate constant of the energy transfer,  $k_{\text{ET}}$ , is given by the following equation:

$$k_{\text{ET}} = \frac{1}{\tau} \left( \frac{R_0}{R} \right)^6 \quad (19.1)$$

where  $R$  is the distance between the molecules,  $R_0$  is a reference distance termed the Förster radius, and  $\tau$  is the fluorescence lifetime of the energy donor molecule without the energy transfer. The Förster radius is dependent on the overlap integral of the fluorescence spectrum of the donor and the absorption spectrum of the acceptor.  $R_0$  is typically of the order of a few nanometers; for example,  $R_0 = 2.2$  nm for phenanthrene–anthracene and 3.3 nm for pyrene–perylene. Therefore, the efficiency of FRET is heavily dependent on the distance between the donor and the



acceptor molecules on the order of nanometers. A quantitative analysis of FRET efficiency from the fluorescence spectrum and the fluorescence decay curve provides information regarding the molecular distance. In polymer systems, FRET spectroscopy has been used for studying the dimensions of polymer chains [29,30] and miscibility among the labeled components [31–33]. The spectroscopic and lifetime measurements can be carried out using a microscope, while the local properties of polymer blends have been discussed based on spatially resolved fluorescence information [12,34–36].

## 19.4

### Fluorescence Microscopy Beyond the Diffraction Barrier

The spatial resolution of conventional optical microscopy is limited by the diffraction limit of light; consequently, two objects that are close to each other cannot be resolved in the fluorescence image. The minimum resolvable distance,  $\Delta x$ , is given as follows:

$$\Delta x = 0.61 \frac{\lambda}{\text{NA}}, \quad (19.2)$$

where  $\lambda$  and NA are the wavelength of light and the numerical aperture of the objective lens, respectively. Two objects closer than  $\Delta x$  will be observed as a single blurred spot in a fluorescence image; hence, because the highest value of NA for a commercially available lens is 1.49, a structure smaller than about 200 nm cannot be resolved in a fluorescence image. Consequently, fluorescence microscopy has been applied to observe the structure of polymer blends at length scales larger than the order of several hundred nanometers. During the past few decades, novel fluorescence imaging methods have been developed to overcome the diffraction barrier; these include near-field optics [37–40] and super-resolution techniques [41–52]. These methods enable optical information to be obtained from a nanometer-scale area in polymer blend systems.

#### 19.4.1

##### Near-Field Optical Microscopy

Near-field optical microscopy is a type of scanning probe microscopy, and is referred to as either scanning near-field optical microscopy (SNOM) or near-field scanning optical microscopy (NSOM). When light is incident to an object that is much smaller than the light's wavelength, there arises not only a propagating field such as scattered light but also a nonpropagating electric field that is restricted around the object. Such the nonpropagating light is termed the optical near-field [39,40]. The nonpropagating optical near-field provides information about the local structure smaller than the wavelength; therefore, the near-field component can achieve a high spatial resolution beyond the diffraction limit. A schematic illustration of a SNOM probe is shown in Figure 19.6. An aperture which is smaller than

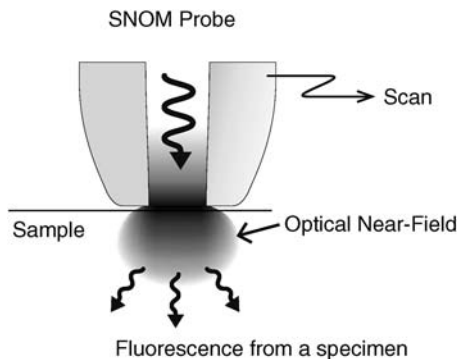


**Figure 19.6** Schematic illustration of a SNOM probe. The optical near-field confined in a nanometric area is generated around an aperture which is much smaller than the wavelength of light. The probe is scanned on the sample surface while monitoring the signal intensity.

the wavelength of light is fabricated at the end of the probe. The SNOM probe illuminates the sample, using the optical near-field that emanates from the aperture. As the probe is scanned the fluorescence signal from the sample will be detected as propagating light. The optical near-field is confined to a nanometric region close to the aperture, which is much smaller than the wavelength of light; therefore, the spatial resolution will be dependent on the size of the aperture. Typically, SNOM can achieve a resolution of less than 100 nm. Because the signal fluorescence can be delivered to any of the detectors used for conventional microscopy measurements, SNOM enables a wide variety of spectroscopic methods to be applied to a nanometric space.

SNOM has been employed for analyses of the phase-separation structure of polymer blends and block copolymers because of its high spatial resolution. At this point, the study of Langmuir–Blodgett (LB) monolayers is described. An LB monolayer is an extremely thin film with a thickness of a single molecule [54,55]. In an LB film made from polymeric materials, the polymer chains have no degree of freedom in the height direction, and therefore such a film can serve as a model system of 2D polymer chains. The phase-separation behavior of polymer blends in two dimensions has been studied using SNOM [10,11,53]. Figure 19.7 shows the fluorescence SNOM images of a monolayer of poly(*iso*-butyl methacrylate) (PiBMA) and poly(octadecyl methacrylate) (PODMA), which were labeled by pyrene and perylene, respectively. The domains of PiBMA and PODMA are brightly observed in the pyrene fluorescence (Figure 19.7a) and perylene fluorescence (Figure 19.7b) images, respectively; moreover, they are complementary to each other, indicating a strong phase separation. Figure 19.7c shows the FRET emission image obtained by detecting perylene fluorescence under the selective excitation of pyrene. Since FRET occurs when the distance between the energy donor (pyrene) and acceptor (peryene) is less than several nanometers, the FRET emission indicates the coexistence of pyrene-labeled PiBMA and perylene-labeled PODMA. Therefore, the

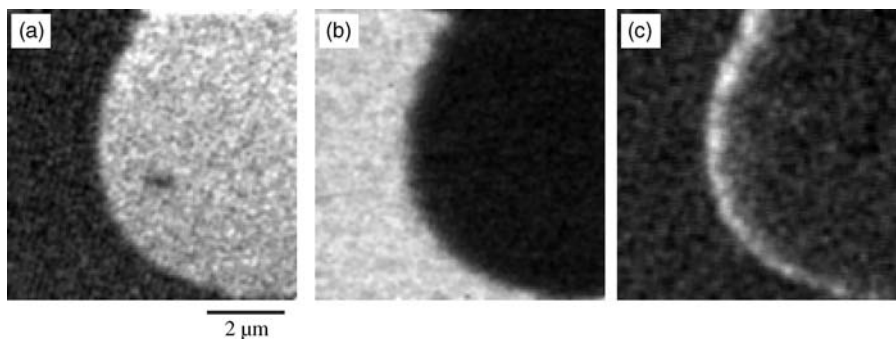


**Figure 19.7** Fluorescence SNOM images of the phase-separation structure of a blend monolayer of pyrene-labeled PiBMA and perylene-labeled PODMA. The SNOM images were observed by collecting the pyrene fluorescence (a), perylene fluorescence (b), and FRET emission (c). Reprinted with permission from Ref. [53]; © 2002, Elsevier.

interface region of the PiBMA and PODMA domains was selectively observed as the bright area in Figure 19.7c. The interface width of the PiBMA–PODMA blend monolayer was evaluated as 100–300 nm from the FRET emission SNOM image; this was far greater than the width of the interface in a 3D bulk system (ca. 3 nm) and indicated an increase in the miscibility of PiBMA and PODMA. These results also revealed directly that the spatial confinement of the polymer chain in two dimensions could alter the miscibility of polymers.

In near-field microscopy, various spectroscopic methods can be combined with fluorescence intensity mapping. For example, fluorescence lifetime SNOM imaging was applied to study the structure of  $\pi$ -conjugated polymers that are used in organic electronics applications. The SNOM images of the phase-separation structure of a blend system of polystyrene (PS) and poly(9,9-dioctylfluorene) (F8) are shown in Figure 19.8. The photoluminescence (PL) intensity image in Figure 19.8c shows the spatial distribution of F8, indicating the phase-separated structure at the length scale of a few micrometers. A comparison of the lifetime image (Figure 19.8e) with the F8 distribution showed that the fluorescence lifetime of the F8-rich domain was less than that of F8 incorporated into the PS-rich domain. This suggested an increase in the diffusion constant of the exciton in the F8-rich domain because of the interchain interaction of F8. Thus, fluorescence lifetime imaging can reveal the molecular properties of  $\pi$ -conjugated polymers.

#### 19.4.2

##### Super-Resolution Optical Microscopy

Whereas, near-field microscopy achieves a high resolution by illuminating a nanometric area with localized light around a small probe tip, the super-resolution techniques extract nanometer-scale information from optical images captured using conventional lens-based optics. Among several super-resolution techniques that have been reported, stimulated emission depletion (STED) microscopy [43–45] and

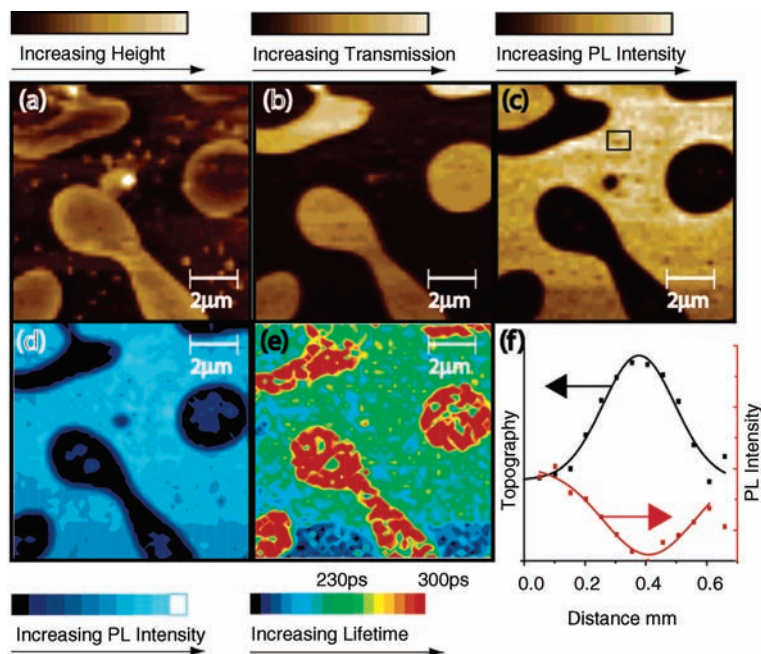


**Figure 19.8** Fluorescence SNOM images of a phase-separated blend of polystyrene and poly(9,9-dioctylfluorene). (a–c) Surface topography, transmittance, and fluorescence images, respectively; (d and e) Mapping of the amplitude and lifetime of the fluorescence decay

curve, respectively; (f) Cross-section profile of the topography and fluorescence images of the area marked by a rectangle in panel (c). Reprinted with permission from Ref. [34]; © 2005, American Chemical Society.

single-molecule localization microscopy [50–52,74,75] have provided fluorescence images with the highest spatial resolution.

STED microscopy is a scanning confocal fluorescence imaging technique. As noted above, confocal microscopy illuminates the sample with a focused light, but the size of the focal spot is limited to approximately 200 nm by the diffraction limit. In STED microscopy, a donut-shaped STED spot is overlapped on the excitation spot, as shown in Figure 19.9. The STED beam has a wavelength of  $\lambda_{\text{STED}}$  that

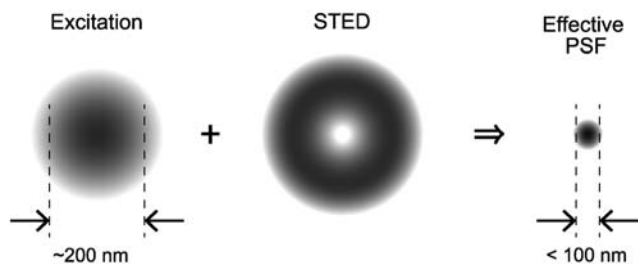


**Figure 19.9** Schematic illustration of the point spread function (PSF) of STED microscopy.

is longer than the peak wavelength of the fluorescence,  $\lambda_{\text{FL}}$ , and this induces the stimulated emission at  $\lambda_{\text{STED}}$ . Consequently, fluorescence at  $\lambda_{\text{FL}}$  is detected only from the center of the excitation spot because the outer side emits at  $\lambda_{\text{STED}}$ . Thus, the STED beam depletes the emission at  $\lambda_{\text{FL}}$  except at the very center of the illuminated spot, which results in an effective point spread function (PSF) of 10–100 nm. Figure 19.10a shows the PSFs of confocal (left) and STED microscopy (right) observed by a 40-nm fluorescent bead, indicating that the spatial resolution of STED microscopy is about 50 nm. By using STED microscopy, the phase-separation structure of a block copolymer of PS and poly(2-vinylpyridine) was studied [46]. In this case, whereas no structural features were observed in a conventional confocal microscopy image (as shown in Figure 19.10b), a micro-phase-separation structure with a periodicity of  $\sim 150$  nm was clearly resolved in Figure 19.10c–e by overlapping the STED beam.

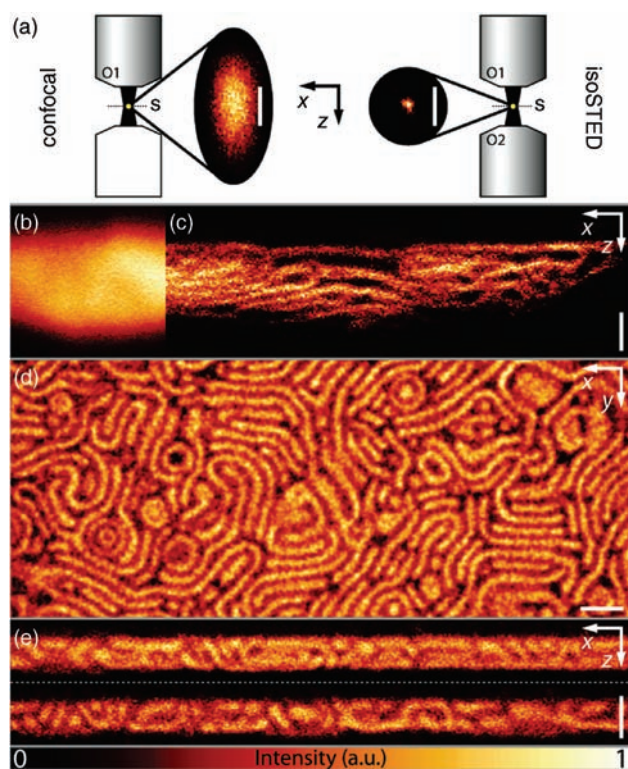


**Figure 19.10** Point spread functions in the  $xz$ -plane of confocal and STED microscopy (a) and the fluorescence images of the phase-separation structure of poly(styrene-block-2-vinylpyridine) (b–e). Panels (b) and (c) were observed using confocal and STED

microscopy, respectively. Panels (d) and (e) indicate the  $xy$ - and two  $xz$ -sections taken at different locations. Scale bars: (a) 250 nm; (c–e) 500 nm. Reprinted with permission from Ref. [46]; © 2009, American Chemical Society.

Single-molecule localization microscopy produces a high-resolution reconstruction image from the coordinate data of the dye molecules introduced to a specimen. When only a single dye molecule is observed in a fluorescence image, the coordinate of the molecule can be determined by fitting a 2D Gaussian function to the observed image. The standard deviation of the localization is given as approximately  $\sqrt{\Delta x/N}$ , where  $\Delta x$  and  $N$  are the observed width of the molecule in a micrograph and the number of the collected photons, respectively [56]. In a typical condition of single-molecule detection, the localization accuracy is of the order of tens of nanometers. Single-molecule localization microscopy can be used to isolate a single dye molecule from the dye molecules introduced to the sample, and determine its position. The measurement procedure for this is as follows. First, all of the dye molecules tagged to a sample are converted to a nonfluorescent state, after which one of the dye molecules is activated stochastically to a fluorescent state and its fluorescence image is recorded. The coordinate of the activated molecule is then analyzed, and finally the observed molecule is converted back to a nonfluorescent state. This cycle is repeated until a number of the dye molecules have been observed. In this way, the coordinates of the dye molecules are determined individually, and by plotting the coordinate data of the dye molecules on an image plane a reconstructed micrograph can be obtained. Switching between the fluorescent and dark states of the dye molecule is implemented by using photochromic dyes for the fluorescence labeling of the sample [50,51]. This technique is referred to as photoactivated localization microscopy (PALM) or stochastic optical reconstruction microscopy (STORM). The spatial resolution of the reconstruction image is determined by the localization accuracy of a single dye molecule, and therefore a resolution of  $<10$  nm can be achieved. Moreover, astigmatic imaging using a cylindrical lens and interference detection by  $4\pi$  imaging optics enhances the depth resolution to 10–100 nm [57,58]. This allows 3D fluorescence imaging with nanometric resolution, both in lateral and depth directions. Thus, super-resolution microscopy can provide spectroscopic information via fluorescence detection, with spatial resolution comparable to that of electron microscopy. Although, to date, the technique has been applied only rarely in the polymer sciences, it may in time serve as a very powerful tool for investigating the 3D structures of polymer systems.

#### 19.4.3

##### **Conformational Analysis of Single Polymer Chain**

The various properties that are characteristic of polymer materials originate from the large degree of freedom of a polymer chain. Indeed, during recent years the statistical conformation and dynamics of polymer chains have been the most important issues in polymer physics, and have been studied extensively by many research groups from both theoretical and experimental viewpoints. The development of atomic force microscopy (AFM) enabled direct observations to be made of the conformation of individual polymer chains adsorbed onto an atomically flat surface [59–62]. However, it is difficult to observe the conformation of a single chain in an actual bulk medium because

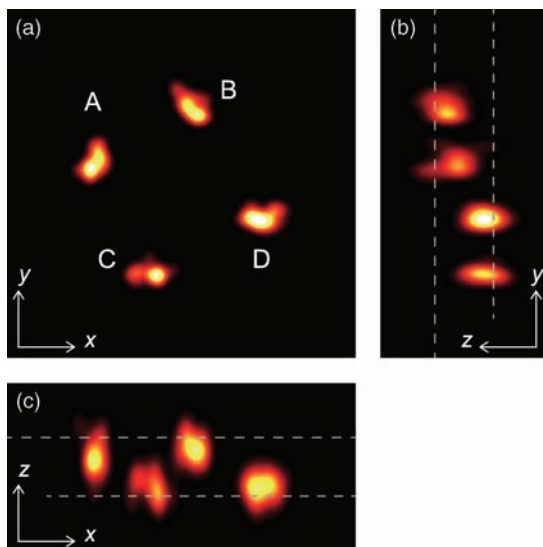


**Figure 19.11** Three-dimensional PALM measurement of single chains of poly(butyl methacrylate). (a–c) Projection images onto the  $xy$ -,  $yz$ -, and  $xz$ -planes, respectively. The dashed lines indicate the interface of the sample film.

The size of the observed volume was  $1250 \times 1250 \times 600$  nm. Reprinted with permission from Ref [64]; © 2012, Royal Society of Chemistry.

the polymer chains therein are expanded in three dimensions and entangled with each other. The great improvements in the spatial resolution of fluorescence imaging by SNOM and PALM allowed the observation of the conformation of a single polymer chain embedded in a bulk medium [63–65]. Figure 19.11 shows the PALM image of single chains of poly(butyl methacrylate) [64], where the conformation of each chain is clearly resolved in the fluorescence image. Consequently, image analysis can provide a variety of information about a single chain, such as the radius of gyration and conformational anisotropy. High-resolution fluorescence imaging can provide indispensable information not previously obtainable by other methods, and has been applied to determine conformational distribution in a phase-separation domain and a phase boundary [66–68].

## 19.5

### Summary

Fluorescence microscopy is an effective technique for studying the structure of polymer blend systems, as it not only reveals the quantitative spatial distribution of polymer components but also provides molecular information from the fluorescence spectrum and decay curve. Real-space observation in three dimensions with high time-resolution can reveal the detailed structure and formation process of the

phase-separation structure of polymer blends. Previously, the spatial resolution of conventional microscopy was limited to about 200 nm by the diffraction barrier; however, recent developments of near-field optics and super-resolution techniques have allowed optical imaging with spatial resolution of the order of tens of nanometers. Nanometric imaging of the fluorescence emission provides a variety of information that is unobtainable using currently available methods. Fluorescence microscopy is expected to contribute greatly to soft materials science as a tool for conducting nanometer-scale observations.

## References

- 1 Birks, J.B. (1970) *Photophysics of Aromatic Molecules*, Wiley-Interscience, New York.
- 2 Turro, N.J. (1991) *Modern Molecular Photochemistry*, University Science Books, Mill Valley, CA.
- 3 Webb, R.H. (1996) *Rep. Prog. Phys.*, **59**, 427.
- 4 Wilson, T. (1990) *Confocal Microscopy*, Academic Press, London.
- 5 Dibbern-Brunelli, D. and Atvars, T.D.Z. (1995) *J. Appl. Polym. Sci.*, **58**, 779.
- 6 White, W.R. and Wiltzius, P. (1995) *Phys. Rev. Lett.*, **75**, 3012.
- 7 Dibbern-Brunelli, D., Atvars, T.D.Z., Joekes, I., and Barbosa, V.C. (1998) *J. Appl. Polym. Sci.*, **69**, 645.
- 8 Nakashima, K., Winnik, M.A., Dai, K.H., Kramer, E.J., and Washiyama, J. (1992) *Macromolecules*, **25**, 6866.
- 9 Li, L., Sosnowski, S., Chaffey, C.E., Balke, S.T., and Winnik, M.A. (1994) *Langmuir*, **10**, 2495.
- 10 Aoki, H., Sakurai, Y., Ito, S., and Nakagawa, T. (1999) *J. Phys. Chem. B*, **103**, 10553.
- 11 Aoki, H. and Ito, S. (2001) *J. Phys. Chem. B*, **105**, 4558.
- 12 Aoki, H., Tanaka, S., Ito, S., and Yamamoto, M. (2000) *Macromolecules*, **33**, 9650.
- 13 Aoki, H., Takahashi, T., Tamai, Y., Sekine, R., Aoki, S., Tani, K., and Ito, S. (2009) *Polym. J.*, **41**, 778.
- 14 Tanaka, K., Tateishi, Y., Okada, Y., Nagamura, T., Doi, M., and Morita, H. (2009) *J. Phys. Chem. B*, **113**, 4571.
- 15 Jinnai, H., Nishikawa, Y., Morimoto, H., Koga, T., and Hashimoto, T. (2000) *Langmuir*, **16**, 4380.
- 16 Jinnai, H., Yoshida, H., Kimishima, K., Funaki, Y., Hirokawa, Y., Ribbe, A.E., and Hashimoto, T. (2001) *Macromolecules*, **34**, 5186.
- 17 Jinnai, H., Nishikawa, Y., Koga, T., and Hashimoto, T. (1995) *Macromolecules*, **28**, 4782.
- 18 Verhoogt, H., vanDam, J., deBoer, A., Draaijer, A., and Houpt, P. (1993) *Polymer*, **34**, 1325.
- 19 Kim, S., Hobbie, E.K., Yu, J.-W., and Han, C.C. (1997) *Macromolecules*, **30**, 8245.
- 20 Kumacheva, E., Li, L., Winnik, M.A., Shinozaki, D.M., and Cheng, P.C. (1997) *Langmuir*, **13**, 2483.
- 21 Newby, B.Z. and Composto, R.J. (2000) *Macromolecules*, **33**, 3274.
- 22 Moffitt, M., Rharbi, Y., Tong, J.-D., Farhina, J.P.S., Li, H., Winnik, M.A., and Zahalka, H. (2003) *J. Polym. Sci. B: Polym. Phys.*, **41**, 637.
- 23 Nivaggioli, T., Tsao, B., Alexandridis, P., and Hatton, T.A. (1995) *Langmuir*, **11**, 119.
- 24 Karpovich, D.S. and Blanchard, G.J. (1995) *J. Phys. Chem.*, **99**, 3951.
- 25 Zachariasse, K.A., Maçanita, A.L., and Kühnle, W. (1999) *J. Phys. Chem. B*, **103**, 9356.
- 26 Vallée, R.A.L., Cotlet, M., Hofkens, J., De Schryver, F.C., and Müllen, K. (2003) *Macromolecules*, **36**, 7752.
- 27 Mundra, M.K., Ellison, C.J., Rittigstein, P., and Torkelson, J.M. (2007) *Eur. Phys. J. Spec. Top.*, **141**, 143.
- 28 Berlman, I.B. (1973) *Energy Transfer Parameters of Aromatic Compounds*, Academic Press, London.
- 29 Bodunov, E., Berberan-Santos, M., and Martinho, J. (2002) *J. Lumin.*, **96**, 269.



- 30 Saini, S., Srinivas, G., and Bagchi, B. (2009) *J. Phys. Chem. B*, **113**, 1817.
- 31 Jiang, M., Chen, W., and Yu, T. (1991) *Polymer*, **32**, 984.
- 32 Dong, L., Hill, D.J.T., Whittaker, A.K., and Ghigginio, K.P. (1994) *Macromolecules*, **27**, 5912.
- 33 Pham, H.H., Farinha, J.P.S., and Winnik, M.A. (2000) *Macromolecules*, **33**, 5850.
- 34 Cadby, A., Dean, R., Fox, A.M., Jones, R.A. L., and Lidzey, D.G. (2005) *Nano Lett.*, **5**, 2232.
- 35 Huang, J.-H., Chien, F.-C., Chen, P., Ho, K.-C., and Chu, C.-W. (2010) *Anal. Chem.*, **82**, 1669.
- 36 Brovelli, S., Meinardi, F., Winroth, G., Fenwick, O., Sforazzini, G., Frampton, M. J., Zalewski, L., Levitt, J.A., Marinello, F., Schiavuta, P., Suhling, K., Anderson, H.L., and Cacialli, F. (2010) *Adv. Funct. Mater.*, 20272.
- 37 Pohl, D.W., Denk, W., and Lanz, M. (1984) *Appl. Phys. Lett.*, **44**, 651.
- 38 Harootunian, A., Betzig, E., Isaacson, M., and Lewis, A. (1986) *Appl. Phys. Lett.*, **49**, 674.
- 39 Paesler, M.A. and Moyer, P.J. (1996) *Near-Field Optics: Theory, Instrumentation, and Applications*, John Wiley & Sons, New York.
- 40 Ohtsu, M. (1998) *Near-field Nano/Atom Optics and Technology*, 1st edn, Springer, Tokyo.
- 41 Hell, S.W. and Wichmann, J. (1994) *Opt. Lett.*, **19**, 780.
- 42 Klar, T.A. and Hell, S.W. (1999) *Opt. Lett.*, **24**, 954.
- 43 Klar, T.A., Jakobs, S., Dyba, M., Egner, A., and Hell, S.W. (2000) *Proc. Natl Acad. Sci. USA*, **97**, 8206.
- 44 Westphal, V., Kastrup, L., and Hell, S.W. (2003) *Appl. Phys. B*, **77**, 377.
- 45 Donnert, G., Keller, J., Medda, R., Andrei, M.A., Rizzoli, S.O., Lührmann, R., Jahn, R., Eggeling, C., and Hell, S.W. (2006) *Proc. Natl Acad. Sci. USA*, **103**, 11440.
- 46 Ullal, C.K., Schmidt, R., Hell, S.W., and Egner, A. (2009) *Nano Lett.*, **9**, 2497.
- 47 Gustafsson, M.G.L. (2000) *J. Microsc.*, **198**, 82.
- 48 Gustafsson, M.G.L. (2005) *Proc. Natl Acad. Sci. USA*, **102**, 13081.
- 49 Mudry, E., Belkebir, K., Girard, J., Savatier, J., Moal, E.L., Nicoletti, C., Allain, M., and Sentenac, A. (2012) *Nat. Photonics*, **6**, 312.
- 50 Betzig, E., Patterson, G.H., Sougrat, R., Lindwasser, O.W., Olenych, S., Bonifacino, J.S., Davidson, M.W., Lippincott-Schwartz, J., and Hess, H. (2006) *Science*, **313**, 1642.
- 51 Hess, S., Girirajan, T., and Mason, M. (2006) *Biophys. J.*, **91**, 4258.
- 52 Rust, M., Bates, M., and Zhuang, X. (2006) *Nat. Methods*, **3**, 793.
- 53 Aoki, H., Kunai, Y., Ito, S., Yamada, H., and Matsushige, K. (2002) *Appl. Surf. Sci.*, **188**, 534.
- 54 Ulman, A. (1991) *An Introduction to Ultrathin Organic Films: From Langmuir-Blodgett to Self-Assembly*, Academic Press, Boston.
- 55 Embs, F., Funhoff, D., Laschewsky, A., Licht, U., Ohst, H., Prass, W., Ringsdorf, H., Wegner, G., and Wehrmann, R. (1991) *Adv. Mater.*, 325.
- 56 Thompson, R. (2002) *Biophys. J.*, **82**, 2775.
- 57 Shtengel, G., Galbraith, J., Galbraith, C., Lippincott-Schwartz, J., Gillette, J., Manley, S., Sougrat, R., Waterman, C., Kanchanawong, P., Davidson, M., Fetter, R., and Hess, H. (2009) *Proc. Natl Acad. Sci. USA*, **106**, 3125.
- 58 Mlodzianoski, M., Juette, M., Beane, G., and Bewersdorf, J. (2009) *Opt. Express*, **17**, 8264.
- 59 Sheiko, S.S. (2000) *Adv. Polym. Sci.*, **151**, 61.
- 60 Kumaki, J., Nishikawa, Y., and Hashimoto, T. (1996) *J. Am. Chem. Soc.*, **118**, 3321.
- 61 Kumaki, J., Kawauchi, T., and Yashima, E. (2006) *Macromolecules*, **39**, 1209.
- 62 Ido, S., Kimura, K., Oyabu, N., Kobayashi, K., Tsukada, M., Matsushige, K., and Yamada, H. (2013) *ACS Nano*, **7**, 1817.
- 63 Ube, T., Aoki, H., Ito, S., Horinaka, J., Takigawa, T., and Masuda, T. (2011) *Macromolecules*, **44**, 4445.
- 64 Aoki, H., Mori, K., and Ito, S. (2012) *Soft Matter*, **8**, 4390.
- 65 Ube, T., Aoki, H., Ito, S., Horinaka, J., and Takigawa, T. (2012) *Soft Matter*, **8**, 5603.
- 66 Yang, J., Sekine, R., Aoki, H., and Ito, S. (2007) *Macromolecules*, **40**, 7573.
- 67 Sekine, R., Aoki, H., and Ito, S. (2009) *J. Phys. Chem. B*, **113**, 7095.
- 68 Tamai, Y., Sekine, R., Aoki, H., and Ito, S. (2009) *Macromolecules*, **42**, 4224.

**Further Reading**

- 1 Lakowicz, J.R. (2006) *Principles of Fluorescence Spectroscopy*, Springer, New York.
- 2 Herman, B. (1998) *Fluorescence Microscopy*, BIOS Scientific Publishing, Oxford.
- 3 Gell, C., Brockwell, D., and Smith, A. (2006) *Handbook of Single Molecule Fluorescence Spectroscopy*, Oxford University Press, Oxford.
- 4 Novotny, L. and Hecht, B. (2006) *Principles of Nano-Optics*, Cambridge University Press, Cambridge.
- 5 Hell, S.W. (2007) *Science*, **316**, 1153.
- 6 Gould, T.J., Verkhusha, V.V., and Hess, S.T. (2009) *Nat. Protocols*, **4**, 291.
- 7 Patterson, G., Davidson, M., Manley, S., and Lippincott-Schwartz, J. (2010) *Annu. Rev. Phys. Chem.*, **61**, 345.

## 20

### Characterization of Polymer Blends with FTIR Spectroscopy

Ufana Riaz and Syed Marghoob Ashraf<sup>1)</sup>

#### 20.1

##### Introduction

Polymer blends are generally defined as mixtures of at least two polymers or copolymers that may be either homogeneous or heterogeneous at the molecular level. *Miscible* polymer blends show homogeneity down to the molecular level and are associated with a negative free energy of mixing, whereas *immiscible* polymer blends are heterogeneous at the molecular scale and are associated with a positive free energy of mixing. The term *compatible* is generally used to describe the beneficial results obtained by blending polymers with enhanced mechanical properties. Three different types of blend can be distinguished: completely miscible blends; partially miscible blends; and fully immiscible blends. As the gain in mixing entropy is negligible due to the high molecular weight of polymer, and the mixing is endothermic in the majority of cases, miscible polymer blends are usually an exception. In fact, few miscible blends have been identified recently. Most polymer blends form immiscible blends, revealing a prominent interface. Adhesion between the two polymer components is poor in such blends, unless they can be compatibilized. It is generally observed that most compatible blends are immiscible, and when the interface morphology of an immiscible blend is modified a polymer alloy is obtained. The first polymer blend was synthesized in 1846, when natural rubber was mixed with *gutta percha* [1], since which time innumerable polymer blends have been synthesized and investigated [2,3]. The major reason for blending polymers is economics; typically, a material can be produced at a lower cost but have the desired synergistic properties that meet the required specifications. There are three main reasons for formulating polymer blends:

- To develop materials with a full set of desired properties.
- To obtain a high performance through synergetic interaction.

1) Now retired

- To adjust the composition of the blend, as per the requirements of customer specifications that satisfies their end use.

Polymer blends exhibit good mechanical properties which are directly related to the adhesion between the constituent polymers, their interaction, and their miscibility. Interactions take place at the interface of the polymers phases to provide good adhesion; moreover, the better the miscibility, the smaller is the size of the interface. An understanding of the factors that affect the miscibility of polymer mixtures is of fundamental importance. It is also essential to have a clear understanding of the basic physical and chemical properties of the constituents associated with this large class of materials.

## 20.2

### Methods of Investigating Miscibility

Various techniques have been adopted to determine the miscibility of polymer blends, including thermal gravimetric analysis (TGA) [4], dynamic mechanical analysis (DMA)[5], small-angle X-ray scattering (SAXS) [6], microscopy [7], and solid-state nuclear magnetic resonance (NMR) [8–13]. In addition, differential scanning calorimetry (DSC) can be used to determine whether one or two glass transition ( $T_g$ ) values and a single  $T_g$  point is obtained. A single composition-dependent glass transition often indicates full miscibility, and this is an established criterion for confirming the miscibility of any polymer blend. In contrast, an immiscible polymer blend will exhibit more than one  $T_g$ -value. Variation in the  $T_g$  of polymer blends as a function of composition can be well interpreted in terms of specific interaction occurring within the polymer blend. The techniques used to analyze polymer blends are listed in Table 20.1.

#### 20.2.1

##### FTIR as a Spectroscopic Tool for the Characterization of Polymer Blends

Most polymer blends are immiscible due to a high degree of polymerization, which predicts the small combinatorial entropy, based directly from a simple Flory–Huggins description of the thermodynamics theory. In order to obtain a one-phase system in polymer blends, it is essential to ensure that favorable specific intermolecular physical or chemical interactions exist between the two base components of the blend, such as hydrogen bonding [14,15]. This type of interaction has been widely described in terms of the association model given by Coleman *et al.* [16]. The strong interactions in miscible polymer blends provide an attractive interest in polymer science due to strong technological incentives arising from their potential applications. The chemical composition and interactions between the functional groups in a polymer blend can be obtained directly by using Fourier transform infrared (FTIR) spectroscopy. The technique has been made more versatile as a characterization tool by combining it with microscopy to

**Table 20.1** Techniques of analysis of polymer blends.

Technique	Characteristics and properties
XRD/WAXRD	Morphology (amorphous/crystalline)
SEM	Surface roughness and Heterogeneous/homogeneous morphology
TEM/HRTEM	Morphology and its development Structural heterogeneities Defect structures
AFM	Crystallization behavior of polymer blends Surface roughness Morphology and microstructure
FTIR	Component identification and quantitative analysis Interfacial interactions (hydrogen bonding) Crystallization and orientation of polymer blends
NMR	Local dynamics of polymer blend chain orientation of polymer blends
SAXS	Dispersion and morphology Phase behavior and structure evolution Lamellar texture and thickness
TGA	Thermal stability
DSC	Melting and crystallization behavior
Cone calorimetry	Flame retardancy, such as heat release rate and carbon monoxide yield Thermal stability
Mechanical test	Young's modulus Tensile strength Elongation at break Viscoelastic properties

provide a deeper analysis of the local structure and the dynamics of blends under different environmental conditions [17–19]. The measurement of FTIR spectra from polymeric samples is relatively rapid and straightforward; indeed, the technique provides high-precision, accurate and reproducible measurements that are accepted for most industrial and research purposes. Nonetheless, several experimental and post-data collection techniques for specialized applications that are not amenable through other routine spectroscopic analyses have also been developed over the years.

Polarized FTIR spectroscopy has been used extensively to study polymer orientation (i.e., the dichroic ratio and dichroic difference are normally obtained from spectra recorded sequentially with the infrared radiation polarized parallel and perpendicular to a reference direction). To improve the sensitivity of this technique, and to follow accurately the dynamics of orientation, FTIR spectroscopy has been coupled with a polarization modulation (PM) technique whereby the dichroic difference spectrum is recorded directly, thus minimizing instrumental and sample fluctuations (this is discussed later in the chapter).

The development of techniques to collect FTIR spectra from small, specific regions of a sample have resulted in the development of IR microspectroscopy.

This technique demonstrates the potential in combining the spatial specificity of microscopy with the powerful chemical specificity of spectroscopy. A balance between the need for sensitive spectral information and a need for high spatial resolution visualization is also necessary for morphological characterization. Hence, infrared microspectroscopy is performed in sequence with emphasis placed on instrumentation capabilities and experimental possibilities.

### 20.2.2

#### Determination of Miscibility Through Hydrogen Bonding

In homogeneous blends, the final properties are often an arithmetic average of the properties of the blend components. In heterogeneous blends, the properties of all blend components are present, although a deficiency in the properties of one component can be hidden to a certain extent by the strengths of other components. Homogeneous miscibility in polymer blends requires a negative free energy of mixing; that is,  $\Delta G_{\text{mix}}$  (the change in free energy)  $< 0$  as per the Flory–Huggins equation.  $\Delta G_{\text{mix}}$  can be negative only if the heat of mixing is near zero or negative ( $\chi_{12}$ , the interaction parameter  $< 0.002$ ). The formation of hydrogen bonds usually induces miscibility of the blends, as shown for many hydrogen-bonded blends. Blends are found to be either partially or fully miscible due to the presence of inter-associated hydrogen bonds. In an effort to address the relationship between hydrogen bonding and miscibility, the details of several types of important hydrogen-bonded polymer blends are summarized in the following sections.

## 20.3

### Characterization of Vinyl Polymer Blends using FTIR Spectroscopy

#### 20.3.1

##### Poly(vinylphenol) (PVPh) Blends

PVPh blends are the most widely studied hydrogen-bonded blends. Landry *et al.* [20] reported blends of PVPh with potential hydrogen bond-accepting groups, including polyesters (aliphatic and aromatic), polycarbonates, polyimides, polyamides, polysulfones, polyurethanes, polyethers, polysiloxanes, poly(amideimides), and cellulose esters. Many of the polyesters, polyamides and cellulose esters showed evidence of interaction and miscibility with PVPh; however, in most of the other cases there were no signs of miscibility and indeed, the miscibility was seen to depend not only on the tacticity of the polymer but also on the preparation conditions. Zhang *et al.* [21] established the relationship between hydrogen bonding and the miscibility of PVPh/poly(methylmethacrylate) (PMMA) blends by using solid-state  $^{13}\text{C}$  NMR. A variety of parameters such as  $^{13}\text{C}$  chemical shifts and  $^{13}\text{C}$  line width were used to examine the intermolecular interaction, miscibility, dominant structure and molecular motion of the PVPh/PMMA blends. The blends were found to be soluble in the domain size of 200–300, and the presence

of an  $\alpha$ -methyl group was seen to affect the miscibility. Dong *et al.* [22], using FTIR and FT-Raman spectroscopy, established the formation of hydrogen bonds between the hydroxyl group of PVPh and the ester group of PMMA, and showed the blends to be partially miscible as they demonstrated weak hydrogen-bonding interactions. Landry and Teegarden [20] investigated the effect of solvent on the miscibility of blends of PVPh with atactic PMMA (aPMMA), and revealed that tetrahydrofuran (THF) induced a phase separation of such blends, whereas 2-butanone promoted their miscibility. The heat of mixing of polymer blends was also reported to play an important role in developing miscibility [23].

Hsu *et al.* [24] investigated the miscibility of PVPh/PMMA blends as a function of the PMMA tacticity [i.e., isotactic PMMA (iPMMA), syndiotactic PMMA (sPMMA) and atactic PMMA (aPMMA)]. In this study, the PMMA polymers with various tacticities were mixed with PVPh using THF and 2-butanone as a solvent to obtain solution blends. When the blends were cast from a THF/2-butanone solution, the calorimetric data indicated that iPMMA was miscible with PVPh, but only partial miscibility/immiscibility was observed with both aPMMA and sPMMA. When pure 2-butanone was used as the solvent, iPMMA and aPMMA were both miscible with PVPh, but the PVPh/sPMMA blends showed only partial miscibility. Whereas, pure THF led to a phase separation of aPMMA and PVPh, 2-butanone produced miscible blends. The  $T_g$  data of these blends were found to be in good agreement with the results of NMR studies. It was also reported that, on increasing the VPh content of the copolymer to 15 mol%, the tacticity of PMMA had no effect on controlling the overall miscibility of the blend system [25,26].

Some groups have also studied the effects on the miscibility of the blends by replacing VPh with styrenated VPh (STVPh). For example, when Jong *et al.* [25] investigated the miscibility of these blends using  $^{13}\text{C}$  solid-state NMR, sPMMA was reported to be miscible with STVPh (the VPh monomer unit content was 5%) in blend compositions containing 30%, 50% and 70% STVPh, whereas iPMMA exhibited miscibility at only 70% STVPh composition. PVPh has also been reported to be miscible with poly(ethyl methacrylate), poly(*n*-propyl methacrylate) and poly(*n*-butyl methacrylate) over the entire blend composition range at temperatures between ambient and 200 °C [27]. PVPh was observed to be immiscible with poly(*n*-hexyl methacrylate) and poly(cyclohexyl methacrylate), however, as the presence of bulky groups inhibited the formation of strong inter-associated hydrogen bonds [28,29]. Many PMMA derivatives have shown miscibility with PVPh, including poly(2-dimethylamino ethyl methacrylate) [30], poly(*N*-methyl-3-piperidinemethyl methacrylate) [31], poly(methyl thiomethyl methacrylate) [32], and poly(2-ethoxyethyl methacrylate) [33]. Polyesters such as poly(3-hydroxyvalerate) (PHV) [34], poly(ethylene succinate), poly(ethylene adipate), poly(butylene adipate) [35] and poly(propylene carbonate) [36] have also shown miscibility with many VPh copolymers. However, phase separation has been observed for blends of PVPh/poly(L-lactide) (PLLA) [37] and PVPh/poly(D,L-lactide) (PDLLA) [38]. Only weak hydrogen-bonding interactions exist between the carbonyl groups of PLLA (or PDLLA) and the hydroxyl groups of PVPh, as concluded from FTIR spectra.

Papageorgiou *et al.* [39] studied poly(ethylene sebacate) (PESeb)/PVPh blends with respect to the miscibility and solidification from the melt state. When the interactions were analyzed using FTIR, absorbance of the carbonyl component of the ester groups of PEsEb was observed at about  $1740\text{ cm}^{-1}$ , while absorbance of the carboxylic group was recorded at  $1710\text{ cm}^{-1}$ . A small shoulder was observed at about  $1730\text{ cm}^{-1}$ , but the peak of the COOH group absorbance was obtained in blends with larger amounts of PVPh (see Figure 20.1a). These results indicated that hydrogen-bonding interactions were present between the ester carbonyl groups as well as the carboxyl end groups of PEsEb and the OH groups of PVPh.

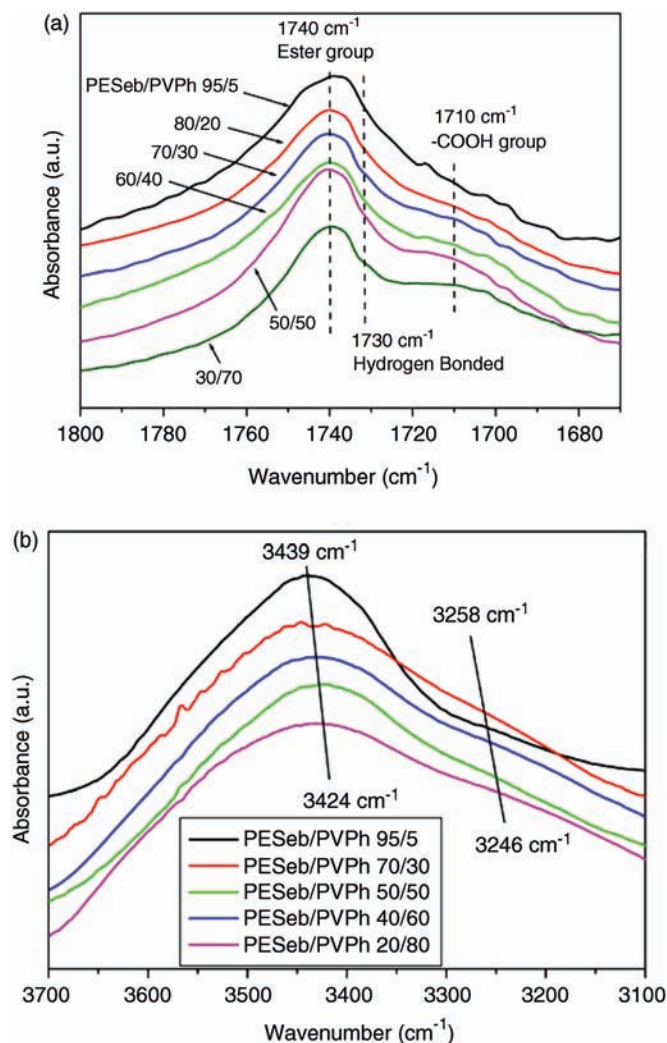


**Figure 20.1** FTIR spectra of the blends. (a) The carbonyl absorbance region; (b) The hydroxyl group absorbance region. Reprinted with permission from Ref. [39]; © 2011, Elsevier.



The characteristic absorbencies of PVPh in the hydroxyl group region were also investigated, and a peak was noted at about  $3424\text{ cm}^{-1}$ , along with a shoulder at  $3246\text{ cm}^{-1}$  which correlated to the OH group (Figure 20.1b). These peaks were found to shift to progressively higher wavenumbers when mixed with PESeb, indicating a change in the chemical environment of the OH groups upon the addition of PESeb. Miscibility between PVPh and polyesters of a similar nature to PESeb, such as poly(hydroxybutyrate) and poly( $\epsilon$ -caprolactone) (PCL), have also been reported. Hydrogen-bonding was confirmed by FTIR in these systems [40,41].

Brisson *et al.* [42] investigated the effect of backbone chain rigidity on the orientation of PVPh/polyethylene terephthalate (PET) blends [43,44]. Experimental investigations using FTIR dichroism were coupled to molecular modeling simulations of the deformation process to gain insights about the orientation of a polymer blend for which the two components differed in chain rigidity. PET also exhibited vibrations related to *gauche* conformers or to aromatic rings; however, these overlapped too severely with PVPh (Figure 20.2). The orientation was calculated for the overall chain by determining the angle between a specific vibration of the repeat unit and the chain axis; this was then averaged over all of the repeat units. In the case of PET, the orientation was reported for *gauche* and *trans* segments of the glycol moiety, and for aromatic cycles; the *trans* segments oriented more than *gauche* segments. A similar trend was seen in the blend although, due to vibrational overlap, they could not be adequately resolved. PVPh/PET blends with PVPh contents greater than 60 mass% surprisingly showed orientation values of zero (within experimental error) for both components. These results were in contrast to those reported for other PVPh-based blends [45,46], but were further verified using birefringence and specular reflection measurements. When the

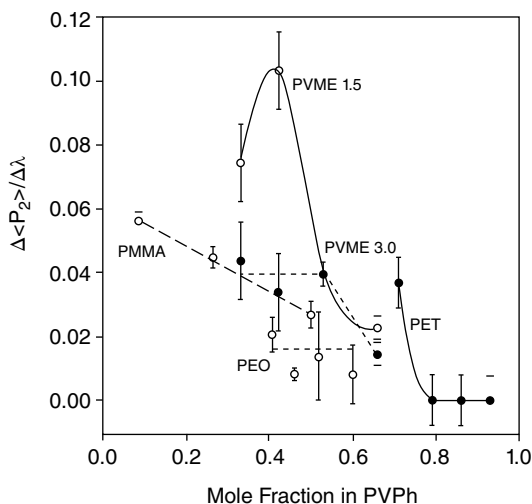


**Figure 20.2** Variation of  $P_2/\Delta\lambda$  with composition for various PVPh-based blends. ●, PEO  $\lambda = 1.5$ ; ○, PEO  $\lambda = 3.0$ ; □, PVME  $\lambda = 1.5$ ; ■, PVME  $\lambda = 3.0$ ; ▲, PET; ◇, PMMA. Reprinted with permission from Ref. [42]; © 2003, Elsevier.

PVPh content was 60 mass%, orientation was clearly detectable and varied linearly for both components of the blend. This was in contrast to the PVPh orientation in blends with polyethylene oxide (PEO) and with polyvinylmethylether (PVME), which was attributed tentatively to a change in the relaxation regime.

### 20.3.2

#### Poly(vinylpyrrolidone) (PVP) Blends

The thermal properties and hydrogen-bonding behavior of polybenzoxazine (PBZZ)/PVP blends were studied by Chang *et al.* [47], using DSC and FTIR. The pure PVP showed a carbonyl absorption peak at  $1680\text{ cm}^{-1}$  [48] (Figure 20.3), but on adding PBZZ into the PVP system the carbonyl stretching frequency was split into two bands at  $1680\text{ cm}^{-1}$  and  $1660\text{ cm}^{-1}$ , corresponding to the free and the

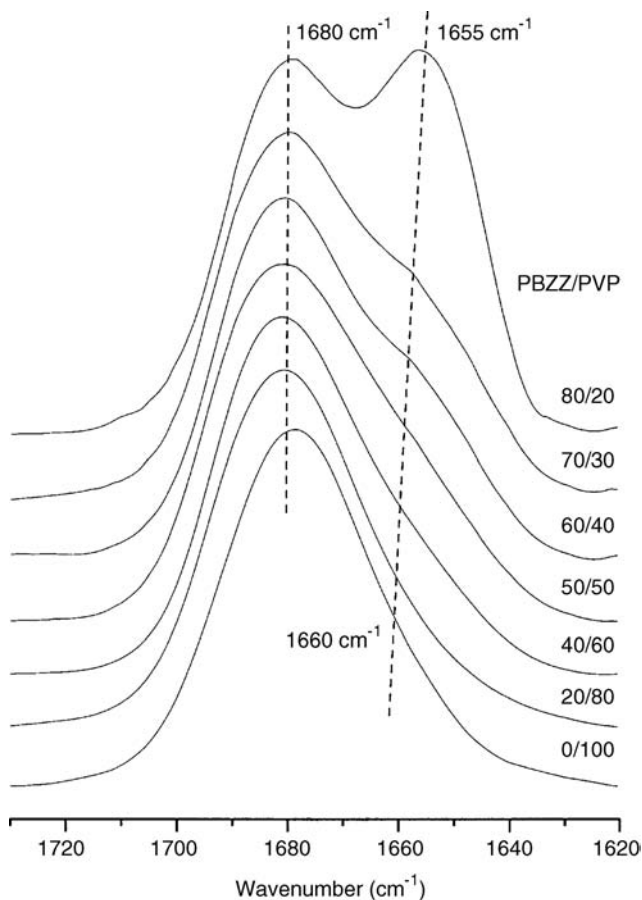


**Figure 20.3** FTIR spectra of (PBZZ)/PVP blends recorded at room temperature between  $1620$  and  $1730\text{ cm}^{-1}$ . Reprinted with permission from Ref. [47]; © 2003, Elsevier.

hydrogen-bonded carbonyl groups, respectively. This free carbonyl band at  $1680\text{ cm}^{-1}$  shifted into the hydrogen-bonded carbonyl band at  $1655\text{ cm}^{-1}$  with increasing PBZZ content in the blend. These two carbonyl bands were also fitted to the Gaussian function and the fraction of the hydrogen-bonded carbonyl group was calculated. Chang and colleagues also studied blends of PVPh with poly(vinylpyrrolidone) (PVP) prepared by solution casting from a *N,N*-dimethylformamide (DMF) solution. The intermolecular interaction between two polymers was detected with FTIR, and the hydroxyl stretching range in the infrared spectrum was found to be sensitive to hydrogen bond formation (Figure 20.4). A temperature of  $150^\circ\text{C}$  was chosen to record the experimental data as this temperature was above the  $T_g$  of both components. Pure PVPh showed a broad band centered at  $3420\text{ cm}^{-1}$  and a shoulder at  $3525\text{ cm}^{-1}$ , corresponding to the multimer hydrogen-bonded hydroxyl group and free hydroxyl group, respectively.

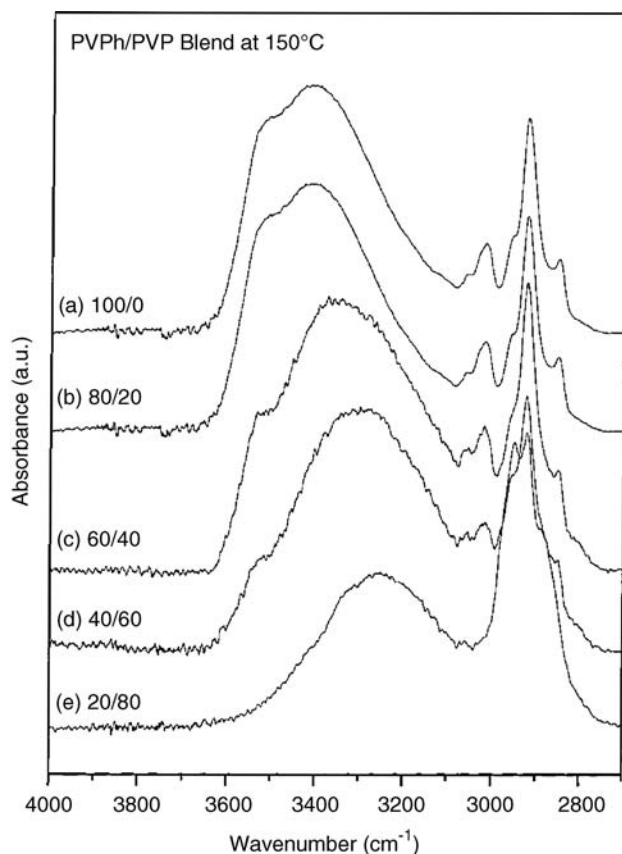


**Figure 20.4** FTIR spectra recorded at  $150^\circ\text{C}$  in the  $2700\text{--}4000\text{ cm}^{-1}$  region for pure PVPh and various PVPh/PVP blends. (a) 100/0; (b) 80/20; (c) 60/40; (d) 40/60; (e) 20/80. Reprinted with permission from Ref. [49]; © 2001, American Chemical Society.

The peak frequency of this broad band shifted to lower wavenumbers with increasing PVP content. The intensity of the free hydroxyl group also revealed a decrease with an increase in the PVP content. Moreover, a new distribution of hydrogen-bond formation resulted from competition between hydroxyl–hydroxyl and hydroxyl–carbonyl interactions. The latter interaction predominated in PVP-rich blends, and was therefore assigned the band at  $3250\text{ cm}^{-1}$  related to hydroxyl group bonded to the carbonyl group. Coleman *et al.* [50] used the frequency difference ( $\Delta\nu$ ) between the hydrogen-bonded hydroxyl absorption and free hydroxyl absorption to investigate the average strength of the intermolecular interaction. The hydroxyl–carbonyl interassociation ( $\Delta\nu = 275\text{ cm}^{-1}$ ) was found to be stronger than the hydroxyl–hydroxyl self-association ( $\Delta\nu = 105\text{ cm}^{-1}$ ). The FTIR spectra of the carbonyl stretching, recorded at  $150^\circ\text{C}$ , ranged from  $1620$  to  $1720\text{ cm}^{-1}$  for blends with various compositions (Figure 20.5), and showed that the carbonyl stretching frequency was split into two bands at  $1680\text{ cm}^{-1}$  and  $1660\text{ cm}^{-1}$ ,

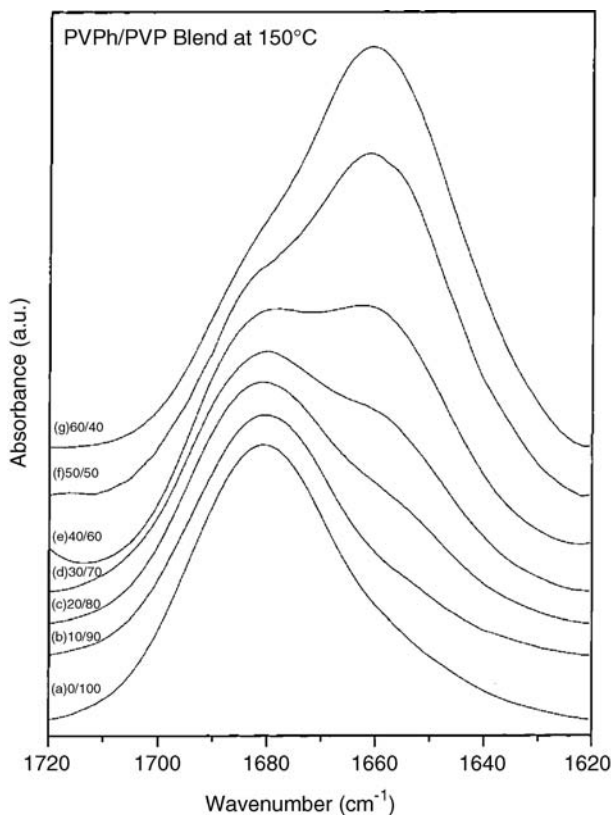


**Figure 20.5** FTIR spectra recorded at  $150^\circ\text{C}$  in the  $1620$ – $1720\text{ cm}^{-1}$  region for PVPh/PVP blends. (a) 0/100; (b) 10/90; (c) 20/80; (d) 30/70; (e) 40/60; (f) 50/50; (g) 60/40. Reprinted with permission from Ref. [49]; © 2001, American Chemical Society.

corresponding to the free and the hydrogen-bonded carbonyl groups. The results were summarized using curve fitting, and indicated that the hydrogen-bonded fraction of the carbonyl group increased with an increase in the PVPh content. The results obtained from FTIR spectroscopy studies at 150 °C in the amorphous state were in complete agreement with those of a miscible blend system. It was also concluded that, with an increase in temperature, miscibility was enhanced as PVP showed a strong transition dipole coupling between neighboring molecules or polymer segments. Labuschagne *et al.* [51] investigated the degree of homogeneity and hydrogen bond interactions in blends of low-molecular-mass poly(ethylene glycol)s (PEGs,  $M_w = 400, 600, \text{ and } 1000$ ) and PVP ( $M_w = 9 \times 10^3$ ) prepared in supercritical  $\text{CO}_2$  (blend<sub>CO<sub>2</sub></sub>) and ethanol (blend<sub>eth</sub>), as well as their (blend<sub>phy</sub>) physical mixtures. Figure 20.6 shows the spectra of the various PEG–PVP blends in the region of  $1760 \text{ cm}^{-1}$  to  $1560 \text{ cm}^{-1}$ . The bands showed significant differences, which were further analyzed by the second-derivative spectra. The (C=O) band was constituted by a multitude of smaller bands that were assigned as carbonyl-unassociated groups ( $>1680 \text{ cm}^{-1}$ ), carbonyl groups bound by PVP–PVP dipole interactions or weakly hydrogen-bonded to another species (ca.  $1679\text{--}1665 \text{ cm}^{-1}$ ), and carbonyl groups that were strongly hydrogen-bonded to another species ( $<1664 \text{ cm}^{-1}$ ) [52–58]. Figure 20.7 shows bands at 1694, 1678, 1669, 1661 and  $1655 \text{ cm}^{-1}$  in the dried PVP. Upon exposure to atmospheric moisture, the intensity of the band at  $1655 \text{ cm}^{-1}$  was increased and shifted to  $1650 \text{ cm}^{-1}$ . In the PEG–PVP blends, strong bands were seen at 1681, 1657 and  $1651 \text{ cm}^{-1}$ . The second-derivate spectra of (PEG-1000–PVP) (Figure 20.6a) showed clear differences between the different preparation methods. A closer examination of Figure 20.6a showed the greatest intensity of the  $1651 \text{ cm}^{-1}$  band in the blend taken as an indication of greater hydrogen-bonding interactions between PEG and PVP. By reducing the molar mass of the PEG component, variations in hydrogen-bonding interaction behavior between the various processing methods became smaller due to the increased diffusion coefficients found with the decreasing  $M_w$  of PEG. The highest variations in hydrogen-bonding were noted for blends containing PEG-1000. Both, blend<sub>phy</sub> and blend<sub>CO<sub>2</sub></sub> revealed reductions in hydrogen-bonding interactions as compared to blend<sub>eth</sub>. The discrepancy in the level of hydrogen-bonding interaction between the blends was correlated to shielding effects of  $\text{CO}_2$  molecules and the time dependence for PEG–PVP hydrogen-bond interactions to reach equilibrium. Due to favorable Lewis acid–base interaction between  $\text{CO}_2$  and the electron-donating ether and carbonyl groups of PEG and PVP, respectively, increased  $\text{CO}_2$  pressure caused an increased sorption of  $\text{CO}_2$  molecules into the polymers [59–62]. The increase in chain mobility showed enhanced diffusion coefficients, followed by polymer inter-diffusion [62]. However,  $\text{CO}_2$  molecules interacting with PVP carbonyl groups reduced the hydrogen-bond interaction between PEG and PVP molecules (Figure 20.7). Thus, while  $\text{CO}_2$  dissolution into the blend enhances PEG–PVP inter-dispersion, hydrogen-bond interaction was not favored. With PEG-1000 being solid, no self-diffusion occurred; however, FTIR spectroscopic analysis demonstrated the presence of some hydrogen-bond interactions between PEG-1000 and PVP.

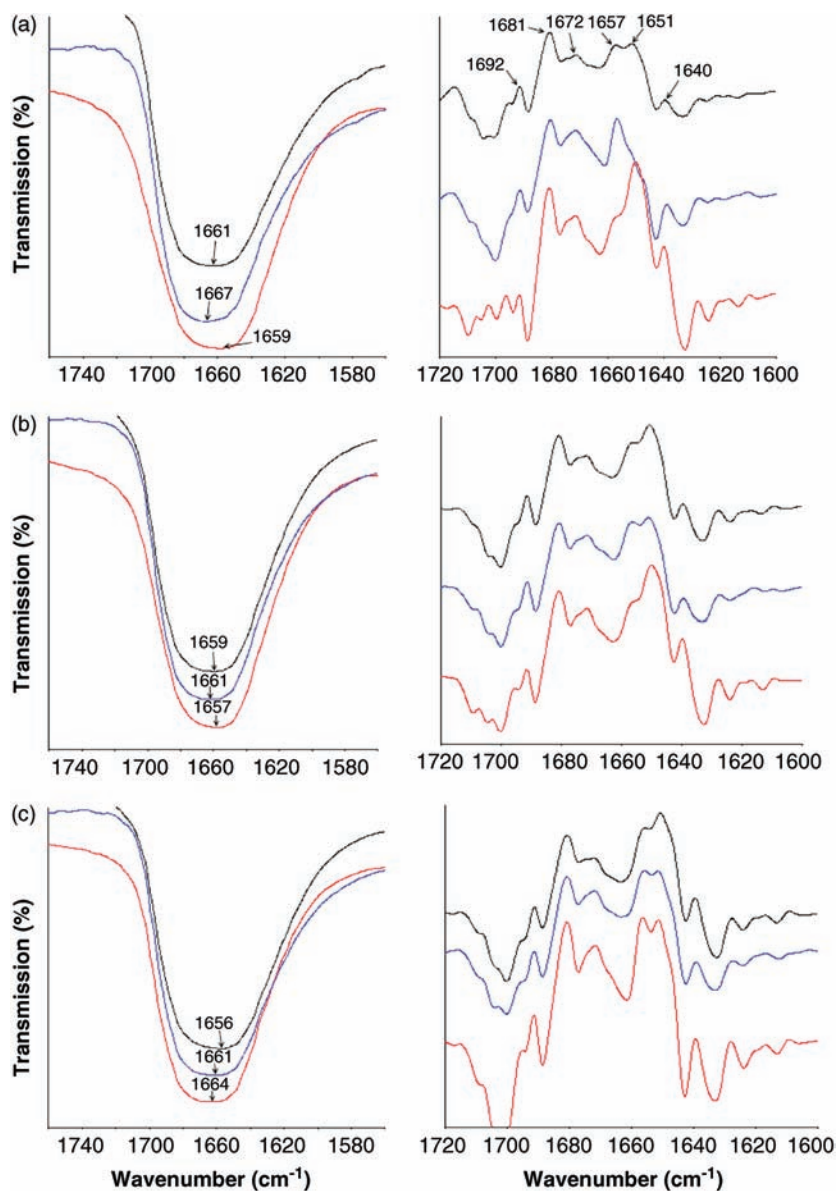


**Figure 20.6** Transmission IR spectra with corresponding second derivative spectra of the C=O region of PVP blends with PEG-1000 (a), PEG-600 (b) and PEG-400 (c) prepared by:

physical mixing (—);  $\text{scCO}_2$ -processing (—); and solvent casting (—). Reprinted with permission from Ref. [51]; © 2010, Elsevier.

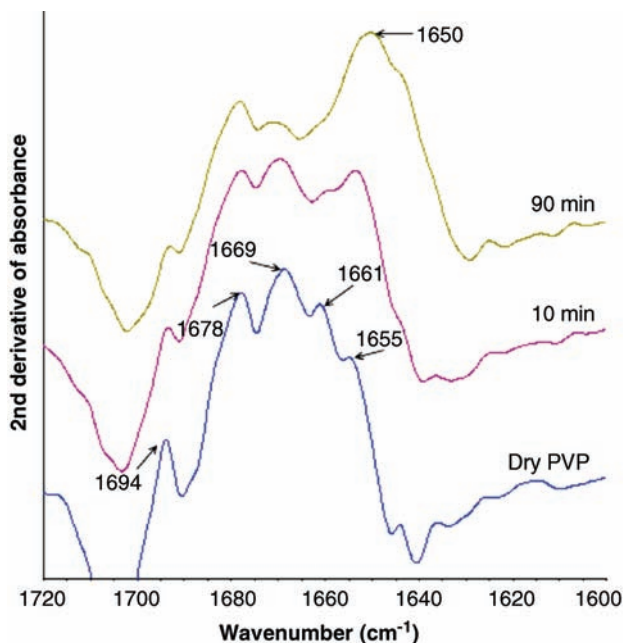


**Figure 20.7** Second-derivative FTIR profiles of the carbonyl band of PVP exposed to atmospheric humidity over a period of 90 min. Reprinted with permission from Ref. [51]; © 2010, Elsevier.

### 20.3.3

#### Poly(vinyl alcohol) (PVA) Blends

Strong hydrogen bonds between PVA and phenolic [63], PVP [64], poly(aspartic acid) sodium [65], hydroxypropyl lignin [66], poly(*N,N*-dimethylacrylamide) [67,68] have been detected with FTIR and other techniques. As a result, these PVA blends are miscible over a wide composition range. Methyl cellulose/PVA [69],  $\beta$ -chitin/PVA [70], PVAc/PVA blends [71], PLA/PVA [72], kraft lignin [73], and PVPy [74,75] are reported to be immiscible. Katime *et al.* [76,77] reported blends of PVA and PEO with relatively high molecular weight ( $M_n$  50 000) prepared by casting from water at 120 °C. FTIR analysis of the blends revealed the existence of specific interactions via hydrogen bonding between hydroxyl groups and the nitrogen of the pyridinic ring, which appeared to be decisive for miscibility. However, Aoi *et al.* [78] noted that PVA was miscible with a low-molecular-weight PEO ( $M_n$  10 300), which suggested that the molecular weight of PEO affected the miscibility. The incorporation of a second comonomer unit (e.g., vinyl acetate or ethylene) into the main chain of PVA limits the formation of self-association hydrogen bonds, and thus enhances the miscibility with many polymers. Lasagabaster *et al.* [79] investigated the use of FTIR spectroscopy to assess the sorption and diffusion process of water through polypropylene (PP)/ethylene alcohol vinyl (EVOH) blends with increasing EVOH content. In addition, they characterized the water–

polymer interactions in order to understand the mechanism of water hydration and its possible effects on physical and transport properties. Water molecules sorbed into the PP/EVOH films were identified in the vibrational spectrum by means of an increase in absorbance, compared to the dry polymer, at specific regions. The vibrations responsible for these changes can be seen in Figure 20.8. The fundamental stretching (OH) vibrations were between  $3700\text{ cm}^{-1}$  and  $3000\text{ cm}^{-1}$ ; the  $2150\text{ cm}^{-1}$  band was assigned to vibrations from the scission and rocking of water; the water OH in-plane bending vibration was observed at  $1652\text{ cm}^{-1}$ , and the  $700\text{ cm}^{-1}$  band arose from the out-of-plane vibrations of OH groups. The OH stretching vibration was divided into two peaks. The peak in the higher-frequency region (ca.  $3520\text{--}3530\text{ cm}^{-1}$ ) was assigned to unassociated water, dimers and loosely bound water, while the peak in the lower-frequency region was associated with water bound by strong hydrogen bonds to the polar groups of the polymer. Sorption curves were also plotted as a percent absorbance gain of the water bending band (OH) versus the square-root of time for PP/EVOH films of increasing EVOH content at a water activity ( $a_w$ ) of 0.998. Appropriate saturated salt slushes were used to provide constant  $a_w$ -values ranging from 0.26 to 0.98, in accordance with standard UNE-EN ISO 483:1988. An ideal behavior is assumed, whence activity is evaluated as the ratio between the pressure of the pure vapor  $[p]$  and the water vapor pressure at  $25\text{ }^\circ\text{C}$   $[p^0]$ ; that is,  $a_w = p/p^0$ .

The diffusion of water in thin layer films of thickness  $L$  is assumed to follow Fick's second law. A widely used approximation is that at short times (up to  $M_t/M_\infty = 0.5$ ), the amount of substance diffused is proportional to  $t^n$  and is given by:

$$M_t/M_\infty = 4/L(Dt/\pi)^n. \quad (20.1)$$

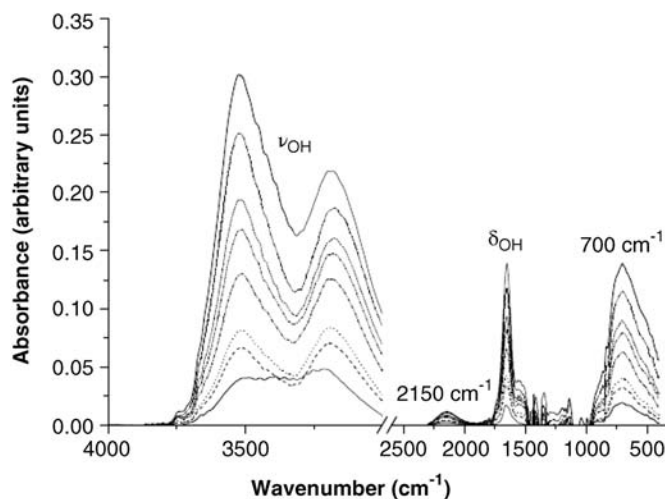


**Figure 20.8** Subtraction of FTIR spectra collected at different sorption times in the case of water vapor sorption test 70/30 PP/PE/EVOH film. Reprinted with permission from Ref. [79]; © 2009, Elsevier.



The FTIR technique does not give the mass of diffusant directly at a given depth, but provides absorbance ( $A_t$  and  $A_\infty$ ) data, which are proportional to the instantaneous mass of the diffusant ( $M_t$  and  $M_\infty$ , respectively) by the Beer–Lambert law, so that Eq. (20.1) may be written as:  $A_t/A_\infty = 4/L(Dt/\pi)^n$ . The value of the exponent  $n$  depends on the mode of sorption, and the sorption results are fitted to a relation of the type:  $A_t/A_\infty = Kt^n$ . If the exponent  $n = 0.5$ , the diffusion is termed as Fickian. The  $n$ -values for the four water bands were approximately 0.5 and independent of the EVOH content and water activity, while the diffusion coefficient ( $D$ ) was assumed to be independent of the concentration of the penetrant (Figure 20.9). The  $D$ -values diminished linearly from 10% to 30% EVOH. The  $D$ -values of the  $3190\text{ cm}^{-1}$  peak were approximately twice the values of the higher frequency band in the four compositions studied. Moreover, the  $D$ -values of the latter were in agreement with those of the other water bands, supporting the idea that the global diffusion process at high water activity was governed by the diffusion of loosely bound water, and that the different types of water were absorbed at different rates. The bending band  $D$ -values for PP/EVOH 90/10 mass% and 70/30 films as a function of water activity are represented in Figure 20.10a. For PP/EVOH 90/10 films,  $D$  was decreased exponentially with water activity, reaching a constant value at  $a_w = 0.82$  ( $r^2 = 0.998$ ). The same trend was observed for the 70/30 films, but the transition occurred at a lower water activity ( $a_w = 0.55\text{--}0.68$ ;  $r^2 = 0.990$ ). Moreover, the 70/30 films displayed significantly lower  $D$ -values than the 90/10 blends over the whole activity range, due to the strong localized interactions that developed between the water molecules and the polar groups in the polymer. The decrease in  $D$ -values with water activity is a consequence of the “sticking” of the first water molecules at the OH groups of the EVOH, thus

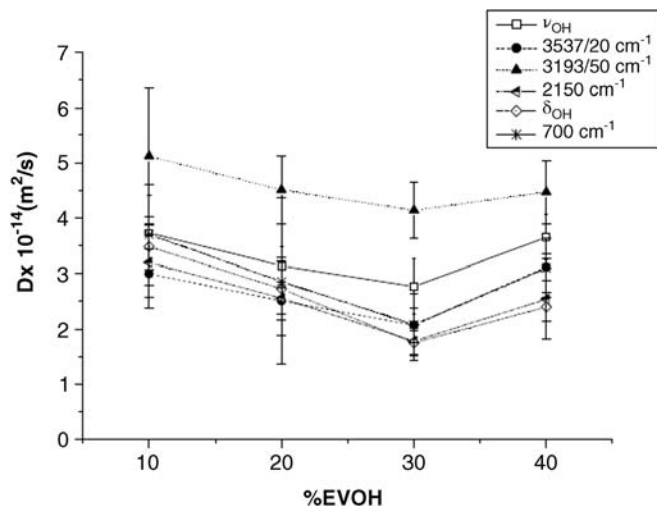


**Figure 20.9** Diffusion coefficients for water vapor at 25 °C and 0.98 water activity in PP/EVOH films as a function of EVOH content. Reprinted with permission from Ref. [79]; © 2009, Elsevier.

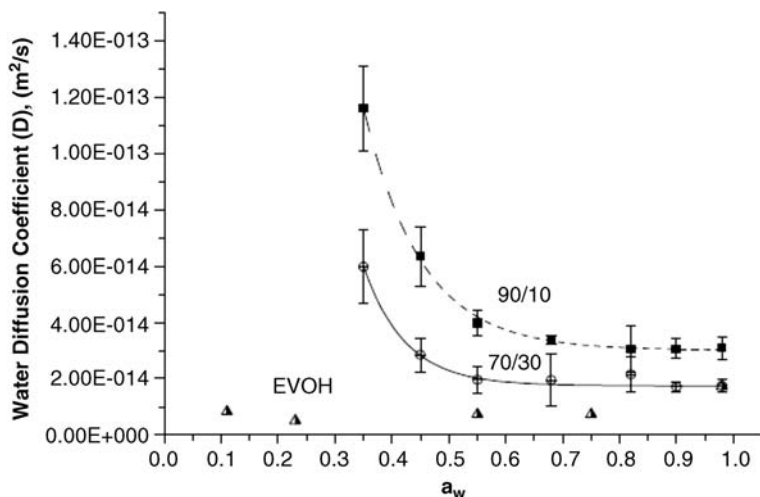


**Figure 20.10** Bending band diffusion coefficients of PP/EVOH 90/10 and 70/30 films compared with those found in literature for pure EVOH. Reprinted with permission from Ref. [79]; © 2009, Elsevier.

forming the first hydration layer, and further aggregation in small clusters around these sites to constitute the effective hydration region. The observed plasticization in the 90/10 and 70/30 blend films was found to be too small to affect diffusion, as the coefficients reach a minimum at the high activity range. The higher number of interacting sites and the greater cluster sizes contribute to further reductions of the effective diffusivity on increasing EVOH content from 10% to 30% at  $a_w = 0.98$ . The consequences reveal lower  $D$ -values and a greater dependence on water concentration; this factor alone failed to explain the different behavior of the 40% EVOH sample (Figure 20.10). A contribution to this observation could come from a higher degree of plasticization, but this was not detected with FTIR. Hence, the effect was attributed to the greater void space around the EVOH spheres, which made the plasticized interface a preferential pathway for moisture diffusion. With regards to pure EVOH, the  $D$ -values were at least one order of magnitude smaller with respect to the 70/30 PP/EVOH blends at low water activities. The reasons for this were the faster free volume blocking, due to the superior number of hydrophilic sites, and the differences in initial free volume owing to the high inter- and intrachain self-association in EVOH copolymers. The  $D$  data appeared to be the lowest not at 0.11 but at 0.23 water activity (Figure 20.10a). The  $D$ -values were found to be superimposable with those of the 70/30 blends at very high water activities, due to the well-known plasticization process by EVOH copolymers in this regime of water activity.

Sankar *et al.* [80] used FTIR spectroscopy to study the intermolecular interactions of blends of Gellan and PVA prepared by the solution casting method. The films were prepared from a total polymer mass of 2 g by casting homopolymer

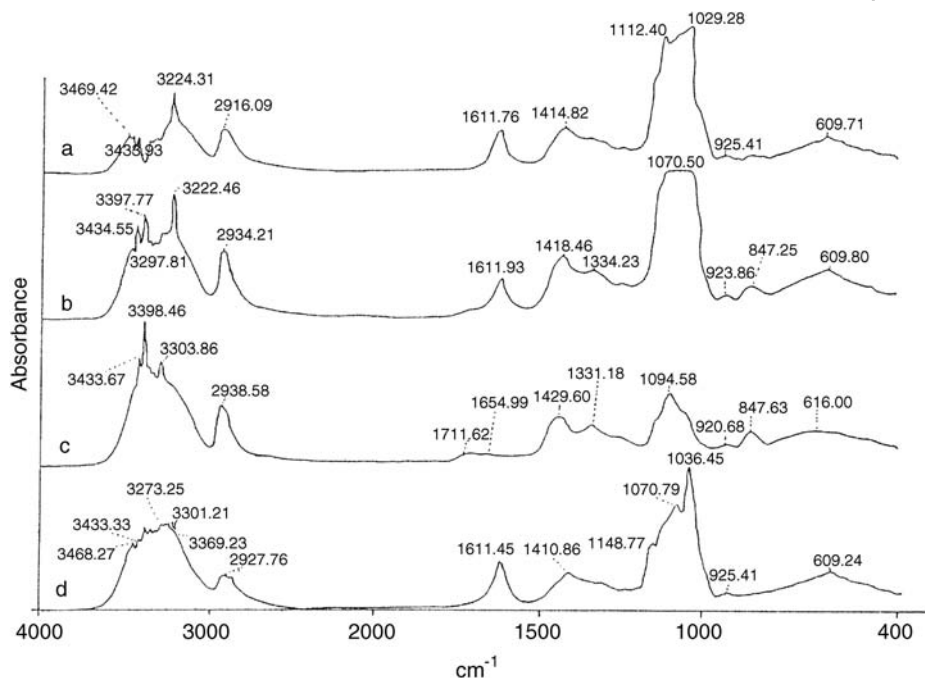


**Figure 20.11** FTIR spectra of Gellan/PVA blends. Spectrum a: subtraction spectra of Gellan and PVA blend D (3:2) from pure PVA; Spectrum b: blend Gellan and PVA, D (3:2);

Spectrum c: pure PVA (B); Spectrum d: pure Gellan (A). Reprinted with permission from Ref. [80]; © 2003, Elsevier.

solutions of Gellan (A) and PVA (B), mixed solutions of Gellan and PVA in the weight ratios as follows: 3:1 (C), 3:2 (D), 1:1 (E), 2:3 (F), and 1:3 (G). Figure 20.11 shows the infrared spectra each of the pure Gellan and the pure PVA components, and the blend and the subtracted spectrum of the blend from pure PVA. The scale factor of the subtraction was chosen so that the  $847\text{ cm}^{-1}$  band of PVA, which was the only absorption band without any superimposition of those due to gellan, was smoothly canceled out. The spectrum of the blend was seen to be similar to that of pure PVA (Figure 20.11, spectrum c), but subtraction of the bands contributed by PVA gave a spectrum similar to that of gellan (, spectrum d). The detailed characteristics of gellan in the range  $1800\text{--}400\text{ cm}^{-1}$  in spectrum d of Figure 20.11 was reproduced in the subtraction spectra (Figure 20.11, spectrum a). This important feature of the subtraction spectrum did not change from one blend sample to the other, except for the difference in band intensities due to the increasing amount of PVA in the blend. Differences in the subtraction spectrum (Figure 20.11, spectrum a), spectrum b and spectrum d were seen to arise from intermolecular interactions between PVA and the gellan in the blend.

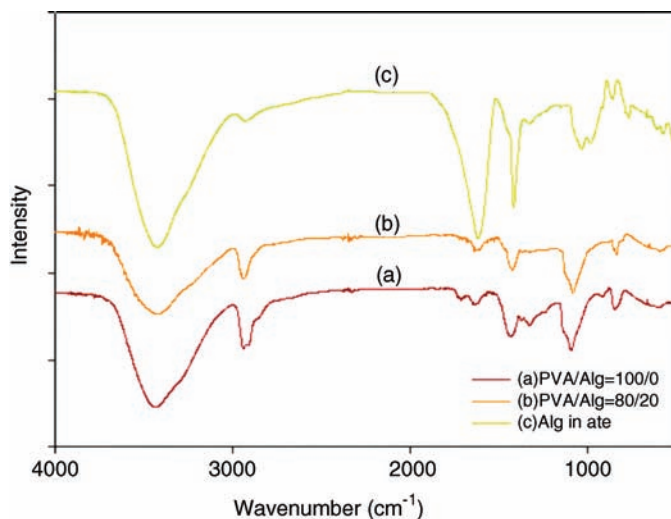


**Figure 20.12** FTIR data of electrospun PVA/Alg blend nanofibers with volume ratios of 10 wt% of PVA to 2 wt% of Alg solutions of (a) 100/0, (b) 80/20 and (c) bulk alginate. Reprinted with permission from Ref. [81]; © 2010, Elsevier.

Karim *et al.* [81] studied Alginate (Alg), blended with PVA, to enhance the mobility of polymer chains during the electrospinning process and to increase the onset temperature of degradation and the thermal stability of PVA at 350 °C. The mechanical properties of the blend nanofibers were improved compared to pure electrospun PVA with the addition of Alg. Figure 20.12 shows the FTIR spectra of electrospun PVA, Alg and PVA/Alg blend nanofibers of different volume ratios of 10 wt% of PVA to 2 wt% Alg solutions of (a) 100/0, (b) 80/20 and (c) bulk alginate. The frequencies and assignments for the pure PVA were 2944  $\text{cm}^{-1}$  for the  $\text{CH}_2$  group stretching vibration, 1096  $\text{cm}^{-1}$  for the C—O group, and 3435  $\text{cm}^{-1}$  for the stretching vibration peak of its side hydroxyl groups. For the pure Alg (spectrum a in Figure 20.12), the band for the hydroxyl groups appeared at 3430  $\text{cm}^{-1}$ . The bands appearing in the region of 3400  $\text{cm}^{-1}$  were assigned to all types of hydrogen-bonded OH groups. The bands at 1615 and 1417  $\text{cm}^{-1}$  belonged to the asymmetric and symmetric —COO— stretching vibrations, respectively. With the addition of Alg (spectrum c in Figure 20.12), the intensities of the absorption peaks of PVA at 849, 1096, 1336, 1440 and 2944  $\text{cm}^{-1}$  were decreased, and some peaks disappeared because of the interaction between PVA and Alg. For Alg (spectrum b in Figure 20.12), the characteristic bands appeared at 1615, 1417 and 3430  $\text{cm}^{-1}$ , and these three bands were observed in the spectra of the blend. It was also noted that the hydroxyl stretching bands showed broadness upon the addition of Alg, which supports the fact that hydrogen bonding occurs between the hydroxyl groups of PVA and Alg. Hence, the inclusion of PVA moderated the interaction between Alg macromolecules, and helped to improve the “electrospinnability” of Alg with PVA.

## 20.4

### Characterization of Blends of Polyethers (PE) using FTIR Spectroscopy

#### 20.4.1

##### Polyethylene Oxide (PEO) Blends

Polyethers such as PEO [82] and PVME [83] are reported to be miscible with PVPh or VPh copolymers over the whole composition range, due to hydrogen-bond formation between the VPh unit and polyethers. Besides PVP [49,84], poly(*N*-acryloylthiomorpholine) [85], poly(2-acrylamido-2-methyl-1-propanesulfonic acid (PAMP) [86] and poly(1-vinylimidazole) (PVIIm) [87,88] form miscible blends with polyesters and polyethers, as a result of the formation of strong interassociated hydrogen bonds with the VPh unit. Muniz *et al.* [89] studied the miscibility of unmodified, cationic and hydrophobic starches with PEO using FTIR microscopy. The use of FTIR-optical microscopy allows a spectroscopic analysis of specific regions of the sample, instead of providing an average of a large region. In the case of polymer blends, FTIR-optical microscopy allows the evaluation of miscibility based on the spectra obtained at specific chosen blend sites [90]. Although the starches (unmodified, cationic and hydrophobic) were chemically different, their FTIR spectra were not significantly different; this confirms that, although the degree of modification is small, it is sufficient to result in different behaviors when blended with PEO. The main differences in the FTIR spectra of the starches used included C—O—C and C—O—H vibrational modes (in the range of 1300–950 cm<sup>-1</sup>). The vibrational modes of PEO and of starch are presented in the spectra shown in Figures 20.13–20.15. The FTIR spectra of PEO and of unmodified starch, and the FTIR microscopy spectra of a 95/05 PEO/unmodified starch blend, obtained at distinct sites (1 and 2) within the sample, are shown in Figure 20.13. It can be verified that the spectra of sites 1 and 2 are quite different with regard to the C—O—C and C—O—H vibrational modes of starch (ca. 1000 cm<sup>-1</sup>), mainly because the band is clearly present in the FTIR spectrum obtained at site 1 of 95/05, but not in the FTIR spectrum at site 2 of this blend. These results reinforce the point of view that, for the ratio of 95/05, the PEO/unmodified starch blend is heterogeneous at the FTIR depth (2–5 μm) [91,92], indicating its immiscibility. The FTIR spectra of PEO, of unmodified starch and of the 90/10 PEO/unmodified starch blend obtained at two distinct sites (1 and 2), are shown in Figure 20.14. Both sites were very similar, at about 1000 cm<sup>-1</sup>, and this was attributed to the C—O—C and C—O—H vibrational modes of the unmodified starch, and a broad band at about 2000 cm<sup>-1</sup>, which was attributed to the asymmetric stretching of PEO. The C—H stretching for PEO and the unmodified starch that appears at about 2880–2890 cm<sup>-1</sup> were also present in the FTIR spectra of the 90/10 blend obtained at sites 1 and 2 (see Figure 20.15). The FTIR spectra obtained at sites 1 and 2 showed a broader band related to band coalescence, which could be attributed to the C—H stretching of PEO (2879 cm<sup>-1</sup>) and of the unmodified starch (2921 cm<sup>-1</sup>). The characteristic features observed were that site 1 was noted to be richer in starch than site 2,

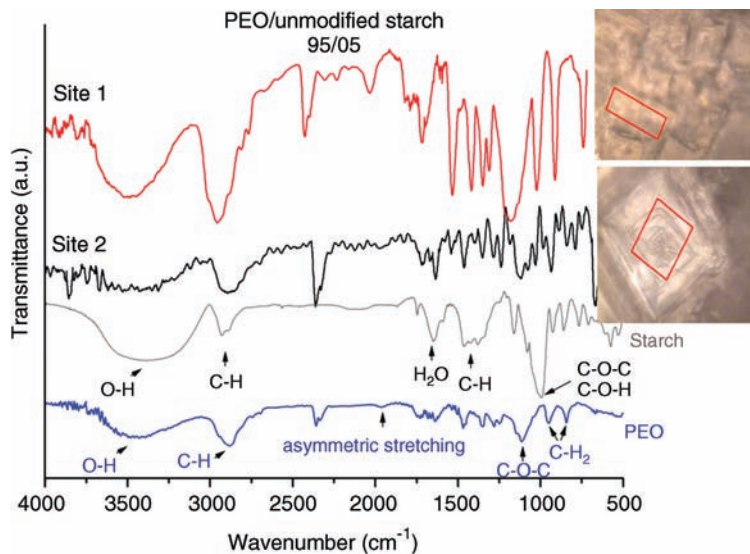


**Figure 20.13** FTIR spectra of PEO, unmodified starch, and two distinct sites of the 90/05 PEO/unmodified starch blend. Reprinted with permission from Ref. [89]; © 2011, Elsevier.

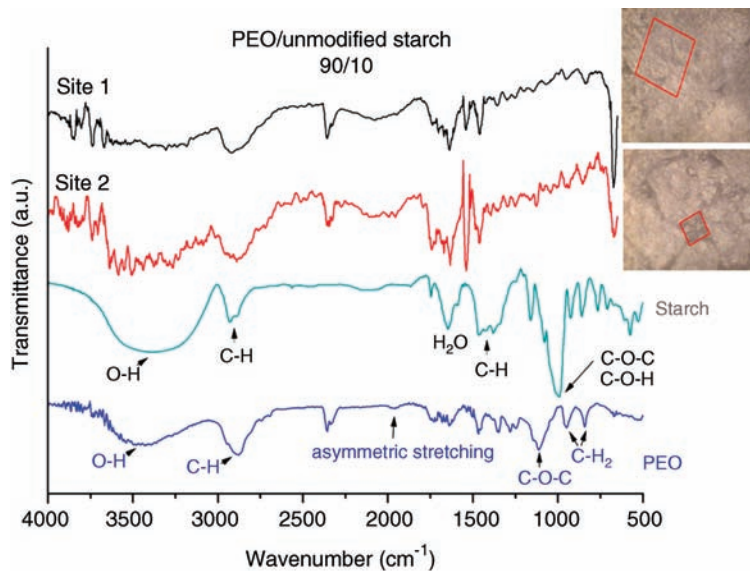


**Figure 20.14** FTIR spectra of PEO, unmodified starch, and two distinct sites of the 90/10 PEO/unmodified starch blend. Reprinted with permission from Ref. [89]; © 2011, Elsevier.

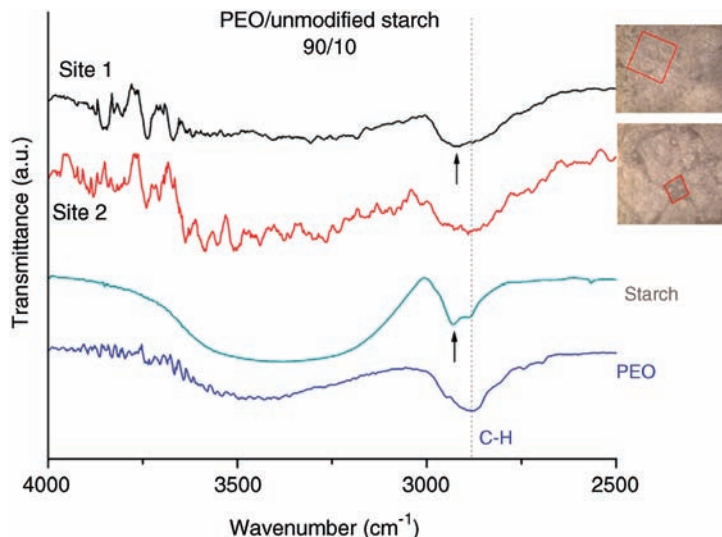


**Figure 20.15** FTIR spectra of PEO, unmodified starch, and two distinct sites at the 90/10 blend composition. Reprinted with permission from Ref. [89]; © 2011, Elsevier.

while the band assigned to PEO in the FTIR spectrum obtained at site 2 was weaker, considering that this blend (90/10) was ninefold richer (in weight) in PEO than in starch. The similarity of the FTIR spectra obtained at sites 1 and 2 indicated that the blend 90/10 PEO/unmodified starch revealed chemical homogeneity, which confirmed the miscibility of this blend ratio. The FTIR spectra of PEO/cationic starch blends did not show any evidence of either interaction between the polymers, or system miscibility in the whole range of studied blend ratios. As the FTIR spectrum obtained at a given site of the sample was very dissimilar to that obtained at another site of the same sample, for the PEO/hydrophobic starch blends, the FTIR spectra were quite similar, regardless of the site chosen.

Inamura *et al.* [93] studied PVA and PEO blends as the two component polymers in solution-cast film blends to investigate the role of interchain hydrogen bonding as the driving force for miscibility. Primary, but not secondary, hydroxyl groups were seen to form interchain hydrogen bonds with the skeletal ether oxygen of PEO. To prove this point, PVA, propylated PVA and two hydroxypropylated PVA derivatives (one with only secondary OH groups and one with a mixture of primary and secondary OH groups) were used as one component which was blended with PEO in solution. The compatibility of the amorphous regions of PVA/PEO blend films was investigated using FTIR analysis. Since PEO with a relatively high average molecular weight was used to avoid any effect of OH groups at the end of the molecular chains, the OH absorption bands contributed by PEO were negligible in the FTIR spectrum. Thus, the OH absorption bands in the range from 3600 to 3000  $\text{cm}^{-1}$  due to the stretching vibration (as shown in Figure 20.16) were attributed only to OH in PVA, which appeared to be highly

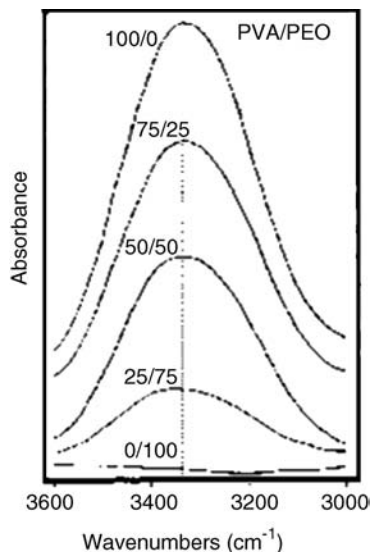


**Figure 20.16** Change in the FTIR spectra of PVA/PEO blend films Reproduced with permission from Ref. [94]; © 1999, American Chemical Society.

amorphous. In the FTIR spectra for the various blend compositions, the OH absorption band peak at  $3340\text{ cm}^{-1}$  due to interior intramolecular hydrogen bonding did not shift as the PEO component was increased, which indicated that the hydrogen bonds in PVA were not affected by blending with PEO. It was concluded that the intermolecular hydrogen bonds were strong enough to maintain their self-assembly in PVA, even though it was in a highly amorphous state. The results obtained strongly suggested that PVA was immiscible with PEO in blend films, and that each component maintained its individual characteristics.

Chang *et al.* [95] also investigated the carbonyl, hydroxyl and ether vibrations to study the mechanism of interpolymer miscibility through the formation of different types of hydrogen bond, both qualitatively and quantitatively, using FTIR spectroscopy of phenolic resin, PEO and PCL. The interassociation equilibrium constant between the phenolic hydroxyl group and the PEO ether group could not be directly determined due to an absence of carbonyl groups that could be used as a measure of the fraction of the hydrogen-bonded group from FTIR analysis in this binary blend. The ether stretching mode near  $1100\text{--}1200\text{ cm}^{-1}$  was found to be a highly coupled mode that was conformationally sensitive and could not be readily resolved into two peaks of free and hydrogen-bonded ether absorptions. However, the interassociation equilibrium constant obtained from model compounds was not exactly the same as that from the true polymer blend.

Figure 20.17a–c show the infrared spectra recorded at room temperature in the hydroxyl, carbonyl and ether, respectively, for a series of ternary blends containing a constant 80 wt mass%. The free hydroxyl group absorption band was located at  $3525\text{ cm}^{-1}$ , while the hydrogen-bonded hydroxyl exhibited a broad absorption at



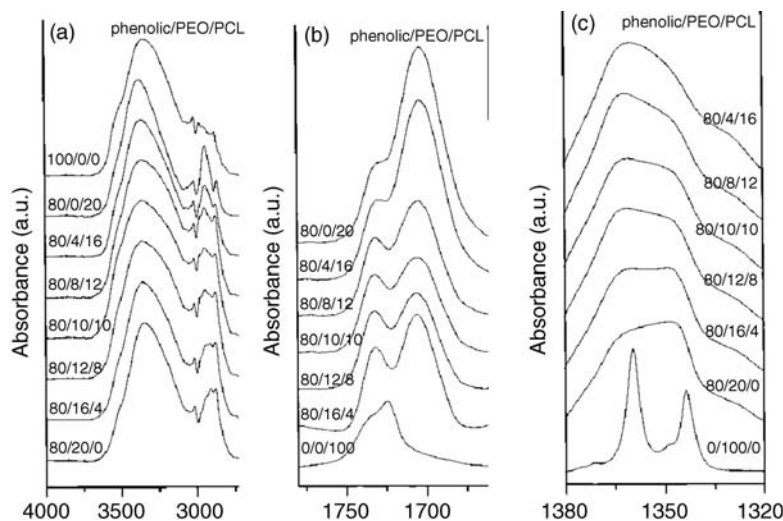


**Figure 20.17** Infrared spectra of ternary blend of phenolic/PEO/PCL containing a constant composition (80 wt%) of phenolic resin at room temperature in the hydroxyl stretching region (a), carbonyl stretching region (b), and ether region (c). Reprinted with permission from Ref. [95]; © 2002, American Chemical Society.

$3350\text{ cm}^{-1}$  due to a wide distribution of hydrogen-bonded hydroxyl groups. In the phenolic/PCL 80/20 binary blend (Figure 20.17a), the hydrogen-bonded hydroxyl group shifted to  $3370\text{ cm}^{-1}$ , reflecting the new distribution of hydrogen bonds between the hydroxyl–hydroxyl and the hydroxyl–carbonyl specific interactions. Furthermore, the band at  $3370\text{ cm}^{-1}$  shifted to  $3345\text{ cm}^{-1}$  (a lower wavenumber) for blends with increasing PEO/PCL ratios. This change was due to the switch from the intermolecular hydroxyl–carbonyl bond to the intermolecular hydroxyl–ether bond, indicating that there are hydrogen-bonding interactions between the PEO ether group and the hydroxyl group of the phenolic resin. The hydroxyl–ether interaction predominated in these ternary blends, so that it was reasonable to assign the band at  $3345\text{ cm}^{-1}$  as the hydroxyl group bonded to the ether group. The frequency difference ( $\Delta\nu$ ) between the hydrogen-bonded hydroxyl absorption and the free hydroxyl absorption was also employed in determining the relative strength of different intermolecular interactions. The phenolic/PEO blends showed a stronger ( $\Delta\nu$ ) than that of the phenolic/PCL blend ( $155\text{ cm}^{-1}$ ), indicating that the hydroxyl ether interassociation was more favorable than the hydroxyl–carbonyl interassociation. Figure 20.17a shows the infrared spectra of carbonyl stretching measured at room temperature, ranging from  $1650$  to  $1780\text{ cm}^{-1}$  for ternary blends. The carbonyl stretching for the pure PCL was split into two bands; absorptions by the amorphous and crystalline conformations were observed at  $1734$  and  $1724\text{ cm}^{-1}$ , respectively. This crystalline conformation at  $1724\text{ cm}^{-1}$  disappeared over the entire ternary blend compositions containing a fixed phenolic content of 80 mass %. Another band appearing at approximately  $1703\text{ cm}^{-1}$  was

assigned as the PCL carbonyl group (i.e., hydrogen-bonded to the phenolic hydroxyl group). The carbonyl stretching frequency split into only two bands at 1734 and 1703  $\text{cm}^{-1}$ , corresponding to the free and hydrogen-bonded carbonyl groups, which were fitted well to the Gaussian function. The hydrogen-bonded fraction of the carbonyl group decreased with an increase in the relative ratio of PEO to PCL. The PCL carbonyl was found to compete with the ether oxygen of PEO to form a hydrogen bond with the hydroxyl group of the phenolic resin. Thus, the interassociation equilibrium constant of hydroxyl–ether was greater than the interassociation equilibrium constant of hydroxyl–carbonyl at room temperature. Chang *et al.* [96] also investigated blends of poly(vinylphenol-*co*-methyl methacrylate) (PVPh-*co*-PMMA) with PEO, prepared by solution casting from THF solution. The miscibility behavior and hydrogen bonding of the blends were investigated using DSC, FTIR and solid-state NMR. Self-association occurred especially by hydroxyl–hydroxyl and hydroxyl–carbonyl hydrogen bonding, taking into account the chemical structure of PVPh-*co*-PMMA. Figure 20.18 shows the IR spectra of the carbonyl stretching measured from 1660 to 1800  $\text{cm}^{-1}$  for PVPh-*co*-PMMA, PEO, and their blends. The carbonyl stretching for the pure PVPh-*co*-PMMA is split into two bands: absorption by free and hydrogen-bonded carbonyl groups at 1730 and 1705  $\text{cm}^{-1}$ , respectively. These bands were resolved into two Gaussian peaks, with areas corresponding to the free carbonyl (1730  $\text{cm}^{-1}$ ) and the hydrogen-bonded carbonyl (1705  $\text{cm}^{-1}$ ) absorptions. By using the respective absorptivity coefficients, it was possible to calculate the fraction of these two carbonyl groups from the relative intensities of the two bands. The fraction of the hydrogen-bonded carbonyl group was calculated from Eq. (20.2), where  $A_b$  and  $A_f$  are the peak areas corresponding.

$$f_b^{\text{C=O}} = \frac{A_b/1.5}{A_b/1.5 + A_f} \quad (20.2)$$

The conversion coefficient of 1.5 was the absorptivity ratio of these two bands, the “free” and “hydrogen-bonded” carbonyl groups, in an ester group blend. Figure 20.18 shows the absorption region of the pure PVPh, the PVPh-*co*-PMMA, and the various PVPh-*co*-PMMA/PEO blends between 2700 and 4000  $\text{cm}^{-1}$  at room temperature. As shown in spectrum (a) of Figure 20.18, the pure PVPh polymer exhibits two bands in the hydroxyl-stretching region of the infrared spectrum. The free hydroxyl group absorption is located at 3525  $\text{cm}^{-1}$ , while the hydrogen-bonded hydroxyl gives a broad absorption at 3350  $\text{cm}^{-1}$  due to a wide distribution of hydrogen-bonded hydroxyl groups. However, the pure PVPh-*co*-PMMA (spectrum (b) in Figure 20.18) shows only one band at about 3400  $\text{cm}^{-1}$  in the hydroxyl-stretching region of the infrared spectrum. This reflects the hydrogen bonding between the hydroxyl–hydroxyl- and the hydroxyl–carbonyl interactions. Furthermore, the band at 3400  $\text{cm}^{-1}$  is shifted to 3350  $\text{cm}^{-1}$  (a lower wavenumber) for blends containing 60 mass% PEO content (spectrum (g) in Figure 20.18). This is due to a change from intramolecular hydroxyl–carbonyl bonding to intermolecular hydroxyl ether bonding, showing that there are hydrogen-bonding

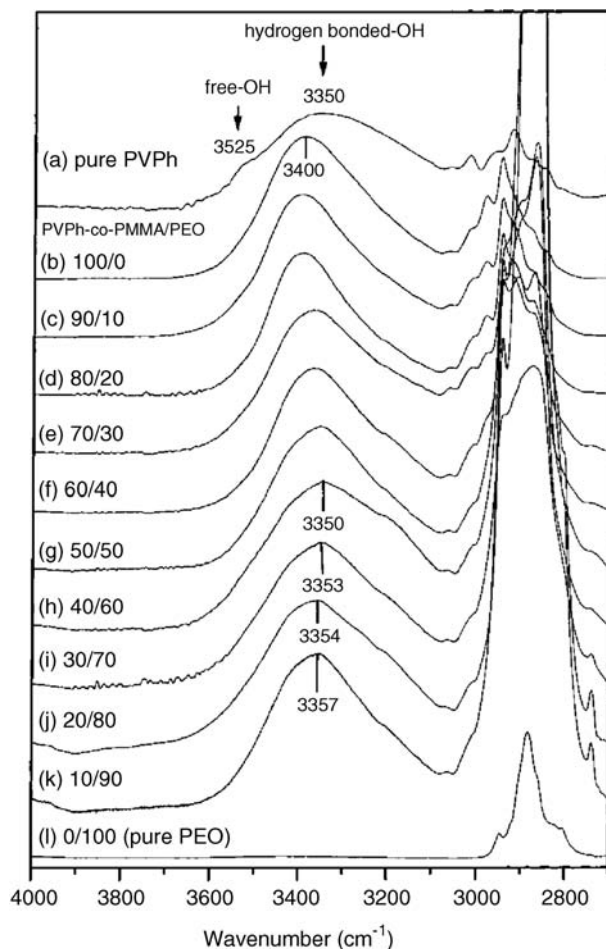


**Figure 20.18** FTIR spectra recorded at room temperature in the  $2700\text{--}4000\text{ cm}^{-1}$  region for pure PVPh and various PVPh-co-PMMA/PEO blends. (a) pure PVPh; (b) 100/0; (c) 90/10;

(d) 80/20; (e) 70/30; (f) 60/40; (g) 50/50; (h) 40/60; (i) 30/70; (j) 20/50; (k) 10/90; (l) 0/100. Reprinted with permission from Ref. [96]; © 2001, American Chemical Society.

interactions between the PEO ether group and the hydroxyl group of PVPh. The  $\text{CH}_2$  wagging region of the pure PEO and PVPh-co-PMMA at  $1360$  and  $1343\text{ cm}^{-1}$  represents the crystalline phase of PEO (Figure 20.19). The intensity of these bands decreases as the PVPh-co-PMMA content increases, and the crystalline bands disappear at the PVPh-co-PMMA/PEO 40/60 blend, which was replaced by a broad band centered at  $1350\text{ cm}^{-1}$ . This shows that PEO crystallization is affected by addition of the amorphous PVPh-co-PMMA polymer.

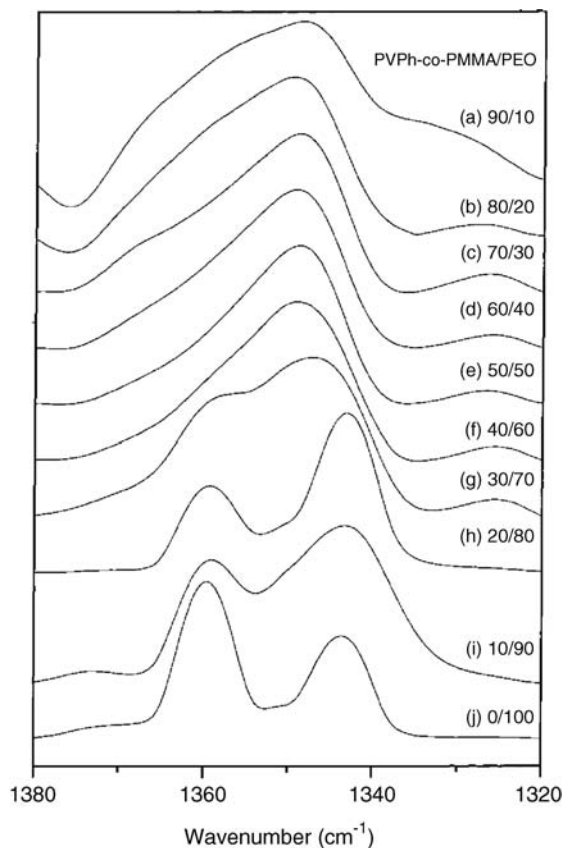


**Figure 20.19** FTIR spectra recorded at room temperature in the 1320–1380  $\text{cm}^{-1}$  region for PVPh-co-PMMA/PEO blends: (a) 90/10; (b) 80/20; (c) 70/30; (d) 60/40; (e) 50/50; (f) 40/60; (g) 30/70; (h) 20/80; (i) 10/90; (j) 0/100. Reprinted with permission from Ref. [96]; © 2001, American Chemical Society.

#### 20.4.2

##### Poly (vinyl methyl ether) (PVME) Blends

Mailhot *et al.* [97] studied the chemical evolution of blends of PVME and PS using infrared spectrometry under conditions of photooxidation. All irradiations were carried out in a SEPAP 12/24 unit designed for studying polymer photodegradation under artificial conditions, corresponding to a medium acceleration of aging and equipped with four medium-pressure mercury lamps. Characterization of the oxidation kinetics permitted the detection of interactions between the two polymers. Irradiation usually leads to noticeable changes of the surface aspect of the polymers. In order to characterize the development of the surface, images of the surface were recorded as a function of the irradiation time using atomic force

microscopy (AFM). The behavior observed by FTIR analysis of the PVME/PS blends of 50/50 mol% irradiated in the presence of oxygen showed two periods. During the first hours of irradiation, the absorption bands observed were very similar to those observed for pure PVME photooxidized under the same conditions (the carbonyl zone presented in Figure 20.20a and b). This result indicated that the FTIR bands observed in the blend reflected mainly the formation of photoproducts of PVME oxidation. After less than 20 h irradiation, under similar conditions, the oxidation of PVME homopolymers reached a limiting value, and the absorbance corresponding to the oxidation products was no longer increased. The changes in the spectra of the blend (Figure 20.20c) reflected the oxidation of pure PS (Figure 20.20d). In order to verify that the increase of the absorbance during this second period could be attributed principally to the formation of photoproducts resulting from the oxidation of PS, a subtraction between the spectrum of the 21 h-irradiated film and the spectra of films irradiated for longer periods was carried out (Figure 20.20e). The shapes of the IR bands were found to differ greatly from that of the pure PS. The spectra in Figure 20.20e showed that, once formed within the first phase, the product (ketonic groups of keto-diester compounds such as dimethyl malonate or 1,3-dimethylacetone dicarboxylate) at  $1733\text{ cm}^{-1}$  progressively disappeared in the second phase. This gave a minimum of absorbance in the carbonyl band between  $1850$  and  $1600\text{ cm}^{-1}$ . Disappearance of the product at  $1733\text{ cm}^{-1}$  increased with the irradiation time, which in turn caused the shape of the carbonyl band arising from the PS photooxidation to be modified. This behavior was observed in the case of the PVME homopolymer and, after a first phase of oxidation leading to an accumulation of the oxidation products, this reflected the loss of some of the oxidation photoproducts. The band at  $1733\text{ cm}^{-1}$  was attributed to ketonic groups of keto-diester compounds such as dimethyl malonate or 1,3-dimethylacetone dicarboxylate. These molecular products either migrated out of the polymeric matrix directly or were photolyzed by a Norrish type I reaction of the ketone, which led to lower-molecular-weight products that were lost by migration. Chemical treatment of the photooxidized blends using ammonia gas were carried out in order to verify if the same photoproducts were formed in the blend and in the homopolymers, and eventually to provide evidence of the formation of new photoproducts. After reaction with ammonia for 86 h, a photooxidized film showed an amide band at  $1670\text{ cm}^{-1}$  (the maxima formed for the homopolymers PS and PVME were  $1669$  and  $1671\text{ cm}^{-1}$ , respectively). The ammonium carboxylate bands were observed at approximately  $1590$  and  $1568\text{ cm}^{-1}$  (large bands), while two maxima were noted in the case of PS at  $1585$  and  $1553\text{ cm}^{-1}$  corresponding, respectively, to aliphatic and aromatic carboxylates. For PVME, the maximum was noted at  $1571\text{ cm}^{-1}$ . The band at  $1568\text{ cm}^{-1}$ , which resulted from treating the blend with ammonia, was progressively shifted to lower wavenumbers when the ammonia treatment was carried out on films of increasing amounts of PS or for increasing irradiation times. This band included the  $1553$  and  $1571\text{ cm}^{-1}$  absorptions.

Hence, FTIR analysis could be used to identify the oxidation products formed upon irradiation, and confirmed that PVME photooxidation was the main cause

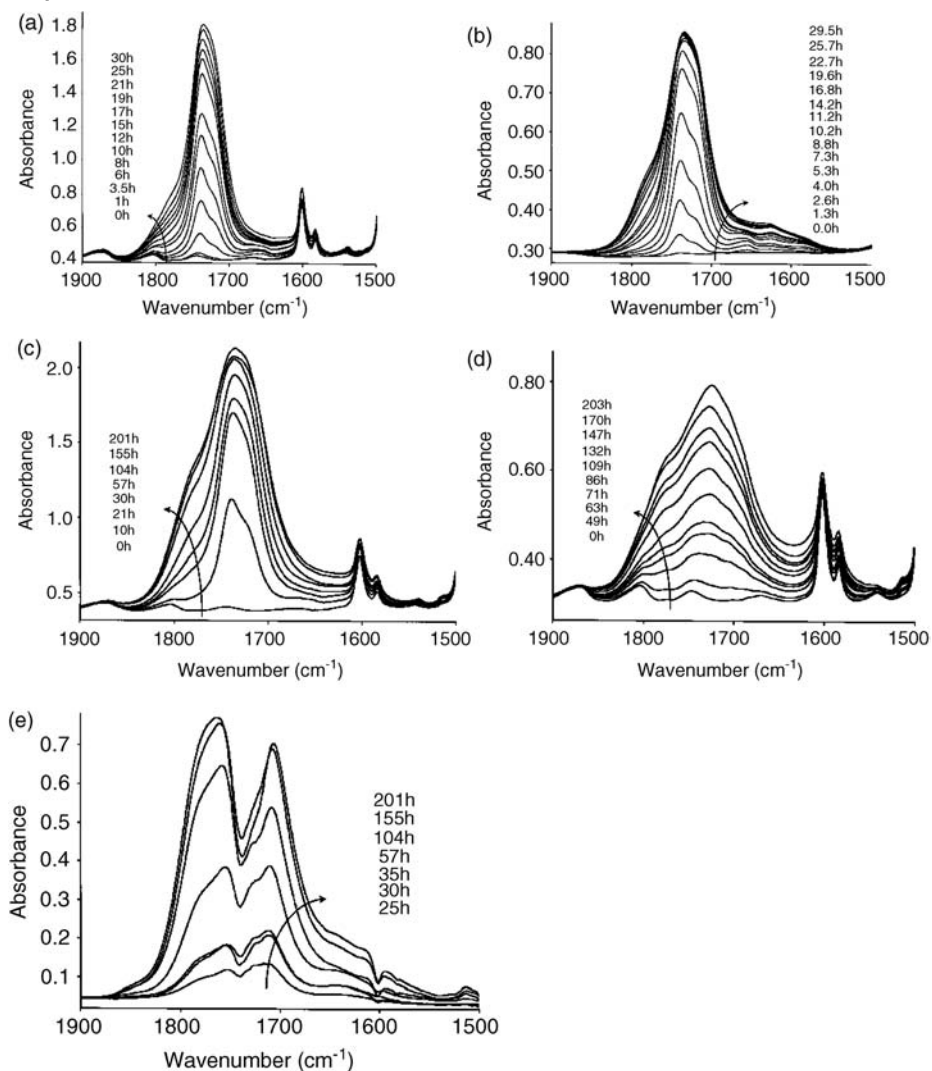


**Figure 20.20** Evolution of the IR spectra of: (a) PVME/PS 50/50 mol% sample ( $32\ \mu\text{m}$ ) during the photooxidation; (b) PVME sample (9 mm) during the photooxidation; (c) PVME/PS 50/50 mol% sample ( $32\ \mu\text{m}$ ) during the photooxidation; (d) PS sample (13 mm) during the photooxidation; (e) PVME/PS 50/50 mol% sample ( $32\ \mu\text{m}$ ) during the photooxidation (subtraction of spectra between the spectrum of the 21 h irradiated film and the spectra of the film irradiated for a longer duration). Reprinted with permission from Ref. [97]; © 2000, Elsevier.

of degradation of the blends. Moreover, PVME had a clear influence on the photo-oxidation of PS, and vice-versa.

Bhutto *et al.* [98] investigated the miscibility and specific interactions of PS and sodium sulfonated polystyrene (Na-SPS) with PVME blends (ranging from 10% to 90% PS by mass), using FTIR spectroscopy. The FTIR studies at different temperatures showed that changes in the spectra of the polymer blends were explained by temperature changes in the pure homopolymers. This indicated that molecular interactions, which were responsible for miscibility, were not detectable by infrared absorptions and were, therefore, of unspecific strength and location. The FTIR analysis of SPS/PVME blends showed that the sulfonate groups of PS affected polymer miscibility through changes in the configuration of molecules, rather than through direct interaction with the PVME. Figure 20.21a and b show the FTIR spectra of PS and PVME, respectively, in the high-frequency region from 2700 to 3200  $\text{cm}^{-1}$ . The high-frequency spectra of PS consisted of seven absorption bands. Those bands with peak locations at 3002, 3026, 3060, 3082 and 3103  $\text{cm}^{-1}$  were due to the C—H stretching of the pendant benzene ring CH groups, while bands with peak positions of 2924 and 2850  $\text{cm}^{-1}$  were assigned to the C—H stretching vibration of the  $\text{CH}_2$  and CH groups on the main PS chain. The high-frequency spectra of PVME consisted of absorption bands with peak positions at 2886, 2931 and 2971  $\text{cm}^{-1}$  due to the C—H stretching vibration of the  $\text{CH}_2$  and  $\text{CH}_3$  groups on the main-chain, respectively, and the band at 2820  $\text{cm}^{-1}$  was assigned to the C—H stretching of the  $\text{CH}_3$  of the pendant methoxy group (Figure 20.21b). Three peaks were found to be most sensitive to changes in the composition of the PS/PVME blends (2820  $\text{cm}^{-1}$  in PVME, and 2850 and 2924  $\text{cm}^{-1}$  in PS). Figure 20.21c shows the FTIR spectrum of the 50/50 (w/w) PS/PVME system. The seven absorption bands of PS and the four bands of PVME in the high-frequency region combined to produce 10 bands, with the PS and PVME bands at 2926  $\text{cm}^{-1}$  superimposed. It was observed that the band which was assigned C—H stretching of CH group on the main PS chain at 2924  $\text{cm}^{-1}$  in pure PS shifted slightly to a higher frequency when PS blended with PVME. This difference in peak position could be expected from the simple addition of two closely spaced broad peaks of different absorbance. As shown in Figure 20.21d (the spectrum of 50:50 PS/PVME and SPS/PVME blends at room temperature), this band was found at 2926  $\text{cm}^{-1}$  in both the sulfonated and unsulfonated blends. Figure 20.21e shows the spectrum of PVME, with a strong doublet at 1085  $\text{cm}^{-1}$  and 1107  $\text{cm}^{-1}$  and a shoulder at 1132  $\text{cm}^{-1}$ . The bands at 1100  $\text{cm}^{-1}$  were assigned to the C—O stretching mode but also included contributions from the  $\text{CH}_3$  rocking and C—C stretching modes. The intensity of the 1085  $\text{cm}^{-1}$  band was greater than that of the 1107  $\text{cm}^{-1}$  component in all blends, with the contribution of 1069  $\text{cm}^{-1}$  of C—H in-plane bending vibration of the PS ring. As the PVME content in the blend was increased, the 1107  $\text{cm}^{-1}$  band became more prominent in comparison to the 1085  $\text{cm}^{-1}$  band. The SPS/PVME blend also showed similar changes to that of PS/PVME blend, except for the appearance of sulfonation peaks at 1229, 1043 and 1011  $\text{cm}^{-1}$ . It was seen from Figure 20.21e that the contribution from the PS peak was small. In addition, the

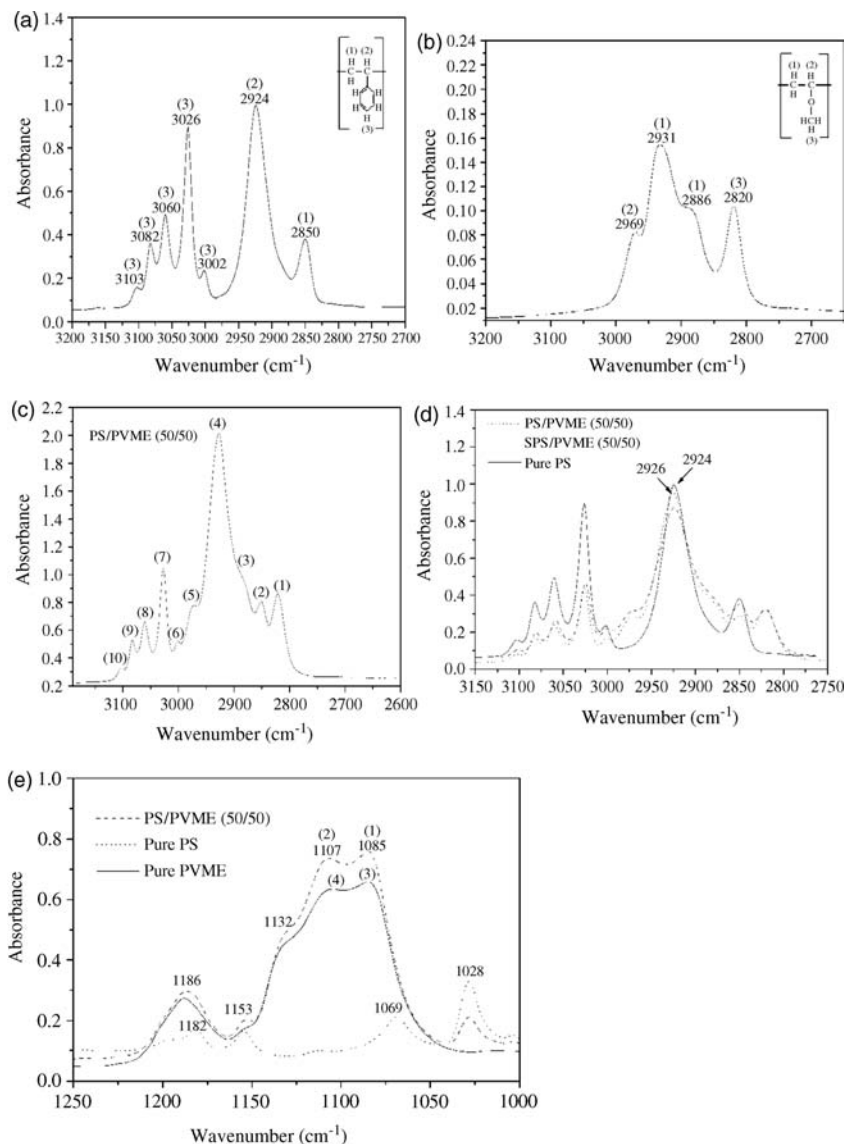


**Figure 20.21** (a) Infrared spectra of pure PS at high-frequency in the 3200–2700 cm<sup>-1</sup> regions measured at room temperature; (b) Infrared spectra of PVME at high-frequency in the 3200–2700 cm<sup>-1</sup> regions measured at room temperature; (c) Infrared spectra of 50:50 (w/w) PS/PVME blends at room temperature in high frequency from 3200 to 2600 cm<sup>-1</sup> regions. Peak frequencies (1)–(10) are 2820, 2850, 2886, 2926, 2971, 3001, 3026, 3060,

3082, and 3103 cm<sup>-1</sup>, respectively; (d) Infrared spectra (2750–3150 cm<sup>-1</sup>) of PS and 50/50 PS/PVME, SPS/PVME blends at room temperature; (e) Infrared spectra (1000–1250 cm<sup>-1</sup>) of PS, PVME and 50/50 PS/PVME blends measured at room temperature. Band: 1, 1085 cm<sup>-1</sup>, absorbance 0.760; 2, 1107 cm<sup>-1</sup>, absorbance 0.728; 3, 1085 cm<sup>-1</sup>, absorbance 0.655; 4, 1107, absorbance 0.635. Reprinted with permission from Ref. [98]; © 2003, Elsevier.



absorbance (peak height) was dependent on sample geometry, spectrometer throughput and temperature. To understand the role played by intermolecular interactions in the miscibility and phase behavior of PS/PVME blends, the nature of the interaction of the homopolymers and blends at different temperatures was examined. Using these results, it was possible to distinguish between the thermal behavior of spectral changes observed in the homopolymers and the miscibility effects of the PS/PVME blends. Spectra for different temperatures were plotted together to identify the spectral shift and peak broadening. Some peaks showed no shift or broadening, while others were shifted and broadened simultaneously, revealing miscibility.

## 20.5

### Characterization of Acrylate Blends with FTIR Spectroscopy

#### 20.5.1

##### Poly(methylmethacrylate) (PMMA) Blends

Ramesh *et al.* [99] investigated polymer electrolytes composed of the blend (PVC/PMMA) with lithium triflate ( $\text{LiCF}_3\text{SO}_3$ ) as a salt, ethylene carbonate (EC) and dibutyl phthalate (DBP) as plasticizers, and silica ( $\text{SiO}_2$ ) as the composite filler. FTIR studies confirmed the complexation between PVC/PMMA blends. The FTIR spectra of pure PVC, pure PMMA and PVC–PMMA samples (Figure 20.22a–e) showed bands that had been reported previously [100]; these bands can be observed in Figure 20.22a (for PVC) and Figure 20.22b (for PMMA). For PVC, the C–H stretching mode was observed at  $2911\text{ cm}^{-1}$ , the  $\text{CH}_2$  deformation mode at  $1333\text{ cm}^{-1}$ , the C–H rocking mode at  $1254\text{ cm}^{-1}$ , the *trans* C–H wagging mode at  $959\text{ cm}^{-1}$ , the C–Cl stretching mode at  $834\text{ cm}^{-1}$ , and the *cis* C–H wagging mode at  $616\text{ cm}^{-1}$ . The peaks at  $2951$ ,  $1721$ ,  $1449$  and  $1159\text{ cm}^{-1}$  were assigned to C–H stretching, C=O stretching,  $\text{CH}_3$  stretching and  $\text{OCH}_3$  stretching vibrations, respectively, in PMMA. Complexation may shift the polymer cage peak frequencies [100]. The characteristic peaks of pure PVC ( $1254$ ,  $959$ ,  $834\text{ cm}^{-1}$ ) were shifted to  $1244$ ,  $966$  and  $841\text{ cm}^{-1}$  in the PVC–PMMA blend, while the peaks of pure PMMA at  $1721$ ,  $1449$  and  $1159\text{ cm}^{-1}$  were shifted to  $1732$ ,  $1435$  and  $1150\text{ cm}^{-1}$ , respectively. Figure 20.22c shows the FTIR spectra of pure PVC, pure PMMA and PVC–PMMA blends in the wave number range from  $1400$  to  $1200\text{ cm}^{-1}$ . The peak at  $1333\text{ cm}^{-1}$  of pure PVC was assigned to  $\text{CH}_2$  deformation. The relative intensity of the peak decreased with decreasing PVC content. The band at  $1254\text{ cm}^{-1}$  was assigned to the C–H-rocking vibration. When PVC was blended with PMMA, a small shoulder appeared in the spectrum at the longer wavenumber. A doublet was found with increasing PMMA content (Figure 20.22d). The FTIR spectra of pure PVC (spectrum a), pure PMMA (spectrum b), PVC–PMMA (70:30) (spectrum c), PVC–PMMA (50:50) (spectrum d) and PVC–PMMA (30:70) (spectrum e) complexes are also shown in Figure 20.22d. The FTIR spectra of pure  $\text{LiCF}_3\text{SO}_3$  was observed at  $1271$  and  $1242\text{ cm}^{-1}$ . The

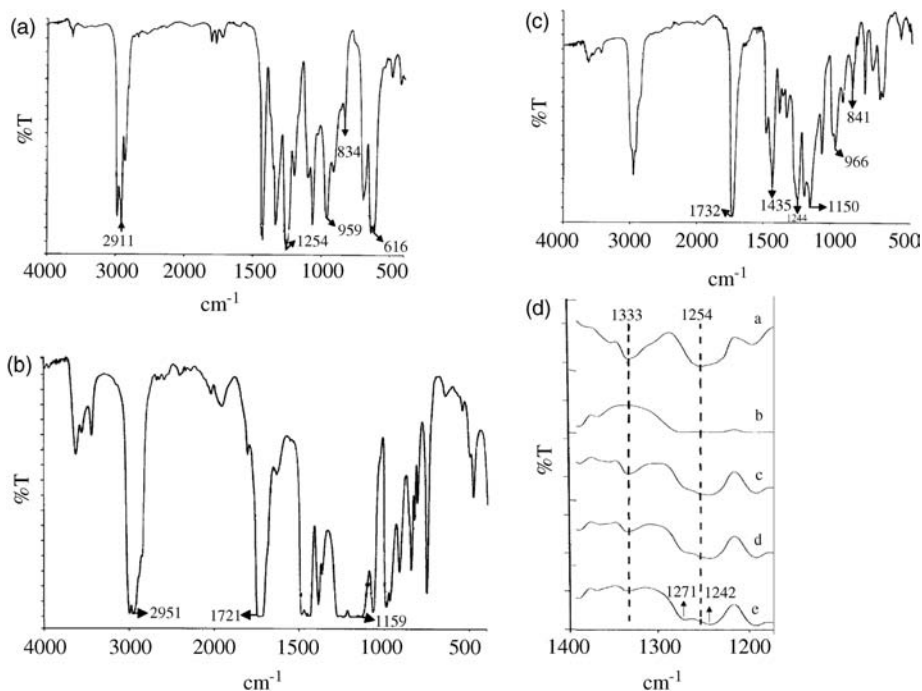


**Figure 20.22** FTIR spectra of: (a) pure PVC; (b) pure PMMA; (c) PVC:PMMA (30:70) blend; (d) (70:30), (spectrum d) PVC:PMMA (50:50) and (spectrum e) PVC:PMMA (30:70) complexes. Reprinted with permission from Ref. [99]; © 2007, Elsevier.

relative intensity of the shoulder was increased with increasing PMMA content such that, when the PMMA content was 70%, the shoulder intensity was higher than that of the original band. The above-described analysis established the complexation of PVC–PMMA blends. Although PMMA and PEMA are only slightly different in structure, they are known to be immiscible. STVPh with a VPh content of 5 mol% was added to an immiscible PMMA–PEMA blend to improve the compatibility. It is expected that poly(styrene-*co*-4-vinylphenol) (PSTVPh) is a compatibilization agent at the interface of the phase-separated PMMA and PEMA domains, since PSTVPh is miscible with both PMMA and PEMA. As expected, the ternary blends composed of PEMA, PMMA and PSTVPh showed a wide miscibility window [99–102]. Similarly, the introduction of PSTVPh into immiscible blends of PS–PEO, PS–PMMA and PS–PBMA caused a notable reduction in the phase domain size with the formation of hydrogen bonds, as shown in Figure 20.23. Poly(styrene-graft-ethylene oxide) has also been used to enhance the compatibility of PS blends with poly(butyl acrylate) (PBA) and poly(butyl acrylate-*co*-acrylic acid) (PBAAA) copolymers [102]. Although no significant effect of the graft copolymer on domain size was found with the PS–PBA blends, the addition of 3 mass% graft copolymer reduced the domain size of the PBAAA phase by a

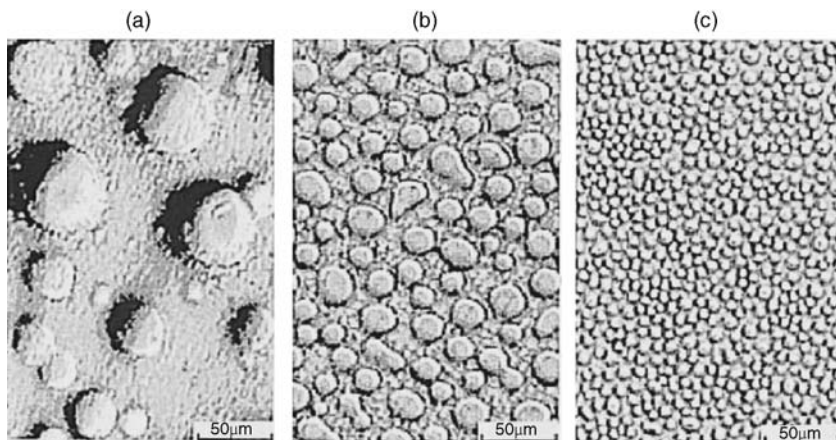


**Figure 20.23** Optical micrographs of 50/50 PS/PEO (MWZ51104/51104) blends. (a) Without STVPh; (b) With 5% copolymer; (c) With 10% copolymer. Reprinted with permission from Ref. [104]; © 1997, American Chemical Society.

factor of 10 in a PS–PBAAA blend. After functionalizing PBA with acrylic acid, the average size of the polyacrylate domains was also reduced considerably by the graft copolymer [103]. These results suggest that the compatibilization effect of the graft copolymer derives from the formation of hydrogen bonds between the PEO side chains in the graft copolymer and the acrylic acid segments in the PBAAA phase.

#### 20.5.2

##### **Poly-(3-hydroxybutyrate-co-3-hydroxyvalerate) (PHBV) Blends**

Dong *et al.* [105] used FTIR spectroscopy to verify the presence of intermolecular hydrogen bonding (inter-H-bond) between PHBV and bisphenol A (BPA). By monitoring the spectral changes during PHBV crystallization and blend dissociation, the absorptivity ratio of C=O bonds in the crystalline and amorphous regions in PHBV, and that of H-bonded and free C=O in PHBV/BPA blends, were determined experimentally as 1.40 and 1.68, respectively. Using a curve-fitting program, the C=O absorption bands of the blends were ascribed to three types of bond, namely amorphous, crystalline, and H-bonded C=O. When the crystallinity of PHBV and the fraction of hydrogen-bonded C=O were calculated, the results indicated that the hydrogen bonding clearly suppressed the PHBV crystallization. In the case of the PHBV/BPA blends studied here, one of the components (PHBV) contained carbonyl groups while the other (BPA) contained hydroxyl groups. Hence, hydrogen bonds (H-bond) can be formed in the blends, and are detectable using FTIR. A broad band with its peak at  $3348\text{ cm}^{-1}$  appeared for pure BPA, and this was attributed to the O—H of hydroxyl groups between individual BPA molecules. In the PHBV/BPA blends, the O—H band shifted to higher wavenumbers with increasing PHBV content. This peak shift was caused

by the occurrence of intermolecular hydrogen bonds (inter-H-bonds) between PHBV and BPA which showed, qualitatively, that the percentage of self-H-bonded O—H groups decreased to the benefit of the formation of inter-hydrogen bonds at higher PHBV composition. For the 10 mass% BPA composition, a single Gaussian-shaped band was observed, centered at  $3453\text{ cm}^{-1}$ ; this frequency was assigned to inter-hydrogen-bonded O—H groups. The self-hydrogen bonds were stronger than the inter-hydrogen bonds; for example, when C=O groups were blended a large proportion of the self-hydrogen bonds was replaced by the weaker inter-hydrogen bonds (Figure 20.24a). However, this replacement could be explained from a statistical point of view. At a 10 wt% BPA composition, the total concentration of the C=O groups was about 11-fold that of the O—H groups and, as a result, the O—H groups of BPA were randomly distributed among a large number of C=O groups and formed inter-H-bonds with C=O groups of PHBV, whereas only 1% of the O—H groups remained free. When the BPA content was increased, the probability that O—H groups would be bound to other O—H groups instead of to C=O groups was increased, and the energy potential was found to play an important role in the resulting ratio of self- and intermolecular hydrogen bonds. Figure 20.24b shows the FTIR spectra of PHBV/BPA blends in the carbonyl stretching vibration (C=O) region, and the change was directly attributed to changes in the PHBV C=O group environments, such as the formation of hydrogen bonds. The apparent shift of the C=O peak of PHBV from  $1723$  to  $1740\text{ cm}^{-1}$  upon blending indicated that the amorphous component predominated over the crystalline in PHBV on adding BPA, because the absorptions at  $1723$  and  $1740\text{ cm}^{-1}$  were attributed to the crystalline and amorphous components, respectively. When the BPA content was further increased, the C=O peak split into a doublet at  $1740$  and  $1713\text{ cm}^{-1}$ . The absorption at  $1713\text{ cm}^{-1}$  was assigned to the H-bonded C=O groups. With an increase in BPA content, the relative absorption of the hydrogen-bonded C=O was increased, while that of the free C=O was decreased. This indicated an increase in the percentage of H-bonded C=O. The highest percentage of this bond was obtained at the 70 wt% BPA composition, which decreased with a higher content of BPA ( $>70\text{ wt}\%$ ).

Ozaki *et al.* [106] studied blends of poly(*R*)-3-hydroxybutyrate (PHB) and PLLA using FTIR microspectroscopy, and showed that crystalline bands were observed due to PHB, whereas those due to PLLA were hardly observed for all PHB/PLLA blends investigated. On the other hand, some crystalline bands of PLLA were observed in the microinfrared spectra of some spots in the 20/80 PHB-co-HHx/PLLA blend. Microinfrared spectra also showed a significant difference in the compatibility and crystalline structures between the PHB-co-HHx/PLLA and PHB/PLLA blends. Figure 20.25a and b show microinfrared spectra in the  $2000$ – $1000\text{ cm}^{-1}$  region of PHB/PLLA and PHB-co-HHx/PLLA blends with 80/20 and 20/80 blending ratios. The differences in the infrared spectra between neat PHB and PHB-co-HHx lie mainly in the intensities of the crystalline and amorphous bands. The ratios of peak intensities of PHB and PLLA bands were dependent on the measurement points in both blends. In the 80/20 PHB/PLLA blend, the spectra of many spots were similar to the crystalline PHB spectrum, but the main

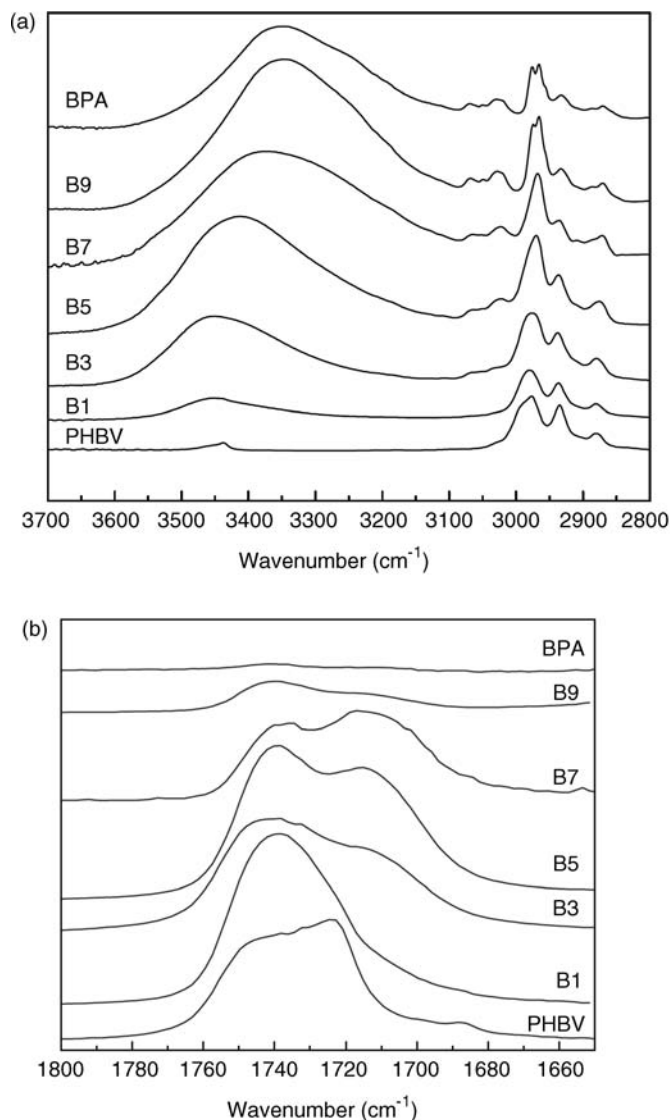


**Figure 20.24** (a) FTIR spectra in  $\nu_{\text{C-H}}$  and  $\nu_{\text{O-H}}$  regions of PHBV/BPA; (b) FTIR spectra in  $\nu_{\text{C=O}}$  region of PHBV/BPA blends. Reproduced with permission from Ref. [105]; © 2003, Elsevier.

PHB crystalline bands observed were the C—O stretching band at  $1720\text{ cm}^{-1}$ , the C—O—C stretching band at  $1275\text{ cm}^{-1}$ , and the band at  $1261\text{ cm}^{-1}$  that was due to the coupling of C—O—C stretching and C—H deformation modes. These bands were clearly identified in the spectra shown in Figure 20.25a and b. The spectra including amorphous PLLA bands at  $1745\text{ cm}^{-1}$  were obtained in some

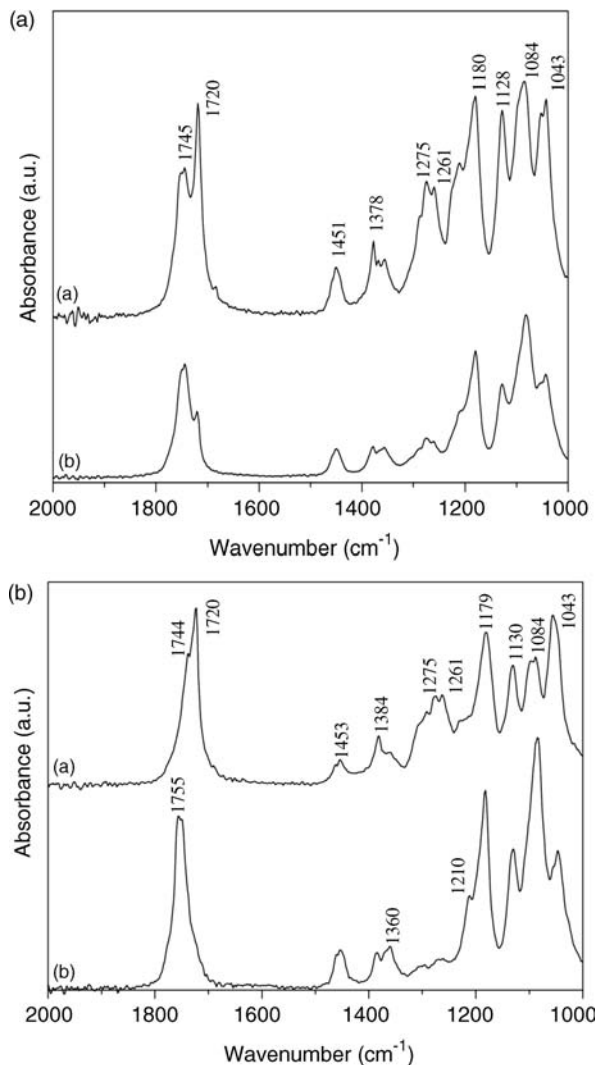


**Figure 20.25** Micro IR spectra of (a) PHB/PLLA and (b) P(HB-co-HHx)/PLLA blends. Spectrum a = 80/20 blend; spectrum b = 20/80 blend. Reproduced with permission from Ref. [106]; © 2003, Elsevier.

spots, as shown in Figure 20.25a; however, as can be seen in Figure 20.25b, the crystalline C=O stretching band at  $1720\text{ cm}^{-1}$  due to PHB was observed in the 20/80 PHB/PLLA blend. The crystalline C=O stretching band of PLLA at  $1755\text{ cm}^{-1}$  appeared weak. PLLA crystalline bands at  $1356$  and  $1210\text{ cm}^{-1}$  were assigned, respectively, to the coupling of the C—H deformation and the  $\text{CH}_3$  symmetric deformation mode, but the C—O—C stretching mode were also not strong. These results indicated that the crystallization of PHB was relatively easy

but that of the PLLA components was difficult, even in the 20/80 PHB/PLLA blend. In the case of PHB-*co*-HHx/PLLA blends, the intensity ratios of PHB-*co*-HHx and PLLA bands were also dependent on the location of measurement points of in the 80/20 and 20/80 blends. In the 80/20 PHB-*co*-HHx/PLLA blend, the crystalline bands of PHB-*co*-HHx were also observed, but those of PLLA were absent from the spectra (as shown in Figure 20.25a). Weak amorphous bands of PLLA were observed in spectra of the 80/20 PHB-*co*-HHx/PLLA blend. In contrast, the crystalline and amorphous bands of PHB-*co*-HHx were not observed in the spectra of some spots of the 20/80 PHB-*co*-HHx/PLLA blend (Figure 20.25b). One of the most characteristic amorphous bands of PLLA at  $1265\text{ cm}^{-1}$ , which was assigned to coupling of the C—O—C stretching and C—H deformation modes was also missing from the spectra of the 20/80 PHB-*co*-HHx/PLLA blend. Thus, the spectra of the 20/80 PHB-*co*-HHx/PLLA blend were very similar to the neat crystalline PLLA spectra. Infrared microspectroscopy revealed that PHB and PHB-*co*-HHx, but not PLLA, were crystallized in the 80/20 blends. These results also indicated that the PHB-*co*-HHx component, when dispersed in a PLLA matrix at a relatively low level, did not undergo significant crystallization.

## 20.6

### Characterization of Synthetic Rubber using FTIR Spectroscopy

Berridi *et al.* [107] used FTIR to study nitrile rubber (NR) and styrenated butadiene rubber (SBR) blends, and the quantification of their composition in used vehicle tires. Figure 20.26a shows the infrared spectrum of the pyrolysis products of a NR-SBR (40/60) blend. The diagnostic bands for SBR and NR pyrolysis products are shown in Figure 20.26b. The spectral region shown corresponded to the out-of-plane bending vibrations of aromatic C—H and C—C groups of PS at  $750$  and  $700\text{ cm}^{-1}$ , respectively, and the out-of-plane bending vibrations of vinyl C—H groups ( $990$  and  $910\text{ cm}^{-1}$ ) and the *trans* CH—CH at  $960\text{ cm}^{-1}$  of butadiene. The band centered at  $815\text{ cm}^{-1}$  was assigned to vibrations of NR. The degradation products of each blend component showed clearly separated bands that were assignable to each component. The high-temperature degradation of NR at between  $300$  and  $500^\circ\text{C}$  showed the formation of variable-length oligomers as a consequence of random polymeric chain scissions. At higher temperatures, the evolution of isoprene, dipentene and different unsaturated volatile products took place. However, PS was degraded in such a way that the monomer was considered as the main degradation product, together with about 30% of low-molecular-weight oligomers. These two types of product were included in the quantification process by FTIR, as both materials displayed bands that were attributable to the deformation vibrations of the aromatic ring.

Bandyopadhyay *et al.* [108] used infrared spectroscopy to identify the polymer, the polymer:blend ratio calculation, the raw material evaluation, the study of reaction mechanism, and the microstructural determination. When NR was characterized using FTIR, the absorbance ratio of specific peaks of different grades of

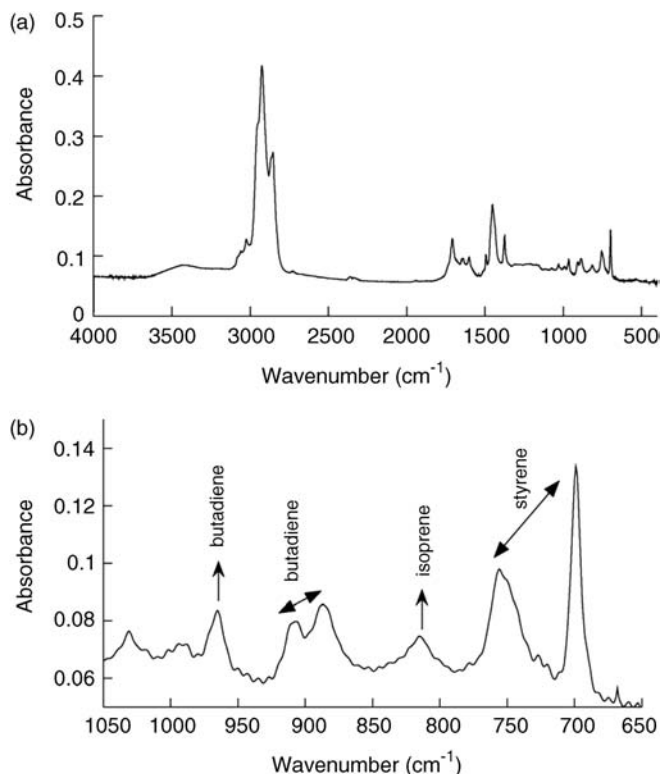


**Figure 20.26** (a) Infrared spectrum of a NR/SBR (40/60) blend; (b) Infrared spectrum in the region between 1050 and 700  $\text{cm}^{-1}$  for a NR/SBR (40/60) blend. Reproduced with permission from Ref. [107]; © 2006, Elsevier.

NR was correlated with the acrylonitrile content measured using the Kjeldhal method. The acrylonitrile content of an unknown acrylonitrile butadiene rubber (nitrile rubber, NBR) was calculated from a calibration graph. The FTIR spectrum of a raw NBR (Figure 20.27a) revealed a nitrile stretching band at 2238  $\text{cm}^{-1}$ , and that of the C—H stretching (out-of-plane) of the butadiene double bond at 969  $\text{cm}^{-1}$ . When this was plotted against the acrylonitrile content of different grades of NBR, the correlation coefficient was found to be 0.99. To verify the correlation coefficient, four fresh samples of NBR with a known acrylonitrile content were prepared and their acrylonitrile contents calculated from the calibration curve in Figure 20.27b. The acrylonitrile content thus calculated showed a good agreement with the experimental value, and the variation in acrylonitrile content was found to be within  $\pm 5.0\%$ . To check the reproducibility of the method, the same sample of NBR with a 33.3% acrylonitrile content was run for seven consecutive days. During this time the acrylonitrile content was measured, using the Kjeldhal method, and a good reproducibility was established.



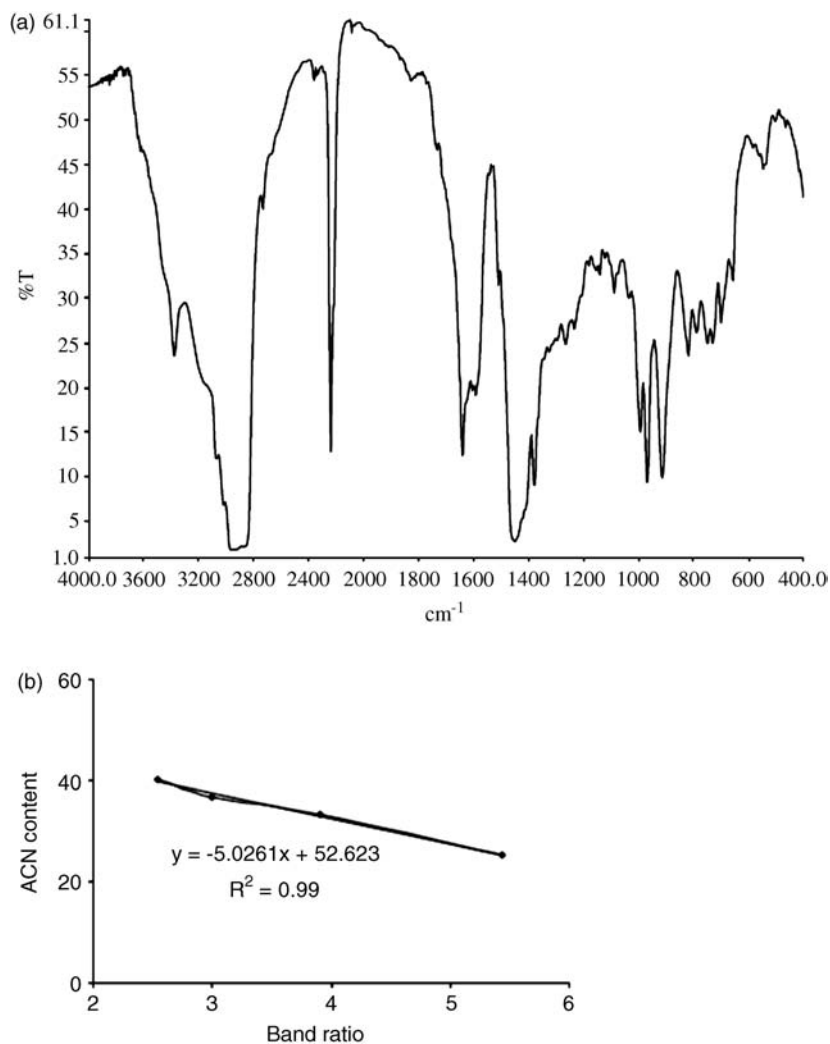


**Figure 20.27** (a) FTIR spectra of acrylonitrile butadiene rubber (film casting); (b) Correlation graph of acrylonitrile content from Kjeldhal method and FTIR. Reproduced with permission from Ref. [108]; © 2007, Elsevier.

## 20.7

### Characterization of Natural Polymer Blends Using FTIR Spectroscopy

#### 20.7.1

##### Collagen Blends

The process of blending collagen with synthetic polymers suffers from the problem of the solubility of the polymeric components in a common solvent. Collagen

solubility depends heavily on the age of the tissue from which it is derived [109–114]. In the case of soluble collagen, it is possible to create a blend with synthetic polymers by forming the blend in a solvent; subsequently, films and sponges can be produced from the blend that are especially useful for biomedical applications. For example, blends of collagen with other hydrophilic polymers can be used as hydrogels, and also as biodegradable polymeric scaffolds in medical applications [115–120]. One important advantage of such biodegradability is the avoidance of surgery to remove the polymer from the body when the implanted device is no longer needed. Highly porous structures of scaffolds maintain large areas to which the cells can attach and proliferate. Various synthetic polymers can be used for blends, including PVP, PVA, PEG and PEO, with thin films, hydrogels and sponges being prepared from the blends. Collagen films can be easily created by solvent evaporation from collagen solution, and by treating the collagen gel solutions with different concentrations of glutaraldehyde and/or other crosslinking agents. Polymeric films based on blends of natural polymers and synthetic polymers have been obtained by solvent evaporation from a collagen solution in acetic acid. Miscibility between the two components has been studied using viscometry, FTIR and DSC. The miscibility of the above-mentioned polymers in thin films has been confirmed by monitoring the FTIR spectra of collagen and collagen/synthetic polymer blends. FTIR is a very powerful technique for detecting intermolecular interactions between two polymers. The inter-molecular interaction through hydrogen bonding can be characterized with FTIR because the specific interaction affects the local electron density (Figure 20.28a), and a corresponding frequency shift can be observed. An example of hydrogen bonding between a collagen molecule and PVP is shown in Figure 20.28a. The shift of the amide bands in the FTIR spectra of the blend suggests an interaction between collagen and PVP by hydrogen bonding. Collagen, which is a hydrogen donor, forms a hydrogen bond with the carbonyl group of PVP. The pyrrolidone rings in PVP contain a proton-accepting carbonyl moiety, while collagen presents hydroxyl and amino groups.

### 20.7.2

#### **Chitosan Blends**

Chitosan is a biodegradable natural polymer with great potential for pharmaceutical and cosmetic applications due to its biocompatibility, high charge density, non-toxicity, and mucoadhesion. Recently, chitosan has attracted attention because of its wide range of applications that include medical, wastewater treatment, biomembranes and hydrogel development. Chitosan has also recently been used widely for drug delivery systems. The macromolecular chain of chitosan can be stiff, yet also have the ability to form a stable liquid crystalline phase in acetic acid solution [122,123]. However, the stiffness of the macromolecular chain of chitosan is very sensitive to pH, with even a small perturbation in pH changing the properties of the chains (Figure 20.28b).

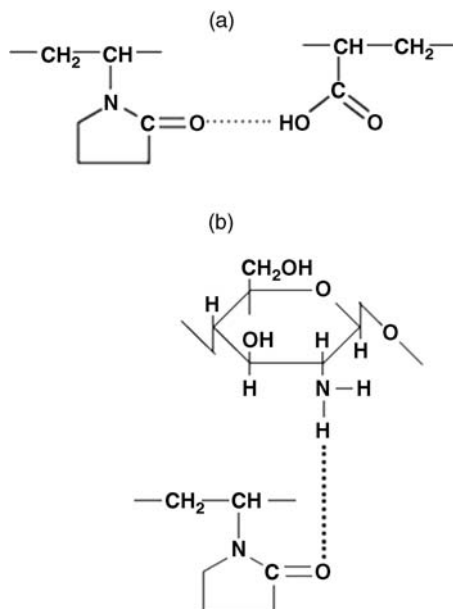


**Figure 20.28** (a) Hydrogen bonding in collagen/PVP blend; (b) Hydrogen bonding between chitosan and synthetic polymer. Reproduced with permission from Ref. [121]; © 2011, Elsevier.

Blends of chitosan with hydrophilic polymers such as PVA, PEO and PVP have been investigated as candidates for oral gingival delivery systems [124,125]. Chitosan–PVP blends can be used in drug-release systems, and also to control the release profile of a drug with poor water solubility. Several research groups have demonstrated the miscibility of chitosan and PVP, and the possibility of using the blended material. PVA, a synthetic polymer, is appropriate for blending with chitosan, especially as chitosan and PVA form an immiscible system in which the interactions between the PVA macromolecules are stronger than those between PVA and chitosan [124]. In a phase-separated system, chitosan–PVA blends were shown to demonstrate interesting and exploitable properties, to be superior to chitosan alone in terms of other properties, and to show great promise as formulations in drug-delivery systems [125]. Several methods have been used to study the interaction of chitosan with the synthetic polymers mentioned above. Results from FTIR analyses have indicated that chitosan/PEO and chitosan/PVP blends each show evidence of miscibility, but the chitosan/PVA blend only shows evidence of interaction when the PVA content is greater than that of the chitosan.

## 20.8

### Study of Blends by Polarization Modulation and 2D-FTIR Spectroscopy

In order to follow the accurate dynamics of orientation, Pérolet *et al.* [126] employed polarized FTIR spectroscopy to study polymer orientation, and coupled

the technique with polarization modulation (PM). This allowed the dichroic difference spectrum to be recorded directly, minimizing instrumental and sample fluctuations. The results obtained confirmed the high efficiency of polarization modulation infrared linear dichroism (PM-IRLD) to determine quantitatively the time dependence of the orientation function of several chemical groups during the orientation and relaxation processes (Figure 20.29a). The *in-situ* dynamics of orientation during the deformation and relaxation processes of DR1M- Random copolymers of 4'-[(2-(methacryloyloxyethyl)ethylaminol]-4-nitroazobenzene BEM-4-nitrophenyl 4-[[2-[(2-methyl-1-oxo-2-propenyl)oxy] ethyl]oxy] benzoate) was presented for both stretched films of PS and PVME blends. The synchronous 2D-IR map of poly(DR1M-*co*-BEM) between 1300 and 1630  $\text{cm}^{-1}$  (see Figure 20.29a and b) showed several correlation peaks. Except for the negative peak at 1527  $\text{cm}^{-1}$ , all remaining peaks were positive, which showed that the bands in the dichroic difference spectra had increased cumulatively in intensity in the same

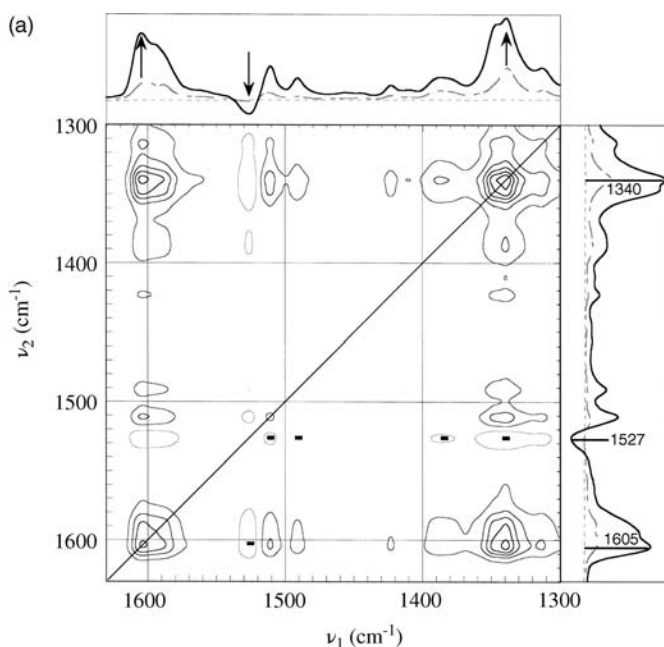


**Figure 20.29** (a) Synchronous 2D-FTIR correlation map of poly\_DR1M-*co*-BEM. with a DR1M mole fraction of 0.23 during the photo-induced orientation process. In this figure, the negative peaks are indicated by a minus sign and the one-dimensional (1D) spectra are the dichroic difference spectra recorded after 5 min (dashed line) and 60 min (solid line) of irradiation; (b) Asynchronous 2D-FTIR

correlation map of poly\_DR1M-*co*-BEM with a DR1M mole fraction of 0.23 during the photo-induced orientation process. In this figure, the negative peaks are indicated by a minus sign and the 1D spectra are the dichroic difference spectra recorded after 5 min (dashed line) and 60 min (solid line) of irradiation. Reproduced with permission from Ref. [126]; © 1998, Elsevier.

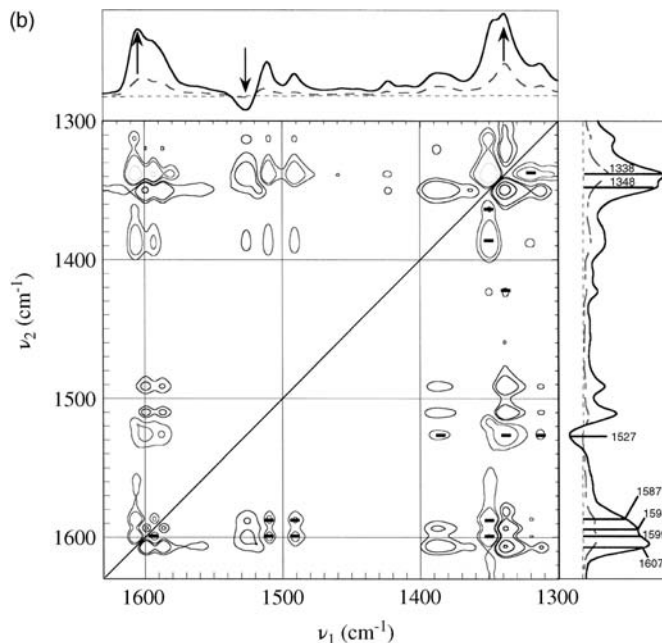


Figure 20.29 (Continued)

direction. The NO vibration of the DR1 M and BEM side chains indicated a strong and unresolved peak around  $1339\text{ cm}^{-1}$ . The negative peak at  $1527\text{ cm}^{-1}$  was assigned to the antisymmetric stretching vibration of the NO group, its transition moment being perpendicular to that of the NO vibration at  $1339\text{ cm}^{-1}$ . The intensity of the bands associated with these two vibrations changed in opposite directions. A strong and highly asymmetric positive cross-correlation peak between the NO vibrations and the C5C stretching vibrations of the *para*-substituted phenyl rings of the DR1 M and BEM side chains were also observed at around  $1339\text{--}1600\text{ cm}^{-1}$ , showing clearly that the DR1 M and BEM groups moved as rigid rods when the polymer was irradiated with polarized visible light. Figure 20.29b shows the spectral resolution markedly enhanced in the asynchronous map of the copolymer that was characterized by several cross-peaks that provide further insight into the reorientation rates of the two types of side chain in the copolymer. This revealed that the NO band contained two components located at  $1338\text{ cm}^{-1}$  and  $1348\text{ cm}^{-1}$ , frequencies which exactly matched those observed in the spectra of DR1 M and BEM homopolymers, respectively w4x. Since the cross peak at  $1338\text{--}1348\text{ cm}^{-1}$  was negative above the diagonal, Noda's rules indicated that the component at  $1338\text{ cm}^{-1}$  grew more rapidly than that at  $1348\text{ cm}^{-1}$ , and that the absorbing DR1 M side chains oriented more rapidly than the inert BEM ones. The two pairs of peaks at  $1587$  and  $1599\text{ cm}^{-1}$  and  $1594$  and  $1607\text{ cm}^{-1}$  are assigned to the  $\nu_{8a}$  and  $\nu_{8b}$  C=C stretching vibrations of the *para*-substituted phenyl rings of the DR1 M and BEM side chains, respectively. With regards to the NO bands, the

frequency of these was in perfect agreement with those of the homopolymers, and their sign showed that the DR1M groups oriented with a faster rate constant than the BEM side chains. The quantitative analysis using a biexponential function of the intensity of the different components after band decomposition shows that for a 23 mol% DR1M content, the fast rate constant of the DR1M groups was fivefold larger than that of the phenyl benzoate side chains [127,128].

## 20.9

### Analysis of Polymer Blends Using FTIR Microspectroscopy

The coupling of an infrared interferometer to a microscope equipped with specialized detectors has been employed widely to examine microscopic areas in polymer FTIR microspectroscopy, and has experienced a renaissance in terms of the capability of instrumentation and visualization afforded for examining multi-component polymer blends. The insight this technique provides information about the composition, formation and behavior of polymeric materials. Phase-separated blends of PVA and poly(vinyl acetate) (PVAc) were studied, and evidence of intra-molecular and inter-molecular specific interactions was reported to depend on the blend composition [129]. Blends with a high PVA content were reported to have large intra-molecular specific interactions, whereas blends with a high PVAc content showed inter-molecular interactions. FTIR mapping spatial resolution was often reported to be insufficient to determine morphological information such as size and shape, which required additional microscopic approaches. A model polymer blend system, poly(methyl methacrylate) (PMMA) and poly(styrene-*co*-acrylonitrile) (PSAN), was studied in an attempt to characterize the phase diagram of the blend system [130]. A poor correlation was found between the phase diagram determined in this manner and that obtained with optical microscopy. The inconsistency developed from the large spot size of the infrared beam and the lack of spatial fidelity of the apertured spectra. Olefinic blends have often been used in utility polymeric articles. In a model blend system, the refractive indices of the two components, isotactic polypropylene (iPP) and syndiotactic polypropylene (sPP), were close enough for their phase-separated blend to be deemed single phase by optical microscopy. However, chemical mapping of the sample showed a clear phase separation based on spectral differences [131]. FTIR imaging allowed the examination of semi-crystalline polymers via their dichroism [132,133]. The spherulitic structure, as visible in polarized optical microscopy, could be reproduced based on the orientation of the transition dipole moments of functional groups. With an infrared polarizer in the beam path, the degree of orientation for each vibrational mode was determined by the generation of spatially resolved dichroic ratio images. When a melt-miscible polymer system was analyzed at temperatures lower than the crystallization temperature of one of the constituents, a phase-separated/single crystalline phase structure was obtained. When the  $T_g$  of the non-crystalline component was lower than the crystallization temperature, the component phase separated as it was rejected from the crystal structure.

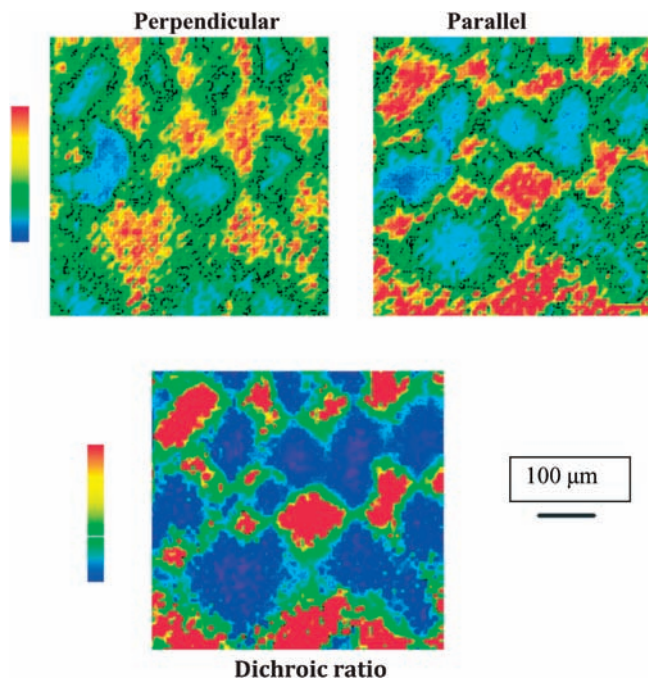


**Figure 20.30** Infrared images of spherulites using perpendicular (left, top) and parallel (right, top) polarized radiation obtained from PEG ( $M_v = 35$  K), quenched from 100°C to room temperature. The images were obtained by plotting the  $1343\text{ cm}^{-1}$ :  $\text{CH}_2$  wag vibrational

mode of the PEG chain. The image at the bottom is a dichroic ratio image obtained by pixel-by-pixel division of the upper two images. Reproduced with permission from Ref. [132]; © 1999, John Wiley & Sons, Inc.

The extent of phase separation could be visualized using IR imaging. PVAc/PEO and high  $M_w$ /low  $M_w$  PEO blends have been imaged to examine the degree of segregation (Figure 20.30) [132]. The morphology, composition and chemical interaction in the interphases were employed to correlate to properties and design better composite materials. High-throughput chemical imaging, as provided by FTIR imaging, can considerably speed up quality checks and characterization of the components of these engineered polymer blends.

## 20.10 Conclusions

Infrared spectroscopy is ideally suited to the qualitative analysis of polymer starting materials, finished products, and the quantification of components in polymer mixtures. FTIR spectroscopy is reliable, fast and cost-effective. This chapter describes several approaches to the quantitative measurement and analysis of IR spectra of typical polymer samples, particularly for the identification of hydrogen

bonding and miscibility in polymer blends. Most commercial blends consist of two polymers combined with small amounts of a third, compatibilizing polymer – typically a block or graft copolymer. The composition analysis of these materials can prove challenging, inasmuch as component compatibilities tend to counteract the ready separation of components. Polymer blends are thus populations of independent molecular distributions, each of which can vary in molar mass and the composition of functional groups. Blends have the potential to be used as membranes for dialysis, wound dressings, artificial skin and implantable devices for the delivery of biologically active compounds. Packaging material for medical devices, drugs and food can also be prepared from blends of natural and man-made polymers, including especially biodegradable materials. Many reports on the properties of newly developed materials have been based on blends of natural and synthetic polymers, although many of these materials are far from commercialization. Nonetheless, the number of reports on polymeric blends suggests that, in the near future, a huge interest in the production of new products should arise based on blends of natural and synthetic polymers.

### Acknowledgments

Dr Ufana Riaz wishes to acknowledge the Department of Science and Technology - Science and Engineering Research Board (DST-SERB) of India, vide sanction no. SB/S-1/PC-070-2013, for grants supporting this research project.

### Abbreviations

<b>Alg</b>	Alginate
<b>BEM</b>	4-nitrophenyl 4-[[2-[(2-methyl-1-oxo-2-propenyl)-oxy] ethyl]oxy] benzoate)
<b>DBP</b>	dibutyl phthalate
<b>DMA</b>	Dynamic mechanical analysis
<b>DM</b>	<i>N,N</i> -dimethylformamide
<b>DR1M</b>	Random copolymers of 4'-[(2-(methacryloyloxy-ethyl)ethylamino)]-4-nitroazobenzene
<b>DSC</b>	Differential scanning calorimetry
<b>EC</b>	ethylene carbonate
<b>EVOH</b>	ethylene alcohol vinyl
<b>FTIR</b>	Fourier transform infrared spectroscopy
<b>LiCF<sub>3</sub>SO<sub>3</sub></b>	lithium triflate
<b>NMR</b>	Nuclear magnetic resonance
<b>NR</b>	Nitrile rubber
<b>PAMP</b>	Poly(2-acrylamido-2-methyl-1-propanesulfonic acid)
<b>PCL</b>	Polycaprolactone
<b>PBA</b>	Poly (butyl acrylate)



PBAAA	Poly(butyl acrylate-co-acrylic acid)
PBZZ	Polybenzoxazine
PDLLA	-Poly(D,L-lactide)
PE	Polyethers
PEMA	Poly(ethylmethacrylate)
PEO	Polyethylene oxide
PESeb	Poly(ethylene sebacate)
PEG	Poly(ethylene glycol)
PET	Polyethylene terephthalate
P(HB- <i>co</i> -HHx)	Poly(R)-3-hydroxybutyrate- <i>co</i> -(R)-3-hydroxyhexanoate)
PHBV	Poly-(3-hydroxybutyrate- <i>co</i> -3-hydroxyvalerate)
PLLA	Poly(L-lactide)
PP	polypropylene
PVME	Poly(vinyl methyl ether)
PVIm	Poly(1-vinylimidazole)
PMMA	Poly(methylmethacrylate)
PVA	Poly(vinyl alcohol)
PVAc	Poly(vinyl acetate)
PVC	Polyvinyl chloride
PVME	Poly (vinyl methyl ether)
PVPh	Poly(4-vinylphenol)
PVP	Poly(vinylpyrrolidone)
SAXS	Small-angle X-ray scattering
SPS	Sodium sulfonated polystyrene
SR	Styrenated rubber
STVPh	Poly(styrene- <i>co</i> -4-vinylphenol)
$T_g$	Glass transition temperature
TGA	Thermogravimetric analysis
THF	Tetrahydrofuran
VPh	Vinylphenol

## References

- Guerra, E.S. and Lima, E.V. (2013) *Handbook of Polymer Synthesis, Characterization and Processing*, John Wiley & Sons, New York.
- Robeson, L.M. (2007) *Polymer Blends: A Comprehensive Review*, Hanser Gardner.
- Utracki, L.A. (2000) *Polymer Blends*, Smithers Rapra, New York.
- Walsh, D.J. (1989) *Comprehensive Polymer Science* (eds C. Booth and C. Price), Pergamon Press, New York.
- Cowie, J.M.G. (1989) *Encyclopedia of Polymer Science and Engineering*, 2nd edn, supplement volume, John Wiley & Sons, New York.
- Olabisi, O., Robeson, L.M., and Shaw, M.T. (1979) *Polymer-Polymer Miscibility*, Academic Press, New York.
- De Juana, R., Hernandez, R., Pena, J.J., Santamaria, A., and Cortazar, M. (1994) Secondary relaxations in a miscible polymer system: poly(hydroxy ether of bisphenol A)/poly(epsilon-caprolactone) blends. *Macromolecules*, **27**, 6980–6984.

- 8 Murayama, T. (1978) *Dynamical Mechanic Analysis of Polymeric Materials*, Elsevier, New York.
- 9 McBrierty, V.J. and Douglass, D.C. (1981) Recent advances in the NMR of solid polymers. *J. Polym. Sci. Macromol. Rev.*, **16**, 295–366.
- 10 Wang, J., Cheung, M.K., and Mia, Y. (2002) Miscibility and morphology in crystalline/amorphous blends of poly (caprolactone)/poly(4-vinylphenol) as studied by DSC, FTIR, and  $^{13}\text{C}$  solid state NMR. *Polymer*, **43** (4), 1357–1364.
- 11 Simmons, A. and Natansohn, A. (1991) Solid-state NMR study of charge-transfer interactions in polymer blends. *Macromolecules*, **24** (12), 3651–3661.
- 12 Zhang, X., Takegoshi, K., and Hikichi, K. (1992) Composition dependence of the miscibility and phase structure of amorphous/crystalline polymer blends as studied by high-resolution solid-state carbon-13 NMR spectroscopy. *Macromolecules*, **25** (9), 2336–2340.
- 13 Chambon, S., Mens, R., Vandewal, K., Clodic, E., Scharber, M., Lutsen, L., Gelan, J., Manc, J., Vanderzande, D., and Adriaenssens, P. (2012) Influence of octanedithiol on the nanomorphology of PCPDTBT:PCBM blends studied by solid-state NMR. *Solar Energy Mater. Solar Cells*, **96**, 210–217.
- 14 Daniliuc, L. and David, C. (1996) Intermolecular interactions in blends of poly(vinyl alcohol) with poly(acrylic acid): 2. Correlation between the states of sorbed water and the interactions in homopolymers and their blends. *Polymer*, **37**, 5219–5227.
- 15 Kubo, S. and Kadla, J.F. (2003) The formation of strong intermolecular interactions in immiscible blends of poly (vinyl alcohol) (PVA) and lignin. *Biomacromolecules*, **4**, 561–567.
- 16 Painter, P.C., Graf, J.F., and Coleman, M.M. (1991) Effect of hydrogen bonding on the enthalpy of mixing and the composition dependence of the glass transition temperature in polymer blends. *Macromolecules*, **24**, 5630–5638.
- 17 Zhang, S.H., Painter, P.C., and Runt, J. (2002) Dynamics of polymer blends with intermolecular hydrogen bonding: broad-band dielectric study of blends of poly(4-vinyl phenol) with poly(vinyl acetate) and EVA70. *Macromolecules*, **35**, 8478–8487.
- 18 Miyoshi, T., Takegoshi, K., and Hikichi, K. (1997) High-resolution solid state  $^{13}\text{C}$  NMR study of the interpolymer interaction, morphology and chain dynamics of the poly(acrylic acid)/poly (ethylene oxide) complex. *Polymer*, **38**, 2315–2320.
- 19 Kuphal, J.A., Sperling, L.H., and Robeson, L.M. (1991) Miscible blends of styrene–acrylic acid copolymers with aliphatic, crystalline polyamides. *J. Appl. Polym. Sci.*, **42**, 1525–1535.
- 20 Landry, M.R., Massa, D.J., Landry, C.J.T., Teegarden, D.M., Colby, R.H., Long, T.E., and Henrichs, P.M. (1994) A survey of poly(vinylphenol) blend miscibility. *J. Appl. Polym. Sci.*, **54**, 991–1011.
- 21 Zhang, X.Q., Takegoshi, K., and Hikichi, K. (1991) Poly(vinylphenol)/poly(methyl acrylate) and poly(vinylphenol)/poly (methylmethacrylate) blends: hydrogen bonding, miscibility, and blending effects on molecular motions as studied by  $^{13}\text{C}$ CP/MAS NMR. *Macromolecules*, **24**, 5756–5762.
- 22 Dong, J. and Yukihiro, O. (1997) FTIR and FT-Raman studies of partially miscible poly(methyl methacrylate)/poly(4-vinylphenol) blends in solid states. *Macromolecules*, **30**, 286–292.
- 23 Christine, J.T.L. and David, M.T. (1991) Heats of mixing of strongly interacting model compounds and miscibility of the corresponding polymers. *Macromolecules*, **24**, 4310–4321.
- 24 Hsu, W.P. (2002) Reexamination of the miscibility of stereoregular poly(methyl methacrylate) with poly(vinyl phenol). *J. Appl. Polym. Sci.*, **83**, 1425–1431.
- 25 Jong, L., Pearce, E.M., and Kwei, T.K. (1993) NMR study of hydrogen bonded polymer blends: influence of the tacticity of poly(methyl methacrylate) on its miscibility with poly (styrene-co-vinylphenol). *Polymer*, **34**, 48–55.
- 26 Hsu, W.P. and Yeh, C.F. (1999) Polymer blends of stereoregular poly (methyl methacrylate) and poly(styrene-co-*p*-hydroxystyrene). *J. Appl. Polym. Sci.*, **73**, 431–440.

- 27 Serman, C.J., Painter, P.C., and Coleman, M.M. (1991) Studies of the phase behavior of poly(vinyl phenol)–poly(*n*-alkyl methacrylate) blends. *Polymer*, **32**, 1049–1058.
- 28 Xu, Y., Graf, J., Painter, P.C., and Coleman, M.M. (1991) Miscibility windows for poly(styrene-co-vinylphenol) blends with poly(*n*-butyl methacrylate) and poly(*n*-hexyl methacrylate): a comparison of theoretical predictions with Fourier transform infrared experimental data. *Polymer*, **32**, 3103–3118.
- 29 Mugica, A., Calahorra, M.E., and Cortazar, M. (2002) Compositional variation of glass-transition temperature in miscible polymer blends involving weak and strong specific interactions. *Macromol. Chem. Phys.*, **203**, 1088–1098.
- 30 Huang, X.D., Goh, S.H., Lee, S.Y., Zhao, Z. D., Wong, M.W., and Huan, C.H.A. (1999) Miscibility and interactions in blends and complexes of poly[2-(dimethylamino)ethyl methacrylate] with poly(*p*-vinylphenol). *Macromolecules*, **32**, 4327–4331.
- 31 Goh, S.H., Lee, S.Y., Luo, X.F., Wong, M.W., and Tan, K.L. (2001) Specific interactions in miscible poly(*p*-vinylphenol)/poly(*N*-methyl-3-piperidinemethyl methacrylate) blends. *Macromol. Chem. Phys.*, **202**, 31–35.
- 32 Yi, J.Z., Goh, S.H., and Wee, A.T.S. (2001) Miscibility and interactions in poly(methylthiomethyl methacrylate)/poly(*p*-vinylphenol) blends. *Macromolecules*, **34**, 7411–7415.
- 33 Hill, D.J.T., Whittaker, A.K., and Wong, K.W. (1999) Miscibility and specific interactions in blends of poly(4-vinylphenol) and poly(2-ethoxyethyl methacrylate). *Macromolecules*, **32**, 5285–5291.
- 34 Zhang, L.L., Goh, S.H., and Lee, S.Y. (1999) Miscible blends containing bacterial poly(3-hydroxyvalerate) and poly(*p*-vinylphenol). *J. Appl. Polym. Sci.*, **74**, 383–388.
- 35 Belfiore, L.A., Qin, C., Ueda, E., and Pires, A.T.N. (1993) Solid-state <sup>13</sup>C detection of the isotropic carbonyl line shape in blends of poly(vinylphenol) with main-chain polyesters. *J. Polym. Sci., Part B: Polym. Phys.*, **31**, 409–418.
- 36 Zhang, Z.H., Mo, Z.S., Zhang, H.F., Zhang, Y., Na, T.H., An, Y.X., Wang, X.H., and Zhao, X.J. (2002) Miscibility and hydrogen-bonding interactions in blends of carbon dioxide/epoxy propane copolymer with poly(*p*-vinylphenol). *J. Polym. Sci., Part B: Polym. Phys.*, **40**, 1957–1966.
- 37 Zhang, L.L., Goh, S.H., and Lee, S.Y. (1998) Miscibility and crystallization behavior of poly(L-lactide)/poly(*p*-vinylphenol) blends. *Polymer*, **39**, 4841–4847.
- 38 Zhang, L.L., Goh, S.H., and Lee, S.Y. (1998) Miscibility and phase behavior of poly(D,L-lactide)/poly(*p*-vinylphenol) blends. *J. Appl. Polym. Sci.*, **70**, 811–816.
- 39 Papageorgiou, Z.G., Bikiaris, D.N., and Panayiotou, G.C. (2011) Novel miscible poly(ethylene sebacate)/poly(4-vinyl phenol) blends: Miscibility, melting behavior and crystallization study. *Polymer*, **52**, 4553–4561.
- 40 Xing, P., Dong, L., An, Y., Feng, Z., Avella, M., and Martuscelli, E. (1997) Miscibility and crystallization of poly(β-hydroxybutyrate) and poly(*p*-vinylphenol) blends. *Macromolecules*, **30**, 2726–2733.
- 41 Woo, E.M. and Chiang, C.P. (2004) Glass transition behavior and miscibility in blends of poly(vinyl *p*-phenol) with two homologous aliphatic polyesters. *Polymer*, **45**, 8415–8424.
- 42 Gestoso, P. and Brisson, J. (2003) Investigation of the effect of chain rigidity on orientation of polymer blends: the case of poly(vinyl phenol)/poly(ethylene terephthalate) blends. *Polymer*, **44**, 7765–7776.
- 43 Gestoso, P. and Brisson, J. (2001) Effect of hydrogen bonds on the amorphous phase of a polymer as determined by atomistic molecular modelling. *Comput. Theor. Polym. Sci.*, **11**, 263–271.
- 44 Hevenqvist, M.S., Bharadwaj, K., and Boyd, R.H. (1998) Molecular dynamics simulation of amorphous poly(ethylene terephthalate). *Macromolecules*, **31**, 1556–1564.
- 45 Rinderknecht, S. and Brisson, J. (1999) Orientation of a miscible polymer blend with strong interchain hydrogen bonds:

- poly(vinylphenol)-poly(ethylene oxide). *Macromolecules*, **32**, 8509–8516.
- 46 Gestoso, P. and Brisson, J. (2001) Orientation of uniaxially stretched poly(vinyl phenol)/poly(vinyl methyl ether) blends. *Polymer*, **42**, 8415–8424.
  - 47 Su, Y.-C., Kuo, S.-W., Yei, D.-R., Xu, H., and Chang, F.-C. (2003) Thermal properties and hydrogen bonding in polymer blend of polybenzoxazine/poly(*N*-vinyl-2-pyrrolidone). *Polymer*, **44**, 2187–2191.
  - 48 Lau, C. and Mi, Y. (2002) A study of blending and complexation of poly(acrylic acid)/poly(vinyl pyrrolidone). *Polymer*, **43**, 823–829.
  - 49 Kuo, S.W. and Chang, F.C. (2001) Studies of miscibility behavior and hydrogen bonding in blends of poly(vinylphenol) and poly(vinylpyrrolidone). *Macromolecules*, **34**, 5224–5228.
  - 50 Moskala, E.J., Varnell, D.F., and Coleman, M.M. (1985) Concerning the miscibility of poly(vinyl phenol) blends – FTIR study. *Polymer*, **26**, 228–234.
  - 51 Labuschagne, P.W., Johna, M.J., and Sadiku, R.E. (2010) Investigation of the degree of homogeneity and hydrogen bonding in PEG/PVP blends prepared in supercritical CO<sub>2</sub>: Comparison with ethanol-cast blends and physical mixtures. *J. Supercrit. Fluids*, **54**, 81–88.
  - 52 Painter, P.C., Pehlert, G.J., Hu, Y., and Coleman, M.M. (1999) Infrared band broadening and interactions in polar systems. *Macromolecules*, **32**, 2055–2057.
  - 53 Hu, Y., Motzer, H.R., Etxeberria, A.M., Fernandez-Berridi, M.J., Iruin, J.J., Painter, P.C., and Coleman, M.M. (2000) Concerning the self-association of *N*-vinyl pyrrolidone and its effect on the determination of equilibrium constants and the thermodynamics of mixing. *Macromol. Chem. Phys.*, **201**, 705–714.
  - 54 Chiu, C.Y., Yen, Y.J., Kuo, S.W., Chen, H.W., and Chang, F.C. (2007) Complicated phase behavior and ionic conductivities of PVP-*co*-PMMA-based polymer electrolytes. *Polymer*, **48**, 1329–1342.
  - 55 Kireeva, P.E., Shandryuk, G.A., Kostina, J.V., Bondarenko, G.N., Singh, P., Cleary, G.W., and Feldstein, M.M. (2007) Competitive hydrogen bonding mechanisms underlying phase behavior of triple poly(*N*-vinyl pyrrolidone)–poly(ethylene glycol)–poly(methacrylic acid-*co*-ethylacrylate) blends. *J. Appl. Polym. Sci.*, **105**, 3017–3036.
  - 56 De Ilarduya, A.M., Iruin, J.J., and Fernandez-Berridi, M.J. (1995) Hydrogen bonding in blends of phenoxy resin and poly(vinylpyrrolidone). *Macromolecules*, **28**, 3707–3712.
  - 57 Lau, C. and Mi, Y. (2001) A study of blending and complexation of poly(acrylic acid)/poly(vinyl pyrrolidone). *Polymer*, **43**, 823–829.
  - 58 Mohamed, M., Tripathy, M., and Majeed, A.A. (2013) Studies on the thermodynamics and solute–solvent interaction of polyvinyl pyrrolidone wrapped single walled carbon nanotubes (PVP-SWNTs) in water over temperature range. *K Arab. J. Chem.*, **298.15**–313.15, DOI: 10.1016/j.arabjc.2013.06.022, (in press).
  - 59 Bernal, A., Kuritka, I., and Saha, P. (2013) Preparation and characterization of poly(vinyl alcohol)-poly(vinyl pyrrolidone) blend: A biomaterial with latent medical applications. *J. Appl. Polym. Sci.*, **127** (5), 3560–3568.
  - 60 Sugimura, K., Teramoto, Y., and Nishio, Y. (2013) Blend miscibility of cellulose propionate with poly(*N*-vinyl pyrrolidone-*co*-methyl methacrylate). *Carbohydrate Polym.*, **98** (1), 532–541.
  - 61 Sugimura, K., Katano, S., Teramoto, Y., and Nishio, Y. (2013) Cellulose propionate/poly(*N*-vinyl pyrrolidone-*co*-vinyl acetate) blends: dependence of the miscibility on propionyl DS and copolymer composition. *Cellulose*, **20** (1), 239–252.
  - 62 Wissinger, R.G. and Paulaitis, M.E. (1987) Swelling and sorption in polymer–CO<sub>2</sub> mixtures at elevated pressures. *J. Polym. Sci., Part B: Polym. Phys.*, **25**, 2497–2510.
  - 63 Shieh, Y.T., Su, J.H., Manivannan, G., Lee, P.H.C., Sawan, S.P., and Spall, W.D. (1996) Interaction of supercritical carbon dioxide with polymers. II. Amorphous polymers. *J. Appl. Polym. Sci.*, **59**, 707–717.
  - 64 Muth, O., Hirth, T., and Vogel, H. (2000) Polymer modification by supercritical impregnation. *J. Supercrit. Fluid*, **17**, 65–72.

- 65 Wu, H.D., Chu, P.P., Ma, C.C.M., and Chang, F.C. (1999) Effects of molecular structure of modifiers on the thermodynamics of phenolic blends: an entropic factor complementing PCAM. *Macromolecules*, **32**, 3097–3105.
- 66 Ping, Z.H., Nguyen, Q.T., and Neel, J. (1989) Investigations of poly(vinyl alcohol)/poly(*N*-vinyl-2-pyrrolidone) blends. 1. Compatibility. *Makromol. Chem.*, **19**, 437–448.
- 67 Wang, P. and Ando, I. (1999) A study of structure and dynamics of poly(aspartic acid) sodium/poly(vinyl alcohol) blends by <sup>13</sup>C CP/MAS NMR. *J. Mol. Struct.*, **508**, 103–109.
- 68 Ciemniecki, S.L. and Glasser, W.G. (1988) Multiphase materials with lignin: 2. Blends of hydroxypropyl lignin with poly(vinyl alcohol). *Polymer*, **29**, 1030–1036.
- 69 Parada, L.G., Cesteros, L.C., Meaurio, E., and Katime, I. (1998) Miscibility in blends of poly(vinyl acetate-co-vinyl alcohol) with poly(*N,N*-dimethylacrylamide). *Polymer*, **39**, 1019–1024.
- 70 Zheng, S.X., Huang, J.Y., Liu, W.Y., Yang, X.T., and Guo, Q.P. (1996) Miscibility and phase behavior in blends of poly(vinyl alcohol) and a copolyamide. *Eur. Polym. J.*, **32**, 757–760.
- 71 Park, J.S., Park, J.W., and Ruckenstein, E. (2001) A dynamic mechanical and thermal analysis of unplasticized and plasticized poly(vinyl alcohol)/methyl cellulose blends. *J. Appl. Polym. Sci.*, **80**, 1825–1834.
- 72 Lee, Y.M., Kim, S.H., and Kim, S.J. (1996) Preparation and characteristics of b-chitin and poly(vinyl alcohol) blend. *Polymer*, **37**, 5897–5905.
- 73 Brunelli, D.D., Atvars, T.D.Z., Joekes, I., and Barbosa, V.C. (1998) Mapping phases of poly(vinyl alcohol) and poly(vinyl acetate) blends by FTIR microspectroscopy and optical fluorescence microscopy. *J. Appl. Polym. Sci.*, **69**, 645–655.
- 74 Shuai, X., He, Y., Asakawa, N., and Inoue, Y. (2001) Miscibility and phase structure of binary blends of poly(L-lactide) and poly(vinyl alcohol). *J. Appl. Polym. Sci.*, **81**, 762–772.
- 75 Kubo, S. and Kadla, J.F. (2003) The formation of strong intermolecular interactions in immiscible blends of poly(vinyl alcohol) (PVA) and lignin. *Biomacromolecules*, **4**, 561–567.
- 76 Cesteros, L.C., Isasi, J.R., and Katime, I. (1994) Study of the miscibility of poly(vinyl pyridines) with poly(vinyl acetate), poly(vinyl alcohol) and their copolymers. *J. Polym. Sci., Part B: Polym. Phys.*, **32**, 223–230.
- 77 Parada, L.G., Cesteros, L.C., Meaurio, E., and Katime, I. (1997) Miscibility and specific interactions in blends of poly(vinyl acetate-co-vinyl alcohol) with poly(ethylloxazoline). *Macromol. Chem. Phys.*, **198**, 2505–2517.
- 78 Aoi, K., Takasu, A., Tsuchiya, M., and Okada, M. (1998) New chitin-based polymer hybrids. Part 3. Miscibility of chitin-graft-poly(2-ethyl-2-oxazoline) with poly(vinyl alcohol). *Macromol. Chem. Phys.*, **199**, 2805–2811.
- 79 Lasagabaster, A.L., Abad, M.J., Barral, L., Ares, A., and Bouza, R. (2009) Application of FTIR spectroscopy to determine transport properties and water–polymer interactions in polypropylene (PP)/poly(ethylene-co-vinyl alcohol) (EVOH) blend films: Effect of poly(ethylene-co-vinyl alcohol) content and water activity. *Polymer*, **50**, 2981–2989.
- 80 Sudhamania, S.R., Prasad, M.S., and Sankar, K.U. (2003) DSC and FTIR studies on Gellan and polyvinyl alcohol (PVA) blend films. *Food Hydrocolloids*, **17**, 245–250.
- 81 Islam, M.S. and Karim, M.R. (2010) Fabrication and characterization of poly(vinyl alcohol)/alginate blend nanofibers by electrospinning method. *Colloids Surf. A: Physicochem. Eng. Aspects*, **336** (1–3), 135–140.
- 82 Cai, H.J., Kadi, A.A., and Brisson, J. (2003) Dynamic rheological analysis of a miscible blend showing strong interactions. *Polymer*, **44**, 1481–1489.
- 83 Pedrosa, P., Pomposo, J.A., Calahorra, E., and Cortazar, M. (1994) On the glass transition behavior, interaction energies, and hydrogen bonding strengths of binary poly(*p*-vinylphenol)/polyether blends. *Macromolecules*, **27**, 102–109.
- 84 Prinos, A., Domprios, A., and Panayiotou, C. (1998) Thermoanalytical and

- spectroscopic study of poly(vinyl pyrrolidone)/poly(styrene-co-vinyl phenol) blends. *Polymer*, **39**, 3011–3016.
- 85 Yi, J.Z., Goh, S.H., and Wee, A.T.S. (2001) Miscibility and interactions in poly(*N*-acryloylthiomorpholine)/poly(*p*-vinylphenol) blends. *Macromolecules*, **34**, 4662–4665.
  - 86 Wang, J., Cheung, M.K., and Mi, Y.L. (2001) Miscibility of poly(ethyl oxazoline)/poly(4-vinylphenol) blends as investigated by the high-resolution solid-state  $^{13}\text{C}$  NMR. *Polymer*, **42**, 2077–2083.
  - 87 Liu, Y., Goh, S.H., Lee, S.Y., and Huan, C.H.A. (1999) Miscibility and interactions in blends and complexes of poly(*N*-acryloyl-*N*<sub>0</sub>-methylpiperazine) with poly(*p*-vinylphenol). *Macromolecules*, **32**, 1967–1971.
  - 88 Luo, X.F., Goh, S.H., and Lee, S.Y. (1999) Miscibility and interpolymer complexation of poly(1-vinylimidazole) with hydroxyl- and carboxyl-containing polymers. *Macromol. Chem. Phys.*, **200**, 399–404.
  - 89 Pereira, A.G.B., Paulino, A.T., Nakamura, C.V., Britta, E.A., Rubira, A.F., and Muniz, E.C. (2011) Effect of starch type on miscibility in poly(ethylene oxide) (PEO)/starch blends and cytotoxicity assays. *Mater. Sci. Eng. C*, **31**, 443–451.
  - 90 He, Y., Zhu, B., and Inoue, Y. (2004) Hydrogen bonds in polymer blends. *Prog. Polym. Sci.*, **29**, 1021–1051.
  - 91 Meier, R.J. (2005) Vibrational spectroscopy: a ‘vanishing’ discipline? *Chem. Soc. Rev.*, **34**, 743–752.
  - 92 Ramesh, S., Yuen, T.F., and Shen, C.J. (2008) Conductivity and FTIR studies on PEO–LiX [ $\text{X}: \text{CF}_3\text{SO}_3^-, \text{SO}_4^{2-}$ ] polymer electrolytes. *Spectrochim. Acta A*, **69**, 670–675.
  - 93 Sawatari, C., Kondo, T., Inamura, I., and Jinbo, Y. (1991) Interchain hydrogen bonds in blend films of poly(vinyl alcohol) and its derivatives with poly(ethylene oxide). *Polym. J.*, **23**, 1143–1147.
  - 94 Sawatari, C. and Kondo, T. (1999) Interchain hydrogen bonds in blend films of poly(vinyl alcohol) and its derivatives with poly(ethylene oxide). *Macromolecules*, **32** (6), 1949–1955.
  - 95 Kuo, S.W., Lin, C.-L., and Chang, F.C. (2002) Phase behavior and hydrogen bonding in ternary polymer blends of phenolic resin/poly(ethylene oxide)/poly(caprolactone). *Macromolecules*, **35**, 278–285.
  - 96 Kuo, S.W. and Chang, F.C. (2001) Miscibility and hydrogen bonding in blends of poly(vinyl phenol-co-methyl methacrylate) with poly(ethylene oxide). *Macromolecules*, **34**, 4089–4097.
  - 97 Mailhot, B., Morlat, S., and Gardette, J.L. (2000) Photooxidation of blends of polystyrene and poly(vinyl methyl ether): FTIR and AFM studies. *Polymer*, **41**, 1981–1988.
  - 98 Bhutto, A.A., Vesely, D., and Gabrys, B.J. (2003) Miscibility and interactions in polystyrene and sodium sulfonated polystyrene with poly(vinyl methyl ether) PVME blends. Part II. FTIR. *Polymer*, **44**, 6627–6631.
  - 99 Ramesh, S., Leen, K.H., Kumuth, K., and Arof, A.K. (2007) FTIR studies of PVC/PMMA blend based polymer electrolytes. *Spectrochim. Acta A*, **66**, 1237–1242.
  - 100 Rajendran, S. and Uma, T. (2000) Effect of  $\text{ZrO}_2$  on conductivity of PVC– $\text{LiBF}_4$ –DBP polymer electrolytes. *Mater. Lett.*, **44**, 208–214.
  - 101 Rajendran, S., Kannan, R., and Mahendran, O. (2001) An electrochemical investigation on PMMA/PVdF blend-based polymer electrolytes. *Mater. Lett.*, **49**, 172–179.
  - 102 Hsu, W.P. (2003) Phase behavior of hydrogen-bonded ternary polymer blends. *J. Appl. Polym. Sci.*, **89**, 2088–2094.
  - 103 Jannasch, P., Gunnarsson, O., and Wesslen, B. (1996) Compatibilizing effects of poly(styrene-graft-ethylene oxide) in blends of polystyrene and butyl acrylate polymers. *J. Appl. Polym. Sci.*, **59**, 619–626.
  - 104 Zhao, J.Q., Pearce, E.M., and Kwei, T.K. (1997) Binary and ternary blends of polystyrene-block-poly(*p*-hydroxystyrene). *Macromolecules*, **30**, 7119–7126.
  - 105 Fei, B., Chen, C., Wu, H., Peng, S., Wang, X., and Dong, L. (2003) Quantitative FTIR study of PHBV/bisphenol A blends. *Eur. Polym. J.*, **39**, 1939–1946.
  - 106 Furukawa, T., Sato, H., Murakami, R., Zhang, J., Noda, I., Ochiai, S., and Ozaki, Y. (2007) Comparison of miscibility and structure of poly(3-hydroxybutyrate-co-3-

- hydroxyhexanoate)/poly(L-lactic acid) blends with those of poly(3-hydroxybutyrate)/poly(L-lactic acid) blends studied by wide-angle X-ray diffraction, differential scanning calorimetry, and FTIR microspectroscopy. *Polymer*, **48** (6), 1749–1755.
- 107 Jose, M., Berridi, F., González, N., Mugica, A., and Bernicot, C. (2006) Pyrolysis-FTIR and TGA techniques as tools in the characterization of blends of natural rubber and SBR. *Thermochim. Acta*, **444**, 65–70.
  - 108 Chakraborty, S., Bandyopadhyay, S., Ameta, R., Mukhopadhyay, R., and Deurib, A.S. (2007) Application of FTIR in characterization of acrylonitrile-butadiene rubber (nitrile rubber). *Polymer Testing*, **26**, 38–41.
  - 109 Cascone, M.G., Giusti, P., Lazzeri, L., Pollicino, A., and Recca, A. (1996) Surface characterization of collagen-based bioartificial polymeric materials. *J. Biomater. Sci. Polym. Ed.*, **7**, 917–924.
  - 110 Rao, K.P. (1995) Recent developments of collagen-based materials for medical applications and drug delivery systems. *J. Biomater. Sci. Polym. Ed.*, **7**, 623–631.
  - 111 Shenoy, V. and Rosenblatt, J. (1995) Diffusion of macromolecules in collagen and hyaluronic acid, rigid-rod-flexible polymer, composite matrices. *Macromolecules*, **28**, 8751–8756.
  - 112 Barbani, N., Lazzeri, L., Cristallini, C., Cascone, M.G., Polacco, G., and Pizzirani, G. (1999) Bioartificial materials based on blends of collagen and poly(acrylic acid). *J. Appl. Polym. Sci.*, **72**, 971–975.
  - 113 Taravel, M.N. and Domard, A. (1995) Collagen and its interaction with chitosan. II. Influence of the physicochemical characteristics of collagen. *Biomaterials*, **16**, 865–871.
  - 114 Taniguchi, T. and Okamura, K. (1998) New films produced from micro fibrillated natural fibers. *Polym. Int.*, **47**, 291–294.
  - 115 Dai, N.T., Williamson, M.R., Khammo, N., Adams, E.F., and Coombes, A.G.A. (2004) Composite cell support membranes based on collagen and polycaprolactone for tissue engineering of skin. *Biomaterials*, **25**, 4263–4271.
  - 116 Lopes, C.M.A. and Felisberti, M.I. (2003) Mechanical behaviour and biocompatibility of poly(1-vinyl-2-pyrrolidone)–gelatin IPN hydrogels. *Biomaterials*, **24**, 1279–1284.
  - 117 Dutoya, S., Lefebvre, F., Deminieres, C., Rouais, F., Verna, A., Kozluca, A., and Le Bugle, A. (1998) Unexpected original property of elastin-derived proteins: spontaneous tight coupling with natural and synthetic polymers. *Biomaterials*, **19**, 147–155.
  - 118 Scotchford, C.A., Cascone, M.G., Downes, S., and Giusti, P. (1998) Osteoblast responses to collagen–PVA bioartificial polymers in vitro: the effects of cross-linking method and collagen content. *Biomaterials*, **19**, 1–11.
  - 119 Sarti, B. and Scandola, M. (1995) Viscoelastic and thermal properties of collagen/poly(vinyl alcohol) blends. *Biomaterials*, **16**, 785–792.
  - 120 Nezu, T. and Winnik, F.M. (2000) Interaction of water-soluble collagen with poly(acrylic acid). *Biomaterials*, **21**, 415–419.
  - 121 Sionkowska, A. (2011) Current research on the blends of natural and synthetic polymers as new biomaterials: Review. *Prog. Polymer Sci.*, **36** (9), 1254–1276.
  - 122 Shanmugasundaram, N., Ravichandran, P., Neelakanta, P.R., Nalini, R., Subrata, P., and Rao, K.P. (2001) Collagen–chitosan polymeric scaffolds for the in vitro culture of human epidermoid carcinoma cells. *Biomaterials*, **22**, 1943–1951.
  - 123 Khor, E. and Lim, L.Y. (2003) Implantable applications of chitin and chitosan. *Biomaterials*, **24**, 2339–2349.
  - 124 Karavas, E., Georgarakis, E., and Bikiaris, D. (2006) Adjusting drug release by using miscible polymer blends as effective drug carriers. *J. Therm. Anal. Calorim.*, **84**, 125–133.
  - 125 Khoo, C.G.L., Frantzich, S., Rosinski, A., Sjoström, M., and Hoogstraate, J. (2003) Oral gingival delivery systems from chitosan blends with hydrophilic polymers. *Eur. J. Pharm. Biopharm.*, **55**, 47–56.
  - 126 Pezoleta, M., Pellerin, C., Prud'homme, R.E., and Beau, T. (1998) Study of polymer orientation and relaxation by polarization

- modulation and 2D-FTIR spectroscopy. *Vib. Spectrosc.*, **18**, 103–110.
- 127 Buffeteau, T., Natansohn, A., Rochon, P., and Pézolet, M. (1996) Study of cooperative side group motions in amorphous polymers by time dependent infrared spectroscopy. *Macromolecules*, **29**, 8783–8787.
  - 128 Noda, I. (1990) Two-dimensional infrared (2D IR) spectroscopy: theory and applications. *Appl. Spectrosc.*, **44**, 550–561.
  - 129 Brunelli, D.D., Atvars, T.D.Z., Joekes, I., and Brabosa, V.C. (1998) Mapping phases of poly(vinyl alcohol) and poly(vinyl acetate) blends by FTIR microspectroscopy and optical fluorescence microscopy. *J. Appl. Polym. Sci.*, **69**, 645–655.
  - 130 Schafer, R., Zimmermann, J., Kressler, J., and Mulhaupt, R. (1997) Morphology and phase behaviour of poly(methyl methacrylate)/poly(styrene-co-acrylonitrile) blends monitored by FTIR microscopy. *Polymer*, **38**, 3745–3752.
  - 131 Kressler, J., Schafer, R., and Thomann, R. (1998) Imaging of semicrystalline polymers and polymer blends by FT-IR microspectroscopy. *Appl. Spectrosc.*, **52**, 1269–1273.
  - 132 Snively, C.M. and Koenig, J.L. (1999) Fast FTIR imaging: A new tool for the study of semicrystalline polymer morphology. *J. Polym. Sci. Polym. Phys.*, **37** (17), 2353–2359.
  - 133 Mirabella, F.M.Jr (1987) Applications of microscopic Fourier transform infrared spectrophotometry sampling techniques for the analysis of polymer systems, in *The Design, Sample Handling and Applications of Infrared Microscopes* (ed. P.B. Rousch), American Society for Testing and Materials, Philadelphia, PA, USA, p. 74.



## 21

# Characterization of Polymer Blends with Solid-State NMR Spectroscopy

Mohammad Mahdi Abolhasani and Vahid Karimkhani

### 21.1

#### Introduction

Controlling the structure of complex systems of macromolecules is a common objective in current materials science research and, indeed, many investigations have been undertaken simply by the mixing of two polymers.

Polymer blending offers a simple and economical means of linking the suitable properties of component polymers [1–6]. Whether a blend retains the original properties of the component polymers or demonstrates an average of their properties depends on the degree of microscopic mixing and its phase morphology [4,5]. The degree of mixing has been defined typically in terms of miscibility of molecular to macroscopic scales, the compositions of each domain, and the phase structure and domain size [7]. In the past, many instrumental methods have been applied to investigate the structures of blends, including differential scanning calorimetry (DSC) to examine miscibility, scattering measurements such as small-angle X-ray scattering (SAXS) and small-angle neutron scattering (SANS), as well as light scattering. Unfortunately, the use of only one of these method results in an incomplete understanding of a blend.

Kwei and coworkers [8] were the first to use solid-state nuclear magnetic resonance (NMR) spectroscopy to examine the microstructure of a polystyrene (PS)/poly(vinyl methyl ether) (PVME) blend, by measuring the  $^1\text{H}$  spin-lattice relaxation time ( $T_1$ ) and spin-spin relaxation time ( $T_2$ ) over a wide temperature range. Nowadays, high-resolution NMR in both liquids and in solids is a widely used technique to analyze the microstructures of polymer blends. To date, several NMR techniques have been applied very effectively to examine the molecular motion, phase structure and heterogeneity of pure polymers. Heterogeneity in blends is much more distinguished compared to pure polymers, which simplifies studies of the domain morphology of the component polymers in a blend.

A review of recent studies indicated that solid-state NMR spectroscopy is still an active research topic and, by including some recently developed NMR techniques, the application of solid-state NMR spectroscopy has continued to provide new

insights into the structure and miscibility of polymer blends. In this chapter, a brief review is provided of recent solid-state NMR studies on the miscibility of polymer blends, with particular emphasis placed on the potential of NMR techniques for characterizing the phase structures, heterogeneity and intermolecular interactions of polymer blends.

## 21.2

### Miscibility

Nuclear Overhauser effect spectroscopy (NOESY) is frequently used in liquid-state NMR, and is one of the standard two-dimensional (2D) methods used to interpret and assign the structures of macromolecules in solution. In addition to solution state, NOESY has been also used in polymeric systems and viscoelastic.

Previously,  $^{13}\text{C}$  NOE spectroscopy under magic angle spinning (MAS) was used to probe polymer miscibility in blends of PS/PVME [9]. As cross-peaks appear only between neighbor spins, NOE can be used as a probe to monitor the degree of mixing at the molecular level. NOE growth rates can also be used to acquire extra information on the molecular structure of the blend. The results of these experiments demonstrated the presence of a specific interaction between the PVME methyl group and the phenyl ring of the PS.

Subsequently, the same technique was used for investigating methyl groups as a source of cross-relaxation in solid polymers such as PS or polycarbonate, [10]. Mirau *et al.* have also shown that static  $^1\text{H}$  2D NOE spectroscopy can be used to measure interchain interactions [11].

In order to investigate the intermolecular interactions responsible for the miscibility in polybutadiene/polyisoprene blends above the glass-transition temperature ( $T_g$ ), the NOESY technique was applied under MAS [12]. The results showed the existence of weak intermolecular interactions between the vinyl side chain of the polybutadiene and the polyisoprene methyl group, thus confirming that intermolecular associations can indeed be probed using this technique.

## 21.3

### Proton Spin-Lattice Relaxation Experiments

The  $^1\text{H}$  spin-lattice relaxation times in the laboratory ( $T_1^H$ ) and rotating ( $T_{1\rho}^H$ ) frames obtained from high-resolution solid-state  $^{13}\text{C}$  cross-polarization (CP)/MAS NMR can provide information regarding the domain size of polymer blends by measuring proton spin diffusion. The latter is not a physical movement of protons, but rather is the equilibration process of nonequilibrium polarizations of spin systems at each local site, which occurs through a mutual exchange of magnetization. For instance, the protons of a well-mixed polymer blend will be thoroughly coupled by a quick spin-spin exchange through dipole-dipole interactions.

These protons then show same relaxation rates, providing the same  $T_{1\rho}^H$  value; however, protons that are in different environments or which are far apart relax independently of one another [13]. Consequently, a partially miscible or immiscible polymer blend would demonstrate, respectively, either a partial averaging of the relaxation rates or no averaging at all.

The extent of mixing of polymer blends on a nanometer scale can be determined by examining the spin-lattice relaxation performance of the  $^1\text{H}$  nuclei. This has been achieved previously in blends of cellulose/poly(vinyl alcohol) (PVOH) [14], wheat proteins/PVOH [15], starch/poly(caprolactone) (PCL) [16] and starch/crosslinked poly(acrylic acid) [17].

Recently, Yoshitake *et al.* [18] reported the miscibility of cellulose acetate (CA) with poly(acryloyl morpholine) (PACMO), in which CA materials with an acetyl degree of substitution (DS) of 1.80–2.95 were used. In these studies, Yoshitake and coworkers used solid-state  $^{13}\text{C}$  CP/MAS NMR measurements to estimate the scale of homogeneity for PACMO/CA miscible blends. In the following, the acetyl DS adopted for the CA component is 2.18 throughout, unless otherwise specified.

The observed values of chemical shift for the two polymer components, the structural formulae of which are shown in Figure 21.1, are summarized in Table 21.1. Both, PACMO and CA possess a carbonyl carbon ( $\text{C}=\text{O}$ ), but the two resonance peaks (ca. 172–174 ppm) were overlapped with each other and hardly separated. With regards to the other carbons of PACMO ( $-\text{O}-\text{CH}_2-$ ,  $-\text{N}-\text{CH}_2$ , and  $\text{CH}_2-\text{CH}-$ ), the respective chemical shifts never showed any clear movement with blend composition (as can be seen in Table 21.1). However, the resonance signals of the pyranose and methyl carbons of the CA component ( $\text{C}1$ ,  $\text{C}_2-\text{C}_5$ , and  $\text{CH}_3$ ) moved to the side of upper field with increasing PACMO content, by approximately 1–1.2 ppm. This implied that the intra- and/or

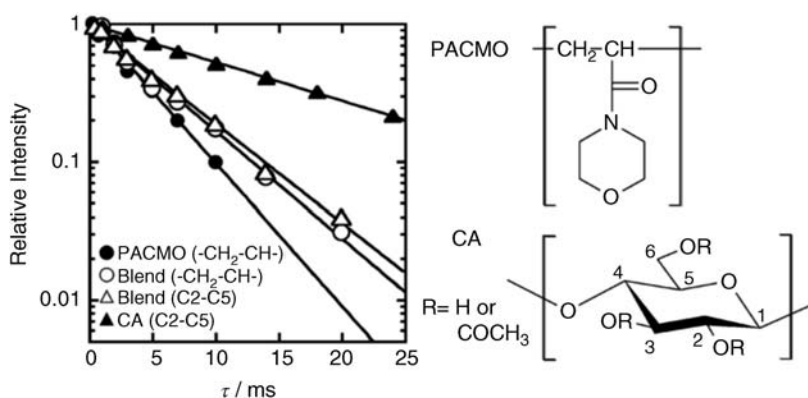


**Figure 21.1** Semi-logarithmic plots of the decay of  $^{13}\text{C}$  resonance intensities as a function of spin-locking time  $\tau$ , for film samples of PACMO, CA (DS = 2.18), and their 50/50 blend. The resonance peak of pyranose  $\text{C}_2-\text{C}_5$

carbons of CA and that of  $-\text{CH}_2-\text{CH}-$  carbons of PACMO were monitored. Reproduced with permission from Ref. [18]; © 2013, Elsevier.

**Table 21.1**  $^{13}\text{C}$  chemical shifts of PACMO, CA, and PACMO/CA blends (acetyl DS = 2.18). Reproduced with permission from Ref. [18]; © 2013, Elsevier.

PACMO/CA	$^{13}\text{C}$ chemical shifts/ppm								
	PACMO component				CA component				
	—C—O	—O—CH <sub>2</sub> —	—N—CH <sub>2</sub> —	—CH <sub>2</sub> —CH—	C1	C2—C5	C6	—C=O	—CH <sub>3</sub>
100/0	174.2	67.7	46.8/43.3	37.1	—	—	—	—	—
70/30	173.6	67.5	46.7/43.3	37.0	101.7	73.0	—	173.6	20.9
50/50	172.4	67.4	46.3/43.0	37.0	102.0	73.3	—	172.4	21.1
30/70	172.0	68.0	46.4/42.9	37.3	102.3	74.3	—	172.0	21.4
0/100	—	—	—	—	102.7	74.5	63.7	171.6	21.7

intermolecular hydrogen bonds in the original unblended CA might have been partly disrupted by blending with PACMO.

A quantitative analysis of the mixing scale in the PACMO/CA (DS = 2.18) blends was carried out through measurements of proton spin-lattice relaxation times in the rotating frame ( $T_{1\rho}^H$ ).  $T_{1\rho}^H$  values can be obtained by practically fitting the decaying carbon resonance intensity to the following single-exponential function:

$$M(\tau) = M(0)\exp\left(\frac{-\tau}{T_{1\rho}^H}\right) \quad (21.1)$$

where  $M(\tau)$  is the magnetization intensity considered and  $\tau$  is the spin-locking time. In a binary polymer blend, if the two constituent polymers are mixed thoroughly enough to allow a cooperative spin-diffusion, the  $T_{1\rho}^H$  values for different protons belonging to the respective components may be equalized to each other [19,20].

The decay behavior of  $^{13}\text{C}$  resonance for PACMO, CA (DS = 2.18), and their 50/50 blend is shown in Figure 21.1. The resonance peak of pyranose C2—C5 carbons (ca. 74 ppm) of CA and that of  $-\text{CH}_2-\text{CH}-$  carbons (ca. 37 ppm) of PACMO were observed in this experiment. The slope of each semi-logarithmic plot gives a  $T_{1\rho}^H$  value as the time constant of the relaxation process.

The  $T_{1\rho}^H$  data thus estimated for PACMO, CA (DS = 2.18), and their blends with 70/30–30/70 compositions are listed in Table 21.2. The relaxation times quantified for the unblended PACMO and CA samples were 4.2 ms and 15.6 ms, respectively. In their blends, the  $T_{1\rho}^H$  value of the PACMO component rises significantly with increasing CA content, whereas that of the CA component diminishes somewhat hastily with increasing PACMO content. Hence, the two  $T_{1\rho}^H$  values at each composition almost coincide with each other. Considering some tolerance in the relaxation measurements, it is rational to assume that the two polymer components in the blends are coexistent within a range where the mutual  $^1\text{H}$ -spin diffusion is acceptable over a period of the homogenized  $T_{1\rho}^H$ , for example, 5.8 ms on average for the 50/50 composition of PACMO/CA.

**Table 21.2**  $T_{1\rho}^H$  values for PACMO, CA, and PACMO/CA blends (acetyl DS = 2.18). Reproduced with permission from Ref. [18]; © 2013, Elsevier.

PACMO/CA	$T_{1\rho}^H$ (ms)	
	PACMO component ( $-\text{CH}_2-\text{CH}-$ )	CA component (C <sub>2</sub> —C <sub>5</sub> )
100/0	4.20	—
70/30	5.43	5.62
50/50	5.59	6.01
30/70	6.54	7.31
0/100	—	15.6

An effective path length  $L$  of the spin diffusion in a time ( $T_{1\rho}^H$ ) is given by the following equation [21]:

$$L \cong (6DT_{1\rho}^H)^{1/2} \quad (21.2)$$

where  $D$  is the diffusion coefficient, usually taken to be  $\sim 1.0 \times 10^{-16} \text{ m}^2 \text{ s}^{-1}$  in organic polymer materials [22–25]. With  $T_{1\rho}^H$  values of 5.4–7.3 ms calculated for the PACMO/CA blends, the diffusion path length can be calculated as  $L = 1.8$ –2.1 nm. Accordingly, it is assured that the relevant blends are homogeneous on a scale of a few nanometers.

Chaléat *et al.* [26] investigated the phase separation and the intermolecular interactions of a series of extruded plasticized starch (PLS)/PVOH blends with various starch:PVOH ratios. The  $^{13}\text{C}$  high-resolution solid-state NMR spectrum of the unprocessed starch is shown in Figure 21.2, where the peak resonances can be assigned as follows: the glycosidic carbon C-1 (102.1 ppm, 100.3 ppm, 99.6 ppm and 93.9 ppm), C-4 (81.0 ppm), C-2, C-3, C-5 (71.7 ppm) and C-6 (61.2 ppm) [27,28]. The different starch crystalline polymorphic forms exhibit different signal multiplicities in the C-1 regions, which reflect the symmetry of the helix packing [27,29]. The A-type polymorph exhibits a characteristic triplet signal multiplicity (100.4 ppm, 99.2 ppm and 98.2 ppm), while the B-type shows doublet signal multiplicity (100.0 ppm and 99.2 ppm) [27]. A high-amylose starch (B-type) has been shown to display extra broad resonances at 103 ppm and 95 ppm for C-1, and 82 ppm for C-4 [29]. This was verified for the high-amylose starch investigated in these studies, with an extra resonance at 102.1 ppm and a broad peak at about 94 ppm (indicated by arrows in Figure 21.2). The additional resonance for C-4 is only distinguished as a shoulder (see Figure 21.2). These peaks (i.e., 102 p pm and

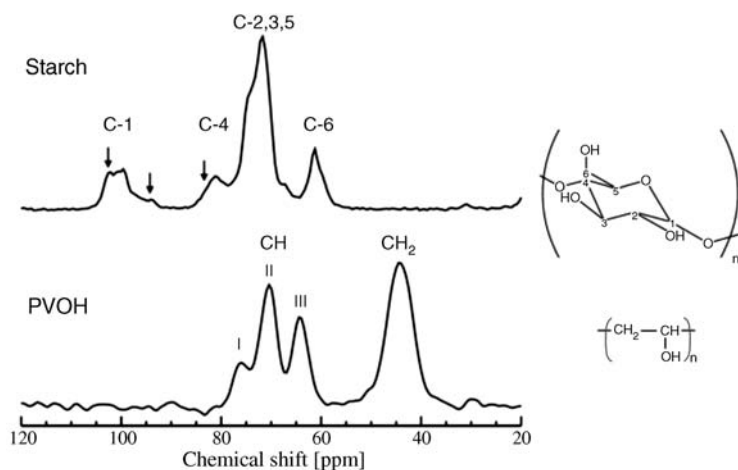


**Figure 21.2**  $^{13}\text{C}$  CP/MAS NMR spectra of the unprocessed starch (top) and the neat PVOH (bottom). The chemical structures of PVOH and the anhydroglucose unit of starch with the

corresponding carbon numbers are indicated. Reproduced with permission from Ref. [26]; © 2012, Elsevier.

82 ppm) have been generally related to the V-type polymorphic structure (single helices), the content of which generally increases with increasing amylose content, whereas the intensity at 94 ppm reflects the contribution of the disordered amorphous starch [30–32].

The  $^{13}\text{C}$  high-resolution solid-state NMR spectrum of neat PVOH is shown in Figure 21.2. The broad, well-separated peak at 44.5 ppm is due to the methylene carbon [33], while the three split peaks at 64.3 ppm, 70.5 ppm and 76.7 ppm can be assigned to CH carbons attached to OH groups. The splitting of these peaks has been studied widely and assigned to the formation of intramolecular hydrogen bonds with neighboring hydroxyl groups [33–35]. The most downfield peak (peak I), the central peak (peak II) and the most upfield peak (peak III), have been attributed to the OH group bonded to the CH carbon forming two hydrogen bonds, one hydrogen bond, and no hydrogen bond, respectively.

$^{13}\text{C}$  CP/MAS spectra of PLS/PVOH blends (50:50, 75:25 and 90:10) and their pure components (0:100 and 100:0) are displayed in Figure 21.3. Changes in chemical shifts and/or in line shapes have previously been detected in the  $^{13}\text{C}$  NMR spectra of blends (e.g., in cellulose or PVOH blends) in comparison with the spectra of the unblended components [19,20,36]. Changes in chemical shifts

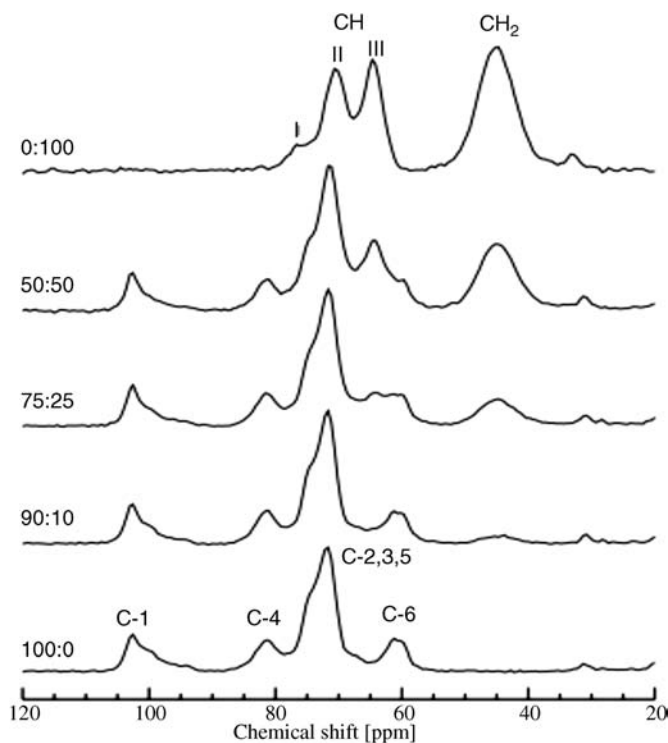


**Figure 21.3**  $^{13}\text{C}$  CP/MAS NMR spectra of the different PLS/PVOH compositions. Reproduced with permission from Ref. [26]; © 2012, Elsevier.

can be associated with the incidence of hydrogen bonding, as this type of interaction has a strong influence on the electron density around the carbons that bear the interacting functionalities.

The C-1 resonance of starch between 98 ppm and 104 ppm, and the methylene carbon peak of PVOH between 40 ppm and 49 ppm, were monitored in the  $T_{1\rho}^H$  determinations. For the raw materials, the pure blend components and all the blends, the  $T_{1\rho}^H$  decay was sufficiently explained by a single-exponential decay function (Eq. (21.1)), resulting in a single  $T_{1\rho}^H$  for each material. The values of the relaxation times are listed in Table 21.3.

For the unblended PLS (100:0) and PVOH (0:100), the  $T_{1\rho}^H$  values are, respectively, 4.2 and 5.9 ms, which is sufficiently different to observe their variations upon blending in different proportions. It can be distinguished that the  $T_{1\rho}$  values decreased in the plasticized starch (100:0) compared to that of the raw starch (5.2 ms), undoubtedly due to the increased molecular mobility of the amylose chains after thermomechanical processing in the presence of a plasticizer. A similar relaxation behavior of wheat proteins after plasticization by glycerol has been previously observed [15]. The relaxation behavior of PVOH was not similarly affected after processing,  $T_{1\rho}$  in the neat PVOH being 5.5 ms.

In the PLS/PVOH blends, although the observed relaxation times do not coincide with those of pure component, the  $T_{1\rho}^H$  values estimated from the starch component resonance are clearly different from those obtained via the PVOH peak, indicating that spin diffusion is not effective. It can be concluded that some phase separation occurred in the system for all compositions.

However, the  $T_{1\rho}^H$  of the PVOH component was lowered by increasing the amount of starch in the blend. Whilst this depression of the  $T_{1\rho}^H$  of PVOH is an indication of mixing, the fact that no averaging takes place between the  $T_{1\rho}$ s of PVOH and starch is a sign that their miscibility is limited, most likely to local regions such as interfaces. It should also be noted that the intrinsic relaxation time of the starch component in the blends is shorter in comparison with values in unblended PLS, indicating that the molecular mobilities of the starch are also

**Table 21.3**  $^1\text{H}T_{1\rho}$  of raw materials and PLS/PVOH blends. Reproduced with permission from Ref. [26]; © 2012, Elsevier.

Sample	$^1\text{H}T_{1\rho}$ (ms)	
	PVOH (40–49 ppm)	Starch (98–104 ppm)
Raw starch	—	5.2
Raw PVOH	5.5	—
0:100	5.9	—
50:50	4.9	3.5
75:25	4.9	4.1
90:10	4.6	4.0
100:0	—	4.2



affected upon blending with PVOH. These results suggest a small degree of miscibility within the blend.

Despite a slight degree of inter-mixing it is clear that, in all investigated PLS/PVOH blends, both components were separated into domains of which the length scale exceeds the maximum diffusive path,  $L$ , over which proton–proton spin diffusion is effective.

Using Eq. (21.2) and a  $D$ -value of  $0.5 \times 10^{-16} \text{ m}^2 \text{ s}^{-1}$  as a reasonable estimate and an average  $T_{1\rho}$  value of 5 ms, the average size of the domains in PLS/PVOH blends can be estimated to exceed 4 nm. To conclude, measurements of the  $T_{1\rho}^H$  relaxation times for both components confirmed the phase separation for all blend compositions, but also suggested a small degree of inter-mixing.

Kuo *et al.* [37] investigated the miscibility of three poly(*N*-phenyl methacrylamide)s – namely poly(*N*-phenyl methacrylamide) (PNPAA), poly(*N*-4-methoxyphenyl methacrylamide) (PMPMA) and poly(*N*-4-bromophenyl methacrylamide) (PBPMA) – by means of DSC, Fourier transform infrared (FTIR) and high-resolution  $^{13}\text{C}$  CP/MAS solid-state NMR analyses.

Figure 21.4 shows the selected  $^{13}\text{C}$  CP/MAS spectra of PNPAA/poly(4-vinylpyridine) (P4VP), PMPMA/P4VP and PBPMA/P4VP at the composition of 20/80, compared with that of pure PNPAA and pure P4VP. Five peaks were also observed for pure P4VP, where the peak at  $\delta = 123.9 \text{ ppm}$  corresponds to the pyridine carbon atom. Clearly, the pyridine carbons shift in PBPMA/P4VP-20/80

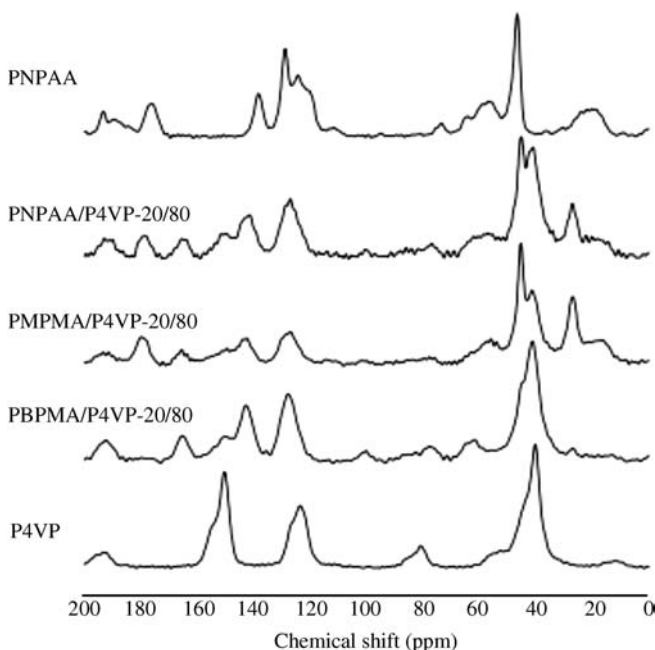


**Figure 21.4**  $^{13}\text{C}$  CP/MAS spectra of PNPAA/P4VP, PMPMA/P4VP and PBPMA/P4VP at the composition of 20/80. Reproduced with permission from Ref. [37]; © 2011, Elsevier.

downfields about 3.8 ppm significantly, also indicating a hydrogen-bonding interaction between the amide group of PBPMA and the pyridine group of P4VP. The pyridine carbons shift in PNPA/P4VP-20/80 and PMPMA/P4VP-20/80 downfield was about 3.2 and 3.0 ppm, respectively, a finding which is consistent with their FTIR spectroscopic analysis.

Kuo and coworkers' results when using DSC revealed that phase separation occurred in PNPA/P4VP and PMPMA/P4VP blends in certain compositions. However, it is worth noting that the compositions with a single transition temperature may be heterogeneous instead of homogeneous, as the dimension of phase separation may be too small to be detected with DSC analysis. Consequently, Kuo *et al.* measured the spin-lattice relaxation time in the rotating frame, using Eq. (21.1).

Figure 21.5 shows the plots of  $\ln(M_t/M_0)$  against  $\tau$ . The homogeneities of these polymer blends were estimated through quantitative analyses based on the main-chain-methylene carbon atom's resonance in poly(methacrylamide) at 46 ppm. Two exponential decays in  $T_{1\rho}^H$  for PNPA/P4VP = 80/20, 20/80 and for PMPMA/P4VP = 80/20, 20/80 can be observed in Figure 21.5 and Table 21.4. The data indicate that two domains possessing distinct mobility are present in PNPA/P4VP and PMPMA/P4VP blends for the entire compositions, except for PNPA blends and PMPMA blends with compositions of 80/20 and 20/80, which appear with a single  $T_g$  in DSC analyses. This observation is consistent with the assumption that the phase separation may not be evaluated in DSC. In contrast, single-exponential decays in  $T_{1\rho}^H$  for PBPMA/P4VP blends are shown in Figure 21.5, which means that both PBPMA blends are homogeneous on the scale at which spin-diffusion occurs within the time  $T_{1\rho}^H$ . Thus, the interaction between PBPMA and P4VP is the largest among these three binary blends. These results are also consistent with those obtained from infrared and DSC analyses.

## 21.4

### Experiments for the Direct Observation of Proton Spin-Diffusion

$^1\text{H}$  spin-diffusion analysis has been confirmed as a powerful tool for examining the miscibility and domain size of polymer blends [38,39].  $^1\text{H}$  spin-diffusion measurements generally consist of three steps:

- 1) A selection period for creating a primary magnetization gradient between dissimilar phase ingredients.
- 2)  $\tau_m$ , through which diffusion of polarization throughout dipolar interactions equilibrate the distribution of magnetization.
- 3) The distribution state of magnetization after mixing time is read out.

By investigating the development of magnetization distribution with mixing time, a quantitative evaluation of the degree of miscibility and domain size can be made.

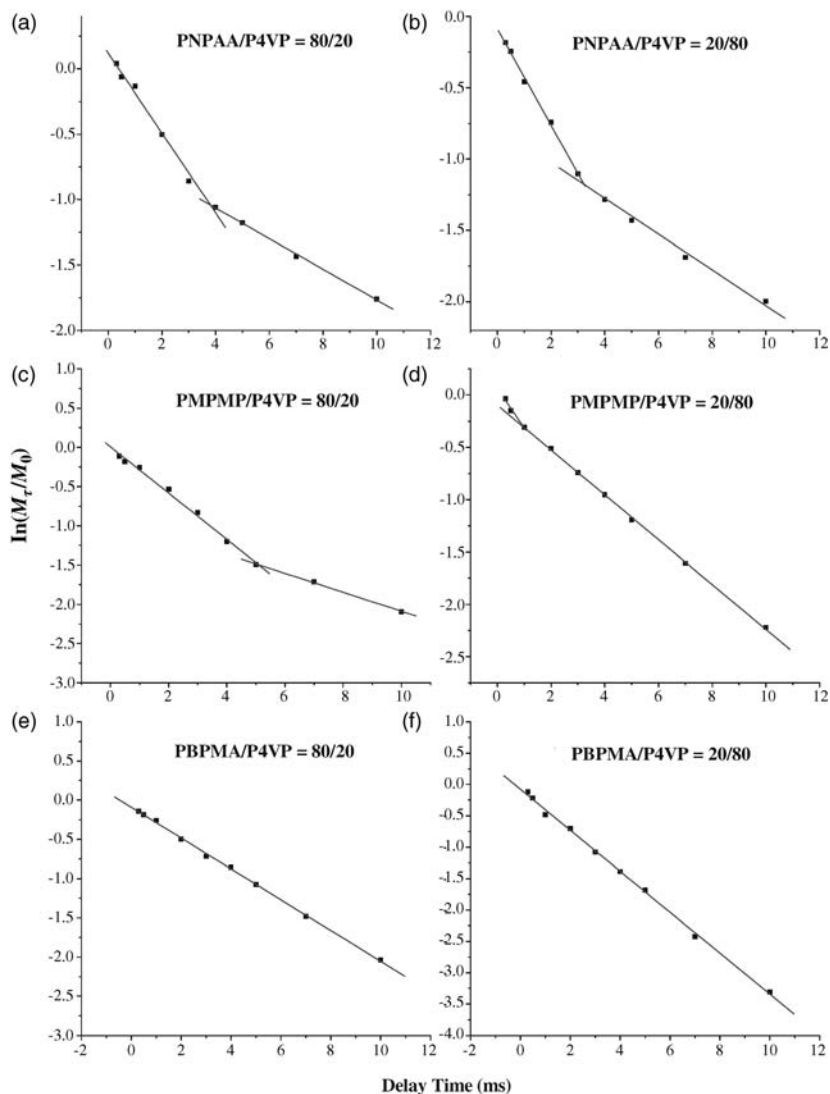


**Figure 21.5** Logarithmic plots of magnetization intensities of 176 ppm versus delay time for PPMA/P4VP blends (a) 80/20 and (b) 20/80; for PMPMA/P4VP blends (c) 80/20 and (d) 20/80; for PBPMA/P4VP blends (e) 80/20 and (f) 20/80. Reproduced with permission from Ref. [37]; © 2011, Elsevier.

The primary magnetization gradient between various phase ingredients can be created by utilizing either the dissimilarity in structures of each phase ingredients, or the difference in mobility. Differences in relaxation times, such as  $^1\text{H}T_2$ ,  $T_{1\rho}^H$ , originated from the mobility difference at experimental temperatures. Different relaxation times make it possible to selectively suppress the polarization of the

**Table 21.4** Value of relaxation time ( $T_{1\rho}^H$ ) for PNPA/P4VP, PMPMA/P4VP and PBPMA/P4VP blends. Reproduced with permission from Ref. [37]; © 2011, Elsevier.

Composition amide/pyridine	$T_{1\rho}^H$ (ms)		
	PNPAA/P4VP	PMPMA/P4VP	PBPMA/P4VP
100/0	4.14	4.71	5.36
80/20	3.33/9.09	3.25/8.33	5.16
20/80	3.03/7.69	2.75/4.76	3.12

phase ingredient with shorter relaxation times, whereas longer relaxation times will hold the magnetization of the component. Goldman–Shen and “dipolar filter” pulse sequences [40,41] are the two most often used spin-diffusion experiments. The selection of magnetization in these experiments are all based on differences in the  $^1\text{H}T_2$  of the components. In contrast, in  $^1\text{H}$  solid-state high-resolution spectra developed by techniques such as CRAMPS, signals due to different structures can be either selectively suppressed or inverted [42,43], and the primary magnetization gradient between different phase ingredients can then also be generated. The read-out step of the spin-diffusion experiments can be fulfilled either by directly analyzing the  $^1\text{H}$  lineshape [22] or by indirectly monitoring the  $^{13}\text{C}$  signal intensity changes via cross-polarization [44].

Today, the investigation of miscibility of polymer blends using  $^1\text{H}$  spin-diffusion remains an active area of research. For example, Fu *et al.* [45] studied the hydrogen bond interactions and dynamics of poly (methyl methacrylate) (PMMA) and poly(4-vinyl phenol) (PVPh) polymer blends, using a variety of advanced solid-state NMR techniques. The possible hydrogen bond interactions between the carbonyl group of PMMA and hydroxyl group of PVPh were successfully elucidated using a two-dimensional (2D)  $^1\text{H}$ – $^1\text{H}$  spin-exchange NMR experiment. For this, three different samples were prepared, and the composition of the PMMA/PVPh polymer blend was fixed at 50/50 wt%. The solution blending was cast from acetone solution, after which the sample was dried for 48 h under vacuum at  $120^\circ\text{C}$  (this was termed the “cast film”). The PMMA and PVPh powders were then physically mixed in a mortar (Blend-0), and the powder mixture then annealed at  $220^\circ\text{C}$  for 120 min (Blend-120), as was the cast film.

In order to confirm the thermal-treatment effects on the diffusion and miscibility of the powder blend samples, 2D  $^1\text{H}$ – $^1\text{H}$  spin-exchange experiments were performed for Blend-0, Blend-120 and the cast film. The 2D spin-exchange spectra provided information on the proximity (due to intermolecular hydrogen-bonding interactions) between the phenolic hydroxyl group (OH) of PVPh and the  $\text{C}=\text{O}$  of PMMA, which is responsible for the miscibility of these PMMA/PVPh blends. Subsequently, 2D spin-exchange spectra were obtained at different spin-diffusion times ( $t_m$ ) of 0.5, 1.0, and 2.0 ms. Example spectra, obtained at  $t_m = 2.0$  ms, are shown in Figure 21.6a–c for Blend-0, Blend-120 and the cast film, respectively. In Figure 21.6a, no intermolecular cross-peak could be seen between the OH and the

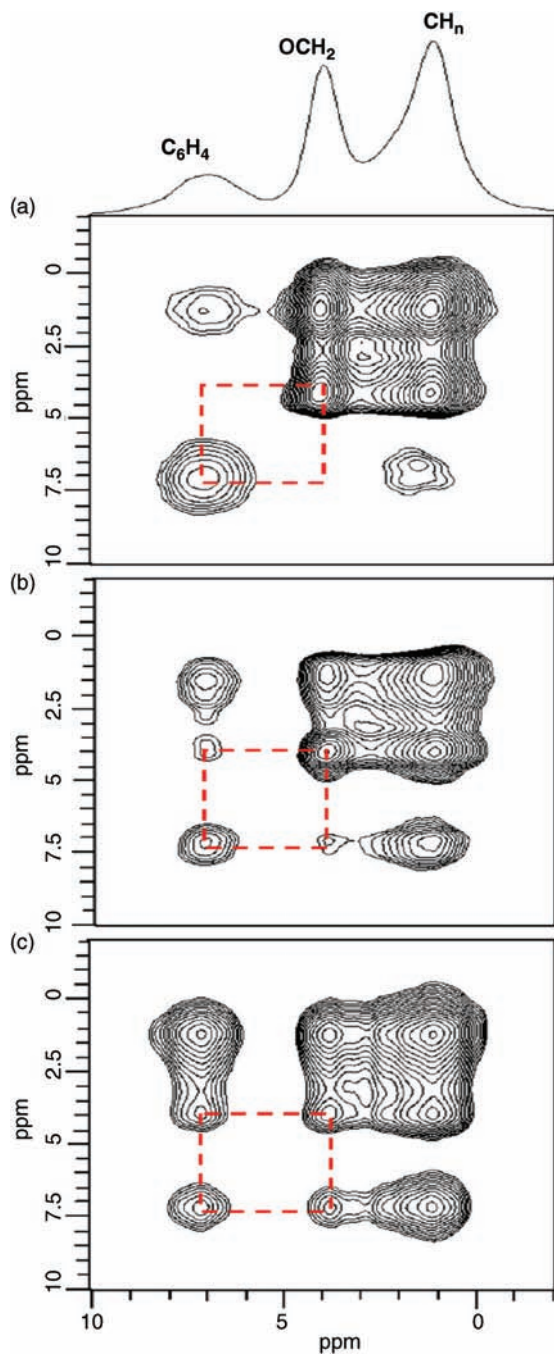


**Figure 21.6**  $^1\text{H}$ – $^1\text{H}$  spin-exchange spectra of the PMMA/PVPh = 1/1 polymer blends at mixing time ( $t_m$ ) of 2 ms, for (a) Blend-0, (b) Blend-120 and (c) cast film. The normal  $^1\text{H}$

MAS spectrum is shown in the upper part of the figure. Reproduced with permission from Ref. [45]; © 2013, Elsevier.

C=O for the pure powder blend (Blend-0), while the mixing time ( $t = 2$  ms) indicated an immiscible polymer blend. For Blend-120, which was annealed at  $220^{\circ}\text{C}$  for 120 min, Figure 21.6b shows the cross-peak of the intermolecular hydrogen bonds when  $t_m = 2$  ms; that is to say, the sample is miscible. The cast film from solution (shown in Figure 21.6c) gave a similar result to Blend-120, with the signal intensity of the cross-peak being strong enough even at a short mixing time of 0.5 ms (not shown here). These results indicated that, as the time of heat treatment was increased, the interchain diffusion of the polymers was also increased and miscibility became more likely. When the time was sufficiently long, the heterogeneous powder blends became homogeneous, as did the miscible blend from solution.

## 21.5

### Molecular Dynamics

Many of the most important macroscopic properties of a blend, such as impact strength and ductility, are affected by the molecular dynamics of the constituent polymers. As blending influences the molecular dynamics of each individual component, characterization of the chain dynamics in polymeric blends is of significant interest. Previously, multidimensional NMR spectroscopy has been identified as a very effective method for revealing structural and dynamical information of polymers, at the molecular level. Compared to the many applications in both solution and solid state, and that information can be provided in important areas such as chain dynamics, local structure, residual couplings (induced by chemical cross-linking and topological constraints), dynamic order parameters, internuclear distances, intermolecular interactions (important for miscibility), the effects of fillers on molecular motions and segmental orientation under mechanical stress, NMR has not been applied widely to viscoelastic polymers [46].

#### 21.5.1

##### $^2\text{H}$ NMR Line Shape Analysis

Quantitative information concerning rotational motion can be acquired by examining the nuclear shielding tensors (anisotropic chemical shift) which dominate NMR spectra. Unfortunately, the tensors are not axially symmetric in aliphatic groups and the anisotropy for nuclear shielding in both  $^1\text{H}$  and  $^{13}\text{C}$  is small, which in turn prohibits the analysis of the dynamics of aliphatic polymers using these methods [47]. Nevertheless, rotational motions can be monitored using  $^2\text{H}$  NMR techniques over a wide range of characteristic frequencies, including fast (200–107 kHz), intermediate (15–150 kHz) and slow (0.4–10 kHz) motions. Reven and coworkers [48] used variable temperature wide-line deuterium NMR spectroscopy to investigate the chain mobility of a series of hydrogen-bonded polymer complexes and multilayers. The  $^2\text{H}$  NMR spectra of a series of acidic water-saturated PMAA complexes over a temperature range of  $21$  to  $70^{\circ}\text{C}$ , is shown in Figure 21.7.

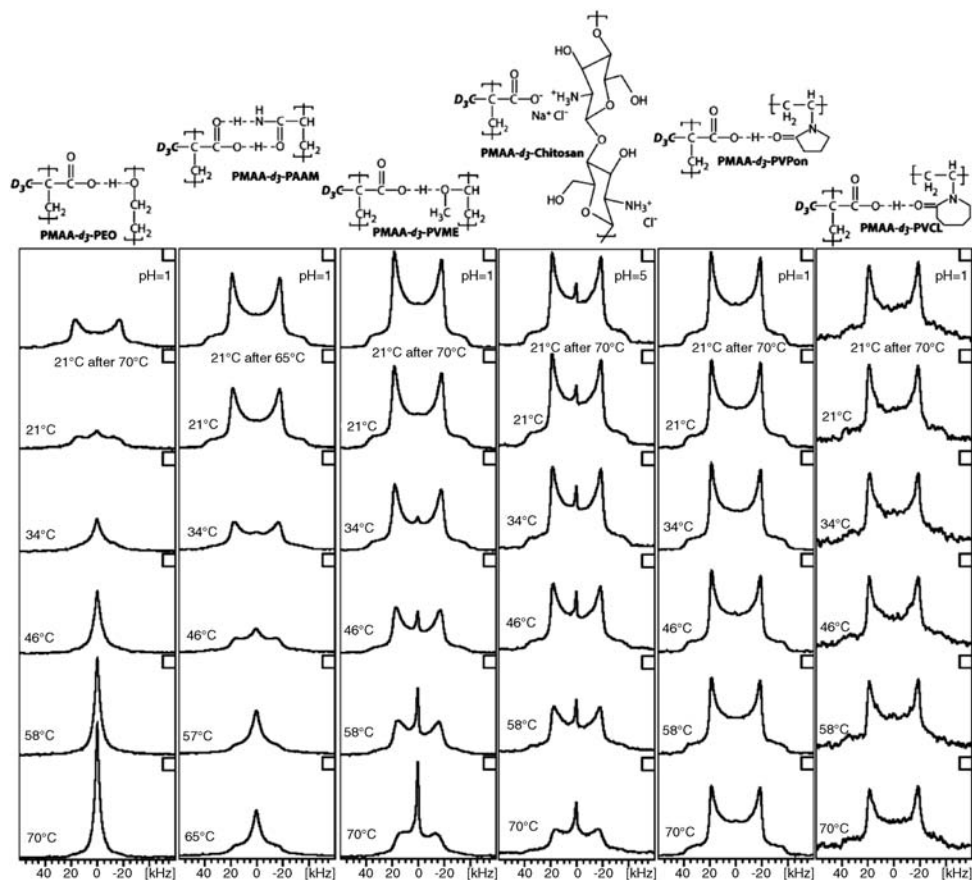


**Figure 21.7** Variable temperature  $^2\text{H}$  NMR of 40 wt% PMAA- $\text{d}_3$  complexes saturated with acidic deuterium-depleted water, with the exception of the chitosan complex which was saturated with untreated deuterium-depleted water. Reproduced with permission from Ref. [48]; © 2011, American Chemical Society.

Averaging of the Pake pattern to an isotropic peak was used to show the onset of chain mobility with increasing temperature. One significant isotropic component is present even before heating for the weak poly(ethylene oxide) (PEO) (low  $T_g$ , higher mobility)/PMAA complex, and the broad component disappears with warming just above room temperature. Unlike the PEO complex, the PVME (low  $T_g$ , higher mobility) and poly(acrylamide) (PAAM) (high  $T_g$ , thermoresponsive polymer)/PMAA complexes keep broad components at the highest temperatures measurement but, similar to previous systems, they exhibit an isotropic component with moderate heating. The determining factors of PMAA dynamics in the PAAM/PMAA system are a lack of hydrophobic stabilization and the thermoresponsive behavior of PAAM (upper critical solution temperature at 25 °C when complexed to PAAM).

As signaled by a slow weakening of the Pake pattern intensity, the poly-electrolyte complex of chitosan-PMAA demonstrates an onset of motion with frequencies in the intermediate rather than fast regime. The chain motion of PMAA remains restricted, with no substantial change in the  $^2\text{H}$  Pake pattern line shapes with heating, unlike the polymers that form the strongest complexes with poly(vinylpyrrolidone) (PVPon). It is well known that complexes of polymers having lower critical solution temperatures are stabilized with heating, and therefore the thermoresponsive properties of PVME and poly(vinylcaprolactam) (PVCL) will have little or no effect on the PMAA chain dynamics.

Reven and coworkers showed that it is possible to tune the chain mobility and related properties of a PMAA-based complex with great precision by selecting the correct polymer partners. These may range from hydrophilic polymers (e.g., PEO or PAAM) with fast dynamics where a rapid isotropic motion is dominant, to partner polymers (e.g., PVPon or PVCL) with significant hydrophobic character and high  $T_g$  and slow dynamics

### 21.5.2

#### Polarization Inversion Spin Exchange at the Magic Angle (PISEMA) Experiment

Polarization Inversion Spin Exchange at the Magic Angle (PISEMA) high-resolution solid-state NMR techniques can be used to investigate the influence of local chain dynamics on cooperative chain motions between the  $\text{OCH}_3$  protons of PMMA and the aromatic protons of PVPh [45,47]. The 2D  $^1\text{H}$ - $^{13}\text{C}$  experimental dipolar spectrum of PMMA/PVPh cast film with the  $^{13}\text{C}$  spectrum, and the corresponding molecular structures obtained using PISEMA method, are shown in Figure 21.8a. In Figure 21.8b, the cast film (made from solution) is indicated by the blue line and Blend-120 (powder blend annealed for 120 min) by the black line. At room temperature, the cross-section of aromatic carbon (C5) at 116.0 ppm has two splits, with the splitting width ( $\Delta\nu$ ) depending on the intensity of the  $^1\text{H}$ - $^{13}\text{C}$  dipolar coupling (especially for strong interactions) and representing the mobility of molecular dynamics. Whereas, the narrower peak results in a wobbling motion of the phenyl ring, a wider splitting denotes a rigid aromatic group. Clearly, in the cast film the intensity of the narrower peak ( $\Delta\nu = 7.8 \text{ kHz}$ ) is stronger, and this can be attributed to its better miscibility, such that methyl-group rotation around the  $\text{O}-\text{CH}_3$  bond in PMMA, via intermolecular hydrogen bonds, increased the amplitude of aromatic protons in PVPh. These observations indicate that an intermolecular cooperative motion is present in the hydrogen-bonded PMMA/PVPh polymer blends.

The temperature-dependency of the side group dynamics of the two polymers should also be considered. Figure 21.8c shows cross-sections of the cast film at room temperature and at  $80^\circ\text{C}$  where, due to a decreasing intensity of the  $^1\text{H}$ - $^{13}\text{C}$  dipolar coupling, the splitting width of the narrower peak is decreased to  $\Delta\nu = 7.2 \text{ kHz}$  at higher temperatures. This indicates that a rotational motion of the methyl group will affect the motion of the aromatic proton, causing a remarkable increase in line with increasing temperature.



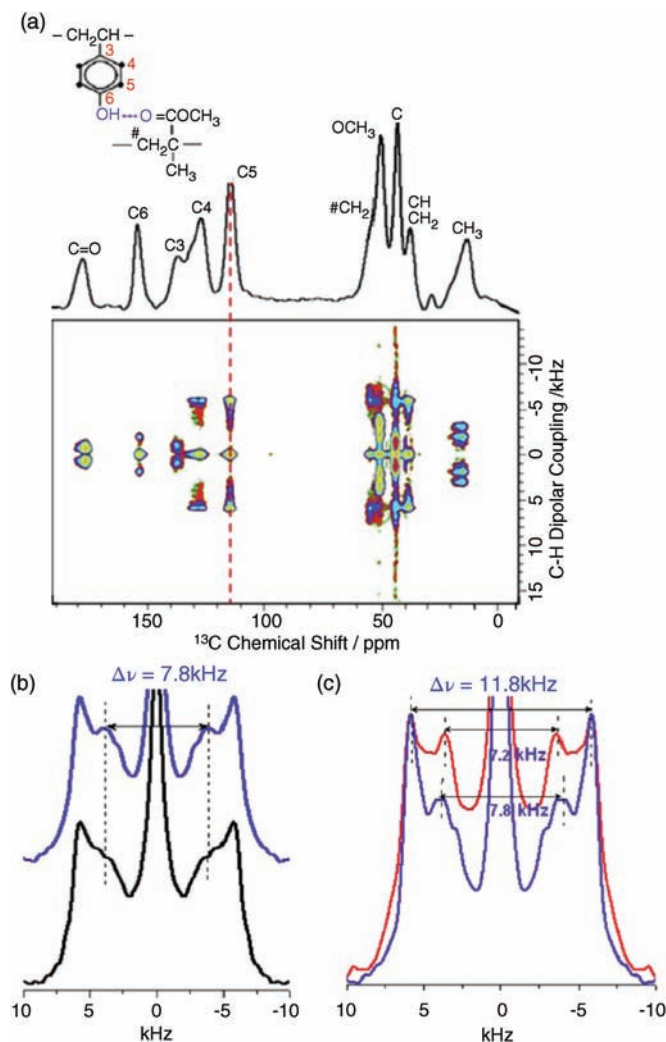


**Figure 21.8** (a) 2D PISEMA spectrum of PMMA/PVPh cast film; (b) Cross-sections of the aromatic proton (d  $^{13}\text{C}$  116.0 ppm) for Blend-120 (bottom) and cast film (top) at

room temperature, and for (c) cast film at room temperature (bottom) and 80 °C (top). Reproduced with permission from Ref. [45]; © 2013, Elsevier.

### 21.5.3

#### Two-Dimensional Wideline Separation (WISE) NMR

As  $T_{1\rho}$  measurements can provide valuable information on the local dynamics of polymer chains, measurements of this quantity are generally used to investigate the effects of blending on local motions in a polymer blend [49]. Molecular

dynamics with frequencies of between 10 and 100 kHz govern C-13  $T_{1\rho}$  relaxation times. In comparison with H-1 spin diffusion, spin diffusion between C-13 nuclei is slow, especially under conditions of MAS. Consequently, while proton  $T_{1\rho}$  relaxation times are partially averaged by spin diffusion, C-13  $T_{1\rho}$  relaxation times are not averaged and therefore information on the motion of each specific site is retained.

WISE NMR is a simple but sophisticated technique to measure the chain dynamics of polymers by correlating the proton line shape with the carbon chemical shift. This method provides information on the dynamics of polymers by measuring the degree to which the proton line shapes are averaged by molecular motion. In solids, the proton lines are broadened through hetero- and homo-nuclear dipolar interactions. However, if the atom is involved in large amplitude fluctuations which, on a time scale of dipolar line widths (50 kHz) are fast, then motionally averaged line shapes will be detected. As revealed in the C-13 chemical shifts and the H-1 line shapes, the WISE experiment constructs a relationship between the chemical structure and segmental dynamics, respectively.

Contour plots of the WISE NMR spectra of polyisoprene (PI)/PMMA 50/50 semi-interpenetrating polymer networks (IPNs) at 298 K are shown in Figure 21.9 [49]. Several well-resolved peaks, including the PI protons of the  $-\text{CH}_2-$  group at 36 ppm, other  $-\text{CH}_2-$  at 30 ppm, and the  $=\text{CH}-$  group at 29 ppm are observed. For PMMA, proton peaks for the  $-\text{CH}_2-$  group at 50 ppm, the  $-\text{OCH}_3$  at 54 ppm and  $-\text{CH}_3$  at 27 ppm are clearly resolved. Peaks at 27 ppm contain overlapped peaks from methyl groups in PMMA and PI. The contour plot indicates that very different proton line widths are observed for the PMMA and PI chains. It can be seen from the contour plot that the line width of PMMA protons at 50 ppm and 54 ppm are much larger than the protons of PI at 36 ppm and 30 ppm. This trend is characteristic of polymeric multicomponent systems, which show phase separation and consist of phases with slow and fast dynamics. For the PMMA phase, the WISE experiment shows that  $-\text{CH}_2-$  protons at 50 ppm are the most rigid, while protons in the ester group (54 ppm) of PMMA have the highest mobility among all protons. Indeed, relaxation measurements showed that, by mixing PMMA with PI chains during semi-IPN formation, the ester group experienced enhanced mobility. Contour plots reveals that the proton in the  $=\text{CH}-$  (129 ppm) group of PI has a lower mobility than protons in the ester group of PMMA. Compared with all other protons in semi-IPNs, the protons in PI chains observed at 36 ppm and 30 ppm are motionally very active.

## 21.6

### Organic Solar Cells

Organic photovoltaic (OPV) materials, as a promising, low-cost solar energy technology, may be manufactured via solution-based printing or coating. Bulk heterojunction (BHJ) devices, which represent some of the most promising OPV morphologies, are composed of a thin film containing a blend of photon-

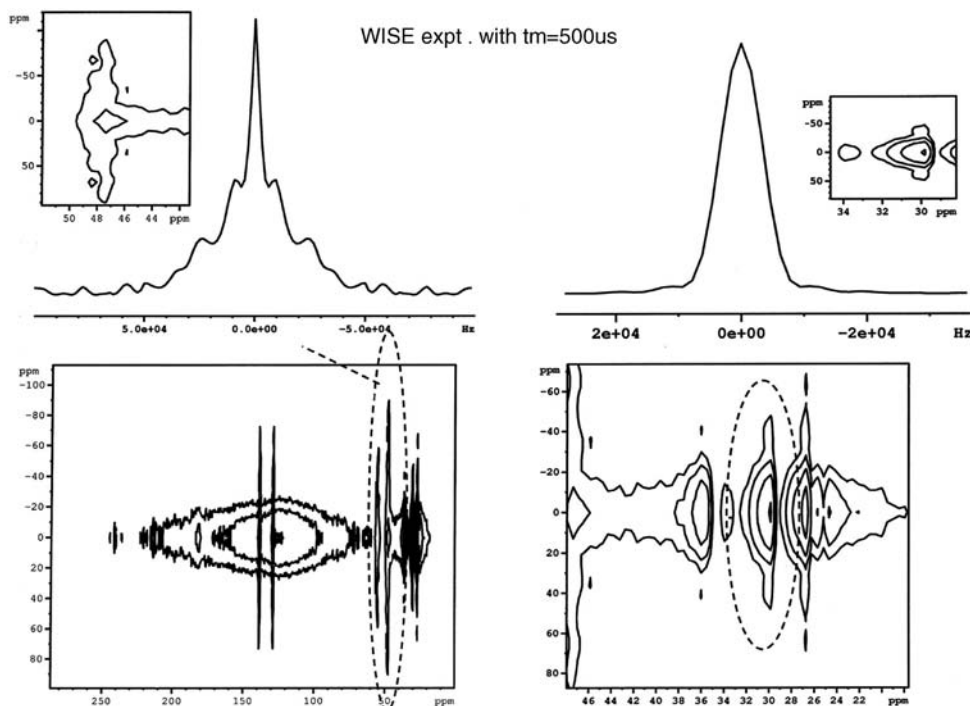


**Figure 21.9** Contour plot of the WISE NMR spectrum of PI/PMMA semi-IPN. Reproduced with permission from Ref. [49]; © 2010, Elsevier.

absorbing (or hole transport, e.g., polymers) and/or electron-accepting (or electron transport, e.g., fullerene derivatives) semiconductors. With regards to carrier photoexcitation, the recombination lengths are typically 10 nm in these disordered materials, while the self-assembly length scale will be on the order of 10–20 nm [50]. The ideal BHJ morphology would comprise pure light absorbing and electron transport phases, with the absorber domains having a smaller dimension than the exciton diffusion length, and with co-continuous paths of both phases leading to the corresponding electrodes. Currently, although BHJ devices have achieved high power conversion efficiencies (power conversion efficiency  $\approx 12\%$ ), an elucidation of the relationship between molecular structure and device performance has been problematic. As both phases are aromatic hydrocarbons, the resolution of finely mixed phases (with length scales of nanometers) using conventional characterization techniques such as light scattering or microscopy has proved very difficult. Moreover, in order to create new OPV materials and fabrication processes to achieve higher efficiencies, a full understanding of the effects of domain size, phase distribution and purity on device performance is required but, as yet, is largely unavailable.

As noted above, solid-state NMR spectroscopy is sensitive to local compositional, structural and dynamical environments in both ordered and disordered regions of

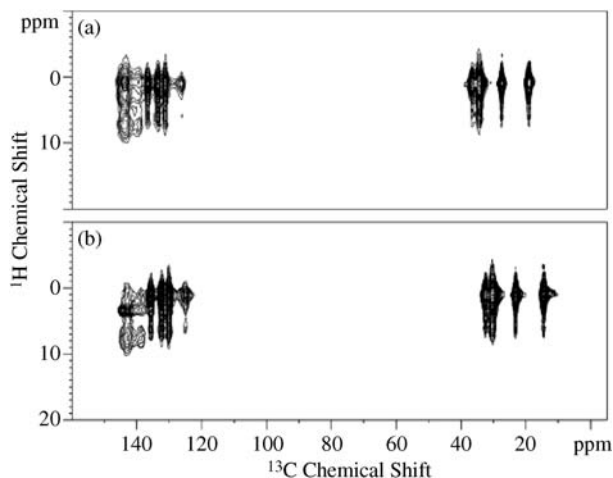


**Figure 21.10** 2D  $^{13}\text{C}$  HETCOR spectra [52] of (a) PCBMCF-RT and (b) PCBMCF-150A. Reproduced with permission from Ref. [51]; © 2006, American Chemical Society.

the materials, which makes it a powerful technique for evaluating the nanoscale structures of polymer blends. In order to study the interfacial molecular structure of blends in OPVs (typically BHJs), a blend of regioregular poly-3-hexylthiophene (rrP3HT) and  $\text{C}_{60}$  or its soluble derivative, [6,6]-phenyl- $\text{C}_{61}$ -butyric acid methyl ester (PCBM) has been examined using 1D and 2D NMR measurements [51]. Chemical shift (CS) data acquired from composite films (CFs) fabricated at room temperature (PCBMCF-RT and  $\text{C}_{60}\text{CF-RT}$ , respectively) and CFs which had later been annealed at  $150^\circ\text{C}$  for 30 min (PCBMCF-A150 and  $\text{C}_{60}\text{CF-A150}$ , respectively), was inferred to clarify the local structure within the interface (Figure 21.10). The alkyl side chains of rrP3HT are close to the  $\text{C}_{60}$  ball in PCBMCF-RT, which causes a wrapping of the  $\text{C}_{60}$  by the alkyl side chains. However, the alkyl side chains in PCBMCF-A150 self-assemble in such way that rrP3HT and PCBM are phase-separated (Figure 21.11).

In the CS spectrum of the  $^{13}\text{C}$  of  $\text{C}_{60}$  in  $\text{C}_{60}\text{CF-A150}$ , a well-defined splitting was observed which was an indication of a distortion from spherical symmetry. Fluctuations in the local magnetic field which arise from the dynamics of the  $\text{C}_{60}$  distortion, were determined from spin-lattice relaxation rate ( $1/T_1$ ) measurements of  $\text{C}_{60}$ .

Nieuwendaal *et al.* showed that because of  $^1\text{H}$  spin diffusion, NMR sensitivity to intermolecular correlations at the nanometer length scale, and its unambiguous chemical contrast, can be used to measure the phase behavior and domain sizes of BHJs of the P3HT/PCBM system [52]. When increasing the efficiency of OPVs, thermal treatment is generally thought of as a vital step in fabrication process; however, the formation of needle-like PCBM crystallites which normally cause a lower efficiency is one unfortunate consequence of thermal treatment.

Martini *et al.* used multinuclear and multitechnique solid-state NMR spectroscopy in comprehensive examinations of P3HT and PCBM and their blends, before

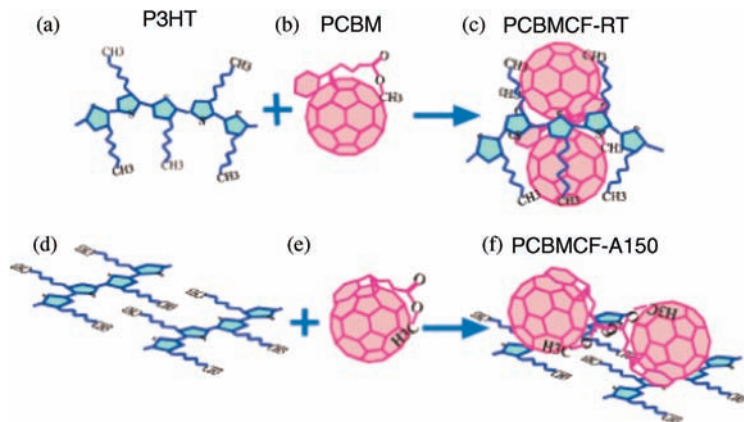


**Figure 21.11** Illustrations of the molecular structure near the interface before (a–c) and after (d–f) annealing. Reproduced with permission from Ref. [51]; © 2006, American Chemical Society.

and after annealing at 150 °C [53]. As a consequence, valuable information on the phase and morphological properties on the nanometric and subnanometric scales of the blends and neat materials were achieved with  $^{13}\text{C}$  CP/MAS spectra, high-resolution  $^1\text{H}$   $T_1$  measurements and low-resolution  $^1\text{H}$  NMR free induction decay analysis. In order to obtain a comprehensive characterization of the dynamic behavior of P3HT in the MHz frequency range for the neat polymer and blends, variable-temperature  $^1\text{H}$  and  $^{13}\text{C}$   $T_1$  measurements have been conducted and the experimental relaxation times analyzed using sophisticated models.

Based on the results obtained, and most likely because of the intimate mixing of P3HT with PCBM, the mobility of the side chains of P3HT were seen to decrease when passing from the neat polymer to the blend before annealing. However, annealing induces phase separation between P3HT and PCBM which leads in turn to an increase in free volume and, consequently, to an increase in the mobility of the alkylic side chains [53].

Solid-state NMR spectroscopy was used by McGehee and coworkers [54] to provide a complementary insight into the molecular structures of poly(2,5-bis(3-hexadecylthiophen-2-yl)thieno[3,2-b]thiophene (PBTTT):fullerene blends (Figure 21.12), including disordered moieties for which X-ray diffraction is less useful. In particular, solid-state 2D  $^{13}\text{C}$  [52] heteronuclear correlation (HETCOR) NMR spectroscopy was used to identify dipole–dipole-coupled  $^{13}\text{C}$  and  $^1\text{H}$  nuclei that are associated with molecularly neighboring moieties, thus providing comprehensive information on the molecular interactions between PBTTT-C16 and PC<sub>71</sub>BM.

As an example, a 2D  $^{13}\text{C}$  [44] HETCOR spectrum acquired for a PBTTT-C16:PC<sub>71</sub>BM blend with a molar ratio of 1 : 1 is shown in Figure 21.13a. This spectrum shows strong 2D intensity correlations (red, blue arrows) from the conjugated polymer (orange) and the fullerene derivative (blue) between  $^{13}\text{C}$  and  $^1\text{H}$  signals

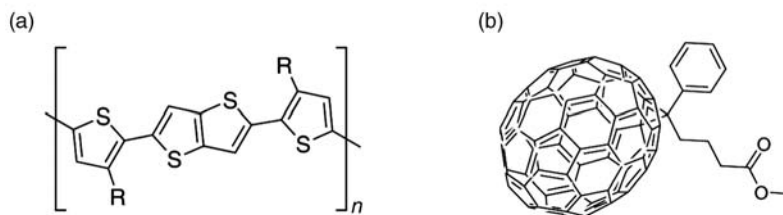


**Figure 21.12** The chemical structures of (a) PBTBT and (b) PC<sub>71</sub>BM. R in the polymer structure can be C<sub>12</sub>H<sub>25</sub>, C<sub>14</sub>H<sub>29</sub>, or C<sub>16</sub>H<sub>33</sub>. Reproduced with permission from Ref. [54]; © 2012, American Chemical Society.

that demonstrates their mutual molecular proximities (<1 nm). Such intensity correlations provide unequivocal evidence for intercalation of the fullerene derivative in the polymer network.

For example, signals associated with <sup>13</sup>C moieties from the PC<sub>71</sub>BM side group (e.g., at 172 ppm from the C=O groups, at 129 ppm from the phenyl rings, and at 36 and 73 ppm from the cyclopropane anchor) are correlated with <sup>1</sup>H signals at 1.4 ppm from the aliphatic PBTBT-C16 polymer side chains. Further intensity correlations are detected between <sup>13</sup>C signals from the C<sub>70</sub> fullerene moieties and <sup>1</sup>H signals at 1.4, 7.2 and 8.7 ppm from the aliphatic side chains and the aromatic backbone protons of conjugated polymer, respectively. Strong interactions – and hence close molecular proximities – between these molecular moieties have been verified by the correlated 2D NMR spectroscopy signal intensities. Moreover, it was also possible to determine the local distances between different aromatic proton moieties by separate solid-state <sup>1</sup>H [52] double-quantum NMR spectroscopy analyses. In detail, the <sup>1</sup>H signals at 7.2 and 8.7 ppm correspond to distinct thienothiophene moieties, and provide important quantitative constraints that allow for a definitive recognition of the structure of the bimolecular crystal [54].

## 21.7

### Conclusions

Solid-state NMR methods provide a powerful tool for understanding miscibility among polymers, with a specific ability to quantify the length scales of mixing below that accessible by other experimental tools (i.e., traditional calorimetric methods), and to detect the inter- and intramolecular interactions that are responsible for miscibility. At present, the area of understanding miscible blend dynamics is of particular interest to many NMR-based investigations, some of which have been reviewed in this chapter. By using solid-state NMR, the details of hydrogen bonding, phase behavior and the dynamics of molecular segments can be investigated. This implies possible new applications in important fields such as tissue engineering and drug delivery. Multinuclear, multi-technique solid-state NMR is especially effective in providing detailed phase, morphological and dynamic information on BHJs prepared from conjugated polymer/fullerene

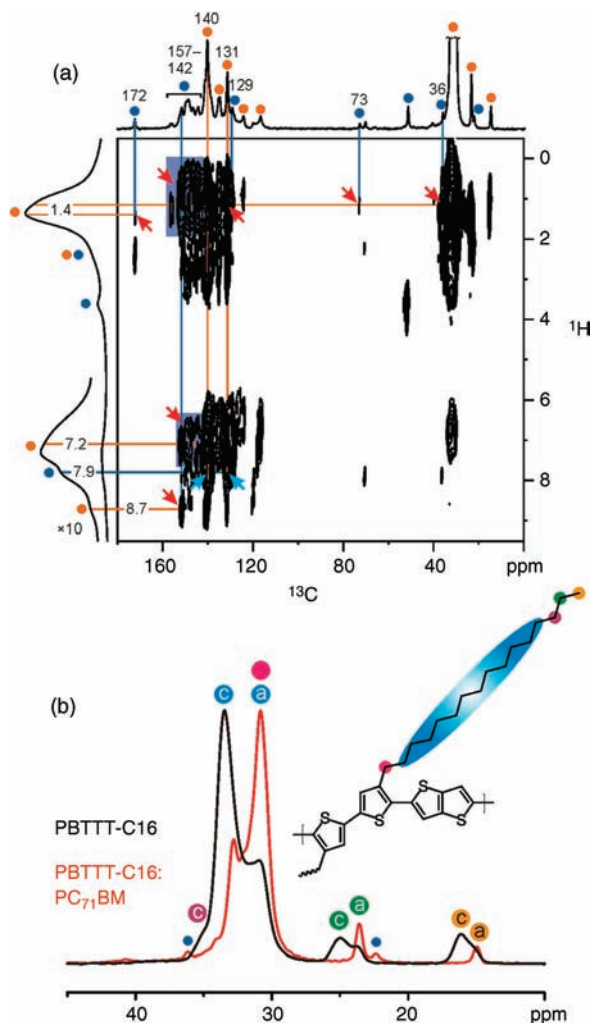


**Figure 21.13** (a) 2D  $^{13}\text{C}$  HETCOR [52] NMR spectrum of a PBTTT-C16:PC $_{71}$ BM blend with a molar ratio of 1 : 1. A corresponding 1D  $^{13}\text{C}\{^1\text{H}\}$ CP/MAS spectrum is shown along the top horizontal axis, and a 1D single-pulse  $^1\text{H}$  MAS spectrum is shown along the left vertical axis. The orange and blue circles indicate spectral contributions from the PBTTT-C16 and the PC $_{71}$ BM, respectively. Lines are shown to aid the identification of correlated signal intensities that establish spatial proximities between specific moieties of the conjugated polymer and the fullerene derivative. The red arrows mark correlated signals between the  $^{13}\text{C}$  moieties of the PC $_{71}$ BM and the  $^1\text{H}$  moieties of the PBTTT-C16, consistent with the proposed crystal

structure. The light-blue arrows mark correlated signals between the aromatic  $^{13}\text{C}$  moieties of the conjugated polymer and the protons from the PC $_{71}$ BM side chain, revealing local structural disorder of fullerene orientations in the polymer crystal; (b) Aliphatic regions of 1D  $^{13}\text{C}\{^1\text{H}\}$ CP/MAS spectra of the PBTTT-C16:PC $_{71}$ BM blend (red) and the neat polymer (black) recorded under MAS conditions of 12.5 kHz with a CP contact time of 2 ms. The colored circles assign the  $^{13}\text{C}$  moieties of the PBTTT-C16 side chains in the crystalline (c) and amorphous (a) regions to their respective signals in the 2D spectrum. Reproduced with permission from Ref. [54]; © 2012, John Wiley & Sons, Inc.

derivative blends which are becoming increasingly common in OPV devices and organic light-emitting diodes.

## References

- Kresge, E., Paul, D., and Newman, S. (1978) *Polymer Blends* (eds D.R. Paul and S. Newman), Academic Press, New York, p. 20.
- Abolhasani, M.M., Azar, A.A., and Shokoohi, S. (2009) PET/EVA/PP ternary blends: An investigation of extended morphological properties. *J. Appl. Polym. Sci.*, **112** (3), 1716–1728.
- Abolhasani, M., Arefazar, A., and Mozdianfard, M. (2010) Effect of dispersed phase composition on morphological and mechanical properties of PET/EVA/PP ternary blends. *J. Polym. Sci. Part B: Polym. Phys.*, **48** (3), 251–259.
- Abolhasani, M.M. *et al.* (2013) Poly (vinylidene fluoride)-acrylic rubber partially miscible blends: Phase behavior and its effects on the mechanical properties. *J. Appl. Polym. Sci.*, **130** (2), 1247–1258.
- Abolhasani, M. *et al.* (2013) Poly (vinylidene fluoride)-acrylic rubber partially miscible blends: Crystallization within conjugated phases induce dual lamellar crystalline structure. *Polymer*, **54** (17), 4686–4701.
- Abolhasani, M.M. *et al.* (2014) Influence of miscibility phenomenon on crystalline polymorph transition in poly(vinylidene fluoride)/acrylic rubber/clay nanocomposite hybrid. *PloS One*, **9** (2), e88715.
- Olabis, O. (1979) *Polymer-Polymer Miscibility*, Academic Press.
- Kwei, T., Nishi, T., and Roberts, R. (1974) A study of compatible polymer mixtures. *Macromolecules*, **7** (5), 667–674.
- White, J.L. and Mirau, P. (1993) Probing miscibility and intermolecular interactions in solid polymer blends using the nuclear Overhauser effect. *Macromolecules*, **26** (12), 3049–3054.
- White, J.L. (1997) Exploiting methyl groups as motional labels for structure analysis in solid polymers. *Solid State Nucl. Magn. Reson.*, **10** (1), 79–88.
- Mirau, P.A., Tanaka, H., and Bovey, F.A. (1988) Two-dimensional NMR studies of polymer mixtures. *Macromolecules*, **21** (10), 2929–2933.
- Heffner, S.A. and Mirau, P.A. (1994) Identification of intermolecular interactions in 1,2-polybutadiene/polyisoprene blends. *Macromolecules*, **27** (25), 7283–7286.
- Kurosu, H. and Chen, Q. (2004) Structural studies of polymer blends by solid-state NMR. *Annu. Rep. NMR Spectrosc.*, **52**, 167–200.
- Masson, J.F. and Manley, R.S.J. (1992) Solid-state NMR of some cellulose/synthetic polymer blends. *Macromolecules*, **25** (2), 589–592.
- Zhang, X. *et al.* (2004) The mechanical property and phase structures of wheat proteins/polyvinyl alcohol blends studied by high-resolution solid-state NMR. *Polymer*, **45** (10), 3305–3312.
- Spěváček, J. *et al.* (2007) Solid-state NMR study of biodegradable starch/polycaprolactone blends. *Eur. Polym. J.*, **43** (5), 1866–1875.
- Ameye, D. *et al.* (2005) Correlation between the molecular morphology and the biocompatibility of bioadhesive carriers prepared from spray-dried starch/Carbopol blends. *Polymer*, **46** (7), 2338–2345.
- Yoshitake, S. *et al.* (2013) Nanoincorporation of layered double hydroxides into a miscible blend system of cellulose acetate with poly(acryloyl morpholine). *Carbohydr. Polym.*, **93** (1), 331–338.
- Masson, J.F. and Manley, R.S.J. (1991) Cellulose/poly (4-vinylpyridine) blends. *Macromolecules*, **24** (22), 5914–5921.
- Masson, J.F. and Manley, R.S.J. (1991) Miscible blends of cellulose and poly (vinylpyrrolidone). *Macromolecules*, **24** (25), 6670–6679.
- McBrierty, V.J. and Douglass, D.C. (1981) Recent advances in the NMR of solid polymers. *J. Polym. Sci. Macromol. Rev.*, **16** (1), 295–366.



- 22 Assink, R. (1978) Nuclear spin diffusion between polyurethane microphases. *Macromolecules*, **11** (6), 1233–1237.
- 23 Radloff, D., Boeffel, C., and Spiess, H. (1996) Cellulose and cellulose/poly(vinyl alcohol) blends. 2. Water organization revealed by solid-state NMR spectroscopy. *Macromolecules*, **29** (5), 1528–1534.
- 24 Spiegel, S. *et al.* (1993)  $^1\text{H}$  spin diffusion coefficients of highly mobile polymers. *Polymer*, **34** (21), 4566–4569.
- 25 Zhang, X., Takegoshi, K., and Hikichi, K. (1992) Composition dependence of the miscibility and phase structure of amorphous/crystalline polymer blends as studied by high-resolution solid-state carbon-13 NMR spectroscopy. *Macromolecules*, **25** (9), 2336–2340.
- 26 Chaléat, C., Halley, P., and Truss, R. (2012) Study on the phase separation of plasticised starch/poly(vinyl alcohol) blends. *Polym. Degrad. Stab.*, **97** (10), 1930–1939.
- 27 Gidley, M.J. and Bociek, S.M. (1985) Molecular organization in starches: a carbon 13 CP/MAS NMR study. *J. Am. Chem. Soc.*, **107** (24), 7040–7044.
- 28 Bogracheva, T.Y., Wang, Y., and Hedley, C. (2001) The effect of water content on the ordered/disordered structures in starches. *Biopolymers*, **58** (3), 247–259.
- 29 Veregin, R. *et al.* (1986) Characterization of the crystalline A and B starch polymorphs and investigation of starch crystallization by high-resolution carbon-13 CP/MAS NMR. *Macromolecules*, **19** (4), 1030–1034.
- 30 Gidley, M.J. and Bociek, S.M. (1988) Carbon-13 CP/MAS NMR studies of amylose inclusion complexes, cyclodextrins, and the amorphous phase of starch granules: relationships between glycosidic linkage conformation and solid-state carbon-13 chemical shifts. *J. Am. Chem. Soc.*, **110** (12), 3820–3829.
- 31 Morgan, K.R., Furneaux, R.H., and Larsen, N.G. (1995) Solid-state NMR studies on the structure of starch granules. *Carbohydr. Res.*, **276** (2), 387–399.
- 32 Tan, I. *et al.* (2007) A method for estimating the nature and relative proportions of amorphous, single, and double-helical components in starch granules by  $^{13}\text{C}$  CP/MAS NMR. *Biomacromolecules*, **8** (3), 885–891.
- 33 Terao, T., Maeda, S., and Saika, A. (1983) High-resolution solid-state carbon-13 NMR of poly(vinyl alcohol): enhancement of tacticity splitting by intramolecular hydrogen bonds. *Macromolecules*, **16** (9), 1535–1538.
- 34 Horii, F. *et al.* (1992) Cross polarization/magic angle spinning  $^{13}\text{C}$  NMR study of solid structure and hydrogen bonding of poly(vinyl alcohol) films with different tacticities. *Polymer*, **33** (11), 2299–2306.
- 35 Horii, F., Masuda, K., and Kaji, H. (1997) CP/MAS  $^{13}\text{C}$  NMR spectra of frozen solutions of poly(vinyl alcohol) with different tacticities. *Macromolecules*, **30** (8), 2519–2520.
- 36 Zhang, X., Takegoshi, K., and Hikichi, K. (1992) High-resolution solid-state  $^{13}\text{C}$  nuclear magnetic resonance study on poly(vinyl alcohol)/poly(vinylpyrrolidone) blends. *Polymer*, **33** (4), 712–717.
- 37 Kuo, S.-W. *et al.* (2011) Substituent-induced delocalization effects on hydrogen-bonding interaction in poly(*N*-phenyl methacrylamide) derivatives. *Polymer*, **52** (12), 2600–2608.
- 38 Schmidt-Rohr, K. and Spiess, H.W. (1994) *Multidimensional Solid-State NMR and Polymers*, Academic Press.
- 39 Asakura, T. and Ando, I. (1998) *Solid State NMR of Polymers*, vol. **84**, Elsevier Science.
- 40 Goldman, M. and Shen, L. (1966) Spin-spin relaxation in  $\text{LaF}_3$ . *Phys. Rev.*, **144** (1), 321.
- 41 Egger, N. *et al.* (1992) Solid state NMR investigation of cationic polymerized epoxy resins. *J. Appl. Polym. Sci.*, **44** (2), 289–295.
- 42 Caravatti, P., Neuenschwander, P., and Ernst, R. (1986) Characterization of polymer blends by selective proton spin-diffusion NMR measurements. *Macromolecules*, **19** (7), 1889–1895.
- 43 Van der Hart, D. *et al.* (2000) Morphological characterization of blends of metal-sulfonated poly(styrene) and a methylated poly(amide) by solid state NMR. *Macromolecules*, **33** (6), 2206–2227.
- 44 Schmidt-Rohr, K. *et al.* (1990) Miscibility of polymer blends investigated by  $^1\text{H}$  spin diffusion and  $^{13}\text{C}$  NMR detection. *Magn. Reson. Chem.*, **28** (13), S3–S9.
- 45 Fu, W., Zhang, R., Li, B., and Chen, L. (2013) Hydrogen bond interaction and

- dynamics in PMMA/PVPh polymer blends as revealed by advanced solid-state NMR. *Polymer*, **54**, 472–479.
- 46 Demco, D. and Blümich, B. (2004) Nuclear magnetic resonance, in: *Encyclopedia of Polymer Science and Technology*, John Wiley; doi: 10.1002/0471440264.pst218.
  - 47 Fu, W. and Sun, P. (2011) Solid state NMR study of hydrogen bonding, miscibility, and dynamics in multiphase polymer systems. *Front. Chem. Chin.*, **6** (3), 173–189.
  - 48 Fortier-McGill, B., Toader, V., and Reven, L. (2011) Chain dynamics of water-saturated hydrogen-bonded polymer complexes and multilayers. *Macromolecules*, **44** (8), 2755–2765.
  - 49 John, J. *et al.* (2010) Main chain and segmental dynamics of semi interpenetrating polymer networks based on polyisoprene and poly(methyl methacrylate). *Polymer*, **51** (11), 2390–2402.
  - 50 Heeger, A.J. (2014) 25th anniversary article: bulk heterojunction solar cells: understanding the mechanism of operation. *Adv. Mater.*, **26**, 10–28.
  - 51 Yang, C., Hu, J.G., and Heeger, A.J. (2006) Molecular structure and dynamics at the interfaces within bulk heterojunction materials for solar cells. *J. Am. Chem. Soc.*, **128** (36), 12007–12013.
  - 52 Nieuwendaal, R.C. *et al.* (2010) Measuring the extent of phase separation in poly-3-hexylthiophene/phenyl-C61-butyric acid methyl ester photovoltaic blends with <sup>1</sup>H spin diffusion NMR spectroscopy. *Chem. Mater.*, **22** (9), 2930–2936.
  - 53 Martini, F. *et al.* (2012) P3HT/PCBM photoactive materials for solar cells: morphology and dynamics by means of solid-state NMR. *J. Phys. Chem. C*, **117** (1), 131–139.
  - 54 Miller, N.C. *et al.* (2012) Use of X-ray diffraction, molecular simulations, and spectroscopy to determine the molecular packing in a polymer-fullerene bimolecular crystal. *Adv. Mater.*, **24** (45), 6071–6079.

## 22

# Characterization of Polymer Blends by Infrared, Near-Infrared, and Raman Imaging

*Harumi Sato, Miriam Unger, Dieter Fischer, Yukihiro Ozaki, and Heinz W. Siesler*

### 22.1

#### Instrumentation for Mid-Infrared and Near-Infrared Imaging

The infrared (IR) or near-infrared (NIR) spectra of a multicomponent sample, when measured with a single-element detector, provide information on the identity of the different components in the sample area being investigated, but do not yield any information on their spatial separation. Since, for many analytical problems, this is the crucial point of an investigation, the development of focal plane array (FPA) detectors [1] for imaging measurements in the mid-IR and NIR wavelength regions has launched vibrational spectroscopy into a new era of analytical applications. By using this technique, several thousand spectra of laterally resolved sample positions can be measured simultaneously within a few minutes, providing chemical images as well as images of other parameters of the sample area under investigation. As a consequence, both mid-IR and NIR imaging techniques have over the past few years proved to be powerful tools for a broad range of industrial and research applications.

The experimental principles of operation are different for these two imaging methods, however. Whereas IR imaging is mainly operated in transmission or attenuated total reflection (ATR) mode as either a macro or (in combination with a microscope) as a micro technique, NIR imaging is primarily applied to diffuse reflection in the macro mode. In this chapter, attention will be focused exclusively on transmission measurements for both wavelength regimes, with polymer sample thicknesses lying in the range of a few microns. This corresponds approximately to the lateral resolution achievable when using the IR/NIR imaging technique.

Over many years the most common method of obtaining a Fourier transform infrared (FT-IR) image has been to perform a point-by-point mapping using a microscope fitted with a computer-controlled motorized stage. Despite automation, this mapping technique was very time-consuming and, due to diffraction limit aperture sizes of  $>15\text{--}20\text{ }\mu\text{m}$  being used, the lateral resolution was limited. In contrast, by using an infrared FPA detector, with  $64 \times 64$  or  $128 \times 128$  detector

elements (pixels), totals of 4096 or 16 384 spectra, respectively, could be measured simultaneously from different locations of the sample, within a few minutes. In Figure 22.1, the mapping (panel b) and FPA imaging (panel c) technique are compared with reference to a silicone oil-in-water emulsion, while the development of color-coded images (panel e) based on the intensities of specific absorption bands of the two components (panel d) are shown in schematic form.

The FT-IR imaging system (Bruker Optik GmbH, Ettlingen, Germany) used for the investigations described in this chapter is shown in Figure 22.2. The system consists of a rapid-scan FT-IR spectrometer, which is connected to an IR microscope (center) and a macrochamber for the investigation of larger imaging areas. Depending on the type of measurement required, the FPA detector can be connected to either the microscope or the macro chamber.

The NIR imaging measurements were performed using a PerkinElmer (Massachusetts, USA) imaging system, which consisted of a FT-NIR spectrometer coupled to a microscope (Figure 22.3). This totally integrated instrument operates in the  $2200\text{--}7600\text{ cm}^{-1}$  wavenumber range, and incorporates a  $16 \times 1$  element ( $400\text{ }\mu\text{m} \times 25\text{ }\mu\text{m}$ ) HgCdTe (MCT) array detector and a single point,  $100\text{ }\mu\text{m} \times 100\text{ }\mu\text{m}$  MCT detector in the same Dewar. The symmetrically arranged objective and condenser provide a sixfold image magnification at 1:1 imaging, and have a numerical aperture of 0.58. Specifically designed optics permit 1:1 or 4:1 imaging of the sampled area on the detector elements, resulting in  $25\text{ }\mu\text{m} \times 25\text{ }\mu\text{m}$  or  $6.25\text{ }\mu\text{m} \times 6.25\text{ }\mu\text{m}$  pixel sizes. For the investigations presented in this chapter, each image was measured in transmission mode for an area of  $320\text{ }\mu\text{m} \times 320\text{ }\mu\text{m}$  with a pixel size of  $6.25\text{ }\mu\text{m} \times 6.25\text{ }\mu\text{m}$  and a spectral resolution of  $16\text{ cm}^{-1}$  by coadding 32 scans for a spectrum.

Variable-temperature measurements were performed for selected investigations. For this purpose, a specifically designed sample holder was built and the experimental temperature was controlled with a High THC-15 unit (Yokohama, Japan) (Figure 22.4).

Before individual examples are discussed, a brief introduction will be provided on the issue of lateral resolution. In theory, the lateral resolution is governed by the Rayleigh criterion [2]:

$$r = 0.61 \frac{\lambda}{\text{NA}} \quad (22.1)$$

where  $r$  is the distance between two measurement points,  $\lambda$  is the wavelength of the radiation, and NA is the numerical aperture defined as:

$$\text{NA} = n \sin \theta \quad (22.2)$$

where  $n$  is the refractive index of the immersion medium between the objective and the sample (i.e., 1.0 for air, 4.0 for Ge in the case of ATR measurements) and  $\theta$  is the half-angle of the maximum cone of light that can enter or exit the condenser or objective. Two objects are completely resolved if they are separated by  $2r$ , and barely resolved if they are separated by  $r$ . As the largest numerical aperture that can generally be achieved for a Cassegrainian optic is approximately 0.6, the

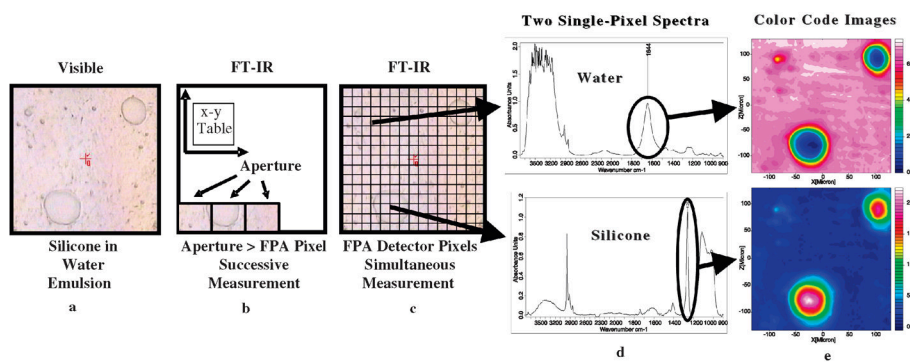


**Figure 22.1** (a) Visible image of a silicone oil-in-water emulsion; (b) Schematic comparison of the FT-IR mapping; (c) FT-IR/FPA imaging technique; (d) Two Single-Pixel Spectra; (e) Color-coded images based on the water-specific (top) and silicone oil-specific (bottom) absorption bands.

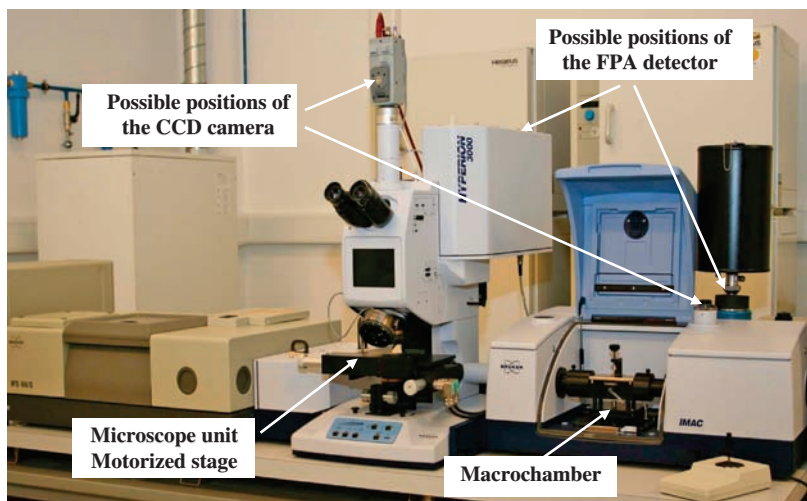


**Figure 22.2** The Bruker FT-IR imaging system used for the investigations described in the text.



**Figure 22.3** The PerkinElmer FT-NIR imaging system used for the investigations described in the text.

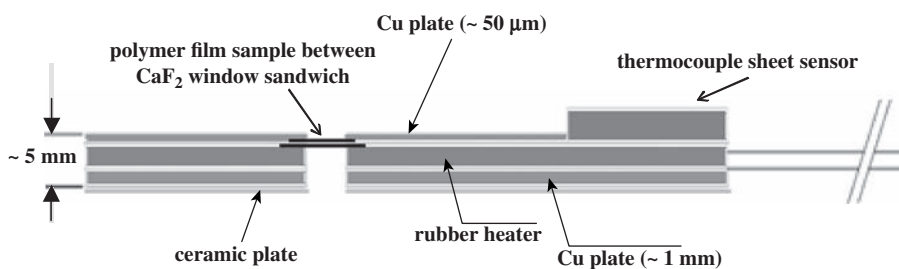


**Figure 22.4** Specifically designed sample holder for temperature-dependent investigations.

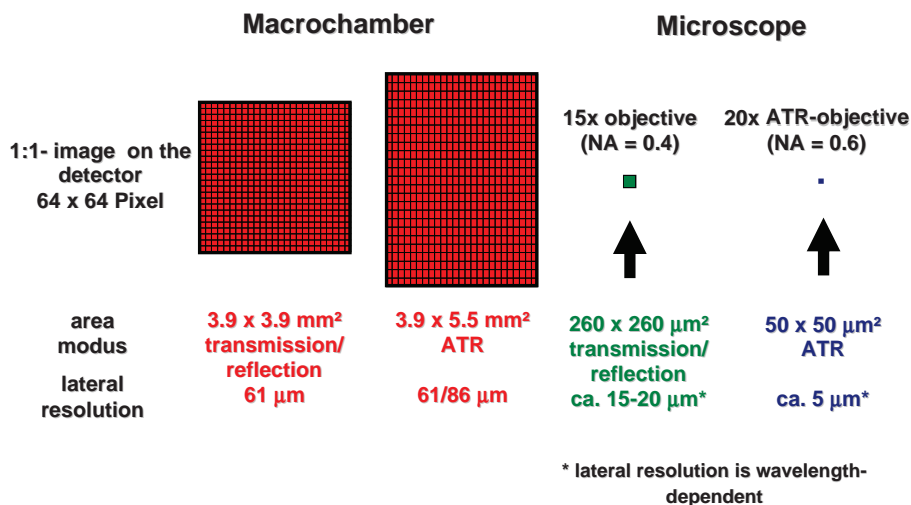


**Figure 22.5** Image areas and corresponding lateral resolutions for different FT-IR imaging measurement modes with a  $64 \times 64$  pixel focal plane array detector.

diffraction-limited spatial resolution is approximately equal to the wavelength of the light when  $n = 1.0$ . Thus, the achievable lateral resolution is wavelength-dependent, which means that the higher the wavenumber (or the lower the wavelength) of the absorption band evaluated for the development of an image, the better will be the lateral resolution of this image. A summary of the achievable lateral resolutions by FT-IR imaging with a  $64 \times 64$  FPA detector in the transmission or ATR mode for different sample areas is shown in Figure 22.5. Distortion of the image dimension in the macro ATR mode occurs because the radiation reflected from the internal reflection element is collected at an angle from the image plane [3].

## 22.2

### Raman Microspectroscopy

In principle, Raman microspectroscopy is attractive because the practical diffraction limit is on the order of the excitation wavelength, which is about 10-fold smaller for Raman spectroscopy with a visible laser than for mid-IR spectroscopy. It is therefore possible to focus visible laser light to much smaller spot sizes (400 nm in air and 240 nm with an oil immersion objective) than may be examined by mid-IR radiation. For various instrument-based reasons [4], charge-coupled device (CCD) Raman spectrometers have in practice proved to be far more successful for Raman microspectroscopy than FT-Raman spectrometers, and most instruments are based on this former concept. One further important instrumental advantage of the microscopes used for Raman microspectroscopy is their confocal design [5]. As the out-of-focus rays from an illuminated volume

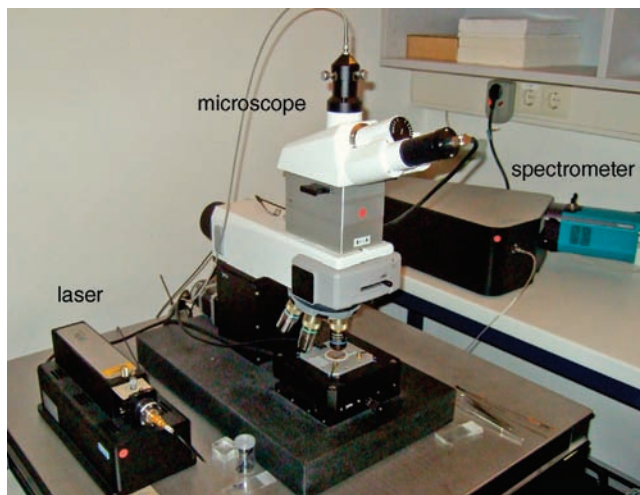


**Figure 22.6** The WITec alpha300R confocal Raman microscope used for Raman mapping investigations described in the text.

element within the specimen are largely removed with this optical design, sharper images are measured than can be acquired from conventional (nonconfocal) microscopy techniques. Mapping is accomplished by moving the sample by small steps after each spectrum has been recorded.

Among the commercially available instruments with confocal optical configurations, the WITec alpha300R (WITec GmbH, Ulm, Germany) is a very powerful and versatile instrument for performing Raman microspectroscopy. This instrument differs from other systems in that it has been designed especially for fast microspectroscopy. With a data acquisition time for an entire spectrum of less than 1 ms, it allows Raman mapping of several tens of thousands of spectra within a few minutes, when the Raman signal is adequate. For the purpose of an improved signal-to-noise ratio and shorter measurement times, the system has been equipped with an electron multiplying CCD (EMCCD) [6].

The confocal Raman microscope alpha300R consists of a microscope fitted with a piezo-driven scan table, a UHTS 300 spectrometer with an ultrafast EMCCD camera, and a Nd:YAG laser with a wavelength of 532 nm (Figure 22.6). All presented measurements were performed with a laser power of 5 mW for the polypropylene (PP)/polyamide 6 (PA6) samples and 10 mW for the poly(3-hydroxybutyrate) (PHB)/poly(L-lactic acid) (PLA) samples, and using a 50 $\times$  microscope objective with a NA of 0.5. The measured area was 50  $\mu\text{m}$   $\times$  50  $\mu\text{m}$  with a lateral resolution of 500 nm (101  $\times$  101 spectra) for the PP/PA6 samples, and 175  $\mu\text{m}$   $\times$  175  $\mu\text{m}$  with lateral resolutions of 1  $\mu\text{m}$  (176  $\times$  176 spectra) or 2  $\mu\text{m}$  (86  $\times$  86 spectra) for the PHB/PLA samples. Mapping of these areas was performed with a measuring time of 500 ms for each individual spectrum. All spectra



and mapping data were evaluated using the WITec Control and Project software or the CytoSpec software (v. 1.4.03; Dr Peter Lasch, Robert-Koch Institute, Berlin, Germany).

## 22.3

### Characterization of Polymer Blends by FT-IR Imaging

One field of materials science for which FT-IR imaging has proved extraordinarily important, from both scientific and practical aspects, is that of polymer analysis and polymer physics. In order to illustrate the broad range of applicability of these disciplines with a special focus on polymer blends, some selected applications will be discussed in detail; these range from phase separation and characterization of the state of order in biopolymer blends, to the use of polarized radiation to produce thickness and anisotropy images of inhomogeneously deformed polymer films.

#### 22.3.1

##### Investigation of Phase Separation in Biopolymer Blends

###### 22.3.1.1 Poly((3-Hydroxybutyrate)(PHB)/Poly(L-Lactic Acid)(PLA) Blends

Polymer blends of PHB and PLA have previously been analyzed by several research groups, using a wide variety of methods [7–9]. In the following, the application of transmission FT-IR and Raman imaging will be discussed as an alternative approach to providing a better understanding of the chemical and physical properties of these blends.

The FT-IR transmission spectrum of a PHB/PLA (50/50 wt%) blend film is shown in Figure 22.7 [10]. For FT-IR imaging, the nonoverlapped left and right wings of the intense  $\nu(\text{C}=\text{O})$  absorption band complex can be used primarily for the characterization of PLA ( $1758\text{ cm}^{-1}$ ) and PHB ( $1724\text{ cm}^{-1}$ ), respectively. The insert to Figure 22.7 has been included to demonstrate that the first overtones of the  $\nu(\text{C}=\text{O})$  absorption bands are even better separated than the bands of the fundamental  $\nu(\text{C}=\text{O})$  vibrations, and can also be used for the image evaluation of samples with larger thickness in the case of too-intense fundamental absorptions.

To provide a comparison of the spectral data obtained by FT-IR and Raman microspectroscopy, the Raman spectra of a PHB-rich and a PLA-rich domain of the same blend film (PHB/PLA; 50/50 wt%) are shown in Figure 22.8. These spectra clearly demonstrate the high selectivity of the PHB and PLA band separation in the  $1710\text{--}1800\text{ cm}^{-1}$  wavenumber region corresponding to the  $\nu(\text{C}=\text{O})$  vibration, and in the  $800\text{--}900\text{ cm}^{-1}$  range which has been assigned to a coupled mode of  $\nu(\text{C}-\text{O})$  and  $\nu(\text{C}-\text{C})$  vibrations [11].

Based on the spectra measured with the FT-IR, FT-NIR and Raman instruments of samples with various mechanical and thermal pretreatments, and under different experimental conditions, images have been derived by exploiting the spectral differences of the blend components.

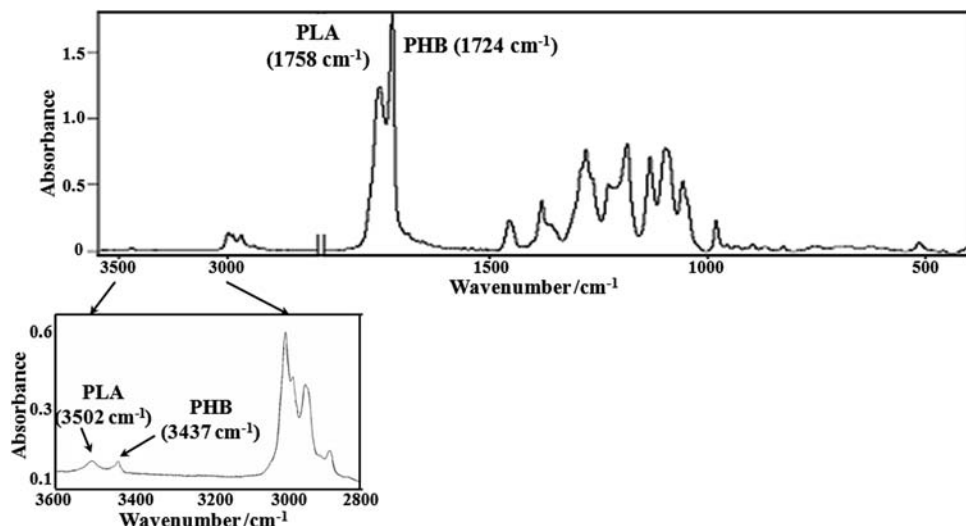


**Figure 22.7** FT-IR transmission spectrum of a PHB/PLA (50/50 wt%) polymer blend film (10  $\mu\text{m}$ ) in the wavenumber region 3600–400  $\text{cm}^{-1}$ . The enlarged insert was recorded from a 25  $\mu\text{m}$  film sample.

The visible images and PHB- and PLA-specific FT-IR images of two PHB/PLA blend films (50/50 and 30/70 wt%) for an area of  $260\text{ }\mu\text{m} \times 260\text{ }\mu\text{m}$  are shown in Figure 22.9. A visual image of the PHB/PLA 50/50 wt% blend with dark, circular-shaped islands embedded in a light matrix is shown in Figure 22.9a (left). In order to prepare the FT-IR contour plots, the PHB- and PLA-specific  $\nu(\text{C}=\text{O})$  absorption wings were integrated for all 4096-pixel spectra. The FT-IR image based on the PHB-specific absorption band (Figure 22.9a, right) indicates a higher concentration of PHB in the islands (red-colored areas), which correlates with the darker areas in the visual image, whereas the matrix has a higher concentration of PLA which can be derived from the red-colored areas in the PLA-specific image

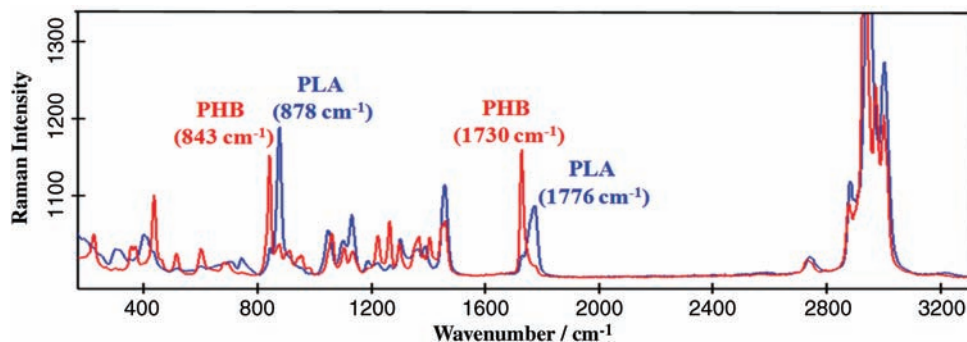


**Figure 22.8** Raman spectra of the PHB-rich (red) and PLA-rich (blue) domains of a PHB/PLA (50/50 wt%) blend film.

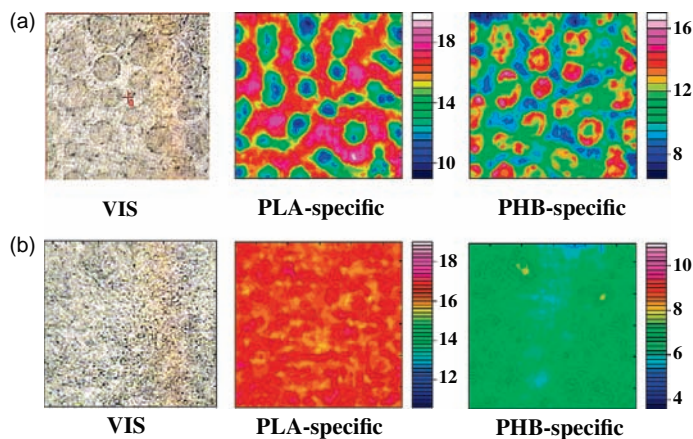


**Figure 22.9** Images of a  $260\ \mu\text{m} \times 260\ \mu\text{m}$  area of PHB/PLA blend films measured at  $25\ ^\circ\text{C}$ . (a) Visible image (left), PLA-specific FT-IR image (center) and PHB-specific FT-IR image (right) of a PHB/PLA (50/50 wt%) blend film; (b) Visible image (left), PLA-specific FT-IR image (center) and PHB-specific FT-IR image (right) of a PHB/PLA (30/70 wt%) blend film.

(Figure 22.9a, center). In contrast, within the available lateral resolution under these experimental conditions and the  $\nu(\text{C}=\text{O})$  wavelength range ( $\sim 20\ \mu\text{m}$ ), no comparable phase separation to the 50/50 wt% blend can be observed in the FT-IR images of the PHB/PLA 30/70 wt% blend film (Figure 22.9b).

In order to obtain a detailed compositional analysis of the blend phases, different PHB/PLA blends ranging from 15/85 to 85/15 wt% were analyzed using FT-IR imaging. To compare these blends in terms of phase homogeneity and composition, the peak maxima of the PHB and PLA  $\nu(\text{C}=\text{O})$  bands were determined for the spectra with the highest absorption intensities for PLA and PHB. The  $\text{PHB}_{\text{max}}/\text{PLA}_{\text{max}}$  intensity ratios were then mapped versus the concentration of PLA (wt%) in Figure 22.10 for the different PHB/PLA blends. The graph obtained clearly indicated that polymer blends with 15, 30, 60, 70 and 85 wt% PLA exhibited only small differences in the  $\text{PHB}_{\text{max}}/\text{PLA}_{\text{max}}$  intensity ratios for the PHB-rich and PLA-rich areas; this, in turn, indicated that these blends are homogeneous, one-phase polymer systems. In contrast, blends with 40 and 50 wt% PLA showed significant differences in the  $\text{PHB}_{\text{max}}/\text{PLA}_{\text{max}}$  intensity ratios of their PHB-rich and PLA-rich phases. Thus, the FT-IR images provided evidence that these blends were separated into two phases with different PHB/PLA compositions; these results were also confirmed by differential scanning calorimetry (DSC) measurements [10].

If a calibration line is drawn through the data points representing the miscible blends (15, 30, 60, 70 and 85 wt% PLA) in Figure 22.10, the compositions of the two phases in the phase-separated blends (40 and 50 wt% PLA) can be derived. In the PHB/PLA 50/50 wt% blend, the PHB-rich phase had a concentration of 39 wt% PLA, while the PLA-rich phase contained 69 wt% PLA. In the case of the PHB/

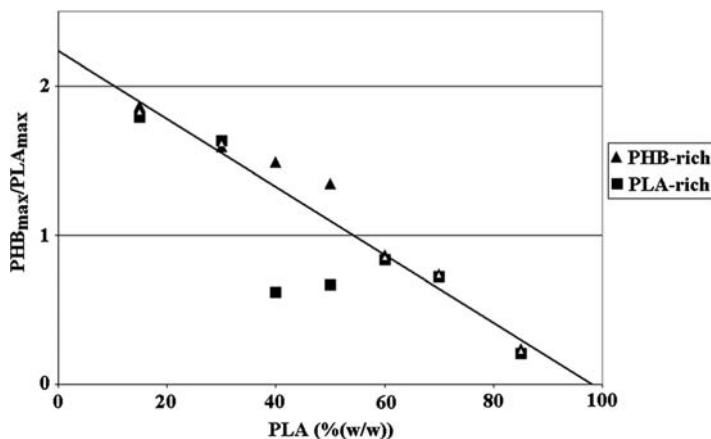


**Figure 22.10** PHB<sub>max</sub>/PLA<sub>max</sub> ratio versus content of PLA for the PHB-rich (▲) and PLA-rich (■) image areas of the different blend compositions (see text for details).

PLA 60/40 wt% blend, PLA contents of 33 and 71 wt% were calculated for the PHB-rich and PLA-rich phases, respectively.

### 22.3.1.2 FT-IR Imaging of Anisotropic PHB/PLA Blend Films

FT-IR imaging has also been applied to analyze phase-separated PHB/PLA blend films which previously had been uniaxially oriented by mechanical elongation. With reference to such anisotropic materials, a significant enhancement of the potential of FT-IR imaging can be achieved by the application of polarized radiation. The first reports of using polarized radiation combined with FT-IR imaging were made by Wilhelm *et al.* [12] and Koenig *et al.* [13]. Based on the polarization spectra obtained, it became clear that not only could images of chemically or physically different species be constructed, but that thickness and anisotropy images could also be developed for samples which had undergone inhomogeneous deformation due to mechanical treatment [14,15].

The extraordinarily informative value of images derived from polarization spectra was demonstrated with a PHB/PLA 50/50 wt% blend film that had an original thickness of 27  $\mu\text{m}$  and had been elongated at room temperature to 50% strain in a miniaturized, computer-controlled stretching machine (Figure 22.11a).

In FT-IR polarization spectroscopy two spectra are generally recorded, with the electric vector of the radiation polarized parallel ( $E_{\parallel}$ ) and perpendicular ( $E_{\perp}$ ), respectively, to a reference direction (e.g., the drawing direction) of the anisotropic sample being investigated. Based on a uniaxial orientation geometry from these experimental data, the intensity of any absorption band, independent of anisotropy, can be expressed by the structural absorbance  $A_0$ , which can be calculated by Eq. (22.3):

$$A_0 = \frac{2A_{\perp} + A_{\parallel}}{3} \quad (22.3)$$

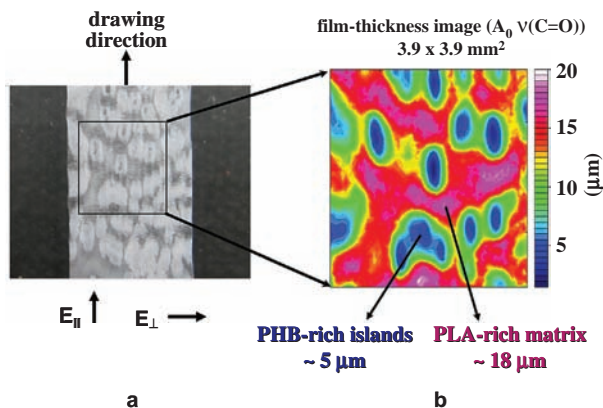


**Figure 22.11** (a) Visible image of a uniaxially drawn PHB/PLA (50/50 wt%) blend film; (b) “Thickness” image based on the structural absorbance of the total carbonyl band  $A_0$   $_{\text{PHB+PLA}}$ .

Based on the absorption intensities of a reference film with known thickness, an image of the marked area in Figure 22.11a was developed by the structural absorbance  $A_0$   $_{\text{PHB+PLA}}$  of the total carbonyl band (Figure 22.11b), which represents the thickness variations of the analyzed film area. Subsequently, from the significantly different contour colors it can be derived that the phase-separated PHB-rich “islands” deform in a different manner and to a much greater extent, and are therefore reduced to a smaller thickness than the PLA-rich matrix (Figure 22.11b). In a further step, “anisotropy” images can also be developed by calculating orientation functions from specific absorption bands of the polarization spectra.

In order to monitor the distribution of chain orientation of the two blend components over the total image area as a consequence of the mechanical treatment, the PHB- and PLA-specific  $\nu(\text{C}=\text{O})$  absorption bands were evaluated in terms of their orientation functions  $f_{\perp}$  (assuming perpendicular transition moments of the  $\nu(\text{C}=\text{O})$  vibrations relative to the PHB and PLA polymer chain direction) by:

$$f_{\perp} = -2 \frac{R - 1}{R + 2} \quad (22.4)$$

where  $R = A_{\parallel}/A_{\perp}$  is the dichroic ratio of the  $\nu(\text{C}=\text{O})$  absorption bands calculated from the two sets of imaging spectra recorded with the radiation polarized parallel and perpendicular to the drawing direction. For more detailed experimental and theoretical principles of FT-IR polarization spectroscopy, the reader is referred elsewhere [16,17].

In Figure 22.12a/b, the chemical images of the phase-separated domains have been developed in analogy to Figure 22.9a. However, in order to eliminate the significant sample thickness inhomogeneities in the stretched polymer (Figure 22.11b), the structural absorbance ratios  $A_{0,\text{PHB}}/A_{0,\text{PLA}}$  and  $A_{0,\text{PLA}}/A_{0,\text{PHB}}$  were applied and clearly indicated that, here too, the islands were PHB-rich and the matrix had a higher PLA content. The orientation function ( $f_{\perp}$ ) images of the

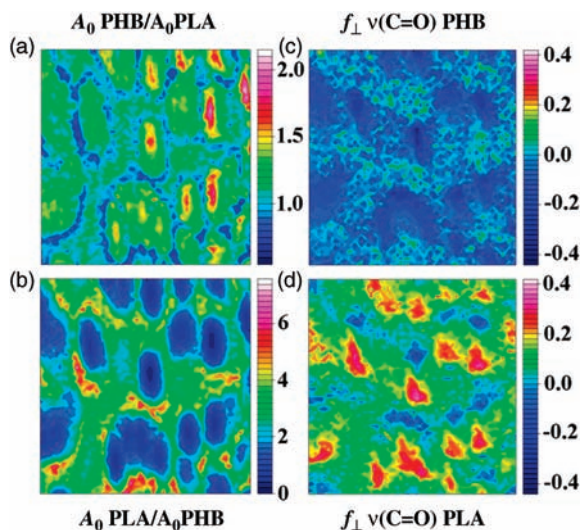


**Figure 22.12** FT-IR images ( $3.9 \times 3.9 \text{ mm}^2$ ) of PHB/PLA (50/50 wt%) blend film. For optimum comparison, the  $f_{\perp}$  images (c) and corresponding orientation function ( $f_{\perp}$ ) images of PHB (c) and PLA (d) of the 50% stretched

two blend components for the investigated sample area were calculated using Eq. (22.4), and are shown in Figure 22.12c,d. From these images a negative orientation ( $f_{\perp} \approx -0.4$ ) can be derived for the PHB chains in the “islands” (Figure 22.12c), whereas the PLA orients positively in the same domains ( $f_{\perp} \approx 0.3$ ) (Figure 22.12d). On the other hand, in the matrix both PHB and PLA orient only very slightly positive ( $f_{\perp}$  between 0 and 0.1) (Figure 22.12c,d). Thus, the two phases of the unstretched PHB/PLA 50/50 wt% blend film with uniform thickness responded completely different to the applied mechanical stress: notably, the PHB-rich phase was oriented to a higher degree and a lower thickness with opposite orientation of the two polymer components (PHB negative, PLA positive), whereas the PLA-rich phase underwent only a small elongation with a comparatively small thickness reduction and a very low positive orientation for both polymer components (see also Figure 22.11b). The opposite orientation behavior of PHB and PLA in the PHB-rich domains (the polymer chains of PHB and PLA were oriented perpendicular and parallel to the drawing direction, respectively) was observed in rheo-optical experiments of phase-separated PHB/PLA blend films, and this was explained in terms of a continuum mechanical orientation mechanism of the crystalline PHB domains relative to the amorphous PLA regions [18]. Thus, the originally isotropic, lamellar PHB domains would be aligned with their long axes in the direction of elongation, which would lead to a preferential perpendicular PHB chain orientation in the anisotropic film (Figure 22.13).

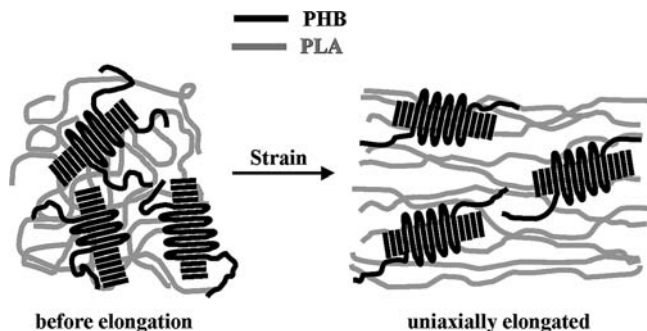


**Figure 22.13** Scheme of the continuum mechanical orientation mechanism of crystalline lamellar PHB domains in a predominantly amorphous PLA matrix.

The benefit of imaging measurements was demonstrated in detail previously [14], because polarization spectra recorded with a single-element detector cannot discriminate the different orientation mechanisms in the phase-separated, anisotropic structure of such polymer blends.

#### 22.3.1.3 Variable-Temperature FT-IR and Raman Imaging Spectroscopy of a Phase-Separated PHB/PLA 50/50 wt% Blend Film

Most pairs of chemically different polymers are mutually immiscible, and mixing usually results in materials which are phase-separated and have weak polymer–polymer interactions/interfaces [19,20]. Moreover, it is also known that the miscibility of different polymers depends on their concentration, the temperature, and their chemical structures [21–23].

Previously, FT-IR imaging spectroscopy was applied to study the miscibility of polymer blends of PHB and PLA as a function of blend composition (see Section 22.3.1.1), and from these investigations the concentration-dependence of phase separation at room temperature was determined. In this context, a phase-separated PHB/PLA 50/50 wt% polymer blend film was analyzed, using FT-IR spectroscopy, between room temperature and 175 °C (which was beyond the melting temperature of both polymers). Furthermore, complementary investigations using Raman imaging were performed in order to exploit the higher lateral resolution of this technique to interpret the structural changes observed as a function of variable temperature. FT-IR imaging measurements were performed using the Perkin Elmer system (see Figure 22.3), while Raman mapping investigations were made using the confocal Raman microscope (alpha300R; WITec GmbH; see Figure 22.6).

The FT-IR transmission spectrum of a PHB/PLA 50/50 wt% polymer blend is shown in Figure 22.7. In order to prepare the FT-IR contour plots for PHB, the  $2 \times \nu(\text{C}=\text{O})$  absorption band was integrated between 3449 and 3426  $\text{cm}^{-1}$ , while for PLA the integrated intensity between 3524 and 3490  $\text{cm}^{-1}$  was evaluated with a common baseline in the region of 3550–3410  $\text{cm}^{-1}$ . In order to visualize the changes in phase separation as a function of temperature, PLA/PHB and PHB/

PLA band ratio images were prepared so as to eliminate the influence of any variation in sample thickness. A constant scaling of the contour colors was applied as a visualization tool for displaying the FT-IR band ratio images. In this case, the colors were assigned based on the maximum and minimum absorbance values of the initial band ratio images at 25 °C. Thus, the colors of the subsequent images were normalized to the absorbance values of the initial images, such that the relationship between the color variation and absorbance values were constant over the interval of the temperature increase.

The visual and the PLA/PHB and PHB/PLA band ratio FT-IR images of the PHB/PLA 50/50 wt% blend are shown for a  $320\text{ }\mu\text{m} \times 320\text{ }\mu\text{m}$  area at 25 °C (panel a), 125 °C (panel b), and 165 °C (panel c) in Figure 22.14. In the visual images (Figure 22.14a and b) of the PHB/PLA 50/50 wt% polymer blend at 25 °C and 125 °C, it was observed that dark, circular islands were embedded in a light matrix. Based on the PLA/PHB band ratio images (Figure 22.14a and b, center images), the bright polymer matrix of the visual images correlated very well with the white/red areas, indicating a PLA-rich phase. In contrast, the FT-IR images based on the PHB/PLA band ratio (Figure 22.4a and b, right images) indicated a higher concentration of PHB in the islands (white/red color in this region), which correlated with the darker areas in the visual images. From these results it can be concluded that, apart from slight changes in the domain boundaries, the phase separation of the PHB/PLA 50/50 wt% polymer blend remained intact over the temperature range from 25 to 125 °C. Interestingly, at 165 °C (beyond the melting temperature of PLA) almost no contrast was detected in the visible image of the PHB/PLA 50/50 wt% blend (Figure 22.14c), but the PLA/PHB and PHB/PLA band ratio FT-IR images still showed small islands of PHB dispersed in the molten PLA matrix (Figure 22.14c, center and right images).

The FT-IR imaging spectra of the investigated PHB/PLA 50/50 wt% polymer blend film recorded at 25 °C and 175 °C are compared in Figure 22.15. Beyond the melting point of the crystalline PHB (174 °C), the disappearance of the crystalline structure led to a decreased intensity of the crystallinity-sensitive band ( $3437\text{ cm}^{-1}$ ) and a concomitant increase in the  $3460\text{ cm}^{-1}$  absorption band, which was characteristic of the amorphous PHB regions. In contrast, due to the low degree of crystallinity, no band shift was observed for the PLA band upon melting (Figure 22.15). Thus, the original band ratio evaluation could no longer be applied at 175 °C, and was replaced by an evaluation of the individual PLA and PHB band intensities. The visible and PLA- and PHB-specific FT-IR images ( $320\text{ }\mu\text{m} \times 320\text{ }\mu\text{m}$ ) of the PHB/PLA blend at 175 °C are shown in Figure 22.16.

At 175 °C neither in the visible nor in the FT-IR images of the PLA- and PHB-specific regions can the structures of phase separation be detected, which confirms that both phases of the PHB/PLA polymer blend are molten and that a more-or-less homogenous liquid phase remains.

The results of Raman imaging measurements of the PHB/PLA 50/50 wt% polymer blend will be discussed at this point. Two band pairs at  $1730/1776\text{ cm}^{-1}$  and  $843/878\text{ cm}^{-1}$  in the Raman spectra (Section 22.3.1.1; see Figure 22.8) were employed to develop PHB/PLA and PLA/PHB ratio images and to characterize



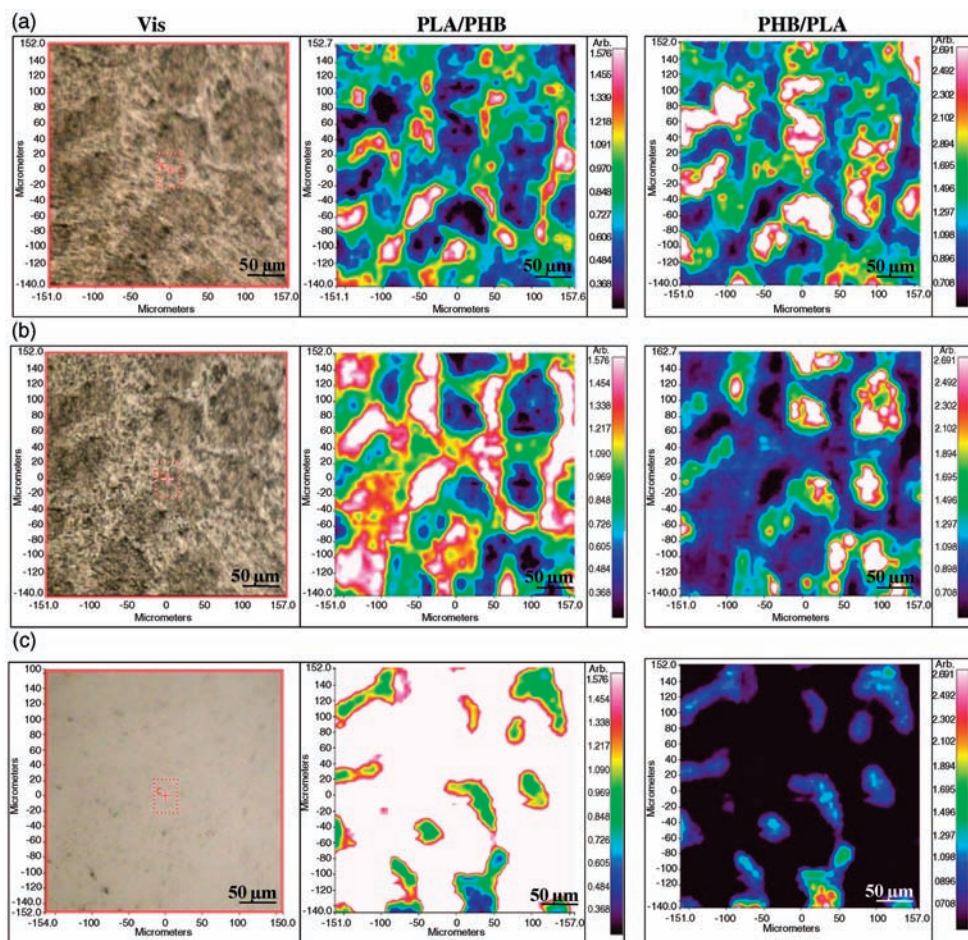


**Figure 22.14** Visual images (left), PLA/PHB band ratio FT-IR images (center) and PHB/PLA band ratio FT-IR images (right) of the PHB/PLA (50/50wt%) blend film at (a) 25 °C, (b) 125 °C, and (c) 165 °C.

the changes in phase separation as a function of temperature. The PHB/PLA images (175 μm × 175 μm) are shown for the two polymer-specific band pairs in Figure 22.17; corresponding images were obtained for the PLA/PHB ratio evaluation, but are not shown here.

Based on the Raman imaging data, two amendments must be made regarding the structural phenomena of the polymer blend and the changes as a function of increasing temperature, as derived from FT-IR data only. First, the originally assumed PHB-rich domains of about 50 μm (see Figure 22.14a and b) are in fact composed of much smaller grain structures of about 1 to 20 μm at 25 °C (see Figure 22.17, left panels). In addition, as a function of temperature this PHB-rich

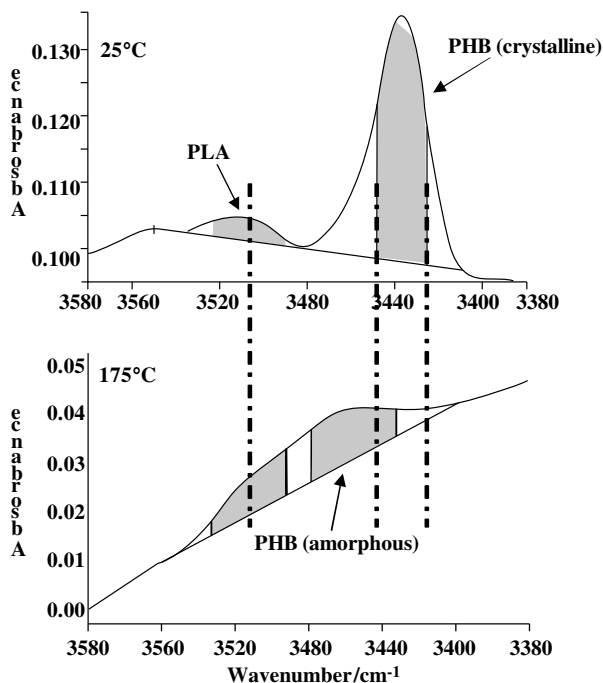


**Figure 22.15** FT-IR imaging spectra of the investigated PHB/PLA (50/50 wt%) blend film. Top: PHB-rich phase, 25 °C; Bottom: molten phases, 175 °C.

grain structure coalesces to somewhat larger domains at 125 °C and 165 °C before the melting of PHB.

#### 22.3.1.4 FT-IR Imaging of the State of Order of PHB/PCL Blend Films

One further application of FT-IR imaging spectroscopy is its combination with DSC. As well as allowing the detection of phase separation in polymer blends (as described above), information on the state of order in blend films also becomes

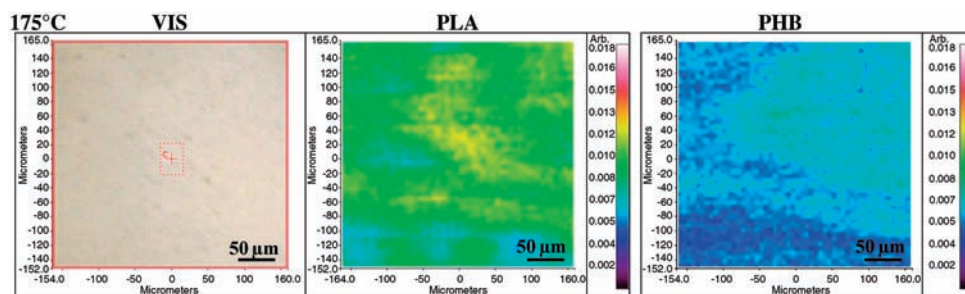


**Figure 22.16** Visual image (left), PLA-specific FT-IR image (center) and PHB-specific FT-IR image (right) of the PHB/PLA (50/50 wt%) blend film at 175 °C.

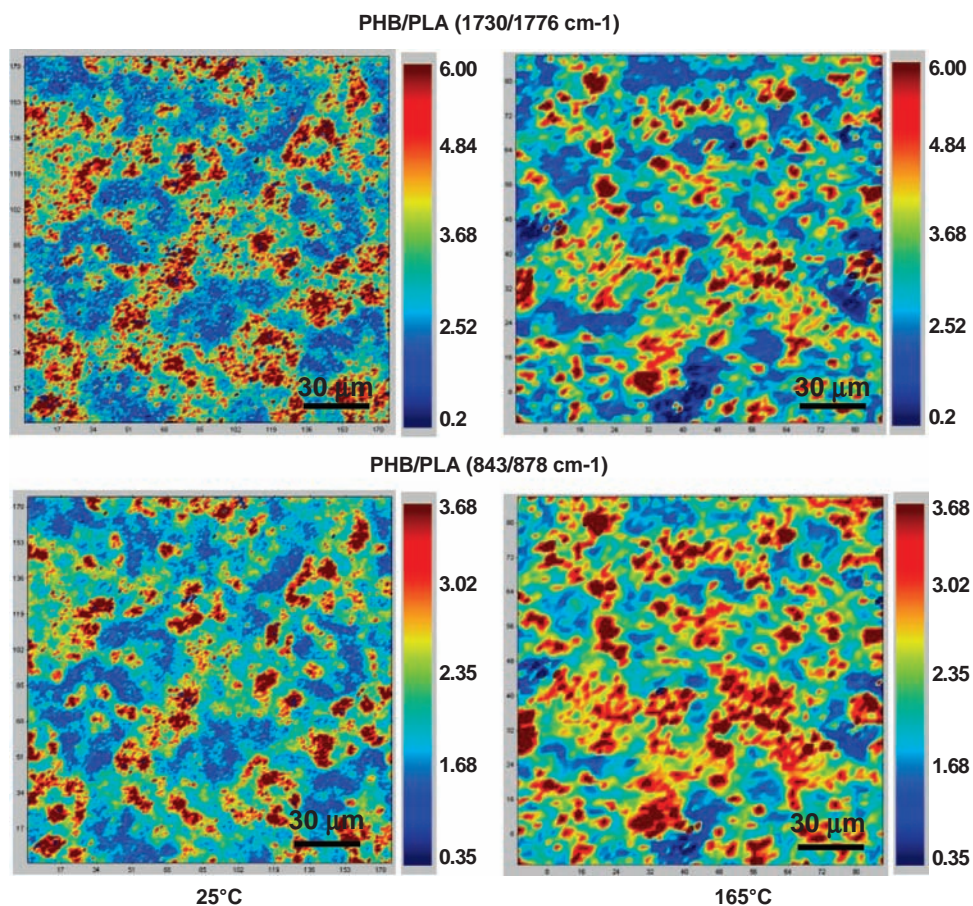


**Figure 22.17** PHB/PLA ratio images of a  $175\text{ }\mu\text{m} \times 175\text{ }\mu\text{m}$  area derived from the  $1730/1776\text{ cm}^{-1}$  (top) and from the  $843/878\text{ cm}^{-1}$  (bottom) specific band pairs of the PHB/PLA polymer blend measured at  $25\text{ }^{\circ}\text{C}$  and  $165\text{ }^{\circ}\text{C}$ .

available, such that FT-IR-specific images based on the degree of crystallinity can be developed.

This procedure is outlined with reference to a phase-separated PHB/PCL 50/50 wt% polymer blend film, with the determination of phase separation of a PHB/PCL 50/50 wt% blend film being discussed first. The FT-IR spectra of the individual polymers are shown in Figure 22.18a, and a spectrum of the PHB/PCL 50/50 wt% blend in the wavenumber region  $1550\text{--}850\text{ cm}^{-1}$  is shown in Figure 22.18b.

In order to develop the FT-IR contour plots, the PHB-specific ( $981\text{ cm}^{-1}$ ) and PCL-specific ( $1473\text{ cm}^{-1}$ ) absorption bands were integrated for all pixel spectra. The visible and FT-IR images of the PHB/PCL 50/50 wt% polymer blend, mapped for a  $260\text{ }\mu\text{m} \times 260\text{ }\mu\text{m}$  area, are shown in Figure 22.19.



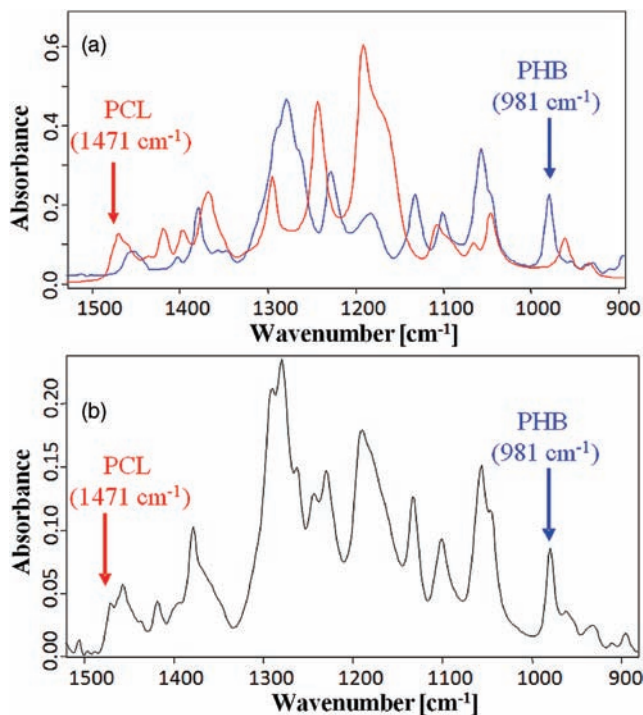


**Figure 22.18** (a) FT-IR spectra of PHB (blue) and PCL (red); (b) FT-IR spectrum of a PHB/PCL (50/50 wt%) blend film.

When compared to the PHB/PLA 50/50 wt% blend discussed in Section 22.3.1.1 (see Figure 22.9a), bright and dark areas could be clearly differentiated in the visual image of the PHB/PCL 50/50 wt% blend (Figure 22.19a). In addition, the dark areas correlated very well with the red areas of the PHB-specific image (Figure 22.19b) and the blue areas in the PCL-specific FT-IR image (Figure 22.19c).

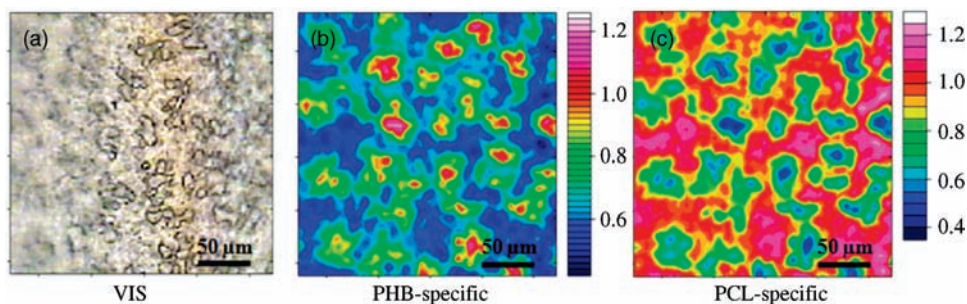


**Figure 22.19** Visual image (a), PHB-specific FT-IR image (b) and PCL-specific FT-IR image (c) of a PHB/PCL (50/50 wt%) blend.

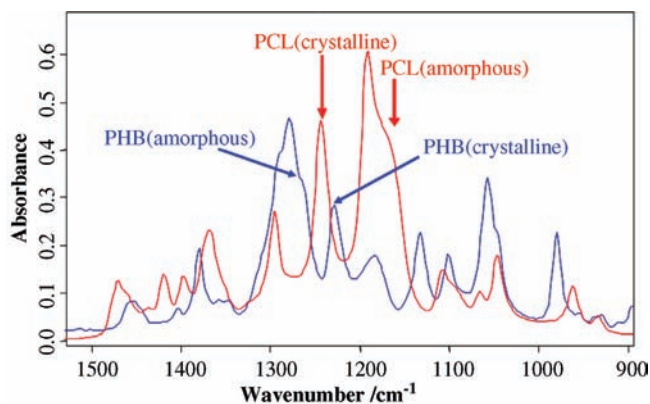


Figure 22.20 FT-IR transmission spectra of PHB (blue) and PCL (red) homopolymers.

Thus, it can be concluded that islands of PHB with a size of 20–25  $\mu\text{m}$  are embedded in a PCL matrix.

The next step was to demonstrate that, by employing a combination of FT-IR imaging and DSC measurements, crystallinity in the observed phase-separated PHB/PCL 50/50 wt% blend could be determined. The individual FT-IR spectra of PHB and PCL are shown, and the characteristic absorption bands of crystalline and amorphous domains are highlighted, in Figure 22.20. According to this figure, a crystallinity-specific band at  $1229\text{ cm}^{-1}$  and a band at  $1265\text{ cm}^{-1}$  for PHB that were characteristic for the amorphous regions were used whilst, for PCL, bands at  $1244\text{ cm}^{-1}$  (crystalline regions) and at  $1165\text{ cm}^{-1}$  (amorphous regions) were selected for further calculations. The DSC–temperature diagram of a PHB/PCL 50/50 wt% polymer blend is shown in Figure 22.21.

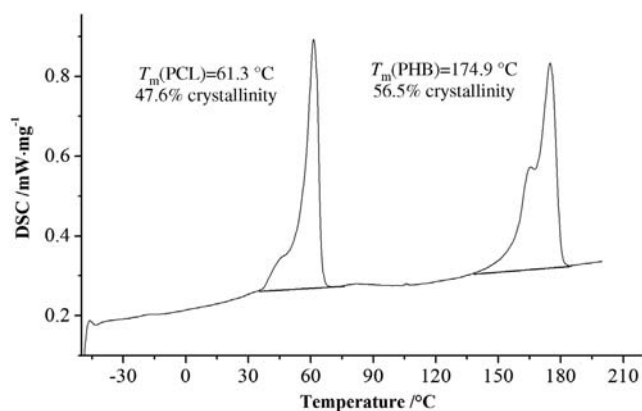
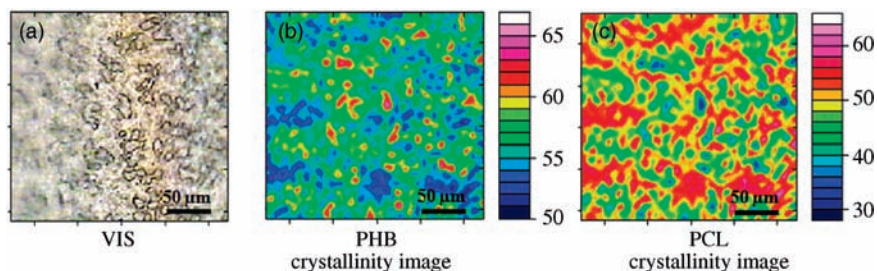


Figure 22.21 DSC curve of a PHB/PCL (50/50 wt%) polymer blend film over the temperature range  $-45$  to  $+200\text{ }^{\circ}\text{C}$ . The heating rate was  $10\text{ }^{\circ}\text{C min}^{-1}$ .



**Figure 22.22** Visual image (a), state-of-order PHB-specific FT-IR image (b) and state-of-order PCL-specific FT-IR image (c) of a PHB/PCL (50/50 wt%) blend. The color scale indicates % crystallinity.

The crystallinity derived from DSC measurements was 56.5% for PHB, and 47.6% for PCL. Assuming that these calculated degrees of crystallinity of PHB and PCL in the blend corresponded to the crystallinity indices derived from conventional FT-IR measurements of a PHB/PCL 50/50 wt% polymer blend, then state of order-specific FT-IR images could be developed. In order to prepare state-of-order specific FT-IR images of PHB and PCL, a crystallinity index was calculated from the intensities of the crystalline- and amorphous-characteristic absorption bands of PHB and PCL for all 4096-pixel spectra, respectively. These crystallinity indices were then transformed into percentage crystallinities corresponding to the DSC analysis of a PHB/PCL 50/50 wt% blend. The visible image, state-of-order PHB-specific and state-of-order PCL-specific FT-IR images of a PHB/PCL 50/50 wt% blend are depicted in Figure 22.22.

In addition to the observed phase separation of the PHB/PCL 50/50 wt% polymer blend, evidence of the degree of crystallinity in the PHB- and PCL-rich domains was also available. The data in Figure 22.22b show that, in the PCL-rich polymer matrix (blue-colored regions), PHB featured a crystallinity of less than 55%, whereas in the PHB-rich “islands” a crystallinity in excess of 60% was observed. In contrast, in the PCL-rich matrix showed a PCL-crystallinity of ca. 55%, whilst in the PHB-rich islands the PCL-crystallinity varied between 30% and 40% (see Figure 22.22c).

#### 22.3.1.5 FT-IR and FT-NIR Imaging of the Spherulitic Structure of Poly(3-Hydroxy-Butyrate) and Cellulose Acetate Butyrate Blends

Suttiwijitpukdee *et al.* [24] studied the crystal melting behavior of PHB and cellulose acetate butyrate (CAB) blends by using both IR and NIR imaging. The variations in the IR and NIR imaging spectra in the regions of the first and second overtones of the C=O stretching vibrations of PHB and CAB revealed the evolution of heterogeneous spherulites during the time-resolved isothermal crystallization process. Based on the results of time-resolved IR and NIR imaging and polarized microscopic studies, it was found that the PHB domains were able to separate from the PHB/CAB blends early in the process. The use of PCA allowed the distribution of the different morphologies of a spherulite to be classified. The

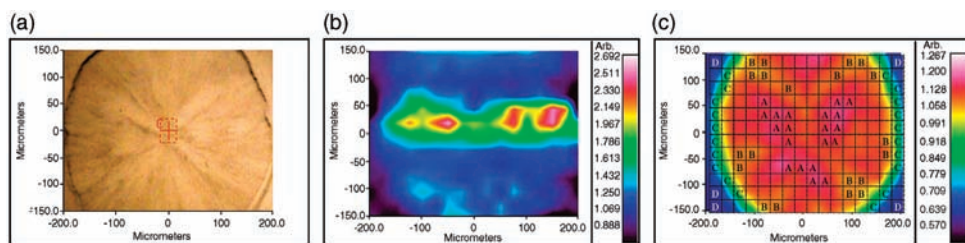


**Figure 22.23** Visual image (a), NIR image (b) and IR image ( $300\mu\text{m} \times 400\mu\text{m}$ ) (c) of the PHB/CAB blend (80/20 wt%) during isothermal crystallization at  $125^\circ\text{C}$  [24].

first principal component suggested that discrimination of the imaging spectra relied largely upon the crystallinity, while the second principal component indicated variations in the amorphous portion of PHB, the CAB contents, and the intermolecular hydrogen bonding of PHB and CAB. The PC1–PC2 scores of different parts of the spherulite suggested that the areas of low crystallinity in the blend spherulite contained both PHB and CAB.

The NIR image (Figure 22.23b) was calculated from the area ratios [25] of the second overtone of the C=O stretching mode of the crystal structure ( $5140\text{--}5090\text{cm}^{-1}$ ) and that of the amorphous part ( $5200\text{--}5150\text{cm}^{-1}$ ). The IR image (Figure 22.23c) was developed from the area ratio of the corresponding first overtone band of the crystalline regions ( $3445\text{--}3390\text{cm}^{-1}$ ) and that of the amorphous domains ( $3480\text{--}3450\text{cm}^{-1}$ ), which cover the crystal peak at  $3445\text{cm}^{-1}$  and the amorphous peak at  $3465\text{cm}^{-1}$ , respectively, to avoid the influence of the peak at  $3485\text{cm}^{-1}$  due to the hydrogen-bonded O–H groups of the CAB content [24,26]. Therefore, the selected range of this amorphous area was narrower than that of other regions. The calculated regions are shown in Figure 22.24. The images

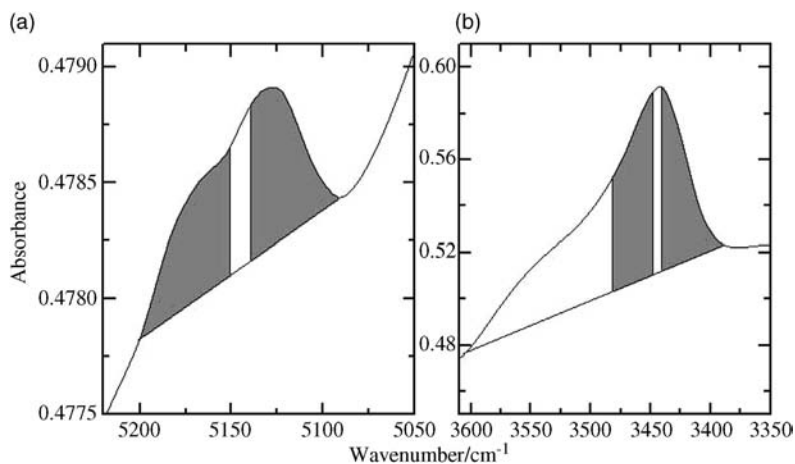


**Figure 22.24** NIR (a) and IR (b) imaging spectra of the PHB/CAB (80/20 wt%) blend film [24].

based on the crystal/amorphous band area ratios yield the high crystallinity of the spherulite (shown in red) and the amorphous part, which is represented by the darker color in the images (see Figure 22.23b and c). The NIR image shows the high crystallinity in the middle part (Figure 22.23b). It should be noted that the IR image shows more clearly the area ratios of the crystalline/amorphous bands, enabling a clearer monitoring of the surface of spherulite morphology than the NIR image. The differences in the band ratios of the NIR and IR images may be caused by two effects. The first effect is that of peak intensity; as the first overtone of the C=O stretching modes of PHB is much stronger than the second overtone, the composed image in the IR region depicts the spherulite morphology more clearly than the NIR image. The second effect is that the first overtone of the C=O stretching vibration in the IR region overlaps with some parts of the O–H stretching band, and the spherulite is affected by intermolecular C=O hydrogen bonding.

By exploiting the advantages of spectroscopic imaging, it may be possible to extract each spectrum from the local areas ( $25\text{ }\mu\text{m} \times 25\text{ }\mu\text{m}$ ), which provide information about the structure at the local points presented in Figure 22.23c. Suttiwijitpukdee *et al.* [24] classified the areas as follows: group A is the highly crystalline area in the spherulite, which is shown in the red color; group B is the low crystalline area shown in the orange color; group C is the interface of the spherulitic edge; and group D is the amorphous region outside the spherulite.

PCA was employed to classify the differences in the spectra for each local area spectrum of the spherulite. Consequently, 20 single spectra were extracted from 20 points of groups A–C, but for group D only five spectra were obtained as the amorphous area is limited (as shown in Figure 22.23c). All spectra in the region of  $5500\text{--}3300\text{ cm}^{-1}$  were subjected to a linear baseline correction and a second derivative pretreatment to highlight subtle differences in the spectral features among the spectra before the PCA calculations.

The PCA score plot of the first principal component (PC1) versus the second principle component (PC2) of each group is illustrated to compare their variations (see Figure 22.25). This plot clearly discriminates between groups A and B and groups C and D. It should be noted that the spectral points of group A are projected nearer to each other than the spectral points of group B, which suggests that group B contains heterogeneity within the group whereas the spectra of group A are similar to each other. The differences between groups A and B indicate that group B is most likely composed of a combination of PHB and a small fraction of CAB, whereas group A is highly crystallized and contains only PHB.

Figure 22.26 presents the loadings plot of PC1 (solid line) and PC2 (broken line), which account for 95% and 4% of the total spectral variance, respectively, of the results shown in Figure 22.25 for the total 65 spectra points. It is evident from the loading plot of PC1 that the important loadings are related to the first overtones of the C=O stretching modes at  $3470\text{ cm}^{-1}$  (amorphous part) and at  $3440$  and  $3424\text{ cm}^{-1}$  (crystalline part). However, judging from the peaks at  $3460$ ,  $3610$ ,  $4350$  and  $4400\text{ cm}^{-1}$  in the PC2 loading plot (broken line), PC2 also imparts



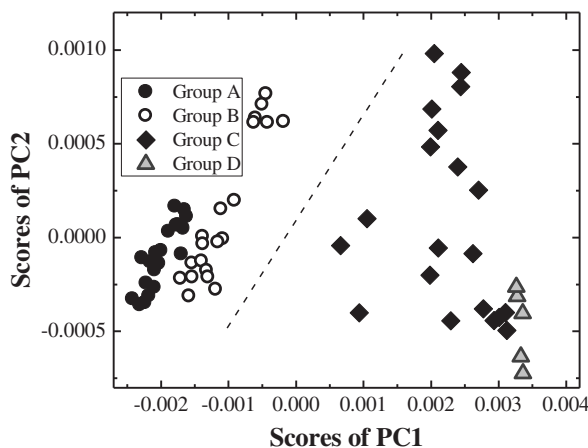


**Figure 22.25** Score plots of PCA factor 1 versus factor 2 for the 65 spectra of groups A, B, C, and D [24].

important information about the intermolecular interactions, even though it accounts for only 4% of the total variance. The highest loading value of PC2 is strongly related to the peak at  $3460\text{ cm}^{-1}$ , which corresponds to the intermolecular hydrogen bonding between CAB and PHB, as reported previously [26]. Furthermore, a weak loading value corresponds to the peak at  $\sim 3610\text{ cm}^{-1}$ , which may be related to the O—H stretching vibration of the CAB in the blends [27]. Therefore, this indicates that PC1 can be explained by introducing the crystallinity of PHB to the blend system, while the loading plot of PC2 indicates the contributions of the amorphous parts of PHB and CAB and the intermolecular hydrogen bonds of PHB and CAB.

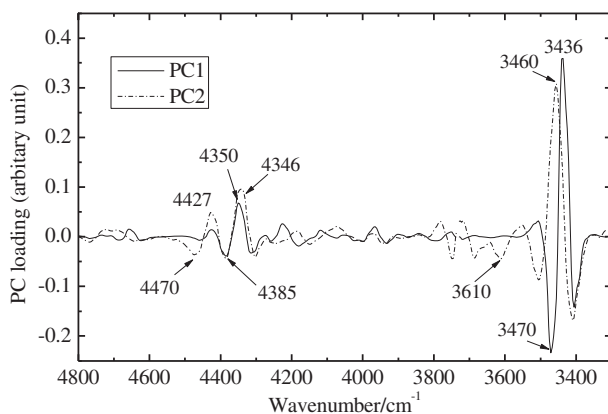


**Figure 22.26** PCA loadings plots of factor 1 and factor 2 of the results shown in Figure 22.25 [24].

### 22.3.1.6 Raman Mapping Measurements of the Influence of a Compatibilizer on Phase Separation of the Polymer Blend Polypropylene/Polyamide 6

In general, polymer blends are mixtures of two different polymers with improved properties in comparison to the individual polymers; however, they tend towards phase separation because of their immiscibility. To overcome this phenomenon, it is necessary to use a compatibilizer which is enriched between the interfaces to connect the immiscible phases. Typically, interactions between the polymer compounds at the interfaces will have a significant effect on the resultant morphology, and thus the macroscopic properties. Investigations into phase separation (and changes thereof) caused by the use of compatibilizers can be performed using Raman mapping, on the basis of its high lateral resolution.

In this case, the polymer blend PP/PA6 was investigated to demonstrate the influence of the compatibilizer maleic anhydride-grafted polypropylene (PP-g-MA) on the phase separation of different blend compositions. The specific Raman bands of PP at  $812\text{ cm}^{-1}$  and of PA6 at  $1640\text{ cm}^{-1}$  were used for development of the images (Figure 22.27). The Raman images developed for these two specific bands are shown in Figure 22.28, where the red areas represent PP and the blue areas correspond to PA6. Figure 22.28a shows the PP/PA6 (60/40 wt%) blend image without compatibilizer, while Figure 22.28b shows the PP/PA6/PP-g-MA (65/30/5 wt%) blend image with compatibilizer. The blend without compatibilizer was seen to exhibit a much stronger phase separation with heterogeneously distributed PA6 particles and significantly different particle sizes (between 1 and

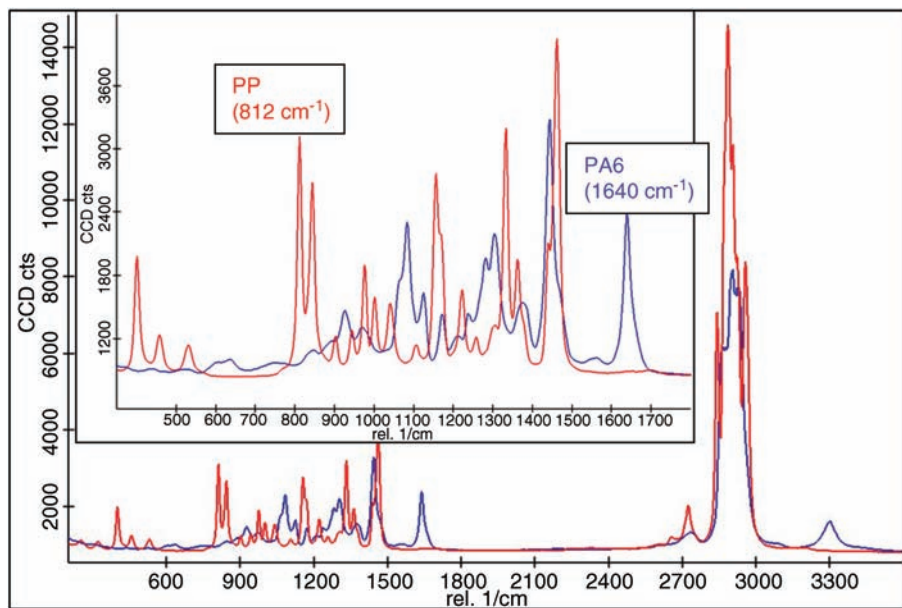
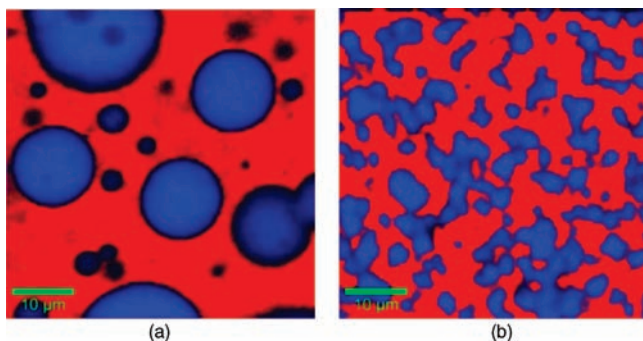


Figure 22.27 Raman spectra of pure PP (red) and PA6 (blue).



**Figure 22.28** Raman images of the blend PP/PA6 (red: PP, blue: PA6) without (a) and with (b) compatibilizer (see text for details).

15 µm). It was clear that the compatibilizer had strongly influenced the morphology in the blend since, after applying the compatibilizer, the blend reflected a completely different phase behavior with much smaller and more homogeneously distributed domains of PA6 in PP.

In addition, the morphology of the same blend components but with different compositions, ranging from 50 to 90 wt% PP without the PP-g-MA compatibilizer (5 wt%), and from 25 to 90 wt% PP with compatibilizer (5 wt%), was investigated. No difference in particle size of PA6 in the PP matrix was observed for the different blends without compatibilizer when compared to Figure 22.28a. However, different morphologies for different compositions were detected for those blends with compatibilizer; these morphologies are shown in Figure 22.29 for four different compositions. Smaller contents of PA6 (20 wt%) were mixed homogeneously with small domains far below 5 µm in both polymers (Figure 22.29a); however, by increasing the concentration of PA6 to 30 wt%, the phase separation was increased and larger domains of PA6 were observed (Figure 22.29b). Finally, by extending the concentration of PA6 to 40 wt% (Figure 22.29c), PA6 particles of up to 10 µm were formed in the phase-separated polymer blend.

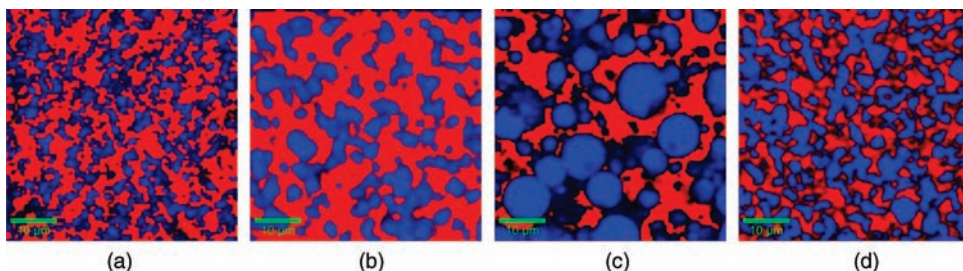


**Figure 22.29** Raman images of the blend PP/PA6 (red: PP, blue: PA6) with 5 wt% of the compatibilizer PP-g-MA. (a) PP/PA6/PP-g-MA (75/20/5 wt%); (b) PP/PA6/PP-g-MA (65/30/5 wt%); (c) PP/PA6/PP-g-MA (55/40/5 wt%); (d) PP/PA6/PP-g-MA (25/70/5 wt%).

A further increase in PA6 content to 70 wt% (Figure 22.29 d) led to domain sizes of the phase-separated polymer components that were comparable to small concentrations of PA6 (Figure 22.29a). This effect could be explained in terms of an optimum performance of the compatibilizer in preventing phase separation, if the content of one component was below 35 wt%.

## References

- Lewis, E.N., Treado, P.J., Reeder, R.C., Story, G.M., Dowrey, A.E., Marcott, C., and Levin, I.W. (1995) *Anal. Chem.*, **67**, 3377–3381.
- Hecht, E. (2001) *Optik*, 3rd edn, Oldenburg Wissenschaftsverlag GmbH, Munich.
- Kazarian, S.G. and Chan, K.L.A. (2010) *Appl. Spectrosc.*, **64** (5), 135A–152A.
- Griffiths, P.R. (2009) *Infrared and Raman Spectroscopic Imaging* (eds R. Salzer and H.W. Siesler), Wiley-VCH, Weinheim, pp. 3–64.
- Everall, N.J. (2009) *Appl. Spectrosc.*, **63** (9), 245A–262A.
- Hollricher, O. and Ibach, W. (2007) *Spectroscopy Suppl.*, **June**, 38–43.
- Blümm, E. and Owen, A.J. (1995) *Polymer*, **36**, 4077–4081.
- Park, J.W., Doi, Y., and Iwata, T. (2004) *Biomacromolecules*, **5**, 1557–1566.
- Furukawa, T., Sato, H., Murakami, R., Zhang, J., Duan, Y.-X., Noda, I., Ochiai, S., and Ozaki, Y. (2005) *Macromolecules*, **38**, 6445–6454.
- Vogel, C., Wessel, E., and Siesler, H.W. (2008) *Biomacromolecules*, **9**, 523–527.
- Jarmelo, S., Marques, D.A.S., Simoes, P.N., Carvalho, R.A., Batista, C.M.S.G., Araujo-Andrade, C., Gil, M.H., and Fausto, R. (2012) *J. Phys. Chem. B*, **116**, 9–21.
- Chernev, B. and Wilhelm, P. (2006) *Monatsh. Chem.*, **137**, 963–967.
- Snively, C.M. and Koenig, J.L. (1999) *J. Polym. Sci. Part B: Polym. Phys.*, **37**, 2353–2359.
- Vogel, C., Wessel, E., and Siesler, H.W. (2008) *Macromolecules*, **41**, 2975–2977.
- Vogel, C., Wessel, E., and Siesler, H.W. (2008) *Appl. Spectrosc.*, **62**, 599–602.
- Siesler, H.W. (1984) *Advances in Polymer Science*, Springer-Verlag, Berlin, Heidelberg, pp. 1–77.
- Siesler, H.W., Hoffmann, G.G., Kolomiets, O., Pfeifer, F., and Zahedi, M. (2007) Variable-temperature rheo-optical Fourier-transform infrared spectroscopy of polymers, in *Vibrational Spectroscopy of Polymers: Principles and Practice* (eds N.J. Everall, J.M. Chalmers, and P.R. Griffiths), John Wiley & Sons Ltd., Chichester, pp. 313–347.
- Vogel, C., Hoffmann, G.G., and Siesler, H.W. (2009) *Vib. Spectrosc.*, **49**, 284–287.
- Strobl, G. (2007) *The Physics of Polymers: Concepts for Understanding Their Structures and Behavior*, Springer, Berlin.
- Utracki, L.A. (1990) *Polymer Alloys and Blends*, Carl Hanser Verlag, München.
- Coleman, M.M., Graf, J.F., and Painter, P.C. (1991) *Specific Interactions and the Miscibility of Polymer Blends*, Technomic Publishers, Lancaster.
- Coleman, M.M. and Painter, P.C. (1984) *Appl. Spectrosc. Rev.*, **20** (3), 255–346.
- Paul, D.R. and Newman, S. (1978) *Polymer Blends*, Academic Press, New York.
- Suttiwijitpukdee, N., Sato, H., Unger, M., and Ozaki, Y. (2012) *Macromolecules*, **45**, 2738–2748.
- Bhargava, R. and Levin, I.W. (2005) *Spectrochemical Analysis Using Infrared Multichannel Detectors*, Blackwell Publishing, Chennai, p. 122.
- Suttiwijitpukdee, N., Sato, H., Zhang, J., Hashimoto, T., and Ozaki, Y. (2011) *Polymer*, **52**, 461–471.
- Workman, J.Jr and Weyer, L. (2008) *Practical Guide to Interpretive Near-Infrared Spectroscopy*, CRC Press/Taylor & Francis Group, New York.

## 23

# Electron Paramagnetic Resonance Spectroscopy and Forward Recoil Spectrometry

Krzysztof Kruczała and Ewa Szajdzińska-Piętek

### 23.1

#### Introduction

In this chapter the fundamentals of electron paramagnetic resonance spectroscopy (EPR) and forward recoil spectrometry (FRES), together with some applications of these techniques in the studies of polymer blends, are described. Both methods are well known and widely used in various areas of research, including that of polymers, despite the fact that polymers are in general not paramagnetic species, and the high-energy ion-beam irradiation involved in FRES might initiate the degradation of these materials while being examined.

EPR is the method of choice for the detection and investigation of paramagnetic centers such as free radicals, transition metal ions (TMIs) and other species with unpaired electrons. Such species may be inherently present in polymeric materials, and include residual post-polymerization radicals, spin charge carriers in conducting polymers, and TMIs added as initiators, stabilizers or catalysts. Macroradicals may be also formed in polymers due to depolymerization reactions, exposure to high-energy radiation, and other degradation processes that occur in these materials. More importantly, EPR is also a powerful tool used in studies of the structure and dynamics of diamagnetic systems. The method, which involves doping the examined material with stable radicals (spin probes) or attachment of the radicals to host molecules by covalent bonds (spin labels), relies on the fact that EPR spectra of the spin probe/label (e.g., the nitroxide radical) are sensitive to its local environment, in terms of polarity, and viscosity, molecular order, and so on.

The second method to be discussed, FRES, is dedicated to measurements of the atomic composition and impurity concentrations in the near-surface regions of solids. In most cases of polymers blends, the surface and interface behavior can differ from that of the bulk material. Following the general rule that the system tends to reduce Gibbs free energy, a constituent with a lower surface energy will migrate to the surface, leading to its surface enrichment. The surface composition can thus change with time, and this phenomenon may affect the usefulness of the

material. Therefore, the surface and interfacial properties of polymer blends are of great technological interest. Forward recoil spectrometry is one of the techniques of ion beam analysis (IBA) that can be used to quantify the depth distribution of components in various materials. When used together with deuterium labeling, FRES is very useful for investigating the surface and interfacial properties and processes of polymer blends, especially those containing polystyrene.

This review of EPR and FRES studies on polymer blends (see Sections 23.2.2 and 23.3.3) is based mainly on reports produced within the past 15 years. However, in other sections reference is also made to earlier publications concerning the development of both methods, and the most relevant data obtained via their use.

## 23.2

### Electron Paramagnetic Spectroscopy

Electron paramagnetic resonance spectroscopy, also known as electron spin resonance (ESR) spectroscopy, is a technique that allows the study of paramagnetic substances (i.e., those having positive magnetic susceptibility) by measuring the magnetic field at which a resonance absorption of monochromatic electromagnetic radiation occurs, leading to a reversal of orientation of the magnetic moments. Paramagnetism is caused by the presence of unpaired electrons. This method was developed during the 1940s in Kazan [1].

EPR is used extensively to detect, identify and follow the fate of radicals involved in polymerization or polymer degradation processes. It is also used extensively to characterize polymeric materials in terms of their morphology, heterogeneity, structural transformations, chain dynamics, and so on [2–5]. For this purpose, one can take advantage of the stable paramagnetic centers present in material to be examined (e.g., residual post-polymerization radicals, or TMIs used as catalytic centers or stabilizers). In most cases, however, external spin probes are added, including spin-labeled macromolecules (see Sections 23.2.1.5 and 23.2.2.1) [6]. The sensitivity and high content of structural information contained in the spin Hamiltonian parameters allow to obtain valuable – and often unique – data on the studied systems [7].

#### 23.2.1

##### EPR Background

As the theory of EPR spectroscopy has been described in numerous books and reviews [2,8–12], at this point only selected basic information will be provided that is essential for readers unfamiliar with the technique and is related to the application of the technique in polymer studies. As mentioned above, EPR spectroscopy is used to investigate substances with unpaired electrons. The electron possesses intrinsic angular momentum called spin ( $S$ ), and since it is a negatively charged particle, its magnetic moment ( $\mu_e$ ) is collinear but anti-parallel to the spin itself

and is given by:

$$\mu_e = -g_e \mu_B S \quad (23.1)$$

where  $g_e$  is the  $g$  factor (for a free electron this is equal to  $\cong 2.002319$ ),  $\mu_B$  is the Bohr magneton ( $e\hbar/2m_e = 9.273 \times 10^{-24} \text{ J T}^{-1}$ , where  $\hbar$  is Planck's constant ( $h$ ) divided by  $2\pi$ , whilst  $e$  and  $m_e$  are the electron charge and mass, respectively).

The component of the spin angular momentum along the  $z$ -direction can only assume two values:

$$S_z = m_s \hbar \quad (23.2)$$

where  $m_s$  is the magnetic spin quantum number.

The  $z$ -direction is assumed as that of the external magnetic field  $\mathbf{B}$  (of induction  $B$ ), and (in an isotropic medium) the energy of the magnetic dipole interaction with this static magnetic field is expressed by the following formula:

$$E = m_s g_e \mu_B B \quad (23.3)$$

Since the magnetic spin quantum number for a single electron can have only two values  $m_s = \pm 1/2$ , therefore, in a magnetic field, two discrete energy levels  $+1/2 m_s g_e \mu_B B$  and  $-1/2 m_s g_e \mu_B B$  associated with parallel ( $\alpha$ ) and anti-parallel ( $\beta$ ) spin orientation with respect to  $\mathbf{B}$ , are produced. The degeneration of the spin levels is thus eliminated and the resulting splitting of energy levels [Eq. (23.4)] in a magnetic field is called the Zeeman effect (cf. Figure 23.1):

$$\Delta E = g_e \mu_B B \quad (23.4)$$

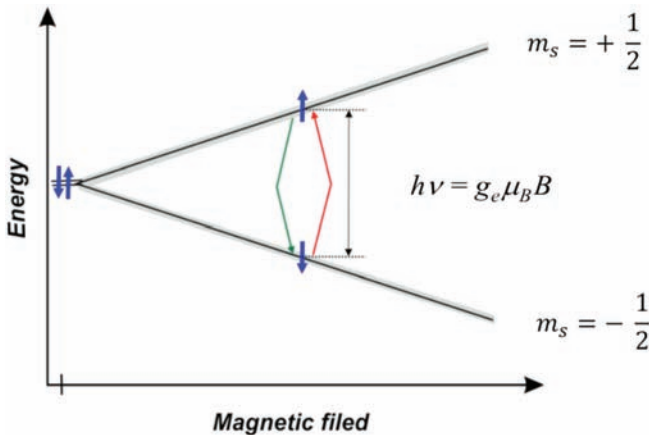


**Figure 23.1** Schematic representation of the splitting of electron spin energy level due to the Zeeman effect. The gray background blur represents the uncertainty of energy levels due to the Heisenberg uncertainty principle:  $\Delta \epsilon \cdot \Delta \tau \geq \hbar/2$ .

The absorption of microwave radiation (with the oscillating magnetic field  $\mathbf{B}_1$  perpendicular to the static magnetic field  $\mathbf{B}$ ) may induce transitions between the two energy levels if the resonance condition is fulfilled. This leads to the fundamental equation of EPR spectroscopy:

$$h\nu = g_e\mu_B B \quad (23.5)$$

where  $\nu$  is the microwave frequency.

The selection rule for EPR absorption is  $\Delta m_s = 1$ , which means that allowed transitions occur only between the adjacent energy levels.

In general, the Zeeman interaction is anisotropic and is described by the second-order  $\tilde{\mathbf{g}}$  tensor, which in the principal coordinate system is represented by the  $3 \times 3$  matrix of the form:

$$\tilde{\mathbf{g}} = \begin{bmatrix} g_{xx} & 0 & 0 \\ 0 & g_{yy} & 0 \\ 0 & 0 & g_{zz} \end{bmatrix} \quad (23.6)$$

in which the diagonal components differ from the  $g$ -factor characteristic of a free electron. However, in the case of carbon centered radicals, the average value of these components is usually close to  $g_e$ , but can vary over a wide range for transition metal complexes.

A full description of static EPR spectra of paramagnetic samples is given by the spin Hamiltonian consisting of several terms which represent, in the order of decreasing energy, electron Zeeman splitting ( $\mu_B \mathbf{B} \cdot \tilde{\mathbf{g}} \cdot \hat{\mathbf{S}}$ ), fine coupling ( $\hat{\mathbf{S}} \cdot \tilde{\mathbf{D}} \cdot \hat{\mathbf{S}}$ ), hyperfine coupling ( $\hat{\mathbf{S}} \cdot \tilde{\mathbf{A}} \cdot \hat{\mathbf{I}}$ ), quadruple interaction ( $\hat{\mathbf{I}} \cdot \tilde{\mathbf{P}} \cdot \hat{\mathbf{I}}$ ), and nuclear Zeeman splitting ( $g_N \mu_N \mathbf{B} \cdot \hat{\mathbf{I}}_B$ ) [13]:

$$\hat{H}_{sp} = \mu_B \mathbf{B} \cdot \tilde{\mathbf{g}} \cdot \hat{\mathbf{S}} + \hat{\mathbf{S}} \cdot \tilde{\mathbf{D}} \cdot \hat{\mathbf{S}} + \hat{\mathbf{S}} \cdot \tilde{\mathbf{A}} \cdot \hat{\mathbf{I}} + \hat{\mathbf{I}} \cdot \tilde{\mathbf{P}} \cdot \hat{\mathbf{I}} - g_N \mu_N \mathbf{B} \cdot \hat{\mathbf{I}} \quad (23.7)$$

where  $\tilde{\mathbf{D}}, \tilde{\mathbf{A}}, \tilde{\mathbf{P}}$  are tensors of fine, hyperfine and quadruple interactions, respectively,  $\hat{\mathbf{S}}, \hat{\mathbf{I}}$ , are operators of electron and nuclear spins, respectively, and  $g_N, \mu_N$  are the nuclear  $g$ -factor and nuclear magneton, respectively.

In the case of polymer systems, most often only two first terms need to be considered, and the spectra are adequately described by the simplified Hamiltonian:

$$\hat{H}_{sp} = \mu_B \mathbf{B} \cdot \tilde{\mathbf{g}} \cdot \hat{\mathbf{S}} + \sum \hat{\mathbf{S}} \cdot \tilde{\mathbf{A}}_n \cdot \hat{\mathbf{I}}_n \quad (23.8)$$

In the above formula, hyperfine interactions with  $n$ -number of nuclei have been considered. Hyperfine structure (HFS) in EPR spectra is due to interaction of the electron magnetic moment with the nuclear magnetic moment ( $\mu_I$ ), which for one nucleus with quantum number  $I$  leads to splitting of the single EPR line to  $N = 2I + 1$  lines (e.g., for  $^{14}\text{N}$ ,  $I = 1$  and  $N = 3$ ). The contribution of an additional magnetic field generated by the nucleus depends on  $\mu_I$  and the electron–nucleus distance. There are two mechanisms of hyperfine coupling: (i) Fermi contact interaction; and (ii) dipole–dipole interaction.

The Fermi contact interactions are responsible for isotropic contribution to the HFS, characterized by the isotropic splitting constant ( $a_{iso}$ ), and are due to the definite probability density of the unpaired electron orbital wavefunction at



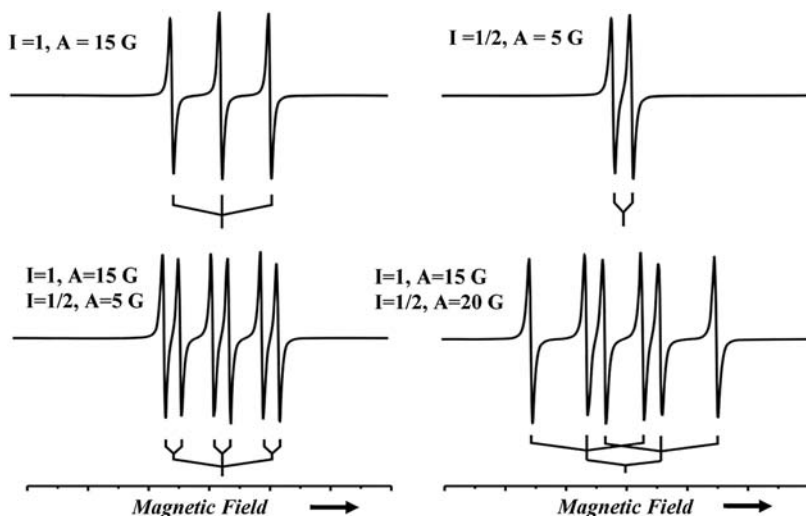


Figure 23.2 Simulated X-band EPR spectra for different isotropic splitting constants  $A$ .

the position of the magnetic nucleus. As the wavefunction at this position does not equal zero only for the atomic  $s$  orbital, the isotropic HFS should not be observed for the electron spin located at other orbitals ( $p$ ,  $d$ ,  $f$ ). In molecular systems, however, isotropic hyperfine coupling is observed in many cases due to spin polarization. The anisotropic part is due to dipole–dipole interactions of electron and nucleus magnetic moments, and can be considered as classical interaction of two dipoles. As the interaction is dependent on the orientation, in the case of fast molecular motion the anisotropic contribution to HFS averages to zero.

The spectra of organic radicals are often characterized by a complex HFS that results from the delocalization of unpaired electrons and their interactions with multiple magnetic nuclei (Figure 23.2).

The HFS is characterized by hyperfine tensor  $\tilde{A}$ , which can be described by a square matrix  $3 \times 3$ ; it consists of isotropic  $a_{iso}$  (Fermi contact interaction) and anisotropic  $\tilde{A}^d$  (dipolar interaction) components, and can be expressed as:

$$\tilde{A} = a_{iso} \cdot \mathbf{1} + \tilde{A}^d = a_{iso} \cdot \begin{bmatrix} 1 & 0 & 0 \\ 0 & 1 & 0 \\ 0 & 0 & 1 \end{bmatrix} + \begin{bmatrix} A_{xx}^d & 0 & 0 \\ 0 & A_{yy}^d & 0 \\ 0 & 0 & A_{zz}^d \end{bmatrix} \quad (23.9)$$

From experimental spectra it is possible to determine the tensors  $\tilde{g}$ ,  $\tilde{A}$ , and line intensity. These parameters, when combined with the information about the line shape and line width, fully describe the EPR spectrum and provide valuable information about the molecular structure of the studied systems [14,15].

**Table 23.1** List of microwave frequency bands and the corresponding resonance magnetic fields for  $g = 2.0$ .

	Band					
	L	S	X	K	Q	W
Frequency, $\nu$ (GHz)	0.8–1.2	2.4–3.8	9–10	$\sim 24$	$\sim 34$	$\sim 94$
Field for $g = 2.0/\text{mT}$	35.0	130.0	340.0	850.0	1220.0	3350.0

Since all magnetic parameters are most often not available directly from the spectrum, computer simulations – combined with the optimization procedure and theoretical calculations – are the only methods that enable a complete analysis of the experimental data (see Section 23.2.1.4) [16].

### 23.2.1.1 Multifrequency EPR

Most continuous-wave EPR (CW-EPR) systems operate at 9–10 GHz microwave frequency – that is, at X-band (Table 23.1). However, in order to distinguish between interactions that are dependent on the magnetic field from the field-independent one, multifrequency EPR needs to be applied [17]. The second most common band is the Q-band at 34 GHz, mainly because it provides a threefold larger Zeeman splitting while still allowing measurements for samples of a reasonable size (which can be easily handled).

The acquisition of EPR spectra at two or more frequencies may help to distinguish two radicals with very similar  $g$  factors and line shapes, which is very often the case for species which can be found in polymer materials. The simulated X-, Q-, and W-band CW-EPR spectra of two radicals differing only by  $\Delta g = 0.0005$  are presented in Figure 23.3a. Whereas, in the X-band spectrum only one isotropic

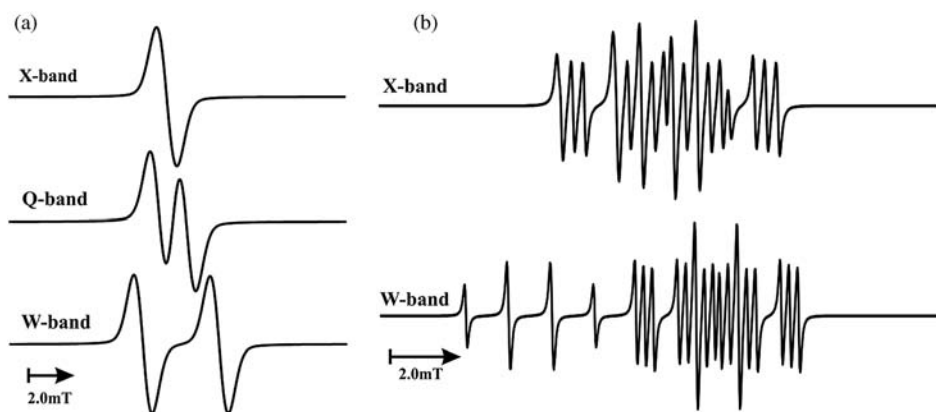


**Figure 23.3** Simulated X-, Q-, and W-band continuous-wave EPR spectra of two radicals. (a) Characterized by  $g$ -factors differing by 0.0005 and no hyperfine interactions;

(b) Characterized by  $g$ -factors differing by 0.004, and hyperfine structure (radical I:  $a_N = a_{H\beta} = 1.5$  mT; radical II:  $a_N = 1.5$  mT,  $a_{H\beta} = 22$  mT,  $a_{H\gamma} = 0.3$  mT).

signal can be observed, the Q-band and especially the W-band spectra show the presence of two signals.

The same procedure may be helpful with spectral analysis in the case of complicated and overlapping HFS. As hyperfine coupling does not depend on frequency, the distance between the HFS lines remains the same but the resonance magnetic field changes according to Eq. (23.5) (cf. Figure 23.3b;  $\Delta g = 0.004$ ).

Continuous-wave multifrequency EPR measurements of the tumbling paramagnetic species such as nitroxide probes (see Section 23.2.1.4) are also helpful for determining a correct motional model. High-field EPR is sensitive only to very rapid components of the probe's rotational motion, and allows discrimination to be made between motional and polarity effects on the spectra [18–21].

### 23.2.1.2 Pulsed EPR

Pulsed EPR [also known as time domain EPR or Fourier transform (FT)-EPR] techniques provide information about weak hyperfine and quadrupolar interactions of a probe electron spin with other electron and nuclear spins in its environment. In a pulsed experiment, a constant magnetic field ( $B_0$ ) is used and the sample is irradiated by sequences of microwave pulses of high power leading to the in a range of transition frequencies. The variations of pulse duration and delay times allow for the separation of weak magnetic interactions and extraction of information that is not accessible when using CW-EPR. The excitation range increases with decreasing pulse duration (typically 10 to 100 ns). An additional advantage of this technique is the fact that a single FT-EPR spectrum can be recorded in a very short time, even of the order of microseconds. In practice, more advanced pulse sequences lead to spectra with low signal-to-noise ratios, which thus require longer acquisition and repetition times. The simplest two-pulse sequence ( $\frac{\pi}{2} \rightarrow \tau \rightarrow \pi \rightarrow \tau$ ) leads to the formation of a Hahn echo [22], which can be converted to an EPR spectrum by using Fourier transform (Figure 23.4) [23]. One of the major areas of applications for this technique includes studies of the structure and dynamics of biomacromolecules, with the use of spin-labeling methods, although similar procedures can be used in the case of other polymeric systems [24]. For example, pulse electron double resonance (PELDOR) or double electron electron resonance (DEER) allow the measurement of distances between spins in the range of 1.5 to 8.0 nm [25–27].

Electron spin echo envelope modulation (ESEEM), as one of the key EPR techniques allowing for the detection of weak hyperfine interactions, was applied to polymer systems in order to provide a qualitative local elemental analysis [28,29]. An appropriate modification of the four-pulse ESEEM leads to a two-dimensional ESEEM technique termed hyperfine sublevel correlation spectroscopy (HYSCORE) [30], which offers an increased resolution [23] and is especially suitable for systems interacting with a large number of different nuclear spins [23]. Pulsed EPR nutation spectroscopy allows the study of high-spin samples containing several spin states with different multiplicities [31,32]. Additionally, it can be used to optimize the oxidative doping process of a high-spin polymer and to determine the optimal stoichiometry between the oxidizing agent and the polymer [33]. Furthermore,

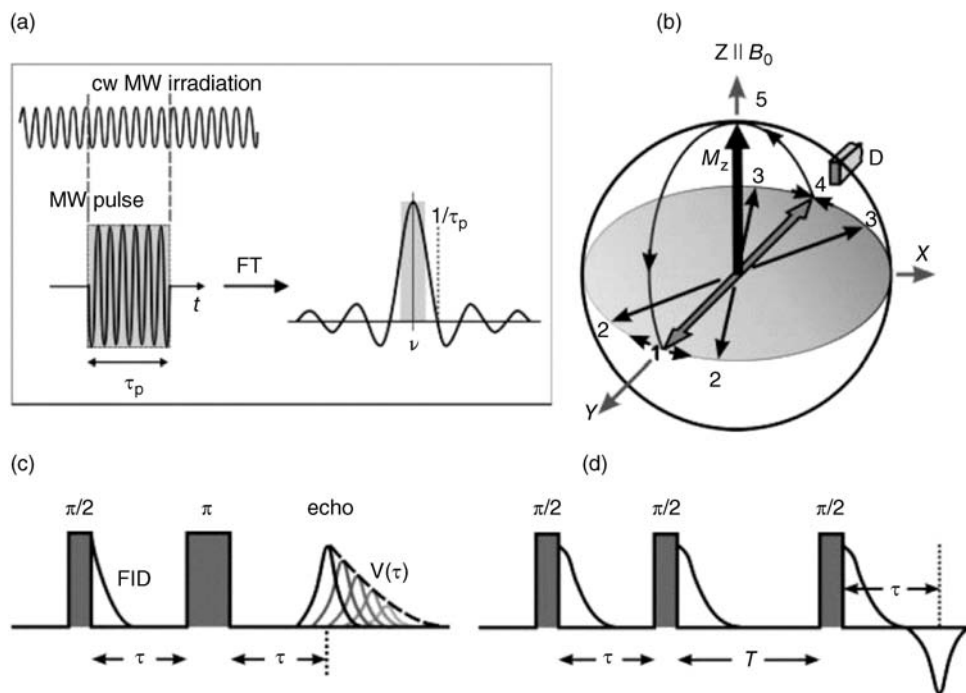


**Figure 23.4** (a) Formation of a microwave pulse of  $\tau_p$  length and the corresponding excitation band obtained after Fourier transformation. (b) Behavior of the magnetization,  $M_0$ , in the rotating frame upon a  $\pi/2 \rightarrow \pi$  pulse sequence, leading to electron spin echo (1) orientation of  $M$  after a strong  $\pi/2$  pulse along the  $x$ -axis; (2) defocusing of spin packets with a rate of  $1/T_m$ ; (3) orientation of spin packets after subsequent

application of  $\pi$  pulse; (4) refocusing of spin packets and formation of an electron spin echo (ESE) signal recorded with detector D; (5) recovery of the longitudinal magnetization with a rate of  $1/\tau_1$ . (FID – free induction decay,  $V(\tau)$  – intensity,  $T_m$  – phase memory time) Pulse sequences for (c) primary (Hahn) echo and (d) stimulated echo. Reprinted with permission from Ref. [36]; © 2013, John Wiley & Sons.

pulsed EPR allows the determination of  $T_1$  and  $T_m$  relaxation times directly from special pulse sequence experiments. Further details on the technique principles and applications are available elsewhere [23,34–36].

### 23.2.1.3 EPR Imaging

In a classic EPR experiment, the applied static magnetic field is homogeneous and the signal is derived from the entire sample volume. EPR imaging (EPRI) allows the spatial distribution of paramagnetic centers in the sample to be determined, such that the macro heterogeneity can be tracked without destroying the sample [37–41]. Traditional EPR spectroscopy can be transformed into EPRI by applying a magnetic field gradient at a site of the sample. In this case, the magnetic field gradient forms a link between the position in the sample and a resonance field, and the information on spatial distribution of paramagnetic centers becomes

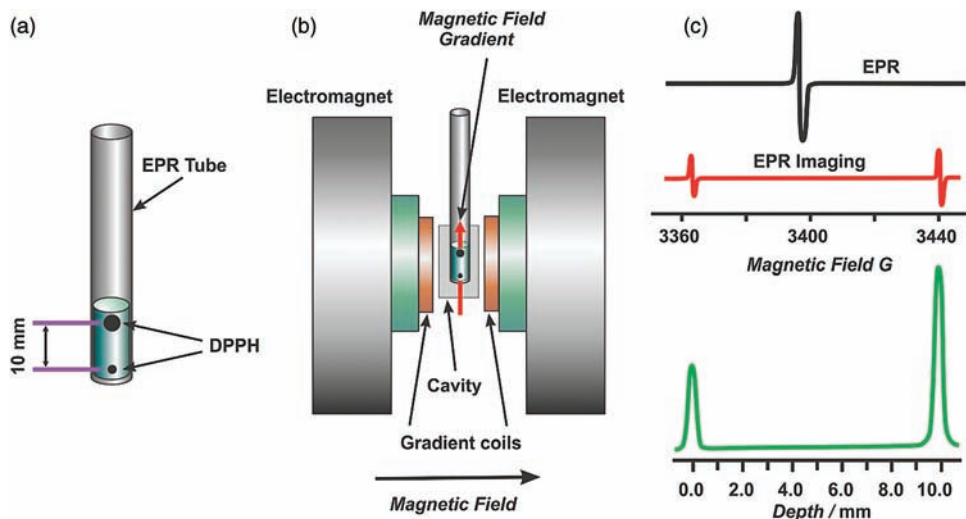


**Figure 23.5** Scheme of the EPR imaging experiment. The application of a magnetic field gradient allows the concentration profile of paramagnetic species within the sample to be determined.

coded in the EPR spectra. Decoding of this information requires the use of advanced numerical procedures [42–44]. In the presence of a magnetic field gradient (generated by an additional coil; cf. Figure 23.5), only paramagnetic species present in a thin layer of the sample fulfill the resonance condition [Eq. (23.5)] at a given value of the homogeneous magnetic field,  $B$ . In the case of the gradient ( $G_x$ ) parallel to the sample axis, the resonance condition is modified in the following manner:

$$h\nu = g\mu_B(B + xG_x) \quad (23.10)$$

where  $x$  is the  $x$ -coordinate (position in the sample).

From a mathematical point of view, the recorded spectrum,  $Y(B)$ , is a convolution of spectrum without gradient  $S(B)$ , concentration profile of paramagnetic species  $P(x)$  and profile of the cavity sensitivity,  $C(x)$ :

$$Y(B) = \int_{-\infty}^{+\infty} (S(B + xG_x) \cdot P(x) \cdot C(x)) dx \quad (23.11)$$

In most cases the sensitivity profile of the cavity is taken as a constant; however, a detailed analysis of the concentration profiles – particularly in the case of long samples ( $l > 3$  mm) – requires that the real sensitivity profile has to be taken into account [39d]. The idea of such experiment is presented in Figure 23.5, where Figure 23.5a shows a model sample of two 2,2-diphenyl-1-picrylhydrazyl (DPPH) crystals of different sizes, placed at a distance of 10 mm from each other. In a classical EPR experiment, the spectrum of this sample

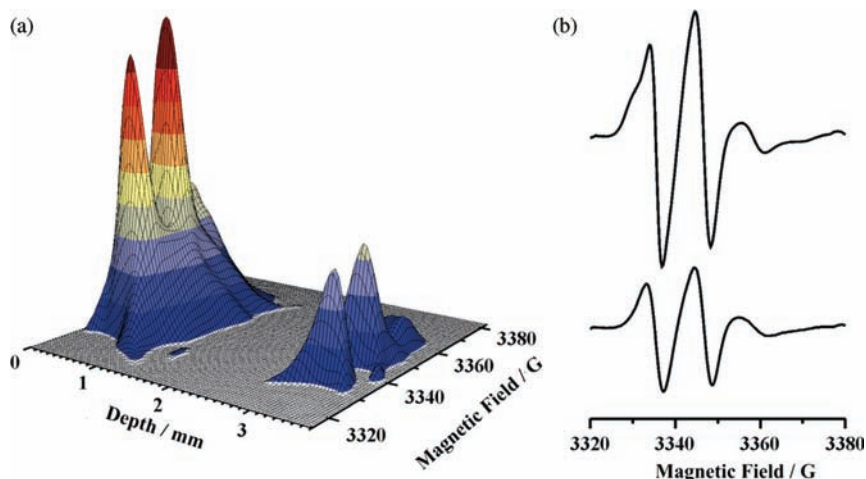


**Figure 23.6** (a) Two-dimensional (2D) spectral-spatial perspective plot of nitroxide biradicals derived from hindered amine stabilizer (HAS) doped in HPEC (copolymer of ethylene and propylene [39c,b]) on one side of the

plaque (left), and in transparent film attached to the plaque on the opposite site (right). (b) Spectral slices determined nondestructively from 2D plot. Adapted with permission from Ref. [46]; © 2008, Elsevier.

consists of one line (Figure 23.5c), but when a magnetic field gradient is applied the resonance will occur at two values of the homogeneous magnetic field. By using an appropriate deconvolution algorithm, the concentration profile of the paramagnetic species can be determined (Figure 23.5c). The profile obtained carries information about the spatial distribution of paramagnetic centers, which in turn makes it possible to deduce the chemical processes taking place in the sample [45].

In order to investigate microheterogeneity of a polymer, it is necessary to apply two-dimensional (or  $n$ -dimensional, where  $n \geq 2$ ) spatial-spectral EPRI [46]. Two-dimensional (spatial-spectral) imaging allows not only a determination of the location and concentration of paramagnetic species but also analysis of spectral changes as a function of the position in the sample (Figure 23.6). This experiment requires the registration of a series of EPR spectra (projections) as a function of the magnetic field gradient, and the use of a reconstruction algorithm [42]. The collected data consist of projections reflecting the test object in spectral ( $B$ ) and spatial ( $L$ ) coordinates (Figure 23.7). For the field gradient equal to zero ( $\alpha = 0$ ), the classical EPR spectrum can be registered, whilst for a field gradient of infinite value it would be possible to obtain a “clean” concentration profile. In practice, however, it is not possible to use an infinitely large gradient and therefore it is not possible to obtain all projections.

The experimentally available maximum projection angle,  $\alpha_{\max}$ , depends on the maximum gradient ( $G_{\max}$ ) that can be used, the sample length ( $L$ ), and the width

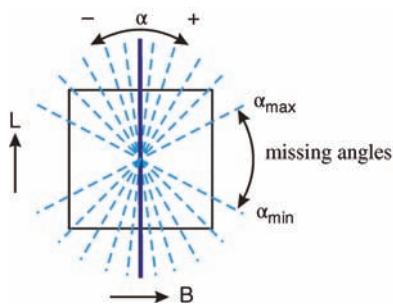


**Figure 23.7** Schematic representation of two-dimensional (2D) (spatial-spectral) projection in 2D EPRI experiment using a discretely changing gradient and the cone of missing angles. Adapted with permission from Ref. [7]; © 2006, John Wiley & Sons.

of the EPR spectrum without gradient ( $\Delta B$ ):

$$\tan(\alpha_{\max}) = \frac{L}{\Delta B} G_{\max} \quad (23.12)$$

For the above-mentioned parameters, it is necessary to register the EPR spectrum by using the sweep width ( $SW_{\max}$ ), calculated according to the following formula:

$$SW_{\max} = \frac{\sqrt{2}\Delta B}{\cos(\alpha_{\max})} \quad (23.13)$$

The shape of the spectra for the missing projections can be considered as the same as that at the maximum available gradient, or it can be calculated with a suitable iterative algorithm [42].

As can be seen from Figure 23.6, the two-dimensional EPRI method allows any changes in the shape and intensity of the EPR spectra to be visualized as a function of position within the sample. From the spectrum shape, information on the local viscosity and polarity can be deduced (see Sections 23.2.1.4 and 23.2.1.5).

#### 23.2.1.4 Simulation of EPR Spectra

The components of  $g$  and  $A$  tensors and their principal axes can be determined experimentally by measuring the angular dependence of EPR spectra of paramagnetic centers in single crystals. However, in most cases of solid-state EPR, including polymer samples, only powder (rigid limit) spectra are experimentally available, which represent a superposition of a large number of individual signals corresponding to random orientations of the paramagnetic center. Therefore, a simulated powder spectrum can be expressed as [47,48]:

$$Y(B, \nu) = C \int_{\theta=0}^{\pi/2} \int_{\varphi=0}^{2\pi} \sum_i P_i(\theta, \varphi, \nu) f(B - B_0[\nu], \sigma_B) d \cos \theta d\varphi \quad (23.14)$$

where  $C$  is a constant that includes all experimental parameters;  $\theta, \varphi$  are the polar and azimuthal angles, respectively, between the external magnetic field and

principal axes of the  $\mathbf{g}$  tensor;  $P(\theta, \varphi, \nu)$  is the transition probability;  $f(B - B_0[\nu], \sigma_B)$  is the line shape function (Lorentzian, Gaussian functions or their combination); and  $\sigma_B$  is the orientation-dependent line width.

In a system that enables rotational diffusion of paramagnetic species, the anisotropy of magnetic interactions is subject to a partial or complete averaging, and this results in changes of the EPR line shape. The correlation time of rotational movements,  $\tau_R$ , is related to the viscosity and temperature of the medium; in the case of isotropic Brownian diffusion of a spherical molecule, it is given by the equation:

$$\tau_R = \frac{V_h}{k_B T} \quad (23.15)$$

where  $\eta$  is viscosity,  $T$  is temperature, and  $V_h$  is the hydrodynamic volume.

In general, to describe the EPR spectrum in a motional regime, a procedure based on the solution of the stochastic Liouville equation should be used [49–52]. However, in low-viscosity media, a very fast molecular tumbling leads to an averaging of the anisotropic part of the spin Hamiltonian to zero, and the spectrum is composed of narrow Lorentzian lines, and is characterized by:

$$g_{iso} = \frac{1}{3}(g_{xx} + g_{yy} + g_{zz}) \quad (23.16)$$

$$a_{iso} = \frac{1}{3}(A_{xx} + A_{yy} + A_{zz}) \quad (23.17)$$

Due to the randomness of molecular motions, yet, the anisotropic Hamiltonian terms fluctuate in time and this leads to a modulation of energy levels and of transition frequencies; consequently, a broadening of the EPR lines is observed. For spectral lines resulting from the hyperfine interaction with a single nucleus, the extent of this broadening will depend on the magnetic nuclear quantum number  $m_I$  of the respective transition. According to Kivelson theory [53], the peak-to-peak line width,  $\Delta B_{pp}$  in frequency units, is given by:

$$\Delta B_{pp}(m_I) = \alpha + \beta \cdot m_I + \varepsilon \cdot m_I^2 \quad (23.18)$$

The coefficient  $\alpha$  includes broadening contributions resulting from other mechanisms (e.g., the presence of oxygen or instrumental factors), whereas  $\beta$  and  $\varepsilon$  are governed by the anisotropy of the  $\mathbf{g}$  and  $\mathbf{A}$  tensors, the viscosity of a medium and its temperature, and the resonance field  $B_0$  (thus the microwave frequency; the broadening is different in X-band than for example in Q-band) [54]:

$$\alpha = \frac{4}{15} b(\Delta\gamma) B_0 \tau_R \quad \text{and} \quad \varepsilon = \frac{1}{8} b^2 \tau_R \quad (23.19)$$

where

$$b = 2\pi(A_{zz} - a_{iso}) = \frac{4}{3}\pi(A_{||} - A_{\perp})$$

$$\Delta\gamma = \beta_e \hbar^{-1} \left[ g_{zz} - \frac{1}{2}(g_{xx} + g_{yy}) \right]$$



In the case of slower movements, in media of high viscosity, the so-called “slow tumbling” EPR spectra are observed – that is, anisotropic signals which directly reflect the distribution of transition frequencies. For nitroxide radicals (which are commonly used as spin probes or labels; *vide infra*), the slow-motional regime corresponds to rotational correlation times in the range  $10^{-6}$  to  $10^{-9}$  seconds. In order to calculate such EPR spectra, two major methods have been used, namely “trajectory methods” or those based on the stochastic Liouville equation. For many years, the line shapes of slow-motional spectra of nitroxide probes/labels have been analyzed using a computer program developed by Freed and colleagues (Cornell University), as described in detail elsewhere [55–57]. Assuming that all of the paramagnetic centers are described by the same spin Hamiltonian, the time evolution of the density matrix operator  $\rho$  is given by the quantum-mechanical Liouville equation:

$$\frac{\partial \rho(t)}{\partial t} = -i[H(t), \rho] \quad (23.20)$$

If the time dependence of the Hamiltonian  $H(t)$  is derived from the interaction of paramagnetic centers with the environment in such a way that the Hamiltonian is defined by a complete set of random parameters  $\Omega$ , and if the time dependence of  $\Omega$  is a stationary Markov process, then:

$$\frac{\partial P(\Omega, t)}{\partial t} = -\Gamma_{\Omega} P(\Omega, t) \quad (23.21)$$

where  $P(\Omega, t)$  is the probability of the paramagnetic species being in a state  $\Omega$  at time  $t$ .

Since this is a stationary process, the evolution operator  $\Gamma_{\Omega}$  acting on random variables is independent of time and spin variables. When used to describe dynamically averaged EPR spectra,  $\Gamma_{\Omega}$  is the operator of rotational diffusion motion, and random variables correspond to Euler angles ( $\Omega \equiv \alpha, \beta, \gamma$ ).

As has been shown previously [51, 57, 58], by assuming  $\Gamma_{\Omega} P_o(\Omega) = 0$  (where  $P_o(\Omega)$  is the unique equilibrium distribution) from Eqs (23.20) and (23.21), the stochastic Liouville equation of motion can be developed:

$$\frac{\partial \rho(\Omega, t)}{\partial t} = -i[H(\Omega), \rho(\Omega, t)] - \Gamma_{\Omega} \rho(\Omega, t) \quad (23.22)$$

In this approach, there is no explicit time dependence of the spin Hamiltonian  $H(t)$ , but it is dependent on Euler angles and its change is expressed by the time evolution of  $\Omega$ . Hence, the spin Hamiltonian [cf. Eq. (23.8)] for systems which exhibit molecular rotational motion can be expressed by the formula:

$$H_{spin} = \mu_B \mathbf{B} \cdot \mathbf{g}^{ef}(\Omega) \mathbf{S}_z + \mathbf{I} \cdot \mathbf{A}^{ef}(\Omega) \cdot \mathbf{S}_z \quad (23.23)$$

This approach is valid for any rate of reorientational movements of the paramagnetic species. For an infinitely slow movement, it leads to a powder spectrum, whereas for fast movements it results in a fully dynamically averaged spectrum (*vide supra*). In the intermediate case, however, the EPR line shape is governed by the manner in which the molecules undergo reorientation, and the computed

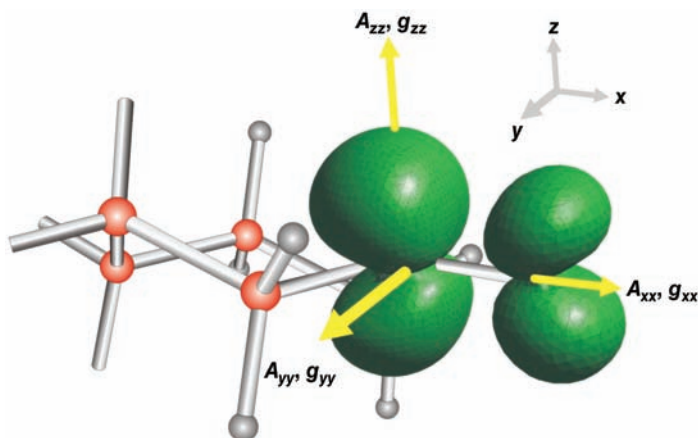


**Figure 23.8** Direction of the principal  $\mathbf{g}$  and  $\mathbf{A}$  axes in relation to nitroxide molecule symmetry. Spin densities on nitrogen and oxygen atoms were calculated using DFT.

spectrum shape depends on the selection of the rotational diffusion model. In the case of nitroxide spin probes, most commonly three models are used: a Brownian diffusion; approximate free diffusion; and jump diffusion [55,59]. In the model of axially symmetric jump diffusion, it is assumed that the spin probe is in a specific orientation for an average time period  $\tau$ , and then immediately jumps to a new orientation. If the probe dynamics is axially symmetric, it is defined by rotational diffusion tensor components  $R_{\parallel}$  and  $R_{\perp}$  (parallel and perpendicular to the molecular symmetry axis of the spin probe molecule), and the angle  $\theta$  between the symmetry axis of diffusion tensor and the axis  $z$  of the molecular coordinate system. The  $z$ -axis is the axis of orbital  $2p_z$  of nitrogen atom and the  $x$ -axis is along the N—O bond (Figure 23.8). This choice of axes causes the main values of the  $\mathbf{g}$  tensor to satisfy the relationship  $g_{xx} > g_{yy} > g_{zz}$ . In the jump diffusion model, the correlation time is associated with the rotational diffusion tensor components by the expression [55,57,59]:

$$\tau_R = \frac{7}{6\sqrt{R_{\parallel}R_{\perp}}} \quad (23.24)$$

In summary, the methods of EPR spectral analysis described here allow the determination of basic spectroscopic parameters of paramagnetic centers (components of the  $\mathbf{g}$  and  $\mathbf{A}$  tensors, line shape), and for gaining insight into their dynamical behavior. This in turn permits conclusions to be drawn on the structure and local properties of the host system (*vide infra*).

### 23.2.1.5 Spin Probes and Spin Labels

Most polymers are not a paramagnetic species, unless they undergo degradation or crosslinking processes involving free radicals [60]. In such a case, stable carbon-centered radicals or radical adducts to the spin trap added to the system



hyperfine splitting constant and a decrease in the  $g$ -factor [69,70]. In particular,  $g_{xx}$  and  $A_{zz}$  are the most sensitive to the polarity of the local environment and to interactions with surrounding molecules [70,71]. In the case of samples having a homogeneous macroscopic distribution of the spin probes, the shape of the EPR spectrum depends on the rate of rotational motion of these radicals. In a medium of low viscosity, due to fast rotational diffusion of the radicals, a motionally averaged triplet is observed (cf. Figure 23.11a), with the distance between the centers of adjacent lines equal to  $a_{iso}$ . For a medium of higher viscosity, an anisotropic signal is recorded which extends over a wide range of the magnetic field. In X-band spectra of slow tumbling probes the distance between the outermost peaks (high-field minimum and low-field maximum) corresponds to  $2A'_{zz}$  – twice the motion-averaged HFS for parallel orientation of the probe axis of rotation with respect to  $\mathbf{B}$ . This extreme line separation increases as the radical dynamics slows down and in the rigid limit (no motion on the EPR time scale) it approaches the value of  $2A_{zz}$  (Figure 23.11b).

In a typical experiment for polymeric systems, EPR spectra are recorded over a wide temperature range and analyzed in terms of the probe dynamics. Quite often (especially for blends), two-component spectra can be observed at certain temperatures that consist of fast- and slow-motional signals (cf. Figure 23.11c). Such a spectrum is indicative of a two-phase morphology and probe partition into different environments. The basic parameters providing information on the examined system are:  $T_a$  and  $T_d$  temperatures which correspond to

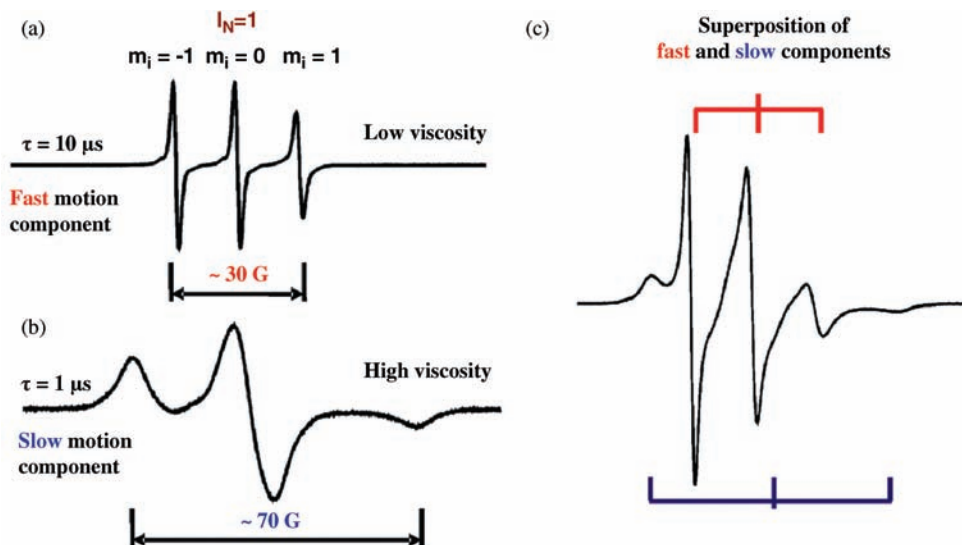


**Figure 23.11** EPR spectra of the nitroxide radical derived from TINUVIN770 in a medium of a low (a) and high (b) viscosity, and the superposition of both signals (c). Estimation of correlation time is based on Ref. [7].

appearance of the fast motion and disappearance of the slow motion, respectively;  $T_{5\text{mT}}$  (or  $T_{50\text{G}}$ ), the temperature at which the extreme line separation ( $2A'_{zz}$ ) is equal to 5 mT;  $\tau_R$ , the rotational correlation time of the probe; and the relative contributions of the two components. The parameter  $T_{5\text{mT}}$  is related to the polymer glass transition temperature ( $T_g$ ); however, its value is higher than the  $T_g$  determined with differential scanning calorimetry (DSC) because of the much shorter time scale of molecular motions monitored by EPR. The relationship between  $T_{5\text{mT}}$  determined from EPR and  $T_g$  measured with DSC depends on the spin probe used and on the type of its interaction with the polymer matrix. The  $\tau_R$  values can be obtained from the line shape simulations, but often these are estimated via approximate formulae from  $A'_{zz}/A_{zz}$  data in the slow-motion regime, or from the width of the central line and relative amplitudes of the motionally averaged triplet [6,53,59].

The intensity of EPR signals (double integral of the EPR line) is correlated with the quantity of paramagnetic species. Determination of the absolute amount of that species ( $N_x$ ) typically involves comparing the sample signal intensity  $A_x$  (area under the absorption curve) with that of the reference signal ( $A_{\text{ref}}$ ) of the known spin content ( $N_{\text{ref}}$ ):

$$N_x = \frac{A_x}{A_{\text{ref}}} N_{\text{ref}} \quad (23.25)$$

### 23.2.2

#### EPR Applications in Studies of Polymer Blends

In this section the potential of EPR techniques as applied to binary polymer blends will be illustrated by examples of selected reports concerning the three issues on three issues: (i) spin probe studies; (ii) radicals generated by ionizing radiation; and (iii) paramagnetic species in conductive materials. All of the experiments described in the following subsections were performed using X-band EPR.

##### 23.2.2.1 Spin Probing of the Structure and Dynamics

Nitroxide radicals are especially useful for probing heterogeneous and microheterogeneous systems; indeed, with a correct selection of probes (or labeling sites) valuable information can be obtained from their EPR spectra on the local properties of various structural domains within the host material. The method is particularly advantageous if used in tandem with other spectroscopic methods, such as infra-red (IR), Raman or fluorescence spectroscopy, and with DSC. It must be emphasized that EPR spectroscopy allows to gain insights on structural and dynamical heterogeneities on a length scale  $<5$  nm, which is too small to be observed using DSC, dynamic mechanical analysis (DMA), or electron microscopy. The application of spin probe techniques in studies of multiphase polymer

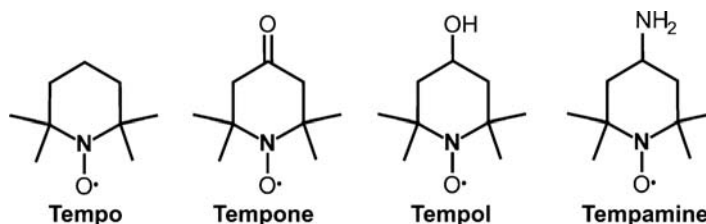


**Figure 23.12** Chemical structures of piperidine nitroxide spin probes.

systems has recently been reviewed, but polymer blends were not discussed extensively in these reports [6,72].

The group of Chen *et al.* successfully examined various polymer blends by using 2,2,6,6-tetramethylpiperidine-1-oxyl (Tempo) or its oxo-, hydroxyl-, and amino- derivatives (Tempone, Tempol, and Tempamine, respectively; see Figure 23.12) [73–76]. Poly(acrylic acid)/poly(ethylene oxide) (PAA/PEO) blends of different compositions were probed with Tempo. The EPR data indicated that the two polymers were not miscible at the molecular level, although DSC experiments revealed only one  $T_g$ -value. The observed fast- and slow-motional spectral components (relative contribution of the former increasing with temperature) were assigned to probe molecules in more flexible PEO-rich domains and more rigid PAA-rich domains, respectively. The probe mobility, characterized by  $2A'_{zz}$  and  $\tau_R$ , was found to diminish with increasing content of PAA in the blend; accordingly, the activation energy for probe rotation, as obtained from the Arrhenius dependence of  $\tau_R$  data, increased. The PAA/PEO system, with composition 1:1 by weight, was also probed with Tempone (a proton acceptor), Tempol, and Tempamine (both proton donors). The experimental data on  $T_{5mT}$ ,  $T_a$  and  $T_d$  indicated clearly that the molecular motion of a probe is determined by not only the probe size but also its capability of hydrogen bonding to functional groups in the polymer matrix [73].

A similar study using Tempol was performed for blends of poly(propylene carbonate) (PPC) with the copolymer poly(styrene-*co*-4-vinyl phenol) of various mole fractions,  $x$ , of hydroxyl groups (STVPh- $x$ ) [74]. In this case, the fast- and slow-motional signals in two-component spectra corresponded to the probe molecules located in PPC-rich and STVPh-rich micro domains, respectively. It was found that the fraction of the *fast* signal (at a given temperature) decreased on increasing the  $x$ -value, while the corresponding  $\tau_R$  increased. At the same time, the activation energy of fast motion increased and the  $T_{5mT}$  shifted to higher temperatures. Taken together, these results reflected a progressive enhancement of the hydrogen-bonding interaction between the hydroxyl groups in STVPh and the carboxyl groups and ether oxygen in PPC, which led to an improved miscibility of the two polymers.

Other studies have involved poly(styrene-*co*-*p*-(hexafluoro-2-hydroxyisopropyl)- $\alpha$ -methyl-styrene) copolymers (PS(OH)- $x$  with the mol.% of hydroxyl groups

$x \approx 2$ –27) blended in a 1 : 1 ratio by weight with PPC [75]. Tempo, Tempol and Tempamine were each used as spin probes, but only the functionalized radicals could provide information on microphase separation or miscibility in these blends. The EPR spectra of Tempo in all examined samples did not disclose two components through the temperature range 100 to 400 K (Figure 23.13).

From the analysis of Tempol and Tempamine spectra, with the fast- and slow-motional components corresponding to the probes in PPC-rich and PS(OH)-rich environments, respectively, the authors again inferred that heterogeneity of the blend decreased with an increasing hydrogen bonding interaction between its constituents – that is, at higher contents of OH groups in the copolymer. This interaction led to the formation of a physical network of the PS(OH) and PPC chains. The results of this study also corroborated with the previous conclusion [73], that the stronger the probe–polymer H-bonds the higher would be the temperature necessary for a thermally activated rapid motion of the probe ( $T_a$ ). However, the temperature range required to obtain a complete motional averaging of the spectra ( $\Delta T = T_d - T_a$ , at a given blend composition) was the same for both probes; that is, it was determined by the polymer matrix rigidity rather than by specific probe–polymer interactions. The enhancement in miscibility due to hydrogen-bonding interactions was fully confirmed by studies of STVPh- $x$  and PS(OH)- $x$  copolymers blended in a weight ratio of 3 : 1 with poly(ethylene oxide) spin labeled at the end-group with the Tempo moiety (SLPEO) [77,78].

Chen and coworkers also examined the systems containing poly(styrene-co-methacrylic acid) (STMAA- $x$ , with the mol.% of MAA units  $x \approx 12$ –38) as a more rigid component and poly(butyl methacrylate) (PBMA) as a more flexible component (1 : 1 by weight) [76]. For these studies a Tempol spin probe was selected, and the behavior of linear polymer blends (LBs) was compared with that of semi-interpenetrating polymer networks (s-IPNs) obtained by the cross-linking of STMAA- $x$  via diamines. For all mixtures, and also for pure STMAA- $x$  samples, the bimodal EPR spectra were observed in a certain temperature region (Figure 23.14). For blends, as for the above-described cases, the spectral parameters  $T_d$ ,  $T_{5mT}$  and  $\tau_c$  (in both fast- and slow-motion regions) increased as a function of the molar fraction of proton-donating groups,  $x$ . For s-IPNs, however, these parameters exhibited an opposite trend, reaching their minimum values at  $x = 29\%$ , followed by higher values at  $x = 38\%$  (cf.  $T_{5mT}$  data in Figure 23.15). The authors concluded that the best polymer miscibility occurred in the sample containing STMAA-29, and the lowest matrix rigidity in this case was due to a predominant plasticizing effect of soft PBMA chains on the hard copolymer network. With further increases in MAA content, the hydrogen-bonding interactions became so intensive that they acted as a cross-linking agent in the formation of point-like and possibly physical crosslinks, and therefore hindered the segmental motion of STMAA.

Miscibility in s-IPNs was also examined for systems consisting of STMAA and the spin-labeled poly( $\epsilon$ -caprolactone) (PCL) [79]. The results of this study led to the conclusion that, in the case of polymers interacting via hydrogen-bonding, the intracomponent crosslinking is not in favor of miscibility. The microphase

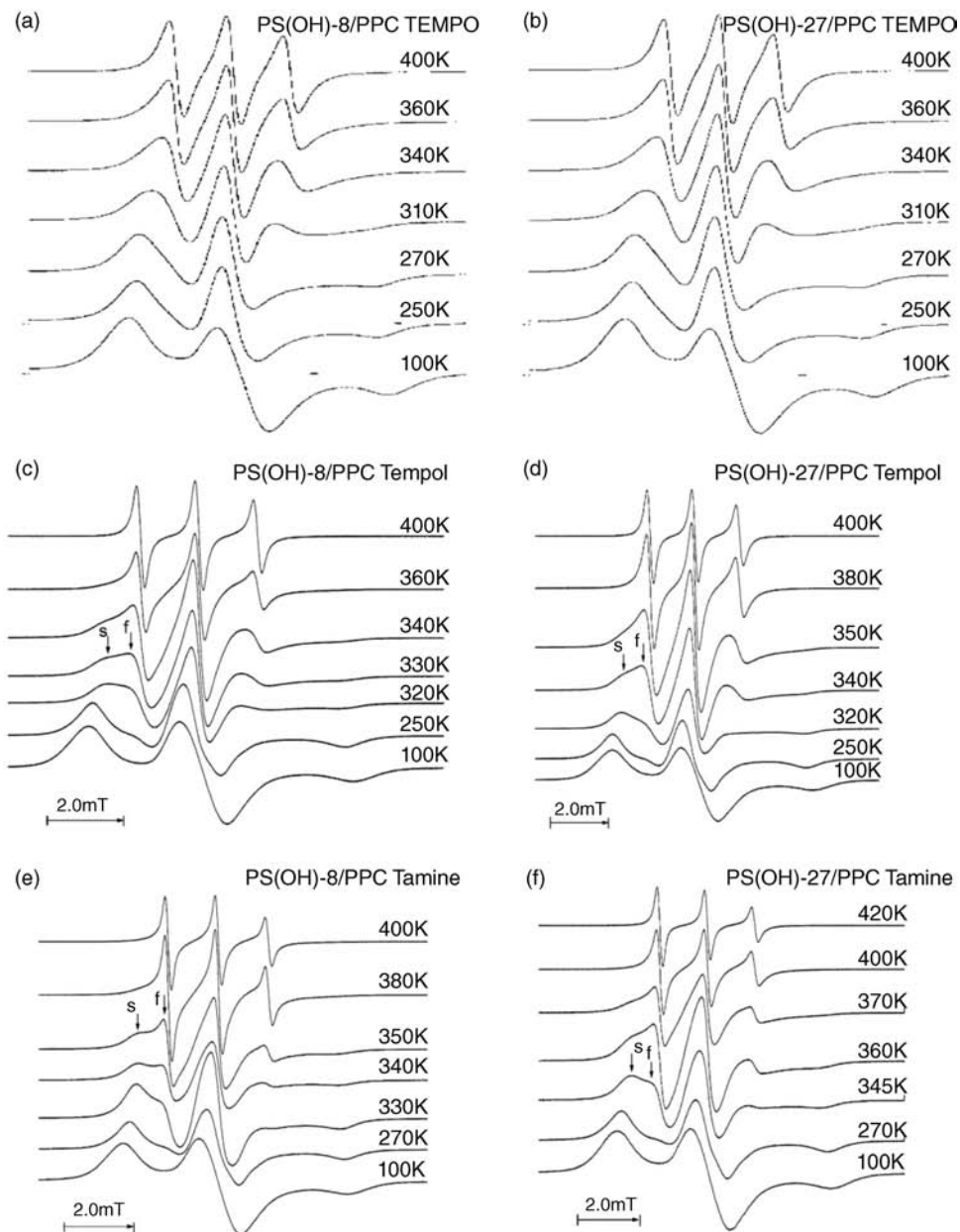


**Figure 23.13** Selected EPR spectra of (a,b) Tempo, (c,d) Tempol, and (e,f) Tempamine in PS(OH)-8/PPC (left column) and PS(OH)-27/PPC (right column) blends. Arrows indicate

low-field lines corresponding to slow- and fast-motional component signals (*s* and *f*, respectively). Reprinted with permission from Ref. [75]; © 2004, Elsevier.



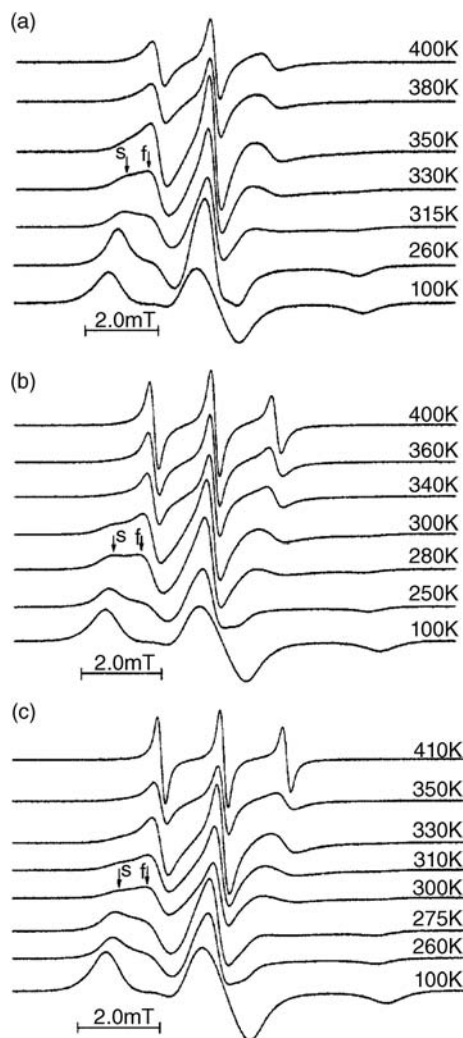


**Figure 23.14** Selected EPR spectra of Tempol spin probe in pure STMAA-12 copolymer (a), its linear blend with PBMA (b), and the respective s-IPN at the copolymer crosslinking density 2% (c). Arrows indicate low-field lines corresponding to slow- and fast-motional component signals (*s* and *f*, respectively). Reprinted with permission from Ref. [76]; © 2005, John Wiley & Sons.

separation is more pronounced with increasing crosslink density of STMAA, as manifested by higher values of  $T_d$  and  $\tau_R$ .

An opposite effect has been reported recently for s-IPNs of polyisoprene (PI, elastic component) and poly(methyl methacrylate) (PMMA, rigid component) probed with Tempol [67]. The EPR spectral features, as well as DMA, SEM and

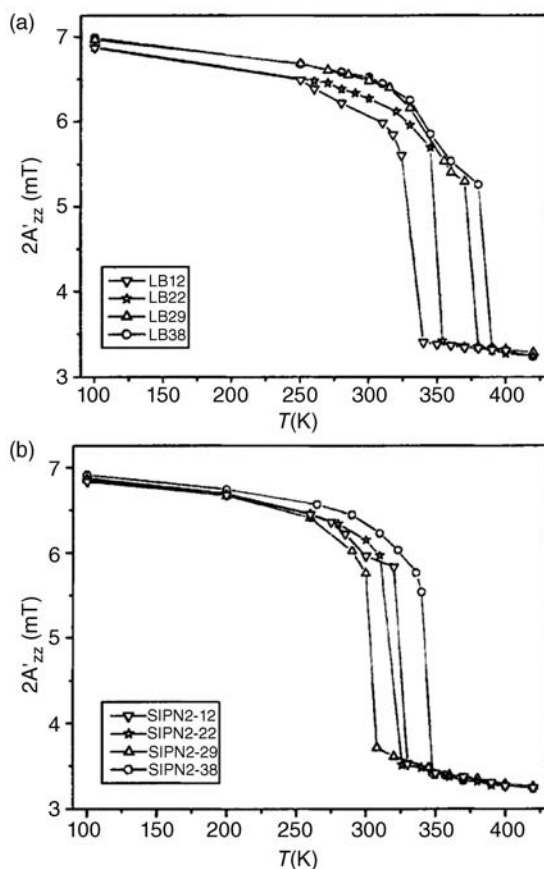


**Figure 23.15** The extreme line separation in Tempol spectra as a function of temperature for (a) linear blends, LB $x$ , and (b) semi-interpenetrating polymer networks, SIPN $y$ - $x$ , of STMAA and PBMA. In the symbols of the

samples  $x$  and  $y$  denote mol.% of MAA units and STMAA crosslinking density, respectively. Reprinted with permission from Ref. [76]; © 2005, John Wiley & Sons.

TEM data, consistently indicated that in this system heavy crosslinking enforced miscibility, leading to smaller PMMA domains within the PI matrix.

Čulín *et al.* used Tempamine as a spin probe of the mixtures of segmented polyether–polyurethane (PU) with carboxylic groups in hard segments and methacrylic copolymer (polymethacrylate; PM) with tertiary amine groups (1:1 by weight at a given concentration of functional groups) [80]. It has been shown that PU itself (unlike PM) exists in two dynamically different phases, and the segmental mobility of both soft and hard segments decreases with increasing content of carboxylic groups, due to intermolecular interactions. For mixtures, the temperature range at which dynamical phase separation occurs is higher than for PU, the fast motional signal appears at a lower temperature (compared to that for pure PU soft

segments), and its contribution increases while  $\tau_R$  (at a given temperature) decreases with respect to the PU data (at the same concentration of functional groups). All of these findings reflect an increased free volume in blends. Taking also into account that the  $T_{5mT}$  of the mixture is between the value for pure PU hard segments and that of PM, the authors suggested a plasticizing effect of PU soft segments on PM chains. In order to acquire information on the molecular dynamics of the PM component, Tempamine was covalently attached to PM chains (via the amide–ester interchange reaction) prior to mixing with (unlabeled) PU. While the spin-labeled PM itself exhibited only slow-motional EPR signals over a wide temperature range (253–393 K), two spectral components were detected in the mixture, and this confirmed the above-mentioned plasticizing effect. Both, the spin probe and spin label experiments consistently indicated that increasing the concentration of the functional groups would lead to a more restricted segmental motion of the blend components ( $T_a$  and  $T_{5mT}$  values shifted to higher temperatures, lower fraction of the *fast* signal, and longer correlation times).

In subsequent studies, Čulin *et al.* [81] employed the spin-labeled PM copolymer (with tertiary amine groups) to examine its blends and s-IPNs (1:1 by weight) with segmented polyester–PU (with carboxylic groups), which exhibits an improved miscibility of hard and soft segments as compared to the polyether–PU analog. Here also, two-component spectra reflected the effect of PU chains on the segmental motion of the PM component below the macroscopic  $T_g$ . An increasing concentration of functional groups restricted this motion, but above a certain concentration ( $0.25 \text{ mmol g}^{-1}$ ) the dynamics of PM segments in the network became faster, which suggested a change in the domain structure that led to a lower local packing density. The PU/PM mixtures revealed similar motional behavior as s-IPNs of the same composition; however, the differences in the fractional amounts of fast and slow motions indicated a better interpenetration and interaction of the two polymers in s-IPNs. The same was inferred from the EPR study on systems consisting of an unlabeled PM component and a PU component spin-labeled at the end of hard segments [82]. In this case, the maximal restriction of segmental motion of PU chains was observed at the critical concentration of functional groups equal to  $0.35 \text{ mmol g}^{-1}$ .

Miwa *et al.* applied the spin-label technique to study local segmental dynamics in miscible blends of poly(cyclohexyl methacrylate) (PCHMA) and poly(cyclohexyl acrylate) (PCHA) which, at any composition, exhibited a single  $T_g$ -value (the higher the PCHA content, the lower  $T_g$ ), as shown with DSC measurements [83,84]. The research group examined the samples containing one component (either PCHMA or PCHA) that had been spin-labeled either inside or at the end of the chain. The EPR spectra recorded for these blends over a wide temperature range represented one signal only, but a comparison of the extreme line separations for individual labeled components clearly indicated that, at a given blend composition, the segmental mobilities of the PCHMA and PCHA chains were different. The experimental data on  $T_{5mT}$  have been analyzed in terms of the self-concentration model suggested by Lodge and McLeish (L–M model) [85] (c.f.

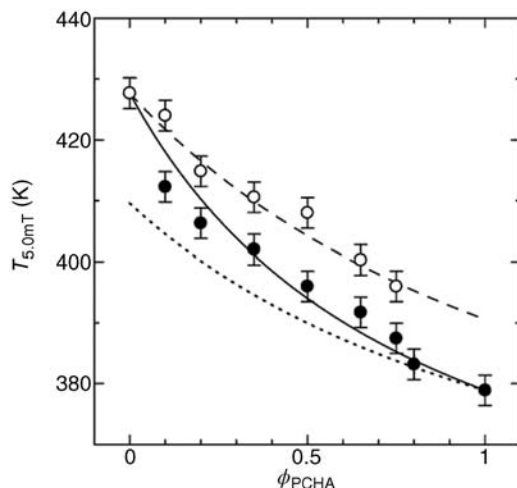


**Figure 23.16** Plots of experimental  $T_{5\text{mT, PCHMA}}$  (open symbols) and  $T_{5\text{mT, PCHA}}$  (solid symbols) values against the PCHA weight fraction in PCHMA/PCHA blends with the one component (as indicated in the subscript) spin labeled at inside sites. Broken and dotted curves correspond to PCHMA and PCHA data, respectively, calculated by the L–M model. The solid curve represents the fit to PCHA data according to Gordon–Taylor equation with  $K=0.4$ . Reprinted with permission from Ref. [83]; © 2004, American Chemical Society.

Figure 23.15 for results obtained with the inside labeled polymers). The model provided an excellent prediction of the segmental dynamics of the PCHMA, while the experimental values for PCHA were somewhat higher than the predicted values. Nevertheless, these results implied that the region explored by the spin-label was comparable to the cube of the Kuhn length, as suggested by Lodge and McLeish.

The experiments with end-labeled polymers revealed that, in blends, the mobility of the PCHMA chain ends is higher than that of the inside segments; this behavior is caused by an increased chain flexibility around the ends, and it was also observed for both homopolymers. For PCHA chains, however, the mobility difference was less pronounced, and at low weight fractions of this component the chain ends were even more mobile than inside segments. This finding has been explained by the locally higher PCHMA content around the PCHA chain ends. An analysis of experimental data within the frames of the L–M model indicated that the self-concentration effect was smaller in the chain end regions, most likely due to the discontinuity of repeat units [84].

Another system examined by Miwa *et al.* is that of binary blends of the AB-type copolymer, polystyrene-*block*-poly(methyl acrylate) (PS–PMA), with homopolymers miscible only with the A (PS) block, including PCHA of different molecular weights ( $M_n=1000$  and  $M_n=17\,300$ , comparable to that of the PS block in the copolymer) and the low-molecular-weight PS homopolymer (PS-1,  $M_n=900$ ) [65]. The copolymer was spin-labeled (using Tempamine) at chemical junction points

between PS and PMA blocks; hence, the respective EPR spectra reflected molecular mobility in the interfacial region of the microphase-separated system. The EPR results, when combined with those of modulated-temperature DSC and small-angle X-ray spectroscopy (SAXS) measurements, indicated that the effects of homopolymers on the dynamics at the interface were related to their spatial distribution in the PS host phase. The most uniformly distributed PS-1 penetrates into the interfacial region and activates the mobility, although – as suggested by  $T_{5mT}$  values of the blends – the interfacial PS-1 concentration remains constant with an increase of the homopolymer content (up to 20 wt%).

Before concluding this subsection, it must be added that the spin probe technique is also widely used in studies of polymeric composites and nanocomposites with inorganic materials, such as silica, clay minerals or organoclays [5,6,86].

#### 23.2.2.2 Radical Processes Induced by Ionizing Radiation

Ionizing radiation is widely used for structural modifications of polymeric materials in order to change their utility properties. Radiation processing inherently involves the generation of macroradicals, and these can be followed using EPR spectroscopy. The primary species formed in ionization spurs undergo secondary reactions leading to chain scissions, crosslinking and oxidative degradation, and the relative contributions of these processes largely depend on the chemical structure and morphology of the polymer as well as on the irradiation conditions. In a polymer mixture, a combination of radicals derived from individual components results in compatibilization of the blend.

Przybytniak *et al.* [87] examined the EPR spectra of blends of high-density polyethylene (PE) with the block copolymer styrene–butadiene–styrene (SBS), irradiated with a beam of 10 MeV electrons from a linear accelerator (e-beam). The aim of these studies was to gain insight into the radical processes occurring in blends, as compared to those in the constituent polymers. The results shown in Figure 23.17 revealed that the spectra of irradiated blends, recorded at one day after irradiation, represented a superposition of the signals of neat PE and SBS. However, their contributions did not correspond to the weight fraction of the blend components, in spite of a phase separation of the two polymers at the microscopic level. Furthermore, based on an analysis of the spectra recorded at shorter post-irradiation periods, the authors suggested that the radiation-induced unsaturation of PE chains was inhibited in the presence of SBS (no conversion of alkyl into allyl macroradicals was found).

In a more recent study, blends of different PEs – including high-density (HD), low-density (LD) and linear low-density (LLD) PE – with polyamide 6 (PA6; 20 wt%) were  $\gamma$ -irradiated with doses of up to 1000 kGy [88]. As seen from Figure 23.18, the EPR spectra of the three examined blends were similar multiplets, the resolution of which decreased in the order HDPE > LLDPE > LDPE. These were interpreted as a superposition of the signals of alkyl ( $-\text{CH}_2-\dot{\text{C}}\text{H}-\text{CH}_2-$ ), allyl ( $-\text{CH}_2-\dot{\text{C}}\text{HCH}=\text{CH}-\text{CH}_2-$ ) and polyenyl ( $-\text{CH}_2-\dot{\text{C}}\text{H}-(-\text{CH}=\text{CH}-)_n-\text{CH}_2-$ ) radicals.

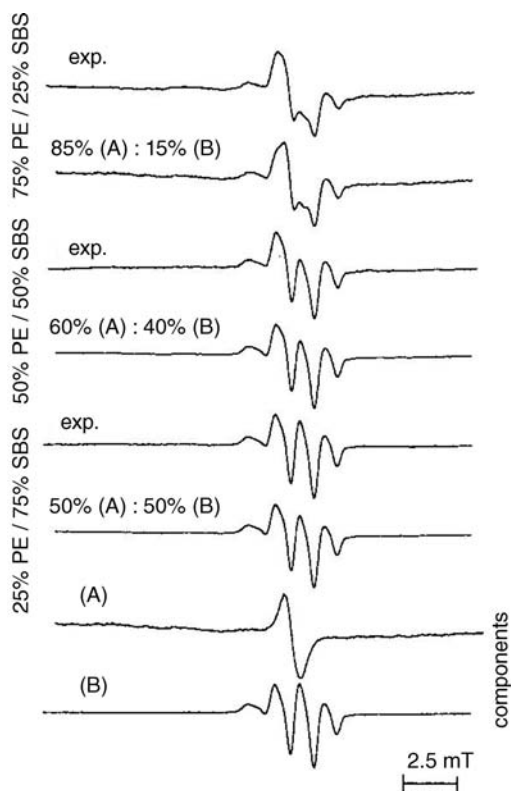


**Figure 23.17** Deconvolution of EPR spectra of PE/SBS blends e-beam-irradiated to 60 kGy; measured at room temperature, 24 h after exposure. (A) and (B) are spectra of neat PE and SBS, respectively. Reprinted with permission from Ref. [87]; © 1999, Elsevier.

When the total radical concentration was determined as a function of the radiation dose, the results showed a clear inhibitory effect of PA6 on radical trapping in the matrix. Moreover, it was noted that the amount of trapped species was significantly higher in the more crystalline HDPE samples as compared to LLDPE and LDPE samples (Figure 23.19).

From the trend of concentration–dose dependence, conclusions can be drawn regarding the relative rates of radical generation and disappearance due to recombination. If the two rates are comparable, a linear dependence would be expected (cf. PA6 and LLDPE data), whereas in the case of recombination being faster than generation, a downward deviation from linearity would occur (cf. HDPE and LDPE data). For all examined blends, however, an upward deviation from linearity was observed, which meant that the process of radical formation (chain scission) was predominant. Based on quantitative determinations for aged samples, it has been concluded that radicals decay more rapidly in blends than in pure polymers, and this can be attributed to a higher chain mobility and facilitated

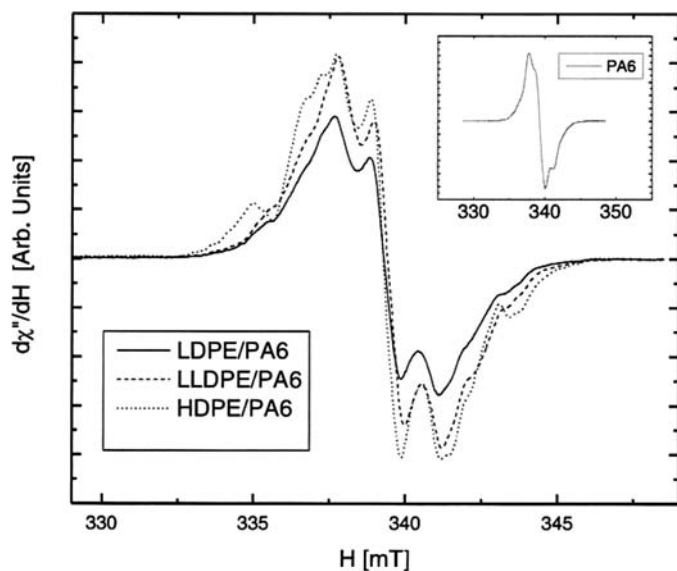


**Figure 23.18** EPR spectra of HDPE/PA6, LDPE/PA6 and LLDPE/PA6 blends irradiated at 930 kGy. Inset: Spectrum of pure PA6 (mainly radicals centered at  $\alpha$ -C with respect to the amide nitrogen). Reprinted with permission from Ref. [88]; © 2006, Springer-Verlag.

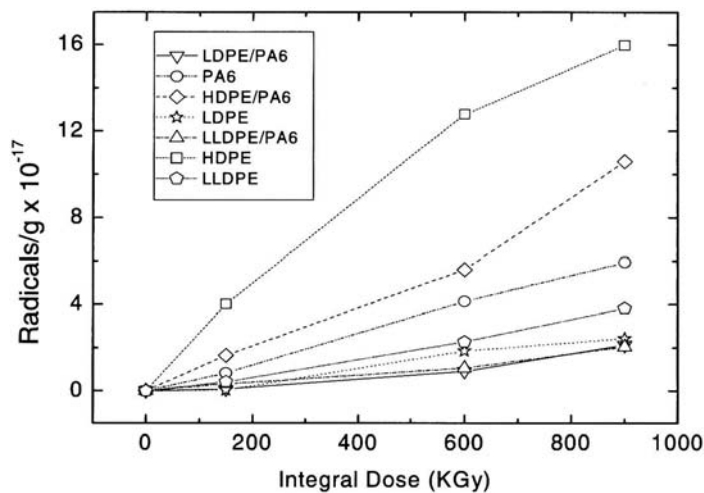


**Figure 23.19** Free radical concentration as a function of the radiation dose for the indicated samples analyzed immediately after exposure. Reprinted with permission from Ref. [88]; © 2006, Springer-Verlag.

recombination in amorphous zones introduced by PA6. At one month after irradiation, the radical concentration had decreased by an order of magnitude.

Ali [89] reported the results of a study on a LDPE blend with an ionomer resin based on ethylene–methacrylic acid copolymer (Surlyn 1857; 10 wt%), which also contained citric acid (1 wt%) as a blowing agent. The blend, as well as the reference samples of pure LDPE and LDPE/citric acid, were e-beam-irradiated at room temperature with a dose of 40 kGy, and the EPR spectra were recorded at different time intervals after irradiation. The septet corresponding to allyl radicals was a dominant spectral component in the initial spectra, the total radical concentration being about 10% higher in the presence of the ionomer due to a contribution of Surlyn-derived radicals. The latter were more stable, such that in the blend the EPR signal was still observed three days after irradiation, whereas in the reference samples the radicals had decayed completely within 3.5 h.

More attention was paid to blends based on isotactic polypropylene (PP), a commonly used commercial polymer that has good mechanical and thermal properties but is prone to degradation upon exposure to ionizing radiation. Zuchowska *et al.* examined e-beam-irradiated mixtures of PP and SBS in various proportions [90]. In this study EPR spectra were recorded as a function of time elapsed after exposure. It was found that radiation generates alkyl radicals from PP ( $-\text{CH}_2\text{C}^\bullet(\text{CH}_3)\text{CH}_2-$ ) which subsequently, in the presence of oxygen, change into peroxy radicals; as a consequence, at three days after irradiation mainly peroxy species were detectable in all samples. In this case, unlike the PE/SBS system (*vide supra*), no signal characteristic for SBS was observed, even at a copolymer content of 75%. The authors deduced that, in the blends, the rate of peroxy radical formation was increased and the transfer of paramagnetic centers  $\text{SBS}^\bullet \rightarrow \text{PP}^\bullet$  took place at higher SBS concentrations.

The effect of  $\gamma$ -irradiation on PP/SBS blends was investigated by Perera *et al.* [91]. The EPR spectra recorded for samples irradiated with 100 kGy (the time interval between exposure and measurement was not specified) (Figure 23.20) were similar to those reported previously [90] that were recorded at three days after e-beam irradiation to 60 kGy. The main signal corresponded to peroxy radicals of PP, and a minor contribution of alkyl radicals tended to disappear with increasing SBS concentration. The authors also presented the total concentration of radicals as a function of the irradiation dose, and inferred from these data that the blend containing 20% SBS exhibited an atypical behavior. At this composition, the relative rate of radical recombination with respect to the rate of radical formation (during irradiation) was similar to that in pure PP, and higher than in other examined blends (10, 30, and 40% SBS).

Another study involved e-beam-irradiated blends of PP with two types of poly(ethylene-co-vinyl acetate) (EVA, 5–13 wt%) differing in weight percentages of vinyl acetate [92]. Here again, two signals were identified in the room-temperature EPR spectra, corresponding to alkyl and peroxy radicals generated in PP regions of the blend. No signal could be assigned to EVA-derived radicals which apparently disappeared during irradiation. In these studies the authors were able to isolate peroxy radical signals from the two-component spectra and follow their growth during post-irradiation storage of the samples. The results shown in Figure 23.21 led to



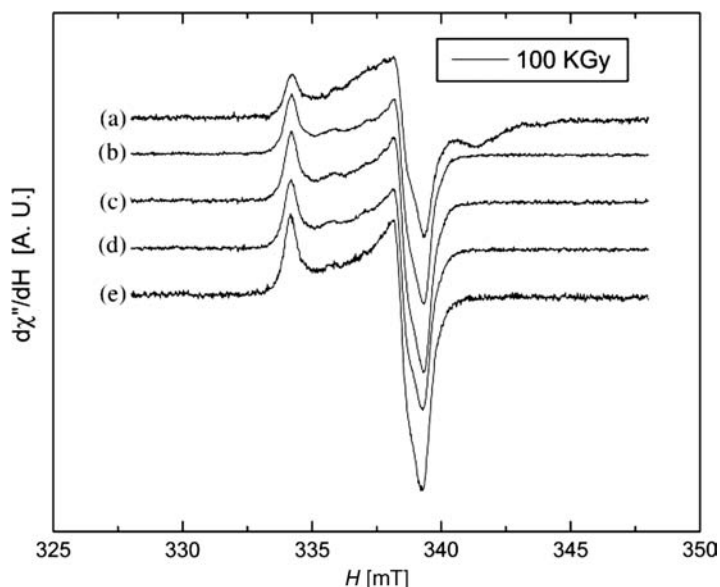


**Figure 23.20** EPR spectra of PP/SBS samples  $\gamma$ -irradiated to 100 kGy. SBS wt%: 0 (a), 10 (b), 20 (c), 30 (d), and 40 (e). Reprinted with permission from Ref. [91]; © 2004, Elsevier.

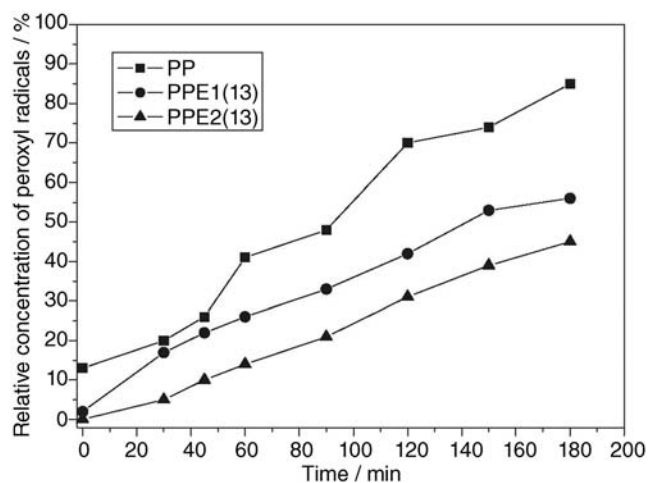


**Figure 23.21** Growth of peroxy radicals during storage of PP and PP/EVA blends e-beam-irradiated with a dose of 25 kGy. PPE1(13) and PPE2(13) are blends with 13 wt% EVA copolymers of vinyl acetate content 18% and 28%, respectively. Reprinted with permission from Ref. [92]; © 2007, Elsevier.

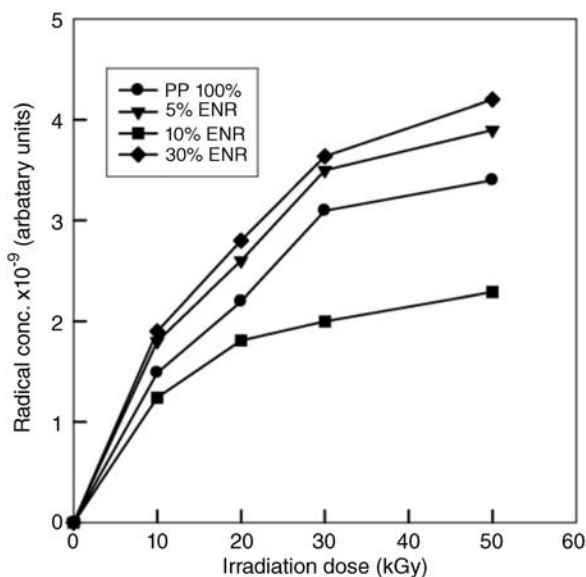


**Figure 23.22** Free radical concentration as a function of e-beam-irradiation dose for PP and PP/ENR blends of the indicated compositions. Reprinted with permission from Ref. [93]; © 2008, Elsevier.

the conclusion that the oxidation of alkyl radical was faster in the original PP than in blends – that is, oxygen diffusion to the blends was restricted. However, it is important to mention that, according to Fourier transform infrared (FTIR) data acquired in the same study, the long-term effect of oxidative degradation (at six months after irradiation) was higher in blends than in PP.

Carbon-centered radicals and peroxy radicals were also observed in the e-beam-irradiated blends of PP with epoxidized natural rubber (ENR, 5–30 wt%) [93]. The former decayed within a few hours after exposure, while the latter survived for more than 20 days. The post-irradiation decrease in total radical concentration proceeded according to a two-step second-order kinetics, with the lifetimes almost independent of the ENR percentage in the blend. Interestingly, the dependence of the initial radical yield versus %ENR was nonmonotonic (Figure 23.22). Hence, the authors suggested that such behavior reflects two effects: (i) the presence of epoxy rings and double bonds of ENR favors radical formation; and (ii) the ENR as an amorphous polymer facilitates recombination processes.

Sonnier *et al.* [94] employed EPR to examine a  $\gamma$ -irradiated PP/HDPE blend (80/20 wt%, obtained via melt extrusion followed by injection-molding). One of important findings here was that radicals were still present in samples stored for 43 days in air at ambient temperature. They can react if a new processing step involving melting of the blend is performed, thereby enhancing the degradation of PP. This would explain why the mechanical properties of a material which has been irradiated before injection-molding are worse than those of the same material when irradiated after molding.

Finally, mention must be made of a study on PS-PP blends in which PP was a minority component (20 wt%). When the blends were  $\gamma$ -irradiated at low doses ( $\leq 70$  kGy) [95], EPR data relating to the concentration of trapped radicals indicated that in these systems the PP was protected against a strong oxidative degradation (chain scission).

### 23.2.2.3 Conductive Materials

During recent years, there has been an increasing research interest in the field of conductive and semi-conductive polymers, both of which are materials of major importance for the development of optoelectronic devices and many other applications. EPR spectroscopy is an especially effective method for the investigation of these materials, because it enables to observe the spin quasi-particles responsible for charge transport. As the mechanical properties and chemical stability of conductive polymers are usually poor, their blends with elastomers or plastics have been considered as alternative materials with improved processability and durability. The most extensively examined of these systems are those which contain polyaniline (PANI) that is brought to a conducting state by doping with an acid (i.e., transition from an emeraldine base form to an emeraldine salt).

Chipara *et al.* [96] used EPR spectroscopy, along with mechanical tests and direct current (dc) electrical conductivity measurements, in studies of polyethylene (PE) that had been blended by mechanical mixing with 5–40 wt% PANI (doped in  $\sim 10\%$  with HCl). The features of room temperature (RT) EPR spectra (single lines located close to  $g=2.00$ ) and the connection between spectral parameters and dc conductivity reflected the major role of polaron hopping in electron transport, and ruled out the presence of spin bipolarons. The reduced asymmetry of the resonance line, with respect to Dysonian shape being typical for a material containing relatively large metallic islands, indicated a mesoscopic structure of the conducting domains. Both, the amount of spins and conductivity have been found to decrease by about 10% after storing the samples for one week. It has been suggested that this effect is due to electron scavenging by macroradicals generated and trapped in the blend during its preparation (the process of “thermo-mechanical mastication”).

More recently, RT EPR signals attributable to polarons (narrow symmetric singlet,  $g=2.0030$ ) have been reported for blends of LLDPE with 5–20 wt% nanorod-polyaniline (NR-PANI, synthesized via a “falling pH” route), prepared by melt extrusion [97]. It should be mentioned here that these blends are good candidates for application as antioxidant packaging materials, as their capability for free radical scavenging increases with NR-PANI content in an over-linear fashion.

Another study which employed RT EPR (complementary to other measurement methods) involved water-soluble blends of sulfosalicylic acid protonated-PANI with poly(vinyl alcohol) (PVA, 10–70 wt%), synthesized by inverted emulsion and emulsion polymerization [98]. Although the mechanical properties and blend morphology were found to depend on the method of synthesis, the EPR spectral parameters were similar for both preparations (symmetric lines of width  $\sim 2$ –5 G, with  $g$  in the range 2.0025–2.0046), typical for the PANI salt.

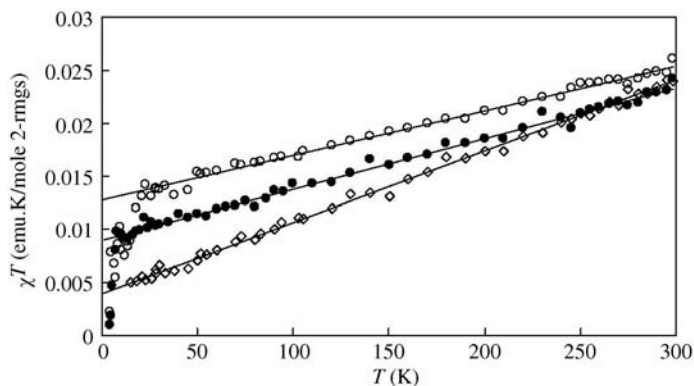


**Figure 23.23**  $\chi \times T$  as a function of temperature ( $T$ ) for a PANI–PEO fiber (closed circles), a PANI–PEO film (open circles), and a PANI film (open diamonds). Reprinted with permission from Ref. [99]; © 2004, Elsevier.

Kahol and Pinto described an EPR study of blends of PANI, fully doped with camphorsulfinic acid (CSA), with polyethylene oxide (PEO, 28 wt%) [99]. The aim of this study was to compare the behavior of electrospun nanofibers (with diameters in the range 200–600 nm) and the cast film. The spectra were recorded over a wide temperature range, down to  $\sim 5$  K, and analyzed in terms of the EPR magnetic susceptibility ( $\chi$ , given as the integrated signal intensity), the line shape, and width. From the data presented in Figure 23.23, the temperature-independent Pauli susceptibility ( $\chi_P$ , proportional to the density of states at the Fermi level) was determined as the slope of the linear dependence observed in the range of higher temperatures. For the blend fibers the value of  $\chi_P$  was higher, and at the same time the EPR lines were narrower while their shape was more Lorentzian as compared to the blend film. All of these results indicated the presence of a better structural order in fibers; evidently, the process of electrospinning brings about an increased chain alignment in the polymer, such that the morphology of the PANI/PEO blends is improved.

Several studies were performed on PANI–PMMA blends which, unlike the PANI–PEO system described above, exhibit Pauli susceptibilities and dc conductivities higher than the respective values for the unblended polyaniline [100–103]. Kahol *et al.* examined the EPR spectra of PANI (doped with *p*-toluenesulfonic acid) and its 40 wt% colloidal dispersion in PMMA for as-prepared samples and for those subjected to overnight annealing at 170 °C [102,103]. As seen from Figure 23.24, before annealing the peak-to-peak line width of the EPR singlet was up to one order of magnitude larger in the blend as compared to neat PANI and the thermal treatment led to a dramatic line narrowing in the blend, but not in PANI. Parallel measurements of the magnetic susceptibility (using a “force” magnetometer) showed, however, that the  $\chi_P$ -values of the two systems (which differed by a factor of ca. 7) remained unchanged. These results were explained in the framework of the inhomogeneous disorder model, and the authors concluded that the PANI and PANI/PMMA systems were structurally different.

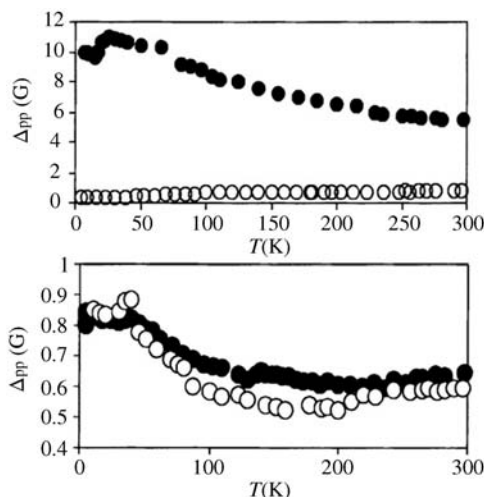


**Figure 23.24** Temperature dependence of peak-to-peak EPR linewidth for unblended PANI (open circles) and PANI–PMMA blend (solid circles), Upper panel, unannealed

samples. Lower panel, annealed samples. Reprinted with permission from Ref. [102]; © 2001, Elsevier.

The group of Chang *et al.* prepared conductive PANI (doped with HCl) blends with PMMA-*co*-glycidyl methacrylate iminodiacetic acid (PMGI) by *in-situ* dispersion polymerization [104]. The EPR spectra were recorded over the temperature range 100–300 K for samples containing different amounts of PANI, and analyzed in terms of *g*-factor, peak-to-peak line width ( $\Delta H_{pp}$ ), line-shapes (Gaussian contribution) and symmetry, and spin concentrations. The data obtained suggested that the spins were of the free electron type ( $g = 2.0033$ – $2.0034$ ; the height ratio of positive to negative peaks of the singlet was close to unity). The increasing spin mobility (at a given temperature) with decreasing PANI content, as indicated by line narrowing, has been interpreted in terms of weaker PANI–PMGI interactions via hydrogen bonding. A similar study performed at the same laboratory concerned PANI blends with the polyamidoamine dendrimer (PAMAM; G2.0) [105]. By using various blending procedures, four materials were produced which exhibited significantly different EPR signals. The results were interpreted taking into account the different intermolecular interactions between PAMAM and PANI (electrostatic and H-bonding, or penetration of PANI inside the dendrimer host).

Souza *et al.* examined the influence of plasticizers, such as dioctyl phthalate (DOP) and cashew nut shell liquid (CNSL), on the electrical properties of blends based on PANI (doped with dodecylbenzene sulfonic acid) and SBS (styrene–butadiene–styrene) copolymer [106,107]. EPR experiments revealed an increase in polaron mobility (a decrease of  $\Delta H_{pp}$ ) as the amount of plasticizer in the blend was increased, with the effect being more pronounced for CNSL (Figure 23.25). This phenomenon is known as a “second doping,” and is achieved without any additional protonation of PANI; rather, it is due to an enhanced conformational

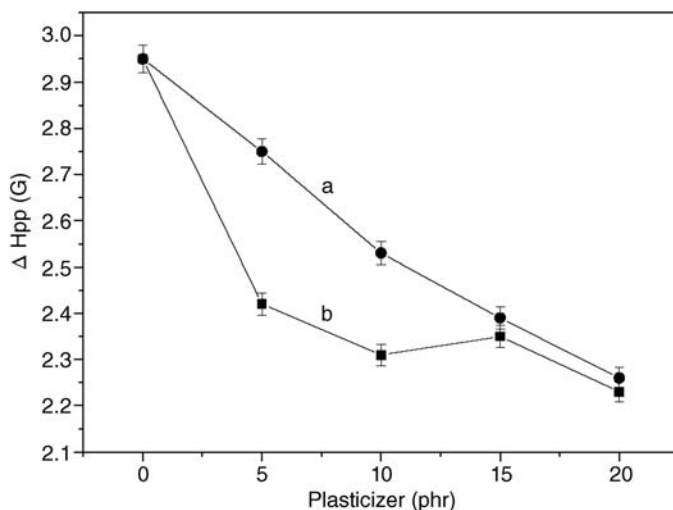


**Figure 23.25** Peak-to-peak line width of EPR signal of PANI-SBS samples plasticized with different amounts of DOP (a) or NCSL (b). Reprinted with permission from Ref. [107]; © 2007, Elsevier.

change of PANI chains from compact to expanded coil, imparted by the phenol moiety of cardanol present in CNSL.

Kanemoto *et al.* investigated iodine-doped regiorandom (RRa) poly(3-octylthiophene) (P3OT) diluted (2 wt%) in a solid matrix of PS [108]. While the pure RRa-P3OT film exhibited isotropic (symmetric) EPR signals, the spectra of the blend were broader and anisotropic (Figure 23.26). The EPR features of the blend were quantitatively evaluated by an analysis of the correlation function, calculated from the Fourier-transformed line shape, and by spectral simulations. The results indicated that the spin motion does not follow the pure one-dimensional model, and this is considered to be due to the coexistence of aggregated and isolated P3OT molecules in the blend which are responsible for isotropic and anisotropic spectral components, respectively. As the latter component was less mobile ( $\Delta H_{pp}$  larger), the authors concluded that the intrachain spin motion was less active than the interchain motion. In addition, as seen from the data presented in Figure 23.27, the spin dynamics in the pure film was dominated by intrachain motion at low temperature, and interchain motion at high temperature.

The EPR technique was also employed in the study of conductive fibers produced by wet-spinning of poly(3,4-ethylenedioxythiophene) doped with poly(styrenesulfonate) (PEDOT:PSS) [109]. The aim of this study was to compare the behavior of the as-spun fibers with those post-treated with ethylene glycol, and also with PEDOT:PSS-PEG fibers obtained by a simplified one-step process of spinning an aqueous blend of PEDOT:PSS and poly(ethylene glycol) (PEG, molecular weight  $200 \text{ g mol}^{-1}$ ). The latter blend exhibited superior conductivity and redox properties. The EPR data (line widths and spin concentrations), together

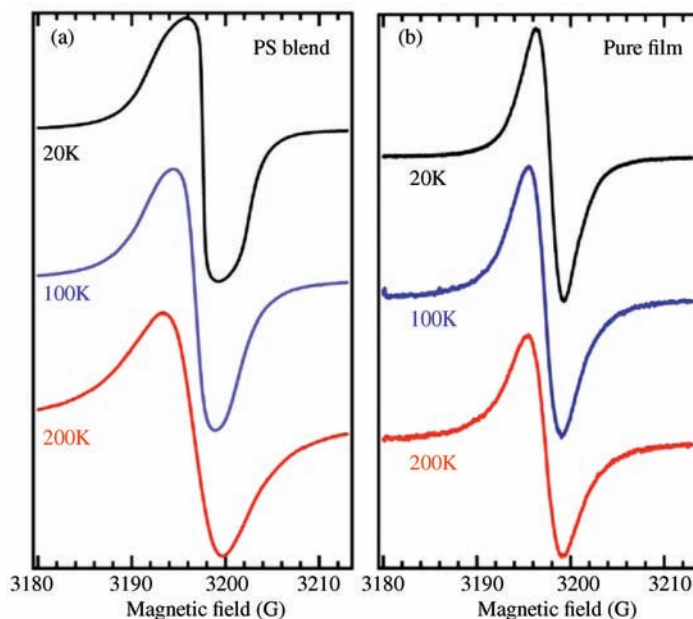


**Figure 23.26** EPR spectra of (a) the polystyrene (PS) blend and (b) a pure film of doped regiorandom (RRA) poly(3-octylthiophene) (P3OT) at indicated temperatures. Reprinted with permission from Ref. [108]; © 2010, Elsevier.

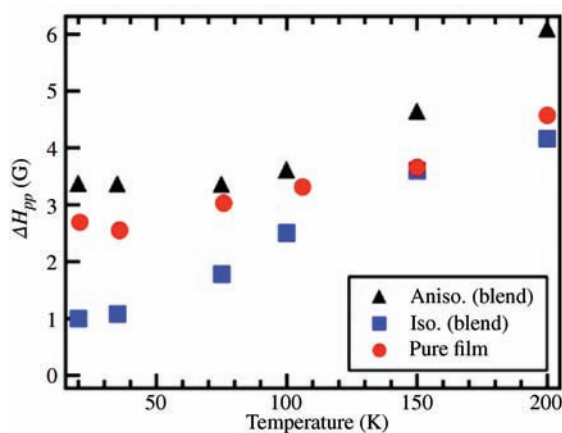


**Figure 23.27** Temperature-dependence of the Lorentzian peak-to-peak linewidth for the anisotropic (Aniso.) and isotropic (Iso.) components in the PS blend determined from

spectral simulations, and the experimental peak-to-peak linewidth in the pure RRA-P3OT film. Reprinted with permission from Ref. [108]; © 2010, Elsevier.

with those of Raman spectroscopy, provided evidence that this was due to a better molecular ordering of the PEDOT chains in the direction of the fiber axis (enrichment of linear or expanded-coil like conformation), which favored the spinless bipolaron formation.

### 23.3

#### Forward Recoil Spectrometry

Forward recoil spectrometry (FRES, FReS or FRS), which is also referred to as elastic recoil detection analysis (ERDA or ERD), is a member of a family of techniques collectively termed ion beam analysis (IBA). FRES is a powerful, standard-free absolute method for the measurement of atomic composition and impurity concentrations in the near-surface region of solids, and is considered a fully non-invasive technique. However, in the case of polymeric materials this assumption is not entirely true, since the projectile ions cause a breaking of covalent bonds (*vide infra*). The method is based on scattering of an incident accelerated-ion beam by the sample, due to nuclear and electrostatic interactions. The collision of the ions with the specimen results – in addition to scattered incident ions – in the ejection of photons, ions, or nuclear decay products, as shown schematically in Figure 23.28 [110].

An analysis of the energy of these particles allows depth profiling with a resolution of a few nanometers for low-energy forward recoil spectrometry (LE-FRES), and a maximum range of up to a few micrometers for nonresonant nuclear reaction (NRA). However, an increasing depth leads to a decreasing resolution, and it becomes necessary to take into account the fact that both parameters depend heavily on the nature of the sample being investigated and the ions used. Detailed descriptions of IBA theory, its applications, limitations and possible

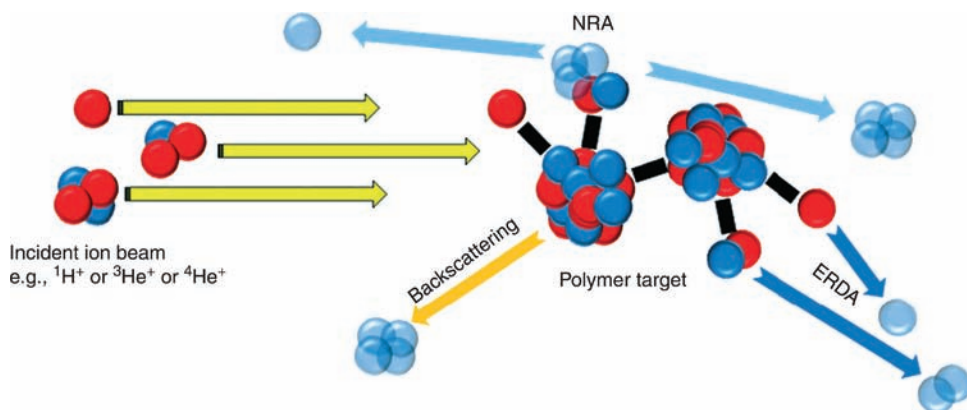


**Figure 23.28** Schematic representation of some of the more common interactions used in ion beam analysis of polymers. Reprinted with permission from Ref. [110]; © 2012, Elsevier.



prospects, are available in numerous books and comprehensive reviews [110–116]. Only a brief description of the technique is provided in the following subsections.

### 23.3.1

#### FRES Fundamentals

A method for the determination of depth profiling of light elements in heavy materials, based on the detection of the former elements recoiling under projectile ions, was first proposed [117] and developed during the 1970s [118]. The method was applied for the first time to a polymer system by Mills *et al.*, who named the technique “forward recoil spectrometry” [119]. Regardless of later discussions and controversy [120], this name and the acronym FRES is commonly used by polymer scientists, and will also be used for the purpose of this section. The set-up for a classical FRES experiment is shown in Figure 23.29, where the incident beam of  $^4\text{He}^+$  or  $^4\text{He}^{2+}$  with energy in the range 1–4 MeV (typically 3 MeV) collides with the sample at an angle  $\alpha$  (usually  $15^\circ$ ). When the projectiles collide with nuclei in a polymer film, some of the protons and deuterons recoil out of the sample and are detected by a silicon surface barrier detector positioned at an angle  $\theta$  (typically  $30^\circ$ ) to the incident beam direction [121]. The lighter elements recoil with the energy:

$$E_{\text{rec}} = k_i E_{\text{inc}} \quad (23.26)$$

where  $E_{\text{rec}}$  is the energy of the recoiled particle just after collision;  $E_{\text{inc}}$  is the energy of the incident particle just before collision; and  $k_i$  is the kinematic factor.

The kinematic factor depends on the mass of the particles and the scattering angle:

$$k_i = \frac{4m_{\text{inc}}m_{\text{rec}}}{(m_{\text{inc}} + m_{\text{rec}})^2} \cos^2 \theta \quad (23.27)$$

where  $m_{\text{inc}}$  is the mass of the incident ion, and  $m_{\text{rec}}$  is the mass of the recoiled ion.

However, not only will these nuclei exit the sample but also the forward-scattered  $^4\text{He}$  (or heavier nuclei) will be present in the ion beam leaving the sample. Since an energy-sensitive detector cannot distinguish the type of ions, a

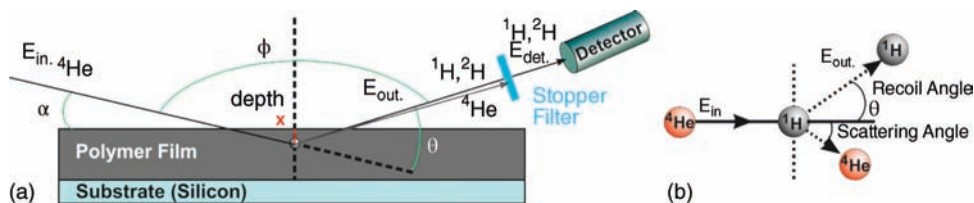


**Figure 23.29** Schematic representation of (a) the typical experimental geometry used in FRES experiments; (b) An elastic scattering.

stopper filter must be applied. This is usually Mylar<sup>TM</sup> foil (polyethylene terephthalate, PET), or sometimes a metal foil made of aluminum or nickel [122,123]. The foil is capable of stopping (low-energy) or slowing down (high-energy) the forward-scattered <sup>4</sup>He nuclei, which therefore do not interfere with hydrogen or deuterium species. However, the foil (in a standard experiment this is 10–12 μm thick) also slows down <sup>1</sup>H and <sup>2</sup>H, leading to a signal broadening and thus decreasing the depth profiling resolution. Additionally, although PET polymer exhibits a high resistivity, forward-scattered <sup>4</sup>He may also recoil <sup>1</sup>H ions from this foil.

Determination of the concentration distributions is based on the energy losses of the impinging and recoiling ions in a sample material. The total energy loss is due to inelastic collisions of the particles with the electrons (electronic energy loss) and the nuclei (nuclear energy loss) in the polymer [124]:

$$S(E) = -\frac{dE}{dx} = -\left[\left(\frac{dE}{dx}\right)_{\text{nuclear}} + \left(\frac{dE}{dx}\right)_{\text{electronic}}\right] \quad (23.28)$$

Therefore, the energy of recoiled <sup>1</sup>H and <sup>2</sup>H nuclei depends on the distance traveled in the sample (i.e., the distance from surface) and kinematic factors. Recoiled particles are detected at a higher energy (high channel numbers) when ejected from the near-surface region compared to those recoiled from the deeper layers within the polymer film. As the number of recoiled nuclei is proportional to the corresponding atom density in the sample, it is possible from the energy spectrum to calculate <sup>1</sup>H and <sup>2</sup>H distribution. The <sup>1</sup>H and <sup>2</sup>H can be distinguished by different kinematic factors, since the factor for deuterium is larger than that for hydrogen, and therefore the <sup>2</sup>H signal is shifted to a higher energy. It should be mentioned here that for the energy range used in FRES experiments (namely, few MeV), the electronic energy loss is three orders of magnitude higher than the nuclear energy loss. A typical FRES technique allows depth profiling up to 750 nm with a maximum of 80 nm resolution [125,126]. The depth resolution in the case of FRES and other IBA methods is defined as [126]:

$$\delta x = \frac{\Delta E_{\text{tot}}}{dE_{\text{det}}/dx} \quad (23.29)$$

where  $\Delta E$  is the total energy resolution, and  $dE_{\text{det}}/dx$  is the effective stopping power of the recoiled particles.

The following phenomena contribute to the total energy resolution: the detector energy resolution; the energy broadening due to multiple scattering; the energy straggling in the sample; the energy straggling in the stopper foil; the geometric broadening due to a beam footprint size and the detector acceptance angle, both causing differences in path lengths; and the kinematic shift induced by the beam energy divergence [116,121,126,127]. The total energy loss can be approximated as a square-root of the sum of squared factors listed above. Additional complications might be introduced by the fact that the surface of the sample thin layer deposited on silica or glass substrates is not always very smooth, whereas FRES is very sensitive to surface roughness due to oblique scattering geometry [128]. For these

reasons, several modifications to the standard FRES set-up have been introduced. A short description of the most important improvements is provided in the following section.

### 23.3.2

#### Technique Developments

In order to achieve the optimum resolution accompanied with a reasonable analyzed depth, the type of incident ions and their energy, the geometry of the experiment, and the detection system must each be optimized. Composto *et al.* demonstrated the effect of finite instrumental resolution by the comparison of calculated volume fraction profiles with the ideal profiles (Figure 23.30) [116].

A poor depth resolution of the conventional FRES is mainly caused by energy straggling in a stopper filter ( $\sim 10.5 \mu\text{m}$  at 3.0 MeV), which decreases the resolution to at the best 80 nm. Therefore, complete stopper filter elimination – or at least a foil thickness reduction – are the possible ways to improve an achievable resolution. The first approach has been used in time-of-flight FRES (TOF-FRES), and the second approach – in low-energy FRES (LE-FRES). The depth resolution can be also improved by using heavy-ion FRES (HI-FRES), although when using heavy-ion beams the polymer sample may be extensively damaged by large

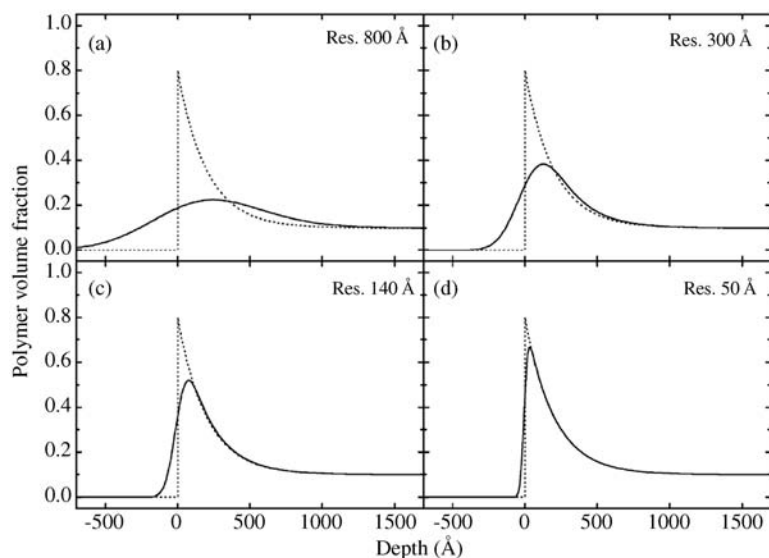


**Figure 23.30** Volume fraction profile (dotted line) for surface segregation in polymer blend having surface and bulk concentrations of 0.8 and 0.1, and the surface excess of 6 nm. The solid lines are obtained by convolution of the

dotted line with a Gaussian instrumental resolution function having FWHM (Full Width at Half Maximum): (a) 800 Å; (b) 300 Å; (c) 140 Å; (d) 50 Å. Reprinted with permission from Ref. [116]; ©2002, Elsevier.

amounts of energy delivered to the sample due to inelastic energy loss processes. Forward recoil spectrometry (including LE- or HI-FRES) may also benefit from optimization of the scattering geometry, see also large (recoil) angle FRES (LA-FRES) [129]. Several other modifications of FRES have been described, including maximum-scattering-angle [130], gas telescope systems [131,132], Bragg ionization chambers [133], the use of a  $E \times B$  filter (crossed electric and magnetic fields) [134,135], coincidence detection [136], and ion-induced electron emission [137], but these have not been used frequently for polymer system investigations and therefore will not be discussed at this point.

It should be added, that several programs have been developed to simulate the ion beam energy spectra, and these can be divided into either analytical (SIMNRA, RUMP, NDF) or Monte-Carlo (TRIM.SP, SRIM, SDTrimSP, MCERD CORTEO) codes [138].

### 23.3.2.1 Time-of-Flight FRES

In this technique, which was introduced during the early 1980s [139,140], the stopper filter is replaced by a time-of-flight detector (Figure 23.31). Depth resolutions below 10 nm were reported for oxygen and carbon in titanium, with detection limits of the order of  $10^{15}$  atoms  $\text{cm}^{-2}$  [140]. This set-up was used by Sokolov *et al.* to investigate surface enrichment of the deuterated component in a blend of high-molecular-weight polystyrene/deuterated polystyrene [141].

The beam of accelerated and collimated  $^4\text{He}^+$  ions collides with the polymer sample, then the recoiled and forward-scattered particles pass through a thin carbon foil and enter a silicon surface barrier detector located at a distance of

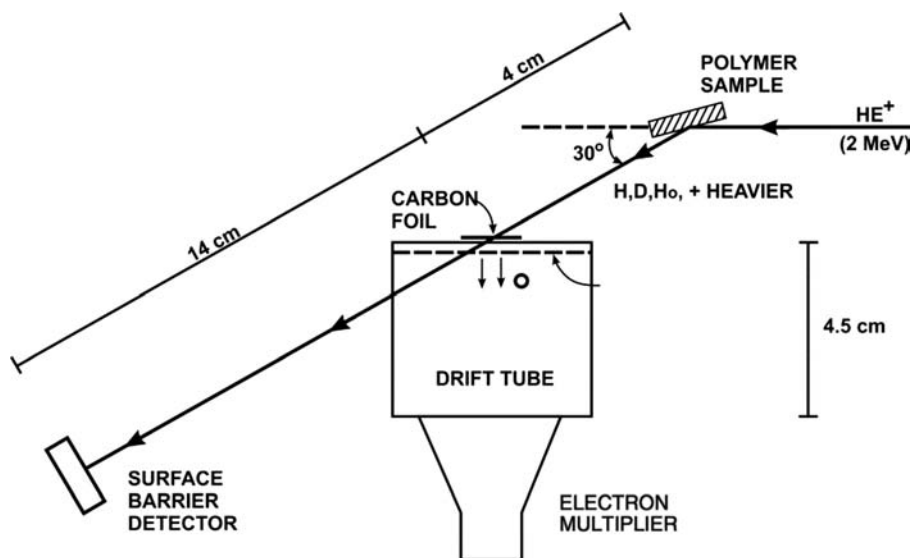


**Figure 23.31** Time-of-flight detector system. Adapted with permission from Ref. [141]; © 1989, AIP Publishing LLC.

several (15–90) centimeters. The secondary electrons generated in the carbon foil by traversing ions produce the start signal for measurements. The particles' flight time is determined by measuring the delay between the detection of electrons, and charged particles at the surface barrier detector. The flight time,  $t_R$ , of particles recoiling from the polymer surface can be estimated with the formula [141]:

$$t_R = \Delta x \sqrt{\frac{m_i}{2k_i E_0}} \quad (23.30)$$

where  $\Delta x$  is the flight path,  $m_i$  is the particle mass,  $k_i$  is the kinematic factor,  $E_0$  is the incident energy.

Because  $^1\text{H}$ ,  $^2\text{H}$ , and  $^4\text{He}$  differ in their masses – and therefore in their kinematic factors – they can be discriminated by using TOF-FRES. In the experiment performed by Sokolov *et al.* ( $E_0 = 2\text{ MeV}$ ), the minimum flight times for recoiling  $^1\text{H}$ ,  $^2\text{H}$  and scattered He were 10.3, 12.4, and 14.2 ns respectively. By using this technique to investigate polymer systems, it is possible to achieve depth resolutions in the range of 30 nm. Unfortunately, the wide use of TOF-FRES is hindered by its relatively complicated and demanding detection system; moreover, its sensitivity for detecting  $^1\text{H}$  and  $^2\text{H}$  is lower in comparison to standard FRES, because the efficiency in generating the secondary electrons decreases with the decreasing mass of particles [141]. Nonetheless, if a high spatial resolution is required then TOF-FRES is the method to be considered.

### 23.3.2.2 Low-Energy FRES

Another approach to the resolution problem of FRES was presented by Genzer, Rothman and Composto, who proposed using an incident beam of 1.3 MeV. This approach benefits from two factors: (i) a thinner stopper filter foil; and (ii) a higher stopper power of forward-scattered ( $^4\text{He}$ ) and recoiled ( $^1\text{H}$  and  $^2\text{H}$ ) ions [126]. When a lower energy is used, a filter of only 3.0–4.5  $\mu\text{m}$  thickness (rather than the usual 10–12  $\mu\text{m}$  thickness) is sufficient to stop forward-scattered helium ions. Due to the energy straggling of  $^1\text{H}$  and  $^2\text{H}$  within the foil, the energy resolutions are limited by the foil thickness, and lowering the thickness from  $\sim 10\text{ }\mu\text{m}$  to  $\sim 4\text{ }\mu\text{m}$  improves the resolution by factor of 1.5. In the case of polystyrene, the stopping power for ions of interest is doubled and, in consequence, the resolution is increased approximately threefold [see Eq. (23.29)]; consequently, for such a set-up a resolution of about 25–30 nm was achieved [126]. Further increases in resolution can be obtained by optimization of the system geometry, for example by varying the incident beam and scattering angles [121,126]. By using a glancing incident or exit geometry, the depth resolution can be improved so as to achieve a value of 20 nm. As the geometry has direct influences both on resolution and probing depth, the correct selection of these angles is crucial. As discussed in detail elsewhere [126], the maximum depth profiling for LE-FRES can be obtained by using a  $71^\circ$  incidence for projectiles,  $30^\circ$  scattering angles, and a 4.5  $\mu\text{m}$  Mylar<sup>TM</sup> foil (Figure 23.32).

The main disadvantage of LE-FRES is a much smaller probing depth (300–400 nm) in comparison to standard FRES ( $\sim 800\text{ nm}$ ).

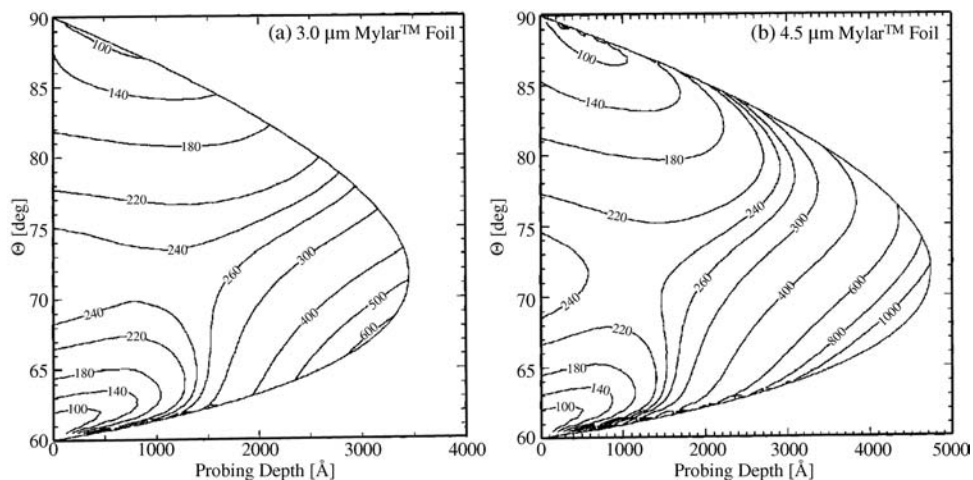


**Figure 23.32** Deuterium depth resolution map for 1.3 MeV  $^4\text{He}^+$  in polystyrene for (a) 3.0  $\mu\text{m}$ - and (b) 4.5  $\mu\text{m}$ -thick Mylar stopper foils. The contour values represent the depth resolution in Angströms. Adapted with permission from Ref. [126]; © 1994, Elsevier.

### 23.3.2.3 Heavy Ion FRES

Another way to improve the depth resolution of FRES is to use heavier projectile ions, as such ions (due to their high masses) exhibit much larger stopping powers [see Eqs (23.27) and (23.29)]. A resolution of 1 nm was reported for a 129 MeV  $^{197}\text{Au}$  beam with  $^{12}\text{C}$  recoil ions from  $^{12}\text{C}/^{11}\text{B}$  multilayers [142]. Although such an incident beam is not suitable for polymer investigations, if special care is taken then ions heavier than  $^4\text{He}$  can be used. For example, during the mid-1980s, Green and Doyle applied  $^{28}\text{Si}^{4+}$  ions with an energy of 20 MeV to study tracer diffusion in polystyrene. Due to the large increase in stopping power, from  $120 \text{ eV nm}^{-1}$  for  $^4\text{He}$  to  $2210 \text{ eV nm}^{-1}$  for  $^{28}\text{Si}$ , a resolution of 20 nm was obtained [143]. However, heavy projectiles in particular – though not exclusively, as Abdesselam *et al.* reported the degradation of a very stable PET film irradiated with a 3.7 MeV  $^4\text{He}^+$  beam [144] – cause the crosslinking (predominantly in polystyrene) and scission of polymer chains that lead to dramatic changes in polymers' properties. Green *et al.* noted that the tracer diffusion coefficient in polystyrene, determined using  $^{28}\text{Si}$  FRES, was 1.6-fold smaller than that measured by  $^4\text{He}$  FRES. These authors attributed these phenomena to the fact that the silicon beam releases not only hydrogen but also carbon nuclei (due to breaking covalent bonds), which in turn alters the polymer density [143]. Able *et al.* investigated changes in the atomic composition (C, H, and D) of thin polystyrene films under  $^4\text{He}$  and  $^{12}\text{C}$  irradiations and showed that, during irradiation by both ions, the loss of  $^1\text{H}$  was faster than that of  $^2\text{H}$ , although the isotopic effect was less pronounced for  $^{12}\text{C}$  [145].

The polymer composition changes with deposited energy density even for a very low dose of radiation (Figure 23.33) [145]. Despite this, several applications of

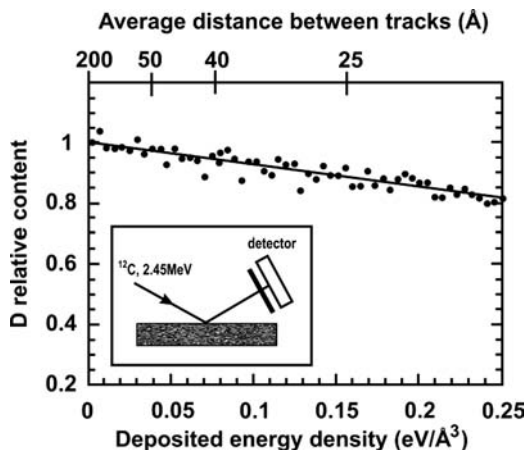


**Figure 23.33** Real-time variation of deuterium content in a 360 Å-thick d-PS film irradiated with a 2.45 MeV  $^{12}\text{C}$  ion beam (beam current  $i = 0.3$  nA, beam diameter  $f = 4$  mm). Insert:

Schematic diagram of ERDA measurements. Adapted with permission from Ref. [145]; © 1995, Elsevier.

HE-FRES with the use of  $^{12}\text{C}^+$  [143,146,147],  $^{20}\text{Ne}^{2+}$  [147], and  $^{40}\text{Ar}^{2+}$  [127] beams for studying polymers have been reported and suggestions are given how to prevent polymer degradation (e.g., by cooling the sample [143]). It seems that with safety precautions being applied, HE-FRES is an acceptable method of investigating relatively stable polymers such as polystyrene.

### 23.3.3

#### Applications to Polymer Blend Studies

The potential of the FRES technique is highlighted in this section, based mainly on papers published in the year 2000 and thereafter. However, as the recent FRES investigations of polymer blends are rather scarce, some examples are also included from earlier studies, many of which were comprehensively reviewed elsewhere [116]. Whilst attention has been focused here on polymer blends, relevant studies of homopolymers, copolymers and polymeric composites will also be presented. The case study examples are divided (to some extent arbitrarily) into four subsections according to the major point of interest, namely diffusion coefficient, interphase behavior, reaction kinetics, and phase separation.

##### 23.3.3.1 Tracer Diffusion

As noted above, the FRES technique was first used to investigate polymers by Mills *et al.* [119], who measured the concentration profiles and tracer diffusion

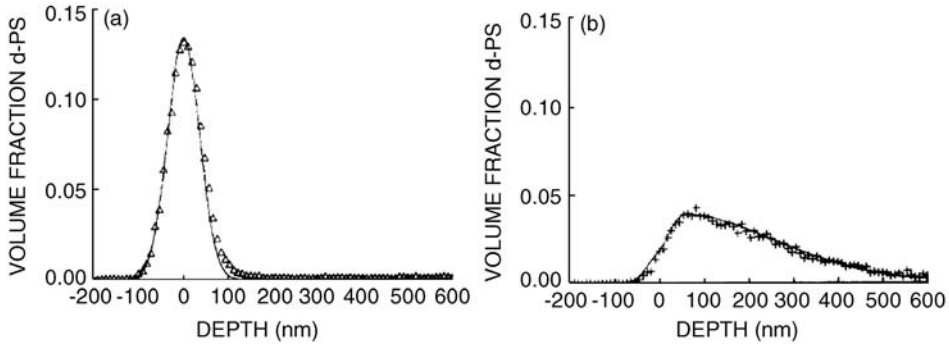


**Figure 23.34** Volume fraction d-PS versus depth  $x$  for (a) the bilayer film before diffusion and (b) the bilayer film after diffusion for 3600 s at 170 °C,  $D = 8 \times 10^{-14} \text{ cm}^2 \text{ s}^{-1}$ . Adapted with permission from Ref. [119]; © 1984, AIP Publishing LLC.

coefficients,  $D$ , of a deuterated polystyrene (d-PS)<sup>1)</sup> diffusing into its hydrogenated analog (h-PS). For this purpose, a standard geometry was used (that is,  $\alpha = 15^\circ$ ,  $\theta = 30^\circ$ ),  $^4\text{He}^{2+}$  ion beam of energy  $E_o = 3.0 \text{ MeV}$ , and  $10.6 \mu\text{m}$  Mylar<sup>TM</sup> foil shielding the silicon surface barrier detector. In this experiment, a thick ( $\sim 4 \mu\text{m}$ ) layer of h-PS was covered by a thin film (10–20 nm) of d-PS (tracer) and diffusion was observed at 170 °C in a vacuum. The measured profiles of the tracer before and after 1 h sample annealing are shown in Figure 23.34.

In order to calculate  $D$ , the equation based on the solution of Fick's second law for the model of very thin film (tracer) diffusing into semi-infinite layer was used:

$$\phi(x) = \frac{1}{2} \left[ \text{erf} \left( \frac{h-x}{\sqrt{4Dt}} \right) + \text{erf} \left( \frac{h+x}{\sqrt{4Dt}} \right) \right] \quad (23.31)$$

where  $\phi(x)$  is the volume fraction of tracer at depth  $x$ ,  $h$  is the thickness of the tracer film;  $t$  is the diffusion time,  $D$  is the diffusion coefficient, and  $\text{erf}$  is the error function.

The authors concluded that the determined value of  $D$ , and its dependence on molecular weight ( $D$  decreases as  $M_w^{-2}$ ), were in agreement with the reptation theory of polymers [148,149]. This theory predicts that for times  $t > \tau_{\text{rep}}$ , where  $\tau_{\text{rep}}$  is the reptation relaxation time, the reptation diffusion coefficient is given by the following equation [150]:

$$D = \frac{4M_0 M_e k_B T}{15 \xi_0 M_w^2} \quad (23.32)$$

where  $M_0$  is the monomer molecular weight,  $M_e$  is the entanglement molecular weight, and  $\xi$  is the monomer friction coefficient.

The same authors used FRES to determine the concentration profiles of d-PS in h-PS with a depth resolution of 80 nm and a sensitivity of 0.1 vol.% d-polymer in

1) Throughout this chapter, deuterated polymers will be marked as d-, while hydrogenated polymers will be marked as h-, followed by an abbreviation of the polymer name.



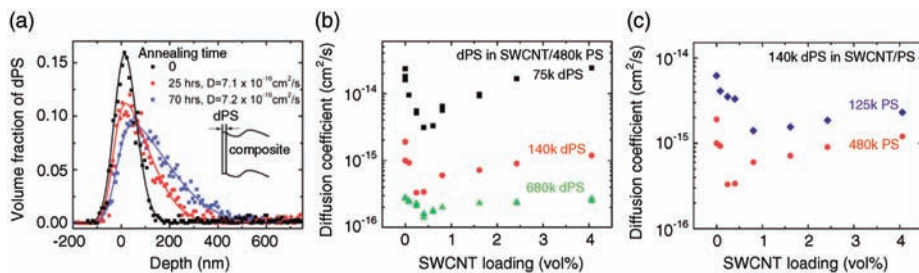


**Figure 23.35** Polymer tracer diffusion in SWCNT/PS nanocomposites measured using ERD. (a) 140 k d-PS distribution in 1.60 vol.% SWCNT/480 k PS nanocomposites as prepared and after annealing at 150 °C for different times. The solid lines are fits of the diffusion equation to obtain the diffusion coefficients. Tracer diffusion in these nanocomposites is independent of annealing time; (b) d-PS tracer diffusion coefficients in SWCNT/480 k PS nanocomposites as a function of SWCNT

concentration for three d-PS molecular weights. For all d-PS tracers the minimum diffusion coefficient occurs at a SWCNT concentration of 0.4 (0.1 vol.%); (c) 140 k d-PS tracer diffusion coefficients at 150 °C as a function of SWCNT concentration in 125 k PS and 480 k PS nanocomposites. The minimum diffusion coefficient appears at 0.8 vol.% SWCNTs in the 125 k PS composites. Adapted with permission from Ref. [154]; © 2009, American Chemical Society.

h-polymer. The value of  $D$  was determined as equal to  $10^{-16} \text{ cm}^2 \text{ s}^{-1}$ . The results presented again confirmed the applicability of a reptation model for macromolecules diffusion [151]. A few years later, Composto *et al.* measured diffusion of the tracer (d-PS and deuterated poly(xylenyl ether), d-PXE) into blends of h-PS and h-PXE [152,153].

Lately, Composto *et al.* investigated the diffusion of polymers in the presence of nanoparticles, and determined the tracer diffusion coefficient of d-PS in single-walled carbon nanotubes/PS nanocomposites (SWCNT/PS) by means of a FRES technique, using classical experimental conditions (see Section 23.3.1) (Figure 23.35) [154]. These authors found that the dependence of  $D$  versus SWCNT loading exhibited a minimum, and explained this phenomenon by assuming the anisotropy of local diffusion near the SWCNT. The assumption was confirmed by a computer simulation using a three-dimensional trap model [154]. In a subsequent report, the same group investigated the diffusion of three tracers that varied in molecular weight, and found that anisotropic diffusion requires the tracer polymer to be larger than the nanotube radius [155]. This group have subsequently published several papers of tracer diffusion (d-PS), in this system [156,157] and other nanocomposite materials such as polystyrene/silica nanoparticles [158,159].

### 23.3.3.2 Reaction Kinetics

Shulze *et al.* applied FRES to follow the extent of reactions at interfaces between perdeuterated, end-functionalized with an aliphatic amine group, polystyrenes (d-PS-NH<sub>2</sub>), and PMMA end-functionalized with anhydride (h-PMMA-anh) [160]. A standard set-up was used for the FRES experiment which allowed a profiling

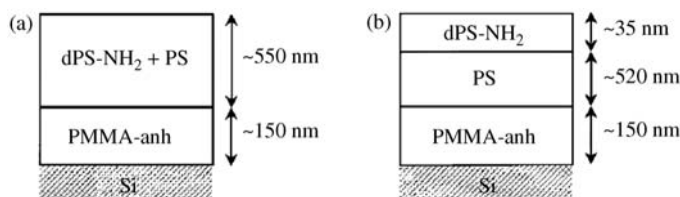


**Figure 23.36** Two sample geometries were used in experiments of Schulze *et al.* (a) Bilayer samples were prepared by floating films containing dPS-NH<sub>2</sub> (8.4 wt%) and PS onto PMMA-anh layers that had been spun from solution onto a Si wafer; (b) Trilayer samples

were prepared by first floating a PS film onto a PMMA-anh layer, followed by floating a thinner dPS-NH<sub>2</sub> film on top of the PS. Adapted with permission from Ref. [160]; © 2000, American Chemical Society.

depth of 700 nm and a depth resolution of about 90 nm. Diffusion might play a key role in reaction kinetics, and in the case of polymers a model of diffusion-controlled reactions is often assumed. Schulze *et al.* measured the diffusion of a d-PS-NH<sub>2</sub> polymer throughout the h-PS matrix by using trilayer sample geometry (as shown in Figure 23.36b). The sample configuration to monitor the extent of the reaction is shown in Figure 23.36a. To calculate  $D$ , the authors used a solution of Fick's law for a thin film diffusing to a reflecting boundary. The results ( $D = 3.0 \times 10^{-13} \text{ cm}^2 \text{ s}^{-1}$  at 174 °C) indicated that the d-PS-NH<sub>2</sub> dispersed itself over 550 nm in about 1 h, whereas reaction products were observed after 24 h. This observation, confirmed by the data obtained using size-exclusion chromatography with fluorescence detection, led the authors to conclude that diffusion in the bulk of the polymer did not limit the rate of reaction, and that a model assuming polymer chain reactivity fitted the data far better [160,161].

### 23.3.3.3 Surface and Interfaces

In general, the properties of surfaces and interfaces differ from those of the bulk. In particular, this phenomenon is important for polymer blends, as they consist of at least two constituents with different surface energies. To obtain materials which combine good mechanical properties of the bulk polymer with specific surface properties, such as hydrophobicity, wettability, adhesion, or biocompatibility, is a challenging issue.

The FRES technique might be applied to investigate real systems as well as model samples used to test theoretical predictions. However, a degree of caution is essential as the technique requires polymer labeling that may affect the interfacial properties. Even typically used deuterium markers can lead to a surface excess of the d-polymer, which increases with the bulk volume fraction of deuterated polymers [162]. (This problem is discussed and described in Chapter 3, and in many books and reviews [163–165]). In this subsection, examples are given of recent FRES-based investigations of polymer blend regions of interest, including: polymer surface (polymer–gaseous phase, usually air, interfaces); interfaces between the phase rich in polymer I and phase rich in polymer II; and polymer–substrate interface.

Kimani *et al.* investigated the surface activity of a polybutadiene blend with chain-end-functionalized polybutadiene with multiple fluorocarbon (h-2CF-PBd) or hydroxyl groups (h-4OH-PBd). In this case, LE-FRES ( $^4\text{He}^+$ , 1.512 MeV,  $78^\circ$  to the sample normal, detection at  $31^\circ$  to the incident beam, 5  $\mu\text{m}$  Mylar foil) was used to determine the depth distribution of the functionalized polymers within the blend film [166]. For FRES experiments, polybutadiene blend films (150 nm thickness) were prepared by codissolution of the 15 wt% end-functionalized polymer with deuterated polybutadiene. The FRES results indicated that h-4OH-PBd-functionalized chains were located close to the polymer–silicon oxide interface, whereas the h-2CF-PBd macromolecules segregated strongly to the polymer–air interface. These phenomena occurred due to the fact that fluoroalkyl additives exhibit a low surface energy, whereas hydroxyl-functionalized additives exhibit a high surface energy.

An excellent example of the capabilities of this technique was provided by Mokarian-Tabari *et al.* [167], who investigated the phase separation of immiscible polymers during spin coating from a common solvent. The FRES technique, combined with NRA, was used for a quantitative analysis of the polymer blend films prepared from a solution of polystyrene (d-PS) and poly(methylmethacrylate) (h-PMMA). The data obtained showed an evident stratification in the film, with a segregation of d-PS to the surface and an increase in PMMA content with distance from the surface (see Figure 23.37).

Unfortunately, due to the low energy used (1.5 MeV beam of  $^4\text{He}^+$  ions), the accessible depth was insufficient to analyze a full thickness of the film, despite the configuration of the experiment which maximized the investigated depth (the beam for the FRES experiment was incident at an angle of  $19^\circ$ , and the scattering angle was  $30^\circ$  [167]).

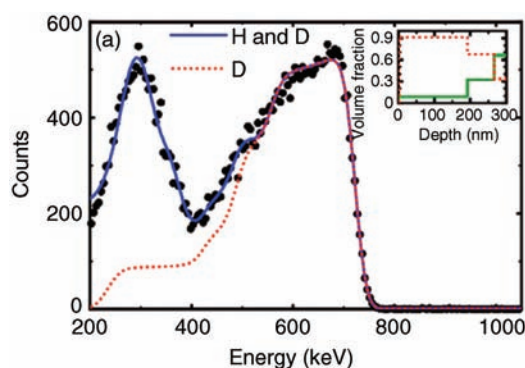


**Figure 23.37**  $^4\text{He}^{2+}$  FRES data for a film prepared in a toluene environment with a partial toluene pressure of 3.8 kPa. The solid line is a fit to the data, whereas the broken line is the d-PS component of that fit. The resulting volume fraction–depth profile is shown in the

inset, in which the broken line indicates the simulated d-PS volume fraction and the solid line the simulated h-PMMA volume fraction. Reprinted with permission from Ref. [167]; © 2010, Springer.

Low-energy FRES was also used to investigate so-called “solvent annealing” (cyclohexane) processes in a 150 nm-thick deuterated polystyrene film blended with fluorocarbon end-capped polystyrene (h-PSF) and poly(styrene-*b*-dimethylsiloxane) (h-PS-PDMS) [168]. The best resolution, 14 nm at the air surface and 20 nm at a depth of 150 nm, was achieved with a 1.82 MeV  $^4\text{He}^+$  beam with a  $66^\circ$  incident angle,  $86^\circ$  grazing exit angle,  $28^\circ$  scattering angle, and 5  $\mu\text{m}$  PET absorber foil. The configuration of these experiments allowed depth profiling up to 150 nm. The measurements revealed that both, solvent and temperature annealing, allowed the h-PSF polymer to diffuse throughout the full thickness of the film. However, only in the case of temperature treatment a surface excess of the hydrocarbon polymer was detected. This observation was rationalized by the assumption that cyclohexane lowers the surface energy of the swollen film, and therefore eliminates the thermodynamic driving force for h-PSF adsorption. Additionally, FRES studies on the annealed d-PS-hPS-PDMS bilayer films showed that the PS-PDMS was only partially miscible with the homopolymer matrix [168].

An interesting study of polymer–substrate interaction was performed by Oslanec *et al.* [169,170], and the results were provided in two papers. In the first report, the authors described an investigation of the adsorption of an asymmetric d-PS-*b*-PMMA block copolymer blended with poly(styrene-*ran*-bromostyrene)(PBr $_x$ S) matrix by LE-FRES (2.0 MeV  $^4\text{He}^+$  ion beam at  $15^\circ$  incident and exit angles, and a 7.5  $\mu\text{m}$  Mylar foil). A depth resolution of 45 nm was achieved at the surface region, and about 70 nm at 220 nm beneath the surface. The deuterated polystyrene block did not adsorb onto the substrate, in contrast to methyl methacrylate. By varying  $x$  in the PBr $_x$ S polymer it was possible to control the unfavorable segmental interaction energy between PBr $_x$ S and dPS ( $\chi_{\text{BM}}$ ). The most interesting part of this study was the finding that the experimental data were in opposition to intuitive (as well as a self-consistent mean-field model) expectation; namely, the interfacial excess,  $z^*$ , of the d-PS block was decreased slightly as  $\chi_{\text{BM}}$  increased. In order to explain these observations, the authors speculated that a competitive adsorption of matrix chains was the reason for a lower than expected d-PS-*b*-PMMA adsorption [169].

In the second report, Oslanec *et al.* investigated the interaction between brominated polystyrene and an inorganic substrate, using LE-FRES with a 1.7 MeV  $^4\text{He}^+$  ion beam at  $15^\circ$  incident and exit angles, and 6  $\mu\text{m}$ -thick Mylar stopper foil. The achieved depth resolution was 55 nm at the surface, and 65 nm at 200 nm beneath the surface. As a polymer model system, blends of d-PBr $_{0.06}$ S with PS (miscible at  $190^\circ\text{C}$ ) were used, with  $\text{SiO}_x$  and SiH as substrates [170]. An interfacial excess of d-PBr $_{0.06}$ S was observed on both investigated surfaces, in contradiction to previous reports (Figure 23.38) [171–173]. Unfortunately, to the best of our knowledge, this discrepancy was not further discussed in literature and remains unexplained.

#### 23.3.3.4 Phase Separation

The phase behaviors of miscible, partially miscible, and immiscible polymers were investigated in the case of sulfonated poly(styrene-*ran*-styrenesulfonate)

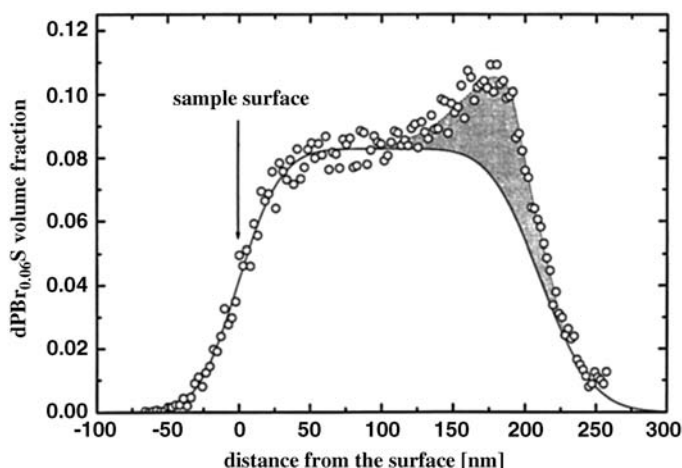


**Figure 23.38** LE-FRES volume fraction profile of d-PBr<sub>0.06</sub>S in a PS:d-PBr<sub>0.06</sub>S blend annealed at 190 °C for 3 days (open circles). The substrate is a SiH-functionalized surface. The volume fraction of PBr<sub>0.06</sub>S in the as-cast sample is  $\phi_{\infty} = 0.092$ . The shaded area represents the d-PBr<sub>0.06</sub>S interfacial excess,  $z^*$ , and the arrow

indicates the position of the sample surface. The solid line depicts an expected dPBr<sub>0.06</sub>S volume fraction profile if no segregation has occurred in the film. Reprinted with permission from Ref. [170]; © 2001, American Chemical Society.

[h-P(S-SS)] with deuterated polystyrene (d-PS) by Zhou *et al.* [174,175]. By annealing samples composed of two layers of d-PS and h-P(S-SS) with 0.02 to 2.6 mol.% sulfonation at 150, 170, and 190 °C, these two polymers were found to be fully miscible when sulfonation was less than 0.2, but became immiscible when the sulfonation reached 2.6 mol.%. This effect was established by detecting the diffusion of d-PS into a layer of P(S-SS) by standard FRES with depth profiling up to 750 nm, although the achieved resolution was not discussed in detail.

After annealing the bilayer sample at an elevated temperature for 72 h, a completely homogeneous deuterated polymer distribution was observed within the sample of a very low degree of sulfonation, whereas for a highly sulfonated d-PS a bimodal concentration profile was observed. As can be seen in Figure 23.39, for a medium degree of sulfonation only a partial diffusion of d-PS was detected [174]. It was also noted that neutralization of the sulfonic acid groups, particularly by divalent cations, reduced the blend miscibility [175]. It was shown in both cases (for blends consisting of acidic and neutralized ionomers) that a standard FRES technique represented an adequate method for creating phase diagrams for these polymer blends.

Using FRES and others techniques, Wang and Composto investigated wetting and phase separation in polymer blend films composed of deuterated poly(methyl methacrylate) (d-PMMA) and poly(styrene-*ran*-acrylonitrile) (h-SAN) at the critical concentration [176–180]. This blend is characterized by a lower critical solution temperature (LCST) behavior with  $T_{LCST} \sim 160$  °C and  $\phi_{d-PMMA} \sim 0.5$  [180]. In this

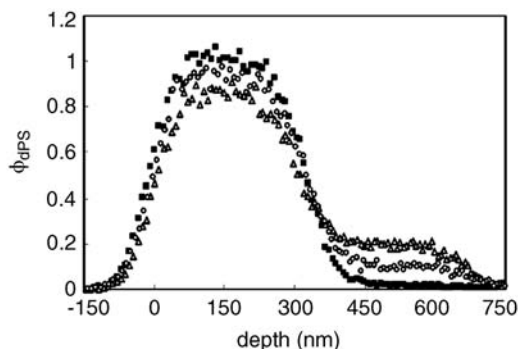


**Figure 23.39** Concentration of deuterated polystyrene as a function of depth in d-PS:P(SS<sub>0.01</sub>) bilayer samples prior to annealing (■) and after annealing for 72 h at 170 °C (○) and 190 °C (Δ). The annealed bilayers indicate partial miscibility, as evidenced by d-PS-rich and P (S-SS<sub>0.010</sub>)-rich layers, and the coexistence

compositions are the averages of the plateaus. At 170 °C,  $\phi_{dPS'} = 0.92 \pm 0.03$  and  $\phi_{dPS''} = 0.10 \pm 0.02$ . At 190 °C,  $\phi_{dPS'} = 0.84 \pm 0.05$  and  $\phi_{dPS''} = 0.20 \pm 0.01$ . Reprinted with permission from Ref. [174]; © 2006, American Chemical Society.

series of reports, the authors provided results of detailed studies of thin films, with thickness,  $d$ , ranging from 5.7 to 8000 nm. In this case, the He ion beam energy was optimized (0.8–3.0 MeV), and in the best case scenario a depth resolution at the surface (defined as the full width at half maximum; FWHM) was as low as 14 nm [180], which is the best value among all reports cited in this chapter for FRES techniques. The phase segregation was monitored when the homogeneous polymer blend was annealed at a temperature above the LCST. In this case four “thickness regimes” were identified with specific evolution pathways as the film thickness changed (Table 23.2).

Regime I is approximately the monolayer of the polymer, and since its thickness is less than the best reported depth resolution it cannot be investigated using FRES. The film evolution in regimes II and III are qualitatively similar, and three stages can be identified. However, due to a thinner polymer layer the process for regime II is more rapid. At the early stage the wetting layers grow by hydrodynamic flow-driven wetting, and at the end of this stage an excess of d-PMMA is observed at the air–polymer and polymer–oxide interfaces (Figure 23.40).

**Table 23.2** Thickness regimes [180].

	Thickness regime			
	Regime I	Regime II	Regime III	Regime IV
Thickness/ $R_g^a$	$d < 1 R_g$	$1 < d < 10 R_g$	$10 < d < 150 R_g$	$d \gg R_g$
Approx. thickness	A few nm	10–100 nm	100–1500 nm	A few $\mu\text{m}$

a)  $R_g$  = radius of gyration.

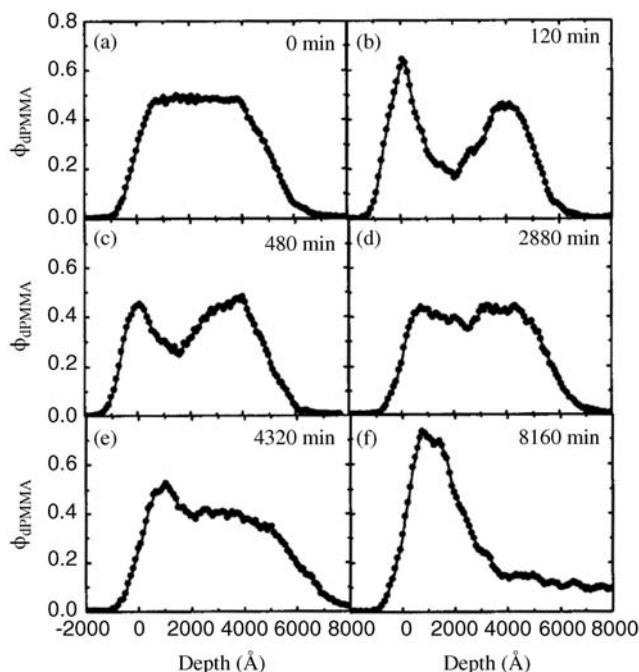


**Figure 23.40** Depth profiles of dPMMA after various annealing times at 185 °C as measured by FRES (regime III). (a) Before annealing, the sample is homogeneous; (b) After 120 min, a trilayer lamella structure of dPMMA-rich/SAN-rich/dPMMA-rich forms; After (c) 480 min and (d) 2880 min, the wetting layers decay and the overall volume fraction profile appears

homogeneous; (e) After 4320 min, a d-PMMA-rich layer reappears at the surface, whereas the volume fraction beneath the surface layer is relatively constant; (f) After 8160 min, the surface layer grows to a thickness of about 2200 Å, and is followed by a d-PMMA-poor region.

Reprinted with permission from Ref. [177];

© 2000, AIP Publishing LLC.

The process leads to a trilayer geometry with external surfaces of the film enriched in d-PMMA, while the interior is h-SAN rich. At the final stage, an excess of the component with lower surface energy, d-PMMA, is observed on the sample edge neighboring the air. As can be seen in Figure 23.40, all of the described processes can be monitored using the FRES technique. In the case of a semi-infinite sample (regime IV), the oscillatory depth profiles are observed (Figure 23.41) which are characteristic of surface-directed spinodal decomposition (SDSD). The phenomenon of SDSD was first observed experimentally by Jones *et al.* in poly(ethylene propylene) and perdeuterated poly(ethylene propylene) blends studied using FRES [181].

In a subsequent report from the Composto's group, the effect of two parameters – film thickness (50–1000 nm) and blend composition ( $\phi_{PMMA} = 0.3–0.8$ ) – were discussed [182]. Variations of these factors led to as many as six pattern development mechanisms.

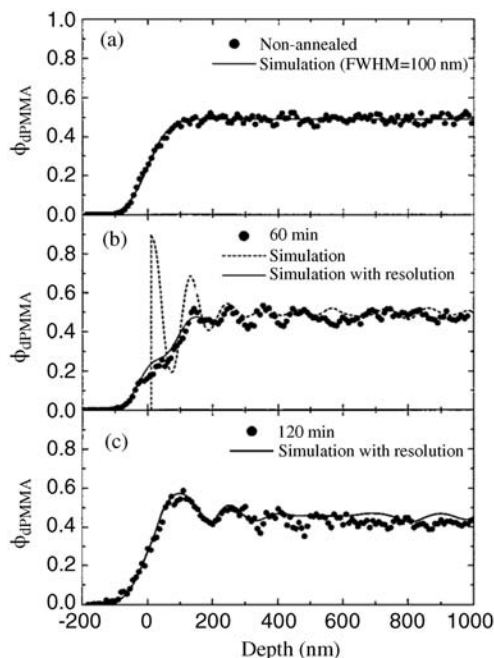


**Figure 23.41** The dPMMA depth profile of a regime IV blend at 185 °C, using 3.0 MeV FRES, where the air–polymer interface is at 0 nm. (a) Before annealing, the composition is uniform. The solid line is a fit with an experimental depth resolution of 100 nm FWHM; (b) After 60 min, compositional oscillations are observed. The dashed line is a cell dynamic

simulation, and the solid line is simulation convoluted with the depth resolution (c.f. the solid line in panel (a)); (c) After 120 min, the wavelength and amplitude of the oscillations increase. The solid line is a cell dynamic simulation convoluted with the depth resolution. Reprinted with permission from Ref. [180]; © 2003, Springer.

In summarizing this subsection, it should be confirmed that FRES is a valuable tool for investigating polymer diffusion, wetting and phase separation in polymer blends, either within thin films or in near-surface regions. However, due to the technique characteristics, the best results can be obtained for polymers, blends, or nanocomposites of polystyrene.

### Acknowledgments

K. K. would like to thank Dr Piotr Pietrzyk for useful discussions and DFT calculations, and Maria Sojka for help with preparing some of the figures. E. S.-P. acknowledges support from the Polish budget for science (Dz.St. 10/2014 at IARR, Lodz Univ. Technol.)



## References

- 1 (a) Zavoisky, E. (1945) *J. Phys. USSR*, **9**, 211; (b) Zavoisky, E. (1946) *Zh. Eksper. Teor. Fiz.*, **16**, 603.
- 2 Ranby, B. and Rabek, J.F. (1977) *ESR Spectroscopy in Polymer Research*, Springer-Verlag, Berlin.
- 3 Smirnov, A. (2002) *Specialist Periodical Reports – Electron Paramagnetic Resonance*, vol. **18** (eds B.C. Gilbert, M.J. Davies, D.M. Murphy, and K.A. McLauchlan) Royal Society of Chemistry, Cambridge, p. 109.
- 4 Bender, C.J. and Berliner, L.J. (eds) (2004) *Instrumental Methods in Electron Magnetic Resonance, Biological Magnetic Resonance*, vol. **21**, Kluwer Academic/Plenum Publishing Corporation, New York, NY.
- 5 Schlick, S. and Jeschke, G. (2012) *Polymer Science: A Comprehensive Reference*, **2**, 221.
- 6 Valić, S., Andreis, M., and Klepac, D. (2011) ESR spectroscopy of multiphase polymer systems, in *Handbook of Multiphase Polymer Systems* (eds A. Boudenne, L. Ibos, Y. Candau, and S. Thomas), John Wiley & Sons, Ltd.
- 7 Schlick, S. (ed.) (2006) *Advanced ESR Methods in Polymer Research*, John Wiley & Sons, Inc.
- 8 Poole, C.P. Jr (1983) *Electron Spin Resonance: A Comprehensive Treatise on Experimental Techniques*, 2nd edn, John Wiley & Sons, Inc.
- 9 Schweiger, A. and Jeschke, G. (2001) *Principles of Pulse Electron Paramagnetic Resonance*, Clarendon, Oxford, UK.
- 10 Weil, J.A. and Bolton, J.R. (2007) *Electron Paramagnetic Resonance: Elementary Theory and Practical Applications*, 2nd edn, John Wiley & Sons, Inc.
- 11 Lund, A., Shiotani, M., and Shimada, S. (2011) *Principles and Applications of ESR Spectroscopy*, Springer, Netherlands.
- 12 Gilbert, B.C., Murphy, D.M., and Chechik, V. (eds) (2012) *Specialist Periodical Reports – Electron Paramagnetic Resonance*, Royal Society of Chemistry, Cambridge, and earlier editions.
- 13 Abragam, A. and Pryce, M.H.L. (1951) *Proc. Roy. Soc. London*, **A205**, 135.
- 14 Poole, C.P. Jr (1997) *Electron Spin Resonance. A Comprehensive Treatise on Experimental Techniques*, A Wiley Interscience Publications.
- 15 DeGray, J.A. and Rieger, P.H. (1987) *Bull. Mag. Res.*, **8**, 95.
- 16 Pietrzyk, P., Podolska, K., and Sojka, Z. (2013) Molecular interpretation of EPR parameters – computational spectroscopy approaches, in *Specialist Periodical Reports – Electron Paramagnetic Resonance*, vol. **23** (eds B.C. Gilbert, D.M. Murphy, and V. Chechik), Royal Society of Chemistry, Cambridge, p. 264.
- 17 Misra, S.K. (2011) *Multifrequency Electron Paramagnetic Resonance: Theory and Applications*, Wiley-VCH Verlag GmbH & Co., Weinheim.
- 18 Livshits, V.A. and Marsh, D. (2000) *J. Magn. Reson.*, **147**, 59.
- 19 Lou, Y., Ge, M., and Freed, J.H. (2001) *J. Phys. Chem. B*, **105**, 11053.
- 20 Kurad, D., Jeschke, G., and Marsh, D. (2004) *Biophys. J.*, **86**, 264.
- 21 Livshits, V.A., Kurad, D., and Marsh, D. (2006) *J. Magn. Reson.*, **180**, 63.
- 22 Hahn, E.L. (1950) *Phys. Rev.*, **80**, 580.
- 23 Schweiger, A. and Jeschke, G. (2001) *Principles of Pulse Electron Paramagnetic Resonance*, Oxford University Press.
- 24 Uvarov, M.N. and Kulik, L.V. (2013) *Appl. Magn. Reson.*, **44**, 97.
- 25 Milov, A.D., Tsvetkov, Y.D., Maryasov, A. G., Gobbo, M., Prinzivalli, C., De Zotti, M., Formaggio, F., and Toniolo, C. (2013) *Appl. Magn. Reson.*, **44**, 495.
- 26 Reginsson, G.W., Kunjir, N.C., Sigurdsson, S.Th., and Schiemann, O. (2012) *Chem. Eur. J.*, **18**, 13580.
- 27 Jeschke, G. (2002) *Macromol. Rapid Commun.*, **23**, 227.
- 28 Dikanov, S.A. and Tsvetkov, Y.D. (1992) *Electron Spin Echo Envelope Modulation (ESEEM) Spectroscopy*, CRC Press, Boca Raton, FL.
- 29 Jeschke, G., Panek, G., Schleidt, S., and Jonas, U. (2004) *Polym. Eng. Sci.*, **44**, 1112.
- 30 Hofer, P., Grupp, A., Nebenfuhr, H., and Mehring, M. (1986) *Chem. Phys. Lett.*, **132**, 279.
- 31 Stoll, S., Jeschke, G., Willer, M., and Schweiger, A. (1998) *J. Magn. Reson.*, **130**, 86.

- 32 Bujak, P., Kulszewicz-Bajer, I., Zagorska, M., Maurel, V., Wielgus, I., and Pron, A. (2013) *Chem. Soc. Rev.*, **42**, 8895.
- 33 Dobrzynska, E., Jouni, M., Gawrys, P., Gambarelli, S., Mouesca, J.M., Djurado, D., Dubois, L., Wielgus, I., Maurel, V., and Kulszewicz-Bajer, I. (2012) *J. Phys. Chem. B*, **116**, 14968.
- 34 Schweiger, A. (1991) *Angew. Chem., Int. Ed. Engl.*, **30**, 265.
- 35 Turro, N.J., Kleinman, M.H., and Karatekin, E. (2000) *Angew. Chem., Int. Ed.*, **39**, 4436.
- 36 Pietrzyk, P., Mazur, T., and Sojka, Z. (2014) Electron paramagnetic resonance spectroscopy of inorganic materials, in *Local Structural Characterisation* (eds D.W. Bruce, D. O'Hare, and R.I. Walton), John Wiley & Sons, Ltd., p. 225.
- 37 Hashem, M., Twig, Y., and Blank, A. (2014) *Appl. Magn. Reson.*, **45**, 63.
- 38 Lucarini, M., Pedulli, G.F., Motyakin, M. V., and Schlick, S. (2003) *Prog. Polym. Sci.*, **28**, 331.
- 39 (a) Kruczała, K., Motyakin, M. and Schlick, S. (2000) *Phys. Chem. B*, **104** (15), 3387; (b) Schlick, S., Kruczała, K., Motyakin, M., and Gerlock, J. (2001) *Polym. Degrad. Stab.*, **73** (3), 471; (c) Kruczała, K., Varghese, B., Bokria, J.G., and Schlick, S. (2003) *Macromolecules*, **36** (6), 1899; (d) Kruczała, K., Bokria, J.G. and Schlick, S. (2003) *Macromolecules*, **36** (6), 1909; (e) Schlick, S. and Kruczała, K. (2005) *J. Coat. Technol. Res.*, **2** (5), 389; (f) Kruczała, K., Aris, W. and Schlick, S. (2005) *Macromolecules*, **38** (16), 6979.
- 40 Motyakin, M.V. and Schlick, S. (2006) *Polym. Degrad. Stab.*, **91**, 1462.
- 41 Schlick, S. and Motyakin, M.V. (2004) 1D and 2D electron spin resonance imaging (ESRI) of transport and degradation processes in polymers, in *Instrumental Methods in Electron Magnetic Resonance. Biological Magnetic Resonance*, vol. 21 (eds C.J. Bender and L.J. Berliner), Kluwer Academic/Plenum Publishing Corporation, New York.
- 42 (a) Eaton, S.S., Eaton, G.R. and Ohno, K. (eds) (1991) *EPR Imaging and In Vivo EPR*, CRC Press, Boca Raton, FL; (b) Eaton, S.S. and Eaton, G.R. (1995) *Concept. Magnetic Res.*, **7**, 49; (c) Eaton, S.S. and Eaton, G.R. (2000) *Specialist Periodical Report on Electron Spin Resonance*, **17**, 109.
- 43 Liang, Z.P. and Lauterbur, P.C. (2000) *Principles of Magnetic Resonance Imaging: A Signal Processing Perspective*, IEEE Press, New York.
- 44 Spalek, T., Kruczała, K., Sojka, Z., and Schlick, S. (2007) *J. Magn. Reson.*, **189** (1), 139.
- 45 (a) Lucarini, M., Pedulli, G.F., Borzatta, V., and Lelli, N. (1996) *Res. Chem. Intermed.*, **22**, 581; (b) Lucarini, M., Pedulli, G.F., Borzatta, V., and Lelli, N. (1996) *Polym. Degrad. Stab.*, **53**, 9; (c) Lucarini, M. and Pedulli, G.F. (1997) *Angew. Makromol. Chem.*, **252**, 179; (d) Lucarini, M., Pedulli, G.F., Lazzari, D., Vitali, M., and Andrews, S.M. (2002) *Macromol. Chem. Phys.*, **203** (15), 2239.
- 46 Schlick, S. and Kruczała, K. (2008) *Molecular Characterization and Analysis of Polymers*, vol. 12 (eds J. Chalmers and Rob Meier), Elsevier, p. 499.
- 47 Pilbrow, J.R. (1990) *Transition Ion Electron Paramagnetic Resonance*, Clarendon Press.
- 48 Spalek, T., Pietrzyk, P., and Sojka, Z. (2005) *J. Chem. Inf. Model.*, **45**, 18.
- 49 Robinson, B., Slutsky, L., and Auteri, F. (1992) *J. Chem. Phys.*, **96**, 2609.
- 50 Tieleman, D.P. and Berendsen, H.J.C. (1996) *J. Chem. Phys.*, **105**, 4871.
- 51 Kubo, R. and Tomita, K. (1954) *J. Phys. Soc.*, **9**, 8.
- 52 Robinson, B., Thomann, H., Beth, A., Fayer, P., and Dalton, L.R. (1985) in *EPR and Advanced EPR Studies of Biological Systems* (ed. L.R. Dalton), CRC Press, Boca Raton, FL.
- 53 Kivelson, D. (1960) *J. Chem. Phys.*, **33**, 1094.
- 54 Nordio, P.L. (1976) General magnetic resonance theory, in *Spin Labeling: Theory and Applications* (ed. L.J. Berliner), Academic Press, New York.
- 55 Earle, A.K. and Budil, E.D. (2006) *Calculation Slow-Motion ESR Spectra of Spin-Labeled Polymers in Advanced ESR Methods in Polymer Research* (ed. S. Schlick), John Wiley & Sons, Inc.
- 56 Polimeno, A., Barone, V., and Freed, J.H. (2011) *Stochastic Methods for Magnetic Resonance Spectroscopies in Computational Strategies for Spectroscopy: From Small*

- Molecules to Nano Systems* (ed. V. Barone), John Wiley & Sons, Inc.
- 57 (a) Freed, J.H. (1972) *Electron Spin Relaxation in Liquids* (eds L.T. Muus and P.W. Atkins), Plenum, New York; (b) Schneider, D.J. and Freed, J.H. (1989) *Biological Magnetic Resonance*, vol. 8 (eds L.J. Berliner and J. Reuben), Plenum, New York, p. 1; (c) Budil, D.E., Lee, S., Saxena, S., and Freed, J.H. (1996) *J. Magn. Reson. A*, **120**, 155.
  - 58 (a) Schneider, D.J. and Freed, J.H. (1989) *Biol. Magn. Reson.*, **8**, 1; (b) Schneider, D.J. and Freed, J.H. (1989) *Adv. Chem. Phys.*, **73**, 387.
  - 59 Freed, J.H. (1976) Theory of slow tumbling ESR spectra for Niroxides, in *Spin Labeling: Theory and Applications* (ed. L.J. Berliner), Academic Press, New York.
  - 60 Qu, B.-j. (2002) *Chin. J. Polym. Sci.*, **4**, 291.
  - 61 Griffith, O.H. and Jost, P.C. (1976) Lipid spin labels in biological membranes, in *Spin Labeling: Theory and Applications* (ed. L.J. Berliner), Academic Press, New York.
  - 62 Miwa, Y., Drews, A.R., and Schlick, S. (2009) *Macromolecules*, **42**, 8907.
  - 63 Ionita, G., Ariciu, A.M., Turcu, I.M., and Chechik, V. (2014) *Soft Matter*, **11**, 1778.
  - 64 Kielmann, U., Jeschke, G., and García-Rubio, I. (2014) *Materials*, **7**, 1384.
  - 65 Miwa, Y., Yamamoto, K., Tanabe, T., Okamoto, S., Sakaguchi, M., Sakai, M., and Shimada, S. (2006) *J. Phys. Chem. B*, **110**, 4073.
  - 66 Dondi, D., Pepori, F., Buttafava, A., Ottaviani, M.F., and Fauticano, A. (2011) *J. Phys. Org. Chem.*, **24**, 1051.
  - 67 John, J., Klepac, D., Didović, M., Sandesh, C.J., Liu, Y., Raju, K.V.S.N., Pius, A., Valić, S., and Thomas, S. (2010) *Polymer*, **51**, 2390.
  - 68 Lucarini, M., Pedulli, G.F., Motyakin, M.V., and Schlick, S. (2003) *Prog. Polym. Sci.*, **28**, 331.
  - 69 Kawamura, T., Matsunami, S., and Yonezawa, T. (1967) *Bull. Chem. Soc. Japan*, **40**, 1111.
  - 70 Owenius, R., Engstrom, M., and Lindgren, M. (2001) *J. Phys. Chem. A*, **105**, 10967.
  - 71 Kurad, D., Jeschke, G., and Marsh, D. (2003) *Biophys. J.*, **85**, 1025.
  - 72 Veksli, Z., Andreis, M., and Rakvin, B. (2000) *Prog. Polym. Sci.*, **25**, 949.
  - 73 Tan, L., Chen, S.M., Ping, Z.H., and Shen, Y.M. (2003) *Magn. Reson. Chem.*, **41**, 481.
  - 74 Qiu, F.R., Chen, S.M., Tan, L., and Ping, Z.H. (2004) *Polym. Adv. Technol.*, **15**, 453.
  - 75 Chen, S.M., Tan, L., Qiu, F.R., Jiang, X.L., Wang, M., and Zhang, H.D. (2004) *Polymer*, **45**, 3045.
  - 76 Qiu, F.R., Chen, S.M., and Ping, Z.H. (2005) *Magn. Reson. Chem.*, **43**, 411.
  - 77 Tan, L., Chen, S., Ping, Z., and Shen, Y. (2004) *Polym. Int.*, **53**, 204.
  - 78 Chen, S.M., Qiu, F.R., and Tan, L. (2004) *J. App. Polym. Sci.*, **92**, 2312.
  - 79 Qiu, F., Chen, S., Ping, Z., and Yin, G. (2005) *Magn. Reson. Chem.*, **43**, 918.
  - 80 Čulin, J., Frka, S., Andreis, M., Šmit, I., Veksli, Z., Anžlovar, A., and Žigon, M. (2002) *Polymer*, **43**, 3891.
  - 81 Čulin, J., Šmit, I., Andreis, M., Veksli, Z., Anžlovar, A., and Žigon, M. (2005) *Polymer*, **46**, 89.
  - 82 Čulin, J., Andreis, M., Veksli, Z., Anžlovar, A., and Žigon, M. (2005) *Eur. Polym. J.*, **41**, 1874.
  - 83 Miwa, Y., Sugino, Y., Yamamoto, K., Tanabe, T., Sakaguchi, M., Sakai, M., and Shimada, S. (2004) *Macromolecules*, **37**, 6061.
  - 84 Miwa, Y., Tanabe, T., Yamamoto, K., Sugino, Y., Sakaguchi, M., Sakai, M., and Shimada, S. (2004) *Macromolecules*, **37**, 8612.
  - 85 Lodge, T.P. and McLeish, T.C.B. (2000) *Macromolecules*, **33**, 5278.
  - 86 Valić, S. (2010) Electron spin resonance in studying nanocomposite rubber materials, in *Rubber Nanocomposites: Preparation, Properties and Applications* (eds S. Thomas and R. Stephen), John Wiley & Sons (Asia), Pte. Ltd., Chapter 15.
  - 87 Przybytniak, G.K., Zagórski, Z.P., and Zuchowska, D. (1999) *Radiat. Phys. Chem.*, **55**, 655.
  - 88 Albano, C., Perera, R., Silva, P., and Sánchez, Y. (2006) *Polym. Bull.*, **57**, 901.
  - 89 Ali, Z.I. (2007) *J. Appl. Polym. Sci.*, **103**, 3461.
  - 90 Zuchowska, D., Zagórski, Z.P., Przybytniak, G.K., and Rafalski, A. (2003) *Int. J. Polym. Mater.*, **52**, 335.
  - 91 Perera, R., Albano, C., González, J., Silva, P., and Ichazo, M. (2004) *Polym. Degrad. Stab.*, **85**, 741.

- 92 Przybytniak, G., Mirkowski, K., Rafalski, A., Nowicki, A., and Kornacka, E. (2007) *Radiat. Phys. Chem.*, **76**, 1312.
- 93 Senna, M.M.H., Abdel-Fattah, A.A., and Abdel-Monem, Y.K. (2008) *Nucl. Instrum. Methods Phys. Res., Sect. B*, **266**, 2599.
- 94 Sonnier, R., Massardier, V., Clerc, L., Lopez-Cuesta, J.M., and Bergeret, A. (2010) *J. Appl. Polym. Sci.*, **115**, 1710.
- 95 Albano, C., Reyes, J., Ichazo, M., González, J., Hernández, M., and Rodríguez, M. (2003) *Polym. Degrad. Stab.*, **80**, 251.
- 96 Chipara, M., Hui, D., Notingher, P.V., Chipara, M.D., Lau, K.T., Sankar, J., and Panaitescu, D. (2003) *Composites B*, **34**, 637.
- 97 Nand, A.V., Ray, S., Travas-Sejdic, J., and Kilmartin, P.A. (2012) *Mater. Chem. Phys.*, **135**, 903.
- 98 Rao, P.S., Subrahmanya, S., and Sathyanarayana, D.N. (2005) *J. Appl. Polym. Sci.*, **98**, 583.
- 99 Kahol, P.K. and Pinto, N.J. (2004) *Synth. Met.*, **140**, 269.
- 100 Srinivasan, D., Natarajan, T.S., Rangarajan, G., Bhat, S.V., and Wessling, B. (1999) *Solid State Commun.*, **110**, 503.
- 101 Rangarajan, G., Srinivasan, D., Angappane, S., and Wessling, B. (2001) *Synth. Met.*, **119**, 487.
- 102 Wessling, B., Kahol, P.K., Raghunathan, A., and McCormick, B.J. (2001) *Synth. Met.*, **119**, 197.
- 103 Kahol, P.K. (2001) *Solid State Commun.*, **117** (1), 37.
- 104 Liu, H.K., Shih, C.C., Wang, G.P., Wu, T.R., Wu, K.H., and Chang, T.C. (2005) *Synth. Met.*, **151**, 256.
- 105 Chao, C.M., Wang, G.P., Wu, K.H., and Chang, T.C. (2006) *J. Polym. Sci., Part B: Polymer Physics*, **44** (1), 1.
- 106 Souza, F.G. Jr, Soares, B.G., Siddaramaiah, Barra, G.M.O., and Herbst, M.H. (2006) *Polymer*, **47**, 7548.
- 107 Souza, F.G. Jr, Pinto, J.C., de Oliveira, G. E., and Soares, B.G. (2007) *Polym. Test.*, **26**, 720.
- 108 Kanemoto, K., Mizutani, N., Muramatsu, K., Hashimoto, H., Baba, M., and Yamauchi, J. (2010) *Chem. Phys. Lett.*, **494** (1–3), 41.
- 109 Jalili, R., Razal, J.M., Innis, P.C., and Wallace, G.G. (2011) *Adv. Funct. Mater.*, **21**, 3363.
- 110 Thompson, R.L. (2012) Ion Beam Analysis, in *Polymer Science: A Comprehensive Reference* (eds M. Moeller and K. Matyjaszewski), vol. **10**, Elsevier Science.
- 111 Wang, Y and Nastasi, M. (eds) (2012) *Handbook of Modern Ion Beam Materials Analysis*, 2nd edn, Cambridge University Press.
- 112 Benka, O. (2011) Elastic Recoil Detection Analysis (ERDA), in *Surface and Thin Film Analysis: A Compendium of Principles, Instrumentation, and Applications*, 2nd edn (eds G. Friedbacher and H. Bubert), Wiley-VCH Verlag GmbH & Co. KGaA, Weinheim.
- 113 Chakraborty, P. (ed.) (2002) *Ion Beam Analysis of Surfaces and Interfaces of Condensed Matter Systems*, Nova Science Publishers Inc.
- 114 Tirira, J., Serruys, Y., and Trocellier, P. (2011) *Forward Recoil Spectrometry: Applications to Hydrogen Determination in Solids*, Springer.
- 115 Kramer, E.J. (1996) *MRS Bull.*, **21**, 37.
- 116 Composto, R.J., Walters, R.M., and Genzer, J. (2002) *J. Mater. Sci. Eng.*, **38**, 107.
- 117 L'Ecuyer, J., Brassard, C., Cardinal, C., Chabbal, J., Deschênes, L., Labrie, J.P., Terreault, B., Martel, J.G., and St. Jacques, R. (1976) *J. Appl. Phys.*, **47**, 381.
- 118 Doyle, L. and Peercy, P.S. (1979) *Appl. Phys. Lett.*, **34**, 811.
- 119 Mills, P.J., Green, P.F., Palmstrom, C.J., Mayer, J.W., and Kramer, E.J. (1984) *Appl. Phys. Lett.*, **45** (9), 957.
- 120 Amsel, G. (1996) *Nucl. Instrum. Methods Phys. Res., Sect. B*, **118**, 52.
- 121 Turos, A. and Meyer, O. (1984) *Nucl. Instrum. Methods Phys. Res., Sect. B*, **4**, 92.
- 122 Tripathi, A., Kruse, O., and Carstanjen, H.D. (2004) *Nucl. Instrum. Methods Phys. Res., Sect. B*, **219–220**, 435.
- 123 Rafailovich, M.H., Sokolov, J., Zhao, X., Jones, R.A.L., and Kramer, E.J. (1990) *Hyperfine Interact.*, **62**, 45.
- 124 Mizohata, K. (2012) *Progress in Elastic Recoil Detection Analysis*, University of Helsinki Report Series in Physics. ISBN 9789521080890.
- 125 Denker, A., Bohne, W., Heese, J., Homeyer, H., Kluge, H., Lindner, S., Opitz-Coutureau, J., Röhrich, J., and

- Strub, E. (2003) *Nukleonika*, **48** (Suppl. 2), S175.
- 126 Genzer, J., Rothman, J.B., and Composto, R.J. (1994) *Nucl. Instrum. Methods Phys. Res., Sect. B*, **86**, 345.
- 127 Ermer, H., Pfaff, O., Straub, W., Geoghegan, M., and Brenn, R. (1998) *Nucl. Instrum. Methods Phys. Res., Sect. B*, **134**, 237.
- 128 Assmann, W., Davies, J., Dollinger, G., Forster, J., Huber, H., Reichelt, T., and Siegele, R. (1996) *Nucl. Instrum. Methods Phys. Res., Sect. B*, **118**, 242.
- 129 Bogdanovic, I., Radovic, I., Steinbauer, E., and Benka, O. (2000) *Nucl. Instrum. Methods Phys. Res., Sect. B*, **170**, 163.
- 130 Ross, G. and Terreault, B. (1980) *J. Appl. Phys.*, **51** (2), 1259.
- 131 Behrooz, A., Headrick, R., Seiberling, L., and Zurmühle, R. (1987) *Nucl. Instrum. Methods Phys. Res., Sect. B*, **28**, 108.
- 132 Stoquert, J., Guillaume, G., Hage-Ali, M., Grob, J., Ganter, C., and Siffert, P. (1989) *Nucl. Instrum. Methods Phys. Res., Sect. B*, **44**, 184.
- 133 Hentschel, E., Kotte, R., Ortlepp, H., Stary, F., and Wohlfarth, D. (1989) *Nucl. Instrum. Methods Phys. Res., Sect. B*, **43**, 82.
- 134 Ross, G.G., Terreault, B., Gobeil, G., Abel, G., Boucher, C., and Veilleux, G.J. (1984) *Nucl. Mater.*, **128/129**, 730.
- 135 Schiettekatte, F., Chewier, A., Chewier, N., Plantier, A., and Ross, G.G. (1996) *Nucl. Instrum. Methods Phys. Res., Sect. B*, **118**, 307.
- 136 Paduschek, P. and Eichinger, P. (1980) *Appl. Phys. Lett.*, **36** (1), 65.
- 137 Steinbauer, E., Benka, O., and Steinbatz, M. (1998) *Nucl. Instrum. Methods Phys. Res., Sect. B*, **136–138**, 695.
- 138 Mayer, M. (2014) *Nucl. Instrum. Methods Phys. Res., Sect. B*, **332**, 176.
- 139 Grolean, R., Gujrathi, S.C., and Martin, I.P. (1983) *Nucl. Instrum. Methods*, **218**, 11.
- 140 Thomas, J.P., Fallavier, M., Ramdane, D., Chevarier, N., and Chevarier, A. (1983) *Nucl. Instrum. Methods*, **218**, 125.
- 141 Sokolov, J., Rafailovich, M.H., Jones, R.A.L., and Kramer, E.J. (1989) *Appl. Phys. Lett.*, **54** (6), 590.
- 142 Dolinger, G., Faestermann, T., and Maier-Komor, P. (1992) *Nucl. Instrum. Methods Phys. Res., Sect. B*, **1–4**, 422.
- 143 Green, P.F. and Doyle, B.L. (1986) *Nucl. Instrum. Methods Phys. Res., Sect. B*, **18**, 64.
- 144 Abdesselam, M., Stoquert, J.P., Djebara, M., Cerruti, C., Chami, A.C., and Montgomery, P. (2011) *Nucl. Instrum. Methods Phys. Res., Sect. B*, **269**, 140.
- 145 Abel, F., Quillet, V., and Schott, M. (1995) *Nucl. Instrum. Methods Phys. Res., Sect. B*, **105**, 86.
- 146 Geoghegan, M. and Abel, F. (1998) *Nucl. Instrum. Methods Phys. Res., Sect. B*, **143**, 371.
- 147 Geoghegan, M., Boue, F., Menelle, A., Abel, F., Russ, T., Ermer, H., Brenn, R., and Bucknall, D.G. (2000) *J. Phys.: Condens. Matter*, **12**, 5129.
- 148 (a) de Gennes, P.G. (1971) *J. Chem. Phys.*, **55** (2), 572; (b) de Gennes, P.G. (1976) *Macromolecules*, **9** (4), 587; (c) de Gennes, P.G. (1976) *Macromolecules*, **9** (4), 594.
- 149 Graessley, W.W. (1980) *Polym. Sci. Polym. Phys.*, **18**, 27.
- 150 Kim, E., Kramer, E.J., Garrett, P.D., Mendelson, R.A., and Wu, W.C. (1995) *J. Mater. Sci.*, **30**, 1709.
- 151 Mills, P.J., Green, P.F., Palmstrom, C.J., Mayer, J.W., and Kramer, E.J. (1986) *J. Polym. Sci., Part B: Polym. Phys.*, **24** (1), 1.
- 152 Composto, R.J., Kramer, E.J., and White, D.M. (1998) *Macromolecules*, **21** (8), 2580.
- 153 Composto, R.J., Kramer, E.J., and White, D.M. (1990) *Polymer*, **31**, 2320.
- 154 Mu, M., Clarke, N., Composto, R.J., and Winey, K.I. (2009) *Macromolecules*, **42** (18), 7091.
- 155 Mu, M., Clarke, N., Composto, R.J., and Winey, K.I. (2009) *Macromolecules*, **42**, 8365.
- 156 Mu, M., Seitz, M.E., Clarke, N., Composto, R.J., and Winey, K.I. (2011) *Macromolecules*, **44**, 191.
- 157 Tung, W.-S., Clarke, N., Composto, R.J., and Winey, K.I. (2013) *Macromolecules*, **46**, 2317.
- 158 Gam, S., Meth, J.S., Zane, S.G., Chi, C., Wood, B.A., Seitz, M.E., Winey, K.I., Clarke, N., and Composto, R.J. (2011) *Macromolecules*, **44**, 3494.
- 159 Gam, S., Meth, J.S., Zane, S.G., Chi, C., Wood, B.A., Winey, K.I., Clarke, N., and Composto, R.J. (2012) *Soft Matter*, **8**, 6512.
- 160 Schulze, J.S., Cernohous, J.J., Hirao, A., Lodge, T.P., and Macosko, C.W. (2000) *Macromolecules*, **33** (4), 1191.

- 161 Schulze, J.S., Moon, B., Lodge, T.P., and Macosko, C.W. (2001) *Macromolecules*, **34**, 200.
- 162 Jones, R.A.L., Kramer, E.J., Rafailovich, M.H., Sokolov, J., and Schwarz, S.A. (1989) *Phys. Rev. Lett.*, **62** (3), 280.
- 163 (a) Cahn, J.W. (1965) *J. Chem. Phys.*, **42**, 93; (b) Binder, K. and Fratzl, P. (2001) Spinodal Decomposition, in *Phase Transformations in Materials* (ed. G. Kostorz), Wiley-VCH Verlag, Weinheim.
- 164 Allen, K.W. (1995) *Polymer Interfaces: Structure and Strength* (ed. R.P. Wool), Carl Hanser Verlag, Munich, Vienna, New York.
- 165 Dimitriou, M.D., Kramer, E.J., and Hawker, C.J. (2014) *Arab. J. Sci. Eng.*, **39**, 1.
- 166 Kimani, S.M., Hardman, S.J., Hutchings, L.R., Clarke, N., and Thompson, R.L. (2012) *Soft Matter*, **8**, 3487.
- 167 Mokarian-Tabari, P., Geoghegan, M., Howse, J.R., Heriot, S.Y., Thompson, R.L., and Jones, R.A.L. (2010) *Eur. Phys. J. E: Soft Matter*, **33**, 283.
- 168 Kiff, F.T., Richards, R.W., and Thompson, R.L. (2004) *Langmuir*, **20**, 4465.
- 169 Oslanec, R., Composto, R.J., and Vlcek, P. (2000) *Macromolecules*, **33**, 2200.
- 170 Oslanec, R. and Brown, H.R. (2001) *Macromolecules*, **34**, 9074.
- 171 Schwarz, S.A., Wilkens, B.J., Pudensi, M.A.A., Rafailovich, M.H., Sokolov, J., Zhao, X., Zhao, W., Zheng, X., Russell, T.P., and Jones, R.A.L. (1992) *Mol. Phys.*, **76**, 937.
- 172 Krausch, G., Kramer, E.J., Rafailovich, M. H., and Sokolov, J. (1994) *Appl. Phys. Lett.*, **64**, 2655.
- 173 Affrossman, S., O'Neill, S.A., and Stamm, M. (1998) *Macromolecules*, **31**, 6280.
- 174 Zhou, N.C., Xu, C., Burghardt, W.R., Composto, R.J., and Winey, K.I. (2006) *Macromolecules*, **39**, 2373.
- 175 Zhou, N.C., Burghardt, W.R., and Winey, K.I. (2007) *Macromolecules*, **40** (17), 6401.
- 176 Wang, H. and Composto, R.J. (2000) *Europhys. Lett.*, **50**, 622.
- 177 Wang, H. and Composto, R.J. (2000) *J. Chem. Phys.*, **113**, 10386.
- 178 Wang, H., Composto, R.J., Hobbie, E.K., and Han, C.C. (2001) *Langmuir*, **17**, 2857.
- 179 Wang, H. and Composto, R.J. (2002) *Macromolecules*, **35**, 2799.
- 180 Wang, H. and Composto, R.J. (2003) *Interface Sci.*, **11**, 237.
- 181 Jones, R.A.L., Norton, L.J., Kramer, E.J., Bates, F.S., and Wiltzius, P. (1991) *Phys. Rev. Lett.*, **66**, 1326.
- 182 Chung, H., Wang, H., and Composto, R.J. (2006) *Macromolecules*, **39**, 153.

### Further Reading

- 1 ESR imaging in solid phase down to sub-micron resolution: methodology and applications. Blank, A., Suhovoy, E., Halevy, R., Shtirberg, L., and Harneit, W. (2009) *Phys. Chem. Chem. Phys.*, **11** (31), 6689.
- 2 RESOLNRA: A new program for optimizing the achievable depth resolution of ion beam analysis methods Mayer, M. (2008) *Nucl. Instrum. Methods Phys. Res., Sect. B*, **266** (8), 1852.
- 3 Computer simulation of ion beam analysis: Possibilities and limitations (Conference Paper) Mayer, M., Eckstein, W., Langhuth, H., Von Schiettekatte, F., and Toussaint, U. (2011) *Nucl. Instrum. Methods Phys. Res., Sect. B*, **269** (24), 3006.
- 4 Geoghegan, M. (1999) MeV ion beam profiling of polymer surfaces and interfaces, in *Polymer Surfaces and Interfaces III* (eds R.W. Richards and S.K. Peace), John Wiley & Sons, Chichester.
- 5 Wetting at polymer surfaces and interfaces Geoghegan, M. and Krausch, G. (2003) *Prog. Polym. Sci.*, **28**, 261.

## 24

# Characterization of Polymer Blends Using UV-Visible Spectroscopy

Mamdouh H. Abou-Taleb

### 24.1

#### Introduction

Polymers are constructed from monomers (molecules capable of bonding in long chains) that are linked by chemical bonds; they are produced by the process of polymerization (the linking up of monomers) and may occur either naturally or synthetically.

A polymer blend is a macroscopically homogeneous mixture of two or more different species of polymer [1]. The number of polymeric components that comprise a blend is often designated by an adjective such as binary, ternary or quaternary. The manufacture of polymer blends has opened an exciting new direction for modification of the structure and physical properties of these materials, while extensive academic research and commercial interest have together led to the development of many applications for these materials.

The process of blending of different polymers provide the ability to adapt new types of polymers varying in order to obtain products with physical and chemical properties of various essential and optimally for use in applications required [2–6]. Molecular structure and the way in which the overlap of the molecules in the solid state are the most important factors that affects the characteristics of the macroscopic and microscopic blending of these polymers. Method of blending polymers is one of the reasons that lie mainly to the different physical and chemical behavior of polymers formed. For example, polymers exhibit two morphological types in the solid state: amorphous and semi crystalline. Inside the amorphous polymer the molecules are oriented arbitrarily and are tangled, and the polymer has a glass-like, transparent appearance. In semi crystalline polymers, the molecules pack together in ordered regions called crystallites. As expected, the linear polymers, having a structure very regular, and perhaps more to be semi-crystalline [7,8].

Morphologically, most polymer blends are semi-crystalline [9,10] as they are mixtures of small crystals and amorphous materials. Semi-crystalline polymers are composed of both amorphous and crystalline regions; the amorphous structure is mainly characterized by entanglements, which are physical nodal points between molecular chains. Semi-crystalline polymers are characterized (beside the

entanglements in the amorphous fraction) by so-called crystalline lamellae. The degree of polymerization, the cooling rate, and the size and shape of the monomer substituent groups are all factors that affect the presence of the semi-crystalline polymer blends. In most polymer blends, the combination of crystalline and amorphous polymer structures leads to the formation of new material structures with more valuable chemical and physical properties [11,12].

The commercial application of polymer blend technology has grown significantly such that, today, compositions are available with properties that once were substantially unattainable with homopolymers. To date, polymer blends have been applied in optical fibers [13,14], microlenses [15], liquid crystal display components [16,17], solar cells [18–20], nonionizing radiation detection [21] and polymer light-emitting diodes [22–24]. In particular, the use of developed polymer blends in optoelectronics applications appears unlimited. Polymer blends may also provide model systems in statistical physics when studying the fundamental aspects of equilibrium and nonequilibrium properties [3], optical properties [25], and mechanical and electrical properties [26].

Currently, research activity in the field of polymer blends – from both theoretical and experimental points of view – is extensive, as is apparent from the many reviews and books available on the subject [27–29]. However, many challenging conceptual problems involving phase separation, phase transition, glass transition, miscibility and immiscibility [30] and optical properties have yet to be resolved for polymer blends [31–34].

Until now, numerous experiments have been conducted to investigate the relationship between the energy of electromagnetic radiation and matter, the aim being to characterize the properties of polymers and their blends. The techniques applied have included nuclear magnetic resonance (NMR) spectroscopy, ultraviolet/visible (UV/VIS) spectroscopy, mass spectroscopy, Raman spectroscopy, and infrared (IR) spectroscopy [35]. Accordingly, spectroscopy is considered as one of the most popular techniques in modern laboratories. In particular, UV/VIS spectroscopy, as pioneered by Beckman in 1940, is one of the oldest and still widely used instrumental techniques. Recently, however, there has been somewhat of a revival in UV spectroscopy, with many new techniques, instruments and data processing methods having been developed [36]. Today, UV spectroscopy is the method of choice in most laboratories involved in the measurement, identification and characterization of polymers and polymer blends, either in the form of solutions or as transparent, colored, or opaque solids.

Spectrophotometry is used to measure light intensity as a function of the light source wavelength or frequency, or the wavenumber. The instrument has been designed to measure the diffusivity on any of the listed light ranges that extend from about 200 nm to 1000 nm. Most advanced spectrophotometers are quick to operate, accurate and reliable, and make only small demands on the time and skills of the operator. This technique has been widely used in many applications, including extraction monitoring, polymer impregnation in the analysis of polymers and their blends, monitoring the miscibility/immiscibility of polymer blends, and in purity determinations. It is important that when



optimizing the functions of the instrument, the operator is able to monitor its performance in critical areas, and has an understanding of the elementary physics of the absorption process, as well as the basic elements of spectrophotometer design. Whilst UV spectrophotometry has certain advantages such as high sensitivity, simplicity, low cost and fast analysis times, it also has some disadvantages in that it has a lack of specificity (for mixtures), it provides only limited qualitative information, and it may be affected by interference (by highly UV-absorbing species).

In this chapter, attention is focused on measuring the optical properties of polymer blends over the ultraviolet and visible ranges of light, notably when investigating the miscibility of polymers and polymer blends. The aim is provide a background for researchers working in different fields who wish to use these analytical (quantitative or qualitative) procedures and who may wish to know more than the “basics.” In fact, almost any scientist whose discipline involves materials analysis, whether molecular biologist, biochemist, geologist, pathologist, pharmacist or metallurgist, may benefit from knowledge of the mechanism of UV/VIS absorption spectrophotometry.

## 24.2

### Electromagnetic Radiation

The term electromagnetic radiation applies to the emission and propagation of energy through space or a material. All radiation possesses energy, either inherently (electromagnetic radiation) or as kinetic energy of motion (particulate radiations). The general characteristics of electromagnetic radiation are:

- Radiation has no mass or physical form.
- It travels at the speed of light  $c$  in a vacuum (or in air).
- It travels in a linear path (until any interaction occurs).

The dominant mechanism of radiation interacting with matter is either absorption or scattering. The absorption of radiation involves the process of transferring the energy of electromagnetic radiation to atoms or molecules of the medium through which the radiation passes [37–39].

Electromagnetic radiation can be described according to the following physical properties: the frequency  $f$ , wavelength  $\lambda$ , wave number  $\nu$  (inverse of wavelength), or photon energy  $E$ . The electromagnetic radiation extends from gamma radiation at the short-wavelength (high-frequency) to long wavelength (low frequencies) used for modern radiocommunications, as shown in Figure 24.1. However, it also covers wavelengths from a fraction of the size of an atom to upwards of thousands of kilometers. For this reason, electromagnetic radiation has been investigated intensively for spectroscopic purposes in the characterization of matter. Whilst the limit for a long wavelength is the size of the universe itself, it is thought that the short wavelength limit is in the vicinity of the Planck length, although in

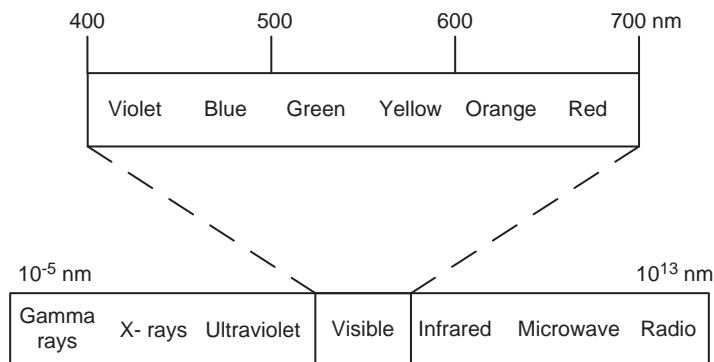


**Figure 24.1** The electromagnetic spectrum. Visible light (400–700 nm) constitutes only a small portion of the spectrum that ranges from gamma rays (<1 pm long) to radiowaves that are thousands of meters long.

principle the radiation is infinite and continuous. The Bohr–Einstein relationship is illustrated by the following:

$$f = \frac{c}{\lambda}, \quad \text{or} \quad f = \frac{E}{h}, \quad \text{or} \quad E = \frac{hc}{\lambda}$$

where  $h$  is Planck's constant,  $\lambda$  is the wavelength,  $E$  is the photon energy, and  $c$  is the velocity of light.

The main aim is to study polymer blends within the spectral range of UV/VIS radiation, which involves wavelengths of 180–380 nm (UV) and 380–780 nm (VIS) of the electromagnetic spectrum. Natural UV light is usually subdivided into three classes: near UV-A (315–380 nm); middle UV-B (280–315 nm) and far UV-C (180–280 nm).

### 24.3

#### Interaction of Radiation (UV/VIS) with Matter

The different regions of electromagnetic radiation exert very different effects upon their interaction with matter. It is a well-known result of quantum mechanics that some aspects of electromagnetic radiation must be described as the behavior of waves, while others can only be understood by describing radiation as a shower of particles, the photons (quanta). The absorption of UV/VIS radiation in the solid phase differs from UV/VIS absorption in the liquid or gaseous phase with respect to the photophysical processes that take place in the crystal lattice, and to the metallic, semiconductor or insulator properties of the absorbing solid [40]. In crystals, multiple atomic or molecular orbitals are combined to form broad energy bands; that is, a valence band fully which is occupied by electrons and a conduction band which is either unoccupied or partially occupied by electrons. Conduction bands and valence bands have different energetic positions relative to one

another, depending on the specific substrate. In a semiconductor cluster, electronic transitions between the valence band and the conduction band require at least UV/VIS radiation with an energy equivalent to the band-gap energy ( $E_g$ ). Band-gap excitation initiates several physical and chemical processes within the semiconductor (SC) particle and on its surface, respectively. Following the absorption of a photon with energy greater than or equal to  $E_g$ , an electron is promoted from the valence band to the empty conduction band of the SC particle, thus creating an electron deficiency in the valence band; this is termed a “defect electron” or a “positive hole.” The electron/hole pair thus formed is called an exciton [41]. The charge carriers (photoelectron and hole) can recombine by different mechanisms and decay channels [42].

The interaction of UV/VIS radiation with atoms or molecules will lead to a reconfiguration of the outer electron shell, due to the absorption of that quantum; this process is frequently called “electronic excitation.” The latter is any process that adds enough energy to an electron of an atom or molecule so that it occupies a higher energy state (i.e., a lower binding energy). The electron remains bound to the atom or molecule but, depending on its role in the bonds of the molecule, molecular break-up may occur. Subsequently, no ions are produced and the atom remains electrically neutral. However, atoms and molecules can exist in many states that are different with respect to the electron configuration, angular momentum, parity, and energy levels. Excited atoms or molecules can return to the ground state as a result of collisions with other molecules, eventually converting the energy of the absorbed photon into heat, or by re-emitting the photons. The re-emitted photons can be detected as a function of wavelength. UV/VIS absorption spectroscopic data is employed to obtain information regarding the nature of the matter, the presence of a particular substance in a sample, qualitative analysis and, in many cases, to quantify the amount of the substance which exists. It also can provide data to explain theoretical models (principally quantum mechanical models), and allow for the absorption spectra of atoms and molecules to be related to other physical properties such as electronic structure, optical properties, band gap energy, miscibility and immiscibility of polymer blends and molecular geometry [43].

A wide range of experimental approaches exist for measuring absorption spectra. The most common arrangement is to generate a beam of radiation at a sample and to detect the intensity of the radiation that passes through that sample. The transmitted and reflected energies can then be used to calculate information about the absorption. The source of radiation, the sample arrangement and detection technique vary significantly depending on the frequency range and the purpose of the experiments.

## 24.4

### The Nature of Electronic Excitations in Matter (Polymer Blends)

A polymer blend is a component of a group of materials in which at least two polymers are blended (i.e., mixed together) to construct a new material with

different physical properties. In order to understand the nature of electronic excitation within the polymer blends, it may be beneficial to return to the principles of the excitation process in atoms and/or molecules in matter [44]. In electromagnetic radiation, either the particle (photons) or the wavelike character is more noticeable; in the UV/VIS wavelength region the latter is the case. The electric field vector of the radiation induces charge separation (polarization) within the molecules. In the UV/VIS region, the sign of the electric field vector changes at ca.  $10^{14}$  Hz, causing the electron density to be polarized at this frequency. The extent of this polarization depends on the dielectric properties of the molecules, their environment, and the wavelength of the radiation [45,46]. Relying on Bohr model and beyond, electrons in the atom can be considered as occupying groups of approximately similar energy levels. Furthermore, sharing the electrons of two or more atoms will construct a molecule, and the sharing of two electrons by two atoms in a molecule is regarded as establishing a chemical bond. These bonds can be classified according to the number of electrons shared: atoms can share one, two or three electrons to form single, double and triple bonds, respectively. These bond designations can be described according to the molecular orbitals (MO) model [47,48].

In this case, MO represent regions in a molecule where an electron is likely to be found, which are obtained from the overlapping atomic orbitals, and can summarize the following aspects:

- Predicts the location of an electron in an atom.
- Specifies the electron configuration of a molecule: the spatial distribution and energy of one (or one pair of) electron(s).
- Describes the behavior of one electron in the electric field generated by the nuclei and some average distribution of the other electrons.

Chemical bonds are formed by overlapping atomic orbitals that result in molecular orbitals of one of three types: bonding (low energy); antibonding (high energy); or nonbonding. Energy absorption is most typically associated with transitions induced in electrons involved in bonding orbitals, and the atoms involved are, for the most part, those containing s+p electron. Two types of bond must be mentioned:

- Single, or  $\sigma$ , bonding orbital; with its related antibonding designed  $\sigma^*$ .
- Double or triple bonds ( $\pi$ -bonding orbital) with the corresponding  $\pi^*$  antibonding orbital.

Nonbonding orbitals ( $n$ ) have no antibonding (lone-pair electrons). The full series of permitted electronic transitions (by UV/V is absorption) are shown in Figure 24.2. The Figure 24.2 shows that  $\sigma \rightarrow \sigma^*$  and  $n \rightarrow \sigma^*$  transitions require relatively high energy and are therefore associated with shorter wavelength radiation (UV). Lower energy  $n \rightarrow \pi^*$  and  $\pi \rightarrow \pi^*$  are UV or visible induced transitions. The absorption of UV or visible radiation by an atomic or molecule can be

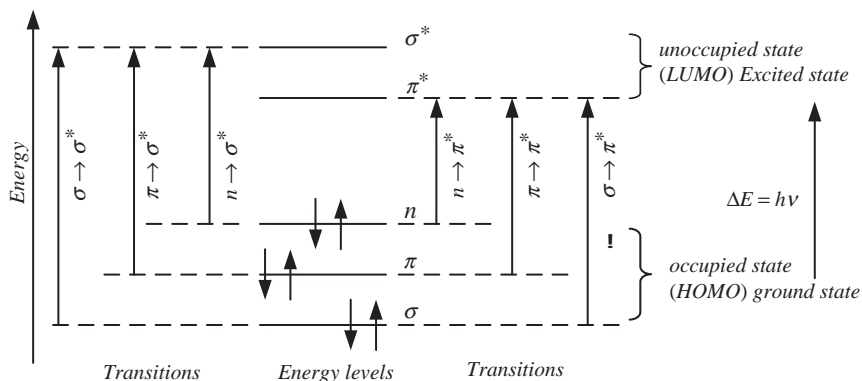


**Figure 24.2** Schematic illustration of six transitions between three types of occupied and two types of unoccupied molecular orbit.

considered as a two-step process:

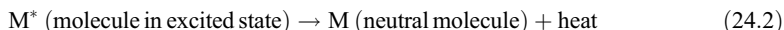
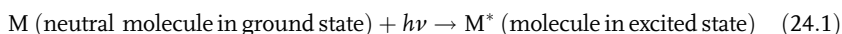
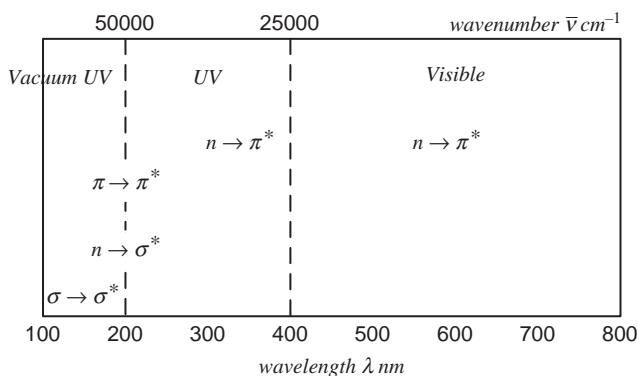


Figure 24.2 depicts this excitation process, which is quantized. The electromagnetic radiation that is absorbed has energy exactly equal to the energy difference between the excited and ground states. For most molecules, the energy necessary to bring about transitions from the highest occupied energy level (HOMO) in the ground state to the lowest unoccupied energy level (LUMO) is less than the energy required to bring about a transition from a lower occupied energy level [49,50].

Thus, in Figure 24.2 an  $n \rightarrow \pi^*$  transition would have a lower energy than  $\pi \rightarrow \pi^*$  transition. For many purposes, the transition of lowest energy is the most important. Not all of the transitions that at first sight appear possible are observed, and certain restrictions – called selection rules – must be considered. One important selection rule states that transitions which involve a change in the spin quantum number of an electron during the transition are not allowed to take place; these are called “forbidden” transitions. Other selection rules deal with the numbers of electrons that may be excited at one time, with symmetry properties of the molecule and of the electronic states, and with other factors that need not be discussed here. Transitions that are formally forbidden by the selection rules are often not observed. However, theoretical treatments are rather approximate, and in certain cases forbidden transitions are observed, although the intensity of the absorption tends to be much lower than for transitions that are allowed by the selection rules. The  $n \rightarrow \pi^*$  transition is the most common type of forbidden transition. The energy differences between electronic levels in most molecules vary from 125 to 650 kJ mol<sup>-1</sup>; this corresponds to a high-frequency (i.e., low-wavelength) absorption band which is observed at 200~800 nm in the UV and visible ranges of detection.



**Figure 24.3** Energy regions corresponding to each type of molecular transition of the interaction between the UV/Vis range with matter.

## 24.5

### Relationship of Structure of Matter to the Electronic Absorption Spectrum

Several structural features are notable for generating light absorption in the visible region (750–400 nm). Many molecules with double bonds – particularly those in which one of the double-bonded atoms has at least one lone pair – absorb radiation in the near-UV region. Molecules containing strong  $\sigma$ -bonds and no lone pairs tend to absorb in the far-UV region. The only promotable electrons are those which form single bonds, and these must receive a large amount of energy in order to undergo a transition to the lowest energy empty orbital of the molecule. Strongly single-bonded molecules with lone pairs on electronegative atoms also tend to absorb only at very short wavelengths (high energy), as shown in Figure 24.3.

## 24.6

### The Correspondence of Color and Transparent Spectrum

Some materials are classified as colored materials, due to the absorption of electromagnetic radiation. Color is an important physical property because it stands as a fingerprint regarding the structure of a material, and is also used with other physical quantities such as density and melting point to describe materials. It is important to have a qualitative understanding of the relationship between the color of light absorbed by a material and the color of light that is perceived when looking through the material. These perspective colors can be considered as complementary colors, while the perceived colors through the transparent materials give different spectra. These spectra contain the attenuation of the light which passes through this transparent medium, and also provide information as to what occurs among specific species of materials, as shown in Figure 24.4.

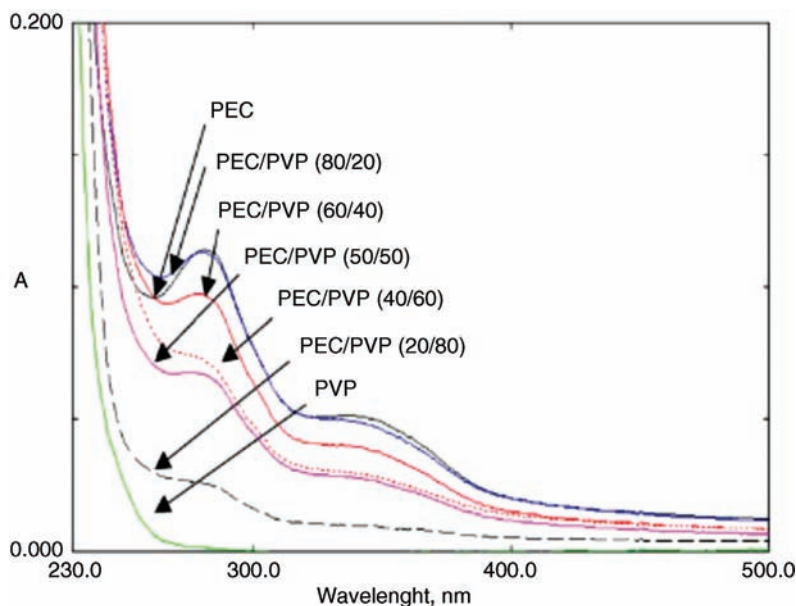


**Figure 24.4** Electronic spectra of pectin (PEC), poly(vinylpyrrolidone) (PVP) and their blends with different compositions in the range of 230–500 nm. In this region, PEC and blends in which its content is dominant exhibit two maxima at about 283 nm and 350 nm [51].

Figure 24.5 shows the designation of pectin (PEC) and the poly(vinylpyrrolidone) (PVP) molecules, while Figure 24.4 represents the electronic spectra (the relationship between wavelength and absorbance) of PEC, PVP and their blends with different weight ratios in the range of 230–500 nm. The data in Figure 24.4

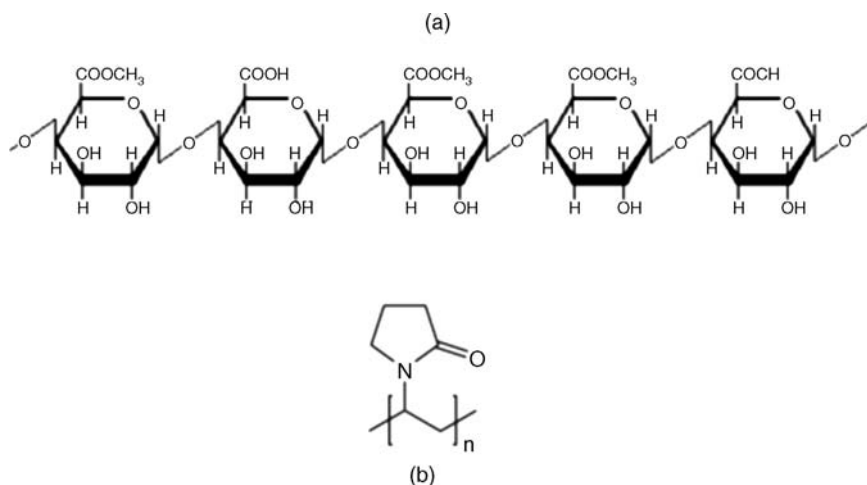


**Figure 24.5** Structures of (a) pectin (PEC) and (b) poly(vinylpyrrolidone) (PVP) polymers.

reveal that the spectrum of PEC is colored, while the PVP spectrum is a transparent medium. The specified information from those types of spectrum is sometimes different. The spectrum from the colored medium provides direct information regarding the type of chromophore and the possible types of transition between different electronic states that characterize the type of material. In contrast, data from the transparent medium provides information about the type of electronic transition, the energy of the band gap, Urbach band tail, and some optical constants [51].

A chromophore is the part (atom or group of atoms) of a molecular entity responsible for the electronic transition in which given spectral band falls within the range of the visible regime. There are two known types of chromophore: one form of the conjugated  $\pi$  system (also known as a resonating system), and the other is the metal complexes. Chromophores which can be detected by UV/Vis spectrophotometry always occupy a multiple bond (such as  $C=C$ ,  $C=O$  or  $C\equiv N$ ) and may be conjugated with other groups to form complex chromophores.

Most UV/Vis absorption spectroscopy of polymers and their blends is based on the transitions of  $n$  or  $\pi$  electrons to the  $\pi^*$  excited state. This is because the absorption peaks for these transitions fall into an experimentally convenient region of the spectrum (200–700 nm). These transitions need an unsaturated group in the molecule to provide the  $\pi$  electrons. The solvent in which the absorbing species is dissolved also has an effect on the spectrum of the species. Peaks resulting from  $n \rightarrow \pi^*$  transitions are shifted to shorter wavelengths (blue shift) with increasing solvent polarity. This arises from the solvent, which increases the number of the lone pair, which in turn lowers the energy of the  $n$  orbital. Often (but not always), the reverse (i.e., red shift) is seen for  $\pi \rightarrow \pi^*$  transitions. This is caused by attractive polarization forces between the solvent and the absorber, which lower the energy levels of both the excited and unexcited states. As this effect is greater for the excited state the energy difference between the excited and unexcited states will be slightly reduced, and this will result in a small red shift. This effect also influences  $n \rightarrow \pi^*$  transitions, but is overshadowed by the blue shift resulting from the solvent of lone pairs.

## 24.7

### Relationship of Polymer Blends to Material Characterization

Polymers and their blends can be classified generally as insulators, conductors, and semiconductors. Some of these polymers and their blends have semiconductor characterization due to the presence of special structural behavior such as conjugation, which is described as the formation of alternating single and double bonds between the neighboring backbone carbon atoms (conjugation). The  $\pi$ -conjugated polymers and their blends can be considered as good examples of the validation of these electrical conducting properties. Semiconducting polymers and their blends have attracted considerable interest due to their broad range of applications. However, the semiconducting behavior can be explained based on



the following approach. The carbon (C) atom is the core building block of most polymers and their blends; the type of bonds that the C-atom's valence electrons construct with other C-atoms or other elements determines the overall electronic characterization of the respective polymer. Polymers and their blends can, in general, be classified as either saturated and unsaturated, based on the number and type of carbon valence electrons involved in the chemical bonding between consecutive C-atoms along the main chain of the polymers and their blends. Saturated polymers are insulators, as all four valence electrons of C-atom used up in covalent bonds, whereas most conductive polymers and their blends have an unsaturated conjugated structure [52]. The  $\pi$ -conjugated polymers and their blends are excellent examples of unsaturated polymers whose electronic configuration branches from their alternate single and double C—C bonds. The fundamental source of the semiconducting property of conjugated polymers and their blends originates from the overlap of the MO formed by the valence electrons of chemically bonded C-atoms. A neutral C-atom has six electrons, which have the electronic structure  $1s^2$ ,  $2s^2$  and  $2p^2$  orbitals. The atomic orbitals (AO) of C-atoms are modified into hybrid orbitals as they form covalent bonds. When two C-atoms combine to form a molecule (bond), one electron from the  $2s$ -state is promoted to the vacant  $2p$  state. These electronic orbitals do not bond separately but hybridize and then mix in linear combinations to produce a set of orbitals oriented towards the corners of a regular tetrahedron. The hybrid orbitals expressed by one  $s$  orbital and three  $p$  orbitals are known as  $sp^3$  hybrid orbitals. The  $sp^3$  hybrids allow a strong degree of overlap in bond formation with another atom, and this produces high bond strength and stability in the molecules. The arrangement of bonds resulting from overlap with  $sp^3$  hybrid orbitals on adjacent atoms gives rise to the tetrahedral structure. In these structures all of the available electrons are tied up in strong covalent bonds, named  $\sigma$ -bonds. Carbon compounds containing  $\sigma$ -bonds formed from  $sp^3$  hybrid orbitals are termed saturated molecules. The saturated hydrocarbons, in general, have high band gaps and, hence, are classified as insulators [53].

As conjugated (alternating bonds) polymers and their blends are composed of alternating single and double bonds,  $sp^3$ -hybridized orbitals cannot account for their electronic structure. The alternating single and double bonds are formed also from  $sp^2$  hybrid orbitals. The mixing of one  $s$  orbital with two of the  $p$  orbitals of the C-atom forms three  $sp^2$  hybrid orbitals, leaving one  $p$  orbital unhybridized. The  $sp^2$  carbon hybrid orbitals are known to form a different bond length, strength and geometry when compared to those of the  $sp^3$ -hybridized molecular orbitals. The  $sp^2$  hybridization has one unpaired electron ( $\pi$ -electron) per C-atom. The three  $sp^2$  hybrid orbitals of a C-atom arrange themselves in three-dimensional space to attain a stable configuration, as shown in Figure 24.6. The geometry that achieves this is termed trigonal planar geometry, where the bond angle between the  $sp^2$  hybrid orbitals is  $120^\circ$ . The unmixed pure  $p_z$  orbital lies perpendicular to the plane of the three  $sp^2$  hybrid orbitals. The  $sp^2$  orbitals give  $\sigma$ -bonds, while the  $p_z$  orbitals form a different type of bond known as  $\pi$ -bonds. The  $p_z$  orbitals of a polymer exhibit  $\pi$ -overlap, which results in the delocalization of an electron along

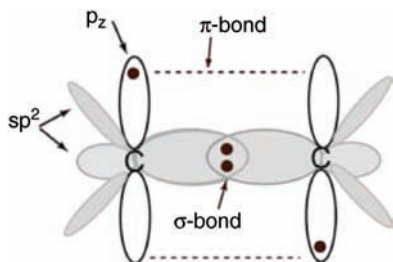


**Figure 24.6** Bonding in conducting conjugated polymers. The  $sp^2$  hybrid orbitals are shown in gray, and the unhybridized  $p_z$  orbitals in white. Electrons are represented by black dots. The two thin  $sp^2$  hybrid orbitals on the side extend in and out of the plane of the paper.

the polymer chain, as shown in Figure 24.6. The  $\pi$ -bonds are, therefore, considered as the basic source of transport band in conjugated systems [54,55].

In terms of an energy-band description, the  $\sigma$ -bonds form completely filled bands, while  $\pi$ -bonds would correspond to a half-filled energy band. The molecular orbitals of a polymer blend form a continuous energy band that lies within a certain energy range. The antibonding orbitals located higher in energy ( $\pi^*$ ) form a conduction band, whereas the lower energy lying bonding orbitals form the valance band. The two bands are separated by a material specific energy gap known as a band gap ( $E_g$ ) (see Figure 24.7). The two separate bands are characterized by two quite important energy levels, namely electron affinity and ionization potential. The electron affinity of a semiconducting polymer

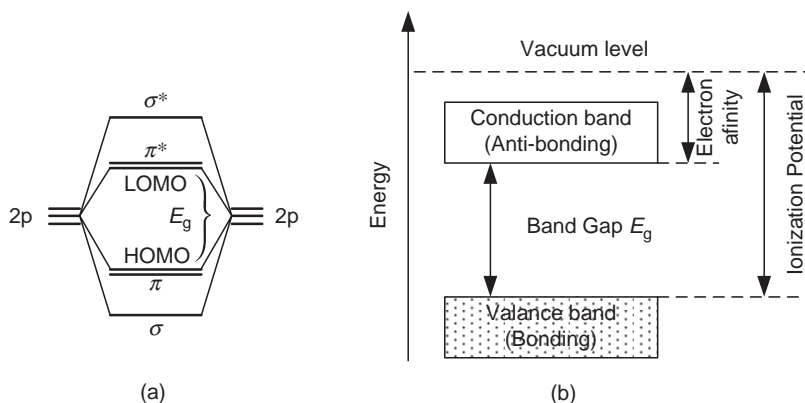


**Figure 24.7** Energy level splitting of orbitals in a conjugated polymer according to a molecular orbital theory (a) HOMO, and LUMO refer to highest occupied molecular orbital and lowest

unoccupied molecular orbital, respectively. Collection of molecular orbitals from bands is separated by an energy gap shown in (b).

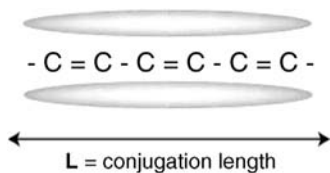


**Figure 24.8** The delocalized cloud of  $\pi$  electrons. The electronic probability density is represented by gray ovals above and below the polymer chain. They are restricted within a conjugation length of the polymer.

corresponds to the lowest state of the conduction band ( $\pi^*$  state) or the lowest unoccupied molecular orbital (LUMO). Likewise, the ionization potential refers to the upper state of the valence band ( $\pi$  state), and corresponds to the highest occupied molecular orbital (HOMO). The band gap of conjugated polymers determined from optical, electrochemical and other spectroscopic measurements is within the semiconductor range of 1 to 4 eV, which covers the whole range from the IR to the UV region. Conjugated polymers and their blends are often considered as quasi-one-dimensional metals due to the fact that the strong intrachain interaction (strong covalent bonding along the chain) and the weak van der Waals-type interchain coupling interactions lead to a delocalization of  $\pi$ -electrons along the polymer chain [54–56]. Every conjugated polymer and its blends have a unique chemical structure that determines their optical and electrical behavior (Figure 24.8).

## 24.8

### Optical Properties of Semiconductors (Polymers and Polymer Blends)

One of the specific objectives of studying UV/VIS optical absorption spectra is to obtain data regarding the physical properties of materials. The spectra obtained include the relationship between the light (transmitted, reflected, or refracted) intensity as a function of photon energy  $E$  or wavelength  $\lambda$ . The information obtained is important for basic science and its applications, and includes many valuable constants that can be calculated to present the optical properties of the medium under investigation. This spectrum can also be evaluated to characterize the polymer blends.

The optical constants (refractive index  $n$  and extinction coefficient  $k$ ) of any medium can be illustrated by the complex index of refraction,  $N = n - ik$ , or the complex dielectric function,  $\epsilon = \epsilon_1 - i\epsilon_2$ , where  $\epsilon$  is related to  $N$  by the relation  $\epsilon = N^2$ , so that  $\epsilon_1 = n^2 - k^2$  and  $\epsilon_2 = 2nk$ . Such nondestructive measurements as supplied by the UV/VIS spectra of a material reveal valuable information about the optical constants, optical band gap, Urbach band tail, band structure, optically active defects, as well as the film thickness. Several reviews are available describing measurements of the optical properties of polymer blends.

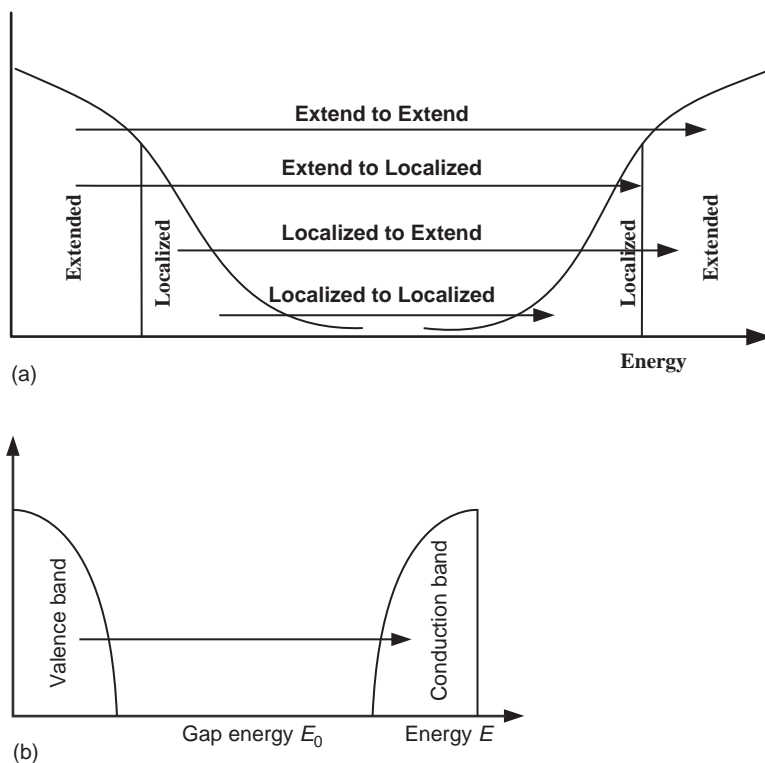


**Figure 24.9** (a) Sketch summarizing the extended and localized states in amorphous semiconductor materials, and the possible transitions between them; (b) Sketch showing

transition between the valence band and conduction band of parabolic bands (without tail states).

## 24.9

### Optical Absorption Spectra of Materials

When continuous radiation passes through a transparent material (semi crystalline), as in the case of a polymer and/or a polymer blend (solution, bulk, and film), a portion of the radiation may be absorbed. The residual radiation – after passing through a dispersion system – will yield an absorption pattern. The absorption coefficient is defined as the ability of a material to attenuate light of a given wavelength per unit length [57,58]. Figure 24.9a shows the limits of electronic densities cases in the inside crystalline material and semi-crystalline which divided into extended and localized states. Figure 24.9a indicates the possible optical transitions between these densities and will be discussed in the following sections. While Figure 24.9b refers to the transition between the valence and conduction bands in a pure semiconductor crystalline materials represented as parabolic bands (without tail states).

## 24.9.1

**Extended-to-Extended State Transitions**

The probabilities of transitions from extended to the extended states are very identical to those identified states for crystalline materials. As can be seen from Figure 24.9a, they determine the absorption of light at high energies (above the gap energy) or recognized by the short wavelength.

This leads to an absorption coefficient of the form:

$$\alpha(\omega) \sim \frac{1}{\omega} (\hbar\omega - E_0)^2$$

Hence, a plot of the following relationship  $\sqrt{\omega\alpha(\omega)} \sim \hbar\omega - E_0$  versus energy  $\hbar\omega$  should produce a straight line, the intersection of which with the y-axis gives the gap energy  $E_0$ , the so-called “Tauc gap.” The Tauc gap is quite often used to characterize the optical properties of amorphous materials [59]. From the considerations given above, it is clear that the Tauc gap provides information on the energy separation of the extended states of valence and conduction bands.

## 24.9.2

**Extended-to-Localized and Localized-to-Extended State Transitions**

The absorption of ideal crystalline materials is not observed when compared to amorphous materials, where below the energy gap a transition from occupied extended states of the valence band to empty tail states of the conduction band may occur. In a similar way, transitions from occupied valence band tail states to empty extended states of the conduction band are possible. Both types of transition should have similar matrix elements. For transitions from localized to extended states (and for extended to localized transitions) with an exponential decay of the density of states of the localized states into the gap, an exponential relationship is found between the absorption coefficient and frequency:

$$\alpha(\omega) \sim \exp\left(\frac{\hbar\omega}{E_U}\right)$$

where  $E_U$  is called “Urbach energy.” Since

$$\ln \alpha(\omega) = C + \frac{\hbar\omega}{E_U}$$

$$E_U = \frac{\hbar}{\frac{d}{d\omega} \ln \alpha(\omega)}$$

it is possible to determine the Urbach energy by plotting the logarithm of the absorption coefficient and taking the inverse of the slope of the linear part of the graph.

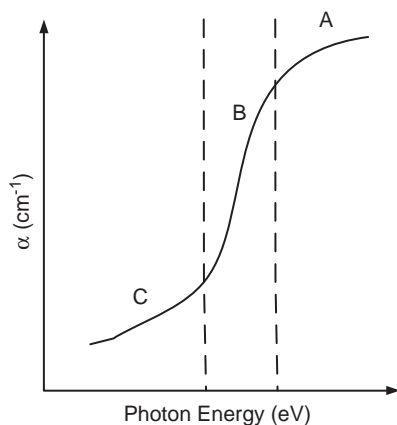


**Figure 24.10** Schematic representation of absorption coefficient versus photon energy.

### 24.9.3

#### Localized-to-Localized State Transitions

These transitions usually are not very important as the number of states involved is low and the transition matrix elements are significantly smaller compared to those of the transitions mentioned above. This is due to the fact that the matrix elements are integrals over all space over the product of two functions (the initial and the derivative of the final state) which are separated in space and hence do exhibit almost no overlap. Transitions from localized to localized states would lead to absorption in the low-energy regions of the spectrum which, in most cases, is the near-IR to the mid-IR region.

The data obtained from the spectrum can be classified as three major regions of interest for the absorption coefficient, namely A, B and C, as shown in Figure 24.10. Region A describes an absorption area in which there are two types of optical transition for the crystalline or semicrystalline materials; these can occur at the fundamental absorption edge, both directly and indirectly.

Direct band gap transition is transition in which the bottom of the conduction band and the top of the valance band occur at the momentum  $k=0$ ; energy released during band-to-band electron recombination (exciton) with a hole is converted primarily into radiation (radiant recombination), the wavelength of which is determined by the energy gap, as shown in Figure 24.11.

By using the parabolic valley model, an expression of  $\alpha(h\nu)$  for each type of transition (allowed or forbidden, depending on the selection rules) has been obtained [60–63]. The absorption coefficient,  $\alpha(h\nu)$ , depends on the density of states for bands containing the initial and final states. The direct energy gap is a prominent feature of the experimental absorption data, due to its rapid variation with energy. The forbidden energy gap of the semiconductor is readily deduced

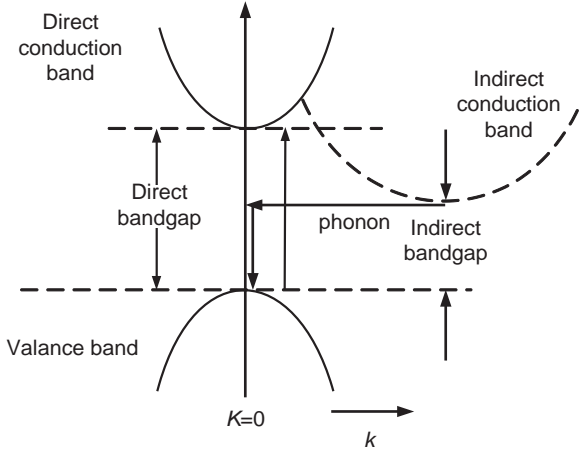


**Figure 24.11** Direct and indirect band gaps for semiconductors.

from the energy of the direct edge and the exciton energy, and can be directly compared to the results of the band structure calculations. For direct transition, the absorption coefficient  $\alpha_d$  is given by:

$$\alpha_d(h\nu) = A(h\nu - E_g^d)^s \quad (24.3)$$

where  $s = 1/2$  or  $3/2$  depending on whether the transition is quantum mechanically allowed direct or forbidden direct transition respectively,  $E_g^d$  is the direct optical energy band gap, and  $A$  is a constant involving the properties of the bands.

There are also indirect-gap transitions, in which the bottom of the conduction band does not lie at the origin. In this case, the electron cannot make a direct transition from the top of the valence band to the bottom of the conduction band because this would violate the momentum selection rule. Such a transition may still take place, but as a two-step process. The electron absorbs both a photon and phonon simultaneously; the photon supplies the energy needed while the phonon supplies the required momentum. The indirect absorption coefficient  $\alpha_i$  is given by:

$$\alpha_i(h\nu) = B(h\nu - E_g^i \mp E_{ph})^s \quad (24.4)$$

where  $s = 2$  or  $3$  depending on whether the transition is quantum mechanically allowed indirect and forbidden indirect transition respectively.  $E_g^i$  is the indirect energy gap and  $B$  is a constant containing parameters pertaining to the bands and the temperature (the latter due to the phonon contribution to the process) and  $E_{ph}$  is the energy of the phonons assisted.  $\alpha_i$  increases as a second power of

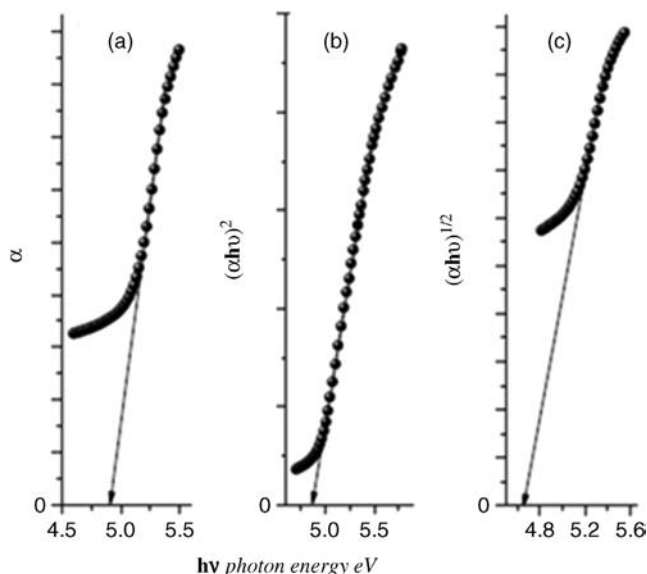


**Figure 24.12** Calculation of: (a) Absorption edge from the relation between  $\alpha$  versus  $h\nu$ ; (b) Direct band gap; (c) Indirect band gap.

$(h\nu - E_g^i)$ , much faster than the half-power of this energy difference, as in the direct transition. Hence, the optical method can be used to discriminate between the direct and indirect energy gap transitions. Consequently, direct band gap transitions are sometimes referred to as “optically active,” and indirect as “optically inactive.”

The dependence of  $(\alpha h\nu)^{1/s}$  versus  $h\nu$  was plotted for different values of  $s$ ; the best fit was obtained for  $s = 2$ , as shown in Figure 24.12, and this result indicates that the indirect transition is the most plausible mechanism. The values of  $E_g$  of the indirect transitions for different compositions can be obtained from the intercept with the abscissa of the  $(\alpha h\nu)^{1/2}$  versus  $h\nu$  plots, as shown in Figure 24.12c.

To determine the nature and width of the band gaps  $\alpha$ ,  $(\alpha h\nu)^2$  and  $(\alpha h\nu)^{1/2}$  were plotted as a function of incident photon energy  $E = h\nu$ , as shown in Figure 24.12a.

The absorption edge values were obtained by extrapolating the linear portions of  $\alpha$  versus  $h\nu$  curves to zero absorption value. The direct band gap values were obtained from the plots of  $(\alpha h\nu)^2$  versus  $h\nu$  (Figure 24.12b), as the absorption coefficient of direct electron transitions depends on the energy of incident photon, according to Eq. (24.3). The intercept on the energy axis, on extrapolating the linear portion of the curves to zero absorption value, gives the value of direct band gap. For indirect electron transitions that require phonon assistance, the absorption coefficient depends on the incident photon energy, according to Eq. (24.4). Hence, the indirect band gap values were obtained from the plots of  $(\alpha h\nu)^{1/2}$  versus  $h\nu$  at the intercepts of the energy axis on extrapolating the linear portion of the curves to zero absorption value in Figure 24.12c.



The B region in Figure 24.10 referred to what is called the “Urbach band tail,” which has been interpreted through suggestions for several mechanisms [62,64], such as band gap variation due to density fluctuations, broadening of the band edge, or the presence of excitonic states induced by internal electronic fields. In addition, other explanations related to have been derived from electronic transitions between (localized) states coming up in the band edge tails, the density of which is assumed to fall off exponentially with energy [65–67]. If this were to occur, as the slopes of the observed exponential absorption edges are the same in a variety of materials, then it would seem unlikely that the tailing would be similar. Rather, it suggests the existence of a correlation between the slope of the Urbach tail and the coordination number and the valence of the state. It is easy to speculate that materials with a lower coordination (i.e., a higher valence) are more easily from an ideal amorphous network which has fewer defects and voids, and perhaps exhibit less departure from optimum covalent band angles and length than do those materials with higher coordination numbers [68].

Region C of Figure 24.10 can be related to intraband transitions and to the density of states (DOS). The procedure for determining the DOS has been to measure the absorption in excess of that identified with an extrapolated Urbach tail.

#### 24.9.4

##### **Exciton Absorption**

In some semiconductor polymer blends the excited electron becomes a free particle in the conduction band and, similarly, the hole left in the valance band also becomes free [69]. This leaves behind a localized positively charged hole. The electron and hole attract each other by electrostatic coulombic forces, however, and may possibly form a bound state in which the two particles revolve together around their center of mass; such a state is referred to as an exciton. The exciton level is in the same neighborhood as the donor level. The energy of the photon involved in exciton absorption is given by:

$$h\nu = E_g - E_{\text{ex}} \quad (24.5)$$

where  $E_{\text{ex}}$  is the exciton binding energy. The electron and hole may have either parallel or antiparallel spins. The spins are coupled by the exchange interaction, giving rise to an exciton fine structure.

#### 24.9.5

##### **Free Carrier Absorption**

Free carriers – both electrons and holes – absorb radiation without becoming excited into the other band. In the case of absorbing a photon, the electron (or hole) makes a transition to another state in the same bands, as shown in Figure 24.13; this is called an intraband transition [70]. Of course, free carrier

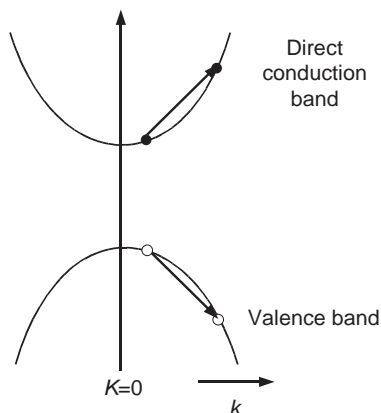


**Figure 24.13** Free carrier absorption.

absorption takes place even when  $h\nu > E_g$ , with both types of absorption fundamental and free carriers occurring simultaneously.

The optical constants are very important because they describe the optical behavior of the materials. The absorption coefficient of the material is a very strong function of photon energy and band gap energy.

Absorbance ( $A$ ) is defined as the ratio between absorbed light intensity ( $I_A$ ) by material and the incident intensity of light ( $I_0$ ) [71,72].

$$A = \frac{I_A}{I_0} \quad (24.6)$$

The transmittance ( $T$ ) is given by reference to the intensity of the transmitting light from the film ( $I$ ) to the intensity of the incident light on it ( $I_0$ )  $T = \frac{I}{I_0}$ , and can be calculated by:

$$T = \exp(-2.303A) \quad (24.7)$$

and the reflectance ( $R$ ) can be obtained from absorption and transmission spectra, in accordance with the law of conservation of energy by the relation:

$$R + T + A = 1 \quad (24.8)$$

The absorption coefficient ( $\alpha$ ) is defined as the ability of a material to absorb the light of a given wavelength

$$\alpha = \frac{2.303A}{t} \quad (24.9)$$

where  $A$  is the absorption of the material and  $t$  is the thickness of the sample (in m).

The refractive index ( $n$ ) of a material is the ratio of the velocity of the light in vacuum to that in the specimen:

$$R = \frac{(n-1)^2 + K^2}{(n+1)^2 + K^2} \quad (24.10)$$

when  $K \approx 0$

$$R = \frac{(n-1)^2}{(n+1)^2} \quad (24.11)$$

$$n = \frac{(1+R)^{1/2}}{(1-R)^{1/2}} \quad (24.12)$$

The extinction coefficient ( $K$ ) was calculated using the following equation:

$$K = \frac{\alpha\lambda}{4\pi} \quad (24.13)$$

## 24.10 Instrumentation

The four main requirements for a UV/VIS spectrophotometer involve: (i) the production of a continuous electromagnetic radiation source; (ii) the creation of a monochromatic wavelength with a dispersive medium, a sample compartment and an optical system; (iii) an optical path whereby a monochromatic light beam is introduced into the material under investigation; and (iv) a detection and measuring system, and the ability to collect and analyze the data acquired. Although spectrophotometers are available in a variety of sizes, shapes, geometries and configurations, two major classes can be identified depending on whether their optical geometry (configuration) is single beam or double beam [36].

Most commercial UV/VIS absorption spectrometers employ one of three overall optical designs: (i) a fixed or scanning spectrometer with a single light beam and sample holder; (ii) a scanning spectrometer with dual light beams and dual sample holders for the simultaneous measurement of  $I$  and  $I_0$  and (iii) a non scanning spectrometer with an array detector for simultaneous measurements at multiple wavelengths. In both single-beam and double-beam spectrometers the light from a lamp is dispersed before it reaches the sample cell. In an array-detector instrument, all wavelengths pass through the sample, while the dispersing element is located between the sample and the array detector.

### 24.10.1 Single-Beam Spectrophotometry

In the single-beam configuration, a single beam of light is emitted from the source. Reference data are acquired to standardize the instrument and are then

removed; a neutral “gray” standard is also measured during the standardization process and a mathematical correction made based on the reflectance of the gray standard, to compensate for the changes. In order for a single-beam configuration to perform well the light source, detector and electronics must be reasonably stable over time. Recent advances in electronics and the stability of the light sources have made reliable single-beam instruments possible. In addition, rapid developments in microprocessor technology has made it possible to achieve excellent results using a single-beam configuration when compared to a double-beam configuration. Comparisons between the reference and sample cells are possible with single-beam instrumentation by feeding the post-detector signal to a microprocessor, which stores the reference data for subtraction from the sample signal prior to printing and/or displaying the reference-corrected result (termed the “baseline”). Signal levels can be compared between different samples at one wavelength, at a series of predetermined wavelengths or, if a wavelength driver is provided, a complete absorption spectrum can be obtained [73].

#### 24.10.2

##### Double-Beam Spectrophotometry

In the double-beam configuration, the beam from the light source is split in two by using a beam splitter. The first beam is used to illuminate the reference standard [R], while the second beam illuminates the material under investigation [S]. All absorption measurements are expressed as the ratio between the incident light intensity  $I_0$  and the transmitted light intensity  $I$ . The beams may be recombined before they reach a single monochromator, but in some cases two monochromators may be used. Splitting of the light beam is normally accomplished either statically, with a partially transmitting mirror or similar device, or by attenuating the beams by using moving optical and mechanical devices. The basic set-up of a double-beam spectrophotometer is shown in Figure 24.14.

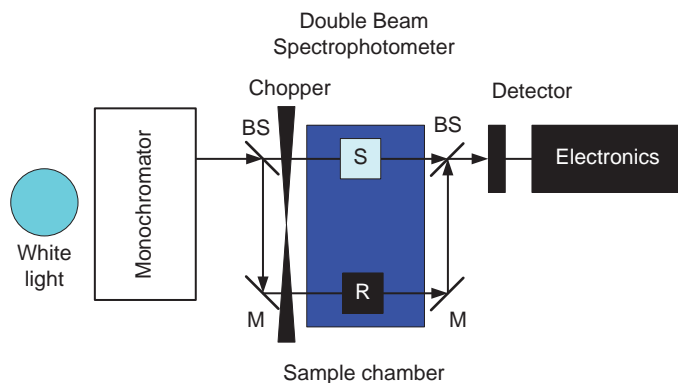


**Figure 24.14** Schematic diagram of the double-beam spectrophotometer.

## 24.11

### Radiation Sources

Stability during the measurement period and the maintenance of an adequate intensity over a wide wavelength region are the main requirements for providing a continuous source of electromagnetic radiation. The various UV radiation sources can include deuterium, hydrogen, tungsten, xenon and mercury arc lamps, while visible radiation sources include tungsten, mercury vapor and carbonone lamps.

Many spectrophotometers employ a deuterium discharge lamp for UV measurements, and a tungsten-halogen lamp for visible and near-infrared (NIR) measurements. The instruments automatically switch lamps when scanning between the UV and visible regions. Most modern spectrophotometers use a xenon lamp as a continuous electromagnetic radiation source with very high brightness, as this will emit a continuous spectrum from UV to the IR range [74].

#### 24.11.1

##### Xenon Lamp (Xenon Arc Lamp)

Xenon lamps are the most frequently used light sources in spectrophotometry when high light intensities are required. The lamp includes a discharge light source in which xenon gas is sealed in a bulb. Xenon lamps are classified as either direct current or alternating current types, according to the lighting method, and exhibit a similar spectral distribution to sunlight, producing a continuous spectrum from UV to NIR.

#### 24.11.2

##### Deuterium Lamp

The deuterium lamp is a discharge light source in which deuterium is sealed in a bulb. These lamps require a large and complex power supply, which makes them more expensive than halogen lamps. However, deuterium lamps represent one of the few continuous-spectrum light sources that are stable in the UV range. Typically, a deuterium lamp will have a short emission wavelength of 400 nm, or less. The window material limits use of the lamp at the short wavelength end of the spectrum.

## 24.12

### Monochromator

The main objective of a monochromator is to divide and transmit a narrow portion of the optical signal that has been selected from a wider range of wavelengths available at the input. In its simplest form, the monochromator is composed of two slits (entrance and exit) and a dispersion element (prism or diffraction grating). The main purpose of the entrance slit is to define the geometric properties

of the investigated radiation. Dispersion or diffraction can only be controlled if the light is collimated – that is, if all the light rays are parallel.

The presence of a prism in the spectrophotometer causes the light to be dispersed into a rainbow. At the exit slit, the different colors of visible light are intense as each arrives at a separate point in the exit slit plane; in this way a series of images of the entrance slit becomes focused on the plane. Rotation of the dispersion element then causes the band of colors to move relative to the exit slit, so that the desired entrance slit image becomes centered on the exit slit (Horiba; <http://www.horiba.com/us/en/scientific/products/optics-tutorial/monochromators-spectrographs/#c3752>).

Most monochromators that are based on diffraction gratings provide a uniform spectral dispersion, with the incoming beam from the entrance slit containing multiple wavelengths that are dispersed to other wavelengths that are no longer parallel but instead leave the grating at slightly different angles. As the light beam passes off the grating at angles depending on its wavelength, it will also be reflected from the mirror “downstream,” at different angles. Consequently, at the second mirror the individual wavelengths will be some distance apart and, after reflecting from this mirror, the beams will diverge even further. In fact, on arriving at the exit slit the beams will be so substantially separated in space that they appear as a “rainbow” across the plane of the exit slit.

#### 24.12.1

##### **Wavelength Selection**

To isolate a wavelength of choice, and to emit it from the monochromator, the position of the “rainbow” must be adjusted so that the desired wavelength passes through the slit but undesired wavelengths strike the edges of the slit and the inside wall of the monochromator close to the slit, and are blocked. This fine-tuning stage, to determine which wavelengths fall where in the exit plane, is accomplished by (very) slightly adjusting the position of the dispersing elements.

#### 24.13

##### **Detection Area and Detectors**

The final optical configuration section is the detection area, which may involve various types of detection. The two factors which affect photodetector choice are wavelength response and sensitivity. The most frequently used detectors are the photomultiplier tube, the silicon diode, and the diode array.

#### 24.13.1

##### **Photomultiplier**

The photomultiplier is a very versatile and sensitive detector of radiant energy in the UV, visible and NIR regions of electromagnetic radiation. The basic radiation

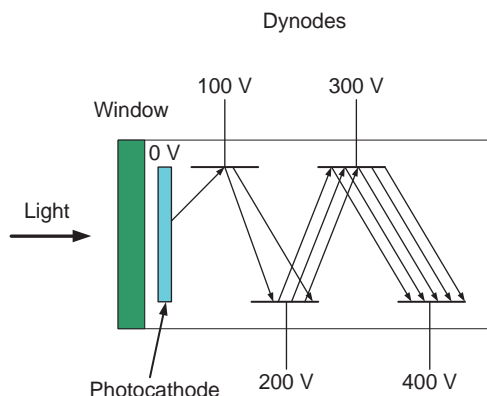


**Figure 24.15** Side view of photomultiplier tube.

sensor is the photocathode, which is located inside a vacuum envelope. During operation, photoelectrons are emitted and directed by an appropriate electric field to an electrode or dynode within the envelope. A number of secondary electrons are emitted at the dynode for each impinging primary photoelectron; these secondary electrons are in turn directed to a second dynode, and so on, until a final gain of perhaps  $10^3$ – $10^8$  is achieved [75]. The electrons from the last dynode are collected by an anode, which provides the signal current that is read out (see Figure 24.15).

#### 24.13.2

##### **Silicon Photodiode**

Silicon photodiodes are solid-state transducers that are used to convert light energy into an electronic signal [76,77]. These devices can be used to detect light in the UV, visible and IR spectral ranges. Photodiodes function by absorbing photons or charged particles and generating a flow of electrons that produces a current in an external circuit, proportional to the incident power. Photodiodes can be used to detect the presence or absence of minute quantities of light, and can be calibrated for extremely accurate measurements from intensities below  $1 \text{ pW cm}^{-2}$  to above  $100 \text{ mW cm}^{-2}$ . Because of their small size, low noise, high speed and good spectral response, silicon photodiodes are currently used for photodetection applications in the most detection systems.

#### 24.13.3

##### **Photodiode Array**

Photodiode arrays (PDAs) are used especially in single-beam spectrophotometer mode, as the spectra are acquired very quickly. The diode is a solid-state semiconductor device that exhibits a nonlinear current voltage characteristic. PDAs, which were first introduced in 1979, incorporate an integrated circuit with an

array of photosensitive spots, or pixels (typically 1024), arranged in linear fashion on a silicon chip. When a PDA is placed along the focal plane of a diffraction grating, each pixel on the array acts as a slit and detector for a given wavelength of dispersed radiation. The PDA detector (optical resolution ca. 1 nm) allows entire spectra to be collected very quickly because all wavelengths of the dispersed radiation are measured simultaneously. However, whereas the sensitivity of UV detectors is normally linear from a few milliabsorbance units (MAU) to 1 or 2 absorbance units (AU), that of PDAs is linear from 0.0001 to 2.0 AU over the entire wavelength range. This allows the purity assessment and accurate quantitation of both major and minor compounds [78].

#### 24.14

##### Data Acquisition

The basic function of a spectrophotometer ends with the collection of a signal (normally an electrical voltage) that is proportional to the absorption of a sample at a given wavelength. The signal handling and measuring systems may be as simple as data acquisition, which is the procedure of sampling signals that measure real-world physical properties and converting the resultant signal(s) into digital numeric values that can be manipulated using a computer. The required components of a data acquisition system will include:

- detectors that convert physical property parameters to electrical signals; and
- analog-to-digital converters, which convert conditioned detector signals to digital values.

Data acquisition applications are typically controlled by software programs that have been developed using various general-purpose programming languages.

#### 24.15

##### Classification of Errors in Spectrophotometry

Experimental measurements are never perfect, even with the most advanced instruments. One of the most well-known problems with spectroscopy measurements is random error, in which unpredictable variations occur in the measured signal from moment to moment or from measurement to measurement; this effect is often referred to as “noise.” There are many sources of noise in physical measurements, including instrument performance criteria in the case of spectrophotometry. These errors derive from the spectral bandwidth and slit width, stray light, wavelength accuracy and slit height, and it is therefore important to check such potential sources of error periodically. Although the fundamental problem in signal measurement is very often to distinguish the signal from the noise, this is not always easy. The signal is the “important” part of the data that needs to be



measured, whether it is the average of signals over a certain period of time or the height of a peak or area under a peak that occurs in the data. These types of error are discussed in the following sections. Problems may also be associated with electronic noise in the detector, while random fluctuations of the photon beam reaching the detector may be apparent in the amplifier output, especially when the beam energy is low. These noise problems may be reduced by integration with respect to time or by storage and enhancement, both of which are techniques to which microprocessors are particularly well suited [79,80].

#### 24.15.1

##### Spectral Band Width and Slit Width

Once a monochromator has been set to a certain wavelength, a beam with a Gaussian intensity distribution of wavelengths emerges from the exit slit. This intensity distribution is depicted in Figure 24.16, where  $\lambda$  and the dotted vertical line represent the wavelength selected on the instrument, and the thick black line represents the distribution of light that reaches the sample. The spectral bandwidth is defined as the width of the triangle at the points where the beam has reached half the maximum value; thus, spectral bandwidth is defined as full width at half-maximum (FWHM) and is represented by the two vertical lines between  $\lambda_{SB1}$  and  $\lambda_{SB2}$  on the wavelength axis. The spectral slit width is defined as the total spread of wavelengths represented by the lines between  $\lambda_{SSW1}$  and  $\lambda_{SSW2}$  in Figure 24.16. The spectral bandwidth of the

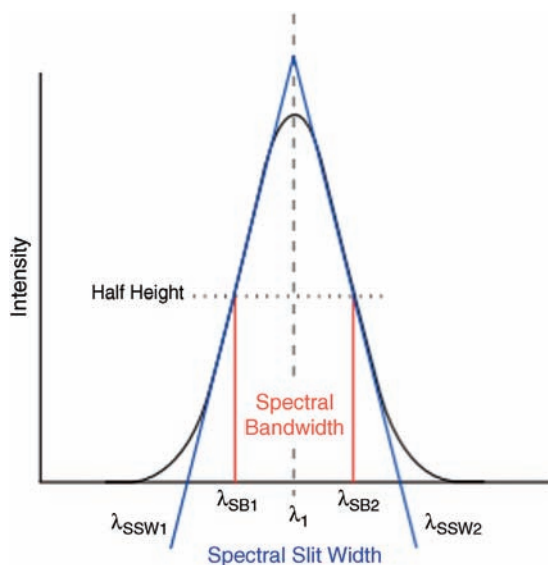


**Figure 24.16** Gaussian intensity distribution of wavelength emerging from the monochromator. The spectral bandwidth is defined by the red boundaries and  $\lambda_{SB}$ . The spectral slit width is depicted by the blue boundaries and  $\lambda_{SSW}$ .

spectrophotometer will always be narrower than the spectral slit width, and is related to the physical slit-width of the monochromator and, therefore, to the resolution capabilities of the instrument.

The resolution of a spectrophotometer is defined as the ability of the instrument to divide a light beam into limited, separate wavelength regions and to distinguish these limited regions one from another. Resolution is mainly ruled by the physical slit width of the instrument, in combination with the inherent optical dispersion of light beam from the exit of the monochromator to the detector of the instrument. Decreasing the slit width will reduce the spectral bandwidth and improve the ability of the instrument to resolve closely spaced peaks. Most instruments use diffraction gratings to obtain advantages of a linear dispersion, and provide fixed slit widths to organize the band width at the exit slit of the monochromator.

Today, many advanced spectrophotometers will have more than one slit width available, providing the users with the opportunity of improved operating photon energy against spectral sensitivity.

#### 24.15.2

##### **Slit Height**

The most common optical systems employ a spherical collimation which most likely will introduce optical aberrations that cause field curvature when the slit images are brought into focus. Occasionally, the slits may be made in a curved shape instead of straight, in order to avoid curvature of the perceived image. This allows the use of taller slits which can gather more light while still achieving a high spectral resolution. An alternative approach would be to use toroidal collimating mirrors to correct the curvature, as this allows higher straight slits without sacrificing the resolution.

#### 24.15.3

##### **Stray Light**

One of the most significant sources of instrument error is stray light, which can be classified as either monochromator stray light or instrumental stray light. Although, in all spectrophotometers, light with a wide range of wavelengths enters the monochromator from the source, only a very narrow band of wavelengths will emerge through the exit slit. Stray light may originate from imperfections in the dispersing element or in other optical surfaces, from diffraction effects, and possibly also from other optical aberrations or from damaged components. The ideal transfer function of such a monochromator is a triangular shape, where the peak of the triangle is at the supposed wavelength chosen. The intensity of the nearby colors will then decrease linearly on either side of this peak until a cut-off value is reached, when the intensity stops decreasing; this is called the "stray light level."

The stray light level is one of the most critical specifications of the spectrophotometer. For example, intense, narrow absorption bands can easily appear to have a peak absorption which is less than the true absorption of the sample,

because the instrument is limited by the stray light level. Many methods have been developed to measure and compensate for stray light in spectrophotometers.

#### 24.15.4

#### Solvents

The choice of a good solvent for use in UV spectroscopy is important, the first criterion being that it should not absorb UV radiation in the same region as the material whose spectrum is being determined. Usually, solvents that do not contain conjugated systems are best-suited for this purpose, although they vary with regards to the shortest wavelength at which they remain transparent to UV radiation. A second criterion applies to the solvent's effect on the fine structure of an absorption band, as both polar and nonpolar solvents can have adverse effects in this respect.

#### References

- 1 Work, W.J., Horie, K., Hess, M., and Stepto, R.F.T. (2004) Definitions of terms related to polymer blends, composite, and multiphase polymeric materials. *Pure Appl. Chem*, **76**, 1985–2007.
- 2 Shonaie, G.O. and Simon, G.P. (1999) *Polymer Blends and Alloys*, Marcel Dekker, New York, pp. 263–451, part II.
- 3 Sanchez, I.C. and Stone, M.T. (2000) *Statistical Thermodynamics of Polymer Solutions and Blends*, vol. 1 (eds C.B. Bucknall and D.R. Paul), John Wiley & Sons, New York, pp. 15–55, Chapter 2.
- 4 Utracki, L.A. (2002) *Polymer Blends Handbook*, vol. 1 (ed. L.A. Utracki), Kluwer Academic, The Netherlands, pp. 1–96, Chapter 1.
- 5 Robeson, L.M. (2002) *Polymer Blends Handbook*, vol. 1 (ed. L.A. Utracki), Kluwer Academic, The Netherlands, pp. 1167–1194, Chapter 17.
- 6 Robeson, L.M. (2007) *Polymer Blends: A Comprehensive Review*, Hanser, Ohio, pp. 11–54, Chapter 2.
- 7 Sabu, T., Boudenne, A., Ibos, L., and Candau, Y. (2011) *Handbook of Multiphase Polymer Systems*, vol. 1 (ed. A. Boudenne), John Wiley & Sons, New York, pp. 1–12, Chapter 1.
- 8 Oudhuis, A.A.C.M., Thiewes, H.J., Van Hutten, P.F., and Brinke, G.T. (1994) *Polymer*, **35**, 3936–3942.
- 9 Agarwal, S. and Speyerer, C. (2010) *Polymer*, **51**, 1024–1032.
- 10 Dreezen, G., Koch, M.H.J., Reynaers, H., and Groeninckx, G. (1999) *Polymer*, **40**, 6451–6453.
- 11 Lei, Y.-G., Cheung, Z.-L., Ng, K.-M., Li, L., Weng, L.-T., and Chan, C.-M. (2003) *Polymer*, **44**, 3883–3890.
- 12 Bartczak, Z., Argon, A.S., Cohen, R.E., and Weinberg, M. (1999) *Polymer*, **40**, 2331–2346.
- 13 Mahapatra, A., O'Riorden, S.M. (2009) US Patent 12, 538, 183, August 10.
- 14 Jouannet, D. and Pham, T.-N. (1997) *Polymer*, **38**, 5137–5147.
- 15 Chari, K., Lander, C.W., Liao, L.-S., and Yacobucci, P.D. (2011) US Patent 7, 931, 515 B2, April 26.
- 16 Demeuse, M.T. and Jaffe, M. (1990) *Polym. Adv. Technol.*, **1**, 181–192.
- 17 Dutta, D., Fruitwala, H., Kohli, A., and Weiss, R.A. (1990) *Polym. Eng. Sci.*, **30**, 1005–1018.
- 18 Ogo, H., Yamanari, T., Taima, T., Sakai, J., Tsukamoto, J., and Yoshida, Y. (2011) *Physics Procedia*, **14**, 231–234.
- 19 Moore, J.R., Albert-Seifried, S., Rao, A., Massip, S., Watts, B., Morgan, D.J., Friend, R.H., McNeill, C.R., and Sirringhaus, H. (2011) *Adv. Energy Mater.*, **1**, 230–240.

- 20 Gang, L., Shrotriya, V., Huang, J., Yao, Y., Moriarty, T., Emery, K., and Yang, Y. (2005) *Nat. Mater.*, **4**, 864–868.
- 21 Saion, Susilawati, E., Doyan, A., Abidin, S. Z., Zulkfli, A., Zaki, A.R.M., Dahlan, K.Z. H., and Karni, T. (2005) *J. Appl. Sci.*, **5**, 1825–1829.
- 22 Lu, L.P., Kabra, D., Johnson, K., and Friend, R.H. (2012) *Adv. Funct. Mater.*, **22**, 144–150.
- 23 Granström, M. and Inganäs, O. (1996) *Appl. Phys. Lett.*, **68**, 147–150.
- 24 Robeson, L.M. (1984) *Polym. Eng. Sci.*, **24**, 587–597.
- 25 Takahashi, S., Okada, H., Nobukawa, S., and Yamaguchi, M. (2012) *Eur. Polym. J.*, **48**, 974–980.
- 26 Jarray, J., Larbi, F.B.C., Vanhulle, F., Dubault, A., and Halary, L. (2002) Polymer blends, Proceedings of 7th European Symposium on Polymer Blends, May 27–29, Lyon-Villeurbanne, France.
- 27 Coleman, M.M., Graf, J.F., and Painter, P. C. (1991) *Specific Interactions and Miscibility of Polymer Blends*, Technomic Publishing Company, Lancaster, pp. 1–45, Chapter 1.
- 28 Sperling, L.H. (2006) *Introduction to Physical Polymer Science*, John Wiley & Sons, Hoboken, New Jersey, pp. 687–728, Chapter 13.
- 29 deGennes, P.G. (1979) *Scaling Concepts in Polymer Physics*, Cornell University Press, New York, pp. 245–258, Chapter X.
- 30 Sionkowska, A. (2006) *J. Photochem. Photobiol. A*, **177**, 61–67.
- 31 Tol, R.T., Mathot, V.B.F., Reynaers, H., and Groeninckx, G. (2006) *Micro- and Nanostructured Multiphase Polymer Blends Systems* (eds S. Thomas, C. Harrats, and G. Groeninckx), CRC Press, pp. 392–420, Chapter 12.
- 32 Van Puyvelde, P. and Moldenaers, P. (2005) *Micro- and Nanostructured Multiphase Polymer Blend Systems Phase Morphology and Interfaces* (eds S. Thomas, G. Groeninckx, and C. Harrats), CRC Press, UK, pp. 421–440, Chapter 13.
- 33 Dell’Erba, R., Groeninckx, G., Maglio, G., Malinconico, M., and Miglizzo, A. (2001) *Polymer*, **42**, 7831–7840.
- 34 Freed, K.F. and Dudowicz, J. (2005) *Adv. Polym. Sci.*, **183**, 63–126.
- 35 Gauglitz, G. and Vo-Dinh, T. (2003) *Handbook of Spectroscopy*, Wiley-VCH Verlag GmbH and Co., Weinheim, Sections II, III, and IV.
- 36 Burns, D.T. (1993) *UV Spectroscopy. Techniques, Instrumentation, Data Handling* (eds B.J. Clark, T. Frost, and M.A. Russell), Chapman & Hall, London, pp. 1–15, Chapter 1.
- 37 Heald, M.A. and Marion, J.B. (1995) *Classical Electromagnetic Radiation*, 3rd edn, Saunders College Publishing, Fort Worth.
- 38 Smith, G.S. (1997) *An Introduction of Classical Electromagnetic Radiation*, Cambridge University Press, Cambridge, pp. 1–107, Chapter 1.
- 39 Serway, R.A. and Beichner, R.J. (2000) *Physics for Scientists and Engineers*, 5th edn, Saunders College, New York, pp. 1075–1103, Part 4, Chapter 34.
- 40 Böttcher, H. (1991) *Technical Applications of Photochemistry*, Deutscher Verlag für Grundstoffindustrie, Leipzig.
- 41 Serpone, N. and Salinaro, A. (1999) *Pure Appl. Chem.*, **71**, 303–320.
- 42 Hoffmann, M.R., Martin, S.T., Choi, W., and Bahneman, D.W. (1995) *Chem. Rev.*, **95**, 69–96; <http://www.horiba.com/us/en/scientific/products/optics-tutorial/monochromators-spectrographs/#c3752>.
- 43 Oppenländer, T. (2003) *Photochemical Purification of Water and Air*, Wiley-Verlag, Weinheim, pp. 37–78, Chapter 3.
- 44 Pavia, L.D., Lampman, G.M., and Kriz, G. S. (2001) *Introduction to Spectroscopy “A Guide for Students of Organic Chemistry”*, Books/Cole, Thomson Learning, Victoria, pp. 353–389.
- 45 Born, M. and Wolf, E. (1999) *Principle of Optics: Electromagnetic Theory of Propagation, Interference and Diffraction of Light*, 7th edn, Cambridge University Press, Cambridge, pp. 286–409.
- 46 Hecht, E. and Zajac, A. (1974) *Optics*, Addison-Wesley, Reading, pp. 86–137, Chapter 4.
- 47 Risteen, A.D. (1895) *Molecules and the Molecular Theory of Matter*, Ginn and Company.
- 48 O’Shea, J.F. (1973) A molecular orbital theory of polymers. PhD Thesis, McMaster University, Hamilton, Ontario.

- 49 Jean, Y. and Volatron, F. (1993) *An Introduction to Molecular Orbitals*, Oxford University Press, New York, pp. 73–99, Chapter 3.
- 50 Fleming, I. (2010) *Molecular Orbitals and Organic Chemical Reaction*, John Wiley & Sons, Inc., UK, pp. 69–122, Chapter 2.
- 51 Kowalonek, J. and Kaczmarek, H. (2010) *Eur. Polym. J.*, **46**, 345–353.
- 52 Yang, Y., Shi, Y., Liu, J., and Guo, T.-F. (2003) The control of morphology and the morphological dependence of device electrical and optical properties in polymer electronics, in S. Hotta (ed.), *Electronic and Optical Properties of Conjugated Molecular Systems in Condensed Phases*, Research Signpost, Kerala, India, pp. 307–354.
- 53 Gadisa, A. (2006) Studies of charge transport and energy level in solar cells based on polymer/fullerene bulk heterojunction bimolecular and organic electronics. PhD thesis, Linköping University, Sweden.
- 54 Salaneck, W.R., Friend, R.H., and Brédas, J.L. (1999) *Phys. Rep.*, **319**, 231–251.
- 55 Heeger, A.J. (2001) *Rev. Mod. Phys.*, **73**, 681–700.
- 56 Heeger, A.J., Kivelson, S., Schrieffer, J.R., and Su, W.P. (1988) *Rev. Mod. Phys.*, **60**, 781–850.
- 57 Stenzel, O.H. (2005) *The Physics of Thin Film Optical Spectra an Introduction*, Springer-Verlag, Berlin, Heidelberg, pp. 214–219, Chapter 12.
- 58 Kittel, C. (2005) *Introduction to Solid State Physics*, John Wiley & Sons, Inc., Chapter 15, pp. 427–450.
- 59 Baranovski, S. (2006) *Charge Transport in Disordered Solids with Applications in Electronics*, John Wiley & Sons, Australia Ltd, pp. 105–110.
- 60 Khan, G.A. and Hogarth, C.A. (1991) *J. Mater. Sci.*, **26**, 412–416.
- 61 Pankove, J.I. (1971) *Optical Processes in Semiconductors*, Dover Publications, New York, pp. 34–86, Chapter 3.
- 62 Tauc, J. (1972) *Optical Properties of Solids* (eds F. Abeles) North-Holland, Amsterdam, pp. 279–300.
- 63 Al-Ani, S.K.J. (1993) *Int. J. Electron.*, **75**, 1153–1163.
- 64 Lanyon, H.P.D. (1963) *Phys. Rev.*, **130**, 134–143.
- 65 Davis, A. and Mott, N.F. (1970) *Philos. Mag.*, **22**, 903–922.
- 66 Fox, M. (2001) *Optical Properties of Solids*, Oxford University Press, New York, pp. 49–71, Chapter 3.
- 67 Fox, M. (2010) *Optical Properties of Solids*, Oxford University Press, New York, pp. 214–245, Chapter 8.
- 68 Urbach, F. (1953) *Phys. Rev.*, **92**, 1324–1324.
- 69 Elliott, R.J. (1957) *Phys. Rev.*, **108**, 1384–1389.
- 70 Li, S.S. (2006) *Semiconductor Physical Electronics*, 2nd edn, Springer Science, pp. 246–283, Chapter 9.
- 71 Gauglitz, G. and Vo-Dinh, T. (2001) *Handbook of Spectroscopy*, vol. 1 (ed. M. Hof), Wiley-VCH, Weinheim, pp. 39–41, Chapter 3.
- 72 Singh, J. (2006) *Optical Properties of Condensed Matter and Applications*, John Wiley & Sons, New York, pp. 1–23, Chapter 1.
- 73 Miller, J.N. (1993) *UV Spectroscopy: Techniques, Instrumentation and Data Handling*, vol. 4 (eds B.J. Clark, T. Frost, and M.A. Russell), Chapman & Hall, London, pp. 17–34, Chapter 2.
- 74 Bart, J.C.J. (2005) *Additives in Polymers: Industrial Analysis and Applications*, John Wiley & Sons, pp. 302–342, Chapter 5.
- 75 Burle Industries, Inc. (1980) *Photomultiplier Handbook*, Burle Industries, Inc., pp. 3–177.
- 76 Friberg, A.T. and Dandliker, R. (2008) *Advances in Information Optics and Photonics* (eds A.P. Knights and J.K. Doylend), SPIE, Washington, pp. 633–640, Chapter 30.
- 77 Bandyopadhyay, A. and Deen, M.J. (2001) Photodetectors for optical fiber communications, in *Photodetectors and Fiber Optics* (ed. H.S. Nalwa), Academic Press, San Diego, pp. 306–368, Chapter 5.
- 78 Sanchez, F., Collados, M., and Vazquez, M. (1992) *Solar Observations: Techniques and Interpretation*, Cambridge University Press, Cambridge, pp. 164–168, Chapter 5.
- 79 Robertson, A.R. (1976) *J. Res. Nat. Bur. Std. Phys. Chem., Section A*, **80**, 625–630.
- 80 Reule, A.G. and Robertson, A.R. (1976) *J. Res. Nat. Bur. Std. Phys. Chem., Section A*, **80**, 609–624.



## 25

### Fluorescence Spectroscopy

*Gabriel Bernardo and Jorge Morgado*

#### 25.1

##### Introduction

Polymer blends have found widespread technological use over the past century [1]. In general, polymers have limited miscibility owing to the relatively small contribution of the entropy of mixing to the reduction of the total Gibbs free energy of the system. The physical properties of polymer blends depend crucially on their phase behavior – that is, the properties of phase-separated blends differ substantially from those of homogeneous mixtures. Although the phase behavior of polymer blends and their structure–property relationships have been a subject of research for many decades, earlier studies were mostly focused on the mechanical properties. Only more recently has the blending of polymers moved into focus, aimed at improving the electronic and optoelectronic properties of the final product, [2,3]. In this context, fluorescence spectroscopy plays a crucial role in the characterization of polymer blends.

The most important characteristic of fluorescence is that it can provide information on the nanometer length scale with very high sensitivity, allowing the system under study to be characterized with high spatial resolution and with time resolutions of a few tens of picoseconds, or even lower. Two-dimensional (2D) plots, in terms of fluorescence intensity dependence on time and wavelength, can be obtained, which can provide valuable information on the photophysical behavior of the system and its relation to the structural/morphological characteristics.

Although fluorescence spectroscopy has been used in polymer science for several decades [4], it has received special attention in recent years, in large part due to its application in the study of a class of newly synthesized fluorescent conjugated polymers, which have important applications in the emerging areas of organic electronics and optoelectronics. Nonconjugated polymeric materials are usually nonfluorescent, but can also be studied using fluorescence spectroscopy upon labeling with fluorescent probes (fluorophores). Emission spectra can be recorded at extremely low fluorophore concentrations and, therefore, a

nonfluorescent polymer may be labeled with such a small amount of a fluorophore that the labeling has only a marginal effect on the properties of the system.

The combination of various fluorescence techniques, such as steady-state and time-resolved fluorescence spectroscopy and fluorescence microscopy, can provide extremely important information on the structure and dynamics of polymer blends. Many relevant examples will be presented in this chapter, with particular emphasis being placed on the most recent investigations.

First, some fundamental aspects of fluorescence spectroscopy will be briefly presented and typical fluorescence experiments discussed. Their use in studies of intrinsically fluorescent polymers and in fluorescent labeled-polymer systems will then be illustrated.

## 25.2

### Fundamentals of Fluorescence Spectroscopy

#### 25.2.1

##### Theory

The energy diagram – known as the Jablonskii diagram – of the states involved in the photoexcitation and luminescence of a molecular system is shown in Figure 25.1 [5,6]. After excitation from a ground state  $S_0$  to an higher-lying  $S_n$  state, the system either relaxes to the vibrational ground state of  $S_1$  or crosses, via

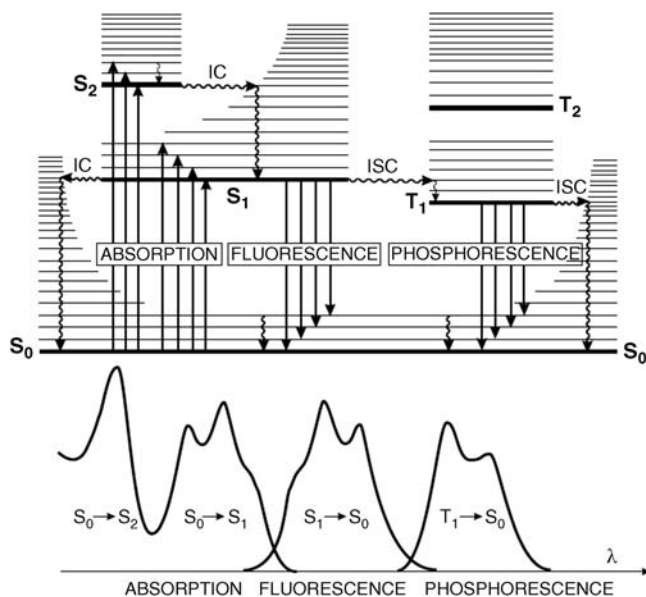


**Figure 25.1** Simplified processes involved in the electronic photoexcitation and fluorescence of a molecular system. Reproduced with permission from Ref. [5]; © 2001, John Wiley & Sons, Inc.



spin-orbit coupling, to the excited triplet manifold, relaxing then to the vibrational ground state of  $T_1$ . It should be noted that the intersystem crossing process ( $S_1 \rightarrow T_1$ ) is spin-forbidden, being only partially allowed by the spin-orbit coupling, which is more relevant for systems based on heavier atoms. The radiative decay takes place from  $S_1$  to the ground state (the Kasha rule), a process termed fluorescence, being symmetry allowed, while the radiative decay of  $T_1$  (strictly spin-forbidden) is termed phosphorescence. The fluorescence-based techniques used to characterize polymer blends will be addressed in this chapter.

Under continuous-wave excitation of a fluorescent molecular system, typically in solution or in solid samples, it is possible to record absorption, fluorescence (both emission and excitation spectra) and phosphorescence spectra.

The fluorescence properties of a given molecular system, namely the intensity (or efficiency) and the spectral shape, recorded under continuous-wave excitation, are sensitive to the medium in which they are embedded (namely solution versus solid state) and the neighboring molecules (chromophores and/or fluorophores). It is this sensitivity that allows information to be obtained on the sample's morphology.

### 25.2.2

#### Steady-State Fluorescence

Steady-state fluorescence is the simplest and the most common type of fluorescence spectroscopy. Measurements are performed with continuous illumination and detection; that is, the sample is illuminated with a continuous beam of light (usually of a specific wavelength) and the emission spectrum (intensity versus wavelength) is recorded.

In a typical steady-state fluorescence spectrometer a continuous beam of light is directed at the sample, where it excites fluorescence. The fluorescence emission is collected at  $90^\circ$  or at a lower angle (known as right-angle and front-face configurations, respectively) from the excitation, to prevent the interference of the excitation light with the detection of the fluorescence emission. The collected fluorescence emission enters a monochromator and a detector (such as a photomultiplier tube) to record the emission spectrum. Alternatively, the fluorescence spectrum detection can be made by a charge-coupled device (CCD) spectrograph coupled to a grating.

### 25.2.3

#### Time-Resolved Fluorescence

A new era of research in fluorescence spectroscopy has emerged with the advent of powerful lasers capable of generating short-lived pulses and with the simultaneous development of sophisticated detection methods. While research groups were previously limited to the study of processes on the microsecond and nanosecond time scale, these developments have expanded the accessible time scale to the pico- and femtosecond. Time-resolved fluorescent measurements are being used, for example, to unravel the dynamics of excited states (excitons) generated in conjugated polymer films (such as stimulated emission) and the processes that

occur in organic photovoltaic systems combining electron-donor and electron-acceptor materials.

Time-resolved measurements provide much more information than is available from the steady-state data [7]. For instance, in blends containing two fluorophores, each with a distinct lifetime, it is not always possible to resolve the emission from the two fluorophores using steady-state measurements (if they emit in the same spectral region) and the nature of the processes that occur following photo-excitation. However, the time-resolved data may reveal the individual decay times and the dynamics of generated excited states.

Two methods of measuring fluorescence lifetime are in widespread use: the time-domain (or pulse-fluorometry) and the frequency-domain (or phase-modulation fluorometry) methods. Here, reference will be made only to the first method.

In pulse-fluorometry the sample is excited with a pulse of light (Figure 25.2). The width of the pulse is made as short as possible, and is preferably much shorter than the excited state decay time  $\tau$  of the sample. The time-dependent intensity is measured following the excitation pulse, and the decay time  $\tau$  is calculated from the slope of a plot of  $\ln I(t)$  versus  $t$ , or from the time at which the intensity decreases to  $1/e$  of the intensity at  $t = 0$ .

The instrumentation for time-resolved fluorescence spectroscopy shares some similarities with that used for steady-state measurements, in the sense that an excitation source and a detection systems are used. The nature of these components may, and usually does, vary significantly. Namely, a pulsed light source is used in time-resolved spectroscopy, which is at variance with the continuous light source used in steady-state fluorescence.

A related experimental method is Time-Correlated Single Photon Counting (TCSPC), which generates a histogram representing the fluorescence intensity over time. This is an efficient method because it counts photons and records their arrival time, which directly represents the fluorescence decay.

Ideally, the recorded fluorescence decay as function of time,  $I(t)$ , would correspond to the intrinsic decay if the excitation pulse would be a  $\delta$ -function. As the

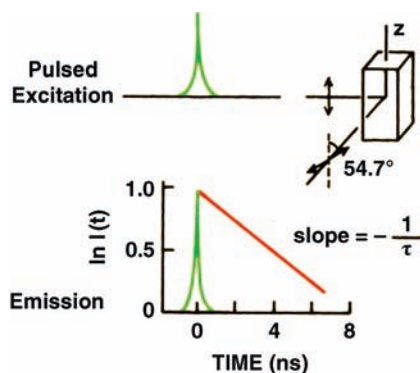


**Figure 25.2** Pulse- or time-domain lifetime measurements. Reproduced with permission from Ref. [8]; © 2006, Springer.

width of the excitation pulse (excitation function) is in fact not zero, there are situations where that width is not negligible with respect to the fluorescence decay data. In such cases, the obtained fluorescence decay (system response) is the result of the convolution of both signals (the  $\delta$ -pulse response and the excitation function). To determine the fluorescence lifetime, that is, based on the  $\delta$ -pulse response of the system, the decay data (actual response of the system) is fitted by taking into account the deconvolution procedure. It is often the case that the measured time-dependent fluorescence is not fitted by a simple exponential function. The  $\delta$ -pulse response can be fitted by a sum of exponential components, each one having an associated decay time,  $\tau_i$ ,

$$I(t) = \sum_i a_i e^{-t/\tau_i} \quad (25.1)$$

where  $a_i$  are the fractional amplitudes, with

$$\sum_i a_i = 1 \quad (25.2)$$

This type of analysis may lead to the identification of different processes, if they have sufficiently distinct decay times. Alternatively, the response may be fitted using stretched exponential functions.

$$I(t) = a e^{-(t/\tau)^\beta} \quad (25.3)$$

In the first case, an average decay time (or lifetime) can be calculated by taking

$$\langle \tau \rangle_f = \frac{\sum_i a_i \tau_i^2}{\sum_i a_i \tau_i} \quad (25.4)$$

known as an intensity-average decay time, or, alternatively,

$$\langle \tau \rangle_a = \sum_i a_i \tau_i \quad (25.5)$$

known as an amplitude-average decay time.

Figure 25.3 shows a simplified diagram (of that shown above in Figure 25.1), specifying the rate constants involved in the various de-excitation channels of an excited  $M^*$  molecular species. In this figure, the rate constant of the radiative

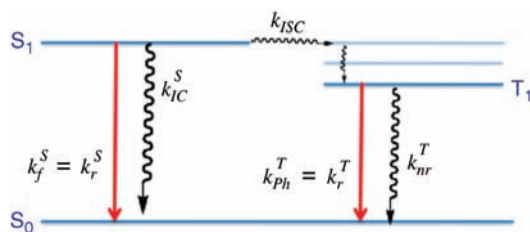
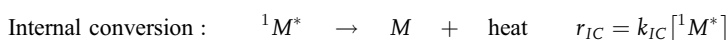
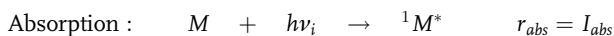


**Figure 25.3** Simplified energy diagram showing the competing processes that follow the photo-excitation of a molecular system. Modified from Ref. [5].

deactivation of  $M^*$  singlet excited state with fluorescence emission ( $k_r^S$ ) competes with the non-radiative decay ( $k_{nr}^S$ ). This has, in turn, two components: the rate of internal conversion ( $k_{IC}^S$ ) and rate of intersystem crossing ( $k_{ISC}^S$ ), meaning that  $k_{nr}^S = k_{IC}^S + k_{ISC}^S$ . In addition, the deactivation of the triplet state  $T_1$  has also two components, the radiative deactivation with phosphorescence emission ( $k_r^T$ ) and the non-radiative deactivation by intersystem crossing  $T_1 \rightarrow S_0$  ( $k_{nr}^T$ ).

Consider a population of molecules  $M$  that are excited by a  $\delta$ -pulse from the ground state ( $S_0$ ) to an upper lying energy state ( $S_n$ ). There is an initial decay of the system from  $S_n$  to  $S_1$  by internal conversion. Starting from  $S_1$ , the following processes occur, with the corresponding rates ( $r$ ):



The molecule can then undergo an internal conversion process down to the lowest excited state,  $S_1$ . The rate of disappearance of these  $M^*$  excited molecules is given by

$$-\frac{d[{}^1M^*]}{dt} = (k_r^S + k_{nr}^S)[{}^1M^*] \quad (25.6)$$

Integration of the above differential equation between time zero and  $t$ , leads to

$$[{}^1M^*] = [{}^1M^*]_0 e^{-(k_r^S + k_{nr}^S)t} = [{}^1M^*]_0 e^{-k t} \quad (25.7)$$

or

$$[{}^1M^*] = [{}^1M^*]_0 e^{-\frac{t}{\tau}} \quad (25.8)$$

where  $[{}^1M^*]_0$  is the concentration of excited molecules at time zero upon incidence of the  $\delta$ -pulse excitation and  $\tau$  is the lifetime of the excited state  $S_1$ , given by

$$\tau = \frac{1}{k_r^S + k_{IC}^S + k_{ISC}^S} \quad (25.9)$$

A radiative lifetime,  $\tau_r$ , is also defined by

$$\tau_r = \frac{1}{k_r^S} \quad (25.10)$$

Considering the steady-state approximation for  $[{}^1M^*]$ , the following is obtained:

$$\frac{d[{}^1M^*]}{dt} = I_{abs} - k_r[{}^1M^*] - k_{ISC}[{}^1M^*] - k_{IC}[{}^1M^*] = 0 \quad (25.11)$$

from which is obtained

$$I_{abs} = (k_r + k_{ISC} + k_{IC}) [^1M^*] \quad (25.12)$$

A fluorescence quantum yield,  $\phi_{FL}$ , can also be defined as

$$\begin{aligned} \phi_{FL} &= \frac{\text{rate of fluorescence}}{I_{abs}} = \frac{k_r [^1M^*]}{(k_r + k_{ISC} + k_{IC}) [^1M^*]} = \frac{k_r}{k_r + k_{ISC} + k_{IC}} \\ &= k_r \tau_S \end{aligned} \quad (25.13)$$

This quantum yield can be defined as fraction of excited molecules that return to the ground state with fluorescence emission. It can be determined by comparing the fluorescence emission intensity with that of a standard (ideally absorbing and emitting in the same spectral region) in solution, or by using an integrating sphere [5].

#### 25.2.4

##### Fluorescence Quenching

The intensity of fluorescence can be decreased (quenched) by several processes, such as collisions (in solution), excimer or exciplex formation, and energy, electron or proton transfer [5]. In the context of polymer blends studies, the process of collisional fluorescence quenching, either static or dynamic (as described by the Stern–Volmer quenching), is not particularly relevant.

Blending components, or having a single component combining different fluorophores, can lead to ground-state interactions, namely charge transfer, which affects both absorption and fluorescence signatures of the individual components or units. Also relevant is the situation when such interactions only occur after photoexcitation, leading to the formation of excimers and exciplexes. In this case, these states are not directly probed from the ground state, being excited state-based spectroscopies, such as fluorescence or pump-probe, the adequate methods for their characterization. Excited-state charge transfer can also quench fluorescence, which occurs when materials with different energy gaps and different LUMO (lowest unoccupied molecular orbital) energies are combined. This is the key process behind organic photovoltaics. This situation is usually identified by a strong fluorescence quenching and a strong reduction in excited states lifetimes.

Additionally, excited-state energy transfer between fluorophores of different energy gaps can take place. This is a quite widely used process when characterizing polymer blends, and in an ideal case it should be possible to excite fluorophores of one of the blend components and to determine the fluorescence coming from a lower-energy gap fluorophore in the second component. Energy donor and acceptor fluorophores may even reside at different locations of a single component. The aim is to use this process to gain insight into the spatial relative distribution of donor and acceptor fluorophores.

It is important to identify the situation where the energy transfer process takes place via a trivial (or radiative) mechanism, in a sequential mode; that is, when the excitation of the accepting fluorophore occurs after the photon has been emitted by the donor fluorophore. Alternatively, energy transfer can take place if there is a coupling between the two fluorophores. The presence of a direct coupling implies that the efficiency of the energy transfer will depend not only on the optical properties of the two fluorophores (namely absorption and fluorescence spectra) but also on the spectral overlap between the donor's fluorescence and the acceptor's absorption spectra, on fluorophores separation, and even relative orientation. This is why fluorescence quenching is a much more valuable tool for characterizing a material's morphology.

The interaction between donor and acceptor fluorophores can be simply divided into dipolar interaction and intermolecular orbital overlap [5]. The dipolar interaction, which is associated with resonance energy transfer (RET) or Förster resonance energy transfer (FRET) [9], is effective at longer distances than the orbital overlap, which is also known as Dexter exchange energy transfer [10]. How these processes occur is shown in Figure 25.4. It is worth mentioning that FRET can only occur by singlet energy transfer, whereas the Dexter mechanism is effective for both singlet and triplet energy transfer. FRET has been widely used to characterize polymer blends [11,12].

In order for FRET to occur, there must be a spectral overlap between the donor emission and the acceptor absorption. In its simplest form, the rate constant for transfer between a donor and an acceptor at a distance  $r$  is:

$$k_T = \frac{1}{\tau_D^0} \left( \frac{R_0}{r} \right)^6 \quad (25.14)$$

where  $\tau_D^0$  is the excited-state lifetime of the donor in the absence of transfer.  $R_0$  is the Förster radius, which is defined as the average intermolecular distance

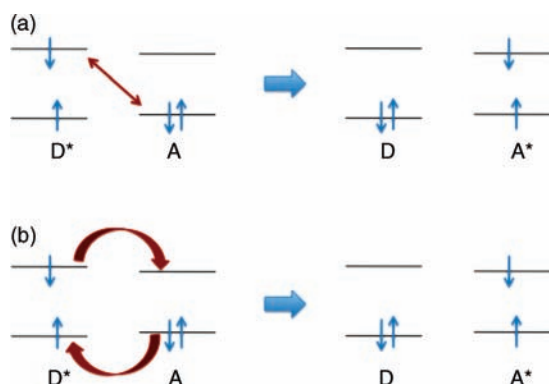


**Figure 25.4** (a) Förster dipole-coupling and (b) Dexter electron-exchange models for energy transfer (from D\* to A).

between donor and acceptor at which the energy transfer rate is equal to the sum of all other spontaneous relaxation decay rates of the excited donor.  $R_0$  is proportional to the spectral overlap of the donor's emission and acceptor's absorption, and can therefore be calculated based on the following expressions [5].

$$R_0(\text{\AA}) = 0.2108 \left[ \kappa^2 \Phi_D^0 n^{-4} \int_0^\infty I_D(\lambda) \varepsilon_A(\lambda) \lambda^4 d\lambda \right]^{1/6} \quad (25.15)$$

where  $\kappa^2$  is the orientational factor,  $\Phi_D^0$  is the fluorescence quantum yield of the donor in the absence of transfer,  $n$  is the refractive index of the medium,  $\varepsilon_A(\lambda)$  is the molar absorption coefficient of the acceptor, and  $I_D(\lambda)$  is fluorescence spectrum of the pure donor, so that

$$\int_0^\infty I_D(\lambda) d\lambda = 1 \quad (25.16)$$

Due to its dependence on  $r^{-6}$ , the Förster transfer rate (Eq. (25.14)) depends heavily on the separation between the donor and acceptor fluorophores/molecules, and efficient transfer only occurs if this separation is less than the Förster transfer radius ( $R_0$ ). Typical values of  $R_0$  are on the order of only a few nanometers, and therefore FRET is very sensitive to distances of this magnitude.

Polymer interfaces are usually much broader than inorganic interfaces because, even in the case of immiscible polymers, some segment interpenetration occurs at the interface between the individual domains, being the interfacial width ( $w$ ) proportional to  $1/\sqrt{(\chi)}$ , where  $\chi$  is the Flory–Huggins chi-parameter [13]. Therefore, even in immiscible polymer blends, polymer interfaces with widths in the range from 1 to 10 nm are typical, and this range matches the typical length scale of FRET. Although the use of FRET in polymers was pioneered by Morawetz during the 1980s, the technique has only recently been extended to acquire quantitative information on polymer interfaces.

In FRET experiments, the time-dependent fluorescence intensity decay (as described in Section 25.2.3) of the donor is usually measured. By fitting the experimental results with a theoretical decay that takes into account the energy transfer process, it is possible to obtain morphological information on the interface, such as the width of the interface between two polymers.

With the development of suitable models for the analysis of the fluorescence decays in restricted geometry with arbitrary distributions of donors and acceptors, it is possible to characterize the density profile of the interfacial region between two polymers. A more detailed description is beyond the scope of this chapter, but other excellent reference sources are available [4,5,8,14].

In general terms, fluorescence quenching can be described by the interaction of a fluorophore with a quencher ( $Q$ ) entity. The analysis of the mechanisms involved can be made using the Stern–Volmer equation, which relates the steady-state fluorescence intensity of the fluorophore in the presence ( $I$ ) and absence ( $I_0$ )

of the quencher with the quencher concentration ( $[Q]$ ):

$$\frac{I_0}{I} = 1 + K_{SV}[Q] \quad (25.17)$$

where  $K_{SV}$  is the Stern–Volmer quenching constant. This equation describes the collisional quenching mechanism, where the excited-state fluorophore returns to the ground state upon collision with a quencher molecule. Deviations from the linear relationship can be observed when the quenching efficiencies are very high, namely when there is some static component (corresponding to an association/interaction between the fluorophore and the quencher) [5].

### 25.2.5

#### Fluorescence Microscopy

Optical microscopy, both fluorescence [15] and confocal [16], is widely used to characterize materials down to the micrometer or sub-micrometer scale. The resolution is diffraction-limited. Depending on the wavelength used for the observation, the Rayleigh criterion establishes that the resolution is roughly half the light wavelength. To circumvent this limit, scanning near-field optical microscopy (SNOM) [17], which operates in the near-field regime, was developed. Laser light is coupled into a single-mode optical fiber and is passed through an aperture at the end of the fiber that is very close to the material's surface. Both dimensions – the aperture of the fiber end and its distance to the material's surface – are in the subwavelength region. The tip of the fiber is scanned across the material's surface, using a piezo-electric-based scanning mechanism similar to that used in atomic force microscopy (AFM). The imaging can be made either in transmission or in fluorescence, and spatial resolution down to about 30 nm can be achieved.

### 25.3

#### Intrinsically Fluorescent Polymer Blends

Conjugated polymers, named in view of the single–double bond alternation along the main chain, are at the origin of the new area of organic electronics and optoelectronics, sharing the arena with small conjugated molecules that are used to prepare thin films showing similar properties. Since the report in 1977 on electrical conductivity in polyacetylene [18], a discovery awarded with the Nobel Prize in Chemistry in 2000 (to Alan Heeger, Alan G. MacDiarmid and Hideki Shirakawa), followed by the report on electroluminescence on poly(*p*-phenylene vinylene) (PPV) by Friend *et al.* in 1990 [19], a huge library of conjugated polymers has been prepared. These combine semiconducting properties, when in the pristine form, with high conductivity, upon charge-transfer doping. Some of the polymers exhibit fluorescence, which has led to the development of polymer-based light-emitting diodes (LEDs). The range of applications varies from thin-film transistors, light-emitting devices, diodes, photodiodes and photovoltaic cells; these materials are also being investigated for applications in bioelectronics [20–24].



In the operation of optoelectronics devices, such as light-emitting devices (diodes, electrochemical cells and transistors), photovoltaic cells (organic photovoltaics; OPVs) and photodiodes, several processes are involved. Depending on the devices, there may occur excitation energy transfer, excited state charge transfer, charge transport, and luminescence quenching. It is often the case that devices based on polymer blends perform better than those based on single polymers, as has been particularly explored in LEDs and OPVs [2]. In the case of LEDs, the selection of polymers to be blended may be determined by their relative hole and electron mobilities (to achieve a balanced charge injection and transport), by the relative fluorescence quantum efficiency, or by the relative energy gaps (for instance, in cases where white light emission is aimed at). In the case of OPVs, the critical process is a splitting of the exciton in separated electrons and holes, a process that is made efficient upon combination of polymers with an offset in their LUMOs and/or HOMOs (highest occupied molecular orbitals), forming a type II heterojunction. The polymer accepting the hole (the polymer with a higher HOMO) should also be a good hole conductor, while the other (with a lower LUMO) should be a good electron conductor so as to allow a rapid charge removal, avoiding recombination. In these two types of device the spatial distribution of both components is of key importance.

Some of the most relevant applications of fluorescence spectroscopy to the characterization of intrinsically fluorescent polymer blends are discussed in the following subsections.

Light-emitting diodes were the first devices based on conjugated polymers to attract a wider attention from the scientific community. The initial studies were mainly focused on poly(*p*-phenylene vinylene)s, but these were later overturned by the polyfluorenes. Among these series of polymers, poly(9,9-dioctylfluorene) (PFO, also known as F8), and a derived copolymer, poly(9,9-dioctylfluorene-*alt*-benzothiadiazole) (F8BT), are certainly among the most well-studied. In terms of device performance, blends based on PFO and F8BT were quite successful; this derives from the fact that PFO and F8BT are complementary in terms of their charge mobilities (PFO is a better conductor of holes, F8BT a better conductor of electrons). Additionally, there is a strong overlap between the PFO emission (photoluminescence) and F8BT absorption spectra, as shown in Figure 25.5. Quite frequently, blends of these two polymers show a green emission (which is ascribed to F8BT) as a result of an efficient energy transfer from PFO to F8BT.

In view of the significant interest directed at this system, a significant number of studies were carried out. In 2001, Bradley and coworkers [25] reported their results on Förster energy transfer in blends of PFO and F8BT using picosecond time-resolved photoluminescence. When blends with compositions ranging from 50% to 0.01% F8BT were investigated, the PFO luminescence was seen to decay faster as the F8BT content increased, a variation that was attributed to an increase in the efficiency of the energy transfer process from PFO to F8BT. The luminescence decay curves, at 440 nm (PFO emission), from the blends with concentrations of F8BT >0.5%, could be fitted to a double-component exponential decay ( $\tau_1 = 12$  ps and  $\tau_2 = 35$  ps). The fluorescence decay of samples with a 0.5% content

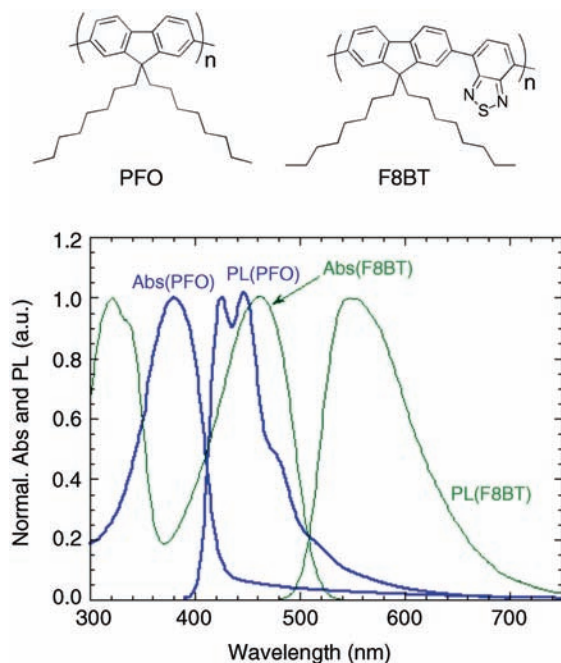


**Figure 25.5** Chemical structures of the conjugated polymers PFO and F8BT, and absorption and photoluminescence spectrum recorded for films of both polymers.

of F8BT were also fitted by two components with lifetimes of 35 ps and 120 ps. Samples with lower F8BT contents (F8BT fraction  $< 0.5\%$ ) needed only a single exponential to adequately fit the fluorescence decay, the lifetime of which increased as the F8BT content decreased, approaching a lifetime of 400 ps, as found in glassy neat PFO films (see Figure 25.6).

The existence of two lifetime components in the PFO luminescence decay (at 440 nm) was interpreted as being due to: (i) an energy transfer between near-neighbor sites (12 ps); and (ii) a two-step process, involving exciton migration along the PFO chains plus energy transfer to F8BT (35 ps component). The authors have tried to rationalize the lifetime of the energy transfer of 12 ps according to Eq. (25.14). Assuming that the donor–acceptor separation is similar to the interchain separation in pure PFO (0.44 nm), Eq. (25.14) gives a Förster radius of 0.8 nm. The use of Eq. (25.15) to calculate this radius in the case of conjugated polymers faces a question about the calculation of the molar absorption coefficient, as either the average molecular weight of the energy-accepting polymer or the molecular weight of a defined segment (which the authors considered to be five repeat units) could be considered that would correspond to the spatial extent of the exciton, created upon photon absorption. In both cases, the  $R_0$  value calculated by Bradley *et al.* was found to be much larger than 0.8 nm. This points to the fact that the application of Förster formalism to conjugated polymers is not

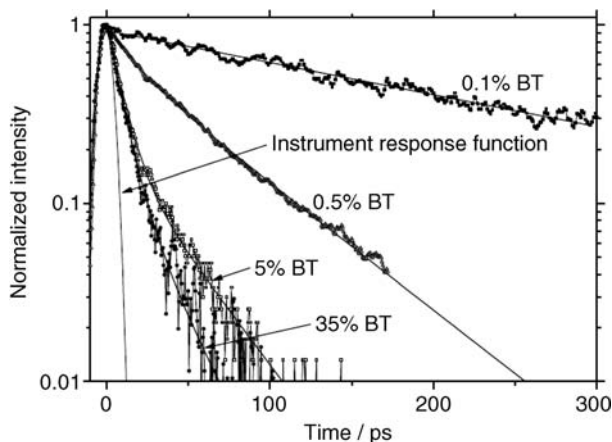


**Figure 25.6** Photoluminescence decay at 440 nm for various PFO/F8BT blends as a function of F8BT content. An increase in F8BT content resulted in a faster decay of PFO fluorescence. Reproduced with permission from Ref. [25]; © 2001, Elsevier.

straightforward as it cannot be considered that the point dipole description is adequate in view of the delocalized nature of the excited states.

Similar PFO/F8BT blends, with F8BT contents of 1, 5 and 50 wt%, spun-cast from two different solvents (chloroform and toluene), were studied by Lidzey and coworkers [26]. Scanning force microscopy showed that the characteristic length-scale of phase-separation was significantly greater when the blend was spin-coated from toluene compared to when a more volatile solvent (e.g., chloroform) was used, in which case a more finely mixed system was obtained. Due to the above-mentioned spectral overlap of the photoluminescence emission of PFO with the absorption of F8BT, which allows for an efficient Förster (dipole–dipole coupling) exciton transfer to occur from PFO to F8BT, Lidzey *et al.* used the residual PFO emission to assess the blend de-mixing (Figure 25.7).

Based on the above-described study, Lidzey *et al.* concluded that in films with a better mixing of the two components there is a more effective energy transfer. In films deposited from chloroform solutions, a content of only 5 wt% F8BT was sufficient to allow a virtually complete energy transfer from PFO to F8BT.

In a subsequent study, the same group used SNOM [27] to map the local efficiency of energy transfer between PFO and F8BT in a ternary blend with the optically transparent polymer poly(methyl methacrylate) (PMMA) in a weight ratio of 80:18:2 (PMMA:PFO:F8BT). When mixed together in solution or cast into a thin film, an efficient energy transfer occurred from PFO to F8BT. However, spectroscopic mapping of the ternary blend using SNOM indicated that energy transfer from PFO to F8BT was hindered, and this effect appeared to be particularly pronounced within the PMMA-rich phase. The authors concluded that the presence of PMMA effectively “diluted” the PFO and F8BT molecules, and thus limited exciton transfer and diffusion (Figure 25.8).

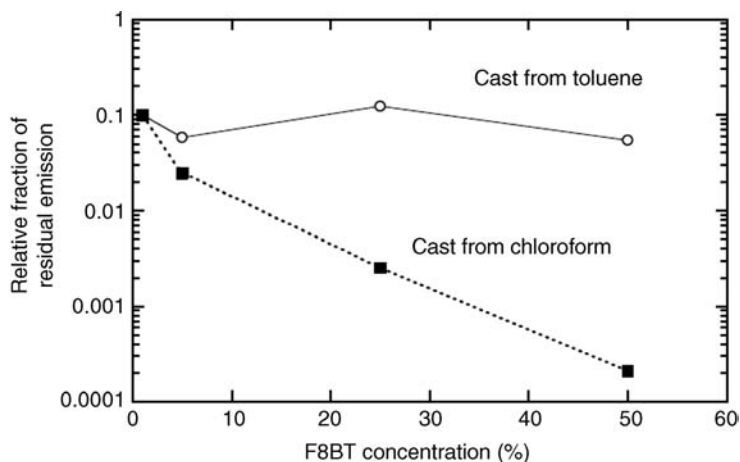


**Figure 25.7** Fractional PFO residual emission (defined as the ratio between PFO emission and the total emission of the blend) as a function of F8BT content. Data are shown for blends cast from both toluene and chloroform.

Note that the fluorescence was generated following laser excitation into the PFO component of the blend. Reproduced with permission from Ref. [26]; © 2005, Elsevier.

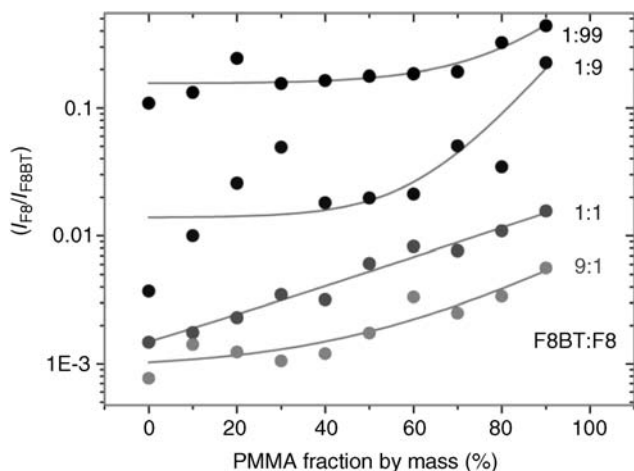


**Figure 25.8** The relative emission ratio of PFO (or F8) to F8BT plotted as a function of PMMA concentration for various F8BT/F8 concentrations (shown next to each data set). The PFO/F8BT emission ratio was determined from far-field measurements of photoluminescence

intensity, by integrating the relative PFO emission between 400 and 480 nm ( $I_{F8}$ ), and comparing this with F8BT emission between 490 and 860 nm ( $I_{F8BT}$ ). Reproduced with permission from Ref. [27]; © 2006, Wiley-VCH.

Cadby *et al.* [28] have used time-resolved SNOM to study the fluorescence emission lifetime of the polymers PFO and F8BT in a phase-separated blend. It was shown that the fluorescence lifetime and quantum efficiency of F8BT varied significantly between the different phase-separated domains, an effect which resulted from the relative efficiency of exciton diffusion to non-radiative defects. Measurements of the PFO emission lifetime indicated that both the PFO- and the F8BT-rich phases contained nanoscale volumes that approximated pure PFO. The PFO decay-lifetime measurements also confirmed the concentration of F8BT to be lower at the interface region between the PFO- and F8BT-rich phases.

Bilayer architectures with well-controlled interfacial roughness were used by Higgins *et al.* [29] to investigate the effect of mixing at a conjugated polymer heterojunction on photoluminescence. It was shown that increased roughness at the PFO/F8BT interfaces would lead to a greatly enhanced Förster transfer from PFO to F8BT chains, and it was concluded that the interfacial roughness is dominated by mixing at the molecular level between the PFO and F8BT chains.

The effect of a poor solvent on the characteristics of the same PFO/F8BT blend films was studied by Cacialli *et al.* [30] using steady-state photoluminescence measurements. In particular, three blends with 25, 15 and 5 wt% of F8BT in PFO, were studied. The photoluminescence of such films was completely dominated by the green-emitting component (F8BT), as the blue-emitting component (PFO) was completely absent as a result of the above-mentioned efficient energy transfer. This was also taken as an indication of the intermixing at a very fine scale of both components. In order to test this hypothesis, the same group treated the films with acetone (which is a poor solvent for both polymers) to promote phase separation between the polymers by swelling. This resulted in a recovery of the PFO blue emission, as shown in the photoluminescence spectra. Subsequent AFM measurements were unable to identify any clear morphological changes between the samples before and after acetone treatment. These findings confirmed that luminescence measurements are more sensitive probes of phase separation than AFM.

Friend *et al.* [31] reported the use of inkjet printing (IJP) to produce thin polymer films with a controlled phase separation of binary polymer blends. Photovoltaic devices comprising a blend of poly(9,9'-dioctylfluorene-*co*-bis-*N,N'*-(4-butylphenyl)-bis-*N,N'*-phenyl-1,4-phenylenediamine) (PFB) with F8BT and LEDs using a blend of F8BT with poly(9,9'-dioctylfluorene-*co*-*N*-(4-butylphenyl)diphenylamine) (TFB) were fabricated (Figure 25.9).

The phase separation in these polymer blends was analyzed using AFM and photoluminescence optical microscopy. The morphology of the films was observed using fluorescence microscopy, under excitations of wide-band ultraviolet or blue illumination. Spin-coating a film of TFB/F8BT blend from a *p*-xylene solution usually yields a lateral phase separation on the order of a few microns, and this can be easily observed by selective absorption using fluorescence microscopy (Figure 25.10a). Whereas, under blue excitation the regions that emit a yellowish-green light (light gray in Figure 25.10a) correspond to the F8BT phase, the areas that remain dark correspond to the TFB phase. Subsequently, islands of TFB up to

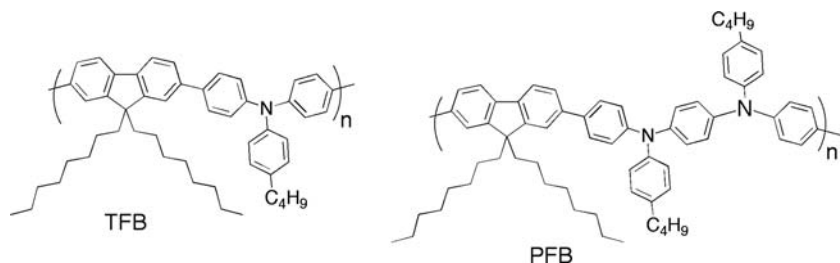


**Figure 25.9** Chemical structures of TFB and PFB.

a few micrometers in size are dispersed in a matrix composed of F8BT. When the blend film is formed by IJP, however, the feature size of lateral phase separation is reduced to around  $1\ \mu\text{m}$  (Figure 25.10b). Although the F8BT-rich regions are still thicker, the film smoothness is greatly improved, with the surface root-mean-square roughness ( $R_{\text{rms}}$ ) reduced to approximately 4.3 nm. By increasing the temperature of the underlying substrates slightly during printing (to ca.  $40^\circ\text{C}$ ), the lateral phase separation is further reduced to about 300 nm, which is beyond the resolution of the optical measurement (Figure 25.10c). The surface becomes very smooth, with  $R_{\text{rms}}$  being reduced to about 1.7 nm; similar results were obtained for the PFB/F8BT blend. It should be noted at this point that the phase separation dimensions range from a few hundred nanometers to a few microns, which is considerably larger than the molecular size. The results show that IJP allows a finer-scale phase separation to be attained than does spin-coating.

The TFB/F8BT blend was also studied by Xia *et al.* [32] using fluorescence microscopy (in combination with oxygen-plasma etching). These authors investigated the internal phase structures of TFB/F8BT blend films and confirmed the presence of a TFB wetting layer close to the substrate. Due to the strong overlap between the emission spectrum of TFB and the absorption spectrum of F8BT, the photoluminescence of TFB was quenched when both phases were present, due to the energy transfer from TFB to F8BT.

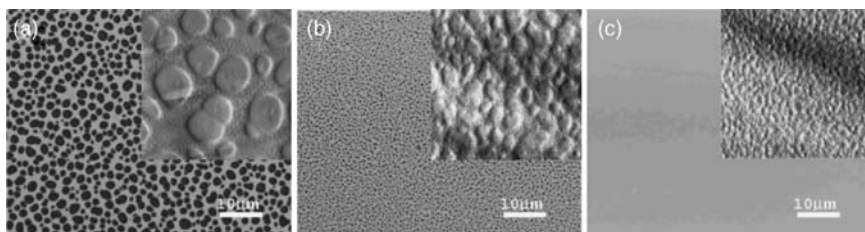


**Figure 25.10** Fluorescence microscopy images ( $10 \times 10\ \mu\text{m}$ ) taken on such films. Blend films were deposited onto indium tin oxide-coated substrates. Reproduced with permission from Ref. [31]; © 2005, American Chemical Society.

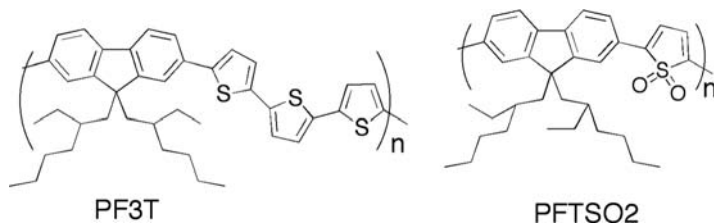
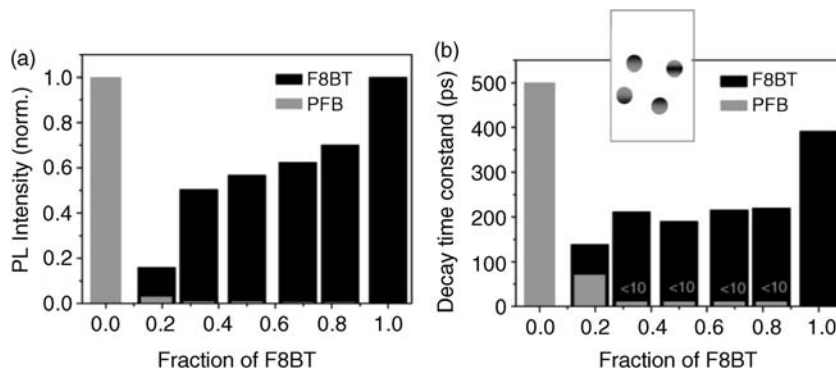


Figure 25.11 Chemical structures of PF3T and PFTSO2.

Blends of PFO with polyfluorene derivatives of lower energy gap, poly(9,9-di(2'-ethylhexyl)fluorene-*alt*-trithiophene) (PF3T) and poly(9,9-di(2'-ethylhexyl)fluorene-*alt*-thiophene-*S,S*-dioxide) (PFTSO2) (see Figure 25.11), were tested in LEDs and characterized by steady-state and picosecond time-resolved fluorescence spectroscopy by Cacialli *et al.* [33]. The blends were prepared with 5 wt% of the lower-energy gap polyfluorene copolymer. The photoluminescence spectrum of the films upon excitation at 400 nm (PFO absorption) was found to be essentially that of the guest copolymer with a residual PFO emission. However, the emission of the guest copolymer was closer to the photoluminescence spectrum in solution, which was blue-shifted to the emission of the neat films. This was interpreted as being associated with exciton confinement in the lower-energy gap polymer.

The picosecond time-resolved fluorescence studies were carried out in the blend films, following excitation at 340 nm, where mainly PFO absorbs. However, when the fluorescence decay was recorded at PFO emission the authors found a much faster decay in the blends than in the neat PFO films, which they explained as being due to energy transfer to the guest copolymer. When the reading was made at the guest copolymer's emission, the authors fitted the fluorescence decay by multiexponential functions (as in Eq. (25.1)) and found that, in both cases, there was a negative component ( $a_i < 0$ ) (rise time), which is a signature of the energy transfer from PFO to each of the guests. The excited state dynamics of the guest copolymers in the blends was found to be similar to that in dilute solutions, indicating exciton confinement to the guest chains (within the blends).

Studies of the morphology of conjugated polymer blend nanoparticles, using fluorescence spectroscopy, have represented a major topic of research during recent years [34–37]. For example, Scherf and coworkers [34] carried out photoluminescence measurements on dilute dispersions of PFB/F8BT nanospheres in water, with the nanospheres having been prepared via a miniemulsion process. This mixture, which consisted of an electron-donor (PFB) and an electron-acceptor (F8BT) combination, was exploited in photovoltaic applications. In view of the relative energy level position (type II heterojunction), excited state charge transfer occurred which, in turn, led to quenching of the PL emission when the second blend component was added. In fact, and as shown in Figure 25.12a, the PFB emission was severely quenched as soon F8BT became present in the particle; the F8BT emission then showed a gradual increase in intensity as the F8BT content was increased. Time-resolved spectra of the diluted nanoparticle dispersions were



**Figure 25.12** (a) Quenching of the photoluminescence of the PFB phase (gray), excited at 380 nm, and the F8BT phase (black), excited at 460 nm, for different ratios of PFB:F8BT in each particle; (b) Fluorescent decay times obtained from time-resolved

photoluminescence spectra for the PFB emission (gray) and the F8BT emission (black) (excitation 394 nm) in pure and blend particles for different ratios. Reproduced with permission from Ref. [34]; © 2004, American Chemical Society.

also recorded. As shown in Figure 25.12b, the photoluminescent decay of the PFB emission became much faster as soon as F8BT became present in the particle, which was consistent with the findings of steady-state photoluminescence emission experiments. The results of these time-resolved experiments indicated that the dissociation of a photogenerated exciton on a PFB chain occurred in less than 10 ps, whereas the dissociation of photogenerated excitons on F8BT was almost one order of magnitude slower. The results obtained were consistent with a morphology that consisted of a phase containing almost exclusively F8BT and a fine scale phase-separated phase of PFB and F8BT.

Nanoparticles based on the same PFB/F8BT blends, prepared also via a miniemulsion process in water, were studied by Landfester and coworkers [36] using photoluminescence measurements. Despite the excited state charge transfer that occurred between these two polymers, a photoluminescence emission (resulting from an interchain exciplex) was detected and used to study the intermixing of the two polymers. The results showed that the PFB-rich phase contained F8BT at a concentration of approximately 15%, while the concentration of PFB in the F8BT-rich phase was in the range 5–10%. The results indicated also that the optical properties of the PFB/F8BT blend systems are mainly determined by the composition of the individual phases, and not by the phase morphology. The photoluminescence which results as a function of blend composition can be easily explained by assuming that the F8BT luminescence originates predominantly from the F8BT-rich phase, while an exciplex emission stems from the PFB-rich phase. This result is quite surprising if the small length scale of phase separation in these particles (as defined by the particle diameter) is borne in mind. Apparently, the minority components in the individual phases largely reduce the exciton diffusion length, and most excitons decay or dissociate within the domains rather than at the domain boundaries.



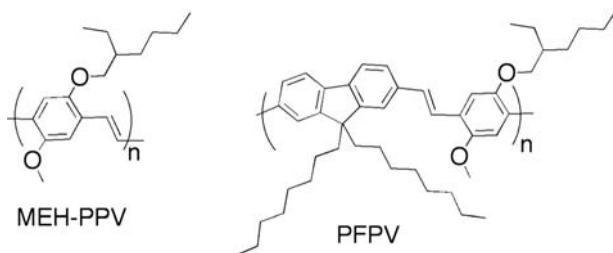


**Figure 25.13** Chemical structures of MEH-PPV and PFPV.

More recently, Gao *et al.* [37] studied energy transfer also in nanoparticles of PFB and F8BT (1 : 1, w/w) using scanning probe and single-particle spectroscopy techniques. The photoluminescence spectra of  $\sim 58$  and  $\sim 100$  nm PFB/F8BT nanoparticles showed an efficient energy transfer from the PFB (donor) component to the F8BT (acceptor) component that was independent of particle size. Based on energy transfer efficiency estimates, the authors proposed that nanoparticles are partially phase-segregated into discrete PFB/F8BT nanodomains on the order of  $\sim 20$ – $40$  nm for both particle sizes.

McNeill *et al.* [35] studied the energy transfer-mediated fluorescence from conjugated polymer nanoparticles consisting of PFO (as host polymer) doped with three different conjugated polymer acceptors, namely the copolymers poly[{9,9-dioctyl-2,7-divinylfluorenylene}-*alt*-{2-methoxy-5-(2-ethylhexyloxy)-1,4-phenylene}] (PFPV); F8BT and the polymer poly[2-methoxy-5-(2'-ethylhexyloxy)-1,4-phenylenevinylene] (MEH-PPV) (Figure 25.13). The fluorescence of the host polymer PFO in the 400–450 nm range possesses a good overlap with the absorption spectra of the three dopant polymers, as would be required for an efficient energy transfer via the Förster mechanism.

The evolution of fluorescence spectra with increasing dopant concentration is shown in Figure 25.14, where the occurrence of a highly efficient energy transfer is clearly evident. The left panels of Figure 25.14 show the fluorescence emission spectra of the three types of blend nanoparticles as a function of the dopant concentration. In the case of the PFO/PFPV nanoparticles, the fluorescence from the PFO host decreased with increasing PFPV content, while that from PFPV increased and reached a maximum at about 6 wt%, after which a further increase in dopant concentration caused a slight reduction in fluorescence intensity. The other two types of blend nanoparticles showed a similar trend in the host fluorescence, but a lower dopant fluorescence intensity that was consistent with the lower fluorescence quantum yields of F8BT and MEH-PPV as compared to PFPV. The dependence of host polymer fluorescence intensity on the concentration of dopant (quencher) was modeled through use of the Stern–Volmer relationship. In the case of PFO/PFPV and PFO/MEH-PPV nanoparticles, the dependence of nanoparticle fluorescence on composition was found to deviate substantially from the Stern–Volmer relationship. This analysis also indicated that approximately 65 PFO

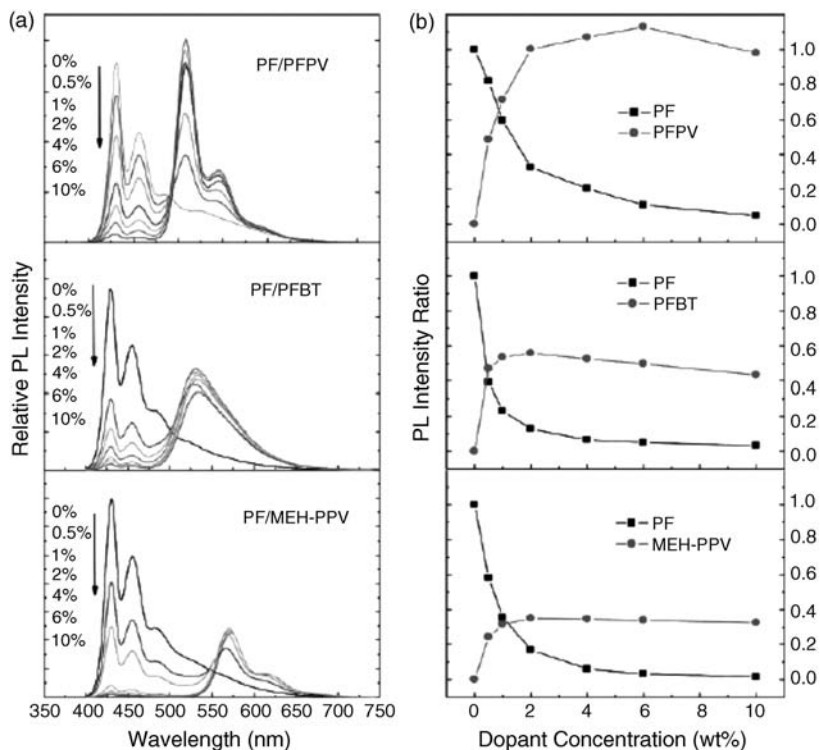


**Figure 25.14** (a) Concentration-dependent fluorescence spectra of polymer blend nanoparticles under 375 nm excitation; (b) Variation of the fluorescence intensity of PFO and dopant polymers in each pair with the dopant

concentration in blend nanoparticles. All fluorescence emission intensities were normalized to the 430 nm emission of pure PFO nanoparticles. Reproduced with permission from Ref. [35]; © 2006, American Chemical Society.

molecules are quenched by a single F8BT molecule, while more than 500 PFO molecules are quenched by a single molecule of either PFPV or MEH-PPV.

## 25.4

### Systems Requiring Extrinsic Fluorescent Labels

As nonconjugated and nonaromatic polymers are nonfluorescent, studies of their phase behavior using fluorescence spectroscopy require the use of extrinsic fluorescent labels [38–40]. These can be either selectively dissolved into the polymer phases [41] or, most commonly, attached covalently to the polymer chains [42–47]. A criticism that is often made of using extrinsic fluorescent probes is the possible local perturbation induced by the probe itself on the nanoenvironment to be probed. In order to minimize such perturbation, the size and shape of the probe should be chosen so as to cause the minimum possible perturbation on the probed region.

The use of fluorescent probes to obtain information about materials distribution in space is most effective when the labeling of both components (in blends) or of different parts of a single component (as is the case for block copolymers) is such that one is labeled with an energy donor fluorophore (D) and the other with an energy acceptor (A) fluorophore. Time-resolved fluorescence studies of the donor can then be used as a tool to assess the relative spatial distribution of the donor- and acceptor-carrying parts. Considering the FRET process that occurs between  $D^*$  and A, and the distance at which this process is effective, an analysis of the dynamics of the D excited states ( $D^*$ ) will provide information on the interface between the two components of a blend, or between the blocks in a copolymer. When addressing the time-dependence of the donor, Eq. (25.1) can be modified to Eq. (25.18), when in the presence of the acceptor,

$$I_D(t) = e^{-t/\tau_D} \cdot q(r, [A]) \quad (25.18)$$

where the decay of the donor excited state is assumed to be, for the sake of simplification, a single exponential function and  $q(r, [A])$  is a quenching-like function due to the energy transfer to A, that leads to a faster fluorescence decay of  $D^*$ , and which depends on the distance between donor and acceptor and on the acceptor concentration. In order to obtain insight about the spatial distribution of D and A in a blend or in a block copolymer, several models have been developed, depending on the geometry of the interface between the A- and D-containing phases. In particular, developments were made for planar [48] and spherical [49,50] symmetries, and also for block copolymers films [51].

Atvars *et al.* [41] performed steady-state fluorescence and time-correlated single-photon counting measurements on samples of poly(vinyl alcohol) (PVA), poly(vinyl acetate) (PVAc) and their blends, labeled noncovalently with fluorescein and/or anthracene probes. The authors determined the interface thickness as being approximately 2.8 nm, and also concluded that the surface-to-volume ratio of PVAc domains was increased in blends with a larger PVAc content.

Roth *et al.* [42] used steady-state fluorescence measurements to study the emission spectra of pyrene and anthracene dyes covalently bonded to polystyrene (PS) upon phase separation from poly(vinyl methyl ether) (PVME). The total fluorescent dye content in the samples was  $<0.02$  mol%. As shown in Figure 25.15a, before phase separation the fluorescence intensity of the spectra decreased slowly with increasing temperature. However, after phase separation (see Figure 25.15b) a sharp increase in fluorescence intensity was observed, which was attributed to the removal of fluorescence quenching of the dye by the local presence of the more polar PVME component in the miscible state. These results showed clearly that the PS/PVME blend displays a lower critical solubility temperature (LCST) type of phase diagram.

Figure 25.15c and d show the temperature dependence of the intensity of 1-pyr-enylmethyl methacrylate-labeled PS (short Py-PS\*) in a (45/5)/50 (PS/PS\*)/PVME blend, where the sharp increase in intensity upon phase separation of the blend is evident. Reproducibility of the measurements across multiple samples is demonstrated in Figure 25.15c, with several time-based measurements of the intensity at

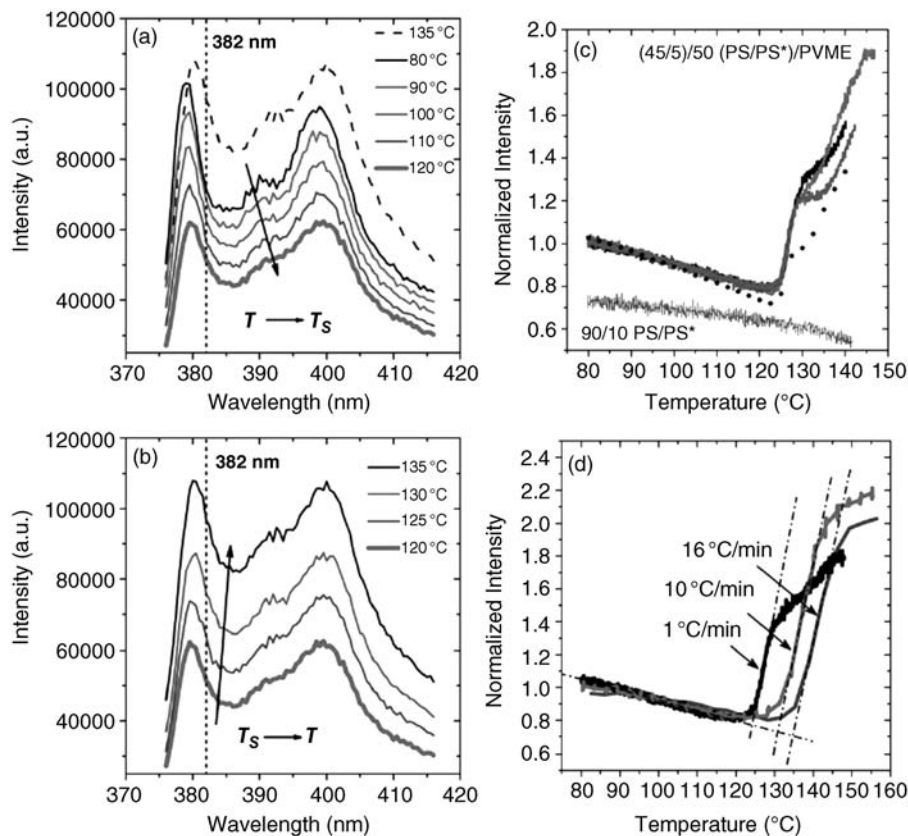


**Figure 25.15** (a, b) Fluorescence emission spectra for short-Py-PS\* in a (45/5)/50 (PS/PS\*)/PVME blend collected at different temperatures; (c, d) Fluorescence intensity of short-

Py-PS\* in a (45/5)/50 (PS/PS\*)/PVME blend as a function of temperature. Reproduced with permission from Ref. [42]; © 2012, John Wiley & Sons, Inc.

382 nm (the vertical dashed line in Figure 25.15a and b) and the integrated intensity from 376 to 416 nm of the emission spectra in Figure 25.15a and b. The authors also found that the specific chemical structure of the fluorescent labels affects the measured phase separation temperature  $T_s$ , with fluorophores covalently attached in closer proximity to the PS backbone identifying phase separation a few degrees earlier.

Steady-state fluorescence spectroscopy has been used by Torkelson *et al.* [43,44] to determine the components' glass transition temperature ( $T_g$ ) in various blends, including blends of PS with poly(*tert*-butyl acrylate) (PtBA), PMMA, and poly(*n*-butyl methacrylate) (PnBMA) [43], as well as in miscible blends of pyrene-labeled PMMA (MPy-labeled PMMA) with poly(ethylene oxide) (PEO) or poly(vinyl chloride) (PVC) over a broad composition range [44]. In the particular case of this latter study [44], the blend  $T_g$ -values were measured upon heating by increasing the

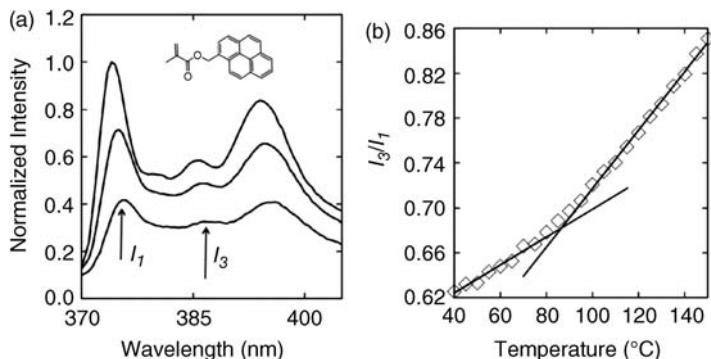


**Figure 25.16** (a) Extrinsic fluorescence spectra of 75 wt% MPy-labeled PMMA in PEO at 150 °C (lowest curve), 100 °C (middle curve), and 50 °C (highest curve), normalized to the first peak intensity at 50 °C (after background subtraction); (b) Intensity ratios as a function

of temperature used to determine  $T_g$ . The value of  $T_g$  is taken from the intersection of the rubbery and glassy state temperature dependences of intensity ratios. Reproduced with permission from Ref. [44]; © 2012, Elsevier.

temperature in 5 °C steps and holding it for 5 min prior to data collection. For MPy-labeled PMMA ( $\lambda_{\text{ex}} = 324$  nm),  $T_g$  was determined via the temperature dependence of the intensity ratio of the third to first vibronic peaks ( $I_3/I_1$ ) of the pyrene dye. The rubbery and glassy state data were fitted with linear regressions, and the intersection of linear regressions was taken as the blend  $T_g$ . Some example results are shown in Figure 25.16 for a 75 wt% MPy-labeled PMMA component blended with PEO.

Fluorescence-SNOM [45] was used for studying the phase behavior of a polymer blend monolayer which consisted of dye-labeled poly(octadecyl methacrylate) (PODMA) and poly(isobutyl methacrylate) (PiBMA), both of which formed stable monolayers at the air–water interface. FRET was observed in the PODMA-rich domain, indicating a mixing of both components at the molecular level. When the temperature was raised to 40 °C, however, phase separation occurred within several minutes and the domain size increased with annealing time. The 2D structure for the completely phase-separated monolayer was studied using time-resolved SNOM.

Atvars *et al.* [46] studied the phase behavior in blends of PS and poly(*n*-butyl methacrylate-*co*-styrene) (*n*BMAS) labeled with anthryl groups, by non-radiative energy transfer (NRET) using both steady-state fluorescence and TCSPC measurements. Miscibility of the blends with several compositions, from 5 to 95% w/w, was studied. For compositions with PS > 80% w/w, a full miscibility was observed, but compositions with 20 < PS < 80% w/w presented a co-continuous morphology with phase separation characteristic of a nucleation-growth mechanism. For blends with PS < 20% w/w, a bicontinuous morphology was observed.

In a related study [47], the same group used steady-state fluorescence spectroscopy coupled to epifluorescence microscopy (fluorescence microspectroscopy) for studying the diffusion of the lower- $T_g$  component during the heating of a binary

blend of the anthracene-labeled poly(*n*-butyl methacrylate-*co*-styrene) (*n*BMAS) with PS.

Extrinsic fluorescent labels have also been used in fluorescence studies of diblock copolymers, as they tend to self-assemble into a diversity of microphase-separated ordered structures such as lamellae, spheres, and cylinders [52–57].

Winnik *et al.* [53] used time-resolved fluorescence spectroscopy (direct non-radiative energy transfer experiments) to determine the interface thickness in films of symmetric poly(styrene-*b*-methyl methacrylate) (PS-PMMA) block copolymers labeled at their junctions with either a 9-phenanthryl or a 2-anthryl group. The corrected donor fluorescence decay profiles were fitted to simulated fluorescence decay curves in which the interface thickness  $\delta$  was the only adjustable parameter. The optimum value of the interface thickness obtained was  $\delta = 4.8$  nm. In similar studies [54–57], the same authors determined the interface thickness value  $\delta = 1.6$  nm in mixtures of two symmetrical poly(isoprene-*b*-methyl methacrylate) (PI-PMMA) block copolymers of similar molar mass and composition [54]; the interface thickness value  $\delta = 1.1$  nm for the lamellar structures formed in films of symmetric PI-PMMA diblock copolymers bearing dyes at the junctions [55]; a cylindrical interface thickness value of  $\delta$  slightly smaller than 1.0 nm in films consisting of mixtures of donor- and acceptor-labeled PI-PMMA (29 vol% PI) that form a hexagonal phase in the bulk state [56]; and the interface thickness  $\delta = 5$  nm on the diblock copolymer poly(styrene-*b*-butyl methacrylate)(PS-*b*-PBMA) [57].

## 25.5

### Conclusions

As exemplified by the numerous examples provided in this chapter, the fluorescent properties of polymer blends are closely related to their corresponding phase behavior and morphology. Therefore, fluorescence spectroscopy is a powerful technique in studies of the phase behavior in polymer blends. The main advantages of the technique are its high spatial and temporal resolutions, whilst its main limitation lays in the fact that it requires the systems under study to be fluorescent.

### Nomenclature

AFM	Atomic force microscopy
BT	Benzothiadiazole
F8 or PFO	Poly(9,9-dioctylfluorene)
F8BT	Poly(9,9-dioctylfluorene- <i>alt</i> -benzothiadiazole)
FRET	Förster (non-radiative) Resonance Energy Transfer
IJP	Ink Jet Printing
LCST	Lower Critical Solubility Temperature

LUMO	Lowest Unoccupied Molecular Orbital
MEH-PPV	Poly[2-methoxy-5-(2'-ethylhexyloxy)-1,4-phenylenevinylene]
<i>n</i> BMAS	Poly( <i>n</i> -butyl methacrylate- <i>co</i> -styrene)
P3HT	Poly(3-hexyl thiophene)
PCBM	[6,6]-phenyl-C61-butyric acid methyl ester
PEO	Poly(ethylene oxide)
PF3T	Poly(9,9-di(2'-ethylhexyl)fluorene- <i>alt</i> -trithiophene)
PFB	Poly(9,9- dioctylfluorene- <i>co</i> -bis- <i>N,N'</i> -(4-butylphenyl)-bis- <i>N,N'</i> -phenyl-1,4-phenylenediamine)
PFBT	Poly[(9,9-dioctylfluorenyl-2,7-diyl)- <i>alt</i> -(1,4-benzo-{2,1',3}-thiadiazole)]
PFPV	Poly[{9,9-dioctyl-2,7-divinyleneffluorenylene}- <i>alt</i> -(2-methoxy-5-(2-ethylhexyloxy)-1,4-phenylene)]
PFTSO2	Poly(9,9-di(2'-ethylhexyl)fluorene- <i>alt</i> -thiophene- <i>S,S</i> -dioxide)
PiBMA	Poly(isobutyl methacrylate)
PI-PMMA	Poly(isoprene- <i>b</i> -methyl methacrylate)
PL	Photoluminescence
PLEDs	Polymer Light-Emitting Diodes
PMMA	Poly(methyl methacrylate)
P <i>n</i> BMA	Poly( <i>n</i> -butyl methacrylate)
PODMA	Poly(octadecyl methacrylate)
PS	Polystyrene
PS- <i>b</i> -PBMA	Poly(styrene- <i>b</i> -butyl methacrylate)
PS-PMMA	Poly(styrene- <i>b</i> -methyl methacrylate)
PtBA	Poly( <i>tert</i> -butyl acrylate)
PVA	Poly(vinyl alcohol)
PVAc	Poly(vinyl acetate)
PVC	Poly(vinyl chloride)
PVME	Poly(vinyl methyl ether)
$R_{rms}$	Root-mean-square roughness
SNOM	Scanning Near-field Optical Microscopy
TCSPC	Time-Correlated Single Photon Counting
TFB	Poly(9,9-dioctylfluorene- <i>alt</i> - <i>N</i> -(4-butylphenyl)diphenylamine)
$T_g$	Glass transition temperature
$T_m$	Melting temperature

## Acknowledgments

G.B. would like to thank the Portuguese Foundation for Science and Technology (FCT) for their support through the program PEst-C/CTM/LA0025/2013 (Strategic Project – LA 25 – 2013-2014). J.M. acknowledges FCT's support under the contract PEst-OE/EEI/LA0008/2013.

## References

- 1 Paul, D.R. and Bucknall, C.B. (1999) *Polymer Blends*, John Wiley & Sons Inc.
- 2 Moons, E. (2002) Conjugated polymer blends: linking film morphology to performance of light emitting diodes and photodiodes. *J. Phys. Condens. Matter*, 14 (47), 12235–12260.
- 3 Schnabel, W. (2007) *Polymers and Light – Fundamentals and Technical Applications*, Wiley-VCH Verlag.
- 4 Guillet, J. (1987) *Polymer Photophysics and Photochemistry – An Introduction to the Study of Photoprocesses in Macromolecules*, Cambridge University Press.
- 5 Valeur, B. (2001) *Molecular Fluorescence – Principles and Applications*, Wiley-VCH Verlag.
- 6 Lanzani, G. (2012) *The Photophysics Behind Photovoltaics and Photonics*, Wiley-VCH, Weinheim.
- 7 Lofroth, J.E. (1986) Time-resolved emission spectra, decay-associated spectra, and species-associated spectra. *J. Phys. Chem.*, 90 (6), 1160–1168.
- 8 Lakowicz, J.R. (2006) *Principles of Fluorescence Spectroscopy*, 3rd edn, Springer, Baltimore.
- 9 Forster, T. (1948) Zwischenmolekulare energiewanderung und fluoreszenz. *Annalen Der Physik*, 2 (1-2), 55–75.
- 10 Dexter, D.L. (1953) A theory of sensitized luminescence in solids. *J. Chem. Phys.*, 21 (5), 836–850.
- 11 Farinha, J.P.S. and Martinho, J.M.G. (2008) Resonance energy transfer in polymer nanodomains. *J. Phys. Chem. C*, 112 (29), 10591–10601.
- 12 Scholes, G.D. (2003) Long-range resonance energy transfer in molecular systems. *Annu. Rev. Phys. Chem.*, 54, 57–87.
- 13 Jones, R.A.L. and Richards, R.W. (1999) *Polymers at Surfaces and Interfaces*, Cambridge University Press.
- 14 Berberan-Santos, M.N. (ed.) (2008) *Fluorescence of Supermolecules, Polymers and Nanosystems*, Springer Series on Fluorescence, vol. 4, Springer-Verlag.
- 15 Tanke, H.J. (1997) Fluorescence microscopy, in *Royal Microscopical Society Microscopy Handbooks*, 2nd edn, Garland Science.
- 16 Mueller, M.A. (2006) *Introduction to Confocal Fluorescence Microscopy*, 2nd revised edn, SPIE Tutorial Texts, SPIE Press, Washington, USA.
- 17 Stevenson, R., Granstrom, M., and Richards, D. (1999) Fluorescence scanning near-field optical microscopy of conjugated polymer blends. *Appl. Phys. Lett.*, 75 (11), 1574–1576.
- 18 Shirakawa, H. *et al.* (1977) Synthesis of electrically conducting organic polymers – halogen derivatives of polyacetylene, (CH) X. *J. Chem. Soc. Chem. Commun.*, (16), 578–580.
- 19 Burroughes, J.H. *et al.* (1990) Light-emitting-diodes based on conjugated polymers. *Nature*, 347 (6293), 539–541.
- 20 Cicoira, F. and Santato, C. (eds) (2013) *Organic Electronics: Emerging Concepts and Technologies*, Wiley-VCH, Weinheim.
- 21 Meller, G. and Grasser, T. (eds) (2010) *Organic Electronics*, in *Advances in Polymer Science*, Springer-Verlag, Berlin, Heidelberg.
- 22 Brütting, W. and Adachi, C. (eds) (2012) *Physics of Organic Semiconductors*, 2nd edn, Wiley-VCH, Weinheim.
- 23 Someya, T. *et al.* (2005) Conformable, flexible, large-area networks of pressure and thermal sensors with organic transistor active matrixes. *Proc. Natl Acad. Sci. USA*, 102 (35), 12321–12325.
- 24 Bauer, S. *et al.* (2014) 25th anniversary article: a soft future: from robots and sensor skin to energy harvesters. *Adv. Mater.*, 26 (1), 149–162.
- 25 Buckley, A.R. *et al.* (2001) Energy transfer dynamics in polyfluorene-based polymer blends. *Chem. Phys. Lett.*, 339 (5–6), 331–336.
- 26 Voigt, M. *et al.* (2005) The interplay between the optical and electronic properties of light-emitting-diode applicable conjugated polymer blends and their phase-separated morphology. *Org. Electron.*, 6 (1), 35–45.
- 27 Cadby, A. *et al.* (2006) Suppression of energy-transfer between conjugated polymers in a ternary blend identified using scanning near-field optical microscopy. *Adv. Mater.*, 18 (20), 2713.



- 28 Cadby, A.J. *et al.* (2007) Imaging the fluorescence decay lifetime of a conjugated-polymer blend by using a scanning near-field optical microscope. *Adv. Mater.*, 19 (1), 107.
- 29 Higgins, A.M. *et al.* (2009) The impact of interfacial mixing on Forster transfer at conjugated polymer heterojunctions. *Adv. Funct. Mater.*, 19 (1), 157–163.
- 30 Morgado, J. *et al.* (2001) De-mixing of polyfluorene-based blends by contact with acetone: Electro- and photo-luminescence probes. *Adv. Mater.*, 13 (11), 810.
- 31 Xia, Y.J. and Friend, R.H. (2005) Controlled phase separation of polyfluorene blends via inkjet printing. *Macromolecules*, 38 (15), 6466–6471.
- 32 Xia, Y.J. and Friend, R.H. (2006) Phase separation of polyfluorene-based blend films and its influence on device operations. *Adv. Mater.*, 18 (11), 1371.
- 33 Charas, A. *et al.* (2002) Excitation energy transfer and spatial exciton confinement in polyfluorene blends for application in light-emitting diodes. *J. Mater. Chem.*, 12 (12), 3523–3527.
- 34 Kietzke, T. *et al.* (2004) A nanoparticle approach to control the phase separation in polyfluorene photovoltaic devices. *Macromolecules*, 37 (13), 4882–4890.
- 35 Wu, C. *et al.* (2006) Energy transfer mediated fluorescence from blended conjugated polymer nanoparticles. *J. Phys. Chem. B*, 110 (29), 14148–14154.
- 36 Kietzke, T. *et al.* (2007) Phase separation of binary blends in polymer nanoparticles. *Small*, 3 (6), 1041–1048.
- 37 Gao, J. and Grey, J.K. (2012) Spectroscopic studies of energy transfer in fluorene co-polymer blend nanoparticles. *Chem. Phys. Lett.*, 522, 86–91.
- 38 Beija, M., Charreyre, M.-T., and Martinho, J.M.G. (2011) Dye-labelled polymer chains at specific sites: Synthesis by living/controlled polymerization. *Prog. Polym. Sci.*, 36 (4), 568–602.
- 39 Wu, J. *et al.* (2003) Synthesis and microstructure characterization of dye-labeled poly(vinyl acetate-co-dibutyl maleate) latex for energy transfer experiments. *Macromolecules*, 36 (21), 8139–8147.
- 40 Guo, R. *et al.* (2012) Facile and efficient synthesis of fluorescence-labeled RAFT agents and their application in the preparation of  $\alpha$ - $\omega$ - and  $\alpha$ , $\omega$ -end-fluorescence-labeled polymers. *Macromol. Chem. Phys.*, 213 (17), 1851–1862.
- 41 Atvars, T.D.Z. *et al.* (1997) Structural study of polymer blends by fluorescence spectroscopy. *J. Lumin.*, 72–74 (0), 467–469.
- 42 Kriisa, A., Park, S.S., and Roth, C.B. (2012) Characterization of phase separation of polystyrene/poly(vinyl methyl ether) blends using fluorescence. *J. Polym. Sci. Polym. Phys.*, 50 (4), 250–256.
- 43 Evans, C.M., Sandoval, R.W., and Torkelson, J.M. (2011) Glass transition temperature of a component near infinite dilution in binary polymer blends: determination via fluorescence spectroscopy. *Macromolecules*, 44 (17), 6645–6648.
- 44 Evans, C.M. and Torkelson, J.M. (2012) Determining multiple component glass transition temperatures in miscible polymer blends: Comparison of fluorescence spectroscopy and differential scanning calorimetry. *Polymer*, 53 (26), 6118–6124.
- 45 Aoki, H. and Ito, S. (2001) Two-dimensional polymers investigated by scanning near-field optical microscopy: Phase separation of polymer blend monolayer. *J. Phys. Chem. B*, 105 (20), 4558–4564.
- 46 de Andrade, M.L. and Atvars, T.D.Z. (2004) Dynamic and static fluorescence spectroscopy applied to miscibility of poly(*n*-butyl methacrylate-co-styrene) with polystyrene and morphological analysis by epifluorescence microscopy. *J. Phys. Chem. B*, 108 (13), 3975–3984.
- 47 de Andrade, M.L. and Atvars, T.D.Z. (2004) Diffusion of a single component in a binary polymer blend upon annealing monitored by fluorescence microspectroscopy. *Macromolecules*, 37 (25), 9626–9630.
- 48 Yekta, A., Duhamel, J., and Winnik, M.A. (1995) Dipole-dipole electronic-energy transfer – fluorescence decay functions for arbitrary distributions of donors and acceptors – systems with planar geometry. *Chem. Phys. Lett.*, 235 (1–2), 119–125.

- 49 Farinha, J.P.S. *et al.* (1996) Latex film formation probed by nonradiative energy transfer: Effect of grafted and free poly (ethylene oxide) on a poly(n-butyl methacrylate) latex. *J. Phys. Chem.*, 100 (30), 12552–12558.
- 50 Yekta, A. *et al.* (1997) Dipole–dipole electronic energy transfer. Fluorescence decay functions for arbitrary distributions of donors and acceptors. 2. Systems with spherical symmetry. *J. Phys. Chem. A*, 101 (10), 1787–1792.
- 51 Farinha, J.P.S. and Martinho, J.M.G. (1997) Electronic energy transfer in restricted geometries – Application to the study of spherical and planar interphases of diblock copolymer films. *J. Lumin.*, 72–4, 914–917.
- 52 Lazzari, M., Liu, G., and Lecommandoux, S. (eds) (2006) *Block Copolymers in Nanoscience*, Wiley-VCH Verlag GmbH & Co. KGaA, Weinheim.
- 53 Rharbi, Y. and Winnik, M.A. (2001) Interface thickness of a styrene-methyl methacrylate block copolymer in the lamella phase by direct nonradiative energy transfer. *Macromolecules*, 34 (15), 5238–5248.
- 54 Yang, J. *et al.* (2003) Energy transfer study of the interface thickness in symmetrical isoprene-methyl methacrylate diblock copolymers. *Macromolecules*, 36 (12), 4485–4491.
- 55 Yang, J. *et al.* (2005) Energy transfer study of symmetric polyisoprene-poly(methyl methacrylate) diblock copolymers bearing dyes at the junctions: Dye orientation. *Macromolecules*, 38 (4), 1256–1263.
- 56 Yang, J. *et al.* (2006) Energy transfer study of the cylindrical interface formed by asymmetric isoprene-methyl methacrylate diblock copolymers bearing a dye at the junction. *Macromolecules*, 39 (6), 2405–2412.
- 57 Spiro, J.G. *et al.* (2006) Experimental and theoretical investigation of the lamellar structure of a styrene-butyl methacrylate diblock copolymer by fluorescence resonance energy transfer, small-angle X-ray scattering, and self-consistent-field simulations. *Macromolecules*, 39 (20), 7055–7063.

## 26

# Characterization of Polymer Blends by Dielectric Spectroscopy and Thermally Simulated Depolarization Current

*Samy A. Madbouly and Michael R. Kessler*

## 26.1

### Introduction

### 26.1.1

#### Dielectric Relaxation Spectroscopy and Thermally Stimulated Depolarization Current

Dielectric relaxation spectroscopy (DRS), also known as electrochemical impedance spectroscopy, is a powerful tool that provides information about the molecular dynamics and the nature of interactions in polymer blends by monitoring the motion of dipolar groups attached to molecular chains. This technique measures the dielectric relaxation properties of polymer materials as a function of frequency and temperature, based on the interactions of an alternating external field with the electric dipole moment of the samples. DRS has been widely used to evaluate the degree of miscibility in polymer blends [1–10]. It has also been used to study the motions of mobile charges or ionic conductivity, data that could not be obtained using dynamic mechanical analysis (DMA). The fact that DRS covers a much wider frequency range than DMA constitutes another advantage. Because of the selective amplification of the dielectric relaxation processes related to the dynamic glass transition of polymers, accurate relaxation data – even for the minor phases in polymer blends – can be obtained. Peak shifting, broadening or changing in dielectric relaxation strength (i.e., dielectric loss peak intensity) are commonly observed in the main segmental  $\alpha$ -relaxation processes of the pure components in miscible or partially miscible polymer blends. DRS requires that at least one of the polymer components has a permanent dipole moment; therefore, it can also be used in blends in which one of the blend components is nonpolar and thus is invisible to the dielectric technique. This permits the specific monitoring of various relaxation processes of the polar component in blends of different compositions.

DRS is not only able to determine the degree of miscibility of polymer blends but also provides an accurate technique to study the crystallization kinetics of amorphous/crystalline polymer blends. The crystallization kinetics are identified by the significant changes in molecular dynamics of the amorphous phase during the isothermal crystallization process [10–18]. It is assumed that the degree of

crystallinity at a certain crystallization time and temperature can be accurately evaluated using the time dependence of the real part of the dielectric permittivity during isothermal crystallization. Therefore, the decrease in permittivity due to transition of the amorphous phase into a crystalline and rigid amorphous phase can be monitored as a function of crystallization time at a constant crystallization temperature, based on the Avrami approach. A combination of wide angle X-ray scattering technique and DRS has been used to monitor in real time the evolution of both, structure in the crystalline phase and dynamics in the amorphous phase during the crystallization process [19,20].

DRS is also an effective tool for investigating the molecular dynamics of reactive polymer blends, including the formation of covalent bonds such as in thermoset polymer blends, blends having transesterification reactions, and immiscible blends with compatibilizers. Here, the peak maximum associated with the glass transition temperature ( $T_g$ ;  $\alpha$ -relaxation process) is normally shifted to lower frequencies (longer relaxation times) as the restriction of chain motion increases with the chemical reaction. The dielectric properties during the curing of thermosetting polymer blends are determined by the changing chemical composition as chemical reactions occur. The changing chemical composition also causes a change in the concentration of various dipolar molecular segments, as well as their rotational degree of freedom [21,22]. The wide frequency range of the DRS technique is especially useful when studying the influence of network modifications on polymer chain mobility.

The thermally stimulated depolarization current (TSDC) method is another dielectric technique used to investigate slow polarization processes in the time domain and to evaluate polymer blend miscibility. This technique is based on measuring the polarization and depolarization currents following the application of a direct current electric field over a wide range of temperatures to observe different dielectric relaxation processes in the material. TSDC is carried out in a very low frequency range, allowing high resolution of different relaxation processes during the heating of the sample from the glassy state to above the  $T_g$ , as shown schematically in Figure 26.1 [23]. The high intensity -peak which appeared above the main  $\alpha$ -relaxation peak is attributed to the depolarization process of ionic conductivity. The temperature dependence of different current maxima in the TSDC spectra can provide accurate information about blend miscibility, segmental, and local dynamics of the polymer components.

### 26.1.2

#### Analysis of Relaxation Spectrum

Suitable theoretical models (e.g., the Havriliak–Negami (HN) model [24]) for analyzing the relaxation behavior of polymer blends (including amorphous/crystalline and thermosetting polymer mixtures) as a function of composition, temperature, crystallization and curing times can be used to evaluate the dielectric relaxation strength of a particular relaxation process and provide suitable information about the number of segments that contribute to the different relaxation processes. In

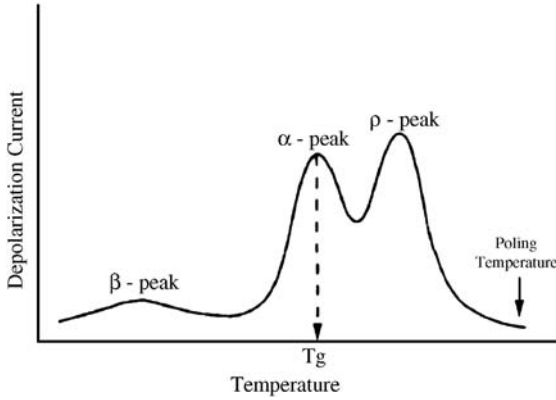


**Figure 26.1** Schematic diagram of the different relaxation processes as a function of temperature. Reprinted with permission from Ref. [23].

general, the HN model provides the most versatile equation for describing the entire dielectric relaxation spectrum, as it can readily account for the asymmetric relaxation broadening typically encountered in polymer blends, particularly in those with physically or chemically crosslinked networks. The HN equation (Eq. (26.1)) is also essential for the simulation of  $\alpha$ - and  $\beta$ -relaxation [24] processes and for studying the variation of the dipole interaction of the polymeric segments with blending:

$$\frac{\epsilon^*(\omega) - \epsilon_\infty}{\epsilon_0 - \epsilon_\infty} = \frac{1}{(1 + (i\omega\tau_0)^b)^c} \quad (26.1)$$

where  $\omega$  is the angular frequency ( $\omega = 2\pi f$ ),  $b$  and  $c$  are parameters describing the shape of the relaxation time distribution function,  $\tau$  is the relaxation time,  $\epsilon^*$  is the complex dielectric permittivity, and  $\epsilon_0$  and  $\epsilon_\infty$  are the limited low- and high-frequency permittivities, respectively. The HN equation reduces to the Cole–Cole relationship (symmetric curves) when  $c = 1$  [25]. The following equation can be used to describe the contribution of ionic conductivity to the dielectric relaxation spectrum:

$$\epsilon'' = \frac{\sigma_{dc}}{\epsilon_0 \omega} \quad (26.2)$$

where  $\sigma_{dc}$  is the direct current conductivity. The HN model provides information on the dielectric relaxation strength,  $\Delta\epsilon$ , the maximum relaxation frequency,  $f_{max}$ , and the distribution parameters of each relaxation process. The relaxation time of each relaxation process,  $\tau_{max} = 1/2\pi f_{max}$  can be calculated using the HN equation as a fitting parameter with the following equation [26]:

$$\tau_{max} = \tau_{HN} \left[ \frac{\sin\left(\frac{\pi ab}{2 + 2b}\right)}{\sin\left(\frac{\pi a}{2 + 2b}\right)} \right]^{1/a} \quad (26.3)$$

where  $\tau_{\max} = \tau_{\text{HN}}$  when  $b = 1$ . The dielectric relaxation strength,  $\Delta\epsilon$ , at a given temperature can be obtained according to the following Frohliche–Onsager equation [27,28]:

$$\Delta\epsilon_\alpha = \epsilon_0 - \epsilon_\infty \propto \frac{n}{T} g(T) \mu^2(T) \quad (26.4)$$

where  $n$  is the number density of dipole moments,  $g$  is the orientation correlation factor, and  $\mu$  is the dipole moment. This approximation shows that  $\Delta\epsilon$  is proportional to the number of dipole moments at a given temperature.

### 26.1.3

#### Effect of Temperature on Relaxation Spectrum

Studying the temperature dependence of different segmental and local relaxation processes ( $\alpha$ -,  $\beta$ -,  $\gamma$ -, and  $\delta$ -) using DRS or TSDC techniques is crucial to understanding the molecular dynamics and miscibility behavior of polymer blends. It is well established that the local relaxation processes of polymers are typically non-cooperative processes originating from the reorientational motions of a small number of molecules or molecular groups confined to certain sites of loose packing created by frozen-in density fluctuations [5–8]. Generally, the dynamics of the local relaxation processes exhibit an Arrhenius behavior; that is, the relationship between relaxation time  $[\log(\tau)]$  and  $1/T$  is linear [29]. However, the glass relaxation process ( $\alpha$ -relaxation) is a large-scale, segmental, micro-Brownian cooperative motion that displays non-Arrhenius behavior. Such processes depend on free volume availability, and can be described by either the Williams–Landel–Ferry (WLF), Vogel–Fulcher–Tammann (VFT) or Meander model. The VFT equation is widely used to interpret the molecular dynamics of  $\alpha$ -relaxation processes according the following equation [30]:

$$\tau = \tau_0 \exp \left[ \frac{B}{T - T_0} \right] \quad (26.5)$$

where  $\tau_0$ ,  $B$ , and  $T_0$  are fitting parameters with different physical significance, while  $\tau$  and  $T$  are relaxation time and temperature, respectively.

Pechhold *et al.* [31,32] developed and defined the concept of free volume for the molecular dynamics of amorphous and semicrystalline polymers. Their “Meander model” considers that the polymer chains are arranged in bundles, which can form a meander cube in a three-dimensional volume, as shown schematically in Figure 26.2.

The temperature dependence of the molecular dynamics of  $\alpha$ -relaxation processes can be well described by the Meander model [31–33]:

$$f_m = \frac{f_0}{\pi} \exp(-Q_\gamma/RT) \{1 - (1 - \exp(-\epsilon_s/RT))^{3r/d}\}^{3(d/s)(3r/d)^2} \quad (26.6)$$

where  $f_0$  is the local vibration frequency of a segment,  $Q_\gamma$  is the local activation energy of a segment,  $\epsilon_s$  is the dislocation energy,  $s$  is the segmental length,  $r$  is the

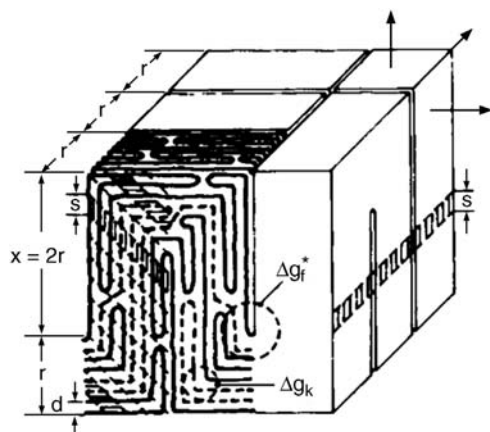


Figure 26.2 Schematic diagram of the Meander cube. Reprinted with permission from Ref. [31].

bundle diameter, and  $d$  is the interchain distance. This model was derived by replacing the free volume theory by the dislocation concept, and is described elsewhere [31–33].

In this chapter, new insights into the molecular dynamics, miscibility, nature of interaction, crystallization behavior, and curing kinetics of representative examples of polymer blends using DRS and TSDC techniques will be reviewed. This should provide a solid basis for understanding the effect of blending on polymer relaxation behavior for a wide range of different types of polymer blends. It will also be shown that the different relaxation processes in polymer blends can be analyzed using the HN model and ionic conductivity equations. The molecular dynamics of the glass relaxation process in blends will also be described, using different theoretical approaches, such as the VFT and Meander models. The variation of the dynamic constraints or the change in the distribution of relaxation times caused by blending for both  $\alpha$ - and  $\beta$ -relaxation processes will be also considered. The real-time crystallization kinetics of different amorphous/crystalline polymer blends will also be described. The crystallization kinetics of blends will be investigated under various experimental variables, such as blend composition, crystallization temperature, and crystallization time. Overall, the chapter will provide a quantitative, experimental and theoretical basis for the description of molecular dynamics and relaxation of a wide range of different polymer blends, the aim being to increase knowledge of the behavior of this important class of polymeric materials and other similar blends.

## 26.2

### Dielectric Relaxation Spectroscopy of Amorphous Polymer Blends

The miscibility and molecular dynamics of different amorphous blend systems, such as poly(methylmethacrylate) (PMMA)/polystyrene (PS), polyisoprene (PI)/

poly(*tert*-butylstyrene) (PtBS), poly(vinyl chloride-*co*-vinylacetate-*co*-2-hydroxypropyl acrylate) (PVVH)/PMMA, poly(vinyl methyl ether) (PVME)/poly(2-vinylpyridine) (P2VPy), PMMA/poly(styrene-*co*-maleic anhydride) (SMA), PMMA/poly( $\alpha$ -methyl styrene-*co*-acrylonitrile) (P $\alpha$ MSAN), poly(4-vinylphenol) (PVPh)/PMMA, and others will be summarized. The effect of blending on the kinetics of glass and local relaxation processes as function of composition, frequency and temperature using DRS and TSDC will be reported. The different relaxation processes in the blends will be analyzed using the HN and ionic conductivity equations, while the glass relaxation process in the blends will be described using the Meander model or VFT equation. In addition, the relaxation strengths ( $\Delta\epsilon$ ) of the  $\alpha$ - and  $\beta$ -relaxation processes will be calculated as a function of composition from the analysis of dielectric relaxation spectra. The variation of the dynamical constraints or the change in the distribution of relaxation times caused by blending for the  $\alpha$ - and  $\beta$ -relaxation processes will also be considered.

Liu *et al.* [34] reported the dielectric relaxation properties of PMMA, PS-*b*-PMMA diblock copolymers and PS/PMMA blends over a wide range of frequencies (0.01 to 1 MHz) and temperatures ( $-40$  to  $150^\circ\text{C}$ ). The dielectric spectrum was resolved into  $\alpha$ - and  $\beta$ -relaxation processes as well as ionic conductivity for different blend compositions. The characteristic relaxation times, fragility indices, activation energies, and dielectric relaxation strengths of PMMA/PS-*b*-PMMA blends were also investigated. It was found that blending significantly suppressed the  $\alpha$ -relaxation process of the copolymers compared to PMMA. The covalent chemical bonds linking PS and PMMA blocks in the diblock copolymers were found to play a dominant role in suppressing the  $\alpha$ -relaxation processes and in decreasing the activation energies of localized  $\beta$ -relaxation processes of the diblock copolymers.

The molecular dynamics of miscible, low-molecular-weight PI and PtBS blends was investigated over the entire composition range, using DRS [35]. The low molecular weights of the two polymer components ( $M_n = 1300$  and  $2300$  Da for PtBS and PI, respectively) were chosen to be well below the entanglement limit of PI. A considerable increase in peak broadening was observed for both low- and high-frequency tails of the normal mode (NM) relaxation process as PtBS concentration was increased and, for a given composition, as the temperature decreased. The magnitude of the broadening in this miscible polymer blend was found to depend on the blend composition, temperature, and dynamic asymmetry (i.e., the difference between the pure component's  $T_g$ ). The observed peak broadening correlated well with freezing of the segmental relaxation of the PtBS component. It was observed that, in blends of PI with high- $T_g$  PtBS, both the  $\alpha$ - and NM-relaxation processes were slowed relative to those observed in the homopolymer. As can be seen in Figure 26.3, the  $\alpha$ -relaxation process shifted to a higher frequency apart with decreasing concentration of PI. In addition, the distance between the  $\alpha$ - and NM-relaxation at 1 Hz ranged from about three decades for a high PI content to almost five to six decades for the 20% PI blends (see Figure 26.3).

The molecular dynamics and dipolar relaxation mechanism of PVVH, PMMA and their blends were investigated using the TSDC technique [36]. Two



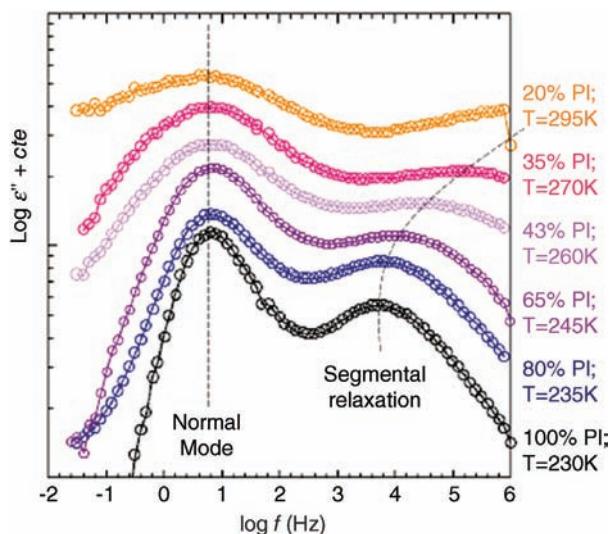


**Figure 26.3** Imaginary part of the relative dielectric permittivity for PI and PI in PI27/PtBS23 blends at different concentrations and temperatures. The different curves have been shifted along the y-axis for clarity. Reprinted with permission from Ref. [35].

$\alpha$ -relaxation processes were observed for PVVH/PMMA blends, indicating that the two polymer components were not completely compatible. The peak maximum of the  $\alpha$ -relaxation process of PVVH was shifted to higher temperatures as the PVVH content decreased. In addition, kinetic parameters such as activation energy, pre-exponential factor and dipole–dipole interaction strength parameter were determined using an iterative technique based on the Arrhenius relaxation model.

Runt and coworkers studied the miscibility and dynamics of intermolecularly hydrogen-bonded polymer blends of poly(*p*-(hexafluoro-2-hydroxyl-2-propyl)styrene) (HFS) with poly(vinyl acetate) (PVAc), poly(ethylene[30%]-*co*-vinyl acetate [70%]), and poly(ethylene[55%]-*co*-vinyl acetate[45%]) (EVA) using DRS [37]. All blend components exhibited local  $\beta$ -relaxation processes that were strongly influenced by the formation of intermolecular associations. Single  $\alpha$ -relaxation processes were observed in all blends, indicating a strong segmental-level coupling. The fragility of the glass-formers was dependent on the volume fraction of intermolecularly associated segments, and the association model predicted which compounds had the highest fragilities. The temperature dependence of the  $\alpha$ -relaxation processes of the blends was well described by the VFT equation. The fragility parameter was calculated from the fitting parameters of the VFT equation [38]. It was reported that the fragility of intermolecularly hydrogen-bonded polymer blends did not depend on the  $T_g$  of the blend, but on the fraction of intermolecularly associated segments [39]. In addition, an  $\alpha$ -relaxation process related to the breaking and reforming of hydrogen bonds was observed at temperatures

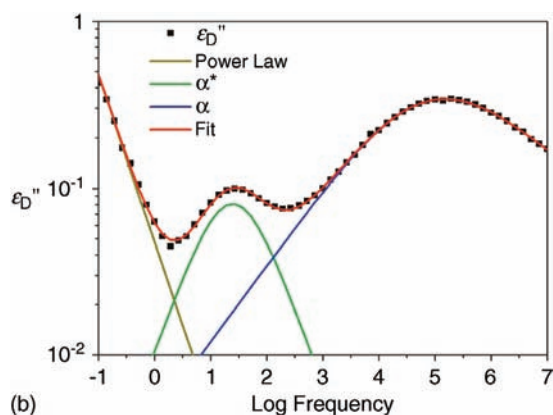
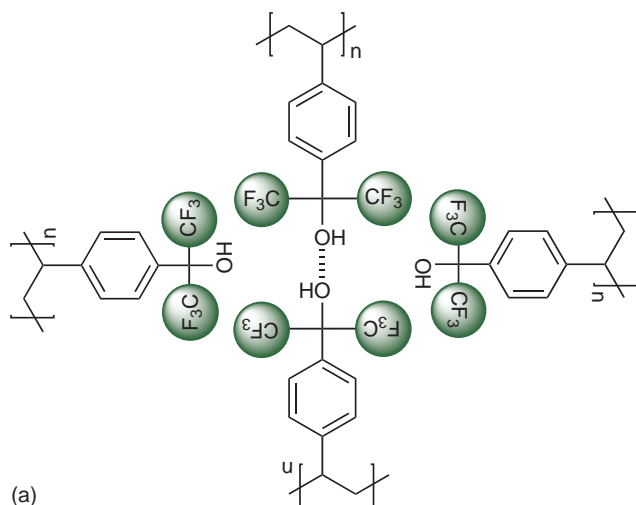


**Figure 26.4** (a) Schematic diagram of the strong intermolecular associations in poly(*p*-(hexafluoro-2-hydroxyl-2-propyl)styrene) (HFS). Reprinted with permission from Ref. [39]; (b) Representative fit of the  $\alpha$ - and  $\alpha^*$ -relaxation processes. Reprinted with permission from Ref. [39].

above the  $\alpha$ -relaxation process, and its temperature dependence varied systematically with ethylene content.

The dynamics of miscible blends of HFS with PVME and P2VPy were investigated via DRS [39]. The HFS moiety forms strong intermolecular associations with proton-accepting polymers, while the steric shielding provided by the two  $\text{CF}_3$  groups minimizes the number of self-associations, as shown schematically in Figure 26.4a. The  $\beta$ -relaxation processes of HFS and PVME (or P2VPy) were significantly suppressed in the blends because of the strong intermolecular hydrogen bonding. When the number of HFS segments was approximately equal to the number of PVME segments, the local relaxation of PVME was almost

undetectable by DRS. A reduced functional group accessibility in P2VPy blends decreased the magnitude of suppression of the  $\beta$ -relaxation processes. A single,  $\alpha$ -relaxation process was observed for each miscible blend. At temperatures above the  $\alpha$ -relaxation process, an additional relaxation was observed,  $\alpha^*$ , which was assigned to the breaking and reforming of hydrogen bonds as the chain relaxed (as seen in Figure 26.4b). The temperature dependence of this process was related to the strength of the hydrogen bonding and the approximate fraction of intermolecularly associated segments. The dielectric spectrum can be resolved into  $\alpha$ - and  $\alpha^*$ -relaxation processes (based on the HN-equation) and ionic conductivity, as described in Figure 26.4b. The  $\alpha^*$ -relaxation process is not related to the phenomenon of electrode polarization, which was observed at still higher temperatures and whose magnitude in the derivative dielectric loss was significantly greater than this relaxation. In addition, dielectric strength, peak broadness and its temperature position were mainly dependent on the numbers and types of hydrogen bonds present in the systems.

The influence of annealing PMMA/SMA blends at temperatures above their  $T_g$  on the molecular dynamics was investigated using DRS [40]. To anneal a blend above the  $T_g$  had a significant effect on segmental motion, including the transition temperature and dynamics. The  $T_g$  was shifted to a higher temperature and the relaxation time ( $\tau_{\max}$ ) was increased due to the increased entanglement density and decreased molecular mobility. As seen in Figure 26.5a, the  $\alpha$ -relaxation process of PMMA/SMA 50/50 blends was shifted considerably to lower frequencies after annealing at different temperatures above  $T_g$  for different time intervals. Figure 26.5 also shows that annealing did not significantly change the peak broadness. The temperature dependence of  $\tau_{\max}$  for the  $\alpha$ -relaxation process at different annealing temperatures was well described by the VFT equation, as shown in Figure 26.5b. Furthermore, side group rotational motion could be freely achieved without overcoming the chain entanglement resistance. Neither the dynamics nor the distribution width of the local relaxation processes ( $\beta$ - and  $\gamma$ -relaxation) were

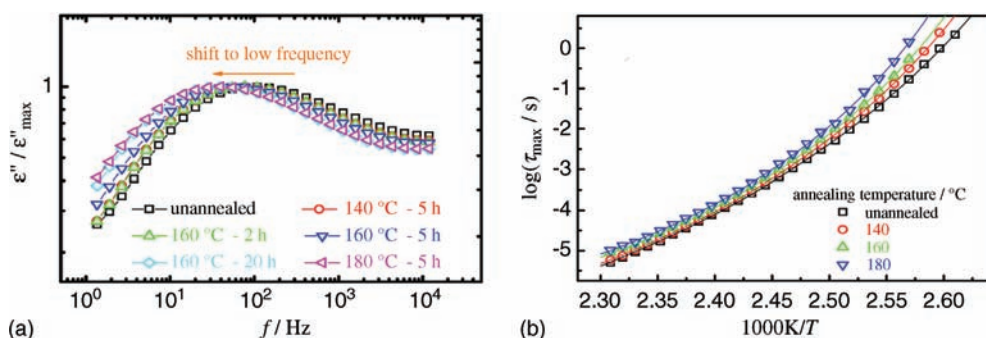


**Figure 26.5** (a) Normalized dielectric loss for PMMA/SMA 50/50 blend at 130 °C after annealing at different temperatures for different time intervals; (b) Relaxation time of the

$\alpha$ -relaxation process as a function of temperature for PMMA/SMA 50/50 blends annealed at different temperatures for 5 h. Both images reprinted with permission from Ref. [40].

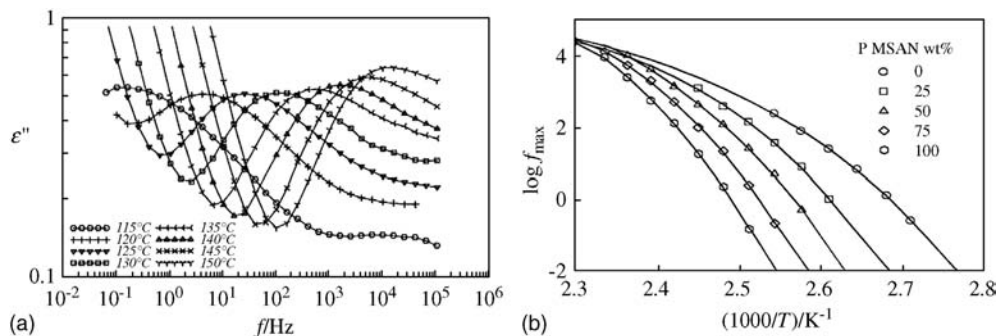


**Figure 26.6** (a) Dielectric loss ( $\epsilon''$ ) of PMMA/P $\alpha$ MSAN 50/50 blend as a function of frequency at different temperatures; (b) Frequency at maximum loss as a function of reciprocal temperature for PMMA/P $\alpha$ MSAN blends of different composition. Both images reprinted with permission from Ref. [41].

affected by chain entanglement resulting from annealing, which indicated that the local environment of the segments was unchanged.

The miscibility of PMMA, and P $\alpha$ MSAN (random copolymer) was studied using DRS [41]. When the molecular dynamics of the  $\alpha$ -relaxation process was investigated as a function of composition, frequency and temperature, respectively, only one common  $\alpha$ -relaxation process was observed for all measured samples, and its dynamics and broadness were composition-dependent (see the dielectric spectrum in Figure 26.6a for a 50/50 PMMA/P $\alpha$ MSAN blend). These findings implied that the two components were miscible and that the molecular dynamics depended on blend composition. In the higher frequency range of the dielectric spectrum, a  $\beta$ -relaxation of the PMMA component was detected (see Figure 26.6a). The frequencies at maximum loss  $f_{\max}$  for the  $\alpha$ -relaxation processes of all measured samples are shown as a function of reciprocal temperature,  $1/T$ , in Figure 26.6b. The activation curves systematically shifted to lower temperatures with increasing PMMA content. This systematic variation of the molecular dynamics with changing composition indicated miscibility of the blend components over the entire range of composition. In Figure 26.6a, the lines were computed using the Meander model (Eq. (26.6)), while the symbols represent experimental results. Miscibility was also confirmed by measuring  $T_g$ -values dielectrically from the activation curves of the  $\alpha$ -relaxation processes of the blends. The composition dependence of the dielectric relaxation strength,  $\Delta\epsilon$ , was also examined for  $\alpha$ - and  $\beta$ -relaxation processes. In addition, the kinetics and broadness of the  $\beta$ -relaxation processes of the PMMA was not affected by blending, which indicated that blending did not change the local environment of each component in the blend.

DRS was used to study the dynamics of hydrogen-bonded polymer blends of poly(2,3 dimethylbutadiene (DMB) [86%]-*co*-hexafluoro-2-hydroxyl-2-propyl)styrene (HFS) [14%]) copolymer with PVME [42]. The copolymer was capable of forming strong intermolecular hydrogen bonds, while minimizing the degree of intramolecular association, and its blends with PVME were miscible over the entire

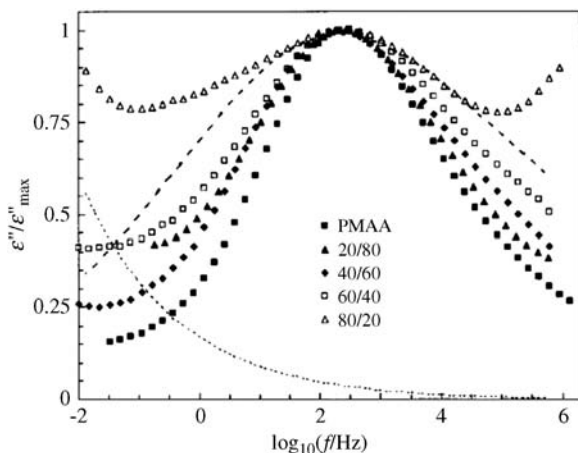


**Figure 26.7** Comparison of the normalized dielectric loss spectra for the local relaxation process of PVPh/PMMA blends at 60 °C. Reprinted with permission from Ref. [43].

composition range. Two segmental processes,  $\alpha$ - and  $\alpha_1$ - relaxations, were observed in blends of 26, 50, and 76 wt% copolymer content. The slower process ( $\alpha_1$ ) was assigned to the segmental motion of the intermolecularly associated copolymer, and the faster process ( $\alpha$ ) to segmental motions of PVME modified by the HFS-*co*-DMB component. A local  $\beta$ -relaxation process for the ether groups of PVME was also observed, but this did not change with blending.

DRS was also used to study the relaxation behavior of hydrogen-bonded poly(4-vinylphenol) (PVPh)/PMMA blends as a function of composition, temperature and frequency [43]. Miscible blends were obtained by solution-casting from a methyl ethyl ketone (MEK) solution, as confirmed by the occurrence of a single  $\alpha$ -relaxation process for each blend. The relaxation time and activation energy of the  $\alpha$ -relaxation process of PMMA were unchanged by blending with PVPh. In addition, the dielectric relaxation strength of the local relaxation process,  $\Delta\epsilon_\beta$ , was proportional to the concentration of PMMA for all blends, which suggested that blending and intermolecular hydrogen bonding did not modify the local intramolecular motion. The  $\alpha$ -relaxation process was shifted to lower frequencies or higher temperatures with increasing PVPh concentration. The dynamics of the  $\beta$ -relaxation process of PMMA exhibited an Arrhenius temperature dependence above  $T_g$ , but with an activation energy larger than that observed below  $T_g$ , because of the increased relaxation amplitude. The effect of blending on the dynamic constraints of the  $\beta$ -relaxation process of PMMA was also considered. Figure 26.7 shows the normalized dielectric loss spectra for the  $\beta$ -relaxation process of PMMA as a function of composition at 60 °C. Here, the peak broadness was significantly increased by blending. The full width at half-maximum of the relaxation-time distribution for neat PMMA was about four decades, while for the 60/40 blends it was six decades at the same temperature. This broadness suggested that the local environment of the relaxing groups became more heterogeneous; that is,

blending may have broadened the distribution of the frozen-in density fluctuations below  $T_g$ .

The molecular dynamics of polyvinyl alcohol (PVA) and carboxymethyl cellulose (CMC) blends was investigated as a function of composition, temperature and frequency using DRS [44]. PVA and CMC were found to be compatible over the range of composition studied. When the dielectric permittivity, loss tangent and a.c. conductivity of all samples were studied as functions of temperature and frequency, the results showed that the dielectric dispersion consisted of both dipolar and interfacial polarization. The frequency dependence of the a.c. conductivity indicated that correlated barrier hopping (CBH) was the most suitable mechanism for conduction.

Both, DRS and TSDC were used to study the molecular dynamics and miscibility of castor oil-based polyurethane (PU) and polyaniline (PANI) blends [45]. A linear relation between the maximum intensity of the depolarization current and the poling electric field was observed. Only one  $\alpha$ -relaxation process was observed in the blends. The temperature dependence of the  $\alpha$ -relaxation process was well described by the VFT equation.

The molecular dynamics and relaxation behavior of miscible PVME and PVPh blends were investigated using DRS [46]. The effect of intermolecular hydrogen bonding on the different relaxation processes was studied and compared to PVME/PS and PVME/poly(2-chlorostyrene) (P2CS) blends. The PVME/PVPh blends exhibited exceptionally strong intermolecular hydrogen bonds compared to PVME/P2CS and PVME/PS blends. The segmental relaxations of PVPh and PVME were coupled in blends controlled by the above-mentioned strong intermolecular hydrogen bonds, while PVME relaxed individually in its blends with P2CS or PS due to intrinsic mobility differences and the absence of any strong intermolecular interactions. In addition, dynamic heterogeneity was observed in PVME/PVPh blends with PVPh concentrations higher than 50 wt%, because of the decoupling arising from the strong intramolecular hydrogen bonding between PVPh segments. The  $\beta$ -relaxation processes of the two components were suppressed significantly by the intermolecular hydrogen bonding, without affecting their temperature-frequency locations. The results obtained suggested that the effect of composition on the molecular dynamics of PVPh/PVME blends was more complicated than that observed in blends without strong intermolecular interactions.

The  $\beta$ -relaxation process of P2VPy in a complex and blends with PVPh was studied using DRS [47]. The polymer complex was formed by mixing PVPh and P2VPy in MEK as a result of the very strong hydrogen bonding between the two polymers. The  $T_g$  of the obtained polymer complex was higher than that of either neat component. The  $\beta$ -relaxation process of P2VPy was significantly suppressed in the complex, and the reduction of its dielectric relaxation strength was approximately proportional to the intermolecular hydrogen-bonding fraction. In addition, the relaxation time of unassociated P2VPy side groups was also slowed down by about one decade compared to that of the neat P2VPy. Homogeneous PVPh/P2VPy blends were obtained in *N,N*-dimethylformamide; however, the degree of

intercomponent hydrogen bonding was much lower in the blends and therefore suppression of the P2VPy local relaxation was less significant than in the complex state. It was concluded that the stronger the intermolecular hydrogen bonding, the more pronounced was the suppression of secondary relaxation processes.

The molecular dynamics of PVPh and EVA (70 wt% vinyl acetate) blends were studied at different temperatures and hydrostatic pressures (up to 750 MPa), using DRS [48]. In this case, pressure was seen to retard the  $\alpha$ -relaxation process, with a consequent increase in  $T_g$ . Although both high pressure and temperature reduced the concentration of hydrogen bonds in the blends, the relaxation time distribution in the blends was narrowed with increasing pressure at a given relaxation time. This behavior was interpreted by considering the additional mobility achieved from breaking hydrogen bonds at high pressures and high temperatures for the hydrogen-bonded (and thus slow) PVPh-EVA segments compared to the fast relaxation of unassociated EVA segments.

The dynamic heterogeneity of the thermodynamically miscible blend of poly(vinyl ethyl ether) (PVEE) and poly(styrene-*co*-hydroxy styrene) (SHS) were investigated using DRS [49]. For SHS/PVEE blends, two segmental relaxations were observed in the DRS spectra, even for blends with a fraction of strong intermolecular hydrogen bonds. This behavior was explained by the existence of unfavorable interactions between PVEE and the styrene units in SHS, which was supported by the immiscibility between PS and PVEE. The repulsive force endowed the non-hydrogen-bonded PVEE segments with more freedom to relax, so that they could be distinguished from the relaxation of intermolecularly hydrogen-bonded PVEE-SHS segments. This experimental result suggested that a significant level of dynamic heterogeneity existed in the SHS/PVEE blends.

The molecular dynamics of PVPh/PVEE blends with a  $T_g$  difference of 186 K were investigated as a function of composition, temperature and pressure, using DRS [50]. Both temperature and volume were found to contribute to the segmental dynamics, with the former having a stronger influence within the temperatures and pressures investigated. Two segmental relaxation processes for blends with low PVPh concentrations were reported; the slow process was attributed to a relaxation of the intermolecular hydrogen-bonded PVPh and PVEE segments, while the fast process was assigned to unassociated PVEE segments. However, for blends with PVPh concentrations  $\geq 30$  wt%, most PVEE segments were hydrogen-bonded to PVPh and the blends exhibited a single  $\alpha$ -relaxation process. This behavior can be compared to that of other miscible blends with a large  $T_g$  difference and weak intermolecular interactions. The observed behavior was explained by the role of intermolecular hydrogen bonding, and the capability of coupling the segmental relaxations of PVEE and PVPh, which would otherwise exhibit two distinct segmental relaxation processes due to their large intrinsic mobility difference. Increases in both temperature and pressure led to a significant broadening in the distribution of relaxation times through the weakening of hydrogen bonds and the associated decoupling of the segmental dynamics, particularly for the PVEE-rich blends. A critical temperature was also identified above which the system became increasingly heterogeneous.

The dipolar relaxation behavior of poly(vinyl chloride) (PVC), PMMA and their blends was investigated over a wide range of temperature, using the TSDC technique [51]. The peak maximum of the  $\alpha$ -relaxation process was found to be strongly blend composition-dependent, and the temperature dependence of the relaxation time of the  $\alpha$ -relaxation process was well described by the VFT equation. The relaxation peak parameters, such as apparent activation energy ( $E$ ), pre-exponential factor ( $\tau_0$ ), and dipole–dipole interaction strength ( $q$ ) were evaluated. Linear behavior between the activation energy and the logarithm of the pre-exponential factor and between the activation enthalpy and activation entropy of the  $\alpha$ -relaxations was established, confirming the validity of the compensation laws. Similar studies have been reported for the molecular dynamics and miscibility of amorphous polymer blends of polycarbonate (PC)/tetramethyl polycarbonate (TMPC) and PS/TMPC [5–8].

### 26.3

#### Dielectric Relaxation Spectroscopy of Semicrystalline Polymer Blends

It is well established that, in semicrystalline materials, the amorphous regions are contained within the spherulitic structure, and that strong interactions exist between these regions and the lamellar crystals. The effect of spherulitic growth rate on the molecular dynamics of constrained amorphous regions in semicrystalline polymers can be accurately investigated using the DRS technique. In general, the common  $\alpha$ -relaxation process of the amorphous phase is typically converted to a more broad and slower  $\alpha'$ -relaxation process for the dynamics of the constrained amorphous phase. In this section, the effect of the crystalline phase on the molecular dynamics of the amorphous phase in semicrystalline polymer blends will be summarized. In addition, the kinetics of the crystallization process of some selected polymer blends will also be examined using the DRS technique. The crystallization kinetics of the blends will be investigated under various experimental variables, such as blend composition, crystallization temperature and crystallization time. The effect of the crystallization process on the dielectric relaxation parameters such as dielectric strength,  $\Delta\epsilon$ , maximum frequency,  $f_{\max}$ , distribution of relaxation time, dielectric storage and loss modulus,  $\epsilon'$  and  $\epsilon''$ , will also be considered. The isothermal crystallization kinetics will be analyzed based on the theoretical approach of Avrami.

The microstructure and dynamics of semicrystalline, melt-miscible poly(ethylene oxide) (PEO)/PVAc blends were investigated using DRS [52]. For crystalline blends with PEO contents up to 50 wt%, the  $\alpha$ -relaxation process was almost identical to that of neat PEO, which indicated the presence of relatively mobile amorphous segments consisting almost entirely of PEO. Multiple overlapping dielectric relaxation processes, including the Maxwell–Wagner–Sillars (MWS) interfacial polarization process (similar to that observed for neat PEO), a slow segmental process associated with amorphous interfibrillar regions, and possibly also a second MWS relaxation, were observed in blends with 30 and 50 wt% PVAc content.



Zardalidis *et al.* [53] investigated the molecular dynamics of PEO/PVAc blends as a function of composition, temperature and pressure. For blends with a high PVAc content, all short-range correlations were dominated by the PVAc component. The fact that an invariant frequency dispersion was observed for different blend compositions under isochronal conditions suggested a covariance of the width of the distribution with structural relaxation time, as found in other glass-forming liquids.

The molecular dynamics of an amorphous/crystalline polymer blend of PVAc and poly(hydroxy butyrate) (PHB) were investigated using DRS over a wide ranges of frequencies (from  $10^{-2}$  to  $10^5$  Hz), temperatures and blend compositions [54]. Two dielectric relaxation processes were detected for neat PHB in both the high- and low-frequency ranges at a given constant temperature above  $T_g$ . These two relaxation peaks were related to the  $\alpha$ - and  $\alpha'$ -relaxations of the amorphous and the rigid amorphous regions in the sample, respectively. The  $\alpha'$ -relaxation process was temperature- and composition-dependent, and was related to the constrained amorphous region located between adjacent lamellae inside the lamellar stacks. In addition, the  $\alpha'$ -relaxation process behaved as a typical glass relaxation process; that is, it originated from the micro-Brownian cooperative reorientation of highly constraint polymeric segments. In the PHB/PVAc blends, only one  $\alpha$ -relaxation process was observed for all measured blends located in the temperature ranges between the  $T_g$ -values of the neat components. The latter finding suggested that the relaxation processes of the two components were coupled due to the small difference in their  $T_g$ -values ( $\Delta T_g = 35^\circ\text{C}$ ) and the favorable thermodynamic interaction between the two polymer components, which consequently led to less dynamic heterogeneity in the blends. The molecular dynamics of the  $\alpha$ - and  $\alpha'$ -relaxation processes was greatly influenced by blending; that is, the dielectric strength, the peak broadness and the dielectric loss peak maximum were all composition-dependent. The dielectric measurements also confirmed a decrease in the rate of the crystallization of PHB in the blends.

DRS was used to investigate the real-time crystallization kinetics of many polar and nonpolar polymer systems by monitoring modifications of the molecular dynamics of the polymer segments in the amorphous phase during the crystallization process. This method was also used to determine the crystallization kinetics of PHB/PVAc blends by real-time measurements of the dielectric spectrum at a given crystallization temperature,  $T_c$  [55]. Figure 26.8 shows the real-time measurements of the segmental relaxation process starting from the glassy state of an amorphous PHB/PVAc 80/20 blend at  $T_c = 30^\circ\text{C}$ . The data in the figure show that the dielectric relaxation spectrum was strongly influenced by the crystallization process of the PHB component in the blend. With increasing crystallization time, both the dielectric constant and dielectric loss were decreased significantly, indicating a reduction of the amorphous region in the blend. In addition, the maximum frequency,  $f_{\text{max}}$ , of the dielectric loss peak remained constant, regardless of the crystallization time, until the peak became undetectable (see, for example, at  $t_c = 85$  min). This relaxation process was mainly related to the percentage amorphous region in the blend. During the late stages of the crystallization process,

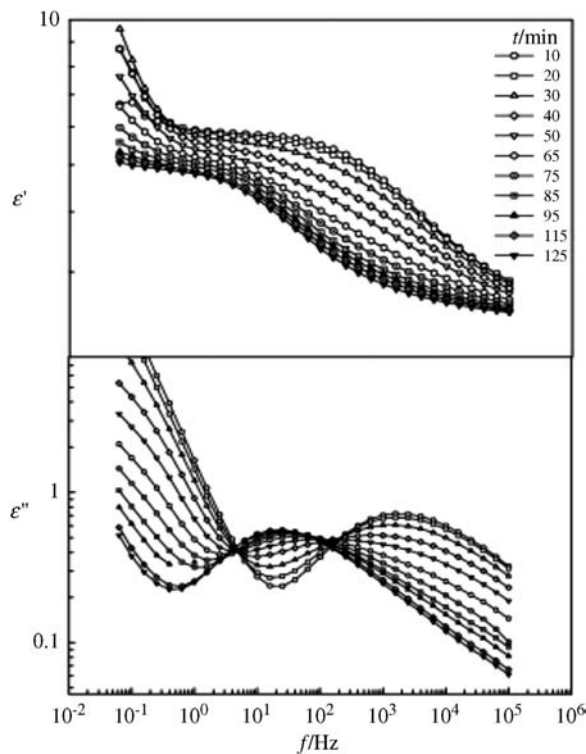


**Figure 26.8** Real-time measurements of the relaxation process of PHB/PVAc 40/60 blend at  $T_c = 50\text{ }^{\circ}\text{C}$ . Reprinted with permission from Ref. [55].

another relaxation peak occurred at a slightly lower frequency range; this peak was attributed to the confinement of some amorphous regions between the crystalline lamellae within the spherulitic structure of PHB. This process usually leads to a reduction in chain mobility and, consequently, to a slower relaxation process for the rigid amorphous regions. At  $t_c = 0\text{ min}$  the sample was completely amorphous and the relaxation segments were almost unconstrained. However, once the PHB began to crystallize in the blends the amorphous phase content was gradually decreased with increasing crystallization time and became more constrained by the crystallized phase, which in turn led to the appearance of a broad relaxation peak. The dielectric strength of the amorphous segments,  $\Delta\epsilon$ , which is directly proportional to the volume fraction of the mobile amorphous phase in the blend, was decreased exponentially with increasing crystallization time. However, the dielectric strength of the rigid amorphous segments,  $\Delta\epsilon_a$ , which is related to the degree of crystallinity in the blend, was increased dramatically with increasing crystallization time.

The miscibility and isothermal crystallization kinetics of poly( $\epsilon$ -caprolactone) (PCL) blends with TMPC and poly(styrene-*co*-acrylonitrile) (SAN) with 27.5 wt% acrylonitrile content were investigated using DRS [56]. The isothermal

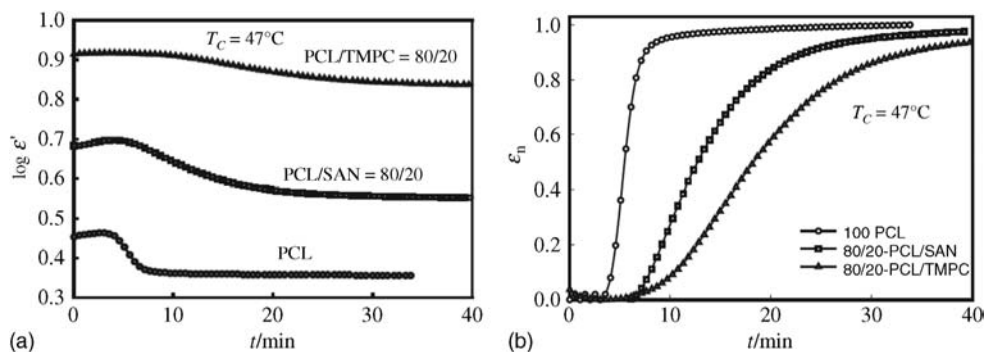


**Figure 26.9** (a) Dielectric constant ( $\epsilon'$ ) of neat PCL, blends of PCL/TMPC 80/20 and PCL/SAN 80/20 as a function of crystallization time at  $47^\circ\text{C}$  and 1 kHz; (b) Normalized dielectric constant ( $\epsilon_n$ ) for neat PCL, blends of PCL/TMPC 80/20 and PCL/SAN 80/20 as a function of crystallization time at 1 kHz and  $T_c = 47^\circ\text{C}$ . Both images reprinted with permission from Ref. [56].

crystallization kinetics of PCL in the different blends was also investigated as a function of  $T_c$ . For neat PCL, the rate of crystallization was  $T_c$ -dependent; that is, the higher the  $T_c$ , the slower the crystallization rate. The crystallization kinetics of the PCL/TMPC blend was much slower than that of PCL/SAN at a constant crystallization temperature, and this behavior was attributed to the higher level of interaction between PCL and TMPC than between PCL and SAN. Consequently, the stronger the higher level of interaction between the two polymer components led to a more pronounced suppression in crystallization kinetics. This specific crystallization kinetics was also attributed to the difference in  $T_g$  between TMPC ( $191^\circ\text{C}$ ) and SAN ( $100^\circ\text{C}$ ), which caused a decrease in the rate of crystallization with increasing  $T_g$  of the amorphous component in the blend. Figure 26.9a shows the crystallization time dependence of the dielectric constant for different PCL blends at 1 kHz and  $T_c = 47^\circ\text{C}$ . All of the samples were melted at  $100^\circ\text{C}$  for 5 min and then quenched to crystallization temperature. During the first few minutes,  $\epsilon'$  was increased to reach a maximum, but this was followed by a rapid decrease to an almost constant value. The initial increase in  $\epsilon'$  was attributed to a pre-order reorientation of the dipoles. This process was followed by crystallization, which greatly restricted the dipolar reorientation and therefore led to a rapid decrease in  $\epsilon'$ . The crystallization kinetics of PCL was significantly affected by blending; that is, the onset crystallization time ( $t_0$ , the time at which  $\epsilon'$  starts to decrease) was increased in the blend, while the value of  $t_0$  for PCL/TMPC was almost twice that of the PCL/SAN blend. This observation led to the conclusion that the reduction in the rate of crystallization of PCL in the blend was caused by a hindrance effect of TMPC and SAN on the arrangement of crystallizable chains in PCL. The change in dielectric constant during the crystallization process was converted to the normalized dielectric constant  $\epsilon_n$ . Figure 26.9b shows the variation in the normalized dielectric constant with time for neat PCL and blends of

PCL/TMPC 80/20 and PCL/SAN 80/20 at 1 kHz. The value of  $\varepsilon_n$  is equivalent to the measurement of the relative degree of crystallization at a given  $T_c$ . The analysis of the isothermal crystallization kinetics was carried out using the theoretical approach of Avrami. The value of the Avrami exponent was almost constant in the neat state and in the blends, which indicated that blending had simply reduced the rate of crystallization, without affecting its mechanism.

The reorientational dynamics of dipoles in a series of blends of polyethylene glycol (PEG) and poly(amidoamine) (PAMAM) dendrimers (polymer materials arranged in many branches, with sub-branches radiating out from a central core) were investigated using DRS [57]. The measurements were performed over a wide range of frequency and temperature. Neat PEG exhibited three relaxation processes: the segmental process in the amorphous phase; and two faster processes that were due to localized motions in the amorphous regions and the rotation of hydroxyl end groups. The addition of dendrimers to the PEG matrix slowed down the segmental process in the amorphous phase, but had no effect on the relaxation time of the local processes in PEG. However, hydrogen-bonding that formed between the PEG oxygen and the amino groups on the dendrimer surface was responsible for the shift of the local processes in dendrimers to lower frequencies. A detailed analysis of the effect of temperature, the concentration of dendrimers and the molecular weight of PEG on the relaxation dynamics was performed. The molecular weight of PEG was found to have minor effects on the average relaxation times of the different relaxation processes of the blend. The time scale of the segmental process in the amorphous phase was also increased with increasing dendrimer concentration, while restrictions in mobility of this system were related to the hydrogen-bonding between the dendrimers and PEG.

The molecular dynamics of a series of PEG/PAMAM blends and PEG-conjugated PAMAM dendrimers was investigated and contrasted over a wide range of frequencies and temperatures, using DRS [58]. The time scale of segmental relaxation decreased with the increasing concentration of dendrimers due to hydrogen-bonding between the PEG oxygen and the amino groups on the surface of the dendrimers. The PEGylated dendrimers exhibited two local processes and one segmental process for the PEG, without any contribution of the epoxy end group, where the PEGylated dendrimer is a PEG with epoxy reactive end groups. The amorphous PEG in the PEGylated dendrimers was constrained not only by the crystallized lamellae but also by covalent bonding with the dendrimer. A comprehensive analysis was also conducted of the effects of morphology, concentration, number of attached PEG chains and temperature on the relaxation time, dielectric relaxation strength and spectral characteristics of various relaxation processes.

The molecular dynamics of semicrystalline, melt-miscible blends of PEO and poly(styrene-*co*-*p*-hydroxystyrene) copolymer (SHS) were investigated, using DRS, by Jin *et al.* [59]. The normalized crystallinity of PEO was almost unchanged by adding SHS up to 20 wt%, but was decreased significantly with further increased in SHS content, reaching almost zero at 50 wt% SHS. The  $\alpha$ -relaxation process shifted to higher temperatures and became broader with increasing concentrations of SHS in the blends. The  $\alpha$ -relaxation process comprised a slower

cooperative segmental relaxation that involved both components, as well as a faster process that was attributed to the less-associated PEO segments. The hydrogen-bonded hydroxystyrene units produced a  $\beta_{S1}$ -relaxation process that was more cooperative than typical local relaxations. The apparent activation energy of the  $\beta_{S1}$ -relaxation process in SHS and the blends (both crystalline and amorphous) was decreased monotonically from 85 to 55 kJ mol<sup>-1</sup> with increasing SHS content from 15 to 100 wt%. The fragility of the neat copolymer was found to be similar to that of PS with a comparable molecular weight, and this was consistent with the idea that intramolecular hydrogen-bonding primarily enhanced the monomer friction coefficient and  $T_g$ , but had little effect on fragility [60]. The blend fragility was increased significantly with SHS content, reflecting the combined contribution of the two components.

The miscibility, melting and crystallization behavior of PHB and oligo[(*R,S*)-3-hydroxybutyrate]-diol (oligo-HB) blends were investigated using DRS [61]. The different relaxation processes in the blends were studied over wide temperature and frequency ranges for various compositions of up to 20 wt% oligo-HB. The fact that only one  $\alpha$ -relaxation process was observed for all measured blends indicated miscibility between the amorphous fractions of PHB and oligo-HB.

The molecular motions in binary blends of isotactic polypropylene (PP), PS and low-density polyethylene (LDPE) were investigated using DRS [62]. The blends were prepared by melt-mixing, and doped with 0.5 wt% of the dielectric probe 4,40-(*N,N*-dibutylamino)-(*E*)- nitro-stilbene (DBANS). The blend composition and blend morphology had no substantial influence on the  $\alpha$ -relaxation process, which indicated that both blend constituents behaved like homogeneous bulk materials. The normalized  $\alpha$ -relaxation process was unchanged, regardless of the blend type and blend composition. These experimental data suggested that the probe molecule, DBANS, was equally distributed over the two blend components in all three polymer combinations LDPE/PP, LDPE/PS, and PP/PS.

The TSDC technique was used to investigate the miscibility of poly(DL-lactide) (PDLLA) and PCL blends over a wide composition range by following changes in local and segmental dielectric relaxations as a function of blend composition [63]. The  $\alpha$ -relaxation process of PCL was slightly shifted to higher temperatures with increasing PDLLA content, indicating a partial miscibility with PDLLA and the formation of a PCL-rich phase. Distribution of the  $\alpha$ -relaxation time of the semicrystalline PDLLA-rich phase was very broad compared to the times of the neat components, mainly due to significant concentration fluctuations, and this confirmed the partial miscibility of these blends. Investigations of blend morphology, using scanning electron microscope (SEM) failed to demonstrate a distinct two-phase system with particles dispersed in a matrix. The profile and strength of the  $\beta$ -relaxation process deviated from the linear mixing rule with composition; however, although these changes followed the same trend as in block copolymers, the effects were less pronounced.

DRS was used to study the molecular dynamics and interactions between polyamide-6,6 (PA-6,6) and hyperbranched (HB) polyamide with amine and alkyl end groups, prepared via a one-pot process, in a PA-6,6 matrix [64]. Three relaxation

processes, namely  $\gamma$ -,  $\beta$ - and  $\alpha$ -relaxations, were observed for the HB polymers and in the blends; these were similar to those observed in PA-6,6 and had comparable activation energies and distribution parameters. Subsequently, the  $T_g$  was increased in line with increasing concentrations of amine-terminated HB, while the molecular mobility of the PA-6,6 chains was decreased. The dielectric spectra of the alkyl-terminated HB polymer blends were indistinct from those of the PA-6,6 matrix.

The molecular dynamics of miscible PC/PCL blends was studied using DRS [65]. The  $\alpha$ -relaxation process of PC in the blends was analyzed isothermally using the HN equation, when PCL was shown to have a significant plasticization effect on the molecular dynamics of PC. The real-time crystallization kinetics of the 90/10 PC/PCL blend was studied by following changes in dielectric loss caused by reductions in the molecular mobility of the amorphous fraction in the blend. Much larger amounts of mobile amorphous chains were shown to have disappeared than had been transferred to the crystallites. A rigid amorphous phase in the blend was formed as the isothermal crystallization of PC developed, and the remaining mobile amorphous phase exhibited unchanged dynamics.

## 26.4

### Dielectric Relaxation Spectroscopy of Chemically Reactive Polymer Blends

In this section, a summary will be provided of the effects of chemically reactive blending on the molecular dynamics of different relaxation processes within the blends. Both, DRS and TSDC are highly sensitive techniques used to monitor changes in the molecular dynamics and dynamical constraints associated with chemical reaction between the blend components, thermoset formation, branching, crosslinking density, and the corresponding bulk properties. The influence of various chemical reactions will be examined dielectrically by following changes in the molecular dynamics of the  $\alpha$ -relaxation process as a function of reaction time, frequency and temperature. In addition, the relaxation strengths ( $\Delta\epsilon$ ) of the  $\alpha$ - and  $\beta$ -relaxation processes will be demonstrated as a function of reaction time from the analysis of dielectric relaxation spectra.

The curing behaviors, thermal and dielectric properties of the blends of cyanate ester (BACY) and two diamine-based benzoxazines (P-ddm and P-oda) were investigated by Lin *et al.* [66]. The experimental data revealed three curing reactions: (i) cyclotrimerization of the cyanate ester, catalyzed by residual phenolic groups in the benzoxazine; (ii) a coreaction between the triazine structure and benzoxazine; and (iii) ring-opening of benzoxazine (self-polymerization). A slight decrease in the dielectric constant was observed when incorporating benzoxazine into BACY. The considerable improvement in the dielectric properties of the blend was related to the rare cyanate ester residual and the formation of less-polar diphenyl ether. The  $T_g$  corresponding to the lowest dielectric constant (2.78 at 1 GHz) was approximately 248 °C, which showed that it was possible to slightly reduce the dielectric constant without sacrificing too much in  $T_g$  in this system.

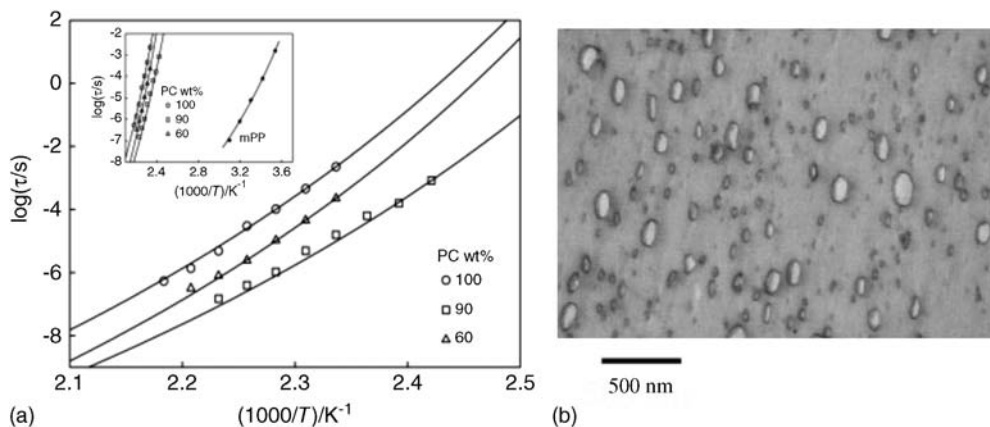


**Figure 26.10** (a) Relaxation time as a function of reciprocal temperature for different PP-g-MA/PC blend compositions. The solid lines show the fitting to the VFT equation. The inset shows the same data plus the activation energy curve of neat mPP. Reprinted with permission from Ref. [67]; (b) STEM image of PP-g-MA/PC 10/90 blend. Reprinted with permission from Ref. [68].

The miscibility and molecular dynamics of nanostructured grafted polypropylene with maleic anhydride (PP-g-MA)/PC blends prepared by the *in-situ* polymerization of macrocyclic carbonates with polypropylene modified with 0.5 wt % maleic anhydride-reactive groups were studied over a wide range of frequencies (from  $10^{-2}$  to  $0.5 \times 10^7$  Hz) at different constant temperatures, using DRS [67]. The molecular dynamics of the  $\alpha$ -relaxation process in the mPP/PC blends appeared in a lower temperature range compared to neat PC. This shift in the molecular relaxation process was attributed to the partial miscibility of the two polymer components in the blends, as confirmed by morphologic analysis using scanning transmission electron microscopy (STEM). Nanoscale morphologies with average domain diameters as small as 50 nm were obtained for the different blend compositions (see the STEM image of a mPP/PC 10/90 blend in Figure 26.10b) [68]. The relaxation spectra of neat PC and PP-g-MA/PC blends were resolved into  $\alpha$ - and  $\beta$ -relaxation processes by using the HN equation and ionic conductivity. The dielectric relaxation parameters, such as relaxation peak broadness, maximum frequency ( $f_{\max}$ ) and dielectric strength ( $\Delta\epsilon$ ) (for both  $\alpha$ - and  $\beta$ -relaxation processes) were blend composition-dependent. The kinetics of the  $\alpha$ -relaxation processes of the blends were well described by the VFT equation, as seen in Figure 26.10a. The local relaxation process of PC was resolved into two relaxation processes,  $\beta_1$  and  $\beta_2$ , associated with the carbonyl groups' motion and the combined motions of the carbonyl and phenylene groups, respectively. Only  $\beta_2$  was shifted to lower frequencies in the blend, while  $\beta_1$  was relatively little affected by blending. The electrical modulus of the blends was used to obtain a sufficient resolution of the different relaxation processes in the samples; that is,  $\alpha$ -,

$\beta$ -relaxation processes, ionic conductivity and interfacial polarization. The blending method used was also found to increase the d.c. conductivity, without affecting the charge carrier transport mechanism.

The molecular dynamics of ternary polymer blends of PP/PA6/acrylonitrile butadiene styrene copolymer (ABS) in the presence of compatibilizers and multi-wall carbon nanotubes (MWNTs) was investigated using DRS [69]. The relaxation time of the PA6 chains was found to have increased significantly when small amounts of compatibilizers (PP-g-MA) or styrene maleic anhydride (SMA) were added. The variation in relaxation time was found to depend heavily on the compatibilizer efficiency. The variation in relaxation time for PA6 in the presence of 1 wt% MWNTs in the respective ternary blends also followed a similar trend; however, the extent of mobility of the PA6 phase was influenced by the state of dispersion of MWNTs in the corresponding blends.

The miscibility of PP/PA6 70/30 wt% blends was also investigated using DRS [70]. In this case, ca. 10 wt% PP functionalized with maleic anhydride was added as a compatibilizer to induce compatibility of the two immiscible components, after which the influence of the compatibilizer on the molecular dynamics of the PA6 phase was determined by monitoring changes induced in the dielectric loss spectra of the blends. Two segmental modes were recorded: (i) a lower temperature mode corresponding to the plasticized material; and (ii) a second, cooperative, mode where the temperature was raised in relation to the dry PA6 amorphous phase. The  $\alpha$ -relaxation process was unaffected by compatibilization. At high temperatures, the high-temperature tail of the segmental mode was much higher in the absence of the compatibilizer.

The molecular dynamics of novel, high-dielectric-permittivity poly(vinylidene fluoride) (PVDF)/PP blends with a small amount of PP-g-MA compatibilizer was reported over a wide range of temperatures and frequencies, using DRS [71]. The results showed that the concentration of PVDF in the composites dominated the changes in dielectric properties, and that the use of PP-g-MA improved the interface interaction between PVDF and PP, resulting in an increased dielectric permittivity.

The polymerization reaction of diglycidyl ether of bisphenol A (DGEBA) epoxy resin with 4,4'-diaminodiphenylmethane (DDM) hardener and a mixture of polysulfone (PSU) and polyetherimide (PEI) as modifier was studied, using DRS [72]. All blends contained 10 wt% of the PSU/PEI mixture. The curing reaction was studied by monitoring the change in the molecular dynamics of the  $\alpha$ -relaxation. The effects of the PEI/PSU ratio on the molecular dynamics and on the curing temperature were also investigated.

The curing reaction of DGEBA epoxy resin with DDM hardener and different amounts of polyoxypropylene triamine (POPTA) oligomer were investigated using DRS [73]. Real-time dielectric measurements were made at different curing temperatures over a wide range of frequencies. A curing-induced phase separation was observed in these systems, and the curing reaction was evaluated by analyzing the change in the main  $\alpha$ -relaxation process of the blends as a function of curing time, curing temperature and the amounts of modifier in the different blend



compositions. The effect of curing reaction on ionic conductivity was also examined for different curing temperatures.

The molecular dynamics of similar chemical structure blends of poly(ethylene terephthalate) (PET) and poly(ethylene naphthalate) (PEN) were investigated using the TSDC technique [74]. Transesterification reactions between the neat components developed during the melt-mixing process. When the  $\alpha$ -relaxation processes of the reactive blends were analyzed into their elementary modes by means of relaxation map analysis, the activation energies of the  $\alpha$ -relaxation process were found not to be significantly affected by the transesterification reaction. However, the polarizability of the blend was considerably decreased as the PEN content increased, due mainly to the increased stiffness of the polymer backbone.

The molecular dynamics of reactively blended PET/PEN of different degrees of ester exchange reaction and composition were investigated using DRS [75]. The dielectric spectra of the  $\alpha$ -relaxation processes of the blends were analyzed based on the HN equation. When the dielectric relaxation broadness and strength were quantified, they were seen to depend on the processing conditions. The molecular coupling of the blends was only minimally affected by the blend composition or the degree of transesterification, although a positive deviation from the linear mixing rule was observed in the composition dependence of activation energies of molecular motions. These findings suggested that there was a greater chain hindrance to the motion of the block and random copolymers formed via the transesterification process.

The molecular mobility and microphase separation in blends of crosslinked PU and SAN prepared by reactive blending were studied using DRS and TSDC over a wide range of frequencies and temperatures [76]. SAN promoted a microphase separation of the hard and soft segments of PU because of the SAN-hard segment interactions, whereas the SAN-soft segment interactions were weak. The TSDC spectra obtained showed that a compensation law holds for the  $\alpha$ -relaxation process of the soft segment, with the compensation temperature being very close to the  $T_g$ -value. An analysis of the  $\alpha$ -relaxation process, in terms of fragility, indicated that the systems under investigation were indeed fragile.

The molecular dynamics and curing kinetics of a thermosetting powder coating that consisted of a carboxylated polyester resin cured with triglycidyl isocyanurate, have been studied using broadband dielectric relaxation spectroscopy over a wide range of frequencies (from  $10^{-1}$  to  $10^6$  Hz) and temperatures (from 70 to 105 °C) for different constant curing times [77]. Two relaxation processes were observed for all measured samples: one for the  $\alpha$ -relaxation process, and another for the  $\beta$ -relaxation process. The dielectric strength,  $\Delta\epsilon$ , of the two relaxation processes was strongly influenced by curing; that is,  $\Delta\epsilon$  was decreased strongly during the early stage of the curing process but then leveled off at the later stages, indicating that the number of reoriented dipoles had decreased as the curing process had proceeded. The comparative dielectric loss and dielectric constant at 85 °C for different samples cured at 200 °C for various times are shown in Figure 26.11a and b. The effect of the curing process on the molecular dynamics of powder coating can be summarized as follows: (i) the maximum of the loss peak shifts to lower

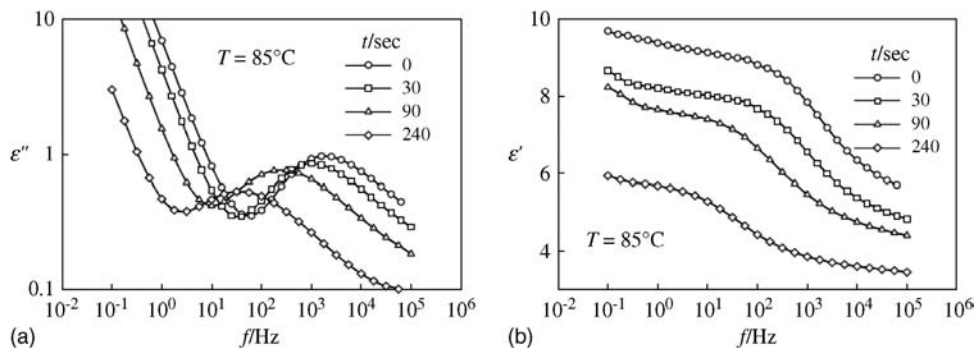


**Figure 26.11** (a) Comparison of dielectric loss ( $\epsilon''$ ) at  $85^\circ\text{C}$  for different samples cured at  $200^\circ\text{C}$  for various times; (b) Comparison of dielectric constant ( $\epsilon'$ ) at  $85^\circ\text{C}$  for different samples cured at  $200^\circ\text{C}$  for various times. Both images reprinted with permission from Ref. [77].

frequency; (ii) the height of the dielectric loss peak decreases; (iii) the broadness of the loss peak increases; (iv) the dielectric constant decreases; and (v) the ionic conductivity decreases with the proceeding of curing process. The above five findings are attributed to the formation of more rigid, highly packing three-dimensional polymer networks. In addition, the Meander model was found to well describe the kinetics of the  $\alpha$ -relaxation process as a function of curing time. The formation of highly packed three-dimensional polymer networks was also found to increase the dislocation energy and to produce additional structural defects.

## 26.5

### Conclusions

This chapter has provided a comprehensive overview of recent developments and progress in the molecular dynamics, miscibility, nature of interaction, crystallization behavior and curing kinetics of representative examples of polymer blends, using DRS and TSDC techniques. Notably, the chapter has provided a solid basis for understanding the effects of blending on polymer relaxation behavior for wide range of different types of polymer blends, including amorphous polymer blends, semicrystalline polymer blends, and chemically reactive polymer blends. Different theoretical approaches, including the VFT and Meander models, were used to describe the molecular dynamics of the  $\alpha$ -relaxation process in blends, while the dynamics of the local,  $\beta$ - and  $\gamma$ -relaxation processes were described using an Arrhenius equation. The dielectric spectra of the polymer blends were analyzed based on HN and ionic conductivity equations. The real-time crystallization kinetics of different amorphous/crystalline polymers was investigated for different polymer blends, with crystallization behavior being studied as a function of blend composition, and of crystallization temperature and time. The influence of

chemical reactions between the blend components, thermoset formation and branching – and the corresponding bulk properties – was examined dielectrically by monitoring changes in the molecular dynamics of the  $\alpha$ -relaxation process at different reaction times, frequencies and temperatures. Overall, this chapter has provided a quantitative, experimental and theoretical basis for determining the molecular dynamics and relaxation of a wide range of different polymer blends. This should, in turn, lead to an increased knowledge of the behavior of this important class of polymeric materials and other similar blends.

## References

- 1 Zidan, H.M., Tawansi, A., and Abu-Elnader, M. (2003) *Physica B: Condens. Matter*, **78**, 339.
- 2 Tang, Y. and Scheinheim, J. (2003) *J. Polym. Sci., Part B: Polym. Phys.*, **41**, 927.
- 3 Zhang, S., Painter, P.C., and Runt, J. (2002) *Macromolecules*, **35**, 8478.
- 4 Fukao, K., Uno, S., Miyamoto, Y., Hoshino, A., and Miyaji, H. (2001) *Phys. Rev. E: Stat. Nonlin. Soft Matter Phys.*, **64**, 051807/1.
- 5 Mansour, A.A. and Madbouly, S.A. (1995) *Polym. Int.*, **36**, 269–277.
- 6 Mansour, A.A. and Madbouly, S.A. (1995) *Polym. Int.*, **37**, 267–276.
- 7 Mansour, A.A., Madbouly, S.A., and Hoehne, G. (1996) *Polym. Int.*, **41**, 395–406.
- 8 Mansour, A.A., Madbouly, S.A., Hoehne, G., and Dollhopf, W. (1997) *Polym. Int.*, **42**, 143–148.
- 9 Mansour, A.A. (1997) *Polym. Int.*, **43**, 70–76.
- 10 Williams, G. (2005) *New Polymeric Materials: ACS Symposium Series*, American Chemical Society, pp. 268–281.
- 11 Ezquerra, T.A., Sics, I., Nogales, A., Denchev, Z., and Balta-Calleja, F.J. (2002) *Europhys. Lett.*, **59**, 417.
- 12 Nogales, A., Ezquerra, T.A., Denchev, Z., Sics, I., Balta-Calleja, F.J., and Hsiao, B.S. (2001) *J. Chem. Phys.*, **115**, 3804.
- 13 Alie, J., Menegotto, J., Cardon, P., Duplaa, H., Caron, A., Lacabanne, C. *et al.* (2004) *J. Pharm. Sci.*, **93**, 218.
- 14 Wurm, A., Soliman, R., and Schick, C. (2003) *Polymer*, **44**, 7467.
- 15 Wurm, A., Soliman, R., Goossens, J.G.P., Bras, W., and Schick, C. (2005) *J. Non-Cryst. Solids*, **351**, 2773.
- 16 vann den Berg, O., Sengers, W.G.F., Jager, W.F., Picken, S.J., and Wübbenhorst, M. (2004) *Macromolecules*, **37**, 2460.
- 17 Napolitano, S. and Wübbenhorst, M. (2006) *Macromolecules*, **39**, 5967.
- 18 Bras, A.R., Viciosa, M.T., Wang, Y., Dionisio, M., and Mano, J. (2006) *Macromolecules*, **39**, 6513.
- 19 Sanz, A., Nogales, A., Ezquerra, T.A., Lotti, N., Munari, A., and Funari, S.S. (2006) *Polymer*, **47**, 1281.
- 20 Alvarez, C., Sics, I., Nogales, A., Denchev, Z., Funari, S.S., and Ezquerra, T.A. (2004) *Polymer*, **45**, 3953.
- 21 Johari, G.P. (1994) *J. Chem. Soc., Faraday Trans.*, **90**, 883.
- 22 Johari, G.P., McAnanaman, J.G., and Wasylyshyn, D.A. (1996) *J. Chem. Phys.*, **105**, 10521.
- 23 Sedita, J.S. and O'Reilly, J.M. (2001) *Polym. Eng. Sci.*, **41**, 15–22.
- 24 Havriliak, S. and Negami, S. (1967) *Polymer*, **8**, 161.
- 25 Cole, R.H. and Cole, K.S. (1941) *J. Chem. Phys.*, **9**, 341.
- 26 Williams, G., Smith, I.K., Holmes, P.A., and Varma, S. (1999) *J. Phys. Condens. Matter*, **11**, A57–A74.
- 27 Boettcher, C.I.F., Van Belle, O.C., and Rip, A. (1973) *Theory of Dielectric Polarization I*, Elsevier Scientific, Amsterdam.
- 28 McCrum, N.G., Read, B.E., and Williams, G. (1991) *Anelastic and Dielectric Effects in Polymeric Solids*, Dover Publications Inc., New York.
- 29 Urman, K., Madbouly, S.A., and Otaigbe, J.U. (2007) *Polymer*, **48**, 1659–1666.
- 30 Ferry, J.D. (1980) *Viscoelastic Properties of Polymer*, Wiley, New York.

- 31 Pechhold, W. and Stoll, B. (1982) *Polym. Bull.*, **7**, 413.
- 32 Pechhold, W., Sautter, E., vonSonden, W., Stoll, B., and Grossmann, H.P. (1979) *Macromol. Chem. Suppl.*, **3**, 247.
- 33 Heinrich, W. and Stoll, B. (1988) *Prog. Colloid Polym. Sci.*, **78**, 37.
- 34 Liu, J., Guo, H., Pang, X., Tan, X., Akinc, M., Lin, Z., and Bowler, N. (2013) *J. Non-Cryst. Solids*, **359**, 27–32.
- 35 Arrese-Igor, S., Alegria, A., Moreno, A.J., and Colmenero, J. (2011) *Macromolecules*, **44**, 3611–3621.
- 36 Ahmed, M.T. and Fahmy, T. (2011) *J. Korean Phys. Soc.*, **59**, 98–104.
- 37 Masser, K.A., Zhao, H., Painter, P.C., and Runt, J. (2010) *Macromolecules*, **43** (21), 9004–9013.
- 38 Fragiadakis, D., Dou, S., Colby, R.H., and Runt, J. (2009) *J. Chem. Phys.*, **130**, 0649071–06490711.
- 39 Masser, K.A. and Runt, J. (2010) *Macromolecules*, **43**, 6414–6421.
- 40 Lin, Y., Tan, Y., Qiu, B., Shangguan, Y., Harkin-Jones, E., and Zheng, Q. (2013) *J. Phys. Chem. B*, **117** (2), 697–705.
- 41 Madbouly, S.A. (2002) *Polym. J.*, **34**, 515–522.
- 42 Masser, K.A. and Runt, J. (2009) *Macromol. Symp.*, **279** (1), 221–227.
- 43 Zhang, H. and Runt, J. (2004) *J. Polym. Sci. Polym. Phys.*, **42** (18), 3405–3415.
- 44 Abd El-Kader, F.H., Shehap, A.M., Abo-Ellil, M.S., and Mahmoud, K.H. (2005) *J. Appl. Polym. Sci.*, **95**, 1342–1353.
- 45 Malmonge, J.A., Dos Santos, M.A., and Sakamoto, W.K. (2005) *J. Mater. Sci.*, **40**, 4557–4560.
- 46 Zhang, S.H., Jin, X., Painter, P.C., and Runt, J. (2004) *Polymer*, **45**, 3933–3942.
- 47 Zhang, S., Painter, P.C., and Runt, J. (2004) *Macromolecules*, **37**, 2636–2642.
- 48 Zhang, S.H., Casalini, R., Runt, J., and Roland, C.M. (2003) *Macromolecules*, **36**, 9917–9923.
- 49 Zhang, S.H., Jin, X., Painter, P.C., and Runt, J. (2003) *Macromolecules*, **36**, 5710–5718.
- 50 Mpoukouvalas, K., Floudas, G., Zhang, S. H., and Runt, J. (2005) *Macromolecules*, **38**, 552–560; Zhang, S.H., Painter, P.C., and Runt, J. (2002) *Macromolecules*, **35**, 9403–9413.
- 51 Migahed, M.D., Ahmed, M.T., and Kotp, A.E. (2000) *J. Phys. D: Appl. Phys.*, **33**, 2108–2116.
- 52 Fragiadakis, D. and Runt, J. (2010) *Macromolecules*, **43**, 1028–1034.
- 53 Zardalidis, G. and Floudas, G. (2012) *Macromolecules*, **45**, 6272–6280.
- 54 Madbouly, S.A., Mansour, A.A., and Abdou, N.Y. (2007) *Eur. Polym. J.*, **43**, 1892–1904.
- 55 Madbouly, S.A., Mansour, A.A., and Abdou, N.Y. (2007) *Eur. Polym. J.*, **43**, 3933–3942.
- 56 Madbouly, S.A., Mansour, A.A., and Abdou, N.Y. (2006) *Macromol. Chem. Phys.*, **207**, 978–986.
- 57 Ristic, S. and Mijovic, J. (2009) *Macromol. Symp.*, **286**, 218–230.
- 58 Natali, S. and Mijovic, J. (2009) *Macromolecules*, **42**, 6799–6807.
- 59 Jin, X., Zhang, S., and Runt, J. (2004) *Macromolecules*, **37**, 4808–4814.
- 60 Jin, X., Zhang, S., and Runt, J. (2003) *Macromolecules*, **36**, 8033–8039.
- 61 Saad, G.R. (2002) *Polym. Int.*, **51**, 338–348.
- 62 Sengers, W.G.F., van denBerg, O., Wübbenhorst, M., Gotsis, A.D., and Picken, S. (2005) *Polymer*, **46**, 6064–6074.
- 63 Newman, D., Laredo, E., Bello, A., Grillo, A., Feijoo, J.L., and Muller, A.J. (2009) *Macromolecules*, **42**, 5219–5225.
- 64 Hakme, C., Stevenson, I., Fulchiron, R., Seytre, G., Clement, F., Odoni, L., Rochat, S., and Varlet, J. (2005) *J. Appl. Polym. Sci.*, **97**, 1522–1537.
- 65 Laredo, E., Grimaub, M., Barriolab, P., Bello, A., and Müller, A.J. (2005) *Polymer*, **46** (17), 6532–6542.
- 66 Lin, C.H., Huang, S.J., Wang, P.J., Lin, H. T., and Dai, S.A. (2012) *Macromolecules*, **45**, 7461–7466.
- 67 Madbouly, S.A. and Otaigbe, J.U. (2007) *Polymer*, **48**, 4097–4107.
- 68 Madbouly, S.A., Otaigbe, J.U., and Ougizawa, T. (2006) *Macromol. Chem. Phys.*, **207**, 1233–1243.
- 69 Panda, B., Bhattacharyya, A.R., and Kulkarni, A.R. (2013) *J. Appl. Polym. Sci.*, **127**, 1433–1445.
- 70 Laredo, E., Grimaub, M., Bello, A., Sanchez, F., Gomez, M.A., Marco, C., Campoy, I., and Arribas, J.M. (2005) *Polym. Sci. Polym. Phys.*, **43**, 1408–1420.
- 71 Dang, Z.M., Yan, W.T., and Xu, H.P. (2007) *J. Appl. Polym. Sci.*, **105**, 3649–3655.

- 72 Kortaberria, G., Arruti, P., and Mondragon, I. (2003) *Macromol. Symp.*, **198**, 389–398.
- 73 Kortaberria, G., Arruti, P., and Mondragon, I. (2001) *Polym. Int.*, **50**, 957–965.
- 74 Sellares, J., Diegoli, J.A., Canadas, J.C., Mudarra, M., Belana, J., Colomer, P., Roman, F., and Calventus, Y. (2012) *J. Phys. D: Appl. Phys.*, **45**, 505301.
- 75 Becker, O., Simon, G.P., Rieckmann, T., Forsythe, J., Rosu, R., Völker, S., and O'Shea, M. (2001) *Polymer*, **42**, 1921–1929.
- 76 Kanapitsas, A. and Pissis, P. (2000) *Eur. Polym. J.*, **36**, 1241–1250.
- 77 Madbouly, S.A., Serag Eldin, A.F., and Mansour, A.A. (2007) *Eur. Polym. J.*, **43**, 2462–2470.



## 27

### Positron Annihilation Spectroscopy: Polymer Blends and Miscibility

*Chikkakuntappa Ranganathaiah*

#### 27.1

##### Introduction

During the past few decades it has been realized that many of the physical and mechanical properties of polymers can be significantly improved by a process called blending. A polymer blend may be defined as a combination of two or more structurally different polymers or copolymers that gives rise to a material with a range of properties that are not deliverable by any of its constituents. The miscibility and phase-separation phenomenon of polymer blends have attracted significant attention in polymer research, due mainly to the multitude of purposes that polymer blends can be applied [1–5]. In order to predict and enhance the material properties of blends, it is important first to understand the nature and the underlying mechanism of blending at the molecular level. One rational approach, which forms the basis of this chapter, is to investigate the correlation between free-volume and miscibility level in blends [2–5]. Although many physical probes exist for characterizing the structure and properties of polymer blends, only a limited number of these probes are capable of characterizing the properties of the free-volume, due to its very small size and its complex evolution. During recent years, positron annihilation spectroscopy (PAS) has emerged as a unique and potent probing tool for characterizing the free-volume properties of polymers and polymer-based materials [5–8]. In PAS, the antiparticle of electron – the positron – is employed as a probe; however, because of its positive electric charge the positron is repelled by the ion cores and becomes localized preferentially in any atomic-sized voids or defects of the material. In polymer-based materials, positronium (the bound state of a positron and an electron) annihilation events are found to be contributed mainly from the free-volume cavities in a polymer matrix. Current reports suggest that PAS has been mainly employed in monitoring *ortho*-positronium (o-Ps, spin triplet state) annihilation lifetimes in polymers. Indeed, it has now been established that the lifetime of the o-Ps, and its probability of formation, are related to the free-volume hole size, fraction and distribution [6–8]. In

the case of polymer blends, PAS analyses have been applied extensively since 1995 [9–62].

Several chapters in this book have described the basics of polymer morphology, the types of polymer and the selection of polymers for the processes of blending, thermodynamic aspects of miscibility and phase separation covering both theoretical developments and experimental aspects in greater detail. Consequently, the reader is presumed now to be knowledgeable on these theoretical treatments, together with experimental techniques such as differential scanning calorimetry (DSC), transmission electron microscopy (TEM), scanning electron microscopy (SEM), and X-ray diffractometry (XRD). Hence, these aspects will not be included in this chapter; rather, attention will be focused immediately on the principles and techniques of PAS, and on its application when studying polymer blend miscibility.

## 27.2

### Positron Annihilation Spectroscopy

#### 27.2.1

##### The Positron Annihilation Process

The positron ( $e^+$ ) is the antiparticle of the electron ( $e^-$ ), and a positron–electron pair is unstable and hence annihilates. The annihilation of positrons in collision with electrons is accompanied by the emission of one, two, or more photons (gamma rays). Single-photon emission by electron–positron annihilation is possible only in the presence of a third body (a nucleus or electrons) that carries away the recoil momentum, whose probability is highly negligible. It has been observed that two-photon annihilation is the most dominant mode of positron annihilation. When a free positron annihilates with a free electron, at least two photons are created to conserve energy. The positron annihilation cross-section (i.e., the probability of annihilation) rapidly decreases with the increase in the number of emitted photons. When the number of created photons increases by one, the annihilation cross-section is multiplied by the fine-structure constant  $\alpha$  (1/137); that is, the probability of the annihilation process decreases by more than two orders of magnitude [65–71]. The cross-section of two-photon annihilation of a free positron and a free electron was calculated in the nonrelativistic approximation by Dirac. This cross-section increases with decreasing relative velocity  $v$  of the colliding particles:

$$\sigma = \frac{\pi r_0^2}{v/c}, \quad v \ll c \quad (27.1)$$

where  $r_0$  is the classical electron radius and  $c$  is the velocity of light in vacuum. Consequently, for a positron embedded in a sea of “cold” electrons with density  $n_e$ , one obtains the decay rate,

$$\lambda = \pi r_0^2 n_e c \quad (27.2)$$



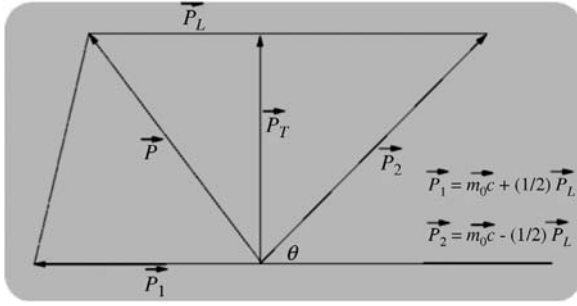


**Figure 27.1** The vector diagram of momentum conservation in the  $2\gamma$ -annihilation process. The momentum of the annihilation pair is denoted by  $P$ ; the subscripts L and T refer to longitudinal and transverse components, respectively.

By measuring the annihilation rate  $\lambda$ , the inverse of which is the mean lifetime  $\tau$  (which means the survival time of the positron in the medium) it is possible to obtain directly the electron density  $n_e$  that is encountered by the positron in the medium. Thus, a positron can serve as a test particle for the electron density of the medium. However, because of the opposite charges, a strong coulombic attraction exists between the positron and electrons of the medium, and as a result of this the electron density  $n_e$  is slightly enhanced from the equilibrium value in the matter medium. The measurement of positron lifetime in a given medium constitutes what is known as positron annihilation lifetime spectroscopy (PALS).

The kinetic energy of the annihilating pair is typically a few electron volts (eV). In their center-of-mass frame, each photon energy is exactly  $m_0c^2 = 511$  keV, and the two photons go strictly in opposite directions; that is, the emission direction is collinear to conserve linear momentum (Figure 27.1). Because of the nonzero momentum of the pair, which is due mainly to the finite momentum of the electron of the material medium, the photons deviate from collinearity in the laboratory frame. The momentum conservation law for the transverse component of the momentum yields a result:

$$\theta \cong \frac{P_T}{m_0c} \quad (27.3)$$

where  $180^\circ - \theta$  is the angle between the two photons in the laboratory frame and  $P_T$  is the momentum component of the electron–positron pair transverse to the photon emission direction. Usually,  $\theta$  is very small ( $< 1^\circ$ ), and hence Eq. (27.3) will be valid. For the pair ( $e^- e^+$ ), the momentum of the thermalized positron is almost zero, and hence the momentum component in Eq. (27.3) corresponds to the momentum of the electron. The experiment in which this deviation from collinearity in the annihilation photons is measured constitutes the angular correlation of annihilated radiation (ACAR). The measured angular correlation curve describes the momentum distribution of electrons of a particular medium in which the positrons are annihilated.

The motion of the electron–positron pair before annihilation also causes a Doppler shift in the energy of the annihilation photons measured in the laboratory system. The frequency shift is  $\Delta\nu/\nu = v_L/c$ , where  $v_L$  is velocity of the pair and  $c$  is the velocity of light. The difference in energies of the annihilation photons can be written as:

$$\Delta E = \pm \frac{v_L}{c}; \quad \Delta E = \pm \frac{cP_L}{2} \quad (27.4)$$

where  $P_L$  is longitudinal momentum of the pair. Thus, in the case of two-photon annihilation, measuring the shift in the frequency or the energy of the annihilation photons constitutes the third experimental method of PAS, namely Doppler broadening of annihilation radiation (DBAR). The Doppler shift in the energy  $\Delta E$  of the annihilation photon from 511 keV makes it possible (at least in principle) to determine the longitudinal component of the momentum of the electron–positron pair in the laboratory frame. In the laboratory, this shift in energy from 511 keV is very small, and is usually described in terms of line shape parameters  $S$  and  $W$  of the annihilation photon. The  $S$  parameter is associated with the contribution of valence electrons to annihilation, while the  $W$  parameter is associated with high-momentum core electrons of the medium to annihilation. This brief introduction to the three methods evolved is based on the “principle of positron annihilation” in material media, while the three above-described techniques constitute the basic methods of PAS.

### 27.2.2

#### Positronium

Thermalized positron (energy  $\sim 0.025$  eV) with an electron of the medium can also form a quasistationary state called the positronium (Ps) atom. Ps is an analog of the hydrogen atom, and positronium is therefore found either in the spin singlet state called *para*-Positronium ( $S=0$ ,  $e^+e^-$  spins antiparallel; p-Ps), or in the triplet state called *ortho*-Positronium ( $S=1$ ,  $e^+e^-$  spins parallel; o-Ps). The cross-section and the nature of annihilation depend on the mutual orientation of the spins of the particles participating in the annihilation process. The probabilities of spontaneous annihilation of p-Ps and o-Ps atoms are also different. Owing to conservation of spin angular momentum, p-Ps will decay by two-photon emission with a rate of  $1/(125 \text{ ps})$ , while o-Ps will decay by three-photon emission with a rate of  $1/(140 \text{ ns})$  in free space. In three-photon emission, the total energy  $2 m_0 c^2$  is shared by all of the photons. Generally, Ps is not formed in metals due to the fact that the positron sees a sea of free electrons (the electron density is high) and the probability of forming Ps is negligible. Rather, Ps is formed in metal oxides, molecular solids, macromolecules, and in liquids and gases which have relatively open structures (i.e., low electron density regions).

The most commonly used experimental methods for observing positron annihilation in matter are the three methods mentioned above: (i) measurement of the positron mean lifetime, using positron lifetime spectroscopy (PLS); (ii) measuring

the deviation from collinearity of the annihilation photons (using ACAR); and (iii) measuring the line shape parameter of the Doppler-broadened annihilation photons (using DBAR). As this technology has continued to develop, however, several other methods have been created such as: (i) a combined measurement of the positron lifetime with DBAR, termed the two-parameter method; and two- and three-dimensional ACAR, coincidence Doppler-broadening (CDB) experiment in which the background level is greatly reduced such that the core electron contribution can be easily and accurately measured. However, these methods are offshoots of the basic principles of positron annihilation [71]. As the thermalization of  $e^+$  in a medium occurs in a very short time, it reaches the bulk of the material quickly and annihilation occurs predominantly from the bulk of the medium. Consequently, in order to make positron annihilation techniques suitable for studying surface phenomena in materials, slow positron beams have been developed that make depth-profiling studies not only possible but also very rewarding [72].

In positron annihilation experiments, the source of positrons is usually a radioactive isotope such as  $^{22}\text{Na}$ . Positrons from  $^{22}\text{Na}$  are born with a kinetic energy of 540 keV and, when injected into a medium, they first slow down very quickly (on the order of  $1\text{--}2 \times 10^{-12}\text{ s}$  or ps) to thermal energies (on the order of  $kT \sim 0.025\text{ eV}$ , where  $k$  is the Boltzmann constant and  $T$  is the temperature). The mean implantation range usually varies from 10 to 1000  $\mu\text{m}$ , depending on the type of medium, which in turn guarantees [65] that positrons reach the bulk of the sample material very quickly. Finally, after living in thermal equilibrium the positron annihilates with an electron from the surrounding medium dominantly into two 511 keV gamma photons. The mean lifetime of positrons is characteristic of each material, and varies from 100 to 500 ps. Figure 27.2 shows, schematically, all three basic positron annihilation experiments. The  $^{22}\text{Na}$  nucleus emits an energetic 1.28 MeV photon within a few picoseconds ( $10^{-12}\text{ s}$ ) after the positron is emitted, and this serves

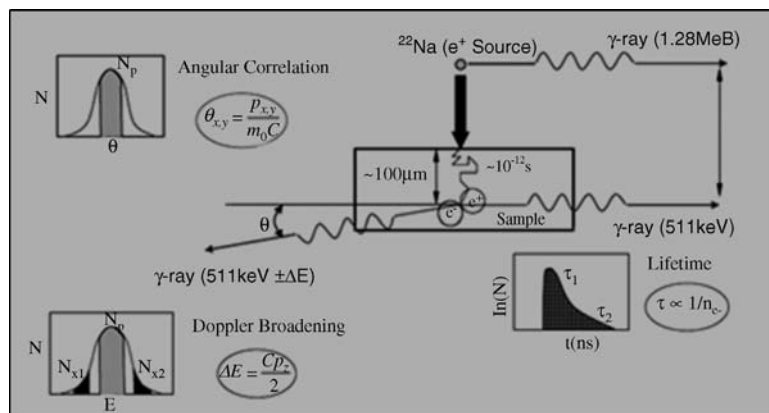


**Figure 27.2** Schematic of  $e^+$  annihilation into two annihilation gamma rays of energy 511 keV, demonstrating the three methods of PAS. Here,  $p_{xy}$  corresponds to  $\theta$  of Eq. (27.3) and  $p_z$  corresponds to  $p_L$  of Eq. (27.4).

as the birth signal for the positron. The lifetime of the positron can thus be measured as the time delay between the birth gamma and one of the annihilation gamma photons. As described above, the momentum of the annihilating electron–positron pair is transferred to the annihilation photon, and this can be detected as a small deviation from collinearity between the 511 keV annihilation photons moving in the opposite direction. The motion of the pair also produces a Doppler shift in the energy of the annihilation photon, which can be measured accurately using a high-energy-resolution HpGe detector.

#### 27.2.2.1 Positron and Positronium Sensitivity to Defects and Free Volume

In the case of metals containing defects of various types, the positron tends to localize in these defects and, if trapped in a defect, it exhibits a characteristic lifetime that is different from annihilation with a free electron. Positron annihilation has been used extensively in the study of metals, metal oxides, alloys and semiconductors [73–81], for the reason that it is possible to determine such important characteristics of metals as the electron momentum distribution, the Fermi energy  $\varepsilon_F$ , the number of free electrons  $Z_C$  per metal atom, and the concentration  $n_e$  (in  $\text{cm}^3$ ) of such electrons in the conduction band, together with the concentration of defects and their type. These characteristics, as is well known, largely determine the mechanical, electrical, magnetic and optical properties of materials [71]. In semiconductors, movement of the Fermi level and defect concentrations can be accurately measured. These studies have established that positron methods are defect-sensitive and nondestructive in nature, as the information is carried away by the annihilation photons and the material can be reused after the test.

The Ps atom also tends to localize in larger defects or cavities called free volume cavities in a similar fashion to the positron. In vacuum, o-Ps decays through three-photon emission, but in condensed matter the Ps atom undergoes many collisions during its lifetime with the surrounding electrons in its localized site, competing with its own electron, and gets annihilated with an electron from the surrounding electron with opposite spin. This process, which is referred to as “pick-off annihilation,” has a rate of about 1/(few ns), which is substantially faster than the vacuum decay rate of o-Ps (1/140 ns). The pick-off process results predominantly in the emission of two photons against three-photon emission. The p-Ps, on the other hand, proceeds through two-photon emission. In the ground state, in the absence of any conversion, one-fourth of all Ps atoms are formed in the singlet state and three-fourths in the triplet spin state. The annihilation of o-Ps reflects the electron momentum similar to positron in metals, and annihilation of the p-Ps mainly reflects the momentum of the Ps atom itself. The positron/Ps lifetime in matter depends on the electron density in the region from where positron/Ps annihilates. In the presence of free volume cavities (voids), the Positronium lifetime determines the void size [76] from where it annihilates. Hence, Ps in condensed media such as polymers and polymer blends provides similar information as does the positron in metals and alloys [73–80].

### 27.2.2.2 Models Predicting Positronium Formation

So far it is clear that, in molecular media, the probability of Ps formation is greater as these materials have open structures of lesser electron density domains, known as free volume cavities. Therefore, it is essential to acquire a brief understanding of the Ps formation mechanism. Over the years, several models have been developed for this purpose. The probability of formation of Ps in a given medium depends on the energy of the electron lying within an energy gap where no other electronic energy transfer processes are possible. In order to capture an electron from a molecule with ionization energy  $E_i$ , the kinetic energy  $E$  of the  $e^+$  must be greater than  $(E_i - E_{ps})$ , where  $E_{ps}$  is the binding energy of Ps. In vacuum,  $E_{ps}$  is 6.8 eV but it may be smaller in the medium. When  $E > E_i$ , the Ps atom is formed with a kinetic energy greater than its binding energy and will immediately break up. Inelastic collisions compete with Ps formation until the  $e^+$  kinetic energy is less than  $E_{ex}$ , the lowest electronic excitation energy. Thus, the probability of Ps formation is highest in the range  $(E_i - E_{ps}) < E < E_{ex}$ , which is called the Ore gap [82], and the Ps yield can be calculated from the size of this gap. Although this model works well for gases, for liquids Mogensen [83] has proposed the spur model of Ps formation. The basic premise of this model is, when the positron loses its last few hundred eV of kinetic energy (the positron in  $^{22}\text{Na}$  is born with a kinetic energy of 540 keV), it creates a track (the so-called “spur”) in which it lives along with electrons, ions, free radicals and excited molecules. The electrostatic attraction between the positron and electron in the spur can result in Ps formation that will compete with other processes mentioned above, including ion–electron recombination, the diffusion of electrons out of the spur, and the annihilation of electrons with positrons. This model provides a correlation between Ps formation probability and the properties of electron spurs studied in radiation chemistry. The main difference between these two theories is that, in the Spur model, Ps is formed only when  $e^+$  is thermalized, whereas in the Ore model Ps is formed during thermalization. Later, Tao [84] modified this theoretical approach to provide a satisfactory explanation of most of these experimental results. Recently, Ito and Zhang [85] proposed a new model of Ps formation called the “resonant model,” which consists of two stages. The first stage refers to the epithermal positron and the ground-state molecule forming the resonant excited state, while the second stage is Ps formation from the near-thermal positron and the excited molecule [85]. Any positron that has failed to form Ps in the epithermal stage will be thermalized in the spur and so can form Ps. Hence, the resonant model of Ps formation contains aspects of both the Ore model and the Spur model to some extent, but requires further experimental verification before it can be used extensively [84].

In the study of polymers and polymer-based systems such as blends, the probe of choice should be sensitive to segmental motions, on a length scale shorter than those responsible for glass transition. At low temperatures, a small size probe will be sensitive to changes in molecular motion. In amorphous polymers, molecular dynamics is influenced not only by the chemical microstructure but also by other processes such as molecular packing, physical aging and crosslinking, all of which

contribute to the motion and structural relaxation. Such systems are often spatially or dynamically heterogeneous. In this context, the concept of free volume is emphatic and emerges as an internal parameter of choice for the study and understanding of the motional phenomena of disordered polymers and blends at the molecular level [86]. This concept has also been applied successfully to methods employing molecular probes. At this point, the concept of free volume in polymers and blends will be introduced very briefly, and indications made of how this can (qualitatively) influence the viscoelastic properties of polymer blends, particularly miscibility. Notably, an attempt is made to provide an understanding of free volume connection to miscibility and real interfaces in polymer blends. In their simplest definition, the nanometer-sized free volume cavities or cavities are the open spaces or voids that have evolved as a result of the molecular architecture and chain folding in polymers. During the past few decades of polymer research, positron annihilation studies of polymers and blends have in particular treated free volume as an internal material parameter through which a quite large number of viscoelastic properties of polymers and blends could be elucidated. The concept of free volume and relevant theories connecting positron annihilation studies are briefly outlined in the following section, though further details are available elsewhere in several related reviews [82–85].

### 27.3

#### Free Volume Theory

A simple theory of free volume was formulated to explain the molecular motion and physical behavior of the glassy and liquid states of matter [87]. This theory has been widely accepted in polymer science because it is conceptually simple and intuitively plausible for understanding many polymer properties at the molecular level. The derived macroscopic properties from free volume perspective are fruitful with the assistance of quantum and statistical mechanical calculations.

Batchinsky [88] considered fluidity in a liquid as being due to the presence of free volume, and developed the simple formula

$$\eta = \frac{1}{V_f} = \frac{1}{(V - V_o)} \quad (27.5)$$

where  $\eta$  is the viscosity,  $V_f$  is the free volume,  $V$  is the total volume, and  $V_o$  is the occupied volume of the molecules of the system. Equation (27.5) is of great intuitive appeal as it qualitatively describes the temperature dependence of viscosity. However, for many systems – and especially for polymers in the fluid state – this formula is only a crude approximation. The viscosity of *n*-alkanes was studied experimentally by Doolittle [87], who proposed the free volume theory used at present. According to Doolittle, the dependence of viscosity on the free volume of the system is expressed as

$$\eta = A_o e^{\left( \frac{B_o V_o}{V_f} \right)} \quad (27.6)$$

where  $A_0$  and  $B_0$  are constants. A similar equation was derived by Fox *et al.* [89], except for the difference that  $V_0$  was replaced by  $V$  since  $V_f \ll V$ . This modified equation was:

$$\eta = A_0 e^{\left(\frac{B_0 V}{V_f}\right)} \quad (27.7)$$

When Williams, Landel and Ferry [90] studied the temperature dependence of free volume, the result was the famous WLF equation:

$$V_f = V_{f,g} [1 + \alpha_o (T - T_g)] \quad (27.8)$$

where  $T_g$  is the glass transition temperature,  $V_{f,g}$  is free volume at  $T = T_g$ , and  $\alpha_o$  is the thermal expansion coefficient of free volume. From this relation, it is clear that  $T_g$  becomes a natural choice as the reference temperature in the study of polymers.

It is a well-known fact that, molecular transport in polymeric materials depends heavily on the amount of free volume or space not occupied by polymer chains in the material. The free volume, whether as static voids created by inefficient chain packing or as transient gaps generated by thermally induced chain segment rearrangements, presents a low-resistance avenue for the transport of diffusing molecules. In fact, the larger the pathways are, the faster are the molecules transported through the polymer. These free volume considerations are embodied in the following statistical model of Cohen and Turnbull [91]:

$$D = a \exp(-bV_A/V_f) \quad (27.9)$$

where  $a$  and  $b$  are positive constants,  $V_A$  is the minimum volume required for penetrant A to execute a diffusion step and hence is a measure of penetrant size, and  $V_f$  is the average free volume size.

### 27.3.1

#### Free Volume Model and Positronium Lifetime Connection

The free volume in an amorphous polymer may be considered to be a cluster of defects which are pinned in space but are of sufficient size to allow motion into the defect of neighboring molecular entities. In a small gas molecule, the species diffusing into the defect may be a molecule or, in the case of macromolecular system such as a polymer, the moving entity may be a small number of backbone units. A simplified quantitative treatment of the free volume model [85,92], assumes that Ps is always localized in a low-density region such as the free volume cavity, and relates the changes in o-Ps lifetime in such a cavity to the change in total volume of the polymer [93–102]. In doing so, an account of the factors influencing the Ps yield is made. A model was formulated to connect both the o-Ps yield and pick-off lifetime to the free volume in molecular materials, and in this way a theoretical relationship can be obtained between the free volume size and the relative number of such cavities [94,95]. A slightly different approach [93]

was developed to explain the lifetime variation with pressure, the free energy-surface tension in the cavity to connect the void size with the Ps annihilation parameters. In polymers, the Ps lifetime is generally in the range 1 to 5 ns. Values of free volume size have been calculated by using the group contribution method [95] or by estimating the occupied volume (van der Waal's) [98]. The size of the free volume cavities can also be calculated using semi-empirical relationships [103].

The viscoelastic properties of polymers can be explained based on the free volume concept. Positron physicists in particular have developed several theoretical models to connect the free volume to positron annihilation parameters, and some of these theoretical models are briefly described here. Ferrell [92] made a theoretical study using liquid helium as a simple example to understand the pick-off behavior of Ps in molecular substances. According to the data obtained, there are two different types of forces which act on the Ps atom and which tend to compensate one another. One force is the attractive van der Waals-type dispersion force, while the other is a repulsive exchange force. In general, the exchange force works against the pick-off force, and is probably the dominant reason for the long lifetime in most materials in which Ps is formed. In about 1960 it was first realized that the temperature dependence of o-Ps lifetime in molecular media should be associated with density changes in the materials. From a quantitative aspect, a greater free volume between the molecules is the result of low density, which in turn leads to a smaller overlap between the Ps wave function and the surrounding molecular electrons with which Ps annihilates. Thus, the rate at which o-Ps pick-off annihilation occurs is inversely proportional to the size of the free volume cavities.

A simplified theory was proposed by Brandt, Berko and Walker [104] in which the positron of Ps wave function in the field of the electron was replaced by the wave function of the Ps atom. The Ps wave function was then calculated for different lattice structures in the Wigner-Seitz approximation. This approximation is generally referred to as the "free volume model," since the free volume is used as one of the parameters in the calculation. This model relates o-Ps lifetime to the average free volume hole size of the medium, and results construed that the o-Ps lifetime would measure the lattice-Ps interaction. Later, Tabata *et al.* [105] and Ogata and Tao [106] each adopted similar – but different – approaches by considering a unit cell and Ps located at the center instead of the center of the molecule, as used by Brandt *et al.* [104].

The correlation between o-Ps lifetimes and dielectric constants in a number of polymers was discussed by Story [107]. The most successful attempt was made by Gray *et al.* [108], who found that the o-Ps quenching cross-section in *n*-alkenes directly correlated with the electron polarizability of the molecule. Wilson *et al.* [93] explained the dependence of pressure on o-Ps lifetimes by using a slightly different description that Ps localizes only in low-density regions. The free volume model developed by Brandt *et al.* [104] has been refined by the same group, with the inclusion of molecular vibrations and the Ore gap Ps yield. Earlier, the same group applied the concept that Ps is formed only if a free volume larger than a certain critical value exists [109]. According to Thosar *et al.* [95], the formation and



decay of Ps atoms is confined to the free volume of the medium, and there is no electron exchange between molecules. Free volume is considered to be divided into a number of sites of average free volume occupied by Ps atoms, which are quenched due to pick-off annihilation. Thus, a theoretical relationship was obtained between the o-Ps lifetime and its intensity to the free volume in molecular materials, including polymers.

## 27.4

### Characterization of Polymer Blends by PAS

Characterization tools are crucial in order to comprehend the basic physical and chemical properties of polymers and their blends. From the point of view of end applications, the tools chosen facilitate the study of emerging materials by providing useful and vital information on some intrinsic properties [3,4]. Various techniques have been employed for the characterization of polymer blends [3,6], the most common being differential scanning calorimetry (DSC) from which the  $T_g$  can be measured and it can be inferred whether the given polymer blend is miscible or immiscible. Viscometry has also been widely used for blends in solution form, and the miscibility properties have been understood through the Flory–Huggins interaction parameter. For morphological studies, techniques such as SEM and TEM have been used [3] to provide surface structure and electronic information of the system. The development of SEM inspired the creation of other “scanning probe” microscopies, notably atomic force microscopy (AFM) [3]. Whereas, unfortunately, these probes are limited by spatial resolution, PAS methods in contrast have become established as powerful defect spectroscopy tools in metals, alloys, ionic materials, polymers, blends and Zeolites, due to their sensitivity and nondestructive nature. As the size of the probe (positron or the positronium) is small enough to probe the molecular and chain motions, PAS is best suited to the study of polymers and polymer blends [110]. Conventional PLS typically probes the free volume at a depth of 200  $\mu\text{m}$  into the sample, so the bulk of the polymer is explored. It is not always true that the surface properties reflect the properties of the bulk at the microscopic level; rather, the optical, SEM, TEM and AFM tools provide surface morphology. In this context, low-energy positron beams are capable of exploring the depth-profile of the free volume in polymers and blends ranging from several nanometers up to several micrometers in depth. Therefore, the application of slow positron methods to polymers and polymer blends has attracted increased attention as it provides a means of obtaining quantitative information on the free volume at different depths in the system. The full details of PAS methods are available elsewhere in books, reviews and in conference proceedings [65,73,74,110–112]. An overview of PAS and its use in studying the miscibility of polymer blends is presented in the following section.

Positron annihilation methods have been used extensively in studies of the microstructure and physical and chemical properties of polymers [113–119], polymer blends [9–62], and recently polymer-based nanocomposites [120,121].

Owing to the complex nature of the microstructure in polymers, positron annihilation measurements were found to be sensitive to the physical properties, which made them unique with respect to glass transition and subglass transitions. During the past 20 years, studies on polymer blends employing positron methods have drastically increased in number, and the quality of data interpretation [9–62]. Several attempts have been made to understand the miscibility behavior of blends with respect to the interface formed between two immiscible polymer components [65,73,74,110–112]. Experimentally, the free volume of a polymer blend can be measured directly and accurately using PALS. In the following sections, details of experiments of positron annihilation are provided, albeit with special emphasis, as this method is invariably used in polymer blend studies. Studies conducted using Doppler broadening and coincidence Doppler broadening will also be reviewed briefly. It is interesting to note that several investigations have reported both discrete lifetime components (average free volume size) analysis and distribution of lifetimes (the probability distribution of free volume cavities) which is rather more close to the real situation in a polymer blend; these two aspects of data reduction are also presented in the following section.

## 27.5

### Experimental Methods of PAS

#### 27.5.1

#### Positron Annihilation Lifetime Spectroscopy (PALS)

The method of positron lifetime measurement with  $^{22}\text{Na}$  as positron source is shown schematically in Figure 27.3a. The positron source emits, almost simultaneously, a gamma ray of 1278 keV energy along with a positron indicating birth of

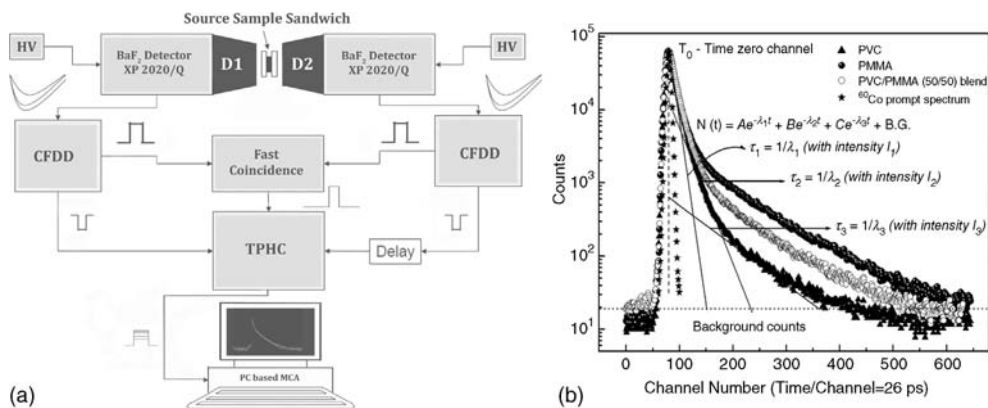


**Figure 27.3** (a) Block diagram of positron lifetime spectrometer; (b) Typical lifetime spectrum of positrons in polymers PVC, PMMA and their blend of 50/50. The instrument's resolution ( $^{60}\text{Co}$  curve) is also shown.

the positron. The lifetimes of individual positrons,  $t$ , can be measured as the time difference between the 1278 keV gamma ray and one of the annihilation photons (511 keV). In reality, positron lifetime measurements involve measuring the time spectrum of delayed coincidences (fast-fast coincidence system) between these two gamma rays. Present-day lifetime spectrometers employ state-of-the-art detectors and advanced electronics, and today even digital lifetime spectrometers have been developed [122]. In Figure 27.3a, the detectors D1 and D2 ( $\text{BaF}_2$  or plastic scintillators) detect the 1278 and 511 keV gamma rays respectively. Fast signals related to the time of emission of corresponding gamma rays are generated by constant-fraction differential discriminators (CFDDs), after which the signals are fed to the start and stop inputs of a time-to-pulse height converter (TPHC). Energy selection (1278 keV for the start, 511 keV for the stop) is also provided by the CFDDs. The fast coincidence circuit produces the gate signal for the TPHC, provided that the coincidence event of gamma rays with proper energies has occurred simultaneously. The TPHC output signal amplitude, which is proportional to the time delay between the 1278 keV and 511 keV gamma rays, is digitalized by an analog-to-digital converter (ADC) and then stored in memory address in a multi-channel analyzer (MCA) [123]; thus, the spectrum of the positron lifetime is obtained as the histogram of counts  $N(t)$ . The resultant time spectrum is a sum of exponentials of lifetimes in a medium. However, in practice only up to three lifetime components can typically be resolved in molecular substances such as polymers and polymer blends, whereas in zeolites up to five to six lifetime components can be resolved. Currently, standard computer programs are available for analysis such as PATFIT [124–126], while PALSfit [127] used by many positron research groups worldwide. The experimentally measured spectra differ from the analytical description given in Eq. (27.10) by the convoluted time resolution function. This resolution function, which is the response of the spectrometer to prompt coincidence events, resembles the Gaussian-like shape and is characterized by the full width at half-maximum (FWHM). In fact, the FWHM and count rate are crucial characteristics of lifetime spectroscopy that determine the quality of the experimental data.

The decay curve of positron lifetimes measured experimentally can be represented mathematically as:

$$y(t) = N_s(t) \sum_{i=1}^n I(t) \alpha_i \lambda_i \exp[-\lambda_i t] \quad (27.10)$$

where  $N_s$  is the total number of counts,  $\alpha_i$  is the fraction of positrons annihilating with annihilation rates  $\lambda_i$ , and  $I(t)$  is the instrumental resolution determined from the lifetime spectrum in a defect-free medium [124–126]. In PATFIT or PALSfit [127], this is provided by the RESOLUTION program. The number of lifetime components “ $n$ ” is equal to number of different states from which positrons annihilate from the medium. In practice, the positron lifetime spectrum of Eq. (27.10) is convoluted with a Gaussian resolution function (sometimes a combination of two or three Gaussians) whose FWHM ranges from 180 to 280 ps depending on

the system configuration. About 8–10% of positrons annihilate in the source material ( $^{22}\text{Na}$  and the source backing), and hence proper “source corrections” shall be made. Constant background counts must be corrected before the spectrum is convoluted [42,43]. In homogeneous crystalline materials, all of the positrons inhabit the same environment and have the same annihilation probability per unit time. Positrons have a deBroglie wavelength of the order of  $10\text{ \AA}$  at room temperature, which is considerably greater than the lattice spacing in crystalline materials. Consequently, only one mode of annihilation is involved in such cases, and the resulting lifetime distribution is a single exponential decay with one lifetime component of the type:

$$N(t) = N_0 + e^{-\lambda_1 t} \quad (27.11)$$

However, in molecular media such as polymers, polymer blends and polymer-based composite materials, positron or Ps will inhabit a different environment and have different lifetimes. As a result, the measured lifetime spectra in such systems will represent many decaying exponentials superposed with the instrumental resolution function. Figure 27.3b shows a typical lifetime spectrum in a polymer blend and its constituents.

Generally, three to four lifetime components are resolved in polymers, and their attribution is as follows. The shortest lifetime component  $\tau_1$  with intensity  $I_1$  is attributed to contributions from free positron annihilation (inclusive of p-Ps lifetime). The intermediate lifetime component  $\tau_2$  with intensity  $I_2$  is considered to be due to the annihilation of positrons trapped at defects present in the crystalline regions, or those trapped at the crystalline–amorphous interface boundaries. The longest-lived component  $\tau_3$  with intensity  $I_3$ , is due to pick-off annihilation of the o-Ps in the free volume cavities present mainly in the amorphous regions of the polymer [42,43]. The simple model of a Ps atom in a spherical potential well of radius  $R$  leads to a correlation between o-Ps lifetime  $\tau_3$  and  $R$  [70,128–130]:

$$(1/\tau_3) = 0.5 \left[ 1 - \left( \frac{R}{R + \Delta R} \right) + \frac{1}{2\pi} \sin \left( \frac{2\pi R}{R + \Delta R} \right) \right] \text{ns}^{-1} \quad (27.12)$$

where  $R$  is the radius of the free volume cavity, and  $\Delta R$  is the fitting parameter termed as a measure of the electron layer thickness around the free volume cavity. A value of  $1.656\text{ \AA}$  has been determined for  $\Delta R$ , empirically making use of the known cavity sizes from data available for molecular media and zeolites [71]. It follows that the average cavity volume,  $V_f$ , can be calculated as  $(4/3)\pi R^3$ . The total fractional free volume,  $F_v$ , of the polymer/blend under study is then calculated as:

$$F_v = C V_f I_3 \quad (27.13)$$

where  $C$  is a constant whose value is found to be  $0.0018\text{ \AA}^{-3}$  [9,28,61]. Despite the simplicity of the model assumptions, Eq. (27.12) seems to hold surprisingly well in the region of  $R$  up to  $10\text{ nm}$ , and constitutes the base for numerous PAS applications to study the free volume and its changes in polymers and polymer blends. Mention is made here of only few studies of polymers by using PAS to

understand glass transitions [77,112] pressure dependencies [77,112], gas transport [131], diffusion [113–116], structural relaxation [117–119], optical properties influenced by diffusion [116] and miscibility and phase separation in blends [42,43,45]. Considerable debate has taken place on the interpretation of o-Ps intensity as a measure of free volume cavity concentration. Indeed, it has been inferred that care must be exercised in attributing this parameter as it is influenced by various factors such as irradiation effects [75,76], and the influence of chemical species affecting Ps formation probability, such as chemical and magnetic quenching [131] and inhibition process [131]. However, the average free volume size  $V_f$  and fractional free volume  $F_v$  derived for polymers and polymer-based materials are well understood and accepted.

### 27.5.1.1 Free Volume Distribution-Lifetime Analysis by Laplace Transform Method

The difficulties encountered in the analysis of positron decay curves, particularly in polymers and blends, limit the determination of free-volume sizes only to average values. In reality, any molecular media will consist of free volume cavities of the same size and also of different sizes, because the evolution of free volume is due to chain folding and molecular packing. As such, the free volume cavities or cavities will be of different sizes and, in order to obtain the distribution of free volume sizes close to the actual situation, advances have been made in the analysis of the positron annihilation lifetime spectrum using integral transform methods. From such an analysis, it is possible to extract continuous distributions of annihilation rate probabilities. One such integral transform method used to derive free-volume and pore-size distributions from the measured positron lifetime spectrum is the CONTIN program [132], although other programs, such as MELT, also exist [133]. All of these advanced programs provide basically the same information, namely the annihilation rate probability density function (PDF).

In many porous media such as polymers, composites and proteins, the heterogeneity of the local molecular environment from which positron annihilation occurs is expected to generate a distribution of lifetimes. In such cases it is necessary to replace the sum in Eq. (27.10) by an integral,

$$y(t) = N_s \int_0^{\infty} \lambda \alpha(\lambda) I(t) \exp(-\lambda_i t) d\lambda \quad (27.14)$$

where  $\alpha(\lambda)$  is the annihilation rate PDF, and other parameters have the same meaning as described above. Reliable algorithms have been developed for the solution of Eq. (27.10) and related Fredholm integral equations based either on eigen function expansions of the Laplace integral [134–136] or on the method of regularization [137–142]. A constrained, regularized least-squares method for the solution of Fredholm integral equations is available as a Fortran program called CONTIN, developed by Provencher [139–142]. Gregory has modified this program to solve integral equations with convoluted exponentials as kernels (CONTIN-PALS2) [143–145]. This approach avoids the direct determination of  $I(t)$ , which is

the resolution function of the spectrometer, by employing the decay curve of a reference material with a well-known short single lifetime,  $\lambda_r^{-1}$ . The CONTIN-PALS2 program includes source components and constant background in the sample and reference decay curves without the need for a direct knowledge of  $I(t)$  [144]. The method can define discrete components in the annihilation rate PDF if their lifetimes are well separated but have the added flexibility to describe continuous distributions of annihilation rates if it is demanded by the data.

The fraction of positrons annihilating with rates between  $\lambda$  and  $\lambda + d\ln\lambda$  is represented as  $\lambda\alpha(\lambda)d\ln\lambda$ . This is the annihilation rate PDF employed by CONTIN-PALS2. The corresponding annihilation lifetime PDF is expressed as  $\lambda^2\alpha(\lambda)$ . The fraction of positrons annihilating with lifetimes between  $\tau + d\tau$  is represented as  $\lambda^2\alpha(\lambda)d\tau$ .

The transformation of the annihilation rate PDF that is,  $\alpha(\lambda)$  to the corresponding radius PDF for the free-volume regions, the sites of o-Ps annihilation is conveniently determined using Newton's method. Therefore, the radius ( $R$ ) PDF is given by

$$f(R) = 2\Delta R \{ \cos[2\pi R/(R + \Delta R)] - 1 \} \alpha(\lambda)/(R + \Delta R)^2 \quad (27.15)$$

where  $\Delta R$  carries the same meaning as described in Eq. (27.12) and takes the value 1.656 Å. The fraction of positrons annihilating in cavities with radii between  $R$  and  $R + \Delta R$  is given by  $f(R)dR$ .

For spherical cavity, the free-volume PDF is expressed as

$$g(V) = f(R)/4\pi R^2 \quad (27.15a)$$

Therefore, the fraction of positrons annihilating in cavities with volumes between  $V$  and  $V + dV$  is written as  $g(V)dV$ . Theoretical treatment using molecular dynamics and kinetic theory [146,147] has predicted that the radii and the free volume cavities in polymer obey the distribution functions  $f(R)$  and  $g(V)$ , respectively.

### 27.5.1.2 Free-Volume Distributions in Polymer Blends

Positron annihilation rate distributions for a typical immiscible polymer blend PVC/PS of (80/20) composition and pure PVC and PS are shown in Figure 27.4a, and the radius and free volume cell size distribution PDFs are shown in Figure 27.4b. These PDFs are obtained from CONTIN-PALS2 analysis of the measured lifetime spectra. It is clear from the distribution curves that the width of the curve for PVC is wider compared to PS, while the blend has a distribution in between the constituent polymer distribution, thus demonstrating the ability of the computer routine CONTIN-PALS2 (from the present authors' studies).

From the radius and free volume size distributions shown below, it becomes very clear that the free volume becomes modified in the blend when the component polymers are blended, and that this distribution is unique from that of both polymers.

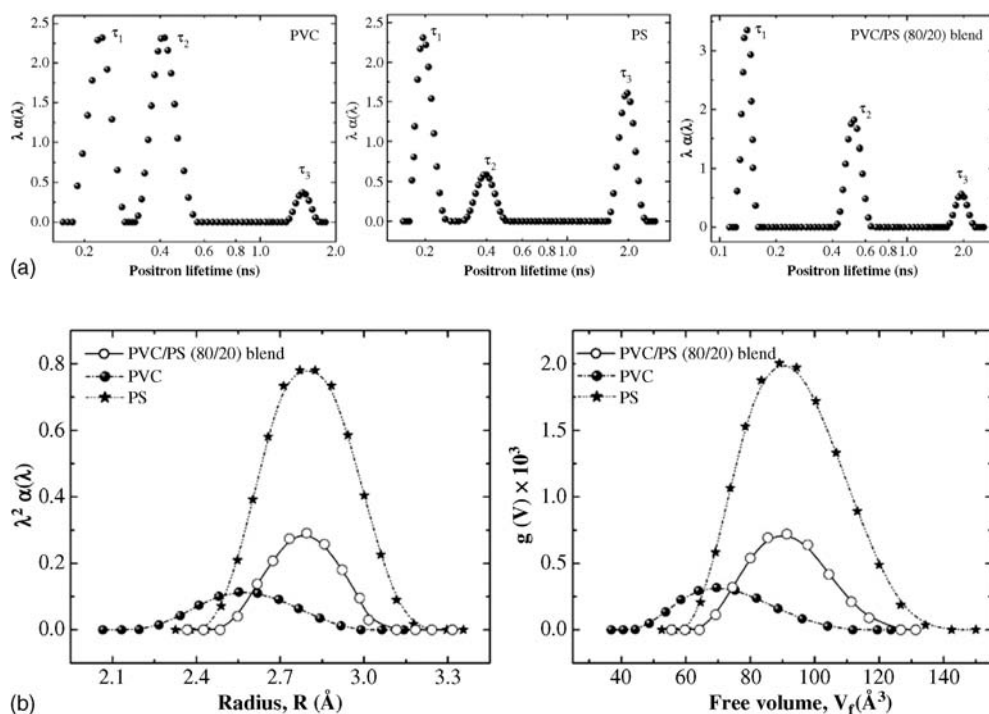


**Figure 27.4** (a) Positron annihilation rate distribution PDF for PVC and PS polymers and their blend PVC/PS (80/20) composition. Three-peak solution obtained from CONTIN-2 program is plotted (authors' studies);

(b) Radius and free volume distribution PDFs for PVC and PS polymers and their blend PVC/PS (80/20) composition. Three-peak solution obtained from CONTIN-2 program is plotted (authors' studies).

### 27.5.1.3 Angular Correlation of Annihilation Radiation (ACAR) Method

The origin of angular correlation of annihilation radiation has been explained earlier (Figure 27.2). Owing to the finite momentum of the ( $e^+e^-$ ) pair, due mainly to the momentum of the electron, there is a deviation from collinearity. Thus, by detecting the two annihilation gamma rays in coincidence as a function of the angle  $\theta$  (the deviation of the gammas flying apart from  $180^\circ$ ), it is possible to determine the momentum of  $e^-e^+$  pairs (which gives electron momentum). Angular correlation experiments provide an excellent momentum resolution (0.2 to 5 mrad) in comparison with DBAR experiments [67,78]. This corresponds to the energy resolution of DBAR measurements in the range of 0.05 to 1.3 keV. As the energy resolution obtainable from modern-day DBAR detectors is limited, ACAR is the preferred technique when momentum resolution is very important. On the other hand, DBAR is a simple experiment that requires very little acquisition time to acquire the same information. ACAR studies have provided very accurate estimates of Fermi energy of the system under study, and activation energy/vacancy migration energies can also be readily obtained. As the angular correlation experiment can resolve neither the angular deviation in the  $x$  direction, nor

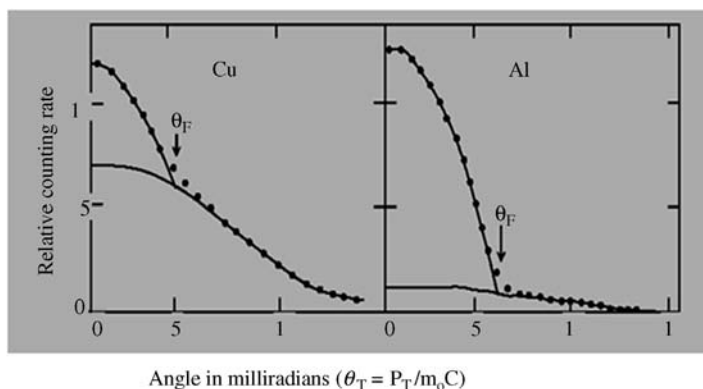


**Figure 27.5** Typical angular correlation curves in metals (Al and Cu).

the Doppler experiment in the  $\gamma$  direction, the counting rate observed experimentally is given by:

$$N(\theta_z) = c \int_{-\infty}^{+\infty} \int_{-\infty}^{+\infty} dp_x dp_y \rho(p_x, p_y, \theta_z m_0 c) \quad (27.16)$$

where  $\rho(p_x, p_y, p_z)$  is the momentum distribution of the annihilating positron-electron pairs in the medium. When the positron is free and is in thermal equilibrium with the medium, its momentum is negligible and the angular correlation curve represents the  $p_z$  – the transverse momentum of the electrons of the medium. As an example, the ACAR curves obtained in the case of single crystals of Cu and Al are shown in Figure 27.5, and it is evident that the Fermi energy can be obtained readily and accurately from ACAR measurements.

It is clear from Figure 27.5, that the contribution of free electrons and the core electrons to the annihilation process are well resolved. The inverted parabolas represent the free electrons contributing to annihilation process, while the broad Gaussian curves represent the contribution of the core electrons.

#### 27.5.1.4 Doppler Broadening of the Annihilation Radiation (DBAR) Method

In relation to Figure 27.2, DBAR is due to the motion of the  $(e^+e^-)$  pair in the medium before annihilation. This is measured with a standard gamma-ray spectrometer equipped with the HpGe semiconductor detector. The energy resolution (FWHM) of such detectors will be around 1.1 keV at 511 keV. The Doppler broadening is characterized by line shape parameters, namely  $S$  and  $W$ . The  $S$ -parameter is defined as the ratio of the area of the central part (Figure 27.6a) of the annihilation photo peak to the total area under the curve, while the  $W$  shape parameter expresses the relative contributions of tails (Figure 27.6a) to the total peak area. The  $S$ -parameter is attributed to the relative contribution of lower-momentum electrons to positron annihilation and is more, while the  $W$ -parameter corresponds to the contribution of the core electrons with a higher momentum to annihilation and is less [110,148]. A typical DBAR spectrum after background



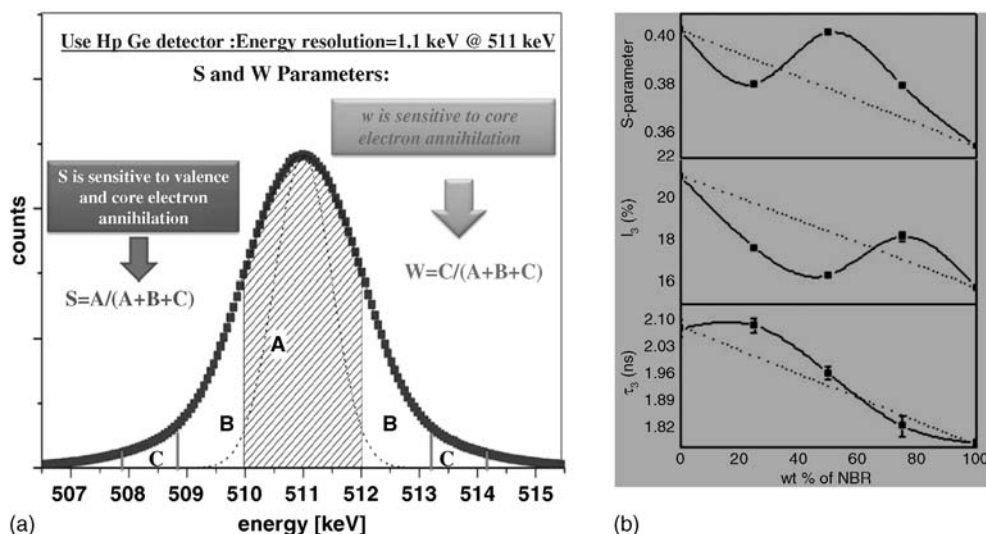


**Figure 27.6** (a) Typical annihilation gamma spectrum obtained with an HpGe detector. The dotted curve represents the true resolution of the spectrometer; (b) Variation of S-parameter,  $I_3$  and  $\tau_3$  with wt% of NBR in the EPDM/NBR blend. The dotted line represents the simple additive rule. Reproduced with permission from Ref. [52].

count subtraction is shown in Figure 27.6a, with the S- and W-parameters defined. For instance, a relative increase in the fraction of positrons trapped at the open-volume defects can be markedly reflected by an increase in the observed S-parameter values. A useful approach here is to present experimental data in terms of the S–W plot, which permits qualitative conclusions to be drawn on the evolution of defects participating in positron trapping and hence to identify the defect type.

An inherent problem in the DBAR experiment is the high background counts due to Compton scattering of 511 and 1278 keV gamma rays [69,148–152]. This is a particularly pronounced problem when measuring the contribution of high-momentum electrons to the annihilation peak, and is important when elucidating the chemical environment of the defects. The background can be drastically reduced by using the coincidence technique, which registers both annihilation gamma rays in coincidence; this method is known as coincidence Doppler broadening (CDB). As the time required for DBAR measurements is very much less than for ACAR, DBAR is often the preferred second method of PAS for any investigation [67,68]. If CDB is employed between the two annihilation gamma rays, again the time required to acquire a statistically good spectrum is greater but the information obtained in this way will be very useful and precise. The chemical environment at the site of positron annihilation can be well understood from CDB experiments, and consequently the technique has recently become much more important in positron experimental research [153].

In polymers, the o-Ps intensity ( $I_3$ ) is a measure of relative number of free volume cavities, and it also represents the probability of Ps formation in such

systems. With adequate precaution exercised for its origin, Jean *et al.* [77] developed an empirical relation connecting the surface area  $S$  encountered by o-Ps in the free volume cavity and the o-Ps intensity as

$$\begin{aligned} I_3 &= 3.0 + 0.033 S; I_3 \text{ is } \% \text{ and } S \text{ is } \text{m}^2\text{g}^{-1} \text{ for } S > 70 \text{ m}^2\text{g}^{-1} \\ I_3 &= 0.080 S; I_3 \text{ is } \% \text{ and } S \text{ is } \text{m}^2\text{g}^{-1} \text{ for } S < 70 \text{ m}^2\text{g}^{-1} \end{aligned} \quad (27.17)$$

Few successful attempts were made in ascertaining this connection [123]. Normally, BET is the standard method used to measure the surface area of mesopores (pores between 2 and 50 nm), but the predictions of Eq. (27.17) have been well supported by BET measurements. Therefore, this relation is effectively used in the development of hydrodynamic interaction method described in the following sections.

## 27.6

### Miscibility in Polymer Blends and Free Volume

A miscible blend is a single-phase system with compact packing of the polymeric segments due to changes in chain configuration/conformation upon blending. Differential scanning calorimetry (DSC) is the most commonly used technique to test whether a polymer mixture has produced a miscible or immiscible blend. It is known that the free volume in polymers is the result of chain ends, folding, and molecular architecture; thus, for miscible blends due to compact packing, the free volume of the blend becomes reduced. The original investigators of positrons used the simple additivity rule for free volume to predict the free volume upon blending. For a binary polymer blend this is written as:

$$F_V = F_{V1}\phi_1 + F_{V2}\phi_2 \quad (27.18)$$

where,  $F_V$  is the free volume fraction of the blend,  $F_{V1}$ ,  $F_{V2}$  are the free volume fractions of the blend components 1 and 2, and  $\phi_1$  and  $\phi_2$  are their corresponding volume fractions. Later it was realized that, unlike volume, free volume is not linearly additive due to the complex nature of its formation. Therefore, a new parameter termed the interchain interaction parameter ( $\beta$ ) [9] was introduced to predict the miscibility of a blend:

$$F_V = F_{V1}\phi_1 + F_{V2}\phi_2 + \beta F_{V1} F_{V2}\phi_1\phi_2 \quad (27.19)$$

where all of the parameters carry their usual meaning. It has been observed that the free volume parameters of the blends exhibit negative and positive deviations from the linear additivity rule (Eq. (27.18)), depending on whether the blend is a single-phase or two-phase system. Accordingly, the interchain interaction parameter  $\beta$  acquires negative and positive values, respectively (Eq. (27.19)). This indicates that, for negative values of  $\beta$ , the blend components establish interactions between themselves and hence the blend is termed as miscible. Positive values of  $\beta$  indicate the absence of any interaction between the components, and hence the blend is termed as immiscible [9,12,25,42–58].

**Table 27.1** DSC scan and interchain interaction parameter results for PP/NBR and PVC/SAN blend systems [57].

Blend	$T_g$ range ( $^{\circ}\text{C}$ )			$\beta$ parameter		
	70/30	50/50	30/70	70/30	50/50	30/70
PP/NBR	-38 to +16	-42 to +16	-25 to +12	0.14	0.07	0.12
PVC/SAN	65 to 98	70 to 100	62 to 100	-0.31	-0.06	0.04

From the compiled data of  $\beta$ -values for various binary polymer blends (see Table 27.2),  $\beta$  parameter values calculated from Eq. (27.19) show no systematic variation as a function of composition. Rather, in certain cases  $\beta$  exhibits a complex behavior such as an oscillation between positive and negative values, so that no meaningful conclusion is possible. Second, a survey of the experimental  $T_g$  values from the DSC experiment as a function of composition revealed that no information on which the composition of a blend would produce good interface adhesion, so that its miscibility level would be the highest for that system. This renders both  $T_g$  and  $\beta$  results inconclusive when deciding the blend composition for the highest miscibility, and this is an important issue for blending two polymers if one is expensive. Further, DSC is not sensitive below a 15 nm domain size of the dispersed phase in a blend. Additionally, if the  $T_g$ -values of the blend constituents are within  $20^{\circ}\text{C}$ , the  $T_g$  of the blend may become broadened and inference might be misleading due to overlap. A typical example of this is the case of PP/NBR and PVC/SAN blends in three compositions (70/30, 50/50 and 30/70) for which  $T_g$  and  $\beta$  data are shown in Table 27.1. It is clear from these data that broader  $T_g$ -values are observed for these compositions. Further, the values of  $\beta$  exhibit complexity, and therefore the measurement of  $\beta$  from free volume and  $T_g$ -values from DSC methods fails to provide the composition-dependent miscibility level. This dogma prompted research groups to seek alternatives to obtain information from the more sensitive positron lifetime measurements, and this in turn led to the development of a new method [54] for measuring composition-dependent miscibility level in miscible and partially miscible blends. This new method, which also provides a means of characterizing the interface in immiscible blends [54,57], is based on hydrodynamic interaction characterized by the  $\alpha$  parameter. It should be noted that free volume of the blend, when measured by positron lifetime experiments, will not indicate whether the change is in the domains of component polymers or at the interface of the two components. This information is essential to understand the characteristics of the interface which decides the miscibility level of the blend. The interactions between the blend component polymers has a direct bearing on the strength of adhesion at the interface, and hence the hydrodynamic interaction. However, hydrodynamic interactions exclude specific interactions between the component polymers of the blend, but depend on the flow behavior of the monomers. As possible interactions between the component polymers of the blends studied are discussed elsewhere in this book, no

further discussions will be undertaken at this point; rather, a brief overview will first be provided on hydrodynamic interactions and their theoretical development, and the connection with free volume.

In the case of polymers, viscosity is considered an important property to explain the viscoelastic behavior of polymers under stress and strain [154]. At this point, two theories are considered which deal with the flow behavior of polymer mixtures: the first, which was proposed by Rouse [155] and is based on the studies of Kargin and Slonimsky, is KSR model; the second, as proposed by Zimm [156] and based on the studies of Kirkwood and Risemann, is the KRZ model.

The KSR model assumes polymer molecules as a set of identical elements (segments) connected in series. Further, each segment in the polymer chain can be visualized as a bead connected linearly, while the macromolecular coil so formed does not disturb the flow rate and no perturbation is introduced to the motion. In other words, the beads in motion are independent of the surrounding medium. In contrast, the KRZ model is the next step in theoretical conceptions of the KSR model; that is, KRZ theory brings in hydrodynamic interaction between segments of the polymeric chains due to flow. The calculations of the KRZ model account for the perturbation of the flow field rates caused by the presence of foreign bodies. In principle, two extreme cases are possible; the first is the case where the polymeric chain does not give rise to perturbations to the flow rate; that is, no hydrodynamic interaction is present. This limiting case is the KSR model itself, while in the other case the space occupied by macromolecules is found to be impermeable to the solvent, and this corresponds to maximum hydrodynamic interaction. The flow generates friction especially at the interface. In case of favorable interactions (for miscible blends), the monomers (beads) are brought closer to each other and this results in excess friction being generated at the interface. This in turn leads to an energy dissipation so that tension at the interface is reduced. The energy dissipation is indicated by a negative sign of the hydrodynamic interaction parameter ( $\alpha$ ). If the miscibility is high at a certain composition of the blend,  $\alpha$  takes on large, negative values [53,54], but for immiscible blends  $\alpha$  will be very small and close to zero, or it may even become positive. This indicates the absence of any favorable interactions between the constituent polymers, and hence very little or no friction at the interface. As a consequence,  $\alpha$  can be considered as a measure of excess friction between the molar surfaces of the component polymers.

Wolf's theory simplifies the above two theories [157,158]. Its considerations can be summarized as: (i) energy dissipation occurs at the molecular interfaces; (ii) the variation in friction between the constituents, as a function of composition, is due to changes in the flow mechanism; and (iii) the energy dissipation, quantified by  $\eta$ , should be governed by the surface fractions of the molecules rather than by their volume or weight fractions. The interrelation between the molar surface fraction ( $\Omega$ ) and volume fraction ( $\phi$ ) of the monomer units is given by (Wolf theory):

$$\Omega = \frac{(1 + \gamma)\phi}{(1 + \gamma\phi)} \quad (27.20)$$

where  $\gamma$  is called the geometric parameter and depends on the molecular architecture of the blend. This is defined in terms of van der Waals surface ( $F$ ) and volume ( $V$ ) of the monomers as:

$$\gamma = \frac{F_2/V_2}{F_1/V_1} - 1 \quad (27.21)$$

and the subscripts 1 and 2 refer to the component polymers 1 and 2, respectively, of the blend.

The excess viscosity (deviation from Arrhenius law) for the mixtures is written as:

$$\Delta \ln \eta = \ln \eta - (1 - \varphi) \ln \eta_1 - \varphi \ln \eta_2 \quad (27.22)$$

where  $\eta$  is the viscosity of the blend, and  $\eta_1$  and  $\eta_2$  are the viscosities of the component polymers. Under the assumption that the energy dissipation takes place at the interfaces between like molecules and unlike molecules and *excluding specific interactions*, for an ideal mixing law, viscosity  $\eta$  in terms of surface fractions  $\Omega$  of its components can be written as:

$$\ln \eta = \Omega_1^2 \ln \eta_{11} + 2 \Omega_1 \Omega_2 \ln \eta_{12} + \Omega_2^2 \ln \eta_{22} \quad (27.23)$$

where  $\eta_{11} = \eta_1$  and  $\eta_{22} = \eta_2$  represent the viscosity contribution to friction between like molecules, and  $\eta_{12}$  corresponds to mutual friction between unlike components.

For binary blends, the expression for  $\eta_{12}$  is given by

$$\eta_{12} = \exp[\alpha + m(1 - \Omega)](\eta_{11}\eta_{22})^{0.5} \quad (27.24)$$

In Eq. (27.24),  $\alpha$  is the hydrodynamic interaction parameter. The parameter  $m$  accounts for the effects of collective motion; it increases the term  $(\alpha + m)$  in the square bracket (correction for nonideal intermolecular friction) in the limit of infinitely dilute solution ( $\Omega \rightarrow 0$ ; nondraining coils). Substituting the above equations into Eq. (27.22) and simplification leads to:

$$\Delta \ln \eta = \left\{ \delta[\gamma(1 + \gamma\varphi)^2 - (1 - \varphi)(1 + \gamma)] + 2\alpha(1 + \gamma)^2\varphi + [\eta]\rho(1 - \varphi) \right\} \frac{\varphi(1 - \varphi)}{(1 + \gamma\varphi)^3} \quad (27.25)$$

where  $\delta$  is defined as

$$\delta = \ln \eta_2 - \ln \eta_1 \quad (27.26)$$

This can be determined by the viscosities of the components of the blend. In Eq. (27.25),  $\rho$  is the density of the blend.

According to Wolf *et al.* [158], a thermodynamic preference of contacts between the molecules of component 1 (solvent) and component 2 (polymer) leads to a

reduction in intermolecular friction due to an increased tendency of the unlike molecules to move conjointly in the blend.

All materials exhibit some viscoelastic response. Viscoelastic materials include amorphous polymers, semicrystalline polymers, biopolymers, metals at very high temperatures, and bituminous materials. To be precise, viscoelasticity is a molecular rearrangement. When stress is applied to a viscoelastic material, such as a polymer, parts of the polymer's long chains will change position; this movement or rearrangement is known as creep. Polymers remain as a solid material even when such parts of their chains are undergoing rearrangement, in order to accompany the stress, but as this occurs it creates a back-stress in the material. Recalling the theory of free volume presented earlier, and its connectivity to viscosity (Eq. (27.5)), it becomes clear that free volume and viscosity are inversely related [90]. Subsequently, by adopting this basic concept Ranganathaiah *et al.* [54] modified the theoretical equations of Wolf *et al.* [157] and deduced an expression for the hydrodynamic interaction parameter  $\alpha$  suitable for a blend in solid phase similar to Eq. (27.25) [53,54]. According to this, in order to determine the hydrodynamic interaction parameter  $\alpha$ , the geometric parameter  $\gamma$  must first be calculated, and this is done by using the experimentally measured values of fractional free volumes and volume fractions in the following equation [53,54]:

$$F_V = \left[ \frac{\varphi_1}{F_{V1}} + \frac{\varphi_2}{F_{V2}} + \delta \left( \frac{\gamma \varphi_1 \varphi_2}{1 + \gamma \varphi_2} \right) \right]^{-1} \quad (27.27)$$

and  $\delta$  is now expressed in terms of fractional free volumes of the component polymers as

$$\delta = [(1/F_{V2}) - (1/F_{V1})] \quad (27.28)$$

The final expression employed for the determination of hydrodynamic interaction parameter  $\alpha$  is

$$\Delta F_V = \left\{ \delta [\gamma(1 + \gamma \varphi_2)^2 - \varphi_1(1 + \gamma)] + 2\alpha(1 + \gamma)^2 \varphi_2 + e^{(\frac{1}{F_V})} \rho \varphi_1 \right\}^{-1} \frac{(1 + \gamma \varphi_2)^3}{\varphi_1 \varphi_2} \quad (27.29)$$

here  $\Delta F_V$  is defined as

$$\Delta F_V = \left[ \frac{1}{F_V} - \frac{\varphi_1}{F_{V1}} - \frac{\varphi_2}{F_{V2}} \right] \quad (27.30)$$

where  $F_{V1}$  and  $F_{V2}$  are the fractional free volumes,  $\phi_1$  and  $\phi_2$  are the volume fractions of constituents 1 and 2 of the blend, respectively, and  $F_V$  is the fractional free volume of the blend. In the original theory,  $\gamma$  was considered to be constant (i.e., composition-independent) and was expressed as:

$$\gamma = (N_2/N_1) - 1 \quad (27.31)$$

where  $N_{i=1,2}$  is the ratio of molar surface fraction to the volume fraction of 1 and 2, respectively. Mertsch and Wolf [159] described  $\gamma$  as being more dependent on

the molar surface fraction, and not on the volume fractions, as the surface fractions quantify the geometric effects in the molecular architecture of the system, particularly those involving conformation that results in close packing. According to the definition of  $\gamma$  (see Eq. (27.21)), it is a constant for a given pair of polymers in a blend. However,  $\gamma$  is certainly not independent of the composition as the geometric molecular arrangement changes with composition, a point strongly supported by Wolf *et al.* and pursued by Ranganathaiah *et al.* in their modification [53,54]. The latter authors have calculated the  $\gamma$  value from free volume data, where the molar surface and molar volume fractions were replaced by the free volume surface area  $S$  and  $F_v$ . Subsequently,  $S$  was calculated from the relationship  $I_3 = 3.0 + 0.033S$ , where  $I_3$  is the o-Ps intensity [53,54]. As an example, the value of  $\gamma$  was calculated from free volume data for SAN/PMMA miscible blend, and was found to be  $-0.256$ . The same  $\gamma$  was calculated according to Bondi's group contribution method [160], based on van der Waals surfaces and van der Waals volumes, for the two-component polymers of SAN and PMMA with the definition (Eq. (27.31)). As this gave a value of  $-0.183$ , it could be concluded that a reasonable agreement between calculations (despite  $\sim 33\%$  deviation) is obtained. The authors of the method [53,54] claimed that the free volume was a better parameter compared to viscosity by comparing the existing data. When Kapnistos *et al.* [161] investigated polystyrene (PS)/poly(vinyl methyl ether) (PVME) miscible blends by viscosity measurements, they evaluated  $\gamma$  as  $-0.35$ , whereas Bondi's method gave a  $\gamma$ -value of  $-0.15$  for the system. When taking into consideration the large discrepancy ( $\sim 80\%$ ) between the viscosity measurements and Bondi's method, it was argued that the free volume measurement was a better parameter as the molecular architecture has a direct bearing on the free volume evolution. This was the first positron measurement (free volume) to evaluate  $\gamma$  for polymer blends, and the claims of the authors were well supported when the method was applied to several polymer blends [50,53,54,57,63,64] and showed clearly that  $\gamma$  does indeed depend on the composition of the blend. Equation (27.29) was then fitted with all of the experimental values, namely fractional free volumes, volume fractions and  $\gamma$  obtained from Eq. (27.27), to obtain the hydrodynamic interaction parameter  $\alpha$ .

#### 27.6.1

##### Free Volume and Miscibility Studies in Blends

The first positron annihilation lifetime (PAL) measurements on polymer blends were conducted by Jean *et al.* [9], who investigated the free volume properties of: (i) a miscible blend, namely tetramethyl-bisphenol A polycarbonate (TMPC) and polystyrene (PS); and (ii) an immiscible blend, namely bisphenol A polycarbonate (PC) and PS. It was observed that TMPC formed a miscible blend with PS as it had larger fractional free volume cavities than PC. For the miscible blend, the free volume showed negative deviation from the linear additivity rule (Eq. (27.19)), whereas for immiscible blend it was observed that the free volume, as detected by o-Ps lifetime as a function of composition, was complicated due to the presence of

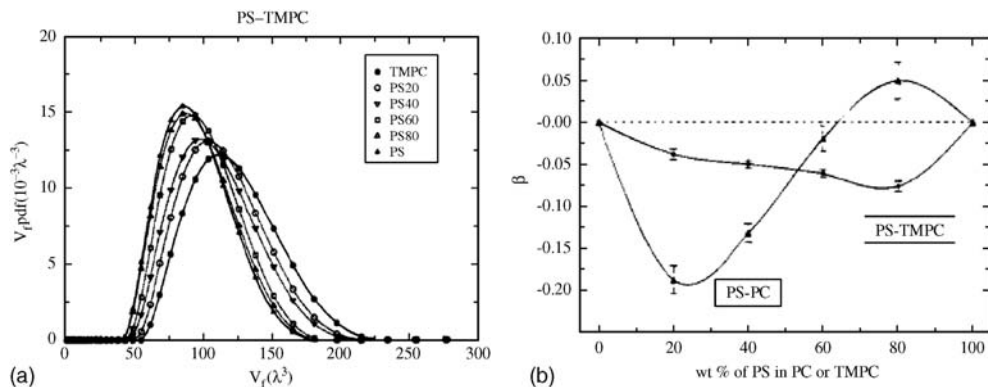


**Figure 27.7** (a) Free volume hole size distributions in PS/TMPC blends; (b) Calculated inter-chain interaction parameter in PS/TMPC and PS/PC blends. Reproduced with permission from Ref. [9].

interfaces. The free-volume cavity distribution is additive in the miscible blend (Figure 27.7a), while a significant broadening was observed in the immiscible blend (not shown here). The observed negative deviation of the free-volume fraction for the miscible blend was interpreted in terms of segmental conformation and packing between dissimilar polymers. The interchain interaction parameter  $\beta$  for the miscible and immiscible blends is shown in Figure 27.7b, where it can be seen that, for the TMPC/PS blend,  $\beta$  was negative throughout the composition range studied, whereas for the PC/PS blend it exhibited both negative and positive values; hence, the latter blend could be considered as miscible up to 60% of PS, beyond which it would be immiscible.

In another early investigation [11], an attempt was made to connect the mechanical properties of the blends to free volume data. It was inferred that the mechanical behavior could be rationalized in terms of the free volume behavior. The polyester blend free volume hole size decreases (i.e., the free volume contracts) on mixing and exhibits higher than average yield strengths and brittle impact responses. The polycarbonate (PC)/poly(aryloxysiloxane) (PAS) blends either retained or gained free volume on mixing, and exhibited average yield strengths and average ductile impact responses of the constituent polymers. A typical variation of the free volume in blends is shown in Figure 27.8a, where it is apparent that the blend loses free volume or that a contraction occurs in the free volume upon blending; as per Equation (27.19),  $\beta$  is negative for the results shown in this figure. The radius distribution of the PP/EPDM blend is shown in Figure 27.8b [12], where the width of the distribution can be seen to be smaller than the width in PP and EPDM. The authors suggested that the size of the free volume is decreased upon mixing, and that such an effect might be due to interactions between the constituent polymers in the blend.

An interesting study to determine the influence of temperature on blend free volume was carried out on PS/PPE blend [19]. Figure 27.9a clearly demonstrates



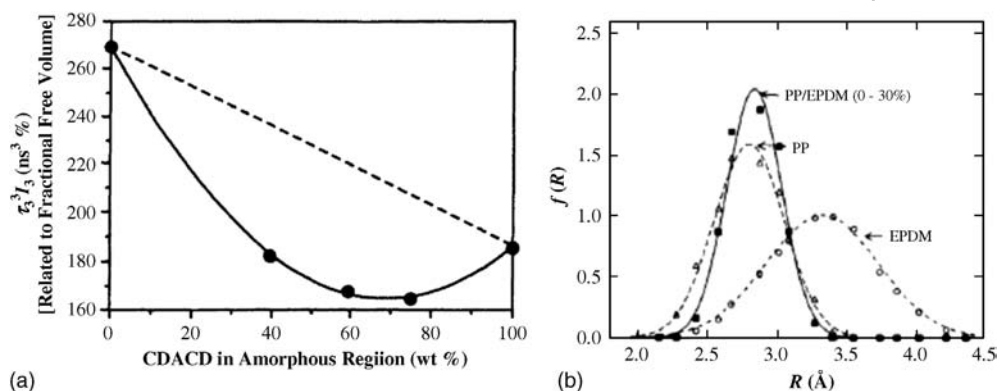


**Figure 27.8** (a) Fractional free volume as a function of % CDACD to show the deviation from additivity rule. Reproduced with permission from Ref. [11]; (b) Free volume radius distribution in PP, EPDM, and PP/EPDM blends with 30% EPDM. Reproduced with permission from Ref. [12].

the influence of temperature on free volume size distribution, as deduced from the measured o-Ps lifetime for a 50/50 composition. In this case, variation was observed in the free volume size distribution, as the average free volume size was increased and the smaller free volume fraction was decreased as the PPE content was increased. The temperature dependence of free volume size was confirmed by the fact that the  $T_g$ -value of the blend (50/50) shifted to a higher temperature as the PPE content was increased. Taken together, this evidence suggested that larger free volumes are generated close to the backbone chain of PPE as the PS content was decreased, and that o-Ps was more favored to annihilate in larger free volumes. One important observation of this study was that the PS/PPE blend

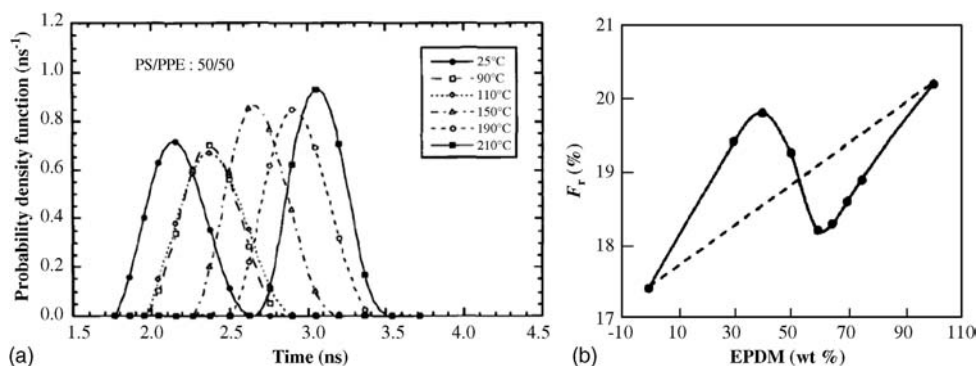


**Figure 27.9** (a) Variation of free volume size distribution (PDF) for PS/PPE blend for different temperatures. Reproduced with permission from Ref. [19]; (b) Fractional free volume as a function of EPDM content in PP/EPDM blend. Reproduced with permission from Ref. [23].

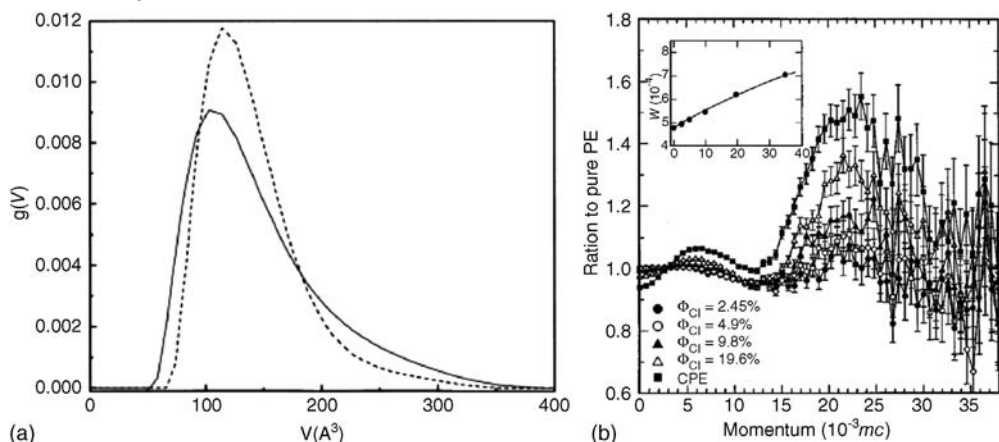


**Figure 27.10** (a) Electron-beam irradiation effects on free volume size variation PPE/EVA blend (PPE = 30%). The solid line indicates unirradiated, the dashed line indicates irradiated at 100 kGy. Reproduced with permission from Ref. [24]; (b) Ratio curves of CDB spectra

for PE/CPE blends. The x-axis is the momentum of the annihilating positron-electron pair in units of  $10^{-3}mc$ . The inset shows the variation of the  $W$  parameter, defined as the fraction of chlorine concentration. Reproduced with permission from Ref. [25].

appeared to be miscible on a macroscopic scale, yet the free volume results on a subnanoscopic scale suggested that they would not mix with each other. In other words, mixing at the molecular level can be understood only from free volume studies.

The positron lifetimes were measured in poly(propylene-co-ethylene) (PPE)/poly(ethylene-co-vinyl acetate) (EVA) blends containing 10, 30, 50 and 60 wt% PPE, before and after electron-beam irradiation. As can be seen from the results (see Figure 27.10a), for the irradiated samples at low electron doses (up to 100 kGy) a crosslinking process of polymer chains was observed which narrowed the width of the free volume size distribution. In comparison with wide angle X-ray diffraction (WAXD) results, free volume results are capable of discerning to some extent the differences in molecular mobility of the elastic (EVA) and plastic (PPE) phases of the blend. At higher doses of electron-beam irradiation, chain scission was indicated by an increase in the width of free volume size distribution. When Kobayashi *et al.* added CPE to PE they observed shorter lifetimes of localized electrons available for Ps formation, while the addition of EVA resulted in a longer lifetime, accompanied by a decrease in Ps formation probability ( $I_3$ ). In the former system, electrons produced by positron irradiation underwent a dissociative attachment to CPE, while the resultant chloride ions captured positrons to form the complex of charge-induced positrons (CIPs), which was clearly evidenced by CDB spectroscopy data (see Figure 27.10b). In the latter system, EVA trapped not only the electrons produced by positron irradiation but also the positrons. The electrons trapped on EVA form Ps, but positron trapping on EVA resulted in a suppression

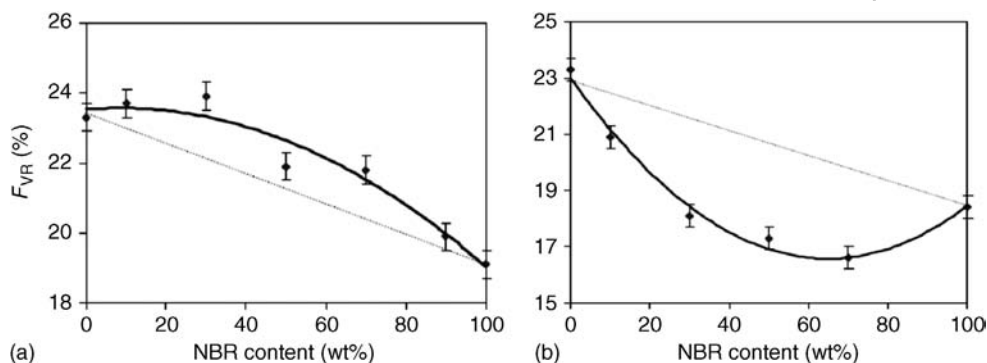


**Figure 27.11** (a) Relative fractional free volume as a function of NBR content in unvulcanized PP/NBR; (b) For vulcanized PP/NBR blend. Solid curves are drawn to guide the eye for experimental data. The dotted line shows the linear additivity rule. Reproduced with permission from Ref. [48].

of Ps formation, which was an interesting result on positron interaction with the structure of the blend.

Studies have also been conducted on polypropylene (PP)/nitrile butadiene rubber (NBR) blends to understand the effect of dynamic vulcanization on blend properties [48]. The results in Figure 27.11a show an increase in free volume size in the nonvulcanized blend as the NBR content was increased, due to the strong incompatibility between the blend components. While the dynamic vulcanization resulted in a significant increase in the free volume size, the fractional free volume was decreased. As can be seen in Figure 27.11a and b, the fractional free volume in the nonvulcanized blend showed a positive deviation from the linear addition, which suggested incompatibility between PP and NBR and hence an additional free volume being evolved during the process of blending. The influence of vulcanization can be clearly seen in Figure 27.11b, that dynamic vulcanization introduces some level of compatibilization between PP and NBR, which results in a decrease in the fractional free volume of the blend and deviates negatively from the additivity rule. In spite of this contrasting free volume behavior in nonvulcanized and vulcanized blends, however, no substantial change was observed in the blends' mechanical properties. Thus, it was concluded that PP and NBR polymers are so incompatible that dynamic vulcanization was insufficient to improve the mechanical properties by establishing chain linkages. However, morphological differences that emerge at the molecular level upon vulcanization can be easily seen in the positron results.

One important polymer used in blending is the ethylene propylene diene monomer (EPDM). An interesting study involving EPDM was conducted with poly(trimethylene terephthalate) (PTT), using PLS and DSC measurements. The DSC results for blends of 50/50 and 40/60 composition showed clearly two  $T_g$  values, indicating a phase-separated blend. No melting point depression was observed for the blend, which strongly supported the incompatibility of the components. Positron results showed increase in both free volume size and fractional free

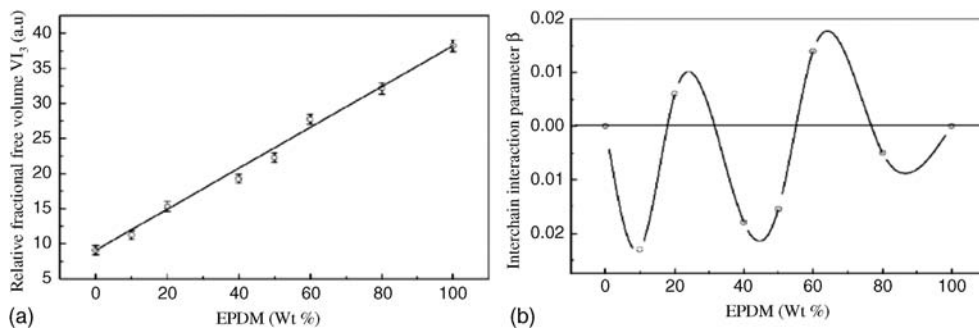


**Figure 27.12** (a) Relative fractional free volume and (b)  $\beta$  parameter for PPT/EPDM blend. Reproduced with permission from Ref. [43].

volume (Figure 27.12a) [43] with increasing EPDM content. This could be due to the creation of free volume and hence resulted in phase separation. An interesting point here was that the fractional free volume exhibited neither a negative nor a positive deviation from the linear additivity rule; in fact, it agreed very well with the additivity rule, which is rarely observed in binary blends (Figure 27.12a). The interchain interaction parameter evaluated from these results showed a complex behavior (Figure 27.12b), however, eliciting its inability to provide information about which composition had produced some compatibility and which composition had produced a high incompatibility resulting in immiscibility. Further support to free volume data was obtained from XRD results; the decrease in crystallinity correlated well with the increase in fractional free volume, which was observed for several other systems.

It is evident from the above discussion that the free volume data derived from positron lifetime measurements is incapable of providing information on the composition-dependent miscibility level of the blend. At this point, a new method based on the same free volume data measured from positron lifetime measurements was introduced to determine the miscibility of binary blends. The new method was based on hydrodynamic interactions (the mathematics required have been explained in detail earlier), and calculations of the  $\gamma$  parameter derived from the hydrodynamic interaction approach were made for three selected polymer blends, namely poly(styrene-co-acrylonitrile) (SAN)/poly(methyl methacrylate) (PMMA) (completely miscible), poly(vinyl chloride) (PVC)/poly(methyl methacrylate) (PMMA) (partially miscible) and poly(vinylchloride) (PVC)/polystyrene (PS) (immiscible) (see Figure 27.13). As can be seen, this parameter behaves similar to the interchain interaction parameter  $\beta$ , in the sense that it exhibits a complex behavior making it difficult to determine the composition-dependent miscibility of the blends.

The hydrodynamic interaction parameter is then plotted as a function of composition, as shown in Figure 27.14 for these blends. It was very clear that, for the miscible blend SAN/PMMA,  $\alpha$  was highest ( $-63.4$ ) at 20% PMMA in the blend and about  $-12.4$  at 50/50 cocontinuous phase. This inferred that an 80/20 composition would be optimal for the SAN/PMMA blend, producing the highest

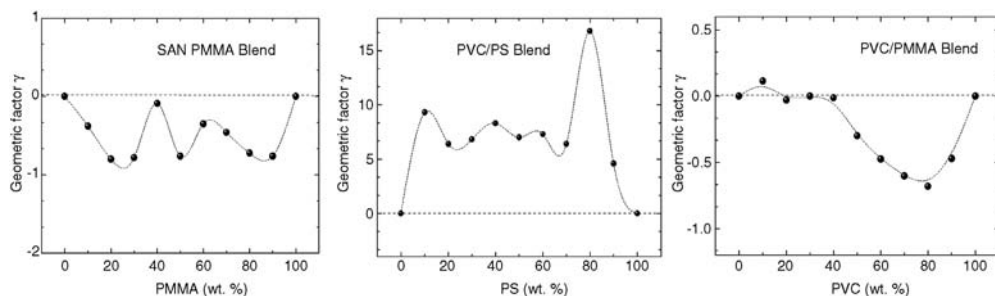


**Figure 27.13** The geometric factor as a function of PMMA, PS and PVC contents in SAN/PMMA, PVC/PS and PVC/PMMA blends. Reproduced with permission from Ref. [63].

miscibility level. In the case of the partially miscible blend PVC/PMMA,  $\alpha$  was very small ( $<1$ ) but showed maxima at 20% and between 70% and 80% PMMA content. Compositions where  $\alpha$  is close to zero produce immiscible blends, whereas for others a miscible blend with a poor miscibility level is produced, as  $\alpha$  is very small but negative; therefore, this is a partially miscible blend. Finally, for the immiscible blend PS/PVC,  $\alpha$  was very small and close to zero for the entire composition range; hence the blend can be concluded as immiscible. Therefore,  $\alpha$  can be regarded as the parameter of choice to provide information on levels of miscibility, since such information is not forthcoming from free volume data alone. This example shows clearly the usefulness and strength of this approach for binary polymer blend studies.

The hydrodynamic interaction approach appears adequate in most cases for describing the composition-dependent miscibility level. Currently, a considerable amount of data is available on binary polymer blends, particularly from positron annihilation studies. Hence, the interpretation offered with regard to miscibility may not be effective, especially in the case of partially miscible blends when some inferences are vague.

In this chapter, data have been presented based on a hydrodynamic interaction approach, and studies conducted by other research groups have been reviewed and reinterpreted to demonstrate the efficacy of this new method. Composition-dependent miscibility studies will clearly throw light on interfaces in binary

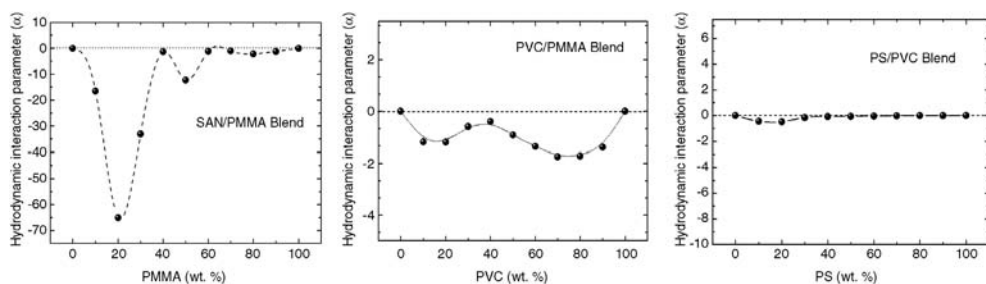


**Figure 27.14** Hydrodynamic interaction parameter ( $\alpha$ ) as a function of PMMA, PVC and PS contents in SAN/PMMA, PVC/PMMA and PS/PVC blends. Reproduced with permission from Ref. [63].

blends that cannot be acquired by any known methods. In Figure 27.14, the  $\alpha$ -values are different from those in earlier studies [54] as relative fractional free volume was used instead of the fractional free volume; hence, in order to bring uniformity to the treatment of these data, the fractional free volume was used for the 25 blends presented in Table 27.2. There was also a small change in the final expression [Eq. (27.29)] from Refs [53] and [54] – hence the difference in the magnitude of  $\alpha$  reported in Table 27.2. When selecting data from the literature, great care was exercised that only free volume data from published studies which provided complete information on the component polymers used in the fabrication of blends (e.g., molecular weight and density) would be considered. However, with this constraint in place, not all of the data available could be used in compiling the hydrodynamic interaction parameter as a function of composition, as reported in Table 27.2.

In Table 27.2, the free volume data (i.e., o-Ps lifetime, o-Ps intensity and fractional free volume) and parameters of the hydrodynamic method namely [i.e.,  $\gamma$  and  $\alpha$ , from Eqs (27.27) and (27.29) respectively], together with the interchain interaction parameter  $\beta$  [from Eq. (27.19)] are tabulated. Also shown are the inferences drawn by the respective research groups (column 6). The final column gives the present author's inference, based on hydrodynamic interaction approach. As can be seen, the main difference between the inferences from the hydrodynamic approach and others is that  $\alpha$  provides the composition of a blend which has the highest miscibility level; the other two parameters,  $\beta$  and  $\gamma$ , do not provide this information, which is totally new and absent from earlier works. The table list seven completely miscible blends, with SAN/PMMA having the highest miscibility ( $\alpha = -63.4$ ) at 80/20 composition and the least miscibility ( $\alpha = -4.85$ ) for PS/TMPC at 20/80 composition. There are six partially miscible blends, with the highest miscibility ( $\alpha = -21.5$ ) being for the PTT/PC blend at 20/80 composition, and the least miscibility ( $\alpha = -2.79$ ) for the PEG/PAM blend at 20/80 composition. In order to scale the results for a standard format, it was designated that if the  $\alpha$ -value was  $<1$  but negative or close to zero or positive, then such blends would be inferred as immiscible. However, if the  $\alpha$ -value was  $>1$  and negative, such blends would be inferred as miscible. The degree of miscibility could be decided on the magnitude of the  $\alpha$ -value (with negative sign), taking the highest level of SAN/PMMA blend. Another important point of observation is that, for partially miscible blends, the DSC or free volume data do not specify the composition-dependent miscibility level, nor which compositions would result in immiscible blends. In contrast, an  $\alpha$ -based inference would provide this information clearly and satisfactorily. Recently a verification of Ranganathaiah's method measuring miscibility level in binary polymer blends is reported from a different laboratory. Meng *et al.* [163] have reported the studies on three blends of SBS/PS covering the all the three types of blends, namely miscible, partially miscible and immiscible by following the method of Ranganathaiah. The  $\alpha$  obtained from free volume data reveal that star-shaped SBS 411 in SBS/PS blend showed the highest miscibility in spite of less styrene proportion (31%). The superior mechanical properties were achieved for this blend compared to linear SBS containing blends.

Table 27.2 Beta-, gamma-, and alpha-values for binary polymer blends from free volume data.

Blend/ Composition	$\tau_3 \pm 0.01$ ns	$I_3 \pm 0.3\%$	$V_f \pm 0.9 \text{ \AA}^3$	$F_V \pm 0.4\%$	Reference and Inference Drawn	Beta ( $\beta$ ) $\pm 1\%$	Gamma ( $\gamma$ ) $\pm 3\%$	Alpha ( $\alpha$ ) $\pm 6\%$	$\alpha$ -Based Inference (Present)
1. PC-based blends									
PS/PC									
20/80	2.11	17.50	107.13	3.37	IM [9]	-0.22	-2.27	-0.15	IM
40/60	2.10	20.00	106.22	3.82		-0.16	-2.00	-0.59	IM
60/40	2.12	23.80	108.05	4.60		-0.10	0.60	-0.40	IM
80/20	2.10	27.00	104.00	5.01		-0.17	1.29	-0.45	IM
PAS/PC									
20/80	2.13	36.20	108.97	7.10	M [11]	0.02	-0.57	-15.06	M
40/60	2.10	35.30	106.22	6.74		0.01	-0.44	-3.25	M
50/50	2.08	34.90	104.80	6.60		0.01	-0.45	-2.30	M
60/40	2.07	34.30	103.90	6.50		0.02	-0.54	-2.15	M
80/20	2.06	34.00	102.62	6.30		0.05	-0.72	-2.25	M
EASTAR/PC									
20/80	1.81	28.70	79.65	4.11	M [11]	-0.02	-0.30	-6.77	M
40/60	1.85	29.30	82.20	4.30		-0.05	-0.50	-4.80	M
60/40	1.89	30.50	87.41	4.80		-0.04	-0.80	-12.96	M
80/20	1.96	31.00	92.13	5.10		-0.09	-0.90	-18.83	M
CDACD/PC									
20/80	1.83	27.00	86.23	4.20	M [11]	-0.12	-1.73	-5.69	M
40/60	1.83	27.20	81.17	3.97		-0.16	-1.50	-4.61	M
60/40	1.87	27.80	82.03	4.10		-0.18	-1.17	-18.19	M
VECTRA/PC									
10/90	2.00	31.00	96.94	5.41	IM [22]	-4.31	1.22	-0.04	IM
20/80	1.98	29.00	94.81	4.95		-2.11	2.79	-0.05	IM
30/70	1.93	26.80	90.24	4.35		-1.50	3.63	-0.07	IM

(continued)

Table 27.2 (Continued)

Blend/ Composition	$\tau_3 \pm 0.01$ ns	$I_3 \pm 0.3\%$	$V_f \pm 0.9 \text{ \AA}^3$	$F_V \pm 0.4\%$	Reference and Inference Drawn	Beta $(\beta) \pm 1\%$	Gamma $(\gamma) \pm 3\%$	Alpha $(\alpha) \pm 6\%$	$\alpha$ -Based Inference (Present)
50/50	1.87	21.00	85.04	3.21	PM [56]	-1.00	4.62	-0.13	IM
75/25	1.70	15.00	70.27	1.90		-0.73	5.34	-0.35	IM
PTT/PC									
10/90	1.64	16.10	68.00	4.53		2.20	10.00	-0.52	IM
20/80	1.68	17.40	70.50	4.14		0.84	20.45	-0.3	IM
30/70	1.71	19.00	72.00	4.03		0.65	13.78	-0.04	IM
40/60	1.77	19.90	76.00	3.65		0.22	4.12	-0.09	IM
50/50	1.80	21.90	82.00	3.47		0.06	2.17	-0.15	IM
60/40	1.82	22.70	83.00	3.14		-0.24	0.33	-0.43	IM
70/30	1.83	24.50	85.00	2.70		-0.78	-0.63	-2.67	M
80/20	1.88	25.60	87.00	2.34	-1.71	-0.91	-21.51	M	
90/10	1.91	26.40	90.00	2.40	-2.07	-0.91	-20.80	M	
2. PVC-based blends									
PVC/PnBMA									
3/97	2.30	28.10	125.94	6.35	M [29]	-5.24	-0.47	-40.29	M
11/89	2.22	24.00	117.62	5.08		-2.51	-0.67	-33.10	M
22/78	2.12	19.00	108.58	3.71		-1.96	-0.68	-16.34	M
42/58	2.02	14.00	98.97	2.49		-1.33	-0.72	-10.01	M
SAN/PVC									
10/90	1.80	7.80	77.60	1.09	PM [55]	0.01	3.03	-1.87	M
20/80	1.78	8.70	75.45	1.15		-0.46	1.23	-2.10	M
30/70	1.81	10.20	79.20	1.45		-0.31	1.82	-0.83	IM
40/60	1.80	11.30	78.90	1.58		-0.47	1.35	-0.71	IM
50/50	1.86	12.00	84.20	2.16		-0.06	1.50	-0.73	IM
60/40	1.84	14.54	82.30	2.15		-0.35	1.80	-0.23	IM
70/30	1.91	16.29	88.60	2.59		0.04	3.15	-0.08	IM
80/20	1.92	18.20	89.80	2.90		0.32	2.51	-0.27	IM



PS/PVC									
10/90	1.85	10.60	83.50	1.59	IM [63]	0.56	9.30	-0.44	IM
20/80	1.98	13.40	95.20	2.30		0.58	6.40	-0.48	IM
30/70	2.00	15.20	96.90	2.65		0.31	6.80	-0.15	IM
40/60	2.01	19.20	98.20	3.39		0.55	8.26	-0.08	IM
50/50	2.01	21.00	98.20	3.70		0.42	6.98	-0.06	IM
60/40	2.01	23.60	98.20	4.19		0.55	7.27	-0.04	IM
70/30	2.02	26.00	99.10	4.66		0.84	6.36	-0.03	IM
80/20	1.99	30.90	96.10	5.34		1.59	16.83	-0.006	IM
90/10	1.99	30.10	96.10	5.21		1.28	4.59	-0.01	IM
PVC/PMMA									
10/90	2.07	17.48	104.10	3.27	PM [63]	-4.18	0.11	-1.18	M
20/80	1.98	14.66	95.20	2.50		-3.17	-0.03	-1.20	M
30/70	1.94	12.17	92.40	2.02		-2.29	-0.001	-0.59	IM
40/60	1.92	10.40	90.00	1.68		-1.89	-0.01	-0.41	IM
50/50	1.95	9.79	92.90	1.64		-1.39	-0.30	-0.92	IM
60/40	1.93	9.49	91.06	1.56		-1.06	-0.47	-1.35	M
70/30	1.95	8.74	92.90	1.46		-0.80	-0.60	-1.73	M
80/20	1.86	8.82	84.60	1.30		-0.61	-0.68	-1.72	M
90/10	1.86	7.30	84.60	1.10		-0.40	-0.75	-1.38	M
EVA/PVC									
10/90	2.06	5.90	105.10	1.12	IM [64]	-0.53	5.34	-0.28	IM
20/80	2.08	7.00	107.10	1.37		-0.74	5.65	-0.62	IM
30/70	2.11	7.25	108.00	1.41		-1.11	3.45	-0.57	IM
40/60	2.22	8.60	118.80	1.84		-1.11	3.26	-0.47	IM
50/50	2.23	8.82	119.70	1.91		-1.52	2.06	-0.41	IM
60/40	2.25	10.25	121.70	2.24		-1.78	1.83	-0.38	IM
70/30	2.29	13.20	125.70	2.99		-1.72	2.41	-0.18	IM
80/20	2.29	15.60	125.70	3.51		-2.09	5.93	-0.12	IM
90/10	2.35	17.40	131.90	4.12		-3.17	1.45	-0.07	IM

(continued)

Table 27.2 (Continued)

Blend/ Composition	$\tau_3 \pm 0.01$ ns	$I_3 \pm 0.3\%$	$V_f \pm 0.9 \text{ \AA}^3$	$F_V \pm 0.4\%$	Reference and Inference Drawn	Beta ( $\beta$ ) $\pm 1\%$	Gamma ( $\gamma$ ) $\pm 3\%$	Alpha ( $\alpha$ ) $\pm 6\%$	$\alpha$ -Based Inference (Present)
<b>3. PMMA-based blends</b>									
PEO/PMMA									
10/90	1.81	27.00	79.69	3.87	IM [13]	-0.08	-0.64	-0.67	IM
25/75	1.97	23.20	93.89	3.92		0.02	0.81	-0.08	IM
35/65	2.12	22.90	108.58	4.47		0.21	-2.40	-0.19	IM
45/55	1.99	23.20	95.90	4.00		0.07	-5.00	-0.05	IM
50/50	1.89	23.90	86.12	3.70		0.01	-0.06	-0.90	IM
75/25	1.90	23.40	87.07	3.66		0.03	1.03	-0.60	IM
PMMA/SAN									
10/90	1.92	20.20	90.00	3.27	M [45]	-0.07	-0.38	-16.50	M
20/80	1.92	20.10	90.00	3.25		-0.12	-0.80	-63.40	M
30/70	1.91	20.56	89.20	3.30		-0.14	-0.78	-33.06	M
40/60	1.97	21.90	94.70	3.73		-0.06	-0.09	-1.29	M
50/50	1.93	21.10	92.00	3.45		-0.18	-0.76	-12.40	M
60/40	1.97	23.69	94.70	4.03		-0.08	-0.35	-1.12	M
70/30	2.04	22.20	101.30	4.05		-0.14	-0.46	-1.00	M
80/20	2.06	23.00	103.00	4.26		-0.17	-0.72	-2.15	M
90/10	2.13	22.50	109.40	4.45		-0.33	-0.76	-1.21	M
PMMA/PS									
10/90	2.06	25.20	103.20	4.69	PM [64]	-0.15	0.62	-1.57	M
20/80	2.08	22.30	105.10	4.23		-0.17	1.04	-0.42	IM
30/70	1.99	20.70	104.10	3.80		-0.20	2.21	-0.09	IM
40/60	2.02	18.40	99.40	3.30		-0.25	21.57	-0.001	IM
50/50	2.07	19.90	105.10	3.80		-0.08	0.37	-0.28	IM
60/40	2.01	20.40	98.50	3.65		-0.08	0.38	-0.18	IM

70/30	2.00	22.40	97.50	3.90		0.04	-0.54	-1.18	M
80/20	2.04	21.20	101.30	3.86		0.11	-0.71	-1.75	M
90/10	2.00	20.70	97.50	3.64		0.17	-0.76	-1.18	M
4. PS-based blends									
PS/TMPC									
20/80	2.30	25.00	125.93	5.67	M [9]	-0.06	-1.18	-4.85	M
40/60	2.25	24.50	120.90	5.33		-0.07	-1.59	-1.26	M
60/40	2.16	27.00	112.25	5.45		-0.06	-0.51	-3.94	M
80/20	2.14	28.50	112.00	5.75		-0.03	-1.75	-4.57	M
PPE/PS									
25/75	2.41	26.33	130.86	6.20	M [19]	0.01	-0.70	-2.32	M
50/50	2.24	21.15	119.96	6.29		0.01	-0.66	-5.32	M
60/40	2.21	30.80	117.62	6.50		0.03	-1.27	-13.28	M
70/30	2.14	29.82	110.79	5.94		-0.04	-2.00	-1.49	M
5. PP-based blends									
HIPS/PP									
10/90	2.25	25.80	120.97	5.62	IM [36]	0.06	2.18	-0.62	IM
20/80	2.26	26.30	121.97	5.77		0.03	1.44	-0.46	IM
30/70	2.20	28.80	116.07	6.02		0.04	1.77	-0.21	IM
40/60	2.22	30.00	118.02	6.37		0.06	3.51	-0.06	IM
50/50	2.19	30.40	115.59	6.33		0.03	1.63	-0.10	IM
60/40	2.18	32.00	114.15	6.58		0.04	2.89	-0.03	IM
70/30	2.15	34.50	111.31	6.91		0.07	10.00	-0.03	IM
80/20	2.13	35.00	108.98	6.87		0.05	8.00	-0.01	IM
90/10	2.11	36.50	107.13	7.04		0.09	5.00	-0.10	IM
NBR/PP									
30/70	2.08	22.70	105.10	4.29	IM [48]	0.14	-4.73	-0.01	IM
50/50	2.08	20.90	105.10	3.95		0.07	4.09	-0.03	IM
70/30	2.15	19.50	112.00	3.93		0.12	7.00	-0.03	IM

(continued)

Table 27.2 (Continued)

Blend/ Composition	$\tau_1 \pm 0.01$ ns	$I_3 \pm 0.3\%$	$V_f \pm 0.9 \text{ \AA}^3$	$F_V \pm 0.4\%$	Reference and Inference Drawn	Beta ( $\beta$ ) $\pm 1\%$	Gamma ( $\gamma$ ) $\pm 3\%$	Alpha ( $\alpha$ ) $\pm 6\%$	$\alpha$ -Based Inference (Present)
6. PEG-based blends									
PEG/PDMAM									
10/90	1.85	26.50	83.08	3.96	PM [35]	0.07	0.50	-3.12	M
20/80	1.96	22.30	93.13	3.74		-0.06	-0.20	-4.47	M
30/70	1.83	24.00	81.16	3.51		-0.12	-2.00	-1.81	M
40/60	1.91	22.50	88.61	3.59		-0.08	-3.56	-0.18	IM
60/40	1.89	20.00	86.61	3.12		-0.20	-1.88	-0.75	IM
70/30	1.99	22.00	95.65	3.79		-0.01	-0.70	-3.88	M
80/20	2.08	20.00	104.40	3.76		-0.02	-3.00	-0.06	IM
90/10	2.10	18.30	106.21	3.50		-0.20	-1.17	-3.33	M
PEG/PAM									
20/80	1.65	21.70	65.87	2.57	PM [35]	-0.05	-0.15	-0.35	IM
40/60	1.80	21.50	78.90	3.05		0.04	-0.53	-2.79	M
60/40	1.65	21.80	65.87	2.58		-0.33	-2.00	-1.62	M
80/20	1.81	20.00	79.65	2.87		-0.51	3.75	-0.09	IM
7. EPDM-based blends									
EPDM/PTT									
10/90	1.82	13.89	80.41	2.01	IM [43]	-0.27	2.00	-0.86	IM
20/80	2.04	14.97	100.41	2.71		-0.15	1.93	-0.46	IM
40/60	2.07	18.37	103.51	3.42		-0.30	1.16	-0.26	IM
50/50	2.16	19.54	112.25	3.95		-0.30	1.25	-0.15	IM
60/40	2.21	23.56	117.04	4.96		-0.13	2.23	-0.06	IM
80/20	2.28	25.76	123.98	5.75		-0.28	1.52	-0.03	IM

NBR/EPDM									
25/75	2.09	17.23	104.24	3.23	IM [52]	-0.20	0.24	-0.96	IM
50/50	1.96	16.10	92.89	2.69		-0.19	0.45	-0.24	IM
75/25	1.82	18.00	79.69	2.58		-0.04	-0.33	-0.46	IM
EPDM/PP									
30/70	2.22	17.00	116.46	3.51	PM [23]	0.02	-0.40	-3.55	M
40/60	2.18	16.80	113.04	3.56		0.05	-0.25	-1.50	M
50/50	2.30	15.90	125.94	3.46		0.03	-0.59	-3.24	M
60/40	2.28	15.20	122.32	3.26		-0.02	0.39	-0.18	IM
65/35	2.29	14.90	123.52	3.28		0.01	-0.07	-0.33	IM
70/30	2.33	14.80	129.62	3.32		0.02	-0.47	-0.83	IM
80/20	2.36	14.60	134.63	3.29		0.04	-0.60	-0.87	IM
PET/PEO									
25/75	2.06	11.00	102.62	2.03	IM [21]	-0.43	-1.70	-0.55	IM
30/70	2.09	10.30	104.86	1.94		-0.46	-1.78	-0.60	IM
35/65	2.08	9.65	103.96	1.81		-0.52	-1.83	-0.71	IM
40/60	2.04	9.40	100.41	1.70		-0.57	-1.92	-0.73	IM
45/55	2.06	9.00	102.62	1.66		-0.58	-2.10	-0.65	IM
CA/PU									
40/60	2.07	18.50	103.17	3.44	PM [37]	-0.10	-0.09	-0.59	IM
60/40	2.02	18.00	97.94	3.17		-0.06	0.11	-0.95	IM
80/20	1.98	15.90	94.89	2.72		-0.13	-0.48	-11.96	M

Note: Numbers in the parenthesis are reference numbers. M = miscible; PM = partially miscible; IM = immiscible. Data reproduced with permission from the respective references.

## 27.7

## Future Outlook

It is clear from these discussions of available free volume data that the measurement of free volume using PLS is in itself insufficient to provide information on the level of miscibility of binary polymer blends. In blending technology, a set of desired properties can generally be obtained by adding a small amount of an expensive polymer to an inexpensive polymer, and hence composition-dependent miscibility level is an important aspect. It has been shown that modeling free volume parameters in order to extract the hydrodynamic interaction parameter, based on well-known theories, has proved to be very effective for this purpose. However, further studies are necessary to understand miscibility in terms of this new approach, which is not forthcoming from any of the presently available analytical tools. The hydrodynamic approach based on free volume could also be extended to ternary blends, an area which is presently faced with complex problems as the number of interfaces becomes three-fold compared to binary blends. Recently, this approach has been shown to work quite well for ternary blends [162], although further studies are needed to establish the method as a qualified standard characterization tool for polymer blends.

## Acknowledgments

The author acknowledges the excellent hospitality extended by Winthrop Prof. J.F. Williams, Nodal Director, ARC Center of Excellence, Center for Antimatter-Matter Studies, School of Physics, University of Western Australia, Australia, where most of this chapter was written while working as Research Professor. The author also thanks the University of Mysore for allowing his research to be carried out at UWA, and his research students for helping to compile and calculate the data presented in this chapter.

## References

- 1 Olabisi, O., Robeson, L.M., and Shaw, M.T. (1980) *Polymer-Polymer Miscibility*, Academic Press, New York.
- 2 Paul, D.R. and Newman, S. (1978) *Polymer Blends*, vols 1 and 2, Academic Press, New York.
- 3 Utracki, L.A. (1999) *Polymer Blends Handbook*, vol. 1, Kluwer Academic Publishers, London.
- 4 Simon, G.P. (2003) *Polymer Characterization Techniques and Their Application to Blends*, American Chemical Society, Washington.
- 5 Jamieson, A.M., Olson, B.G., and Nazarenko, S. (2010) *Polymer Physics: From Suspensions to Nanocomposites and Beyond* (eds L.A. Utracki and A.M. Jamieson), John Wiley, Hoboken.
- 6 Stevens, J.R. (1980) *Methods of Experimental Physics*, Academic Press, London.
- 7 Jean, Y.C. (1990) *Microchem. J.*, **42**, 72–102.
- 8 Wu, S.J. (1987) *Polym. Sci. Part B: Polym. Phys.*, **25**, 2511–2529; Steller, R. and Zuchowska, D. (1991) *J. Appl. Polym. Sci.*, **38**, 1411.
- 9 Liu, J., Jean, Y.C., and Hsinjin, Y. (1995) *Macromolecules*, **28**, 5774–5779.
- 10 McCullagh, C.M., Yu, Z., Jamieson, A.M., Blackwell, J., and McGerve, J.D. (1995) *Macromolecules*, **28**, 6100–6107.

- 11 Hill, A.J., Zipper, M.D., Tant, M.R., Stack, G.M., Jordan, T.C., and Shult, A.R. (1996) *J. Phys.: Condens. Matter*, **8**, 3811–3827.
- 12 Wang, C.L., Wang, S.J., and Qi, Z.N. (1996) *J. Polym. Sci.: Part B: Polym. Phys.*, **34**, 193–199.
- 13 Wastlund, C., Frans, H., and Maurer, J. (1997) *Macromolecules*, **30**, 5870–5876.
- 14 Wastlund, C., Berndtsson, H., and Maurer, F.H.J. (1998) *Macromolecules*, **31**, 3322–3327.
- 15 Wastlund, C., Schmidt, M., Schantz, S., and Maurer, F.H. (1998) *J. Polym. Eng. Sci.*, **38**, 1286–1294.
- 16 Peng, Z.L., Olson, B.G., Srithawatpong, R., McGervey, J.D., Jamieson, A.M., Ishida, H., Meier, T.M., and Halasa, A.F. (1998) *J. Polym. Sci. Part B: Polym. Phys.*, **36**, 861–871.
- 17 Dlubek, G., Alam, M.A., Stolp, M., and Radusch, H.J. (1999) *J. Polym. Sci. Part B: Polym. Phys.*, **37**, 1749–1752.
- 18 Xiao, C., Wu, J., Yang, L., and Yee, A.F. (1999) *Macromolecules*, **32**, 7913–7920.
- 19 Li, H.L., Ujihira, Y., Nanasawa, V., and Jean, Y.C. (1999) *Polymer*, **40**, 349–355.
- 20 Srithawatpong, R., Peng, Z.L., Olson, B.G., Jamieson, A.M., Simha, R., McGervey, J.D., Maier, T.R., Halasa, A.F., and Ishida, H. (1999) *J. Polym. Sci. Part B: Polym. Phys.*, **37**, 2754–2770.
- 21 Wang, B., Zhang, M., Zhang, J.M., He, C.Q., Dai, Y.Q., Wang, S.J., and Ma, D.Z. (1999) *Phys. Lett. A*, **262**, 195–205.
- 22 Hsieh, T.T., Tiu, C., Hsieh, K.H., and Simon, G.P. (2000) *J. Appl. Polym. Sci.*, **77**, 2319–2330.
- 23 Jiang, Tao, Jiang, Xue-liang, Cheng, Shi-yuan, Dai, Yi-qun, Wang, Shao-jie, and Wang, Bo (2000) *Chin. J. Polym. Sci.*, **18**, 123–126.
- 24 Misheva, M., Mihaylova, M., Djourelov, N., Kreteva, M., Kreteva, V., and Nedkov, E. (2000) *Radiat. Phys. Chem*, **58**, 39–47.
- 25 Wang, C.L., Kobayashi, Y., Zheng, W., Zhang, C., Nagai, Y., and Hasegawa, M. (2001) *Phys. Rev. B*, **63**, 064204 9.
- 26 Cowie, J.M.G., McEwan, I., McEwen, I.J., and Pethrick, R.A. (2001) *Macromolecules*, **34**, 7071–7075.
- 27 Wang, C.L., Kobayashi, Y., Zheng, W., and Zhang, C. (2001) *Polymer*, **42**, 2359–2364.
- 28 Hsieh, Tsung-Tang, Tiu, C., and Simon, G.P. (2001) *Polymer*, **42**, 8007–8011.
- 29 Dlubek, G., Pionteck, J., Bondarenko, V., Pompe, G., Taesler, C.H., Petters, K., and Krause-Rehberg, R. (2002) *Macromolecules*, **35**, 6313–6323.
- 30 Gunther-Schade, K., Schubert, D.W., and Faupel, F. (2002) *Macromolecules*, **35**, 9074–9078.
- 31 Dlubek, G., Bondarenko, V., Pionteck, J., Kilburn, D., Pompe, G., Taesler, C., Redmann, F., Petters, K., Rehberg, R.K., and Alam, M.A. (2003) *Radiat. Phys. Chem.*, **68**, 369–373.
- 32 Li, Y., Zhang, R., Chen, H., Zhang, J., Suzuki, R., Ohldaira, T., Feldstein, M.M., and Jean, Y.C. (2003) *Biomacromolecules*, **4**, 1856–1864.
- 33 Dai, Y.Q., Wang, B., Wang, S.J., Jiang, T., and Cheng, S.Y. (2003) *Radiat. Phys. Chem.*, **68**, 493–496.
- 34 Dlubek, G. and Alam, M.A. (2002) *Polymer*, **43**, 4025–4031.
- 35 Ribeiro, M.E.S., Silva, E., Machado, J.C., Mano, V., and Silva, G.G. (2003) *J. Polym. Sci. Part B: Polym. Phys.*, **41**, 1493–1520.
- 36 Hu, Y., Qi, C., Liu, W., Wang, B., Zheng, H., Sun, X., and Zheng, X. (2003) *J. Appl. Polym. Sci.*, **90**, 1507–1514.
- 37 Zhou, Q., Zhanga, L., Zhang, M., Wang, B., and Wang, S. (2003) *Polymer*, **44**, 1733–1739.
- 38 Garcia, A., Iriarte, M., Uriarte, C., Iruin, J., Etxeberria, A., and delRio, J. (2004) *Polymer*, **45**, 2949–2957.
- 39 Liu, R.Y.F., Bernal-Lara, T.E., Hiltner, A., and Baer, E. (2004) *Macromolecules*, **37**, 6972–6979.
- 40 Aravind, I., Albert, P., Ranganathaiah, C., Kurian, J.V., and Thomas, S. (2004) *Polymer*, **45**, 4925–4937.
- 41 Kwak, S.Y., Kim, S.H., and Suzuki, T. (2004) *Polymer*, **45**, 8153–8163.
- 42 Ravikumar, H.B. and Ranganathaiah, C. (2005) *Polym. Int.*, **54**, 1288–1295.
- 43 Ravikumar, H.B., Ranganathaiah, C., Kumaraswamy, G.N., and Thomas, S. (2005) *Polymer*, **46**, 2372–2380.
- 44 Soares, B.G., Almeida, M.S.M., Deepa Urs, M.V., Kumaraswamy, G.N., Ranganathaiah, C., Siddaramaiah, R., and Mauler, R. (2006) *J. Appl. Polym. Sci.*, **102**, 4672–4681.
- 45 Kumaraswamy, G.N., Ranganathaiah, C., Deepa Urs, M.V., and Ravikumar, H.B. (2006) *Eur. Polym. J.*, **42**, 2655–2666.

- 46 Fang, Z., Xu, Y., and Tong, V. (2006) *J. Appl. Polym. Sci.*, **102**, 2463–2469.
- 47 Jiang, Z.Y., Jiang, X.Q., Huang, Y.J., Lin, J., Li, S.M., Li, S.Z., and Hsia, Y.F. (2006) *Nucl. Instrum. Methods B*, **245**, 491–494.
- 48 Soares, B.G., Almeida, M.S.M., Ranganathaiah, C., Deepa Urs, M.V., and Siddaramaiah (2007) *Polym. Test.*, **26**, 88–94.
- 49 Gomaa, E. (2007) *J. Appl. Polym. Sci.*, **105**, 2564–2570.
- 50 Raj, J.M., Ranganathaiah, C., and Ganesh, S. (2008) *Polym. Eng. Sci.*, **48**, 1495–1503.
- 51 Minfeng, Z., Xudong, S., Yun, W., Xiandong, Y., Huiquan, X., Baoyi, W., and Chenze, Q. (2008) *Radiat. Phys. Chem.*, **77**, 1062–1066.
- 52 Mostafa, N. (2008) *J. Appl. Polym. Sci.*, **108**, 3001–3008.
- 53 Jamieson, A.M., Olson, B.G., and Nazarenko, S. (2010) *Polymer Physics: From Suspensions to Nanocomposites and Beyond* (eds L.A. Utracki and A.M. Jamieson), John Wiley, Hoboken, p. 491.
- 54 Ranganathaiah, C. and Kumaraswamy, G.N. (2009) *J. Appl. Polym. Sci.*, **111**, 577–588.
- 55 Raj, J.M. and Ranganathaiah, C. (2009) *Polym. Degrad. Stab.*, **94**, 397–403.
- 56 Aravind, I., Ahn, K.H., Ranganathaiah, C., and Thomas, S. (2009) *Ind. Eng. Chem. Res.*, **48**, 9942–9951.
- 57 Raj, J.M. and Ranganathaiah, C. (2009) *J. Polym. Sci. Part B: Polym. Phys.*, **47**, 619–632.
- 58 Gomaa, E., Aly, E.H., and Mohsen, M. (2009) *J. Polym. Sci. Part B: Polym. Phys.*, **47**, 227–238.
- 59 Dębowska, M., Rudzińska-Girulska, J., Serwaczak, M., Kiersnowski, A., and Pigowski, J. (2010) *Nukleonika*, **55**, 57–64.
- 60 Manjula, M.K., Lokanatha Rai, K.M., Raj, J.M., Manjula, C.S. Siddaramaiah, and Ranganathaiah, C. (2010) *J. Polym. Res.*, **17**, 89–98.
- 61 Ratna, D. and Simon, G.P. (2010) *J. Appl. Polym. Sci.*, **117**, 557–564.
- 62 Harms, S., Ratzke, K., Pakula, C., Zaporotchenko, V., Thomas, S., Egger, W., Sperr, P., and Faupel, F. (2011) *J. Polym. Sci. Part B: Polym. Phys.*, **49**, 404–408.
- 63 Kumaraswamy, G.N. (2007) Free volume microprobe studies on the miscible property of polymer blends by positron lifetime spectroscopy and differential scanning calorimetry. PhD Thesis, University of Mysore, India.
- 64 Raj, J.M. (2009) A free volume study on the phase morphology modifications in binary polymer blends by electron beam irradiation and other routes. PhD Thesis, University of Mysore, India.
- 65 Dupasquier, A. and Mills, A.P.Jr (1995) Positron spectroscopy of solids, in *Proceedings, International School Physics - Enrico Fermi, Course CXXV, Varenna 1993*, IOS Press, Amsterdam.
- 66 West, R.N. (1973) Positron studies of condensed matter. *Adv Phys.*, **22**, 263–383.
- 67 Saarinen, K., Hautajarvi, P., and Corbel, C. (1998) Identification of defects in semiconductors, in M. Stavola (ed.), *Semiconductors and Semimetals*, vol. **51A**, Academic Press, San Diego.
- 68 Krause-Rehberg, R. and Leipner, H.S. (1999) *Positron Annihilation in Semiconductors*, Springer-Verlag, Berlin.
- 69 Brandt, W. and Dupasquier, A. (1983) *Positron Solid State Physics*, North-Holland, Amsterdam.
- 70 Nakanishi, Y., Wang, S.J., and Jean, Y.C. (1988) *Positron Annihilation Studies of Fluids*, World Science, Singapore.
- 71 Jean, Y.C. and Deng, F. (1992) *J. Polym. Sci. Part B: Polym. Phys.*, **30**, 1359–1364.
- 72 Shultz, P.J. and Lynn, K.G. (1988) *Rev. Mod. Phys.*, **60**, 701–779.
- 73 Hautajarvi, P. (1979) *Positrons in Solids*, Springer-Verlag, Berlin, Heidelberg: NY.
- 74 Sharma, S.C. (1987) *Positron Annihilation in Fluids*, World Scientific, Singapore.
- 75 Grafutin, V.I. and Prokop'ev, E.P. (2002) *Physics – Uspekhi Fizicheskikh Nauk*, Russian Academy of Sciences.
- 76 Puska, M.J. and Nieminen, R.M. (1994) *Rev. Mod. Phys.*, **66**, 841–897.
- 77 Venkateswaran, K., Cheng, K., and Jean, Y. C. (1984) *J. Phys. Chem.*, **88**, 2465–2469.
- 78 Goldanskii, V.I. (1967) *Positron Annihilation*, Academic Press, New York.
- 79 Goldanskii, V.I. (1968) *At. Energy Rev.*, **6**, 3–148.
- 80 Mackenzie, I.K. (1983) *Positron Solid State Physics*, North Holland, Amsterdam, p. 214.
- 81 Grafutin, V.I., Prokop'ev, E.P., Myasishcheva, G.G., and Funtikov, Y.V. (1999) *Phys. Solid State*, **41**, 843–847.



- 82 Ore, A. and Powell, J.L. (1949) *Phys. Rev.*, **75**, 1963–1963.
- 83 Mogensen, O.E. (1974) *J. Chem. Phys.*, **60**, 998–1004.
- 84 Tao, S.J. (1976) *Appl. Phys.*, **10**, 67–79.
- 85 Zhang, Z. and Ito, Y. (1990) *J. Chem. Phys.*, **93**, 1021–1029.
- 86 Ferry, J.D. (1970) *Viscoelastic Properties of Polymers*, John Wiley, New York.
- 87 Doolittle, A.K. (1951) *J. Appl. Phys.*, **22**, 1471–1475.
- 88 Batchinsky, A.J. (1913) *Z. Phys. Chem.*, **84**, 644–645.
- 89 Fox, T.G., Gratch, S., and Losheak, S. (1956) *Rheology*, vol. 1, Academic Press, New York.
- 90 Williams, M.L., Landel, R.F., and Ferry, J.D. (1955) *J. Am. Chem. Soc.*, **77**, 3701–3707.
- 91 Cohen, M.H. and Turnbull, D. (1959) *J. Chem. Phys.*, **31**, 1164–1169.
- 92 Ferrell, R.A. (1956) *Rev. Mod. Phys.*, **28**, 308–337.
- 93 Wilson, R.K., Johnson, P.O., and Stump, R. (1963) *Phys. Rev.*, **129**, 2091–2095.
- 94 Brandt, W., Berko, S., and Walker, W.W. (1961) *Phys. Rev.*, **121**, 1864–1864.
- 95 Thosar, B.V., Kulkarni, V.G., Laci, R.G., and Chandra, G. (1969) *Phys. Lett. A*, **28** (1), 760–761.
- 96 Thosar, B.V., Kulkarni, V.G., Laci, R.G., and Chandra, G. (1973) *Phys. Status Solidi B*, **55**, 415–426.
- 97 Van Krevlan, D.W. and Hoftzer, P.J. (1976) *Properties of Polymers*, 2nd edn, Elsevier, New York.
- 98 Lee, W.M. (1980) *Polym. Eng. Sci.*, **20**, 65–69.
- 99 Brandt, W. and Wilkenfeld, J. (1975) *Phys. Rev.*, **B12**, 2579–2587. 1976, **B13**: 2243–2243.
- 100 Brandt, W. and Spim, I. (1966) *Phys. Rev.*, **142**, 231–237.
- 101 Brandt, W. and Feibus, H. (1968) *Phys. Rev.*, **174**, 454–459.
- 102 Brandt, W. and Feibus, H. (1969) *Phys. Rev.*, **184**, 277–281.
- 103 Fujita, H. (1968) *Diffusion in Polymers*, Academic Press, New York.
- 104 Brandt, W., Berko, S., and Walker, W.W. (1960) *Phys. Rev.*, **120**, 1289–1295.
- 105 Tabata, Y., Ito, Y., and Oshima, K. (1968) Proceedings, Symposium of Organic Solid State Chemistry, Brookhaven National Laboratory, vol. 417, pp. 47–48.
- 106 Ogata, A. and Tao, S.J. (1970) *J. Appl. Phys.*, **41**, 4261–4265.
- 107 Story, E.J. (1960) Positron research. MS thesis, Vanderbilt University.
- 108 Gray, P.R., Cook, C.F., and Sturm, G.P. (1968) *J. Chem. Phys.*, **48**, 1145–1157.
- 109 Brandt, W. and Wilkenfeld, J. (1975) *Phys. Rev. B.*, **13**, 479.
- 110 Pethrick, R.A. (1997) *Prog. Polym. Sci.*, **22**, 1–47.
- 111 Brandt, W. and Dupasquier, A. (1983) *Positron Solid State Physics*, North-Holland, Amsterdam, p. 432.
- 112 Schrader, D.M. and Jean, Y.C. (1988) *Positron and Positronium Chemistry*, Elsevier Science, Amsterdam.
- 113 Ramani, R. and Ranganathaiah, C. (2001) *Polym. Int.*, **50**, 237–248.
- 114 Ramani, R., Ramachandra, P., Ramgopal, G., and Ranganathaiah, C. (1997) *Eur. Polym. J.*, **33**, 1753–1758.
- 115 Shariff, G., Sathyanarayana, P.M., Thimmegowda, M.C., Ashalatha, M.B., Ramani, R., Avasthi, D.K., and Ranganathaiah, C. (2002) *Polymer*, **43**, 2819–2826.
- 116 Deepa Urs, M.V., Ranganathaiah, C., Ramani, R., and Alam, S. (2006) *J. Appl. Polym. Sci.*, **102**, 2784–2794.
- 117 Ashalatha, M.B., Sathyanarayana, P.M., Shariff, G., Thimmegowda, M.C., Ramani, R., and Ranganathaiah, C. (2004) *Appl. Phys. A.*, **78**, 565–573.
- 118 Sathyanarayana, P.M., Shariff, G., Thimmegowda, M.C., Ashalatha, M.B., Ramani, R., and Ranganathaiah, C. (2002) *Polym. Int.*, **50**, 765–771.
- 119 Ramachandra, P., Ramani, R., Ramgopal, G., and Ranganathaiah, C. (1997) *Eur. Polym. J.*, **33**, 1707–1711.
- 120 deSousa, E.M.B., deMogalhaes, W.F., and Mahalle, N.D.S. (1999) *J. Phys. Chem. Solids*, **60**, 211–221.
- 121 Harms, S., Ratzke, K., and Faupel, F. (2010) *Macromolecules*, **43**, 10505–10511.
- 122 Nissila, J., Rytola, K., Aavikko, R., Laakso, A., Saarinen, K., and Hautajarvi, P. (2005) *Nucl. Instrum. Methods A*, **538**, 778–789.
- 123 Sathyanarayana, P.M., Shariff, G., Thimmegowda, M.C., Ashalatha, M.B., Ramani, R., and Ranganathaiah, C. (2002) *Polym. Int.*, **50**, 765–771.

- 124 Kirkegaard, P., Pedersen, N.J., and Eldrup, M. (1989) PATFIT-88: A data-processing system for positron annihilation spectra on mainframe and personal computers. Riso Nat. Lab. Report, Denmark, M-2740.
- 125 Marquardt, D.W. (1963) *J. Soc. Ind. Appl. Math.*, **11**, 431–441.
- 126 Kirkegaard, P. and Eldrup, M. (1971) The least squares fitting program POSITRONFIT: Principles and formulas. Riso Nat. Lab. Report, Denmark, M-1400.
- 127 Kirkegaard, P., Olsen, J.V., Eldrup, M., and Pedersen, N.J. (2009) PALSfit: A computer program for analyzing positron lifetime spectra. Riso Nat. Lab. Report, Denmark, R-1652.
- 128 Tao, S.J. (1972) *J. Chem. Phys.*, **56**, 5499–5510.
- 129 Eldrup, M., Lightbody, D., and Sherwood, J.N. (1981) *Chem. Phys.*, **63**, 51–58.
- 130 Ranimol, S., Ranganathaiah, C., Varghese, S., Joseph, K., and Thomas, S. (2006) *Polymer*, **47**, 858–870.
- 131 Merrigan, J.A., Green, J.H., and Tao, S.J. (1972) *Techniques of Chemistry - 1, Part IIID – Physical Methods of Chemistry*, Wiley-Interscience, New York.
- 132 Gregory, R.B. (1991) *J. Appl. Phys.*, **70**, 4665–4670.
- 133 Shukla, A., Peter, M., and Hoffmann, L. (1993) *Nucl. Instrum. Methods A*, **335**, 310–317.
- 134 Delves, L.M. and Mohamed, J.L. (1985) *Computational Methods for Integral Equations*, University Press, Cambridge.
- 135 McWhirter, J.G. and Pike, E.R. (1978) *J. Phys. A: Math. Gen.*, **11**, 1729–1745.
- 136 Schrader, D.M. and Usmar, S.G. (1988) *Positron Annihilation Studies of Fluids*, World Scientific, Singapore, p. 215.
- 137 Tikhonov, A.N. and Aisenin, V.Y. (1977) *Solutions of Ill-Posed Problems*, Winston, Washington, DC.
- 138 Groetsch, C.W. (1984) *The Theory of Tikhonov Regularization for Fredholm Equations of the First Kind*, Pitman, Boston.
- 139 Provencher, S.W. (1982) *Comput. Phys. Commun.*, **27**, 229–242.
- 140 Livesey, A.K. and Skilling, J. (1985) *Acta Crystallogr. A*, **41**, 113–122.
- 141 Livesey, A.K. and Brochon, J.C. (1987) *Biophys. J.*, **52**, 693–706.
- 142 Provencher, S.W. (1982) *Comput. Phys. Commun.*, **27**, 213–227.
- 143 Gregory, R.B. and Procyk, A. (1988) *Positron Annihilation in Fluids*, World Scientific, Singapore, p. 524.
- 144 Gregory, R.B. and Zhu, Y. (1990) *Nucl. Instrum. Methods A*, **290**, 172–182.
- 145 Gregory, R.B. (1991) *Nucl. Instrum. Methods A*, **302**, 496–507.
- 146 Rigby, D. and Roe, R.J. (1990) *Macromolecules*, **23**, 5312–5319.
- 147 Robertson, R.E., Simha, R., and Curro, J. G. (1985) *Macromolecules*, **18**, 2239–2246.
- 148 Davis, W.J. and Pethrick, R.A. (1998) *Polym. Int.*, **45**, 395–402.
- 149 Robertson, R.E. (1992) *Computational Modeling of Polymers*, Marcel Dekker, Midland.
- 150 Deng, Q. and Jean, Y.C. (1992) *Proc. Am. Chem. Soc. Polym. Mater. Sci. Eng.*, **67**, 151–153.
- 151 Davis, W.J. and Pethrick, R.A. (1998) *Eur. Polym. J.*, **34**, 1747–1754.
- 152 Jean, Y.C. (1990) *Positron and Positronium Chemistry*, World Scientific, Singapore.
- 153 Lynn, K.G., Donald, J.R.M., Boie, R.A., Feldman, L.C., Gabbe, J.D., Robbins, M. F., Bonderup, E., and Golovchenko, J. (1977) *J. Phys. Rev. Lett.*, **38**, 241–244.
- 154 Riande, E., Diaz-Calleja, R., Prolongo, M. G., Masegosa, R.M., and Salom, C. (2000) *Polymer Viscoelasticity: Stress and Strain in Practice*, Marcel Dekker, New York.
- 155 Rouse, P.J. (1953) *J. Chem. Phys.*, **21**, 1272–1280.
- 156 Zimm, B.J. (1956) *J. Chem. Phys.*, **24**, 269–278.
- 157 Schnell, M. and Wolf, B.A. (2000) *J. Rheol.*, **44**, 617–628.
- 158 Schnell, M. and Wolf, B.A. (2001) *Polymer*, **42**, 8599–8605.
- 159 Mertsch, R. and Wolf, B.A. (1994) *Ber Bunseng. Phys. Chem.*, **98**, 1275–1280.
- 160 Bondi, A. (1964) *J. Phys. Chem.*, **68**, 441–451.
- 161 Kapnistos, M., Hinrichs, A., Vlassopoulos, D., Anastasiadis, S.H., Stammer, A., and Wolf, B.A. (1996) *Macromolecules*, **29**, 7155–7163.
- 162 Meghala, D. and Ranganathaiah, C. (2012) *Polymer*, **53**, 842–850.
- 163 Meng, X., Liu, X., Li, Z., and Zhou, Q. (2013) *Polym. Engg. Sci.* DOI 10.1002/pen.23614.

## Index

### **a**

ABS copolymer image 563  
 absorption coefficient 803  
 – vs. photon energy 804  
 absorption edge 806  
 acrylonitrile 139, 171  
 acrylonitrile butadiene rubber, FTIR spectra 663  
 acrylonitrile–butadiene–styrene (ABS) copolymer 562, 870  
 activation energies 151, 153  
 – apparent 136  
 – crosslinking 139  
 adhesion energy 110  
 adsorbate–adsorbent interactions 329  
 Alginate macromolecules 642  
 – electrospinnability 642  
*n*-alkanes 12  
 amide–ester interchange reaction 753  
 amonochromator 815  
 amorphous/crystalline polymer blends 160, 161  
 amorphous semiconductor materials 802  
 amplitude-average decay time 825  
*Anabaena* cyanobacterium 601  
 analog-to-digital converter (ADC) 889  
 analytical vs. inverse gas chromatography 328  
 angular correlation of annihilated radiation (ACAR) 879  
 anisotropic hyperfine interaction 746  
 anisotropic nanometric fillers 151  
 annealing PMMA/SMA blends 857  
 annihilating pair, kinetic energy of 879  
 annihilation gamma photons 882  
 2 $\gamma$ -annihilation process  
 – vector diagram of momentum conservation 879  
 antidegradants 108  
 antiplasticizers 381

$\alpha$ -relaxation process 850  
 Arrhenius behavior 380  
 Arrhenius equation 395, 399  
 Arrhenius plot 139  
 Arrhenius relationship 135  
 atactic PHB (aPHB) 431  
 atactic PMMA (aPMMA) 629  
 atomic force microscopy (AFM) 3, 309, 523, 524, 830  
 – data 283  
 – morphological information 524  
 attenuated total reflection (ATR) mode 705  
 – IR/NIR imaging technique 705  
 average decay time 825  
 Avrami approach 850  
 azoisobutyronitrile (AIBN) 171

### **b**

band gap transition 804  
 – direct and indirect 805  
 BCPs. *see* block copolymers (BCPs)  
 benzoxazine 868  
 binary polymer blends  
 – beta-, gamma-, and alpha-values for 909–915  
 – of crystalline-amorphous diblock copolymers 226  
 binary systems 374–376  
 binodal curve 104  
 biocompatibility 7, 55, 312, 313, 431, 664, 776  
 biodegradability 7, 45, 51, 53, 56, 282, 431, 537, 664  
 biodegradable blends 7  
 biodegradable polyesters-based polymer blends 29  
 biodegradable polymeric scaffolds 664  
 biomedical devices 1  
 bioplastics 383  
 bisphenol A-based benzoxazine (BA-a) 374

- bisphenol A-based cyanate ester (BACY) 374, 375
- bisphenol A polycarbonate (PC) 377
- blending ratios 314
- block copolymer/PS weight ratio 565
- block copolymers (BCPs) 133, 150, 218, 224, 260–264, 513–515
  - blends of 224–228
  - ordered phases 264–267
  - phase diagram 266
  - shearing into single domain texture and 266
- body-centered cubic (BCC) 224, 225
- Bohr–Einstein relationship 792
- Bohr magneton 733
- Boltzmann constant 881
- Boltzmann's law 9
- Bondi's method 901
- Bragg angle 212
- Bragg–Brentano configuration 210
- Bragg ionization chambers 770
- Bragg-peaks 224, 265
- Bragg-reflections 265
- Bragg's law 211
- Brownian diffusion 742, 744
- Brownian motion 119
- Bruggeman formula 302
- Bruggemann effective medium approximation (BEMA) model 311
- Bruker FT-IR imaging system 708
- bulk heterojunction (BHJ) devices 696
- butadiene-rich phase 561
- 1-butyl-3-methyl imidazolium chloride 383
- c**
- cadmium sulfide (CdS) 545
- Cahn–Hilliard theory 106
- Cahn–Hilliard equation 464, 465, 515, 516
- camphorsulfonic acid (CSA) 762
- Capronor system 170
- carbon black 151
- carbon nanotubes (CNTs) 377
- carboxylated polyester resin 871
- carboxyl-terminated copolymer of
  - butadiene 139
- carboxymethyl cellulose (CMC) blends
  - molecular dynamics 860
- cashew nut shell liquid (CNSL) 763
- castor oil-based polyurethane (PU) 860
- Cauchy function 302
- $^{13}\text{C}$  cross-polarization (CP) 680
- CDACD, PC-based blends
  - fractional free volume 903
- cellulose 52
  - blends containing 54, 55
  - cellulose acetate (CA) 681
  - poly(acryloyl morpholine) (PACMO) 681
  - $T_{1\rho}^H$  values 683
  - cellulose acetate butyrate (CAB) 51
  - cellulose acetate butyrate blends 724, 725
  - FT-IR and FT-NIR imaging of 724–727
  - spherulitic structure of 724–727
  - cellulose acetate propionate (CAP) 51
  - charge carriers 793
  - charge coupled devices (CCDs) 213, 823
  - charge-induced positrons (CIPs) 904
  - chemisorption 341
  - chemometric methods 336
    - application of 336, 337
  - chemorheology 153
    - MMTmodified epoxy 152, 153
  - chitosan blends 52, 418, 664, 665
    - blends containing 55
    - modification 419
    - SCP ratio 419, 420
    - water vapor transmission rate 420
  - chitosan particles spray
    - SEM images of 569
  - chitosan-poly (vinyl alcohol) (PVA) blend 418
    - films 419
    - interpenetrating polymer networks 419
    - isotherm curves of sorption 419
    - sorptive properties 419
  - chlorinated polyethylene (CM) 272
  - chlorinated polyethylene (CPE) 386
  - chlorosulfonated polyethylene (CSM) 272
  - chord distribution function (CDF) 232
  - chromophore 798
  - cis-polyisoprene (CPI) 381
  - cis-polyisoprene/trans-polyisoprene (CPI/TPI) blends 375
  - cloud-point determination 162–165
  - cohesive energies 17, 18
  - coincidence Doppler broadening (CDB) 895
    - experiment 881
  - Cole–Cole relationship 851
  - collagen 52
  - collagen/synthetic polymer blends
    - FTIR spectra 664
  - commercial products based on miscible blends 159
    - polystyrene (PS)– poly(phenylene oxide) (PPO) 159
    - poly(vinyl chloride) (PVC)–nitrile rubber 160
    - poly(vinylidene fluoride) (PVDF)–poly(methyl methacrylate) (PMMA) 159

- COMPASS software 20
- compatibilization 120, 121, 269, 282
- kinetic criteria 121
  - morphology development in compatibilized blends 121–123
  - influence of compatibilizer concentration on 123
  - Marangoni stress 121, 122
  - steric repulsion 122
  - objectives of compatibilizers in blending process 120
  - techniques 94, 123, 124
  - addition of preprepared copolymer 124
  - addition of reactive low-molecular-weight compounds 125, 126
  - addition of reactive polymer 125
  - solid-state shear pulverization 126
- compatibilizer 109
- competition, of phase dissolution and crystallization 190–197
- complementary dissimilarity 16
- complex refractive indices 299
- complex viscosity 137
- frequency dependence 137
- confocal microscopy 3, 610, 613
- polymer blends, characterization of 543–547
- conjugated polymers, bonding in conducting 800
- constant-fraction differential discriminators (CFDDs) 889
- CONTIN-PALS2 program 892
- CONTIN program 891
- continuous-wave EPR (CW-EPR) systems 736, 737
- copolymerization 138, 159
- block-and-graft 159
  - random 159
- copolymers 83, 84, 260
- correlated barrier hopping (CBH) 860
- corrosion-resistant 1
- coumaroneindene (CI) 381
- Cox–Merz rule 137
- creep compliance 398
- creep data 405
- creep polymers 395
- creep response 397
- crosslinkers 382
- storage modulus curve 382
- crystalline–amorphous interface boundaries 890
- crystalline lamellar PHB domains 717
- crystallites 228, 789
- crystallization kinetics 181
- CTBN rubber 139
- curing kinetics 137
- curing process 134
- curing temperature 134, 136
- current–voltage characteristics 317
- cyanate ester (BACY), thermal and dielectric properties 868
- cyclohexane 341
- d**
- DBAR measurements 893
- deBroglie wavelength 890
- deflection temperature under load (DTUL) 384
- deformation micromechanisms 554
- deformed lamellar SBS triblock copolymer
- higher-magnification TEM images of 572
- dehydrochlorination reaction 358
- density of states (DOS) 807
- 2D EPRI experiment, schematic representation 741
- deuterated PB (DPB) 613
- bicontinuous structures, time evolution of 614
- deuterated poly(methyl methacrylate) (d-PMMA) 585, 779
- depth profiles 781, 782
- deuterated polystyrene (d-PS) 780
- phase separation 778
  - polymer blend films 777
  - vs. depth, volume fraction 774
- deuterated poly(xyleyl ether) (d-PXE) 775
- deuterium lamp 811
- deuterium NMR spectroscopy 692
- Dexter exchange energy transfer 828
- 2D-FTIR spectroscopy 665–668
- DGEBA epoxy 139
- resin 151
- 4,4'-diamino-3,3'-dimethyl dicyclohexyl methane 139
- 4,4'-diaminodiphenylmethane (DDM) hardener 870
- 4,4'-diaminodiphenylsulfone (DDS) 307
- diblock copolymers 260, 266, 267
- 1,2-dichloroethane 171
- dielectric loss peak intensity 849
- dielectric relaxation spectroscopy 849
- amorphous polymer blends, dielectric relaxation spectroscopy of 853–862
  - chemically reactive polymer blends 868–872
  - relaxation spectrum analysis 850–852

- relaxation spectrum, temperature effect 852, 853
  - semicrystalline polymer blends 862–868
  - differential scanning calorimetry (DSC) 222, 274, 626, 747, 878, 887, 896
  - measurements 713
  - diffraction 211
  - diglycidyl ether of bisphenol A (DGEBA)-based epoxy resins 138, 565
  - diaminodiphenyl-methane (DDM) cured blends of 565
  - N,N*-dimethylformamide 860
  - solution 633
  - dioctyl phthalate (DOP) 763
  - dip coating 552–553
  - 2,2-diphenyl-1-picrylhydrazyl (DPPH) crystals 739
  - dipole–dipole interactions 2, 3, 99
  - DMA. *see* dynamic mechanical analysis (DMA)
  - DMTA. *see* dynamic mechanical thermal analysis (DMTA)
  - Doppler broadening of annihilation radiation (DBAR) 880, 881
  - Doppler shift 880
  - double-beam configuration 810
  - double-beam spectrophotometer 810
  - double electron electron resonance (DEER) 737
  - ductile fracture mode 38
  - dynamic mechanical analysis (DMA) 626, 747, 849
  - dynamic mechanical experiment 396
  - dynamic-mechanical relaxation times 136
  - dynamic mechanical thermal analysis (DMTA) 4, 365, 366, 395, 396
  - analyzers 366, 367
  - to analyze viscoelastic behavior of polymers 368, 369
  - geometries of experimental testing 367
  - modeling viscoelastic behavior 373
  - viscoelastic spectra 369
  - – flowing 373
  - – glass–rubber relaxation 371, 372
  - – glassy state 369–371
  - – recrystallization or curing 372, 373
  - – rubbery plateau 372
  - dynamic oscillation rate 137
  - Dysonian shape 761
- e**
- EC plasticization 362
  - elastic recoil detection analysis (ERDA) 766
  - elastic scattering 767
  - electrochemical impedance spectroscopy 849
  - electroluminescent polymer blends 586
  - electromagnetic radiation 791
  - electromagnetic spectrum 792
  - electronic energy transfer processes 882
  - electronic excitation 793
  - electronic photoexcitation 822
  - electron magnetic moment 733
  - electron microscopy (EM) 551
  - electron multiplying CCD (EMCCD) 710
  - electron paramagnetic resonance spectroscopy 731
  - background 732–747
  - deuterated polystyrene 780
  - deuterium depth resolution map 772
  - deuterium, real-time variation of 773
  - dPMMA, depth profiles 781, 782
  - electron spin resonance (ESR) spectroscopy 732
  - forward recoil spectrometry (FRES) 766
  - free radical concentration 757
  - FRES experiments 767
  - HAS stabilizer 745
  - HDPE/PA6 757
  - $^4\text{He}^{++}$  FReS data 777
  - imaging experiment 739
  - LE-FRES volume fraction profile 779
  - Lorentzian peak-to-peak linewidth 765
  - microwave frequency bands 736
  - microwave pulse, formation 738
  - missing angles, cone of 741
  - nitroxide biradicals, two-dimensional (2D) spectral-spatial perspective plot 740
  - nitroxide molecule symmetry 744
  - PANI–PEO fiber 762
  - PCHA weight fraction in PCHMA/PCHA blends 754
  - peak-to-peak line width signal 763, 764
  - PE/SBS blends e-beam-irradiation 756
  - piperidine nitroxide spin probes, chemical structures of 748
  - polymer blend, volume fraction profile 769
  - polymers, ion beam analysis of 766
  - polystyrene (PS) blend 765
  - PP and PP/ENR blends e-beam-irradiation 760
  - PP/EVA blends e-beam-irradiation 759
  - PP/SBS samples 759
  - PS film onto PMMA-anh layer 776
  - simulated X-band EPR spectra 735
  - spin probe general formula 745
  - STMAA-12 copolymer, tempol spin probe 751

- STMAA crosslinking density 752
- SWCNT/PS nanocomposites, polymer tracer diffusion 775
- tempamine, in PS(OH)-8/PP 750
- temperature dependence 763
- thickness regimes 780
- time-of-flight detector system 770
- TINUVIN770 746
- volume fraction d-PS *versus* depth 774
- X-, Q-, and W-band continuous-wave EPR spectra 736
- electron–positron annihilation 878
- electron spin echo envelope modulation (ESEEM) 737
- electron spin echo (ESE) signal 738
- electron spin energy level, schematic representation 733
- electron spin resonance (ESR) spectroscopy 5, 732
- electrostatic coulombic forces 807
- ellipsometric porosimetry 311
- ellipsometry 3, 299
- energy diagram 822
- enthalpy 2, 8, 10, 11, 330
  - of mixing 95, 96
  - regular solution 11
  - of vaporization 17
- entropy 8, 9, 138, 330
  - combinatorial 10, 332
  - factor 2
  - of mixing 96–98
  - mixing of ideal solutions 8
- environmental scanning electron microscopy (ESEM) 569
- EOC-rich blends 558
- EPDM elastomer 275
- epoxidized (eSBS) block copolymer 566, 567
- epoxidized natural rubber (ENR) 354
- epoxidized natural rubber/ethylene propylene diene monomer (ENR/EPDM) blends 274
- epoxidized styrene-butadiene linear diblock copolymer-modified epoxy 150
- epoxy/amine system 136
- epoxy monomers 150
- epoxy-phenolic system 137
- epoxy resin-based nanostructured blends 565
- epoxy resin/PEI blend 432
- epoxy system 137
- EPR imaging (EPRI) 738, 739
- EPR signals 747
- EPR spectra hyperfine structure (HFS) 734

- EPR spectral analysis 744
- EPR spectroscopy 741, 747
  - continuous-wave 747
- equilibrium phases 104
- ethylbenzene 171
- ethylene alcohol vinyl (EVOH) 637, 639
  - bending band diffusion coefficients 640
- diffusion coefficients 639
- ethylene-propylene-diene-based (EPDM) rubbers 381
- ethylene propylene diene monomer (EPDM) 905
- ethylene-trifluoroethylene copolymer (ETFE) 588
- ethylene vinyl alcohol (EVOH) 375
- Euler angles 743
- excitation function 825
- exothermic curing reaction 137
- extinction coefficient 300, 809

## *f*

- F8BT blend 586
- F8BT photoluminescence spectra 839
- F8BT:TFB blend thin films 586
- Fermi contact interactions 734, 735, 745
- Fermi energy 893
- Fick's law, for thin film diffusing 776
- Fick's second law 638
- film, by dropping 552
- film-formation, mechanisms in systems
  - containing polymer 316
- finite concentration of test solutes (FC-IGC) 329
- Flory–Huggins chi-parameter 829
- Flory–Huggins description, thermodynamics theory 626
- Flory–Huggins equation 102, 417
- Flory–Huggins interaction 103, 331
  - parameters 261, 307, 340, 887
  - for “multiple” systems 333, 334
- extension of model to systems with specific interactions 19–24
- Flory–Huggins parameters 340
- Flory–Huggins solute-polymer interaction parameter 332
- Flory–Huggins theory 7, 9, 10, 13–17, 98, 246, 335
- fluorescence microscopy 3, 610, 612
  - diffraction barrier 615
  - fundamentals of 609–612
  - measurements 611
  - polymer blend systems

- 3D structure, real-space measurement 612–614
  - spectroscopic information 614–615
  - fluorescence resonant energy transfer (FRET) 614
  - fluorescence-SNOM 843
  - images 617
  - fluorescence spectroscopy 821, 823
  - extrinsic fluorescent labels 844
  - fundamentals of 822
  - microscopy 830
  - nonconjugated polymeric materials 821
  - polymer blends 830–840
  - quenching 827–830
  - steady-state fluorescence 823
  - systems requiring extrinsic labels 840–844
  - theory 822, 823
  - time-resolved fluorescence 823–827
  - time-resolved measurements 824
  - fluorescent moiety 611
  - fluorescent molecular system, continuous-wave excitation of 823
  - focal plane array (FPA) detectors 705
  - FT-IR imaging measurement 709
  - forbidden transitions 795
  - Förster (dipole–dipole coupling) exciton transfer 833
  - Förster radius 614
  - Förster resonance energy transfer (FRET) 828, 829
  - forward recoil spectrometry (FRES) 731, 766
  - Fourier transform (FT)-EPR techniques 737
  - Fourier transform infrared (FTIR) spectroscopy 3, 26, 314, 625, 626, 628, 637, 687, 706, 720
  - analysis techniques 627
  - bisphenol A (BPA) 657
  - characterization of polymer blends 626–628
  - emission image 616
  - image 705
  - investigating miscibility, methods of methods of 626
  - microspectroscopy 668, 669
  - natural polymer blends
  - chitosan blends 664, 665
  - collagen blends 663, 664
  - polarization modulation/2D-FTIR spectroscopy 665–668
  - polarization spectroscopy 714
  - polyethylene oxide (PEO) blends 643–650
  - poly-(3-hydroxybutyrate-co-3-hydroxyvalerate) (PHBV) blends 657–661
  - poly(methylmethacrylate) (PMMA) blends 655–657
  - poly (vinyl methyl ether) (PVME) blends 650–655
  - poly(vinyl alcohol) (PVA) blends 637–642
  - poly(vinylphenol) (PVPh) blends 628–632
  - poly(vinylpyrrolidone) (PVP) blends 632–637
  - synthetic rubber 661–663
  - techniques 5
  - thermal gravimetric analysis (TGA) 626
  - Fourier transform-ion cyclotron resonance (FT-ICR) 590
  - Fox equation 274
  - FPA imaging technique 706
  - fractional PFO residual emission 834
  - emission ratio 834
  - fragile glass-formers 380
  - fragility index 379–381, 380
  - free carrier absorption 808
  - FT-ICR analyzers 590
  - FT-IR imaging, polymer blends 630, 711
  - anisotropic PHB/PLA blend films 714–717
  - poly((3-hydroxybutyrate)(PHB)/poly(L-lactic acid)(PLA) blends 711–714
  - FT-Raman spectroscopy 629
  - full width at half-maximum (FWHM) 224, 780, 815, 889
- g**
- gas permeation
  - BCPC/PMMA blend 450, 451
  - CA/PMMA blend 447, 448
  - CELL/PVA blend 449
  - EVA-45/H-48 blend 448
  - matrimid/PBIs 447
  - matrimid/P84 blends 446, 447
  - matrimid/PSF blends 446
  - PS/PC blends 444
  - PS/PPO blends 445
  - PS/PTMPS blends 445
  - PS/PVME blend 448, 449
  - PTMSMMA/3-methylsulfolane blend 450
  - PU/PMMA blend 448
  - PVA/PEI/PEG blends 444
  - TLCP/PET blend 449
  - trogamid blend 449, 450
  - Gaussian contribution 763
  - Gaussian curves 894
  - Gaussian functions 620, 633, 648, 742
  - Gaussian intensity distribution, of wavelengths 815
  - Gaussian resolution function 889



- gelation 134, 139
  - behaviors 148–150
- gellan/PVA blends
  - FTIR spectra of 641
- gel point 134
- gel time 134
  - criteria for determination 135
- Gibbs energy 2, 100, 102, 105, 106
- Gibbs free energy 13, 23, 25, 95, 261, 330, 331, 731, 821
- Ginzburg number 259
- glass–rubber relaxation 371, 372
  - temperature 381
- glass transition temperature ( $T_g$ ) 34, 305, 329
- glycidyl methacrylate (GMA) 395
- glycidyl methacrylate grafted poly(ethylene octane) (PLA/mPEO) 376
- glycol moiety
  - *gauche* and *trans* segments of 631
- glycolyzed poly(ethylene terephthalate) (GPET) 424
  - sorption and diffusion in water 424
- Gnuplot program 601
- Gordon–Taylor equation 274
- grazing-incidence small-angle x-ray scattering (GISAX) 211
- green-emitting component 835
- Groblér–Balizs procedure 328
- h**
- HAS stabilizer 745
- Havriliak–Negami (HN) model 850, 851
- HC-blended systems 381
- HC tackifier 381
- HDPE lamellae 557
  - crystals 559
- HDPE/PA6 EPR spectra 757
- heat distortion temperature (HDT) 384–386, 385
- heavy-ion FRES (HI–FRES) 769
- $^4\text{He}^{++}$  FReS data 777
- Helfand–Tagami model 109
- Helfand theory 307
- heterogeneous polymer blends 3, 94, 348
- hexagonal closed pack (HCP) 224
- HFS. *see* hyperfine structure (HFS)
- HgCdTe (MCT) array detector 706
- high-density polyethylene (HDPE) 340, 556
- high-density polyethylene and poly(vinyl alcohol) (rHDPE/PVA) blends 384
- high-density polyethylene (HDPE)/isotactic polypropylene (i-PP) blends 276
- highest occupied molecular orbitals (HOMOs) 795, 800, 831
- high-frequency ultrasound 270
  - in-line monitoring 278
  - static characterization 270
- high-impact polystyrene (HIPS) 380
- high-molar-mass polymer systems 265
- high-molecular-weight epoxy (HMWE) monomer 380
- Hildebrand approach 17, 18
- Hildebrand–Scatchard solution theory 336
- hindered amine stabilizers (HAS) 745
- HNBR latex 403
- homogeneous polymer blends 348
- homopolymers 17, 133, 218, 308
  - blends of 219, 220
- Hookian spring, behavior under excitation of constant load 398
- horizontal precipitation Langmuir–Blodgett (HP–LB) method 599
- HpGe semiconductor detector 894
  - high-energy-resolution 882
  - typical annihilation gamma spectrum 895
- $^1\text{H}$  spin-diffusion analysis 688
- Hv light scattering
  - crystallization kinetics by 181–190 (*see also* optical microscopy)
- hydrocarbon (HC) 381
- hydrodynamic interaction parameter 900, 906
- hydrogen-bonded carbonyl groups 648
- hydrogen-bonded hydroxyl absorption 634, 647
- hydrogen bonding 2
  - enthalpies of 26
- hydroxyl–carbonyl interassociation 634
- hyperbranched (HB) polyamide 867
- hyperbranched poly(ester amide) (HBP) 49, 50
- hyperbranched polymers 327
- hyperfine coupling 734
- hyperfine structure (HFS)
  - in EPR spectra 734
  - nuclear spin quantum number 742
- hyperfine sublevel correlation spectroscopy (HYSCORE) 737
- hyperfine tensor 735
- i**
- ideal gases 8
- ideal polymer blend 382
- IGC. *see* inverse gas chromatography (IGC)
- illumination techniques and contrast mechanisms 525
- immiscible polymer blends 2, 94, 625
- impact-modified plastics 160

- index of crystallinity 224
  - indium tin oxide (ITO)/glass substrate 317
  - inelastic collisions 883
  - infrared interferometer 668
  - infrared microscopy 3
  - infrared microspectroscopy 628
  - infrared spectroscopic ellipsometry (IRSE) 304
  - infrared variable angle spectroscopic ellipsometry (IR-VASE) 304
  - in-situ* polymerization 400
  - intensity-average decay time 825
  - interaction energy 11, 12, 23
    - density 12
    - per lattice site 12
  - interfaces 94
    - in polymer blends 107–111
    - segmental density profile across 109
  - intermolecular interactions 11
  - internal energy 10, 11
  - interphase boundaries/border compositions 38, 39
    - electron microscopy 39
  - interphase distribution function (IDF)
    - calculation 223
    - PCL/PVC blends 223
  - intradband transition 807
  - intrinsically conducting polymers (ICPs) 540
  - inverse gas chromatography (IGC) 18, 327–329, 334
    - advantages 341, 342
    - capillary column 327
    - drawbacks 341, 342
    - packed column 327
    - procedures in experiments leading to determination of polymer blend characteristics 334–336
    - theoretical background 328–330
    - transport properties of polymeric mixtures 337–339
    - vs. analytical 328
  - iodine-doped regiorandom (RRa) 764
  - ion beam analysis (IBA) 732, 766
  - ion-bombardment-induced emission processes 590
  - ionization potential/ionization potential 800
  - ionizing radiation 755
  - iPHB/aPHB blend 431, 432
  - iPHB/PECH blend 431, 432
  - iPMMA/PLLA blends 74
  - iPP1/iPP2 blends 224
  - IR microspectroscopy 627
  - isotactic PMMA (iPMMA) 629
  - isotactic polypropylene (iPP) 224, 340, 395, 668
  - isothermal behavior 134
  - isothermal conditions 137
  - isothermal crystallization 229
  - isothermal curing reactions 136
  - ITO/F8BT:TFB blend, power efficiency voltage characteristics 587
- j**
- Jablonskii diagram 822
  - James–Martin coefficient 329
- k**
- Kelvin equation 311
  - kinetic transitions 134
  - Kivelson theory 742
  - Kjeldhal method 662
  - Kohlausch–Williams–Watts model 373
  - Kramers–Kronig consistency 302
  - KRZ model 898
  - KSR model 898
- l**
- Langmuir–Blodgett (HP-LB) method 581
    - horizontal precipitation 599
    - monolayers 616
  - Laplace integral 891
  - large-amplitude oscillatory preshear 151
  - large angle (LA)-FRES 770
  - laser scanning confocal microscopy (LSCM) 543
  - latex compounding technique 400
  - lattice fluid model 100
  - LCST (lower critical solution temperature) 160, 171
  - LDPE/i-PP blends 395
  - LDPE-LLDPE blends 383
  - LDPE/PA6 blends, EPR spectra of 757
  - Lewis acid–base interaction 635
  - light-emitting diodes (LEDs) 581, 831
  - light scattering 161, 162
    - $V_V$  profile, of PCL/SAN-27.5 (80/20) blend 174
  - linear blends (LB) 749
  - linear low-density polyethylene (LLDPE) 376
    - EPR spectra of 757
  - linear polyethylene 556
  - linear viscoelastic behavior 137
  - linoleic acid 382
  - Liouville equation 742
    - quantum-mechanical 743
  - liquid-like behavior 151
  - liquid-liquid phase separation (LLPS) 160, 230
  - liquid-liquid phase transition 160

- liquid metal ion gun (LMIG) 593
- liquid–solid phase separation 160
- liquid–solid phase transition 160
- Lorentz-corrected SAXS profile 220, 221
  - plot 222
  - polymer blends (iPP1/iPP2) 225
- Lorentzian functions 742
- Lorentzian peak-to-peak linewidth
  - temperature-dependence of 765
- Lorenz microscopy mode 561
- low-density polyethylene (LDPE) 370, 371, 395
- lower critical solubility temperature (LCST) 3, 100, 103, 104, 258, 330, 841
  - behavior 779
  - thickness regimes 780
  - phase diagrams 24
- lowest unoccupied molecular orbital (LUMO) 795, 801
  - energies 827
- low-molecular-weight epoxy (LMWE) 380
- LSCM images
  - of poly(styrene-ranbutadiene) and polybutadiene blend 545
  - of PS/PMMA blend 545
  - quality improvement and 3D reconstruction 544
  - showing phase separated morphologies 546
- m**
- magic angle spinning (MAS) 680
- magnetic spin quantum number 733
- maleic anhydride (MA) 125
- maleic anhydride-grafted polypropylene (MA-g-PP) 308, 378
- Markov process 743
- matrix-assisted pulsed laser evaporation (MAPLE) 313
- Maxwell–Garnett EMA 301
- Maxwell model 119
- Maxwell–Wagner–Sillars (MWS) interfacial polarization process 862
- MD simulations
  - interaction parameter from 20, 21
  - PLLA/PVPh
  - interaction parameter from 20, 21
  - using the COMPASS force-field 45
- Meander model 852
  - schematic diagram 853
- mean-field approach 246
- mean-field random phase approximation 254, 258
- mechanical thermal analysis 3
- medium-angle x-ray scattering (MAXS) 218
- MEH-PPV, chemical structures of 839
- melting point 171
- mesoscale morphologies, in polymer blends 526, 528
  - crystallization morphologies in stereocomplexationable chiral blends 537–540
  - mesoscale morphologies in conducting polymer blends 540–543
  - optical characterization of 528
  - role of polymer tacticity on polymer blend morphologies 535–537
- metal-containing block copolymer 523
- methylene dianiline (MDA)-cured DGEBA-based epoxy resin 566
- methyl ethyl ketone (MEK) solution 859
- microcontact printing (mCP) 584
- microcrystallites 526
- micromechanical deformation processes 554
- microphase separation temperature (MST) 264
- microtomy 553
- microwave pulse, formation 738
- microwave radiation, absorption of 734
- mid-infrared instrumentation, polymer blends 705–709
- milliabsorbance units (MAU) 814
- miscibility 13, 94, 373. *see also* miscible blends
  - binary systems 374–376
  - classification of region 16
  - complete, requirement 22
  - gap 101
  - glass–rubber relaxation temperature
  - compositional rules based on 379
  - theoretical approaches to calculating 379
  - heterogeneous 374
  - homogeneous 373
  - immiscibility 374
  - influence of type of processing 376, 377
  - nanoparticles, influence of 377, 378
  - partial miscibility 374
  - polymer blending, recovering plastic waste by 377
  - of polymers 330
  - rubbery plateau as an indicator 378
  - ternary systems 376
  - upon heating 24
- miscible blends 160
  - PCL/PDLA 38
  - PDLLA/PMMA 42
  - PHB/PDLLA 64
  - PHB/PLLA 68
  - PHB/starch 53

- PLA/PCL 37–40, 38, 39
- PLA/PEG 78
- PLA/PEO 35
- PLA/PESu 47
- PLA/PHB 40, 41, 75
- PLA/PLA 30–34
- PLA/PS 48
- PLA/PVAc 36, 66
- PLA/PVPh 43–45, 50
- PLA/TKGM 75
- PLLA/EVAc70 37
- PLLA/EVAc85 37
- PLLA/PCL 39
- PLLA/PDLA 30
- PLLA/PHB 40
- PLLA/PMMA 42, 70
- PLLA/PVA 68
- PLLA/PVPh 24, 44, 46, 62
- PMMA/PLLA 73
- polymer blends 2, 625
- PS/PE blends
- PTMC/PLLA blends 48
- starch/PCL blends 99
- miscible systems 27
- enthalpically driven 28, 29
- entropically driven 27, 28
- MMT/epoxy nanocomposites 153
- MMT-modified systems 153
- molar fractions 10
- molecular dynamics (MD) simulations 20, 27
- for the PLLA/PVPh system 20, 21
- molecular fractionation 104
- molecular modeling techniques 20
- monochromator 811, 812
- montmorillonite (MMT) 151, 386
- morphology 111–114
- of blend, stability 119, 120
- development during melt processing 114–118
- EPDM/PB blends, torque ratios 113
- polystyrene/polyethylene (PS/PE) blend 107
- multi-channel analyzer (MCA) 889
- multicomponent polymers, electron
- microscopic analysis 418
- deformation studies 571–574
- morphological characterization 555
- amorphous polymers 561–563
- nanostructured copolymers 563–567
- semicrystalline polymers 555–561
- special techniques and applications 567–571
- overview 551–552
- sample preparation techniques 552
- fracture behavior analysis 554–555
- surface, etching of 554
- thin-film preparation 552, 553
- thin sections, staining of 553, 554
- multivariate analysis (MVA) methods 595
- multivariate curve resolution (MCR) 595
- multi-wall carbon nanotubes (MWNs) 378, 870
- modified with 378
- Mylar™ foil 768
- n**
- nanoparticle-filled systems 151
- nanoparticle-modified thermosets 150
- nanoscale secondary ion mass spectrometry (NanoSIMS) 580
- high lateral resolution SIMS analysis 598
- HP-LB film, mass-resolved negative ion maps of 600
- ion optical set-up 597
- ion optics, schematics of 598
- mass analyzers 591
- mass spectrometer 597–598
- nanoscale secondary ion mass spectrometry technique 597
- polymer blend surface 580
- Nd:YAG laser 710
- near-field scanning optical microscopy (NSOM) 615
- near-infrared (NIR)
- imaging measurements 706, 811
- imaging, polymer blends 705–709
- microscopy 3
- neutron reflectivity (NR) 3, 304
- spectroscopy 585
- nitrile butadiene rubber (NBR) blends
- relative fractional free volume 905
- nitrile rubber (NR) 661
- SBR, infrared spectrum of 662
- 2-(4-nitro-2,1,3-benzoxadiazol-7-yl)aminoethyl (NBD) dye 543
- nitroxide molecule symmetry, direction 744
- nitroxide species 745
- NOESY technique 680
- nonbonding orbitals 794
- nondestructive experimental method 299
- nonelectrolyte solutions 12
- nonlinearity factors 397
- non-radiative energy transfer (NRET) 843
- nonrandomness 24
- nonresonant nuclear reaction (NRA) 766
- nonvolatile component 336
- nuclear magnetic resonance (NMR) 210

- spectroscopy 3, 4, 790
  - nuclear overhauser effect spectroscopy (NOESY) 680
  - nuclear shielding tensors 692
  - nucleation 160, 228, 229
    - and growth (NG) 138
    - heterogeneous 229
    - homogeneous 229
  - numerical method 465, 466
  - numerical simulation, on a heterogeneously functionalized substrate
  - of phase separation of immiscible polymer blends 466, 467
  - of self-assembly of a polymer–polymer–solvent ternary system 481
  - verification of self-assembly of a polymer–polymer–solvent ternary system on 497
- o**
- oligo[(R,S)-3-hydroxybutyrate]-diol (oligo-HB) blends 867
  - OM. *see* optical microscopy (OM)
  - online extrusion compounding of polymer blend 402
  - online-manufacturing concept, of polymer blends 399–402
    - materials systems studied 402, 403
  - o-Ps lifetime 885
  - optical micrographs, of PCL/SAN-27.5 (80/20) blend 173
  - optical microscopic techniques, resolution limits 525
  - optical microscopy (OM) 138, 181, 523, 552, 595
    - crystallization kinetics by 181–190
    - effect of aging/hydrolysis on 541
    - morphological differences in PAni.DBSA/TPU blends 542
    - morphological information 524
    - PCL/SAN-27.5 (80/20) blend
  - order–disorder transition 150, 265
  - organic photovoltaics (OPVs) 696, 831
  - organophilic MMT 151
  - ortho*-positronium (o-Ps) 877
  - oscillatory measurements 151
  - osmium tetroxide vapor 564
  - Ostwald ripening theory 120
- p**
- PA6 blends, EPR spectra of 757
  - PA-6/HNBR blend 408–412
    - creep master curves 411
    - creep rate *vs.* time traces 410
    - difference in *E*-moduli 409
    - effect of testing temperature 409
    - effect on creep 409
    - *E'* *vs.* *T* and *tan δ vs. T* traces 408
    - fracture toughness 412
    - incompatibility 408
    - parameters of the Findley power law 409, 411
  - Painter–Coleman association model (PCAM) 25, 26
  - PA66/mSEBS blends 377
  - PANI–PMMA blend, temperature dependence 763
  - PANI–SBS samples
    - peak-to-peak line width of EPR signal 764
  - para*-Positronium (p-Ps) 880
  - particle sizes 3, 107
    - in immiscible blends, evaluation of 204, 205
  - pattern shapes, effects of 513–515
  - PBI/PI blend 428
    - polymer–polymer interaction parameter 428
    - specific free volume 428
  - PBTTT-C16:PC<sub>71</sub>BM blend 701
  - PBTTT-C16 polymer side chains
    - <sup>1</sup>H signals 700
  - PCBMCF-RT
    - 2D <sup>13</sup>C HETCOR spectra 698
    - molecular structure 699
  - PCL-*b*-PB copolymers 226
  - PCL carbonyl 648
  - PCL homopolymers, FT-IR transmission spectra 723
  - PCL/SAN-27.5 blend
    - change of light-scattering profile 176
    - evolution of characteristic wavenumber
    - light-scattering *V<sub>v</sub>* profile 174
    - optical micrographs 173
    - phase diagram 172
    - Plot of  $R(q)/q^2$  *vs.*  $q^2$  179, 180
    - wavelength of concentration fluctuations *vs.* time 175
  - PCL-specific FT-IR image 722
  - PC/PVDF blend
    - ToF-SIMS F<sup>+</sup> images 581
  - pectin (PEC), electronic spectra 797
  - PEDOT-PSS layer 317
  - PEDOT:PSS–PEG fibers 764
  - PEI–PBT/mPEO blends 376
  - PEO, FTIR spectra 644, 645
  - PEOX blends 422
    - addition to PES, and water vapor diffusion coefficient 422

- blends of water-soluble PEOX with copolymers
- water sorption and transport properties 422
- PerkinElmer FT-NIR imaging system 708
- Perkin Elmer system 717
- permanganic etching 554
- peroxyl radicals, growth of 759
- pervaporation 434
  - acetic acid/water mixture 435
  - 1,4-dioxane/water 436, 437
  - DMF/water mixtures 436
  - ethanol/water mixture 435, 436
  - THF/water mixtures 434, 435
- PES/PEO blend 422
- degree of crystallization 423
- water sorption isotherms 422
- PES/phenoxy blends 423
- PET/mPEO blends 377
- PFB phase
  - nanoparticles 838
  - photoluminescence quenching 838
  - photoluminescence spectra 839
- PFO/MEH-PPV nanoparticles 839
- PF3T, chemical structures of 839
- PF3T, chemical structures 837
- PFTSO<sub>2</sub>, chemical structures 837
- phase dissolution 172
  - apparent diffusion coefficient for 180
  - model, development in time derived from light-scattering data 177
  - poly( $\epsilon$ -caprolactone)/poly(styrene-co-acrylonitrile) blend 172
- phase inversion, EPDM/PS blends 275
- phase-modulation fluorometry methods 824
- phases
  - behavior 100
  - contrast microscopy 525
  - decomposition 138
  - diagrams 101–104, 266 (*see also* phase diagram of a diblock copolymer melt)
  - morphology 554
  - separation 104–107
- phase separation 138, 140, 172
  - apparent diffusion coefficient for 180
  - poly( $\epsilon$ -caprolactone)/poly(styrene-co-acrylonitrile) blend 172
- phase transformation 160
- phase transition 160
- PHB/PCL blend films, FT-IR imaging of 720–724
- PHB/PCL, DSC-temperature diagram of 723
- PHB/PVAc, relaxation process of 864
- PHB-specific FT-IR image 722
  - state-of-order 724
- phenolic/PEO/PCL, ternary blend, infrared spectra of 647
- phenomenological theory, of block copolymers 261
- phenoxy blends 423
- phenoxy polymer 423
- [6,6]-phenyl-C61-butyric acid methyl ester (PCBM) blend 318, 602
- p*-(hexafluoro-2-hydroxyisopropyl) (HHIS) 424
  - diffusion coefficients 425
  - poor chain packing 425
  - positive excess volumes 425
- photoactivated localization microscopy (PALM) 620
- photodiode arrays (PDAs) 813
- photoexcitation, of molecular system 825
- photolithography 580
- photoluminescence (PL) intensity 617
- photomultiplier tube 813
- photooxidized blends, chemical treatment 651
- photovoltaics 581
- p*-hydroxybenzoate–poly(ethylene terephthalate) (PET) 376
- p*-hydroxystyrene (HS) 424
  - clustering of sorbed water molecules 425
  - diffusivity values 425
  - sorption isotherms 425
- physical gel 151
- physico-chemical data 341
- physico-chemical interactions 151
- physico-chemical parameters 332
- pick-off annihilation 882
- piperidine nitroxide spin probes, chemical structures of 748
- PI/PMMA semi-IPN, WISE NMR spectrum of 697
- PI27/PtBS23 blends, dielectric permittivity for PI and PI 855
- PISEMA method 694
- Planck length 791
- PLA/PHB blend
  - band ratio images 718
  - FT-IR imaging spectra 718
  - Raman imaging measurements 718
- PLA polymer chain direction 715
- PLA/poly(4-vinylphenol) (PVPh) 43–45, 50
- PLA-specific FT-IR image 720
- plastic deformation 572
- plasticized starch (PLS) 684
- plasticizers 108, 381, 382
  - storage modulus curve 382

- PLS/PVOH blends
  - $^{13}\text{C}$  CP/MAS NMR spectra 685
  - $T_{1\rho}^H$  values 686
- PNPAA/P4VP
  - $^{13}\text{C}$  CP/MAS spectra of 687
  - magnetization intensities, logarithmic plots of 689
  - relaxation time, value of 690
- point spread function (PSF) 619
- polarization modulation (PM) 665–668, 666
  - technique 627
- polarization modulation infrared linear dichroism (PM-IRLD) 666
- polarizer-compensator-sample-analyzer (PCSA) ellipsometer 304
- poly(acrylamide) (PAAM) 693
- poly(acrylic acid) (PAA) 314
- poly(acrylic acid)/poly(ethylene oxide) (PAA/PEO) 748
- poly(acryloyl morpholine) (PACMO) 681
  - $^{13}\text{C}$  chemical shifts 682, 683
  - cellulose acetate 681, 683
  - semi-logarithmic plots of 681
  - $T_{1\rho}^H$  values 683
- polyamide (PA) 48, 278, 308, 355, 728
- poly(amidoamine) (PAMAM)
  - dendrimers 763, 866
- polyaniline (PANI) blends 761, 860
- poly(aryloxysiloxane) (PAS) blends 902
- poly(aspartic acid-*co*-l-lactide) (PAL)
  - copolymers 33
- polybenzoxazine (PBZZ), FTIR spectra of 632
- poly(benzyl methacrylate) (PBzMA) 50
- poly(2,5-bis(3-hexadecylthiophen-2-yl)thieno [3,2-*b*]thiophene) (PBTtT)
  - chemical structures 700
  - fullerene blends 699
- polybutadiene (PB) 613, 680
- polybutadiene-urethane oligomer 341
- poly(butyl acrylate) (PBA) 656
- poly(butyl acrylate-*co*-acrylic acid) (PBAAA)
  - copolymers 656
- poly(butylene adipate-*co*-terephthalate) (PBAT) 282
- poly(butylene succinate) (PBS) 45–47
- poly(butylene terephthalate) (PBT) 376
- poly(butyl methacrylate) (PBMA) 749
  - three-dimensional PALM measurement 621
- poly(*tert*-butylstyrene) (PtBS) 854
- polycaprolactone (PCL)/poly(vinyl chloride) PCL/PVC blend 223
- poly(carbonate) (PC) 50, 580, 862, 901, 902
  - bisphenol A blend 377
  - partial negative ToF-SIMS spectra 589
  - TEM image of 567, 568
  - ToF-SIMS spectra 589
- polycarbosilane-derived b-SiC particles (SiC-MWCNTs) 378
- polychloroprene/ethylene–propylene–diene-monomer rubber (PCR/EPDM rubber) blends 377, 378
- polycondensation reaction 29
- poly(cyclohexyl acrylate) (PCHA) 753
- poly(cyclohexyl methacrylate) (PCHMA) 753
- poly(2-dimethylamino ethyl methacrylate) 629
- poly(2,3 dimethylbutadiene) (DMB) 858
- poly(2,6-dimethyl-1,4-phenylene oxide) (PPO) 306
- poly(dimethylsiloxane) (PDMS) 314
- poly[2,7-(9,9-di-*n*-octylfluorene-*alt*-benzothiadiazole)] (F8BT)
  - thin-film morphologies of 585
- poly(9,9-dioctylfluorene) (PFO) 831
  - chemical structures 832
  - photoluminescence decay 833
- poly(9,9'-dioctylfluorene-*co*-benzothiadiazole) (F8BT) 570
- poly(9,9-dioctylfluorene-*co*-*N*-(4-butylphenyl)diphenylamine) (TFB) 570, 835
  - chemical structures of 836
  - fluorescence microscopy 836
- polydisperse systems 108
- poly(DL-lactide) (PDLLA) 58, 65, 867
  - blends 74, 79
  - chains in parallel orientation 33
- poly\_DR1M-*co*-BEM, synchronous 2D-FTIR correlation map of 666
- poly( $\epsilon$ -caprolactone) (PCL) blends 7, 37–40, 50, 170, 631, 749, 864
- poly( $\epsilon$ -caprolactone)-*block*-polybutadiene copolymer 226
- poly( $\epsilon$ -caprolactone)/poly(ethylene glycol) blends 230
- poly( $\epsilon$ -caprolactone)-poly(vinyl chloride) (PCL-PVC) blends 340
- poly(epichlorohydrin) (PECH) 51, 431
- polyester poly(lactic-*co*-glycolic acid) copolymer (PLGA) 312
- polyester/PVPh systems 45
- polyesters 629
- polyetherimide (PEI) 140, 376, 870
- poly-ether–polyurethane (PU) 752
- poly(ether urethane)/modified carbonate silicate fillers 341
- polyethylene 280

- poly(ethylene adipate) 629
- poly(3,4-ethylenedioxythiophene) (PEDOT) 317
- polyethylene glycol (PEG) 34–36, 313, 866
- poly(ethylene naphthalate) (PEN) 871
  - molecular dynamics 871
- polyethylene oxide (PEO) blends 34–36, 65, 347, 349, 381, 632, 643–650, 692, 762, 862
- poly(ethylene oxide)/poly(methylmethacrylate) (PEO/PMMA) blends 433
- polyethylene/polypropylene blends 407, 595
- poly(ethylene sebacate) (PESeb) 630
- poly(ethylene succinate) (PES) 45–47, 51
- polyethylene terephthalate (PET) blends 49, 76, 631, 768, 871
  - molecular dynamics 871
  - nanocomposites 423, 424
  - TEM image of 567, 568
- poly(9,9-dioctylfluorene), fluorescence SNOM images 618
- poly(glycolic acid) (PGA) 52
- polyglycolide (PGA) 7, 29, 52
- poly(*p*-(hexafluoro-2-hydroxyl-2-propyl)styrene) (HFS) 855
- poly(3-hexylthiophene) (P3HT) 602
- poly(hydroxyalkanoates) (PHA) 431
- poly(3-hydroxybutyrate-*co*-3-hydroxyvalerate) (PHBHV) 52, 657–661
  - C–O–C stretching 659
  - FTIR spectroscopy 657, 659
- poly(3-hydroxybutyrate)(PHB) 7, 29, 50, 51, 710, 863
  - blend 82
  - C=O stretching modes 726
  - FT-IR spectra of 722
  - FT-IR transmission spectrum 717, 718, 719
  - homopolymers, FT-IR transmission spectra 723
  - infrared microspectroscopy 661
  - micro IR spectra 660
  - PHB-*co*-HHx/PLLA blend 661
  - poly(*R*)-3-hydroxybutyrate 658
  - polymer chain direction 715
  - Raman imaging measurements 718
  - variable-temperature FT-IR/Raman imaging spectroscopy 714–717
- poly(3-hydroxybutyrate)(PHB)/poly(*L*-lactic acid)(PLA) blends
  - FT-IR transmission spectrum of 711, 712
  - polymer blend, band pairs 721
  - Raman spectra of 712
  - ratio images 721
- poly(3-hydroxy-butyrates), spherulitic structure 724–727
- poly(hydroxystyrene) (PHOST) 310
- poly(4-hydroxystyrene-*co*-methoxystyrene) (HSMS) 50
- poly(3-hydroxyvalerate) (PHV) 629
- poly(isobornyl acrylate) (PIBA) 359
- poly(isobutyl methacrylate) (PiBMA) 616, 843
- polyisoprene (PI) blends 680, 853
- polyisoprene (PI)/PMMA, WISE NMR spectra of 696
- poly(lactic acid) (PLA) 29, 57, 58, 170, 376
  - blends containing 29, 30
  - film 315
- poly(lactide) 29, 75
  - blended with 29–50, 60, 66–70, 72, 77, 78, 81, 82
  - commercial forms 30
  - *n* biomedicine and packaging 30
  - properties 29
- polylactide/polyamide11 blends (PLA/PA11) 383
- polylactide/polyhydroxyalkanoate (PLA/PHBV) blends 376
- polylactides 7
- poly(*L*-lactic acid)(PLA) blends
  - FT-IR transmission spectrum 717, 718, 719
  - Raman imaging measurements 718
  - variable-temperature FT-IR/Raman imaging spectroscopy 714–717
- poly(*L*-lactide) (PLLA) 57, 59, 77, 629
  - amorphous unit cells of PLLA/PVPh blends 46
  - blends 60–64, 66, 69, 70, 72–74, 80, 81
  - crystalline bands 660
  - micro IR spectra 660
  - with poly(glycolic acid)-*co*-*L*-lactic acid) 33
- polymer-based systems 883
- polymer blends 1, 347, 526, 527
  - based on poly(lactide) (PLA) 57–82
  - characteristics 334
  - commercialization of 365
  - confocal microscopy characterization of 543–547
  - morphology 219
  - nanoparticles, concentration-dependent fluorescence spectra 840
  - numerical models for 457–460
  - polypropylene/polyamide 6, Raman mapping measurements of 728–730
  - principle of 348



- theoretical models to explain viscoelastic behavior 374
- thermal analysis (*see* thermal analysis (TGA))
- thin films 580, 586
- ToF-SIMS imaging of 595
- polymer crystallization 228
- polymer degradation processes 732
- polymer electrolytes 348
- polymer-filler blends 1, 133
- polymer-filler composition 332
- polymeric delivery system 316
- polymeric mixtures, transport properties 337–339
- polymeric scaffolds, biodegradable 664
- polymeric systems 746
- polymerization process 104, 138, 347
- polymer–polymer interaction 335
  - coefficient 334
- polymer–polymer interfaces 111
- polymer–polymer miscibility 340
- polymers 83, 84
  - high-molecular-weight 14
  - interfaces 829
  - ion beam analysis of 766
  - microheterogeneity 740
  - microscopy, thin films for 552
  - molecules 10
  - orientation 279, 280
- polymer–solvent interactions 341
- polymer–solvent systems 342
- polymer–test solute systems 331
  - Flory–Huggins interaction parameter 331–333
- polymer toughness 394, 395
- poly(methyl acrylate) (PMA) 41–43
- poly(methyl methacrylate) (PMMA) 41–43, 347, 381, 424, 580, 628, 655–657, 668, 751, 853, 906
  - cluster function 425
  - dielectric loss for 857
  - geometric factor 907
  - $^1\text{H}$ - $^1\text{H}$  spin-exchange spectra 691
  - homopolymer 355
  - hydrodynamic interaction parameter 907
  - molecular dynamics and dipolar relaxation mechanism 854
  - PMMA/HHIS blend 424, 425
  - PMMA/HS blend 424, 425
  - PMMA/PEO blends 381
  - PMMA/PVPh cast film, 2D PISEMA spectrum of 695
  - PMMA/SMA 50/50 blends 857
  - side-chain-labeled 612
  - system 588
- poly(methyl methacrylate)/poly(butadiene) (PMMA/PB) 348
- poly(methyl methacrylate)/poly(vinylidene fluoride) (PMMA/PVDF) 348
- poly(methyl thiomethyl methacrylate) 629
- poly(*N*-4-bromophenyl methacrylamide) (PBPMA) 687
- poly(*n*-butyl methacrylate-co-styrene) (nBMAS) 843
- poly(*N*-methyl-3-piperidinemethyl methacrylate) 629
- poly(*N*-phenyl methacrylamide)s 687
- poly(*n*-vinyl pyrrolidone) (PVP) 423
- poly(octadecyl methacrylate) (PODMA) 616
  - dye-labeled 843
- polyoxypropylene triamine (POPTA) 139
  - oligomer 870
- poly(*p*-chlorostyrene) (PpClIS) 50
- poly(*p*-dioxanone) (PPDO) 7, 29, 51, 52
  - with poly(vinyl phenol) (PPDO/PVPh) blends 379
- polyphenols 50
- poly(phenylene oxide)/poly(styrene) (PPO/PS) 348
- poly(phenyl methacrylate) (PPhMA) 50
- polypropylene (PP) 308, 637, 905
  - e-beam-irradiated blends 758
  - Raman spectra 728, 729
- poly(propylene carbonate) (PPC) 47, 48
  - rich micro domains 748
- poly(propylene-co-ethylene) (PPE)/poly(ethylene-co-vinyl acetate) (EVA) blends
  - electron-beam irradiation effects on 904
  - positron lifetimes 904
- polypropylene/polyethylene terephthalate (PP/PET) blends 384
- poly(propylene) (PP)–PS and poly(propylene)–poly(ethylene) (PE) 2
- polypropylene with maleic anhydride (PP-g-MA)/PC blend compositions
  - relaxation time 869
- poly(vinyl acetate-co-vinyl alcohol) (P(VAc-co-VA) 51
- poly(vinyl ethyl ether) (PVVE) 861
- poly(vinyl methyl ether) (PVME) blends 50, 650–655
- poly(vinylpyrrolidone) (PVPon) 694
- poly(2-vinylpyridine) (P2VP) polymer blend 583
- poly((*R*)-3-hydroxybutyric acid) (PHB) 40, 41, 59, 75

- polysaccharides 52
- polystyrene (PS)
  - infrared spectra of 645
  - latex, transmission electron microscopy image 401
  - PS–PBAAA blend 657
- poly(styrene-acrylonitrile) (SAN)–poly(methyl methacrylate) (PMMA) 2, 308
- polystyrene (PS) blend 48, 103, 280, 306, 583, 612, 841, 853, 901
  - EPR spectra of 765
  - fluorescence SNOM images 618
  - 1-pyrenylmethyl methacrylate-labeled 841
  - ToF-SIMS chemical maps 583
  - ultrathin polymer-blend films, phase separation of 584
- poly(styrene-*block*-ferrocenyldimethylsilane) 523
- polystyrene-*block*-poly(methyl acrylate) (PS–PMA) 754
- poly(styrene-*b*-methyl methacrylate) (PS–PMMA) block copolymers 844
- poly(styrene-*co*-acrylonitrile) (PSAN) 50, 170, 171, 307, 341, 668, 906
- poly(styrene-*co*-hydroxy styrene) (SHS) 861
- polystyrene (PS)/polyamide (PA6) blends 378
- poly(styrene)/poly(ethylene) (PS/PE) 348
- polystyrene–poly(ethylene propylene)–polystyrene block copolymer network 266
- polystyrene–polyisoprene diblock copolymers 266
- polystyrene (PS) polymer blend, in ultrathin film 582
- polystyrene/poly(methylstyrene) blend 258
- poly(styrene) (PS)–poly(phenylene oxide) (PPO) 2
- poly(styrenesulfonate) (PSS) 317
- poly(styrenesulfonate)-doped
  - poly(3,4-ethylenedioxythiophene) (PEDOT-PSS) 586
- poly(styrene-*co*-4-vinylphenol) (PSTVPh) 656
- polysulfone (PSU) 870
- poly(*tert*-butyl acrylate) (PtBA) 842
- poly(trimethylene carbonate) (PTMC) 47, 48
  - blend 76
- poly(trimethylene terephthalate) (PTT) 377, 905
- poly(3-(4'-(1'',4'',7''-trioxaoctyl)phenyl)thiophene) (PEOPT) 317
- polyurethane (PU) 337
- poly(vinyl acetate) (PVAc) 36, 37, 668, 855
- polyvinyl alcohol (PVA) 36, 37
  - molecular dynamics 860
- poly(vinyl alcohol) (PVA) blends 637–642, 681
  - FTIR spectroscopy 641
- poly(vinyl chloride) (PVC) 50, 347
  - dipolar relaxation behavior of 862
- poly(vinyl chloride) (PVC)/poly( $\alpha$ -methylstyrene-acrylonitrile) ( $\alpha$ -MSAN) blends 386
- poly(vinyl chloride)/poly(ethylene-*co*-vinyl acetate) (PVC/EVA) 348
- poly(vinyl chloride)/poly(methyl methacrylate) (PVC/PMMA) 348
- poly(vinylidene chloride-*co*-acrylonitrile) (P(VDC-AN)) 51
- poly(vinylidene fluoride) (PVDF) blend 580
- poly(vinylidene fluoride) (PVDF)/PP blends
  - gh-dielectric-permittivity 870
- poly(vinyl methyl ether) (PVME) 103, 632, 841, 854, 901
- poly(4-vinylphenol) (PVPh) 43–45, 50, 854
- poly(vinylphenol) (PVPh) blends 628–632
- poly(4-vinylphenol-*b*-styrene) (PVPh-*b*-PS) 225
- poly(vinylphenol-*co*-methyl methacrylate) (PVPh-*co*-PMMA) 648
- poly(4-vinyl phenol) (PVPh) polymer blends 690
- poly(vinylpyridine) 611
- poly(4-vinylpyridine) (P4VP) 225
- poly(vinylpyrrolidone) (PVP) blends 632–637, 633
- poly(vinyl pyrrolidone) (PVP)-poly(ethylene glycol) (PEG) blends 418
- POM images of PDLA/LMw-PLLA blends 538
- POM/PU blend
  - $\alpha$ - and  $\beta$ -relaxations 403
  - atomic force microscopy image 401
  - creep data 405
  - creep master curves 407
  - effect of temperature on tensile creep 406
  - $E'$  vs.  $T$  and  $\tan \delta$  vs.  $T$  traces 405
  - Findley power law model 405
  - mechanical loss factor 403
  - scanning electron microscopy image of fracture surfaces 404
  - storage modulus 403
  - transmission electron microscopy image 404
  - weight loss vs. temperature 407
- pore size distribution (PSD) 311
- pore sizes 310
- Porod–Ruland model 221
- positron annihilation 892

- lifetime (PAL) measurements 901
- lifetime spectroscopy (PALS) (*see* positron annihilation spectroscopy)
- methods 887
- principle 880
- rate distribution 893
- positron annihilation spectroscopy (PAS) 877, 879
  - experimental methods
    - Al/Cu, angular correlation curves 894
    - angular correlation of annihilation radiation (ACAR) method 893, 894
    - Doppler broadening of the annihilation radiation (DBAR) method 894–896
    - free volume distribution-lifetime analysis, by Laplace transform method 891, 892
    - free-volume distributions, in polymer blends 892, 893
    - positron annihilation lifetime spectroscopy (PALS) 888–891
    - free volume theory 884
    - positronium lifetime connection 885–887
    - miscibility
      - free volume 901–915
      - in polymer blends 896–901
    - models predicting positronium formation 883, 884
    - polymer blends, characterization of 887, 888
    - positronium 880–882
      - sensitivity to defects and free volume 882
    - process of 878–880
  - positron lifetime spectrometer, block diagram 888
  - power conversion efficiency 697
  - power law 151
  - power ultrasound 280
    - batch melt mixing 281
    - compatibilization 282, 283
    - extrusion 283, 284
    - injection molding 280
    - melt mixer equipped with an ultrasonic device 282
    - tensile stress of injection molded PS and PS/HDPE (90/10) blend
  - PP/EVA blend 428–430
    - diffusivity 430
    - *D*-values 430
    - water-solubility coefficients 429
    - water sorption isotherms 428, 429
  - principal component analysis (PCA) 336
  - probability density function (PDF) 891
  - protein-adsorption behavior 313
  - proton–proton spin diffusion 687
  - pseudo*-Voigt function 227
  - PS/PEO blend, optical micrographs 657
  - PS-PMMA blend
    - cross-sectional image of 613
    - film 309
  - PS–polydiene, nonpolar systems 225
  - PS/PPE blend, free volume size distribution (PDF) 903
  - PS/PVME blends 655
  - PS/TMPC blends, free volume hole size distributions in 902
  - PSU/mPEO 377
  - PU (polyurethane)-B2 compositions 337
  - pulsed beam characterization 593, 594
    - duty cycle 594
  - pulse–echo technique 273
  - pulse electron double resonance (PELDOR) 737
  - $\delta$ -pulse response 825
  - pure poly(ethylene oxide) (PEO)
    - thermal analysis( TGA) 359, 360
    - thermogravimetric curve 356
  - pure poly(vinyl chloride) (PVC)
    - in energy-based applications 349
    - labeled TGA thermogram 354
    - thermal analysis( TGA) 355–359
    - thermogravimetric curve 355
  - PVA/Alg blend nanofibers, electrospun, FTIR data 642
  - PVA/P(AA-AMPS) blend 430, 431
    - acetate and sulfonic groups 430
    - polymer–water interactions 431
    - sorption and diffusion 430
    - water diffusion 430
    - water uptake 430
  - PVC/EVAc blend 425–427
    - selectivity to water 427
    - transport parameters for 426
    - water permeation 427
    - water solubility 427
  - PVC/PEO blends 349, 350
    - interpolymer hydrogen bonding 350
    - thermogravimetric curve 356
  - PVC/PEO:LiCF<sub>3</sub>SO<sub>3</sub> blends 350, 351, 360, 361
    - thermogravimetric curve 356, 357
  - PVC/PEO-LiCF<sub>3</sub>SO<sub>3</sub>-DBP-EC:SiO<sub>2</sub> blends 351, 361, 362
    - thermogravimetric curve 357, 358
  - PVC/SAN blend systems 897
  - PVME/PS blends
    - FTIR spectra 651
  - PVOH, <sup>13</sup>C CP/MAS NMR spectra 684, 685

PVPh-based blends 631  
 PVPh, molecular dynamics of 861  
 PVPh/PMMA blends 859  
 PVPh-co-PMMA/PEO blends 648  
 – FTIR spectra 649, 650  
 PVP/PEG blend 431  
 PVP-PEG-poly(acrylic acid) (PAA) blends 418  
 PVP/polysulfone blend 420–422  
 – equilibrium sorption isotherms 420, 421  
 – interpretations, by behavior of diffusion coefficient 420  
 – water sorption and transport behavior 420  
 – water vapor diffusion coefficient vs. activity 421  
 P2VP/PS blend, HP-LB film of 600  
 PVVH 854  
 pyridine fragments 588

## q

3D quadrupole ion trap mass analyzer 591  
 quantitative analysis, SIMS techniques 588

## r

Raman/fluorescence spectroscopy 747  
 Raman imaging 3  
 Raman microspectroscopy 709–711  
 – charge-coupled device (CCD) 709  
 – WITec alpha300R confocal 710  
 Raman spectroscopy 790  
 Ranganathaiah's method 908  
 Rayleigh criterion 830  
 $\gamma$  rays 553  
 reaction-induced microphase separation (RIPS) 150  
 reactive ion etching (RIE) 554  
 reflection coefficients 299  
 reflectometry 239  
 refractive indices 300, 313, 314  
 regioregular poly-3-hexylthiophene (rrP3HT) 698  
 regular solution 10  
 – enthalpy 10, 11  
 – interaction energy 11  
 – van Laar-type equation 12  
 resonance energy transfer (RET) 828  
 resonant model 883  
 rheological measurements 104, 137  
 rheological models 150  
 rheological properties 133  
 rheological testing 137  
 rheology, of polymers 365  
 ring-opening polymerization (ROP) 29

RPA-structure factor 262  
 RPA theory 263  
 rubber blends 160  
 rubber latex 402  
 rubber-modified epoxy resins 138  
 rubber-thermosetting blends 1  
 rubbery polymer 329  
 ruthenium tetroxide ( $\text{RuO}_4$ ) 553, 559

## s

SAN particles. *see* poly(styrene-acrylonitrile) (SAN)  
 SAN/PMMA miscible blend 901  
 SARINA (SPM Assisted Reconstruction of SIMS recorded nano-volumes) 600  
 – SIMS and AFM data 601  
 SAS. *see* small-angle scattering (SAS)  
 scanning electron microscopy (SEM) 3, 138, 275, 308, 311  
 scanning near-field optical microscopy (SNOM) 615  
 – probe, schematic illustration of 616  
 scanning probe microscopy (SPM) 552, 887  
 scanning transmission X-ray microscopy (STXM) 569, 571  
 scattering function and thermodynamics 249, 250  
 – beyond mean field 258–260  
 – concentration fluctuations 249  
 – forward scattering 250–254  
 – random phase approximation (RPA) 254–258  
 – spatially correlated fluctuations 250  
 – thermal density fluctuations 249  
 Scherrer equation 224  
 SE. *see* spectroscopic ellipsometry (SE)  
 secondary electron (SE) 554  
 secondary ion mass spectrometry (SIMS) techniques 4, 579  
 – 3D quadrupole ion trap mass analyzer 591  
 – Fourier transform-ion cyclotron resonance (FT-ICR) 590  
 – mass analyzers 591  
 – mode of action 589  
 – NanoSIMS 597  
 – polymer blends, 3D imaging of 599–602  
 – quantitative analysis 588  
 – regions of interest (ROI) 593  
 – time-of-flight 592  
 segmental dynamics 379–381  
 semiconducting polymers 586  
 semi-crystalline

- molecular dynamics 866
- polymers 209, 212, 229, 789
- semi-interpenetrating polymer networks (s-IPNs) 749, 752
- shear 266
- viscosity 137
- signal-to-noise ratio (SNR) 275
- silica fillers 151
- silicate delamination 151
- silicon surface barrier detector 770
- siloxane-containing oligomers 138
- simplified Hamiltonian 734
- SIMS. *see* secondary ion mass spectrometry (SIMS) techniques
- single-phase blends 160
- single-walled carbon nanotubes/PS nanocomposites (SWCNT/PS) 775
- small-angle neutron scattering (SANS) 3, 111, 305, 679
  - data identifying spinodal and binodal temperatures 253
  - polystyrene (PS) and poly(methylstyrene) (PMS) blends 257
  - polystyrene (PS) and poly(vinylmethylether) (PVME) blends 258
  - scattering pattern 266
- small-angle scattering (SAS) 237–239
  - contrast 239–242
  - Gaussian chain 244, 245
  - illustration of 238
  - interference between wave-like radiation 238
  - measurements 218
  - by x-rays (SAXS)/neutrons (SANS) 237
- small-angle x-ray scattering (SAXS) 111, 209, 626, 679
  - “block” collimation system in a Kratky-camera 213
  - characteristic features, of melting process 229
  - instrumentation and synchrotron advantage 212, 213
  - scattering profile for neat diblock copolymer (PVPh-*b*-PS) 225
  - signatures, reversed in 229
  - structural characterization of data 220
  - techniques for polymers 212
  - time evolution, profiles for isothermal crystallization of PCL/PEG blend 230, 231
  - transmission-mode for 210
- small-angle x-ray spectroscopy, measurements 755
- solid-state NMR spectroscopy 679
  - miscibility 680
  - molecular dynamics 692
  - organic solar cells 696–697
  - polystyrene (PS)/poly(vinyl methyl ether) (PVME) blend 679
  - proton spin-diffusion, direct observation of 688–692
  - proton spin-lattice relaxation experiments 680–688
- solid-state physics 209
- solubility 138
  - parameters 340
  - testing 18
- solution-casting procedures 554
- spectrophotometry. *see* various spectrometric techniques
- spectroscopic ellipsometry (SE) 299, 311
  - analysis of interfacial thickness and interfacial reaction 305
  - applications in characterization of polymer blend films 304
  - averaging effective medium approximation 301
  - biomaterial surfaces 312
  - Bruggeman EMA 302
  - complex dielectric function 301
  - composite layers for organic solar cells 317–322
  - configuration 300
  - depth profiling 303
  - sample preparation 303
  - effective dielectric function 301
  - effective-medium theory 301
  - film thickness 300
  - linear EMA 301
  - macroscopically homogeneous effective medium 301
  - Maxwell–Garnett EMA 301
  - optical model 300
  - pattern formation in nanolayers 309–312
  - phase separation morphology 309
  - real-time measurement 304
  - resolution 300
  - roughness 309–312
  - surface modification, adsorption from solution 312, 313
  - types of instrument and measurements 303, 304
- spherulites 223, 229, 526, 527
  - birefringence structure 527
  - induction periods 540
  - infrared images of 669
  - radial growth rates of 540

- spin-cast polymer blend films 584
- spin coating 552, 554, 581
  - film formation, schematic model 582
  - process 582
  - schematic model 582
- spin Hamiltonian parameters 732
- spinodal decomposition 3, 104, 106, 138, 461–464, 584, 613
  - change of  $\ln(I_{VV})$  in time during 178, 179
- spin probe, formula 745
- spur model 883
- starch, blends containing 52–54
- static secondary ion mass spectrometry (SSIMS) 580
- static tests 137
- steady-state fluorescence spectroscopy 842
- steady-state viscosity 137
- Stern–Volmer quenching constant 830
- stimulated emission depletion (STED) microscopy 617, 619
  - point spread function (PSF) of 618
  - point spread functions 619
- stochastic optical reconstruction microscopy (STORM) 620
- stress–strain curves 286
- structure–property relationship 138
- structure–thermomechanical relationships 394
- STVPh-rich micro domains 748
- styrenated VPh (STVPh) 629
- styrene and acrylonitrile (SAN) 377
  - copolymers of 171
- styrene/butadiene star block copolymer, TEM image of 564
- styrene/butadiene/styrene (SBS) 755
  - triblock copolymer 565
- styrene maleic anhydride (SMA) 870
- sulfonated polystyrene 779
- surface-directed spinodal decomposition (SDSD) 781
- surface roughness vs. blend composition 287
- SWCNT/PS nanocomposites, polymer tracer diffusion 775
- swelling measurements 18
- symmetrical-reflection geometry 210
- syndiotactic PMMA (sPMMA) 629
- synthetic rubber 661–663
- t**
- Tauc gap 803
- tempamine spectra 749
  - EPR spectra 750
- temperature 24
  - composition behavior 160
  - dependence of interaction parameter 24
  - vs. blend composition plane 160
- tensile cryofracture surfaces, SEM images of 574
- tensile fracture surfaces, higher-magnification SEM images of 573
- tensile strength 280, 286
- ternary systems 376
- tetrahydrofuran (THF) 341, 629
- 2,2,6,6-tetramethylpiperidine-1-oxyl (Tempo)
  - EPR spectra 749, 750
- tetramethyl polycarbonate (TMPC) 862
- TFB/F8BT blend 570
- thermal analysis( TGA) 347–362
  - formulated system 349
  - gas environment 352
  - heating rate 353
  - information obtained from TGA 353
  - instrumentation 351
  - pure PEO 359, 360
  - pure PVC 355–359
  - PVC/PEO blends 349, 350
  - PVC/PEO:LiCF<sub>3</sub>SO<sub>3</sub> blends 350, 351, 360, 361
  - PVC/PEO-LiCF<sub>3</sub>SO<sub>3</sub>-DBP-EC:SiO<sub>2</sub> blends 351, 361, 362
  - sample weight 352
  - testing temperature range 352
  - thermal process 353, 354
  - value of the TGA information 354, 355
- thermal composition fluctuations 259
- thermal gravimetric analysis (TGA) 626
- thermalized positron 880
- thermally stimulated depolarization current (TSDC) method 5, 849, 850
- thermocouple sheet sensor 707
- thermodynamics, of polymer blends 95
  - average energy 247
  - average enthalpic energy 247
  - critical point 249
  - enthalpy of mixing 95, 96
  - entropy of mixing 96–98
  - Flory–Huggins theory 98–100
  - free energy function 249
  - Helmholtz free energy 247, 248
  - lattice model for polymer blend 246
  - and solutions 246
  - spinodal points 248, 249
  - stability 160
  - theory 7
- thermogravimetric analysis (TGA) 3, 395, 399

- thermogravimetric balance, schematic construction 400
  - thermo-oxidative stability of the POM matrix 406
  - thermoplastic alloys 159
  - thermoplastic Konjac glucomannan (TKGM) 50
  - thermoplastic polyurethane (TPU)/polypropylene (PP) blends 378
  - thermoplastic starch/poly(lactic acid) (TPS/PLA) blends 382
  - thermoplastic–thermoplastic blends 1
  - thermoplastic (linear polymer)-thermoplastic polymer blends 133
  - thermoplastic-thermosetting polymer blends 1, 133
  - thermoset rheological behaviors 133, 134
  - thermosetting blend systems 137, 138
  - thermosetting powder coating 871
  - thermosetting systems, with nanostructures 150–153
  - thin films
    - photovoltaic device structure 318
    - polymer blends 580–582
    - applications of 586, 587
    - phase-separation 583–586
  - Time-Correlated Single Photon Counting (TCSPC) 824
  - time-of-flight (TOF) 593
    - detector system 770
    - FRES (TOF-FRES) 769
  - time-of-flight secondary ion mass spectrometry (ToFSIMS) 579
    - chemical maps 583
    - $F^-$  images 581
    - spectra 588
  - time-resolved light scattering 165
    - crystallization by  $H\nu$  light scattering 169, 170
    - immiscible blends 165, 166
    - spinodal decomposition 166–169
  - time-resolved SAXS measurements 229
    - using synchrotron sources 229
  - time–temperature superposition (TTS) principle 398
  - time-to-pulse height converter (TPHC) 889
  - titanium oxide ( $\text{TiO}_2$ ) 362
  - transesterification 283
  - transition metal ions (TMIs) 731
  - translational entropy 10
  - transmission electron microscopy (TEM) 3, 311, 523
    - morphological information 524
  - transmission IR spectra 636
  - trans*-polyisoprene and liquid *cis*-polyisoprene (TPI/CPI) 384
  - triglycidyl *p*-aminophenol (epoxy)/poly(ether sulfone) (PES) 306
  - TTT (Time-Temperature-Transformation) isothermal cure diagram 134
  - two-dimensional detector 210
  - tyrosine-derived polycarbonates 314
- u**
- UCST (upper critical solution temperature) 160
  - ultramicrotomy 553
  - ultrasonic attenuation 276
    - temperature relationships 274
  - ultrasonic device 282
  - ultrasonic interferometer 271
  - ultrasonic technology 279, 280
  - ultrasonic velocity 271
  - ultrasound 269
    - frequency range 270
    - high-frequency 269
    - lifetime of a cavitation bubble 270
    - low-power 269
  - ultrathin films. *see also* thin films
    - phase separation, applications of 586, 587
    - of polymer blends 580–582
  - ultraviolet/visible (UV/VIS) spectroscopy 790
  - universal testing machines 3
  - unsaturated polyester resin (UPR) 380
  - upper critical solution temperature (UCST) system 3, 24, 25, 103, 258, 330
  - Urbach band tail 801
  - Urbach energy 803
  - UV-absorbing species 791
  - UV-visible spectroscopy 789
    - color/transparent spectrum, correspondence of 796–798
    - data acquisition 814
    - detection area/detectors 812
    - electromagnetic radiation 791–792
    - electronic absorption spectrum 796
    - electronic excitations nature in matter 793–796
    - instrumentation 809
    - monochromator 811, 812
    - optical absorption spectra 802
    - optical properties of semiconductors 801–802
    - polymer blends to material characterization 798–801
    - polymer blend technology 790
    - radiation (UV/VIS) interaction with matter 792, 793

- radiation sources 811
- semi-crystalline polymers 789
- spectrophotometer 809
- wavelength region 794

**v**

- van't Hoff-type plot 26
- vapor permeation 437
  - chitosan/CPA 437
  - EEA-CB blends 442, 443
  - LCP blends 441, 442
  - natural rubber blends 437–440
  - NBR blends 440, 441
  - PHB/PEO blends 443
  - PHB/PMMA blends 443
  - PU/PDMS blends 442
  - PVA/PAA blends 443, 444
  - PVC/EVAc blends 443
- variable angle spectroscopic ellipsometry (VASE) 304
- VFT equation 857
- VFTH equation 381
- vibrational energies 17
- vinyl ester resin 137
- vinyl polymer blends
  - using FTIR spectroscopy 628
- virtual UCST behavior, determination 197–204
- viscoelastic behavior 153
  - theoretical models to explain 374
- viscoelastic creep compliance 397
- viscoelasticity 134
  - influence of chemical and physical crosslinkers on 383, 384
  - of polymer blend 365
- viscoelastic materials 900
- viscoelastic properties 143–148
  - of polymers 886
- viscosity 1, 135, 136, 137, 139, 150, 269, 283
  - data 136
  - dependent empirical model 136
- vitrification 134, 139, 153, 160
- Vogel–Fulcher–Tamman–Hesse model 380, 852

**w**

- Waals surface 899
- Waals-type dispersion force 886
- water vapor sorption test 70/30 PP/PE/EVOH film 638
- water vapor transmission rate (WVTR) 420
- wide angle x-ray diffraction (WAXD) 218, 904
- wide-angle x-ray scattering (WAXS) 209, 210, 218
  - crystallinity of WAXS data 224
  - time evolution, profiles for isothermal crystallization of PCL/PEG blend 230
  - transmission-mode for 210
- Wigner–Seitz approximation 886
- Williams–Landel–Ferry (WLF) equation 136, 151, 399, 852, 885
- WITec alpha300R confocal Raman microscope 710
- Wolf's theory 898

**x**

- xenon lamps 811
- $x_N$ -value 265
- x-ray diffraction (XRD) 209, 311
  - experimental X-ray set-up 210
- x-ray photoelectron spectroscopy (XPS) 588
- x-ray reflectivity (XR) 304
- x-ray scattering 209
  - basics 213
  - elastic scattering, of electromagnetic radiation 213–215
  - scattered intensity 216–218
  - scattering by assembly of electrons 215, 216

**y**

- Young's modulus 397

**z**

- Zeeman effect 733
- Zeeman interaction 734
- Zhao–Choi procedure 335, 337, 341
- Ziegler–Natta initiators 383



# **WILEY END USER LICENSE AGREEMENT**

Go to [www.wiley.com/go/eula](http://www.wiley.com/go/eula) to access Wiley's ebook  
EULA.